AERODYNAMIC ANALYSES REQUIRING ADVANCED COMPUTERS

Part I

A conference held at
LANGLEY RESEARCH CENTER
Hampton, Virginia
March 4–6, 1975

NATIONAL AERONAUTICS AND SPACE ADMINISTRATION

AERODYNAMIC ANALYSES REQUIRING ADVANCED COMPUTERS

Part I

A conference held at
Langley Research Center in Hampton, Virginia
on March 4–6, 1975

Prepared by Langley Research Center

Scientific and Technical Information Office 1975
NATIONAL AERONAUTICS AND SPACE ADMINISTRATION
Washington, D.C.

For sale by the National Technical Information Service
Springfield, Virginia 22161
Price – $15.25

PREFACE

This compilation consists of papers presented at a conference on Aerodynamic Analyses Requiring Advanced Computers held at the NASA Langley Research Center on March 4-6, 1975.

The purpose of the conference was to present results of recent theoretical research on aerodynamic flow problems requiring the use of advanced computers. The conference was divided into the following sessions: (1) Viscous Flows, (2) Internal Flows, (3) Two-Dimensional Configurations, and (4) Three-Dimensional Configurations. Papers were presented by members of NASA Centers, Universities, and Industry.

Page Intentionally Left Blank

CONTENTS

Part I

INTERNAL FLOWS

Chairman: Bernhard H. Anderson

Part II*

TWO-DIMENSIONAL CONFIGURATIONS

Chairman: Alfred Gessow

THREE-DIMENSIONAL CONFIGURATIONS

Subsonic and Supersonic Aircraft

Chairman: Roy V. Harris, Jr.

*Papers 23 to 52 are presented under separate cover.

INTRODUCTORY REMARKS

Attendees at the conference were welcomed by Edgar M. Cortright of the Langley Research Center, J. Lloyd Jones of NASA Headquarters, and Dean R. Chapman of the Ames Research Center. The welcoming speakers made observations on the advancements in theoretical aerodynamics since the NASA conference in 1969 on "Analytical Methods in Aircraft Aerodynamics" and on the changing role of theory and experiment in fluid-flow research and aircraft design. In addition, their remarks provided a preview of the accomplishments that were described in the conference and of the long-range prospects for theoretical aerodynamics. In effect, the three speakers did an excellent job of setting the stage for the detailed technical papers presented. It is appropriate then that transcriptions of their talks be used to give this same perspective to the conference proceedings. The talks are given in the order in which they were presented.

Edgar M. Cortright, Director, Langley Research Center:

I'm Ed Cortright, Director of Langley, and I'm delighted to welcome you ladies and gentlemen to this Conference on "Aerodynamic Analyses Requiring Advanced Computers." We debated that title an inordinately long time and that was the best thing we could come up with to describe what you folks are doing these days. It's particularly pleasant for me to have this group here at Langley. There was a day when I felt I knew something about the flow of air but now I'm relegated to the flow of paper. Perhaps during the next three days I'll be able to spend enough time here to learn a little and see many things that I probably will have trouble understanding. This is the first conference of this type that's been held since 1969 when we had one at Ames on "Analytical Methods in Aircraft Aerodynamics." Since that time a tremendous amount of water seems to have flowed under the bridge. For example, there has been extensive progress in the calculation of viscous flows including separation and in our ability to model turbulence. We can now calculate flows over two-dimensional sections in all speed ranges, as well as the inverse problem of calculating the shapes to give us the pressures we want. This extends to three-dimensional configurations these days. So we've come a long way and there's still a long way to go.

It appeared to us that the time was now right to get you folks together and have an exchange such as this. I hope this meeting proves that to be a good judgement. The progress that has been made, and which we will be dealing with the next three days, relates to the use of very high speed digital computers; the CDC 6000 series, the

CDC 7600, and the IBM 360/85 are typical of machines which are fairly widely available and these computers are indispensable to the problem solving that we're talking about. However, what's become very apparent as the state of the art progresses is that we run out of computer capacity even with machines as fast as the 7600. Hence we're now looking to super machines, such as the ILLIAC and the CDC STAR, and even beyond to machines that someday will perhaps be several orders of magnitude faster. It may be of course, and probably will be, that many companies will not be able to afford machines of the super computer size immediately, although that's not clear. But certainly the smaller companies, general aviation companies for example, will not. In that regard it seems reasonable for these types of number crunching problems that remote terminals will be quite appropriate, and during the course of this conference there will be a demonstration of the use of the ILLIAC at Ames accessed from a remote terminal here at Langley.

Now the papers that you're going to see and hear sort of run the gamut. Many are all theoretical, maybe at least half of them, but others are a combination of theory and experiment which has sort of been the NASA hallmark over the years. Since we're endowed with so many fine facilities, we've made a special point to attempt to check theoretical solutions with experimental data. In this regard, an example of how the theoretical developments are influencing the experimental trends might be made with the two-dimensional section work that is going on today. In the "good old days," as we sometimes say, we'd run a whole family of airfoils, like the old NACA four digit series, in order that the aircraft designers could pick by interpolation, if they couldn't find exactly the airfoil they wanted. Today in the transonic airfoil area, as well as in the subsonic range for general aviation application, we're going to test just a few selected sections which will be designed theoretically and count on the computer to do the interpolation and the design in between these experimental check points.

I do want to say a word, however, about what I believe to be the continuing role of the wind tunnel. There are quite a few people today with a lot of vision who are beginning to see the day when the computer will replace the wind tunnel, and I believe that's feasible. Although I had been a doubter, I'm beginning to come around to think maybe that's going to happen someday. It's a way off though; I think even you will concede that, and in the interim there's going to be a continuing role to check the more intricate flow fields, particularly where separation is present. We are continuing to work in the NASA to improve our wind-tunnel capability, particularly, at the moment, in the direction of high Reynolds number. I would like to comment on a cryogenic wind tunnel that we've been working on using nitrogen gas at several hundred degrees F below zero. We're aspiring to Reynolds numbers over a hundred million on full configurations based on mean chord. This looks very feasible, and we already, with a small cryo test tunnel, are reaching fifty million with two-dimensional models. These tunnels, I believe, will be used to check your more advanced calculations and will play a major role in helping you define theoret-

ical models, in detecting the defects in the theoretical solutions, and in developing the improvements required to really hit these predictions on the head. I believe that role will continue for a considerable period of time.

Now another aspect of this conference, I'd like to point out, is that it's far from a NASA show. While there is a predominance of NASA papers, at least 25 to 35 percent are from industry and universities; there's no monopoly at NASA on brains or ideas. What's really happening around the country is a joint effort with participation by everyone – universities, industry, and government – to make this rather fantastic capability come true.

J. Lloyd Jones, Deputy Associate Administrator (Aeronautics Technology), Office of Aeronautics and Space Technology, NASA Headquarters:

It is indeed a pleasure for me to be here this morning, to welcome you to this conference, and to express NASA Headquarters support of the computational aerodynamics program that you'll be hearing about at this conference. A long personal involvement with both experimental and analytic aerodynamics leads to my recognizing and welcoming the present capabilities and the exciting future promise of this computational aerodynamics effort.

The last NASA conference on this subject, as Dr. Cortright indicated, was in October of 1969 at the Ames Research Center. In fact, I was organizer and chairman of that conference. I was interested in reviewing the conference to note what progress we've made in the past five and a half years. A major difference, arising from the recent availability of the very high-speed computers, is that we now have direct solutions to the governing flow equations with much less use of approximate methods. We can now, as compared to that time, calculate transonic mixed flows with embedded shock waves. Before, we couldn't calculate even a single 2D case; now, we're calculating wing-body mixed flows. The emphasis then was on simple shapes such as conical bodies, and now we have entire sessions on flows about complex configurations, for example, the shuttle. Another major difference is our capability of attacking viscous flows in a more realistic manner. In 1969, for example, there was one review paper on a crude Navier-Stokes solution, one review paper on turbulent boundary layers using simple mixing length functions, and one paper on laminar separation using first-order integral schemes, and that was the extent. Today, we have sessions on higher order turbulence modeling and are tackling laminar and turbulent separated flows in a very serious way. So, in summary, it looks like we've come to the point where we're facing realistic problems in a head-on manner by trying to solve the complete flow field about complex shapes. In 1969 we were

still idealizing the physics of the flow in order to get tractable equations which we could solve.

Although we've made a great deal of progress and we're applying this capability to many practical problems, there are still many potential flow problems that require the use of advanced computers which do not appear to be getting the attention I think they deserve; for example, the calculation of interacting systems of vortex wakes behind aircraft. An expanded capability to calculate such wake systems might very well lead to a near-term solution to the wake vortex hazard problem through innovative changes in the design of the lift and propulsive systems of large transport aircraft. Examples of other problems that deserve attention include calculation of helicopter wakes and V/STOL aerodynamics. I'm sure that there are those of you in industry who are tackling these problems now, but from what I've seen available in the literature there's a great field there that requires attention.

In NASA we're now in the process of going through our budget hearings for our Fiscal 1976 program. In aeronautics we're discussing our program with emphasis placed on various program elements. Our testimony addresses, for example, technology for short-haul aircraft where the emphasis is on powered lift, long-haul aircraft where the emphasis is on fuel conservation, supersonic cruise aircraft, military aircraft with emphasis on high maneuverability, rotorcraft, and general aviation. In planning our program we have long and protracted discussions about the emphasis and the priorities which should be placed on these various systems concepts. However, we strongly feel that the heart of the NASA program is the discipline-oriented research. I'm sure I don't have to explain that concern to the members in this audience. I think the aerodynamic capability that we're leading to with the efforts being reported here will have great impact in all of these aircraft systems areas. It is clear that you recognize this point also. This capability has the potential for ensuring us that we have a closer approach to optimum design and that we will be able to develop greater confidence in our ability to achieve the performance which we set out to achieve in an aircraft design. And more important is the potential for reduced cost in the design and development process. So that's what we're about.

I sincerely hope that you find this conference to be a valuable experience, and I'm sure that you see the same potentials that I do in this aerodynamic capability that is forthcoming here or you wouldn't be present. Thank you very much.

Dean R. Chapman, Director of Astronautics, Ames Research Center:

I'm Dean Chapman from the Ames Research Center and in my introductory comments I'd like to sketch for you the perspective which we at Ames see regarding the

motivations and the objectives for advancing the technology of computerized flow simulations. Many of you are aware, I believe, that computational fluid dynamics is one of the areas that we have selected to emphasize at Ames primarily because of its tremendous potential for revolutionizing the way our profession has been doing business during the last seventy years; that is, since the time of Stanton and the Wright Brothers when wind tunnels were first used as a vital part of the aerodynamic design process. We see three major objectives in this work. I want to go over them quickly, not in the order of their importance as we judge them, but in the order they are now being accomplished and will be accomplished.

The first major objective is to provide those flow simulations which are either impossible or impractical to obtain in ground-based facilities. One example is flow very near Mach number of 1, for which wind-tunnel wall interference and support interference restrict the usefulness of the experimental data. Another example, covered in one of the papers in this Conference, is that of simulating the chemically reacting flow over the shuttle orbiter as it enters the atmosphere. This is a flow field simulation which is not possible to obtain in any existing ground-based facility.

The second major objective that we see is one already mentioned by Lloyd Jones in his introductory remarks. That is to use the computer to lower the time and the cost that will be required to obtain those flow simulations which are necessary in the design of new aerospace vehicles. We already have one example of this. It happens to pertain to the flow over a defense interceptor missile as it flies through the blast wave of one of its brethren missiles. It's a rather complicated flow field and in this case the cost of the computer simulations to do essentially the same job, in fact a more complete job than the experimental simulations, was less than 10 percent of the experiment cost.

The third major objective, and the one I personally believe will turn out to be the most important in the long run, is to provide more accurate simulations of flight conditions than wind tunnels can provide. There are some compelling reasons for being optimistic that this third objective will be achieved. One is that the inherent limitations on the accuracy of wind tunnels are more severe than the inherent limitations in computer simulations. All wind tunnels, as you are well aware, are limited in the size of model that can be put in them and the density that they can be pumped up to; hence, they are limited in Reynolds number. Subsonic and transonic tunnels are limited by wall interference and all tunnels are limited to some extent by model interference. Very high Reynolds number transonic tunnels will be limited by the artificial aeroelastic distortions that the high dynamic pressures will bring about. Finally, wind tunnels are limited by the atmospheres that can be put in them and by the degree of uniformity of the stream that they can produce. The computers are not limited in any of these ways, and the inherent limitation on the accuracy by which the governing differential equations of motion, the Navier-Stokes equations, represent reality is much less severe. Of course

the complication is that these full governing differential equations are simply too complicated, too intricate, to be solved in a practical amount of time and at a practical cost right now by any of the currently available computers. Another reason that we are optimistic that this third and most important objective will be accomplished stems from past experience, and experience in other fields of computational physics. In ballistics, for example, which is governed by Newton's equations of motion with air forces thrown in, the computer has long ago displaced ballistic ranges as the principal source of the data that are needed to construct artillery tables. Also in the field of neutronics, which is governed by the Boltzmann integro-differential equation, computers of the 1960's began to displace, and by now have largely displaced, the experimental critical test facilities as the principal source of design information for nuclear reactors. When future computers obtain the capability of solving the complete Navier-Stokes equations with dispatch, then, if history is a guide, the wind tunnels can be expected to play a secondary role to the computers in aerodynamics just as the neutronics critical test facilities now perform a secondary role to the computers in neutron transports mechanics and just as ballistic ranges now perform secondary roles to computers in trajectory mechanics.

I've attempted to make a rough estimate of the time that it will take before computers attain this capability, and that's illustrated on the only slide that I have to show you.

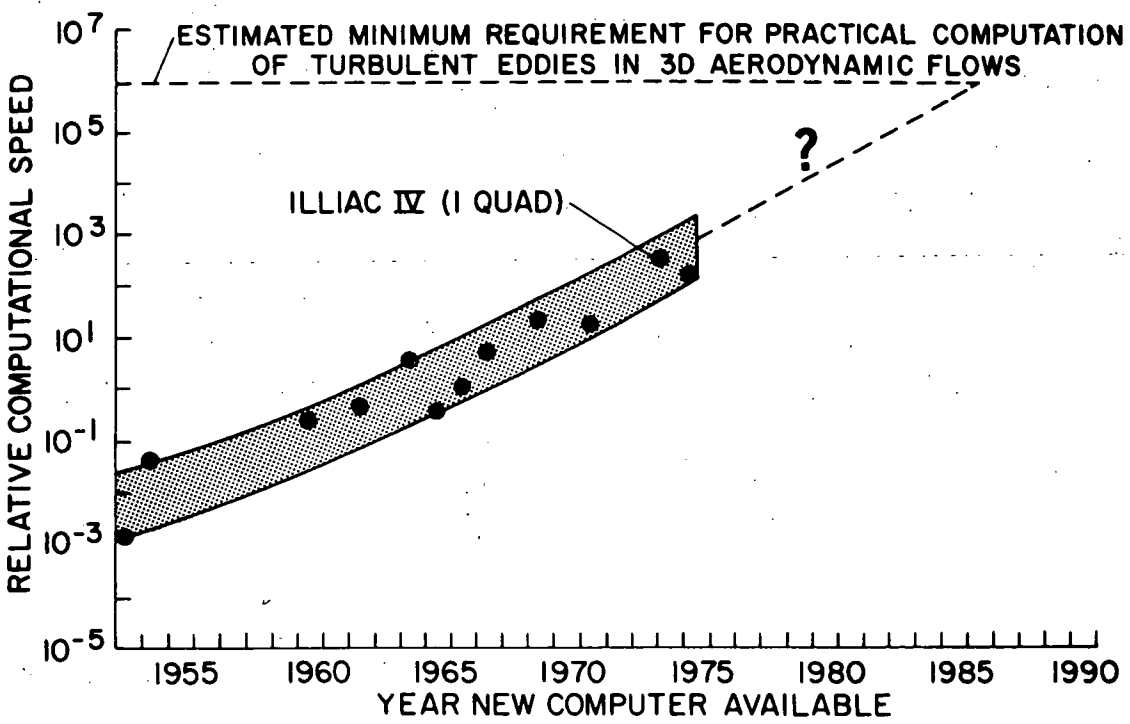

This is a graph of the relative speed of computers plotted as a function of the year that each new computer became available. We estimate that solving the full time-dependent Navier-Stokes equations for a configuration such as an aircraft, say a wing-body-tail combination, will require the use of the order of 10^9 grid points or flow elements in the field. To solve a problem of this magnitude in a reasonable amount of time will require a computer having a relative speed on this graph of about 10^6. The figure shows that if the past trends continue, such a computational capability will be available in the mid or latter part of the 1980's. I'd like to note in concluding that there is no fundamental reason for limiting computers to this capacity; that is, the fundamental limitations like speed of light, circuitry, and so forth only limit the capability of computers for speeds well beyond the limits of the figure. So, we believe that it's not a question of whether this capability will be achieved, or whether computers will be able to simulate flight conditions more accurately than wind tunnels, but it's just a question of when.

Page Intentionally Left Blank

REMOTE ACCESS OF THE ILLIAC IV

By K. G. Stevens, Jr.

NASA Ames Research Center

2

SUMMARY

Until a few years ago, most computational aerodynamic flow simulations were made on general-purpose computers physically located near the researcher wishing the flow simulation. In recent years alternate computer resources have become available. These particular resources are very attractive because they are larger and faster than older computers. This paper will discuss the use of one of these alternate computer resources, namely, the ILLIAC IV.

This discussion will have two major sections. The first section will describe the hardware, that is, the ILLIAC IV, the Illiac system, The Advanced Research Projects Agency (ARPA) computer network, and the IMLAC PDS-1. The second section will trace the execution of the Space Shuttle flow simulation on this hardware. An actual demonstration of this flow simulation will be presented at this conference.

ILLIAC IV

To understand the ILLIAC IV hardware we will look at its four functional parts. Those parts are the control unit, the 64 processing elements, the processing element memories, and the Illiac main memory. (See figure 1 for a diagram of the hardware described below.)

The Control Unit (CU) contains the instruction stack which interprets all instructions, some of which may be completely executed within the CU. Instructions are partially executed and then broadcast to the 64 processing elements; there, the execution is completed by all the processing elements in lock-step. Thus the Illiac operates on up to 64 sets of operands simultaneously. If each operand is viewed as a component of a vector, one may think of the Illiac as a Vector or Array Processor. In addition to managing the Instruction stack, the CU may be thought of as a small self-contained computer. It has four accumulators which are capable of a full set of shifting, bit-setting, and Boolean operations, as well as addition and subtraction. Furthermore, these accumulators may be used as index registers for fetching and storing in the processing elements.

A Processing Element (PE) has six programmable registers, called RGA, RGB, RGS, RGR, RGX, and RGD. The RGA is the accumulator and RGB is its extension; RGS is a scratch register. The remaining registers are somewhat peculiar to the Illiac architecture. RGR is used for inter-PE communications of data. Data may be rotated end-around (data from PE 1 going to PE 64) within the

64 RGRs. RGX acts as an index for intra-PE fetching. This register allows independent fetching depths in each of the PE memories. The RGD contains fault bits and test result bits for that PE. It also contains the bits, called mode bits, which, when set, allow the PE to take part in instructions and, when reset, protect the PE memory as well as RGA, RGS, and RGX from change. The speed of a PE is approximately equal to that of a CDC 6600.

The Processing Element Memories (PEMs) may be thought of in two ways: (1) collectively as 131,072 64-bit words of memory from the CU's point of view, and (2) as a 64 x 2048 matrix of 64-bit words from the point-of-view of the PEs. In the latter case, each PE is able to access its own column of 2048 words. (Note that the RGX indexing permits the PEs to fetch independently any word within their own column.)

The main memory of the Illiac is logically a 16-million word drum. The drum is divided into 52 bands (tracks) each of which contains 300 Illiac pages (an Illiac page is 1024 64-bit words). The drum may be mapped, that is, data may be stored upon it in predetermined locations, and accessed asynchronously. This enables the programmer to ensure that the data he wishes to fetch are coming under the read/write heads when he needs them. This allows the full billion-bit-per-second transfer rate to be realized during execution. (A detailed description of the Illiac hardware may be found in reference 1.)

THE ILLIAC SYSTEM

The Illiac system includes the ILLIAC IV, the central system, and a B6700. (See figure 2 for a diagram of the hardware described below.) The central system consists of various processors, memories, and devices that interface the Illiac, B6700 and the outside world. The main processor in the central system is currently a PDP-10 running under the TENEX operating system.

File storage is provided by a hierarchy of devices from central memory (PDP-10 memory) to the Unicon laser memory. Files are moved through the storage hierarchy depending on their activity and space availability. The permanent mass storage device is the laser memory which has an on-line capacity of 700 billion bits.

The Burroughs B6700 computer performs utility functions such as assemblies and compilations of GLYPNIR programs. (For a detailed description of this system see reference 2.)

ARPA NETWORK

The ARPA network now has about 50 nodes connected by 50 kilobit lines. (See figure 3 for typical geographical locations.) These nodes fall into one

of two categories, either a Terminal Interface Message Processor (TIP) or an Interface Message Processor (IMP). An IMP can connect up to four computers to the ARPA network. Their basic function is to send to and receive from other IMPs and TIPs strings of bits (either character data or bit data). Figure 4 shows the wide range of computers currently on the network.

A TIP in addition to performing the same functions as an IMP may support dial-up terminals. Almost any terminal is compatible with the TIP. (A complete description of how to use the TIP may be found in reference 3.)

IMLAC PDS-1

IMLAC's PDS-1 consists of a dynamic cathode ray tube (CRT) and a solid-state keyboard controlled by a sixteen-bit 4096-word miniprocessor. This device is capable of emulating a teletype and an IBM 2250 Display Unit.

An acoustic coupler will be used to dial up a TIP. The TIP will then allow the user to access the Illiac system through its IMP. This original connection will be made as a teletype. When graphics data are being transmitted, the PDS-1 will emulate the 2250 Display Unit and display the graphics data on the CRT. When the system stops transmitting graphics data, the PDS-1 will again emulate a teletype so that further instructions may be issued.

THE SHUTTLE CODE

The demonstration problem has been coded by Davy and Reinhardt and resides in the central system memory. This problem consists of computing the inviscid, frozen flow over the first ten meters of a Shuttle Orbiter-like vehicle (based on design version 147). The free-stream conditions correspond to a Mach number of 10 at an altitude of 20 km. The flow field is computed with an angle of attack of 5 degrees to accentuate the relationship between the body shape and the shock shape. A detailed description of the code may be found in reference 4.

THE DEMONSTRATION

The demonstration will make use of most of the hardware and software described above. (See figure 5 for a diagram of the hardware configuration.) The IMLAC PDS-1 will be connected to the MITER TIP via an acoustic coupler and the conventional telephone system. The TIP will connect the IMLAC, via the ARPA network, to the Illiac system's IMP. At this point the IMLAC is logged into the Illiac's PDP-10. To run this version of the shuttle code two parameters are needed. After supplying these two parameters, Illiac execution

may be requested. This request is usually made by submitting a batch job. However, for this demonstration the shuttle code will be run interactively.

The demonstration program will compute two flow fields. The first computation is without canopy, and the fuselage has simply been faired smoothly through the canopy region. The body profile is shown on the screen in solid-line-plot mode. (See figure 6 for a sample CRT picture.) Also displayed on the screen by solid lines are the bow shock locations and the computed body pressure at the leeward symmetry plane as a function of Z, the integration direction.

For the second computation of the flow field, a canopy shape described by a two-parameter (the input parameters) analytical function is added to the fuselage. Results of the flow field as well as the canopy shape are now displayed on the CRT screen in point-plot mode so that they may be contrasted with the previous computation.

While the ILLIAC IV is calculating these two flow fields, the resulting graphics data are stored in Illiac main memory. When the calculations are completed the graphics data are transferred from the Illiac main memory to the central memory. At this point a simple PDP-10 routine is used to transmit the graphics data to the IMLAC where it may be viewed.

This demonstration is intended to show the feasibility of using an advanced computer from a remote location. It also is meant to demonstrate the practicality of using computer flow-field simulations and their graphical representations in solving aerodynamics problems.

REFERENCES

1. Burroughs Corporation: ILLIAC IV Systems Characteristics and Programming Manual. NASA Contractor Report 2159, 1972.

2. Institute for Advanced Computation: Systems Guide for the ILLIAC IV User. IAC Doc. No. SG-I10000-0000-D, Moffett Field, CA, March 1974.

3. Bolt, Beranek and Newman Inc.: User's Guide to the Terminal IMP. Report No. 2183, December 1974.

4. Davy, W. C.; and Reinhardt, W. A.: Computation of Shuttle Nonequilibrium Flow Fields on a Parallel Processor. Aerodynamic Analyses Requiring Advanced Computers, Part II, NASA SP-347, 1975, pp. 1351-1376.

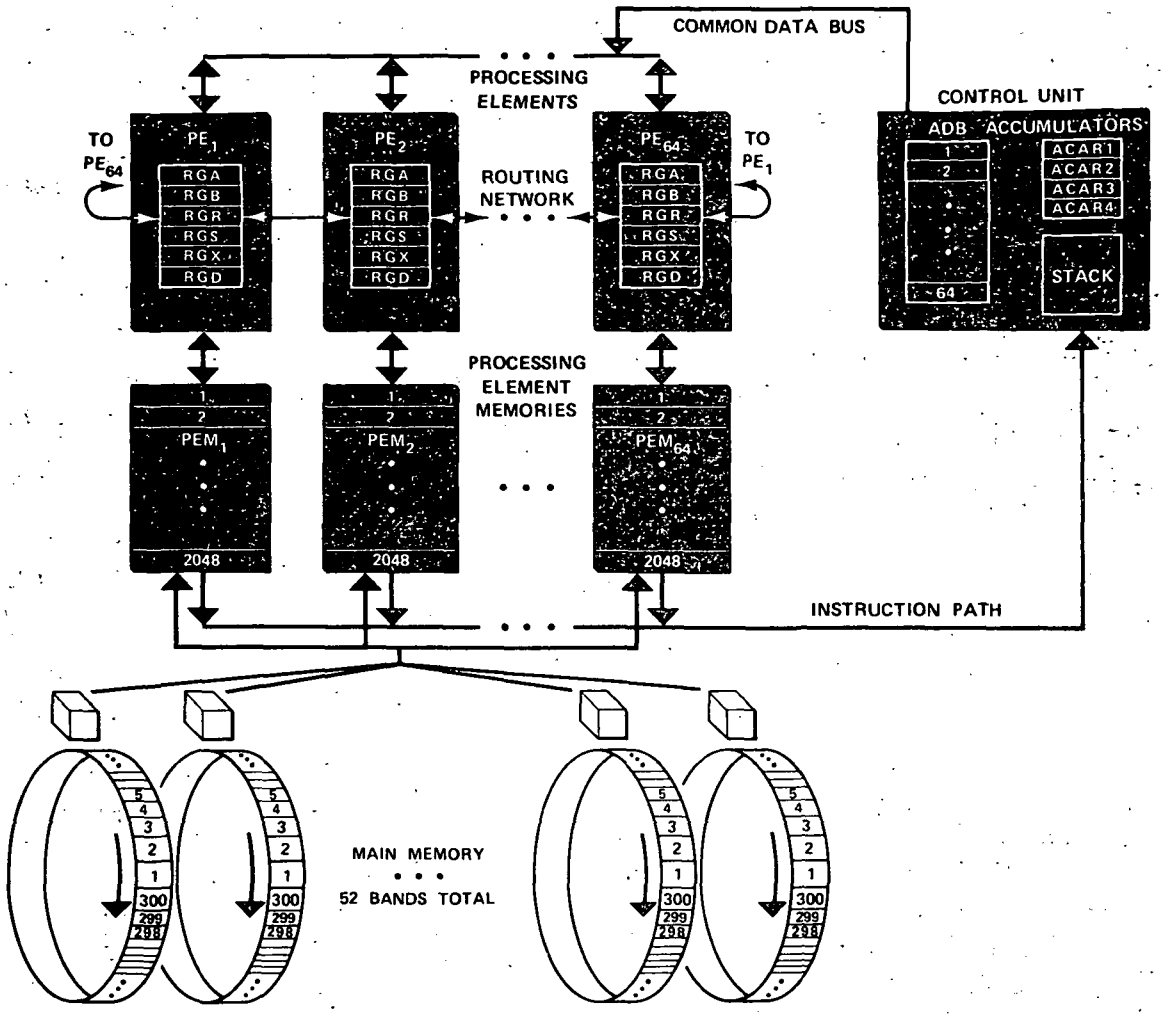

Figure 1.- ILLIAC IV.

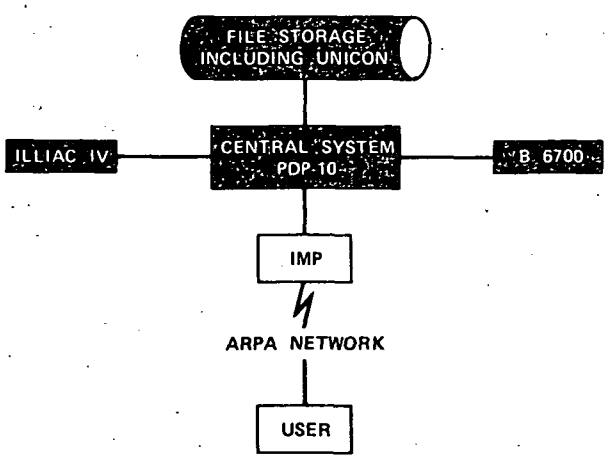

Figure 2.- Illiac system.

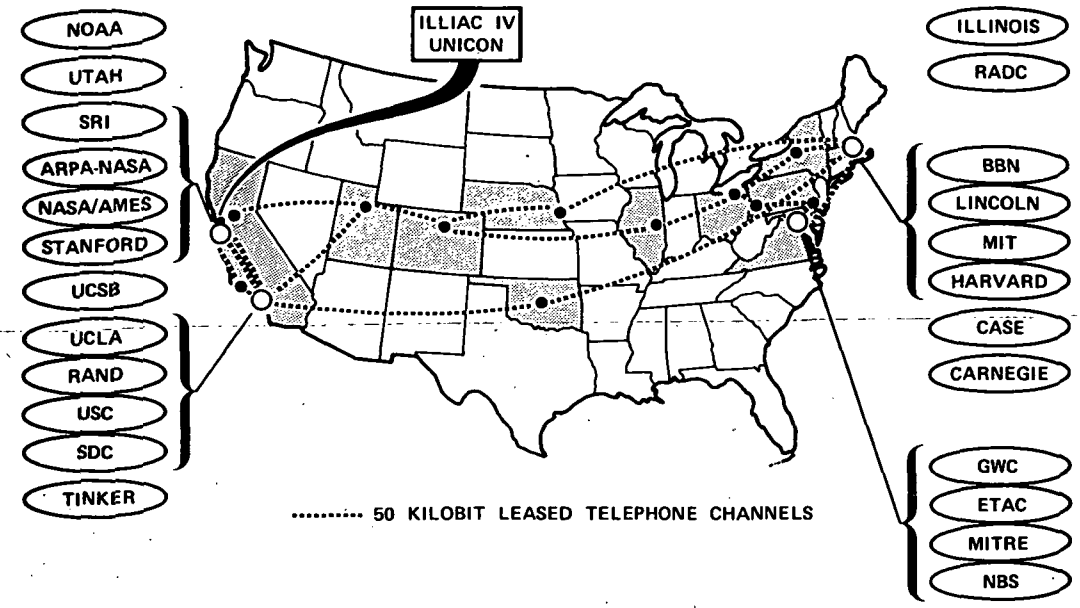

Figure 3.- ARPA computing network.

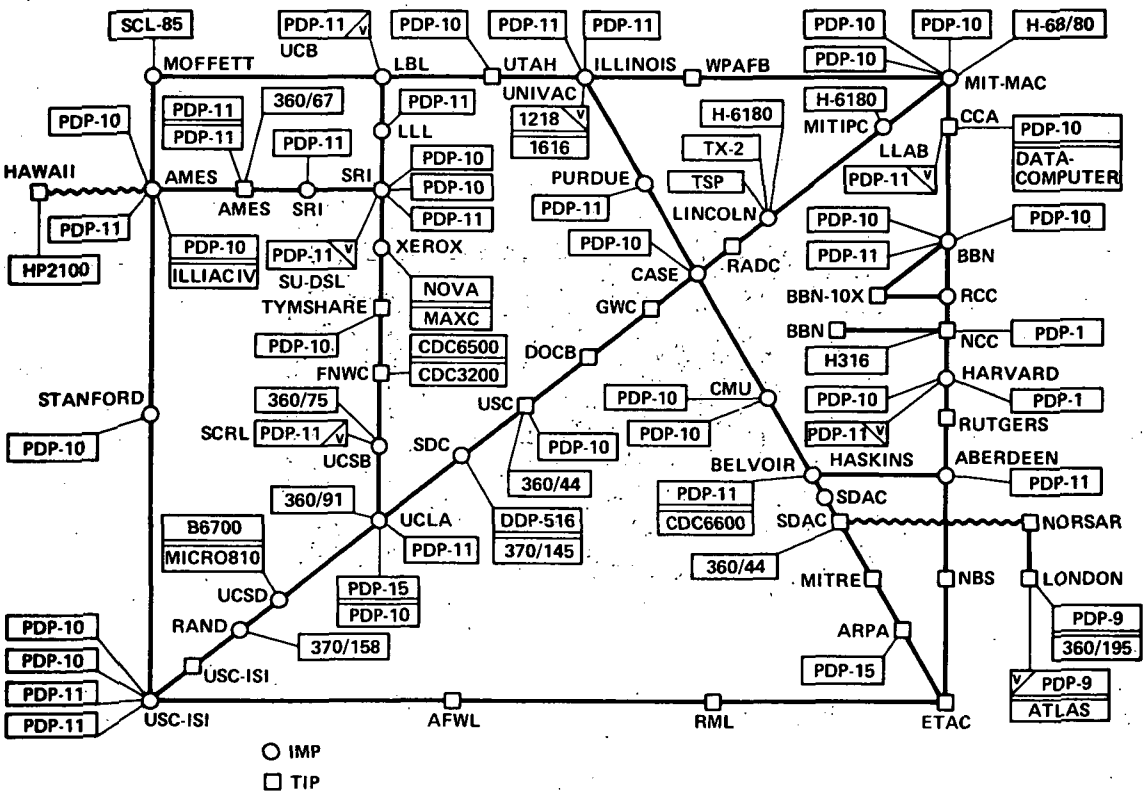

Figure 4.- ARPA network logical map, November 1974.

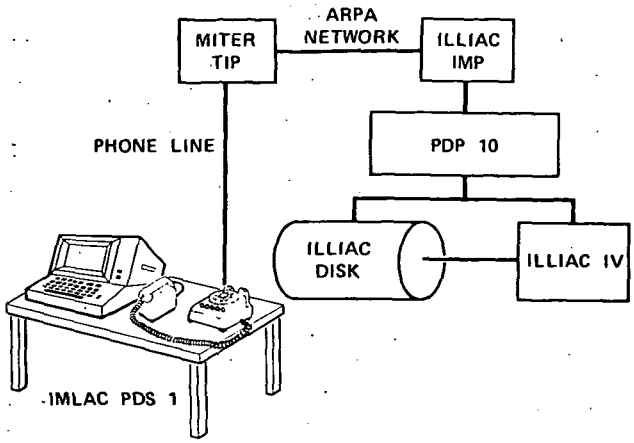

Figure 5.- Demonstration hardware.

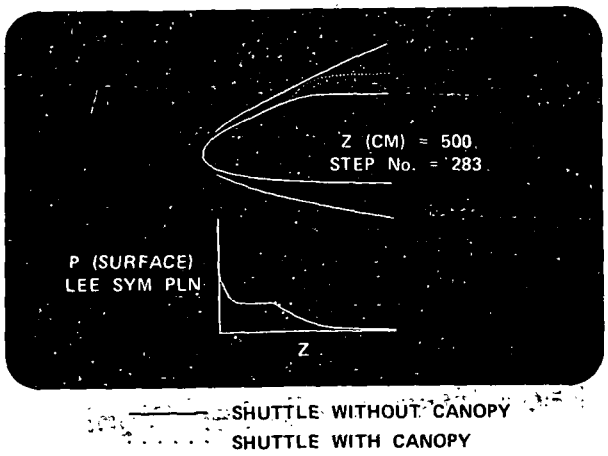

Figure 6.- Demonstration frame.

Page Intentionally Left Blank

CALCULATION OF THREE-DIMENSIONAL COMPRESSIBLE LAMINAR AND TURBULENT BOUNDARY LAYERS

PREFACE

By Julius E. Harris
NASA Langley Research Center

The complexity and cost of designing aerospace vehicles together with the availability of large-storage high-speed computer systems have resulted in focused research in the area of developing numerical solution techniques and user-oriented computer codes for the compressible three-dimensional laminar and turbulent boundary-layer equations. The numerical program for three-dimensional boundary-layer flows at the NASA Langley Research Center can be divided into the three following categories: (1) in-house development of an implicit finite-difference technique for general problem definition and turbulence modeling studies, (2) contract development of a perfect-gas computer code for arbitrary wing planforms, such as the supercritical wing (NASA Contract No. NAS 1-12821 with Douglas Aircraft Company; paper by Tuncer Cebeci and others), and (3) contract development of a real-gas (equilibrium/frozen) computer code for complete configurations, such as the Space Shuttle (NASA Contract No. NAS 1-12424 with Aerotherm Division of Acurex Corporation; paper by Robert M. Kendall and others).

The in-house research has been directed toward (1) development of efficient and accurate finite-difference procedures for solving the governing nonlinear three-dimensional boundary-layer equations, (2) studies of optimum transformations to reduce the number of mesh points required for high Reynolds number turbulent flows, and (3) calibration and verification of turbulence models for the Reynolds stress terms. The initial stage of the in-house research program was concerned with problem definitions common to general three-dimensional boundary-layer flows for aeronautical and aerospace vehicles; these areas included the following: (1) optimum coordinate system for general configurations, (2) characteristics of various numerical procedures including computer storage and processing time as a function of vehicle scale and aerothermal environment (perfect-gas or real-gas flows), and (3) requirements and/or availability of three-dimensional inviscid flow-field solutions (computer code availability and range of application).

The outgrowth of the in-house research program resulted in the initiation of two contract efforts which, in principle, cover the broad requirements of the aerospace industry. The Aerotherm Division of Acurex Corporation was given the task of develop-

ing a user-oriented computer program in which the numerical procedure and coordinate system were optimized for complete configurations for which the aerothermal environment (real-gas flows) is important. The Douglas Aircraft Company was given the task of developing a user-oriented computer program in which the numerical procedure and coordinate system were optimized for wing geometry. Two independent contract efforts were initiated as a result of in-house and contract studies of computer storage and processing times required for these two classes of flows.

CALCULATION OF THREE-DIMENSIONAL COMPRESSIBLE LAMINAR AND TURBULENT BOUNDARY LAYERS

AN IMPLICIT FINITE-DIFFERENCE PROCEDURE FOR SOLVING THE THREE-DIMENSIONAL COMPRESSIBLE LAMINAR, TRANSITIONAL, AND TURBULENT BOUNDARY-LAYER EQUATIONS

By Julius E. Harris
NASA Langley Research Center

SUMMARY

An implicit finite-difference procedure is presented for solving the compressible three-dimensional boundary-layer equations. The method is second-order accurate, unconditionally stable (conditional stability for reverse cross flow), and efficient from the viewpoint of computer storage and processing time (60000_8 storage and 0.002 second per nodal point on the CDC 6600 computer). The Reynolds stress terms are modeled by (1) a single-layer mixing length model and (2) a two-layer eddy viscosity model. These models, although simple in concept, accurately predicted the equilibrium turbulent flow for the conditions considered. Numerical results are compared with experimental wall and profile data for a cone at an angle of attack larger than the cone semiapex angle. These comparisons clearly indicate that the numerical procedure and turbulence models accurately predict the experimental data with as few as 21 nodal points in the plane normal to the wall boundary. Research continues in the areas of convergence accelerator techniques (reduction of computer processing time), turbulence modeling, and extension of the computer code to general configurations (general geometry package development).

INTRODUCTION

A current design and analysis requirement of the aerospace industry is development of accurate and efficient numerical techniques and corresponding user-oriented computer codes for solving the compressible three-dimensional laminar, transitional, and turbulent boundary-layer equations for flows over general configurations. These codes would substantially reduce the cost and time currently required for the development of advanced aircraft through the substitution of numerical simulation for time-consuming and expensive experimental simulation and testing. The research focused on three-dimensional boundary-layer flows can be attributed to (1) experience gained over

the past decade in developing user-oriented codes for two-dimensional and axisymmetric flows, including the development of numerical procedures and simple but accurate mean-field turbulence models and (2) the increased availability of large-storage high-speed digital computer systems.

Experience gained in two-dimensional and axisymmetric boundary-layer flows indicates that computer codes for three-dimensional turbulent flows, if they are to be accepted as design/analysis tools by the aerospace industry, will require efficient and accurate numerical methods with suitable turbulence models for the Reynolds stresses. Numerical experimentation and detailed experimental turbulent boundary-layer research has resulted in the development and verification of mean-field turbulence models (eddy viscosity/mixing length) for two-dimensional boundary-layer flows which are sufficiently accurate for application to a broad range of flow and boundary conditions. (See refs. 1 to 4.) The numerical techniques developed for this class of flow can be directly applied, with minor modifications, to three-dimensional flows; however, zones of dependence and independence must be carefully treated for three-dimensional flows (see refs. 5 and 6). Although the extension of two-dimensional mean-field turbulence models to three-dimensional flows appears to be straightforward, numerical experimentation in which numerical results are compared with accurate three-dimensional profile and wall data is required before any evidence can be produced to prove or disprove this assumption (refs. 7 to 9).

If one assumes that accurate and efficient numerical procedures together with sufficiently realistic turbulence models can be developed on the basis of experience with two-dimensional flows, a number of problem areas still remain to be solved for general three-dimensional boundary-layer flows; these include: (1) selection and development of an optimum boundary-layer coordinate system; (2) development of general transformations which will remove numerical problems associated with the generation of initial data planes, reduce the growth of the boundary layer in the computational region, and reduce the sensitivity of the numerical procedure to mesh-point distributions in the two spatial surface coordinates; and (3) availability and/or use of accurate three-dimensional inviscid flow-field solutions which are required for edge boundary condition specification. (See ref. 10.) Problems associated with (1) and (3) make it manditory that the boundary-layer codes be coupled with the three-dimensional inviscid flow-field codes to avoid excessive and time-consuming data manipulation as well as to provide the possibility of accounting for displacement surface effects on numerical results. For general aerospace configurations the problem associated with obtaining accurate three-dimensional inviscid flow-field data may well be the most difficult. However, substantial progress has been made in this particular area of research. Progress has also been made in the area of three-dimensional boundary-layer flows over the past few years (refs. 11 to 15). A crit-

ical review of computational techniques for boundary-layer flows (two- and three-dimensional) is presented in reference 16.

In this paper a technique under development at the NASA Langley Research Center for solving the compressible three-dimensional laminar, transitional, and turbulent boundary-layer equations is presented. The advantages and disadvantages of the implicit finite-difference procedure and Crocco transformation are discussed. The Reynolds stress terms are modeled by two mean-field (scalar invariant) models. Numerical results are presented and compared with experimental data to determine the validity of the simple turbulence models and the accuracy of the numerical procedure.

SYMBOLS

A	damping term in turbulence model (eq. (12))
a_1,a_2	coefficients in boundary condition on shear equation (see eq. (25b))
C	coefficient of geometric progression for mesh-point distribution, $\Delta\zeta_{k+1}/\Delta\zeta_k$
$C_{f,e}$	skin-friction coefficient
c_p	specific heat at constant pressure
D	Van Driest damping factor (eq. (11))
ds	incremental arc length
$\bar{e}$	$= \frac{\mu}{T}\left(1 + \frac{\epsilon}{\mu}\Gamma\right)$
F	$= u/u_e$
G	$= v/v_e$
H	$= w/u_e$
h_1,h_2,h_3	metric coefficients (eq. (5))

$k_1, k_2, \ldots, k_6$ coefficients in turbulence models (eqs. (9) to (17))

$\bar{k}_{eff}$ effective thermal conductivity (eq. (8))

$\bar{L}$ reference length

ℓ_1, ℓ_2 mixing lengths (eqs. (10) and (17))

M_∞ free-stream Mach number

N number of mesh points in the plane normal to the wall boundary

N_{Pr} Prandtl number

$N_{Pr,t}$ static turbulent Prandtl number

p pressure

$R_{\infty,L}$ Reynolds number based on reference length

T temperature

$\bar{U}_\infty$ free-stream velocity

$U_{e,t}$ total velocity at edge of boundary layer

u, v, w velocity component in the ξ-, η-, and ζ-direction, respectively

x_1, x_2, x_3 physical coordinates

$Y_1, Y_2, \ldots, Y_6$ coefficients for derivative relations (eqs. (33) to (38))

$\bar{\alpha}$ angle of attack

$\alpha_1, \alpha_2, \ldots, \alpha_5$ coefficients in standard equation (eq. (24))

$\beta_1,\beta_2,\beta_3,\beta_4$	coefficients in equation (40)
γ	ratio of specific heats
$\tilde{\gamma}$	normal intermittency function (eq. (13))
Γ	streamwise intermittency function
$\Delta\xi,\Delta\eta,\Delta\zeta$	incremental mesh-point spacing in the ξ,η,ζ coordinates
$\overline{\delta}^*$	incompressible displacement thickness (eq. (19))
ϵ	eddy viscosity
ζ	transformed normal coordinate
η	transformed cross-flow coordinate
θ	$= T/T_e$
κ_1,κ_2	geodesic curvatures (eq. (6))
μ	molecular viscosity
μ_{eff}	effective viscosity (eq. (7))
ξ	transformed streamwise coordinate
$\tilde{\xi}$	similarity parameter
ρ	density
τ	total shear stress
Φ	shear parameter (eq. (23))
ϕ	circumferential angle

ω dummy variable

ω_s surface streamline angle

Subscripts:

e boundary-layer edge quantity

i,j,k grid point indices

p,q,r dummy indices

w wall value ($\zeta = 1$)

ξ,η direction of quantity

A bar over a symbol designates a dimensional quantity.

GOVERNING EQUATIONS

The governing equations are written in general form as follows (see fig. 1 for coordinate system; bar over a symbol designates a dimensional quantity):

Continuity

$$\frac{\partial}{\partial\xi}\left(\bar{h}_2\bar{h}_3\bar{\rho}\bar{u}\right) + \frac{\partial}{\partial\eta}\left(\bar{h}_1\bar{h}_3\bar{\rho}\bar{v}\right) + \frac{\partial}{\partial\zeta}\left(\bar{h}_1\bar{h}_2\bar{\rho}\bar{w}\right) = 0 \tag{1}$$

ξ-momentum

$$\frac{\bar{u}}{\bar{h}_1}\frac{\partial\bar{u}}{\partial\xi} + \frac{\bar{v}}{\bar{h}_2}\frac{\partial\bar{u}}{\partial\eta} + \frac{\bar{w}}{\bar{h}_3}\frac{\partial\bar{u}}{\partial\zeta} - \bar{u}\bar{v}\bar{\kappa}_2 + \bar{v}^2\bar{\kappa}_1 = -\frac{1}{\bar{\rho}\bar{h}_1}\frac{\partial\bar{p}}{\partial\xi} + \frac{1}{\bar{\rho}\bar{h}_3}\frac{\partial}{\partial\zeta}\left(\frac{\bar{\mu}_{eff}}{\bar{h}_3}\frac{\partial\bar{u}}{\partial\zeta}\right) \tag{2}$$

η-momentum

$$\frac{\bar{u}}{\bar{h}_1}\frac{\partial\bar{v}}{\partial\xi} + \frac{\bar{v}}{\bar{h}_2}\frac{\partial\bar{v}}{\partial\eta} + \frac{\bar{w}}{\bar{h}_3}\frac{\partial\bar{v}}{\partial\zeta} + \bar{u}^2\bar{\kappa}_2 - \bar{u}\bar{v}\bar{\kappa}_1 = -\frac{1}{\bar{\rho}\bar{h}_2}\frac{\partial\bar{p}}{\partial\eta} + \frac{1}{\bar{\rho}\bar{h}_3}\frac{\partial}{\partial\zeta}\left(\frac{\bar{\mu}_{eff}}{\bar{h}_3}\frac{\partial\bar{u}}{\partial\zeta}\right) \tag{3}$$

Energy

$$\frac{\bar{u}}{\bar{h}_1}\frac{\partial\bar{T}}{\partial\xi} + \frac{\bar{v}}{\bar{h}_2}\frac{\partial\bar{T}}{\partial\eta} + \frac{\bar{w}}{\bar{h}_3}\frac{\partial\bar{T}}{\partial\zeta} = \frac{1}{\bar{\rho}\bar{c}_p}\left\{\left(\frac{\bar{u}}{\bar{h}_1}\frac{\partial p}{\partial\xi} + \frac{\bar{v}}{\bar{h}_2}\frac{\partial\bar{p}}{\partial\eta}\right) + \frac{\bar{\mu}_{eff}}{\bar{h}_3{}^2}\left[\left(\frac{\partial\bar{u}}{\partial\zeta}\right)^2 + \left(\frac{\partial\bar{v}}{\partial\zeta}\right)^2\right] + \frac{1}{\bar{h}_3}\frac{\partial}{\partial\zeta}\left(\frac{\bar{k}_{eff}}{\bar{h}_3}\frac{\partial\bar{T}}{\partial\zeta}\right)\right\} \tag{4}$$

where h_1, h_2, and h_3 represent the metric coefficients for the incremental arc length $d\bar{s}$; that is

$$d\bar{s}^2 = \left(\bar{h}_1\, d\xi\right)^2 + \left(\bar{h}_2\, d\eta\right)^2 + \left(\bar{h}_3\, d\zeta\right)^2 \tag{5}$$

The parameters $\bar{\kappa}_1$ and $\bar{\kappa}_2$ are the geodesic curvatures of the curves ξ = Constant and η = Constant, respectively; namely

$$\left.\begin{aligned} \bar{\kappa}_1 &= -\frac{1}{\bar{h}_1\bar{h}_2}\frac{\partial \bar{h}_2}{\partial \xi} \\ \bar{\kappa}_2 &= -\frac{1}{\bar{h}_1\bar{h}_2}\frac{\partial \bar{h}_1}{\partial \eta} \end{aligned}\right\} \tag{6}$$

The governing system is completed with the perfect gas equation of state and Sutherland's molecular viscosity law.

Closure of equations (1) to (4) requires that the effective viscosity $\bar{\mu}_{eff}$ and thermal conductivity $\bar{k}_{eff}$ be expressed in terms of the dependent variables. These relations are formulated as follows:

$$\bar{\mu}_{eff} = \bar{\mu}\left(1 + \frac{\bar{\epsilon}}{\bar{\mu}}\,\Gamma\right) \tag{7}$$

and

$$\bar{k}_{eff} = \frac{\bar{c}_p\bar{\mu}}{N_{Pr}}\left(1 + \frac{\bar{\epsilon}}{\bar{\mu}}\frac{N_{Pr}}{N_{Pr,t}}\,\Gamma\right) \tag{8}$$

where $\bar{\mu}$, $\bar{\epsilon}$, N_{Pr}, and $N_{Pr,t}$ represent the molecular viscosity, eddy viscosity, Prandtl number, and static turbulent Prandtl number, respectively. The streamwise intermittency function Γ (ref. 17) models the transitional region of flow and is a function of ξ and η; $0 \leqq \Gamma \leqq 1$. In the present analysis the initiation and completion of the transitional flow process are empirically specified; however, correlation relations could be directly incorporated into the computer code. The eddy viscosity is assumed to be a scalar function independent of coordinate direction (refs. 8 and 18). The following simple scalar invariant turbulence models are considered:

Single-layer mixing length model:

$$\bar{\epsilon} = \bar{\rho}\bar{\ell}_1^2\left\{\frac{1}{\bar{h}_3^2}\left[\left(\frac{\partial \bar{u}}{\partial \zeta}\right)^2 + \left(\frac{\partial \bar{v}}{\partial \zeta}\right)^2\right]\right\}^{1/2}\tilde{\gamma} \tag{9}$$

where

$$\frac{\bar{\ell}_1}{\bar{x}_{3,e}} = k_2 \tanh\left(\frac{k_1}{k_2}\frac{\bar{x}_3}{\bar{x}_{3,e}}\right) D \tag{10}$$

$$D = 1 - \exp\left(-\frac{\bar{x}_3}{A}\right) \tag{11}$$

$$\bar{A} = k_3\left(\frac{\bar{\mu}}{\bar{\rho}}\right)_w\left(\frac{\bar{\tau}}{\bar{\rho}}\right)_w^{-1/2} \tag{12}$$

$$\tilde{\gamma} = \frac{1 - \operatorname{erf}\left(k_5 \dfrac{\bar{x}_3}{\bar{x}_{3,e}} - k_6\right)}{2} \tag{13}$$

$$\bar{\tau} = \left(\bar{\tau}_\xi{}^2 + \bar{\tau}_\eta{}^2\right)^{1/2} \tag{14}$$

Two-layer eddy viscosity model:

Inner law

$$\epsilon_{inner} = \bar{\rho}\bar{\ell}_2{}^2\left\{\frac{1}{\bar{h}_3{}^2}\left[\left(\frac{\partial\bar{u}}{\partial\bar{\zeta}}\right)^2 + \left(\frac{\partial\bar{v}}{\partial\bar{\zeta}}\right)^2\right]\right\}^{1/2}\tilde{\gamma} \qquad \left(0 \leqq \bar{x}_3 \leqq \bar{x}_{3,c}\right) \tag{15}$$

Outer law

$$\epsilon_{outer} = k_4\bar{\rho}\bar{U}_{e,t}\bar{\delta}^*\tilde{\gamma} \qquad \left(\bar{x}_{3,c} < \bar{x}_3 \leqq \bar{x}_{3,e}\right) \tag{16}$$

where

$$\bar{\ell}_2 = k_1\bar{x}_3 D \tag{17}$$

$$\bar{U}_{e,t} = \left(\bar{u}_e{}^2 + \bar{v}_e{}^2\right)^{1/2} \tag{18}$$

$$\bar{\delta}^* = \int_0^{\bar{x}_{3,e}}\left[1 - \frac{\left(\bar{u}^2 + \bar{v}^2\right)^{1/2}}{\bar{U}_{e,t}}\right] d\bar{x}_3 \tag{19}$$

The point where the inner and outer laws are matched $\bar{x}_{3,c}$ is obtained from the continuity of eddy viscosity. For the results presented in this paper, k_1, k_2, k_3, k_4, k_5, k_6, and $N_{Pr,t}$ were assigned values of 0.435, 0.09, 26, 0.0168, 5, 0.78, and 0.95, respectively. These represent the classical values generally accepted for equilibrium two-

dimensional boundary-layer flows (see refs. 3 and 4); however, note that although the assigned values are sufficient over a broad range of flow and wall boundary conditions, modifications are required for certain classes of flow. (See refs. 4 and 10, for example.)

TRANSFORMATION

The use of physical coordinates introduces a number of problems for three-dimensional boundary-layer flows which can be circumvented by the introduction of a suitable transformation. If physical coordinates are used, three main problems are encountered as follows: (1) the numerical procedure and resultant solution are sensitive to the mesh-point distribution in the two surface spatial coordinates $(\Delta\bar{x}_1$ and $\Delta\bar{x}_2)$; (2) the growth of the boundary layer in the streamwise $(\bar{x}_1)$ and cross-flow $(\bar{x}_2)$ directions requires the addition of nodal points in the $\bar{x}_3$-direction as the solution progresses (these two factors result in excessive computer processing time and/or computer code logic); and (3) initial data planes cannot be generated where the initial boundary-layer thickness is zero (for example, at the tip of a sharp body). Consequently, in the present procedure a transformation is introduced which avoids these problems and, in addition, minimizes the computer processing time and storage requirements.

Equations (1) to (19) are first nondimensionalized (see ref. 11 for definition of nondimensional variables), and a similarity-type transformation is introduced for the normal coordinate and velocity as follows:

$$\bar{h}_3 = \tilde{\xi}\,\frac{\rho_e}{\rho}\,\frac{\bar{L}}{\sqrt{R_{\infty,L}}}\,h_3 \tag{20}$$

$$\bar{w} = \frac{1}{\tilde{\xi}\sqrt{R_{\infty,L}}}\,\frac{\rho_e}{\rho}\,\bar{u}_\infty w \tag{21}$$

where $\bar{u}_\infty$ is the reference velocity and for a sharp cone $\tilde{\xi} = \sqrt{\xi}$. The metric coefficients h_2 and h_3 are arbitrary functions of the coordinates. In order to cast the equations into Crocco-type form, the following function is defined:

$$\zeta = (1 - F)^{1/2} \tag{22}$$

where $F = u/u_e$. The continuity and ξ-momentum equations are combined to form the shear equation, where the shear parameter Φ is defined by

$$\Phi = -\frac{1}{h_3}\,\frac{\mu}{T}\left(1 + \frac{\epsilon}{\mu}\,\Gamma\right) \tag{23}$$

Consequently, F is replaced by Φ as a new dependent variable, and $H = w/u_e$ is uncoupled from the system. The governing system of equations reduces to three coupled

nonlinear partial differential equations in θ, G, and Φ together with an explicit algebraic relationship for H. The system assumes the following form:

$$\frac{\partial^2 \omega}{\partial \zeta^2} + \alpha_1 \frac{\partial \omega}{\partial \zeta} + \alpha_2 \omega + \alpha_3 + \alpha_4 \frac{\partial \omega}{\partial \xi} + \alpha_5 \frac{\partial \omega}{\partial \eta} = 0 \tag{24}$$

where ω represents θ, G, and Φ, and α_1, α_2, α_3, α_4, and α_5 are nonlinear coefficients.

The boundary conditions on equation (24) are as follows:

when $\zeta = 0$

$$\theta = 1 \qquad G = 1 \qquad \Phi = 0 \tag{25a}$$

when $\zeta = 1$

$$\left.\begin{aligned} &\theta = \theta_w \quad \text{or} \quad \left(\frac{\partial \theta}{\partial \zeta}\right)_w = f(\xi,\eta) \\ &G = 0 \\ &\left(\frac{\partial \Phi}{\partial \zeta}\right)_w = -\left(a_1 H + a_2 \frac{\bar{e}\theta}{\Phi} + \Phi\right)_w \end{aligned}\right\} \tag{25b}$$

where a_1 and a_2 are functions of geometry and the inviscid edge conditions.

The primary advantage of the Crocco-type transformation is that the solution domain is bounded between the definite limits $0 \leq \zeta \leq 1$. The only disadvantage of the transformation is that velocity overshoot in F is not allowed; that is, F must increase monotonically from the specified wall value (slip at the surface can be specified) to unity at the edge boundary. Edge vorticity and streamline swallowing are not considered in this paper.

SOLUTION TECHNIQUE

Equation (24) is solved in an iterative mode with a marching implicit finite-difference technique suggested by Dwyer (ref. 19) and modified by Krause (ref. 20). The method is second-order accurate and unconditionally stable (conditional stability for reverse cross flow; see ref. 20). For turbulent flows a minimum of two mesh points in the ζ-plane must be located in the viscous sublayer; consequently, a variable mesh-point distribution is used. In the present study a geometric progression is assumed; that is, $\Delta\zeta_{k+1}/\Delta\zeta_k = C$ for $\kappa = 2, 3, \ldots, N - 1$ (ref. 3). Variable mesh-point distributions are also used in the ξ- and η-planes to minimize the computer processing time and storage requirements. A schematic of the difference molecule is presented in figure 2. Equation (24) is written at the point (i-1/2,j,k) and solved for the values of the dependent

variables θ, G, Φ, and H at the point (i,j,k). Consequently, the partial derivatives of equation (24) at the point (i-1/2,j,k) are expressed as follows:

$$\left(\frac{\partial^2\omega}{\partial\zeta^2}\right)_{i-1/2,j,k} = \frac{\left(\frac{\partial^2\omega}{\partial\zeta^2}\right)_{i-1,j,k} + \left(\frac{\partial^2\omega}{\partial\zeta^2}\right)_{i,j,k}}{2} \tag{26}$$

$$\left(\frac{\partial\omega}{\partial\zeta}\right)_{i-1/2,j,k} = \frac{\left(\frac{\partial\omega}{\partial\zeta}\right)_{i-1,j,k} + \left(\frac{\partial\omega}{\partial\zeta}\right)_{i,j,k}}{2} \tag{27}$$

$$\left(\frac{\partial\omega}{\partial\xi}\right)_{i-1/2,j,k} = \frac{\omega_{i,j,k} - \omega_{i-1,j,k}}{\Delta\xi_{i-1}} \tag{28}$$

$$\left(\frac{\partial\omega}{\partial\eta}\right)_{i-1/2,j,k} = \frac{\frac{\omega_{i-1,j+1,k} - \omega_{i-1,j,k}}{\Delta\eta_j} + \frac{\omega_{i,j,k} - \omega_{i,j-1,k}}{\Delta\eta_{j-1}}}{2} \tag{29}$$

$$(\omega)_{i-1/2,j,k} = \frac{\omega_{i-1,j,k} + \omega_{i,j,k}}{2} \tag{30}$$

The derivative quantities in equations (26) and (27) are obtained from

$$\left(\frac{\partial^2\omega}{\partial\zeta^2}\right)_{p,q,r} = Y_1\omega_{p,q,r+1} - Y_2\omega_{p,q,r} + Y_3\omega_{p,q,r-1} \tag{31}$$

$$\left(\frac{\partial\omega}{\partial\zeta}\right)_{p,q,r} = Y_4\omega_{p,q,r+1} - Y_5\omega_{p,q,r} - Y_6\omega_{p,q,r-1} \tag{32}$$

where

$$Y_1 = \frac{2}{\Delta\zeta_r(\Delta\zeta_r + \Delta\zeta_{r-1})} \tag{33}$$

$$Y_2 = \frac{2}{\Delta\zeta_r\,\Delta\zeta_{r-1}} \tag{34}$$

$$Y_3 = \frac{2}{\Delta\zeta_{r-1}(\Delta\zeta_r + \Delta\zeta_{r-1})} \tag{35}$$

$$Y_4 = \frac{\Delta\zeta_{r-1}}{\Delta\zeta_r(\Delta\zeta_r + \Delta\zeta_{r-1})} \tag{36}$$

$$Y_5 = \frac{\Delta\zeta_{r-1} - \Delta\zeta_r}{\Delta\zeta_r \, \Delta\zeta_{r-1}} \tag{37}$$

$$Y_6 = \frac{\Delta\zeta_r}{\Delta\zeta_{r-1}(\Delta\zeta_r + \Delta\zeta_{r-1})} \tag{38}$$

For equally spaced mesh-point distributions in the ζ-plane, equations (33) to (38) assume the values

$$\left.\begin{aligned} Y_1 &= \frac{1}{\Delta\zeta^2} & Y_2 &= 2Y_1 \\ Y_3 &= Y_1 & Y_4 &= \frac{1}{2\Delta\zeta} \\ Y_5 &= 0 & Y_6 &= Y_4 \end{aligned}\right\} \tag{39}$$

When a converged solution cannot be obtained at the most leeward plane, $\phi = 180^o$ (for example, for separation on leeward surface), a cubic Crank-Nicolson differencing scheme is used at the maximum η-station (ref. 14). If this procedure were not incorporated into the program logic, one η-station would be lost for each incremental $\Delta\xi$ because of the Krause differencing scheme; that is, equation (29) assumes the existence of a converged solution at the point (i-1,j+1,k) for $K = 2, 3, \ldots, N - 1$.

The marching procedure cannot be initiated without the existence of two orthogonal initial data planes. For a sharp right circular cone these planes of initial data are generated directly from the governing equations by using a second-order Crank-Nicolson scheme for the two planes $\xi = 0$, $0 \leq \eta \leq \eta_{max}$ and $0 \leq \xi \leq \xi_{max}$, $\eta = 0$ where similarity exists. A discussion of problems associated with obtaining initial data planes for general configurations is presented in reference 10.

Substitution of equations (26) to (30) into equation (24) results in a system of coupled algebraic equations whose coefficient matrix is of tridiagonal form which can be efficiently solved for the dependent variables (Thomas' algorithm). The primary problem associated with equation (24) is that the coefficients (α_1, α_2, etc.) are highly nonlinear. The shear equation controls the convergence rate of the numerical procedure (iterations required) as the system is sequentially iterated. Equation (24) can be written for Φ as

$$\frac{\partial^2\Phi}{\partial\zeta^2} + \left(\frac{h_1}{\zeta} + \frac{\beta_1}{\Phi^2}\right)\frac{\partial\Phi}{\partial\zeta} - \frac{h_1}{\zeta^2}\Phi + \frac{\beta_2}{\Phi} + \frac{\beta_3}{\Phi^2}\frac{\partial\Phi}{\partial\zeta} + \frac{\beta_4}{\Phi^2}\frac{\partial\Phi}{\partial\eta} = 0 \tag{40}$$

where β_1, β_2, β_3, and β_4 are functions of geometry, inviscid edge conditions, and previous iterate values of the dependent variables F and θ and their derivatives. The problem is further complicated by the inclusion of the turbulence models (eqs. (9) to (19)), since in the transformed plane Φ appears explicitly in the transformed relationships.

Consequently, the coefficients (β_1, β_2, etc.) also depend on Φ for turbulent flows (for laminar flows this dependence is removed). The system of equations will not converge if the shear equation is written as shown in equation (40) because of the Φ^{-1} term. Convergence can be achieved by using a Taylor's series expansion of Φ^{-1} about the previous iterate value Φ_G; that is

$$\frac{1}{\Phi} = \frac{1}{\Phi_G}\left(2 - \frac{\Phi}{\Phi_G}\right) + O(\Phi^2) \tag{41}$$

Substitution of equation (41) into equation (40) yields

$$\frac{\partial^2\Phi}{\partial\zeta^2} + \left(\frac{h_1}{\zeta} + \frac{\beta_1}{\Phi^2}\right)\frac{\partial\Phi}{\partial\zeta} + \left(-\frac{h_1}{\zeta^2} - \frac{\beta_2}{\Phi_G{}^2}\right)\Phi + 2\frac{\beta_2}{\Phi_G} + \frac{\beta_3}{\Phi^2}\frac{\partial\Phi}{\partial\zeta} + \frac{\beta_4}{\Phi^2}\frac{\partial\Phi}{\partial\eta} = 0 \tag{42}$$

Equation (42) converges in an average of five to seven iterations for high Reynolds number turbulent flow. The wall boundary condition on Φ (see eq. (25b)) also presents a problem since Φ_w is unknown; however, the wall derivative relationship can be directly incorporated in the iterative solution procedure. In principle, it should be possible to reduce the average number of iterations substantially to a maximum of three. Research continues in the areas of (1) restructuring equation (42), (2) treatment of the Φ wall boundary conditions, and (3) the problem associated with Φ in the transformed turbulence models. Note however that the present procedure requires essentially the same processing time per mesh point (0.002 sec) as the Cebeci-Keller Box method (ref. 10) and that this time may be substantially reduced through convergence accelerator procedures and/or the inclusion of Newton-Raphson iteration.

RESULTS AND DISCUSSION

The numerical procedure and turbulence models have been applied to a number of flows (current geometry limited to sharp right circular and elliptic cones). In this paper, numerical results are compared with experimental wall and profile data for a cone with a 12.5° semiapex angle at an angle of attack of 15.75°. The free-stream Mach number, total pressure, and total temperature were 1.8, 172.4 kN/m^2, and 294 K, respectively. Transition was assumed to be initiated and completed in the region $0.03 \leq \bar{x}_1/\bar{L} \leq 0.08$ ($\bar{L}$ = 105.6 cm). The adiabatic wall boundary condition was imposed on the energy equation (see eq. (25b)); that is, $\left(\frac{\partial\theta}{\partial\zeta}\right)_w = 0$. No experimental data were input into the viscous flow solution. The inviscid pressure distribution $p_e = p_e(\xi,\eta)$ was obtained from a numerical solution of the three-dimensional inviscid flow equations. Experimental data for verification of the accuracy of the numerical procedure and turbulence models were obtained from reference 21.

The numerical results for F, G, and θ are compared with experimental data in figure 3 for circumferential locations of $\phi = 0^o$, 45^o, 90^o, and 135^o. In order to evaluate the effect of nodal-point spacing in the ζ-plane, a parametric study was made for $N = 301$, 201, 101, 61, and 21 with $\Delta\zeta_{k+1}/\Delta\zeta_k = 1.02$. The results for $N = 301$ and 201 were essentially identical, and those for $N = 101$ were within 0.5 percent of the $N = 301$ results. The agreement between the experimental and numerical results is very good for 301 points and, in general, good for 21 points. The two turbulence models (eqs. (9) to (19)) produced essentially identical results. The two-layer model results presented in figure 3 are for $N = 301$; however, the two-layer results for $N = 21$ were essentially identical to the $N = 21$ results of the single-layer model. A comparison of the numerical results for $C_{f,e}$ presented in figure 4(a) indicates that the difference between the results for 61 points and 301 points is approximately 1 percent and between 21 points and 301 points is approximately 3 percent. In figure 4(b), $C_{f,e}$ is presented as a function of ϕ. Figures 3 and 4 indicate that as few as 21 points normal to the wall boundary can be used to obtain results to within 3-percent accuracy (compared with $N = 301$ results). Numerical results for surface streamline direction $\omega_s = \tan^{-1}\left(\tau_\eta/\tau_\xi\right)_w$ obtained for $N = 301$ and 21 are compared with experimental data in figure 5. The agreement is good considering that the inviscid pressure distribution was obtained from the inviscid equations and not from experimental data; that is, displacement surface effects are not included in the viscous/inviscid calculations.

The major points which should be noted in these comparisons are (1) that the numerical procedure is efficient and accurate and (2) that the turbulence models are satisfactory for high Reynolds number equilibrium turbulent boundary-layer flows. The Crocco-type transformation and the numerical procedure allow the generation of accurate solutions for a minimum of 21 points normal to the wall boundary. The computer code requires 60000_8 storage (the i-1,j,k data plane is stored on disk) and approximately 0.002 second per grid point processing time on a CDC 6600 computer system. Current studies indicate that it may be possible to substantially reduce the processing time through convergence accelerators for the shear equation (eq. (42)) and/or the inclusion of a Newton-Raphson iteration procedure. The current program is comparable in both storage and processing time with the Cebeci-Keller Box method (ref. 10).

CONCLUDING REMARKS

Solutions of the compressible three-dimensional turbulent boundary-layer equations have been obtained and compared with experimental data. The agreement between the numerical results and experimental data indicates that accurate results can be obtained with a minimum of 21 nodal points in the plane normal to the wall boundary layer for high Reynolds number equilibrium turbulent flows. The turbulence models, although simple in

concept, were adequate for the class of flow considered; however, previous experience indicates that caution should be exercised in extending these models to more demanding boundary-layer flows. The numerical procedure is second-order accurate and unconditionally stable (conditional stability for reverse cross flow). The computer code requires 60000_8 storage and approximately 0.002 second per grid point processing time (CDC 6600 computer system). Studies indicate that the processing time may be further reduced through convergence accelerator and Newton-Raphson iteration procedures; however, the current computer requirements of storage and speed compare favorably with other procedures under development.

REFERENCES

1. Kline, S. J.; Morkovin, M. V.; Sovran, G.; and Cockrell, D. J., eds.: Computation of Turbulent Boundary Layers – 1968 AFOSR-IFP-Stanford Conference. Vol. I – Methods, Predictions, Evaluation and Flow Structure. Stanford Univ., c.1969.

2. Compressible Turbulent Boundary Layers. NASA SP-216, 1969.

3. Harris, Julius E.: Numerical Solution of the Equations for Compressible Laminar, Transitional, and Turbulent Boundary Layers and Comparisons With Experimental Data. NASA TR R-368, 1971.

4. Cebeci, Tuncer; and Smith, A. M. O.: Analysis of Turbulent Boundary Layers. Academic Press, Inc., 1974.

5. Raetz, G. S.: A Method of Calculating Three-Dimensional Laminar Boundary Layers of Steady Compressible Flows. Rep. No. NAI-58-73, Northrop Aircraft, Inc., Dec. 1957.

6. Wang, K. C.: On the Determination of the Zones of Influence and Dependence for Three-Dimensional Boundary-Layer Equations. J. Fluid Mech., vol. 48, no. 2, July 28, 1971, pp. 397-404.

7. Bradshaw, P.: Effects of Streamline Curvature on Turbulent Flow. AGARDograph No. 169, Aug. 1973.

8. Nash, John F.; and Patel, Virendra C.: Three-Dimensional Turbulent Boundary Layers. Sci. & Business Consultants, Inc., 1972.

9. Bradshaw, P. (appendix by V. C. Patel): The Strategy of Calculation Methods for Complex Turbulent Flows. Rep. No. 73-05, Aeronaut. Dep., Imp. Coll. Sci. & Technol., Aug. 1973.

10. Cebeci, Tuncer; Kaups, Kalle; Mosinskis, G. J.; and Rehn, J. A.: Some Problems of the Calculation of Three-Dimensional Boundary-Layer Flows on General Configurations. NASA CR-2285, 1973.

11. McGowan, J. J., III; and Davis, R. T.: Development of a Numerical Method To Solve the Three-Dimensional Compressible Laminar Boundary-Layer Equations With Application to Elliptical Cones at Angle of Attack. ARL 70-0341, U.S. Air Force, Dec. 1970.

12. Adams, John C., Jr.: Analysis of the Three-Dimensional Compressible Turbulent Boundary Layer on a Sharp Cone at Incidence in Supersonic and Hypersonic Flow. AEDC-TR-72-66, U.S. Air Force, June 1972. (Available from DDC as AD 743 003.)

13. Popinski, Zenon; and Davis, R. T.: Three-Dimensional Compressible Laminar Boundary Layers on Sharp and Blunt Circular Cones at Angle of Attack. NASA CR-112316, 1973.

14. Blottner, F. G.; and Ellis, Molly: Three-Dimensional, Incompressible Boundary Layer on Blunt Bodies. Part I: Analysis and Results. SLA-73-0366, Sandia Corp., Apr. 1973.

15. Wang, K. C.: Three-Dimensional Laminar Boundary Layer Over Body of Revolution at Incidence. Part VI. General Methods and Results of the Case of High Incidence. AFOSR-TR-73-1045, U.S. Air Force, May 1973. (Available from DDC as AD 763 831.)

16. Blottner, F. G.: Computational Techniques for Boundary Layers. Paper for AGARD Lecture Series 73 on Computational Methods for Inviscid and Viscous Two- and Three-Dimensional Flow Fields (Von Karman Inst.), Feb. 17-22, 1975.

17. Dhawan, S.; and Narasimha, R.: Some Properties of Boundary Layer Flow During the Transition From Laminar to Turbulent Motion. J. Fluid Mech., vol. 3, pt. 4, Jan. 1958, pp. 418-436.

18. Hunt, James L.; Bushnell, Dennis M.; and Beckwith, Ivan E.: The Compressible Turbulent Boundary Layer on a Blunt Swept Slab With and Without Leading-Edge Blowing. NASA TN D-6203, 1971.

19. Dwyer, Harry A.: Solution of a Three-Dimensional Boundary-Layer Flow With Separation. AIAA J., vol. 6, no. 7, July 1968, pp. 1336-1342.

20. Krause, Egon: Comment on "Solution of a Three-Dimensional Boundary-Layer Flow With Separation." AIAA J., vol. 7, no. 3, Mar. 1969, pp. 575-576.

21. Rainbird, William John: Turbulent Boundary-Layer Growth and Separation on a Yawed Cone. AIAA J., vol. 6, no. 12, Dec. 1968, pp. 2410-2416.

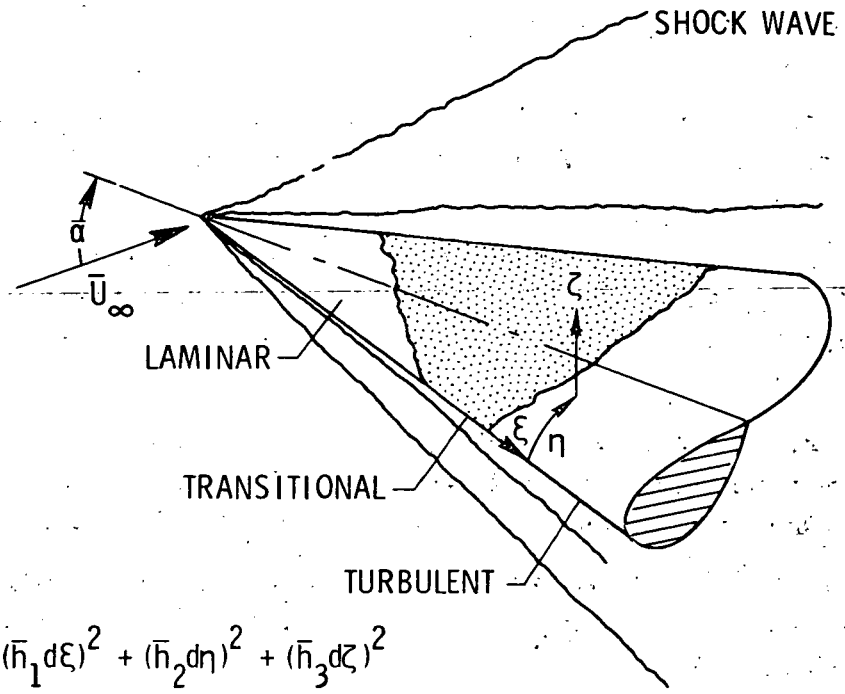

Figure 1.- Coordinate system.

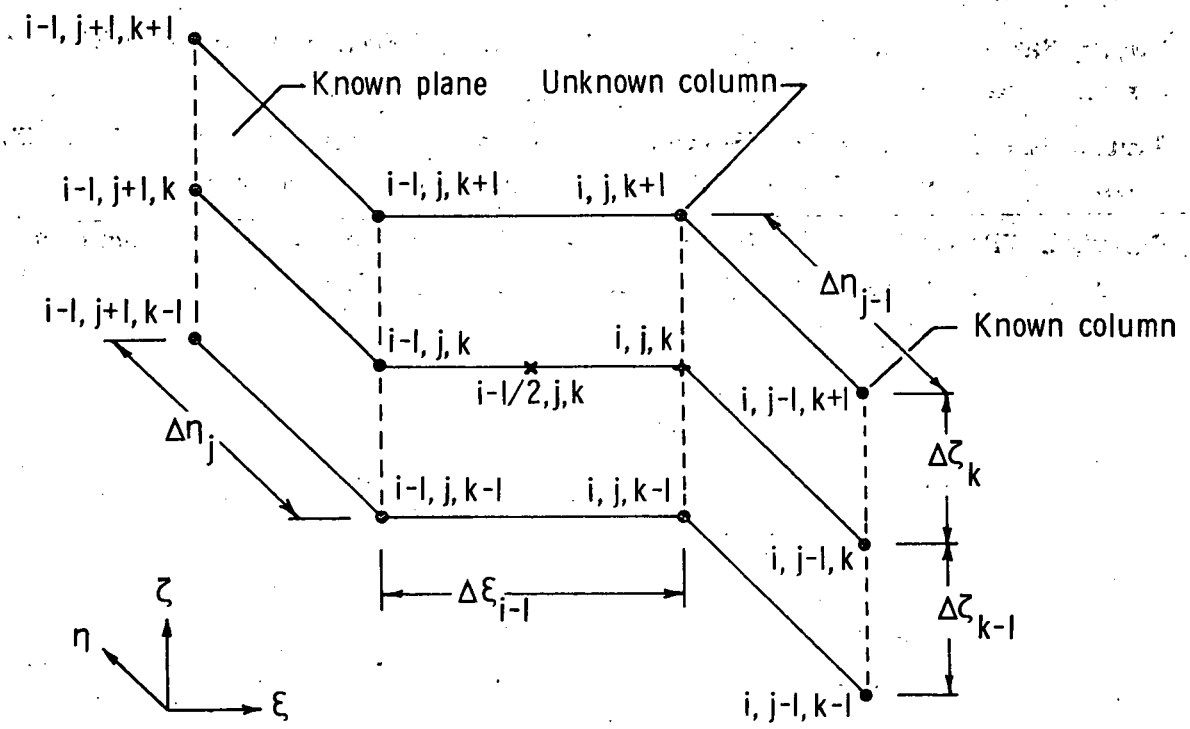

Figure 2.- Difference grid nomenclature.

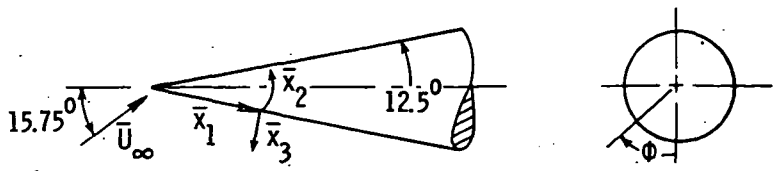

Experimental data		Numerical results	N
○	u/Q_e	Mixing length model	
□	v/Q_e	———	301
△	T/T_e	- - - - - - - - - -	21
		Eddy viscosity model	
		x	301

STORAGE/PROCESSING ON CDC 6600 COMPUTER

N	CPU time per mesh point, sec	Storage	Total CPU time, sec
301	0.002	170000_8	900
21	.002	60000_8	60

(a) Details of figure 3.

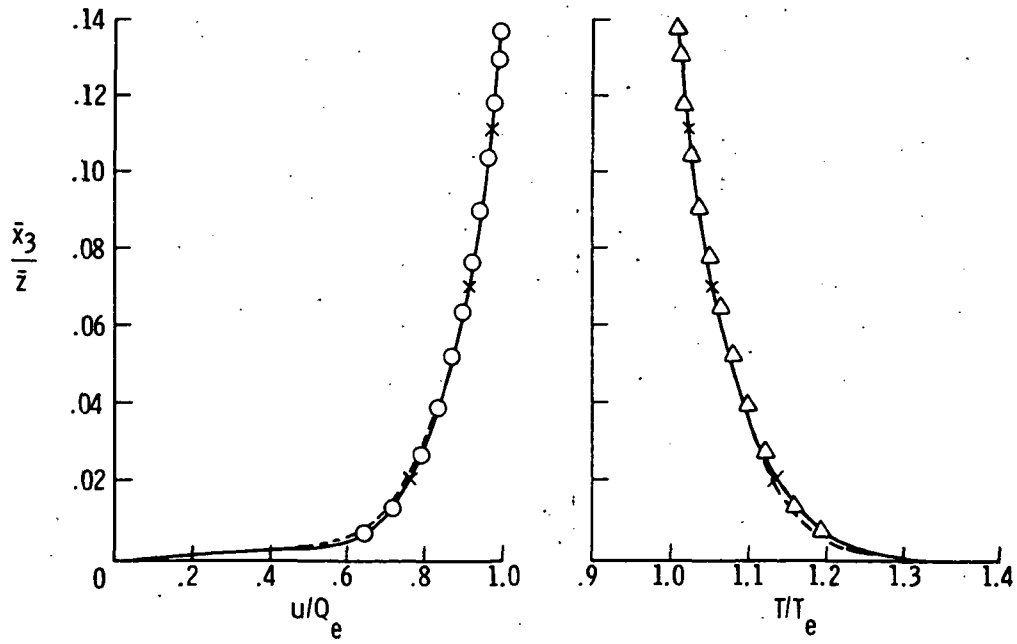

(b) $\phi = 0°$.

Figure 3.- Profile comparisons. $M_\infty = 1.8$; $R_{\infty,\bar{L}} = 25 \times 10^6$; $\gamma = 1.4$; $\bar{z} = 2.54$ cm; $\bar{L} = 105.6$ cm; $Q_e = \sqrt{u_e^2 + v_e^2}$.

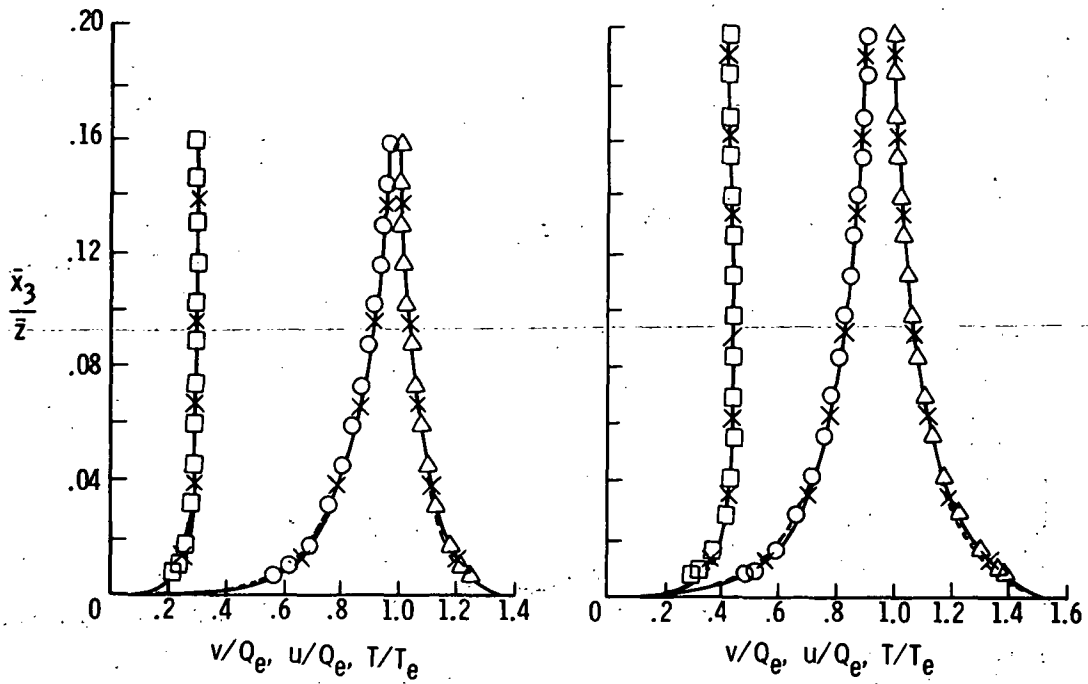

(c) $\phi = 45^o$.

(d) $\phi = 90^o$.

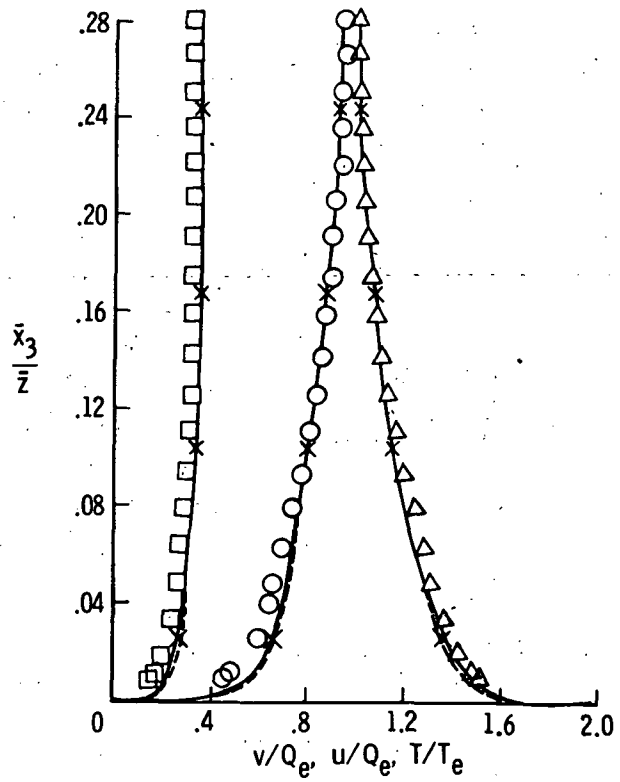

(e) $\phi = 135^o$.

Figure 3.- Concluded.

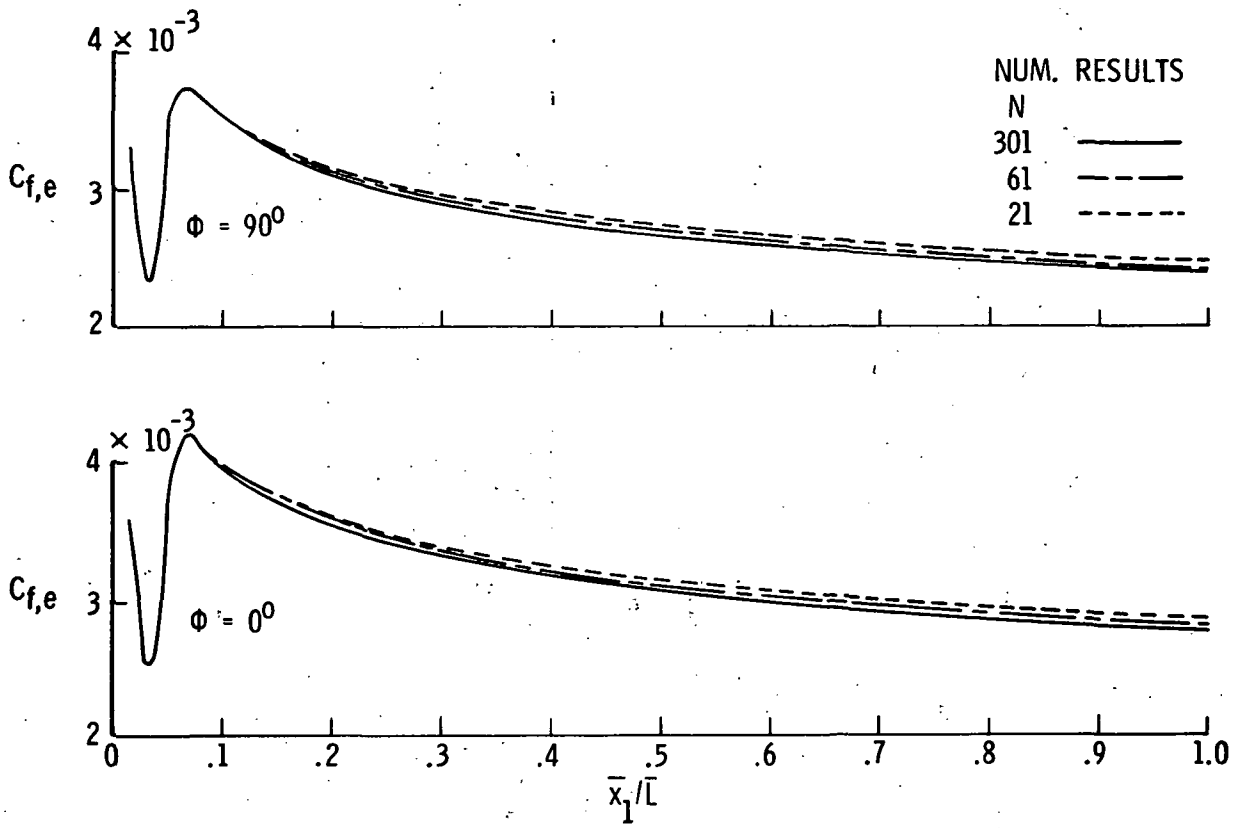

(a) $\phi = 0^{o}; 90^{o}$.

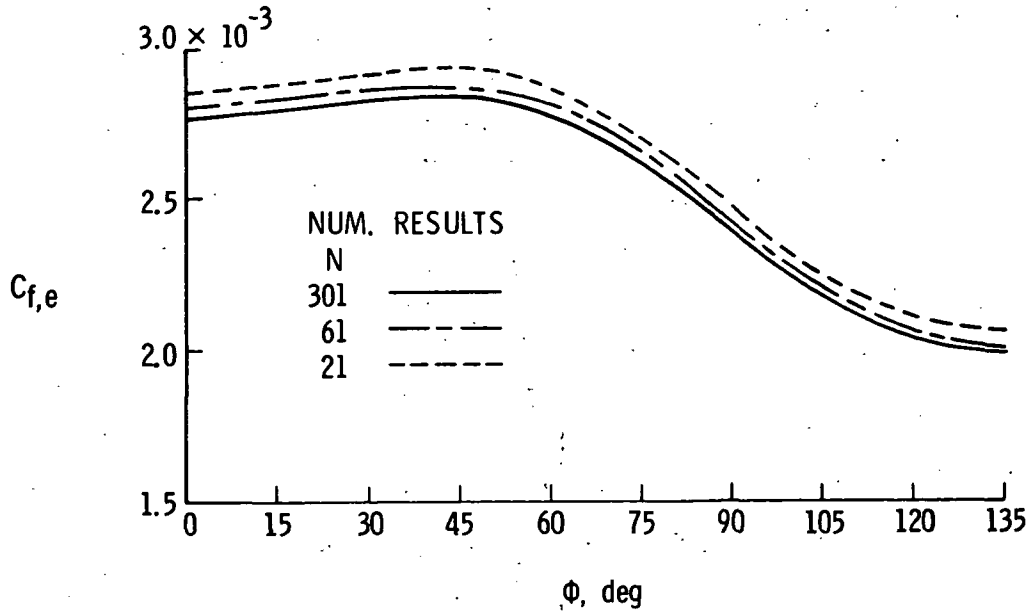

(b) $\bar{x}_1/\bar{L} = 1$.

Figure 4.- Effect of nodal spacing on skin friction.

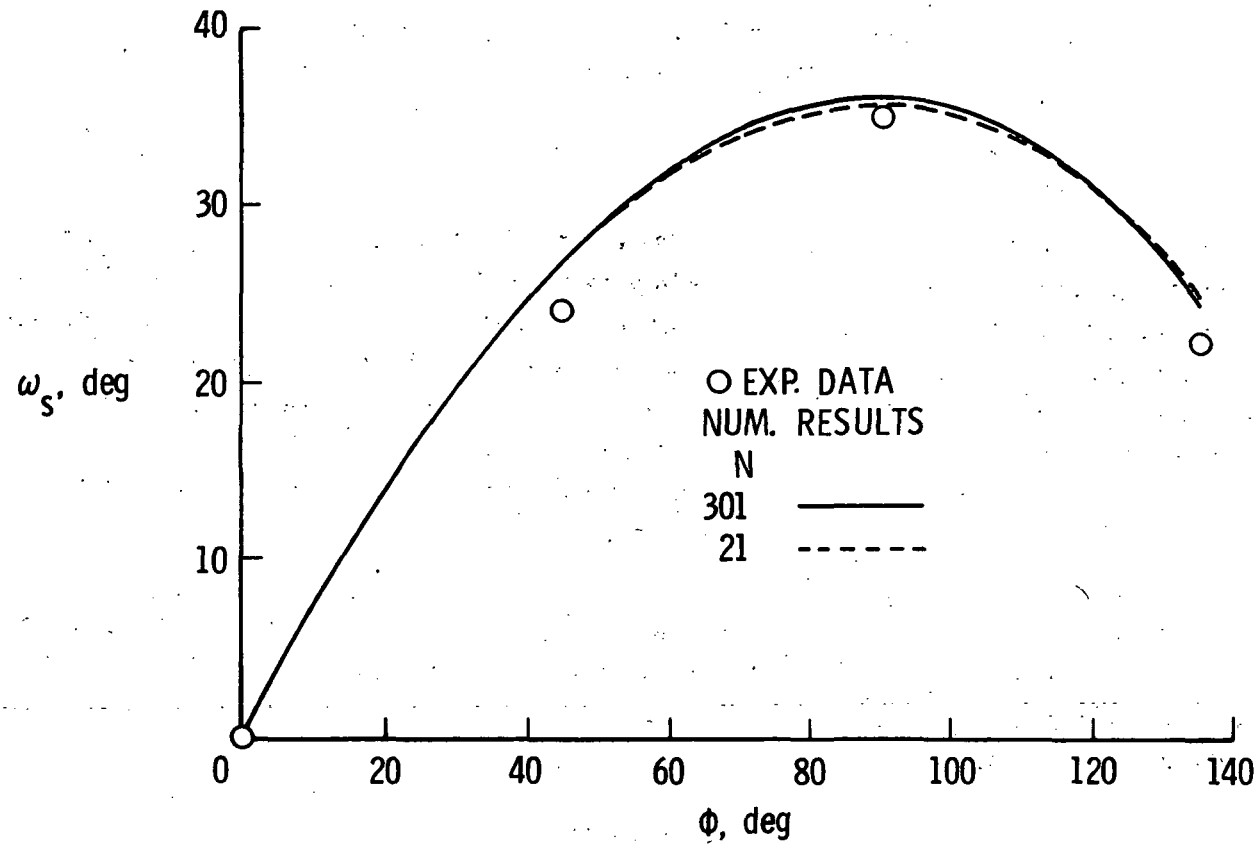

Figure 5.- Surface flow direction. $\bar{x}_1/\bar{L} = 1$.

CALCULATION OF THREE-DIMENSIONAL COMPRESSIBLE LAMINAR AND TURBULENT BOUNDARY LAYERS

CALCULATION OF THREE-DIMENSIONAL COMPRESSIBLE BOUNDARY LAYERS ON ARBITRARY WINGS

By Tuncer Cebeci, Kalle Kaups, Judy Ramsey, and Alfred Moser
Douglas Aircraft Company

SUMMARY

A very general method for calculating compressible three-dimensional laminar and turbulent boundary layers on arbitrary wings is described. The method utilizes a non-orthogonal coordinate system for the boundary-layer calculations and includes a geometry package that represents the wing analytically. In the calculations all the geometric parameters of the coordinate system are accounted for. The Reynolds shear-stress terms are modeled by an eddy-viscosity formulation developed by Cebeci. The governing equations are solved by a very efficient two-point finite-difference method used earlier by Keller and Cebeci for two-dimensional flows and later by Cebeci for three-dimensional flows.

Preliminary results for a swept wing look very encouraging. A typical computation time (CPU) for one surface of the wing which roughly consists of 30 z-stations and 20 x-stations with 30 η-points across the boundary layer is a little over 30 sec on an IBM 370/165 computer.

INTRODUCTION

The development of an efficient and accurate method to compute three-dimensional boundary layers on wings of arbitrary shape requires:

(1) The velocity distribution at the boundary-layer edge

(2) A convenient coordinate system

(3) A model for the Reynolds stresses

(4) A numerical method to solve the governing equations

The velocity distribution must be obtained from the pressure distribution. In general, the pressure distribution can be obtained either theoretically or experimentally.

When obtained theoretically, the velocity components in the streamwise and spanwise directions can be calculated without too much difficulty and thus satisfy the first requirement. When the pressure distribution is obtained experimentally, the calculation of the velocity components is rather difficult. Certain approximations must be made to get the velocity distribution from the experimental pressure distribution. In the section "Governing Equations," the difficulties and the procedure used to calculate the velocity components from the experimental pressure distribution are discussed.

In selecting a coordinate system for the boundary-layer calculations, an important point to consider is that the coordinate system should be calculated only once for each geometrical configuration. This rules out the streamline coordinate system since for each angle of attack the streamlines must be calculated repeatedly. Another important point to consider is dictated by utility. The measured or calculated external velocity distributions are usually given in planes containing the local chord line. Hence it is natural to select one surface coordinate in planes parallel to the defining sections. The other surface coordinate may be lines either orthogonal or nonorthogonal to that coordinate line. However, the selection of an orthogonal system causes a number of inconveniences together with lengthy interpolation procedures. As a result, a nonorthogonal coordinate system appears to be the most convenient system with which to perform the boundary-layer calculations as discussed in detail in the section "Coordinate System."

For turbulent flows the governing boundary-layer equations contain the Reynolds stress terms which require closure assumptions such as mixing-length, eddy-viscosity concepts or "higher order turbulence" models. Although the latter have the potential to compute more complicated turbulent flows, mixing-length, eddy-viscosity approaches have proven to yield quite satisfactory results for boundary-layer flows. (See refs. 1 to 4.) The use of higher order turbulence models also increases the complexity of already complex equations leading to high computation times. Furthermore, for compressible flows their accuracy may not be as good as the simple mixing-length, eddy-viscosity methods. For this reason, in our study the Reynolds stresses are modeled by using an accurate eddy-viscosity formulation (see the section "Turbulence Model") developed by Cebeci. (See refs. 3 and 4.)

When physical coordinates are used, the solutions of the governing boundary-layer equations are quite sensitive to the spacings in the streamwise direction (x) and to the spanwise direction (z) and require a large number of x- and z-stations. In calculations such as the ones considered here where the computation time and storage become important, it is necessary to remove the sensitivity to Δx- and Δz-spacings. This can be done by expressing and solving the governing equations in transformed coordinates. Therefore, in the section "Transformation of the Governing Equations," a convenient transformation to express the boundary-layer equations in terms of transformed variables is considered.

In the section "Numerical Method," the solution of the governing equations by the Cebeci-Keller Box method is discussed. This is a very efficient two-point finite-difference method developed by H. B. Keller and applied to the boundary-layer equations by Keller and Cebeci. (See, for example, refs. 5 and 6.)

In the section "Results and Discussion," results for a planar turbulent boundary-layer flow approaching a three-dimensional obstacle and results for a swept wing are presented. Finally in the section "Future Work," additional work that needs to be done in order to develop a complete design tool for computing the flow field past an arbitrary wing is discussed.

SYMBOLS

A	Van Driest damping length, $26(\nu/u_\tau)(\rho/\rho_w)^{1/2}$
b	$= C(1 + \epsilon_m^+)$
C	$= \rho\mu/(\rho_e\mu_e)$
C_p	pressure coefficient, $2(p - p_\infty)/(\rho_\infty u_\infty^2)$
c	the ratio ρ_e/ρ; local chord
c_f	skin-friction coefficient
E	total enthalpy ratio, H/H_e
f	transformed vector potential for ψ
G	$= E'$
g	transformed vector potential for Φ
g'	$= w/w_e$
H	total enthalpy

h, h_1, h_2 metric coefficients

$\vec{i}, \vec{j}, \vec{k}$ unit vectors in $\bar{x}$-, $\bar{y}$-, and $\bar{z}$-directions of Cartesian coordinate system in which wing is defined

$\vec{K}$ curvature vector of coordinate line

$K_1 = K_{g_1}$
$K_2 = K_{g_2}$ geodesic curvatures

K_{12}, K_{21} geometric parameters

L modified mixing length

M_∞ free-stream Mach number

N_{Pr} Prandtl number

$\vec{n}$ unit vector normal to the surface

P parameter denoting either coordinate, ϕ or $\bar{y}$; point

$P_1, P_2, \ldots, P_{10}$ parameters in transformed differential equations

p static pressure

p_t total pressure

R_e $= u_e s_1 / \nu_e$, Reynolds number

r see figure 7

$\vec{r}$ position vector for point on surface, $(\bar{x}, \bar{y}, \bar{z})$

S stagnation point

s distance along a streamline

s_1	curve length along x-coordinate line
t	time
$\vec{t}$	unit tangent vector along coordinate line
u,v,w,t	dependent variables in first-order, transformed differential equations, f', f'', g', and g''
$\bar{u}$	see figure 7
u_s	total velocity (u_t evaluated at the edge)
u_t	total or resultant velocity
u_τ	friction velocity, $\sqrt{\tau_{t,w}/\rho_w}$
v	velocity normal to surface in physical differential equations
x,z,y	independent coordinates in boundary-layer equations
$\bar{x},\bar{y},\bar{z}$	Cartesian coordinate system used for wing definition
α	local geometric angle of attack of wing section chord lines
β	$= \sin^{-1}(u_p/u_s)$
γ	ratio of specific heats, $\gamma = 1.4$
ϵ(or ϵ_m),ϵ_H	eddy viscosity and eddy conductivity, respectively
η	transformed coordinate normal to surface
θ	angle in tangent plane between x- and z-coordinate lines
λ	local sweep angle, measured between plane normal to free-stream velocity vector and z-coordinate line

μ	molecular viscosity
μ_1,μ_2,μ_3	parameters in transformed energy equation
ν	kinematic viscosity
ρ	density
$\tau_{t,w}$	resultant wall shear stress
τ_x,τ_z	shear stresses
ϕ	stretching variable defined in figure 3
Φ,ψ	two-component vector potentials, equation (56)

Subscripts:

e	outer edge
g	geodesic
I	input stations
i,j,n	indices
in,out	inner and outer regions for eddy viscosity
le	leading edge
p	pivotal points, i.e., stations at which boundary layer is computed
t	wing tip
te	trailing edge
w	wall

∞ free-stream conditions

Primes denote differentiation with respect to η.

GOVERNING EQUATIONS

The governing boundary-layer equations for a nonorthogonal coordinate system are given in references 7 and 8. With a slight change of notation for compressible laminar and turbulent flows, they are given by

Continuity equation:

$$\frac{\partial}{\partial x}(\rho u h_2 \sin\theta) + \frac{\partial}{\partial z}(\rho w h_1 \sin\theta) + \frac{\partial}{\partial y}(\overline{\rho v} h_1 h_2 \sin\theta) = 0 \tag{1}$$

x-momentum equation:

$$\rho \frac{u}{h_1}\frac{\partial u}{\partial x} + \rho \frac{w}{h_2}\frac{\partial u}{\partial z} + \overline{\rho v}\frac{\partial u}{\partial y} - \rho K_1 u^2 \cot\theta + \rho K_2 w^2 \csc\theta + \rho K_{12} uw$$

$$= -\frac{\csc^2\theta}{h_1}\frac{\partial p}{\partial x} + \frac{\cot\theta \csc\theta}{h_2}\frac{\partial p}{\partial z} + \frac{\partial}{\partial y}\left(\mu \frac{\partial u}{\partial y} - \rho\overline{u'v'}\right) \tag{2}$$

z-momentum equation:

$$\rho \frac{u}{h_1}\frac{\partial w}{\partial x} + \rho \frac{w}{h_2}\frac{\partial w}{\partial z} + \overline{\rho v}\frac{\partial w}{\partial y} - \rho K_2 w^2 \cot\theta + \rho K_1 u^2 \csc\theta + \rho K_{21} uw$$

$$= \frac{\cot\theta \csc\theta}{h_1}\frac{\partial p}{\partial x} - \frac{\csc^2\theta}{h_2}\frac{\partial p}{\partial z} + \frac{\partial}{\partial y}\left(\mu \frac{\partial w}{\partial y} - \rho\overline{w'v'}\right) \tag{3}$$

Energy equation:

$$\rho \frac{u}{h_1}\frac{\partial H}{\partial x} + \rho \frac{w}{h_2}\frac{\partial H}{\partial z} + \overline{\rho v}\frac{\partial H}{\partial y} = \frac{\partial}{\partial y}\left[\frac{\mu}{N_{Pr}}\frac{\partial H}{\partial y} + \mu\left(1 - \frac{1}{N_{Pr}}\right)\frac{\partial}{\partial y}\left(\frac{u_t^2}{2}\right) - \rho\overline{v'H'}\right] \tag{4}$$

where $\overline{\rho v} = \rho v + \overline{\rho' v'}$ and h_1 and h_2 are metric coefficients. The latter are functions of x and z, that is,

$$h_1 = h_1(x,z) \qquad h_2 = h_2(x,z) \tag{5}$$

Also, θ represents the angle between the coordinate lines x and z. For an orthogonal system $\theta = \pi/2$. The parameters K_1 and K_2 are known as the geodesic curvatures of the curves z = Constant and x = Constant, respectively. They are given by

$$\left.\begin{aligned} K_1 &= \frac{1}{h_1 h_2 \sin\theta}\left[\frac{\partial}{\partial x}(h_2 \cos\theta) - \frac{\partial h_1}{\partial z}\right] \\ K_2 &= \frac{1}{h_1 h_2 \sin\theta}\left[\frac{\partial}{\partial z}(h_1 \cos\theta) - \frac{\partial h_2}{\partial x}\right] \end{aligned}\right\} \tag{6}$$

The parameters K_{12} and K_{21} are defined by

$$K_{12} = \frac{1}{\sin\theta}\left[-\left(K_1 + \frac{1}{h_1}\frac{\partial\theta}{\partial x}\right) + \cos\theta\left(K_2 + \frac{1}{h_2}\frac{\partial\theta}{\partial z}\right)\right] \tag{7a}$$

$$K_{21} = \frac{1}{\sin\theta}\left[-\left(K_2 + \frac{1}{h_2}\frac{\partial\theta}{\partial z}\right) + \cos\theta\left(K_1 + \frac{1}{h_1}\frac{\partial\theta}{\partial x}\right)\right] \tag{7b}$$

The total velocity within the boundary layer u_t is given by

$$u_t = (u^2 + w^2 + 2uw\cos\theta)^{1/2} \tag{8}$$

One obvious procedure to calculate the velocity components u_e and w_e from the given pressure distribution is to evaluate equations (2) and (3) at the edge of the boundary layer. This gives

$$\frac{u_e}{h_1}\frac{\partial u_e}{\partial x} + \frac{w_e}{h_2}\frac{\partial u_e}{\partial z} - K_1 u_e^2 \cot\theta + K_2 w_e^2 \csc\theta + K_{12} u_e w_e = -\frac{\csc^2\theta}{h_1\rho_e}\frac{\partial p}{\partial x} + \frac{\cot\theta\csc\theta}{h_2\rho_e}\frac{\partial p}{\partial z} \tag{9}$$

and

$$\frac{u_e}{h_1}\frac{\partial w_e}{\partial x} + \frac{w_e}{h_2}\frac{\partial w_e}{\partial z} - K_2 w_e^2 \cot\theta + K_1 u_e^2 \csc\theta + K_{21} u_e w_e = \frac{\cot\theta\csc\theta}{h_1\rho_e}\frac{\partial p}{\partial x} - \frac{\csc^2\theta}{h_2\rho_e}\frac{\partial p}{\partial z} \tag{10}$$

Equations (9) and (10), which may be expressed in the form

$$\frac{u_e}{h_1}\frac{\partial u_e}{\partial x} + \frac{w_e}{h_2}\frac{\partial u_e}{\partial z} = F(u_e, w_e, x, z) \tag{11}$$

and

$$\frac{u_e}{h_1}\frac{\partial w_e}{\partial x} + \frac{w_e}{h_2}\frac{\partial w_e}{\partial z} = G(u_e, w_e, x, z) \tag{12}$$

constitute a system of first-order quasi-linear partial differential equations in u_e and w_e. The differential relationships for these variables are

$$du_e = \frac{\partial u_e}{\partial x}\,dx + \frac{\partial u_e}{\partial z}\,dz \tag{13}$$

$$dw_e = \frac{\partial w_e}{\partial x}\,dx + \frac{\partial w_e}{\partial z}\,dz \tag{14}$$

If we let s denote the distance along a streamline, and u_s the total velocity (u_t evaluated at the edge), that is,

$$u_s = \left(u_e^2 + w_e^2 + 2u_e w_e \cos\theta\right)^{1/2} \tag{15}$$

equations (13) and (14) can be expressed in the form

$$u_s \frac{du_e}{ds} = \frac{u_e}{h_1}\frac{\partial u_e}{\partial x} + \frac{w_e}{h_2}\frac{\partial u_e}{\partial z} \tag{16}$$

and

$$u_s \frac{dw_e}{ds} = \frac{u_e}{h_1}\frac{\partial w_e}{\partial x} + \frac{w_e}{h_2}\frac{\partial w_e}{\partial z} \tag{17}$$

by noting that

$$u_s = \frac{ds}{dt} \qquad u_e = h_1\frac{dx}{dt} \qquad w_e = h_2\frac{dz}{dt} \tag{18}$$

Comparison of equations (11) and (12) with equations (16) and (17) gives

$$\frac{du_e}{ds} = \frac{F}{u_s} \qquad \frac{dw_e}{ds} = \frac{G}{u_s} \tag{19}$$

In addition, we have the following relationships

$$\frac{dx}{ds} = \frac{u_e}{h_1 u_s} \qquad \frac{dz}{ds} = \frac{w_e}{h_2 u_s} \tag{20}$$

The system of four first-order differential equations (eqs. (19) and (20)) allows one to calculate the variation of u_e, w_e, x, and z along a streamline. In principle, these equations can be solved as an initial-value problem. However, it can be shown that the system of differential equations (11) and (12) has characteristics which are identical to the inviscid streamlines. As a result, the initial-value problem cannot be started from lines which are streamlines. Thus, with initial points on the stagnation line or in the plane of symmetry, the solution is quite difficult except for the initial lines themselves. To obtain the solutions over the entire surface, the initial values of u_e and w_e must be known along a line which is not a streamline itself. However, this information is not available in general. A satisfactory solution requires considerable study. In this study approximate methods are used. The simple sweep theory is known to give reasonable answers

when applied to regions of high-aspect-ratio wings that are outside the influence of root and tip effects. In the absence of spanwise pressure gradients, this approximation is almost exact. Thus, for weak spanwise pressure gradients, we can obtain the velocity components on the midportion of a swept wing with reasonable accuracy by using the sweep theory. In regions of root and tip influence, the simple sweep theory with a correction to the sweep angle is applied. The procedure is explained below.

Consider the velocity vector in the tangent plane at a point P on the wing. (See fig. 1.) The basic assumption for the simple sweep theory is that the velocity component u_p in the z-direction is given by:

$$u_p = u_\infty \sin \lambda \tag{21}$$

The sweep angle λ represents the angle between the spanwise direction and the z-coordinate line through the point P. The parallelogram addition of vector components yields

$$\frac{u_e}{u_\infty} = \frac{u_s}{u_\infty} \frac{\cos \beta}{\sin \theta} \tag{22}$$

$$\frac{w_e}{u_\infty} = \frac{u_s}{u_\infty} \frac{\sin \beta \sin \theta - \cos \theta \cos \beta}{\sin \theta} \tag{23}$$

where $\sin \beta = \frac{u_\infty \sin \lambda}{u_s}$.

Elimination of β from equations (22) and (23) yields

$$\frac{u_e}{u_\infty} = \frac{\sqrt{(u_s/u_\infty)^2 - \sin^2 \lambda}}{\sin \theta} \tag{24}$$

$$\frac{w_e}{u_\infty} = \sin \lambda - \frac{u_e}{u_\infty} \cos \theta \tag{25}$$

The total velocity ratio u_s/u_∞ is calculated from

$$\left(\frac{u_s}{u_\infty}\right)^2 = 1 + \frac{1 - \left[\frac{p_{t,1}}{p_{t,2}}\left(1 + \frac{\gamma}{2} C_p M_\infty^2\right)\right]^{(\gamma-1)/\gamma}}{\frac{(\gamma - 1)M_\infty^2}{2}} \tag{26}$$

with $p_{t,1}$ and $p_{t,2}$ denoting the values of total pressure before and after the shock, respectively, and C_p is the pressure coefficient, $C_p = (p - p_\infty)/(1/2\rho u_\infty^2)$. Equation (26) is valid for an adiabatic flow through a shock wave, but since the total pressure ratio across the shock is seldom known, its effect will be neglected. This approximation

introduces only an error of a few percent into the velocity calculations because the total pressure jump across a swept shock is small even for free-stream Mach numbers approaching unity. The total pressure ratio must also remain close to one for the first-order boundary-layer theory to be valid in front of and behind the shock wave.

Equations (24) to (26) are approximately valid for the root and tip regions if the local sweep angle λ is replaced by an effective sweep angle λ_{eff}

$$\left.\begin{aligned}\lambda_{eff} &= \lambda - F_r\lambda_r \\ \lambda_{eff} &= \lambda - F_t\lambda_t\end{aligned}\right\} \tag{27}$$

where λ_r and λ_t denote the root and tip sweep angle for the given z-coordinate line and F_r and F_t are the spanwise interpolation factors for the root and tip, respectively. These parameters are shown schematically in reference 9 as a function of nondimensional spanwise distance in terms of root or tip chord.

COORDINATE SYSTEM

The wing is defined in the $\bar{x},\bar{y},\bar{z}$ coordinate system. Here, the $\bar{x}$-axis is in the direction of the airplane's longitudinal axis and the $\bar{y}$-axis is in the spanwise direction. It is assumed that the wing is defined by a number of airfoil sections in the planes $\bar{y}$ = Constant, which involve the specification of $\bar{z}_i$ and $\bar{x}_i$ for constant values of $\bar{y}_i$. It is also assumed that the pivotal points along the chordwise direction $(\bar{x}/c)_p$ where c denotes local chord are given, as are the spanwise stations $\bar{y}_p$ where the boundary-layer calculations are to be made. These parameters are shown schematically in figure 2.

The defining airfoils are usually given by n pairs of values of $\bar{x}_i$ and $\bar{z}_i$. But because all aerodynamic data related to airfoils are customarily given in terms of fraction of the total chord c, the input data are converted to an xz-coordinate system (see fig. 3) based on the local chord (maximum length line). The relationships between x, $\bar{x}$, z, and $\bar{z}$ are

$$\frac{x}{c} = \frac{1}{c}\left[\left(\bar{x} - \bar{x}_{le}\right)\cos\alpha - \left(\bar{z} - \bar{z}_{le}\right)\sin\alpha\right] \tag{28}$$

$$\frac{z}{c} = \frac{1}{c}\left[\left(\bar{x} - \bar{x}_{le}\right)\sin\alpha + \left(\bar{z} - \bar{z}_{le}\right)\cos\alpha\right] \tag{29}$$

where

$$c = \left[\left(\bar{x}_{te} - \bar{x}_{le}\right)^2 + \left(\bar{z}_{te} - \bar{z}_{le}\right)^2\right]^{1/2} \tag{30}$$

$$\alpha = -\tan^{-1} \frac{\bar{z}_{le} - \bar{z}_{te}}{\bar{x}_{le} - \bar{x}_{te}} \tag{31}$$

The subscripts le and te refer to the points at the leading and trailing edges. They must be specified.

The curves $\bar{y}_j$ = Constant and the curves connecting the points x/c = Constant on all the defining airfoils form a convenient coordinate system. However, the movement of the stagnation point S with angle of attack gives rise to ambiguity. For example, the same x/c value may correspond to two z/c values on a given section. To avoid this problem, another variable ϕ defined by

$$\frac{x}{c} = \frac{1}{2}(1 - \cos \phi) \tag{32}$$

is introduced. Here, $\phi = 0$ corresponds to the leading edge, $\phi = \pi$ corresponds to the trailing edge. The value of ϕ is positive for the upper surface. On the lower surface ϕ is negative.

Other Possible Coordinate Systems

In this section, other possible coordinate systems are discussed. Because of impracticalities with these systems, the nonorthogonal coordinate system is the most convenient to perform the boundary-layer calculations for wing surfaces.

As pointed out in the Introduction, one surface coordinate must be chosen in planes parallel to the defining sections. Consider an orthogonal system in which the orthogonals are constructed between the intersections of planes parallel to the defining sections and the wing surface. Trial calculations showed that orthogonals started from the wing-root congregate at the leading edge, leaving large portions of the wing uncovered. (See fig. 4.) This is especially true for a wing with a sharp trailing edge. A rounded trailing edge rectifies the situation somewhat but there is still a large area of the wing where the orthogonals are sparse.

The orthogonal coordinate system in figure 4 was constructed with the polar angle $\phi = x_2$ at the root section as the other surface coordinate. As is seen from this figure, there are computational difficulties at the trailing edge. To show this, consider figure 5, in which the surface coordinates x_1 and x_2 are obtained by extending the surface coverage with the dashed lines. Here, AA'' is the stagnation line, AB is the root section, and D is a point on the trailing edge. Starting from the initial lines, the boundary layer can be calculated along the line BC'' including the root chord. However, the point D cannot be obtained in a straightforward manner. This is also true for the rest of the trailing-edge points D', D'', and D'''. Because of the difficulty in calculating these trailing-edge points, the orthogonal coordinate system is not practical.

Another possible coordinate system can be obtained by representing the wing by one or more separate conical surfaces. Figure 6 shows such a representation. Here, the wing panels ABDC and CDFE form two conical surfaces with apexes at P and Q, respectively. The shape of the panel ABDC and the coordinate system in the developed plane are shown in figure 7. The initial lines are AC and AB. Line AC is the stagnation line and AB is the wing-fuselage junction. Calculations can be started at corner A. A linear coordinate transformation can be used to avoid marching into the negative r direction. Such a coordinate system without taking the thickness into account (this amounts to representing wing sections by flat plates) was used by Nash and Scruggs (ref. 10). The disadvantage of this coordinate system is the difficulty of doing calculations in the overlap region.

Present Coordinate System

The most convenient coordinate system on the wing surface and the one used in this study is a nonorthogonal coordinate system given by the lines $\bar{y}$ = Constant and ϕ = Constant. The new independent variables ϕ and $\bar{y}$ are selected to correspond to the independent boundary-layer parameters x and z, respectively, in equations (1) to (4). Before the boundary-layer calculations are performed, it is necessary to decide on the surface locations for which the boundary-layer solutions will be output. The best method is a chordwise point distribution in terms of percent chord. The information can then be converted to give the ϕ_p-values for the pivotal points. As is likely to happen, the points on the wing defining sections will not correspond to the pivotal points for the boundary-layer calculations. Thus interpolation is necessary. At each spanwise defining station, the ϕ_I corresponding to the input data can be found by using equations (28) to (32). Next, $\bar{x}_I$ versus ϕ_I and $\bar{z}_I$ versus ϕ_I are curve fitted with cubic spline functions and $\bar{x}_{pI}$ and $\bar{z}_{pI}$ are interpolated for at each spanwise station. Then the $\bar{x}_{pI}$ and $\bar{z}_{pI}$ are spline fitted versus $\bar{y}_j$ for each ϕ_p and are interpolated for $\bar{x}_p$ and $\bar{z}_p$ at $\bar{y}_p$.

Calculation of the Geometric Parameters of the Coordinate System

Once the coordinate system is selected, it is necessary to calculate its geometric parameters, namely, the metric coefficients h_1 and h_2 and K_1 and K_2 which appear in the governing boundary-layer equations. These are calculated by the procedure described below.

The metric coefficient along one curve in space is given by

$$h^2 = \left(\frac{d\bar{x}}{dP}\right)^2 + \left(\frac{d\bar{y}}{dP}\right)^2 + \left(\frac{d\bar{z}}{dP}\right)^2 \tag{33}$$

with P denoting a parameter. For $P = \phi$ along the curves $\bar{y}$ = Constant, equation (33) can be written for h_1 as

$$h_1^2 = \left(\frac{\partial \bar{x}}{\partial \phi}\right)_{\bar{y}}^2 + \left(\frac{\partial \bar{z}}{\partial \phi}\right)_{\bar{y}}^2 \tag{34}$$

Similarly, for $P = \bar{y}$ along the curves ϕ = Constant

$$h_2^2 = 1 + \left(\frac{\partial \bar{x}}{\partial \bar{y}}\right)_{\phi}^2 + \left(\frac{\partial \bar{z}}{\partial \bar{y}}\right)_{\phi}^2 \tag{35}$$

The derivatives in equations (34) and (35), namely $(\partial \bar{x}/\partial \phi)_{\bar{y}}$, $(\partial \bar{z}/\partial \phi)_{\bar{y}}$, $(\partial \bar{x}/\partial \bar{y})_{\phi}$, and $(\partial \bar{z}/\partial \bar{y})_{\phi}$, can be obtained as byproducts of spline-fitting the points along the chordwise and spanwise directions at the pivotal points.

The unit tangent vector $\vec{t}$ along a curve is given by

$$\vec{t} = \frac{d\vec{r}}{ds} = \frac{d\vec{r}}{dP}\frac{1}{ds/dP} = \frac{1}{h}\frac{d\vec{r}}{dP} \tag{36}$$

The unit tangent vector $\vec{t}_1$ along the curve $\bar{y}$ = Constant is

$$\vec{t}_1 = \frac{1}{h_1}\left[\left(\frac{\partial \bar{x}}{\partial \phi}\right)_{\bar{y}}\vec{i} + \left(\frac{\partial \bar{z}}{\partial \phi}\right)_{\bar{y}}\vec{k}\right] \tag{37}$$

where $\vec{i}$, $\vec{j}$, and $\vec{k}$ are unit vectors in the coordinate directions $\bar{x}$, $\bar{y}$, and $\bar{z}$, respectively. The unit tangent vector $\vec{t}_2$ along the curve ϕ = Constant is

$$\vec{t}_2 = \frac{1}{h_2}\left[\left(\frac{\partial \bar{x}}{\partial \bar{y}}\right)_{\phi}\vec{i} + \vec{j} + \left(\frac{\partial \bar{z}}{\partial \bar{y}}\right)_{\phi}\vec{k}\right] \tag{38}$$

The angle between the coordinate lines is then

$$\cos\theta = \vec{t}_1 \cdot \vec{t}_2 = \frac{\left(\frac{\partial \bar{x}}{\partial \phi}\right)\left(\frac{\partial \bar{x}}{\partial \bar{y}}\right) + \left(\frac{\partial \bar{z}}{\partial \phi}\right)\left(\frac{\partial \bar{z}}{\partial \bar{y}}\right)}{h_1 h_2} \tag{39}$$

The curvature of a curve in space is given by

$$\vec{K} = \frac{d\vec{t}}{ds} = \frac{d\vec{t}}{dP}\frac{1}{ds/dP} = \frac{1}{h}\frac{d\vec{t}}{dP} \tag{40}$$

The geodesic or tangential curvature K_g of a curve on the surface can be obtained from

$$K_g = (\vec{t} \times \vec{n}) \cdot \vec{K} \tag{41}$$

Here, $\vec{n}$ is the vector normal to the surface which by definition is

$$\vec{n}\sin\theta = \vec{t}_1 \times \vec{t}_2 \tag{42}$$

or

$$\vec{n} = \frac{1}{h_1 h_2 \sin\theta}\left[-\left(\frac{\partial \bar{z}}{\partial \phi}\right)\vec{i} - \left(\frac{\partial \bar{x}}{\partial \phi}\frac{\partial \bar{z}}{\partial \bar{y}} - \frac{\partial \bar{x}}{\partial \bar{y}}\frac{\partial \bar{z}}{\partial \phi}\right)\vec{j} + \left(\frac{\partial \bar{x}}{\partial \phi}\right)\vec{k}\right] \tag{43}$$

With the use of equation (36), equation (40) can be written as

$$\vec{K} = \frac{1}{h^2}\frac{d^2\vec{r}}{dP^2} - \frac{1}{h^3}\frac{d\vec{r}}{dP}\frac{dh}{dP} = \frac{1}{h^2}\left(\frac{d^2\bar{x}}{dP^2}\vec{i} + \frac{d^2\bar{y}}{dP^2}\vec{j} + \frac{d^2\bar{z}}{dP^2}\vec{k}\right) - \frac{1}{h^4}\left(\frac{d\bar{x}}{dP}\vec{i} + \frac{d\bar{y}}{dP}\vec{j} + \frac{d\bar{z}}{dP}\vec{k}\right)\left(\frac{d^2\bar{x}}{dP^2}\frac{d\bar{x}}{dP}\right.$$

$$\left. + \frac{d^2\bar{y}}{dP^2}\frac{d\bar{y}}{dP} + \frac{d^2\bar{z}}{dP^2}\frac{d\bar{z}}{dP}\right) \tag{44}$$

The geodesic curvature K_{g_1} for a curve $\bar{y}$ = Constant is

$$K_{g_1} = -\left(\vec{t}_1 \times \vec{n}\right) \cdot \vec{K}_1 \tag{45}$$

The minus sign on the right-hand side of equation (45) is introduced to obtain $K_{g_1} = -(1/h_1 h_2)(\partial h_1/\partial z)$ in the case of an orthogonal coordinate system. With ϕ as the parameter, the expression for $\vec{K}_1$ is

$$\vec{K}_1 = \frac{1}{h_1{}^2}\left(\frac{\partial^2\bar{x}}{\partial\phi^2}\vec{i} + \frac{\partial^2\bar{z}}{\partial\phi^2}\vec{k}\right) - \frac{1}{h_1{}^4}\left[\left(\frac{\partial\bar{x}}{\partial\phi}\vec{i} + \frac{\partial\bar{z}}{\partial\phi}\vec{k}\right)\left(\frac{\partial^2\bar{x}}{\partial\phi^2}\frac{\partial\bar{x}}{\partial\phi} + \frac{\partial^2\bar{z}}{\partial\phi^2}\frac{\partial\bar{z}}{\partial\phi}\right)\right] \tag{46}$$

Substituting equations (37), (43), and (46) into equation (45) gives, after simplifications

$$K_{g_1} = \frac{1}{h_1{}^4 h_2 \sin\theta}\left(\frac{\partial\bar{x}}{\partial\phi}\frac{\partial\bar{z}}{\partial\bar{y}} - \frac{\partial\bar{x}}{\partial\bar{y}}\frac{\partial\bar{z}}{\partial\phi}\right)\left(\frac{\partial^2\bar{x}}{\partial\phi^2}\frac{\partial\bar{z}}{\partial\phi} - \frac{\partial^2\bar{x}}{\partial\phi^2}\frac{\partial\bar{x}}{\partial\phi}\right) \tag{47}$$

The geodesic curvature K_{g_2} for a curve ϕ = Constant is given by

$$K_{g_2} = \left(\vec{t}_2 \times \vec{n}\right) \cdot \vec{K}_2 \tag{48}$$

With $\bar{y}$ as the parameter, the expression for $\vec{K}_2$ is

$$\vec{K}_2 = \frac{1}{h_2{}^2}\left(\frac{\partial^2\bar{x}}{\partial\bar{y}^2}\vec{i} + \frac{\partial^2\bar{z}}{\partial\bar{y}^2}\vec{k}\right) - \frac{1}{h_2{}^4}\left(\frac{\partial\bar{x}}{\partial\bar{y}}\vec{i} + \vec{j} + \frac{\partial\bar{z}}{\partial\bar{y}}\vec{k}\right)\left(\frac{\partial^2\bar{x}}{\partial\bar{y}^2}\frac{\partial\bar{x}}{\partial\bar{y}} + \frac{\partial^2\bar{z}}{\partial\bar{y}^2}\frac{\partial\bar{z}}{\partial\bar{y}}\right) \tag{49}$$

The expression for the geodesic curvature K_{g_2} is obtained by substitution of equations (38), (43), and (49) into equation (48):

$$K_{g_2} = \frac{1}{h_1 h_2{}^4 \sin\theta}\left[\left(\frac{\partial\bar{x}}{\partial\phi}\frac{\partial\bar{z}}{\partial\bar{y}} - \frac{\partial\bar{x}}{\partial\bar{y}}\frac{\partial\bar{z}}{\partial\phi}\right)\left(\frac{\partial^2\bar{x}}{\partial\bar{y}^2}\frac{\partial\bar{z}}{\partial\bar{y}} - \frac{\partial^2\bar{z}}{\partial\bar{y}^2}\frac{\partial\bar{z}}{\partial\bar{y}}\right) + \left(\frac{\partial^2\bar{x}}{\partial\bar{y}^2}\frac{\partial\bar{x}}{\partial\phi} + \frac{\partial^2\bar{z}}{\partial\bar{y}^2}\frac{\partial\bar{z}}{\partial\phi}\right)\right] \tag{50}$$

The second-order partial derivatives appearing in equations (47) and (50) are also obtained as a byproduct of the spline-fitting technique. In terms of parameters appearing in boundary-layer equations, we set $K_1 = K_{g_1}$ and $K_2 = K_{g_2}$. In addition to θ, h_1, h_2, K_1, and K_2, the boundary-layer equations contain K_{12} and K_{21} which are functions of the previously mentioned parameters. Also, the partial derivatives, $\partial\theta/\partial\phi$ and $\partial\theta/\partial\bar{y}$, are contained in the boundary-layer equations and obtained by spline-fitting θ versus ϕ and $\bar{y}$.

TURBULENCE MODEL

The solution of the system of equations (1) to (4) requires closure assumptions for the Reynolds stresses, $-\rho\overline{u'v'}$, $-\rho\overline{w'v'}$, and $-\rho\overline{v'H'}$. This can be done by a number of approaches. One approach is to use simple eddy-viscosity and mixing-length formulas for the Reynolds stresses. This method, also called the mean-field method, has been used by Cebeci and Smith (ref. 11), Bushnell and Beckwith (ref. 1), and Harris (ref. 2) as well as several others. Another approach is to use expressions that consider the rate of change of the Reynolds stresses in the governing equations. This method, called transport-equation method, has been used by Bradshaw (ref. 12), Donaldson and Sullivan (ref. 13), Hanjalić and Launder (ref. 14), and several others. In reference 15, Bradshaw presents an excellent discussion of both these methods.

For low-speed flows, both approaches work equally well. For high-speed flows, however, the mean-field method seems to be slightly better than the transport-equation method, chiefly because of the inadequate closure assumption accounting for the mean compression or dilatation effect. However, a recent report by Bradshaw (ref. 16) seems to improve substantially the predictions of his method for compressible flows. In either case, equations (1) to (4) are already quite difficult to solve, and there is no need to increase the computation time by using higher order turbulence models. For this reason, an eddy-viscosity formulation developed by Cebeci (refs. 3 and 4) is used in this study. According to this formulation, the boundary layer is divided into two regions, called inner and outer regions, and eddy-viscosity formulas are defined separately in each region.

For a nonorthogonal system (assuming no mass transfer), the inner eddy viscosity is defined by

$$\epsilon_{m,in} = L^2\left[\left(\frac{\partial u}{\partial y}\right)^2 + \left(\frac{\partial w}{\partial y}\right)^2 + 2\cos\theta\left(\frac{\partial u}{\partial y}\right)\left(\frac{\partial w}{\partial y}\right)\right]^{1/2} \tag{51}$$

where

$$L = 0.4y\left[1 - \exp\left(-y/A\right)\right] \tag{52}$$

The total shear stress evaluated at the wall is

$$\tau_{t,w} = \mu\left[\left(\frac{\partial u}{\partial y}\right)_w^2 + \left(\frac{\partial w}{\partial y}\right)_w^2 + 2\cos\theta\left(\frac{\partial u}{\partial y}\right)_w\left(\frac{\partial w}{\partial y}\right)_w\right]^{1/2} \tag{53}$$

The outer eddy viscosity is defined by the formula

$$\epsilon_{m,out} = \alpha\left|\int_0^\infty (u_{t,e} - u_t)dy\right| \tag{54}$$

where

$$u_{t,e} = \left(u_e^2 + w_e^2 + 2u_e w_e \cos\theta\right)^{1/2} \tag{55a}$$

$$u_t = \left(u^2 + w^2 + 2uw\cos\theta\right)^{1/2} \tag{55b}$$

and $\alpha = 0.0168$.

TRANSFORMATION OF THE GOVERNING EQUATIONS

Boundary-Layer Equations

Two-component vector potentials ψ and ϕ are defined such that

$$\left.\begin{aligned} \rho u h_2 \sin\theta &= \frac{\partial\psi}{\partial y} \\ \rho w h_1 \sin\theta &= \frac{\partial\Phi}{\partial y} \\ \overline{\rho v} h_1 h_2 \sin\theta &= -\left(\frac{\partial\psi}{\partial x} + \frac{\partial\Phi}{\partial z}\right) \end{aligned}\right\} \tag{56}$$

The following transformations are also defined

$$x = x \tag{57a}$$

$$z = z \tag{57b}$$

$$d\eta = \left(\frac{u_e}{\rho_e\mu_e s_1}\right)^{1/2}\rho\, dy \tag{57c}$$

$$\psi = \left(\rho_e\mu_e u_e s_1\right)^{1/2} h_2\, f(x,z,\eta)\sin\theta \tag{57d}$$

$$\Phi = \left(\rho_e\mu_e u_e s_1\right)^{1/2}\frac{w_e}{u_e}\, h_1\, g(x,z,\eta)\sin\theta \tag{57e}$$

where

$$s_1 = \int_0^x h_1 \, dx \tag{58}$$

Substituting equations (56) and (57) into equations (2) to (4), after considerable algebra, gives the following:

x-momentum equation:

$$(bf'')' + P_1 ff'' + P_2\left[c - (f')^2\right] + P_5(c - f'g') + P_6 f''g + P_8\left[c - (g')^2\right] = xP_{10}\left[f' \frac{\partial f'}{\partial x} - f'' \frac{\partial f}{\partial x} + P_7\left(g' \frac{\partial f'}{\partial z} - f'' \frac{\partial g}{\partial z}\right)\right] \tag{59}$$

z-momentum equation:

$$(bg'')' + P_1 fg'' + P_4(c - f'g') + P_3\left[c - (g')^2\right] + P_6 gg'' + P_9\left[c - (f')^2\right] = xP_{10}\left[f' \frac{\partial g'}{\partial x} - g'' \frac{\partial f}{\partial x} + P_7\left(g' \frac{\partial g'}{\partial z} - g'' \frac{\partial g}{\partial z}\right)\right] \tag{60}$$

Energy equation:

$$\left(\mu_1 E'\right)' + \mu_2 E' + \mu_3' = xP_{10}\left[f' \frac{\partial E}{\partial x} - E' \frac{\partial f}{\partial x} + P_7\left(g' \frac{\partial E}{\partial z} - E' \frac{\partial g}{\partial z}\right)\right] \tag{61}$$

Here, primes denote differentiation with respect to η and

$$P_1 = \frac{1}{2} + \frac{s_1}{2u_e h_1} \frac{\partial u_e}{\partial x} + \frac{s_1}{2\rho_e \mu_e h_1} \frac{\partial}{\partial x}(\rho_e \mu_e) - s_1\left(K_1 \cot\theta - \frac{K_{12}\cos\theta + K_{21}}{\sin^2\theta}\right) \tag{62a}$$

$$P_2 = \frac{s_1}{u_e h_1} \frac{\partial u_e}{\partial x} - K_1 s_1 \cot\theta \tag{62b}$$

$$P_3 = \frac{s_1}{u_e h_2} \frac{\partial w_e}{\partial z} - K_2 s_1 \frac{w_e}{u_e} \cot\theta \tag{62c}$$

$$P_4 = \frac{s_1}{w_e h_1} \frac{\partial w_e}{\partial x} + K_{21} s_1 \tag{62d}$$

$$P_5 = \frac{w_e}{u_e}\left(K_{12}s_1 + \frac{s_1}{u_e h_2}\frac{\partial u_e}{\partial z}\right) \tag{62e}$$

$$P_6 = \frac{w_e}{u_e}\left[\frac{s_1}{w_e h_2}\frac{\partial w_e}{\partial z} - \frac{s_1}{2u_e h_2}\frac{\partial u_e}{\partial z} + \frac{s_1}{2\rho_e \mu_e h_2}\frac{\partial}{\partial z}(\rho_e \mu_e) + \frac{1}{2h_2}\frac{\partial s_1}{\partial z}\right.$$

$$\left. - s_1\left(K_2 \cot\theta - \frac{K_{12} + K_{21}\cos\theta}{\sin^2\theta}\right)\right] \tag{62f}$$

$$P_7 = \frac{h_1}{h_2}\frac{w_e}{u_e} \tag{62g}$$

$$P_8 = \left(\frac{w_e}{u_e}\right)^2 K_2 s_1 \csc\theta \tag{62h}$$

$$P_9 = \frac{u_e}{w_e} K_1 s_1 \csc\theta \tag{62i}$$

$$P_{10} = \frac{s_1}{x h_1} \tag{62j}$$

and

$$\mu_1 = C\left(1 + \epsilon^+ \frac{N_{Pr}}{N_{Pr,t}}\right)\frac{1}{N_{Pr}} \tag{63a}$$

$$\mu_2 = P_1 f + P_6 g \tag{63b}$$

$$\mu_3 = C\frac{u_e^2}{H_e}\left(1 - \frac{1}{N_{Pr}}\right)\left[f'f'' + \frac{w_e^2}{u_e^2} g'g'' + \cos\theta \frac{w_e}{u_e}(g'f'' + f'g'')\right] \tag{63c}$$

$$E = \frac{H}{H_e} \tag{63d}$$

$$C = \frac{\rho\mu}{\rho_e \mu_e} \tag{63e}$$

$$b = C(1 + \epsilon_m^+) \tag{63f}$$

$$c = \frac{\rho_e}{\rho} \tag{63g}$$

In the preceding equations, eddy-viscosity and eddy-conductivity concepts have been used in order to satisfy the closure conditions for the Reynolds stresses. They are defined by

$$-\rho\overline{u'v'} = \rho\epsilon_m \frac{\partial u}{\partial y} \qquad -\rho\overline{w'v'} = \rho\epsilon_m \frac{\partial w}{\partial y} \qquad -\rho\overline{v'H'} = \rho\epsilon_H \frac{\partial H}{\partial y} \tag{64}$$

The turbulent Prandtl number $N_{Pr,t}$ and the dimensionless transport coefficients are defined by

$$N_{Pr;t} = \frac{\epsilon_m^+}{\epsilon_H^+} \qquad \epsilon_m^+ = \frac{\epsilon_m}{\nu} \qquad \epsilon^+ = \sqrt{2}\,\epsilon_m^+ \qquad \epsilon_H^+ = \frac{\epsilon_H}{\nu} \tag{65}$$

Equations (59) to (61) are subject to the following boundary conditions:

$$\left.\begin{array}{llll} \eta = 0 & f = g = 0 & f' = g' = 0 & E' = 0 \quad \text{(adiabatic wall)} \\ \eta \to \eta_\infty & f' \to 1 & g' \to 1 & E \to 1 \end{array}\right\} \tag{66}$$

Eddy-Viscosity Equations

The eddy-viscosity formulas given by equations (51) to (55) can also be transformed and expressed as

$$\epsilon_{m,in}^+ = \frac{\mu_e}{\mu}\left[0.4\left(\int_0^\eta \frac{\rho_e}{\rho}\,d\eta\right)\left(1 - e^{-y/A}\right)\frac{\rho}{\rho_e}\right]^2 \left\{R_e\left[(f'')^2 + \frac{w_e}{u_e}\,g''\left(2f'\cos\theta + \frac{w_e}{u_e}\,g''\right)\right]\right\}^{1/2} \tag{67}$$

$$\epsilon_{m,out}^+ = 0.0168\left(\frac{\mu_e\rho}{\rho_e\mu}\right)\sqrt{R_e}\left(\int_0^{\eta_\infty} \frac{\rho_e}{\rho}\left\{\left[1 + \frac{w_e}{u_e}\left(2\cos\theta + \frac{w_e}{u_e}\right)\right]^{1/2}\right.\right.$$

$$\left.\left. - \left[(f')^2 + \frac{w_e}{u_e}\,g'\left(2f'\cos\theta + \frac{w_e}{u_e}\,g'\right)\right]^{1/2}\right\} d\eta\right) \tag{68}$$

where

$$\frac{y}{A} = \frac{1}{26}\left(\frac{\mu_w}{\mu_e}\right)^{1/2} R_e^{1/4}\left[\frac{(\rho/\rho_e)^2}{C}\int_0^\eta \frac{\rho_e}{\rho}\,d\eta\right]\left[(f_w')^2 + \frac{w_e}{u_e}\,g_w''\left(2f_w'\cos\theta + \frac{w_e}{u_e}\,g_w''\right)\right]^{1/4} \tag{69}$$

NUMERICAL METHOD

The Cebeci-Keller Box method is used to solve the governing boundary-layer equations given by equations (59) to (61). This is a two-point finite-difference method devel-

oped by H. B. Keller (ref. 17) and applied to the boundary-layer equations by Keller and Cebeci (refs. 5 and 6). The method is discussed in detail in references 6 and 11. For this reason only a brief description will be given here.

One of the basic ideas of this method is to write the governing system of equations in the form of a first-order system. Thus, derivatives of some quantities with respect to the "normal" variable must be introduced as new unknown functions. Derivatives with respect to all other variables occur only to first order as a consequence of the boundary-layer approximations. With the resulting first-order system and an arbitrary rectangular net, centered difference quotients and averages at the midpoints of net rectangles and net segments are used, as required, to get $O(h^2)$ accurate finite-difference equations.

This method is unconditionally stable; however, the equations are highly implicit and nonlinear. Newton's method is employed to solve them. In order to do this with an efficient and stable computational scheme, a block-tridiagonal factorization scheme is used.

Numerical Formulation of the Momentum Equations

New dependent variables $u(x,z,\eta)$, $v(x,z,\eta)$, $w(x,z,\eta)$, and $t(x,z,\eta)$ are introduced, so that equations (59) and (60) can be written as

$$(bv)' + P_1 fv + P_2(c - u^2) + P_5(c - uw) + P_6 gv + P_8(c - w^2) = xP_{10}\left[u\frac{\partial u}{\partial x} - v\frac{\partial f}{\partial x} + P_7\left(w\frac{\partial u}{\partial z} - v\frac{\partial g}{\partial z}\right)\right] \tag{70a}$$

$$(bt)' + P_1 ft + P_4(c - uw) + P_3(c - w^2) + P_6 gt + P_9(c - u^2) = xP_{10}\left[u\frac{\partial w}{\partial x} - t\frac{\partial f}{\partial x} + P_7\left(w\frac{\partial w}{\partial z} - t\frac{\partial g}{\partial z}\right)\right] \tag{70b}$$

$$f' = u \tag{70c}$$

$$u' = v \tag{70d}$$

$$g' = w \tag{70e}$$

$$w' = t \tag{70f}$$

For the net cube shown in figure 8, the net points are

$$x_0 = 0 \qquad x_n = x_{n-1} + k_n \qquad (n = 1, 2, \ldots, N) \tag{71a}$$

$$z_0 = 0 \qquad z_i = z_{i-1} + r_i \qquad (i = 1, 2, \ldots, I) \tag{71b}$$

$$\eta_0 = 0 \qquad \eta_j = \eta_{j-1} + h_j \qquad (j = 1, 2, \ldots, J) \tag{71c}$$

where k_n, r_i, and h_j are defined in figure 8.

The difference equations which are to approximate equations (70c) to (70f) are obtained by averaging about the midpoint $\left(x_{n-\frac{1}{2}}, z_{i-\frac{1}{2}}, \eta_{j-\frac{1}{2}}\right)$

$$\frac{f_j^{n,i} - f_{j-1}^{n,i}}{h_j} = u_{j-\frac{1}{2}}^{n,i} \tag{72a}$$

$$\frac{u_j^{n,i} - u_{j-1}^{n,i}}{h_j} = v_{j-\frac{1}{2}}^{n,i} \tag{72b}$$

$$\frac{g_j^{n,i} - g_{j-1}^{n,i}}{h_j} = w_{j-\frac{1}{2}}^{n,i} \tag{72c}$$

$$\frac{w_j^{n,i} - w_{j-1}^{n,i}}{h_j} = t_{j-\frac{1}{2}}^{n,i} \tag{72d}$$

where, for example,

$$u_{j-\frac{1}{2}}^{n,i} = \frac{1}{2}\left(u_j^{n,i} + u_{j-1}^{n,i}\right)$$

The difference equations used to approximate equations (70a) and (70b) are rather lengthy. To illustrate the difference equations, an example equation similar to equations (70a) and (70b) is chosen as follows:

$$v' + P_1 f v = x\left(u \frac{\partial u}{\partial x} + P_7 w \frac{\partial u}{\partial z}\right) \tag{73}$$

The difference equations for this equation are

$$\frac{\bar{v}_j - \bar{v}_{j-1}}{h_j} + (P_1)_{i-\frac{1}{2}}^{n-\frac{1}{2}} \overline{(fv)}_{j-\frac{1}{2}} = x^{n-\frac{1}{2}}\left[\bar{u}_{j-\frac{1}{2}}\left(\frac{\bar{u}_n - \bar{u}_{n-1}}{k_n}\right) + (P_7)_{i-\frac{1}{2}}^{n-\frac{1}{2}} \bar{w}_{j-\frac{1}{2}}\left(\frac{\bar{u}_i - \bar{u}_{i-1}}{r_i}\right)\right] \tag{74}$$

where, for example,

$$\bar{v}_j = \frac{1}{4}\left(v_j^{n,i} + v_j^{n,i-1} + v_j^{n-1,i-1} + v_j^{n-1,i}\right)$$

$$\bar{u}_n = \frac{1}{4}\left(u_j^{n,i} + u_j^{n,i-1} + u_{j-1}^{n,i} + u_{j-1}^{n,i-1}\right)$$

$$\bar{u}_i = \frac{1}{4}\left(u_j^{n,i} + u_j^{n-1,i} + u_{j-1}^{n,i} + u_{j-1}^{n-1,i}\right)$$

$$P_{i-\frac{1}{2}}^{n-\frac{1}{2}} = \frac{1}{4}\left(P_i^n + P_{i-1}^n + P_i^{n-1} + P_{i-1}^{n-1}\right)$$

The boundary conditions for equations (70) evaluated at $x = x_n$ and at $z = z_i$ are

$$\left.\begin{array}{lll} f_0^{n,i} = 0 & g_0^{n,i} = 0 & u_0^{n,i} = 0 \\ w_0^{n,i} = 0 & u_J^{n,i} = 1 & w_J^{n,i} = 1 \end{array}\right\} \tag{75}$$

If $\left(f_j^{n-1,i-1}, u_j^{n-1,i-1}, v_j^{n-1,i-1}, g_j^{n-1,i-1}, w_j^{n-1,i-1}, t_j^{n-1,i-1}\right)$, $\left(f_j^{n,i-1}, u_j^{n,i-1}, v_j^{n,i-1}, g_j^{n,i-1}, w_j^{n,i-1}, t_j^{n,i-1}\right)$, and $\left(f_j^{n-1,i}, u_j^{n-1,i}, v_j^{n-1,i}, g_j^{n-1,i}, w_j^{n-1,i}, t_j^{n-1,i}\right)$ are assumed to be known for $0 \leq j \leq J$, then the difference equations (70a), (70b), (72), and (75) yield an implicit nonlinear algebraic system of $6J + 6$ equations in as many unknowns $\left(f_j^n, u_j^n, v_j^n, g_j^n, w_j^n, t_j^n\right)$. This nonlinear system is solved by means of Newton's method. The resulting linearized system is then solved very efficiently by using the block elimination method discussed by Isaacson and Keller (ref. 18).

Numerical Formulation of the Energy Equation

A new dependent variable $G(x,z,\eta)$ is defined as

$$G = E' \tag{76a}$$

and equation (61) is written as

$$\left(\mu_1 G\right)' + \mu_2 G + \mu_3' = xP_{10}\left[u\frac{\partial E}{\partial x} - G\frac{\partial f}{\partial x} + P_7\left(w\frac{\partial E}{\partial z} - G\frac{\partial g}{\partial z}\right)\right] \tag{76b}$$

The difference equation for (76a) is written again by averaging about the midpoint $\left(x_n, z_i, \eta_{j-\frac{1}{2}}\right)$, and is similar to those given by equation (72). The difference equation for equation (76b) is written similar to equation (74). The boundary conditions for an adiabatic wall are

$$G_0^{n,i} = 0 \qquad E_J^{n,i} = 1 \tag{77}$$

The resulting algebraic system of $2J + 2$ equations in as many unknowns $\left(E_j^{n,i}, G_j^{n,i}\right)$, which is linear, is directly solved by the block elimination method.

RESULTS AND DISCUSSION

One obvious difficulty in evaluating the accuracy of the three-dimensional turbulent boundary-layer calculations on wings is the lack of complete, reliable data. Fortunately, however, there are a few good data available for flows with simple geometries. Calculations for these flows serve the useful purpose of evaluating the turbulence models used for the Reynolds stresses. References 3 and 4 present several comparisons of calculations with experimental data. Although these comparisons are for flows over simple geometries and the calculations are for a coordinate system different than the one considered here, the generally good agreement observed in those calculations gives some confidence in the accuracy of the turbulence model used in this study. Figure 9, taken from reference 19, shows the flow geometry and comparisons of calculated and experimental results for a planar turbulent boundary-layer flow approaching a three-dimensional obstacle. The results shown are for velocity profiles in a gradually steepening adverse pressure gradient flow off the plane of symmetry. The calculations were made for a Cartesian coordinate system which can be obtained from the present equations by setting $h_1 = h_2 = 1$, $K_1 = K_2 = K_{12} = K_{21} = 0$, and $\theta = \pi/2$.

Skin-friction coefficients are presented in figure 10 for the upper surface of a swept wing whose planform is given in reference 10. The calculations were made by obtaining the velocity components from the experimental pressure distribution by the procedure discussed earlier. To simulate the actual geometry, a reasonable thickness distribution was added to the planar wing considered in reference 10. As in reference 10, the calculations were made for a unit Reynolds number of 4.92×10^6 per meter and for a free-stream Mach number M_∞ of 0.5. In the figure $z = 1.778$ m represents an inboard station on the wing and $z = 4.572$ m represents a station in the middle of the outboard panel of the wing. The skin-friction coefficients are defined as surface shear-stress components normalized with free-stream dynamic pressure. Here, $c_{f,x}$ represents the shear-stress component in the x-coordinate direction and $c_{f,z}$ represents the shear-stress component normal to the x-coordinate in the tangent plane. In physical and transformed coordinates, they are defined by the following formulas:

$$c_{f,x} = \frac{\tau_x + \tau_z \cos\theta}{\frac{1}{2}\rho_\infty u_\infty^2} = \frac{2C_w}{\sqrt{R_e}}\left(\frac{\rho_e}{\rho_\infty}\right)\left[\left(\frac{u_e}{u_\infty}\right)^2 f_w'' + \frac{u_e w_e}{u_\infty^2} g_w'' \cos\theta\right] \tag{78}$$

$$c_{f,z} = \frac{\tau_z \sin\theta}{\frac{1}{2}\rho_\infty u_\infty^2} = \frac{2C_w}{\sqrt{R_e}}\left(\frac{\rho_e}{\rho_\infty}\right)\frac{u_e w_e}{u_\infty^2} g_w'' \sin\theta \tag{79}$$

Although the present results and those of reference 10 are qualitatively similar, there are several quantitative differences between the two predictions. One possible reason for the differences could be the starting procedure used to compute the initial conditions along the spanwise direction. Our calculations were made for a turbulent flow starting at approximately 3-percent chord whereas the calculations of reference 10 were made with transition to turbulent flow occurring at 10-percent chord. Another possible reason for the differences could be the procedure used to get the velocity components from the experimental pressure distribution.

The method described in the previous section resulted in the three computer programs which are used separately from each other. One computer program deals with the calculation of the velocity components from the experimental pressure distribution by using the sweep theory. Obviously if the velocity components are known from the inviscid flow theory, then this program is not needed. The second computer program deals with the calculation of the nonorthogonal coordinate system and its geometric parameters, namely, the metric coefficients h_1, h_2, K_1, and K_2 appearing in the governing boundary-layer equations. Through the use of this program, the coordinate system and its geometric parameters are calculated once and for all for a given wing. The data is punched out on cards to be stored. If no changes are made in the airfoil cross sections, then this data can be used for any number of boundary-layer calculations without using the second computer program again. The third computer program deals with the solution of the governing boundary-layer equations for a nonorthogonal system using the very efficient and accurate Cebeci-Keller Box method. This program assumes that initial conditions on two intersecting lines are given. In the present program, the two intersecting lines correspond to the wing-fuselage junction and to a line along the span a small fraction of the chord length away from the leading edge. This computer program solves the boundary-layer equations in a surprisingly small amount of time for a given external velocity distribution (either experimental or theoretical) and for a given wing coordinate system for both incompressible and compressible flows. The results in figure 10, for example, were obtained for a wing consisting of 29 z-stations and 19 x-stations with 30 η-points across the boundary layer. The total central-processing-unit (CPU) time for all stations is approximately 30 sec on an IBM 370/165 computer.

FUTURE WORK

The method described here has been tested for only one flow condition. It lacks certain important features and capabilities that may become very useful at different flow conditions, particularly for the third computer program which solves the boundary-layer equations. These features and capabilities conveniently can be divided into three separate tasks.

1. It is desirable and useful to include the capability of starting the calculations at the stagnation line rather than some small distance aft of the stagnation line as in the present procedure. This task involves the solution of a special set of equations, called attachment-line equations. With this capability, the solution of one of the initial lines (stagnation line) becomes exact but remains approximate (though a good approximation) on the other initial line (wing-fuselage juncture) as before.

2. In the present method, the dimensionless cross-flow velocity is defined by $g' = w/w_e$. However, this definition is not very convenient. In some problems where the outer velocity component w_e changes sign, certain ambiguities arise. For example, if the cross flow at the outer edge of the boundary layer becomes slightly negative but remains positive in the rest of the boundary layer, the value of g' will suddenly change sign from one station to the next. This introduces some discontinuity in the flow field since as w_e goes through zero, the value of g' becomes infinite at some net point between the two calculation stations. To avoid this problem, the transformation needs to be changed slightly and the cross-flow velocity w normalized by some reference velocity which does not change sign.

3. A very important study that needs to be conducted involves the procedure with which the calculations are advanced in the spanwise direction. In the present program, a special solution at the root station is obtained prior to calculating the boundary layers on consecutive spanwise stations. At each spanwise station the solution starts with an initial profile and proceeds along the chord until w_e becomes negative. At that point, the program proceeds to the next spanwise station and initiates the calculation at the leading edge and so on. With this procedure the wing is covered from the root to the tip. It should be noted that region I is defined to be the region where w_e is positive. The calculations in region II (this corresponds to the region where w_e is negative) start from the wing tip. The same approximate boundary-layer equations are solved as for the wing-root section to generate the initial conditions along the chord at the wing tip. The rest of the calculation procedure is identical to region I except that now marching is in the inboard direction as the boundary layer is calculated in consecutive spanwise stations all the way to the wing root.

This procedure of marching back and forth requires further study. If there is another region where the cross-flow velocity w_e changes sign, proper logic must be incorporated in the computer program.

An alternative procedure to define separate regions can be utilized by the appearance of negative cross-flow velocity. In such cases, a procedure similar to the present marching procedure can be used. The proper marching procedure requires an extensive and careful study since the locus of streamlines is unknown a priori on complex geometries. An efficient method can only be found by making the actual calculations and changing and testing the logic as required.

REFERENCES

1. Bushnell, Dennis M.; and Beckwith, Ivan E.: Calculation of Nonequilibrium Hypersonic Turbulent Boundary Layers and Comparisons With Experimental Data. AIAA J., vol. 8, no. 8, Aug. 1970, pp. 1462-1469.

2. Harris, Julius E.: Numerical Solution of the Equations for Compressible Laminar, Transitional, and Turbulent Boundary Layers and Comparisons With Experimental data. NASA TR R-368, 1971.

3. Cebeci, Tuncer: Calculation of Three-Dimensional Boundary Layers. I. Swept Infinite Cylinders and Small Cross Flow. AIAA J., vol. 12, no. 6, June 1974, pp. 779-786.

4. Cebeci, Tuncer: A General Method for Calculating Three-Dimensional Incompressible Laminar and Turbulent Boundary Layers. Rep. No. MDC J6517 (Contract No. N00014-72-C-0111), McDonnell Douglas Corp., Mar. 1974. (Available from DDC as AD 779 616.)

5. Keller, Herbert B.; and Cebeci, Tuncer: Accurate Numerical Method for Boundary Layer Flows. I. Two Dimensional Laminar Flows. Proceedings of the Second International Conference on Numerical Methods in Fluid Dynamics. Volume 8 of Lecture Notes in Physics, Maurice Holt, ed., Springer-Verlag, 1971, pp. 92-100.

6. Keller, Herbert B.; and Cebeci, Tuncer: Accurate Numerical Methods for Boundary-Layer Flows. II: Two-Dimensional Turbulent Flows. AIAA J., vol. 10, no. 9, Sept. 1972, pp. 1193-1199.

7. Squire, L. C.: The Three-Dimensional Boundary-Layer Equations and Some Power Series Solutions. R. & M. No. 3006, British A.R.C., 1957.

8. Hansen, Arthur G.: Compressible, Three-Dimensional, Laminar Boundary Layers – A Survey of Current Methods of Analysis. Douglas Paper 3105, Douglas Aircraft Co., Inc., Sept. 28, 1964.

9. Method for Predicting the Pressure Distribution on Swept Wings With Subsonic Attached Flow. Transonic Data Mem. 6312, Roy. Aeronaut. Soc. (London), Dec. 1963.

10. Nash, J. F.; and Scruggs, R. M.: Three-Dimensional Compressible Boundary-Layer Computations for a Finite Swept Wing. NASA CR-112158, [1972].

11. Cebeci, Tuncer; and Smith, A. M. O.: Analysis of Turbulent Boundary Layers. Academic Press, Inc., 1974.

12. Bradshaw, P.: Calculation of Three-Dimensional Turbulent Boundary Layers. J. Fluid Mech., vol. 46, pt. 3, Apr. 13, 1971, pp. 417-445.

13. Donaldson, Coleman duP.; and Sullivan, Roger D.: An Invariant Second-Order Closure Model of the Compressible Turbulent Boundary Layer on a Flat Plate. Contract No. NASW-2224, Aeronaut. Res. Assoc. Princeton, Inc., June 1972. (Available as NASA CR-128172.)

14. Hanjalić, K.; and Launder, B. E.: A Reynolds Stress Model of Turbulence and Its Application to Thin Shear Flows. J. Fluid Mech., vol. 52, pt. 4, Apr. 25, 1972, pp. 609-638.

15. Bradshaw, P.: The Understanding and Prediction of Turbulent Flow. J. Roy. Aeronaut. Soc., vol. 76, no. 739, 1972, pp. 403-418.

16. Bradshaw, P.: Anomalous Effects of Pressure Gradient on Supersonic Turbulent Boundary Layers. Rep. No. 72-21, Aeronaut. Dep., Imperial College Sci. & Technol., Nov. 1972.

17. Keller, Herbert B.: A New Difference Scheme for Parabolic Problems. Numerical Solution of Partial Differential Equations – II, Bert Hubbard, ed., Academic Press, Inc., 1971, pp. 327-350.

18. Isaacson, Eugene; and Keller, Herbert Bishop: Analysis of Numerical Methods. John Wiley & Sons, Inc., c.1966.

19. East, L. F.; and Hoxey, R. P.: Low-Speed Three-Dimensional Turbulent Boundary-Layer Data. Parts 1 and 2. R. & M. No. 3653, British A.R.C., 1971.

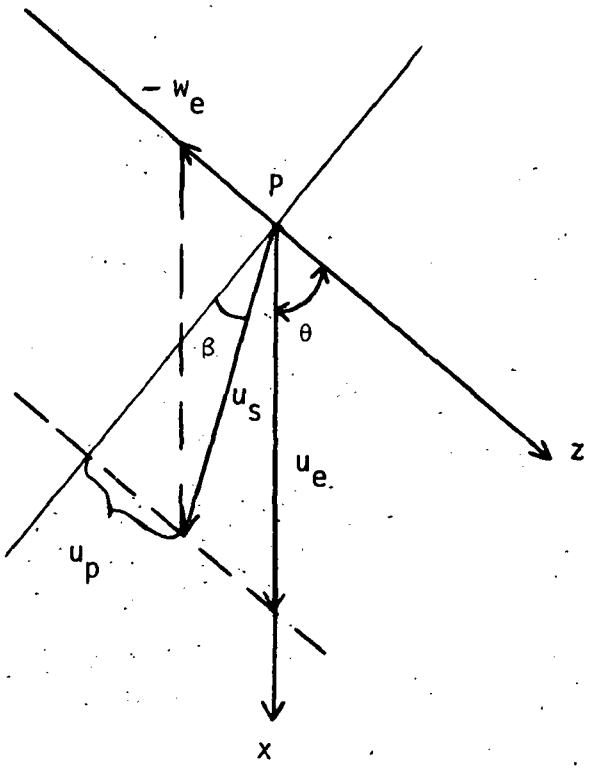

Figure 1.- Velocity vector in the tangent plane at a point P on the wing.

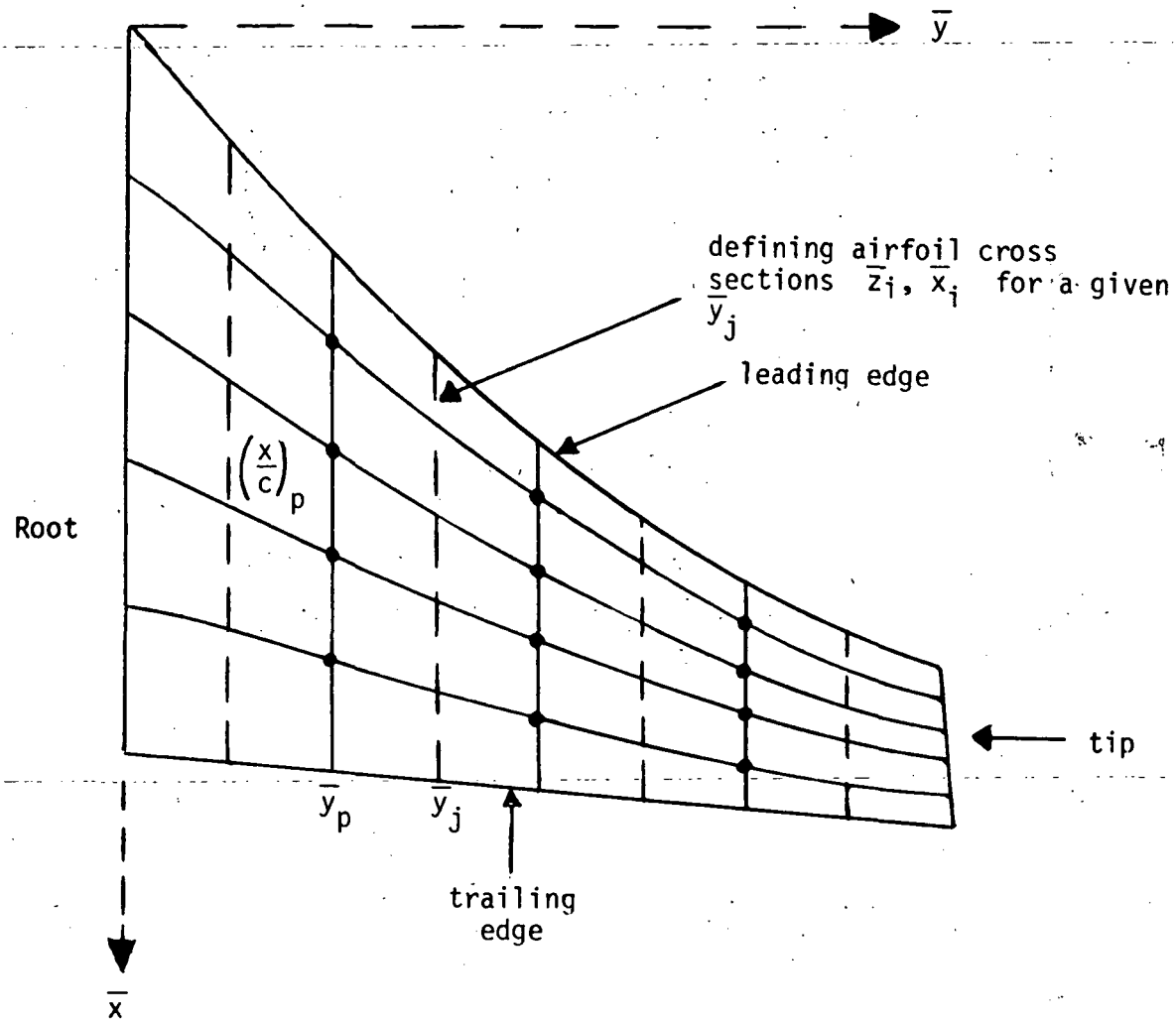

Figure 2.- Schematic of typical wing.

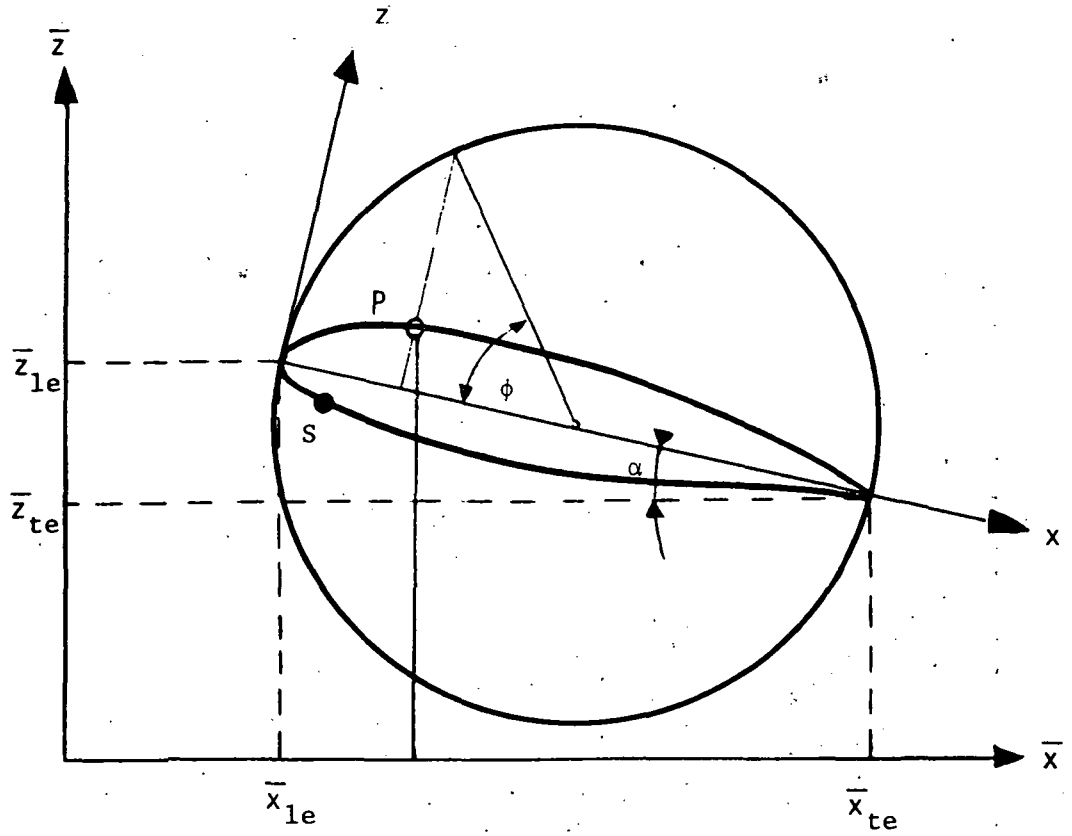

Figure 3.- Notation for the airfoil section for a given $\bar{y}_j$.

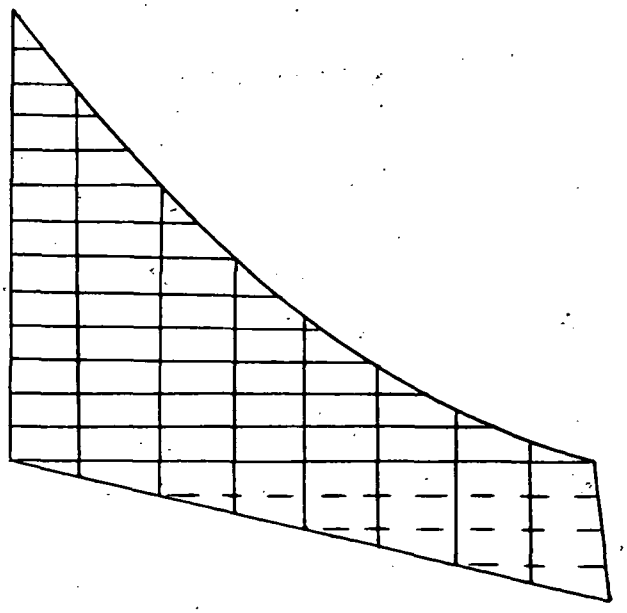

Figure 4.- An orthogonal system for the wing.

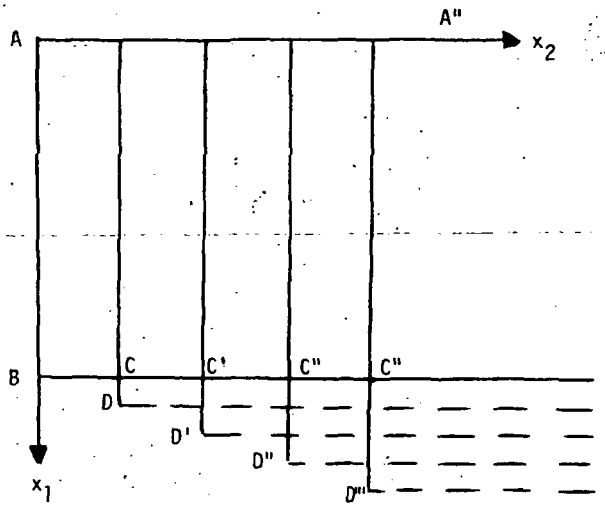

Figure 5.- Wing in the x_1 and x_2 plane.

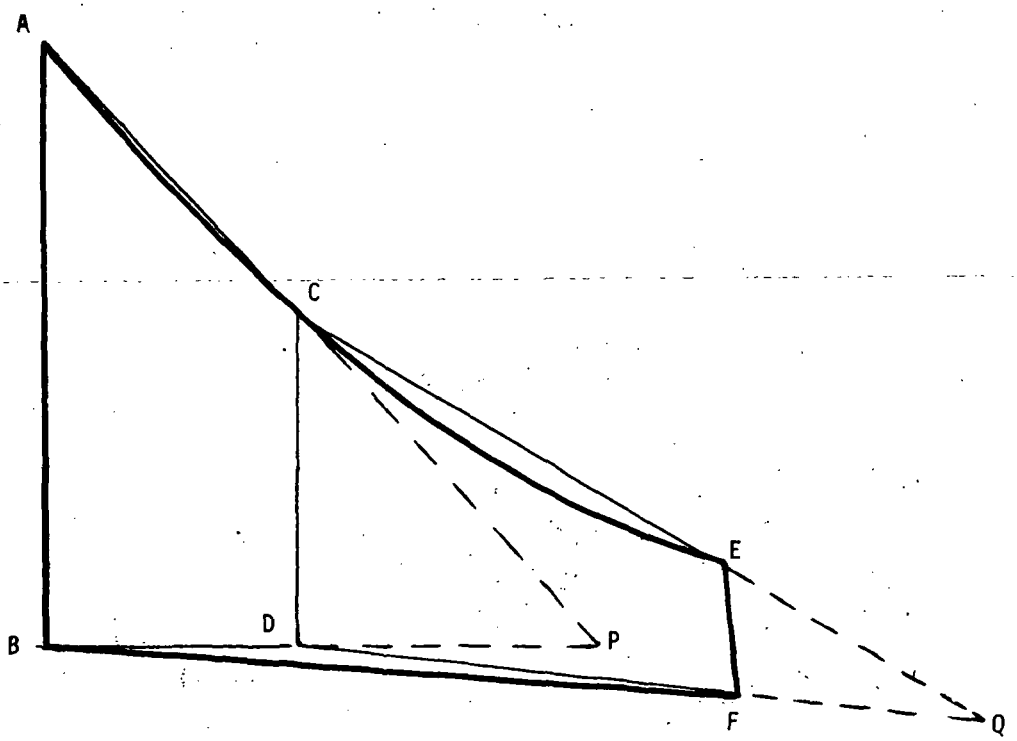

Figure 6.- Representation of the wing by conical sections.

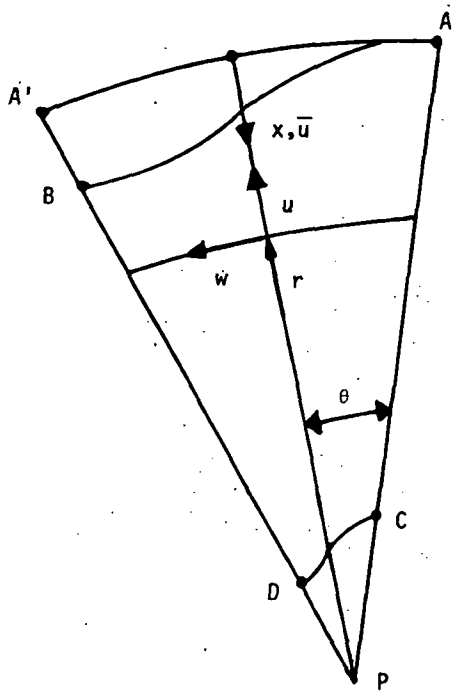

Figure 7.- Notation for conical section ABDC and the coordinate system in the developed plane.

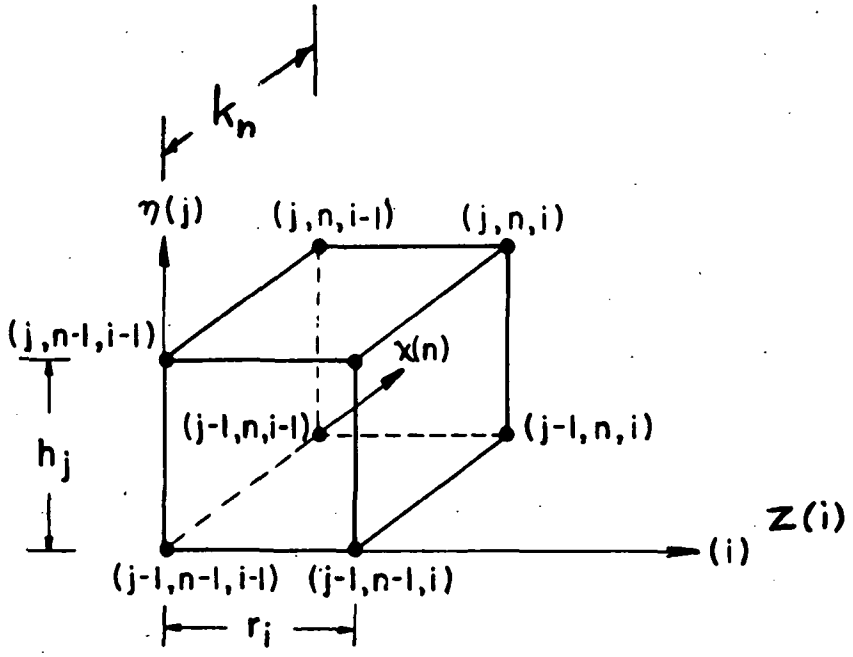

Figure 8.- Net cube for the difference equations for three-dimensional flows.

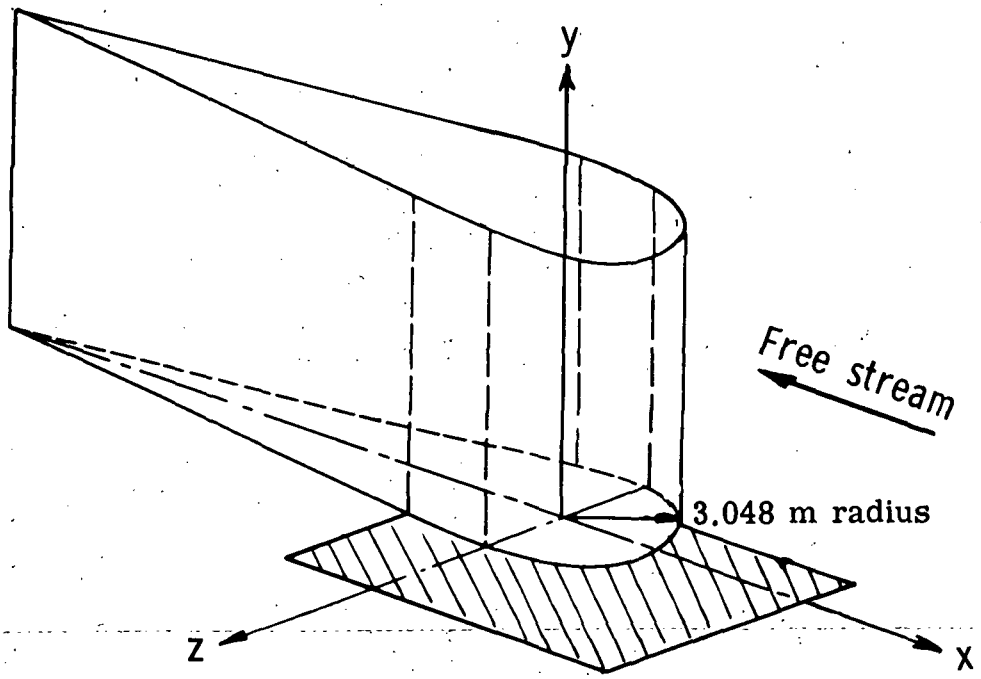

(a) Schematic drawing of test setup.

Figure 9.- Comparisons of numerical results with experimental data.

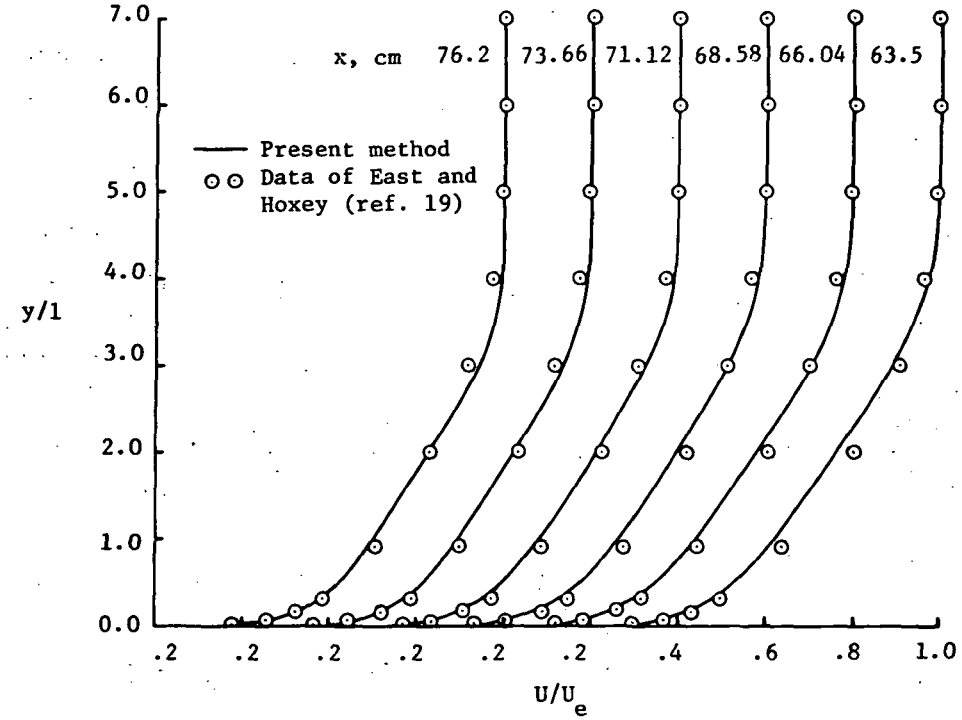

(b) z = 5.09 cm (1 = 2.54 cm).

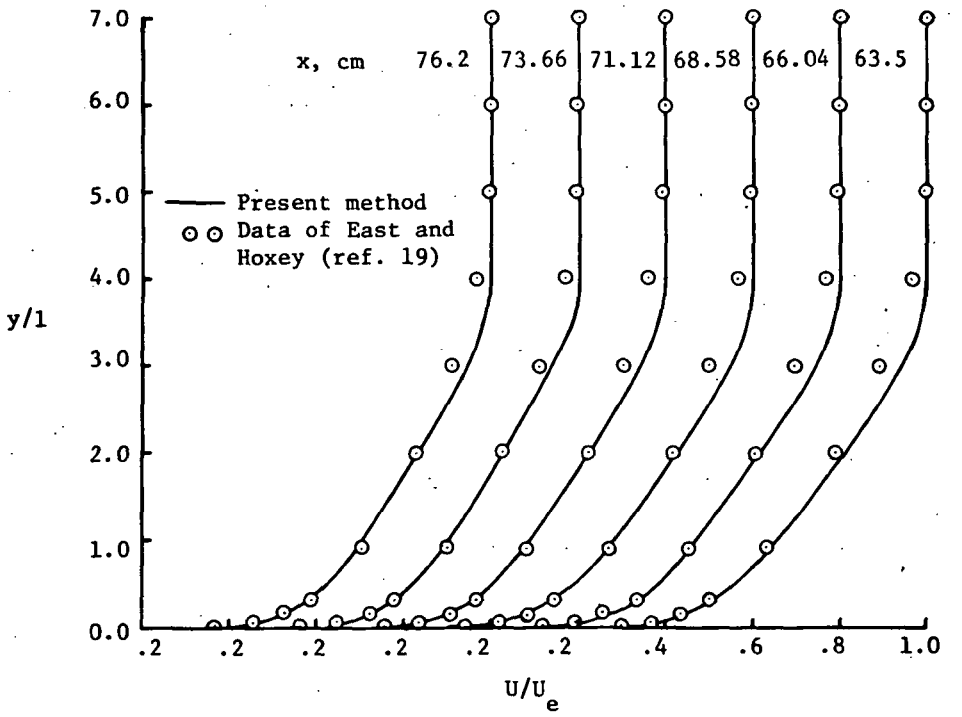

(c) z = 7.62 cm (1 = 2.54 cm).

Figure 9.- Concluded.

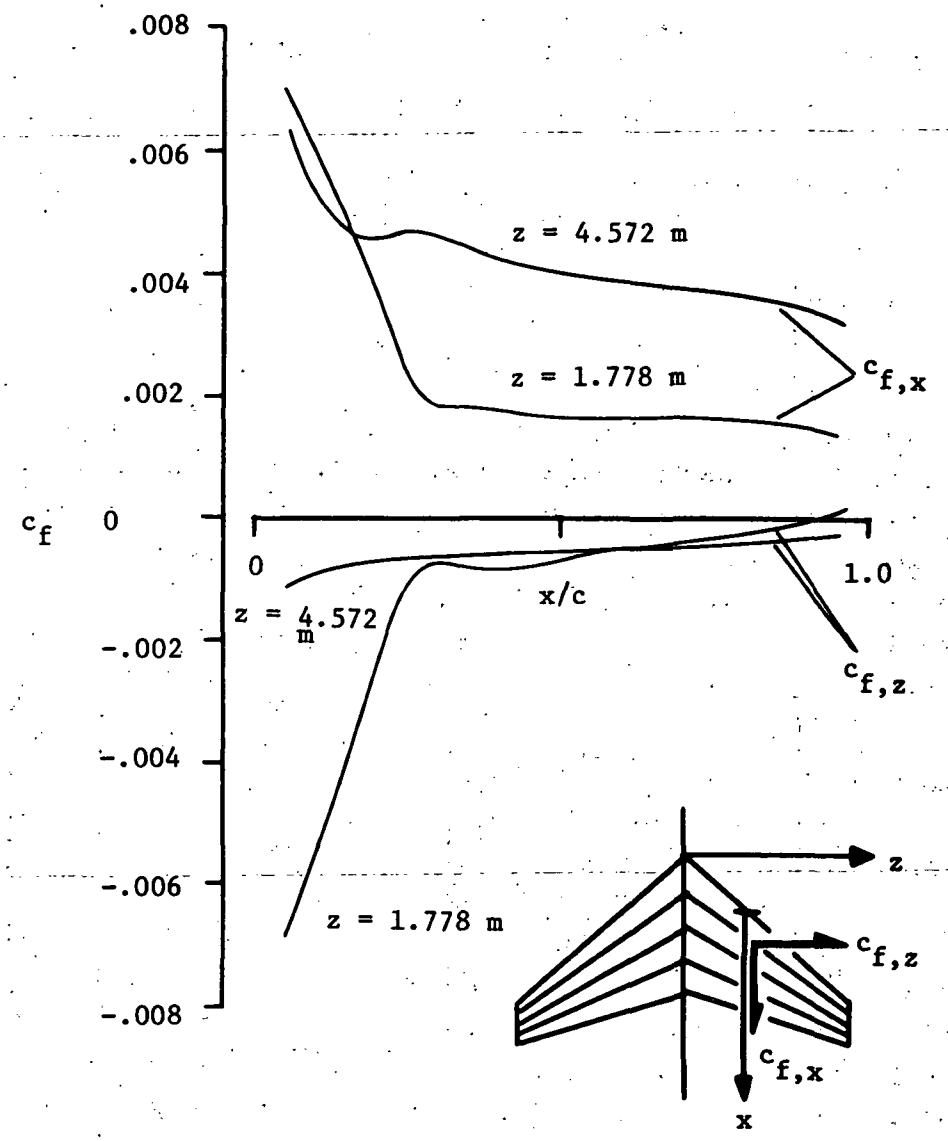

Figure 10.- Calculated skin-friction coefficients for upper surface of a swept wing. Schematic of planform illustrates notation and does not represent calculated wing.

CALCULATION OF THREE-DIMENSIONAL COMPRESSIBLE LAMINAR AND TURBULENT BOUNDARY FLOWS

THREE-DIMENSIONAL COMPRESSIBLE BOUNDARY LAYERS OF REACTING GASES OVER REALISTIC CONFIGURATIONS

By Robert M. Kendall, William S. Bonnett, Charles T. Nardo, and Michael J. Abbett
Aerotherm Division, Acurex Corporation

SUMMARY

A three-dimensional boundary-layer code has been developed for particular application to realistic hypersonic aircraft, but it is very general and can be applied to a wide variety of boundary-layer flows. Laminar, transitional, and fully turbulent flows of compressible, reacting gases can be efficiently calculated by use of the code. A body-oriented orthogonal coordinate system is used for the calculation and the user has complete freedom in specifying the coordinate system within the restrictions that one coordinate must be normal to the surface and the three coordinates must be mutually orthogonal.

The boundary-layer equations are discretized and integrated step by step. The integration is fully implicit in the streamwise direction, a condition that is especially important for realistic configurations since it enables one to calculate flows having cross-flow attachment and detachment lines off the pitch plane. The code is restricted to those flows which are adequately represented by the boundary-layer equations; the analysis must be extended to adequately describe flows in which cross-flow diffusion effects are important near cross-flow attachment lines. The numerical algorithm includes splined functions for dependent variables between nodes to minimize the number of nodes normal to the surface. This condition results in an extremely efficient solution procedure for reacting boundary layers. Finally, the code includes the capability to account for surface normal entropy gradient effects.

INTRODUCTION

The design of aircraft and aerospace vehicles requires consideration of the inviscid/viscous flow field over the vehicle. Historically, the aerothermal environment of such aircraft in realistic flight conditions has been predicted by synthesizing empirical

data from ground-level test facilities with simplified analyses to correlate the test results with the anticipated flight environment. This approach depends on the development of scaling laws between ground and flight conditions. As flight regimes are further extended in altitude and speed to those appropriate to space shuttle and hypersonic research aircraft, the range of applicability of scaling laws and correlations relating results from existing test facilities to flight conditions becomes more uncertain. The cost of constructing test facilities which will yield data of sufficient quality and range to duplicate realistic vehicles and trajectories is prohibitive.

Parallel with the increased flight range typified by spacecraft, space shuttle, and hypersonic research aircraft has been a rapid increase in the ability to obtain numerically exact solutions to the complete gas dynamic equations for the inviscid/viscous flow field about such configurations. Currently, under contract NAS 1-11525 (ref. 1), The National Aeronautics and Space Administration is supporting the development of a computer code which will obtain the inviscid flow field solution. To predict adequately the viscous drag and heat flux distributions, one must obtain the solution of the three-dimensional boundary-layer equations describing the viscous layer adjacent to the vehicle surface. In this paper recent efforts which have culminated in the development of a computer code for solving general three-dimensional laminar and turbulent chemically reacting boundary layers are summarized.

The numerical approach used is based on the results of two pilot codes for calculating three-dimensional boundary layers on pointed cones at angle of attack as well as broad experience in developing and applying boundary-layer codes in two dimensions. Key elements in the approach are:

(a) Splined functions to minimize nodes through the boundary-layer thickness

(b) Finite differences used for cross-flow derivatives

(c) Physical variables, simplifying analyses, and changes in turbulent transport properties model

(d) Fully implicit solution procedure; thereby the convenient calculation of flows having off-pitch-plane attachment and detachment lines is permitted

(e) Relative ease in incorporating a wide variety of turbulence models and boundary conditions, including entropy layer, specified surface temperature or heat flux, surface catalysis, mass addition, coupling with surface ablation calculations, etc.

(f) Very reasonable computing time

The result is a code which can accurately describe laminar boundary-layer profiles with 7 to 10 nodes and turbulent profiles with 12 to 15 nodes through the boundary layer. The number of nodes through the boundary layer is important for reacting boundary layers

because the time required to evaluate the chemical state dominates the time spent in matrix inversion for macroscopic quantities u, v, w, and T where T is the temperature. Hence, the time implication of the number of nodes is more serious than it would be for homogeneous boundary layers. Conventional implicit finite-difference approaches are less complicated analytically but require significantly more nodes in the plane normal to the wall boundary than do splined function procedures, simply because the latter relate not only the dependent variables but also their derivatives with the nodal variation of the independent variables.

Three-dimensional boundary layers exhibit certain physical and mathematical characteristics which have important implications on the selection of a numerical solution technique. Particularly important to this effort are physical and mathematical modeling in the vicinity of outflow and inflow lines, lines where the surface streamlines diverge or converge. The windward side pitch plane line of a pointed cone at incidence is an example of an outflow line, whereas the leeward side pitch plane meridian at small incidence typifies an inflow line. These lines are often found off the pitch plane on both the windward and leeward sides of configurations such as the space shuttle. They are important physically because they are often regions of local maximum or minimum heat flux rates. Mathematically, they are extremely important because of a numerical approach often taken in solving three-dimensional boundary-layer flows, namely, integrating with cross flow.

Consider the pointed cone at incidence. Because the flow direction is strictly away from the windward pitch plane (except right on the pitch plane), one expects and finds that by assuming small circumferential derivatives, the solution of the boundary layer in the pitch plane can be determined completely independent of the boundary-layer solution off the pitch plane.[1] Assume for the moment that one has the entire flow field solution (inviscid and boundary layer) at some axial station x_0 and wishes to advance to $x_1 = x_0 + \Delta x$ where the inviscid solution is known (Δx is the mesh point spacing). As noted above, the windward pitch plane solution can be obtained directly. Then, by recalling that the initial value problem is hyperbolic-like with respect to the circumferential coordinate and parabolic with respect to the surface normal, the boundary-layer solution can be obtained by marching around the cone from the windward to the leeward side.

In contradistinction is the class of fully implicit solution procedures in which the solution at $x_1 = x_0 + \Delta x$ is obtained simultaneously at all points. In the fully implicit procedure each point at x_1 is influenced by and influences every other point. The influ-

[1] Of course, one needs information about the behavior of the edge inviscid flow in the vicinity of the pitch plane and of the pressure, temperature, velocity components, etc. (that is, not only p_e, T_e, u_e, etc., but also $\partial p_e/\partial \phi$, etc.).

ence will be large or negligibly small according to the actual physical influences, provided that the numerical scheme is accurate.

The circumferential marching methods require that one integrate the system in the direction of positive cross-flow velocity in order to obey the laws of propagation of signals. Marching against the cross flow results in instability. On a cone at very small incidence this is no problem, for the cross flow is always from windward to leeward. At higher incidence the cross-flow inflow line moves off the leeward meridian, and it is necessary to march from both the windward and the leeward meridians toward the cross-flow inflow line. Furthermore, the marching methods can have stability limits on the streamwise integration step size, and the allowable step size decreases linearly with the meridional spacing. Fully implicit schemes usually have no such integration step size limit, the only limit being one of accuracy.

Having used the pointed cone problem to clarify the situation, consider now a realistic configuration such as the space shuttle. Typical outflow and inflow lines on the windward side are shown in sketch (a). Obviously, the solution along the pitch plane out-

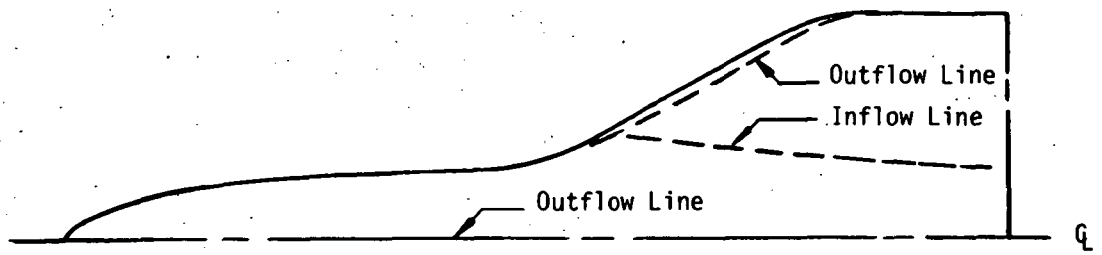

Sketch (a).- Schematic of inflow and outflow lines.

flow line can be obtained independently of the rest of the boundary layer by assuming small cross-flow derivatives. This is not the case for the wing leading edge because there are no symmetry conditions there which could be used to simplify the three-dimensional boundary-layer equations. In fact, without solving the complete problem, one does not know the locus of the outflow line there. Swept cylinder theory could be used to obtain an approximate solution along the wing leading edge, but this would be inconsistent with the spirit of an exact boundary-layer calculation. This is particularly important since the wing leading edge is a region of locally very high heat fluxes. The advantage of the fully implicit approach is apparent, for the exact solution including the wing leading-edge region can be obtained without resort to approximations.

There is another very important inflow line consideration. It is well known that there appear to be no physically meaningful similar solutions to the full three-dimensional boundary-layer equations on the leeside of a pointed cone at angle of attack α for values of α/θ_c in certain ranges. (See refs. 2 and 3.) (θ_c is the half-core angle.) One

expects comparable results to hold for inflow lines on realistic configurations. Lin and Rubin (ref. 3) suggest extending the three-dimensional boundary-layer equations to account for cross-flow diffusion, and they report results that show excellent agreement with experiment for values of α/θ_c for which they could not obtain numerical solutions on the leeside by using the standard three-dimensional boundary-layer equations. At even higher values of α/θ_c, however, they could obtain solutions with the three-dimensional boundary-layer equations (without cross-flow diffusion), but these solutions were in poor agreement with the experimental heat flux. Calculations using the extended equations agreed well with the experimental data.

ANALYSIS

Geometry and Coordinate Considerations

The selection of a coordinate system to describe the development of a boundary layer over a three-dimensional surface is of major importance and can significantly affect the eventual usefulness and applicability of the final computer code. The numerical algorithm utilized herein required the use of Taylor series spline functions (in the normal direction) and a Newton-Raphson iteration technique to obtain the final solution vectors. Both of these concepts are discussed in more detail later; however, it is useful to emphasize that such a solution procedure requires one to generate many correction coefficients for each individual term in the equation set. As a result, it becomes extremely desirable to keep the number of terms in the equation set to a minimum. Consequently, and because the flows to be computed will be generally highly nonsimilar, it was elected to retain both dependent and independent variables in their primitive forms (except for nodal-point stretching in the direction normal to the wall). Utilization of stream functions and similarity variables would result in significant increases in the number of terms in the equation set. In addition, such transformations can result in major difficulties as far as future code modifications and/or changes are concerned, especially in updating turbulence models.

The boundary-layer approximation is impractical to implement in any other than surface-oriented coordinate systems. Once this is recognized, the only remaining question is one of orthogonal compared with nonorthogonal coordinate systems. Regardless of which system is chosen, one constraint should be recognized, namely, that one coordinate direction must always be normal to the surface at all times. As a result, if one selects an orthogonal coordinate system, only one other coordinate direction is independent, as the third will automatically be determined from the orthogonality condition. For example, if the streamwise coordinate is selected (for example, to be coincident to the body cross sections), the nodal-point distribution in the circumferential direction is automatically determined. However, if the nodal point distribution in the circumferential

direction is specified, then constant streamwise coordinate stations will be, in general, skewed surfaces and will not lie along the body cross-section planes. On the other hand, if a nonorthogonal coordinate system is chosen, one may select both streamwise and circumferential nodal point distributions. To decide whether to stay orthogonal or nonorthogonal requires one to investigate the form of the equations in both instances. Consider the metric tensor g_{ij} in both coordinates:

For orthogonal systems:

$$g_{ij} = \begin{pmatrix} h_1^2 & 0 & 0 \\ 0 & h_2^2 & 0 \\ 0 & 0 & 1 \end{pmatrix}$$

For nonorthogonal systems:

$$g_{ij} = \begin{pmatrix} h_1^2 & h_1 h_2 \cos\theta & 0 \\ h_1 h_2 \cos\theta & h_2^2 & 0 \\ 0 & 0 & 1 \end{pmatrix}$$

where h_1 and h_2 are the scale factors.

The nonorthogonal metric tensor results in only two additional terms in the continuity equation beyond its orthogonal counterpart. In the momentum and energy equations, however, there is a threefold increase in the number of terms. By assuming that each term generates, on the average, three correction coefficients, one can easily assess that the nonorthogonal coordinate system results in a nominal tenfold increase in the number of correction coefficients.[2]

Although the desirability of choosing both surface coordinate point distributions is enticing, the additional complexity added to the analysis is not felt to be warranted. As a result, an orthogonal coordinate system was chosen. It was elected to have the flexibility of choosing a circumferential nodal-point distribution since it is necessary to be able to concentrate nodal points in regions of large cross-flow gradients (for example, wing leading edges). Since the other coordinate direction is normal to the wall, the third (streamwise) coordinate direction is automatically determined from the cross product. As a result, constant streamwise surfaces will not lie along body cross sections. This

[2]This result is only true if one considers cross-flow diffusion terms within the equation set. For no cross-flow diffusion, the increase is minimal. Although the equations presented herein do not include these additional terms, it is expected that their inclusion in the near future will be necessary in order to handle the cross-flow separation problem and for this reason the argument has been presented.

condition is inconvenient in that more handling and interpolation of edge conditions will be required to obtain a consistent set of edge boundary conditions.

It should be emphasized that the particular orthogonal system described is used in automatically coupling the boundary-layer code to the three-dimensional inviscid supersonic flow field code developed by Marconi et al. (ref. 1) for application to space shuttle problems. The boundary-layer code is written in general orthogonal surface coordinates, and one has the freedom to select any coordinate system within that class (for example, streamline coordinates), provided one can provide the inviscid edge data to the boundary-layer code.

Dependent and Independent Variable Selection

The governing equations are solved in primitive variables, but with stretching the independent variable normal to the surface for computational convenience. Transformations to similarity variables are useful in analytically studying similarity solutions. For the numerical solution of nonsimilar solutions their usefulness is of questionable value, provided nodal points are sensibly selected and streamwise derivatives are accurately represented. Cebeci et al. report (ref. 4) that fewer nodes were necessary for calculating turbulent boundary layers when they used a similarity transformation of the dependent variables, nodal spacing increasing geometrically from the wall. They would have had better results had they varied the nodal spacing logarithmically near the wall as the solution varies. Their experience simply indicates that geometrically spaced nodal distributions coupled with transformed dependent variables resulted in a nodal spacing which was closer to logarithmic in physical space than a straight geometric progression in physical space. To illustrate this condition, results of the 3-D code using physical variables and 8 nodes agrees very well with the BLIMP code (ref. 5) predictions using similarity variables and 7 nodes, as shown in figure 1. To minimize the number of points required, it is necessary to identify the edge of the boundary layer. This is done by scaling the lengths normal to the surface by the local boundary-layer thickness, an unknown quantity, which is obtained by introducing the auxiliary condition that the total enthalpy H_t at the second (or third) nodal point from the edge is a fixed ratio of the local edge enthalpy (for example, $H_t/H_{t,e} = 0.9$ at $x_3/x_{3,e} = 0.5$ where e denotes edge).

Governing Equations

The three-dimensional boundary-layer equations are written in general, orthogonal, body surface coordinates. One coordinate is normal to the local tangent plane, one is in the tangent plane in the general direction of the edge velocity,[3] and the third is in the tangent plane normal to the other two. As noted, coordinate stretching is performed normal to the surface. Within this context, the three-dimensional boundary-layer equations are

[3]This is necessary if the problem is to be solved as an initial value problem.

(subscript 1 indicates the general streamwise coordinate; subscript 2, the cross-flow coordinate; and subscript 3, the surface normal coordinate):

Continuity:

$$\frac{\partial}{\partial x_1}(h_2 \rho v_1) + \frac{\partial}{\partial x_2}(h_1 \rho v_2) + \frac{\partial}{\partial x_3}(h_1 h_2 \rho v_3) = 0 \tag{1}$$

Axial momentum:

$$\frac{v_1}{h_1}\frac{\partial v_1}{\partial x_1} + \frac{v_2}{h_2}\frac{\partial v_1}{\partial x_2} + v_3\frac{\partial v_1}{\partial x_3} + \frac{v_1 v_2}{h_1 h_2}\left(\frac{\partial h_1}{\partial x_2}\right) - \frac{{v_2}^2}{h_1 h_2}\left(\frac{\partial h_2}{\partial x_1}\right) = -\frac{1}{\rho h_1}\frac{\partial p}{\partial x_1} + \frac{1}{\rho}\frac{\partial}{\partial x_3}\left[(\mu + \epsilon)\frac{\partial v_1}{\partial x_3}\right]\frac{1}{Re} \tag{2}$$

Cross-flow momentum:

$$\frac{v_1}{h_1}\frac{\partial v_2}{\partial x_1} + \frac{v_2}{h_2}\frac{\partial v_2}{\partial x_2} + v_3\frac{\partial v_2}{\partial x_2} + \frac{v_1 v_2}{h_1 h_2}\left(\frac{\partial h_2}{\partial x_1}\right) - \frac{{v_1}^2}{h_1 h_2}\left(\frac{\partial h_1}{\partial x_2}\right) = -\frac{1}{\rho h_2}\frac{\partial p}{\partial x_2} + \frac{1}{\rho}\frac{\partial}{\partial x_3}\left[(\mu + \epsilon)\frac{\partial v_2}{\partial x_3}\right]\frac{1}{Re} \tag{3}$$

Normal momentum:

$$0 = -\frac{1}{\rho}\frac{\partial p}{\partial x_3} \tag{4}$$

Energy:

$$\rho\left(\frac{v_1}{h_1}\frac{\partial H}{\partial x_1} + \frac{v_2}{h_2}\frac{\partial H}{\partial x_2} + v_3\frac{\partial H}{\partial x_3}\right) = \frac{1}{Re}\frac{\partial}{\partial x_3}\left(B\left\{\epsilon - \frac{\epsilon}{2}\left[\frac{\hat{C}_p}{N_{Pr,t}} + \frac{1}{N_{Sc,t}}\left(\sum_i \frac{\partial K_i}{\partial h} h_i\right)\right] + \mu - \frac{\lambda_m}{2}\right\}\frac{\partial}{\partial x_3}\left({v_1}^2 + {v_2}^2\right) + \left\{\epsilon\left[\frac{\hat{C}_p}{N_{Pr,t}} + \frac{1}{N_{Sc,t}}\left(\sum_i \frac{\partial K_i}{\partial h} h_i\right)\right] + \lambda_m\right\}\frac{\partial H}{\partial x_3}\right) \tag{5}$$

where p is the pressure, μ is the molecular viscosity, and

$$\lambda_m = \frac{1}{\mu_{ref}}\left[\lambda\frac{\partial T}{\partial h} - \sum_i j_i h_i\left(\frac{dh}{dx_3}\right)^{-1}\right]$$

$$\hat{C}_p = C_p\frac{\partial T}{\partial h}$$

and ϵ is the eddy viscosity. These equations are nondimensionalized, all dimensional quantities being divided by appropriate constant reference quantities. Important nondimensional groups are listed in table I.

TABLE I.- IMPORTANT NONDIMENSIONAL GROUPS

Group symbol	Elements		Common name
R_e, R, R_N, R_∞, $R_{e,\infty}$ $= \frac{\rho u \ell}{\mu}$	ρ	reference density	Reference Reynolds number
	u	reference velocity	
	ℓ	reference length	Reynolds number based on nose radius
	μ	reference viscosity	Free-stream Reynolds number
			Reference free-stream Reynolds number
$B = \frac{u^2}{h}$	u	reference velocity	
	h	reference enthalpy	
$N_{Pr,t} = \frac{C_p \epsilon}{\lambda}$	C_p	specific heat	Turbulent Prandtl number
	ϵ	eddy viscosity	
	λ	thermal conductivity	
$N_{Sc,t} = \frac{\epsilon}{\rho D_{12}}$	ϵ	eddy viscosity	Turbulent Schmidt number
	ρ	density	
	D_{12}	binary diffusion coefficient	

Numerical Procedures

To simplify the discussion, consider a three-dimensional Cartesian coordinate system x,y,z with velocity components u, v, and w. The x-coordinate corresponds to the direction of integration, y is locally normal to the surface, and z designates the cross-flow direction. The solution domain is covered by a nodal network as schematized in figure 2. It is assumed that the entire flow is known at some value $x = x_i$ and is to be determined at $x_{i+1} = x_i + \Delta x$. For a solution at x_{i+1} to be obtained, which satisfies the governing partial differential equations (PDEs) and the imposed boundary conditions, the functional form of the x, y, and z derivatives is specified and is substituted into the PDEs along with the boundary conditions. The result is a system of algebraic relations between unknown dependent variables at the nodal points at station $x = x_{i+1}$. Essentially all numerical solutions to the PDEs reduce to this same process. What distinguishes one procedure from another is the functional form chosen to relate nodal values of dependent variables and their derivatives, one to another.

Normal to the wall boundary, the dependent variables are represented by a splined Taylor series between each node. Letting j denote a nodal index running from 1 at the wall to JMAX at the outer edge of the boundary layer results in

$$\left.\begin{aligned} u_{j+1} &= u_j + u'_j\,\Delta y + u''_j\,\frac{\Delta y^2}{2} \\ u'_{j+1} &= u'_j + u''_j\,\Delta y \end{aligned}\right\} \tag{6}$$

In addition, the PDEs are integrated with respect to y between each node which insures that the conservation laws are satisfied exactly between nodes and greatly simplifies the calculation of diffusion terms by eliminating second derivatives.

In the cross-flow direction where variations are generally much less severe than in the normal direction, second-order-accurate centered finite differences are used to represent the cross-flow derivatives; for example, $\partial U/\partial z$ for equal spacing is represented as

$$U_z = \frac{U_{j,k+1} - U_{j,k-1}}{z_{k+1} - z_{k-1}} \tag{7}$$

where k is the index associated with the z coordinate.

Axial derivatives $\partial U/\partial x$ are represented by simple backward difference quotients of the form

$$U_x = \frac{U_{i+1,j,k} - U_{i,j,k}}{x_{i+1} - x_i} \tag{8}$$

where i is the index associated with the x coordinate.

The solution is obtained fully implicitly. Thus, equations (6) and (7) are evaluated at station x_{i+1}. Upon introduction of the boundary conditions (for example, $U_{i+i,JMAX,k} = U_e(x,y,z)$, etc.), the result is a system of nonlinear algebraic equations for primary (u, ρ, etc.) and secondary (u', ρ', etc.) variables at each nodal point.[4] This system is solved by Newton-Raphson iteration as outlined in the following paragraph.

Consider the system of nonlinear equations to be represented by

$$F_m(U_n) = 0 \tag{9}$$

where m is an equation index and U_n is one of the dependent primary or secondary variables ($U_{i+1,j,k}$, etc.). Assume a value of $U_n = U_n^*$ and expand F_m (see eq. (9)) in a Taylor series about U_n^*

[4]Actually, obtaining the solution is usually enhanced if the derivative terms (u', ρ', etc.) are treated as the primary variables and the primitive variables (u, ρ, etc.) as the secondary variables.

$$F_m(U_n) = F_m(U_n^*) + \sum_{\ell} (U_\ell - U_\ell^*) \frac{\partial F_m}{\partial (U_\ell)_{U_\ell = U^*}} = 0 \tag{10}$$

This equation can be written in matrix form as

$$A(U - U^*) + F = 0 \tag{11}$$

or

$$U = U^* - A^{-1}F \tag{12}$$

where

$$A^{-1} = \left[\frac{\partial F_m}{\partial U_\ell}\right]^{-1} \tag{13}$$

Thus, the solution basically reduces to the problem of inverting a large matrix, and thereby solving a system of linear algebraic equations for the unknown U.

The matrix A is composed of a number of submatrices, illustrated in figure 3 for the case of five meridional (cross-flow) planes. It is block tridiagonal because cross-flow derivatives are represented with centered finite differences (if splined polynomials were used in the cross-flow direction as well, A would be dense matrix). The submatrices along the diagonal are relatively dense because they include information which is transmitted through the boundary layer as well as that which is transmitted in the cross-flow direction. The off-diagonal submatrices are relatively sparse because they only contain cross-flow derivative information.

A schematic of a typical diagonal submatrix for one meridional plane is shown in figure 4. Denote the submatrices by A_{ij} and decompose the unknown vector U into subvectors U_i. For a given value of U denote the error in the equation by E, which is a vector which can be similarly decomposed into subvectors E_i. Then the elements of the submatrix A_{ij}, which are denoted by a_{mn}, represent the rate of change of the mth equation at that node with respect to the nth dependent variable. The equations being considered are the Taylor series equations used in the spline fits of dependent variables, the governing PDEs, and certain constraint equations used in imposing boundary conditions.[5] Since the form of the Taylor series is invariant from node to node and station to station, the corresponding elements are constant. By taking advantage of this constancy, the submatrix can be further reduced as follows.[6]

---

[5]For example, $H/H_{te} = 0.9$ at $y/y_e = 0.5$. Additional constraints are appropriate for calculations involving vortical-layer effects.

[6]Do not confuse the sub submatrix A above with the complete matrix A of figure 3 and equation (11).

$$\underset{\text{Taylor series}}{\uparrow\downarrow} \quad \overset{\text{Submatrix reduction}}{\begin{bmatrix} A & B \\ C & D \end{bmatrix} \begin{bmatrix} U_1 \\ U_2 \end{bmatrix} = \begin{bmatrix} 0 \\ E_2 \end{bmatrix}} \tag{14}$$

or

$$U_2 = \left(D - CA^{-1}B\right)^{-1} E_2 \tag{15}$$

and

$$U_1 = A^{-1}BU_2 \tag{16}$$

Return now to the complete system equations (9). Since A is block tridiagonal, it can be reduced by Gaussian reduction. In this reduction, it is necessary to invert a number of submatrices. Because of the properties of the submatrices (see discussion of eqs. (14) to (16)), it is only necessary to invert matrices whose size is

$$\underset{\text{Equations per node}}{\underset{\uparrow}{4}} \times (\text{Number of nodes}) + \underset{\text{Constraint equations}}{\underset{\uparrow}{3}} \tag{17}$$

Thus, even though the complete matrix A is very large, the maximum matrix size which must be inverted is quite manageable, being typically about 35×35 for laminar flow and 63×63 for turbulent flow.

Stagnation-Point Solution

It is assumed that the flow is similar at the stagnation point. By placing the coordinate system origin at the stagnation point and orienting it near the stagnation point, the edge velocities can be expressed in the form[7]

$$\left.\begin{aligned} U_e &= U\frac{x}{\ell} \\ W_e &= W\frac{z}{\ell} \end{aligned}\right\} \tag{18}$$

where U and W are constants supplied by the inviscid solution. In the vicinity of the stagnation point

$$\left.\begin{aligned} \frac{du}{dx_1} &= \frac{u}{x_1} \\ \frac{dw}{dx_1} &= \frac{w}{x_1} \end{aligned}\right\} \tag{19}$$

[7]These expressions are for Cartesian coordinates.

and it is noted that

$$\frac{dg}{dx_1} = 0 \tag{20}$$

where g is the static enthalpy. In polar coordinates,

$$U_e = U \cos^2 \phi + W \sin^2 \phi \frac{x_1}{\ell} \tag{21}$$

$$W_e = (W - U)\cos \phi \sin \phi \frac{x_1}{\ell} \tag{22}$$

Since the cross-flow derivatives are well behaved at the stagnation point, the stagnation-point solution can be numerically generated by representing the streamwise derivatives as

$$\frac{du}{dx_1} = d_1 U_\ell - d_2 U_{\ell-1} \tag{23}$$

where

$$d_1 = -d_2 = \frac{1}{\Delta x_i} \tag{24}$$

By taking

$$\left.\begin{aligned} d_1 &= \frac{1}{x_e} \\ d_2 &= 0 \end{aligned}\right\} \tag{25}$$

for $\frac{du}{dx_1}$ and $\frac{dw}{dx_1}$ and $d_1 = d_2 = 0$ for $\frac{dg}{dx_1}$, the solution can be numerically generated very near the stagnation point. The predicted velocity profiles for the stagnation-point flow on a 4:1 prolate spheroid are compared with Howarth's analytical solution (ref. 6) in figure 5.

Entropy-Layer Effects

It is usually relatively simple to account for entropy-layer effects in two-dimensional or axisymmetric hypersonic flow over a blunt body. The usual procedure is to relate the mass flux in the boundary layer with the position on the bow shock wave encompassing the same amount of mass flux, as illustrated in sketch (b). That is, y_s is determined so that the mass flux between AA' equals that across the boundary layer BB'. The local edge conditions at B are then determined by isentropically expanding the streamline from behind the shock at A to the local surface pressure at B'. It is relatively easy to account for the effects of normal entropy gradient as well. Naturally,

the solution at BB' must be obtained iteratively in order to simultaneously satisfy the mass balance as indicated.

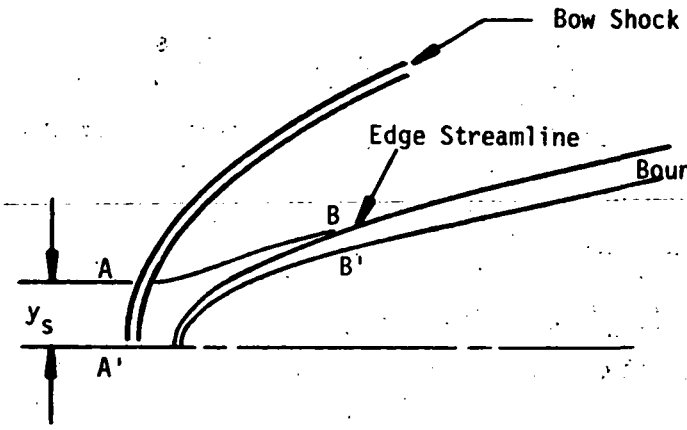

Sketch (b).- Schematic of 2-D or axisymmetric mass flux balance used in accounting for entropy layer effects.

In three dimensions the problem is somewhat more complicated, but not tremendously so. Again, for ease of exposition, revert to simple Cartesian coordinates. The idea is to match the viscous and inviscid solutions in some common region of overlap. To this end, define a stream surface S in the inviscid region, where the boundary-layer equations are still valid. Conservation of mass gives

$$\left.\begin{aligned} \frac{\partial F_x{}^i}{\partial x} + \frac{\partial F_z{}^i}{\partial z} &= 0 \\ \frac{\partial F_x}{\partial x} + \frac{\partial F_z}{\partial z} &= (\rho v)_{wall} \end{aligned}\right\} \tag{26}$$

where

$$\left.\begin{aligned} F_x{}^i &= \int_0^S (\rho u)^i dy \\ F_x &= \int_0^S (\rho u) dy \\ &\vdots \end{aligned}\right\} \tag{27}$$

Define

$$\left.\begin{aligned} \Delta F_x &= F_x - F_x{}^i \\ \Delta F_z &= F_z - F_z{}^i \end{aligned}\right\} \tag{28}$$

then

$$\frac{\partial \Delta F_x}{\partial x} + \frac{\partial \Delta F_z}{\partial z} = (\rho v)_{wall} \tag{29}$$

Note that $F - F^i = \text{Constant}$ outside the boundary layer (that is, in the overlap region). Thus ΔF_x and ΔF_z are independent of the location of S and are functions of x and z only so long as S is chosen to be in the overlap region. Equation (29) and one of equations (28) are the relations necessary to account for entropy-layer effects in three dimensions. They are implemented in the code as follows.

From the inviscid solution the values of the ΔF_x and ΔF_z functions at each (x,z) location are determined; next, the edge conditions are determined as functions of ΔF_x and ΔF_z, namely

$$U_e = f_1\left(x,z,F_x{}^i = F_x + \Delta F_x\right) \tag{30}$$

$$F_z{}^i = f_2\left(x,z,F_x{}^i = F_x + \Delta F_x\right) \tag{31}$$

etc. The two new equations at each meridional plane are introduced

$$\frac{\partial \Delta F_x}{\partial x} + \frac{\partial \Delta F_z}{\partial z} = (\rho v)_{wall} \tag{32}$$

$$\Delta F_z = F_z - F_z{}^i = F_z - f_2(x,z,F_x,\Delta F_x) \tag{33}$$

where F_x and F_z are available within the existing B/L solution logic. Equations (27) and (30) are the two constraint equations associated with entropy-layer effects previously discussed.

Turbulence Modeling

Mean field turbulence models are utilized in the present paper. The turbulent eddy viscosity model currently implemented in the code is the Bushnell-Beckwith model (ref. 7) as extended to three-dimensional flows by Harris. The eddy viscosity is given by

$$\epsilon = \rho \ell^2 \sqrt{\left(\frac{\partial u}{\partial x}\right)^2 + \left(\frac{\partial w}{\partial z}\right)^2} \tag{34}$$

where

$$\left.\frac{\ell}{\delta}\right|_{\frac{u}{u_e}=0.995} = K_1 \tanh\left(\frac{K_2}{K_1}\frac{y}{\delta}\right) D\bar{\gamma} \tag{35}$$

and

D wall damping function

$\overline{\gamma}$ y-direction intermittency function

In the transition region, ϵ is multiplied by a streamwise intermittency function. The turbulent Lewis and Prandtl numbers are taken to be constant.

Introduction of different turbulent eddy viscosity models is a straightforward task, but it does require the derivation of certain terms needed in the Newton-Raphson iteration (for example, $\partial\epsilon/\partial\rho$, $\partial\epsilon/\partial u$, etc.).

Thermochemistry

The code has ideal gas and chemical equilibrium options. In the latter case, the state relation is obtained by solving exactly for the species equilibrium relations in a special, optimized air equilibrium routine. Details are given in reference 5. It is a straightforward matter to replace the air equilibrium routine with a Mollier fit, if desired.

PRELIMINARY RESULTS

A number of test cases are currently in progress. In this section the results of predictions are compared with experimental heat-transfer data for two three-dimensional flows.

The first is for a laminar boundary layer on a 10° half-angle cone at an angle of attack of 4°. The experimental data were obtained by Tracy (ref. 8) at $M_\infty = 7.95$ and $R_{e,\infty} = 1.25 \times 10^6$ per foot. The inviscid edge data for the boundary-layer calculation were obtained from Jones' tables (ref. 9). The predicted circumferential distribution of heat-transfer coefficient is compared with the experimental data in figure 6, where it is seen that the agreement is excellent.

The second sample problem is for laminar flow over a 2.79-cm (1.1-in.) R_N sphere/15° cone at an angle of attack of 10°. The tests were conducted at free-stream Mach and Reynolds numbers of 10.6 and 4.1×10^6 per meter (1.2×10^6 per foot) (Cleary, ref. 10). Theoretical heat-transfer distributions are compared with experimental data in figures 7 and 8. Axial distributions along different meridional rays are given in figure 7 and the circumferential distribution at one fixed axial station is given in figure 8. The theoretical calculations were generated by using normal-shock entropy. In general, the agreement between theory and experiment is very good. Slightly higher predictions

on the windward side at $x/R_N < 2$ probably result from a rather large axial step size and the resulting inaccuracies in numerically calculating the local edge pressure gradient.

CONCLUDING REMARKS

The three-dimensional boundary-layer code reported herein has been developed for particular application to realistic hypersonic aircraft, but it is very general and can be applied to a wide variety of boundary-layer flows of interest. Laminar, transitional, and fully turbulent flows of compressible, reacting gases can be efficiently calculated by use of the code. The calculation is performed in a general body-oriented orthogonal coordinate system. The user has complete freedom in specifying the coordinate system within the restrictions that one coordinate must be normal to the surface and the three coordinates must be mutually orthogonal.

The boundary-layer equations are discretized and integrated step by step. The integration is fully implicit in the streamwise direction. This is especially important for realistic configurations since it enables one to calculate flows having cross-flow attachment and detachment lines off the pitch plane. The code is restricted to those flows which are adequately represented by the boundary-layer equations; the analysis must be extended to describe adequately flows in which cross-flow diffusion effects are important near cross-flow attachment lines. The numerical algorithm includes splined functions for dependent variables between nodes to minimize the number of nodes normal to the surface. This condition results in an extremely efficient solution procedure for reacting boundary layers. Finally, the code includes the capability to account for surface normal entropy gradient effects.

Currently, the code is being coupled to the supersonic, inviscid flow field code which was developed by Marconi et. al., Grumman Aerospace Corporation, under contract to the National Aeronautics and Space Administration. Upon completion of the inviscid/viscid code coupling, extensive comparisons for more complex configurations will be made.

REFERENCES

1. Marconi, Frank; Yaeger, Larry; and Hamilton, H. Harris: Computation of High-Speed Inviscid Flows About Real Configurations. Aerodynamic Analyses Requiring Advanced Computers, Part II, NASA SP-347, 1975, pp. 1411-1455.

2. Murdock, John W.: The Solution of Sharp Cone Boundary Layer Equations in the Plane-of-Symmetry. SAMBO TR-71-209, U.S. Air Force, July 1971. (Available from DDC as AD 730 598.)

3. Lin, T. C.; and Rubin, S. G.: Viscous Flow Over a Cone at Moderate Incidence. II. - Supersonic Boundary Layer. AFOSR-TR-73-0219, U.S. Air Force, Sept. 1972. (Available from DDC as AD 755 862.)

4. Cebeci, Tuncer; Kaups, Kalle; Mosinskis, G. J.; and Rehn, J. A.: Some Problems of the Calculation of Three-Dimensional Boundary-Layer Flows on General Configurations. NASA CR-2285, 1973.

5. Kendall, Robert M.: An Analysis of the Coupled Chemically Reacting Boundary Layer and Charring Ablator. Pt. V – A General Approach to the Thermochemical Solution of Mixed Equilibrium-Nonequilibrium, Homogeneous or Heterogeneous Systems. NASA CR-1064, 1968.

6. Rosenhead, L., ed.: Laminar Boundary Layers. Clarendon Press (Oxford), 1963.

7. Bushnell, Dennis M.; and Beckwith, Ivan E.: Calculation of Nonequilibrium Hypersonic Turbulent Boundary Layers and Comparisons With Experimental Data. AIAA J., vol. 8, no. 8, Aug. 1970, pp. 1462-1469.

8. Tracy, Richard R.: Hypersonic Flow over a Yawed Circular Cone. Hypersonic Res. Proj. Mem. No. 69 (Contract No. DA-31-124-ARO(D)-33), Graduate Aeronaut. Lab., California Inst. Technol., Aug. 1, 1963.

9. Jones, D. J.: Tables of Inviscid Supersonic Flow About Circular Cones at Incidence $\gamma = 1.4$. AGARDograph 137, Pts. I and II, Nov. 1969.

10. Cleary, Joseph W.: Effects of Angle of Attack and Bluntness on Laminar Heating-Rate Distributions of a 15° Cone at a Mach Number of 10.6. NASA TN D-5450, 1969.

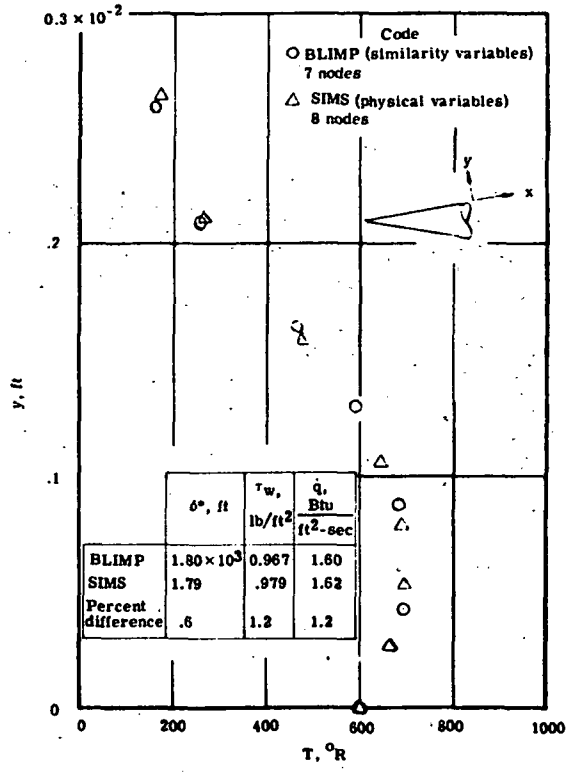

Figure 1.- Illustration that physical variables require no more nodes than transformed variables. Laminar flow; $M_\infty = 8$; $\gamma = 1.4$; $R_\infty = 8.5 \times 10^6$; $\theta_c = 10^o$; $\alpha = 0^o$; γ, ratio of specific heat; τ_w, shear stress at wall; δ^*, displacement thickness; and q, heat transfer.

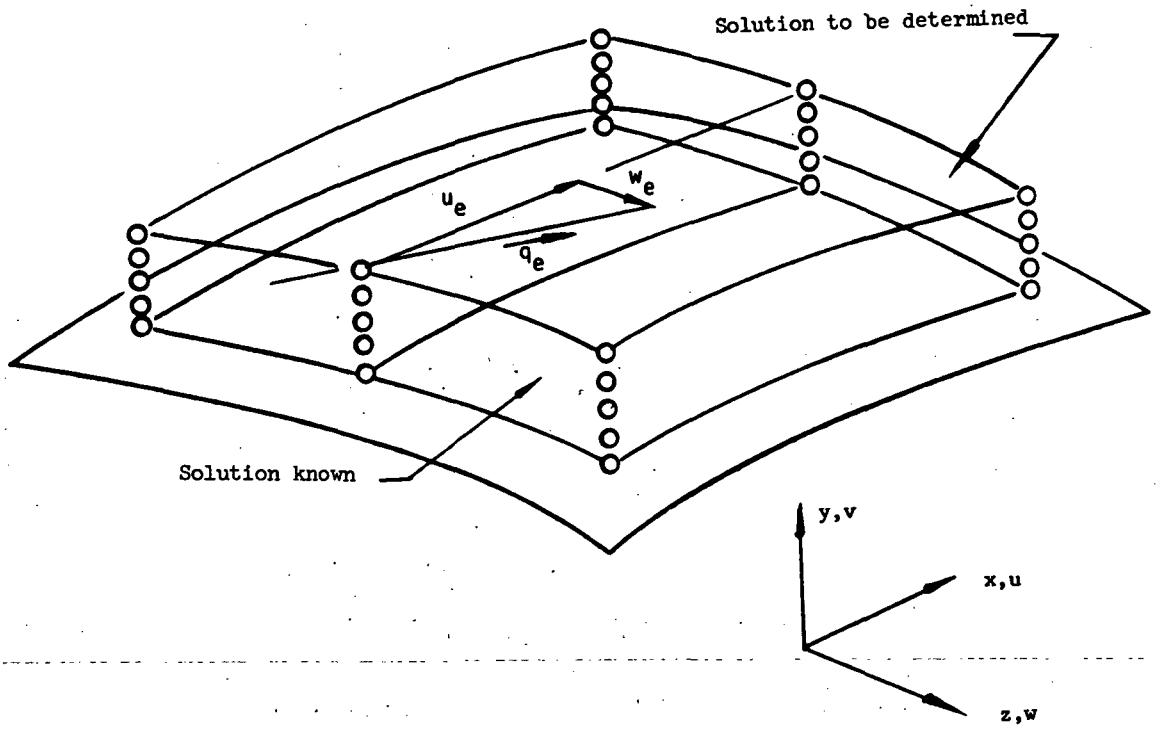

Figure 2.- Schematic of discretization. Boundary layer is covered by a nodal network.

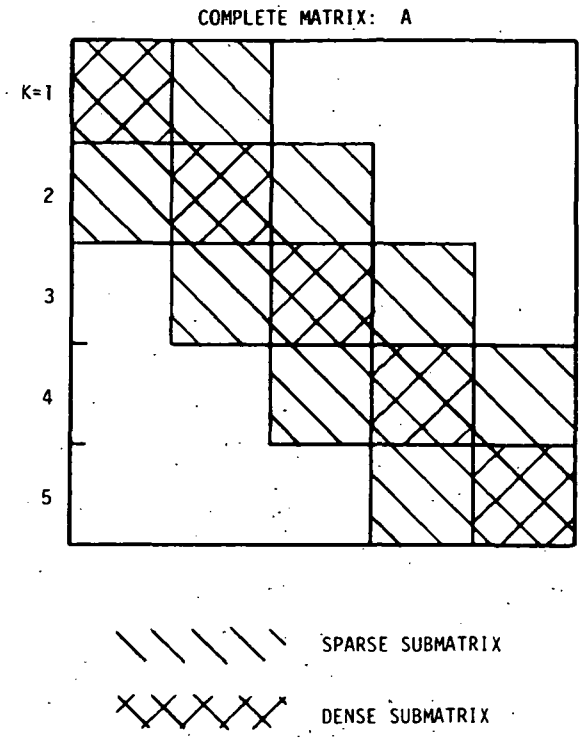

Figure 3.- Schematic of form of matrix A for the case of five meridional planes.

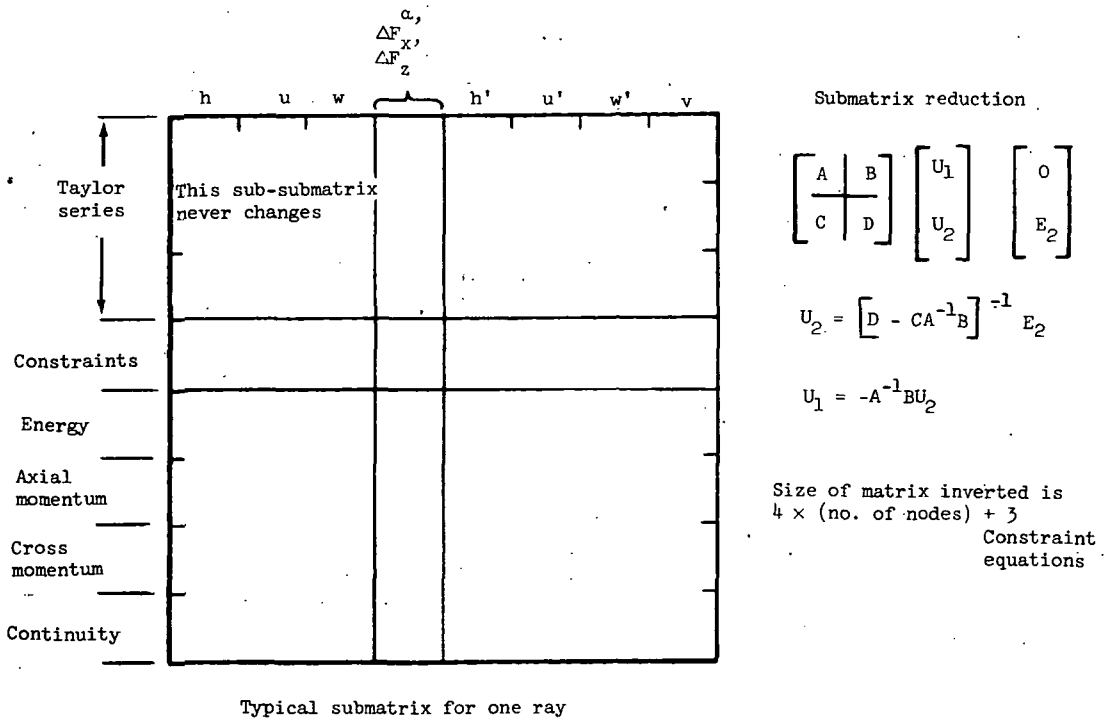

Figure 4.- Schematic of submatrix.

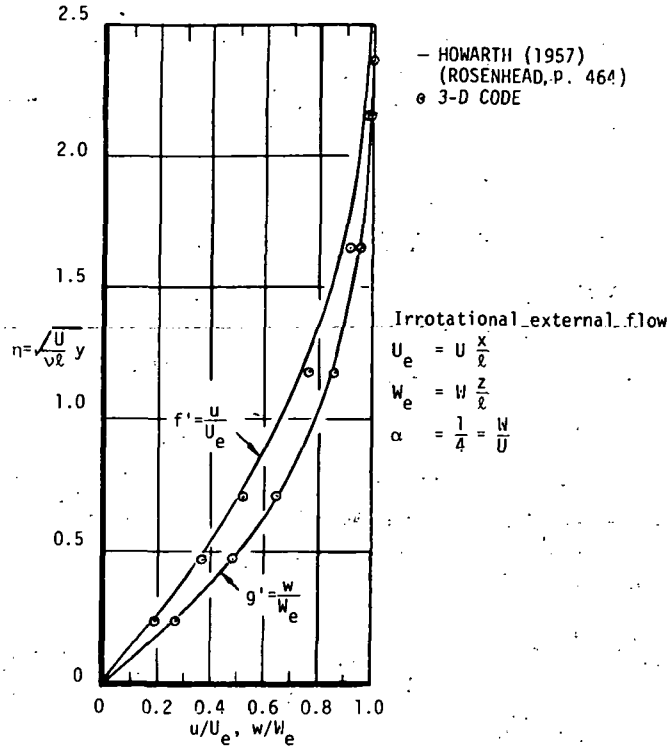

Figure 5.- Comparison of exact and approximate general 3-D stagnation-point solution. ν is kinematic viscosity.

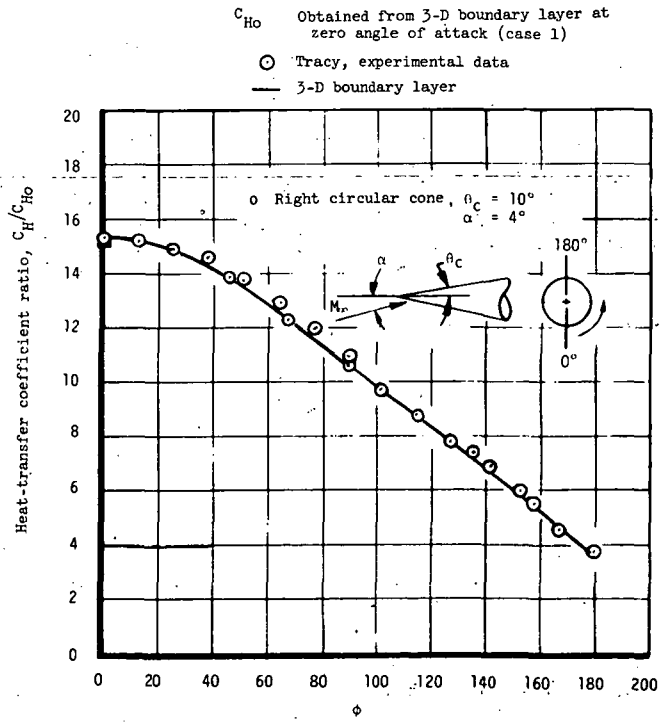

Figure 6.- Comparison of 3-D boundary-layer solution to experimental data.

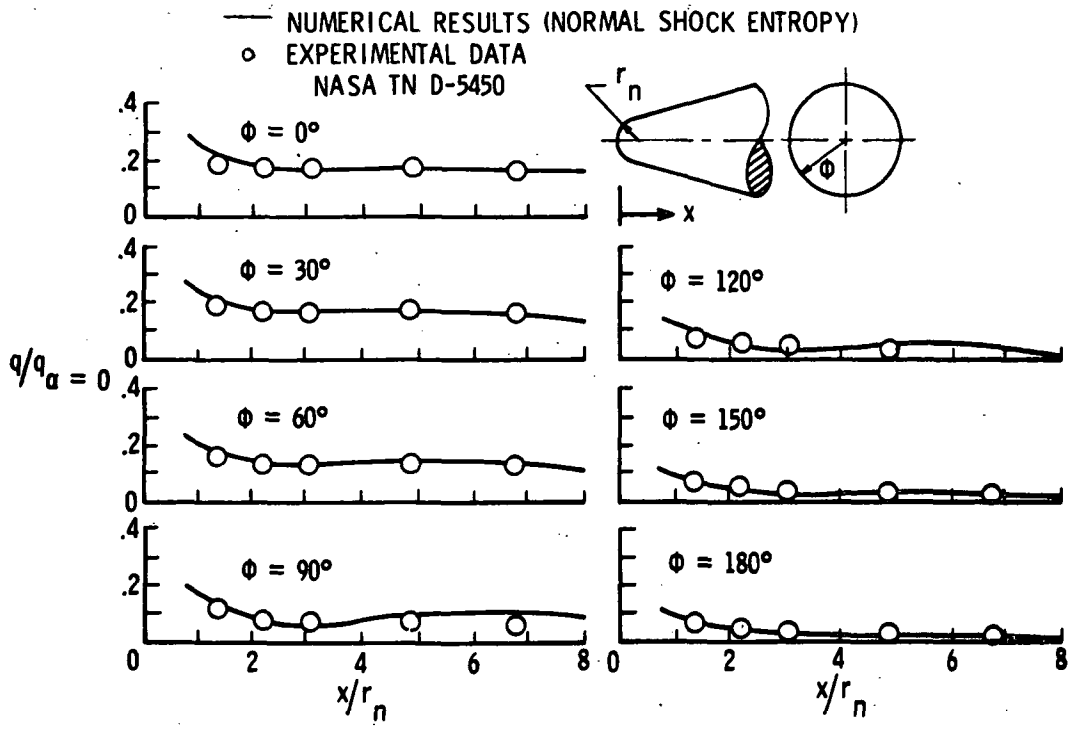

Figure 7.- Comparison of numerical results with experimental data. Axial heat-transfer distributions for 15° cone; $M_\infty = 10.6$; $R_\infty = 1.2 \times 10^6$; and $\alpha = 10°$.

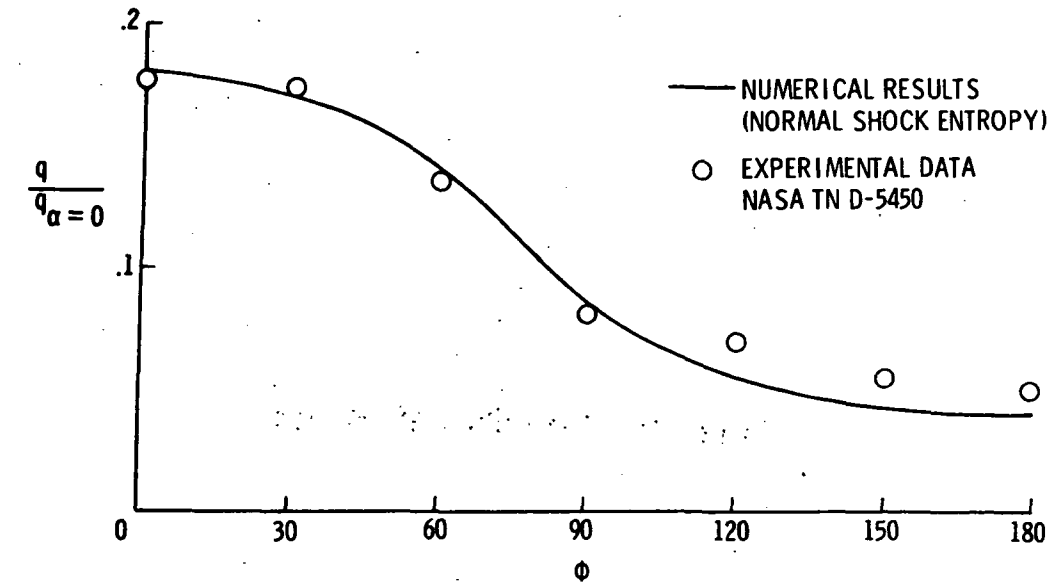

Figure 8.- Comparison of numerical results with experimental data. Circumferential heat-transfer distribution. $M_\infty = 10.6$; $R_\infty = 1.2 \times 10^6$; $\alpha = 10°$; and $x/r_n = 2.23$.

Page Intentionally Left Blank

A NUMERICAL METHOD FOR THE PREDICTION OF HIGH-SPEED BOUNDARY-LAYER TRANSITION USING LINEAR THEORY*

By Leslie M. Mack

Jet Propulsion Laboratory

SUMMARY

This paper describes a method of estimating the location of transition in an arbitrary laminar boundary layer on the basis of linear stability theory. After an examination of experimental evidence for the relation between linear stability theory and transition, a discussion is given of the three essential elements of a transition calculation: (1) the interaction of the external disturbances with the boundary layer; (2) the growth of the disturbances in the boundary layer; and (3) a transition criterion. A brief discussion is given of the computer program which carries out these three calculations. The program is first tested by calculating the effect of free-stream turbulence on the transition of the Blasius boundary layer, and is then applied to the problem of transition in a supersonic wind tunnel. The effects of unit Reynolds number and Mach number on the transition of an insulated flat-plate boundary layer are calculated on the basis of experimental data on the intensity and spectrum of free-stream disturbances. Reasonable agreement with experiment is obtained in the Mach number range from 2 to 4.5.

INTRODUCTION

One of the most difficult problems in theoretical aerodynamics is the prediction of transition from laminar to turbulent flow, a problem that is especially severe for supersonic and hypersonic boundary layers. Examples ranging from high-velocity reentry vehicles to the wind-tunnel testing of transonic airfoil sections can be put forward to illustrate the dramatic effects on flow characteristics which result from differences in the location of transition. The search for some method of estimating whether the boundary layer will be laminar or turbulent for a particular external flow has mostly focussed on empirical correlations of some type. These methods are limited in scope and should be replaced by a more fundamental approach which involves the calculation of the development of the perturbed boundary layer as it responds to its disturbance environment. The direct solution of the three-dimensional time-dependent Navier-Stokes equation of compressible flow, which could be of great benefit, still lies in the future. The use of turbulence model equations is a promising approach although it remains to be demonstrated if enough of the complexity of the transition

*Research supported by NASA under Contract No. NAS 7-100.

process is retained in these time-averaged equations, which were primarily intended for fully developed turbulent flow, to make them useful as a prediction technique. A third possibility is the use of linear stability theory. This approach might at first appear to be of little value because of the evident nonlinearity of the final breakdown of laminar flow. However, it does have the considerable advantage that within the restrictions of linearity and locally parallel flow one is dealing with solutions of the unsteady Navier-Stokes equations. Furthermore, in many disturbance environments most of the region preceding transition will involve a disturbance of small amplitude. In these cases, the process by which the dominant external disturbances form an organized wave structure in the boundary layer, and the subsequent growth of the internal boundary-layer disturbances both lie within the scope of a linear theory. Nonlinearity occurs only in a small region immediately preceding transition. Consequently, it should follow that at least the change in the transition Reynolds number as the mean boundary layer or the disturbance environment changes can be calculated from linear theory.

In reference 1, a detailed investigation was carried out to determine whether in a supersonic wind tunnel the change in the transition Reynolds number of a flat-plate boundary layer with Mach number and surface cooling can indeed be accounted for by linear theory. The results reported there are sufficiently promising to encourage taking the next step, which is to use linear theory to make a quantitative estimate of the transition Reynolds number. It is the purpose of this paper to describe a numerical method and computer program which combine information about the external disturbances with stability theory and a transition criterion to provide estimates of transition location in a wide variety of cases. As examples, the effect on transition of free-stream turbulence in low-speed flow, and of Mach number and unit Reynolds number in a supersonic wind tunnel are given.

SYMBOLS

A	disturbance amplitude
A_1	free-stream disturbance amplitude
A_0	initial disturbance amplitude
A_t	amplitude transition criterion
c_p	phase velocity, ω/α_r
$E(\omega)$	energy density of normalized power spectrum
f	frequency

F	dimensionless frequency, $\omega^* \nu_1^* / U_1^{*2}$
L^*	length scale
L_x^*	integral length scale of turbulence
M	Mach number
p'	pressure fluctuation
Re	free-stream x-Reynolds number
R_L	Reynolds number based on L_x^*
R_{δ^*}	displacement-thickness Reynolds number
u', v'	velocity fluctuations
U	mean longitudinal velocity
U_s	average source velocity
x,y,z	longitudinal, transverse and lateral coordinates
α	complex wave number in x-direction, $\alpha_r + i\alpha_i$
β	complex wave number in z-direction, $\beta_r + i\beta_i$
γ	ratio of specific heats
μ	viscosity coefficient
ν	kinematic viscosity coefficient
τ_R	Reynolds stress ratio
$(\tau_R)_t$	Reynolds stress transition criterion
ψ	wave angle, $\tan^{-1}(\beta_r/\alpha_r)$
ω	circular frequency

Superscripts:

$(\ )^*$	dimensional quantity
$(\ )'$	fluctuation quantity

($\overline{\ }$) average quantity

Subscripts:

t transition

1 free-stream condition

o neutral-stability condition

LINEAR STABILITY THEORY AND TRANSITION

The idea of calculating boundary-layer transition by means of linear stability theory would be on much more solid ground if it were possible to point to experimental evidence that there is indeed a direct quantitative relation between linear instability and transition. Schubauer and Skramstad (ref. 2) demonstrated the correctness of the theory of Tollmien and Schlichting as a description of the behavior of small disturbances in the laminar boundary layer preceding transition. They also showed that the location of transition could be changed by varying either the frequency or amplitude of an artificial disturbance, but no quantitative results were given.

Apparently the only published experiment that does offer quantitative results in this regard is the one described in reference 3 by Jackson and Heckl. An axisymmetric model of circular cross section on which a Blasius boundary layer formed was mounted in a wind tunnel of moderate turbulence level (0.2 - 0.4%). A loudspeaker was placed inside the model and the sound introduced into the boundary layer through a circumferential slit located 12 in. from the effective start of the boundary layer. Transition was fixed at a point 15 in. downstream of the slit for a range of frequencies by adjusting the amplitude of the loudspeaker. The amplitude of the disturbance created in the boundary layer was monitored with a hot-wire anemometer located in the boundary layer above the slit. Transition was measured by a hot wire located at the downstream (15 in.) station and was judged to have occurred when the disturbance spectrum changed to a turbulent form. Thus the end rather than the start of transition was being measured.

For a given free-stream velocity U_1^* (asterisks refer to dimensional quantities) the frequency and amplitude were varied to find the frequency which resulted in transition at the downstream station with the smallest initial amplitude. These frequencies are called the critical frequencies and are shown on a typical stability diagram in figure 1 where the dimensionless frequency $F = \omega^* \nu_1^* / U_1^{*2}$ is plotted against Re, the free-stream x-Reynolds number, and R_{δ^*}, the displacement-thickness Reynolds number. In terms of linear stability theory, the experimental procedure was equivalent to finding the frequency with maximum total amplification at a given Reynolds number. Consequently, if the location of transition is determined by the linear instability of the undisturbed laminar boundary layer, the

critical-frequency data points should lie along the theoretical line of maximum amplification. Figure 1 shows that this condition is satisfied. Furthermore, this close relation between transition and linear instability is not restricted to what are commonly thought of as small disturbances. The transition Reynolds numbers of figure 1 are between 0.3×10^6 and 1.2×10^6 which would correspond to free-stream turbulence levels of 0.4 to 1.6% if transition were caused solely by free-stream turbulence.

Finally, it must be remarked that stability and transition experiments with artificially produced sound as the disturbance source are notoriously difficult to carry out, a situation already noted and discussed at some length in reference 2. It would be highly desirable to repeat the same type of experiment as in reference 3 with a different method of producing the artificial disturbances.

With some experimental support available for the idea of using linear theory for transition prediction, it only remains to decide on how to apply the theory. Any naturally occurring disturbance will have its energy distributed over a range of frequencies, and in the most general case its development in a boundary layer can only be calculated by considering the separate development of all frequencies with a significant portion of the total energy. However, amplification in a boundary layer is selective, and for small initial disturbance levels the selectivity, or tuning, is sufficiently sharp so that by the time transition is approached most of the disturbance energy is concentrated in a narrow band about the most-amplified frequency. This phenomenon suggests simplifying the application of stability theory by considering only disturbances of a single frequency. Such a procedure is possible because the amplification is linear and there is no transfer of energy from one frequency to another. Therefore, transition will be predicted in this paper on the basis of the single-frequency disturbance of maximum amplitude at each Reynolds number. Since the amplitude of a disturbance at any Reynolds number depends on its initial amplitude as well as on the amplification it has undergone, it is necessary to consider the initial energy spectrum of the complete wide-band disturbance to arrive at the single-frequency disturbance of maximum amplitude.

A comparison of the growth of the theoretical single-frequency disturbance of maximum amplitude at transition with the measured growth of the same frequency component is shown in figure 2 for an insulated flat-plate boundary layer in a supersonic wind tunnel at $M_1 = 4.5$ and Re/in. $= 1.8 \times 10^5$. The dimensionless frequency of the two growth curves, $F = 0.3 \times 10^{-4}$, is the theoretical frequency of the disturbance of maximum amplitude only if the initial energy distribution of all single-frequency disturbances is identical to the power spectrum of the free-stream disturbances as measured by Laufer (ref. 4). The experimental narrow-band disturbance growth is taken from Kendall's measurements (ref. 5) in the JPL 20-in. wind tunnel, the same tunnel as used by Laufer. Because of the interaction of the irradiated sound from the turbulent boundary layers on the tunnel walls with the laminar boundary layer near the leading edge of the flat plate, there is no experimentally discernible neutral-stability point. The theoretical and experimental disturbance amplitudes are matched at the theoretical neutral point.

The theoretical disturbance of maximum amplitude has a wave angle ψ equal to 60°, while the experimental narrow-band disturbance includes all wave angles. Unfortunately, the distribution of energy with respect to wave angle in the experiment is unknown. Even so, the growths of the two disturbances are seen to be closely related. By coincidence, the two growth curves cross at almost exactly the start-of-transition Reynolds number measured by Coles (ref. 6), also in the JPL 20-in. wind tunnel. The fact that transition occurs where the theoretical disturbance is growing rapidly means that a transition criterion based on amplitude has a good chance of predicting the start of transition provided only that the region of maximum growth does vary, as assumed, with the mean-flow parameters in the same way as the transition Reynolds number.

REQUIREMENTS OF TRANSITION CALCULATION

In addition to the calculation of the velocity and temperature profiles of the mean boundary layer, the transition calculation can be divided into three distinct parts: (1) the interaction of the external disturbances which lead to transition with the boundary layer to form the internal boundary-layer disturbances of Tollmien-Schlichting type; (2) the growth of the internal disturbances; and (3) a transition criterion based on some property of the growing disturbances. In this section each of these three aspects will be discussed separately starting with the second for reasons of clarity in the exposition.

Spatial Stability Theory

The calculation of the disturbance growth in the boundary layer is the element which brings in the traditional linear stability theory. A detailed account of compressible stability theory may be found in reference 7. What is required of the theory are the eigenvalues of the stability equations for a spatially growing disturbance. For the parallel-flow form of the stability equations, a Fourier component of a typical three-dimensional fluctuation quantity is given by

$$q'(x,y,z,t) = Q(y) \exp\left[i(\alpha x + \beta y - \omega t)\right] \qquad (1)$$

where q' is a small quantity; x,y,z are the longitudinal, transverse and lateral coordinates; $Q(y)$ is a complex amplitude function; ω is the real circular frequency; and α and β are the complex wave numbers

$$\alpha = \alpha_r + i\alpha_i \quad , \quad \beta = \beta_r + i\beta_i \qquad (2)$$

All quantities have been made dimensionless with respect to a length scale L^* and a velocity scale V^*. The disturbance wave angle is

$$\psi = \tan^{-1}(\beta_r/\alpha_r) \tag{3}$$

and β_i/α_i is assumed equal to β_r/α_r. The phase velocity is

$$c_p = \omega/\alpha_r \tag{4}$$

and the imaginary part of α is the amplification rate

$$(1/A)(dA/dx) = -\alpha_i \tag{5}$$

The notation A has been introduced as the amplitude in equation (5) to emphasize that in the parallel-flow theory all flow variables grow at the same rate and independently of y. The amplitude is given as a function of Reynolds number by

$$A(Re)/A_o = \exp\left(-\int_{Re_o}^{Re} \alpha_i \, dRe\right) \tag{6}$$

The subscript o refers to the lower-branch neutral point, i.e., where the disturbance has its minimum amplitude and first starts to amplify. The initial amplitude A_o is obviously of as much importance in determining the amplitude A as the amplification, and is the quantity that must be obtained from the external disturbance and an interaction relation.

The eigenvalues α_i and c_p are obtained from repeated numerical integrations of the stability equations. For a three-dimensional compressible disturbance, the equations form an eighth-order system of complex linear ordinary differential equations (ref. 7). The four solutions which satisfy the boundary conditions as $y \to \infty$ provide the initial conditions for the numerical integration which proceeds from the free stream to the wall at $y = 0$. There are a total of 64 real equations to integrate. At $y = 0$, a linear combination of the four solutions satisfies three of the four homogeneous boundary conditions. With Re and the dimensionless frequency F fixed, an iterative linear search procedure finds the eigenvalues α_i and c_p which satisfy the remaining boundary condition.

Interaction of External Disturbances

Quantities computed directly from the linear stability theory such as the minimum critical Reynolds number and amplification rate are inherent properties of the mean boundary layer on the same basis as the displacement thickness or skin-friction coefficient. On the other hand, the transition Reynolds number is not at all an inherent property as it depends not only on the instability of the boundary layer, but also on external disturbances which interact with the boundary layer to form the internal disturbances which lead ultimately to transition. With no disturbances, transition can not occur no matter how unstable the boundary layer is. The external disturbances can arise from any one of several sources of unsteadiness such as free-stream turbulence, sound or vibration. Ideally, one would like to have a theory to give the initial amplitude of each Fourier component of the internal disturbance from the known external disturbance, but no such theory exists. A forced response of the boundary layer can be computed in certain instances, and the initial amplitude of the free internal disturbance assumed to be related in some way to the forced internal disturbance. An example of such a procedure is given in reference 1, where the effect of irradiated sound on the stable region of a laminar boundary layer is calculated from a simple forcing theory.

Yet a third procedure for determining the initial amplitude is to adopt an empirical relation. The simplest of these assumes that the square of the amplitude of each frequency component of the internal disturbance is directly proportional to the energy density of the same frequency of the external disturbance, and that the constant of proportionality is the same for all frequencies. That is, the initial amplitude A_0 of the single-frequency internal disturbance of frequency ω is related to A_1, the amplitude of the external disturbance, by

$$A_0(\omega) = A_z E^{\frac{1}{2}}(\omega) A_1 \qquad (7)$$

where $E(\omega)$ is the normalized (unit area) energy density of the one-dimensional power spectrum of A_1. The constant A_z can be regarded as an interaction or coupling coefficient which "couples" the external to the internal disturbance. It is determined by adjusting the calculated transition Reynolds number to a measured value. Once A_z is determined in conjunction with a specific transition criterion and for a specific disturbance source, there are no more free constants in the entire calculation. More generally, A_z is a function of ω and is so given when calculated from a forcing theory.

Equation (7) is in accord with the stated procedure of applying stability theory in the form of single-frequency disturbances. Otherwise, A_0^2 in equation (7) would be an energy density, and the internal disturbance amplitude A_d would be given by

$$A_d^2 = \int_0^\infty (A/A_0)^2 \, A_0^2(\omega) \, d\omega \qquad (8)$$

where A/A_0 is the frequency-dependent amplification ratio given by equation (6). There is one circumstance under which A_d differs from the A of the most amplified frequency only by a constant, and that is when A/A_0 has the character of a delta function. For transition in a low-disturbance environment where large amplifications take place, A/A_0 does resemble a delta function near transition, but in many cases it does not. It must be kept in mind that the development of a disturbance composed of a whole spectrum of frequencies is being represented by a fictitious disturbance of only a single frequency. Such a representation can not always be adequate, and it is most likely to be seriously in error when the amplification is small.

A potentially serious problem for which there is no solution at the present time is that the available disturbance spectra both in the free stream and the boundary layer are one-dimensional. As can be seen from equation (1) the elementary disturbance of stability theory is an oblique wave in the x-z plane. For supersonic flow, the most unstable first-mode disturbance is oblique with a wave angle ψ of between 50° and 60° over a wide range of Mach numbers (ref. 7). What is needed, therefore, is the energy distribution with respect to ψ as well as frequency. In the absence of any measurements, it will be assumed that the frequency power spectra are the same for all wave angles.

Transition Criterion

The final step in the transition calculation is to apply a transition criterion, the simplest of which is an amplitude criterion based on a value of A, say A_t. The theoretical disturbance growth curve of figure 2 shows that the choice of A_t is not critical, as a rather large change in A_t makes only a small difference in the corresponding Reynolds number Re_t which is to be identified with the transition Reynolds number. The use of A itself as the transition criterion avoids the troublesome problem in the application of the parallel-flow theory of having to identify A with a particular fluctuation quantity. In a growing boundary layer, the eigenfunctions are functions of Re and as a result the different flow variables do not all grow in the same manner. Even within the scope of an amplitude criterion, one could identify A with, say, the mass-flow fluctuation and use the pressure fluctuation as the transition criterion with somewhat different results than if the mass-flow fluctuation were the transition criterion.

Some 30 years ago Liepmann (ref. 8), in an exceptionally clear presentation of the requirements of a transition calculation based on linear theory, proposed that transition starts when the Reynolds stress equals the mean viscous stress, i.e., when

$$\tau_R = \rho \overline{u'v'}/\mu \, \partial U/\partial y = 1 \qquad (9)$$

The basis of this idea is that when the Reynolds stress reaches such a value the mean velocity profile must change in an important way. Liepmann's criterion can be modified somewhat by selecting a value $(\tau_R)_t$ different from unity as the criterion.

In order to calculate τ_R, it is necessary to first calculate the eigenfunctions. Since the amplitude in linear stability theory is arbitrary, A must be identified with the peak value of a particular fluctuation to set the amplitude, and only then can τ_R be calculated. Thus, as mentioned above, the transition Reynolds number obtained will depend to some extent on which fluctuation is chosen.

At present it is not clear how to use Liepmann's criterion in compressible flow. There are other momentum transfer terms besides $\overline{\rho u'v'}$, and even if this single term can properly represent the distortion of the mean velocity profile there are still fluctuation heat-flux terms which perhaps should be included as a measure of the distortion of the mean temperature profile. For these reasons, only the amplitude criterion will be used in this paper for compressible flow.

A third criterion which also involves the Reynolds stress has recently been proposed by R. Kaplan of the University of Southern California. This criterion is based on an argument concerning the total stress tensor. Transition is considered to start when the transverse principal stress vanishes, a condition that is satisfied when

$$\rho \overline{u'v'} + \mu \, \partial U/\partial y = (\overline{u'^2} \, \overline{v'^2})^{\frac{1}{2}} \qquad (10)$$

Again this criterion will only be used for incompressible flow.

COMPUTER PROGRAM

The computer program developed for the transition calculation is based on the author's stability program (ref. 9) which has been used for several years to work on a variety of incompressible and compressible boundary-layer stability problems. The stability program was first simplified and put in single-precision arithmetic except for the independent variable of the differential equations. The first new feature to be added was the automation of the eigenvalue computations so that a large number of eigenvalues can be obtained in a single computer run. Up to 12 dimensionless frequencies

F may be calculated at a given initial Reynolds number at either equal increments in F or at unequally spaced specified values of F. Then for each F in turn, up to 14 eigenvalues are computed over a range of Reynolds numbers which may also be unequally spaced.

The eigenvalue search procedure is set up to do a minimum of two iterations. Only one perturbation integration is required per iteration because with F and Re fixed, the secular determinant is an analytic function of the complex variable α for a spatial disturbance. Thus two iterations require four integrations of the 64 equations (16 for incompressible flow). Convergence is usually achieved after the two mandatory iterations, but if not, and the search has started to converge, up to two more iterations are allowed. If there is still no convergence, or the search did not give adequate signs of converging after the first two iterations, the increment in F or Re is halved, and if necessary, halved a second time. If nonsimilar boundary-layer profiles are being used, the Re increment can not be halved as the program is set up to use precomputed profiles which are read in from mass storage as needed.

After the eigenvalues have been obtained over a sufficient Reynolds number range for a given frequency, the next step is to compute the Reynolds numbers of the neutral-stability points. Up to four neutral points can be computed to allow for the possibility of two separate unstable regions. The neutral points are found by interpolation, and if desired the interpolated neutral points can be further refined by applying an eigenvalue search procedure which requires a minimum of six additional integrations per neutral point. When the lower-branch neutral point Re_o has been found, A/A_o is calculated from equation (6).

The next step is the calculation of the initial amplitude A_o from equation (7). For an empirical interaction relation, A_1 and A_2 are both input quantities and $E(\omega)$ is calculated from one or several formulas which are specific to a particular problem. If the sound-forcing theory is used to calculate A_2, then two integrations of 80 equations each are needed for this purpose. With both A/A_o and A_o known, A(Re) can be calculated and the amplitude transition criterion applied. When A exceeds A_t, the corresponding Re_t is computed by inverse interpolation. When this series of calculations has been carried out for all of the frequencies of importance, the minimum Re_t is the predicted transition Reynolds number.

The evaluation of the Reynolds stress criteria requires the computation of the eigenfunctions at each Reynolds number. Two integrations are needed for this purpose. The peak value of the mass-flow fluctuation is identified with A to assign a magnitude to the eigenfunctions and thus to the Reynolds stress. The Liepmann and Kaplan criteria are evaluated, and when either criteria is exceeded the equivalent transition Reynolds number is found by inverse interpolation.

Storage and Time Requirements

The program requires a total of 49,000 single-precision words (36 bits) of storage, or 31,200 words with segmentation (overlays). On the UNIVAC 1108 time-sharing system, the basic integration time is 7.4×10^{-4} sec to integrate one equation across one step. For incompressible flow, where 80 steps are adequate and there are 16 equations for a two-dimensional disturbance, it requires 0.95 sec for each integration, and a total of 3.8 sec for each eigenvalue provided there is convergence in two iterations. For compressible flow with 100 steps and 64 equations, the respective times are 4.7 and 19 sec.

A minimum requirement for a transition calculation is about four frequencies with eight Reynolds numbers for each frequency. Consequently, to find the eigenvalues requires 122 sec for incompressible flow and 608 sec for compressible flow if all eigenvalue searches converge in two iterations. The time required to obtain the neutral-stability points by interpolation, evaluate the integral of α_i, calculate A_0 and determine Re_t on the basis of the amplitude criterion is negligible. For example, the results to be presented at $M_1 = 4.5$ were obtained with five frequencies and a total of 45 Reynolds numbers. The time to compute the eigenvalues was 855 sec, but to do all of the other calculations took only 1.5 sec.

The Reynolds stress transition criteria require two integrations per Reynolds number, and thus 50% as much time as the computation of the eigenvalues if the transition criteria are to be evaluated at all Reynolds numbers. However, if an Re_t is obtained first from the amplitude criterion, then the eigenfunction calculation need not start until one or two stations before this Reynolds number. In practice, the two Reynolds stress criteria required about 25% more time than for the eigenvalue calculation alone.

Since the transition Reynolds number is often computed as a function of some mean-flow parameter such as Mach number or altitude, a great many different boundary layers have to be evaluated. At 10-15 minutes per boundary layer, a large amount of computer time can be involved and a faster computer than the UNIVAC 1108 would be an advantage. It is estimated that the program would run about ten times faster on a CDC 7600. On a parallel-processor computer such as the ILLIAC, a further time advantage could be realized by integrating the independent solutions simultaneously instead of consecutively as at present, and by calculating the eigenvalues and eigenfunctions of different frequencies simultaneously.

EFFECT OF FREE-STREAM TURBULENCE

In order to debug the final program as economically as possible, but still work on an important problem, a calculation was made of the effect of free-stream turbulence on the transition of the Blasius boundary layer.

Figure 3 shows the published measurements as taken from reference 10. The ordinate is the start-of-transition Reynolds number, and the abscissa is the rms intensity of free-stream turbulence which is identified here with the amplitude A_1. The curve is from the present calculation and is discussed below. Unfortunately, none of the experimenters measured either the turbulence spectrum or the scale. In the absence of this essential information, the spectrum was assumed to be the Dryden spectrum (ref. 11) of isotropic turbulence,

$$U_1^* E^*(\omega^*)/L_x^* = 4/[1 + (\omega^* L_x^*/U_1^*)^2] \qquad (11)$$

where L_x^* is the integral length scale of turbulence. Although it is not necessary to set individual values of U_1^* and L_x^* in the present calculation at a single turbulent Reynolds number ($R_L = U_1^* L_x^*/\nu^*$), the spectrum is entered in the program as given by equation (11) in order to be able to calculate the separate effects of U_1^* and L_x^*. Therefore, U_1^* and L_x^* had to be assigned and the values chosen were

$$U_1^* = 44 \text{ ft/sec} \quad , \quad L_x^* = 2.18 \text{ in.} \qquad (12)$$

With $E^*(\omega^*)$ known, the next step is to set the interaction constant A_z. For this purpose, the start-of-transition Reynolds number $Re_t = 2.8 \times 10^6$ measured by Schubauer and Skramstad (ref. 2) for $A_1 = 0.1\%$ was used. Although the lowest measured disturbance level in their tunnel (0.02 - 0.03%) was mostly sound, particularly for the unstable frequencies, it will be assumed that disturbances of 0.1% and greater are primarily turbulence. Since the Kaplan transition criterion is the only one that does not require a numerical value to be chosen, it was used to calculate A_z. With A identified as the peak value of u', the rms longitudinal velocity fluctuation referenced to the free-stream mean velocity, it was found that $A_z = 0.086$ gives $Re_t = 2.8 \times 10^6$. With this A_z, the same Re_t is obtained with the amplitude criterion set at $A_t = 0.04$, or with the Liepmann criterion set at $(\tau_R)_t = 0.14$ instead of Liepmann's suggested value of 1.0.

At this point everything should be in readiness to calculate the effect of A_1 on Re_t. However, the change of A_0 with A_1 as given by equation (7) and the Dryden spectrum, together with the frequency dependence of A/A_0 for a two-dimensional instability wave in the Blasius boundary layer, does not begin to give a large enough effect on Re_t to account for figure 3. There is no experimental information on the relation between the turbulence intensity in the free stream and the amplitude of the instability wave, so only conjectures are possible. One possibility is that the interaction is not linear as assumed by equation (7). A second possibility is that there is indeed a linear interaction, but that the initial

disturbance forms in the damped region rather than at the neutral point. As a result, A_0 would vary with F along the neutral curve just from the different damping ratios between the initial point and the neutral point. Since the frequency of the disturbance of maximum growth also changes with A_1, the second possibility is in a certain sense equivalent to the first. Consequently, it will be assumed without further inquiry into its meaning that

$$A_z = 0.043 \left[1 + (A_1/0.001)^{2.3}\right] \qquad (13)$$

where the multiplicative constant is just one-half the previous value of A_z in order to give the same Re_t as before when $A_1 = 0.1\%$. The exponent 2.3 was chosen to fit the experimental curve at $A_1 = 0.4\%$. As a note of caution, equation (13) is not intended to relate the entire free-stream spectrum to the internal spectrum, but only to give the A_0, and hence the amplification ratio, that is required to account for the initial rapid decrease of Re_t with increasing A_1.

Re_t was computed with equations (7), (13) and the amplitude criterion of 4% up to $A_1 = 2\%$, and the result is the curve shown in figure 3. It is surprising that agreement with the experimental results is obtained all the way to $A_1 = 2\%$ where transition is not far from the minimum critical Reynolds number.

The curve shown in figure 3 is not much more than an empirical fit to the data. Unfortunately, until the amplitudes of Tollmien-Schlichting waves can be related in a fundamental way, either theoretically or experimentally, to the free-stream turbulence, nothing better can be done at the present time. The advantage of the present procedure over a direct curve fit of Re_t to the data is that the effects of turbulence scale, spectrum and free-stream velocity on Re_t, as well as the influence of turbulence on the transition of arbitrary boundary layers, can all be calculated with no further assumptions. Furthermore, it is possible to use the method to compare results obtained with the three transition criteria, and some of these calculations have been carried out. Simply stated, the computed transition Reynolds numbers appear to depend very little on the particular criterion used. For $A_1 < 0.5\%$, there is virtually no difference between the criteria; for $A_1 = 1\%$, the results for the amplitude, Liepmann and Kaplan criteria are, respectively, 0.567×10^6, 0.600×10^6 and 0.609×10^6, a maximum difference of 7%.

TRANSITION IN SUPERSONIC WIND TUNNELS

Determination of Input Quantities

Transition in a supersonic wind tunnel above $M_1 = 2\text{-}3$ is dominated by the sound radiated from the turbulent boundary layers on the tunnel walls.

In reference 1, linear stability theory was used together with an amplitude criterion to calculate the variation of Re_t with M_1 for an insulated flat-plate boundary layer. The external disturbances were included by the simple expedient of taking $A_0 \sim M_1^2$, as suggested by Laufer's finding in reference 4 that the free-stream rms pressure fluctuation p_1' varies essentially as M_1^2. The calculated variation of Re_t with M_1 bore a striking resemblance to the experimental measurements, although the unit Reynolds number dependence of p_1' was not sufficient to explain the measured dependence of Re_t on unit Reynolds number. The spectrum of p_1' plays an essential role in this dependence and must be included in the calculation.

With the interaction in the form of equation (7), $E^*(\omega^*)$ was obtained from the measurements of Laufer (ref. 4). The faired experimental spectra are shown in figure 4. The spectrum at $M_1 = 4.5$, Re/in. $= 3.4 \times 10^5$ is approximated in the computer program by curve fits accurate to about 5%. A unit Reynolds number correction as given by the spectrum at $M_1 = 4.5$, Re/in. $= 1.8 \times 10^6$, and a Mach number correction as given by the spectrum at $M_1 = 2.0$, Re/in. $= 3.4 \times 10^5$ are both included in the program. The energy density and frequency $f^*(= \omega^*/2\pi)$ were made dimensionless by Laufer with L_x^*, the integral length scale of the wall pressure fluctuations, and U_s^*, the average velocity of the sound sources. Both of these quantities are entered in the program as curve fits to the measured values.

Laufer measured p_1' at two Re/in. from $M_1 = 1.6$ to 5.0. Other measurements (ref. 12) have shown that p_1' varies with Re/in. as $(\text{Re/in.})^n$. The power that agrees best with Laufer's two values over the Mach number range is $n = -0.2$. Consequently, the value of A_1 entered in the program is

$$A_1 = 0.00045\ \gamma M_1^2\ [(\text{Re/in.})/(3.4 \times 10^5)]^{-0.2} \qquad (14)$$

where $\gamma = 1.4$.

The remaining quantity in equation (7) is the coupling coefficient A_z. The program provides for A_z to be computed by the sound-forcing theory presented in reference 1. This theory requires a value of the sound source velocity which in turn defines ψ_c, the cut-off value of the wave angle ψ beyond which there is no sound radiation. The angle ψ_c is usually less than the angle of the disturbance of maximum amplification and can result in a marked reduction in the amplification ratio A/A_0. In addition, the source velocity is a strong function of frequency and this dependence has been measured only at $M_1 = 4.5$ (ref. 13). Even though with an average value of the source velocity the theory gives the result that A_z is inversely proportional to F and increases slowly with M_1 in agreement with the measurements of Kendall (ref. 5), it was decided that the uncertainties involved in using the sound-forcing theory in the present calculations are greater than just assuming A_z to be constant.

With an amplitude transition criterion of 1%, the constant A_z was adjusted to give $Re_t = 1.45 \times 10^6$ at $M_1 = 4.5$, Re/in. $= 3 \times 10^5$, the start-of-transition Reynolds number measured by Coles (ref. 6). It must be pointed out that the amplitude criterion is here completely arbitrary. A different value of A_t would merely change A_z in proportion. What is really being set is the amplification A/A_o needed for transition at the specified Reynolds number. The coefficient A_z would acquire a physical meaning only if the entire spectrum were being used to compute the amplitude rather than a single frequency. However, it is helpful to use constants whose magnitudes make physical sense, and 1% was chosen on the idea that it represents the pressure fluctuation. The mass-flow and pressure fluctuation both become large in the free stream as M_1 increases. In the boundary layer, the mass-flow fluctuation, which is mostly a density fluctuation at high Mach numbers, is larger than in the free stream. On the other hand, p' is smaller than in the free stream and declines relative to the mass-flow fluctuation as M_1 increases. Since it is known that a boundary layer at hypersonic Mach numbers can support large mass-flow fluctuations without becoming turbulent, it may be that p' is the more suitable quantity to relate to transition.

Results of Calculations

With the constant A_z set once and for all, a series of calculations were carried out for $M_1 = 2.2$, 3.0 and 4.5, and $1 < \text{Re/in.} \times 10^{-5} < 4$. These Mach numbers were chosen because most of the eigenvalues needed were already available. The results are shown in figures 5 and 6 where they are compared with Coles' measurements at four Mach numbers, only one of which is the same as the Mach numbers of the calculations. Figure 6 is cross plotted from figure 5, and there is one additional point shown at $M_1 = 1.6$ that does not appear in figure 5.

There is seen to be reasonable agreement between the calculated and experimental values, with a maximum difference of about 15%. The unit Reynolds number effect has been a particularly difficult one to account for in anything resembling a fundamental manner (ref. 14), and it is encouraging to see some features of the measured effect appear in the calculated results. Many measurements of the unit Reynolds number effect can be fitted by the relation

$$Re_t \sim (\text{Re/in.})^m \tag{15}$$

A common value of m is 0.4, although a wide range of values have been encountered, and there are measurements which do not fit this relation at all. The measurements for $M_1 = 2.57$ in figure 5 fall into this latter category when the entire Re/in. range is included. However, for Re/in. $> 1 \times 10^5$ a power law is a reasonable fit to the data with m = 0.28, 0.36, 0.63, 0.47 at $M_1 = 2.0$, 2.57, 3.7, 4.5, respectively. The calculated

slope at $M_1 = 2.2$ is $m = 0.35$ which is close to the experimental value at $M_1 = 2.57$. Although the calculated curves at the other two Mach numbers are not straight lines, they are in agreement with experiment to the extent that their slopes increase with Mach numbers.

The increased slope calculated at the lower Re/in. may possibly be a reflection of this same tendency in the experimental results for $M_1 = 2.57$, but it more likely comes from an inadequacy in the method. The best agreement is found at $M_1 = 2.2$, and this agreement would be even better as to the magnitude of Re_t if the actual measured value of $p_1'/\gamma M_1^2$ at $M_1 = 2.2$, 0.00055, were used instead of the average value 0.00045. At $M_1 = 2.2$, the total amplification at Re/in. $= 1.5 \times 10^5$ is 11.1, and the representation of the disturbance growth by a single frequency should be valid. In contrast, at $M_1 = 4.5$ the amplification at the same Re/in. is only 3.5, and it is possible that the single-frequency approximation at this and lower Re/in. is not valid because of the small overall amplifications involved.

In support of this conjecture, a calculation made by the author a number of years ago (ref. 7, fig. 13-46) is helpful. In this calculation, growth curves were obtained at $M_1 = 4.5$ with the complete frequency spectrum taken into account, but with still only a single wave angle of 60° (there is a similar calculation with energy distributed uniformly with respect to ψ). In this calculation the spectrum and p_1' were assumed to be independent of Re/in., and α_i was computed approximately from the temporal stability theory. Of these simplifications, the most serious is believed to be the one concerning p_1'. A unit Reynolds number effect smaller than in the present calculation was found. With an amplitude criterion set to yield $Re_t = 1.45 \times 10^6$ at Re/in. $= 3 \times 10^5$ as here, the Re_t at Re/in. $= 1 \times 10^5$ can be determined from reference 7 to be 1.15×10^6. This value can be compared with $Re_t = 0.66 \times 10^5$ of the present calculation with $n = -0.20$ in equation (14). If n is set equal to zero, then Re_t increases to 0.83×10^6. If the influence of n on the result with the complete spectrum is in the same ratio as with a single frequency, then with $n = -0.20$, Re_t would decrease from 1.15×10^6 to 0.91×10^6. It can be seen from figure 5 that this value fits the measurements quite well, and the value of m in equation (15) is 0.43 as compared to the experimental value of 0.47.

Figure 6 requires little comment except to point out that computations are needed at more Mach numbers to better define the curves drawn in the figure. In order to extend the calculations to higher Mach numbers, additional p_1' and spectrum measurements are needed. For $M_1 < 2$, there is a different sort of problem. With decreasing Mach number, the influence of the irradiated sound decreases and that of free-stream vorticity increases. Consequently, the nature of the interaction changes and A_z can not be expected to remain constant. The present indications are that the sound is more effective in creating instability waves than is vorticity, so that A_z should decrease below $M_1 = 2$ with resulting larger values of Re_t. In support of this reasoning, $Re_t = 3.4 \times 10^6$ at $M_1 = 1.6$, Re/in. $= 3 \times 10^5$ in figure 6, while an experiment by Kendall in the JPL 20-in. tunnel showed no transition on a flat plate at Re $= 4.3 \times 10^6$ with Re/in. $= 3.4 \times 10^5$.

CONCLUDING REMARKS

The origin of transition has been viewed here as the result of specific external disturbances with well-defined characteristics interacting with the boundary layer and being amplified according to linear stability theory until a critical state is reached. The example of the effect of free-stream turbulence on transition could not be carried to a conclusion because not enough is known of the all important interaction process. It is in the supersonic wind tunnel that the most complete information exists. The free-stream disturbances have been measured in the necessary detail, transition data are available, and the interaction appears to be linear and of such a nature that it can be represented by a simple relation. In these favorable circumstances, linear stability theory has been shown capable of providing reasonable estimates of the start of transition as a function of unit Reynolds number and Mach number for the simplest possible boundary layer, the boundary layer on a smooth, insulated, flat plate. However, there appears no reason to doubt that the method, perhaps modified to include the complete spectrum, will work for more complicated boundary layers and in different disturbance environments if the interaction can be properly accounted for.

Further progress would seem to require more study of each of the three parts of the transition calculation. The stability theory must be extended beyond flat-plate boundary layers; the spectral characteristics of the disturbances which occur in different flow environments must be measured; and the interaction of these disturbances with the boundary layer to create instability waves must be understood. Some factors which influence transition and are commonly thought of as causes of transition, such as surface roughness and waviness, are not true sources of instability waves in the absence of an unsteady local separation, but act to influence existing disturbances which have arisen from other sources. This influence is exerted through a modification of the mean boundary layer which sharply increases the instability amplification (ref. 15). The requirement in these instances is the capability of computing the modified mean boundary layer.

To the objection that it is very difficult to obtain the necessary information about the external disturbances, it can be replied that otherwise the prospects for real progress in the ability to predict transition are indeed bleak. Repeated experimentation in similar disturbance and flight environments can result in some definite conclusions, but once the environment is changed the whole procedure must start all over again. Even when it becomes possible, as it will one day, to replace the linear stability theory with the three-dimensional time-dependent Navier-Stokes equations, this part of the problem will not change. The interaction can then be solved directly, but the necessity of defining the external disturbances will remain exactly what it is today. Without quantitative knowledge of the disturbances, transition prediction, difficult enough in any case, is likely to remain forever just out of reach.

REFERENCES

1. Mack, L. M.: Linear Stability Theory and the Problem of Supersonic Boundary-Layer Transition. AIAA Journal, vol. 13, Mar. 1975.

2. Schubauer, G. B. and Skramstad, H. K.: Laminar Boundary-Layer Oscillations and Transition on a Flat Plate. NACA Report 909, 1948.

3. Jackson, F. J. and Heckl, M. A.: Effect of Localized Acoustic Excitation on the Stability of a Laminar Boundary Layer. Report 62-362, Aeronautical Research Lab., Wright-Patterson Air Force Base, Ohio, 1962.

4. Laufer, J.: Some Statistical Properties of the Pressure Field Radiated by a Turbulent Boundary Layer. Physics of Fluids, vol. 7, no. 8, Aug. 1964, pp. 1191-1197.

5. Kendall, J. M.: Wind Tunnel Experiments Relating to Supersonic and Hypersonic Boundary Layer Transition. AIAA Journal, vol. 13, Mar. 1975.

6. Coles, D.: Measurements of Turbulent Friction on a Smooth Flat Plate in Supersonic Flow. Journal of Aeronautical Sci., vol. 21, no. 7, July 1954, pp. 433-448.

7. Mack, L. M.: Boundary-Layer Stability Theory. Internal Document 900-277, Rev. A, Jet Propulsion Lab., Pasadena, Calif., 1969.

8. Liepmann, H. W.: Investigation of Boundary-Layer Transition on Concave Walls. NACA WR W-87, 1945. (Formerly NACA ACR 4J28.)

9. Mack, L. M.: Computation of the Stability of the Laminar Compressible Boundary Layer. Methods in Computational Physics, Volume 4, B. Alder, ed., Academic Press, Inc., 1965, pp. 247-299.

10. Dryden, H. L.: Transition from Laminar to Turbulent Flow. In Turbulent Flows and Heat Transfer, Princeton Univ. Press, Princeton, N. J., 1959, pp. 3-74.

11. Dryden, H. L.: A Review of the Statistical Theory of Turbulence. Q. Appl. Math., vol. 1, 1943, pp. 7-42.

12. Beckwith, I. E. and Bertram, M. H.: A Survey of NASA Langley Studies of High-Speed Transition and the Quiet Tunnel. NASA TM X-2566, 1972.

13. Kendall, J. M.: Supersonic Boundary Layer Stability Experiments. Proc. of Boundary Layer Transition Study Group Meeting, vol. II, Aerospace Corp., San Bernardino, Calif., 1967.

14. Potter, J. L.: The Unit Reynolds Number Effect on Boundary Layer Transition. Ph.D. Dissertation, Vanderbilt Univ., Nashville, Tenn., May 1974.

15. Klebanoff, P. S. and Tidstrom, K. D.: Mechanism by which a Two-Dimensional Roughness Element Induces Boundary-Layer Transition. Physics of Fluids, vol. 15, no. 7, July 1972, pp. 1173-1188.

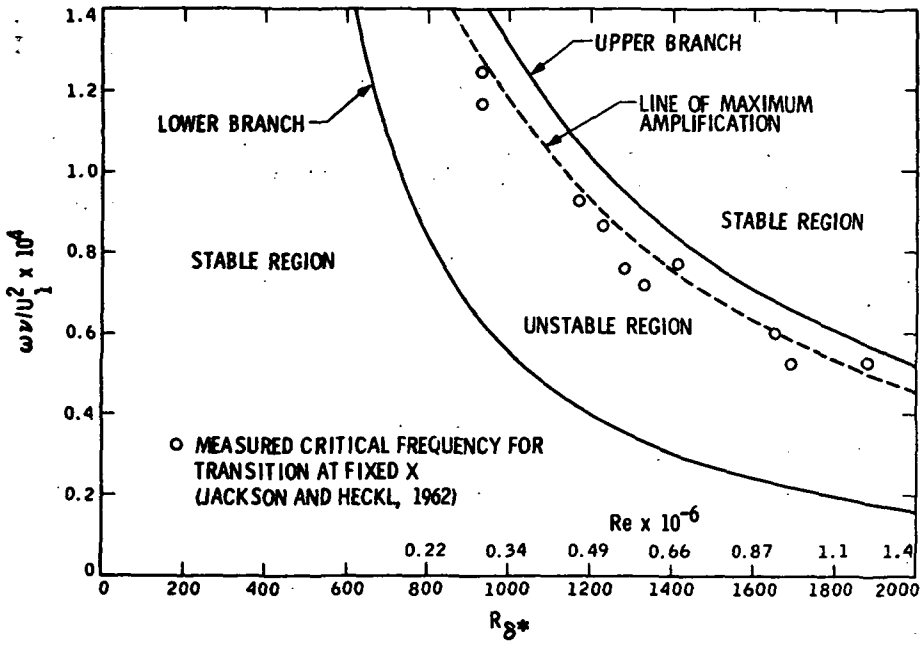

Figure 1. Experimental evidence for the relation between transition and linear stability theory.

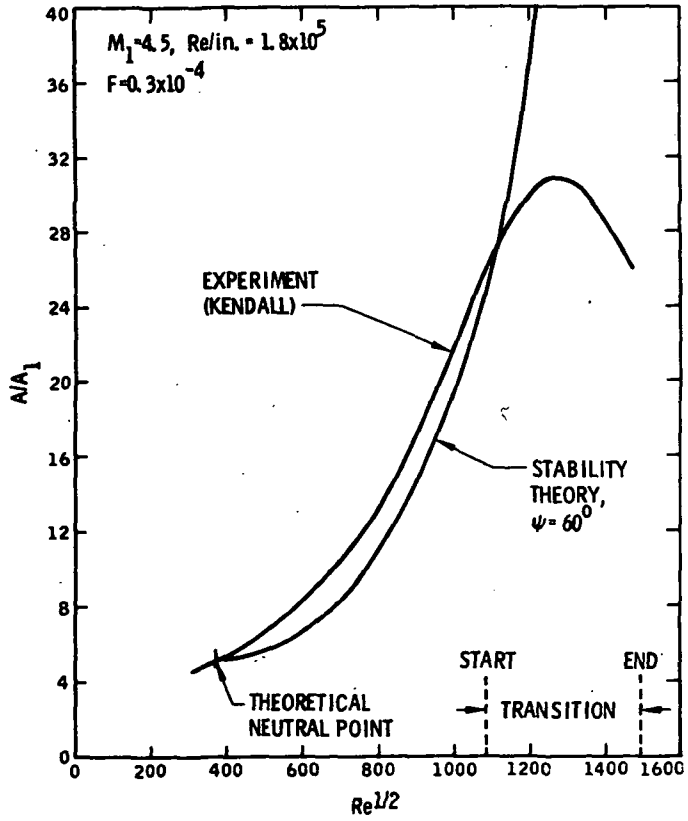

Figure 2. Comparison of the theoretical and experimental growth of a single-frequency disturbance.

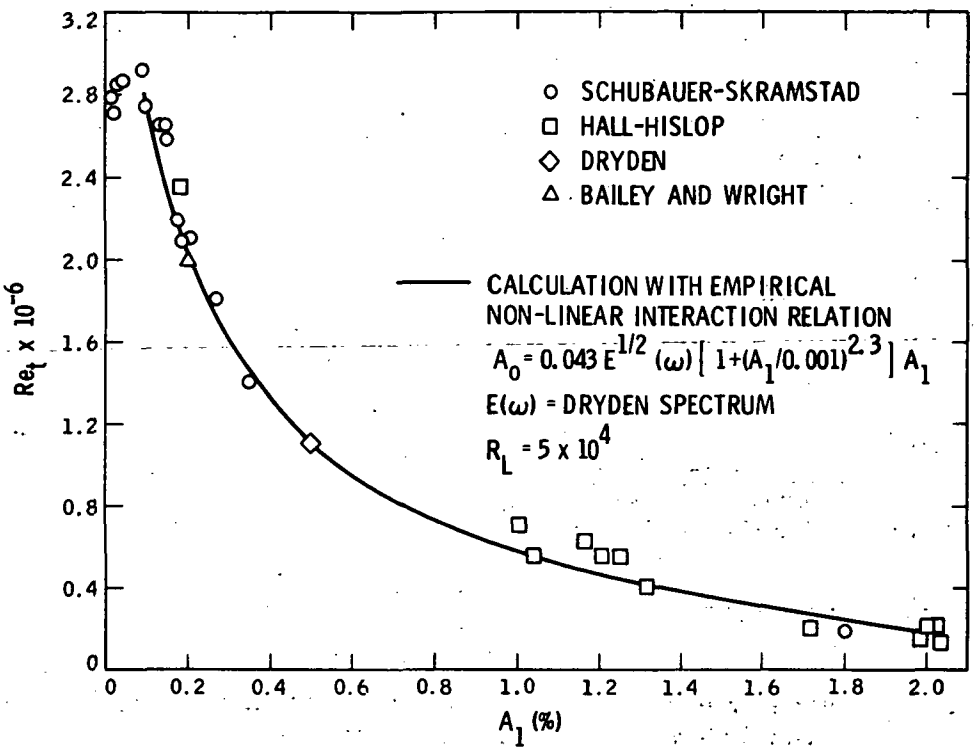

Figure 3. Effect of free-stream turbulence on transition.

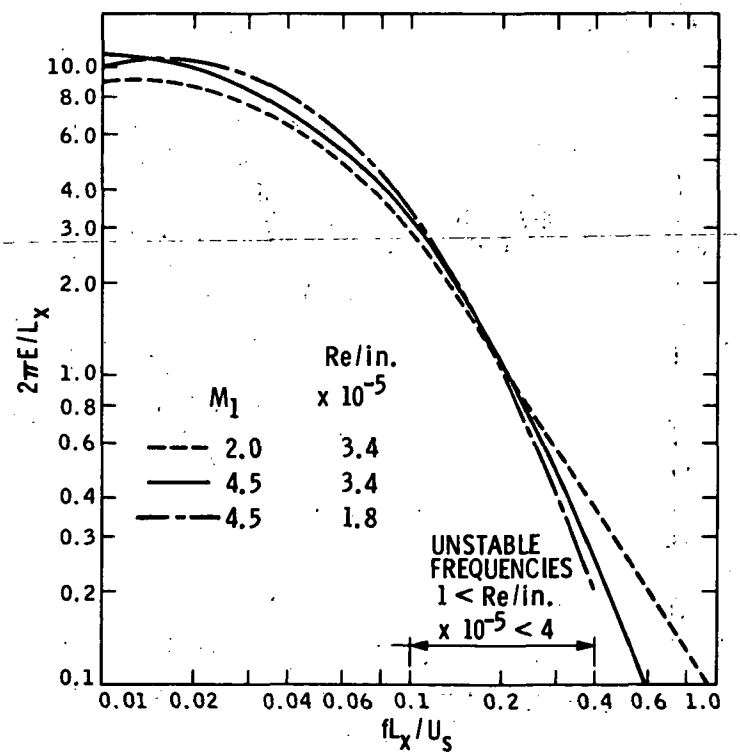

Figure 4. Experimental free-stream disturbance spectra (ref. 4).

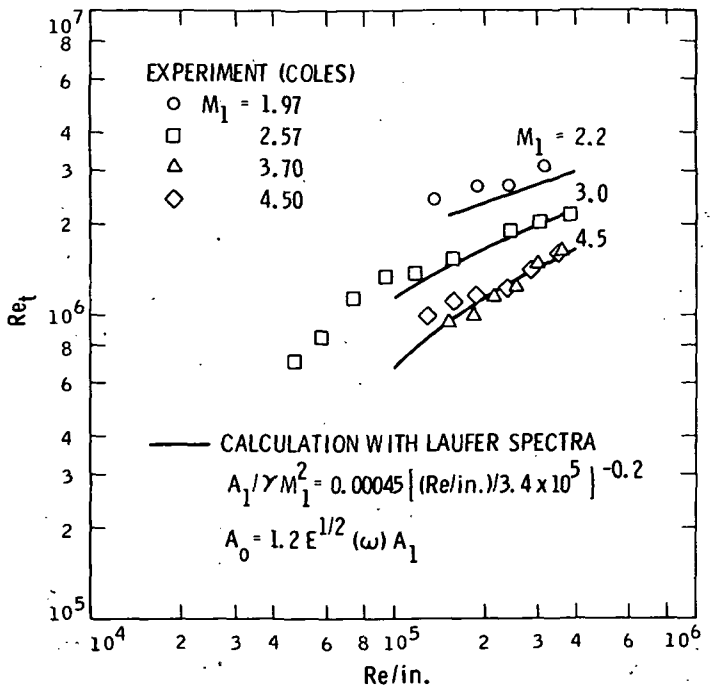

Figure 5. Calculated effect of unit Reynolds number on the transition of insulated flat-plate boundary layers at M_1 = 2.2, 3.0, 4.5 and comparison with experiment.

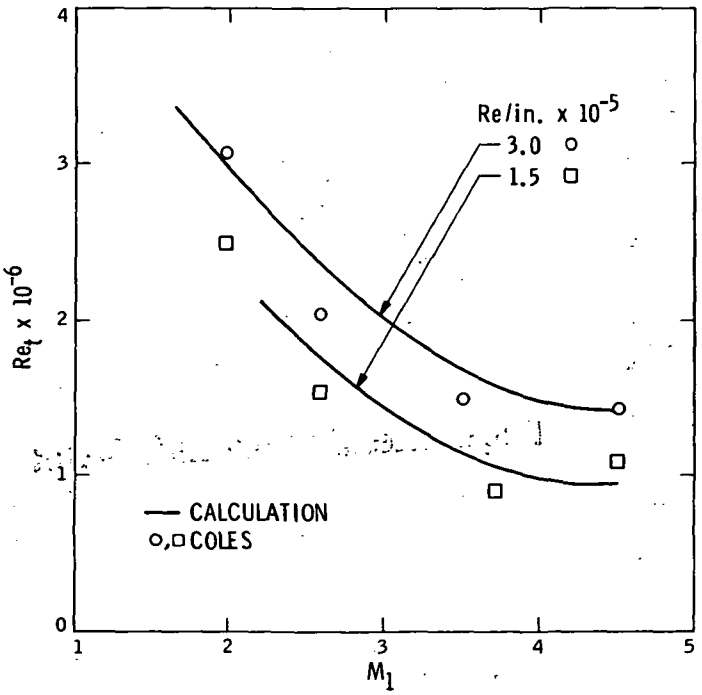

Figure 6. Calculated effect of Mach number on the transition of insulated flat-plate boundary layers at Re/in. x 10^{-5} = 1.5 and 3.0 and comparison with experiment.

Page Intentionally Left Blank

SOLUTIONS FOR INCOMPRESSIBLE SEPARATED BOUNDARY LAYERS INCLUDING VISCOUS-INVISCID INTERACTION

By James E. Carter and Stephen F. Wornom
NASA Langley Research Center

SUMMARY

Numerical solutions are presented for the laminar and turbulent boundary-layer equations for incompressible flows with separation and reattachment. The separation singularity is avoided by using an inverse technique in which the displacement thickness is prescribed and the pressure is deduced from the resulting solution. The turbulent results appear qualitatively correct despite the use of a two-layer eddy-viscosity model which is generally assumed appropriate only for mild-pressure-gradient flows. A new viscous-inviscid interaction technique is presented in which the inviscid flow is solved inversely by prescribing the pressure from the boundary-layer solution and deducing the new displacement thickness from the solution of a Cauchy integral. Calculations are presented using this interaction procedure for a laminar flow in which separation and reattachment occur on a solid surface.

INTRODUCTION

The development of theoretical prediction techniques for flows involving boundary-layer separation is of fundamental importance since separation is a common occurrence on most aerodynamic surfaces. Significant progress has been made in recent years for laminar supersonic flows which contain large viscous-inviscid interactions, such as those which occur at the point of incidence of a shock wave on a flat plate or in the vicinity of a compression corner. Werle and Vatsa (ref. 1) and Dwoyer (ref. 2), as well as others, have demonstrated that the boundary-layer equations including interaction with the inviscid flow provide an accurate model which gives results that agree with experiment and solutions of the Navier-Stokes equations (ref. 3). In addition these techniques are currently being extended to turbulent flows (ref. 4).

In supersonic flows the interaction between the viscous and inviscid flow can be computed locally since the inviscid flow is hyperbolic. As a result the singularity which occurs in solutions of the boundary-layer equations when the pressure is prescribed is removed by allowing the boundary layer to modify the pressure to give a regular solution at the separation point. This technique cannot be used for subsonic flows since the invis-

cid flow is elliptic and hence, the pressure at any given point depends on the entire displacement body distribution.

Alternate procedures which are appropriate for subsonic flows and do not rely on interaction to eliminate the separation singularity are the inverse boundary-layer solution techniques which have been recently developed. Catherall and Mangler (ref. 5), and later Carter (ref. 6), have demonstrated that regular solutions can be obtained if the displacement thickness is prescribed and the pressure is deduced from the resulting solution. Similarly, regular solutions at separation can be obtained by prescribing the skin friction as shown by Kuhn and Nielsen (ref. 7), Klineberg and Steger (ref. 8), and Carter (ref. 6). Another inverse procedure, which was developed earlier by Klineberg and Steger (ref. 9) and later used by Tai (ref. 10), is to use the transverse component of velocity at the boundary-layer edge as the prescribed condition.

In contrast with these inverse techniques, Briley and McDonald (ref. 11) have made calculations for subsonic flow using a direct procedure in which the unsteady boundary-layer equations are repeatedly solved until a steady-state solution is obtained. After each time step the prescribed pressure is updated from thin airfoil theory, thereby accounting for the displacement thickness interaction. Although this technique seems feasible, it needs further examination since Briley and McDonald obtained a regular solution at a laminar separation point for a case with no interaction. The absence of the singularity in this case is probably due to numerical inaccuracy since a first-order scheme was used with a coarse grid. Hence, it is not clear in those cases in which interaction was included whether the solution at separation would be regular if a second-order scheme were used.

In using the inverse boundary-layer procedures discussed above, it is necessary to incorporate a description of the inviscid flow to completely describe a viscous-inviscid interaction. For example, Kuhn and Nielsen (ref. 7) developed an iterative procedure in which Murman's inviscid transonic flow program (ref. 12) is solved iteratively with their inverse boundary-layer technique. Kuhn and Nielsen made calculations for the turbulent separated flow behind a bump placed on a wind-tunnel wall. The skin friction was updated for each new boundary-layer calculation based on the difference between the pressure computed from the boundary-layer solution and that obtained from the inviscid flow calculation for the displacement body. This procedure is not straightforward as it is not clear how to update the skin friction based on this pressure mismatch. A simpler procedure, which was recommended by Kuhn and Nielsen and is the subject of the present paper, is to combine the displacement-thickness-prescribed, inverse boundary-layer procedure with a suitable representation of the inviscid flow. In the present study of incompressible flow, the inviscid calculations are made by using an inverse Cauchy integral from thin airfoil theory.

The Cauchy integral relating pressure and body slope is used in an inverse manner so that a new displacement body can be found from the pressure obtained in the inverse boundary-layer calculation. The displacement thickness is then updated by subtracting the prescribed body from the displacement body and the iteration is continued to convergence. This procedure is similar to that used by Jobe and Burggraf (ref. 13) and by Melnik and Chow (ref. 14) in solving the asymptotic equations developed by Stewartson (ref. 15) governing the flow at the trailing edge of a flat plate. An important feature of this inverse procedure is that the results require no smoothing, as has been typically found necessary in direct calculations of inviscid-viscous interaction (refs. 16 and 17). This result is not surprising since the inverse procedure primarily uses numerical integration, which is inherently a smoothing process, in contrast to the numerical differentiation used in the direct procedure.

A second purpose of this paper is to present some calculations which have been made for turbulent flows involving separation and reattachment. These calculations, which do not include interaction, have been made by incorporating a two-layer eddy-viscosity model in the displacement-thickness-prescribed procedure used in the laminar analyses. The variable grid scheme analyzed by Blottner (ref. 18) is incorporated in these calculations to reduce the number of grid points across the boundary layer and simultaneously maintain second-order accuracy.

SYMBOLS

A_n, B_n, C_n, D_n	coefficients in tridiagonal system of equations
C_n', D_n'	coefficients in Thomas algorithm
C_f	skin-friction coefficient
C_p	pressure coefficient
L	reference length
ℓ	coefficient in vorticity-transport equation (see eqs. (1) and (8))
m,n	indices for ξ- and η-directions, respectively
N	computational coordinate

ΔN	increment in computational coordinate
$R_{\infty,L}$	free-stream Reynolds number, $\left(\frac{\rho UL}{\mu}\right)_\infty$
R	reattachment point
S	separation point
t	thickness (see fig. 3)
U_∞	free-stream velocity
u	velocity component parallel to surface
u_e	velocity component parallel to surface at edge of boundary layer
u'v'	Reynolds stress component
x	coordinate along surface
Δx	increment in coordinate along surface
x_0	upstream interaction boundary
x_1	downstream interaction boundary
x'	integration variable
y	coordinate normal to surface
α	coefficient of artificial time term
Δ	increment in displacement thickness
δ	boundary-layer thickness
δ^*	displacement thickness
$\bar{\delta}^*$	$= \delta^* \sqrt{R_{\infty,L}}$

ϵ	eddy-viscosity coefficient
η	transformed y-coordinate
$\Delta\eta$	grid spacing in η-direction
μ	molecular viscosity coefficient
ν	kinematic coefficient of viscosity
ξ	transformed x-coordinate
$\Delta\xi$	grid spacing in ξ-direction
ρ	density
ψ	stream function
$\overline{\psi}$	$= \psi\sqrt{R_{\infty,L}}$
$\tilde{\psi}$	transformed stream function
ω	vorticity
$\overline{\omega}$	$= \omega\Big/\sqrt{R_{\infty,L}}$

Subscripts:

B	body
DB	displacement body
FP	flat plate
max	maximum
o	denotes value at upstream boundary
tr	transition

Governing Equations

The governing equations for an incompressible boundary-layer flow for a prescribed displacement thickness can be given in terms of the following vorticity-transport and stream-function equations:

$$u\bar{\delta}^{*2}\frac{\partial\overline{\omega}}{\partial\xi} - \bar{\delta}^{*}\left\{\frac{\partial}{\partial\xi}\left[\tilde{\psi} + (\eta - 1)\left(u\bar{\delta}^{*}\right)\right]\right\}\frac{\partial\overline{\omega}}{\partial\eta} = \frac{\partial^2\ell\overline{\omega}}{\partial\eta^2} \tag{1}$$

$$\frac{\partial\tilde{\psi}}{\partial\eta} = \bar{\delta}^{*2}(1 - \eta)\overline{\omega} \tag{2}$$

These equations are solved subject to the boundary conditions

$$u(\xi,0) = \tilde{\psi}(\xi,0) = 0 \tag{3}$$

$$\overline{\omega}(\xi,\eta) \quad \text{and} \quad \tilde{\psi}(\xi,\eta) \to 0 \quad \text{as} \quad \eta \to \infty \tag{4}$$

The independent variables are $\xi = x$ and $\eta = y/\bar{\delta}^{*}$ where $\bar{\delta}^{*}$ is the displacement thickness which is defined in the usual manner. Equations (1) and (2) are nondimensional and the dependent variables which are barred have been scaled in the usual manner by $\sqrt{R_{\infty,L}}$ which is appropriate for laminar boundary layers. The transformed stream function $\tilde{\psi}$ is related to the usual stream function $\overline{\psi}$ by $\tilde{\psi} = \overline{\psi} - u\bar{\delta}^{*}(\eta - 1)$ where u is the x-component of velocity. The vorticity is denoted by $\overline{\omega}$ and after it is obtained from equation (1), u is given by

$$u(\xi,\eta) = \bar{\delta}^{*}\int_0^{\eta}\overline{\omega}\left(\xi,\eta_1\right)d\eta_1 \tag{5}$$

After equations (1), (2), and (5) are solved, the unknown edge velocity u_e is obtained from the x-momentum equation which is evaluated at the surface to give

$$u_e\frac{du_e}{d\xi} = -\frac{1}{\bar{\delta}^{*}}\frac{\partial\overline{\omega}}{\partial\eta}\bigg|_{\eta=0} \tag{6}$$

This value should agree with the value obtained from equation (5) and thus serves as a check on the calculation. Equation (6) is integrated from the upstream boundary to give $u_e(\xi)$ and the corresponding pressure coefficient is given by

$$C_p = 1 - u_e^2 \tag{7}$$

Further details of the preceding formulation for laminar flow are presented by Carter (ref. 6).

For laminar flows the quantity ℓ appearing in equation (1) is set equal to unity, whereas for turbulent flow

$$\ell = 1 + \frac{\epsilon}{\mu} \tag{8}$$

where ϵ/μ is the ratio of the eddy viscosity to the molecular viscosity coefficient. The eddy-viscosity coefficient is used to relate the Reynolds stress to the velocity gradient in the usual manner

$$\overline{\rho u'v'} = -\epsilon \frac{\partial u}{\partial y} \tag{9}$$

In the present calculations a two-layer eddy-viscosity formulation has been used which is similar to that used by Harris (ref. 19), Cebeci and Keller (ref. 20), and others. In the inner region a combination of Prandtl's mixing length model along with the Van Driest damping factor is used and is given as follows in dimensional quantities:

$$\left(\frac{\epsilon}{\mu}\right)_{inner} = \frac{(0.4yD)^2}{\nu}\left|\frac{\partial u}{\partial y}\right| \tag{10}$$

where the damping factor D has been modified for separated flows and is given by

$$D = 1 - \exp\left[-\frac{y}{26}\sqrt{\frac{1}{\nu}\left|\frac{\partial u}{\partial y}\right|_{max}}\right] \tag{11}$$

In the outer region Clauser's velocity defect model is used along with the Klebanoff intermittency factor

$$\left(\frac{\epsilon}{\mu}\right)_{outer} = \frac{0.0168 u_e \delta^*}{\nu}\left[\frac{1}{1 + 5.5(y/\delta)^6}\right] \tag{12}$$

where δ is the boundary-layer thickness defined as the point where $u = 0.995u_e$. The boundary between the inner and outer regions is the point at which

$$\left(\frac{\epsilon}{\mu}\right)_{\text{inner}} = \left(\frac{\epsilon}{\mu}\right)_{\text{outer}} \tag{13}$$

Equations (10) to (13) relate the Reynolds stress to the mean flow and thereby complete the formulation for turbulent flows. This two-layer eddy-viscosity model has been widely used for attached flows with mild pressure gradients; its applicability to separated turbulent flows is unknown at the present time. Nonetheless, the purpose of the present paper is to develop a numerical scheme for separated turbulent flows; in the future, refinements of the turbulent empiricism will be made to assess the quantitative results in comparison with experiment.

Numerical Procedure

Figure 1 gives a schematic diagram of the computational schemes and boundary conditions used for the boundary-layer calculations. In an earlier paper Carter (ref. 6) presented a global iteration procedure in which the finite-difference scheme is switched in the reversed-flow region to properly account for the reversed-flow direction. The global iteration technique requires repeated streamwise iterations until convergence is obtained. More recently, Carter and Wornom (ref. 21) have shown that a separated boundary layer can be computed much more rapidly with the usual forward-marching procedure used for attached boundary layers provided that the tridiagonal equations are diagonally dominant and that the streamwise convection of vorticity is neglected in the reversed-flow region; that is, if $u < 0$, then set

$$u\bar{\delta}^{*2}\frac{\partial\bar{\omega}}{\partial\xi} = 0 \tag{14}$$

This approximation is somewhat similar to that used by Reyhner and Flügge-Lotz (ref. 22) for neglecting the streamwise convection of momentum in the reversed-flow region. Use of this approximation eliminates the well-known instability of marching in a direction opposite to that of the flow; in addition, the accuracy is essentially unaffected if the magnitude of the reversed-flow velocity is less than $0.1U_\infty$, as shown by Carter and Wornom (ref. 21).

The streamwise gradients which are typically encountered as a boundary layer approaches separation are quite large, and thus, from numerical experimentation it has been found necessary to use a fully second-order-accurate scheme for $u > 0$. The Crank-Nicolson scheme, including the reversed-flow approximation discussed previously, is used in the laminar calculations and has been previously discussed in references 6 and 21. The turbulent forward-marching procedure, which is presented subsequently, is quite similar although the computational molecule shown in figure 1 is used since the

Crank-Nicolson scheme resulted in oscillatory solutions for some of the turbulent calculations. In this case the streamwise derivatives are represented by the second-order difference expression

$$\left.\frac{\partial \omega}{\partial \xi}\right|_{m,n} = \frac{1}{2\,\Delta\xi}\left(3\omega_{m,n} - 4\omega_{m-1,n} + \omega_{m-2,n}\right) \tag{15}$$

The bars, which were used previously to denote Reynolds number scaling, are deleted for convenience in the presentation of the numerical procedure. The computational molecule for $u < 0$ in the global turbulent calculation is the same as that reported for laminar flow by Carter (ref. 3). A constant grid spacing is used in the stream direction and hence $\xi = m\,\Delta\xi$. In the normal direction a variable grid is used, second-order accuracy being maintained by using the difference expressions developed by Blottner (ref. 18) which are given as

$$\left.\frac{\partial \omega}{\partial \eta}\right|_{m,n} = \frac{\omega_{m,n+1} - \omega_{m,n-1}}{\eta_{n+1} - \eta_{n-1}} + 0(\Delta N^2) \tag{16}$$

$$\left.\frac{\partial^2 \ell\omega}{\partial \eta^2}\right|_{m,n} = \frac{2}{\eta_{n+1} - \eta_{n-1}}\left[\frac{(\ell\omega)_{m,n+1} - (\ell\omega)_{m,n}}{\eta_{n+1} - \eta_n} - \frac{(\ell\omega)_{m,n} - (\ell\omega)_{m,n-1}}{\eta_n - \eta_{n-1}}\right] + 0(\Delta N^2) \tag{17}$$

Blottner showed that a variable grid scheme is equivalent to a coordinate stretching method if the coordinate η can be related to a computational coordinate N in which the grid is evenly spaced. In the present calculations the grid is varied at a constant rate; that is, $\Delta\eta_n = K\,\Delta\eta_{n-1}$, which can be written in terms of a computational coordinate N as follows

$$\eta_n = \eta_{max}\frac{K^{N_n/\Delta N} - 1}{K^{1/\Delta N} - 1} \tag{18}$$

where $N_n = (n - 1)\Delta N$ and $0 \leqq N \leqq 1$. In the present calculations K, the ratio of adjacent grid spacings, equals 1.09, $\eta_{max} = 31$, and 93 grid points are used across the boundary layer. This grid point distribution insures a minimum of 15 points in the viscous sublayer. However, no numerical study was made to determine the optimum value of K or the minimum number of grid points. By using equations (15) to (17) the vorticity transport equation can be written in the following form where q denotes the column iteration level:

$$A_n^q \omega_{m,n-1}^{q+1} + \left(B_n + \alpha\right)^q \omega_{m,n}^{q+1} + C_n^q \omega_{m,n+1}^{q+1} = D_n^q + \alpha \omega_{m,n}^q \tag{19}$$

where

$$\left.\begin{aligned}
A_n &= -\left(C_\eta + K\ell_{m,n-1}\right) \\
B_n &= (K+1)\ell_{m,n} + 3C_\xi \\
C_n &= C_\eta - \ell_{m,n+1} \\
D_n &= C_\xi\left(4\omega_{m-1,n} - \omega_{m-2,n}\right) \\
C_\xi &= K(K+1)\left(\delta_m^* \Delta\eta_{n-1}\right)^2 \frac{u_{m,n}}{4\Delta\xi} \\
C_\eta &= -\frac{K\delta_m^* \Delta\eta_{n-1}}{2} \frac{\partial}{\partial\xi}\left[\tilde{\psi} + (\eta - 1)(u\delta^*)\right]\Big|_{m,n} \\
\alpha &= 2\left|C_\eta\right| + \ell_{m,n+1} + K\ell_{m,n-1} - (K+1)\ell_{m,n}
\end{aligned}\right\} \tag{20}$$

In the reversed-flow region the streamwise convection of vorticity is neglected; as a result $C_\xi = 0$.

Repeated application of equation (19) from the wall to the outer boundary results in a tridiagonal system of linear equations for the vorticity. These equations are solved by the Thomas algorithm which can be written as

$$\omega_{m,n}^{q+1} = D_n' + C_n' \omega_{m,n-1}^{q+1} \tag{21}$$

where

$$D_n' = \frac{D_n - C_n D_{n+1}'}{B_n + C_n C_{n+1}'} \qquad C_n' = \frac{-A_n}{B_n + C_n C_{n+1}'} \tag{22}$$

In equation (19) a timelike term $\alpha\left(\omega_{m,n}^{q+1} - \omega_{m,n}^q\right)$ has been introduced to provide the unconditional diagonal dominance

$$|B_n + \alpha| \geq |A_n| + |C_n| \qquad (23)$$

and thereby prevent error growth in the back substitution procedure given in equation (21). Introduction of this term is a modification of the usual implicit technique used to solve the boundary-layer equations and is the subject of a recent paper by Carter and Wornom (ref. 21).

The quantities D_n' and C_n' are computed, beginning at the outer boundary where the boundary condition $\omega(\xi,\infty) = 0$ is imposed and proceeding to the wall. Equation (21) is then used to obtain $\omega_{m,n}^{q+1}$ once the value at the wall $\omega_{m,1}^{q+1}$ is known. The wall vorticity is found by simultaneously solving for the stream function from equation (2) across the boundary layer and imposing the surface boundary condition given in equation (3). Details of this procedure are the same as those used for laminar flow which are presented by Carter (ref. 6). After the back substitution in equation (21) is completed, the coefficients in equation (19) are updated and the process continued until convergence is obtained. Convergence is assumed when the maximum change in all the dependent variables between two successive column iterations is less than 10^{-5}. In most of the calculations it was necessary to use underrelaxation for the iterative column solution, as was discussed by Carter (ref. 6). The relaxation factor typically used in both the laminar and turbulent calculations was 0.6.

INVISCID FLOW AND INTERACTION PROCEDURE

In this section the inviscid flow, which is approximated by small-disturbance theory, and the interaction procedure shown in figure 2 are discussed. This procedure is applied to the laminar flow over the surface shown schematically in figure 3 in which flow separation and reattachment occur. The strong viscous-inviscid interaction region is assumed to be limited to the region shown in figure 3 in order to replace the infinite limits in the Cauchy integral, which is used to compute the inviscid flow, with finite values. Thus, it is assumed that the region of strong interaction is located a large distance from the leading edge and the Blasius flat-plate displacement thickness at this location results in a negligible pressure gradient. These assumptions are discussed in further detail later.

The calculation is begun with an assumed displacement thickness distribution for $x_0 \leq x \leq x_1$, which is input to the boundary-layer equations. The resulting solution yields the surface pressure $C_{p,DB}$ from equation (7) which results from the inviscid flow over the displacement body. The displacement body coordinate y_{DB} is given by

$$y_{DB} = y_B + \delta^* \qquad (24)$$

where y_B is the prescribed body surface. The displacement thickness can be written as

$$\delta^*(x) = \frac{1.7208\sqrt{x}}{\sqrt{R_{\infty,L}}} + \Delta(x) \tag{25}$$

where the first part is the Blasius flat-plate solution and the second part $\Delta(x)$ is the result of the nonzero pressure gradient. Since the inviscid flow is linear, the pressure on the displacement body can be written as

$$C_{p,DB} = C_{p,B} + C_{p,\Delta} + C_{p,FP} \tag{26}$$

where $C_{p,B}$ is the pressure on the prescribed surface when no viscous effects are present and is found from the direct Cauchy integral

$$C_{p,B}(x) = -\frac{2}{\pi}\int_{-\infty}^{\infty} \frac{\left(dy_B/dx'\right)dx'}{x - x'} \tag{27}$$

where the usual small-disturbance approximations have been made. It is necessary, of course, to compute $C_{p,B}$ only once. In equation (26) $C_{p,\Delta}$ is the pressure coefficient due to Δ, the deviation of the displacement thickness from that generated by a flat plate. Also, in equation (26) $C_{p,FP}$ denotes the pressure coefficient induced by a flat-plate displacement thickness, which in the present study will be approximated as

$$C_{p,FP} = 0 \tag{28}$$

This approximation, which is discussed by Van Dyke (ref. 23), is the result of second-order boundary-layer theory for the flow over a semi-infinite flat plate. Furthermore, it should be noted that the pressure gradient induced by a flat-plate displacement thickness increases as the leading edge is approached and thus, if $C_{p,FP} \neq 0$, then there is no logical point at which a downstream, relatively local interaction calculation can be initiated other than at $x_0 = 0$.

Since the boundary-layer solution is computed inversely, the iteration procedure is simplified by also solving the inviscid flow with an inverse technique. The inverse Cauchy integral relating the pressure on the displacement body to the rate of growth of the displacement body is given by

$$\frac{dy_{DB}}{dx}(x) = \frac{1}{2\pi}\int_{-\infty}^{\infty} \frac{C_{p,DB}(x')dx'}{x - x'} \tag{29}$$

Similarly, the inverse relation for the prescribed surface is given by

$$\frac{dy_{B}}{dx}(x) = \frac{1}{2\pi}\int_{-\infty}^{\infty} \frac{C_{p,B}(x')dx'}{x - x'} \tag{30}$$

If equation (30) is subtracted from equation (29), then from the previous discussion it follows that

$$\frac{d\Delta}{dx}(x) = \frac{1}{2\pi}\int_{-\infty}^{\infty} \frac{C_{p,\Delta}(x')dx'}{x - x'} \tag{31}$$

The end points on this integral pose a problem since the boundary-layer solution which gives $C_{p,\Delta}$ is computed only in the range $x_0 \leqq x \leqq x_1$. In the present study the lower limit on the integral in equation (31) has been replaced with x_0 and thus, the interaction is assumed negligible upstream of x_0; that is, $C_{p,\Delta} = 0$ for $x \leqq x_0$. Downstream of the interaction at $x = x_1$, it is expected that $C_{p,\Delta}$ will be small but not zero, particularly in the early stages of iteration. It is noted that since the prescribed surface returns to a flat plate as $x \to \infty$, then $C_{p,B} = C_{p,\Delta} = 0$ is the required downstream boundary condition. This boundary condition is imposed in the inviscid calculation since the boundary-layer problem is parabolic and is solved independently of a downstream boundary condition. To avoid the discontinuity which would be encountered by setting $C_{p,\Delta} = 0$ at $x = x_1$, the following extrapolation is used for $x \geqq x_1$:

$$\tilde{C}_{p,\Delta} = \frac{a_1}{x} + \frac{a_2}{x^2} + \frac{a_3}{x^3} \tag{32}$$

where $\tilde{C}_{p,\Delta}$ denotes the extrapolated value of $C_{p,\Delta}$ and the coefficients a_1, a_2, and a_3 are computed by matching equation (32) with $C_{p,\Delta}$ obtained in the boundary-layer solution at $x = x_1$. Numerical tests on the approximate treatment of the limits in equation (31) will be discussed later.

On the basis of the preceding discussion, equation (31) is rewritten as

$$\frac{d\Delta}{dx}(x) = \frac{1}{2\pi}\left[\int_{x_0}^{x_1} \frac{C_{p,\Delta}(x')dx'}{x - x'} + \int_{x_1}^{\infty} \frac{\tilde{C}_{p,\Delta}(x')dx'}{x - x'}\right] \tag{33}$$

The first integral is evaluated numerically with a third-order-accurate quadrature formula in which the singularity at $x' = x$ is isolated in the same manner as was done by Jobe and Burggraf (ref. 13). The second integration is performed analytically with equation (32). In solving equation (33) $d\Delta/dx$ is obtained at the midpoints between the grid nodes of the boundary-layer solution. Thus, Δ at the boundary-layer points $x = \xi = m\,\Delta\xi$ is then obtained to second-order accuracy from

$$\Delta_m = \Delta_{m-1} + \left.\frac{d\Delta}{dx}\right|_{m-\frac{1}{2}} \Delta x + 0(\Delta x^2) \tag{34}$$

beginning at $x = x_0$ where $\Delta = \Delta_0$ which is found by solving the boundary-layer equations in Görtler variables from the leading edge with $C_{p,B}$ prescribed. Note that Δ_0 must be small since the interaction is assumed negligible upstream of $x = x_0$. As shown in figure 2 the new displacement thickness is computed from equation (25), and the resulting value is multiplied by $\sqrt{R_{\infty,L}}$ to give $\bar{\delta}^* = \sqrt{R_{\infty,L}}\delta^*$ in order to conform to the usual boundary-layer scaling. At this point in the iteration cycle a check on convergence is made which is defined in the present study as

$$\max_m \left|\bar{\delta}_m^{*i+1} - \bar{\delta}_m^{*i}\right| < 10^{-4} \tag{35}$$

where i denotes the iteration cycle. Generally, it is found that when equation (35) is satisfied, the corresponding maximum change in C_p is about 10^{-6}. Underrelaxation was used in the present calculations at the indicated points in figure 2. A relaxation factor of 0.2 was used in the calculations; several attempts were made to increase this value, but these calculations diverged.

RESULTS AND DISCUSSION

Turbulent Boundary-Layer Calculations

Calculations with the inverse boundary-layer procedure are first discussed for the turbulent flow over a flat plate in which the input displacement thickness is computed from

a direct solution of the boundary-layer equations in Görtler variables. A comparison of the skin-friction distribution obtained from the direct and inverse calculations is shown in figure 4 along with the experimental measurements of Wieghardt and Tillman (flow number 1400 in the 1968 Stanford Conference, ref. 24). The excellent agreement between the direct and inverse boundary-layer calculations is expected since the same eddy-viscosity model is used in both of these calculations. In the inverse calculations it is found that with $\Delta x = 0.025$ the deduced edge velocity deviates from unity by 5 percent, whereas with $\Delta x = 0.0125$ this error is less than 2 percent. These boundary-layer solutions are also shown in figure 4 to be in good agreement with the experimental data. The direct solution starts at the leading edge with a laminar boundary layer and transition is assumed to occur at $x = 0.001$m. The inverse calculation begins at $x = 0.087$m, the direct solution at that station being used for the upstream boundary condition. Better agreement with the data could be obtained either by using a more detailed modeling of the transition region or by using the experimental data for the starting conditions, as was done by most of the investigators in the Stanford Conference.

Further calculations were made by using the displacement thickness distributions shown in figure 5 as input conditions to the present inverse boundary-layer procedure. The resulting solutions for the skin friction and edge velocity are shown in figures 6 to 8. Figure 6 shows the large separated region computed for laminar flow with the δ^* distribution designated as case 1 in figure 5. Note that the edge velocity, and hence the pressure, shows a plateau region between separation and reattachment which is characteristic of separated flows. This laminar calculation is the same as that designated as case B in reference 21 where additional details are presented. The turbulent boundary-layer solution corresponding to this same δ^* distribution is shown in figure 7 where it is seen that separation did not occur despite the 30-percent decrease in the edge velocity. The qualitative trend here is correct since it is well known that a turbulent boundary layer requires a larger pressure rise than a laminar boundary layer before separation occurs. As a check on the solution shown in figure 7, the deduced velocity u_e was used as an input to the boundary-layer equations expressed in Görtler variables. The resulting skin-friction distribution is seen in figure 7 to be in good agreement with that obtained in the inverse solution. There is some difference in the two solutions near the point of maximum boundary-layer thickness and is probably due to a lack of resolution across the boundary layer in the direct solution.

A more severe case was computed by using the displacement thickness distribution designated as case 2 in figure 5 as the prescribed condition. The resulting skin-friction distribution is shown in figure 8 and it indicates that separation and reattachment occur for this case. It is seen that there is no difference between the solution obtained with the approximate forward-marching procedure and that found by the global iteration technique, in which the finite-difference scheme is switched in the reversed-flow region to properly account for the reversed-flow direction. In this case the magnitude of the reversed-flow

velocity is only about $0.02U_\infty$, which at least for laminar flows is quite accurately computed by the approximate forward-marching procedure, as shown in reference 21.

An attempt was made to compute the same case as a direct calculation with u_e prescribed to see whether or not a singularity exists at the separation point as in laminar flow. The preliminary results indicate that the direct solution has a much steeper skin-friction gradient near separation, although further grid refinements as well as analysis are needed to determine the precise behavior in this region. Furthermore, the significance of this study is unclear since the solution behavior near separation will depend on the turbulent formulation, which is quite approximate in the present paper.

Laminar Viscous-Inviscid Interaction

The prescribed surface, for which interaction calculations are presented, is given by

$$y_B = t \operatorname{sech} 4(x - 2.5) \tag{36}$$

where $t = -0.03$ in figure 9 and $t = -0.015$ in figure 12. For these results $x_0 = 1.0$, $x_1 = 4.0$, and $\Delta x = 0.025$ which results in 121 grid points in the x-direction. The Reynolds number based on free-stream conditions and the distance from the leading edge to the assumed start of the interaction is $R_{\infty,L} = 8 \times 10^4$. In the boundary-layer calculation 87 points were used across the viscous layer; thus, a total of 10 527 grid points were used which were found to require approximately 25 sec on the CDC 6600 computer to complete one iteration cycle shown in figure 2. The results shown in figure 9 were obtained with a relatively crude initial guess on δ^* as seen in figure 10 and were found to require 64 iterations to meet the convergence criterion given in equation (35). No attempt was made to optimize the convergence rate of these calculations.

In the lower part of figure 9 the deduced displacement body is shown in comparison with the prescribed body. The points S and R refer to the separation and reattachment points, respectively, and are connected by the dividing streamline which separates the inner recirculating flow from the outer, forward flow. The displacement thickness distribution is better seen in figure 10 where the initial and final distributions are compared with the Blasius flat-plate solution. A comparison of the pressure distributions on the displacement and prescribed body shapes is shown in the upper part of figure 9. The difference in these two curves is $C_{p,\Delta}$, which is about half of the uninteracted pressure level at the bottom of the trough; this shows the large influence the boundary layer exhibits in this flow field. It is observed that $C_{p,\Delta}$ approaches zero as both the upstream and downstream boundaries are approached, which indicates that the interaction is adequately contained in this region. Additional calculations were made to insure that the results are independent of x_0, x_1, and the extrapolation given in equation (32), provided that these

boundaries are placed sufficiently far from the bottom of the trough. As a further numerical test the grid spacing in the x-direction was reduced from 0.025 to 0.0125; the results of these two calculations differ only slightly. From previous studies (ref. 6) the grid spacing across the boundary layer is considered sufficiently small and thus, the results shown in figures 9 and 10 are considered an accurate solution of the governing partial differential equations.

The skin-friction distribution for this case is shown in figure 11 along with the Blasius flat-plate distribution and that obtained by a direct calculation of the boundary-layer equations with the inviscid pressure distribution prescribed. This latter calculation demonstrates the usual singularity at separation where the slope of the skin-friction curve is infinite, whereas the solution obtained including interaction has a large but finite gradient at separation. The column iterative procedure used in the direct calculation no longer converges downstream of the separation point. As expected, the point of separation is predicted further downstream when the effects of interaction are included since the boundary layer reduces the adverse pressure gradient and thus delays separation. It is observed that the gradient is even larger near reattachment and is followed by an overshoot of the flat-plate result which is characteristic of the usual neck region downstream of a separated flow. Comparison of figures 10 and 11 shows that the maximum in skin friction corresponds to the minimum in displacement thickness in the neck region.

The results of an additional calculation in which $t = -0.015$ in equation (36) are presented in figures 12 and 13. Comparison of these results with those discussed previously for $t = -0.03$ show that the shallower trough results in a smaller but not negligible viscous-inviscid interaction. In figure 13 it is seen that for this case the inclusion of the viscous-inviscid interaction relieves the adverse pressure gradient such that the flow remains attached, despite the prediction of separation from a first-order boundary-layer calculation using the inviscid pressure distribution which is given in figure 12.

CONCLUDING REMARKS

In the present paper a technique is demonstrated for solving laminar and turbulent separated boundary layers. The turbulent separation results appear qualitatively correct; however, the quantitative accuracy of this solution technique must be evaluated by making comparisons with experimental data. It is anticipated that modifications of the eddy-viscosity model used in the present study will be required.

A new viscous-inviscid interaction procedure for separated flows is discussed and several calculations using this technique are presented. This iterative procedure requires none of the smoothing techniques usually required in numerically matching a boundary-layer and inviscid flow solution. Further studies are needed to optimize the efficiency of this interaction procedure.

REFERENCES

1. Werle, M. J.; and Vatsa, V. N.: New Method for Supersonic Boundary-Layer Separations. AIAA J., vol. 12, no. 11, Nov. 1974, pp. 1491-1497.

2. Dwoyer, D. L.: Supersonic and Hypersonic Two-Dimensional Laminar Flow Over a Compression Corner. AIAA Computational Fluid Dynamics Conference, July 1973, pp. 69-83.

3. Carter, James E.: Numerical Solutions of the Navier-Stokes Equations for the Supersonic Laminar Flow Over a Two-Dimensional Compression Corner. NASA TR R-385, 1972.

4. Bertke, S. D.; Werle, M. J.; and Polak, A.: Finite Difference Solutions to the Interacting Supersonic Turbulent Boundary Layer Equations, Including Separation Effects. Rep. No. AFL-74-4-9 (Contract N00019-73-C-0223), Dep. of Aerosp. Eng., Univ. of Cincinnati, Apr. 1974.

5. Catherall, D.; and Mangler, K. W.: The Integration of the Two-Dimensional Laminar Boundary-Layer Equations Past the Point of Vanishing Skin Friction. J. Fluid Mech., vol. 26, pt. 1, Sept. 1966.

6. Carter, James E.: Solutions for Laminar Boundary Layers With Separation and Reattachment. AIAA Paper No. 74-583, June 1974.

7. Kuhn, Gary D.; and Nielsen, Jack N.: Prediction of Turbulent Separated Boundary Layers. AIAA Paper No. 73-663, July 1973.

8. Klineberg, John M.; and Steger, Joseph L.: On Laminar Boundary-Layer Separation. AIAA Paper No. 74-94, Jan.-Feb. 1974.

9. Klineberg, John M.; and Steger, Joseph L.: Calculation of Separated Flows at Subsonic and Transonic Speeds. Proceedings of the Third International Conference on Numerical Methods in Fluid Mechanics, Volume II. Volume 19 of Lecture Notes in Physics, Henri Cabannes and Roger Temam, eds., Springer-Verlag, 1973, pp. 161-168.

10. Tai, Tszé C.: Transonic Laminar Viscous-Inviscid Interaction Over Airfoils. AIAA Paper No. 74-600, June 1974.

11. Briley, W. R.; and McDonald, H.: Numerical Prediction of Incompressible Separation Bubbles. Rep. N110887-3, United Aircraft Corp., June 1974.

12. Murman, Earll M.; and Cole, Julian D.: Calculation of Plane Steady Transonic Flows. AIAA J., vol. 9, no. 1, Jan. 1971, pp. 114-121.

13. Jobe, C. E.; and Burggraf, O. R.: The Numerical Solution of the Asymptotic Equations of Trailing Edge Flow. Proc. Roy. Soc. London, Ser. A, vol. 340, no. 1620, Sept. 3, 1974, pp. 91-111.

14. Melnik, R. E.; and Chow, R.: Asymptotic Theory of Two-Dimensional Trailing-Edge Flows. Aerodynamic Analyses Requiring Advanced Computers, Part I, NASA SP-347, 1975, pp. 177-249.

15. Stewartson, K.: On the Flow Near the Trailing Edge of a Flat Plate II. Mathematika, vol. 16, June 1969, pp. 106-121.

16. Stevens, W. A.; Goradia, S. H.; and Braden, J. A.: Mathematical Model for Two-Dimensional Multi-Component Airfoils in Viscous Flow. NASA CR-1843, 1971.

17. Bauer, Frances; and Garabedian, Paul: Computer Simulation of Shock Wave Boundary Layer Interaction. Commun. Pure & Appl. Math., vol. 26, no. 5/6, Sept./Nov. 1973, pp. 659-665.

18. Blottner, F. G.: Variable Grid Scheme Applied to Turbulent Boundary Layers, Comput. Methods Appl. Mech. & Eng., vol. 4, no. 2, Sept. 1974, pp. 179-194.

19. Harris, Julius, E.: Numerical Solution of the Equations for Compressible Laminar, Transitional, and Turbulent Boundary Layers and Comparisons With Experimental Data. NASA TR R-368, 1971.

20. Keller, Herbert B.; and Cebeci, Tuncer: Accurate Numerical Methods for Boundary-Layer Flows. II: Two-Dimensional Turbulent Flows. AIAA J., vol. 10, no. 9, Sept. 1972, pp. 1193-1199.

21. Carter, James E.; and Wornom, Stephen F.: A Forward Marching Procedure for Separated Boundary-Layer Flows. AIAA J., vol. 13, no. 8, 1975. (To be published.)

22. Reyhner, T. A.; and Flügge-Lotz, I.: The Interaction of a Shock Wave With a Laminar Boundary Layer. Int. J. Non-Linear Mech., vol. 3, no. 2, June 1968, pp. 173-199.

23. Van Dyke, Milton: Perturbation Methods in Fluid Mechanics. Academic Press, Inc., 1964.

24. Coles, D. E.; and Hirst, E. A., eds.: Computation of Turbulent Boundary Layers – 1968. AFOSR-IFP-Stanford Conference. Volume II – Compiled Data. Stanford Univ., c.1969.

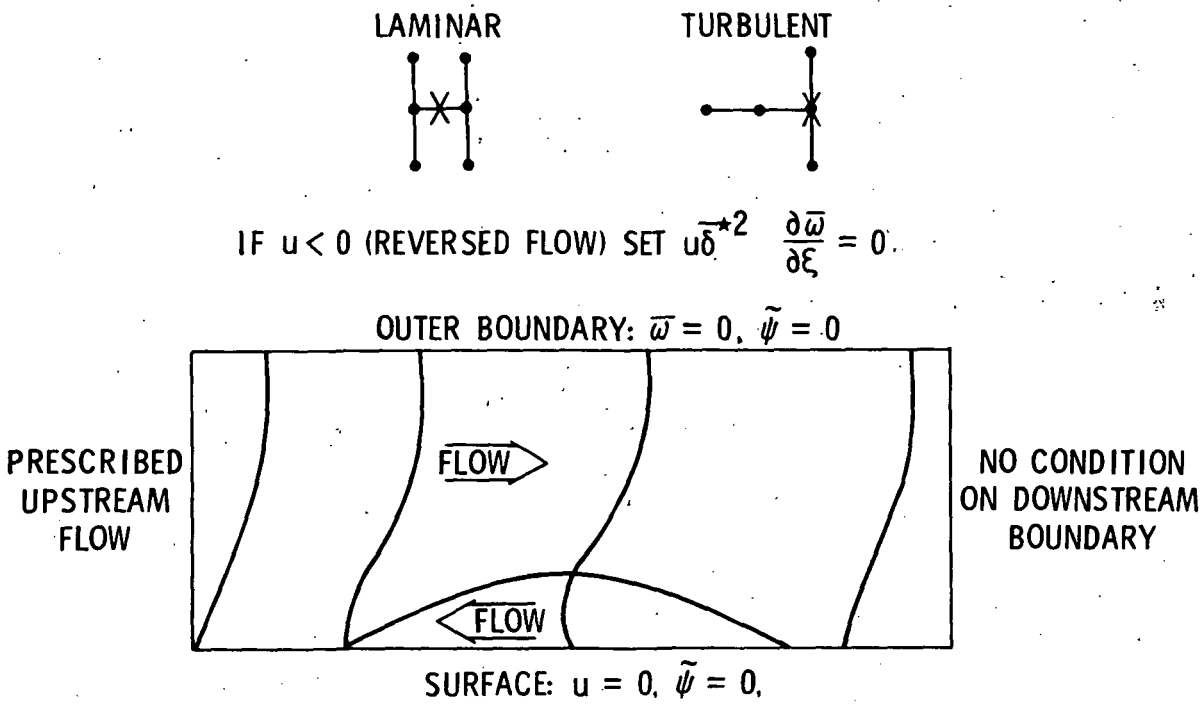

Figure 1.- Boundary-layer computational schemes and boundary conditions.

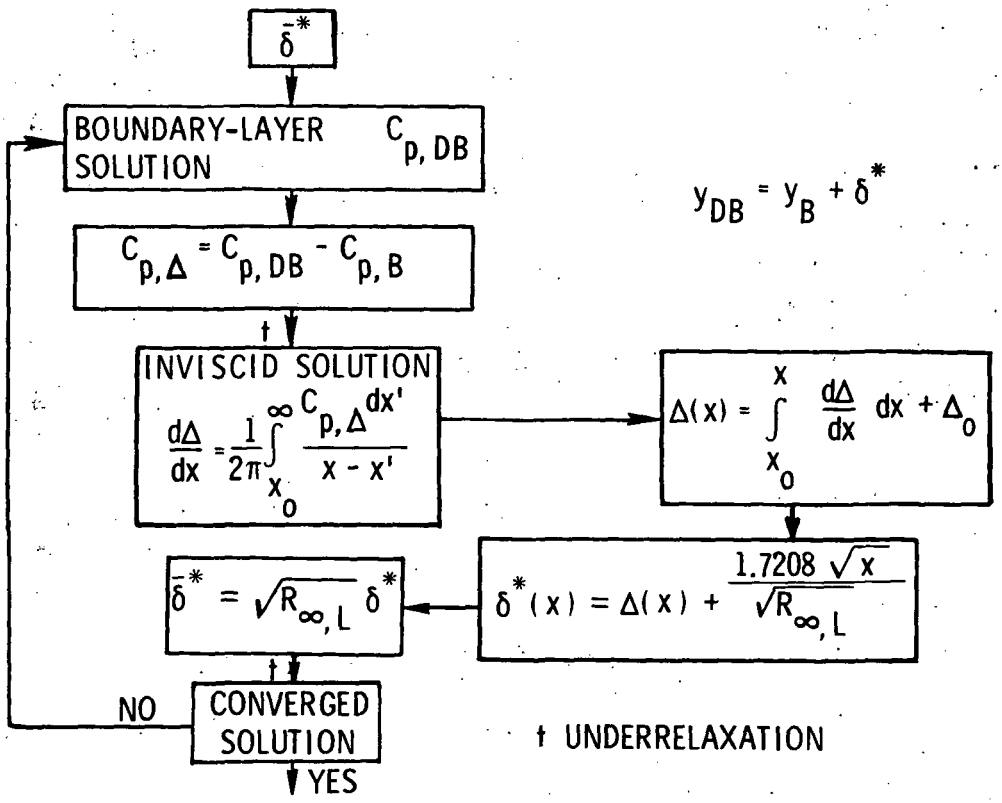

Figure 2.- Inverse viscous-inviscid interaction procedure.

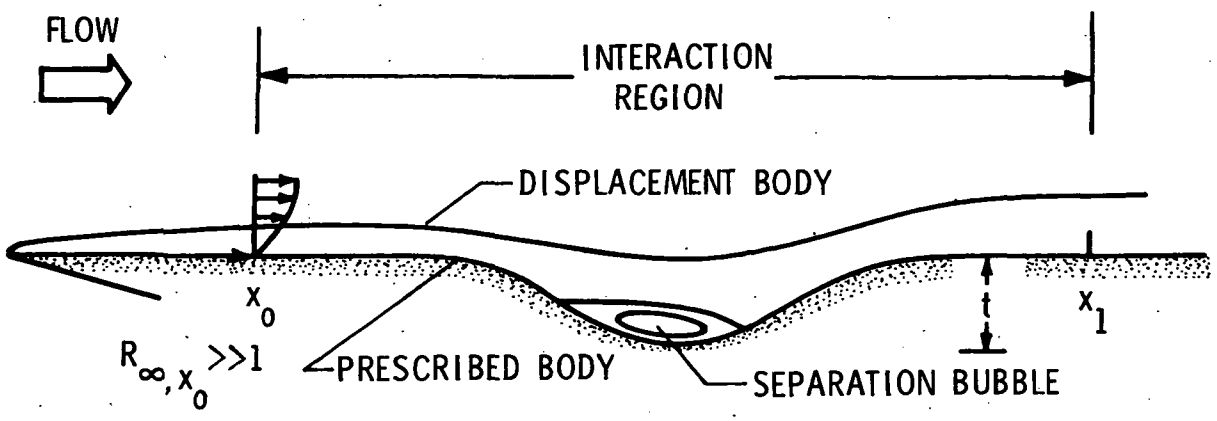

Figure 3.- Schematic diagram of interaction region.

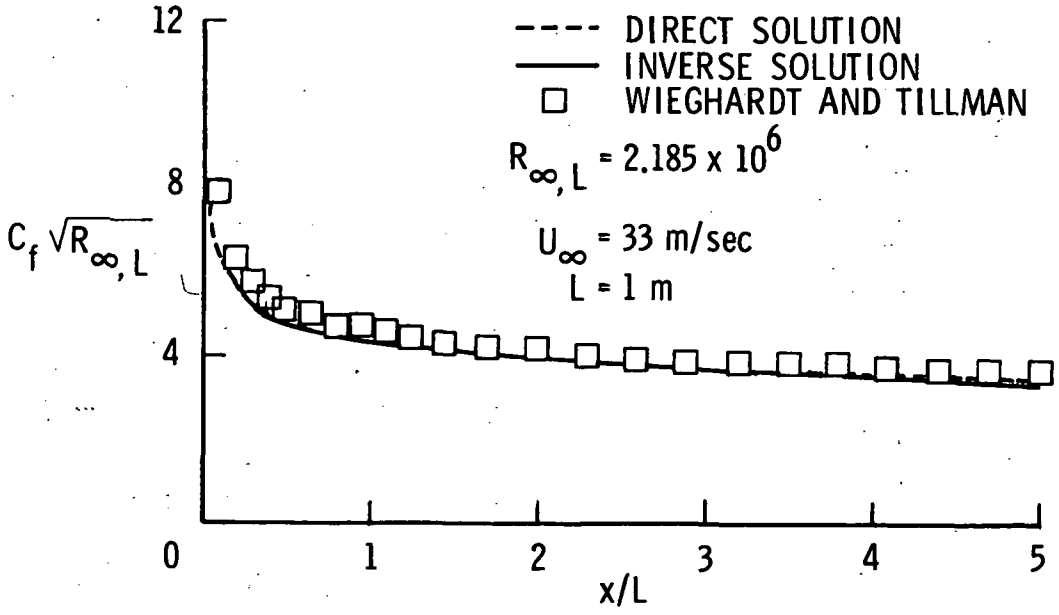

Figure 4.- Flat-plate skin-friction comparisons.

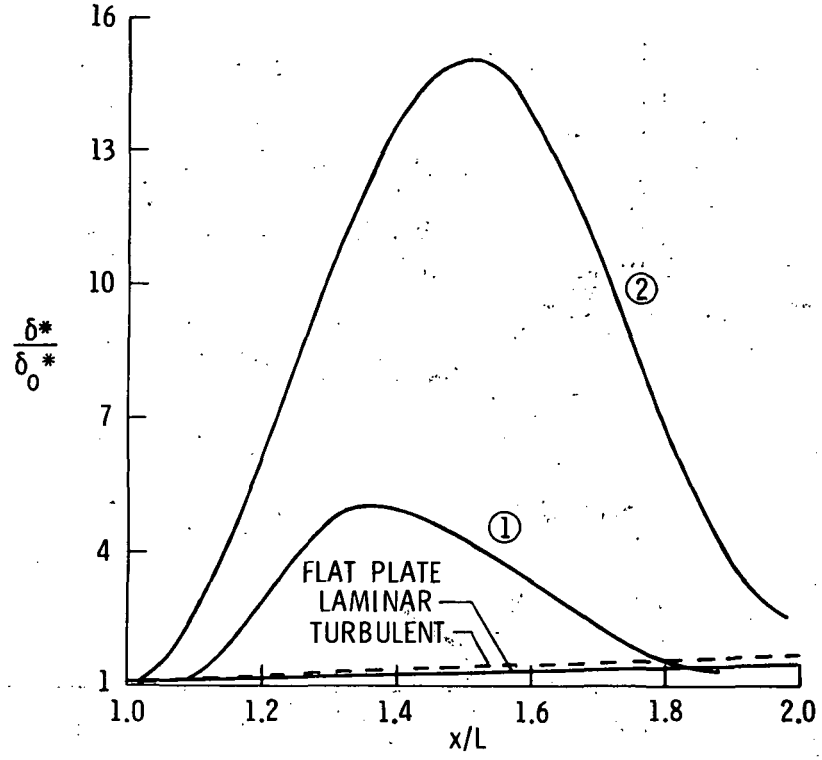

Figure 5.- Prescribed displacement thickness.

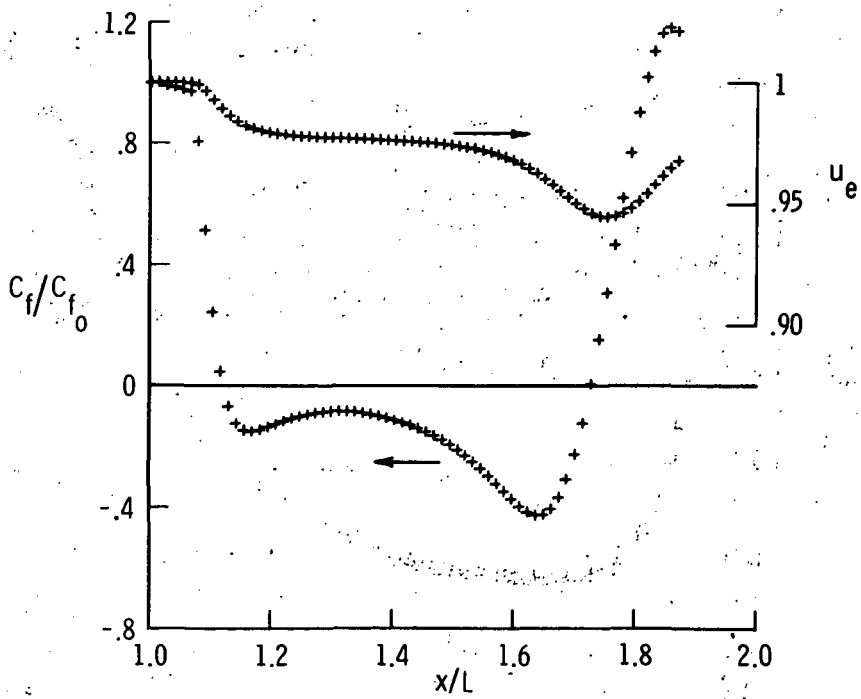

Figure 6.- Skin friction and edge velocity for case 1 – laminar flow.

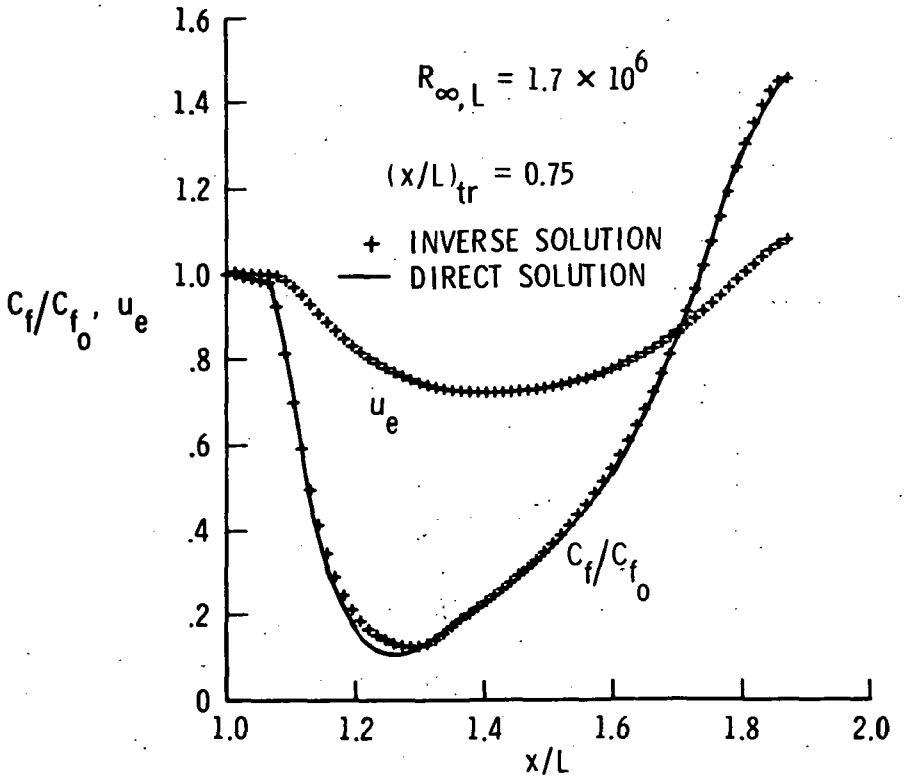

Figure 7.- Skin friction and edge velocity for case 1 – turbulent flow.

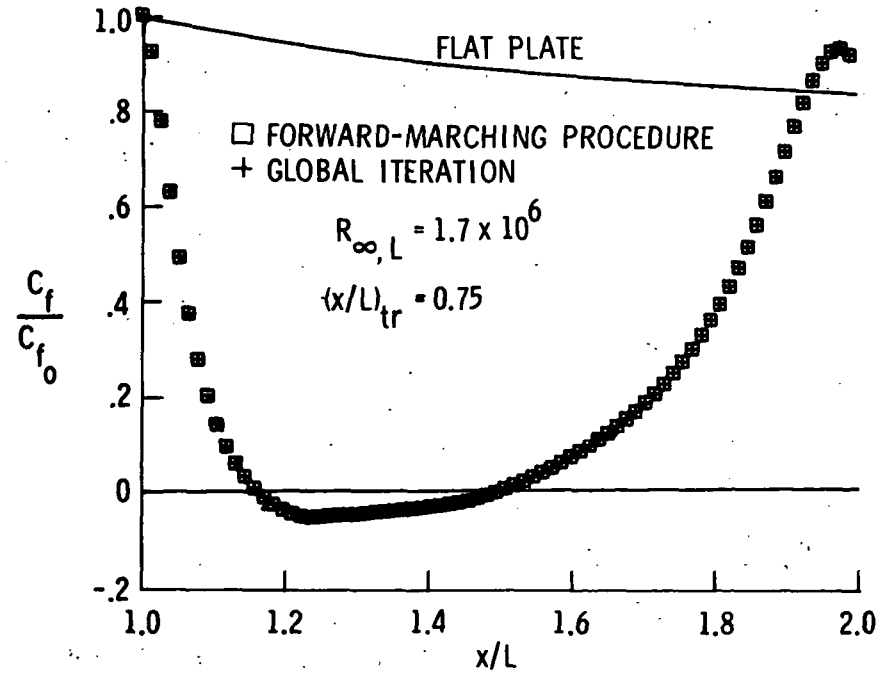

Figure 8.- Skin friction for case 2 – turbulent separation and reattachment.

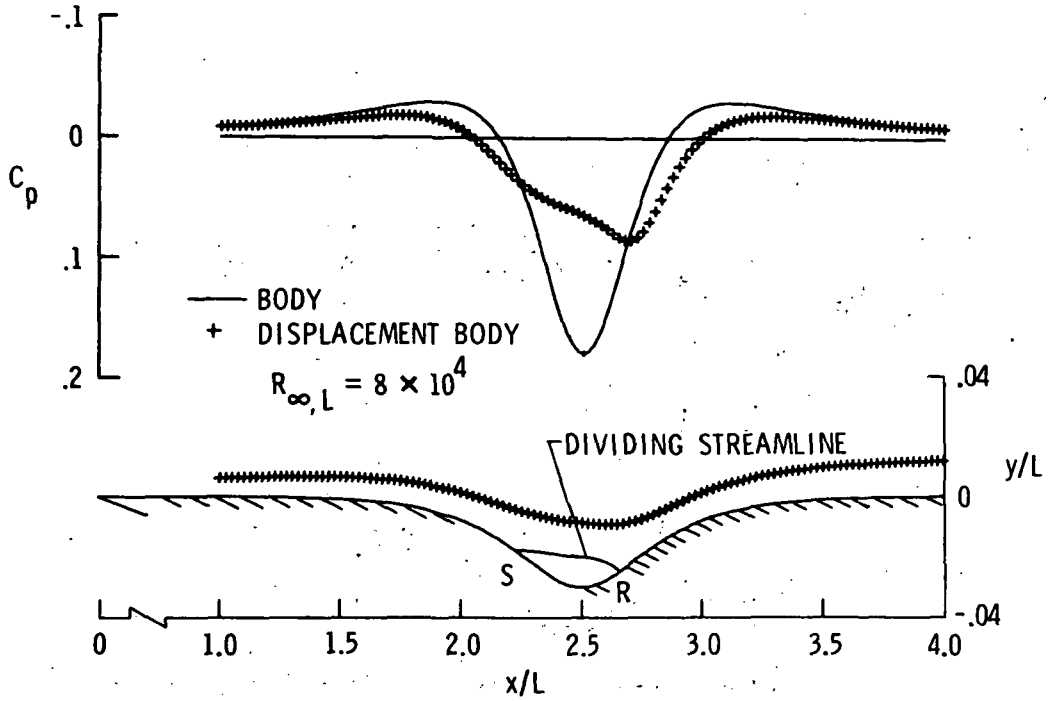

Figure 9.- Laminar viscous-inviscid interaction results; t = -0.03.

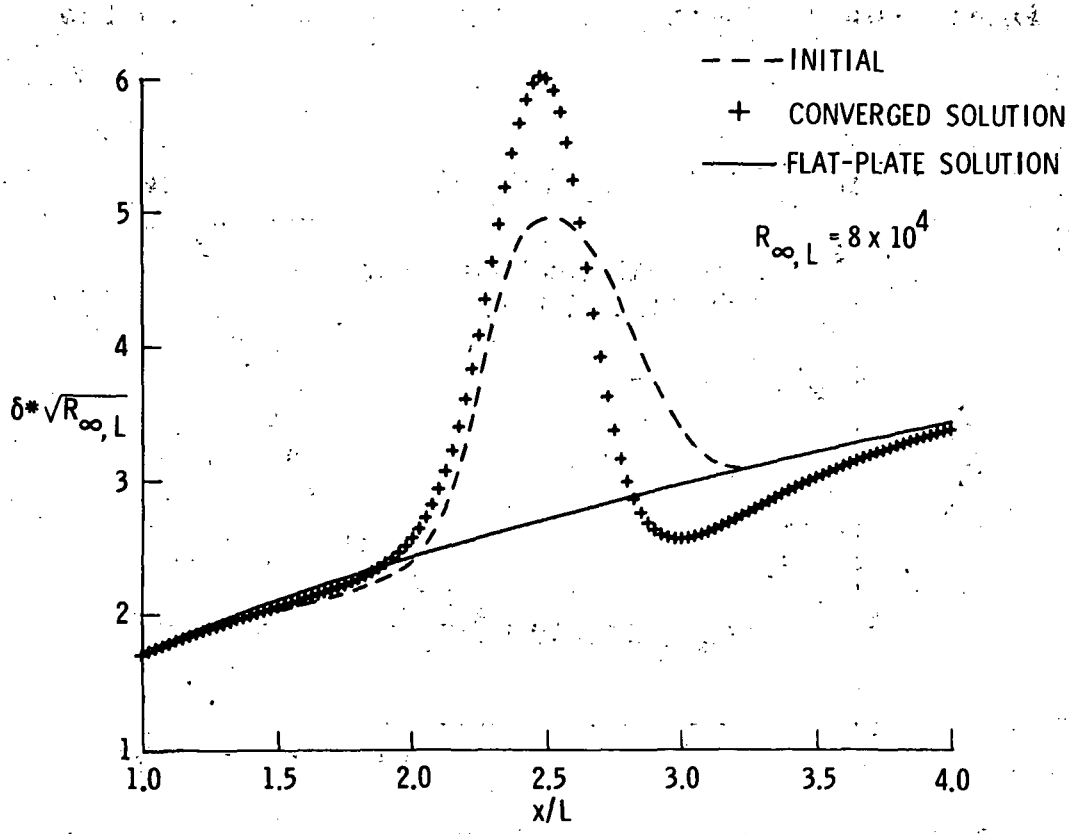

Figure 10.- Initial and final displacement thickness distributions; t = -0.03.

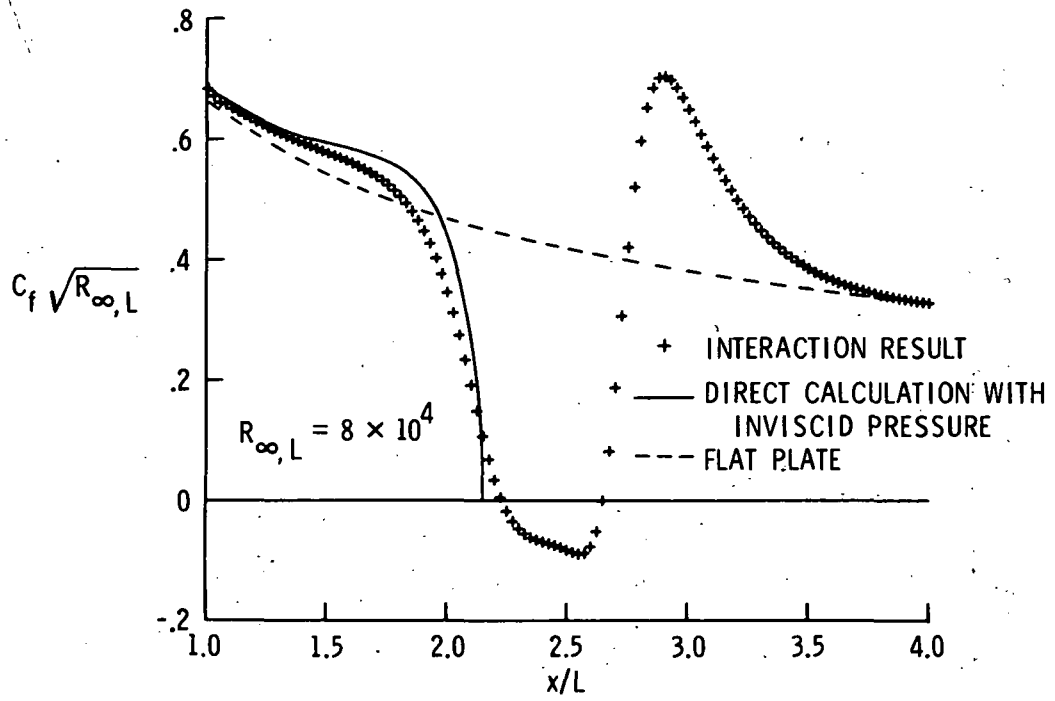

Figure 11.- Laminar interaction skin friction; t = -0.03.

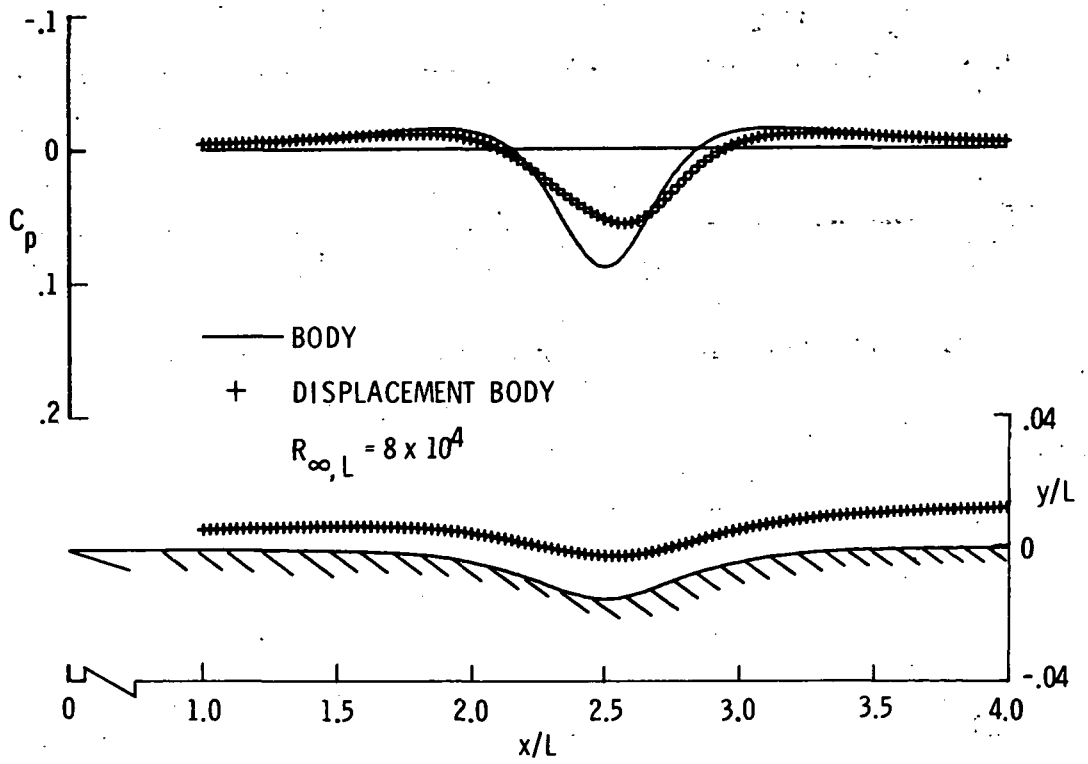

Figure 12.- Laminar viscous-inviscid interaction results; t = -0.015.

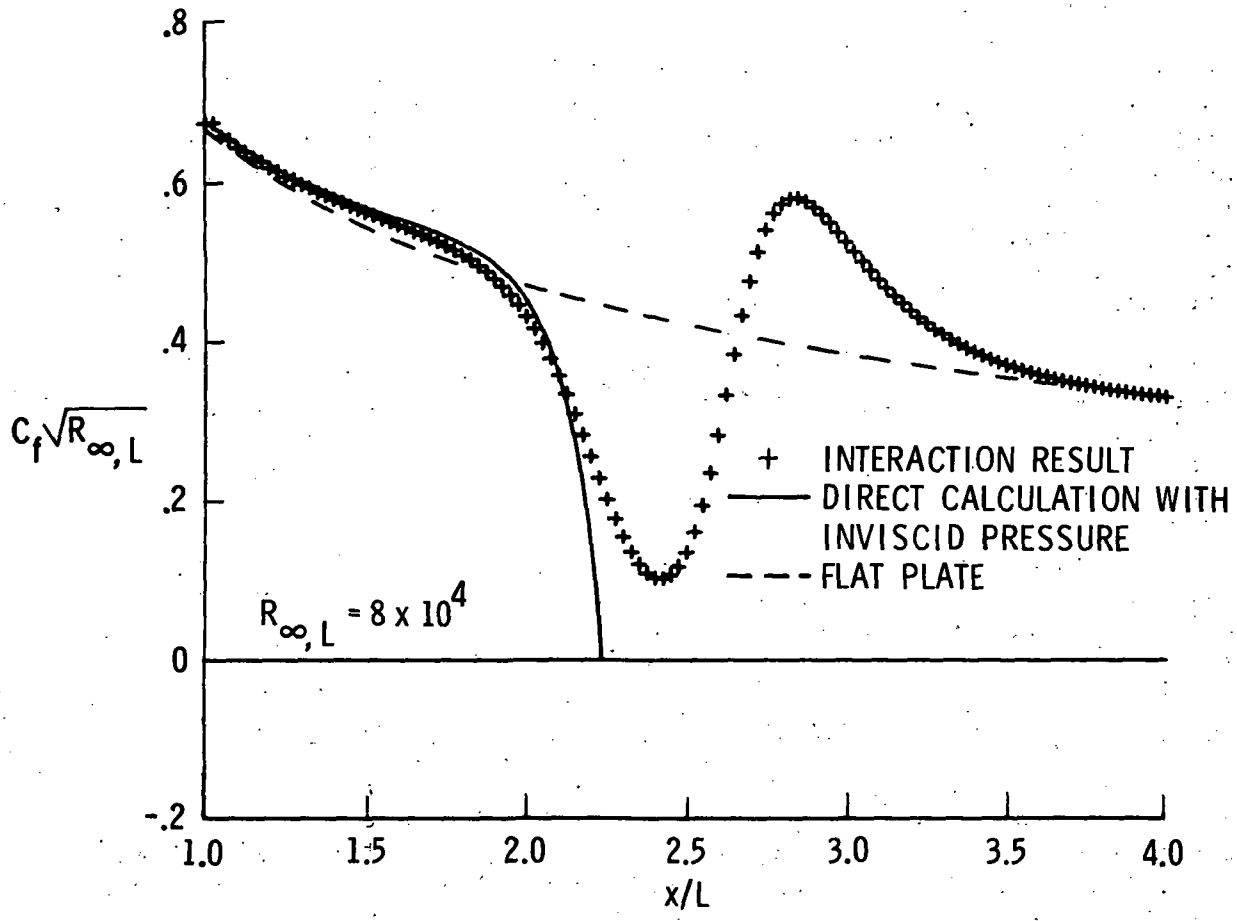

Figure 13.- Laminar interaction skin friction; t = -0.015.

ON THE CALCULATION OF SUPERSONIC SEPARATING AND REATTACHING FLOWS

By John D. Murphy, Leroy L. Presley, and William C. Rose

NASA Ames Research Center

SUMMARY

A method is developed for solving the laminar and turbulent compressible boundary-layer equations for separating and reattaching flows. Results of this method are compared with experimental data for two laminar and three turbulent boundary-layer, shock-wave interactions. Several Navier-Stokes solutions were obtained for each of the laminar boundary-layer, shock-wave interactions considered. Comparison of these solutions indicates a first-order sensitivity in C_f to the computational mesh selected in *both* the viscous and inviscid portions of the flow.

Three turbulent boundary-layer, shock-wave interactions were considered, one unseparated interaction at $M = 3$ and two separated interactions at $M = 1.47$ and 3. Boundary-layer theory appeared to be adequate to describe the first two of these interacting flows. However, for the separated interaction at $M = 3$, boundary-layer theory failed.

Comparison of the present boundary-layer solutions with the Navier-Stokes solutions and with data for a given Mach number indicates that as long as $|v_e/u_e|$ is small, the boundary-layer approximation yields solutions whose accuracy is comparable to the Navier-Stokes solutions. A more general parameter might indicate boundary-layer theory to be valid if some function of Mach number times $|v_e/u_e|$ is small.

Since the present boundary-layer solution is an inverse method, that is, $C_f(x)$ is specified rather than $P(x)$, a criterion for selecting the correct C_f distribution is required. It was originally anticipated that this criterion would be supplied by coupling the boundary-layer solutions to a shock-capturing, finite-difference solution to the inviscid-flow equations. Although several modes of coupling have been attempted, only slight success has been obtained to date because the shock-capturing scheme imposes a relatively thick shock wave on the viscous flow, which in turn requires an almost discontinuous change in flow angle at the boundary-layer edge. The inconsistency of this behavior in the two solutions has thus far obstructed attempts to obtain meaningful coupled solutions. Therefore, a truncated Navier-Stokes system of equations was examined and it appears that this technique circumvents these difficulties.

INTRODUCTION

It is generally agreed that the problem of separating and reattaching flows is one of the more challenging and technologically relevant problems in

computational fluid mechanics. In recent years, the computational attack has taken place on two fronts - the engineering approach by way of boundary-layer theory and the pure numerical approach by way of the Navier-Stokes equations. Reasonably complete summations of the status of these two approaches up to about 1970 are contained in references 1 to 3. During the past two or three years, substantial additional progress has been made in the boundary-layer theory approach by Klineberg and Steger (ref. 4) and Carter (ref. 5), and in the Navier-Stokes equation approach as represented by references 6 through 11. The basic position taken by each of these schools of thought can be summarized as follows: the Navier-Stokes equations are undoubtedly the correct equations for describing the flow fields in question and, since we can solve them, why settle for an approximation? The boundary-layer contingent would concur with the above but they would add that the cost of Navier-Stokes solutions both now and in the foreseeable future is far too high to permit their use as design tools.

The present study examines these positions in some detail. In particular, we are concerned with establishing, at least qualitatively, the limits of applicability of the boundary-layer approximation for both laminar and turbulent separating and reattaching flows. Secondly, we are concerned with the development of an economical and reasonably accurate engineering calculation scheme for such flows.

SYMBOLS

C	Chapman-Rubesin constant
C_f	skin-friction coefficient, $C_f = \tau_w/(1/2)\rho_o u_o^2$
DC	difference coefficient multiplying quantities at x
DM	difference coefficient multiplying quantities at $x-\Delta x$
DP	difference coefficient multiplying quantities at $x+\Delta x$
E	Eckert number, $u_e^2/2H_e$
F	defined in equation (12)
f	dimensionless stream function
H	total enthalpy $h + (u^2/2)$
h	static enthalpy
ℓ	mixing length
M_o	initial Mach number

M	number of nodes in x direction
N	number of nodes in y direction
p	pressure
Pr	Prandtl number
Pr_T	turbulent Prandtl number
R	gas constant
r	body radius
S	entropy
T	temperature
U	defined in equation (12)
u	velocity component in x direction
v	velocity component in y direction
x	streamwise variable
y	cross stream variable
α	weighting factor in type dependent differencing
β	boundary-layer pressure gradient parameter = $\frac{2\xi}{u_e}\frac{du_e}{d\xi}$
γ	ratio of specific heats
Δ	difference in quantities
δ	boundary-layer thickness or stream angle
δ^*	displacement thickness
ε	residual error
ζ	y_n/y_ℓ
ρ	density
σ	defined in equation (18)
μ	viscosity or Mach angle ($\mu = \sin^{-1}(1/M)$)
τ	shear stress

ξ transformed x variable

η transformed y variable

$( )'$ differentiation with respect to η

Subscripts

e evaluated at boundary-layer edge

f evaluated at final conditions downstream of interaction

i evaluated at ith x point

j evaluated at jth y point

ℓ lower boundary

o evaluated on initial line

t evaluated at stagnation conditions

u upper boundary

w evaluated at wall conditions

ANALYSIS

Viscous-Flow Calculations

The procedure used to solve the viscous-flow portion of the calculation is a generalized Galerkin method (refs. 12 and 13) applied to the boundary-layer equations. The equations considered are

$$\frac{\partial \rho u r^k}{\partial x} + \frac{\partial \rho v r^k}{\partial y} = 0 \tag{1}$$

$$\rho u \frac{\partial u}{\partial x} + \rho v \frac{\partial u}{\partial y} = - \frac{dP}{dx} + \frac{\partial}{\partial y}\left(\mu \frac{\partial u}{\partial y} + \rho\tau\right) \tag{2}$$

$$\rho u \frac{\partial H}{\partial x} + \rho v \frac{\partial H}{\partial y} = \frac{\partial}{\partial y}\left[\frac{\mu}{Pr} \frac{\partial H}{\partial y} + \frac{\mu}{2}\left(1 - \frac{1}{Pr}\right) \frac{\partial u^2}{\partial y}\right] + \frac{\partial}{\partial y}\left\{\rho\tau\left[\frac{1}{Pr_T} \frac{\partial H/\partial y}{\partial u/\partial y} + u\left(1 - \frac{1}{Pr_T}\right)\right]\right\} \tag{3}$$

$$P = \rho R T \tag{4}$$

$$\rho\tau = \rho \ell^2 \left|\frac{\partial u}{\partial y}\right| \frac{\partial u}{\partial y} \tag{5}$$

Only adiabatic flows with $Pr = Pr_T = 1$ are treated here; hence equation (3) is replaced by $h + (u^2/2) = \text{const}$. To suppress the streamwise growth of the boundary layer and to facilitate initialization, equations (1) and (2) are combined under the Levy-Lees-Dorodnitsyn transformation $(x,y) \rightarrow (\xi,\eta)$ where

$$\xi = \int_o^x \rho_o u_o \mu_o r^{2k} dx \quad , \quad \eta = \frac{\rho_o u_o r^k}{\sqrt{2\xi}} \int_o^y \frac{\rho}{\rho_o} dy$$

$$f = \frac{1}{\sqrt{2\xi}} \int_o^y \rho u \, dy \quad , \quad f' = \frac{u}{u_e}$$

which results in

$$(Cf'')' + ff'' + \beta\left(\frac{\rho_e}{\rho} - f'^2\right) + K_1\rho\tau - 2\xi\left(f' \frac{\partial f'}{\partial \xi} - f'' \frac{\partial f}{\partial \xi}\right) = 0 \qquad (6)$$

where $K_1 = \sqrt{2\xi}/\mu_e r^k$ and the primes indicate differentiation with respect to η. The following analysis closely parallels that of Kendall and Bartlett (ref. 13). The present method extends that of reference 13 to treat separated flow and is restricted to calorically and thermally perfect gases.

y-dependent differencing—To apply the generalized Galerkin method, the approximations for the stream functions, velocity, and shear between adjacent nodes are chosen as

$$f_{j+1} = f_j + f'_j\Delta\eta + f''_j \frac{\Delta\eta^2}{2} + f'''_j \frac{\Delta\eta^3}{3} + f'''_{j+1} \frac{\Delta\eta^3}{24} \qquad (7)$$

$$f'_{j+1} = f'_j + f''_j\Delta\eta + f'''_j \frac{\Delta\eta^2}{3} + f'''_{j+1} \frac{\Delta\eta^2}{6} \qquad (8)$$

$$f''_{j+1} = f''_j + f'''_j \frac{\Delta\eta^2}{2} + f'''_{j+1} \frac{\Delta\eta^2}{2} \qquad (9)$$

These relations are obtained by a Taylor series expansion to terms including f^{IV} and substitution of $f_j^{IV} = (f'''_{j+1} - f'''_j)/\Delta\eta$. Equations (7) to (9) are substituted in equation (6) and the results integrated with respect to a unit square-wave weighting function from η_j to η_{j+1} to yield:

$$Cf''\Big|_{\eta_j}^{\eta_{j+1}} + ff'\Big|_{\eta_j}^{\eta_{j+1}} - \left[1 + \frac{2\beta}{2-E}\right]\sum_{k=1}^{4} f_j^k \, XPK + \frac{\beta}{2-E}\,\eta\Big|_{\eta_j}^{\eta_{j+1}} + K_1\bar{\rho}\tau\Big|_{\eta_j}^{\eta_{j+1}}$$

$$-2\xi\int_{\eta_j}^{\eta_{j+1}} f' \frac{\partial f'}{\partial \xi} d\eta + 2\xi\int_{\eta_j}^{\eta_{j+1}} f'' \frac{\partial f}{\partial \xi} d\eta = 0 \qquad (10)$$

where

$$\sum_{k=1}^{4} f_j^k XPK = f_j' XP1 + f_j'' XP2 + f_j''' XP3 + f_{j+1}''' XP4 = \int f'^2 d\eta$$

and

$$XP1 = \Delta\eta\left(f_j' + f_j'' \frac{\Delta\eta}{2} + f_j''' \frac{\Delta\eta^2}{8} + f_{j+1}''' \frac{\Delta\eta^2}{24}\right)$$

$$XP2 = \frac{\Delta\eta^2}{2}\left(f_j' + f_j'' \frac{2\Delta\eta}{3} + f_j''' \frac{11\Delta\eta^2}{60} + f_{j+1}''' \frac{\Delta\eta^2}{15}\right)$$

$$XP3 = \frac{\Delta\eta^3}{8}\left(f_j' + f_j'' \frac{11\Delta\eta}{15} + f_j''' \frac{66\Delta\eta^2}{315} + f_{j+1}''' \frac{5\Delta\eta^2}{63}\right)$$

$$XP4 = \frac{\Delta\eta^3}{24}\left(f_j' + f_j'' \frac{4\Delta\eta}{5} + f_j''' \frac{5\Delta\eta^2}{21} + f_{j+1}''' \frac{2\Delta\eta^2}{21}\right)$$

The two terms remaining to be integrated are discussed under x-Dependent Differencing. This procedure yields a consistent differencing method that is fourth-order accurate in η and equations (7) to (9) ensure that the stream function, velocity, and shear are defined everywhere (not only at nodal points) and are continuous everywhere. Equations (7) to (10) provide a sequence of $4(N-1)$ equations in $4N$ unknowns, where N is the number of nodes normal to the wall. Note that $3(N-1)$ of these equations are linear algebraic equations while $(N-1)$ equations are nonlinear ordinary differential equations. The remaining four equations are imposed as boundary conditions:

$$f = f' = 0 \quad \text{at} \quad \eta = 0$$

$$f' = 1, \quad f'' = 0 \quad \text{at} \quad \eta = \infty$$

The complete system is solved by use of a Newton-Raphson iteration scheme by differentiating with respect to f_j, f_{j+1}, . . ., f_j''', f_{j+1}''', and for separated flows β, to yield

$$J(f)\Delta f_j^k = -\varepsilon_j^k$$

where $J(f)$ is the $(4N \times 4N)$ Jacobian, ε is the residual error, and Δf_j^k is the incremental change in the solution parameters per iteration.

To speed up the iteration process, the equations are ordered so that the $3(N-1)$ linear algebraic equations plus the boundary condition $f'(0) = 0$ occupy the first $3N-2$ matrix rows. The matrix has the partitioned form (see ref. 14):

$$\begin{bmatrix} L_1 & L_2 \\ NL_1 & NL_2 \end{bmatrix} \begin{bmatrix} \Delta f_L \\ \Delta f_{NL} \end{bmatrix} = -\begin{bmatrix} \varepsilon_L \\ \varepsilon_{NL} \end{bmatrix}$$

The submatrix L_1 is a function of the nodal configuration only and can be inverted just once and used in all subsequent calculations. Formal manipulation and back substitution yield

$$\Delta f_{NL} = \left[NL_2 - NL_1 L_1^{-1} L_2\right]^{-1}\left[-\epsilon_{NL} + NL_1 L_1^{-1}\epsilon_L\right]$$

$$\Delta f_L = L_1^{-1}\left[-\epsilon_L - L_2 \Delta f_{NL}\right]$$

The matrix $\left[NL_2 - NL_1 L_1^{-1} L_2\right]$ must be inverted every iteration, but it is only of order (N+2).

x-dependent differencing—The streamwise differencing is carried out in a manner similar to that of reference 4. The term

$$-2\xi \int_{\eta_j}^{\eta_{j+1}} f' \frac{\partial f'}{\partial \xi}\, d\eta$$

is decomposed and integrated by parts as

$$-\int_{\eta_j}^{\eta_{j+1}} f'\left[DPf'_{i+1} + DCf'_i + DMf'_{i-1}\right]d\eta = -\left[DP \sum f^k_{i+1,j} XPK + DC \sum f^k_{i,j} XPK + DM \sum f^k_{i-1,j} XPK\right]$$

where, for attached flow,

$$DP = 0\ , \quad DC = 2/\ell n\ \xi_i/\xi_{i-1}\ , \quad DM = -DC$$

and for separated flow

$$DP = (1-\alpha)/\ell n\ \xi_{i+1}/\xi_i \quad ; \quad \alpha = 1 \quad \text{for} \quad f' > 0.01$$

$$DM = -(1+\alpha)/\ell n\ \xi_i/\xi_{i-1} \quad ; \quad \alpha = 100f'\ , \quad -0.01 \le f' \le 0.01$$

$$DC = -(DP + DM) \quad ; \quad \alpha = -1\ , \quad f' < -0.01$$

This procedure incorporates backward differencing when the flow is in the mainstream direction, forward differencing when the flow is reversed, and a central difference on and near the zero velocity streamline. The remaining term is decomposed as above, integrated by parts, and expanded in Taylor series to yield:

$$2\xi \int_{\eta_j}^{\eta_{j+1}} f'' \frac{\partial f}{\partial \xi}\, d\eta = DC\, f_i f_i' \Big|_{\eta_j}^{\eta_{j+1}} + DP\, f_{i+1} f_i' \Big|_{\eta_j}^{\eta_{j+1}} + DM\, f_{i-1} f_i' \Big|_{\eta_j}^{\eta_{j+1}} + DC \sum f_{i,j}^k XPK_i$$

$$+DP \sum f_{ij}^k XPK_{i+1} + DM \sum f_{ij}^k XPK_{i-1}$$

where, for attached flow, excluding the points of separation and reattachment yields

$$DC = 2/\ell n\ \xi_i/\xi_{i-1}\ , \quad DP = 0\ , \quad DM = -DC$$

and for separated flow,

$$DC = 0\ , \quad DP = 2/\ell n\ \xi_{i+1}/\xi_{i-1}\ , \quad DM = -DP$$

As shown, a straightforward marching routine is used in the attached flow while, for separated flow, the entire separation region must be relaxed simultaneously.

The present method requires no under relaxation and a typical well-separated flow with 20 η points and 10 ξ points can be relaxed to a maximum residual $0(10^{-4})$ in about 22 iterations compared to 800 for the method of reference 4 and 100 to 200 iterations for the method of reference 5. Although the present method may require more operations per iteration, it is at least competitive with other methods cited. The speed of the present method primarily results from the splined Taylor series used as approximating functions. First, they provide an effective fourth-order-accurate, finite-difference representation in the y direction which permits a relatively sparse nodal array to yield high accuracy and, second, the spline character enhances the stability markedly.

Inviscid-Flow Equations and Coupling Schemes

In this section, the technique used to solve for the inviscid flow field and to obtain the effects due to the boundary layer on that flow is described. A technique for obtaining fully coupled interactive solutions of the inviscid and viscous flows is being developed, but is not sufficiently advanced to discuss here. Rather, at this point, boundary-layer solutions for a pressure and skin-friction distribution, appropriate to the data of reference 13, have been obtained and then various schemes for matching this solution with the inviscid flow have been investigated. The inviscid flow is for supersonic flow between a shock-wave generator and some matching line given by the boundary-layer solution.

Inviscid-flow equations—The basic equation used in the inviscid flow-field analysis is similar to that of reference 15. The key features, however,

are described here for completeness. In a Cartesian coordinate system, the steady, inviscid, two-dimensional fluid dynamic equations (continuity, x and y momentum) are written in conservative form as

$$\tilde{U}_x + \tilde{F}_y = 0 \tag{11}$$

The three components of the vectors $\tilde{U}$ and $\tilde{F}$, which represent the conservative variables, are defined as

$$\tilde{U} = \begin{bmatrix} \rho u \\ kp+\rho u^2 \\ \rho uv \end{bmatrix}, \quad \tilde{F} = \begin{bmatrix} \rho v \\ \rho uv \\ kp+\rho v^2 \end{bmatrix} \tag{12}$$

where $k = (\gamma-1)/2\gamma$. The units of these equations were normalized by dividing both pressure and density by their respective stagnation conditions, while the velocities were divided by the maximum adiabatic velocity. With this normalization and the further restriction that the flow be adiabatic, the energy equation can be written:

$$\frac{p}{\rho} + u^2 + v^2 = 1 \tag{13}$$

To calculate two-dimensional flow between two nonparallel walls, in this case the shock-wave generator and the lower coupling boundary, it is most convenient to normalize the coordinate system so that the upper and lower boundaries become parallel. The transformed coordinates are

$$\left.\begin{aligned} x &= x \\ \xi &= y - \frac{y_\ell}{y_u - y_\ell} = y - \frac{y_\ell}{\zeta} \end{aligned}\right\} \tag{14}$$

where $y_u = y_u(x)$ and $y_\ell = y_\ell(x)$. Applying this transformation to equation (11) results in

$$U_x + F_\zeta = 0 \tag{15}$$

where $U = \zeta\tilde{U}$ and $F = \tilde{F} + \tilde{U}\left[y'_\ell(\xi-1) - y'_u\right]$. (In this section, the primes denote differentiation with respect to x.)

The above differential equation is integrated using MacCormack's second-order-accurate differencing scheme (see ref. 15). For flow-field points, that is, points on neither the upper nor lower boundary, the predictor and corrector equations are

$$\bar{U}_j^{n+1} = U_j^n - \left(\frac{\Delta x}{\Delta \xi}\right)\left(\bar{F}_{j+1}^n - F_j^n\right) \quad \text{(predictor)} \tag{16}$$

Subscript j identifies particular points on a data line as follows: 1, lower body point; 2, 3, . . ., $N_{\xi-1}$, flow-field points; and N_ξ, upper body point. The data lines are identified by the superscripts n and n+1. The bars indicate a predicted value.

$$U_j^{n+1} = \frac{1}{2}\left[U_j^n + \overline{U_j^{n+1}} - \left(\frac{\Delta x}{\Delta \xi}\right)\left(\overline{F_j^{n+1}} - \overline{F_{j-1}^{n+1}}\right)\right] \quad \text{(corrector)} \tag{17}$$

The above equations are applied to the three vector components of U.

The step size in the x direction is found by determining the maximum slope of the characteristic surface, inclined at the local Mach angle μ relative to the local stream angle δ, for each point as follows:

$$\sigma_j^n(\pm) = \left|\tan(\pm\mu + \delta)_j^n\right| \tag{18}$$

where the $\pm$ denote positive and negative directions of the Mach angle from each point. The entire data line n is surveyed to determine $\left|\sigma_j^n(\pm)\right|_{max}$. Depending on the sign associated with the maximum slope, Δx is found from

$$\Delta x(+) = K\left[\frac{\xi_{j+1}^{n+1}\zeta^{n+1} - \xi_j^n\zeta^n - y_\ell^n + y_\ell^{n+1}}{\sigma_j^n(+)_{max}}\right] \tag{19}$$

or

$$\Delta x(-) = K\left[\frac{\xi_j^n\zeta^n - \xi_{j-1}^{n+1}\zeta^{n+1} - y_\ell^{n+1} + y_\ell^n}{\sigma_j^n(-)_{max}}\right] \tag{20}$$

where K is a constant that controls the step size. If $K = 1$, the CFL condition is satisfied identically.

Application of the finite-difference equations (16) and (17) yields predicted and corrected values of the three components of the conservative-variable vector U on the new data line. These must be decoded after the predictor step and corrector step in turn. This decoding into physical variables is accomplished by solving the following:

$$\left.\begin{aligned} v &= \left.\frac{U_1}{U_2}\right|_j^{n+1} \\ u &= \left.\frac{U_2 + \sqrt{U_2^2 - 4U_1^2k(1-k)(1-v^2)}}{2U_1(1-k)}\right|_j^{n+1} \\ \rho &= \left.\frac{U_1}{\zeta u_1}\right|_j^{n+1} \quad ; \quad p = \rho(1-u^2-v^2) \end{aligned}\right\} \tag{21}$$

Constructing a technique that will give a physically realistic solution of the conditions on a solid boundary is difficult in a predictor-corrector sequence since strict application requires an imaginary point inside the body. Abbett (ref. 16) developed a technique that satisfies the surface tangency

condition and relies on information provided by the finite-difference equations. For the upper and lower surfaces, respectively, the predictor equations are written as

$$\overline{U_{N_\xi}^{n+1}} = U_{N_\xi}^{n} - \left(\frac{\Delta x}{\Delta \xi}\right)\left(F_{N_\xi}^{n} - F_{N_\xi - 1}^{n}\right) \tag{22}$$

and

$$\overline{U_{1}^{n+1}} = U_{1}^{n} - \frac{\Delta x}{\Delta \xi}\left(F_{2}^{n} - F_{1}^{n}\right) \tag{23}$$

Modified corrector equations that maintain second-order accuracy at the upper and lower surfaces, respectively, are given by

$$U_{N_\xi}^{n+1} = \frac{1}{2}\left[U_{N_\xi}^{n} + \overline{U_{N_\xi}^{n+1}} - \frac{\Delta x}{\Delta \xi}\left(\overline{F_{N_\xi}^{n+1}} - \overline{F_{N_\xi - 1}^{n+1}}\right) - \frac{\Delta x}{\Delta \xi}\left(F_{N_\xi}^{n} - 2F_{N_\xi - 1}^{n} + F_{N_\xi - 2}^{n}\right)\right] \tag{24}$$

and

$$U_{1}^{n+1} = \frac{1}{2}\left[U_{1}^{n} + \overline{U_{1}^{n+1}} - \frac{\Delta x}{\Delta \xi}\left(\overline{F_{2}^{n+1}} - \overline{F_{1}^{n+1}}\right) - \frac{\Delta x}{\Delta \xi}\left(F_{3}^{n} - 2F_{2}^{n} - F_{1}^{n}\right)\right] \tag{25}$$

After the corrector equations are decoded at the boundaries, the flow variables will not necessarily satisfy the boundary conditions at the wall. The technique for satisfying the boundary conditions depends on a scheme for matching the boundary-layer solution.

The coordinates of the upper boundary are determined from

$$y_u = y_{u_o} + x \tan \delta_u \tag{26}$$

where δ_u is the deflection angle of the upper wall. When matching to the output of the boundary-layer solution, the lower boundary is specified by a table of coordinates. These coordinates are used to fit a parabola of the form

$$y = ax^2 + bx + c \tag{27}$$

between each set of three consecutive points. The three points used to determine the coefficients in the above equation were chosen so that two of the points should have $x > x^{n+1}$. The slope of the boundary is found from the derivative of equation (27).

Matching scheme—Two techniques for matching the inviscid and viscous solutions were investigated: (1) requiring tangency along the matching contour and (2) forcing the inviscid solution to agree with the u and v velocity components from the viscous solutions along the matching line. For the first matching scheme, the flow angle from the decoded corrector equations on the boundary is found from

$$\delta = \tan^{-1}\frac{v}{u} \tag{28}$$

This flow angle is compared with the slope of the boundary at x^{n+1}. If the two angles disagree, then a Prandtl-Meyer turning is applied at the new body point using

$$\frac{p}{p_j^{n+1}} = 1 - \gamma M \Delta\delta + \frac{\gamma M}{M}\left[\frac{\gamma+1}{4}(M^2) - 1\right]\Delta\delta^2 \tag{29}$$

where $\Delta\delta$ is the difference in the two angles and

$$M = M^2/\sqrt{M^2-1} \tag{30}$$

Note that the sign of $\Delta\delta$ will result in either an expansion ($\Delta\delta > 0$) or an isentropic compression ($\Delta\delta < 0$) and the pressure, resulting from equation (19), is taken as the predicted pressure on the body at data line N+1. The density is found from

$$\rho_j^{n+1} = \left[pC\right]^{1/\gamma} \tag{31}$$

where $C = e^{-S-S_r/c_v}$ and S_r is some reference entropy. Once p and ρ are known at the boundaries, the total velocity is obtained from

$$q = \sqrt{1 - (p/\rho)} \tag{32}$$

The velocity components then result from the tangency condition at the boundaries. This technique was applied on the upper boundary throughout both matching schemes investigated. With this matching scheme, two different matching boundaries were considered - δ^* and an arbitrary streamline where the Mach number remained supersonic throughout the interaction. Results are presented only for the latter case since similar results were obtained for both matching contours.

The second matching scheme forced the inviscid solution to match values of u and v given by the viscous solution along the matching contour, here taken as the boundary-layer edge. This technique does not impose the tangency condition along the matching boundary, but rather allows for mass exchange from the inviscid to viscous portions of the flow, a physically realistic situation. Since u and v along the matching contour are now taken to be known, these values are used in the decode equations (21) to solve for p^{n+1} and ρ^{n+1}.

Navier-Stokes Solutions

Solutions to the Navier-Stokes equations presented here were obtained from several sources. Solutions of MacCormack (ref. 3), MacCormack and Baldwin (ref. 11), Messina (unpublished), and Skoglund and Gay (ref. 6) were obtained from the sources cited, while additional solutions were obtained in the present study using the computer codes of MacCormack and Baldwin (ref. 11) and Carter (ref. 10).

Space does not permit a detailed description of the differences and similarities of the several codes considered. There are, however, some striking differences and similarities in the several solutions presented which warrant discussion in some detail. Figure 1 shows the envelope of four Navier-Stokes solutions obtained from references 3 and 10 to 12, together with the data of Hakkinen et al. (ref. 17), for an unseparated, laminar-boundary-layer, shock-wave interaction at $M = 2$. Two points immediately come to mind: first, the large discrepancy in skin friction and the relatively small discrepancy in surface pressure. At first glance, this implies a low sensitivity of the pressure distribution to the skin-friction distribution and a lack of uniqueness in the Navier-Stokes solutions. However, a sequence of solutions obtained here using MacCormack and Baldwin's (ref. 11) code, with successive mesh refinement in the outer inviscid flow, shows differences in C_f of the same order as those shown in figure 1. This arises from the fact that for the coarsest mesh considered, the externally generated shock wave takes on a thickness that, when projected onto the boundary layer, is of the same order as the length of interaction. The viscous flow is then responding to a continuous compression rather than an imposed shock wave. As the nodal structure was refined, the skin-friction distribution approached a single curve.

Figure 2 shows a similar envelope of Navier-Stokes solutions obtained from references 6, 8, 10, and 11, together with experimental data for a well-separated, laminar-boundary-layer, shock-wave interaction (ref. 17). The results here are similar to those discussed above and the same conclusions can be drawn.

The point of the foregoing presentation is not to show how poorly Navier-Stokes solutions perform but rather to induce the user of Navier-Stokes codes to examine his results critically and, in particular, to examine the computational mesh dimensions in the light of the smallest relevant physical scale in the problem under consideration.

In subsequent sections, the boundary-layer calculation scheme developed is compared to the Navier-Stokes solutions of MacCormack (ref. 3).

RESULTS

The results of the inverse boundary-layer method are compared with Navier-Stokes solutions and with experimental data. The flows considered all occur on a flat plate and the pressure rise is caused by an externally generated shock wave. The specific flow parameters and experiments considered are listed in table 1.

Table 1

Reference	M_∞	Re	p_f/p_o	Remarks
17*	2	1.84×10^5	1.2	Laminar
17*	2	1.96×10^5	1.4	Laminar
18	1.47	4×10^6/ft	2.25	Turbulent
19	2.93	5.7×10^7/m	2.5	Turbulent
19*	2.93	5.7×10^7/m	5.0	Turbulent

*Navier-Stokes solutions available.

Finally, we will describe the progress made, to date, in coupling the inverse boundary-layer method to the inviscid calculation scheme to provide a complete flow-field prediction method.

Laminar-Boundary-Layer, Shock-Wave Interaction

Two laminar-boundary-layer, shock-wave interactions are considered: an unseparated interaction at $M = 2.0$ having an overall pressure rise p_f/p_o of 1.2 and a well-separated interaction at $M = 2.0$ having an overall pressure rise p_f/p_o of 1.4. These two interactions correspond to the experiments of Hakkinen et al. (ref. 17), as shown in figures 6a and 6b, respectively, of that report. For convenience, these interactions will be called Hakkinen 6a and 6b.

Note that in this and all subsequent comparisons with Navier-Stokes solutions, the skin-friction distribution obtained from the Navier-Stokes solution was input to the inverse boundary-layer method. This procedure ensures that a comparison of other parameters, that is, velocity and pressure distributions, provides a true measure of the validity of the boundary-layer assumption, without the peripheral considerations of downstream boundary conditions or matching conditions between viscous and inviscid flow. However, some differences can arise even in this case because of the order of the difference approximation used. The present inverse method is third-order accurate in wall shear as opposed to first-order accuracy imposed by assuming a linear variation of velocity with distance away from the wall in the Navier-Stokes solutions. An examination of the differences attributable to this assumption indicates that C_f can vary ±10 percent for the same velocity profile, depending on the order of curve fit used to deduce the derivative at the wall.

Figure 3 compares the pressure distribution obtained from present methods with a refined mesh Navier-Stokes calculation using Hung and MacCormack's code (ref. 9) for Hakkinen 6a. The two solutions are nearly indistinguishable everywhere and they are in reasonable agreement with the data. In figure 4, the velocity distributions at the x location corresponding to the minimum value of C_f (fig. 3) are compared. The differences between the present method and MacCormack's solution are not large and are largely attributable to differences in transport properties, that is, $Pr = 1$ and $\mu/\mu_o = T/T_o$ in the present method and $Pr = 0.72$ and μ from the Sutherland law in MacCormack's code.

Figure 5 shows the streamwise pressure distribution for Hakkinen 6a, for $y = 0$, $\delta/2$, δ, as computed by MacCormack (ref. 3). These curves are essentially indistinguishable and hence, within the boundary layer, $\partial p/\partial y \simeq 0$. This, in turn, implies a trivial solution to the y momentum equation which, from the usual boundary order-of-magnitude arguments, indicates that the boundary-layer equations are adequate for this flow.

Figure 6 compares the pressure distribution obtained from the present method with that of MacCormack's solution for Hakkinen 6b. For this case, a slight difference in surface pressure distribution is obtained near $x/L = 0.15$.

Figure 7 compares the velocity profiles obtained from the present method and from MacCormack's method for Hakkinen 6b. Differences between the profiles are explicable in terms of differences in transport properties discussed previously. Figure 8 shows the streamwise pressure distributions for Hakkinen 6b, as computed by MacCormack (ref. 3). This figure shows the normal pressure gradient developing in about the same region noted in figure 6 ($x/L = 0.15$ corresponds to $x/\Delta x = 20$). This normal pressure gradient appears to be an inertial effect associated with strong streamline curvature in the outer portion of the boundary layer where $M(y) \rightarrow M_e$. For this case, the boundary-layer method predicts a relatively large value of $|v_e/u_e|$ (not shown), which indicates the beginning of a breakdown of the boundary-layer approximation.

Turbulent Boundary-Layer, Shock-Wave Interaction

The question of the validity of boundary-layer theory in turbulent boundary-layer, shock-wave interactions is somewhat less clear than for laminar interactions. This is true for three reasons. First, few Navier-Stokes solutions with simple turbulence models are available for comparison (ref. 18). Second, the current turbulence models are demonstrably inadequate for flows with rapidly changing boundary conditions and, third, only a few experiments are available in supersonic turbulent flow which are sufficiently detailed to permit a useful comparison. Because of these facts, only a cursory comparison of results of the present method with both Navier-Stokes solutions and experimental data can be made.

Figure 9 compares the present method with the data of Seddon (ref. 19), for a normal shock-wave, turbulent-boundary-layer interaction with an initial Mach number of 1.47. For this case, the experimentally determined value of $C_f(x)$ was input to the inverse boundary-layer method in the attached-flow regime. For the reversed-flow region, where no data were available, three estimates of C_f were made (defined by the solid, dashed, and dot-dashed lines in the upper half of figure 9). The corresponding pressure distributions are shown in the lower half of figure 9. Two conclusions can be drawn from this figure: first, the boundary-layer equations are capable of reproducing the observed behavior and, second, the pressure distribution is sufficiently sensitive to variations in C_f to permit a coupled solution to distinguish between similar distributions of skin-friction coefficient.

Figure 10 shows a comparison of a direct calculation using the present method with the data of reference 20. The experimental skin-friction distribution shown was deduced from the measured mean velocity profiles using the method of reference 21. These data were taken at a free-stream Mach number of 2.93 and a unit Reynolds number of 5.7×10^7 m^{-1}. The pressure rise was effected by a shock generator set at 7^o incidence to the oncoming flow. As noted above, the predicted results were obtained for this case by calculation in the direct mode, that is, $P(x)$ was specified and C_f computed. The two predicted skin-friction distributions shown in the upper portion of figure 10 result from two

turbulence models used for this calculation. The equilibrium model is that described above while the exponential lag model is that suggested by Rose and Johnson (ref. 22) and subsequently used with some success in the Navier-Stokes calculations of reference 23 (see also ref. 18). One may conclude then that, given the appropriate turbulence model, the boundary-layer equations are adequate to describe flows of this type.

The last case considered was also taken from references 20 and 21. The initial flow properties were the same as those discussed in figure 10 but the shock generator angle was set at 13^{o} to the oncoming flow. As shown in the upper portion of figure 11, the flow has an extensive region of separation $(x_{reatt} - x_{sep}) \simeq 4\delta$. For this case, the inverse boundary-layer method failed. The predicted pressure distribution shown in figure 11 indicated nearly twice the pressure rise observed experimentally. Direct solutions employing the experimentally observed pressure distribution failed to predict any separation. This might be attributed to three-dimensional effects in the experiment except that the Navier-Stokes solutions of Baldwin and Rose (see ref. 18), using a similar turbulence model, did a plausible job of predicting the flow. An examination of this solution shows extensive regions of significant normal pressure gradient.

Coupled Solutions

Figure 12 compares the pressure distributions resulting from the two coupling schemes for the Hakkinen 6b case with that given by the Navier-Stokes program of reference 3. Neither coupling scheme appears to be adequate when applied in a noniterative manner. The tendency of shock-capturing techniques to smear the shock wave over several grid points and to overshoot the pressure rise through the shock-wave reflection is evident. Perhaps the best overall qualitative agreement with the Navier-Stokes results is provided by the u-v coupling scheme; however, as noted earlier, the discontinuity in v that results from the boundary-layer calculations will strongly affect this scheme.

Truncated Navier-Stokes Equations

To circumvent the difficulties encountered in coupling viscous and inviscid flows, an alternative procedure was considered. Rather than solve coupled viscous and inviscid equations in an iterative mode, we proposed to solve the following system of equations:

$$\frac{\partial \rho}{\partial t} + \frac{\partial \rho u}{\partial x} + \frac{\partial \rho v}{\partial y} = 0$$

$$\frac{\partial \rho u}{\partial t} + \rho u \frac{\partial u}{\partial x} + \rho v \frac{\partial u}{\partial y} + \frac{\partial p}{\partial x} = \frac{\partial \tau_{xy}}{\partial y}$$

$$\frac{\partial \rho v}{\partial t} + \rho u \frac{\partial v}{\partial x} + \rho v \frac{\partial v}{\partial y} + \frac{\partial p}{\partial y} = 0$$

together with an equation of state and a consistent energy conservation relation. This was accomplished by simply removing the appropriate terms from the computer code of MacCormack and Baldwin (ref. 11). These equations converged everywhere within 1 percent of full Navier-Stokes solution for the Hakkinen cases 6a and 6b using the same mesh configuration (results not shown). The above method was slightly more efficient than the solution of the full Navier-Stokes equations because fewer operations need to be performed in the computer code.

One can deduce, however, that these equations can be solved and since they are parabolic in the streamwise variable, they can be solved by a forward-marching procedure. This latter fact would allow a first-order improvement in computational efficiency. Unfortunately, these conclusions were reached very late in the present study and time did not permit significant exploitation of the properties of these equations.

CONCLUDING REMARKS

We have demonstrated the validity of the boundary-layer equations applied to certain shock-wave, boundary-layer interactions. As has been suggested (e.g., ref. 2), solutions to the boundary-layer equations begin to depart significantly from those of the Navier-Stokes equations under the same conditions for which nontrivial normal pressure gradients are first observed in the Navier-Stokes solutions. Based on the physical argument that high-velocity flow, turning through a large angle, requires the action of a large force over a short distance, one may deduce that the normal pressure gradient arises primarily from the inviscid characteristics of the flow field. From this one may conclude that when some parameter involving both Mach number and turning angle, for example, $M_e|v_e/u_e|$, exceeds a critical value, boundary-layer theory will fail.

Despite the fact that boundary-layer theory can be shown to fail at high supersonic Mach numbers when extensive separations occur, it would appear that, for many technological problems, boundary-layer theory is quite satisfactory. This should be particularly true in the design of transonic airfoils and for engine inlets to be used on transonic and low supersonic flight vehicles when high angle-of-attack trajectories are not required.

Note that a typical solution presented here required about 3 min of CPU time on the IBM 360/67. Our experience indicates a factor of about 25 reduction in CPU time when the CDC 7600 is used. While the present inverse method is not yet a complete predictive method, it shows substantial promise if the coupling problems can be solved. Alternatively, if these problems defy solution, the truncated Navier-Stokes system described earlier appears to be potentially useful.

REFERENCES

1. Brown, S. N.; and Stewartson, K.: Laminar Separation, edited by W. R. Sears and M. Van Dyke, Annual Review of Fluid Mechanics, vol. 1, Annual Reviews, Inc., Palo Alto, Calif., 1969, pp. 45-72.

2. Murphy, J. D.: A Critical Evaluation of Analytic Methods for Predicting Laminar Boundary Layer, Shock Wave Interaction, NASA TN D-7044, 1971.

3. MacCormack, R. W.: Numerical Solution of the Interaction of a Shock Wave with a Laminar Boundary Layer, Proceedings of the 2nd International Conference on Numerical Methods in Fluid Dynamics, Lecture Notes in Physics, vol. 8, Springer-Verlag, 1971.

4. Klineberg, J. M.; and Steger, J. L.: The Numerical Calculation of Laminar Boundary Layer Separation, NASA TN D-7732, 1974.

5. Carter, J. E.: Solutions for Laminar Boundary Layers with Separation and Reattachment, AIAA Paper 74-583, 1974.

6. Skoglund, V. J.; and Gay, B. D.: Improved Numerical Techniques and of a Separated Interaction of an Oblique Shock Wave and a Laminar Boundary Layer, Bur. of Engin. Res. Rept. ME 41(69)S-068, Univ. of New Mexico, June 1969.

7. Staiano, E. F.: A General Numerical Procedure for Solutions of Viscous Compressible Flows with Shock Waves, Ph.D. dissertation, Univ. of New Mexico, May 1967.

8. MacCormack, R. W.: An Introduction to the Numerical Solution of the Navier-Stokes Equations, AIAA Paper 75-1, 1975.

9. Hung, C. M.; and MacCormack, R. W.: Supersonic and Hypersonic Laminar Flows Over a Two-Dimensional Compression Corner, AIAA Paper 75-2, 1975.

10. Carter, J. E.: Numerical Solutions of the Navier-Stokes Equations for the Supersonic Laminar Flow Over a Two Dimensional Compression Corner, NASA TR R-385, 1972.

11. MacCormack, R. W.; and Baldwin, B. S.: A Numerical Method for Solving the Navier-Stokes Equations with Application to Shock Boundary Layer Interactions, AIAA Paper 75-1, 1975.

12. Murphy, J. D.: Application of the Generalized Galerkin Method to the Computation of Fluid Flow, Presented at the AIAA Computational Fluid Dynamics Conference, Palm Springs, Calif., July 19-20, 1973.

13. Kendall, R. M.; and Bartlett, E. P.: Non-Similar Solutions of the Multicomponent Laminar Boundary Layer by an Integral Matrix Method, AIAA Preprint 67-218, 1967.

14. Lanczos, C.: Applied Analysis, Prentice-Hall, Englewood Cliffs, N.J., 1964.

15. Presley, L. L.; and Kutler, P.: Comparison of a Discrete-Shock Finite-Difference Technique and the Method of Characteristics for Calculating Internal Supersonic Flows, Presented at the AIAA Computational Fluid Dynamics Conference, Palm Springs, Calif., July 19-20, 1973.

16. Abbett, M. J.: Boundary Condition Calculation Procedures for Inviscid Supersonic Flow Fields, Presented at the AIAA Computational Fluid Dynamics Conference, Palm Springs, Calif., July 19-20, 1973.

17. Hakkinen, R. J.; Greber, I.; Trilling, L.; and Abarbanel, S. S.: The Interaction of an Oblique Shock Wave with a Laminar Boundary Layer. NASA MEMO 2-18-59W, 1959.

18. Baldwin, B. S.; and Rose, W. C.: Calculation of Shock-Separated Turbulent Boundary Layers. Aerodynamic Analyses Requiring Advanced Computers, Part I, NASA SP-347, 1975, pp. 401-417.

19. Seddon, J.: The Flow Produced by Interaction of a Turbulent Boundary Layer with a Normal Shock Wave of Strength Sufficient to Cause Separation, ARC R & M 3502, 1967.

20. Reda, D. C.; and Murphy, J. D.: Shock Wave Turbulent Boundary Layer Interaction in Rectangular Channels, Part II, The Influence of Side Wall Boundary Layers on Incipient Separation and Scale of the Interaction, AIAA Paper 73-234, 1973.

21. Rubesin, M. W.; Murphy, J. D.; and Rose, W. C.: Wall Shear in Strongly Retarded and Separated Turbulent Boundary Layers, AIAA J., vol. 12, no. 10, Oct. 1974, pp. 1442-1444.

22. Rose, W. C.; and Johnson, D. A.: A Study of Shock Wave Turbulent Boundary Layer Interaction Using Laser Velocimeter and Hot Wire Anemometer Techniques, AIAA Paper 74-95, 1974.

23. Shang, J. S.; and Hankey, W. L., Jr.: Numerical Solutions of the Navier-Stokes Equations for Supersonic Turbulent Flow Over a Compression Corner, AIAA Paper 75-4, 1975.

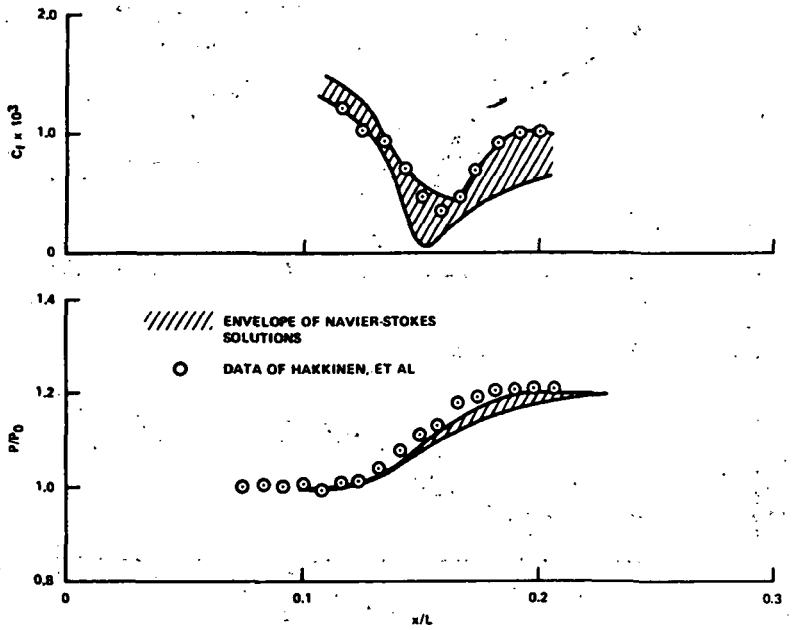

Figure 1.- Comparison of envelope of four Navier-Stokes solutions with the data of Hakkinen et al.; M = 2, $Re_{shock} = 2.84 \times 10^5$, $p_f/p_o = 1.20$.

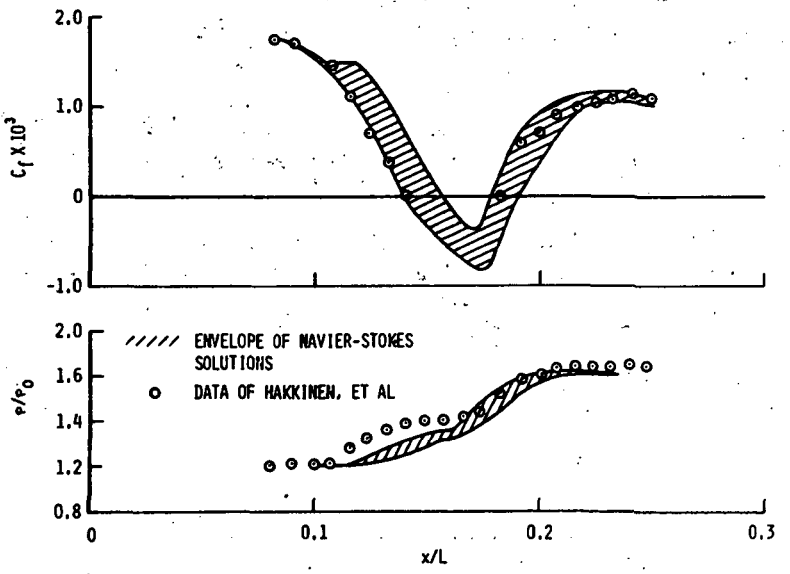

Figure 2.- Comparison of envelope of four Navier-Stokes solutions with the data of Hakkinen et al.; M = 2, $Re_{shock} = 2.96 \times 10^5$, $p_f/p_o = 1.40$.

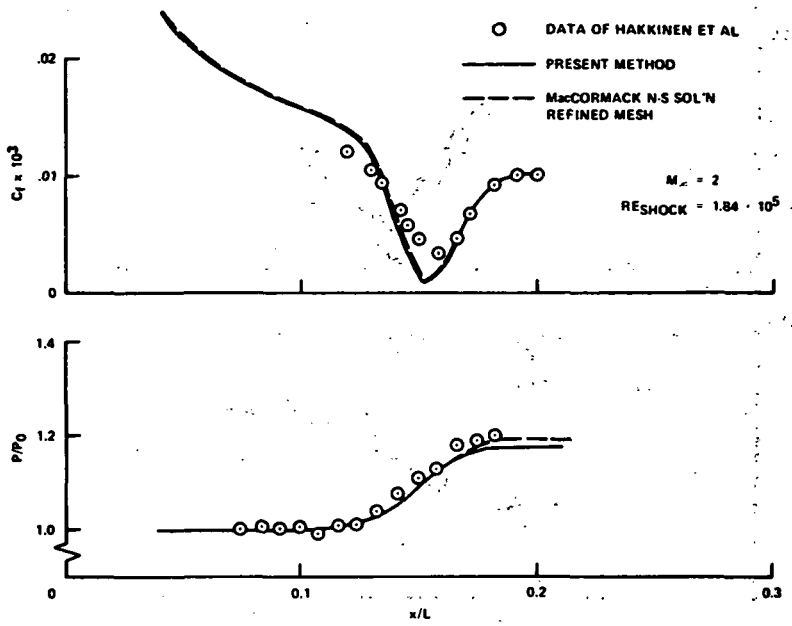

Figure 3.- Comparison of results of the present method with refined mesh calculations using Hung and MacCormack's code.

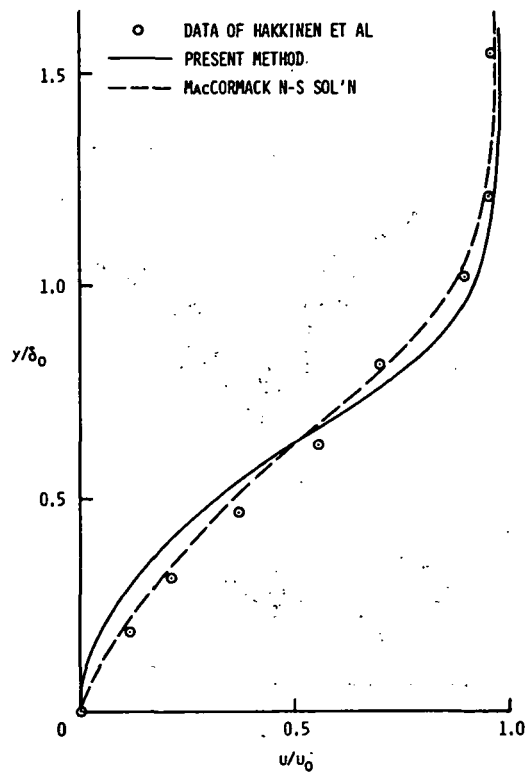

Figure 4.- Comparison of predicted velocity profiles at minimum C_f.

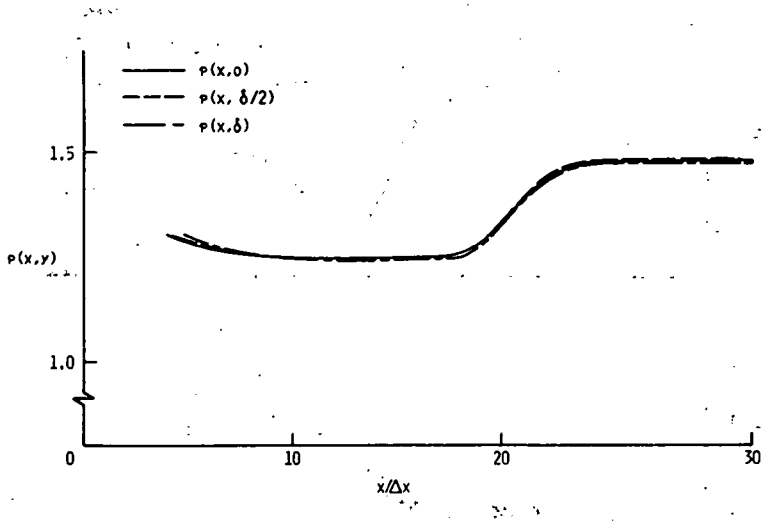

Figure 5.- Predicted pressure distributions for an unseparated laminar boundary-layer, shock-wave interaction; calculations of MacCormack.

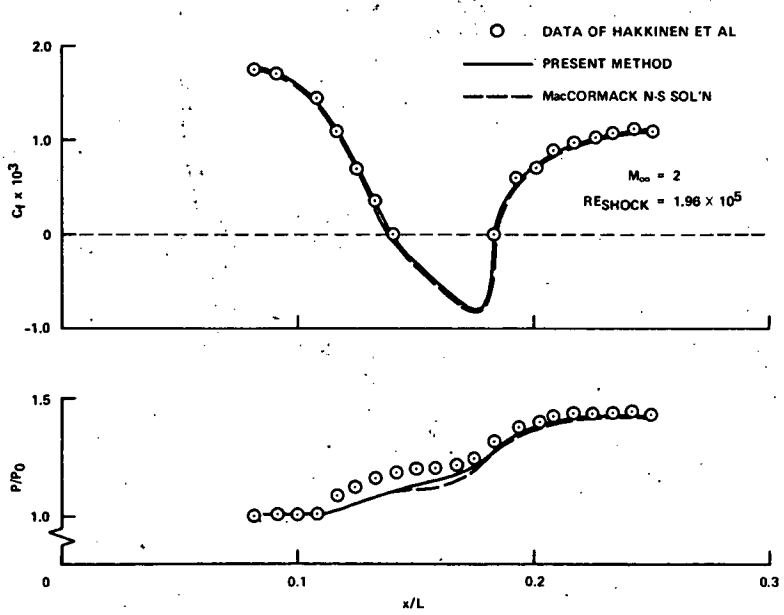

Figure 6.- Comparison of results of present method with calculations of MacCormack.

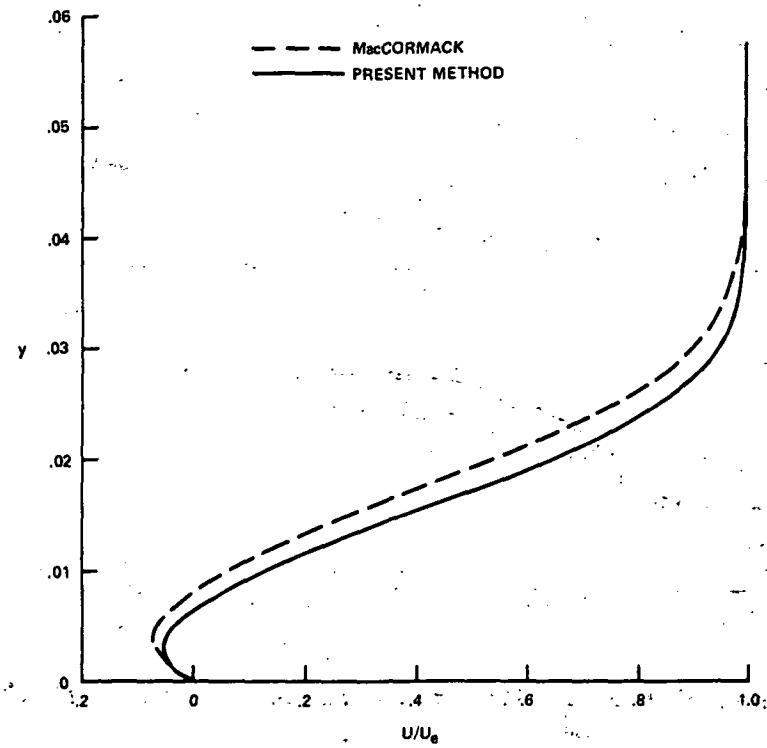

Figure 7.- Comparison of predicted velocity profiles at minimum C_f.

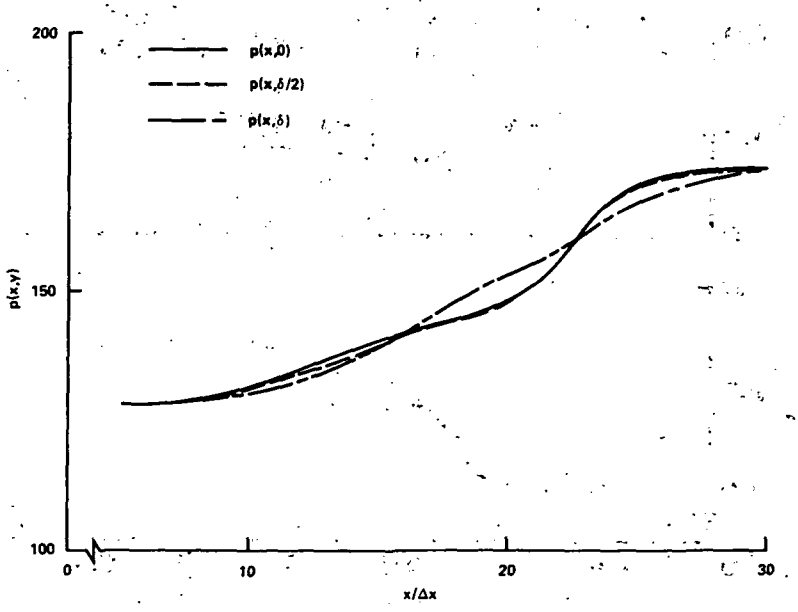

Figure 8.- Predicted pressure distributions for a separated laminar boundary-layer, shock-wave interaction; calculations of MacCormack.

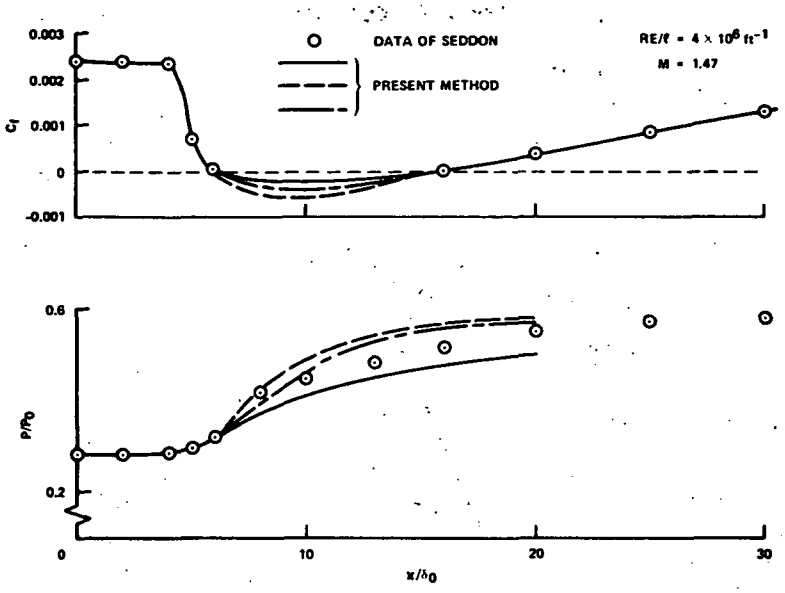

Figure 9.- Comparison of the results of the present method with the data of Seddon (ref. 18).

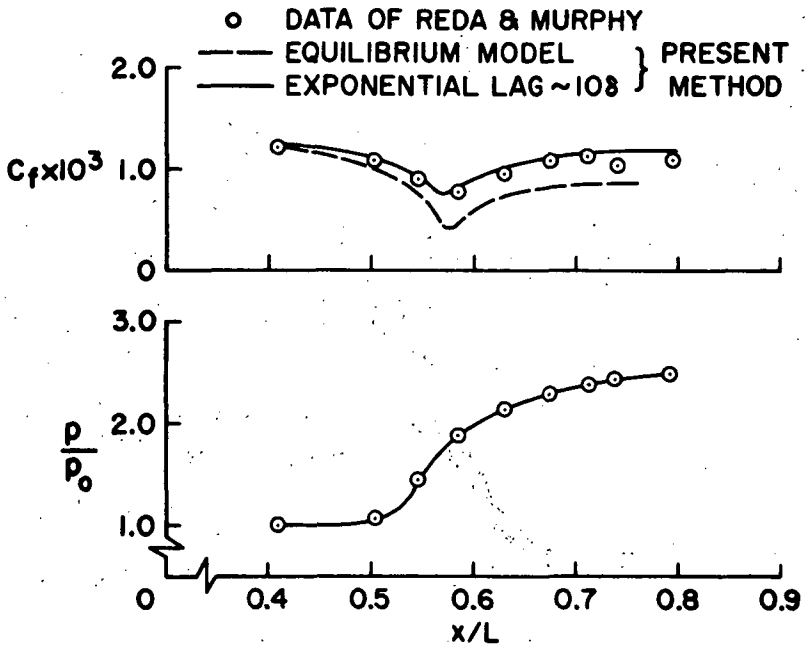

Figure 10.- Comparison of the present method with the data of reference 19; turbulent unseparated flow.

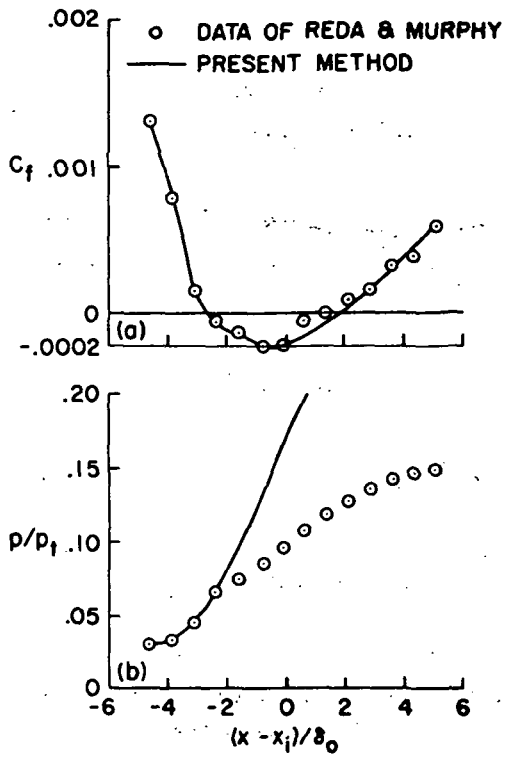

Figure 11.- Comparison of the present method with the data of reference 20; turbulent separated flow.

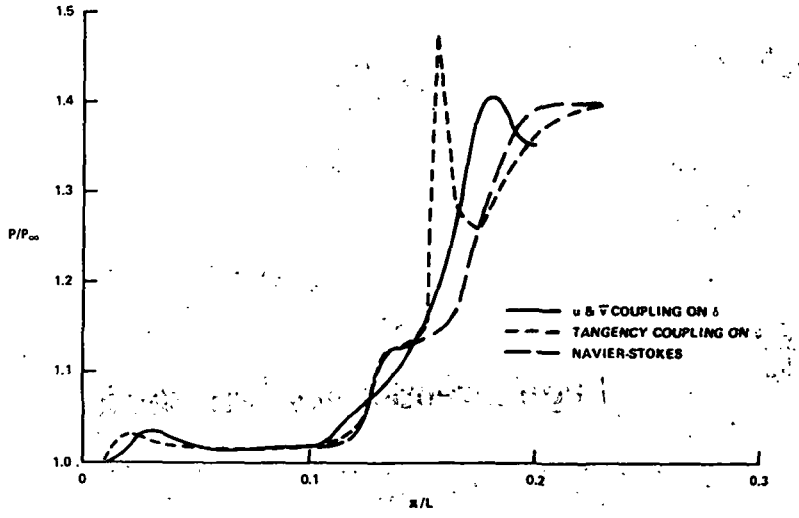

Figure 12.- Comparison of coupling schemes.

Page Intentionally Left Blank

ASYMPTOTIC THEORY OF TWO-DIMENSIONAL TRAILING-EDGE FLOWS*

By R. E. Melnik and R. Chow
Grumman Aerospace Corportation

SUMMARY

In this investigation, problems of laminar and turbulent viscous interaction near trailing edges of streamlined bodies are considered. The laminar study is based on the triple-deck formulation of Stewartson, Messiter, and Brown. This theory is developed from asymptotic expansions of the Navier-Stokes equations in the limit of large Reynolds numbers. The expansions describe the local solution near the trailing edge of cusped or nearly cusped airfoils at small angles of attack in compressible flow. A complicated inverse iterative procedure, involving finite-difference solutions of the triple-deck equations coupled with asymptotic solutions of the boundary values, is used to accurately solve the viscous interaction problem. Results are given for the correction to the boundary-layer solution for drag of a finite flat plate at zero angle of attack. A solution is also presented for the viscous correction to the lift of an airfoil at incidence. A comparison of the present results with triple-deck solutions recently obtained by other investigators for the symmetric problem is presented. Also presented are some comparisons of the present solution with low Reynolds number ($R \leqq 200$) solutions of the Navier-Stokes equations and with experimental data. These comparisons indicate that the asymptotic triple-deck theories are accurate over a surprisingly wide range of Reynolds numbers down to Reynolds numbers as low as 10 or less.

In the second part of this investigation, the problem of turbulent interactions at airfoil trailing edges is considered. It is demonstrated that second-order boundary-layer theory fails at airfoil trailing edges and that the concept of the flow over an equivalent body formed from the displacement thickness is not appropriate for turbulent flows near trailing edges. A rational asymptotic theory is developed for treating turbulent interactions near trailing edges and is shown to lead to a multilayer structure of turbulent boundary layers. The flow over most of the boundary layer is described by a Lighthill model of inviscid rotational flow. The main features of the model are discussed and a sample solution for the skin friction is obtained and compared with the data of Schubauer and Klebanoff for a turbulent flow in a moderately large adverse pressure gradient.

*This research was performed under NASA Langley Contract No. NAS 1-12426.

INTRODUCTION

The problem of trailing-edge flows is of considerable importance in aerodynamics. Most streamlined bodies end in a sharp trailing edge that is cusped or nearly cusped in order to provide a smooth transition of the flow into the wake. The flow near the trailing edge is important in establishing the lift and drag forces on the body.

At high Reynolds numbers the solution of the Navier-Stokes equations can be expanded in descending powers (and logarithms) of the Reynolds number. The leading term is governed by inviscid flow equations over most of the domain and by boundary-layer equations in a thin layer near the surface and in the wake. To lowest order, the lift is determined by solutions of the inviscid-flow equations, subject to the Kutta condition. Skin-friction drag is determined by solutions of the boundary-layer equations with the pressure distribution obtained from the inviscid solution. Within this approximation, form drag is computed from the surface pressures induced by the effect of the boundary layer on the external inviscid flow and is, therefore, a second-order effect in the theory.

Although the inviscid and boundary-layer solutions provide the leading approximation for the flow over streamlined bodies, higher order corrections are important in many problems. A major impediment in the determination of the correction is due to the fact that the underlying asymptotic expansions are not uniformly valid at trailing edges. The nonuniformity is caused by the appearance of singularities in solutions of both the laminar and turbulent boundary-layer equations at trailing edges. The nature of the singularity differs in the laminar and turbulent cases, but in both cases, the major effect is the production of a displacement thickness that is singular at the trailing edge. This in turn leads to singularities in the induced pressures at the trailing edge. As a result, the second-order Kutta condition cannot be satisfied and the viscous correction to lift cannot be determined. In addition, corrections to the boundary-layer solutions for skin friction and form drag are not correctly determined by standard second-order boundary-layer theory. Most existing engineering methods for predicting viscous effects on lift are based on iterative solutions of the second-order boundary-layer equations. These methods experience difficulties at trailing edges which are circumvented by an ad hoc smoothing of the displacement surface determined from the solution of the boundary-layer equations.

In spite of its importance and the continuing interest of many investigators, it is only recently that a comparatively complete theory of trailing-edge flows has been developed and this only for laminar flows. The recent advances in laminar trailing-edge problems are based on the triple-deck formulation of Stewartson (ref. 1) and Messiter (ref. 2) developed originally for a symmetric flat plate at zero angle of attack. These theories were then extended the following year by Brown and Stewartson (ref. 3) to the lifting flat plate. The triple-deck theories are applicable to general airfoils with a cusped or nearly cusped

trailing edge in compressible flow. For Mach numbers not near one, compressibility enters into the theory only through a scaling of dependent and independent variables. However, even though a number of properties of the solution were determined and the singular behavior was explained, accurate numerical solutions were not obtained in these early works.

The first part of this paper deals with the laminar-viscous interaction near airfoil trailing edges in the limit of large Reynolds numbers. The approach used is to develop the appropriate numerical procedures to solve the boundary-value problem formulated by Stewartson, Messiter, and Brown. A general discussion of the laminar-flow problem along with a summary of the triple-deck formulation and the resulting boundary-value problem is presented in the section "The Laminar-Flow Problem." The following section, entitled "The Numerical Method," deals with all aspects of the numerical methods used to solve this problem. First, an inverse iterative scheme to solve the coupling between the various layers of the triple deck is discussed. Then finite-difference methods based on the Keller "box" scheme (refs. 4 and 5) are formulated to solve the triple-deck equations. Methods are also discussed for the evaluation of the Hilbert integrals arising from the analysis. Also presented in the section on numerical methods is a description of the accuracy and convergence properties of the numerical methods. A discussion of the results for both zero and nonzero incidence follows in the Results. Solutions to the symmetric problem have also been recently obtained by Jobe and Burggraf (ref. 6) and by Veldman and Van De Vooren (ref. 7). Detailed comparisons between the present solution and those of references 6 and 7 are provided. Also the solution for the drag of a finite flat plate at zero incidence is compared with the experimental data of Janour (ref. 8) and with finite-difference solutions of the complete Navier-Stokes equations recently obtained by S. C. R. Dennis, who provided numerical data from his unpublished results. The solution for the velocity profile in the wake of the symmetric solution is compared with experimental data of Sato and Kuriki (ref. 9).

Currently, understanding of turbulent interactions at trailing edges is rather less complete. Recent attempts to develop a rational theory of turbulent trailing-edge flows include the investigations of Spence (ref. 10) and Küchman (ref. 11). In reference 10, the main correction to boundary-layer theory is assumed to arise from the pressure change across the wake generated by the singular curvature of the inviscid trailing streamline. This leads to a jet-flap model of trailing-edge flows. Spence's model is inconsistent and leads to unacceptable oscillatory solutions downstream. The failure of Spence's theory is caused by the neglect of convective acceleration terms in the normal momentum equations. It is interesting that a scaling analysis of Spence's interaction equation indicates the need to retain these terms in the lowest order theory. The investigation of Küchman in reference 11 is based on a Lighthill model of turbulent boundary layers near the trailing edge, which is treated as an inviscid rotational flow. Some examples of rotational flow in

a wedge-shaped compression corner are presented. Although these results are of interest, there is no attempt to develop a complete, rational theory and no consideration is given to the trailing-edge region on a lifting airfoil.

A more promising approach for a rational theory of turbulent flows follows from asymptotic expansions of the time-averaged Navier-Stokes equations in the limit of large Reynolds numbers. Similar asymptotic techniques have been applied to noninteracting turbulent boundary layers by Mellor (ref. 12), Yajnik (ref. 13), and Bush and Fendell (refs. 14 and 15) and to transonic shock-wave—boundary-layer interactions by Melnik and Grossman (ref. 16) and by Adamson and Feo (ref. 17).

In the second part of the present investigation (Turbulent Trailing-Edge Flows) it is shown that asymptotic analysis leads to a three-layer description of turbulent interaction near trailing edges with a streamwise length scale that is on the order of a boundary-layer thickness. The flow in the outermost layer is governed by inviscid, linearized rotational-flow equations. The description near the wall requires two layers, involving just Reynolds stresses in the middle layer and both Reynolds and laminar stresses in the innermost wall layer. The solution in the outer layer is unaffected to lowest order by the two inner layers and can, therefore, be completely determined independently of the details of the inner layers. This leads to a Lighthill model for the outer problem that must be solved to determine the pressure distribution and lift forces. Here, only the incompressible problem will be considered and a brief description of the essential features of the interaction model, together with a formulation of a boundary-value problem governing the outer inviscid flow will be provided. Also a sample solution for the skin friction determined from matching the inner and outer solutions is given and the results are compared with the low-speed data of Schubauer and Klebanoff (ref. 18).

SYMBOLS

a_1, a_2 parameters related to lift coefficient and constant defined by equation (19b)

A displacement function in triple-deck theory

A_1^-, A_1^+ constants related to behavior of A near the origin

b_1 constant in asymptotic solution for $|X| \to \infty$

B_P constant defining y-grid distribution

B_α constant related to second-order boundary-layer solution for displacement thickness (turbulent)

C_f skin-friction coefficient, $\dfrac{\tau_w^*}{\frac{1}{2}\rho U_\infty^2}$

$C_{f,o}$ skin-friction coefficient of noninteracting boundary-layer solution at trailing edge (turbulent)

C_{ij} constant appearing in asymptotic solutions of triple-deck equations, where i and j = 1, 2, 3, . . .

C_L lift coefficient

C_o coefficient of singular pressure gradient in wake

C_α constant related to singularity of inviscid solution near trailing edge

d normalized shear stress gradient in computation plane, $\partial\tau/\partial y$

d_1 constant in asymptotic solution for $|X| \to \infty$

d_2 constant in triple-deck solution for drag coefficient

D shear stress gradient in Z-direction, $\partial\tau/\partial Z$

f Blasius function

F_1 similarity function related to symmetric triple-deck solution for $|X| \to -\infty$

G_o Hakkinen-Rott similarity function related to triple-deck solution for $X \to 0$

h_1, h_2, h_3 functions appearing in differential equations for H_1, H_2, and H_3, respectively

H shape factor, δ_1^*/δ_2^*

H_1, H_2, H_3 similarity functions related to triple-deck solutions for $X \to -\infty$

I integer, running index for X-mesh

I_p integer related to X-mesh

I_1, I_2, I_3	integers defining X-mesh
J	integer, running index for y-mesh
J_{inner}	number of points in inner mesh in wake
J_P	number of mesh points in y-mesh on plate
J_W	number of mesh points in y-mesh in wake
K_i	parameter defining mesh distribution, where $i = 1, 2, \ldots$
$\ell(y^+)$	mixing length, turbulent flow
L	length of plate or chord, dimensional
L_0, L_1, L_{max}	parameters related to X-mesh
p	pressure
p_∞	free-stream pressure, dimensional
P	normalized pressure appearing in triple-deck theory
P_1, P_2, P_3	constants related to behavior of P near origin
R	Reynolds number, $U_\infty L/\nu$
R_{ij}	functions related to asymptotic behavior of U as $Z \to \infty$, where i and $j = 1, 2$
T_i	integrals defined by equations (45), where $i = 1, 2, 3$
u	velocity in streamwise direction
u_τ	friction velocity, $\sqrt{\tau_w/\rho}$
U	normalized velocity in streamwise direction in triple-deck theory
U_∞	free-stream velocity, dimensional

v	velocity in direction normal to plate
V	normalized velocity in direction normal to plate in triple-deck theory
W	Coles wake function (turbulent flow)
x	Cartesian coordinate along plate
X	normalized coordinate along plate in triple-deck theory
X_P	end point of boundary-layer calculation
y	computational coordinate normal to plate for laminar flow and physical coordinate for turbulent flow
y_M	coordinate defining outer boundaries of y-mesh
Z	physical coordinate normal to plate for laminar flow
α	normalized angle of attack in triple-deck theory
α^*	angle of attack in radians
γ	constant appearing in behavior of triple-deck solution near origin for $\alpha \neq 0$
$\Gamma(\,)$	Gamma function
δ	boundary-layer thickness
δ_1	displacement thickness
δ_2	momentum thickness
δ_c	boundary-layer camber, $\frac{1}{2}(\delta_T - \delta_B)$
ϵ	small parameter, $R^{-1/8}$ for laminar flow and $\sqrt{\frac{C_{f,o}}{2}}$ for turbulent flow
$\hat{\epsilon}$	small parameter related to wall-layer thickness, $(\epsilon^2 R)^{-1}$ in turbulent flow

ζ vorticity (turbulent flow); also variable defined by equations (38) and (39)

η independent variable in similarity solutions of triple-deck equations, $|Z|/2|2X|^{1/3}$

θ parameter used to scale wake location, related to wake centerline

κ Karman constant, approximately equal to 0.41

λ constant, equal to 0.33206, appearing in Blasius solution, $f''(0)$

λ_1 normalized skin friction at trailing edge in triple-deck solution

$\Lambda_{10}, \Lambda_{02}, \Lambda_{23}$ integrals defined by equations (46)

ν coefficient of kinematic viscosity, dimensional

ξ variable used in definition of X-grid distribution

$\tilde{\pi}$ Coles wake parameter

ρ density, dimensional

σ parameter used to scale wake location, related to wake thickness

τ normalized skin friction in laminar study; also Reynolds stress in turbulent problem

τ_w skin friction

ψ normalized stream function in computational plane

Ψ stream function

ω relaxation parameter

Superscripts:

$*$ dimensional quantity

+	denotes wall-layer variable in turbulent analysis
^	denotes blending-layer variable in turbulent analysis
'	denotes differentiation with respect to indicated variable and perturbation quantity in turbulent flow

Subscripts:

B	bottom surface of airfoil
BL	perturbation quantity arising from upstream boundary layer in turbulent analysis
e	local quantity evaluated at edge of boundary layer
inv	perturbation quantity arising from outer inviscid flow in turbulent analysis
T	top surface of airfoil
TE	quantity evaluated at trailing edge, $X = 0$

THE LAMINAR-FLOW PROBLEM

Problems of laminar flow at large Reynolds numbers are usually analyzed by a combination of inviscid-flow and boundary-layer techniques. This approach is based on asymptotic expansions of the complete Navier-Stokes equations in the limit of Reynolds numbers approaching infinity. The inviscid and boundary-layer equations arise as the basic equations governing the leading approximation in the outer and inner regions, respectively. This approach leads to accurate and useful solutions of viscous-flow problems in many instances and has tended to dominate the history of fluid mechanics. However, in spite of its central role in fluid flows, the underlying structure of the asymptotic expansions are only relatively well understood for flows that are not separated and for geometries that are smooth.

It is well known that the inviscid and boundary-layer descriptions break down near separation points or near singular points of the geometry, such as sharp leading edges, corners, and trailing edges. A comprehensive review of these matters, including a discussion of higher order approximations, has been given by Van Dyke (ref. 19) and Stewartson (ref. 20).

In the trailing-edge problem, the nonuniformity of the basic expansions is caused jointly by a discontinuity in the surface boundary conditions at the trailing edge and by a singularity in the inviscid solution at the trailing edge of a lifting airfoil. The discontinuity in boundary conditions leads to a singularity in the boundary-layer solution at the trailing edge that is described by Goldstein's near wake solution (ref. 21). Goldstein's solution shows that the displacement surface develops a sharp corner with a vertical tangent on the downstream side of the trailing edge, as illustrated in figure 1. Goldberg and Cheng (ref. 22) have examined the second-order inviscid solution over a finite-length flat plate at zero incidence and have demonstrated that the inviscid flow over this displacement surface is singular, with the induced pressures approaching plus (minus) infinity on the downstream (upstream) side of the trailing edge.

The inviscid solution for subsonic flow near the trailing edge of a cusped airfoil at angle of attack exhibits a square-root singularity in the surface pressure distribution, as sketched in figure 1. The surface pressure is bounded but the pressure gradients are unbounded as the trailing edge is approached. The singular pressure gradients lead to singularities in the boundary-layer solution and to breakdown of the basic asymptotic expansions.

There have been numerous attempts to correct these defects and to develop an asymptotic theory that is uniformly valid at trailing edges, but for the most part, these were completely unsuccessful. It was only in the recent work of Stewartson (ref. 1) and, independently, Messiter (ref. 2) that a correct and rational treatment of the flow near trailing edges was given. In these works it was shown that the flow develops a characteristic multilayer structure near trailing edges that also arises in many other laminar interaction problems and which is referred to by Stewartson as a triple-deck model. A general discussion of viscous problems involving triple-deck structure is found in the recent review by Stewartson in reference 20.

The Triple-Deck Formulation

Stewartson and Messiter presented a rational treatment for the flow near a trailing edge. By using the method of matched asymptotic expansions, these investigators have shown that solutions of the Navier-Stokes equations near the trailing edge can be developed in asymptotic series in the limit of large Reynolds numbers. The solutions are cast in terms of a fundamental small parameter ϵ given in terms of the Reynolds number

$$\epsilon = R^{-1/8} \tag{1}$$

where R is the Reynolds number based on the length of the plate and the constant flow velocity far from the plate. Stewartson and Messiter considered the idealized case of incompressible flow over a finite flat plate at zero incidence. The theory was extended

to angle of attack by Brown and Stewartson in reference 3 for angles of attack α^* on the order of $\epsilon^{1/2}$. Although the theory of references 1 to 3 was developed for incompressible flow over finite flat plates, the basic theory is applicable to more general airfoils provided the airfoil is closely approximated by a flat plate near the trailing edge. For example, this requires the trailing-edge angle of an airfoil with thickness to be less than $0(\epsilon^2)$. The equations for the leading approximation are also applicable to compressible flows provided the Mach number of the inviscid solution is not near one in the trailing-edge region. In these cases compressibility effects enter only through a scale transformation of dependent and independent variables as given in references 3 and 20.

The structure of the triple-deck region is sketched in figure 2. The flow upstream and downstream of the triple-deck region is governed by standard inviscid and boundary-layer equations. The leading term in the outer inviscid region is given by constant uniform flow, while the solution in the upstream boundary layer is given by the Blasius solution and in the downstream wake by a modified Goldstein near wake solution, as described in reference 3. In the intermediate region between the Blasius and Goldstein region, the flow develops the multilayer structure sketched in figure 2. The ratio of the length scale of each region to the length of the plate L is also indicated in the figure. The streamwise length scale is $0(\epsilon^3)$, which is an order of magnitude larger than a boundary-layer thickness. Viscous effects are important only in the lower deck where the solution is governed by classical (incompressible) boundary-layer equations. Both pressure and viscous forces are negligible in the main deck to lowest order. The main role of the essentially passive main deck is to transmit flow deflections generated by the sublayer to the outer edge of the boundary layer. These flow deflections provide an inner boundary condition for the solution in the upper deck which is governed by inviscid small-disturbance equations. The solution in the inviscid upper deck is governed by elliptic partial differential equations which provide for the long upstream influence that was missed in many previous theories.

From the preceding discussion, it can be seen that the triple-deck formulation leads to a description of the flow as an interaction between the outer inviscid stream and the displacement thickness generated by the sublayer. The solution in the inviscid upper deck can be reduced to an integral relationship between the surface pressure and the flow deflection generated by the sublayer.

Solution of the triple-deck problem is thus reduced to that of determining solutions to the boundary-layer equations valid in the sublayer. These solutions must match the rotational flow in the main deck and must result in a displacement thickness and pressure distribution that satisfies the linear integral relationship arising from the outer solution.

The notation employed in references 1 to 3 and 20 varies. Here the notation employed by Stewartson in reference 1 will be followed with some exceptions. Physical

quantities are denoted by an asterisk, free-stream quantities by the subscript ∞, and the plate length by L. The quantities x^* and y^* are Cartesian coordinates parallel and transverse, respectively, to the plate with origin at the trailing edge, u^* and v^* are velocity components in the x^*- and y^*-directions, respectively, p^* is the pressure, ρ the density, α^* the angle of attack, and λ is a constant, equal to 0.33206, associated with the Blasius solution for the wall shear stress. Nondimensional variables for the lower deck are given by

$$\left.\begin{aligned} X &= \lambda^{5/4}x^*/\epsilon^3 L & Z &= \lambda^{3/4}y^*/\epsilon^5 L \\ U &= u^*/\epsilon\lambda^{1/4}U_\infty & V &= v^*/\epsilon^3\lambda^{3/4}U_\infty \\ P &= (p^* - p_\infty)/\epsilon^2\lambda^{1/2}\rho U_\infty^2 & \alpha &= \alpha^*/\epsilon^{1/2}\lambda^{9/8} \end{aligned}\right\} \tag{2}$$

(These scalings are for incompressible flow; for compressible flow, see refs. 3 and 20.) The Reynolds number R is given by $U_\infty L/\nu$, where ν is the kinematic viscosity coefficient.

For future reference, the solution for incompressible, inviscid flow over a flat plate of length L at incidence α^* is given by (for $y^* = 0$)

$$v^* = 0 \qquad u^* = U_\infty - U_\infty\alpha^* \frac{x^* + B}{\left[(-x^*)(L + x^*)\right]^{1/2}} \operatorname{sgn} y^* \qquad (-L < x^* < 0) \tag{3a}$$

$$u^* = U_\infty \qquad v^* = U_\infty\alpha^* \frac{x^* + B}{x^*(L + x^*)^{1/2}} \qquad (0 < x^*) \tag{3b}$$

The lift coefficient C_L corresponding to the solution is given by

$$C_L = 2\pi\alpha^*\left(1 - \frac{2B}{L}\right) \tag{4}$$

where B is a constant to be determined. The value of the constant B, determined by the Kutta condition applied to the trailing edge, would be zero. Here, however, the trailing-edge interaction leads to a nonzero value which gives a viscous correction to the lift coefficient. In reference 3 it was shown that this constant is $0(\epsilon^3 L)$ which leads to a viscous correction to the lift that is $0(\epsilon^3)$. A nondimensional circulation constant a_1 is introduced according to the definition

$$a_1 = \frac{B\lambda^{5/4}}{\epsilon^3 L} \tag{5}$$

The boundary-layer equations governing the flow in the lower deck are written in the form

$$\frac{\partial U}{\partial X} + \frac{\partial V}{\partial Z} = 0 \tag{6}$$

$$U \frac{\partial U}{\partial X} + V \frac{\partial U}{\partial Z} = - \frac{dP}{dX} + \frac{\partial^2 U}{\partial Z^2} \tag{7}$$

where the pressure P is a function of X alone.

Equations (6) and (7) are to be solved subject to the following boundary conditions:

$$U \to |Z| + \ldots \qquad (X \to -\infty) \tag{8a}$$

$$U = V = 0 \qquad (Z = 0;\ X < 0) \tag{8b}$$

$$P_T(X) = P_B(X) \qquad (X \geq 0) \tag{8c}$$

$$U \to |Z| + \ldots \longrightarrow \begin{cases} A_T(X) & (Z \to +\infty) \quad (8d) \\ -A_B(X) & (Z \to -\infty) \quad (8e) \end{cases}$$

where $P_T(X)$ and $P_B(X)$ are the pressures on the top and bottom of the X-axis, respectively, and $A_T(X)$ and $A_B(X)$ are perturbations of the displacement thickness from the undisturbed Blasius value at the trailing edge.

Finally, the pressure distribution must satisfy the following asymptotic condition in order to match the upstream inviscid solution

$$P_{T,B} \to -\alpha\sqrt{-X}\ \operatorname{sgn} Z \qquad (X \to -\infty) \tag{9}$$

where the subscript T,B is introduced for convenience to represent either the top of the bottom and $\operatorname{sgn} Z$ should be taken as plus for $Z > 0$ and minus for $Z < 0$. The pressure should decay to zero for $Z \to +\infty$ in order to match the Goldstein solution downstream.

Equation (8a) is a requirement that the velocity profile match to the inner portion of the Blasius solution far upstream. Equation (8c) follows from the requirement that the pressure be continuous across the wake. The application of this condition at the trailing edge ($X = 0$) is equivalent to the Kutta condition and serves to determine the constant a_1 defined by equation (5) and, therefore, the viscous correction to the lift coefficient.

Solution of the inviscid flow equations in the upper deck leads to the following integral relationship between the functions $A_{T,B}(X)$ and $P_{T,B}(X)$:

$$\frac{dA_T(X)}{dX} = -\frac{1}{\pi} \fint_{-\infty}^{+\infty} \frac{P_T(X_1)}{X - X_1}\, dX_1 \tag{10a}$$

$$\frac{dA_B(X)}{dX} = +\frac{1}{\pi} \fint_{-\infty}^{+\infty} \frac{P_B(X_1)}{X - X_1}\, dX_1 \tag{10b}$$

where the double slash on the integral sign means that Hadamard "finite part" of the divergent integral is to be taken. The integrals in equations (10) do not converge in the ordinary sense because of the behavior of the pressure for large negative X indicated in equation (9). A form more suitable for computation is given in the numerical methods section. Equations (10) are an inversion of the relationships given in reference 3 and are in a form that is most suitable for the numerical procedures used in the present investigation.

The preceding formulation indicates that to solve the triple-deck problem, the boundary-layer equations must be integrated subject to the vortical outer boundary conditions given by equations (8d) and (8e). The vorticity arises from the boundary-layer solution valid in the upstream flow. The upstream vorticity leads to additional algebraically growing terms in equations (8d) and (8e), as will be discussed later.

The pressure and displacement functions appearing in the boundary-layer equations and boundary conditions are unknown and must be determined as part of the solution of the boundary-layer equations such that the linear relation given in equations (10) is satisfied. The form of the pressure for large negative X is given by

$$P_{T,B} = \left(-\alpha\sqrt{-X} + \alpha a_1/\sqrt{-X} + \ldots\right) \operatorname{sgn} Z \tag{11}$$

where a_1 is related to the lift coefficient by equations (4) and (5). The lift coefficient can be obtained by solving the boundary-layer equations and extracting the constant a_1 from the expansion given in equation (11).

Asymptotic Properties of the Triple Deck

Equations (4) to (11) provide a complete formulation of the triple-deck problem. Useful asymptotic results were provided in references 1 to 3 and are extended and summarized in the following. (Corrections to a number of the signs are incorporated; see also ref. 6.)

For $X \to -\infty$, the solution must approach the perturbed Blasius solution and have the form

$$U = |Z| + 1.784|X|^{-1}F_1'(\eta) + \alpha|X|^{1/6}H_1'(\eta)\,\mathrm{sgn}\,Z + \alpha^2 H_2'(\eta) + \alpha^3|X|^{-1/6}H_3'(\eta)\,\mathrm{sgn}\,Z + \ldots \tag{12a}$$

and

$$\eta = \frac{|Z|}{3|2X|^{1/3}} \tag{12b}$$

where primes denote differentiation with respect to η. The similarity functions $F_1(\eta)$, $H_1(\eta)$, $H_2(\eta)$, and $H_3(\eta)$ satisfy ordinary differential equations given in references 1 and 3. The differential equations, boundary conditions, and asymptotic behavior required in the present work are listed in the appendix.

Other results for $X \to -\infty$ are

$$P(X) = -0.3433|X|^{-2/3} - 0.6867b_1|X|^{-5/3} - 0.0816X^{-2}\ln|X| + \frac{d_1}{|X|^2} + \ldots$$

$$- \alpha\left(|X|^{1/2} - a_1|X|^{-1/2} + 0.2368|X|^{-5/6} + \ldots\right)\mathrm{sgn}\,Z + \ldots \tag{13a}$$

$$A(X) = 0.3265|X|^{-1} + \alpha C_{12}|X|^{1/6}\,\mathrm{sgn}\,Z - \alpha^2 C_{21}\left(\frac{1}{3}\ln|X| + \ln K\right) + \alpha^2(C_{21} + C_{22})$$

$$+ \alpha^3 C_{33}|X|^{-1/6}\,\mathrm{sgn}\,Z + \ldots \tag{13b}$$

$$\left.\frac{\partial U}{\partial Z}\right|_{Z=0} = 1 + 0.3106|X|^{-4/3} - \alpha(2.1539)|X|^{-1/6}\,\mathrm{sgn}\,Z + \ldots \tag{13c}$$

where K and the C_{ij}'s are known constants listed in the appendix.

For $X \to +\infty$ the velocity profile approaches the inner solution of Goldstein's near wake solution. The behavior of $P(X)$, $A_{T,B}(X)$, and $U(X,0)$ are given by

$$P(X) = 0.1717X^{-2/3} + 0.3433b_1X^{-5/3} - 0.0816X^{-2}\ln X + d_1X^{-2} + \ldots \tag{14a}$$

$$A_{T,B}(X) = 1.416\left(\frac{1}{4}X\right)^{1/3}\mathrm{sgn}\,Z + 1.416\left(\frac{1}{4}\right)^{1/3}b_1X^{-2/3}\,\mathrm{sgn}\,Z - \alpha\left[\frac{2}{3}X^{3/2} + 2a_1X^{1/2}\right.$$

$$\left. - \left(\frac{1}{6}\right)^{1/6}2^{3/2}\left(-\frac{1}{3}\right)!X^{1/6}\right] + \ldots \tag{14b}$$

$$U(X,0) = 1.611X^{1/3} + 1.611b_1X^{-2/3} + 0.052X^{-1} + \ldots \tag{14c}$$

The solution of the triple-deck equations develops a singularity at the trailing edge that is described by the Goldstein solution (ref. 21) for $\alpha = 0$ and by the Hakkinen-Rott near wake solution (ref. 23) for $\alpha \neq 0$. In both cases the velocity profile has the following form for X and $Z \to 0$

$$U = \frac{1}{3}\left(\frac{1}{4}X\right)^{1/3} G_0'(\eta) \tag{15}$$

where η is given by equation (12b) and G_0 satisfies an ordinary differential equation studied in reference 23 and listed in the appendix.

For zero incidence, the local solution for $X \to 0$ is given as follows:

For $X < 0$,

$$P = P_{TE} + P'_{TE}X + \left(P_2 \ln|X| + P_3\right)X^2 + \ldots \tag{16a}$$

$$A = A_{TE} + A'_{TE}X - \left(3^{3/2}/5\right)C_0|X|^{5/3} + \frac{1}{2}A_1^-X^2 + \ldots \tag{16b}$$

$$\left.\frac{\partial U}{\partial Z}\right|_{Z=0} = \lambda_1 \tag{16c}$$

and for $X > 0$,

$$P = P_{TE} + \frac{3}{2}C_0X^{2/3} + P_1X + \ldots \tag{17a}$$

$$A = A_{TE} + A'_{TE}X + \left(3^{3/2}/10\right)C_0X^{5/3} + \frac{1}{2}A_1^+X^2 + \ldots \tag{17b}$$

$$U = 1.4061C_0^{1/2}X^{1/3} + \ldots \tag{17c}$$

$$C_0 = 0.4089\lambda_1^{4/3} \tag{17d}$$

The local solution for $X \to 0$ when $\alpha \neq 0$ is slightly more complicated for $X < 0$. Equation (16a) now takes the form

$$P_{T,B} = P_{TE} + \left(P'_{TE}\right)_{T,B}X + \left[\left(P_2\right)_{T,B} + \left(P_3\right)_{T,B}X\right]X^{-2}\ln|X| + \ldots \tag{18a}$$

Equation (16b) has different expressions for A_T and A_B

$$A_T = \left(A_{TE}\right)_T + \left(A'_{TE}\right)_T X - \left(3^{3/2}/5\right)C_o|X|^{5/3} + \tfrac{1}{2}\left(A_1^-\right)_T X^2 + \ldots \tag{18b}$$

$$A_B = \left(A_{TE}\right)_B + \left(A'_{TE}\right)_B X + \left(3^{3/2}/5\right)C_o|X|^{5/3} + \tfrac{1}{2}\left(A_1^-\right)_B X^2 + \ldots \tag{18c}$$

and

$$\left.\frac{\partial U}{\partial Z}\right|_{Z=0^+,X=0} = \lambda_{1,T} \qquad \left.\frac{\partial U}{\partial Z}\right|_{Z=0^-,X=0} = \lambda_{1,B} \tag{18d}$$

For $X > 0$, equation (17a) has the same form. Equation (17b) becomes

$$A_T = \left(A_{TE}\right)_T + \left(A'_{TE}\right)_T X + \left(3^{3/2}/10\right)C_o X^{5/3} + \tfrac{1}{2}\left(A_1^+\right)_T X^2 + \ldots \tag{18e}$$

$$A_B = \left(A_{TE}\right)_B + \left(A'_{TE}\right)_B X - \left(3^{3/2}/10\right)C_o X^{5/3} + \tfrac{1}{2}\left(A_1^+\right)_B X^2 + \ldots \tag{18f}$$

and equations (17c) and (17d) assume the forms, respectively,

$$U = \gamma C_o^{1/2} X^{1/3} + \ldots \tag{18g}$$

$$C_o = C_o\left(\lambda_{1,T}, \lambda_{1,B}\right) \tag{18h}$$

where γ and C_o are now functions of $\lambda_{1,T}$ and $\lambda_{1,B}$ and are determined by solving the merging asymmetrical shear flow problems of Hakkinen and Rott.

The two sets of constants (a_1, b_1, d_1) and $\left(P_{TE}, P'_{TE}, P_2, P_3, A_{TE}, A'_{TE}, A_1^-, A_1^+, \text{ and } \lambda_1\right)_{T,B}$ appearing in the preceding expansions are not determined by the local solution. The first set relates to the far-field solution while the second set relates to the local solution near the trailing edge. Values for all but d_1 have been estimated for $\alpha = 0$ by fitting the asymptotic forms to the numerical solutions obtained in the present study.

For future reference the behavior of the velocity profile for large Z and fixed X is given as

$$U = |Z| + \left(\alpha C_{11}/K^{1/2}\right)|Z|^{1/2}\,\mathrm{sgn}\,Z + \alpha^2 C_{21}\ln|Z| + \left(\alpha^3 C_{31}K^{1/2}/2\right)\left(|Z|^{-1/2}\ln|Z|\right)\mathrm{sgn}\,Z$$
$$+ A_{T,B}\,\mathrm{sgn}\,Z + \left\{\left(\alpha C_{11}/2K^{1/2}\right)A_{T,B} + \left(\alpha^3/2K^{1/2}\right)\left[C_{11}(C_{21} - C_{22})\right.\right.$$
$$\left.\left. + KC_{34}\right]\mathrm{sgn}\,Z\right\}|Z|^{-1/2} - a_2|Z|^{-3} + \ldots \qquad (19a)$$

The constants C_{ij} and K are listed in the appendix and

$$a_2 = 1.784\left[\frac{\Gamma(4/3)}{3^{25/6}\left(-\frac{1}{3}\right)!}\right] \qquad (19b)$$

The preceding expansion was obtained by expanding the solution of the boundary-layer equations for large Z and matching to the asymptotic expansion of the initial profile defined by equations (12). (See results in appendix.) This matching enabled the set of arbitrary constants appearing in equations (10) to be identified with the constants given in the appendix. Equations (19) are used to set the far-field boundary conditions in a finite difference procedure described in the following section.

THE NUMERICAL METHOD

The boundary-value problem to be solved for the trailing-edge solution is illustrated in figure 3. The boundary-layer equations must be solved such that the solution matches the Blasius solution far upstream and the Goldstein solution far downstream. No-slip conditions must be satisfied on both sides of the flat plate and asymptotic boundary conditions must be satisfied on each side of the boundary layer and wake for $|Z| \to \infty$. The pressure gradient appearing in the momentum equation and the displacement functions $A_T(X)$ and $A_B(X)$ appearing in the outer boundary condition must be determined such that they satisfy the linear integral relationship imposed by the outer inviscid solution. In addition, the condition that the pressure decays to zero as $X \to +\infty$ must be imposed in order to match the Goldstein solution. In the present approach, a fixed point iteration between the inviscid and boundary-layer equations is employed. The principal difficulties in the numerical solution of the boundary-layer equations are due to a singularity at the trailing edge and to a slow algebraic decay of the solution for $|X|$ and $|Z| \to \infty$. These problems are treated by using asymptotic solutions to set the far-field boundary conditions at finite distances and to describe the singular solution near the trailing edge. A highly nonuniform mesh distribution is also employed to obtain proper resolution near the trailing edge and to allow for the slow decay of the solution in the far field.

The boundary-layer equations are solved by the Keller-Cebeci (refs. 4 and 5) finite-difference scheme for parabolic partial differential equations. This method is well suited to the present problem since it is second-order accurate, unconditionally stable, and permits highly nonuniform mesh distributions. The Hilbert transformations in equations (10), which provide the inviscid solution, are evaluated by special quadrature formula on the same mesh distribution employed in the boundary-layer calculation. This avoids the need to interpolate between the inviscid and viscous solutions. The resulting computation has uniform second-order accuracy, including the far field and the singular point at the trailing edge.

The Iteration Scheme

The iteration procedure is indicated in figure 3. The path of the iteration is in a direction inverse to that usually employed in similar viscous interaction problems. Here, the displacement functions $A_{T,B}(X)$ are obtained from solutions of the inviscid equations (i.e., eqs. (10)) with the pressure distribution prescribed. The pressure distributions $P_{T,B}(X)$ are determined from solutions of the boundary-layer equations. Since the unknown pressure gradient appears in these equations, an additional relation is needed to complete their solution. This is supplied by the previous evaluation of the displacement function $A_{T,B}(X)$ which provides an outer boundary condition for the solution of the viscous equations. This indirect iteration sequence is followed because it provides a convenient and simple treatment of the trailing-edge singularity. In a conventional iteration, the solution of the boundary-layer equations for a prescribed pressure distribution results in a discontinuity in the slope of the displacement function at the trailing edge. This, in turn, leads to unbounded pressures in the inviscid solution and to divergence of the iteration sequence.

The iteration starts with estimated pressure distributions $P_T(X)$ and $P_B(X)$ which appear in the integrands of the Hilbert integrals. The integrals are evaluated by a second-order-accurate quadrature scheme to yield expressions for dA_T/dX and dA_B/dX. The displacement functions A_T and A_B are then obtained by integration using a trapezoidal rule with initial values determined from the upstream asymptotic expansions given in equation (13b). This half-cycle yields an intermediate solution for the displacement functions $A_{T,B}(X)$.

In the next half-cycle the boundary-layer equations are integrated. A minor difficulty arises because of the presence of the unknown pressure gradient in the differential equations. To deal with this problem the momentum equation is differentiated with respect to Z. This eliminates the pressure but increases the order of the equations from a third- to a fourth-order system of partial differential equations. An additional boundary condition is required to close the system. This is supplied by using the known functions

$A_{T,B}(X)$ in the asymptotic expansion given in equations (19) to yield a condition on the streamwise velocity component as $|Z| \to \infty$. This condition and the conditions that the shear stress approach one for $|Z| \to \infty$ and that both velocity components vanish on the plate result in a well-posed problem. A finite-difference scheme, described in the next subsection, is employed to integrate the boundary-layer equations starting from an initial station far upstream of the trailing edge. Profiles at the initial station are determined from the first five terms of the asymptotic solution given in equations (12). The boundary-layer equations are solved by marching downstream to the trailing edge on the top and bottom of the plate independently. A local solution describing the singular behavior at the trailing edge is obtained by numerically solving the similarity equations, first considered by Hakkinen and Rott in reference 23. The similarity solution is used to construct a "composite" profile across the sublayer at a station just downstream of the trailing edge. The solution is then marched downstream, employing two boundary conditions on each side of the wake, as indicated in figure 3. After completion of the sweep, the pressure gradient is determined from the momentum equation evaluated on the X-axis at $Z = 0$. The pressure is then computed from a trapezoidal integration of the gradient. Two arbitrary constants of integration, the trailing-edge pressure and the circulation constant a_1 (see eq. (11)) are evaluated by matching the pressure to the upstream data and by requiring the pressure difference to vanish at the trailing edge.

The boundary-layer solution cannot be continued downstream to very large distances because of the appearance of a growing solution $P = P_G X^{2/3}$ for $X \to +\infty$. The solution is induced by a wake thickness distribution $\frac{1}{2}(A_T + A_B) \approx A_G X^{1/3}$ which appears in the outer boundary conditions. The constant P_G vanishes and the unwanted solution is excluded if the constant A_G is exactly equal to the Goldstein value ($A_G = 0.892\ldots$). However, because of the finite arithmetic carried in the computer, this solution cannot be excluded from the numerical solution and it eventually dominates the far-field behavior. Consequently, the boundary-layer solution must be terminated at a station $X = X_P$ that is taken to be upstream of the region where the spurious growing solution starts to dominate. This raises a minor problem, since a solution for the pressure distribution $P(X)$ along the entire X-axis must be supplied for the evaluation of the Hilbert integral. This is easily remedied by using an analytic expression to represent the pressure distribution downstream of the terminal point $X = X_P$. In the computer program an expression is employed that matches both the pressure and pressure gradient at $X = X_P$ and has the correct asymptotic behavior for $X \to +\infty$. Numerical experiments, to be discussed at the end of the section, have indicated that this procedure provides a smooth continuation of the solution downstream of $X = X_P$ and has a negligible effect on the upstream solution.

This half-cycle results in a complete solution for the pressure distribution which can be substituted into the Hilbert integral to obtain new estimates for the displacement

functions. The integration is continued until the solution converges to a required tolerance. As usually required in this type of problem, the solution must be underrelaxed in order to obtain convergence.

The value of $P(X)$ is relaxed according to the formula

$$P(X) = \omega P(X)_{new} + (1 - \omega)P(X)_{old}$$

where P_{old} is the pressure at the start of the boundary-layer computation, P_{new} is the pressure computed at the most recent sweep, and ω is a relaxation parameter ($\omega < 1$) that is adjusted to obtain convergence. In the present scheme it is found that the value of ω must be reduced as the extent of the streamwise interval is increased in the downstream direction. Accordingly, the following strategy is employed. The calculation starts with a given relaxation parameter small enough to obtain convergence with an initial choice of $X_p = 3$. The solution is converged with these choices, the terminal point is moved further downstream, ω is reduced, and the calculations repeated. Converged results have been obtained starting with values of $\omega = 0.15$ and $X_p = 3$ and ending with $\omega = 0.02$ and $X_p = 20.791$.

Solution of the Boundary-Layer Equations

The boundary-layer equations are solved by the Keller-Cebeci "box" scheme (refs. 4 and 5). The unknown pressure gradient is eliminated from the boundary-layer equations by application of a Z-derivative to the momentum equations. A stream function Ψ is introduced and the boundary-layer equations are written as a system of four first-order partial differential equations. The wake thickness and centerline position become unbounded as $X \to \infty$. To control the wake growth the Z-coordinate is scaled such that wake position is bounded in the computational plane. A scale transformation is defined in terms of two parameters $\sigma(X)$ and $\theta(X)$ by the following relation:

$$y = \frac{Z - \theta(X)}{\sigma(X)} \tag{20}$$

where y is a scaled coordinate in the direction normal to the plate and the functions $\sigma(X)$ and $\theta(X)$ are given in terms of $A_{T,B}(X)$ by

$$\sigma(X) = \begin{cases} \sigma_o & (X < L_1) \quad (21a) \\ \sigma_o + \frac{1}{2}\left[A_T(X) - A_B(X)\right] - \frac{1}{2}\left[A_T(L_1) - A_B(L_1)\right] & (X \geq L_1) \quad (21b) \end{cases}$$

$$\theta(X) = -\frac{1}{2}\left[A_T(X) + A_B(X)\right] + \frac{1}{2}\left[A_T(L_1) + A_B(L_1)\right] \qquad (X \geq L_1) \qquad (22)$$

where σ_o is a constant scale parameter and L_1 is a small positive number that identifies the streamwise station where the wake solution is initialized. The functions $\sigma(X)$ and $\theta(X)$ control the wake thickness and position, respectively. The choice of $\theta(X)$ was previously discussed in reference 3. This scaling minimizes the variations of wake location in the far field and as a result, the computations can be carried out with fixed outer boundaries in the y-plane. In addition the coordinates approach similarity variables appropriate to the Goldstein solution for $X \to +\infty$. Scaled dependent variables are also introduced according to the relations

$$\Psi = \sigma(X)^2 \psi(X,y) \tag{23a}$$

$$U = \sigma(X)\, u(X,y) \tag{23b}$$

$$\tau = \tau(X,y) \tag{23c}$$

$$D = \sigma(X)^{-1} d(X,y) \tag{23d}$$

where Ψ, U, τ, and D are, respectively, the stream function, streamwise velocity component, shear stress, and derivative of shear stress with respect to Z $\left(\text{i.e., } D = \frac{\partial \tau}{\partial Z}\right)$ and where ψ, u, τ, and d are, respectively, scaled versions of the stream function, streamwise velocity component, shear stress, and derivative of shear stress with respect to Z. With these transformations and with the elimination of the pressure gradient, the governing equations can be written in the form

$$\frac{\partial \psi}{\partial y} = u \tag{24a}$$

$$\frac{\partial u}{\partial y} = \tau \tag{24b}$$

$$\frac{\partial \tau}{\partial y} = d \tag{24c}$$

$$\frac{\partial d}{\partial y} = \sigma(X)^3 \left(u \frac{\partial \tau}{\partial X} - d \frac{\partial \psi}{\partial X} \right) - 2\sigma(X)^2 \sigma'(X) \psi d \tag{24d}$$

In this formulation the boundary condition on V given in equation (8b) is replaced by the equivalent condition on the stream function

$$\psi = 0 \qquad (y = 0;\ X < 0) \tag{25}$$

A general, nonuniform rectangular mesh is introduced and equations (24) are differenced according to the box scheme along the lines indicated in figure 4. The X-columns

are labeled by an index I and the horizontal rows by an index J starting from J = 1 on the lower boundary and continuing to $J = J_P$ on the upper boundary, where J_P is the number of points in the y-mesh on the top of the plate. The first three equations do not involve X-derivatives. These are central differenced about a midpoint of a y-interval on the most forward marching column. Equation (24d), which is nonlinear and involves derivatives in both directions, is central differenced about the midpoint of the box, as indicated in figure 4. The nonlinear coefficients are evaluated as four point averages at the midpoint of the box. This difference approximation leads to a nonlinear set of difference equations for the vector unknowns $(\psi,u,\tau,d)_J$ along the column I + 1. The difference approximation is second-order accurate and implicit since it couples all the unknowns along the I + 1 column.

The boundary conditions along the plate involve the specification of the two components $\psi(X_{I,0})$ and $u(X_{I,0})$ for $X < 0$. Outer boundary conditions are imposed on the vector components u and d. The conditions are given in the form of a ratio at the outer two points of the mesh J_P and J_{P-1}. The ratios for the conditions on top of the plate are computed from the asymptotic far-field expansion given in equations (19) as follows:

$$\frac{\sigma(X)u_{J_P} - R_{11}\left(Z_{J_P},X\right) - A_T(X)}{\sigma(X)u_{J_{P-1}} - R_{11}\left(Z_{J_{P-1}},X\right) - A_T(X)} = \frac{R_{12}\left(Z_{J_P},X\right)}{R_{12}\left(Z_{J_{P-1}},X\right)} \tag{26a}$$

$$\frac{d_{J_P}/\sigma(X) + R_{21}\left(Z_{J_P},X\right)}{d_{J_{P-1}}/\sigma(X) + R_{21}\left(Z_{J_{P-1}},X\right)} = \frac{R_{22}\left(Z_{J_P},X\right)}{R_{22}\left(Z_{J_{P-1}},X\right)} \tag{26b}$$

where

$$R_{11}(Z,X) + Z + \frac{\alpha C_{11}}{K^{1/2}} Z^{1/2} + \alpha^2 C_{21} \ln Z + \alpha^3 \frac{C_{31}}{2} K^{1/2} Z^{-1/2} \ln Z \tag{27a}$$

$$R_{12}(Z,X) = \left\{\frac{\alpha C_{11}}{2K^{1/2}} A_T(X) + \frac{\alpha^3}{2K^{1/2}}\left[C_{11}(C_{21} - C_{22}) + KC_{34}\right]\right\} Z^{-1/2} - a_2 Z^{-3} \tag{27b}$$

$$R_{21}(Z,X) = \frac{\alpha C_{11}}{4K^{1/2}} Z^{-3/2} + \alpha^2 C_{21} Z^{-2} - \frac{3}{8}\alpha^3 K^{1/2} C_{31} Z^{-5/2} \ln Z \tag{28a}$$

$$R_{22}(Z,X) = \frac{3}{8K^{1/2}}\left[\alpha C_{11} A_T(X) + \alpha^3\left(-C_{11}C_{22} + KC_{34} - \frac{5}{3} C_{11}C_{21}\right)\right] Z^{-5/2} - 12a_2 Z^{-5} \tag{28b}$$

where Z is related to the computational coordinate y by

$$Z = \theta(X) + \sigma(X)y \tag{29}$$

This procedure for satisfying the far-field boundary conditions was motivated by the work of Ackerberg and Phillips (ref. 24). Similar expressions are applied to the bottom boundary of the mesh. For the wake computations $(X \geq L_1)$, only the outer boundary conditions are to be satisfied and the expressions are identical to those of equations (26), (27), and (28).

The difference equations are solved by a Newton-Raphson technique. The nonlinear equations are linearized about a previous estimate to form a linear system of algebraic equations for the perturbation quantities $(\delta\psi, \delta u, \delta\tau, \delta d)_J^{I+1}$. The differential equations and boundary conditions result in a linear system that has a block tridiagonal form. In the present problem the main blocks are 4×4 square matrices. The equations are solved by an efficient Gaussian elimination technique as described in reference 5. The form of the outer boundary conditions given in equations (26) automatically falls into this block structure.

Solutions at the most recently computed station (e.g., station I in fig. 4) are employed as initial estimates. Quadratic convergence was observed to occur with these starting values. The iteration was continued until a convergence criterion based on the relative error was satisfied at all mesh points. The criterion

$$\frac{|\delta f(I+1,J)|}{|f(I+1,J) + \delta f(I+1,J)|} < \epsilon_1 \tag{30}$$

is employed, where f stands for any one of the dependent variables.

The calculation proceeds by marching in the X-direction starting from an initial station $X = L_0$. Initial profiles are determined from the asymptotic solution given in equations (12). The similarity functions $F_1(\eta)$, $H_1(\eta)$, $H_2(\eta)$, and $H_3(\eta)$ appearing in the asymptotic solutions are determined from a numerical integration of the two-point boundary-value problems formulated in the appendix. These solutions are obtained with the same subroutine employed in the marching calculation.

When the trailing edge $(X = 0)$ is reached, a composite solution is formed to describe the initial wake profile a short distance $(\Delta X = L_1)$ downstream of the trailing edge. The composite profile is obtained from a coordinate expansion for X and $Z \to 0$. It is written as the sum of an outer and inner solution less the "common part." The structure of the local solution is similar to Goldstein's near wake solution except for the presence of a singular, self-induced pressure gradient in the similarity equation. Solutions were first

obtained by Hakkinen and Rott in reference 23 and are further discussed in references 1 to 3 and 20. The wake initial profile is given by

$$U(L_1,Z) = U_T(0,Z) + \frac{1}{3}\left(\frac{1}{4}L_1\right)^{1/3} G_0'(\eta) - \lambda_{1,T}Z \qquad (Z > 0) \qquad (31)$$

$$U(L_1,Z) = U_B(0,Z) + \frac{1}{3}\left(\frac{1}{4}L_1\right)^{1/3} G_0'(\eta) - \lambda_{1,B}Z \qquad (Z < 0) \qquad (32)$$

where U_T and U_B are the velocity profiles at the trailing edge on the top and bottom of the plate, respectively, G_0' is the similarity function describing the "inner" Hakkinen-Rott solution, η is a similarity variable defined by equation (12b), and $\lambda_{1,T}$ and $\lambda_{1,B}$ are the skin-friction coefficients at the trailing edge. (See eq. (18d).) Profiles for the variables ψ, τ, and d can be formed in a similar manner. The function $G_0'(\eta)$ is determined as part of the solution by integrating the two-point boundary-value problem formulated in the appendix. The solution in the wake is then continued downstream, starting from the initial wake station $(X = L_1)$ and terminating at a station $(X = X_p)$ chosen at the start of the calculations, as discussed in the beginning of this section.

The pressure distribution is determined after completion of the forward sweep by integrating the streamwise momentum equation

$$\frac{dP}{dX} = \frac{d(X,0)}{\sigma(X)} + \sigma(X)^2\left[\tau(X,0)\frac{\partial\psi(X,0)}{\partial X} - u(X,0)\frac{\partial u(X,0)}{\partial X}\right] - \frac{u^2(X,0)}{2}\frac{d\sigma^2(X)}{dX} \qquad (33)$$

All quantities on the right side of equation (33) are known from the most recent sweep. Separate equations hold on the top and bottom of the plate. The pressure is determined by a simple trapezoidal integration

$$P_{T,B}(I+1) - P_{T,B}(I) = \left[X(I+1) - X(I)\right]\left(\frac{dP_{T,B}}{dX}\right)_{I+1/2} \qquad (34)$$

where the pressure gradient is evaluated by averaging equation (33) over the stations $X(I+1)$ and $X(I)$. Two constants of integration are required to complete the solutions given in equation (34). These are determined from the asymptotic solutions given in equation (13a), which give

$$P_T(X = L_0) = -\alpha\sqrt{|L_0|} + \frac{\alpha a_1}{\sqrt{|L_0|}} - \frac{0.3433}{|L_0|^{2/3}} - \frac{0.2368\alpha}{|L_0|^{5/6}} \qquad (35a)$$

$$P_B(X = L_0) = \alpha\sqrt{|L_0|} - \frac{\alpha a_1}{\sqrt{|L_0|}} - \frac{0.3433}{|L_0|^{2/3}} + \frac{0.2368\alpha}{|L_0|^{5/6}} \qquad (35b)$$

Note that these relations involve the unknown circulation constant a_1 which must be determined before the solution can be completed. The circulation constant a_1 is determined from a generalized Kutta condition as follows. By definition

$$\left.\begin{aligned} P_T(0) &= P_T(X = L_o) + \int_{L_o}^{0} \left(\frac{dP_T}{dX}\right) dX \\ P_B(0) &= P_B(X = L_o) + \int_{L_o}^{0} \left(\frac{dP_B}{dX}\right) dX \end{aligned}\right\} \tag{36}$$

If equations (35) are substituted into equations (36) and the Kutta condition that the pressure is continuous at the trailing edge $\left(\text{i.e., } P_T(0) = P_B(0)\right)$ is imposed, the following relations are obtained:

$$P_T(0) = P_B(0) = -\frac{0.3433}{|L_o|^{2/3}} + \frac{1}{2}\int_{L_o}^{0} \left(\frac{dP_T}{dX} + \frac{dP_B}{dX}\right) dX \tag{37a}$$

$$a_1 = |L_o| + \frac{0.2368}{|L_o|^{1/3}} - \frac{\sqrt{|L_o|}}{2\alpha}\int_{L_o}^{0} \left(\frac{dP_T}{dX} - \frac{dP_B}{dX}\right) dX \tag{37b}$$

Equations (37) should be interpreted as asymptotic relations valid for $L_o \to -\infty$. The present results indicate that the solution is not overly sensitive to the magnitude of L_o and that a_1 can be evaluated to two decimal places for $L_o = -17$. Equation (37a) has been employed in conjunction with equation (34) to determine the surface pressure by sweeping equation (34) from the trailing edge.

The differential equations are differenced in Cartesian coordinates on a nonuniform mesh. The grid-point distribution is determined from simple transformations that map a uniform grid to a nonuniform grid. The parameters of the mapping are adjusted to concentrate mesh points in regions of large gradients that occur on the axis ($y = 0$) and at the trailing edge ($X = 0$). The distribution of y-grid points is given as follows for the upper half-plane. The mesh points in the lower half-plane are obtained by reflection about the X-axis.

On the plate side ($X < 0$) the $y(J)$ distribution is defined by the relations

$$y(J) = \frac{\zeta y_M}{1 + B_p(1 - \zeta)} \tag{38a}$$

$$B_p = \frac{J_p - 1}{K_1}\left(\frac{1 - K_1}{J_p - 2}\right) \tag{38b}$$

and

$$\zeta = \frac{J - 1}{J_p - 1} \qquad \left(1 \leq J \leq J_p\right) \tag{38c}$$

where y_M is the upper boundary of the computational domain, J is a running index, and K_1 is a parameter employed to control the relative spacing of the increments. Equations (38) reduce to a uniform mesh for $K_1 = 1$ and to a nonuniform mesh with a concentration of mesh points near the wall for $K_1 < 1$.

On the wake side of the field, a two-piece grid consisting of a fine uniform grid was employed near the axis, and a stretched grid was used in the outer part of the wake. The grid for $X > 0$ is defined by the following relations. For the inner region

$$y(J) = y_{inner}\frac{J - 1}{J_{inner} - 1} \qquad \left(1 \leq J \leq J_{inner};\ 0 \leq y \leq y_{inner}\right) \tag{39a}$$

and for the outer region

$$y(J) = y_{inner} + \left(y_M - y_{inner}\right)\left[\frac{\zeta}{1 + B_p(1 - \zeta)}\right]\left[1 + K_2(1 - \zeta) + K_3(1 - \zeta)^2\right] \tag{39b}$$

where

$$\zeta = \frac{J_W - J}{J_W - J_{inner}} \qquad \left(J_{inner} < J \leq J_W;\ y_{inner} < y \leq y_M\right) \tag{39c}$$

where y_{inner} is the upper boundary of uniform mesh region, J is a running index, J_{inner} is the number of mesh points in the inner region, J_W is the total number of mesh points employed in the wake, and K_2 and K_3 are parameters that control the mesh distribution in the outer region. They are chosen such that (1) the mesh increment is continuous across the boundary between the inner and outer regions and (2) the outermost increment $y\left(J_W\right) - y\left(J_W - 1\right)$ is equal to the corresponding increment on the plate. The mesh distribution in the marching or X-direction is chosen to provide for a concentration of mesh points on the wake side of the trailing edge and for a gradual stretching in the far field for $X \to \pm\infty$.

On the plate side ($X < 0$) the following transformation is employed:

$$X(I) = L_0\xi\left(\frac{1 - K_4}{1 - K_4\xi}\right)^3 \tag{40a}$$

where

$$\xi = \frac{I_p - I}{I_p - 1} \qquad \left(1 \leqq I \leqq I_p;\ L_0 \leqq X \leqq 0\right) \tag{40b}$$

L_0 is the value of X at the initial station, I is a running index, I_p is the number of X-mesh points used on the plate, and K_4 is a parameter that controls the relative spacing of the mesh points on the plate. Equations (40) generate a uniform mesh for $K_4 = 0$ and a nonuniform mesh for $K_4 > 0$. A relation between K_4 and the minimum mesh increment Δ_1 is given by

$$K_4 = \frac{\left(I_p - 1\right) + \left(I_p - 1\right)\left[\Delta_1\left(I_p - 1\right)/L_0\right]^{1/3}}{\left(I_p - 1\right) - \left[\Delta_1\left(I_p - 1\right)/L_0\right]^{1/3}} \tag{41}$$

With equations (40) and (41), a mesh distribution can be generated with a specified minimum increment Δ_1 at the trailing edge that smoothly expands to the initial point $\left(X = L_0,\ I = 1\right)$.

The streamwise mesh distribution in the wake is given in three parts: a nonuniform region near the trailing edge that concentrates points near the origin, an intermediate region with a uniform mesh, and a nonuniform region with an expanding grid in the downstream direction. A good distribution is generated by the following relations:

$$X(I) = \frac{\Delta_2\left(I - I_p\right)^3}{\left(I_1 - I_p\right)^2 - \left(I_1 - I_p - 1\right)^3} \qquad \left(I_p < I \leqq I_1\right) \tag{42a}$$

$$X(I) = X(I - 1) + \Delta_2 \qquad \left(I_1 < I \leqq I_2\right) \tag{42b}$$

$$X(I) = X\left(I_2\right) + \frac{\Delta_2\left(I - I_3\right)}{\left[1 - K_5\left(I - I_3\right)\right]^3} \qquad \left(I_2 \leqq I < I_3\right) \tag{42c}$$

and

$$K_5 = \left\{1 - \left[\frac{\Delta_2(I_3 + 1 - I_2)}{L_{max} - X(I_2)}\right]^{1/3}\right\}\left(\frac{1}{I_3 + 1 - I_2}\right) \tag{43}$$

where Δ_2 is a parameter that controls the first mesh increment in the wake, I_1, I_2, and I_3 are the values of the running index I that separate the three mesh regions, and L_{max} is the coordinate of the downstream boundary of the mesh. Note that I_3 is also equal to the total number of points used in the streamwise direction. Attention is called to the fact that L_{max} need not be equal to the terminal point of the boundary-layer calculation, $X = X_p$.

Evaluation of the Hilbert Integral

The most recent sweep of the boundary-layer equations provides updated solutions for the pressure distributions required for the evaluation of the Hilbert integrals given in equations (10). The main difficulties in the numerical evaluation of these integrals are associated with the infinite range of integration, the algebraic singularity in the integrand for $X \to -\infty$, the pole singularity at $X = X_1$, and the infinite pressure gradient for $X \to 0^+$.

The first two problems are treated by dividing the integration interval into a number of segments. The outer two segments contain the unbounded intervals $X \to +\infty$ and $X \to -\infty$. In these regions, the pressure distribution is approximated by the asymptotic expressions given in equations (13a), (13b), and (14a), and the integrals are evaluated in closed form. This reduces the numerical problem to one involving an integration over a finite range and also provides for a correct evaluation of the singular "finite part" integral for $X \to -\infty$. The remaining integrals are over a finite range and are evaluated by numerical quadrature using the mesh distribution employed in the boundary-layer calculation. Difficulties with the pole singularity are avoided by evaluating the integrals only at the midpoints of the integration intervals used in the quadrature. Excessive truncation error due to the singular pressure gradients near the trailing edge is avoided by using a special quadrature formula that accounts for this behavior. On the plate, the integration interval is split into two segments, $-\infty < X \leq L_0$ and $L_0 < X < 0$, while in the wake, $0 < X < L_1$, $L_1 < X < L_2$ and $L_2 < X < +\infty$. Note that segment boundaries L_1, L_2, and L_3 need not line up with the boundaries of the mesh defined by equations (42). With this division, the integrals can be expressed as the following summation

$$A'_{T,B}(X) = \frac{a}{\pi} T_1 - \operatorname{sgn} Z\left(T_2 + T_3 + \Lambda_{10} + \Lambda_{02} + \Lambda_{23}\right) \tag{44}$$

where the far-field expressions have been used to evaluate the integrands of the integrals T_1, T_2, and T_3 as follows:

$$T_1 = \int_{-\infty}^{L_o} \frac{\sqrt{-X_1}\,dX_1}{X - X_1} - a_1 \int_{-\infty}^{L_o} \frac{dX_1}{\sqrt{-X_1}(X - X_1)} + \frac{(-1/3)!}{\sqrt{3}(6)^{2/3}} \int_{-\infty}^{L_o} \frac{dX_1}{(-X)^{5/6}(X - X_1)} \tag{45a}$$

$$T_2 = -\frac{1.784}{3\sqrt{3}} \int_{-\infty}^{L_o} \frac{dX_1}{(-X)^{2/3}(X - X_1)} \tag{45b}$$

$$T_3 = \frac{0.892}{3\sqrt{3}} \int_{L_3}^{+\infty} \frac{dX_1}{(X_1)^{2/3}(X - X_1)} \tag{45c}$$

$$\Lambda_{10}(X) = \int_{L_1}^{0} \frac{P_{T,B}(X_1)\,dX_1}{X - X_1} \tag{46a}$$

$$\Lambda_{02}(X) = \int_{0}^{L_2} \frac{P(X_1)\,dX_1}{X - X_1} \tag{46b}$$

$$\Lambda_{23}(X) = \int_{L_2}^{L_3} \frac{P(X_1)\,dX_1}{X - X_1} \tag{46c}$$

The integrals in equations (45) are evaluated in closed form and those in equations (46) are evaluated by numerical quadrature.

The range of integrations of the integrals in equations (46) is segmented by using the mesh distribution $X(I)$ employed in the boundary-layer calculation, and the integrals in equations (46a) and (46c) are expressed as a finite sum of integrals over the mesh increments $X(I + 1) - X(I)$. The individual integrals over these increments are then evaluated in closed form by using a piecewise linear approximation for the pressure distribution $P_{T,B}(X)$ and/or $P(X)$ over the mesh increment. The integral in equation (46b) is evaluated with a piecewise linear approximation for the function $P(X) - \frac{3}{2} C_o^{2/3} X^{2/3}$, where C_o is the constant appearing in the Hakkinen-Rott similarity solution (eqs. (18)). With this procedure all integrations are second-order accurate. The displacement functions can be evaluated from a trapezoidal integration as follows:

$$A_{T,B}(I + 1) = A_{T,B}(I) + \left[X(I + 1) - X(I)\right] A'_{T,B}\left(I + \tfrac{1}{2}\right) \tag{47}$$

with $A'_{T,B}\left(I + \frac{1}{2}\right)$ evaluated from equations (44) to (46). Two constants of integration appear. These are evaluated from the asymptotic solutions given in equation (13b) at the initial station $X(1) = L_o$, which yields

$$A_{T,B}(I = 1) = 0.3265\left|L_o\right|^{-1} + \alpha C_{12}\left|L_o\right|^{1/6} \operatorname{sgn} Z - \alpha^2 C_{21}\left[\frac{1}{3}\ln\left|L_o\right| + \ln 3\left(2^{1/3}\right)\right]$$

$$+ \alpha^2\left(C_{21} + C_{22}\right) + \alpha^3 C_{33}\left|L_o\right|^{-1/6} \operatorname{sgn} Z \qquad (48)$$

This procedure results in a convenient method for determining the values of $A_{T,B}$ at the mesh points $X(I)$ given the pressure at the same points. A number of numerical experiments have been carried out for sequences of mesh distributions and for pressure distributions that could be integrated in closed form. These results clearly indicated that the quadrature errors reduced quadratically with mesh size and that the preceding evaluations of $A_{T,B}(X)$ were second-order accurate at all points of the mesh including those near the trailing edge. The results of this study will be presented in a separate publication.

Accuracy and Convergence Considerations

A number of numerical experiments were carried out to check the accuracy of the complete program. These tests were carried out for the symmetric problem (i.e., $\alpha = 0$) by using a version of the program that was modified to allow for the symmetry of the solution. The angle-of-attack terms were deleted and a symmetry condition was imposed on the wake axis. With the modified program it was necessary to compute the solution only in the upper half-plane; thus the number of mesh points required was reduced by one-half.

Calculations were performed to determine the effect of varying the locations of the upstream $(X = L_o)$ and downstream $(X = X_P)$ boundaries of the mesh and the position of the upper boundary y_M. The number of mesh points employed in the horizontal and vertical directions were also varied, as were the parameters controlling the relative spacing of the grid. Computations were carried out using up to 99 points normal to the plate and 300 points in the streamwise direction. These results indicated that a good distribution of mesh points is generated with the following choices.

For the y-mesh

$$y_M = 8.0 \qquad K_1 = 2/5 \qquad (49)$$

and 25 points are employed on the plate side $(J_P = 25)$ and 44 points on the wake side $(J_W = 44)$ of the trailing edge. Of the 44 points in the wake, 12 $(J_{inner} = 13)$ are dis-

tributed uniformly in the region $0 \leqq y \leqq 0.5555$. With these choices the minimum increment occurs on the axis and is equal to

$$(\Delta y)_{min} = 0.1333 \qquad (X < 0) \qquad (50a)$$

$$(\Delta y)_{min} = 0.0427 \qquad (X > 0) \qquad (50b)$$

The mesh spacing smoothly increases to a maximum at the upper boundary where it is equal to (for all X)

$$(\Delta y)_{max} = 0.8027 \qquad (51)$$

For the X-mesh the upstream L_0 and downstream L_{max} boundaries are chosen as

$$L_0 = -17 \qquad L_{max} = 30 \qquad (52)$$

Fifty-one points are employed on the plate and 124 points in the wake. The boundaries of the various segments in the wake are taken at

$$I_1 = 81 \qquad I_2 = 151 \qquad I_3 = 175 \qquad (53)$$

and, therefore, a total of 175 grid points are employed in the streamwise direction.

The initial station in the wake is taken at $I = 57$ which occurs at

$$X(57) = 0.004136 \qquad (54)$$

The minimum mesh increment on the plate occurs at the trailing edge and is equal to

$$(\Delta X)_{min} = 0.05 \qquad (X < 0) \qquad (55)$$

In the wake the minimum increment occurs at the wake initial station $X(57)$ and is equal to

$$(\Delta X)_{min} = 0.002432 \qquad (X > 0) \qquad (56)$$

These choices lead to very high concentrations of mesh points in the initial parts of the wake. About 10 points of the y-grid fall in the inner region of the wake initial profile where the solution is described by the Hakkinen-Rott similarity solution. Numerical

experiments have indicated that solutions on this mesh are accurate to about one part in the third decimal place.

Convergence criteria were set on both iterative loops employed in the program to achieve three-place accuracy. The error tolerance ϵ_1 used in the Newton-Raphson solution of the difference equation (see eq. (30)) was set at 10^{-2}. This resulted in solutions to the difference equations that are accurate to 10^{-8} or better in two cycles per streamwise step at most stations. A third cycle is occasionally required near the trailing edge.

The overall interaction between the boundary-layer and inviscid programs is continued until the solution has converged to the third decimal place. Twelve iterations were required to converge the main loop with $\omega = 0.15$ and $X_p \approx 3$. Each cycle consists of a sweep through the boundary layer and the evaluation of the Hilbert integral. Most of the computer time is taken in the boundary-layer routine. The computations were performed on an IBM 370/165 digital computer and required about 20 seconds per cycle, or about 4 minutes to complete the first 12 iterations. A total of 28 additional cycles were employed to move the terminal point X_p downstream to $X_p = 20.791$. The influence of the value of X_p on the upstream solution was investigated and was found to amount to an increment of no more than 0.002 in the solution at $X = X_p$, which decreased rapidly upstream. Similar conclusions hold for the angle-of-attack problem except that the computer times were about doubled because of additional mesh points on the lower side of the flow field.

The present program used significantly fewer iterations and less computer time than that required by similar methods developed by Jobe and Burggraf (ref. 6) to treat the zero angle-of-attack problem. This is apparently due to their use of a fixed point iteration scheme to solve the finite-difference equations and to the use of a separate iterative scheme to compute the pressure at each streamwise station. Jobe and Burggraf were able to use larger values of ω in the outer loop and, as a result, obtained solutions with somewhat fewer outer cycles. However, this advantage did not nearly overcome the longer cycle times required in their program. It should be pointed out, however, that the symmetric problem does not involve free parameters and, hence, needs to be solved just once. Therefore, computing efficiency is not a real issue in this problem. It was, however, important to develop an efficient code for the full problem since there are twice the number of mesh points and since solutions must be obtained for various values of the normalized incidence α.

RESULTS

The triple-deck formulation reduces the trailing-edge problem to one involving a single parameter α, a normalized angle of attack defined in equations (2). The computer

program described in the previous section has been employed to obtain solution for two values of α equal to 0 and 0.10. Initial estimates to start the iteration were obtained from the approximate solution of Messiter (ref. 2) for $\alpha = 0$ and the linear solution of Brown and Stewartson (ref. 3) for nonzero angles of attack. Numerical experiments carried out in the study indicates that the present solution for the symmetric case is accurate to three decimal places. The symmetric solution was obtained by using a special version of the code in which the angle-of-attack terms appearing in the boundary and initial conditions were set to zero. In addition, a symmetry condition was imposed on the axis (i.e., $\psi = \tau = 0$ at $y = 0$) and the solution was computed only in the upper half-plane. The solution for $\alpha = 0.10$ was obtained with an early version of the code that employed a somewhat coarser mesh and, hence, is likely accurate to just two decimal places.

The results obtained for the symmetric problem are compared with solutions of the triple-deck equations recently obtained by Jobe and Burggraf (ref. 6) and Veldman and Van De Vooren (ref. 7). The computations in these studies were based on finite-difference techniques that differed in a number of respects from the method employed here. The main difference being that a second-order Crank-Nicolson scheme was employed in references 6 and 7, while a Keller-Cebeci box scheme was employed in the present study. The computations in reference 6 were carried out on a nonuniform mesh using up to 180 points in the vertical direction and 480 points in the streamwise direction. In reference 7 a nonuniform mesh was employed with a maximum of 40 points in each direction. These are to be compared with the 24×175 point nonuniform mesh used in the present computation. The inviscid solution was obtained in reference 6 and in the present study from a numerical quadrature of the Hilbert integral. In reference 7 the inviscid solution was determined from a finite-difference solution of Laplace's equation in the outer deck by using a 40×40 point mesh distribution. The iterative techniques used in the present scheme appear to be more effective and require significantly less computer time than the methods employed in references 6 and 7. Comparisons given in this section indicate that the overall agreement between the three sets of solutions is quite good, with differences amounting to a few parts in third decimal places at most points of the flow field. However, the solutions of reference 6 are somewhat less accurate near the trailing edge due to the poor resolution of the trailing-edge singularity obtained with the uniform mesh distribution used in that study. The computation in reference 7 loses some accuracy in the far field due to the large mesh spacing used in that region.

Solutions to the symmetric problem are presented in figures 5 to 17. The pressure distribution on the axis is given in figures 5 to 7. The effect of the wake in generating a significant favorable pressure gradient on the plate is clearly shown in figure 5. The pressure starts from the free-stream level far upstream and falls to a value of

$$P_{TE} = -0.394 \tag{57}$$

at the trailing edge. This should be compared with the values of P_{TE} of -0.388 and -0.392 obtained in references 6 and 7, respectively. The pressure then rises steeply from this trailing-edge value to a small positive maximum and then approaches the free-stream value slowly from above. These results clearly show a large adverse pressure gradient in the wake just downstream of the trailing edge. The pressure gradient is bounded on the upstream side and is unbounded on the downstream side of the trailing edge. The numerical solution is seen to blend smoothly into the asymptotic far-field solution for $X \to \pm\infty$ and match smoothly with the singular solution at the trailing edge for $X \to 0^+$. The coefficient of the third term of the trailing-edge solution (eq. (17a)) has been extracted from the present numerical results as

$$P_1 = -0.52 \tag{58}$$

The agreement between the present solution and the solutions of references 6 and 7 is quite favorable, with the differences between the results being indiscernible on the scale of figure 5.

The pressure distribution near the trailing edge is shown on a greatly expanded scale in figure 6. Differences between the three sets of results are apparent on this scale. The present results and those of Veldman and Van De Vooren are virtually identical with the three term expansion given in equation (17a) with the constant P_1 given by equation (58). The use of a nonuniform mesh with a fine grid near the trailing edge provides excellent resolution of the singular trailing-edge behavior in the present calculations and in those of Veldman and Van De Vooren. The results of Jobe and Burggraf, which were obtained on a uniform mesh, definitely appear to have a higher truncation error and to lose some resolution as the origin on the wake side of the trailing edge is approached. Their results, however, appear to improve as the mesh size is reduced.

On the basis of analytical considerations, Stewartson in reference 1 has indicated that the pressure gradient is finite on the plate side of the trailing edge and that logarithmic terms must arise in the expansion of the pressure distribution as $X \to 0^-$. (See eq. (16a).) The present results plotted in figure 7 seem to confirm Stewartson's conjecture. In figure 7, the numerical solution for the pressure gradient is compared with the analytic expression given in equation (16a). The numerical constants P'_{TE}, P_2, and P_3 were extracted from the numerical solution and were found to have the following values:

$$P'_{TE} = -0.301 \qquad P_2 = 0.12 \qquad P_3 = -0.14 \tag{59}$$

This is to be compared with the value $P'_{TE} = -0.278$ given in reference 6. The numerical solution clearly indicates a vertical tangent at the origin and shows creditable agreement with the analytical solution using the constants given previously. Four mesh points in the region $X < -0.5$ fall on the analytical curve given in figure 7.

The solution for the skin friction is given in figure 8. The solution is seen to match smoothly to the weak interaction solution given in equation (13c). The results clearly show the strong effect of the wake-induced pressure gradient on the skin friction. The skin friction at the trailing edge is increased by a factor of λ_1 over the Blasius value, where

$$\lambda_1 = 1.351 \tag{60}$$

This is to be compared with the values of $\tau_w(0) = 1.343$ and $\tau_w(0) = 1.352$ predicted in references 6 and 7, respectively. Comparisons of the triple-deck solution with the second-order boundary-layer solution of Schneider and Denny (ref. 25) are given in reference 6.

The solution for the centerline velocity in the wake is given in figure 9, together with a comparison of the Goldstein solution for $X \to +\infty$ and with the Hakkinen-Rott solution for $X \to 0^-$. Both analytic solutions exhibit an $X^{1/3}$ behavior and appear as linear distributions in the scale used in the figure. Also included is a comparison with two terms of the Goldstein solution. The second term, involving the constant b_1, corresponds to a shift in the origin of the asymptotic solution. The value of the constant b_1 has been extracted from the present numerical solution, as will be discussed later in this section. It can be seen that the triple-deck solution provides a smooth blending between the trailing-edge and far-field solutions. The effect of the shift is clearly evident in the results.

In figure 10, the solution for the centerline velocity is compared with the results of references 6 and 7 on an expanded scale near the origin. The present results show good agreement with the solution of Veldman and Van De Vooren and with the singular solution of Hakkinen and Rott right to the trailing edge. The nonuniform mesh employed here and in reference 7 permits a very high resolution of the singular trailing-edge behavior. The results of Jobe and Burggraf (ref. 6) again show higher truncation errors and somewhat poorer resolution near the trailing edge owing to the larger mesh intervals employed in their uniform mesh solutions.

The solution of Veldman and Van De Vooren employs a highly stretched mesh with relatively large mesh increments in the region away from the trailing edge. The results in figure 10 indicate that this leads to somewhat larger truncation errors in the downstream region than those that arise in the present solution.

The present solution for the displacement function $A(X)$ is compared with the far-field asymptotic expansions in figure 11. Again the numerical solution blends smoothly

into the asymptotic solutions for $X \to \pm\infty$. The effect of the origin shift in the downstream solution is again evident in the comparison. The inclusions of the b_1 term in the asymptotic solution is seen to extend the region of agreement well into the near field. The results are seen to be in good agreement with the solutions given in references 6 and 7, with no apparent differences on the scale employed in figure 11.

Comparison of the present results for the slope of the displacement surface with the solutions of Jobe and Burggraf shows some discrepancy as indicated in figure 12. The dashed line in figure 12, representing the solution of reference 6, was obtained from a graphical reading of a figure in reference 6 using an automatic digitizer. Some of the differences are surely due to errors in reading the graphical data. However, the main differences are in the trailing-edge region, and these are likely caused by the larger grid spacing used in reference 6. The present results clearly show the vertical tangent at the origin implied by the singular solution given in equation (17b). This is seen more clearly on the expanded scale used in figure 13. In figure 13, the present numerical solution for $A'(X)$ is compared with the singular expansion given in equation (17b) and with the solution of reference 6 as tabulated in the thesis of Jobe (ref. 26). The present solution is seen to blend very smoothly with three terms of the singular solutions. The constants in equation (17b) were evaluated by fitting equation (17b) to the present numerical solutions and were found to have the following values:

$$A_{TE} = 0.338 \qquad A'_{TE} = 0.402 \qquad A_1^+ = -1.3 \qquad A_1^- = -2.1 \tag{61}$$

These are to be compared with the values $A_{TE} = 0.335$, $A'_{TE} = 0.335$, and $A_1^+ = 0.56$ given in reference 6. The results agree relatively well with the solution of reference 6 except for the grid point nearest the trailing edge and the values of the constant A_1^-.

The constant b_1 appearing in the second term of the far-field solution has been evaluated by fitting equations (14b) and (14c) to the present numerical solutions for $A(X)$ and $U(X,0)$. The results are denoted by $b_A(X)$ and $b_U(X)$ and are displayed as functions of X in figure 14. The results seem to approach a limiting value that is given by

$$b_1 = -0.285 \pm 0.005 \tag{62}$$

which is to be compared with the value $b_1 = -0.27 \pm 0.03$ quoted in reference 6. Also shown for comparison is a similar plot taken from reference 26. The difference between the two sets of results is likely caused by somewhat higher truncation error and by the abrupt termination procedure employed in the calculation of references 6 and 26.

The drag coefficient for the finite flat plate can be evaluated from an integration of the skin-friction distribution on the plate as follows:

$$C_D = 1.328R^{-1/2} + d_2R^{-7/8} + 0\left(R^{-1}\right) \tag{63a}$$

where the constant d_2 is given by

$$d_2 = 2\lambda^{-1/4} \int_{-\infty}^{\infty} \left[\tau(X,0) - 1\right] dX \tag{63b}$$

Use of the present solution for the skin friction and a trapezoidal integration of the preceding integral leads to the following evaluation:

$$d_2 = 2.660^{\,1} \tag{63c}$$

In figure 15 the drag coefficients predicted by equations (63) are compared with experimental data obtained in 1935 by Janour (ref. 8) for flow of oil over a finite flat plate. Also included is a comparison with solutions of the full Navier-Stokes equations recently obtained by Dennis in 1973 (as mentioned in the Introduction) for Reynolds numbers in the range $1 \leqq R \leqq 200$. The results in the figure show that the correction to the Blasius result is large in this range and that it is accurately predicted by equations (63) to within a few percent for Reynolds numbers as low as $R = 10$.

Dennis later extracted the value of d_2 by fitting an equation of the form of equation (63a) to his numerical solutions. His results for d_2 are plotted in figure 16 together with the limiting values (i.e., for $R \to +\infty$) predicted by the triple-deck solutions as obtained in the present study and in references 6 and 7. The agreement of all three triple-deck solutions with Dennis' results is quite good with the present solution yielding the best agreement.

The preceding results indicate that the triple-deck solution is accurate over a surprisingly wide range of Reynolds numbers. Indeed the maximum difference with the Dennis solution for the drag coefficient is about 8 percent at a Reynolds number R of 1. The close agreement with the Navier-Stokes solutions implies that the next term in the asymptotic solution, which is formally on the order of $0\left(R^{-1}\right)$ must be very small. Further comparisons and discussions of the drag coefficient are given in references 6, 20, and 26.

Sato and Kuriki (ref. 9) carried out wind-tunnel experiments on the flow in the wake of a thin plate. The flow was determined to be two-dimensional. The plate was 300 millimeters long and the flow velocity was 10 meters/second. The investigators were primarily interested in exploring the transition of the wake from laminar to turbulent flow. They

[1] A value of $d_2 = 2.644$ attributed to the present authors in references 6 and 7 was obtained on a coarser mesh than the one employed in the present computations and is, consequently, less accurate than the above value.

measured mean as well as fluctuating velocity profiles in the wake. The Reynolds number of the test was 2.1×10^5 ($\epsilon = 0.216$). The mean velocity profile given in figure 17 was measured at a station 30 millimeters behind the trailing edge where the flow was fully laminar (the nonlinear transition region started about 40 to 60 millimeters behind the plate). At this Reynolds number the pressure peak predicted by the triple-deck theory occurs at 40 millimeters behind the plate. Thus, the measuring station for the profiles in figure 17 was in a region where the theory predicted a strong adverse pressure gradient.

The triple-deck solution was used to construct a composite velocity profile at $X = 30$ millimeters. The solution was represented as the sum of an "outer and inner solution" minus the "common part," as follows:

$$\frac{U_{comp}}{U_\infty} = f'(\eta) + 0.4945A(X)\left[f''(\eta) - f''(0)\right] + 0.1642\left(U_{inner} - Z\right) \tag{64a}$$

where

$$\eta = 0.4941Z \tag{64b}$$

and the physical distance normal to the wake axis is given by

$$y_{min} = 0.325Z \tag{64c}$$

The function $f(\eta)$ is the Blasius function for the semi-infinite flat plate solution and $U_{inner}(Z)$ is the triple-deck solution for the wake profile at $X = 2.49$. The displacement function at this station is given by

$$A(2.49) = 1.052 \tag{64d}$$

The profile given by equations (64) is compared with the measured profile of Sato and Kuriki in figure 17. The theoretical and experimental profiles are seen to be in good agreement across the entire wake. The main differences occur in the outer region where viscous and pressure gradient terms have been neglected in the theoretical solutions. Also indicated is the centerline velocity predicted by the one-term Goldstein solution. The effect of the interaction in reducing the centerline velocity is significant and readily discernible in this experiment. It is also of some interest to call attention to the fact that transition was observed to start at a station 40 millimeters behind the plate, which coincided with the location of the theoretical pressure peak in the wake. This result suggests that self-induced pressures may play an important role in the transition of a wake from laminar to turbulent flow. As a corollary it also indicates that the effect of wake-induced pressure gradients may have to be accounted for in theoretical transition calculations.

The numerical methods developed in the present investigation have been found to provide an effective means for solving the triple-deck equations. Because of the overall efficiency of the differencing and iterative techniques employed, it is practical to use these methods to solve the angle-of-attack problem. An early version of the code described in previous sections was used to obtain solutions for α (normalized angle of attack) equal to 0.10. This solution was obtained without the terms of $0(\alpha^2)$ or greater that appear in the outer boundary condition given in equations (26) to (27) and in the initial condition given by equations (12). These terms are quite small and are believed to have a small influence on the solution at the value $\alpha = 0.10$ for which the computations are carried out.[2]

In figure 18 the solution for the pressure distributions on the top and bottom of the plate and on the wake axis is compared with an approximate solution developed in reference 3. The approximate solution was based on a simple linearization of the triple equations about a linear streamwise velocity profile. As was noted in reference 3, the linearization is clearly not valid in the wake, where the velocity gradient $\partial U/\partial y$ must vanish on the axis. However, the errors in the wake are not expected to have a strong influence on the solution upstream of the trailing edge. If this holds true, the linearized solution should provide a reasonably good approximation to the angle-of-attack solution. The results in figure 18 bear this out. The agreement between the present numerical solution of the full triple-deck equations and the linearized solution given in reference 3 is seen to be quite good. The effect of incidence on the pressure distribution in the wake is barely noticeable on the scale used in figure 18. The circulation constant a_1 appearing in the formula for the viscous correction to the lift coefficient in equations (4) and (5) is determined as part of the present solution and is given as

$$a_1 = 0.55 \tag{65}$$

This is to be compared with the value determined from the linearized solution of Brown and Stewartson, namely

$$a_1 = 0.79 \tag{66}$$

The agreement for a_1 is not nearly as good as for the pressure distribution but is probably as good as one should expect from such a simple approximation.

In figure 19, the numerical solution for the pressure distribution is compared with the inviscid solution on the plate and with asymptotic solution valid for upstream. The numerical solution is seen to blend smoothly into the upstream asymptotic solution. Comparison with the zero angle-of-attack solution given in figure 5 indicates that the approach to the far-field solution is much slower in the angle-of-attack case. The difference

---

[2]Computations including all terms appearing in equations (26) to (29) have been carried out since this paper was written and the results confirm this conclusion.

between the numerical and inviscid solutions in the far field is due mainly to the circulation term a_1. This term can be interpreted as a shift of the origin in the far-field asymptotic solution for $X \to -\infty$. The effect of the shift is clearly evident in the comparison in figure 19. The results in figure 19 clearly show the large changes in the inviscid pressure distribution induced by the wake. These changes take two main forms: one is the shift in the pressure distribution in the far field mentioned previously, and the other is the complete change in the shape of the pressure distribution near the trailing edge.

The effect of the induced pressures on the solution for the skin friction is indicated in figure 20. In this figure, the numerical solution for the skin friction on the top and bottom of the plate is compared with the asymptotic solution valid far upstream. The numerical solution is seen to join smoothly to the asymptotic solution. The far-field solution plotted in figure 20 contains three terms: the basic Blasius value, the second due to inviscid pressure gradients induced by incidence, and the third term due to the favorable pressure gradient induced by the wake interaction. These terms combine to yield a skin-friction variation that is quite small except very close to the trailing edge. The effect of incidence is seen to have a fairly large effect on the value of skin friction at the trailing edge, which was equal to $C_f(0) = 1.349$ for $\alpha = 0$. Clearly, a much larger value of incidence will be required to drive the skin friction to zero on the upper service. The present result seems to indicate that the point of vanishing skin friction should first arise at a station upstream of the trailing edge.

The solution for the displacement functions $A_T(X)$ and $A_B(X)$ is given in figure 21 where it is compared with the far-field asymptotic solutions. The strong effect of incidence in displacing the wake centerline is clearly evident in this result. Again, attention is called to the smooth blending of the numerical and asymptotic solutions in the far field.

TURBULENT TRAILING-EDGE FLOWS

The numerical solutions obtained in this study and in references 6 and 7 have completely confirmed the triple-deck model and the local asymptotic solutions developed in references 1 to 3. These works provide a sound theoretical framework for analyzing laminar interactions at trailing edges of streamlined bodies. Unfortunately, the boundary layer on an airfoil usually undergoes transition to turbulent flow at the Reynolds numbers of interest. Most theoretical methods for predicting the effect of boundary layers on airfoil characteristics are based on classical second-order boundary-layer theory. Although not generally recognized, second-order boundary-layer theory for turbulent flows breaks down at airfoil trailing edges. Consequently, the theory does not provide a satisfactory basis for computing boundary-layer corrections to inviscid airfoil solutions. It is, therefore, important to develop a systematic theory for treating turbulent interactions in airfoil problems.

In the present study, a formal asymptotic theory has been developed for turbulent interacting flows, following broadly along the lines of the laminar triple-deck theories. Of course, turbulent boundary layers differ greatly from laminar flows and are controlled by quite dissimilar physical mechanisms. Particularly significant is the fact that turbulent boundary layers tend to retain high velocities much closer to the wall than in a laminar flow. This effect is one of the main reasons for the small upstream influence observed in turbulent interactions. However, the general idea of the triple-deck approach in seeking formal asymptotic solutions of the Navier-Stokes equations in the limit of large Reynolds numbers is also useful for the turbulent problem.

Accordingly, solutions of the turbulent airfoil problem will be developed as formal asymptotic expansions of the full Navier-Stokes equations in the limit $R \to \infty$. The turbulent analysis is carried out by using the basic framework developed in references 1 to 3 for laminar trailing-edge problems. Incompressible flow over a thin airfoil with a cusped or nearly cusped trailing edge at angle of attack is considered. The airfoil is assumed sufficiently thin so that the inviscid flow is described to lowest order by the flat plate solution given, for example, by equations (3) and (4) of this paper. Here, however, the angle of attack α^* is assumed to be $0(1)$ and not necessarily small. Transition is assumed to occur upstream of the trailing edge and the boundary layers are assumed to be fully developed turbulent flows in the trailing-edge region. More specifically, the velocity profiles in the noninteracting region are assumed to have a small defect form in the main part of the boundary layer and the usual logarithmic behavior near the wall.

In this section, the main features of a turbulent interaction theory that can be developed under these general conditions are outlined. First the behavior of boundary-layer theory near trailing edges is examined. It is shown that a singularity arises in the solution which causes a breakdown of the second-order theory near trailing edges. This analysis will show that a Kutta condition for the second-order solution cannot be satisfied and that the lift correction cannot be determined.

The failure of second-order theory is resolved by the introduction of a local solution that correctly describes the flow near trailing edges. The local solution is shown to have a three-layer structure that superficially resembles the triple-deck structure of the laminar problem. However, in the turbulent problem the physical mechanisms leading to this structure and the basic equations holding in each region are very different from those arising in the laminar flows.

In the present discussion, only a very brief description of the turbulent interaction theory is presented. The asymptotic structure of the local solutions governing the flow near the trailing edge will be described and the boundary-value problem that must be solved to complete the solution in the trailing-edge region will be outlined. Also a simple solution for the skin friction in the trailing-edge region that follows from the theory is

presented. The skin-friction solution is compared with experimental data of Schubauer and Klebanoff (ref. 18) and with numerical solutions of the boundary-layer equations.

Second-Order Solution

The second-order solution for viscous flow over an airfoil is determined in the following steps:

(1) Determine the inviscid solution for flow over the prescribed airfoil shape and compute the pressure distribution on the surface

(2) Solve the boundary-layer equations with the pressure distribution obtained from the inviscid solution and compute the displacement thickness

(3) Use the displacement surface to compute the equivalent source/sink distribution on the airfoil and wake surface and solve the inviscid equations with the source distribution as a surface boundary condition. Alternatively, the displacement thickness can be used to form an equivalent airfoil shape that serves as a new geometry in the inviscid solution.

This well-known procedure can be embedded in a formal asymptotic expansion for large Reynolds numbers. However, because of the presence of a singularity in the inviscid solution, this expansion is not uniformly valid at trailing edges. Consequently, the second-order solution cannot be completed and the boundary-layer corrections to the lift coefficient cannot be determined. Previous airfoil calculations based on second-order boundary-layer concepts relied on numerical smearing of the trailing-edge singularity to obtain solutions.

A singularity appears at the trailing edge in the inviscid solution for all lifting airfoils with a sharp trailing edge. For an airfoil with a cusped trailing edge, the pressure distribution on the surface exhibits a square-root behavior. This is illustrated in figure 22 where the steps leading to the nonuniformity of the second-order theory are outlined. Near the trailing edge, the pressure distribution is given by

$$P^* = P^*_{TE} - \rho U^{*2}_{TE}\left(C_\alpha \sqrt{-x^*/L}\ \operatorname{sgn} y + \ldots\right) \tag{67a}$$

where L is the airfoil chord and C_α is a constant that depends on the incidence α^* and the shape of airfoil. For a flat plate (or a sufficiently thin airfoil) C_α can be determined from the solution given in equations (3), namely

$$C_\alpha = \alpha^* \tag{67b}$$

and $P^*_{TE} = p_\infty$ and $U^*_{TE} = U_\infty$.

The behavior of the displacement thickness near the trailing edge can be determined from the momentum integral equation

$$d\delta_2^* + \delta_2^* dx^* (H + 2) \frac{dU_e^*}{U_e^* dx^*} = \frac{1}{2} C_f \tag{68}$$

where δ_2^* is the momentum thickness, H is the shape factor, U_e^* is the streamwise velocity external to the boundary layer, and C_f is the skin-friction coefficient. The displacement thickness δ_1^* is given by

$$\delta_1^* = H\delta_2^* \tag{69}$$

With the external velocity evaluated from the inviscid solution (eqs. (67)), the second term in equation (68) is unbounded at the trailing edge. Since the variation of skin friction due to pressure variations can be shown to be equal to the order of the pressure change, the singular acceleration term in equation (68) can only be balanced by the gradient of momentum thickness. Thus, equations (67) to (69) lead to the following expansion for the displacement thickness as $x^* \to 0$:

$$\delta_{1,T}^* = \delta_{1,T}^*(0)\left\{1 - C_\alpha\left[H_T(0) + 2\right]\sqrt{-x^*/L} + \ldots\right\} \qquad (x^* < 0) \tag{70a}$$

$$\delta_{1,B}^* = \delta_{1,B}^*(0)\left\{1 + C_\alpha\left[H_B(0) + 2\right]\sqrt{-x^*/L} + \ldots\right\} \qquad (x^* < 0) \tag{70b}$$

where the subscripts T and B refer to the top and bottom of the airfoil, respectively. The boundary layer thickens on the top and thins on the bottom of the airfoil due to the imposed pressure distribution. This leads to an equivalent camber distribution δ_c^* given by

$$\delta_c^* = \frac{1}{2}\left(\delta_{1,T}^* - \delta_{1,B}^*\right) = \delta_c^*(0) + B_\alpha\sqrt{-x^*/L} + \ldots \tag{71a}$$

where

$$\delta_c^*(0) = \frac{1}{2}\left[\delta_{1,T}^*(0) - \delta_{1,B}^*(0)\right] \tag{71b}$$

$$B_\alpha = -\frac{1}{2} C_\alpha \left[\delta_{1,T}^*\left(H_T + 2\right) - \delta_{1,B}^*\left(H_B + 2\right)\right]_{x^*=0} \tag{71c}$$

The slope of the equivalent camber distribution given in equations (71) is singular at the trailing edge. The antisymmetric part of the second-order outer solution is determined by computing the inviscid flow over this camber distribution. It follows from potential

flow considerations that the second-order solution for the surface velocity must have the following behavior for $x^* \to 0^-$:

$$\frac{U^*}{U^*_{TE}} = 1 + \left[C_\alpha \sqrt{-x^*/L} + \frac{(B_\alpha/\pi) \ln (x^*/L) + \Delta\Gamma}{\sqrt{-x^*/L}} + \ldots \right] \operatorname{sgn} y \tag{72}$$

where C_α and B_α are the constants defined previously and $\Delta\Gamma$ is an arbitrary constant.

The first two terms in equation (72) arise from the inviscid solution and the last two are induced by the interaction. Notice that both interaction terms are singular. The logarithmic term is induced by the singularity in the camber distribution, while the $\Delta\Gamma$ term is an arbitrary homogeneous solution that satisfies Laplace's equations and the boundary conditions. Ordinarily this term would be excluded by the Kutta condition, which requires the solution to be bounded at the trailing edge. It is clear from equation (72) that this condition cannot be satisfied for any value of the constant $\Delta\Gamma$. Thus, the second-order solution cannot be completed and the boundary-layer correction to lift cannot be determined. It is curious that this conclusion, which follows from the simple analysis given previously in this paper, has gone unrecognized in previous viscous airfoil analyses.

Interaction Theory

The results given previously clearly demonstrate that the standard second-order boundary-layer theory is not uniformly valid at trailing edges. To develop complete solutions of viscous airfoil problems, the basic theory must be corrected to better account for the flow near the trailing edge. In the present investigations, the method of matched asymptotic expansions was used to develop formal solutions for the trailing-edge region. This approach is based on the time-averaged Navier-Stokes equations with a turbulence closure employing a turbulent kinetic equation and an algebraic length-scale relation. Solutions were developed in terms of a small parameter ϵ which here is related to the friction velocity u^*_τ in the noninteracting region upstream of the trailing edge. That is,

$$\epsilon = \frac{u^*_{\tau,o}}{U^*_\infty} = \sqrt{\frac{1}{2} C_{f,o}} \tag{73}$$

where $C_{f,o}$ is the skin-friction coefficient at the trailing edge, as determined from solution of the noninteracting boundary-layer equations on the top of the airfoil. Asymptotic solutions are developed for $R \to \infty$ or equivalently for $\epsilon \to 0$. The analysis follows very closely a similar theory developed for interactions between turbulent boundary layers and normal shock waves in reference 16.

In the brief discussion of the theory given here, only a general description of the main results of the analysis will be provided. In addition, the present discussion will be limited to incompressible flows. A more complete discussion of the analysis leading to these results along with a simple extension to compressible trailing-edge flows will be provided in future publications.

From the present analysis, it has been determined that the streamwise extent of the interaction region at the trailing edge is on the order of a boundary-layer thickness; that is, $\Delta y^* \approx \delta^* \approx \epsilon L$. The flow near the trailing edge was found to develop a multilayered structure, as illustrated in figure 23. The solution upstream of the interaction is divided into standard potential flow and boundary-layer regions over a streamwise length scale $0(L)$. The solution in the boundary layer has a two-layer structure typical of turbulent flows; an outer wake-like region and an inner wall layer. The velocity profile in the outer region has a small defect form, which on the top of the plate can be written in the form

$$\frac{U^*}{U^*_{e,T}} = 1 + \epsilon f\left(y^*/\delta^*_T, x^*\right) \tag{74}$$

where U^*_e is the velocity at the edge of the boundary layer and δ^*_T is the local boundary-layer thickness. The velocity profile in the inner layer is expressed in a law of the wall form

$$\frac{U^*}{U^*_{e,T}} = \epsilon F(y^+, x^*) \tag{75a}$$

where y^+ is a wall variable defined by

$$y^+ = y^* u^*_{\tau,T}/\nu \tag{75b}$$

where ν is the kinematic coefficient of viscosity. Similar expressions hold for the boundary-layer profiles on the lower surface. The solution for noninteracting turbulent boundary layers has been embedded in a formal asymptotic structure by Mellor (ref. 12), Yajnik (ref. 13), and Bush and Fendell (refs. 14 and 15). These authors have shown that the law of the wall and velocity defect profiles appear as the leading terms of an asymptotic expansion for $R \to \infty$. Thus, fully developed turbulent boundary-layer flows can be viewed as limiting solutions valid in this limit. The present analysis should be considered as an extension of these works to the trailing-edge interaction problem.

The solution in the interaction region develops the three-layer structure illustrated in figure 23.

The three layers required in the solution are

(1) An outer, basically inviscid rotational stream. This region includes most of the boundary layer and a part of the irrotational flow outside the boundary layer that is on the order of a boundary-layer thickness.

(2) An inner wall layer that is a continuation of the wall layer from upstream.

(3) An intermediate, or blending layer that occurs between the outer and wall layers. The blending layer is thinner than the outer layer but thicker than the wall layer.

The wall-layer thickness is defined in terms of the parameter $\hat{\epsilon}$ introduced by Mellor in reference 12

$$\Delta y^* \approx \epsilon \hat{\epsilon} L \tag{76a}$$

where

$$\hat{\epsilon} = \left[\epsilon^2 R\right]^{-1} \tag{76b}$$

In the outer layer both the Reynolds and viscous stresses are small compared to the inertia terms in the momentum equation. Vorticity is generated in the upstream boundary layers and is convected, unchanged, along streamlines in the trailing-edge region. This leads to a description of the flow as an inviscid rotational stream. A similar model was first proposed by Lighthill in 1953 (ref. 28) for treating interactions of oblique shock waves with turbulent boundary layers at supersonic speeds.

The flow in the inner layer is a local equilibrium flow in the sense of Townsend (ref. 29). To lowest order, the total stress (viscous plus Reynolds stresses) is constant across the layer and the solution is completely determined by the local skin friction.

An intermediate region is required because of a mismatch that develops between the Reynolds stresses in the inner and outer layers. In the outer layer, the Reynolds stresses are frozen at their upstream values. In the inner layer, the Reynolds stresses are in a local equilibrium determined by the wall friction because of the small-scale structure of the turbulence in this region. As a result, a discontinuity in Reynolds stresses develops between the inner and outer regions. This discontinuity is resolved by the blending layer. Solutions in the blending layer are governed by linearized boundary-layer equations that involve Reynolds stresses, but not viscous stresses. Turbulent closure models are required to complete the lowest order solutions in the wall and blending layer regions but not in the outer region. Displacement effects generated by the two inner layers are small and do not affect the first few terms of the solution in the inviscid outer region. Thus, the leading terms of the outer solution can be determined without consideration of the flow near the wall.

Next the form of the expansions in each region is considered. The expansion parameter ϵ defined in equation (73) is equal to the friction velocity of the upstream flow on the top of the airfoil. It should not be confused with the previous definition of ϵ used in the laminar study $\left(\text{i.e., } \epsilon_{\text{laminar}} = R^{-1/8}\right)$.

Outer Layer

The coordinate stretchings for the outer region are given by

$$X = (x^*/L)\epsilon^{-1} \qquad y = (y^*/L)\epsilon^{-1} \tag{77}$$

where the coordinate system employed in the laminar study is used. There will be some minor differences from the notation used for the laminar analysis but the changes will be clear and should not cause confusion.

The solution in the outer layer is dominated by contributions from the irrotational airfoil solution. The first terms in the expansion are obtained by expressing the airfoil solution in the inner variables defined in equations (77) and expanding the result in powers of ϵ. The next term comes from the upstream boundary layer and is determined by simply adding the defect part of the upstream profile to the irrotational contribution.

Physically, this approximation is based on the idea that velocity variation across the boundary layer is small in the limit of large Reynolds numbers. (See eq. (74).) Thus, the physical picture is one of a basically irrotational flow that is slightly perturbed by small shear flow disturbances near the wall. The resulting linear superposition of the boundary-layer and inviscid solutions leaves the pressure distribution in the field and the lift coefficient of the airfoil unchanged. The nonlinear interaction of these terms produces perturbations in the pressure distribution and lift coefficient. Thus, the expansion in the outer region is written in the form

$$\frac{\psi^*}{U^*_{TE}} \equiv \psi = y + \epsilon^{1/2}\psi_{inv}(X,y) + \epsilon\psi_{BL}(y) + \epsilon^{3/2}\psi'(X,y) + \ldots \tag{78a}$$

$$\frac{u^*}{U^*_{TE}} \equiv u = 1 + \epsilon^{1/2}u_{inv}(X,y) + \epsilon u_{BL}(y) + \epsilon^{3/2}u'(X,y) + \ldots \tag{78b}$$

where ψ and u are the nondimensional stream function and the streamwise velocity component, respectively, U^*_{TE} is the velocity at the trailing edge predicted by the irrotational outer solution, and $*$ denotes the corresponding dimensional quantities. The velocity components u and v are related to the stream function by the usual relations

$$u = \partial\psi/\partial y \qquad v = -\partial\psi/\partial X \tag{79}$$

The first two terms in equations (78) arise from the airfoil solution written in inner variables and then expanded in powers of ϵ. For a general airfoil with a cusped trailing edge this yields the result

$$\psi_{inv} = -\frac{2}{3} C_\alpha r^{3/2} \cos\frac{3}{2}\theta \tag{80a}$$

$$u_{inv} = C_\alpha r^{1/2} \sin\frac{1}{2}\theta \tag{80b}$$

where r and θ are polar coordinates, with θ measured from the positive X-axis, given by

$$r = \sqrt{x^2 + y^2} \tag{81a}$$

$$\theta = \tan^{-1}(y/X) \tag{81b}$$

Substitution of the assumed expansion into the time-averaged Navier-Stokes equations leads to the following equation for the perturbation stream function:

$$\nabla^2\psi' = -\zeta'(X,y) = -\frac{d^2u_{BL}(y)}{dy^2}\,\psi_{inv}(X,y) \tag{82}$$

where ∇^2 is the Laplacian operator and ζ' is the perturbation vorticity. This is a simple Poisson equation that relates the disturbance stream function to the perturbation in vorticity ζ'. The vorticity perturbation arises from the convection of the vorticity in the upstream boundary layer along the curved streamline of the irrotational airfoil solution, as illustrated in figure 24.

The Poisson equation must be solved subject to the boundary conditions

$$\psi'(X,y) \to 0 \qquad (r \to \infty) \tag{83a}$$

$$v' = -\frac{\partial\psi'}{\partial x} = 0 \qquad (y = 0;\ x \leq 0) \tag{83b}$$

where v' is the perturbation velocity normal to the surface. The perturbations in streamwise velocity and static pressure are given by the relations

$$u' = \frac{\partial\psi'}{\partial y} \tag{84a}$$

$$p' = -u' = -\frac{\partial\psi'}{\partial y} \tag{84b}$$

These boundary conditions lead to well-posed boundary-value problems for the outer solution. The outer solution leads to a "slip" velocity on the surface that is resolved by the inner layers.

The solution of the boundary-value problem can be represented as the sum of a particular solution plus a complementary solution. The particular solution satisfies equation (82) but not the boundary conditions. This solution leads to a downwash on the surface that violates the boundary condition on v' (eq. (83a)). The complementary solution is a solution of Laplace's equation that cancels this downwash. The solution for the particular integral depends on the form of the initial velocity profile $u_{BL}(y)$ and on the expression for the irrotational stream function ψ_{inv}. For general profiles, the particular and homogeneous solutions must be found by numerical means. However, if the initial profile is represented by a Coles law of the wall/law of the wake correlation, a closed-form expression for the particular integral can be found by analytic function theory. Coles form for the defect profile on the upper surface can be written in the form

$$u_{BL}(y) = \begin{cases} \frac{1}{\kappa}\ln\left(y/\delta_T\right) - \frac{\tilde{\pi}_T}{\kappa} W\left(y/\delta_T\right) & \left(0 \leq y \leq \delta_T\right) \\ 0 & \left(\delta_T < y\right) \end{cases} \tag{85}$$

where δ_T is a nondimensional boundary-layer thickness defined by the relation

$$\delta_T^* \equiv \epsilon L \delta_T \tag{86}$$

κ is the Karman constant, $\tilde{\pi}_T$ is the Coles wake parameter, and $W\left(y/\delta_T\right)$ is the wake function which can be represented by a simple polynomial approximation to the cosine function usually employed in this description. Similar expressions hold for the profile on the lower surface.

The particular integral evaluated in this fashion leads to closed-form expressions for the downwash velocity on the top and bottom of the plate. The homogeneous solution which cancels this downwash can be found in the usual way from thin airfoil theory. This leads to a representation of the homogeneous solution in terms of a Hilbert integral that must, in general, be evaluated by numerical quadrature. A Kutta condition, requiring the solution to be finite at the trailing edge, is imposed as part of the solution of the homogeneous problem. This condition determines the value of an arbitrary constant appearing in the trailing-edge solution that is directly related to the circulation constant $\Delta\Gamma$ appearing in the second-order boundary-layer solution (eq. (72)). Matching the trailing-edge solution to the second-order solution valid outside the trailing-edge region leads to an expression for the lift coefficient in the form

$$C_L = 2\pi\alpha^*\left(1 + a_1\epsilon^2 \ln \epsilon + a_2\epsilon^2 + \ldots\right) \tag{87}$$

where a_1 is a known constant and a_2 is a constant to be determined from a complete solution of the trailing-edge problem. The constant a_1 as determined by matching to the upstream solution (eq. (72)) is given by

$$a_1 = 1/\pi\left[\delta_{1,T}\left(H_T + 2\right) - \delta_{1,B}\left(H_B + 2\right)\right]_{X=0} \tag{88}$$

where $\delta_{1T,B}$ and $H_{T,B}$ are the (nondimensional) displacement thicknesses and shape factors at the trailing edge, respectively, as determined from the noninteraction boundary-layer solution. The nondimensional displacement thicknesses $\delta_{1T,B}$ are defined by the relation

$$\delta^*_{1T,B} = \epsilon^2 L \delta_{1T,B} \tag{89}$$

where $\delta^*_{1T,B}$ are the dimensional displacement thicknesses. Notice that the leading correction to the lift coefficient, as given in equation (87) is $0\left(\epsilon^2 \ln \epsilon\right)$. This term is completely missed in standard second-order theory which leads to a correction that is $0\left(\epsilon^2\right)$.

Equations (87) and (88) indicate that the lift correction is due primarily to the difference in boundary-layer thicknesses on the top and bottom of the airfoil. In the usual situation, $\delta_{1,T} > \delta_{1,B}$, and the effect of the log term is to reduce the lift coefficient. The effect of this term is most important on rear-loaded airfoils where the rear loading tends to dramatically increase the difference in boundary-layer thickness on the top and bottom of an airfoil. The effect of the shape of the boundary-layer profiles also influences the lift correction through the values of H_T and H_B appearing in equation (88). Rear loading tends to make the boundary layers less full on the top of the airfoil compared with the bottom. This implies that $H_T > H_B$ and this, in turn, also leads to a reduction in lift. This effect is formally of higher order since

$$H_{T,B} = 1 + 0(\epsilon) \qquad (R \to \infty) \tag{90}$$

However, in practice, H is significantly different from one at Reynolds number of interest (e.g., $H \approx 1.4$ for a flat plate at $R \approx 10^6$) and this effect can be numerically significant.

Inner Layers

Next briefly the form of the expansions in the two inner layers near the wall is considered. (See fig. 23.) Only the solution on the airfoil surface upstream of the trailing

edge is considered. The evolution of the inner layers into the wake leads to a similar structure. However, solutions in the inner layers of the wake are much more complex and have not yet been fully developed. A major uncertainty in the wake solution is concerned with the choice of a closure hypothesis to properly deal with a change in the sign of the Reynolds stress near the axis.

Only the solutions on the upper surface are dealt with explicitly. The expressions to be presented also hold on the lower side with an obvious change of notation. In the innermost layer the solutions for the streamwise velocity u^* and Reynolds stress τ^* are represented in the form of a law of the wall as

$$u^* = u^+\sqrt{\tau_w^*(X;\epsilon)/\rho}\,(y^+,X;\epsilon) \tag{91a}$$

$$\tau^* = \tau_w^*(X;\epsilon)\tau^+(y^+,X;\epsilon) \tag{91b}$$

$$y^* = y^+\nu/\sqrt{\tau_w^*/\rho} \tag{91c}$$

where $\tau_w^*(X;\epsilon)$ is the skin friction and u^+, τ^+, and y^+ are nondimensional wall-layer variables.

Substitution of these variables into the time-averaged Navier-Stokes equations with $\epsilon \to 0$ leads to the well-known condition that the total stress (laminar plus Reynolds stresses) is constant across the wall layer to all orders in ϵ. This conclusion follows from the fact that the wall-layer thickness is transcendentally small in ϵ. The wall-layer formulation is completed by the choice of a closure condition relating Reynolds stress to mean velocity. Analysis indicates that a balance of production and dissipation in the wall layer is a rational result that follows from the turbulent energy equation in the limit $\epsilon \to 0$. With the usual model of dissipation this leads to a mixing length formula

$$\tau^+ = \ell^2(y^+)(\partial u^+/\partial y^+)^2 \tag{92}$$

where $\ell(y^+)$ is the mixing length distribution. In this formulation the choice of $\ell(y^+)$ is strictly empirical. Careful consideration of the magnitude of the pressure gradients in the present problem indicates that the choices commonly used for moderate-pressure-gradient flows are appropriate here. For example, the two-layer model of Cebeci and Smith with a Van Driest damping factor is known to give very accurate solutions in incompressible wall layers. It is known that the mixing length distribution is linear for large y^+ and that this leads to the usual logarithmic velocity profile for $y^+ \to \infty$. Thus, if

$$\ell(y^+) = \kappa y^+ \qquad (y^+ \to \infty) \tag{93}$$

where κ is the Karman constant, it follows that

$$u^* \to \sqrt{\tau_w^*(X;\epsilon)/\rho}\left(\kappa^{-1} \ln y^+ + B^+\right) \qquad (y^+ \to \infty) \qquad (94a)$$

$$\tau^* \to \tau_w^*(X;\epsilon) \qquad (y^+ \to \infty) \qquad (94b)$$

where B^+ is a universal constant, independent of the local value of skin friction. With $\tau^*(X;\epsilon)$ expanded in a series in ϵ, the preceding result leads to an asymptotic solution for $\epsilon \to 0$ and $y^+ \to \infty$ that must be matched to the inner limit of the outer solution.

The solution for the velocity in the outer inviscid region has a similar behavior for $y \to 0$. However, because the Reynolds stresses are frozen in the outer region, the coefficient of the logarithmic term in the outer solution remains constant, equal to the friction velocity in the noninteracting boundary layer upstream. Thus the solution in the wall layer does not match the outer solution. It follows that an intermediate or blending layer must be inserted between the outer and wall layers in order to obtain a continuous solution for the Reynolds stresses across the boundary layer.

The requirement that the Reynolds stress be continuous leads to the condition that the shear stress term must be retained as a leading term in the streamwise momentum equation in the limit $\epsilon \to 0$. This condition determines the thickness of the blending layer to be $0(\epsilon^2 L)$. Thus a new stretched variable $\hat{y}$ is introduced to represent the solution in the blending layer, where

$$y^* = \epsilon^2 L \hat{y} \qquad (95)$$

Consideration of the form of the velocity profile in the upstream region and in the outer and wall layers leads to an assumption for a solution in the blending layer of the form

$$u = 1 + \epsilon^{1/2} u_{inv}(X,0) + \epsilon \ln \epsilon (1/\kappa) + \epsilon \hat{u}_{BL}(\hat{y}) + \epsilon^{3/2} \ln \epsilon \hat{u}_{21}(X) + \epsilon^{3/2} \hat{u}_{22}(X,y) + \ldots \qquad (96a)$$

$$v = \epsilon^{3/2} \hat{v}_2(X,\hat{y}) + \ldots \qquad (96b)$$

$$P = P_{TE} + \epsilon^{1/2} P_{inv}(X) + \epsilon^{3/2} \hat{P}_2(X) + \ldots \qquad (96c)$$

$$\tau = \epsilon^2 \left[1 + \epsilon^{1/2} \hat{\tau}_2(X,\hat{y}) + \epsilon^{3/2} \ln \epsilon \hat{\tau}_{31}(X) + \epsilon^{3/2} \hat{\tau}_{32}(X,\hat{y}) + \ldots\right] \qquad (96d)$$

where $u_{inv}(X,0)$ and $\hat{u}_{BL}(\hat{y})$ are deduced from equations (80b) and (85) and are given by

$$u_{inv}(X,0) = C_\alpha \sqrt{-X}\ \mathrm{sgn}\ y \tag{97a}$$

$$\hat{u}_{BL}(\hat{y}) = \kappa^{-1}\left[\ln\left(\hat{y}/\delta_T\right) - 2\tilde{\pi}_T\right] \tag{97b}$$

The ln terms appearing in the preceding expansions are required in order to match similar logarithmic terms in the inner expansions of the outer solution. These terms enter the expansion from the logarithmic behavior of the initial profile for small y. Consideration of the transverse momentum equation leads to the conclusion that the pressure is constant across the blending layer to the order considered in equation (96c). Thus the unknown function $\hat{P}_2(X)$ appearing in equation (96c) can be identified with the surface value of the pressure distribution of the outer solution. The requirement that the blending layer solution match the solution in the wall layer leads to the conclusion that the expansion for the Reynolds stress must have the same form as the expansion for the streamwise velocity component. It also follows that the relative change in skin friction in the trailing-edge region is on the order of the pressure change; that is, $\Delta_T/\epsilon^2 = 0(\epsilon^{1/2})$ as indicated in equation (96d).

Substitution of the preceding expansions into the momentum equation leads to the simple result

$$\hat{u}_{21}(X) = -\kappa^{-1} u_{inv}(X,0) \tag{98}$$

The solution for the vertical velocity component $\hat{v}_2$ is obtained from integration of the continuity equation

$$\hat{v}_2(X,\hat{y}) = -\left[du_{inv}(X,0)/dX\right]\hat{y} \tag{99}$$

The solutions for $\hat{u}_{22}$ and $\hat{\tau}_2$ are governed by two coupled first-order, linear, partial differential equations. These equations are derived from the streamwise momentum equation and from a turbulent closure hypothesis relating Reynolds stress to mean velocity. Since the pressure gradients on an airfoil can be relatively large, the closure assumption is based on the turbulent energy equation. Since the solution of these equations is not being considered in this presentation, they will not be written out here. Note simply that the momentum equation leads to a balance of linearized convective terms with shear stress and pressure gradient terms. Only the Reynolds stresses contribute to the shear stress gradients. The pressure gradient term is impressed from the outer inviscid solution $\left(dP_2(X)/dX\right)$.

The turbulent energy equation leads to a balance of advection, production, and dissipation of the Reynolds stress perturbation $\hat{\tau}_2$. The contribution from pressure diffusion and other terms in the energy equation are formally smaller than these main terms.

The present formulation leads to a simple form for the skin friction that is independent of the particular closure model assumed in the analysis. Matching of the blending and wall-layer solutions for u^* given in equations (94) and (96) leads to the following expression for the skin-friction coefficient:

$$\frac{C_f(X)}{C_{f,o}} = 1 - C_p(X;\epsilon) + 2\left(\frac{\epsilon}{\kappa} \ln \frac{\epsilon}{\kappa}\right) C_p(X;\epsilon) + \cdots \tag{100}$$

where $C_{f,o} = 2\epsilon^2$ and $C_p(X;\epsilon)$ is a pressure coefficient based on reference conditions from the inviscid solution at the trailing edge. Equation (100) is a simple relation for the skin-friction coefficient in terms of the pressure coefficient. It is a direct requirement of matching and follows simply from the three-layer structure of turbulent boundary layers near trailing edges. It involves only two turbulence parameters $C_{f,o}$ and κ. The parameter $C_{f,o}$ is the skin coefficient upstream of the trailing edge and κ is the Karman constant which enters from the logarithmic term in the initial profile.

Although the skin-friction result was derived here in the context of the trailing-edge problem, it can be given a more general and useful interpretation. The three-layer structure of turbulent flows also appears to apply to situations with large imposed pressure gradients. In this case equation (100) is valid with $C_{f,o}$ identified with the skin-friction coefficient upstream of the large-pressure-gradient region. The pressure coefficient is then defined with respect to reference quantities at the beginning of the pressure change. To check these concepts the skin-friction coefficient predicted by equation (100) was compared with data of Schubauer and Klebanoff (ref. 18). In reference 18 Schubauer and Klebanoff measured the skin-friction and pressure distributions in turbulent boundary layers approaching separation in a moderately large adverse pressure gradient. The skin-friction coefficient was computed by using the experimentally determined pressure coefficient in equation (100). The results are compared with the data in figure 25. Comparisons with the turbulent boundary computations of Bradshaw, Ferris, and Atwell (ref. 30) obtained with a turbulent energy approach are also included.

In this figure the combination $1 - C_p(X;\epsilon)$ is referred to as the first term. This one-term solution is equivalent to the assumption of a constant local skin-friction coefficient (i.e., a skin-friction coefficient based on the local dynamic pressure at the edge of the boundary layer). This result correctly indicates the main trend of the skin-friction variation with pressure but is in relatively poor agreement with the data. The inclusion of the logarithmic term in the solution greatly improves the agreement with the experimental data.

The numerical solutions given in figure 25 were obtained with and without a curvature correction. The present results should be compared with the numerical solution without the correction since it is not included in the present results. The agreement with the uncorrected numerical solution is seen to be quite good throughout the pressure rise. The better agreement with the experimental data and with the corrected numerical solution is probably fortuitous. However, the comparisons in figure 25 clearly indicate that the logarithmic interaction term is large and that very good results are obtained with its inclusion. These results also suggest that equation (100) can be made the basis of a separation criteria. The comparisons given tend to confirm the multilayer structure of turbulent flows proposed in the present study.

Concluding Remarks

In the present investigation a formal asymptotic description of turbulent interactions at airfoil trailing edges was developed. The most important result of the present study was the formulation of a boundary-value problem that governs the solutions for the interaction pressure distribution and lift coefficient on an airfoil. The interaction can be described as an inviscid rotational flow governed by a linearized Poisson equation. Work is currently in progress to complete the solution of these equations. Also the analysis has recently been extended to compressible flow and it has been demonstrated that the basic formulation applies to the case with minor modification provided the Mach number near the trailing edge is less than one. Both of these developments will be described in future publications on the subject.

The results discussed in this section are concerned with the lifting, basically antisymmetric problem. The effect of wake-induced displacement pressures, which was so important in the laminar problem, is absent to the order of the small parameter ϵ considered so far in the turbulent problem. The present solutions can be carried to higher order in ϵ. The next terms in the series are likely to the order of $\epsilon^2 \ln \epsilon$ and ϵ^2. These terms involve the thickness effects of the boundary layers on the airfoil and in the wake. However, the resulting problem is symmetric and so the solution would not affect the lift coefficient to this order. The major unsolved aspects of the problem concern the structure of the expansions in the inner layers of the wake. Further analysis is required to clarify the nature of the solution of this complex problem.

APPENDIX

THE SIMILARITY FUNCTIONS

The function $F_1(\eta)$ arising in the symmetric problem for X large and negative satisfies the differential equation and boundary conditions

$$F_1''' - 18\eta^2 F_1'' - 36\left(\eta F_1' - F_1\right) = -2^{5/3}3^{-1/2} \tag{A1a}$$

$$F_1(0) = F_1'(0) = 0 \qquad F_1''(\eta) \to 0 \qquad (\eta \to \infty) \tag{A1b}$$

It follows that

$$F_1 \to \left[3^{-7/6}(1/3)!/(-1/3)!\right]\eta \qquad (\eta \to \infty) \tag{A1c}$$

The functions $H_i(\eta)$ arising in the angle-of-attack problem for X large and negative satisfy the differential equations and boundary conditions

$$H_i''' - 18\eta^2 H_i'' + 9(4 - i)\left(\eta H_i' - H_i\right) = h_i \tag{A2a}$$

$$H_i(0) = H_i'(0) = 0 \qquad H_i''(\eta) \to 0 \qquad (\eta \to \infty) \tag{A2b}$$

where

$$h_1 = 9/2^{1/3} \tag{A2c}$$

$$h_2 = \left(3/2^{1/3}\right)\left(3H_1H_1'' - H_1'^2\right) \tag{A2d}$$

$$h_3 = \left(3/2^{1/3}\right)\left(2H_1''H_2 - H_2'H_1' + 3H_2''H_1\right) \tag{A2e}$$

It can be shown that the $H_i(\eta)$'s have the following asymptotic behavior for

$$H_1 = \tfrac{2}{3}C_{11}\eta^{3/2} + C_{12}\eta + C_{13} + \ldots \tag{A3a}$$

$$H_2 = C_{21}\eta \ln \eta + C_{22}\eta + C_{23}\eta^{1/2} + C_{24} + \ldots \tag{A3b}$$

$$H_3 = C_{31}\eta^{1/2} \ln \eta + C_{32} \ln \eta + C_{33}\eta + C_{34}\eta^{1/2} + C_{35} + \ldots \tag{A3c}$$

where the constants C_{ij} have been determined from analytical studies in references 1 to 3 and from numerical solutions obtained in the present investigation to be

$$\left.\begin{array}{lll} C_{11} = -3(2)^{1/6}(-2/3)!/(1/6)! & C_{12} = 6^{1/3}(-1/3)! & C_{13} = -1/K \\ C_{21} = -3.255 & C_{22} = 3.082 & C_{23} = C_{11}C_{22}/K \\ C_{24} = C_{12}^2/2K & C_{31} = C_{11}C_{21}/K & C_{32} = C_{12}C_{21}/K \\ C_{33} = -17.408 & C_{34} = 16.900 & C_{35} = (C_{21} + C_{22})C_{12}/K \end{array}\right\} \quad \text{(A4)}$$

where $K = 3(2)^{1/3}$.

The function $G_o(\eta)$ governing the trailing-edge behavior satisfies the following differential equations and boundary conditions:

$$G_o''' + 2G_oG_o'' - G_o'^2 = 27(2)^{4/3}C_o \qquad \text{(A5a)}$$

$$G_o'(\eta) - 18\lambda_{1,T}\eta = D_T \to 0 \qquad (\eta \to \infty) \qquad \text{(A5b)}$$

$$G_o'(\eta) - 18\lambda_{1,B}\eta = D_B \to 0 \qquad (\eta \to -\infty) \qquad \text{(A5c)}$$

where $\lambda_{1,T}$ and $\lambda_{1,B}$ are the values of the skin friction $\partial U/\partial Z\big|_T$ and $\partial U/\partial Z\big|_B$ at the trailing edge and C_o is a constant to be determined as part of the solution. Further details, together with typical solutions, are given in references 3 and 23.

REFERENCES

1. Stewartson, K.: On the Flow Near the Trailing Edge of a Flat Plate II. Mathematika, vol. 16, 1969.

2. Messiter, A. F.: Boundary Layer Flow Near the Trailing Edge of a Flat Plate. SIAM J. Appl. Math., vol. 18, 1970.

3. Brown, S. N.; and Stewartson, K.: Trailing Edge Stall. J. Fluid Mech., vol. 42, 1970.

4. Keller, H.: A New Difference Scheme for Parabolic Problems. Numerical Solutions of Partial Differential Equations, J. Bramble, ed., Academic Press, New York, 1970.

5. Keller, H.; and Cebeci, T.: Accurate Numerical Methods for Boundary Layer Flows. II: Two-Dimensional Turbulent Flows. AIAA J., vol. 10, no. 9, 1972.

6. Jobe, C. E.; and Burggraf, O. R.: The Numerical Solutions of the Asymptotic Equation of Trailing Edge Flow. Proc. Royal Soc. London, A340, 1974. (See ref. 26.)

7. Veldman, A. E. P.; and Van De Vooren, A. I.: Drag of a Finite Flat Plate. Proceedings of the Fourth International Conference Numerical Methods in Fluid Dynamics. Volume 35 of Lecture Notes in Physics, Springer-Verlag, 1975.

8. Janour, Z.: Resistance of a Flat Plate at Low Reynolds Numbers. NACA TM 1316, 1951.

9. Sato, H.; and Kuriki, K.: The Mechanism of Transition in the Wake of a Thin Plate Placed Parallel to a Uniform Flow. J. Fluid Mech., vol. 11, 1961.

10. Spence, D. A.: Wake Curvature and the Kutta Condition. J. Fluid Mech., vol. 44, 1970.

11. Küchman, D.: Inviscid Shear Flow Near the Trailing Edge of an Airfoil. Z. Flugwiss, vol. 15, 1967.

12. Mellor, G. L.: The Large Reynolds Number Asymptotic Theory of Turbulent Boundary Layers. Int. J. Eng. Sci., vol. 10, 1972.

13. Yajnik, K.: Asymptotic Theory of Turbulent Shear Flows. J. Fluid Mech., vol. 42, 1970.

14. Bush, W. B.; and Fendell, F.: Asymptotic Analysis of Turbulent Channel and Boundary Layer Flow. J. Fluid Mech., vol. 56, 1972.

15. Bush, W. B.; and Fendell, F.: Asymptotic Analysis of Turbulent Channel Flow for Mean Turbulent Energy Closures. Phys. Fluids, vol. 16, 1973.

16. Melnik, R. E.; and Grossman, B.: Analysis of the Interaction Between a Weak Normal Shock Wave With a Turbulent Boundary Layer. AIAA Paper 74-598, 1974.

17. Adamson, T. C., Jr.; and Feo, A.: Interactions Between a Shock Wave and a Turbulent Boundary Layer in Transonic Flow. SIAM J. App. Math., vol. 29, no. 1, July 1975.

18. Schubauer, G.; and Klebanoff, P. S.: Investigation of Separation of the Turbulent Boundary Layer. NACA Rep. 1030, 1951. (Supersedes NACA TN 2133.)

19. Van Dyke, M. D.: Higher Order Boundary Layer Theory. Annual Review of Fluid Mechanics, vol. 1, 1969, pp. 265-292.

20. Stewartson, K.: Multistructural Boundary Layers. Advances in Appl. Mech., vol. 14, 1974, pp. 145-239.

21. Goldstein, S.: Concerning Some Solutions of Boundary Layer Equations in Hydrodynamics. Proc. Cambridge Phil. Soc., vol. 26, 1930.

22. Goldburg, A.; and Cheng, S. I.: An Anomaly in the Application of Poincare-Lighthill-Kuo and Parabolic Coordinates to the Trailing Edge Boundary Layer. J. Math. Mech., vol. 10, 1961.

23. Hakkinen, R. J.; and Rott, N.: Similar Solutions for Merging Shear Flows. AIAA J., vol. 3, 1965.

24. Ackerberg, R. C.; and Phillips, J. H.: A Numerical Method for Highly Accelerated Laminar Boundary-Layer Flows. SIAM J. Numer. Anal., vol. 10, 1973.

25. Schneider, L. I.; and Denny, V. E.: Evolution of the Laminar Wake Behind a Flat Plate and Its Upstream Influence. AIAA J., vol. 9, 1971.

26. Jobe, C. E.: The Numerical Solution of the Asymptotic Equations of Trailing Edge Flow. Ph. D. Diss., The Ohio State University, 1973.

27. Stewartson, K.: On the Asymptotic Theory of Separated and Unseparated Fluid Motions. SIAM J. Appl. Math., vol. 28, no. 2, 1975.

28. Lighthill, M. J.: On Boundary Layers and Upstream Influence. II: Supersonic Flows Without Separation. Proc. Royal Soc. London, Ser. A, vol. 217, 1953.

29. Townsend, A. A.: Equilibrium Layers and Wall Turbulence. J. Fluid Mech., vol. 11, 1961.

30. Bradshaw, P.; Ferris, D. H.; and Atwell, N. P.: Calculation of Boundary-Layer Development Using the Turbulent Energy Equation. J. Fluid Mech., vol. 28, 1967.

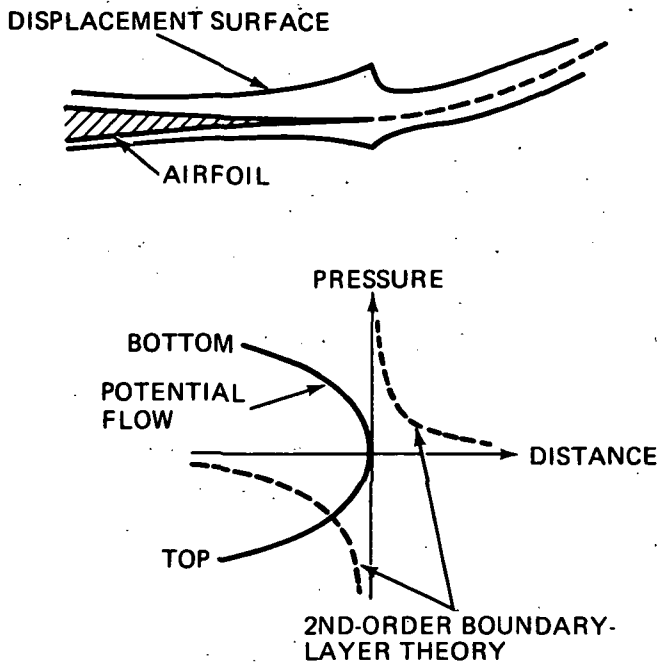

Figure 1.- Trailing-edge flow.

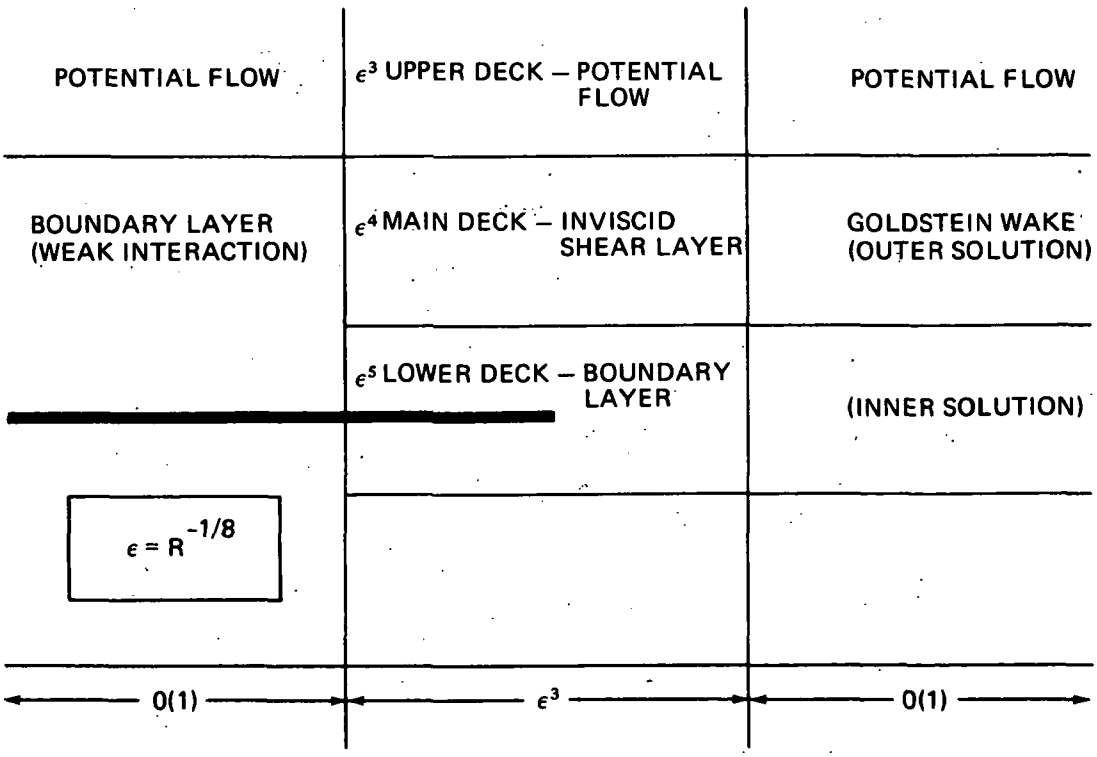

Figure 2.- Triple-deck structure.

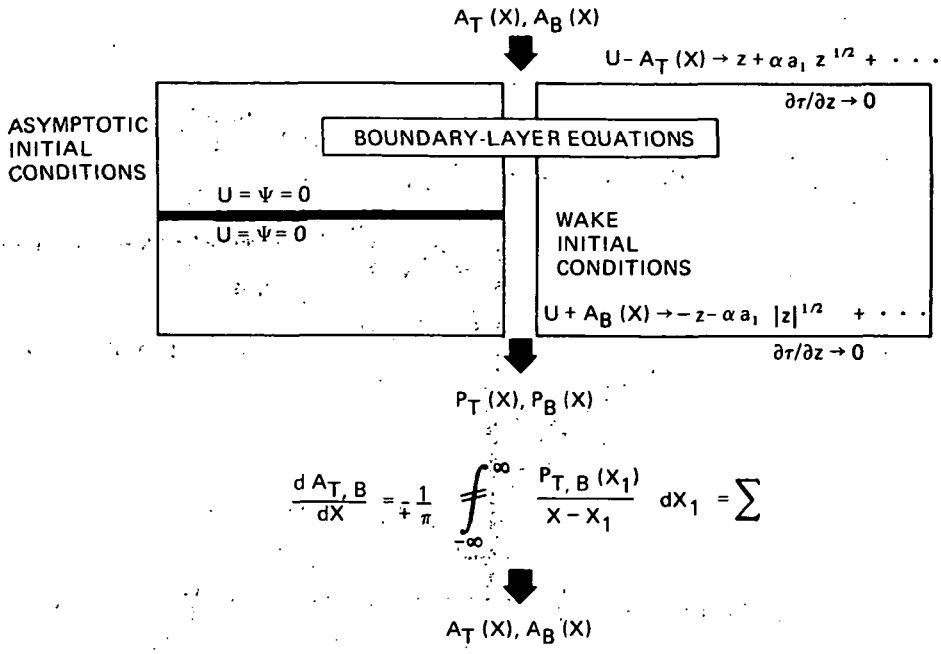

Figure 3.- Boundary-value problem for triple-deck solution.

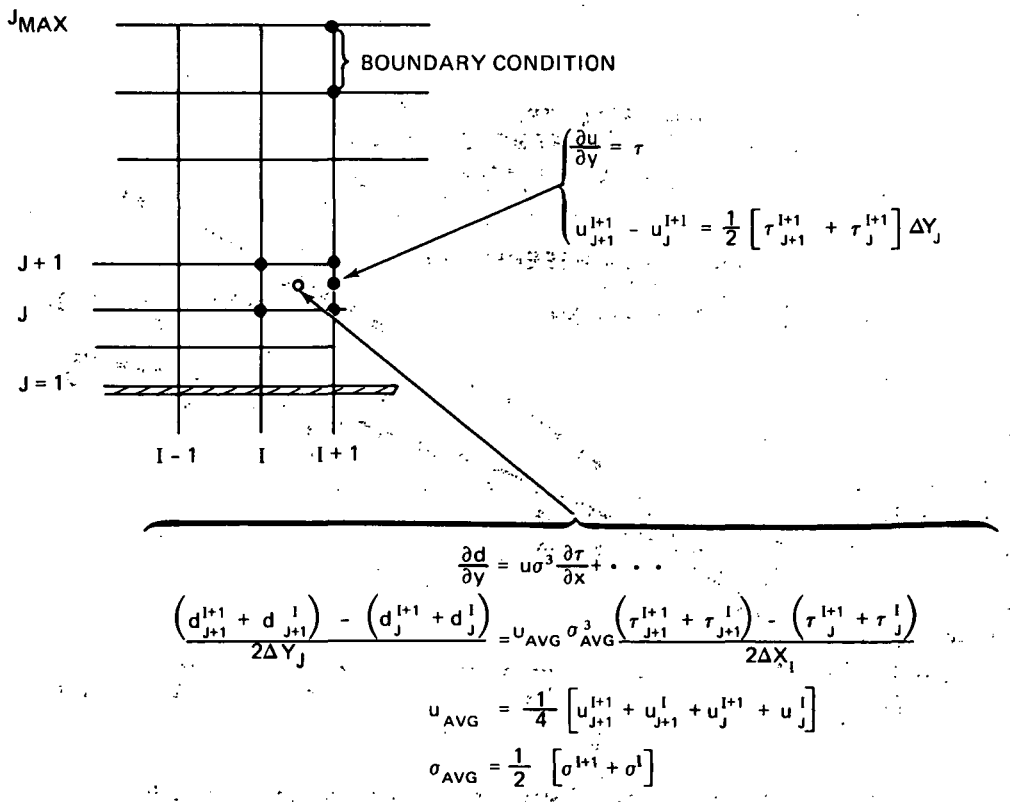

Figure 4.- Finite-difference approximation ("box" scheme).

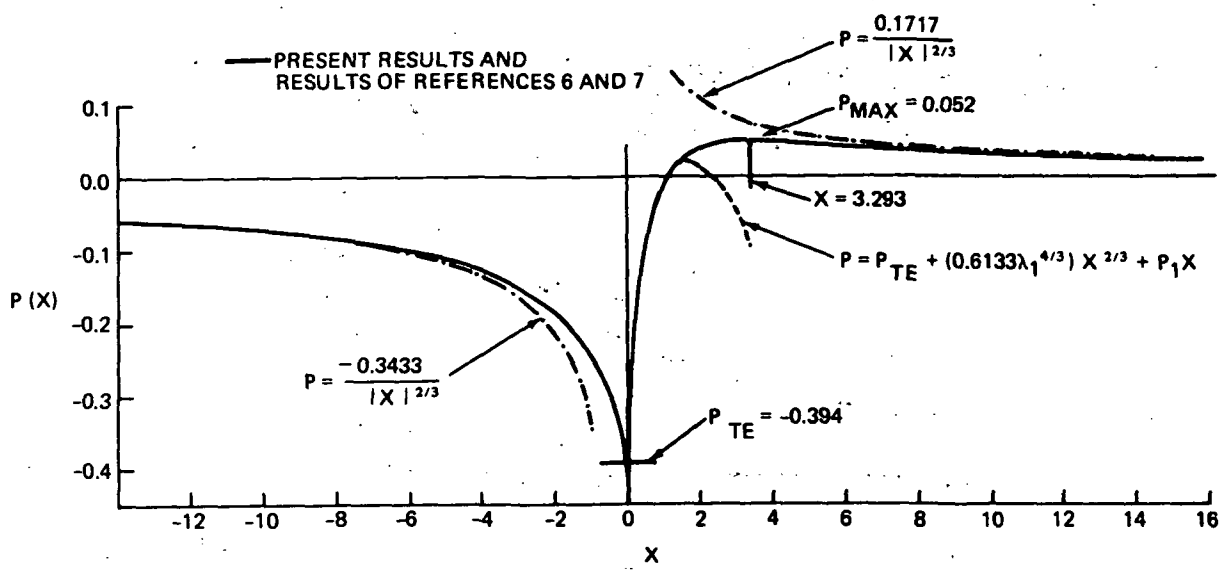

Figure 5.- Surface pressure distribution; $\alpha = 0$.

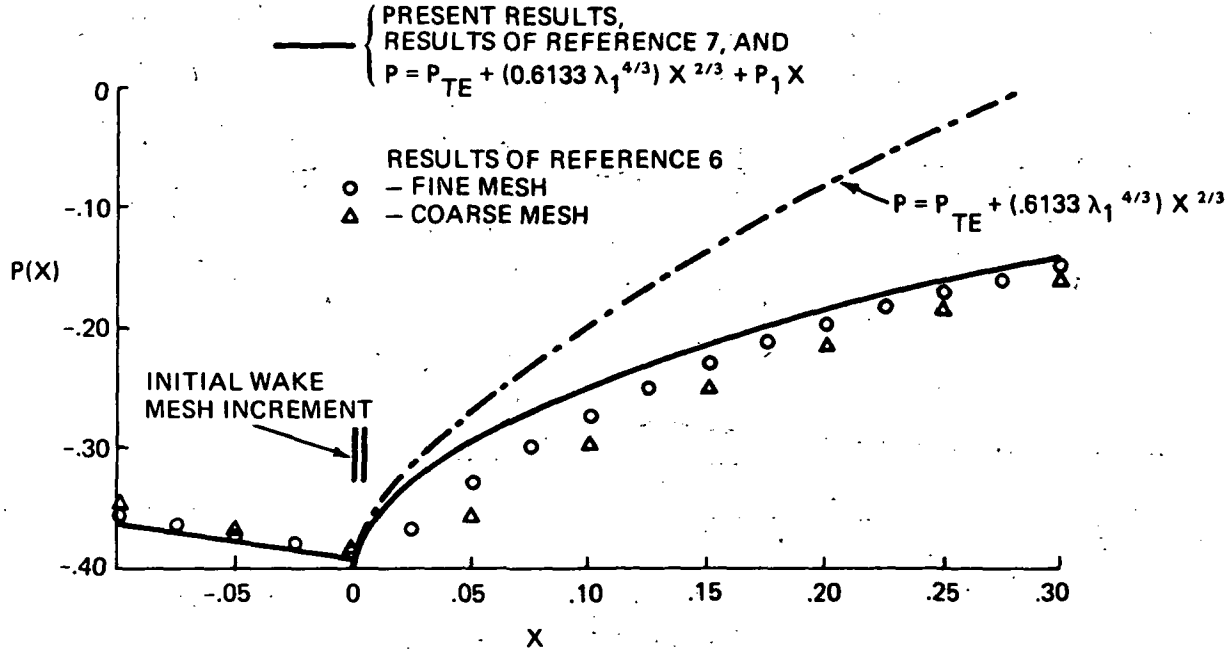

Figure 6.- Pressure distribution near origin; $\alpha = 0$.

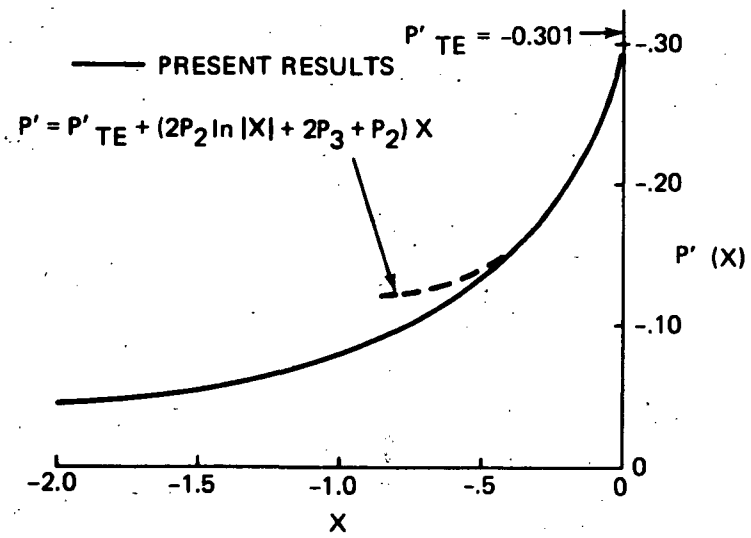

Figure 7.- Pressure gradient on plate near origin; $\alpha = 0$.

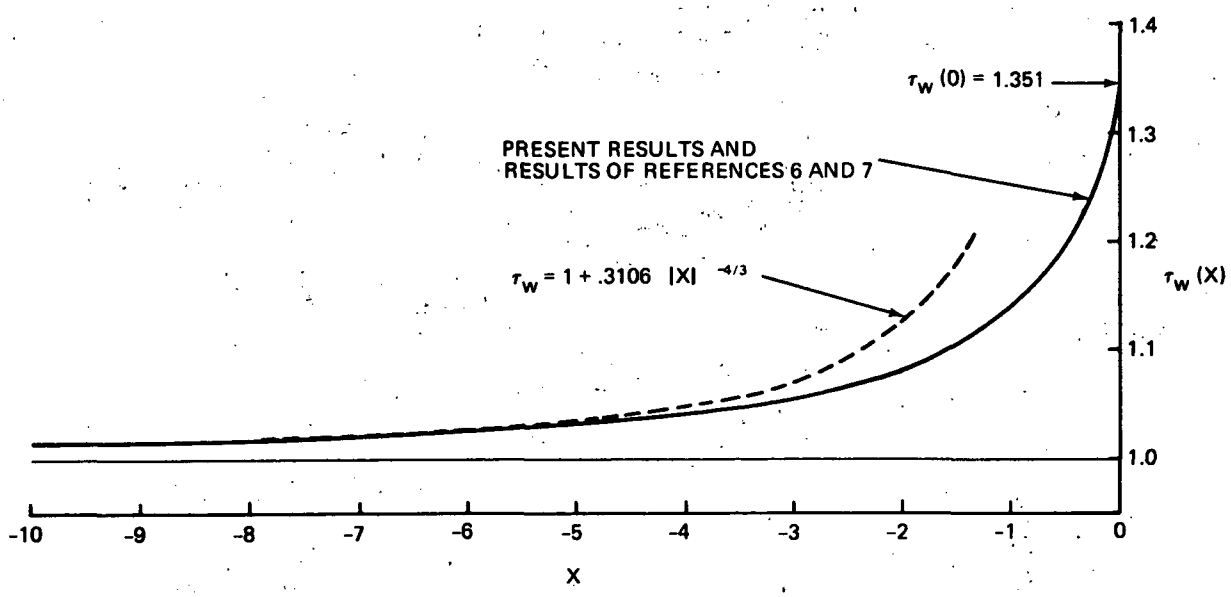

Figure 8.- Skin friction; $\alpha = 0$.

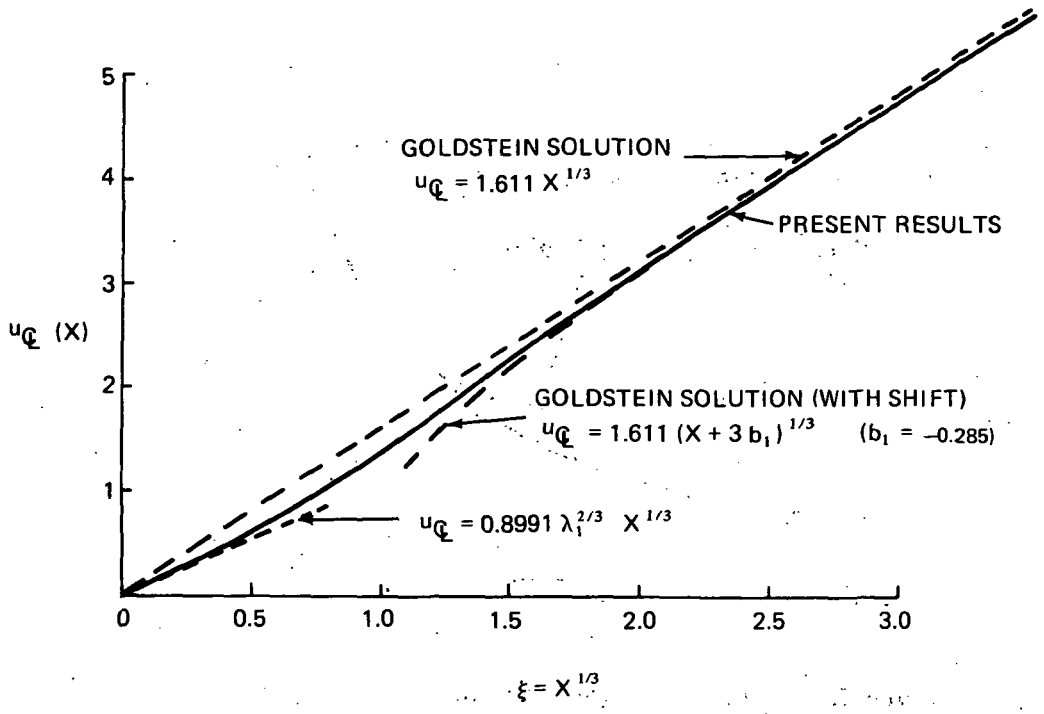

Figure 9.- Comparison of centerline velocity with singular solutions for $X \to 0$ and for $X \to \infty$; $\alpha = 0$.

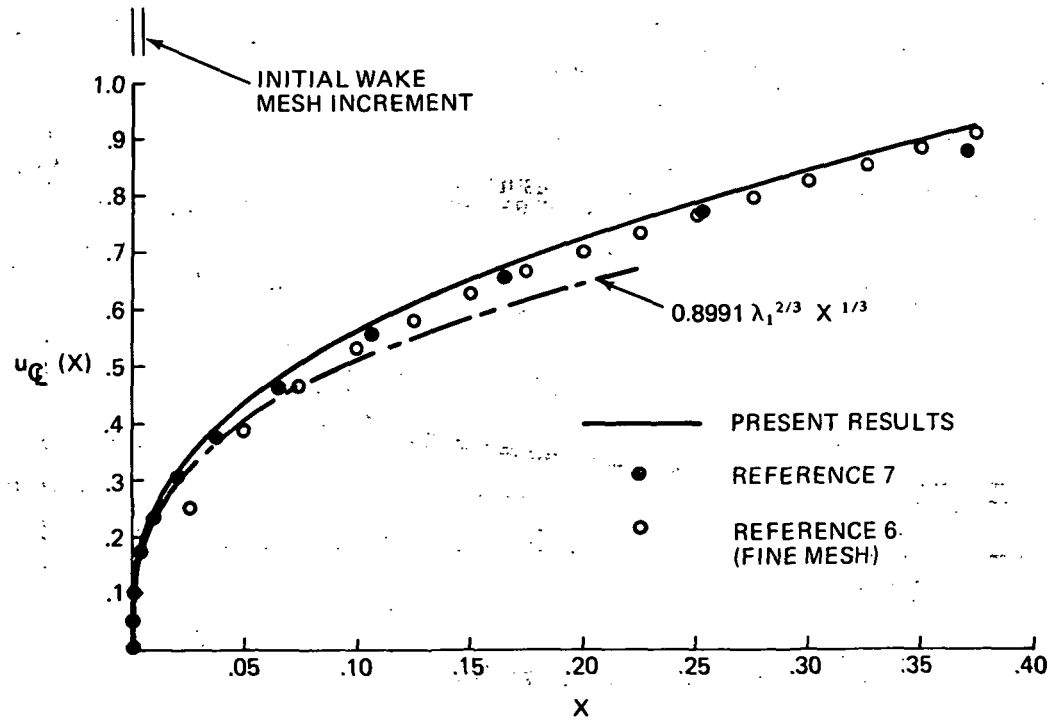

Figure 10.- Centerline velocity near origin; $\alpha = 0$.

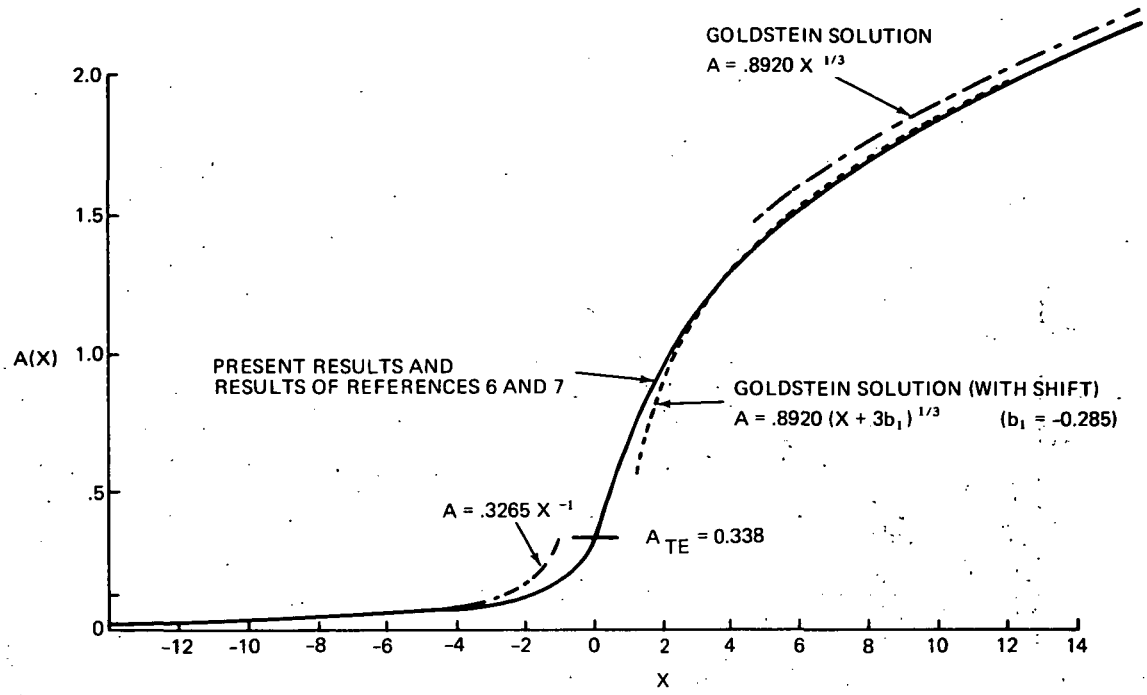

Figure 11.- Displacement function; $\alpha = 0$.

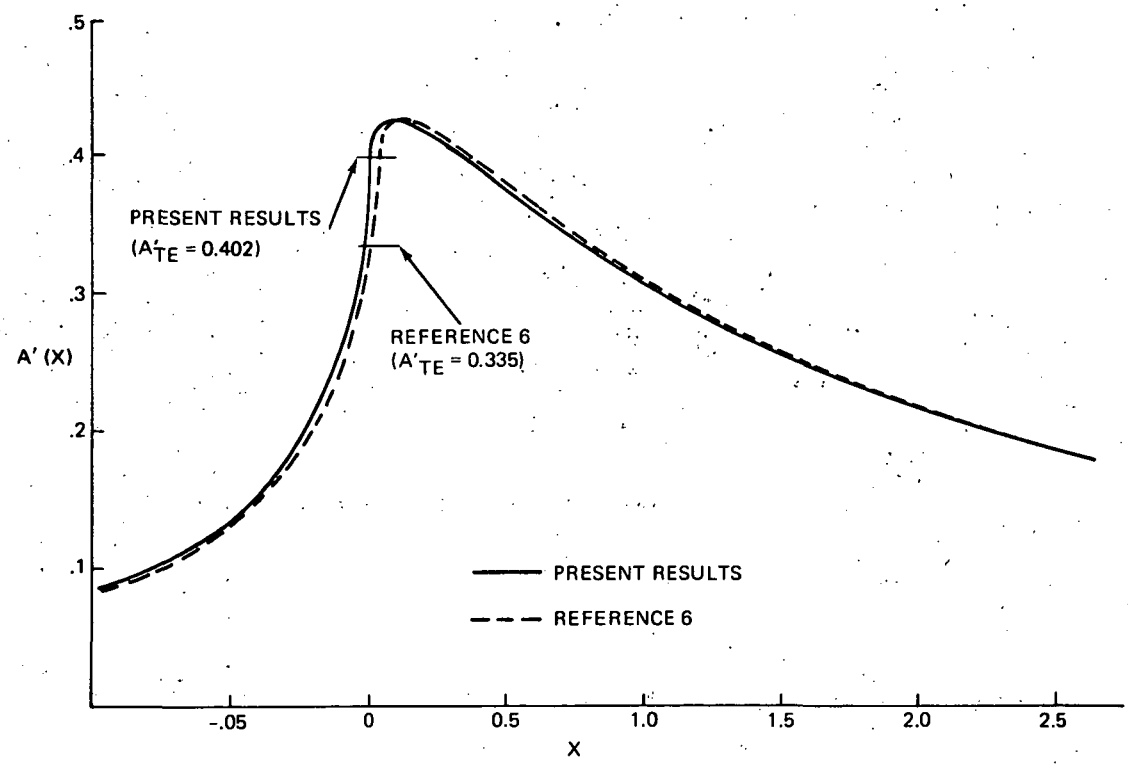

Figure 12.- Displacement surface slope A'(X); $\alpha = 0$.

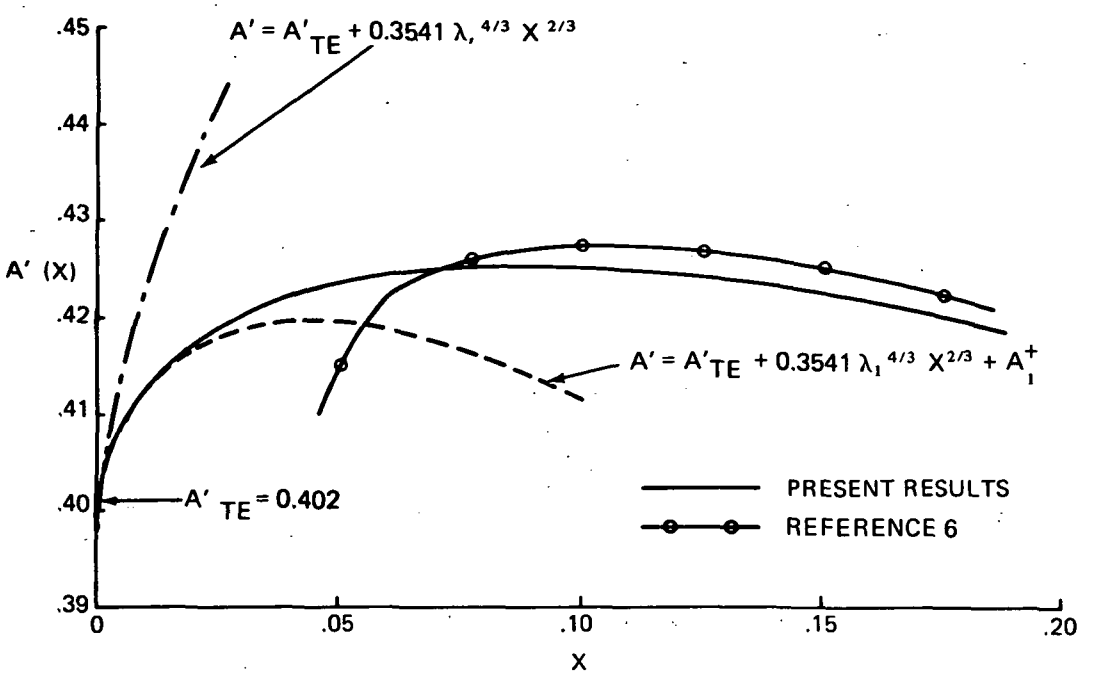

Figure 13.- Behavior of slope function near origin; $\alpha = 0$.

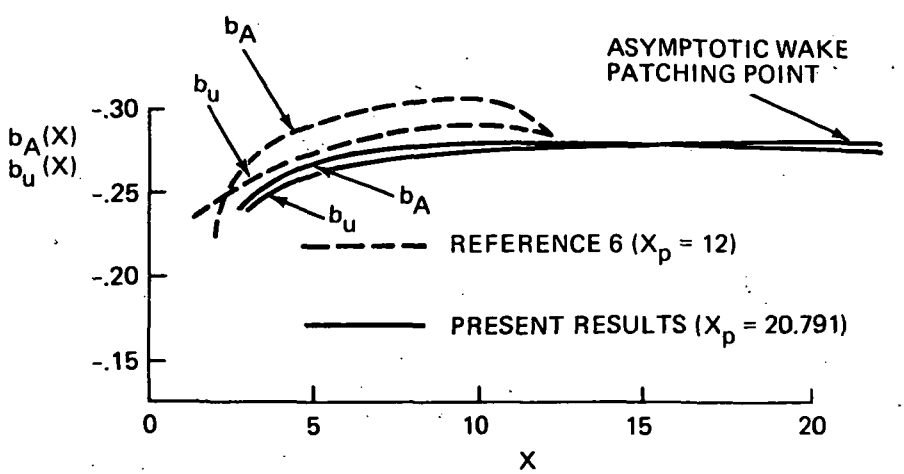

Figure 14.- Asymptotic behavior for large positive X; $\alpha = 0$.

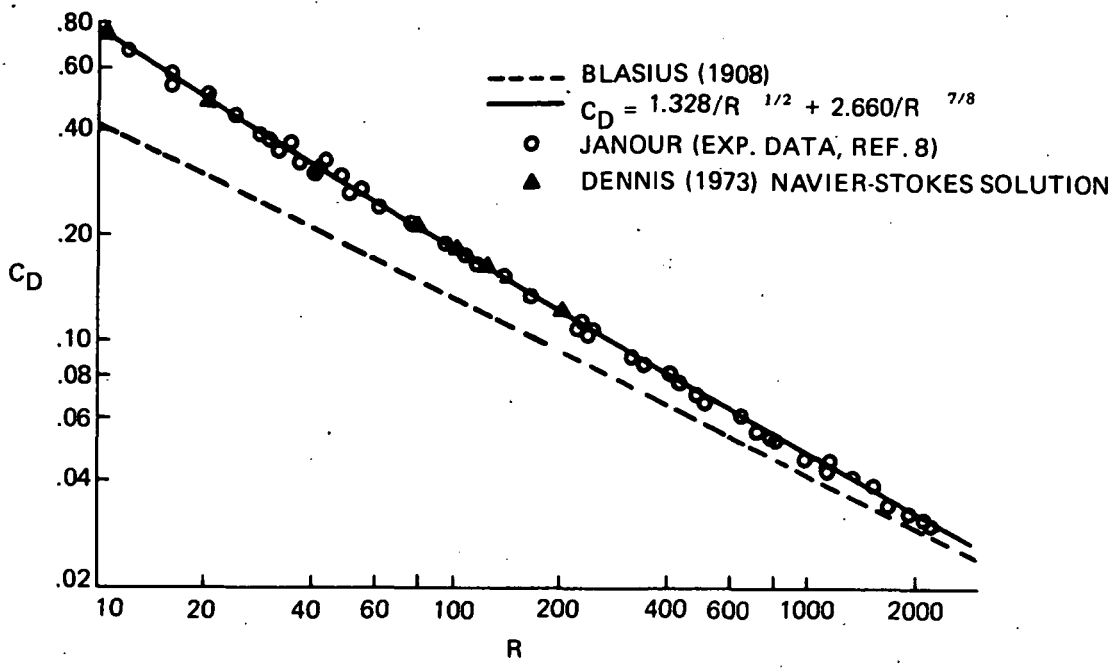

Figure 15.- Drag of finite flat plate as a function of Reynolds number at zero angle of attack.

						∞		
R	40	75	100	125	150	REF. 6	REF. 7	PRESENT
d_2	2.546	2.609	2.632	2.646	2.655	2.694	2.651	2.660

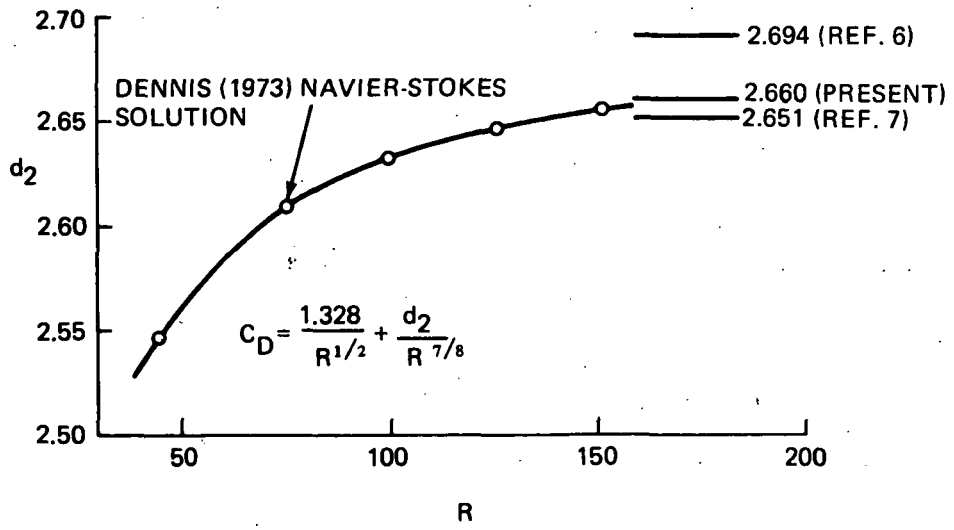

Figure 16.- Comparison between triple-deck and Navier-Stokes solutions for drag constant.

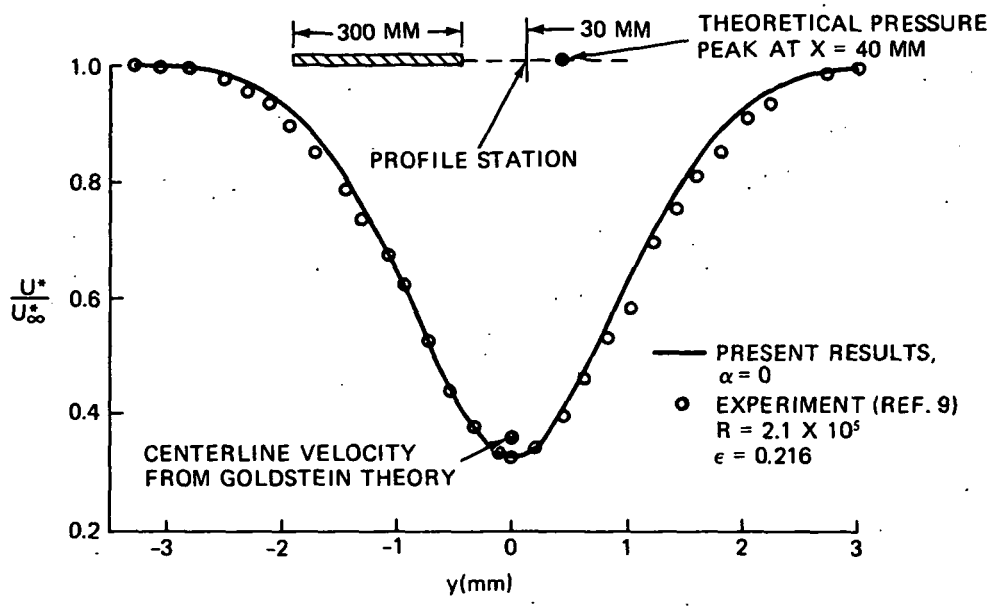

Figure 17.- Comparison of triple-deck velocity profile in wake of symmetric plate with data of Sato and Kuriki (ref. 9).

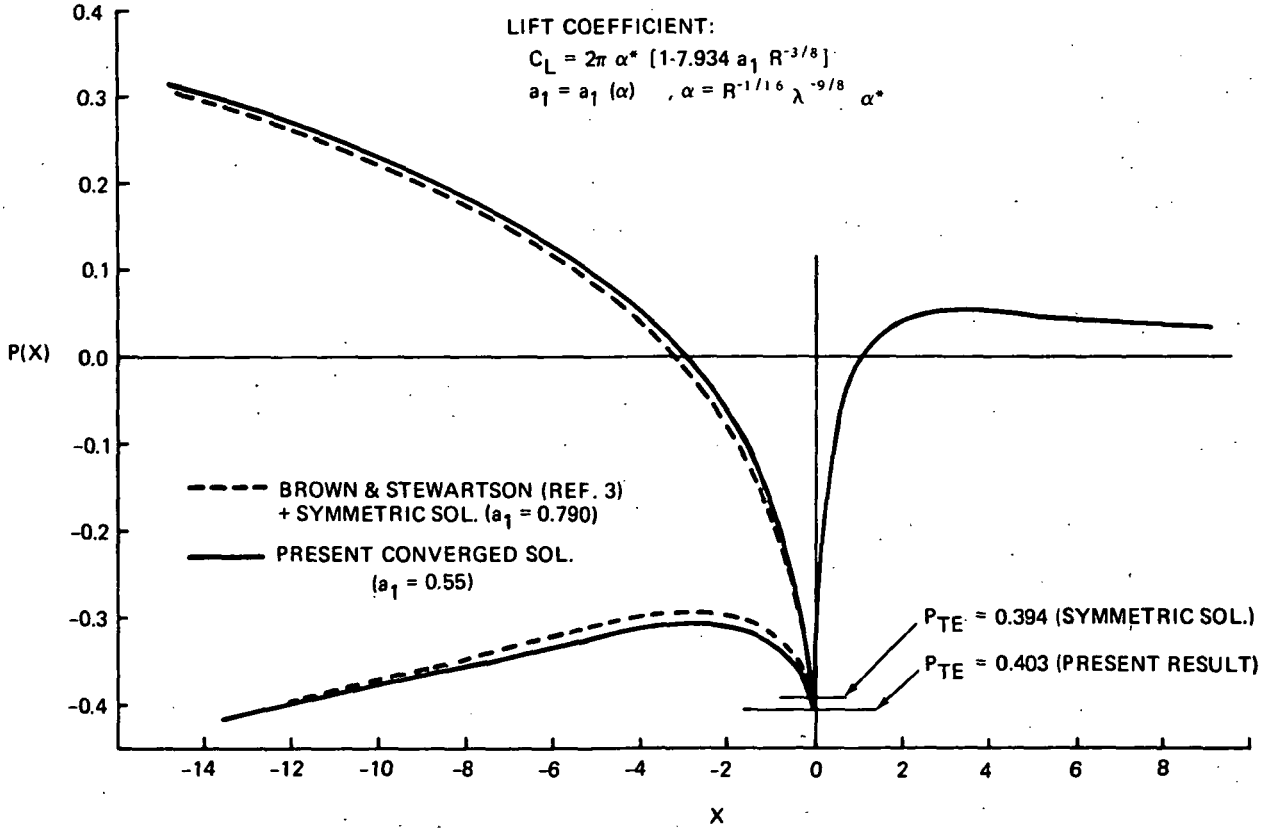

Figure 18.- Comparison of present solution with linearized solution of reference 3; $\alpha = 0.1$.

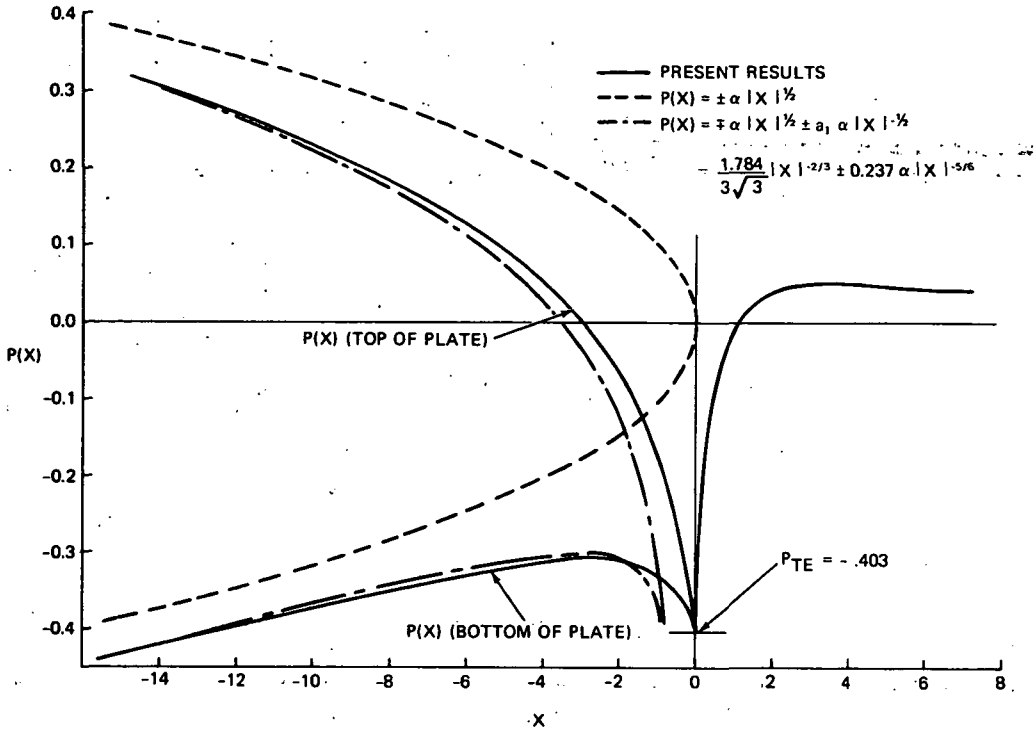

Figure 19.- Surface pressure distribution; $\alpha = 0.1$.

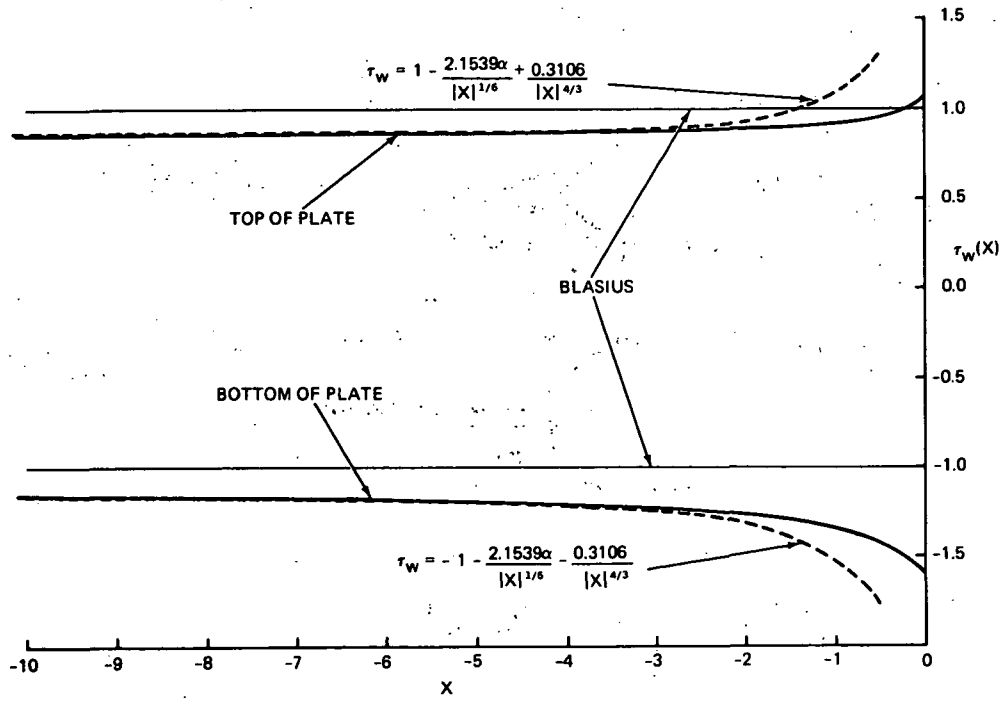

Figure 20.- Skin friction; $\alpha = 0.1$.

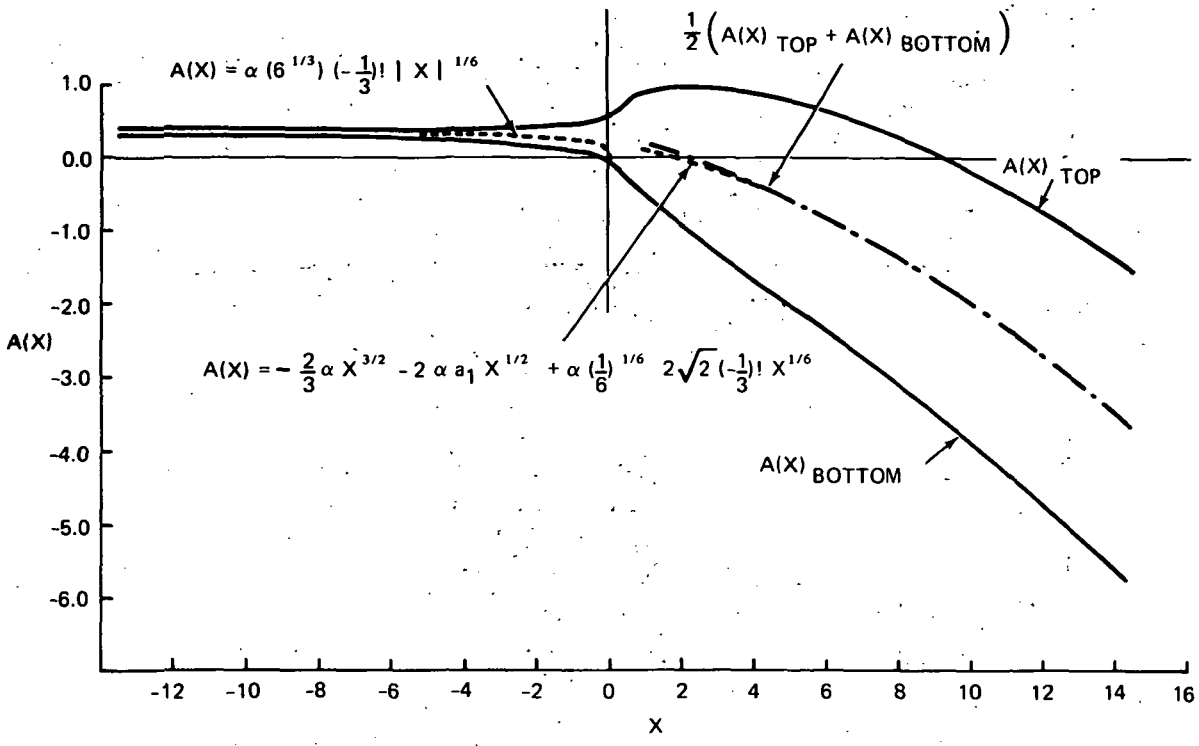

Figure 21.- Displacement function; $\alpha = 0.1$.

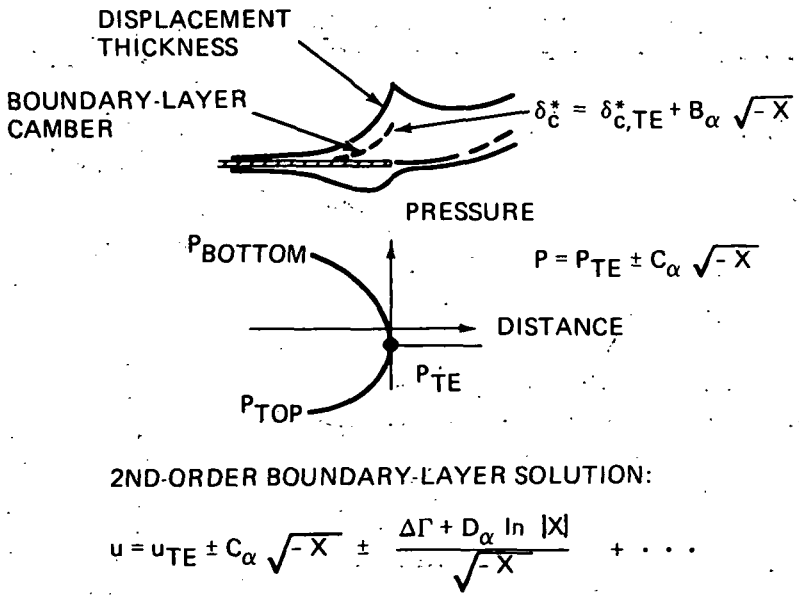

2ND-ORDER BOUNDARY-LAYER SOLUTION:

$$u = u_{TE} \pm C_\alpha \sqrt{-X} \pm \frac{\Delta\Gamma + D_\alpha \ln |X|}{\sqrt{-X}} + \cdots$$

Figure 22.- Second-order boundary-layer theory – turbulent flow.

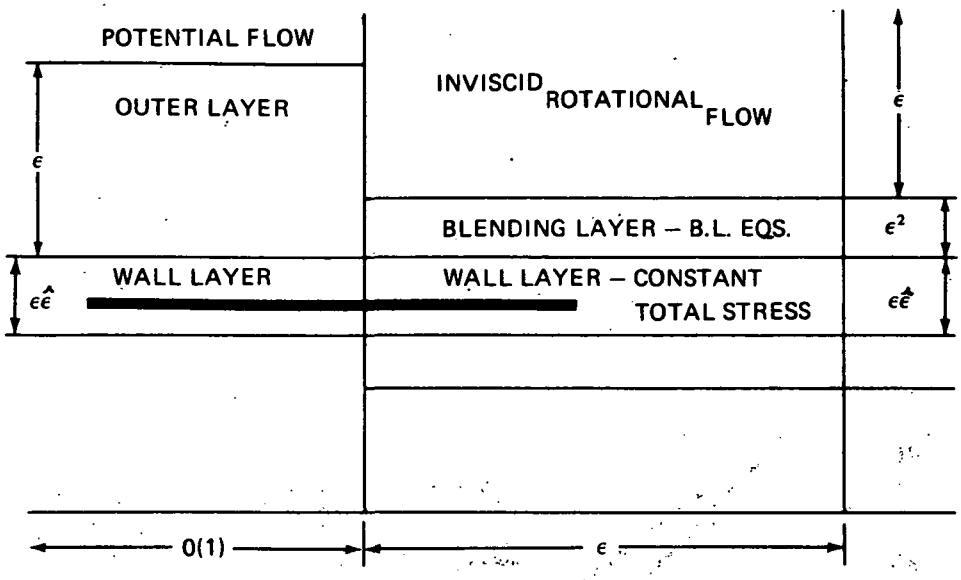

$\epsilon = \sqrt{C_{f,o}/2}$ (FRICTION VELOCITY)

$\hat{\epsilon} = (\epsilon^2 R)^{-1}$

LIMIT: $\epsilon \to 0 \quad (R \to \infty)$

Figure 23.- Flow field structure – turbulent interaction.

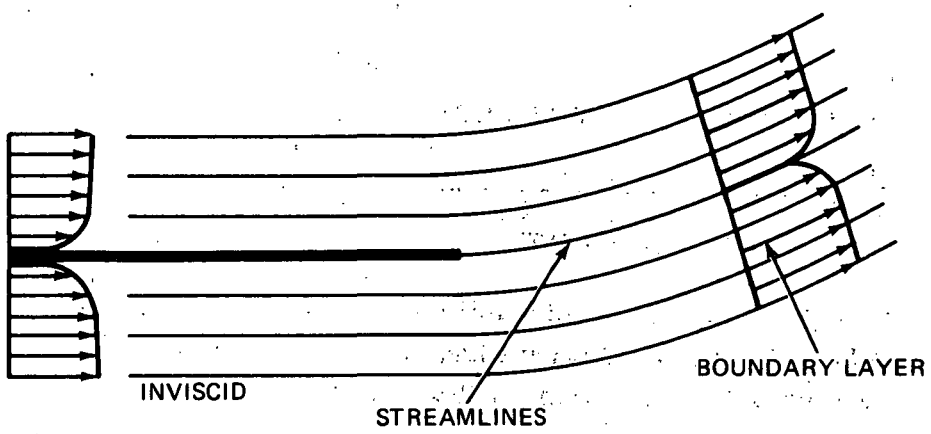

$$\psi = \psi_{INV} + \psi_{BL} + \psi'$$

$$\nabla^2 \psi' = \zeta(x, y) = -u_{BL}(y)\, \psi_{INV}(x, y)$$

$$v' = \frac{\partial \psi'}{\partial X} \text{ (DOWNWASH VELOCITY)}$$

SOLUTION YIELDS: $C_L = 2\pi\alpha [\, 1 + a_1 \epsilon^2 \ln \epsilon + a_2 \epsilon^2]$

Figure 24.- Outer problem.

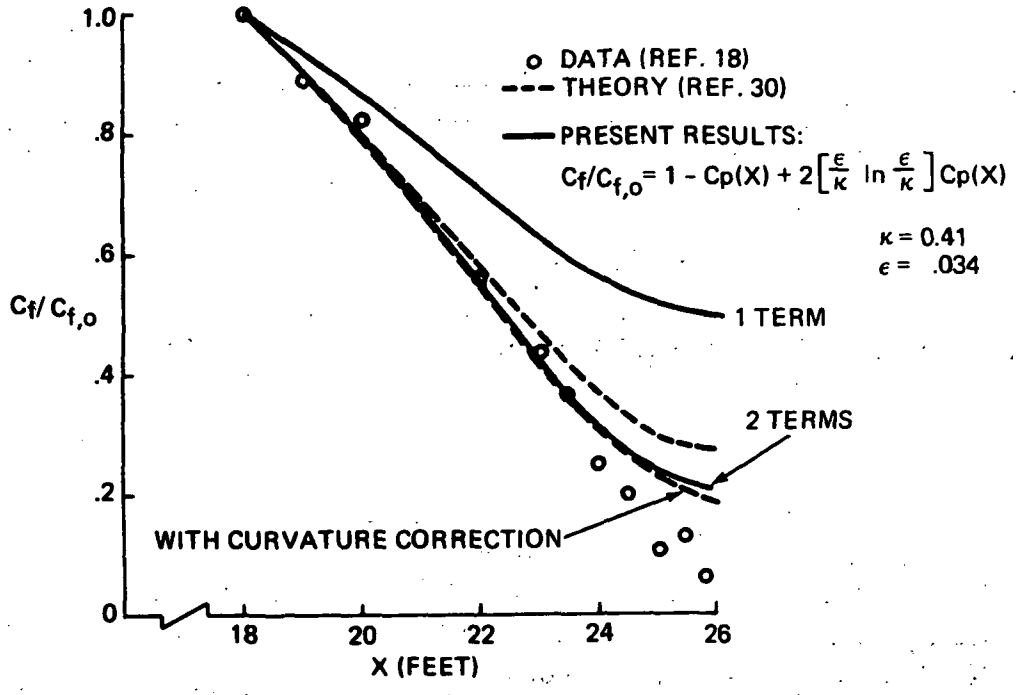

Figure 25.- Comparison of solution for skin friction with data of Schubauer and Klebanoff (ref. 18) and a turbulent boundary-layer solution. 1 ft = 0.3048 m.

Page Intentionally Left Blank

ANALYTICAL STUDY OF MIXING AND REACTING THREE-DIMENSIONAL SUPERSONIC COMBUSTOR FLOW FIELDS*

By A. J. Baker,**
Bell Aerospace Division of Textron

R. Clayton Rogers,
NASA Langley Research Center

and S. W. Zelazny
Bell Aerospace Division of Textron

SUMMARY

An analytical investigation is presented of mixing and reacting hydrogen jets injected from multiple orifices transverse and parallel to a supersonic airstream. The COMOC computer program, based upon a finite-element solution algorithm, was developed to solve the governing equations for three-dimensional, turbulent, reacting, boundary-region and confined flow fields. The computational results provide a three-dimensional description of the velocity, temperature, and species-concentration fields downstream of hydrogen injection. Detailed comparisons between cold-flow data and results of the computational analysis have established validity of the turbulent-mixing model based on the elementary mixing-length hypothesis. A method is established to initiate computations for reacting flow fields based upon cold-flow correlations and the appropriate experimental parameters of Mach number, injector spacing, and pressure ratio. Key analytical observations on mixing and combustion efficiency for reacting flows are presented and discussed.

INTRODUCTION

The hydrogen-fueled scramjet engine is a prominent candidate for propulsion of advanced hypersonic cruise vehicles. (See, for example, Becker and Kirkham (ref. 1) and Bushnell (ref. 2).) An airframe-integrated underbody engine configuration (figs. 1(a) and (b)) has been suggested (ref. 3), and design considerations are discussed by Henry and Anderson (ref. 4). Many alternative scramjet designs have been proposed by the U.S. Air Force, the U.S. Navy, and NASA. In all cases, however, fuel introduction typically consists of rows of circular, choked-flow fuel injector orifices mounted flush and

*This work was supported principally by NASA under Contracts NAS1-11214 and NAS1-13165.

**Visiting Professor, Old Dominion University.

normal to the combustor wall or in fins spanning the combustor inlet. (See fig. 1(c).) The various proposed component designs have largely emerged from laboratory experimentation wherein empirical relations have established a preliminary configuration. Detailed experimental parametric evaluations are then utilized to optimize design configuration.

The ability to analytically predict turbulent, mixing, and reacting three-dimensional flows, and hence avoid the more costly exclusively experimental approach, has been the long-range goal of rocket and ramjet designers for more than a decade. Three very difficult problems must yield to solution to attain this goal. First, a computational technique for solving the appropriate three-dimensional flow field with a predominant flow direction is required. Second, proper turbulent diffusion models must be selected or developed, since the accuracy of the predictive calculation is strictly dependent upon the adequacy of these models for combined laminar and turbulent diffusion of mass, momentum, and energy. Consequently, detailed baseline data characterizing the flow phenomena over a reasonably wide range of flow parameters must be obtained to confirm the validity of the theoretical modeling.

The objective of this investigation is to describe analytically the mixing and reaction of hydrogen in a supersonic airstream simulating the combustion of a scramjet engine. Current combustor design concepts (ref. 4) for scramjet engines employ fuel injection both from transverse wall injectors and from internal struts containing both parallel and transverse injection orifices. Therefore, the analytical characterization of both fuel injection modes is sought. In particular, the problem areas considered are illustrated in figure 2 for the mixing and reaction zones downstream of a row of transverse injection orifices (fig. 2(a)) and the parallel strut injectors (fig. 2(b)). Details of the mixing and reaction promoted by these distinct geometric configurations are computed by using a considerable extension of the exploratory theoretical studies documented in references 5, 6, and 7.

Experimental data for comparison with these analyses are provided from references 8, 9, 10, and 11. In references 8 and 9, detailed velocity and concentration measurements were made in a nonreacting, three-dimensional, hydrogen-air mixing region downstream of a row of laterally spaced circular orifices. The hydrogen was injected from the orifices, at various pressures, transverse to a turbulent Mach 4 air boundary-layer flow over a flat plate. In the experiments reported in reference 10, ambient-temperature hydrogen was injected at nominal equivalence ratios of 0.5 and 1.0 transverse to a hot supersonic test gas (vitiated air) from rows of circular orifices in opposite walls of a two-dimensional duct. Data measurements included static pressure distributions at the duct wall and pitot pressure and gas composition surveys at the duct exit, from which the reacted fraction of injected hydrogen was deduced. Additional reacting-flow data are available from the experimental investigation reported in reference 11,

where two distinct strut fuel injectors were tested in a hot supersonic duct flow. In the transverse injection strut, hydrogen was injected from orifices just downstream of a rearward-facing step. In the parallel configuration, hydrogen was injected parallel to the main flow from conical nozzles drilled at the base of the strut wedge. Data measurements were similar to those of the previously discussed hot-flow experimentation. Generated predictions are compared with select data sets from each of these experimental investigations.

Long-term support has been given to finite-element research in computational fluid mechanics by Bell Aerospace Division of Textron. Significant contributions were provided by W. T. Rushmore and J. A. Orzechowski.

SYMBOLS

a	boundary-condition coefficient
A	species; area
b	coefficient
B	species
c	coefficient
c_p	specific heat
C	species
C_f	skin friction
d	differential; orifice diameter
f	function of known argument
g	function of known argument
h	static enthalpy; duct height
H	stagnation enthalpy; hydrogen

i	index
$\hat{i},\hat{j},\hat{k}$	unit vectors of rectangular Cartesian coordinate system
k	thermal conductivity; constant
K	generalized diffusion coefficient; equilibrium constant
ℓ	differential operator; number; mixing length
L	characteristic length; differential operator
m	number
M	Mach number; number of finite elements
n	unit normal vector; number; nodes per element; dimensionality
N	nitrogen; composition matrix
N_{Pr}	Prandtl number
N_{Re}	Reynolds number
N_{Sc}	Schmidt number
O	oxygen
p	pressure
q	generalized dependent variable
q_r	dynamic pressure ratio
Q	generalized discretized dependent variable
R	domain of elliptic operator; universal gas constant

s	injector spacing
S	mass source term; finite-element assembly operator
T	temperature
u,U	velocity
W	molecular weight
x_i	rectangular Cartesian coordinate system
X	species mole fraction
Y	species mass fraction
β	pressure gradient parameter
γ	ratio of specific heats
∂R	closure of elliptically coupled solution domain
δ	boundary-layer thickness
Δ	increment
ϵ	kinematic eddy viscosity
η	mixing efficiency
κ	coefficient
λ	multiplier; turbulence sublayer constant
μ	viscosity
ρ	density
σ	integral kernel

τ integral kernel; wall shear

ϕ equivalence ratio, $\dfrac{(\rho u_1)_{jet}}{0.034(\rho u_1)_{air}}$

Φ functional

χ domain of initial-value operator

ω turbulence damping factor

Ω global solution domain

Superscripts:

e effective value

T matrix transpose

α species identification

$\hat{}$ unit vector

* approximate solution

Subscripts:

e local reference condition

i,j,k tensor indices

m mth subdomain

o initial

t stagnation or total

T turbulent

α	species identification
β	elemental species
∞	global reference condition

Notation:

$\{\}$	column matrix
$[\,]$	square matrix
$\cup$	union
$\cap$	intersection
$\sum$	summation
$\in$	belongs to

THEORETICAL DEVELOPMENT

Many researchers are now giving attention to numerical solution of three-dimensional parabolic and/or boundary-region flow fields. Most procedures employ a finite-difference solution algorithm for variously combined forms of the continuity, momentum, and energy equations. Note that the three-dimensional boundary-layer equations result from this parabolic set for flow fields wherein diffusion in one direction only is important and the corresponding pressure gradient is negligible. Several researchers have obtained solutions for the three-dimensional boundary-region flow of single-species fluids. Pal and Rubin (ref. 12) employ asymptotic expansions of the flow variables for laminar incompressible flow after transformation to modified stream function and vorticity. Results of extending the theory to a compressible perfect fluid in physical variables are reported by Cresci et al. (ref. 13), who used an extension of the numerical technique common to boundary-layer solutions. Extension to handle streamwise pressure gradients and refinement of the overall method are reported by Rubin and Lin (ref. 14). Caretto et al. (ref. 15) present a finite-difference algorithm for solution of three-dimensional boundary-region flows with extension to the "parabolic" Navier-Stokes equations. The results of computations for transitional internal flows in rectangular ducts are presented

by Curr et al. (ref. 16). Refinement of the overall procedure with particular attention to solution of the parabolic Navier-Stokes equations is given by Patankar and Spalding (ref. 17). The key feature of their theory is a procedure for splitting the pressure field computation such that a two-dimensional boundary-value problem results for pressure in the transverse plane coupled to an assumed uniform streamwise pressure gradient computed from global continuity. The latter step is similar to methods employed for computations in two-dimensional hydrodynamics (ref. 18).

Characterization of an n-species, three-dimensional boundary-region or parabolic flow field requires solution of (n - 1) species-continuity equations in addition to those previously mentioned. Caretto (ref. 15) and Patankar and Spalding (ref. 17) include results of a finite-difference solution of heat, mass, and momentum transfer in three-dimensional parabolic flows. Baker (ref. 19) presents a finite-element solution algorithm for multiple-species diffusion in supersonic, three-dimensional boundary-region flow. However, no general three-dimensional solution algorithm has been published which considers mixing and reacting three-dimensional confined flows.

The system of partial differential equations governing such three-dimensional, confined unidirectional flows of a compressible, reacting fluid is obtained as an approximation to the full three-dimensional Navier-Stokes equations. This approximation, now known as the "parabolic Navier-Stokes equations," describes steady, confined three-dimensional flows wherein (1) a predominant flow direction is uniformly discernible; (2) in this direction (only), diffusion processes are negligible compared with convection; and (3) no disturbances are propagated upstream antiparallel to this direction. The three-dimensional boundary-region equations are obtained as a subset of the parabolic Navier-Stokes equations with the single but significant assumption that a known pressure distribution is superimposed upon the flow field. The velocity vector lying on a three-dimensional Euclidean space spanned by a rectangular Cartesian coordinate system x_i is identified as

$$u_i \equiv u_1\hat{i} + u_2\hat{j} + u_3\hat{k} \tag{1}$$

For development of the governing equation system, assume that $\hat{i}$ is parallel to the predominant flow direction. Identify the two-dimensional vector differential operator

$$(\,)_{,k} \equiv \hat{j}(\,)_{,2} + \hat{k}(\,)_{,3} \tag{2}$$

where the comma identifies the gradient operator. In Cartesian tensor notation, with summation over 2 and 3 for repeated Latin subscripts, the parabolic Navier-Stokes equation system for a multiple-species, compressible, reacting flow takes the form

$$0 = (\rho u_i)_{,i} + (\rho u_1)_{,1} \tag{3}$$

$$\rho u_1 Y^{\alpha}_{,1} = \left(\frac{\mu^e}{N_{Sc}N_{Re}} Y^{\alpha}_{,k}\right)_{,k} - \rho u_k Y^{\alpha}_{,k} + S^{\alpha} \tag{4}$$

$$u_1 u_{j,1} = \left(\frac{\mu^e}{N_{Re}} u_{j,k}\right)_{,k} - u_k u_{j,k} - p_{,j} \tag{5}$$

$$\rho u_1 H_{,1} = \left(\frac{\mu^e}{N_{Re}N_{Pr}} H_{,k}\right)_{,k} - \rho u_k H_{,k} - \gamma M_\infty{}^2 \left[\frac{1 - N_{Pr}}{N_{Pr}} \frac{\mu^e}{2N_{Re}} \left(u_j{}^2\right)_{,k}\right]_{,k}$$

$$- \left(\frac{N_{Sc} - N_{Pr}}{N_{Sc}N_{Pr}} \frac{\mu^e}{N_{Re}} \sum h^{\alpha} Y^{\alpha}_{,k}\right)_{,k} \tag{6}$$

The variables appearing in equations (3) to (6) are nondimensionalized with respect to ρ_∞, U_∞, H_∞, and a length constant L, and have their usual interpretation in fluid mechanics. The Reynolds number N_{Re}, Prandtl number N_{Pr}, and Schmidt number N_{Sc} are defined for a combination of laminar and turbulent contributions as, for example,

$$\frac{\mu^e}{N_{Pr}} \equiv \frac{\mu}{N_{Pr}} + \frac{\rho\epsilon}{(N_{Pr})_T} \tag{7}$$

In equation (7), μ is the laminar viscosity, ϵ is the kinematic eddy viscosity, and the subscript T denotes a turbulent reference parameter. The stagnation enthalpy is defined in terms of species static enthalpies as

$$H \equiv \sum_{\alpha} h^{\alpha} Y^{\alpha} + \frac{1}{2} u_k{}^2 \tag{8}$$

The static enthalpy includes the heat of formation h^{α}_o of the species in its definition as

$$h^{\alpha} \equiv \int_{T_o}^{T} c_p^{\alpha}\, dT + h^{\alpha}_o \tag{9}$$

An equation of state is required to close the system. Assuming perfect-gas behavior for each species, from Dalton's law,

$$p = \rho R T \sum_{\alpha} \frac{Y^{\alpha}}{W^{\alpha}} \tag{10}$$

where R is the universal gas constant and W^{α} is the molecular weight of the αth species.

There are two approximate methods which may be effectively used to describe reacting hydrogen-oxygen-air systems. In the first case, assume that prototype scramjet combustors are adequately described by equilibrium combustion. The following reactions are operative:

$$\left.\begin{aligned} &2H + O \rightleftharpoons H_2O \\ &2H \rightleftharpoons H_2 \\ &2O \rightleftharpoons O_2 \\ &H + O \rightleftharpoons OH \\ &N_2 + 2O \rightleftharpoons 2NO \end{aligned}\right\} \tag{11}$$

The equilibrium composition of the combustion byproducts is determined by applying the law of mass action (ref. 6) to each reaction defined in equations (11). This yields definition of a set of equilibrium constants K, which, for the simple reaction $nA + mB \rightleftharpoons \ell C$, are expressed in terms of species mole fraction X^{α} as

$$K \equiv \frac{\left[X^A\right]^n \left[X^B\right]^m}{\left[X^C\right]^{\ell}} \tag{12}$$

Solution of equation (11), coupled with equation (12) and conservation of total and elemental mass, yields an algebraic equation system for determination of the equilibrium composition of the system, of the form

$$\left[N_{\alpha\beta}\right]\left\{X^{\alpha}\right\} = \left\{\text{Constant}\right\} \tag{13}$$

In equation (13), the elements of the matrix [N] account for the distribution of the particular species mole fraction $\left\{X^{\alpha}\right\}$ containing the βth elemental material, for example, O, H, and N.

Solution of the equilibrium temperature and species concentration requires an iterative solution to a nonlinear algebraic equation system. A considerably less expensive method (from the standpoint of computer time) may be employed to obtain an upper limit on the effects of heat release on the flow field development. The mole fractions of the dissociated species O and H are usually small compared with those of O_2 and H_2. Equations (11) may then be considerably simplified by assuming that the complete reaction

$$H_2 + \frac{1}{2} O_2 \rightarrow H_2O \tag{14}$$

is the only reaction that occurs. In this case all the H_2 reacts with the available O_2 to form H_2O. By describing the variation of specific heats with temperature through a polynomial relationship of the form $c_p \equiv a + bT + cT^2$, the temperature is solved explicitly in terms of the enthalpy and pressure without iteration.

For internal flows, characterized by boundary-layer thicknesses which are small in comparison with the overall internal duct dimension, the pressure distribution can be accurately approximated by inviscid flow solutions. However, in the alternate case where the flow is confined in a duct whose lateral dimension is not large with respect to the boundary-layer thickness, this approach is invalid. Here, boundary-layer development directly influences the pressure distribution within the duct, and an axial pressure gradient is induced by viscous effects. For these flows, a quasi-one-dimensional integral treatment of equations (3) and (5) has been suggested (refs. 17 and 20), wherein for steady flows, equations (3) and (5) are integrated across the duct transverse dimensions to obtain an equivalent expression written on mass-averaged dependent variables defined by

$$Q \equiv \frac{1}{\dot{m}A} \int_{A(x_1)} \rho u_1 q \, d\tau \tag{15}$$

In equation (15), $A(x_1)$ is the duct area, which may be a function of axial location x_1; $\dot{m}$ is the mass flow rate

$$\dot{m} \equiv \rho u_1 A \tag{16}$$

and q represents a generalized dependent variable which may be selectively streamwise velocity u_1, static temperature T, or density ρ. Taking the logarithmic differential of equation (16) gives

$$\frac{dA}{A} = \frac{d\dot{m}}{\dot{m}} - \frac{du_1}{u_1} - \frac{d\rho}{\rho} \tag{17}$$

The integral momentum equation (eq. (5)) implies

$$A \, dp + F \, dx_1 + u_1 \, d\dot{m} + \dot{m} \, du_1 = 0 \tag{18}$$

where F is the retarding force per unit length of duct exerted by viscous interaction of the confined flow with the wall. The equation of state for a perfect fluid of constant molecular weight may be logarithmically differentiated to yield

$$\frac{d\rho}{\rho} = \frac{dp}{p} - \frac{dT}{T} \tag{19}$$

Combining equations (15) to (19) yields an explicit relation for axial pressure gradient as

$$p_{,1} = \frac{-\frac{F}{A} - \frac{2u_1}{A}\dot{m}_{,1} + \frac{\dot{m}u}{A^2}A_{,1} - \frac{\dot{m}u_1}{AT}T_{,1}}{1 - \frac{\dot{m}u_1}{Ap}} \tag{20}$$

If an initial pressure level and the detailed flow field at a given station are known, equation (20) can be evaluated and integrated to yield downstream pressure levels. To achieve this, the friction force per unit duct length is related to the wall shear stress τ as

$$F \equiv \tau p \tag{21}$$

where p is the wetted perimeter of the duct. For the rectangular combustor geometries considered herein as bounded by symmetry planes,

$$\frac{F}{A} = \frac{\tau}{x_2^w} \tag{22}$$

where τ is evaluated as a function of the local velocity gradient at the wall (ref. 20) and x_2^w is the distance from the center plane of the duct to the wall.

Calculation of the change in mass flow rate with respect to axial distance requires a computational distinction between the actual mass flow $\dot{m}^r$ and the computed mass flow $\dot{m}^f$. The difference between $\dot{m}^r$ and $\dot{m}^f$ provides an estimate of the pressure and pressure gradient required to maintain conservation of mass. The rate of change of mass flow with respect to x_1 is defined as

$$\dot{m}_{,1} = \frac{\Delta\dot{m}}{\Delta x_1} \tag{23}$$

where

$$\Delta\dot{m} = \Delta\dot{m}^f - \Delta\dot{m}^r \tag{24}$$

and

$$\Delta\dot{m}^r = \dot{m}^r(x_1 + \Delta x_1) - \dot{m}^r(x_1) \tag{25a}$$

$$\Delta\dot{m}^f = \dot{m}^r(x_1) - \dot{m}^f(x_1) \tag{25b}$$

$$\Delta x_1 \equiv (x_1)_{new} - (x_1)_{old} \tag{26}$$

In equation (25a), $\Delta\dot{m}^r$ represents the mass flow increment which results from the mass addition, whereas $\Delta\dot{m}^f$ (eq. (25b)) represents the mass flow error obtained at the

upstream station x_1. Examination of equations (20) and (23) to (25) shows that use of equation (23) will always provide a pressure gradient which tends to make the computed and actual mass flow discrepancy decrease and hence models the physical flow.

For the analyses presented herein, flow-field turbulence has been modeled by means of an eddy-coefficient hypothesis. It should be noted that more sophisticated alternatives exist; their application to the problem class at hand will occur as the data base expands, as has occurred for modeling turbulence in two-dimensional and simple three-dimensional flows (refs. 21 and 22). The computer code implementing the finite-element algorithm for the equation system has been developed so that higher order turbulence models may be directly incorporated into the governing equation set and solution vectors. Elementary mixing-length theory (MLT) has proved very useful in characterizing the mixing of mass, momentum, and energy over a wide variety of flow conditions (ref. 23). Bearing this in mind, as well as the essential boundary-layer character of the considered flows, the baseline turbulent model was selected as the MLT and was employed to compute the evolutionary (downstream) development of all dependent variables. The success of more sophisticated turbulence modeling may then be assessed on a quantitative basis to evaluate explicitly any improvements at the expense of introducing additional empirical relationships and/or constants.

The MLT model is employed to compute the eddy diffusivities of momentum ϵ, mass $\epsilon(N_{Sc})_T^{-1}$, and thermal energy $\epsilon(N_{Pr})_T^{-1}$. Each is expressed in terms of the mixing length ℓ, the mean longitudinal velocity u_1, and distance normal to the wall x_2, according to the equation

$$-\overline{uv} \equiv \epsilon \frac{\partial u_1}{\partial x_2} = \ell^2 \left| u_{1,2} \right| u_{1,2} \tag{27}$$

The mixing length is defined as

$$\ell \equiv \begin{cases} kx_2\omega & (0 \leq x_2 \leq \lambda\delta/k) \\ \lambda\delta\omega & (x_2 > \lambda\delta/k) \end{cases}$$

where

k	$= 0.435$
λ	sublayer constant
δ	boundary-layer thickness
x_2	coordinate normal to wall

The Van Driest damping coefficient is

$$\omega \equiv 1 - \exp\left(-\frac{\tilde{x}_2}{A}\right)$$

where

$\tilde{x}_2$ $\equiv \frac{\tilde{u}x_2}{\nu}$

$\tilde{u}$ friction velocity, $\sqrt{\tau/\rho}$

τ skin friction

ρ density at wall

ν kinematic viscosity

A $\equiv 23.5$

FINITE-ELEMENT SOLUTION ALGORITHM

The parabolic Navier-Stokes equation system and the three-dimensional boundary-region equation system excepting global continuity (eq. (3)) are uniformly constituted as initial boundary-value problems of mathematical physics. Each of the subject partial differential equations (eqs. (4) to (6)) is a special case of the general, second-order, nonlinear partial differential equation

$$L(q) \equiv \kappa\left[K(q)q_{,k}\right]_{,k} + f(q,q_{,i},x_i) + g(q,\chi) = 0 \tag{28}$$

where q is a generalized dependent variable identifiable with each computational dependent variable. In equation (28), f and g are specified functions of their arguments, χ is identified with x_1 for parabolic flows, and x_i are the coordinates for which second-order derivatives exist in the lead term. The finite-element solution algorithm is based upon the assumption that $L(q)$ is uniformly parabolic within a bounded open domain Ω; that is, the lead term in equation (28) is uniformly elliptic within its domain R, with closure ∂R, where

$$\Omega = R \times \left[\chi_o,\chi\right) \tag{29}$$

and $\chi_o \leqq \chi$. If equation (28) is uniformly parabolic, unique solutions for q are obtained upon specification of functional constraints on $\partial\Omega = \partial R \times \left[\chi_o,\chi\right)$ and an initial-condition specification on $R \cup \partial R \times \chi_o$. For constraints on $\partial\Omega$, the general form relates the function and its normal derivative everywhere on the closure ∂R as

$$\ell(q) \equiv a^{(1)}q(\bar{x}_i,\chi) + a^{(2)}Kq(\bar{x}_i,\chi)_{,k}n_k - a^{(3)} \equiv 0 \tag{30}$$

In equation (30), the $a^{(i)}(\bar{x}_i,\chi)$ are user-specified coefficients, the superscript bar notation constrains x_i to ∂R, and n_k is the local outward-pointing unit normal vector. For an initial distribution, assume that

$$q(x_i,\chi_o) \equiv q_o(x_i) \tag{31}$$

is given throughout $R \cup \partial R \times \chi_o$.

The finite-element solution algorithm is established for the equation system (28) to (31) by using the method of weighted residuals (MWR) formulated on a local basis. Since equation (28) is valid throughout Ω, it is valid within disjoint interior subdomains Ω_m described by $(x_i,\chi) \in R_m \times [\chi_o,\chi)$, called finite elements, wherein $\cup R_m = R$. An approximate solution for q within $R_m \times [\chi_o,\chi)$, called $q^*_m(x_i,\chi)$, is formed by expansion into a series solution of the form

$$q^*_m(x_i,\chi) \equiv \{\Phi(x_i)\}^T\{Q(\chi)\}_m \tag{32}$$

In equation (32), the functionals $\Phi_k(x_i)$ are subsets of a function set that is complete on R_m. The expansion coefficients $Q_k(\chi)$ represent the unknown χ-dependent values of $q^*_m(x_i,\chi)$ at specific locations interior to R_m and on the closure ∂R_m, called nodes of the finite-element discretization of R.

To establish the values taken by the expansion coefficients in equation (32), require that the local error in the approximate solution to both the differential equation $L(q^*_m)$ and the boundary-condition statement $\ell(q^*_m)$, for $\partial R_m \cap \partial R \neq 0$, be rendered orthogonal to the space of the approximation functions. By employing an algebraic multiplier λ, the resultant equation sets can be combined as

$$\underset{m}{S}\left[\int_{R_m} \{\Phi(x_i)\}\, L(q^*_m)\, d\tau - \lambda \int_{\partial R_m \cap \partial R} \{\Phi(x_i)\}\, \ell(q^*_m)\, d\sigma\right] \equiv \{0\} \tag{33}$$

where $\underset{m}{S}$ is the mapping function from the finite-element subspace R_m to the global domain R, commonly termed the assembly operator. The number of equations (33) prior to assembly is identical with the number of node points of the finite element R_m.

Equation (33) forms the basic operation of the finite-element solution algorithm and of the COMOC computer program. The lead term can be rearranged, and λ determined by means of a Green-Gauss theorem:

$$\int_{R_m} \{\Phi(x_i)\}\, \kappa\left[Kq^*_{m,k}\right]_{,k} d\tau = \kappa \oint_{\partial R_m} \{\Phi(x_i)\}\, Kq^*_{m,k} n_k\, d\sigma - \kappa \int_{R_m} \{\Phi(x_i)\}_{,k} Kq^*_{m,k}\, d\tau \tag{34}$$

For $\partial R \cap \partial R_m$ nonvanishing (eq. (34)), the corresponding segment of the closed-surface integral will cancel the boundary-condition contribution (eq. (33)) by identifying $\lambda a^{(2)}$ with κ of equation (28). The contributions to the closed-surface integral (eq. (34)), where $\partial R_m \cap \partial R = 0$, can be made to vanish (ref. 6). When equations (30) to (34) are combined, the globally assembled finite-element solution algorithm for the representative partial differential equation system becomes

$$\underset{m}{S}\left[-\kappa \int_{R_m} \{\Phi\}_{,k} K q^*_{m,k} d\tau + \int_{R_m} \{\Phi\}(f^*_m + g^*_m) d\tau \right.$$

$$\left. - \kappa \int_{\partial R_m \cap \partial R} \{\Phi\}\left(a^{(1)}_m q^*_m - a^{(3)}_m\right) d\sigma \right] = \{0\} \tag{35}$$

The rank of the global equation system (eq. (35)) is identical with the total number of node points on $R \cup \partial R$ for which the dependent variable requires solution. Equation (35) is a first-order, ordinary differential system, and the matrix structure is sparse and banded. Solution of the ordinary differential equation system is obtained by using a predictor-corrector finite-difference numerical integration algorithm (ref. 6).

A solution algorithm is required for the continuity equation, which is retained as equation (3) for boundary-region flows. Since equation (3) is an initial-value problem on ρu_2 as a function of x_2, with x_1 and x_3 appearing as parameters, the approximation function need span only the transverse coordinate direction as

$$(\rho u_2)^*_m = \{\Phi(x_2)\}^T \{\rho V(x_1, x_3)\}_m \tag{36}$$

The matrix elements of $\{\rho V\}$ are nodal values of ρu^*_2; their functional dependence requires solution of equation (3) along lines (x_1, x_3) equal a constant. Since equation (3) exists in standard form as an ordinary differential equation, direct numerical quadrature yields the required solution at node points of the discretization.

COMOC COMPUTER PROGRAM

The COMOC computer program system is being developed to transmit the rapid theoretical progress in finite-element solution methodology into a viable numerical solution capability. In the course of generating this general-purpose system, several variants of COMOC have been developed for specific problem classes, including transient thermal analysis and the two-dimensional Navier-Stokes equations as well as the three-dimensional boundary-region equations. The present operational variant of COMOC is capable of solving each of these problem classes and has been extended to include the parabolic Navier-Stokes equation system. An on-line restart feature allows the user to

switch between boundary-region and parabolic Navier-Stokes systems according to the requirements of the problem at hand. Generated solutions determine the three-dimensional distribution of all dependent variables and solution parameters for flow of a viscous, heat-conducting, multiple-species, compressible fluid including combustion. The flow may be external or confined, subsonic or supersonic, laminar and/or turbulent, and can contain up to nine or more distinct species in frozen composition or undergoing equilibrium or complete chemical reaction for a hydrogen-oxygen-air system.

The finite-element solution algorithm is utilized to cast the original initial-valued, elliptic boundary-value problems into large-order systems of purely initial-value problems. The program then integrates the discretized equivalent of the governing equation system in the direction parallel to the predominant flow. Initial distributions of all dependent variables may be arbitrarily specified, and boundary constraints for each can be specified by the user on arbitrarily disjoint segments of the solution domain closure. The solutions for each dependent variable, and all computed parameters, are established at node points lying on a specifiably nonregular, computational lattice formed by plane triangulation of the elliptic portion of the solution domain. Each of the computational triangles is spanned by a linear approximation function used for all independent and dependent variables as well as each solution parameter.

The COMOC system is built upon the macrostructure illustrated in figure 3. The main executive routine allocates core by means of a variable dimensioning scheme based upon the total degrees of freedom of the global problem. The size of the largest problem that can be solved is thus limited only by the available core of the computer in use. The precise mix between number of dependent variables (and parameters) and fineness of the discretization is user-specifiable and widely variable. The input module serves its standard function for all arrays of dependent variables, parameters, and geometric coordinates. The discretization module forms the finite-element discretization of the elliptic solution domain and evaluates all required finite-element nonstandard matrices and standard-matrix multipliers. The initialization module computes the remaining initial parametric data required to start the solution. The integration module constitutes the primary execution sequence of problem solution. It utilizes a highly stable, predictor-corrector integration algorithm for the column vector of unknowns of the solution. Calls to auxiliary routines for parameter evaluation (viscosity, Prandtl number, source terms, combustion parameters, etc.) as specified functions of dependent and/or independent variables are governed by the integration module. The user has considerable latitude to adapt COMOC to the specifics of his particular problem by directly inserting readily written subroutines to compute special forms of these parameters. The output module is similarly addressed from the integration sequence and serves its standard function via a highly automated array display algorithm. COMOC can execute distinct problems in sequence and contains an automatic restart capability to continue solutions.

EXPERIMENTAL DATA

The presented theoretical model has been applied to the prediction of mixing and reaction of hydrogen in a supersonic flow field simulating a scramjet combustor. Two hydrogen injector arrangements were considered: (1) a row of circular orifices on the wall that inject hydrogen transverse to the main flow and (2) strut injectors in both a parallel and a transverse injection configuration. Before discussing the comparisons between theory and experiment, it is appropriate to review the source and nature of the experimental data.

Nonreacting Flow

In the experimental investigation reported in references 8 and 9, hydrogen was injected from multiple, laterally disposed circular orifices transverse to a nominal Mach 4 airstream over a flat plate. The turbulent boundary layer was approximately 3 injector diameters thick at the injector station (without injection). Tests were conducted for ratios q_r of jet dynamic pressure to main-stream dynamic pressure of 0.5, 1.0, and 1.5. Each of these conditions was sufficient to maintain the injectors in a choked condition. For each value of q_r, data were obtained at stations $x_1/d = 7$, 30, 60, and 120 downstream of the point of injection, and for individual injector spacings s/d of ∞ (single jet), 12.5, and 6.25. At each test condition (q_r and s/d) and at each station x_1/d, the hydrogen-air mixing region was mapped by making a vertical survey directly downstream of the center jet and horizontal surveys at three elevations above the plate surface. In each survey, the measurements consisted of a two-dimensional mapping of local pitot and static pressures and the molar concentration of hydrogen. From these data, profiles of velocity, mass flux, and hydrogen mass fraction were determined. Details of the probe design, measurements, and data reduction may be found in references 8 and 9.

Reacting Flow

An experimental investigation of the reaction of hydrogen in a hot supersonic test gas flowing through a two-dimensional duct is reported in reference 10. The hydrogen was injected at ambient temperature and transverse to the main flow from rows of circular orifices in opposite walls of the duct. The test gas, a simulation of supersonic airflow at altitude, was supplied by a burner in which hydrogen, oxygen, and air mixtures were reacted in such proportions that the resulting oxygen concentration of the mixture was 21 percent by volume (vitiated air). Nominal stagnation conditions of the test gas were 2200 K and 2.7 MN/m^2 at a Mach number of 2.7. Details of the burner operation are given in references 24 and 25. Several injector configurations differing in the number, size, and spacing of the distinct injectors were tested at nominal equivalence ratios

ϕ of 0.5 and 1.0. An equivalence ratio of unity signifies a stoichiometric mixture; less than unity indicates fuel-lean operation. Data measurements consist of two-dimensional distributions of wall static pressure, bulk heat transfer to the water-cooled wall, and surveys of pitot pressure and gas composition across the horizontal center plane of the duct exit.

Strut Injector Tests

Additional reacting-flow data have been obtained (ref. 11) for parallel and perpendicular (to the main flow) injection of hydrogen from strut injectors spanning the combustor. The objective of these tests was to determine the flow fields produced by simple strut injectors and to compare these results with theory based on a one-dimensional analysis and empirical mixing models. For these tests a hot-gas simulation of Mach 7 flight was made. The test gas was supplied by the hydrogen-oxygen-air burner mentioned in the previous section. For the perpendicular injection strut, the hydrogen was injected from equally spaced, choked orifices drilled just downstream of a modest rearward-facing step located at the maximum strut thickness. The parallel injection strut employed five equally spaced conical nozzles in the base of strut. Aerodynamically, both struts were simple 6° half-angle wedges that spanned the width of the duct. Data acquisition consisted of distributions of duct-wall static pressure and surveys of pitot pressure and gas composition on the horizontal center plane at the duct exit. Details on the operation of the hydrogen-oxygen-air burner, the probe measurements, and data reduction can be found in references 24 and 25.

NUMERICAL RESULTS

The objective of this study is to formulate and evaluate a theoretical model for describing the complex three-dimensional phenomena associated with scramjet combustion of hydrogen-air systems at supersonic speeds. It has been hypothesized that the finite-element solution algorithm for the governing three-dimensional equation systems, coupled with elementary mixing-length turbulence modeling and constant Schmidt and Prandtl numbers, represents an adequate first step toward the desired goal. The numerical results presented in this section verify this supposition and its limitations and are presented in three categories. First, it is essential that the accuracy and convergence character of the finite-element solution algorithm be numerically assessed and verified. Results which provide this required information are presented for lower dimensional problems involving laminar and turbulent flows. Second, it is necessary to validate the hypothesized turbulence model by correlation of predictions with experimental test data over a wide range of design parameters. Finally, for the theoretical model to be viable as a design tool, it is necessary to establish a means for extending the initialization pro-

cedures to hot flow and to obtain correlation with experimental data for practical combustor configurations. The numerical results of these three distinct phases are correspondingly discussed in this section.

Accuracy and Convergence

As noted in the Introduction, the conventional two- and three-dimensional boundary-layer equations represent a dimensionally degenerate subset of the equation systems under study for application to supersonic combustion devices. With the boundary-condition versatility that is intrinsic in the finite-element solution technique, it is possible to establish a two-dimensional solution within the three-dimensional solution domain and solve the corresponding supersonic boundary-layer problem without alteration to the code. The generated results may then be evaluated for accuracy and convergence by comparison with solutions produced by finite-difference techniques and with a similarity solution for constant specific heat. The check case corresponds to a nominal Mach 5, laminar, two-dimensional, air boundary-layer flow over an adiabatic wall in a favorable pressure gradient. With the assumption of constant specific heat, the flow is isoenergetic and it is necessary only to solve the x_1 momentum equation and the continuity equation. The initial distribution for longitudinal velocity u_1 is established from the similar solution for $\beta = 0.5$ and $S = 0$ of reference 26. The initial distribution for u_2 is obtained iteratively, and Sutherland's law is employed to compute viscosity.

The test case is initialized at $x_1 = 0.03$ m downstream from the leading edge. The boundary-layer thickness at this station δ_o is 0.0039 m, the local Mach number M_e is 3.77, the Reynolds number N_{Re} is 0.83×10^5 per meter, and the adiabatic wall temperature T_w is 1000 K. Shown in figure 4 are the COMOC computed distributions of skin friction, local free-stream Mach number, and boundary-layer thickness for the case of constant specific heat. These were obtained with two uniform finite-element discretizations corresponding to four and eight elements spanning the initial boundary-layer thickness. The input static pressure distribution $p_e(x_1)$ is also presented for reference. The boundary-layer thickness has increased more than fourfold within the solution domain. Only small differences, on the order of about 2 percent, exist between the two solutions, the finer discretization producing a slightly larger skin friction and smaller local Mach number. Superimposed in figure 4 for comparison purposes are the results for the similar solution (ref. 26) and a 20-zone finite-difference solution obtained with the Von Mises coordinate transformation. Agreement among the four solutions is excellent (within 2 percent) for skin friction. The similar solution for M_e lies between the COMOC and finite-difference solutions, and overall agreement is within ±3 percent.

Shown in figure 5 are computed velocity profiles at $x_1/\delta_o = 22.7$, which is about midway through the presented solution domain. Shown for reference is the initial longi-

tudinal velocity profile with the node locations of the four-element discretization superimposed. Both COMOC solutions produce u_1 distributions that are slightly more concave upward in the midregion in comparison with the similar or finite-difference solution. The eight-element COMOC solution lies closer to the similar solution in the region where the two finite-element solutions differ. The finite-difference solution lies appreciably below both the COMOC and similar solutions near the free stream. The computed transverse velocities, which are also plotted in figure 5, show only slight differences between the two discretization solutions. The trends of the COMOC solutions are in excellent agreement with the established procedures; unfortunately, since each method of solution is distinctly numerical, no absolute accuracy assessment is established. However, for an incompressible boundary-layer flow, absolute accuracy and convergence rates for the finite-element solution have been established to be close to theoretically predicted values (ref. 27).

This check case establishes an accuracy assessment of solution of three-dimensional boundary-region equations. A similar evaluation of the parabolic Navier-Stokes equation system has been obtained for three different channel flow configurations. Figure 6 summarizes the results for a nonreacting subsonic flow to evaluate the ability of the pressure solution algorithm (eq. (20)) to compute a constant streamwise gradient. For the fully developed channel flow, streamwise velocity and the pressure gradient are computationally maintained to within ±2.5 percent of their initial values. The computations for developing channel flow correctly predicted the downstream distance required to attain fully developed flow; that is, COMOC predicted that the flow was fully developed at $x_1/h = 33$ (compared with $x_1/h = 30$ reported in ref. 28). A similar evaluation was performed to assess channel flow computations with heat addition. Conditions were selected such that in the initial portion of the flow, reaction of hot air with cold hydrogen induces a favorable pressure gradient (heat addition in subsonic flow). However, after the available oxygen supply is exhausted, the continued mixing of the cold hydrogen with the heated combustion products produces an overall temperature drop and, hence, an adverse pressure gradient. The computational results are summarized in figure 7; the trends are observed to have been correctly captured by COMOC while maintaining conservation of mass to within ±1.0 percent.

Correlation With Cold-Flow Data

Early design studies of a prototype injection scheme for a supersonic combustor (ref. 3) considered the transverse injection of hydrogen as the primary means of fuel introduction into the airstream. Consequently, as discussed in the previous section, detailed concentration, velocity, and pressure measurements were made for an appropriately scaled experimental configuration (shown in fig. 8). As a function of the dynamic pressure ratio, the sonically injected hydrogen penetrates the turbulent supersonic air

boundary layer to a certain distance and in the process turns downstream as illustrated. This complex turning phenomenon exerts considerable influence on the initial mixing of the injectant with the main flow. Furthermore, and of equal importance, the subsequent hydrogen distributions (fig. 8) are convected downstream by the main flow while the hydrogen diffuses in the plane transverse to this direction. For multiple-injector configurations, the concentration patterns merge as illustrated; thus, a three-dimensional effect in addition to mixing and reaction is imposed.

To verify a viable theoretical model, it is necessary to evaluate the appropriateness of the hypothesized mixing-length turbulence model. The detailed experimental results of Rogers (refs. 8 and 9) for the configuration illustrated in figure 8 provide the necessary data base for comparison of predictions. Initial conditions for the predictions were established from these data, and the downstream station at $x_1/d = 30$ was selected as the initialization station. The original raw data consist of a single vertical traverse and three lateral traverses on the transverse plane at several x_1 stations. The measured hydrogen mass fraction distributions appear of Gaussian shape; however, the symmetry plane of the data was variously displaced from the geometric symmetry plane. Although the entire flow field could be computed numerically, the strong appearance of a data symmetry plane suggested establishment of a corresponding computational solution domain. Therefore, a cubic spline interpolation program was applied to the raw data program to establish the x_3/d location of the data symmetry plane via a minimization criteria on the wings of the Gaussian-type distributions. The spline package then interpolated the raw data for hydrogen mass fraction and u_1 and output the evaluation of the interpolation polynominals at node points of the finite-element discretization of the transverse plane. A representative case of the spline-computed distributions of hydrogen mass fraction is shown in figure 9 in comparison with the spread and context of the experimental data.

Although plots of the form of figure 9 are geometrically aesthetic, the transition from the initial distributions and significant detail on solution accuracy and trends are better obtained by plotting concentration profiles $(x_2/d$ against $Y^H)$ along planes $x_3/d = \text{Constant}$ at each longitudinal station for which data measurements exist. The parameters evaluated experimentally include dynamic pressure ratio q_r and discrete injector spacing s/d for a Mach 4 flow in an unconfined geometry:

Discrete injector spacing, s/d	Dynamic pressure ratio, q_r		
	0.5	1.0	1.5
∞	✓	✓	✓
12.5	✓	✓	✓
6.25	✓		

Computational evaluation of the influence of all conditions has been made with the three-dimensional boundary-region variant of COMOC and a nonuniform discretization of the transverse plane (R in eq. (29)) into 100 finite elements. As the study progressed, computational evaluations were also made of the influence of a nonzero transverse velocity component u_3 as well as the magnitude of the sublayer constant λ in the mixing-length model.

Presented in figures 10 and 11 are the computed distributions of hydrogen mass fraction on planes $x_3/d = \text{Constant}$ at downstream stations $x_1/d = 60$ and 120 for the test conditions $q_r = 1.0$ and $s/d = 12.5$. In addition, the "universally" accepted value $\lambda = 0.09$ of the mixing-length model (eq. (27)) was employed, and zero transverse velocity was assumed. In all cases, the symbols represent data or data spread corresponding to "best symmetry" at the particular location. The solid curves denote the computed distributions, and each dashed curve corresponds to the initial distribution faired through the data at $x_1/d = 30$, which is presented for reference. At the first downstream station (fig. 10), agreement of the computational predictions with data is generally acceptable everywhere except near the plate surface for the first two profiles corresponding to the plane of symmetry and the next adjacent plane, $x_3/d = 0$ and 1.0. Agreement with data is degraded somewhat at the far downstream station (fig. 11), with predictions missing data points both near the wall and near the peak for the first two representations. Out of the core region of the jet, agreement with data remains quite good, however.

The correlation between predictions and data for the test case shown in figures 10 and 11 is a significant improvement over previous attempts (ref. 5). For good agreement in the centroidal region of the hydrogen jet, it is necessary that the maximum hydrogen concentration remain off the wall. Therefore, either from three-dimensional effects or a complex turbulence interaction between the jet and the wall, there is a mechanism in play capable of resisting the unidirectional trend of maximum diffusion to the wall. It has been hypothesized, as a result of the initial studies (ref. 5), that the existence of a mass flux transverse to the main flow direction and along the plate surface might account for the experimentally measured centroidal peak. Such a transverse mass flux could be initiated by the displacement effect of the sonic hydrogen jet issuing transverse to the main flow, since in such an interaction problem, the jet appears to the mainstream flow in many ways similar to an impervious body. Consequently, immediately downstream of the transverse jet, there must exist an approximately spheroidal fixed recirculation region near the wall, and a transverse mass flux would be required to alleviate a localized low-pressure area just downstream of this bubble.

This hypothesis was computationally evaluated for the test case just described by imposition of a small negative, transverse velocity distribution beneath the measured hydrogen concentration maximum at $x_1/d = 30$. The magnitude and vertical extent of the imposed transverse velocity on the symmetry center plane are shown in figure 12(a).

Figure 12(b) illustrates the lateral spread of the imposed transverse velocity distribution. For reference purposes, figure 12(a) also illustrates the longitudinal velocity distribution u_1 on the center plane at the initial station $x_1/d = 30$ as well as the predicted distributions at the remaining downstream data stations.

The influence of the imposed transverse velocity on the predicted distributions of hydrogen mass fraction at the two downstream data stations is shown in figures 13 and 14. The selected u_3 velocity distribution is observed not to alter significantly the mass fraction distributions above the peak but does substantially promote the existence of a local off-plate maximum in the centroidal region at $x_1/d = 60$. However, by the time the last data station is reached (fig. 14), the imposed transverse velocity distribution has been essentially dissipated (see fig. 12), and the computed distributions of hydrogen mass fraction in the centroidal region are noted to revert to the form of the maximum existing at the plate surface. It can be concluded, therefore, that transverse mass flow is probably of influence in the near region downstream of the point of injection. However, there is as yet some undetermined mechanism for maintaining the off-axis peak in the mass fraction distribution at stations far downstream. This undoubtedly points to some deficiency in the turbulent mixing model for this configuration and serves to emphasize the need for a more comprehensive theoretical model for describing three-dimensional turbulent mass mixing. For example, an approach based on turbulent kinetic energy and dissipation function might prove valuable.

After some computational experimentation, it was determined that all data could be correlated with superior accuracy by changing the value of the mixing-model sublayer coefficient λ to 0.07 and keeping $(N_{Pr})_T = 0.7$. (It should be noted that essentially the same hydrogen distributions could be predicted using the combination of $\lambda = 0.09$ and $(N_{Pr})_T = 0.90$. The difference between solutions obtained using $\lambda = 0.07$ and $(N_{Pr})_T = 0.7$ would be primarily in the velocity field.) Although this differs from the universally accepted value, it is certainly not unreasonable to expect this value to change somewhat because of the three-dimensional character of the problem being studied. The effect of λ on predicted distributions of hydrogen mass fraction is shown in figures 15 and 16 for the test case $q_r = 1.0$ and $s/d = 12.5$. The previous good agreement obtained at station $x_1/d = 60$ (fig. 3) has not been degraded and has actually been improved away from the core region. More importantly, at $x_1/d = 120$, a distinct improvement in agreement with the data for all profiles is indicated. Since the purpose of the present study is not a detailed development of a mixing model per se but evaluation of the analytical concept, the value of $\lambda = 0.07$ is used uniformly in all subsequent data correlations for both cold- and hot-flow configurations.

The influence of injectant dynamic pressure ratio q_r on the validity of the hypothesized mixing-length turbulence model has been evaluated for the test cases $s/d = 12.5$,

$\lambda = 0.07$, and $u_3 = 0$ at $q_r = 0.5$, 1.0, and 1.5. A summary of the results is presented in figure 17, which shows the comparison between predictions and data on the symmetry center plane $x_3/d = 0$ and at the lateral plane $x_3/d = 2.0$. By and large, agreement with data is consistent except for the low-pressure case ($q_r = 0.5$ on the symmetry plane), where overdiffusion is predicted. The trend of these results might have been anticipated in that the test case at the lowest dynamic pressure ratio corresponds to a weak jet dominated by near-wall effects. Imposition of a transverse velocity field u_3 might enhance agreement. This has not been verified, however, since low dynamic pressure ratios are of marginal practical interest.

The influence of spacing between discrete ejectors s/d has been computationally evaluated for $q_r = 1.0$ and $s/d = 12.5$ and ∞. Although more data exist for $q_r = 0.5$, the results of this comparison are liable to be inconclusive on the basis of the relatively poorer agreement seen in figure 17. Computed distributions of hydrogen mass fraction are shown in figure 18 in comparison with data for the symmetry center plane $x_3/d = 0$ and one other plane ($x_3/d = 2.0$ for $s/d = 12.5$ and $x_3/d = 2.5$ for $s/d = \infty$). The values $\lambda = 0.07$ and $u_3 = 0$ were retained for this comparison, and agreement of the predictions with data on the symmetry plane is observed to be consistent with previous experience. Somewhat poorer agreement exists off the symmetry plane for the single jet ($s/d = \infty$). This result might be expected, as three-dimensional diffusion effects are probably more dominant for the single jet, since it diffuses into a doubly unbounded domain. All multiple-jet configurations are expanding into only a singly unbounded domain downstream of merged interaction.

As with any multidimensional computations in compressible viscous fluid mechanics, it is important to establish a quantitative accuracy assessment. For the cold-flow configuration studied and reported herein, an accuracy measure of the adequacy of the employed discretization is possible by determining the conservation properties of the solution. For the cold mixing case, the species-continuity equation for hydrogen mass fraction can be written in explicit conservation form. Integrating this equation over a three-dimensional control volume and using Gauss' theorem (ref. 5) determines that the total hydrogen mass flow, that is, $\rho u_1 Y^H$, would be rigorously conserved by an analytic solution. COMOC evaluates this parameter at each output station by using linear finite-element approximation functionals for each variable and performing the integrations analytically. (Thus, the order of accuracy of the evaluation is consistent with that of the solution of the partial differential equations.)

For the test conditions $q_r = 1.0$, $s/d = 12.5$, and $u_3 = 0$, with $\lambda = 0.07$ (see figs. 15 and 16), a monotonically increasing loss of hydrogen mass flow with increasing distance downstream was computed; at $x_1/d = 120$, the computed loss equaled 8.8 percent of the mass flow computed at station $x_1/d = 30$. The 100-element standard nonuniform discretization was refined by a factor of 2 in each coordinate direction to produce

400 finite elements spanning R (see fig. 19, diagonals omitted), and the computation was repeated on $30 \leq x_1/d \leq 60$. Over this interval, the coarse discretization yielded a computed 5-percent loss in hydrogen mass flow. The fine discretization produced a modest variation in computed hydrogen mass flow over the initial interval, with a $1\frac{1}{2}$-percent net loss computed by $x_1/d = 60$. The resulting detailed differences in computed distributions of hydrogen mass fraction are shown in figure 20. Above the peak and outside the core region, differences are undiscernible on the scale of the plots. Within the core region, the maximum difference in computed hydrogen levels is less than 8 percent, which compares favorably with the 10- to 20-percent spread of the "best symmetry" data. The computational expense of these comparison solutions differed by over an order of magnitude. On an IBM 360/65, using no out-of-core devices for either case, the CPU time of the 100-element solution was about 250 seconds; on the same interval, the 400-element solution required 2600 seconds! Two parts constitute this increase (see ref. 6): a factor of about 4, due to the fact that the element DO loops in COMOC were 4 times longer, and a multiplicative factor of about 2, due to increased solution stiffness resulting from the refined grid itself. The ability of coarse finite-element discretizations, using low-order functionals, to preserve adequate engineering solution accuracy appears a distinct feature of the algorithm.

From these extensive correlations with data and the comprehensive numerical experimentation, it appears that the mixing-length turbulence model coupled with the finite-element solution of the three-dimensional boundary-region equation system provides an adequately accurate diagnostic tool for three-dimensional mixing of cold hydrogen injected into a supersonic turbulent boundary layer for dynamic pressure ratios q_r greater than 0.5 and for multiple jet configurations. Hence, the results discussed in these two sections give sufficient basis to pursue the computations detailed in the next section.

Extension to Hot-Flow and Combustor Correlations

A distinct feature of the three-dimensional boundary-region and parabolic Navier-Stokes equation systems is the capability to obtain a three-dimensional solution while marching in one coordinate direction. Elimination of the requirement for a downstream boundary condition is particularly important. For the subject mixing and combustion studies, however, the corresponding penalty is that an accurate initial condition is required to model adequately the complex near-injection flow field under study. In the previous section, the computations took advantage of detailed experimental profiles for the establishment of initial conditions. In the more general case, and in particular for hot-flow cases with combustion, detailed distributions of initial conditions are specifically unavailable, and a theoretical device for establishing the starting point of the solutions is required. Flow fields involving the parallel injection of dissimilar fluids present no dif-

ficulty, since smooth transitions occur and boundary-layer and shear-layer concepts are appropriate. However, for transverse injection, this is not the case, and some alternative means is required.

In anticipation of this need, a task in the early phases of the study was to evaluate the concept of a numerical "virtual source" as a means for eliminating the requirement for detailed initial conditions (ref. 5). Injection of a jet from an orifice in a plate transverse to a supersonic airstream has been the subject of a number of investigations. The important correlating parameter appears to be dynamic pressure ratio q_r. Most experimental data are for large values of q_r, for which the jet has sufficient momentum to penetrate the boundary layer and produce a complicated separation region and bow shock ahead of the jet. However, for the present cases, q_r ranges between 0.5 and 1.5, and a significant part of the jet remains within the turbulent boundary layer. Hence, mixing is initiated immediately downstream of injection. From these considerations, a theoretical model was proposed for establishing a barrel-shock—Mach disk hypothesis for turning of the transverse jet parallel to the main flow (see fig. 21). An analysis based on one-dimensional considerations was developed to characterize the jet turning. The important parameters in the model are dynamic pressure ratio q_r and free-stream Mach number M_∞, and the output is injectant momentum and flow area. Details of the model are presented in reference 5.

The validation of the concept of the virtual source as an initial-condition generator was accomplished by using the detailed cold-flow experimental data discussed in the previous section. Shown in figure 22 is the initial condition velocity surface, u_1 vs. (x_2,x_3), corresponding to a transverse cold hydrogen jet embedded (within the depression in the velocity surface) within the turbulent boundary-layer profile at $q_r = 1.0$. The detailed predicted distribution of hydrogen mass fraction are shown in figures 23 and 24 for the virtual-source simulation of the standard test case $(q_r = 1.0$ and $s/d = 12.5)$. For these computations, transverse velocity u_3 was assumed zero and $\lambda = 0.07$ in the turbulence model. Even after marching only 30 diameters downstream from the point of injection, agreement between the predictions and the data (fig. 23) is admirable, especially in the centroidal region, where there is an excellent prediction of an off-plate peak. At the final station $x_1/d = 120$ (fig. 24), agreement between the virtual-source simulation and data is excellent, being essentially identical with the results starting with data at $x_1/d = 30$ (fig. 11).

Shown in figure 25 is an alternative method for presenting these data which will be extended to the hot-flow comparisons. This figure presents the peak hydrogen concentration as a function of distance downstream. The agreement with data is excellent in the range $30 \leq x_1/d \leq 120$. The disagreement at $x_1/d = 7$ is not serious in light of the further downstream agreement; the indicated data point may well be significantly in error. Shown also in figure 25 are the trajectories of the peak hydrogen concentration above the

plate x_2/d and the lateral spread of the jet determined at the x_3/d coordinate where the local hydrogen concentration equals 10 percent of the local maximum. Observe that the local peak of the elevation trajectory sinks to the plate surface downstream of $x_1/d = 60$, as was observed for the multitudinous cold-flow data. The agreement of lateral spreading rate with data is excellent.

At the lower right in figure 25 is a computation of mixing efficiency η, defined as the fraction of hydrogen, integrated over the flow cross-sectional area at a given station, that would react if complete reaction with the available oxygen were to occur. This parameter has been used for correlating cold-flow data (ref. 9) and is readily computed by COMOC as an output parameter by means of the integration techniques utilized for measuring hydrogen mass flow. Hence, figures 23 to 25 demonstrate that the virtual-source concept of transverse hydrogen injection for the cold-flow configuration effectively simulates the injection phenomenon.

It is therefore hypothesized that the virtual-source concept is appropriate for combustion studies as well, and the experimental verification of this hypothesis is sought. As a first step, it is appropriate to measure the influence of combustion on the virtual-source cold-flow configuration. Shown also in figure 25 are computations carried out to $x_1/d = 30$ for the cold-flow simulation, but combustion of the hydrogen is now allowed to occur according to the complete-reaction hypothesis (eq. (14)). Note that the trajectory of maximum hydrogen mass fraction lies considerably above that for the cold-flow, nonreacting configuration. However, on the basis of mixing efficiency η, there is very little difference in overall mixing between the cold reacting and nonreacting cases.

The cold-flow problem is of marginal interest, however, since the average equivalence ratio of the cold-flow configuration ($\phi = 0.04$) lies well below the design level for a practical combustor. Note that equivalence ratio is defined (ref. 11) strictly in terms of the global mass flows of hydrogen and air. For stoichiometric combustion, $\phi = 1$; for fuel-lean operation, ϕ is less than 1. It is coincidental that the cold-flow virtual-source configuration can be thermodynamically altered (only) to correspond to conditions similar to test point 4 of reference 10. To simulate the test configuration, the cold flow was computationally vitiated by imposing an arbitrary uniform background hydrogen concentration (of 1 percent) and augmenting the oxygen level of the base flow such that the corresponding composition of the computational test gas simulates the hot (wet) air used for the experiment. The total temperature of the computational simulation was approximately 2000 K; the corresponding mass flow of cold hydrogen for the vitiated virtual source yielded $\phi = 0.4$, in comparison with $\phi = 0.5$ for the experiment. Shown in figure 25 are the trajectory of maximum hydrogen mass fraction, the elevation trajectory, and the lateral spreading rate for the vitiated virtual-source simulation of the test con-

figuration. Note that the elevation trajectory of the hot-flow configuration follows very closely the cold-flow data, a result possibly of the cold-wall ($T_w \equiv 0.5T_t$) boundary condition used for the computational simulation. It may also reflect the somewhat lessened lateral spreading rate for the vitiated reacting case, as shown in figure 25. Mixing efficiency was not computed for this vitiated combustion case. However, equivalence ratio, as a node point parameter, can be computed at any point in the solution domain. At the far right of the mixing-efficiency curve in figure 25, the experimentally determined range of equivalence ratio for test point 4 (ref. 10) is compared with the computed values. The presented computational values are in qualitative agreement with the experimental extremums on the center plane at the duct exit.

Of greatest practical importance, recent thinking on design of scramjet combustors hypothesizes that, depending upon flight Mach number, two fuel injection modes will be required. For example, an experimental model of a strut injector system (fig. 26) is currently under construction at Langley Research Center for evaluation of combustor performance as a function of injection mode. Design of this device was augmented by an earlier experimental program intended to evaluate the essential character of the two distinctly different injection modes proposed for this type of combustor (ref. 11). Sketches of the perpendicular and parallel injection struts that are associated with current design technology are shown in figure 27. In each case, given nearby is a virtual-source simulation of the proposed injection mode showing the location of the discrete injectors as well as the orientation of the virtual source within the computational domain. In the lower half of figure 27, an exploded view of the virtual-source simulation for the perpendicular injection mode is shown. The parallel injector corresponds to coaxial injection; its computational source domain is also shown in figure 27.

Velocity surface distributions for longitudinal velocity u_1 calculated for the virtual-source simulation of each injector configuration are shown in figures 28 and 29. Note that for the perpendicular injection strut (fig. 28), the cold hydrogen is embedded in a subsonic jet indicated by the severe depression in the velocity surface. This depression rapidly vanishes, as shown in the surface plot at the downstream station. Conversely, for the parallel injection mode (fig. 29), the simulation requires a supersonic hydrogen jet embedded within the air boundary-layer flow, hence the local velocity peak. This peak, likewise, is completely dissipated by the time the flow has proceeded downstream. To model this combustor, which employed a combustion duct with a modestly expanding cross-sectional area, the measured experimental pressure distribution was used for the computations, since COMOC is not yet operational with coordinate stretching functions in three dimensions.

Shown in figure 30 is the trajectory of the maximum hydrogen concentration as a function of injection mode for the experimental results reported in reference 11. Note

indeed that the perpendicular injection mode promotes much stronger mixing and hence produces a combustion process that proceeds considerably more rapidly than that corresponding to the parallel injection mode. Also plotted in figure 30 are the pressure distributions used for the computations, as well as the computed distribution of equivalence ratio on the center plane at $x_1/d = 150$ across one-half of a jet. Note that for the parallel injection mode, the range of computed equivalence ratio is twice that of the perpendicular case, in qualitative agreement with the data ranges from reference 11. Furthermore, the experimental evaluation of the differences in the flame shape for the two injection modes (ref. 11) with respect to apparent mixing rate is in agreement with the maximum hydrogen trajectories computed by the virtual-source simulation.

Hence, the analytical predictions are certainly not contrary to the available experimental information; more positively, they appear to be in essential agreement with the experimentally determined trends. Refinement of the theoretical model is certainly required, but the crucial confirmative results are at hand. The greatly detailed information available from the computational solutions may encourage the experimentalist to utilize the analytical capability to guide the design of future experiments. In this manner, important and relevant experimental data crucial to the ultimate verification of the validity of the analytical approach can be obtained. The availability of a computational and theoretical model that closely simulates the actual experimental configuration may thus enhance the overall value of the combustor design program in terms of information gained per unit expenditure of dollars and/or man hours. For example, when domain discretizations involving about 100 triangular finite elements were used, the parallel-strut test required only 1000 seconds of CPU time on an IBM 360/65 to run to $x_1/d = 200$. The perpendicular-strut test, with its much stronger mixing (and hence a stiffer differential equation system), required only 1500 seconds of CPU time to run to $x_1/d = 150$. Operation of the COMOC program is highly automated, and the same error criterion was used for both tests. An experienced user can prepare an entirely new data deck in about an hour. Execution of each test case, requiring evaluation of about 15 parameters and dependent variables at each node point of the discretization of R and at each downstream computational station, required about 340 000 bytes of rapid-access core in the computer. The next generation of computer hardware will significantly reduce present constraints with regard to both core requirements and CPU time.

CONCLUDING REMARKS

An analytical investigation has been presented on the turbulent mixing and reaction of hydrogen jets injected from multiple orifices transverse and parallel to a supersonic airstream. The proposed three-dimensional differential equation systems were solved by means of a finite-element algorithm in concert with a turbulent-mixing model based

on the elementary mixing-length hypothesis. The computational results have provided three-dimensional descriptions of the velocity, temperature, and species-concentration fields downstream of injection for geometries appropriate in practical combustor designs. Detailed comparisons between the predicted results and available experimental data have verified the validity of the analytical model and its ability to computationally simulate the experimental configuration with high fidelity. Thus, it appears that the newly emerged computational "laboratory" may well both supplement and supplant the experimental evaluation of prototype designs and, in particular, may facilitate detailed parametric studies.

REFERENCES

1. Becker, John V.; and Kirkham, Frank S.: Hypersonic Transports. Vehicle Technology for Civil Aviation – The Seventies and Beyond, NASA SP-292, 1971, pp. 429-445.

2. Bushnell, Dennis M.: Hypersonic Airplane Aerodynamic Technology. Vehicle Technology for Civil Aviation – The Seventies and Beyond, NASA SP-292, 1971, pp. 63-84.

3. Henry, John R.; and Beach, H. Lee: Hypersonic Air-Breathing Propulsion Systems. Vehicle Technology for Civil Aviation – The Seventies and Beyond, NASA SP-292, 1971, pp. 157-177.

4. Henry, John R.; and Anderson, Griffin Y.: Design Considerations for the Airframe-Integrated Scramjet. NASA TM X-2895, 1973.

5. Baker, A. J.; and Zelazny, S. W.: A Theoretical Study of Mixing Downstream of Transverse Injection Into a Supersonic Boundary Layer. NASA CR-112254, 1972.

6. Baker, A. J.; and Zelazny, S. W.: COMOC: Three-Dimensional Boundary Region Variant. Theoretical Manual and User's Guide. NASA CR-132450, 1974.

7. Orzechowski, J. A.; and Baker, A. J.: COMOC: Three-Dimensional Boundary Region Variant. Programmer's Manual. NASA CR-132449, 1974.

8. Rogers, R. Clayton: A Study of the Mixing of Hydrogen Injected Normal to a Supersonic Airstream. NASA TN D-6114, 1971.

9. Rogers, R. Clayton: Mixing of Hydrogen Injected From Multiple Injectors Normal to a Supersonic Airstream. NASA TN D-6476, 1971.

10. Rogers, R. C.; and Eggers, J. M.: Supersonic Combustion of Hydrogen Injected Perpendicular to a Ducted Vitiated Airstream. AIAA Paper No. 73-1322, Nov. 1973.

11. Anderson, Griffin Y.; and Gooderum, Paul B.: Exploratory Tests of Two Strut Fuel Injectors for Supersonic Combustion. NASA TN D-7581, 1974.

12. Pal, Alexander; and Rubin, Stanley G.: Viscous Flow Along a Corner. Part I. Asymptotic Features of the Corner Layer Equations. AFOSR-69-1225TR, U.S. Air Force, May 1969. (Available from DDC as AD 693 630.)

13. Cresci, R. J.; Rubin, S. G.; Nardo, C. T.; and Lin, T. C.: Hypersonic Interaction Along a Rectangular Corner. AIAA J., vol. 7, no. 12, Dec. 1969, pp. 2241-2246.

14. Rubin, Stanley G.; and Lin, Tony C.: A Numerical Method for Three-Dimensional Viscous Flow: Application to the Hypersonic Leading Edge. J. Comput. Phys., vol. 9, no. 2, Apr. 1972, pp. 339-364.

15. Caretto, L. S.; Curr, R. M.; and Spalding, D. B.: Two Numerical Methods for Three-Dimensional Boundary Layers. Comput. Methods Appl. Mech. & Eng., vol. 1, no. 1, June 1972, pp. 39-57.

16. Curr, R. M.; Sharma, Devraj; and Tatchell, D. G.: Numerical Predictions of Some Three-Dimensional Boundary Layers in Ducts. Comput. Methods Appl. Mech. & Eng., vol. 1, no. 2, Aug. 1972, pp. 143-158.

17. Patankar, S. V.; and Spalding, D. B.: A Calculation Procedure for Heat, Mass and Momentum Transfer in Three-Dimensional Parabolic Flows. Int. J. Heat & Mass Transfer, vol. 15, no. 10, Oct. 1972, pp. 1787-1806.

18. Amsden, Anthony A.; and Harlow, Francis H.: The SMAC Method: A Numerical Technique for Calculating Incompressible Fluid Flows. LA-4370, Los Alamos Sci. Lab., Univ. of California, Feb. 17, 1970.

19. Baker, A. J.: Finite Element Solution Theory for Three-Dimensional Boundary Flows. Comput. Methods Appl. Mech. & Eng., vol. 4, no. 3, Nov. 1974, pp. 367-386.

20. Patankar, S. V.; and Spalding, D. B.: Heat and Mass Transfer in Boundary Layers. Second ed. Int. Textbook Co. Ltd. (London), c.1970.

21. Free Turbulent Shear Flows. Volume I – Conference Proceedings. NASA SP-321, 1973.

22. Wheeler, A. J.; and Johnston, J. P.: An Assessment of Three-Dimensional Turbulent Boundary Layer Prediction Methods. Trans. ASME, Ser. I: J. Fluids Eng., vol. 95, no. 3, Sept. 1973, pp. 415-421.

23. Launder, B. E.; and Spalding, D. B.: Lectures in Mathematical Models of Turbulence. Academic Press, Inc., 1972.

24. Russin, William Roger: Performance of a Hydrogen Burner To Simulate Air Entering Scramjet Combustors. NASA TN D-7567, 1974.

25. Eggers, James M.: Composition Surveys of Test Gas Produced by a Hydrogen-Oxygen-Air Burner. NASA TM X-71964, 1974.

26. Christian, James W.; Hankey, Wilbur L.; and Petty, James S.: Similar Solutions of the Attached and Separated Compressible Laminar Boundary Layer With Heat Transfer and Pressure Gradient. ARL 70-0023, U.S. Air Force, Feb. 1970. (Available from DDC as AD 705 581.)

27. Popinski, Z.; and Baker, A. J.: An Implicit Finite Element Algorithm for the Boundary Layer Equations. J. Comp. Phys. (To be published, 1975).

28. Schlichting, Hermann (J. Kestin, transl.): Boundary-Layer Theory. Sixth ed. McGraw-Hill Book Co., Inc., 1968.

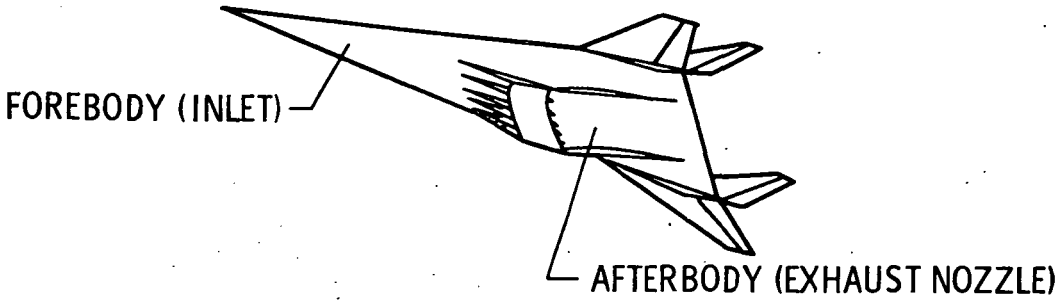

(a) Isometric view.

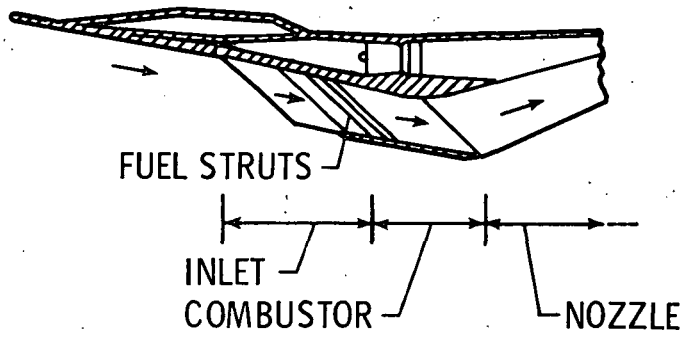

(b) Schematic of hypersonic propulsion system – scramjet operation above Mach 3.

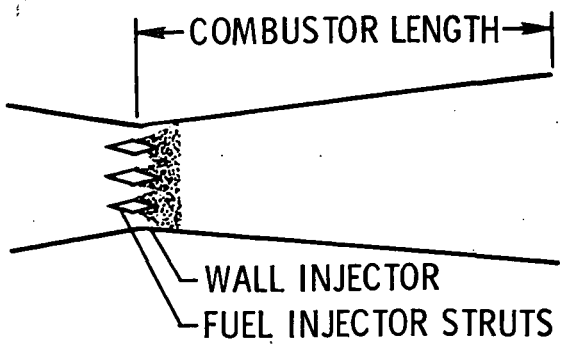

(c) Combustor length with in-stream fuel injection.

Figure 1.- NASA hypersonic research airplane.

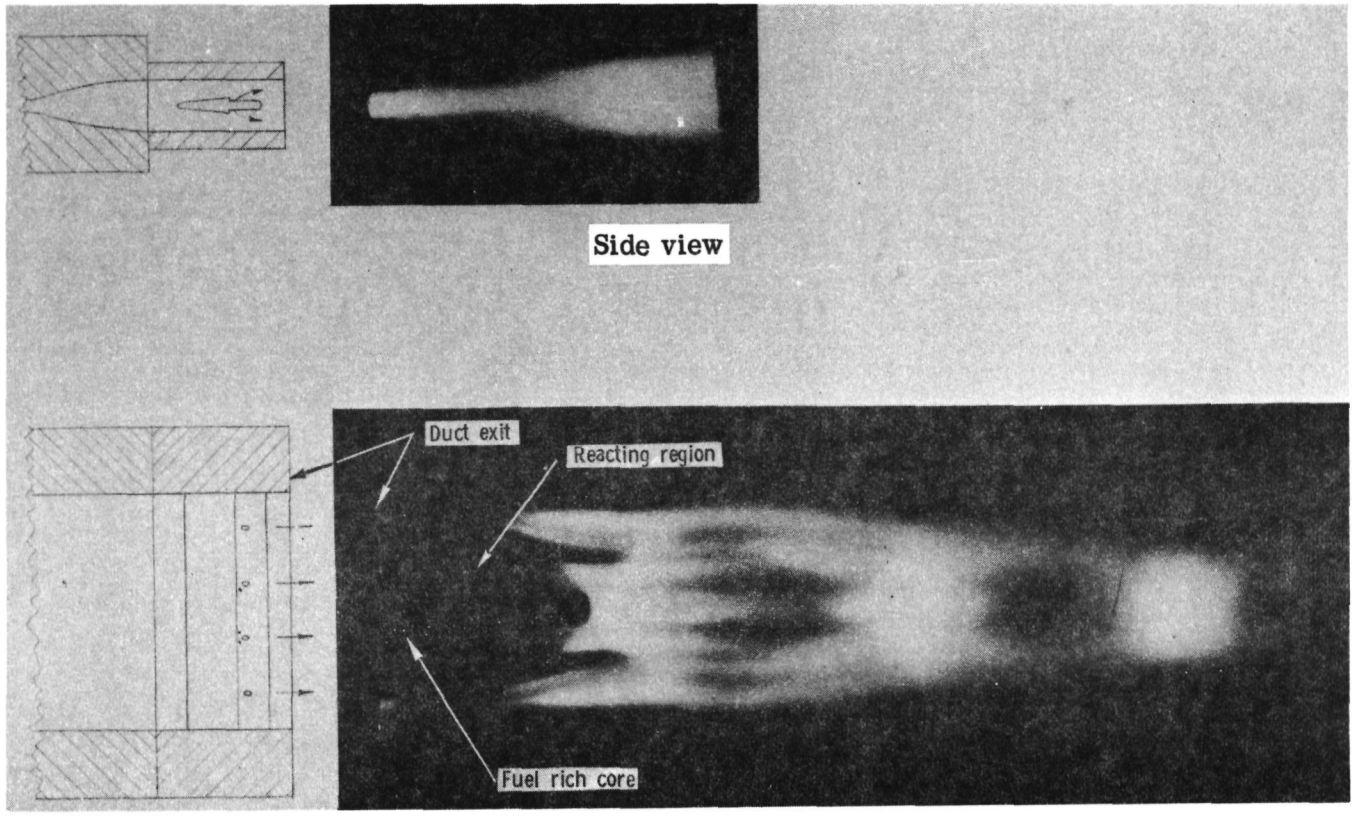

L-74-1011

(a) Perpendicular strut.

Figure 2.- Flame photographs of injection struts in short duct.

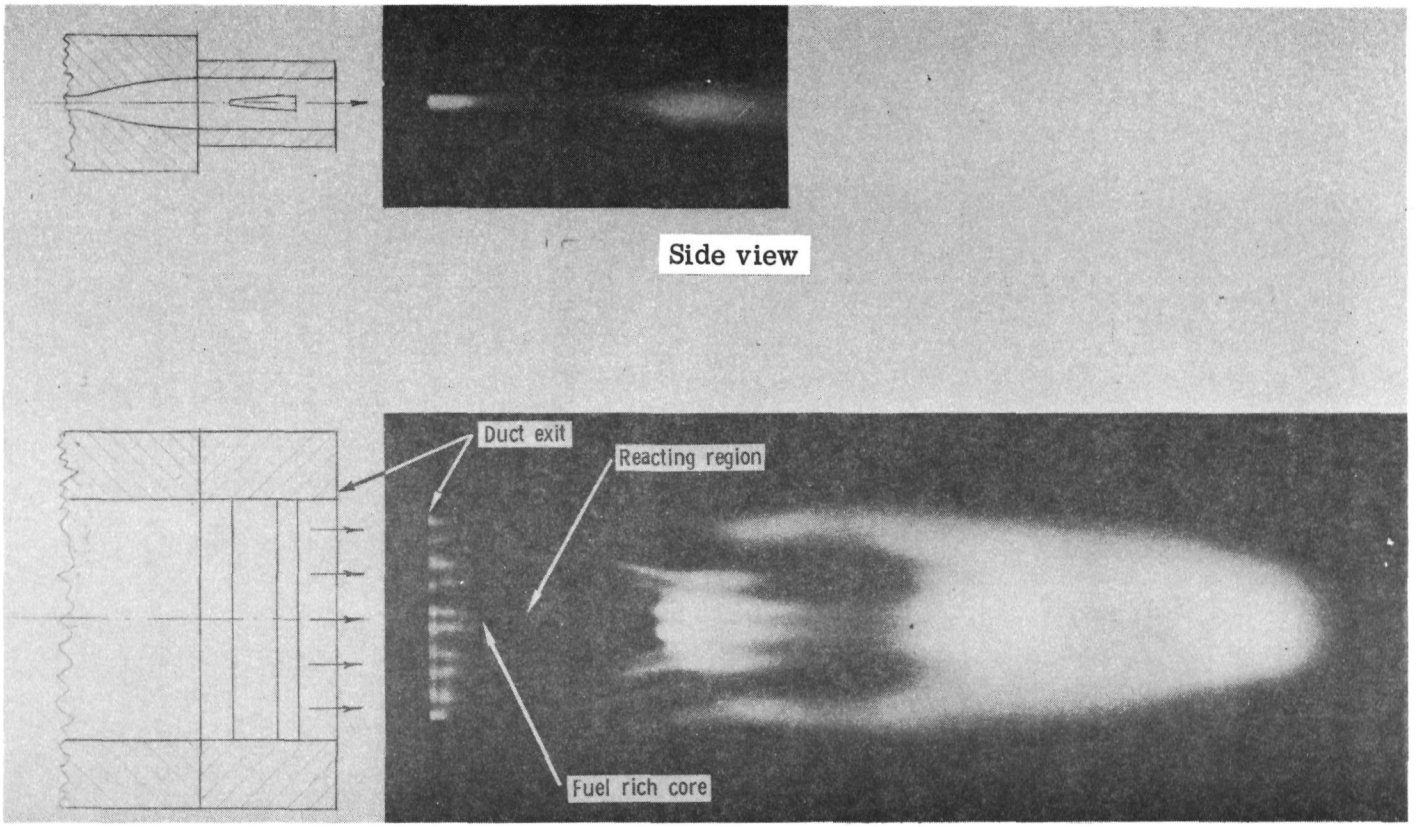

L-74-1010

(b) Parallel strut.

Figure 2.- Concluded.

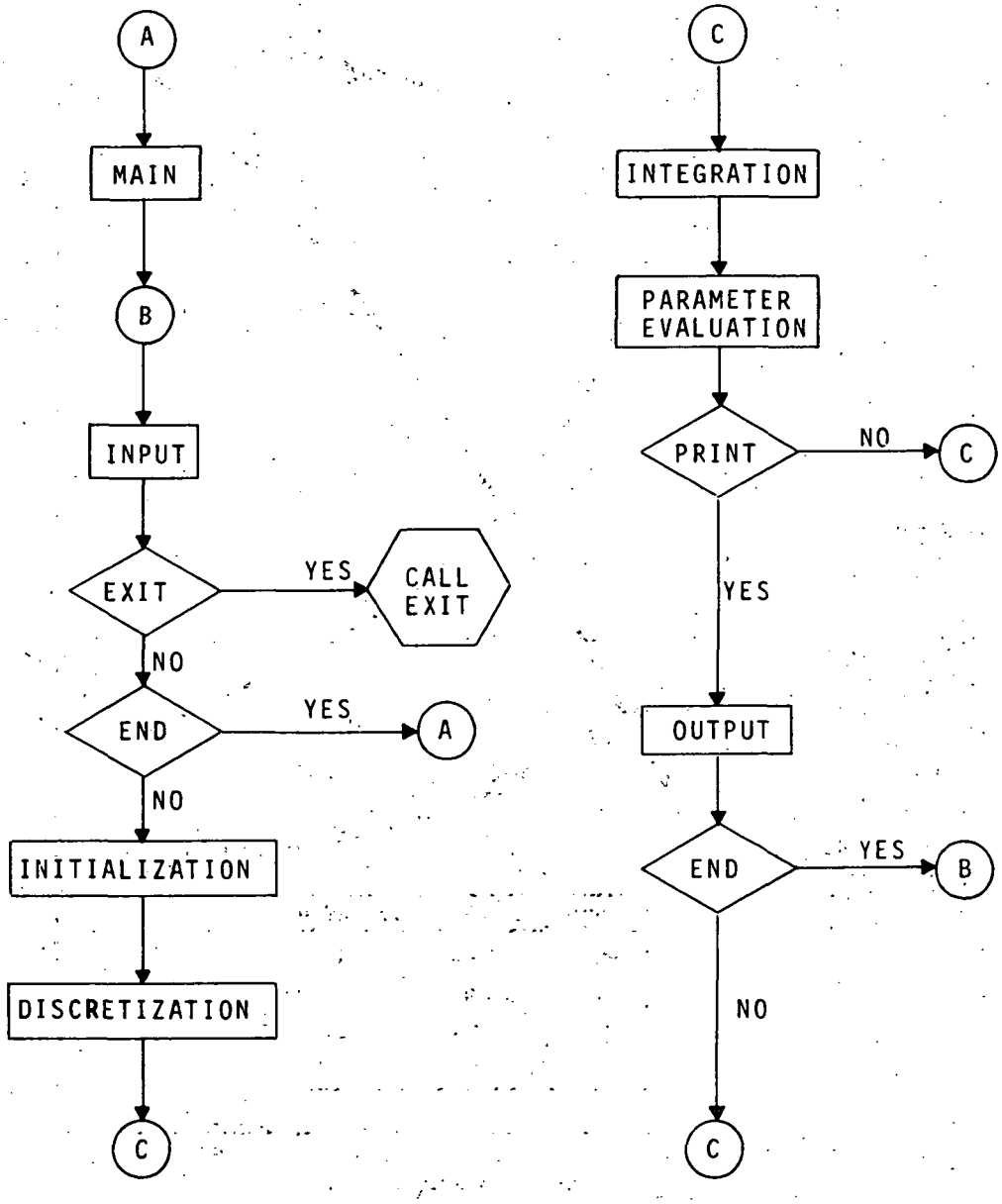

Figure 3.- COMOC macrostructure.

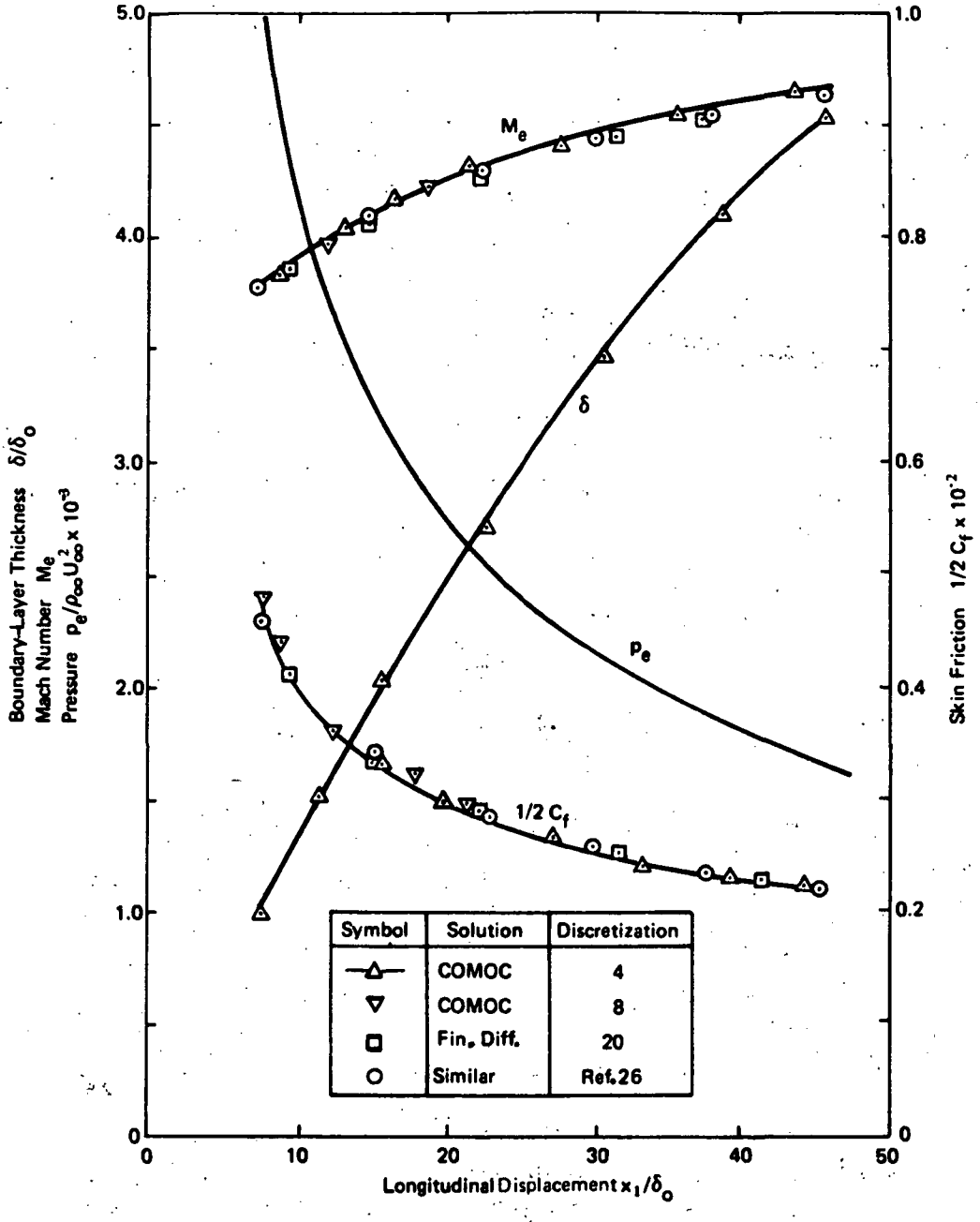

Figure 4.- Computed supersonic boundary-layer parameters. M = 5; $N_{Re} = 0.83 \times 10^5$ per meter; $\beta = 0.5$.

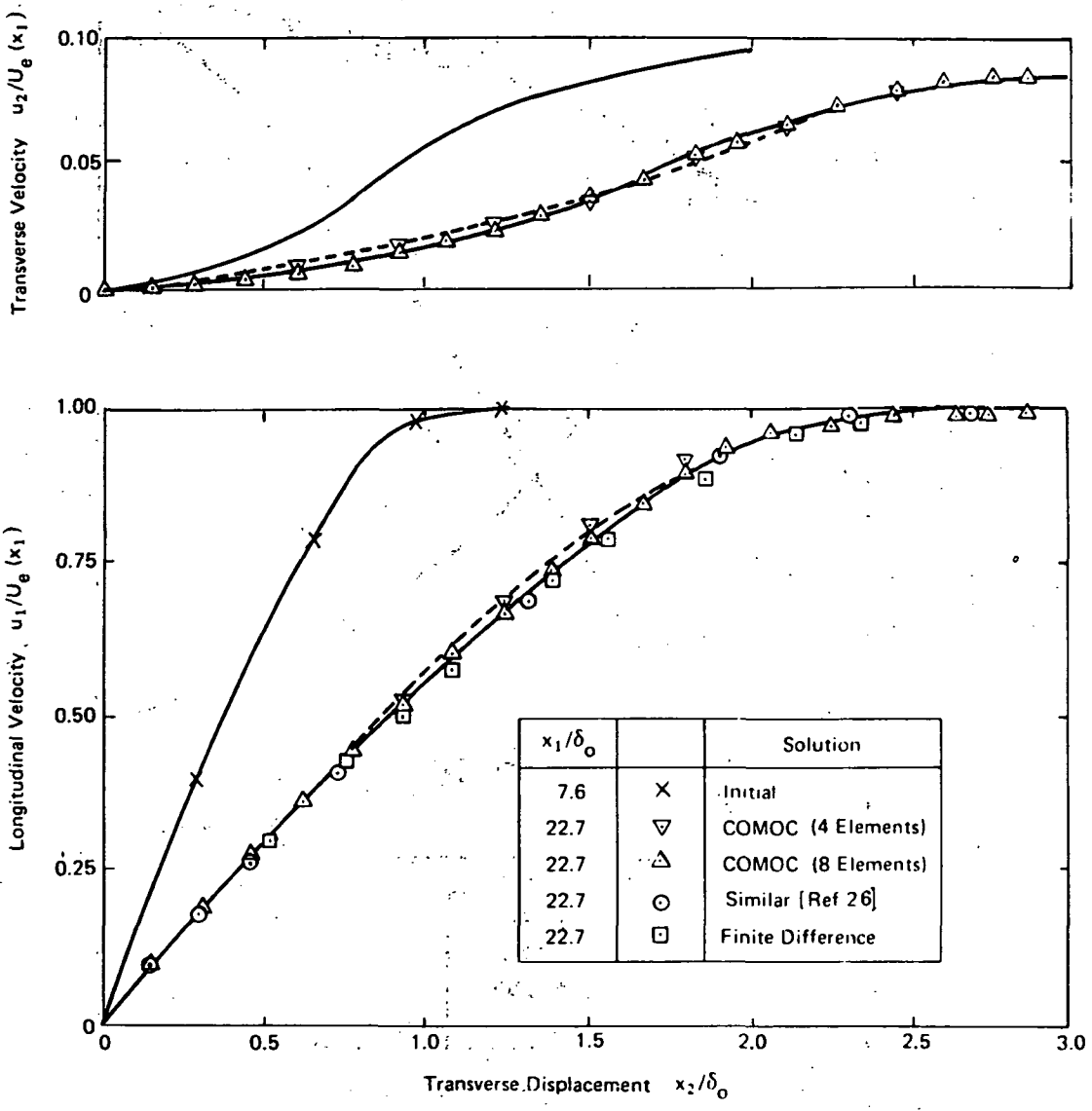

Figure 5.- Computed supersonic boundary-layer velocity profiles. M = 5; $N_{Re} = 0.83 \times 10^5$ per meter; $\beta = 0.5$.

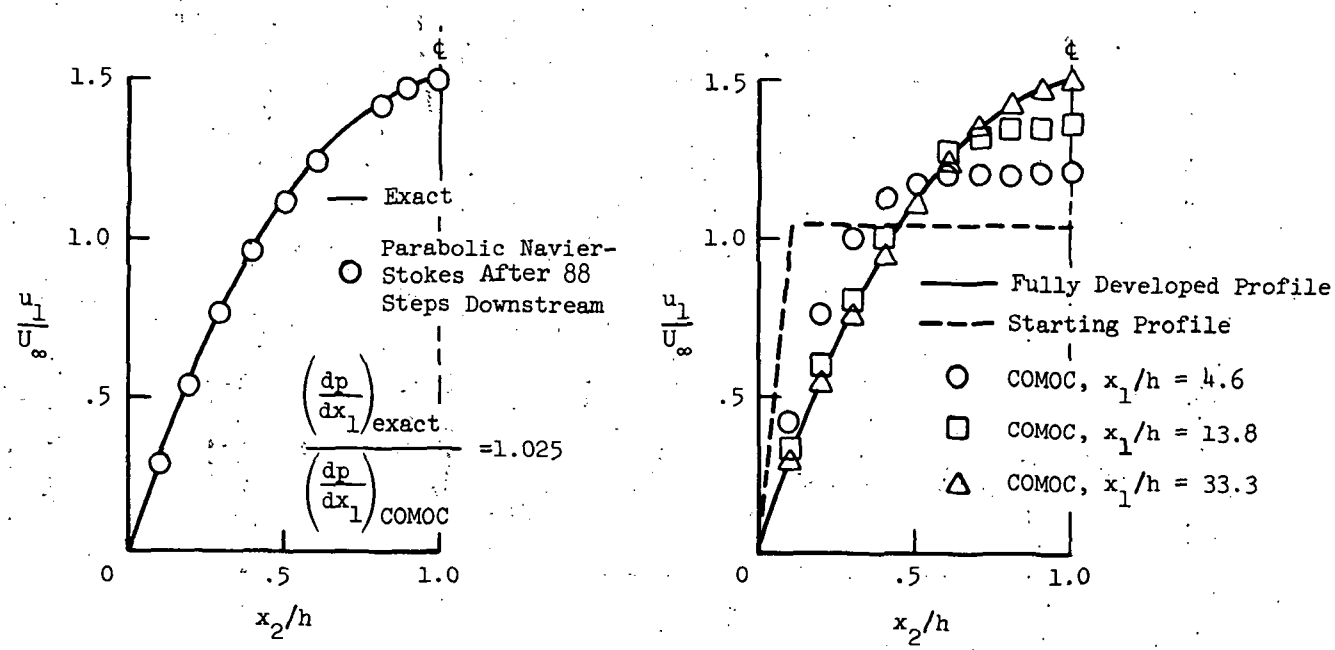

(a) Fully developed.

(b) Developing.

Figure 6.- Channel flow solutions computed with the parabolic Navier-Stokes equations.

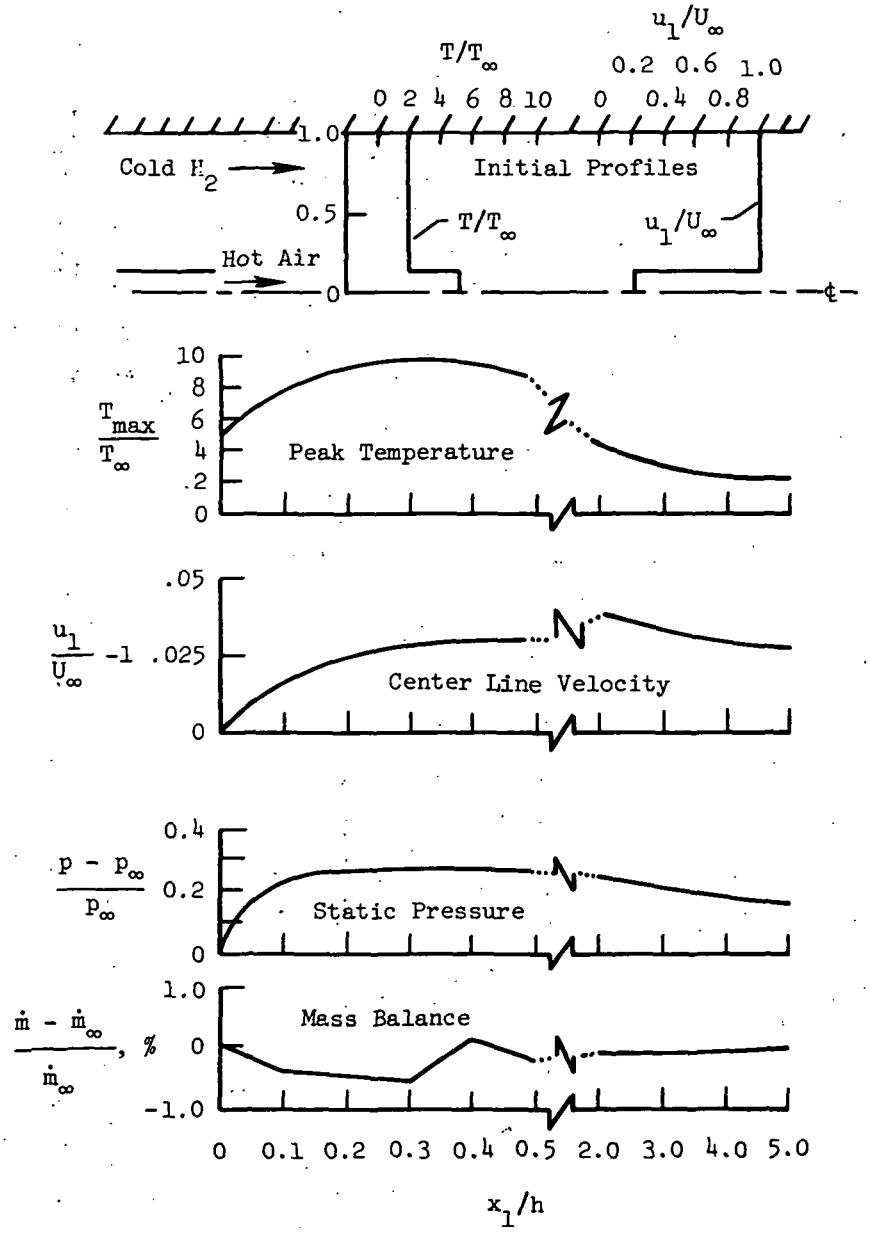

Figure 7.- Mixing and reacting channel flow. T_∞ = 400 K; U_∞ = 305 m/sec; h = 0.15 m.

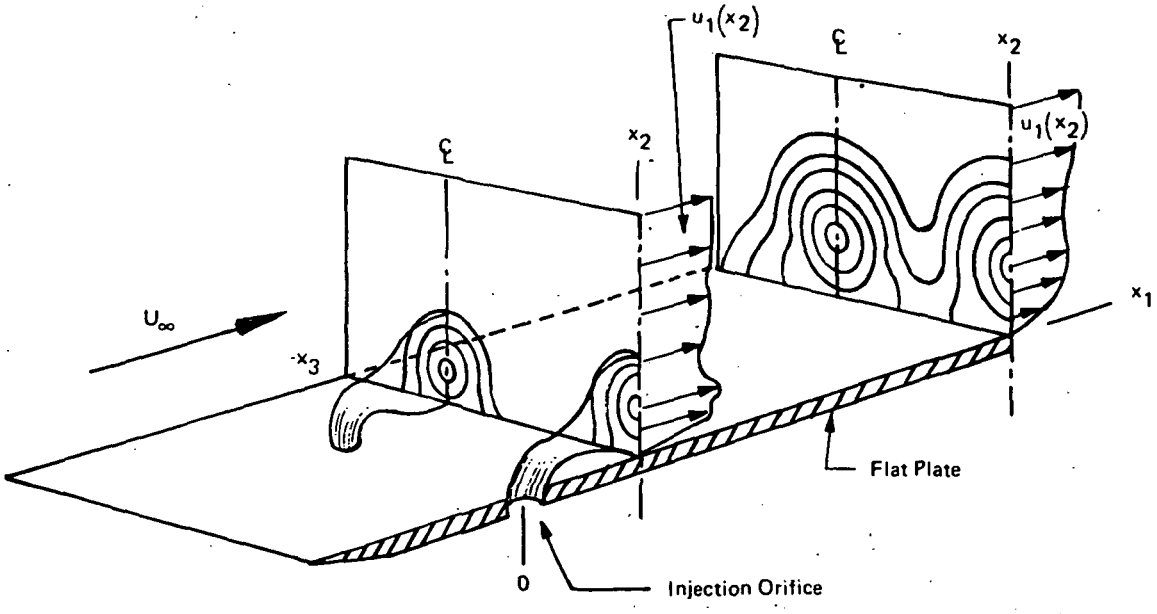

Figure 8.- Three-dimensional flow field downstream of transverse injection from discrete orifices.

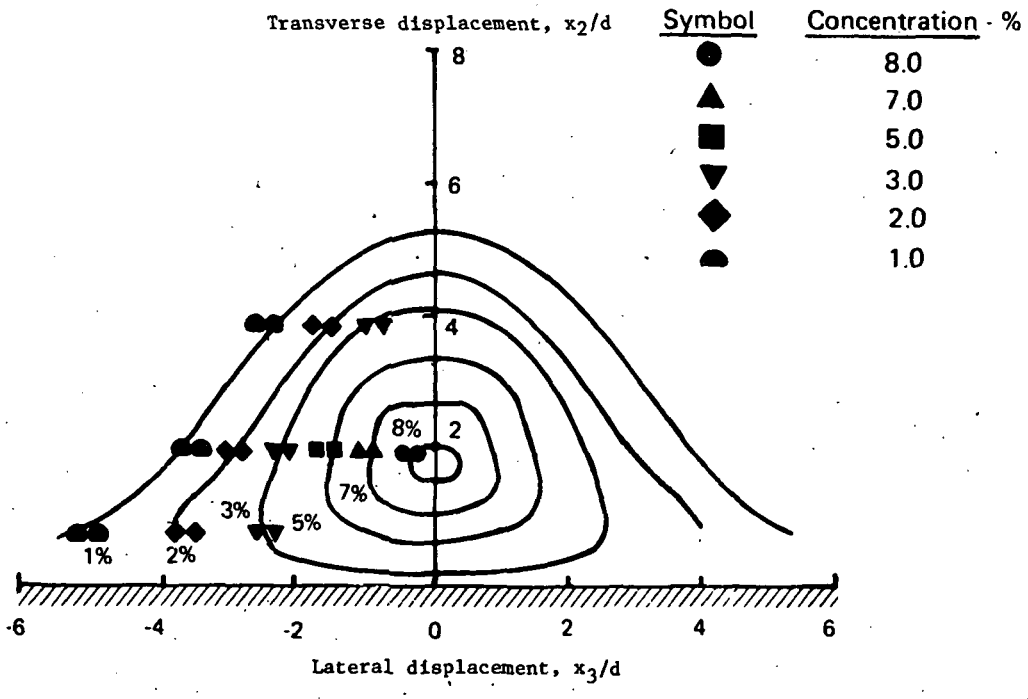

Figure 9.- Cubic-spline interpolated contours of hydrogen mass fraction. $q_r = 1.0$; $x_1/d = 30$; $s/d = \infty$. (Symbols are "best symmetry" fit for data of Rogers (ref. 8).)

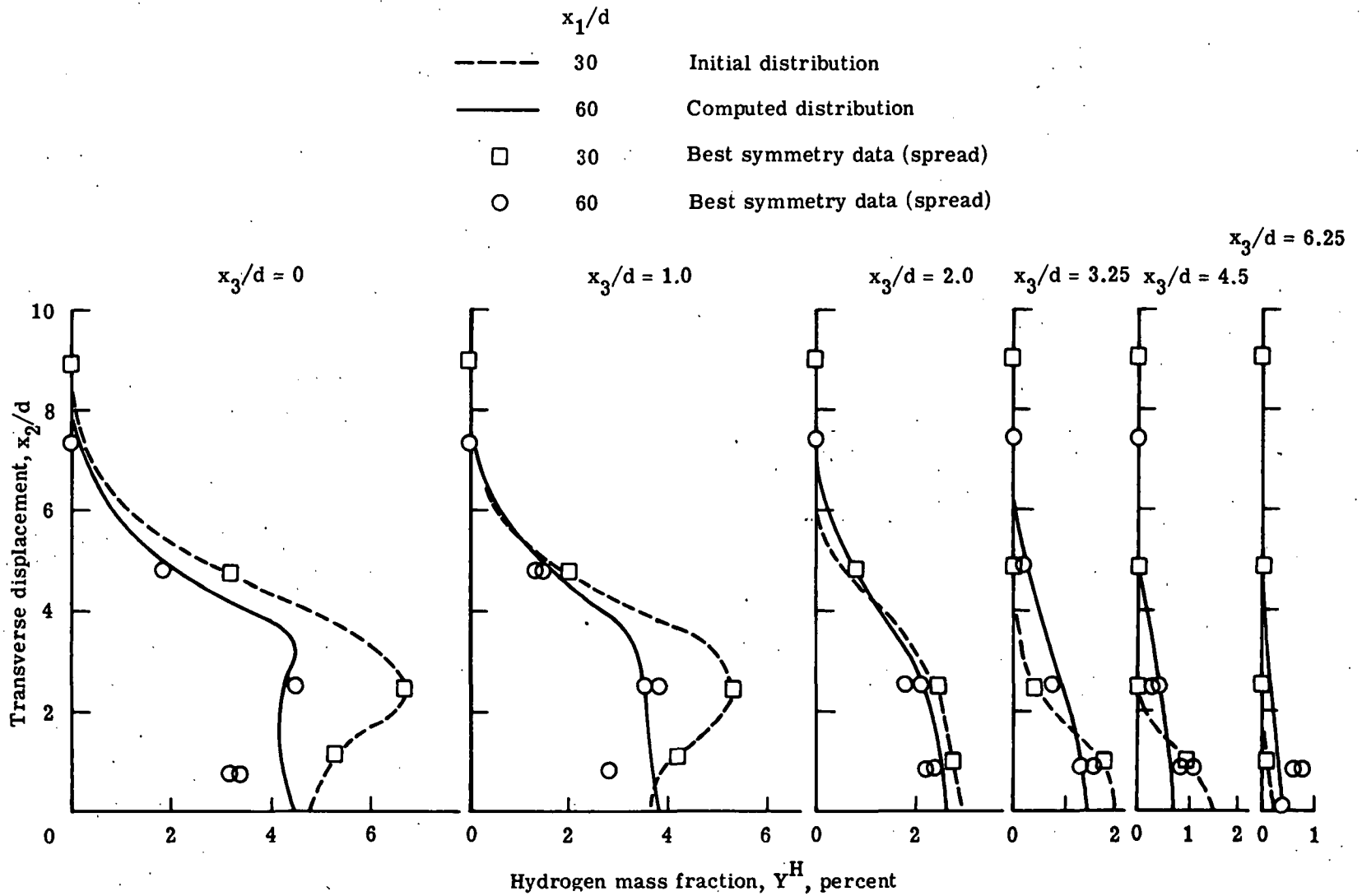

Figure 10.- Computed distribution of hydrogen mass fraction at $x_1/d = 60$.
$q_r = 1.0$; $s/d = 12.5$; $u_3 = 0$; $\lambda = 0.09$.

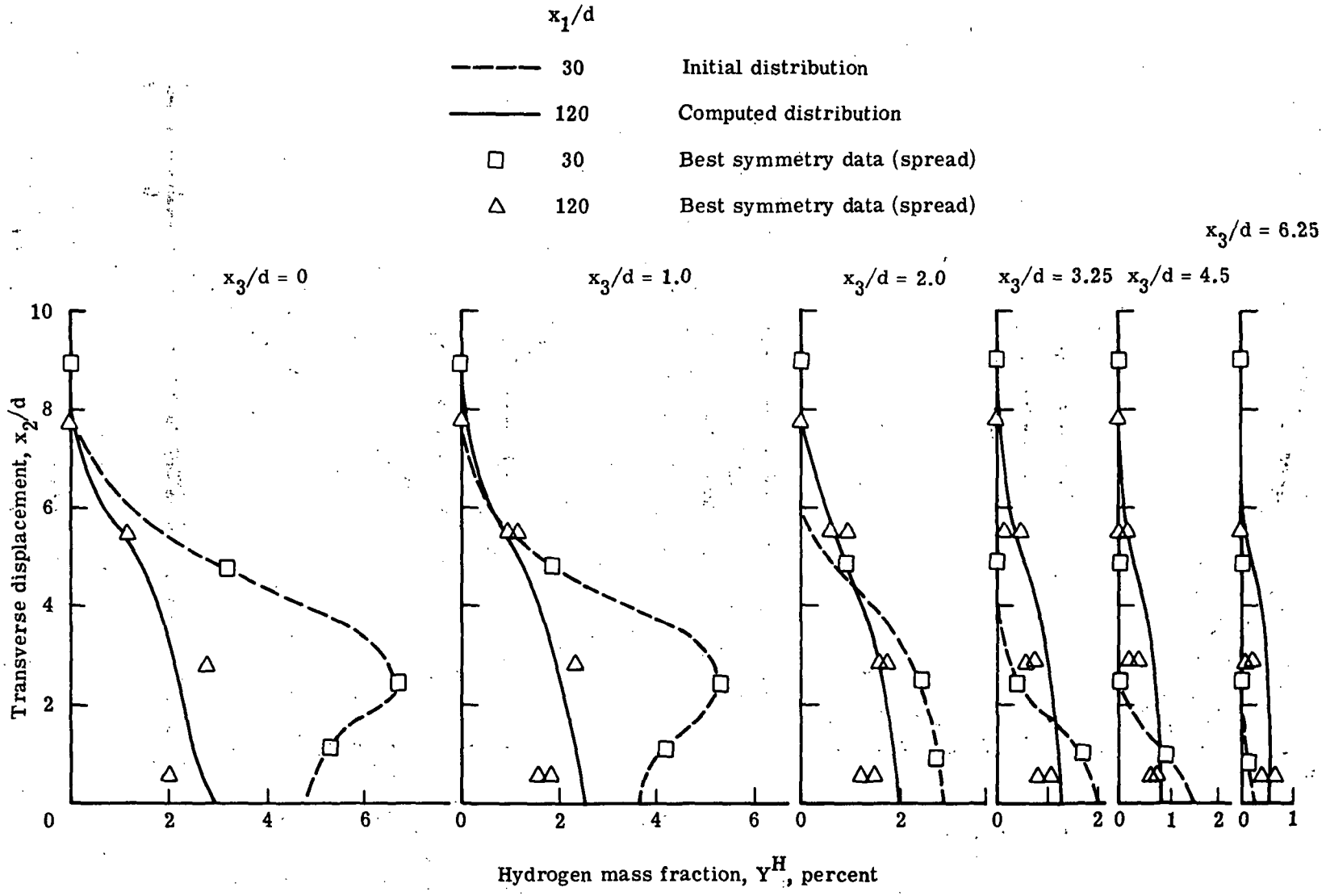

Figure 11.- Computed distribution of hydrogen mass fraction at $x_1/d = 120$. $q_r = 1.0$; $s/d = 12.5$; $u_3 = 0$; $\lambda = 0.09$.

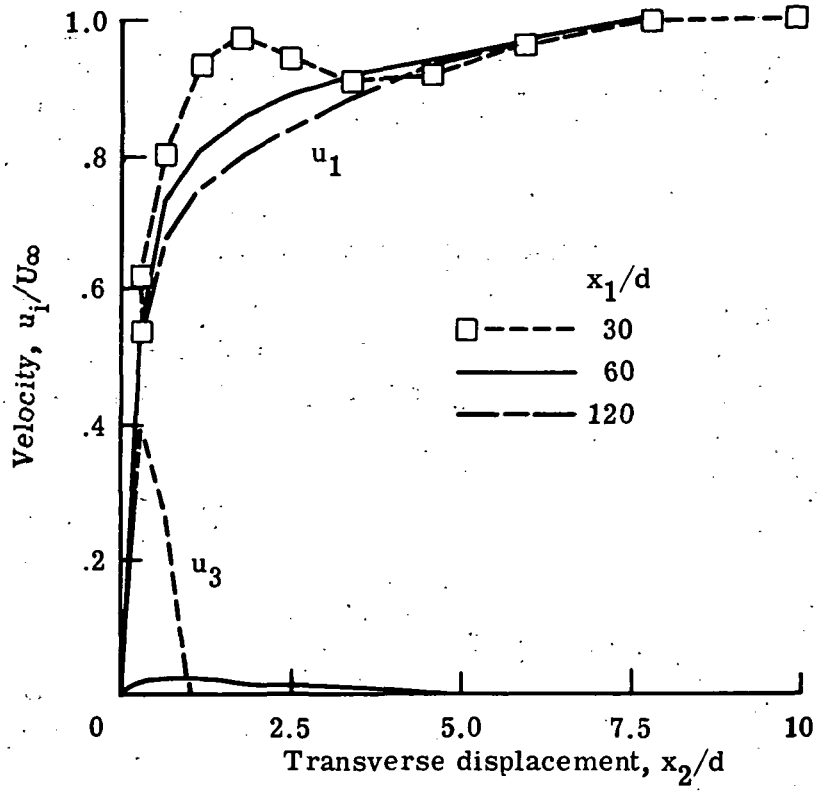

(a) Longitudinal and lateral velocities.

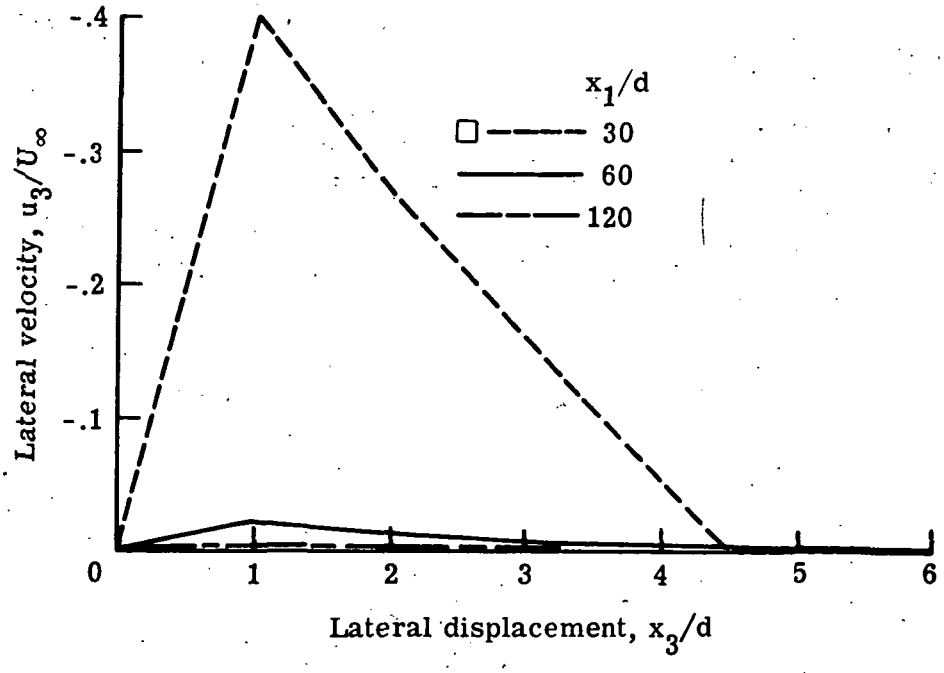

(b) Lateral velocity.

Figure 12.- Imposed transverse velocity.

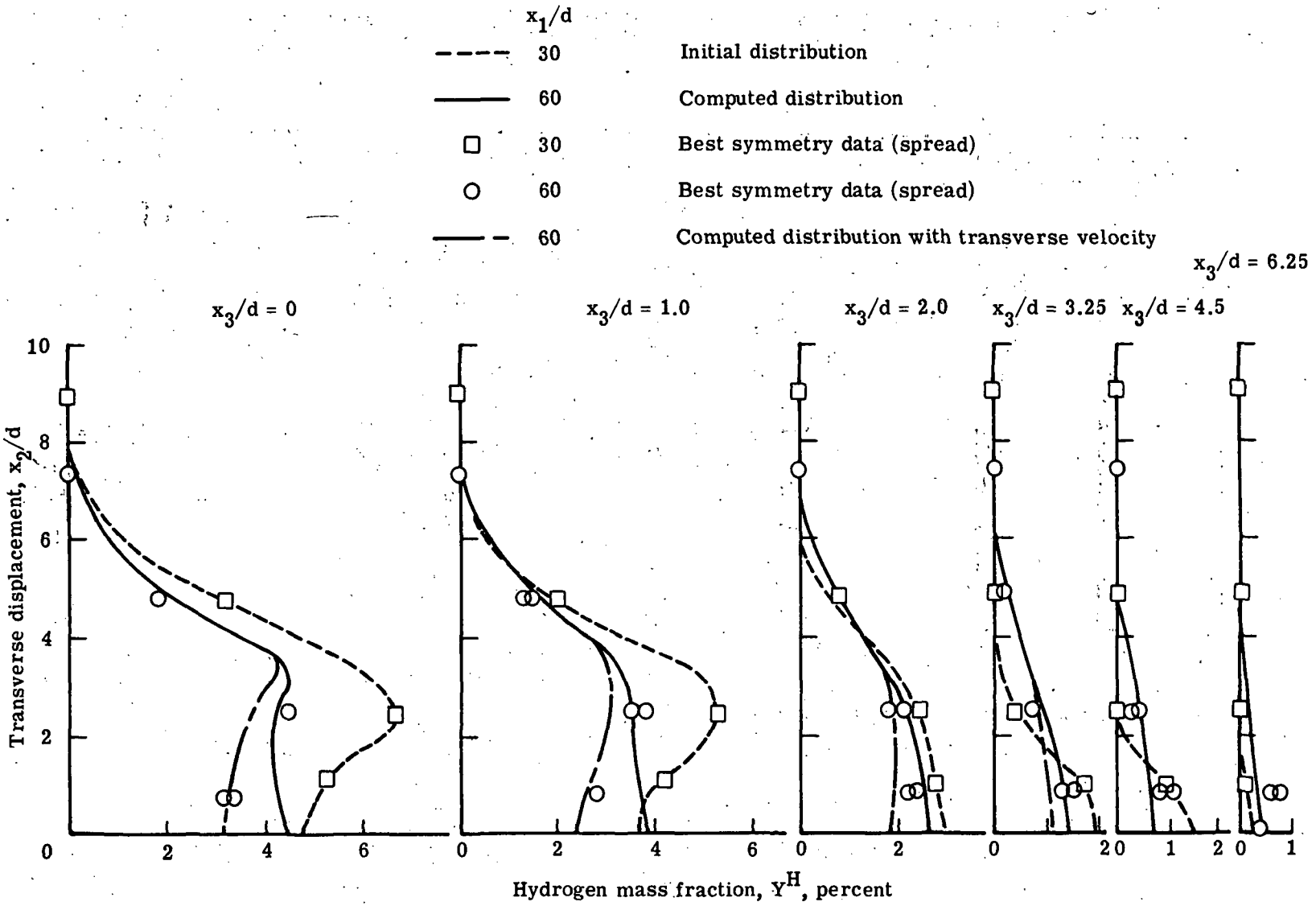

Figure 13.- Effect of transverse velocity on computed distributions of hydrogen mass fraction at $x_1/d = 60$. $q_r = 1.0$; $s/d = 12.5$; $u_3 \neq 0$; $\lambda = 0.09$.

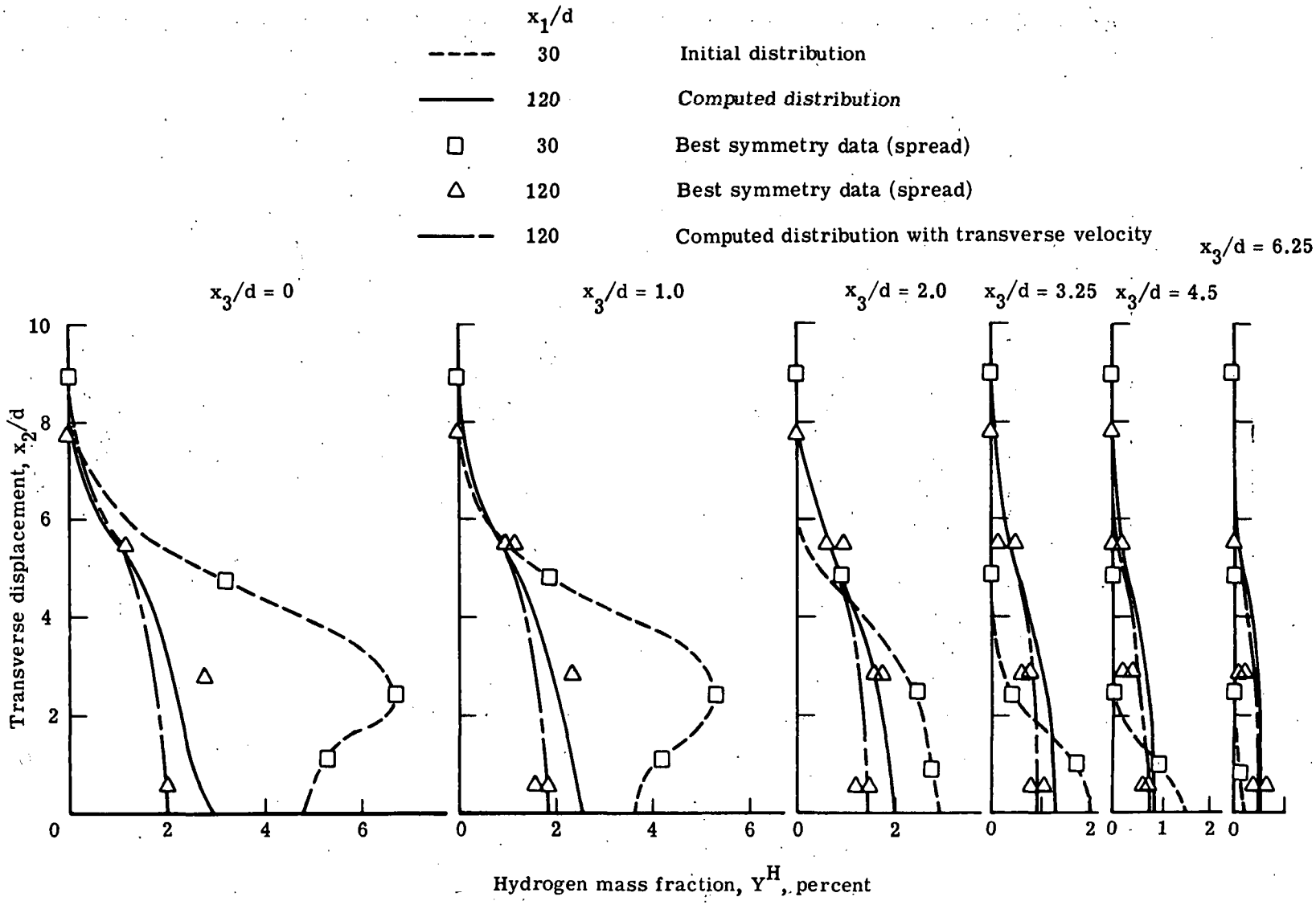

Figure 14.- Effect of transverse velocity on computed distribution of hydrogen mass fraction at $x_1/d = 120$. $q_r = 1.0$; $s/d = 12.5$; $u_3 \neq 0$; $\lambda = 0.09$.

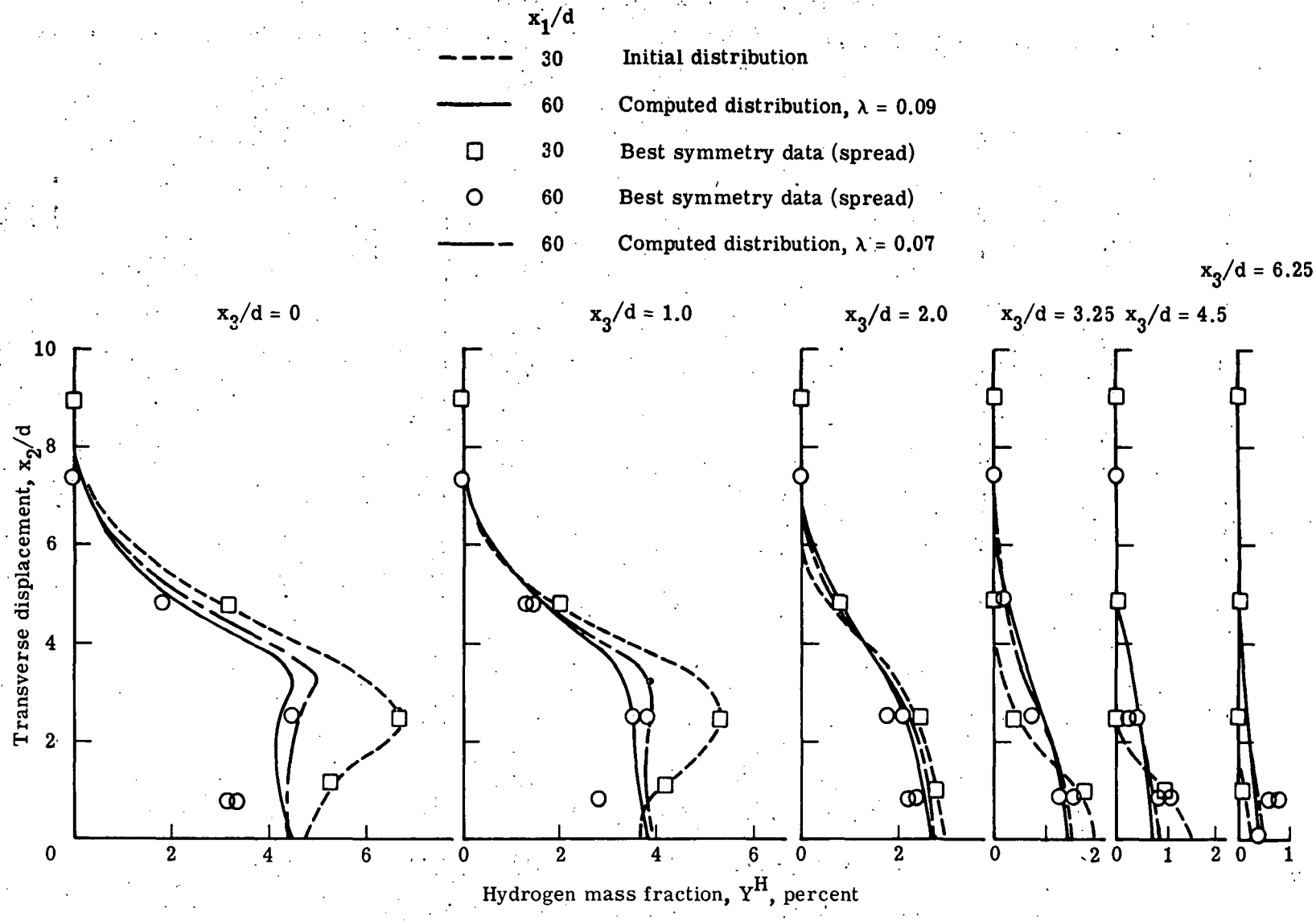

Figure 15.- Effect of turbulent sublayer constant on computed distribution of hydrogen mass fraction at $x_1/d = 60$. $q_r = 1.0$; $s/d = 12.5$; $u_3 = 0$.

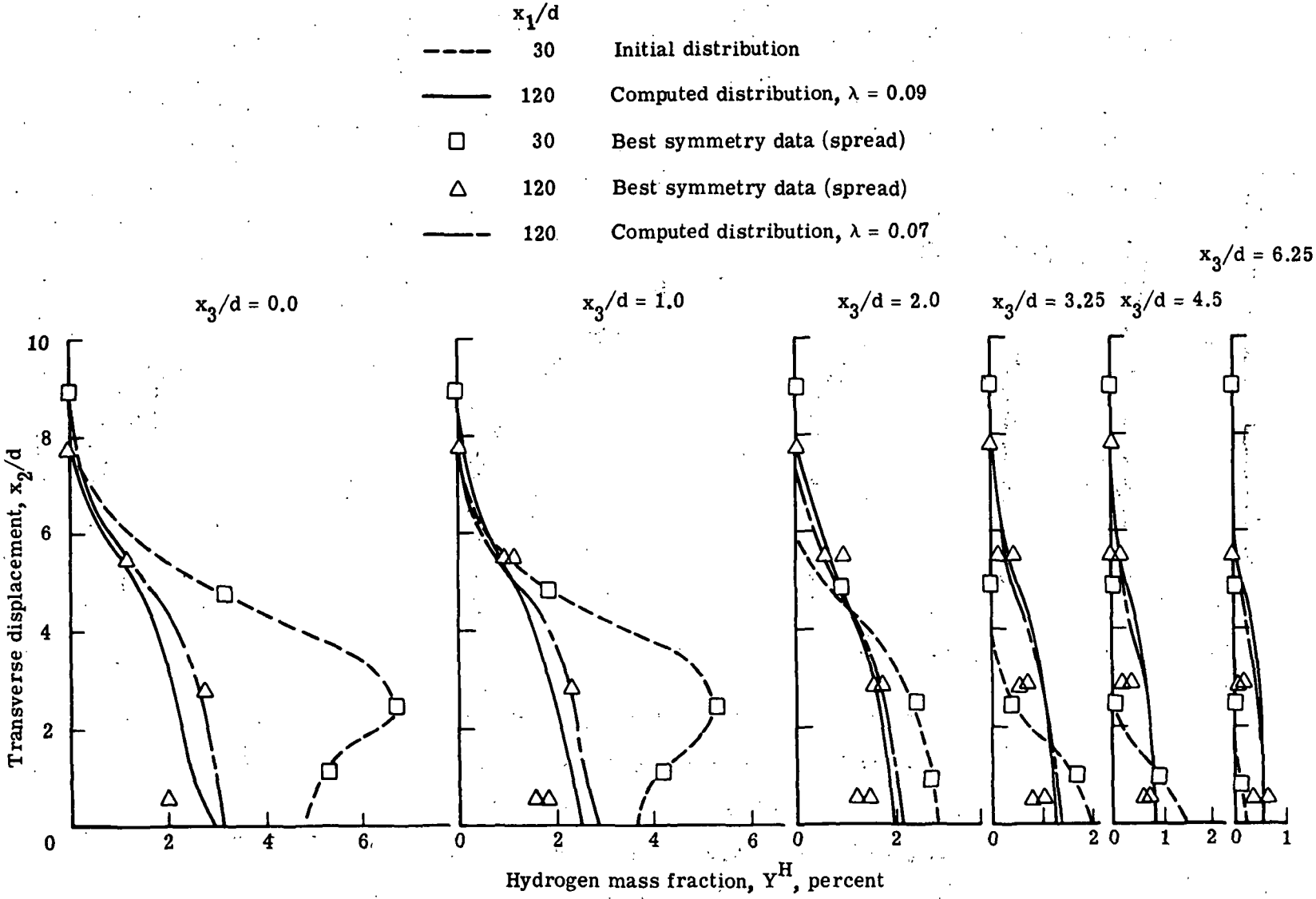

Figure 16.- Effect of turbulent sublayer constant on computed distribution of hydrogen mass fraction at $x_1/d = 120$. $q_r = 1.0$; $s/d = 12.5$; $u_3 = 0$.

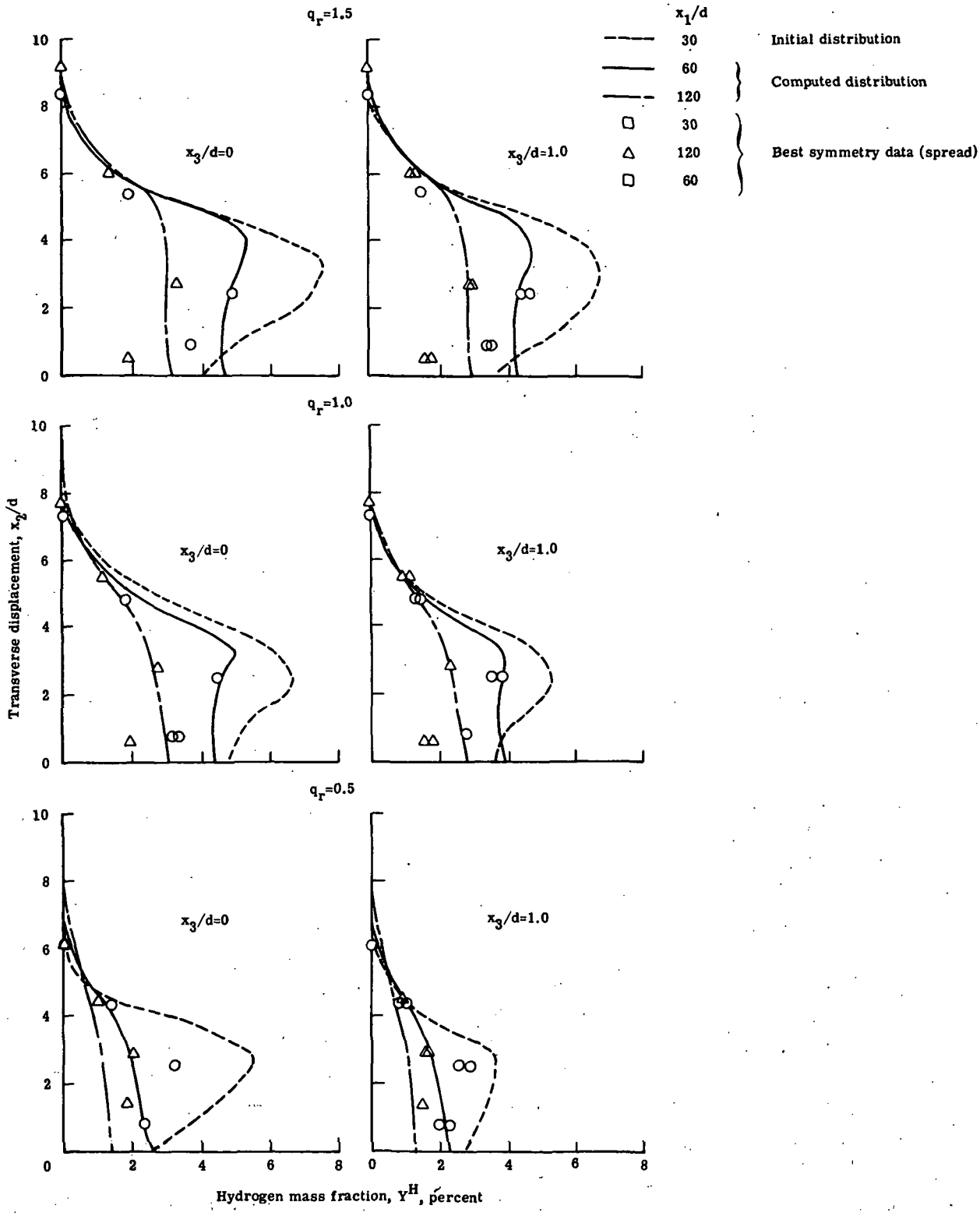

Figure 17.- Distributions of hydrogen mass fraction as a function of q_r. $s/d = 12.5$; $\lambda = 0.07$; $u_3 = 0$.

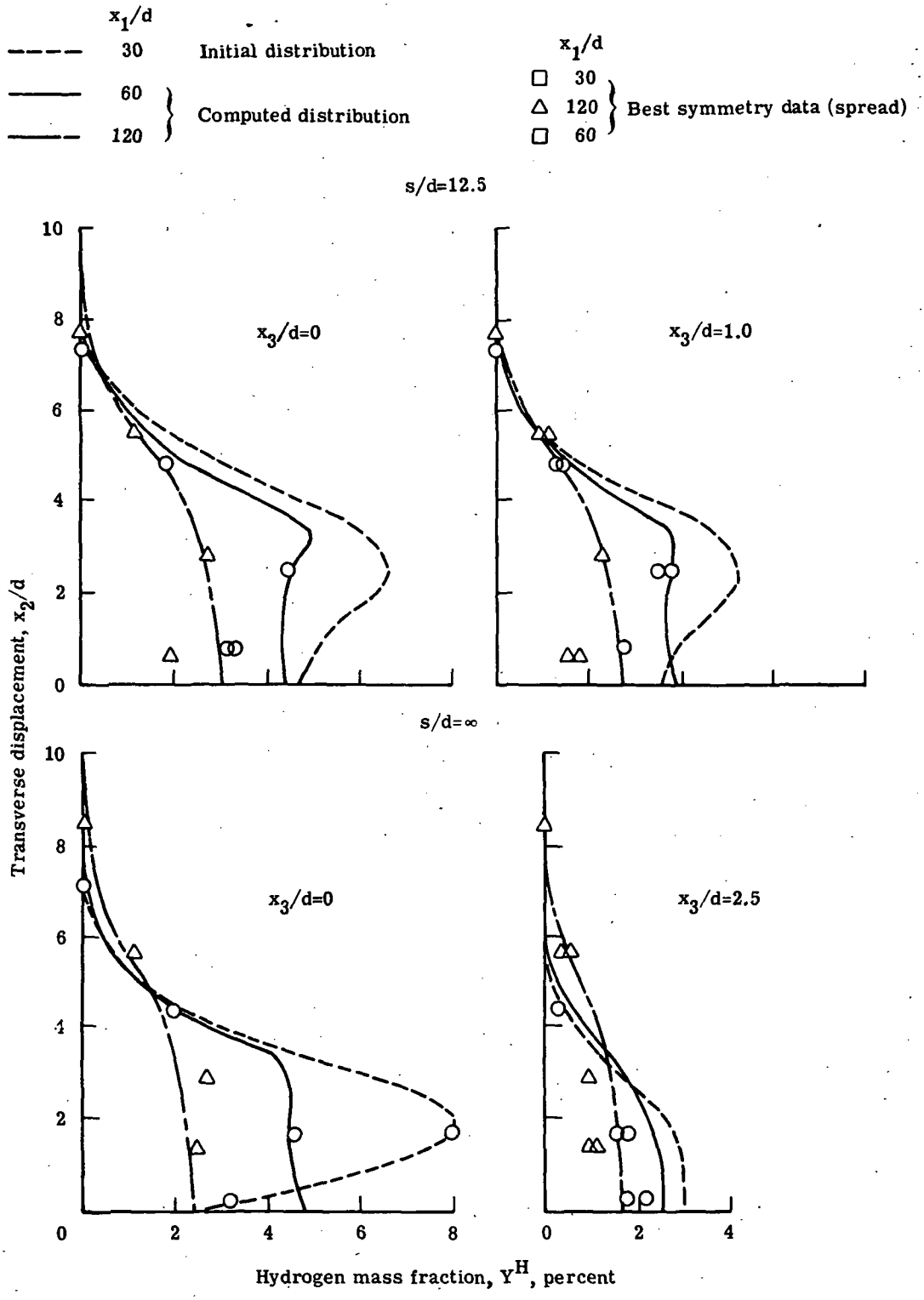

Figure 18.- Computed distribution of hydrogen mass fraction as a function of injector spacing s/d. $q_r = 1.0$; $u_3 = 0$; $\lambda = 0.07$.

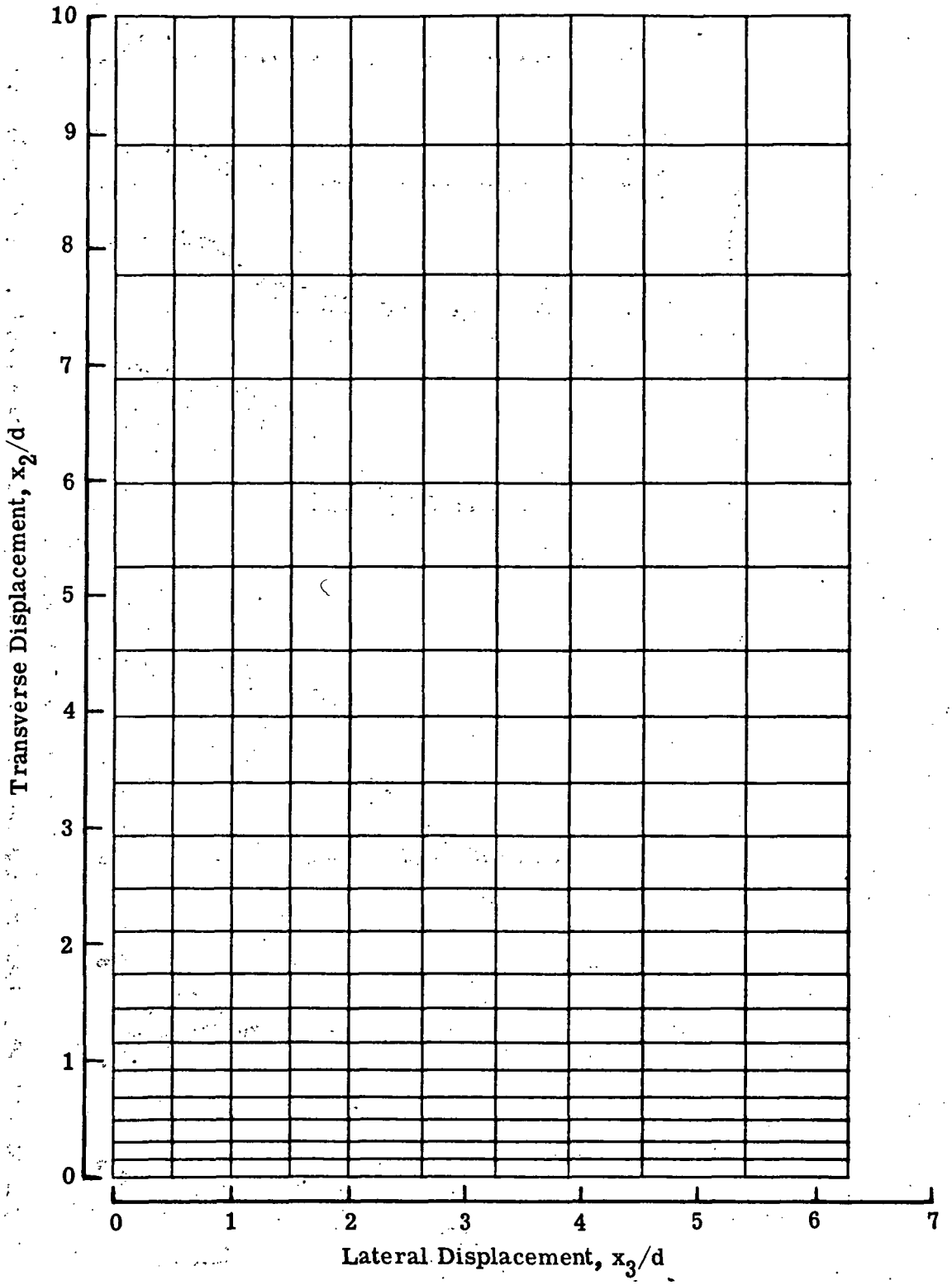

Figure 19.- Finite-element double discretization of injector solution domain.

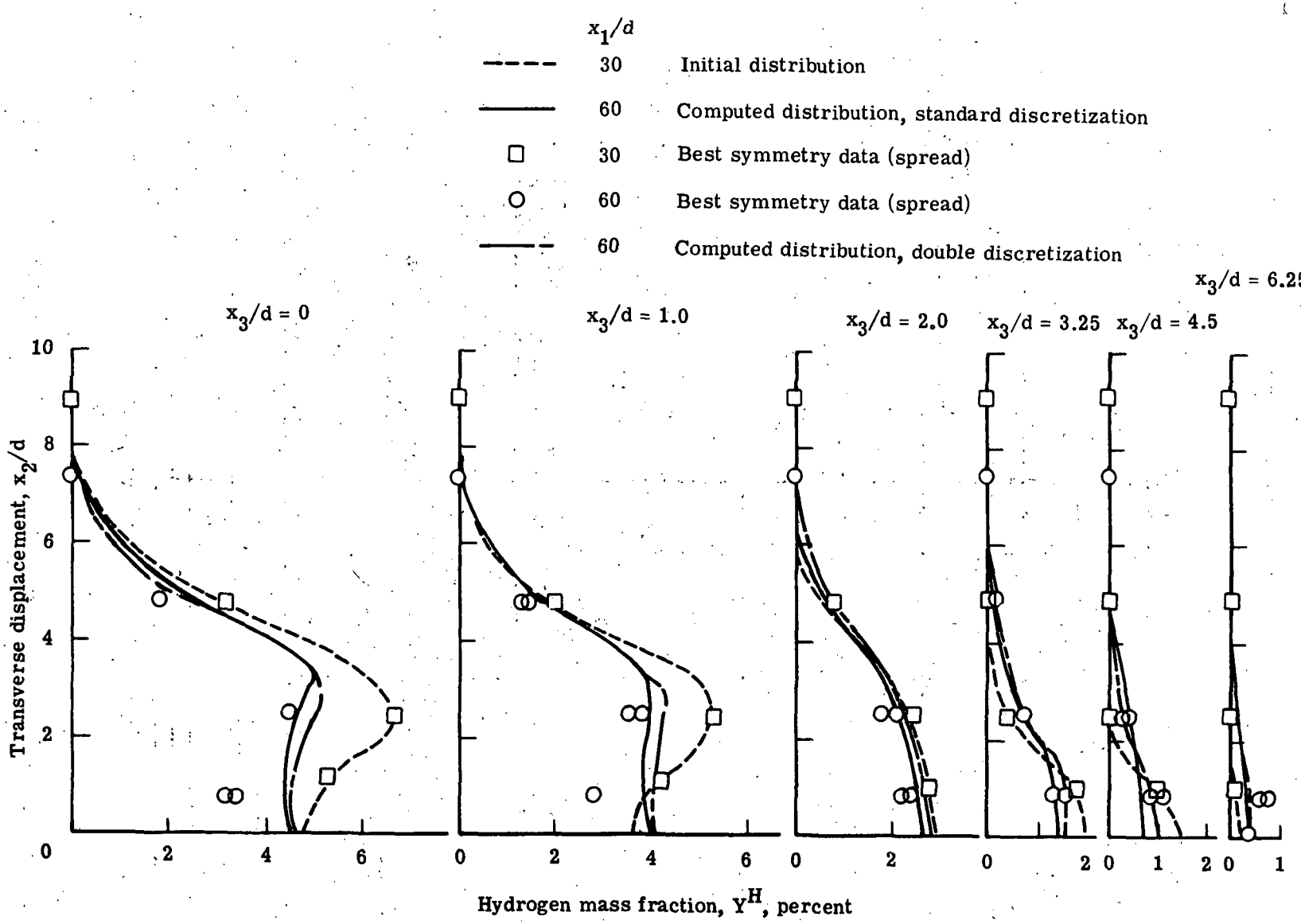

Figure 20.- Effect of discretization on computed distribution of hydrogen mass fraction at $x_1/d = 60$. $q_r = 1.0$; $s/d = 12.5$; $u_3 = 0$; $\lambda = 0.07$.

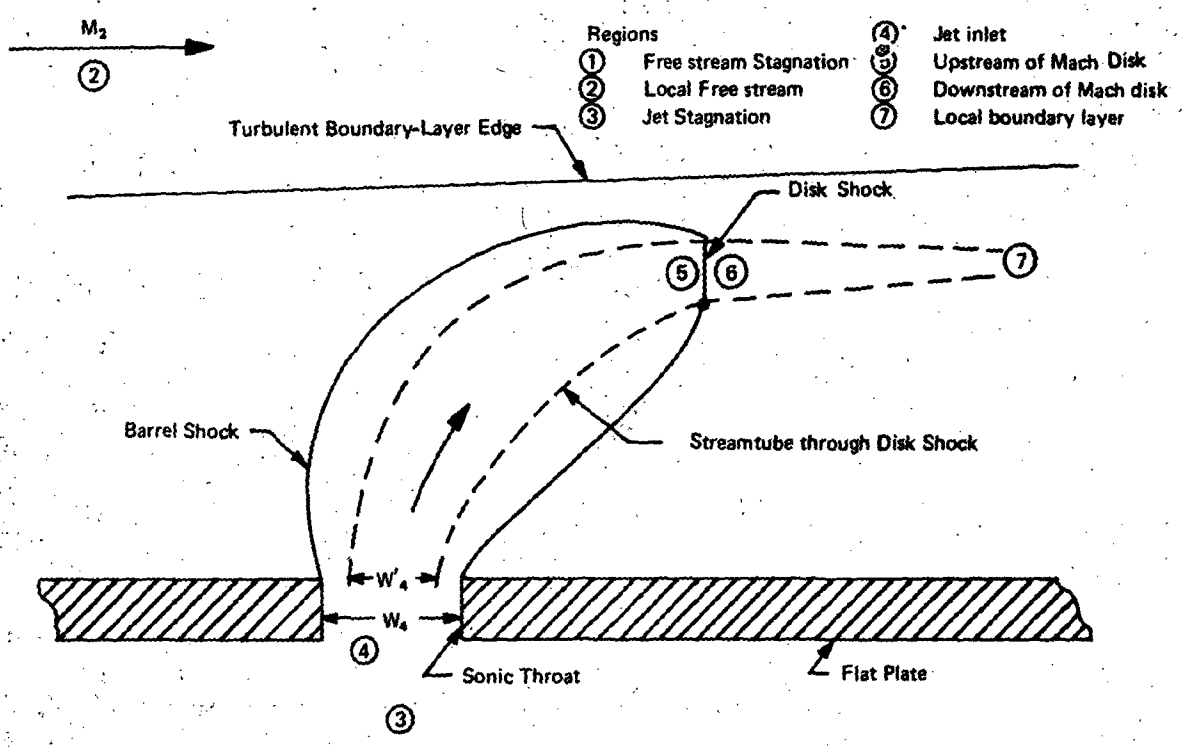

Figure 21.- Transverse injection into a turbulent boundary layer.

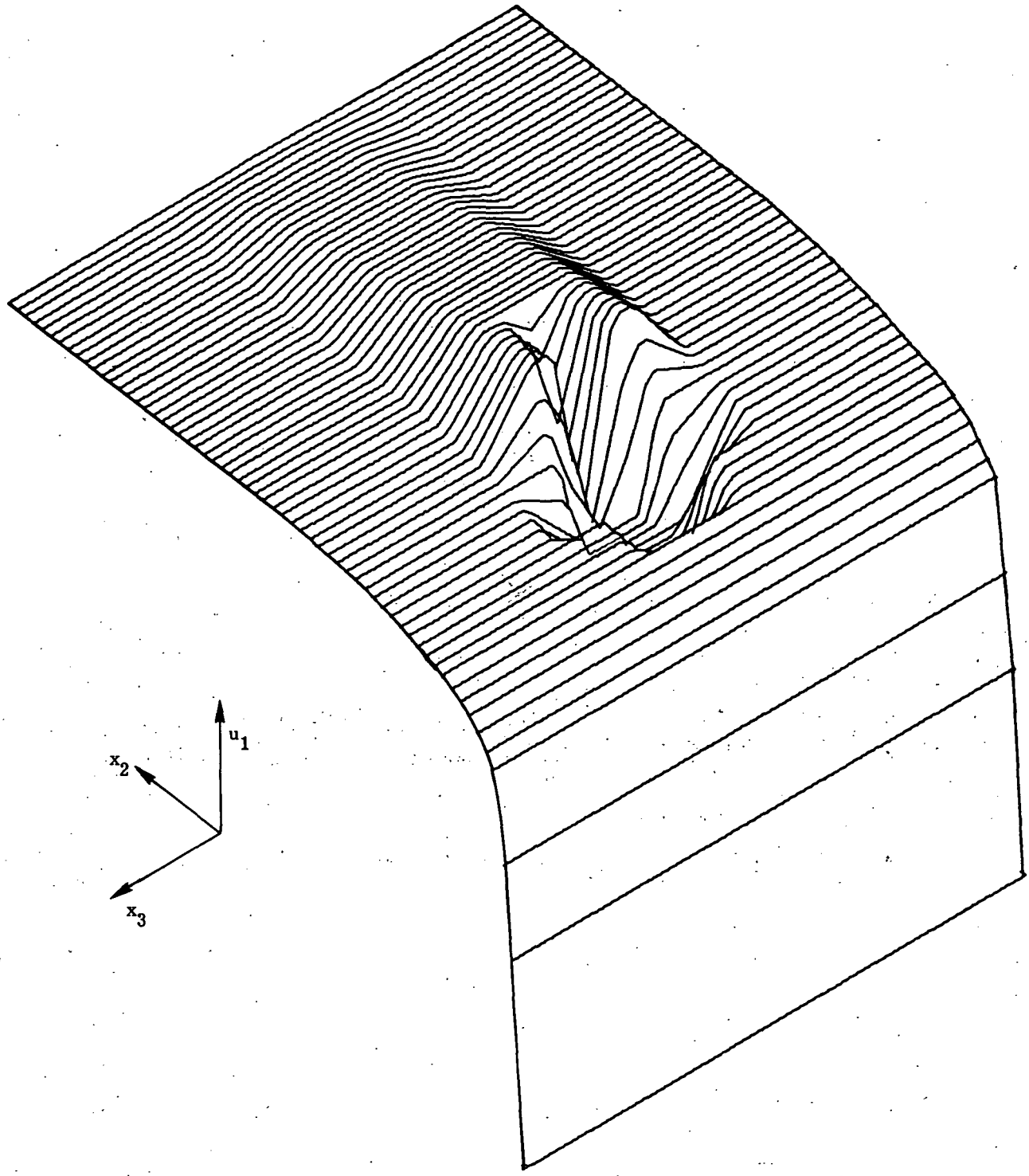

Figure 22.- Initial u_1 velocity distribution for virtual-source simulation of cold transverse hydrogen injection.

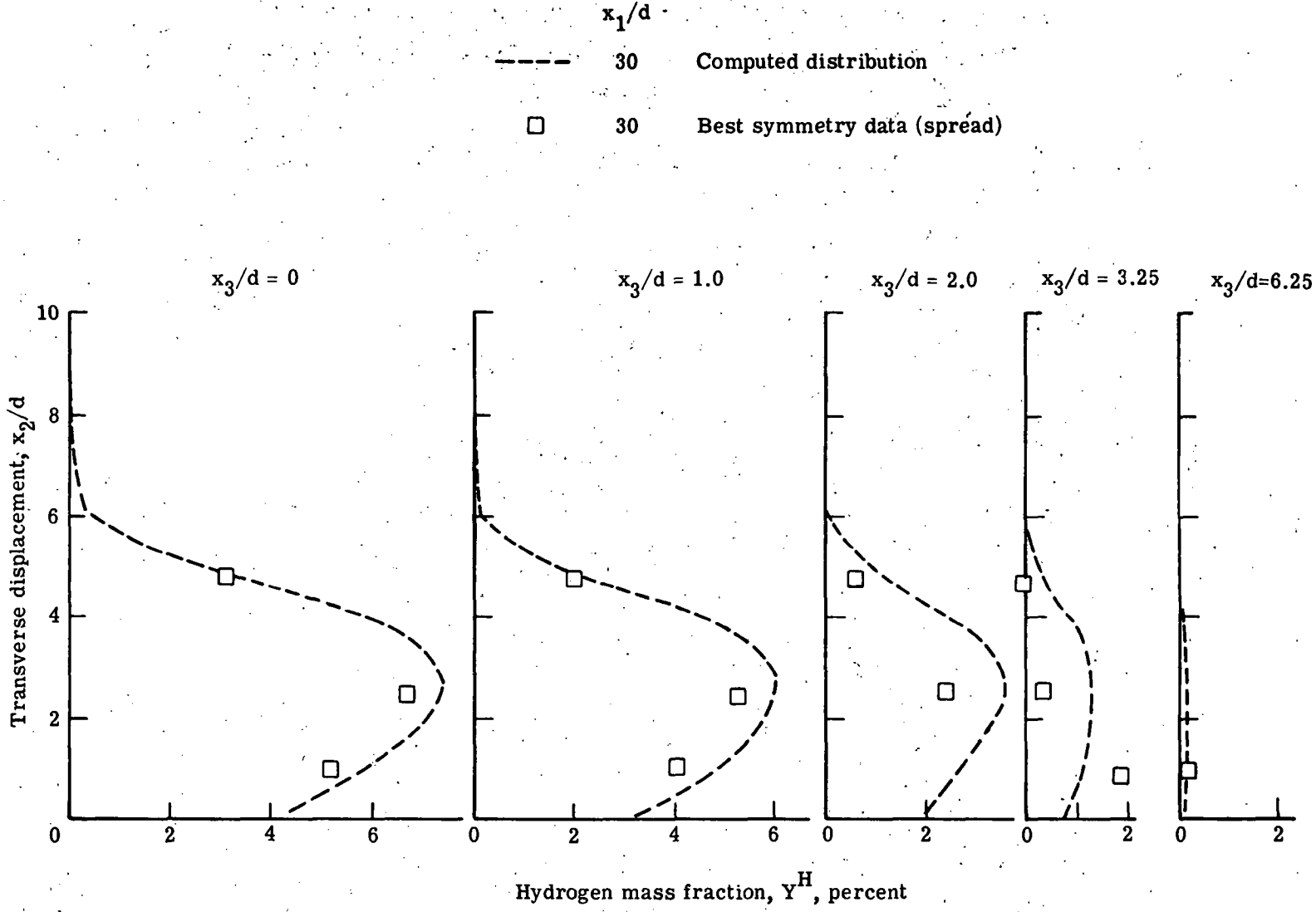

Figure 23.- Computed distributions of hydrogen mass fraction at $x_1/d = 30$ for virtual-source simulation of standard test conditions. $q_r = 1.0$; $s/d = 12.5$; $u_3 = 0$; $\lambda = 0.07$.

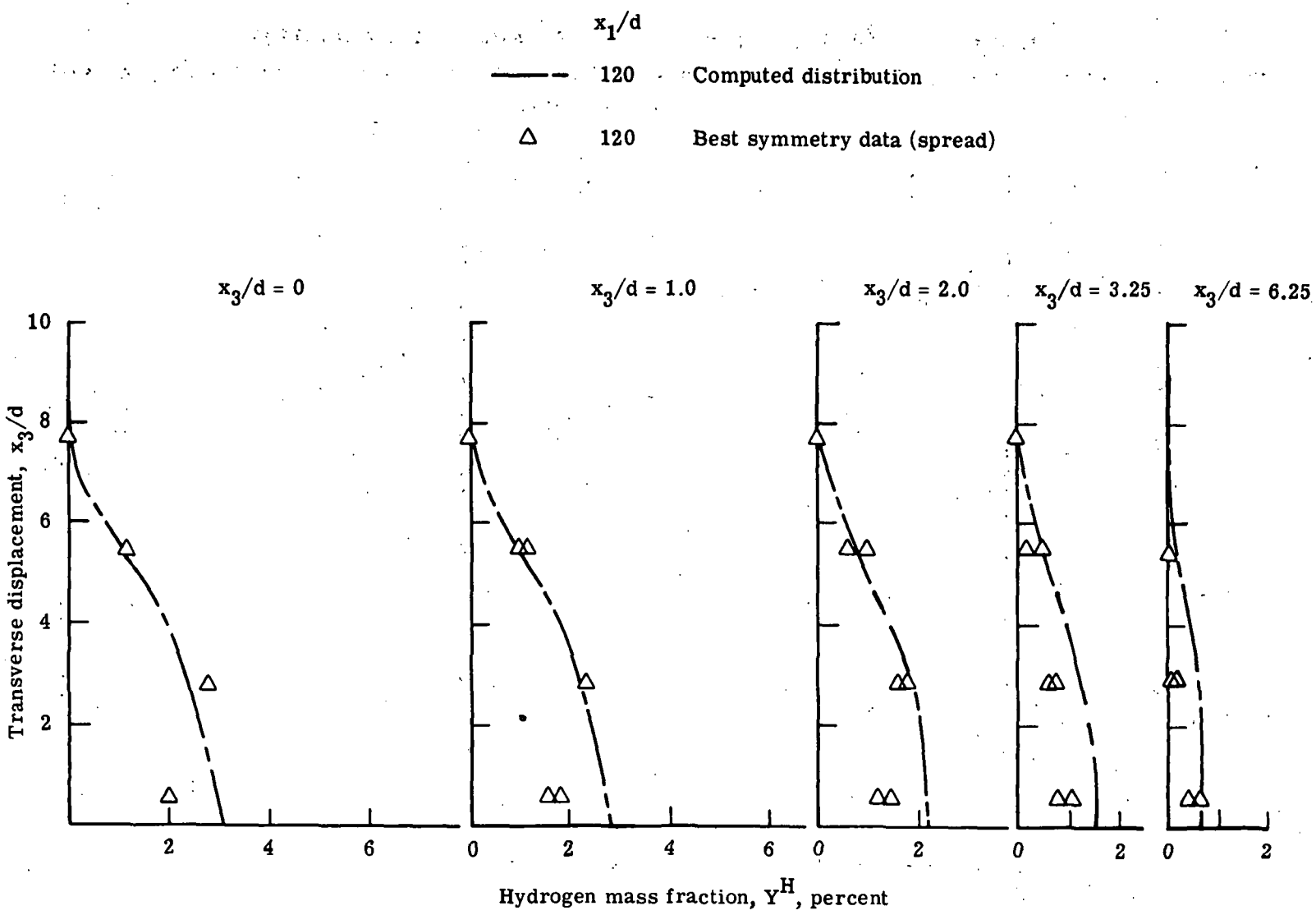

Figure 24.- Computed distribution of hydrogen mass fraction at $x_1/d = 120$ for virtual-source simulation of standard test conditions. $q_r = 1.0$; $s/d = 12.5$; $u_3 = 0$; $\lambda = 0.07$.

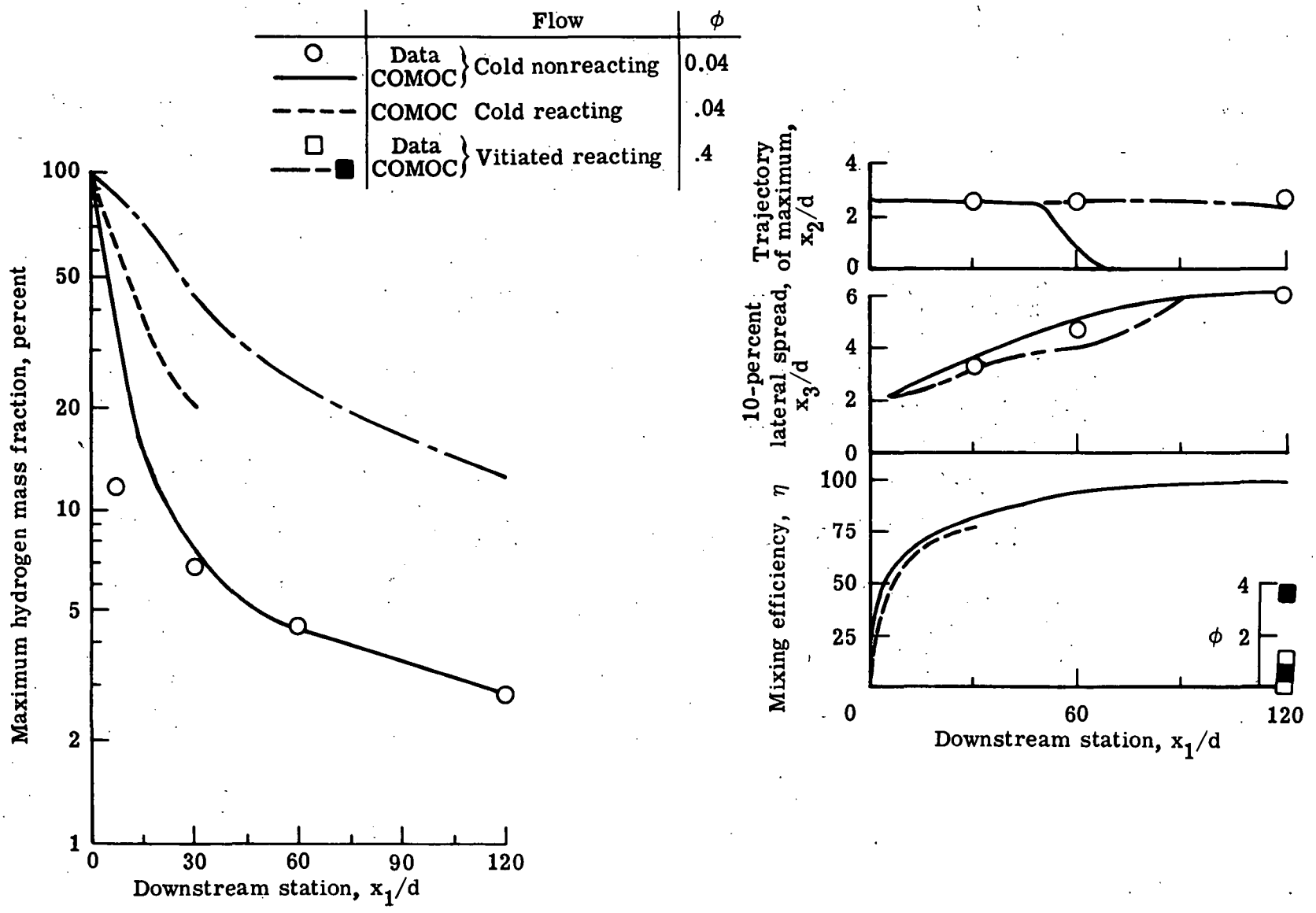

Figure 25.- Transverse cold hydrogen injection – virtual-source simulation. $q_r = 1.0$; $s/d = 12.5$.

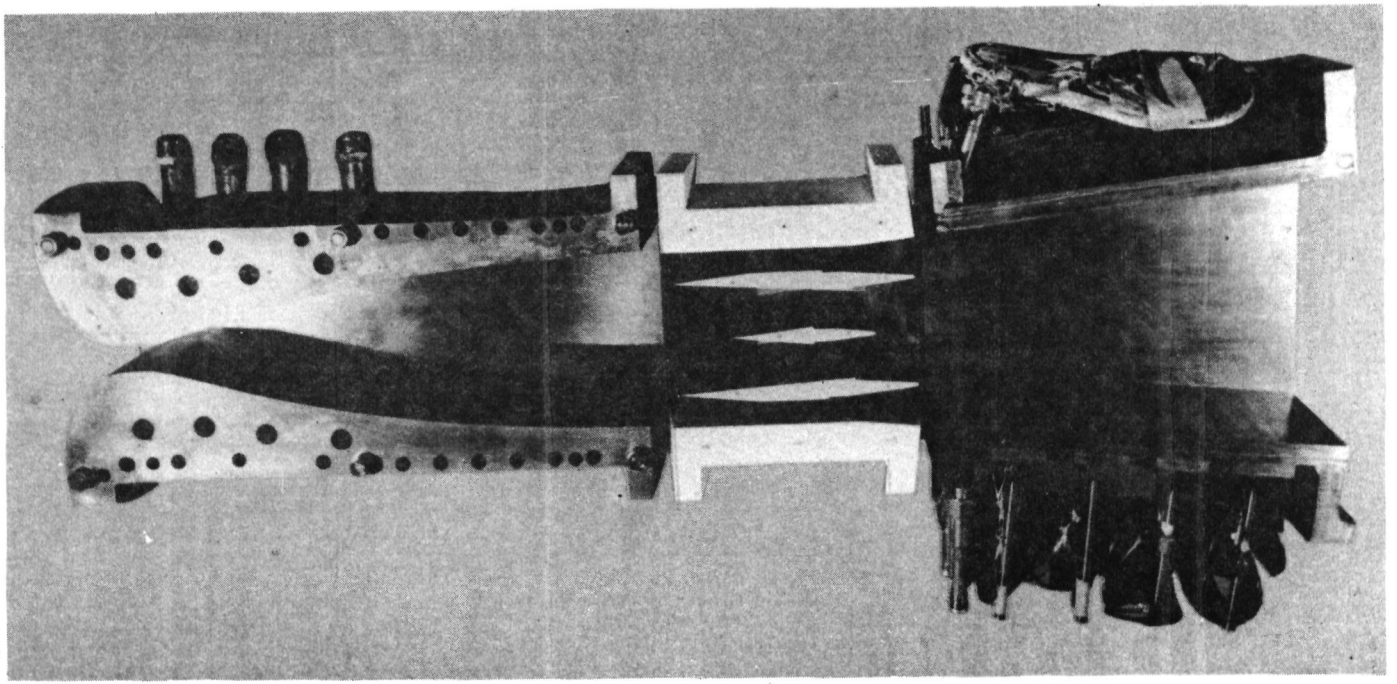

Figure 26.- Scramjet combustor model.

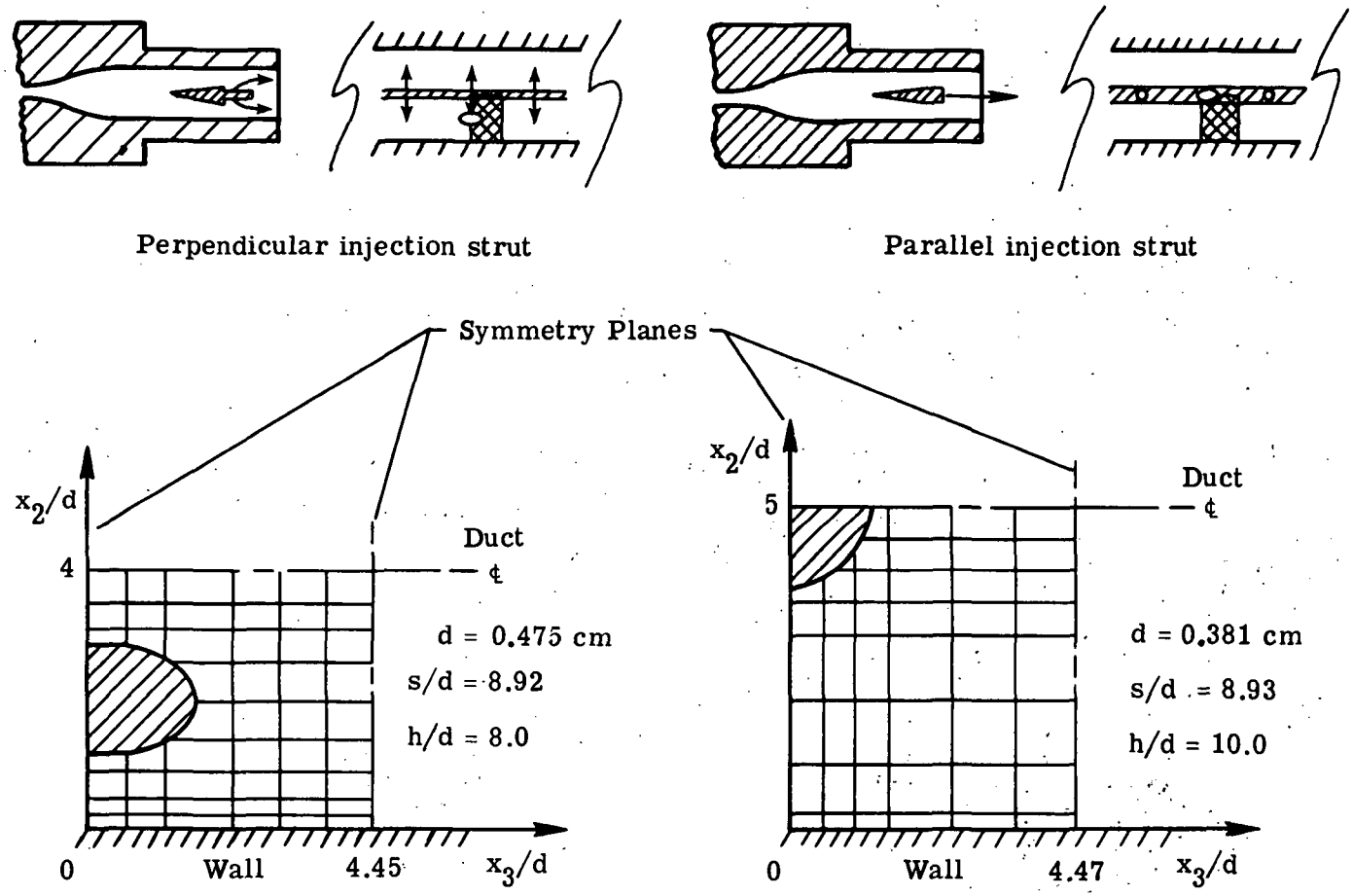

Figure 27.- Two fuel injector struts (ref. 11) for supersonic combustion, with virtual-source simulation.

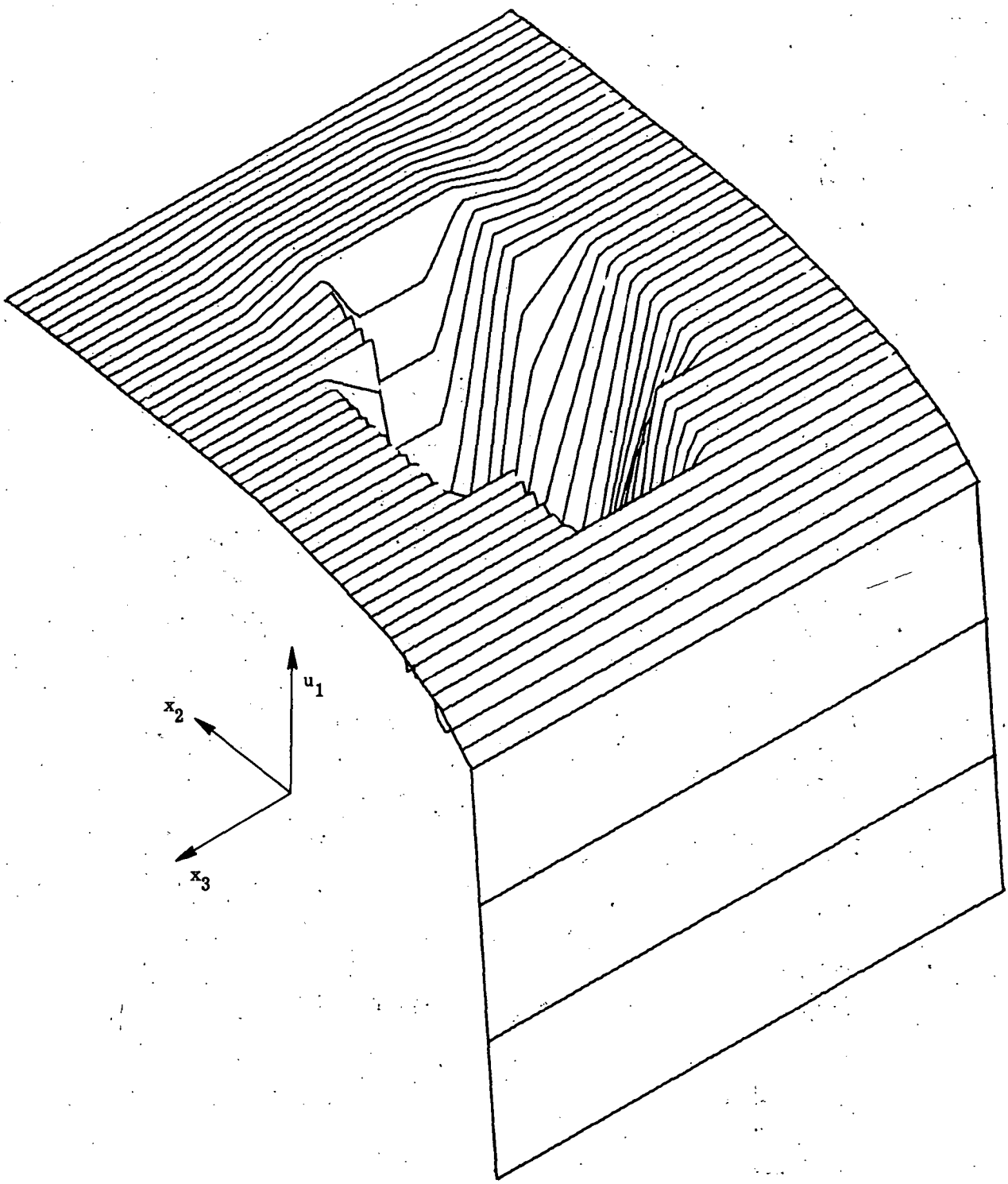

(a) $x_1/d = 0.$

Figure 28.- Longitudinal velocity distributions from virtual-source simulation of perpendicular injector.

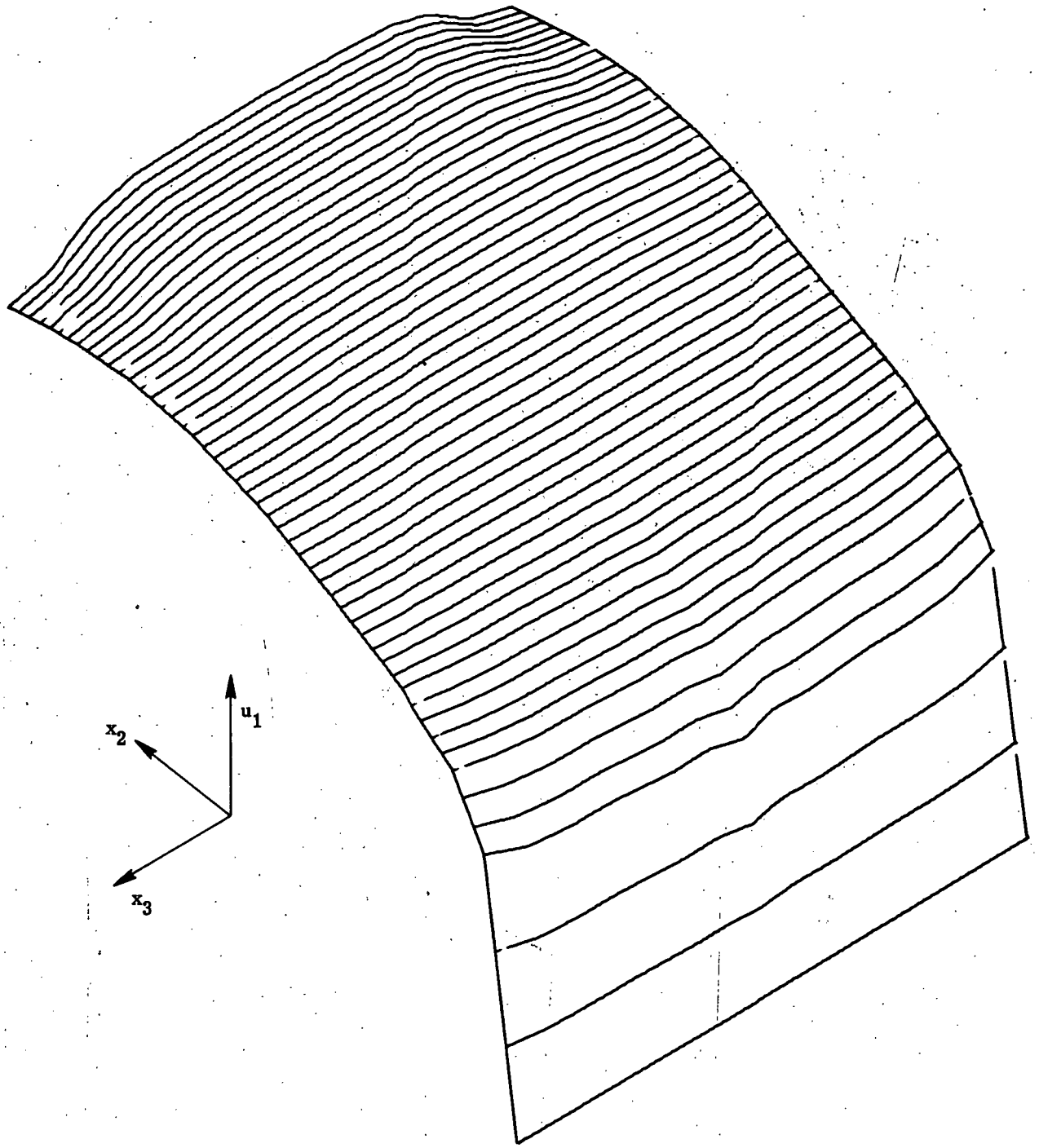

(b) $x_1/d = 150.$

Figure 28. - Concluded.

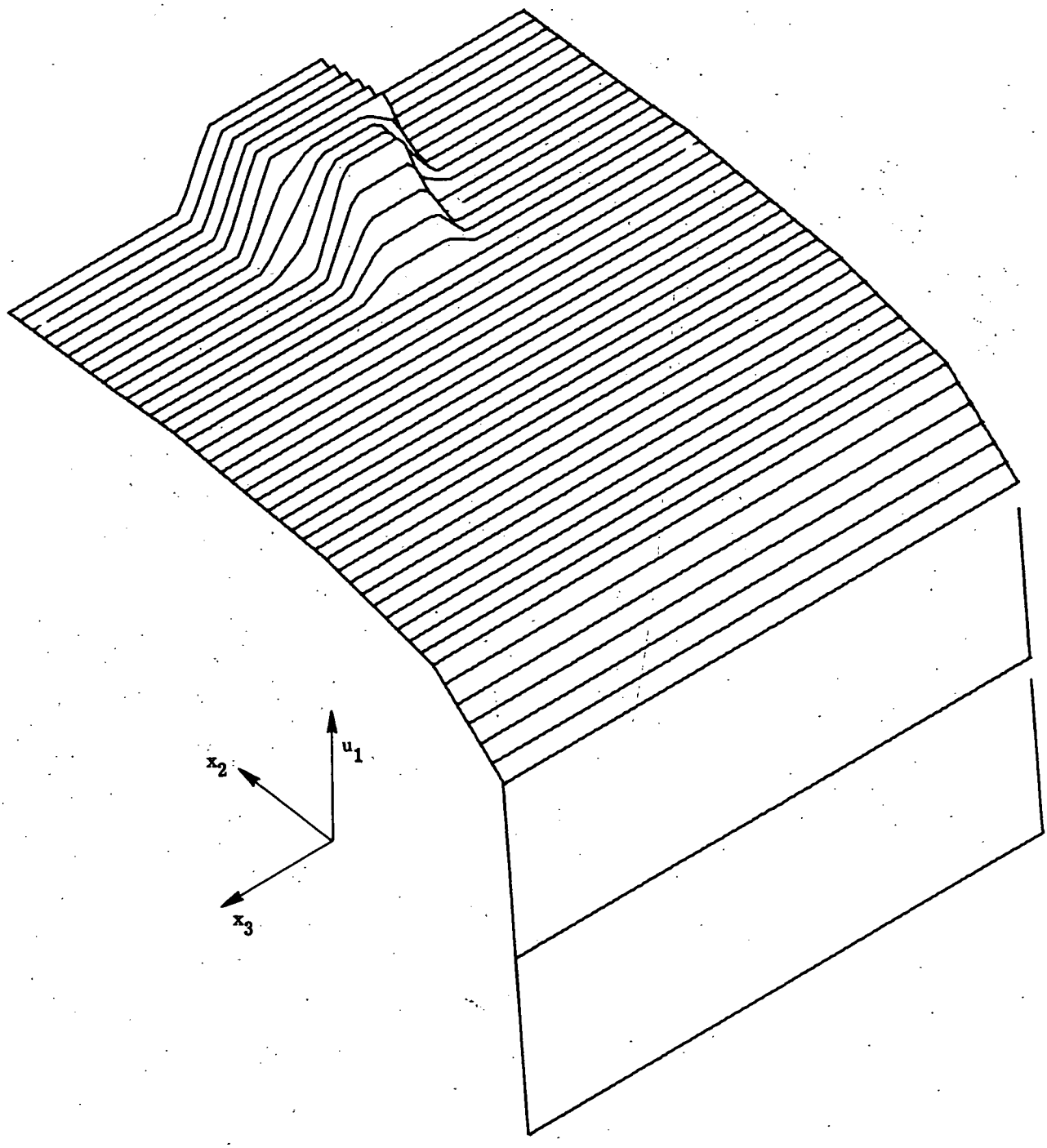

(a) $x_1/d = 0.$

Figure 29.- Longitudinal velocity distributions from virtual-source simulation of parallel injector.

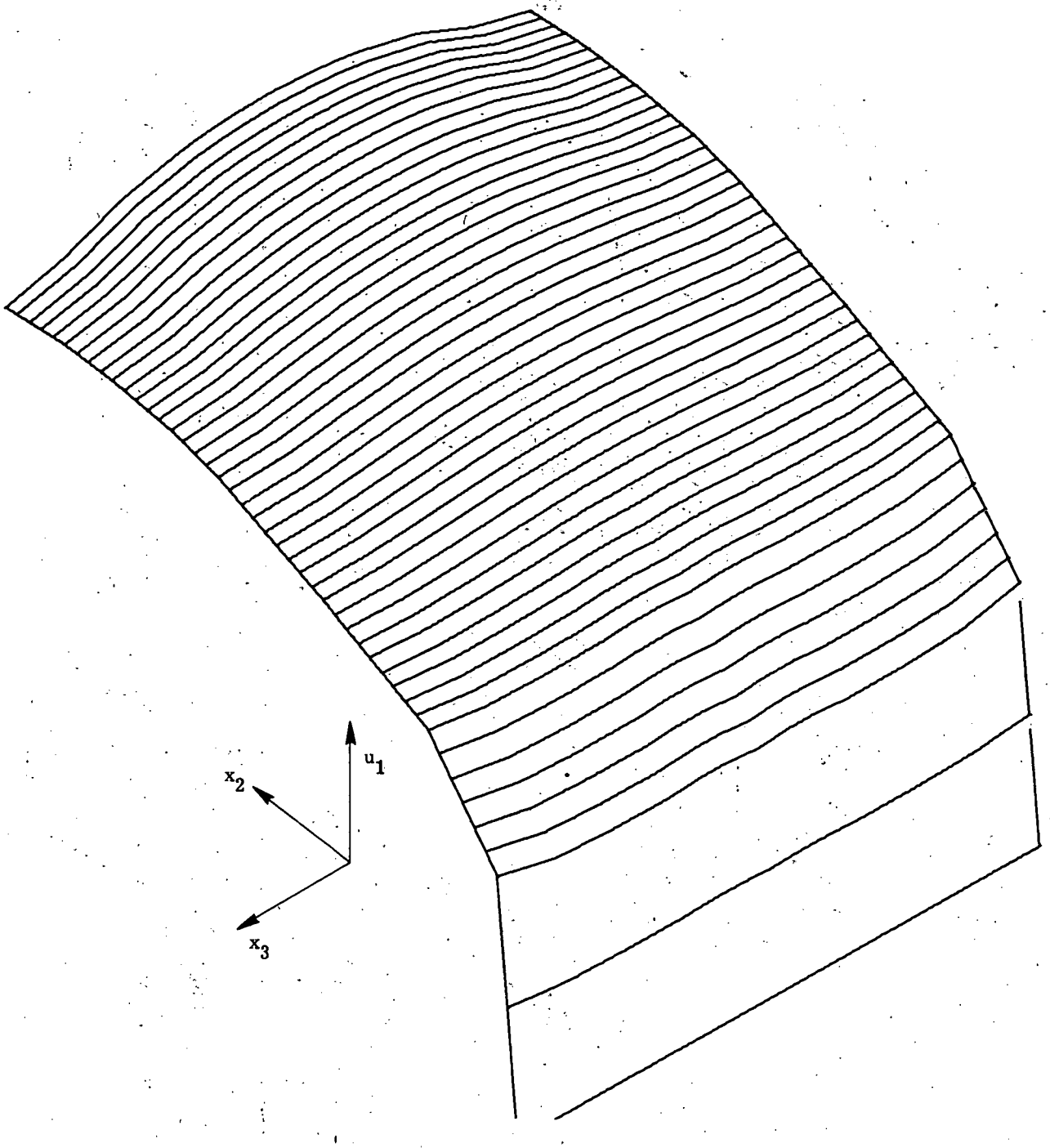

(b) $x_1/d = 150.$

Figure 29.- Concluded.

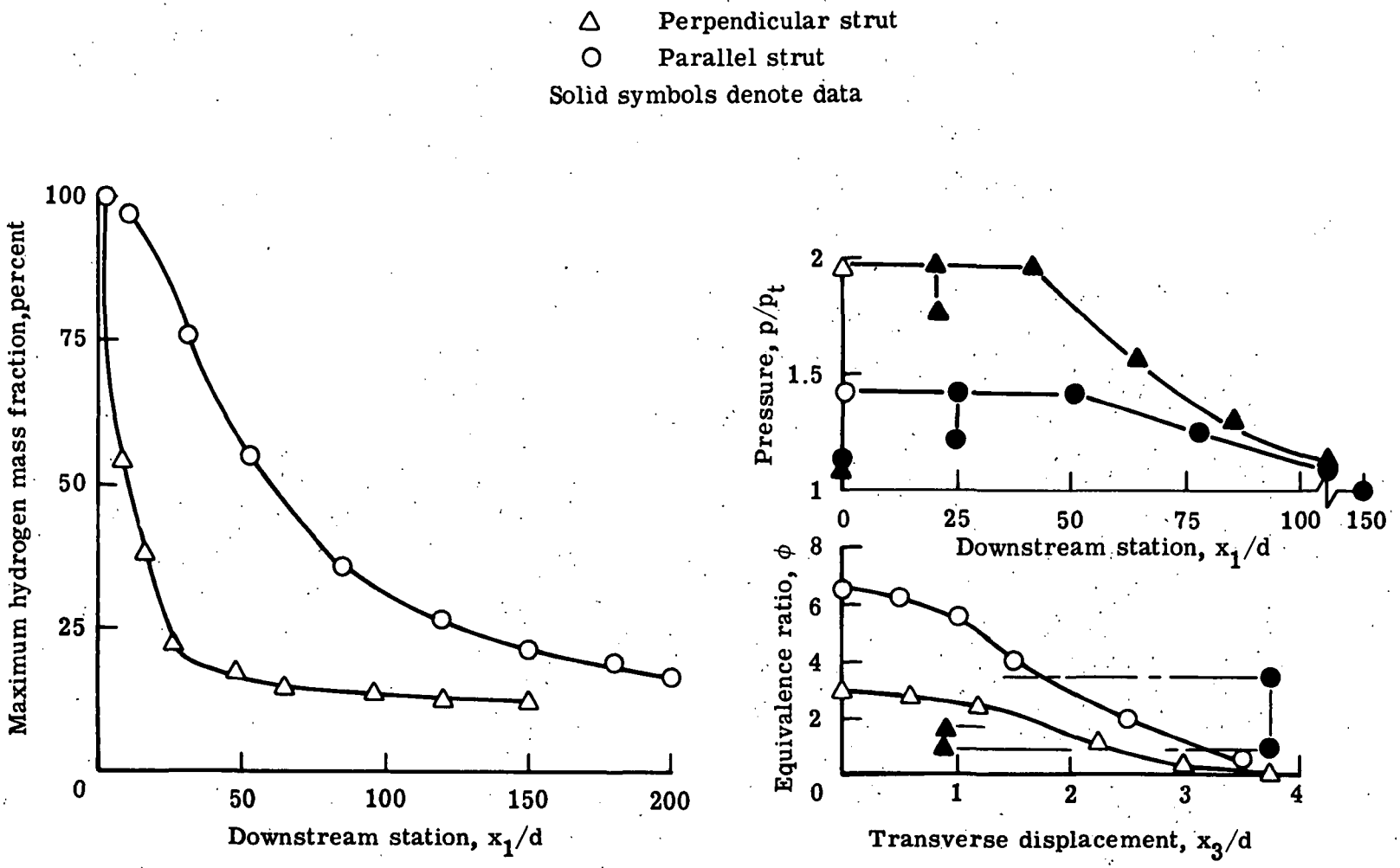

Figure 30.- Analytical evaluation of two supersonic strut injectors from virtual-source simulation. M = 3; ϕ = 0.6; s/d = 9.

Page Intentionally Left Blank

SUBGRID- OR REYNOLDS STRESS-MODELING FOR THREE-DIMENSIONAL TURBULENCE COMPUTATIONS

By Morris W. Rubesin

NASA Ames Research Center

SUMMARY

A review is given of recent advances in two distinct computational methods for evaluating turbulence fields, namely, statistical Reynolds stress modeling and turbulence simulation, where large eddies are followed in time. It is shown that evaluation of the mean Reynolds stresses, rather than use of a scalar eddy viscosity, permits an explanation of streamline curvature effects found in several experiments. Turbulence simulation, with a new volume averaging technique and third-order accurate finite-difference computing is shown to predict the decay of isotropic turbulence in incompressible flow with rather modest computer storage requirements, even at Reynolds numbers of aerodynamic interest.

INTRODUCTION

It is generally accepted that the Navier-Stokes equations represent the physics of Newtonian fluid flow fields at points in space and time away from sharp discontinuities such as shock waves. The intense shear layers present in turbulence fields, for example, the superlayer, extend over a much larger space than do shock waves, so that it can be expected that the Navier-Stokes equations will apply uniformly over the turbulence fields. Mathematically, turbulence can be considered, then, as the very complex solutions to these equations reflecting their nonlinear character and random sets of initial and boundary conditions. Because of the large set of possible solutions, unique solutions in turbulent flow can be expressed only in terms of averaged quantities over the time and/or space in the expectation that the turbulence is a slowly varying or stationary random process.

The nonlinear character of the equations forces the use of numerical computations, yet attainment of these solutions of the time-dependent Navier-Stokes equations is not possible now or in the foreseeable future. The reason for this is contained in certain features of turbulence that are inimical to finite difference computations. At a point in space, turbulent flow is irregular in time, random in character. In addition, it is three-dimensional and composed of different structures having a large range of length and time scales. To compute the irregularities, it is necessary to employ computational methods that are accurately time dependent. Techniques appropriate to asymptotic solutions that permit overshoots or employ artificial damping cannot be employed because they introduce errors in the instantaneous flow-field development that are likely to grow. The

small-scale dimensions, also, impose numerical stability or accuracy restraints on the allowable advancing time steps in the time-dependent solutions. For example, in an aerodynamic boundary layer, the smallest significant scale requires mesh spacing 10^{-5} of the boundary-layer thickness. The three-dimensionality of the flow, together with the small scale, requires on the order of 10^{17} mesh points to define the flow field of an entire aircraft. The corresponding allowable time step is 1 microsecond of real time. Clearly, these requirements for storage capacity and computer speeds are many orders of magnitude beyond the best of current computers or those contemplated in the foreseeable future. To circumvent these difficulties it is necessary to resort to "turbulence modeling."

The term "turbulence modeling" involves two distinct stages. The first eliminates the small-scale structure of the dependent variable through an averaging of some sort (ensemble, space, or time) that can be carried out with mathematical rigor. The new averaged dependent variables are relatively slow varying so they can be resolved with finite difference methods utilizing mesh dimensions and time intervals compatible with current computers. The nonlinear terms of the basic equations, however, introduce averages of moments of the dependent variables that must be expressed in terms of the averaged quantities retained to avoid a proliferation of dependent variables in excess of the numbers of equations available (the "closure" problem). The manner of doing this is the second stage of the "turbulence modeling" process and in this stage, considerable reliance is placed on comparisons with experimental data to compensate for the "physics" lost in the earlier averaging process.

The name "Statistical Theory of Inhomogenous Turbulence," references 1 and 2, has been applied to the process where averaging is performed at a point in space over a period of time long compared to the time scales of the largest eddies of the turbulence. The method is most suitable to steady-state mean flow fields, although it can be applied as well to flow fields that are slowly varying compared to the large eddy time scales. The resulting dependent variables represent the slowly varying mean flow field and are completely devoid of eddy structure. An alternative method, sometimes called "turbulence simulation," depends on averaging the Navier-Stokes equations over space volumes that are smaller than the largest eddies, but much larger than the tiniest eddies. The new dependent variables (the volume averages) retain their time dependence, but possess scales resolvable by current computer techniques.

The NASA Ames Research Center has been sponsoring research in both of these areas. It is believed that in the short term most practical aerodynamic computations will be based on the statistical theory of turbulence. The aerodynamicist is interested in the mean properties of the flow fields with which he deals so that the behavior of individual eddies is more information than he needs. On the other hand, the modeling hypotheses made in the statistical theory are largely intuitive and supported rather tenuously by a meager supply of data. It hasn't been possible to provide experimental information on all of the multitude of variables that appear in the modeling equations. Turbulence simulation, once verified, will be able to be applied

to a variety of simple flow fields that emphasize particular modeling effects. For example, simulation of homogeneous turbulence decay can shed light on modeled turbulence dissipation in the statistical theory. Simple shear flows can yield information on the diffusion of turbulence kinetic energy, or of pressure fluctuations. Thus, turbulence simulation will provide an excellent basis for guiding statistical modeling. Ultimately, however, the technique of turbulence simulation may go beyond merely providing modeling assistance to statistical theory and become the basis for practical turbulence computation. Inherent in turbulence simulation is its direct evaluation of the large eddies that are characteristic of particular flow fields and modeling of the small scales that are known to be universal in character. These are certainly the elements of a practical prediction scheme.

In this paper, a review will be given of some recent progress in the work sponsored by Ames. The recent contributions to the statistical theory of turbulence were performed at DCW Industries under Contract NAS2-8192. The work in turbulence simulation has been conducted at Stanford University under Grant NGR 05-020-622.

SYMBOLS

e, q^2	specific kinetic energy of turbulence
E	power spectral density
f	function
k	wave number
L	dimension of flow volume
M	turbulence generation grid mesh spacing
p	pressure
S_{ij}	rate of strain of mean motion
t, t^*	time, dummy variable of integration over time period
T	period of integration > > turbulence scale
u, v, w	velocity components in x, y, z directions
u_i	component of velocity in ith direction
u_τ	friction velocity, $\sqrt{\tau_w/\rho}$
U_o	channel mean velocity

x_i	coordinate in ith direction
y	distance normal to surface
Γ	irrotational strain
δ	boundary-layer thickness
δ_{ij}	Kronecker δ
Δ	mesh spacing
Δ_{avg}	dimension for space averaging (see table 1)
ε or ν_T	eddy diffusivity or eddy kinematic viscosity
ν	kinematic viscosity
κ	Von Kármán constant
ρ	density
τ	turbulent shear in boundary layer
$\tau_{ij}, \overline{u_i' u_j'}$	turbulent shear stress in direction i on surface normal to j
τ_w	wall shear
χ	parameter in dissipation term of equation (16)
ω	Saffman's "pseudo vorticity" or dissipation rate

Superscripts:

$(\bar{})$, $< >$	average quantity
$( )'$	instantaneous fluctuating quantity

Subscripts:

e	edge of boundary layer
i,j,k,m,n	tensor indices

STATISTICAL THEORY OF INHOMOGENOUS TURBULENCE

To place the Wilcox contribution (ref. 3) into the proper context of current turbulence modeling it is necessary to review briefly the basis of the statistical theory of turbulence. For simplicity, attention will be confined to incompressible fluid flow. The Navier-Stokes equations are

$$\frac{\partial u_i}{\partial t} + \frac{\partial}{\partial x_j}\left(u_i u_j\right) = -\frac{1}{\rho}\frac{\partial p}{\partial x_i} + \frac{\partial}{\partial x_j}\left(\nu \frac{\partial u_i}{\partial x_j}\right) \tag{1}$$

where the notation of repeated indices represents summation over all the coordinate directions. The local velocity components, or pressure, are written as

$$u_i\left(x_j, t^*\right) = \bar{u}_i\left(x_j, t\right) + u'\left(x_j, t, t^*\right) \tag{2}$$

which allows for slow variation of the mean quantity $\bar{u}_i$ in time t and expresses the fluctuating component within the integration period relative to the mean over the period. The averaging process is defined as

$$\bar{f}\left(x_j, t\right) = \frac{1}{T}\int_{t-T/2}^{t+T/2} f\left(x_j, t^*\right)\, dt^* \tag{3}$$

With equation (2), equation (3) becomes

$$\bar{u}_i\left(x_j, t\right) = \frac{1}{T}\int_{t-T/2}^{t+T/2} \left[\bar{u}_i\left(x_j, t\right) + u'\left(x_j, t, t^*\right)\right] dt^* \tag{4}$$

which reduces to the requirement

$$\frac{1}{T}\int_{t-T/2}^{t+T/2} u'\left(x_j, t, t^*\right)\, dt^* = 0 \tag{5}$$

When equation (1) is averaged according to equations (3) and (5), there results

$$\frac{\partial \bar{u}_i}{\partial t} + \frac{\partial \bar{u}_i \bar{u}_j}{\partial x_j} = -\frac{1}{\rho}\frac{\partial \bar{p}}{\partial x_i} + \frac{\partial}{\partial x_j}\left(\nu \frac{\partial \bar{u}_i}{\partial x_j} - \overline{u_i' u_j'}\right) \tag{6}$$

Before equation (6) can be solved it is necessary to express the moments $\overline{u_i' u_j'}$ (the Reynolds stresses) in terms of the mean flow $\bar{u}_j$ and the characteristics of the turbulence. If equation (1) is manipulated to yield a differential equation for $\overline{u_i' u_j'}$, reference 1, in addition to terms containing $\overline{u_i' u_j'}$ and $\bar{u}_j$, new quantities involving quadratures of u_j' and p' and $\overline{u_i' u_j' u_k'}$ appear. An additional set of equations for $\overline{u_i' u_j' u_k'}$ leads to many new higher moments. In general, equations for higher moments lead to more new dependent variables than new equations. The means of stopping this diverging process is achieved through "closure" hypothesis.

The most widely used closure method has been based on the concept of an eddy viscosity; for example, where it is hypothesized that the turbulence Reynolds stresses $\overline{u_i'u_j'}$ are proportional to the rate of strain of the mean flow, with the factor or proportionality, the eddy viscosity, being a scalar quantity. The similarity to Stokes stress relations in laminar flow and the role of viscosity is evident. With the eddy viscosity, ε,

$$\overline{u_i'u_j'} = 2\varepsilon S_{ij} - 2/3\,\delta_{ij}e \tag{7}$$

where the mean rates of strain, S_{ij}, are

$$S_{ij} = \frac{1}{2}\left(\frac{\partial \bar{u}_i}{\partial x_j} + \frac{\partial \bar{u}_j}{\partial x_i}\right) \tag{8}$$

for an incompressible fluid. Turbulence kinetic energy, e, is

$$e = \frac{1}{2}\overline{u_i'u_i'} \tag{9}$$

The earliest theories, due to Prandtl, expressed

$$\varepsilon = \varepsilon\left(x_2, S_{ij}, \kappa\right) \tag{10}$$

through an algebraic expression with κ an empirical constant. Since this "closed" the problem at the level of equation (6), it has been termed "first-order closure." The method was quite successful for pipe flows and boundary layers where changes occurred gradually. In fact, extensions of this method to compressibility has provided several decades of usefulness through accurate prediction of skin friction at high Mach numbers for two-dimensional aerodynamic configurations, evaluations of aerodynamic heating phenomena, and the assessment of concepts such as transpiration cooling or ablation for alleviating the effects of aerodynamic heating. The method is most accurate when restricted to simple shapes. Its cost effectiveness in numerical computations, however, has made its use attractive in heuristic investigations even for conditions where it cannot be expected to be accurate, namely, the zones of interaction between a shock wave and a turbulent boundary layer that is the topic of several of the papers in this conference.

For more general body shapes, especially those having rapidly varying boundary-layer edge conditions, the introduction of rate processes in the development in the turbulence is necessary. Here the eddy viscosity is expressed as a function of two turbulence quantities equivalent to velocity and time or length scales. As an example, the Saffman model (ref. 4) sets

$$\varepsilon = \frac{e}{\omega} = \frac{\text{turbulent specific kinetic energy}}{\text{"pseudo vorticity" or "dissipation rate"}} \tag{11}$$

where

$$\frac{De}{Dt} = f_1\left(e,\omega,S_{ij}\right) \tag{12}$$

and

$$\frac{D\omega^2}{Dt} = f_2\left(e,\omega,S_{ij}\right) \tag{13}$$

The functions f_1 and f_2 are not the exact terms that can be derived from equation (1), but are "modeled" to express the physical quantities actually present, rates of turbulence production, dissipation, and diffusion, in functional forms containing a closed set of dependent variables. These functional forms are dimensionally consistent and contain empirical constants that are expected to be insensitive to the character of individual flow fields. A review of a large number of such two-equation models, where the modeling takes place in the equations for the turbulence quantities and is called "second-order closure," is given in reference 5.

There are flow conditions, especially cases of three-dimensional flows, where the concept of the scalar eddy viscosity fails. For these conditions it is necessary to evaluate the Reynolds stresses $\overline{u_i'u_j'}$ directly. Several investigators have devised models of the direct Reynolds stress equations, references 6 through 8. The method described in this paper possesses desirable features. It is relatively simple, reducing to the simple Saffman eddy viscosity model when flow conditions permit, and it is easily extendable to compressible flows through the use of mass averaged dependent variables, reference 9. Furthermore, as is shown later, it has proved to be quite successful in explaining the streamline curvature effects documented in Bradshaw's monograph, reference 10.

The equation representing the Reynolds stresses of equation (6) can be written exactly as

(Convection) (Production) (Dissipation)

$$\frac{\partial \tau_{ij}}{\partial t} + \bar{u}_k \frac{\partial \tau_{ij}}{\partial x_k} = - \tau_{ik} \frac{\partial \bar{u}_j}{\partial x_k} - \tau_{jk} \frac{\partial \bar{u}_i}{\partial x_k} + 2\nu \overline{\frac{\partial u_i'}{\partial x_k} \frac{\partial u_j'}{\partial x_k}}$$

(Tendency to Isotropy)

$$- \overline{\frac{p'}{\rho} \left[\frac{\partial u_j'}{\partial x_i} + \frac{\partial u_i'}{\partial x_j} \right]}$$

(Turbulent Diffusion of Pressure)

$$+ \frac{\partial}{\partial x_k} \left[\delta_{ik} \overline{u_j' \frac{p'}{\rho}} + \delta_{jk} \overline{u_i' \frac{p'}{\rho}} \right]$$

(Molecular and Turbulent Diffusion of Stress)

$$+ \frac{\partial}{\partial x_k} \left[\nu \frac{\partial \tau_{ij}}{\partial x_k} + \overline{u_k' u_i' u_j'} \right] \qquad (14)$$

where

$$\tau_{ij} = - \overline{u_i' u_j'} \qquad (15)$$

The terms on the left represent the convection of the Reynolds stresses. The first two terms on the right are the production terms; for example, where the mean flow strain interacts with the Reynolds stresses. The third term on the right is the dissipation term. It depends on quadratures of the instantaneous velocity gradients and therefore is largely dependent on the small scales of the turbulence. The next term, involving correlations of pressure and velocity gradient correlations, permits exchange between the individual Reynolds stresses and is termed the "tendency toward isotropy." This term vanishes for incompressible flow when equation (14) is contracted to yield an equation for the turbulent kinetic energy. The next term is the diffusion of pressure fluctuations by turbulence. Finally, the last term on the right, a divergence form, represents the diffusion of the Reynolds stresses by molecular and turbulent mechanisms. Dave Wilcox of DCW Industries models the Reynolds stress equation as

(Convection) (Production) (Dissipation)

$$\frac{\partial \tau_{ij}}{\partial t} + \bar{u}_k \frac{\partial \tau_{ij}}{\partial x_k} = - \tau_{ik} \frac{\partial \bar{u}_j}{\partial x_k} - \tau_{jk} \frac{\partial \bar{u}_i}{\partial x_k} + \frac{2}{3} \beta^* \left[1 - \chi + \chi^2 \right] e\omega\delta_{ij}$$

(Tendency to isotropy) (Production redistribution)

$$- \lambda^* \omega \left[\tau_{ij} + \frac{2}{3} e\delta_{ij} \right] + 4 \frac{e}{\omega} \left[S_{im} S_{mj} - \frac{1}{3} S_{mn} S_{mn} \delta_{ij} \right]$$

(Molecular and turbulent diffusion)

$$+ \frac{\partial}{\partial x_k} \left[\left(\nu + \sigma^* \frac{e}{\omega} \right) \frac{\partial \tau_{ij}}{\partial x_k} \right] \qquad (16)$$

where

$$\chi = \sqrt{\frac{2 S_{mn} S_{mn}}{\beta^* \omega^2}}$$

The turbulent dissipation rate, ω, is given by

$$\frac{\partial \omega^2}{\partial t} + \bar{u}_k \frac{\partial \omega^2}{\partial x_k} = \left[\alpha \sqrt{\frac{\partial \bar{u}_i}{\partial x_j} \frac{\partial \bar{u}_i}{\partial x_j}} - \beta\omega \right] \omega^2 + \frac{\partial}{\partial x_k} \left[\left(\nu + \sigma \frac{e}{\omega} \right) \frac{\partial \omega^2}{\partial x_k} \right] \qquad (17)$$

after Saffman, reference 4. The turbulent kinetic energy, e, obtained as the contraction of equation (16), is

$$\frac{\partial e}{\partial t} + \bar{u}_k \frac{\partial e}{\partial x_k} = \left[\alpha^* \sqrt{2 S_{mn} S_{mn}} - \beta^* \omega \right] e + \left[\tau_{ij} - 2 \frac{e}{\omega} S_{ij} \right] \frac{\partial \bar{u}_i}{\partial x_j}$$

$$+ \frac{\partial}{\partial x_k} \left[\left(\nu + \sigma^* \frac{e}{\omega} \right) \frac{\partial e}{\partial x_k} \right] \qquad (18)$$

where

$\alpha = 0.2638 \qquad \beta^* = \alpha^{*2} = 8/81 = .0988$

$\beta = 0.18$

$\sigma = 0.50 \qquad \sigma^* = 0.5 \qquad \lambda^* = (9/2)\ \beta^*$

These constants are consistent with the Saffman formulation. Wilcox introduced an additional constant λ^*, which he evaluated by requiring the normal stresses in a flat plate boundary layer to have the ratio $\overline{u'^2} : \overline{v'^2} : \overline{w'^2}$ equal to 4:2:3 to conform to experiment.

A comparison of the exact equation (14) and the modeled equation (16) indicates that modeling has been applied to all the terms other than turbulence production. The form of the modeled terms are expressed in a limited invariant tensor form, as compared to reference 7. Consistent with the Saffman model, the dissipation term does not represent the energy dissipated by molecular processes at the smallest scales, but rather accounts for the energy cascaded to the smallest eddies by the larger eddies. Saffman assumed that the scales of the smallest eddies adjust to accommodate the turbulence passed to them, and thereby avoids the need for two length scales. The quantity $1 - \chi + \chi^2$ in equation (16) is always greater than zero, giving dissipation its proper sign. One can consider that the terms labeled "tendency to isotropy" and "production redistribution" together model the "tendency to isotropy" term of equation (14) as the contraction of all these terms is zero. The current Wilcox model neglects the "turbulent diffusion of pressure." Finally, the "turbulent diffusion of stress," the third order correlation, is modeled through an eddy viscosity assumption supplemented by an effective turbulent Prandtl number, σ^*.

One of the first problems to which this model was applied was the effect of streamline curvature in attached turbulent boundary layers. Considered was a constant pressure flow over a curved surface having a radius of curvature R in the plane of the two-dimensional mean flow. From a perturbation solution of equations (6) and (16) to (18) corresponding to the wall region of the boundary layer, Wilcox found that mean velocity could be expressed in the usual wall layer dimensionless quantities as

$$\left(1 - \phi \frac{y}{R}\right) \frac{u}{u_\tau} = \frac{1}{\kappa} \log \frac{u_\tau y}{\nu} + \text{Constant} \tag{19}$$

with

$$\phi = 15.4 \tag{20}$$

The corresponding turbulence quantities were found to be

$$e = \frac{u_\tau^2}{\alpha^*} \left[1 + 0 \left(\frac{y}{R} \log \frac{u_\tau y}{\nu} \right)^2 \right] \tag{21}$$

$$\omega = \frac{u_\tau}{\alpha^* \kappa y} \left[1 + 2.4 \frac{y}{R} \log \frac{u_\tau y}{\nu} + \ldots \right] \tag{22}$$

$$\overline{u'^2} = \frac{8}{9}\frac{u_\tau^2}{\alpha^*}\left[1 + 3\frac{y}{R}\log\frac{u_\tau y}{\nu} + \ldots\right] \tag{23}$$

$$\overline{v'^2} = \frac{4}{9}\frac{u_\tau^2}{\alpha^*}\left[1 - 10\frac{y}{R}\log\frac{u_\tau y}{\nu} + \ldots\right] \tag{24}$$

$$\overline{w'^2} = \frac{6}{9}\frac{u_\tau^2}{\alpha^*}\left[1 + \frac{8}{3}\frac{y}{R}\log\frac{u_\tau y}{\nu} + \ldots\right] \tag{25}$$

In addition, the local shear turned out to be expressible in terms of an eddy viscosity

$$\tau = \frac{1}{\lambda^*}\frac{\overline{v'^2}}{\omega}\frac{\partial \bar{u}}{\partial y} \tag{26}$$

These results are very significant in several ways. First, the law of the wall expression, equation (19), has the same form found to correlate experimental data measured over a curved wall. The value of ϕ found experimentally by R. N. Meroney, was $\phi \cong 12$, which is in reasonable agreement with the modeled value of equation (20). Furthermore, the specific kinetic energy of the turbulence, equation (21), is shown to be relatively unaffected by the streamline curvature. Again, this is in agreement with experimental data for corresponding flow conditions where So and Mellor, reference 11, found ϵ_{max}/u_τ^2 unaffected by curvature for convex walls. A comparison of equations (23) through (25) shows that streamline curvature affects the individual normal stresses differently. The normal stresses along and across the surface increase, while the normal stress perpendicular to the surface decreases and in an amount larger than the others. The difference in sign of the behavior of the normal stresses demonstrates why the specific kinetic energy remains essentially constant. It is interesting that the expression equation (26) for the shear stress, τ, shows an eddy viscosity form, but where the characteristic turbulence velocity scale is not the specific kinetic energy, e, reference 4, but the normal stress $\overline{v'^2}$. The sensitivity of $\overline{v'^2}$ to the effects of streamline curvature and its direct effect on the shear explains much of the streamline curvature effect discussed by Bradshaw, reference 10.

Another comparison of the Wilcox Reynolds stress computations with experimental data is shown in figure 1. These data were obtained by Bradshaw, reference 12, in a turbulent boundary layer on a flat plate on which an adverse pressure was suddenly applied. The data include profiles of the three individual normal Reynolds stresses, the shear stress, the specific kinetic energy, and the mean velocity at a station 1.52 m after the adverse pressure gradient was applied. To initiate the computations, extensive use was made of the Bradshaw mean flow and hot-wire data at the start of the adverse pressure gradient. The initial mean velocity and

specific kinetic energy profiles were directly obtained from the data. The ω profile was deduced from the measured turbulent shear stress and mean velocity profiles by utilizing the eddy viscosity relationship

$$\tau = \rho \frac{e}{\omega} \frac{\partial \bar{u}}{\partial y} \tag{27}$$

Because the shear τ and $\partial\bar{u}/\partial y$ both approach zero near the boundary-layer edge, the determination of ω there becomes uncertain and is a source of error. The value of ω found at the boundary layer edge and used at all stations as a boundary condition on equation (17) was $\omega_e = 10^{-4}\, u_e^2/\nu$.

The Reynolds stress theory, shown in figure 1 as the solid lines, does a good job in predicting the maximum levels of the normal stresses, however, the shapes of the profiles for $\overline{u'^2}$ and $\overline{w'^2}$ are missed badly. In contrast, the $\overline{v'^2}$, the normal stress perpendicular to the surface, is predicted quite well everywhere in the boundary layer. It should be noted that after experiencing the adverse pressure gradient, the ratio $\overline{u'^2}_{max} : \overline{v'^2}_{max} : \overline{w'^2}_{max}$ is 9:5:7, which the theory seems to predict without modification of the constant λ^*. The comparisons with the data for the shear stress, turbulent energy, and mean velocity also contain the predictions by the eddy viscosity model of Saffman indicated by the dashed lines. Because the Wilcox model relies so heavily on the Saffman model, it is not surprising that the two theories give such similar results, especially at a station where the turbulence is nearly in equilibrium. For these quantities, the predictions, while encouraging, yield results that can stand improvement.

From this brief comparison with data, it can be concluded that the Wilcox Reynolds stress model with second-order closure predicts the effects of streamline curvature rather accurately in the wall region of a boundary layer. Of the normal stresses, the $\overline{v'^2}$ is most strongly affected. This, in turn, affects the shear stress since in this region $\tau \simeq 1/\lambda^*(\overline{v'^2}/\omega)(\partial\bar{u}/\partial y)$. The latter is a most important practical result in that it shows that current eddy viscosity models with $\overline{v'^2}$ replacing the turbulence energy as the characteristic turbulence velocity still may apply in regions of streamline curvature. Despite the success of the model near the surface, modeling improvements are required to increase the accuracy of predictions away from the surface. Perhaps the diffusion of pressure fluctuations by turbulence cannot be neglected. Further, it may be necessary to modify the constants of the Saffman theory for particular flow fields to enhance accuracy at the sacrifice of generality.

TURBULENCE SIMULATION

The turbulence simulation calculations to be described here are being conducted at Stanford University, with Profs. William Reynolds and Joel Ferziger as the principal investigators. The primary goal of the Stanford activity is to derive turbulence simulation techniques ultimately suitable for use with compressible fluids and complex aerodynamic configurations. The initial stages of the program, however, have been confined to very simple

flow fields and to incompressible fluids so that comparisons of the techniques employed could be made with the results of other workers in turbulence simulation and with certain fundamental experiments based on hot-wire measurements.

The program began with a careful reconsideration of the volume averaging process by Leonard, reference 13. The new averaged equations contained second order terms that required finite difference methods with truncation errors fourth order in space and second order in time. These equations have been used to study the decay of incompressible, isotropic flow with different numerical techniques and alternative models for subgrid closure. The work is being extended, currently, to flows with irrotational plane strain, simple shear, and a jet into an axial stream.

Table 1 and figure 2 compare the bases of the averaging technique devised by Leonard with those of the more conventional approach. The averaged Navier-Stokes equation shown at the top of table 1 is common to both methods. The dependent variables, however, have different meaning. The conventional average quantity is a uniformly weighted average over a volume of dimension Δ_j around the point x_j. The volume dimension Δ_j is customarily set equal to the finite difference mesh dimension. The Leonard average is weighted toward the center of the averaging volume x_j as $G(x_j-x_j')$ is required to decay to a zero value with increasing distance x_j-x_j'. Specifically, in most of the numerical work a Gaussian weighting function has been adopted with Δ_{avg}, not necessarily set equal to the mesh spacing, as a parameter. In either averaging method, the gradient of an average equals the average of a gradient. Key to the difference in the averaging techniques is the manner in which the local velocity vector is divided into the resolvable and irresolvable eddy contributions. This is shown mathematically in table 1 and diagramatically in the figure 2. In the conventional case, the resolvable velocity is identified with the mean velocity in the box so that the irresolvable component, then, averages to zero. With this definition the averaged nonlinear moment can be expressed as the product of the individual average velocity components plus the Reynolds stress. It is emphasized that this Reynolds stress is time dependent, just as are the averaged velocities related to the large eddies. In Leonard averaging, the resolvable component of velocity $\bar{u}_i$ is treated as a continuously varying quantity across the averaging volume, and the irresolvable fluctuations are defined relative to the local $\bar{u}_i$. The averaged nonlinear moment is much more complex containing a term representing the divergence of the quadrature of the mean velocities as well as a series of quantities that are identified in the aggregate as a Reynolds stress. The modeling of the Reynolds stresses, although they are inherently different quantities, is the same functionally in either method. The Reynolds stress of the unresolved components, R_{ij}, for either averaging method is expressed in terms of an eddy viscosity and the instantaneous strain of the resolved eddies. The definition of the eddy viscosity follows Smagorinsky, reference 14, where the length scale is set equal to the mesh spacing and the frequency scale is related to the root of the sum of the squares of all the strain elements. An alternative eddy viscosity has been utilized by the Stanford group wherein the frequency scale depends on the vorticity of the resolved eddies,

having the advantage of going to zero where the flow is irrotational. The latter approach may aid in defining the boundaries between turbulent and nonturbulent, irrotational flow regions.

The main contribution resulting from the Leonard averaging process is the addition of the term $\Delta^2_{avg}/24(\partial^2/\partial x_j^2)(\bar{u}_i\bar{u}_j)$ to the expression for the averaged moment. Since this term is contained within an operator $\partial/\partial x_j$ it is of third order when expressed in finite difference form. To retain the significance of this term, the Stanford group was forced to adopt finite difference methods with fourth-order truncation errors in space, reference 15. The usual second-order finite differencing in time was retained.

The results of some of the Stanford computations of the decay of homogeneous, isotropic turbulence are shown in figures 3 through 6. The data used for comparison were measured by Compte-Bellot and Corrsin, reference 16, in a uniform flow behind a turbulence generating grid at a Reynolds number per foot of about 200,000. The experimental three-dimensional turbulent energy spectrum at a fixed position in the channel downstream of the grid, shown in figure 3, was adopted as the initial conditions for the calculations. Because the mean flow rate is uniform, the distance along the channel serves as the independent variable of the problem and can be expressed in time as tU_o/M, where M is the mesh spacing of the turbulence generation grid. At the higher wave numbers, the spectrum possesses the $k^{-5/3}$ distribution expected of homogeneous, isotropic turbulence according to the theory of Kolmogoroff, reference 17. The vertical lines in figure 3 define the range of wave numers, k, resolved in the calculations by mesh spacings where each side of the calculational volume is divided into 16 or 32 parts. The lower bound results from the imposition of periodic boundary conditions on opposite faces of the cubic volume, so that

$$k_{min} = \frac{2\pi}{L} \tag{28}$$

where L is the length of the side of the cube. For the cube divided in 16^3 parts, L is taken to be 24 cm. For the cube divided in 32^3 parts, L is 32 cm. The corresponding k_{min}, from equation (28), are 0.26 cm^{-1} and 0.2 cm^{-1}, respectively. The upper value of the resolved k is dependent on the computational mesh dimension, being smaller for the 32^3 mesh division. Within these bounds, the 32^3 mesh division can resolve eddies that account for 80% of the total turbulence energy, whereas the 16^3 mesh division only accounts for about 71% of the energy.

The next three figures (4 to 6) show the evolution of the turbulence spectra at times, or distances beyond the turbulence generating grid, after the initial value set at the farthest upstream test station. All of the figures represent the case of the cube divided into 16^3 parts and with computational mesh spacings of 1.5 cm. The results found from the 32^3 case showed no marked improvements in the calculations. The computation was initiated by expressing the turbulence in a 3-dimensional Fourier series. The Fourier transform of this velocity series to wave-number space then was matched directly to the experimental energy spectrum to give the magnitude of the

coefficients corresponding to each wave-number vector. These vectors were then randomly oriented with a random number generator. Finally, an inverse Fourier transform was applied to achieve the initial turbulence field compatible with the measured energy in physical space. The decay of the turbulence field was then computed using the time-dependent methods described earlier.

Figure 4 shows the effect of setting $\Delta_{avg} = 0$ and utilizing the Smagorinsky subgrid eddy viscosity model (see table 1) in the computations. The dashed lines represent the data at the initial time, $tU_o/M = 42$, and a subsequent time, $tU_o/M = 98$. The computed spectra are represented with the solid lines. Initially the computations are made to agree with the $tU_o/M = 42$ data line as described earlier. The development of the spectra after this time is the test of the method and the subgrid model. From table 1, it is noted that with $\Delta_{avg} = 0$, the weighting function in the Leonard averaging is a Dirac function and the averaged Navier-Stokes equation is formally the same as in conventional averaging, although the meaning of the dependent variable $\bar{u}_i$ is different. For $\Delta_{avg} = 0$, as time progresses, a piling up of energy occurs at the high wave-number end that becomes progressively worse.

Figure 5 shows the evolution of the energy spectrum if the averaging volume dimension is increased to equal to the computational mesh dimensions, $\Delta_{avg} = \Delta$. Again, the Smagorinsky eddy viscosity model is used for the subgrid Reynolds stresses. Note that the dashed lines representing the data are different from those in the previous figure because the data have been averaged according to the Leonard formula with $\Delta_{avg} = \Delta$ in order to express the data in the same dependent variables as in the computations. The unusually high energy at the high wave numbers evident in the previous figure for $\Delta_{avg} = 0$ at $tU_o/M = 98$ is reduced here for $\Delta_{avg} = \Delta$. Finally, in figure 6, the results of using $\Delta_{avg} = 2\Delta$ are shown. Again the data have been averaged to make the data and computation dependent variables correspond. The dashed line at $tU_o/M = 98$ is the averaged data. The points in symbols show the computed spectrum at $tU_o/M = 98$ for both the Smagorinsky and vorticity models of the subscale eddy viscosity (see table 1). There is little to choose between the different models for this example. Both show excellent agreement with the data, and the piling-up of the calculations at high wave number is no longer evident. It appears that the use of $\Delta_{avg} = 2\Delta$ is most appropriate for this type of problem and that the additional term in the Leonard averaging process acts to redistribute the energy within the spectrum in an appropriate manner.

The last figure, figure 7, shows some early results of computations of the distortion of homogeneous turbulence by irrotational plane strain. A field of homogeneous isotropic, turbulence is passed through the transition section shown schematically in the upper left of the figure. The cross-sectional area is constant so that $\bar{w}$, the mean velocity in the z direction remains constant. In the center portion, the walls perpendicular to the y-axis move in to just balance the outward movement of the walls perpendicular to the x-axis, resulting in a constant irrotational plane strain of the mean flow. Downstream of the transition region, the walls again become parallel.

The development of the mean normal stresses with distance along the channel as computed by turbulence simulation is shown in the lower portion of the figure. Again, a cubic volume of 16^3 mesh points was employed. At station 0 the turbulence, initiated as described earlier for the decay problem, is nearly isentropic $\overline{u'^2} = \overline{v'^2} \cong \overline{w'^2}$. In the region of constant irrotational strain, the normal stress in the expanding direction, $\overline{u'^2}$, diminishes, whereas, $\overline{v'^2}$, in the contracting direction increases. The axial normal stress remains relatively unchanged. In the downstream parallel section, the turbulence appears to be returning to isotropy as expected, but very slowly.

The results of turbulence simulation calculations described here are most encouraging. Through adjustment of the volume-averaging process and the use of higher order finite differencing, it has been possible to accurately predict the decay rate and spectral content of the large eddies of homogeneous, isotropic turbulence in incompressible flow. No difficulties have been encountered for the decaying type of flow with the standard subgrid modeling techniques. In addition, early attempts at handling more complex flows are yielding reasonable results with relatively little extra effort. Perhaps the most important result to date is the attainment of accurate turbulence prediction at Reynolds numbers of aerodynamic interest with the rather small number of mesh points employed.

CONCLUDING REMARKS

The success of the Reynolds stress modeling in the statistical theory of turbulence within a boundary layer in the immediate vicinity of the wall is most encouraging. Although improvements in modeling are still required for the wake region of the boundary layer, a way of doing this other than by reasoned intuition seems to be close at hand through turbulence simulation. In the near future, significant advances can be expected through the intersection of these seemingly disparate approaches to the evaluation of turbulence flows. Solutions to simple problems at aerodynamic Reynolds numbers appear to be possible currently as computer storage requirements and subgrid modeling do not seem to be as critical as was anticipated earlier.

REFERENCES

1. Rotta, J.: Statistische Theorie nichthomogener Turbulenz. 1. Mitteilung. Z. Phys., Bd. 129, 1951, pp. 547-572. (Available as NASA TT F-14560).

2. Rotta, J.: Statistische Theorie nichthomogener Turbulenz. 2. Mitteilung. Z. Phys., Bd. 131, 1951, pp. 51-77. (Available as NASA TT FF-11696).

3. Wilcox, D. C. and Chambers, T. L.: Streamline Curvature Effects on Turbulent Boundary Layers. DCW Industries Report DCW-R-04-01, Feb. 1975.

4. Saffman, P. G.: A Model for Inhomogeneous Turbulent Flow. Proc. Roy. Soc. Lond. A, vol. 317, 1970, pp. 417-433.

5. Launder, B. E., and Spalding, D. B.: Mathematical Models of Turbulence. Academic Press, London, 1972.

6. Daly, B. J., and Harlow, F. H.: Transport Equations in Turbulence, Physics of Fluids, vol. 13, no. 11, Nov. 1970, pp. 2634-2649.

7. Donaldson, C duP., Sullivan, R. D., and Rosenbaum, H.: A Theoretical Study of the Generation of Atmospheric Clear Air Turbulence, AIAA Journal, vol. 10, no. 2, Feb. 1972, pp. 162-170.

8. Hanjalac, K. and Launder, B. E.: A Reynolds Stress Model of Turbulence and its Application to Thin Shear Flows. J. Fluid Mech., vol. 52, pt. 4, 1972, pp. 609-638.

9. Rubesin, M. W. and Rose, W. C.: The Turbulent Mean-Flow, Reynolds Stress, and Heat-Flux Equations in Mass-Averaged Dependent Variables. NASA TM X-62,248, March 1973.

10. Bradshaw, P.: Effects of Streamline Curvature on Turbulent Flow. AGARD-AG-169 (1973).

11. So, R. M. C. and Mellor, G. L.: An Experimental Investigation of Turbulent Boundary Layers Along Curved Surfaces. NASA CR-1940, 1972.

12. Bradshaw, P.: The Response of a Constant-Pressure Turbulent Boundary Layer to the Sudden Application of an Adverse Pressure Gradient. NPL Aero Rep. 1219, Brit. A.R.C., Jan. 6, 1967.

13. Leonard, A.: Energy Cascade in Large-Eddy Simulations of Turbulent Fluid Flows. Advances in Geophysics, vol. 18A, F. N. Frankiel and R. E. Munn (Ed.) Academic Press, N.Y., 1974.

14. Smagorinsky, J.: General Circulation Experiments with the Primitive Equation: I The Basic Experiment. Monthly Weather Review, vol. 91, No. 3, Mar. 1963, pp. 99-164.

15. Shanaan, S. and Ferziger, J. H.: A Direct Method of Solution of Poisson Equation Accurate to Fourth Order. Report No. TF-3, Stanford University, August 1974.

16. Compte-Bellot, G. and Corrsin, S.: Simple Eulerian Time Correlation of Full- and Narrow-Band Velocity Signals in Grid-Generated, "Isotropic" Turbulence. J. Fluid Mech., vol. 48, pt. 2, July 28, 1971, pp. 273-337.

17. Hinze, J. O.: Turbulence, McGraw-Hill Book Co., New York, 1959.

TABLE 1. COMPARISON OF CONVENTIONAL AND LEONARD AVERAGING

$$\frac{\partial \bar{u}_i}{\partial t} + \frac{\partial}{\partial x_j}(\overline{u_j u_i}) = -\frac{1}{\rho}\frac{\partial \bar{p}}{\partial x_i} + \frac{\partial}{\partial x_j}\left(\nu \frac{\partial \bar{u}_i}{\partial x_j}\right)$$

CONVENTIONAL	LEONARD
$\bar{f}(x_j) = \frac{1}{\Delta_j}\int_{x_j-\Delta_j/2}^{x_j+\Delta_j/2} f(x_j')dx_j'$	$\bar{f}(x_j) = \int_{-\infty}^{+\infty} G(x_j-x_j')\, f(x_j')dx_j'$

$$\frac{\partial \bar{f}}{\partial x_j} = \frac{\partial \bar{f}}{\partial x_j}$$

$$G(x_j-x_j') = \left\{\sqrt{\frac{6}{\pi}}\frac{1}{\Delta_{avg}}\right\}^2 \exp\left\{-\frac{6(x_j-x_j')^2}{\Delta_{avg}^2}\right\}$$

$u_i(x_j) = \bar{u}_i(x_j) + u_i'(x_j,x_j')$	$u_i(x_j') = \bar{u}_i(x_j') + u_i'(x_j')$
$\overline{u_i'} = 0$	$\overline{u_j'} \neq 0$
$\overline{\bar{u}_i\bar{u}_j} = \bar{u}_i\bar{u}_j + \underbrace{\overline{u_i'u_j'}}_{R_{ij}}$	$\overline{\bar{u}_i\bar{u}_j} = \bar{u}_i\bar{u}_j + \frac{\Delta_{avg}^2}{24}\frac{\partial^2}{\partial x_j^2}(\bar{u}_i\bar{u}_j) + \underbrace{\overline{u_i'\bar{u}_j} + \overline{\bar{u}_iu_j'} + \overline{u_i'u_j'}}_{R_{ij}}$

WHERE $R_{ij} = -2\nu_T S_{ij} + \frac{1}{3}R_{ii}$ $\qquad S_{ij} = \frac{1}{2}\left(\frac{\partial \bar{u}_i}{\partial x_j} + \frac{\partial \bar{u}_j}{\partial x_i}\right)$

SMAGORINSKY $\qquad \nu_T = C_S\Delta^2(2S_{mn}S_{mn})^{1/2}$

VORTICITY $\qquad \nu_T = C_V\Delta^2(\bar{\omega}_n\bar{\omega}_n)^{1/2}$ $\qquad \bar{\omega}_k = \left(\frac{\partial \bar{U}_i}{\partial x_j} - \frac{\partial \bar{U}_j}{\partial x_i}\right)$

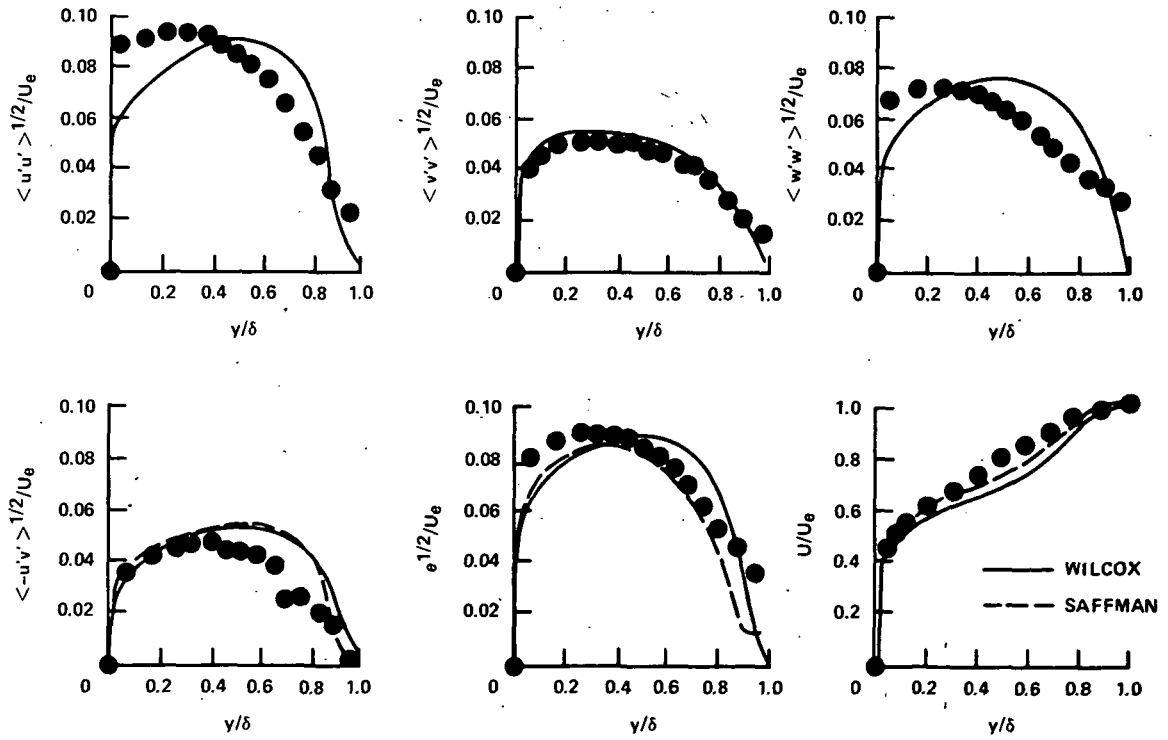

Figure 1. Comparison of Reynolds stress computations with experimental data of Bradshaw (adverse pressure).

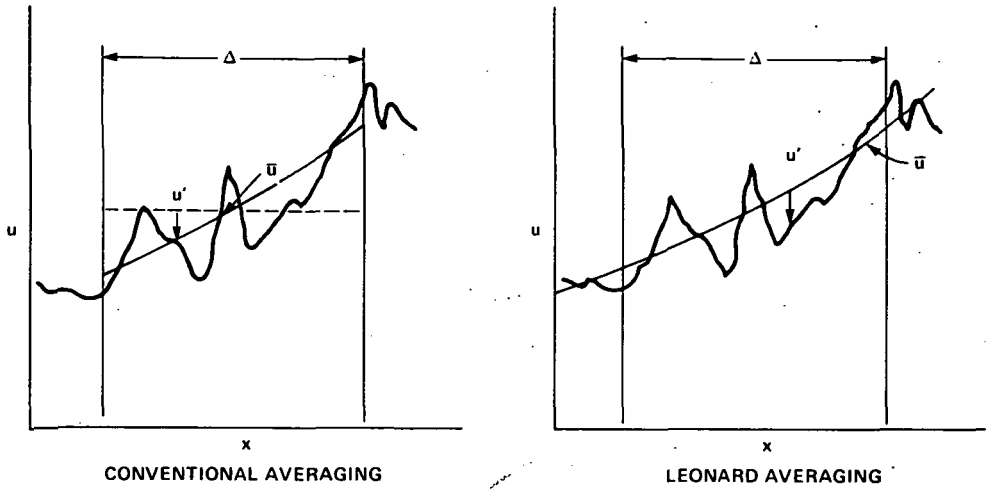

Figure 2. Volume-averaging dependent variables.

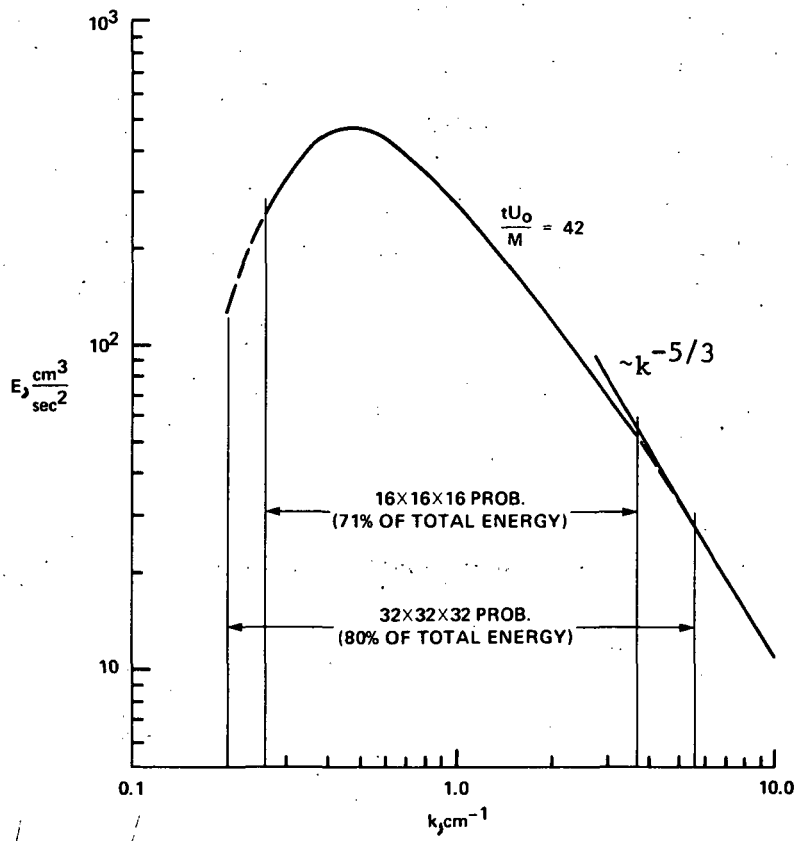

Figure 3. Initial energy spectrum. Data from reference 16.

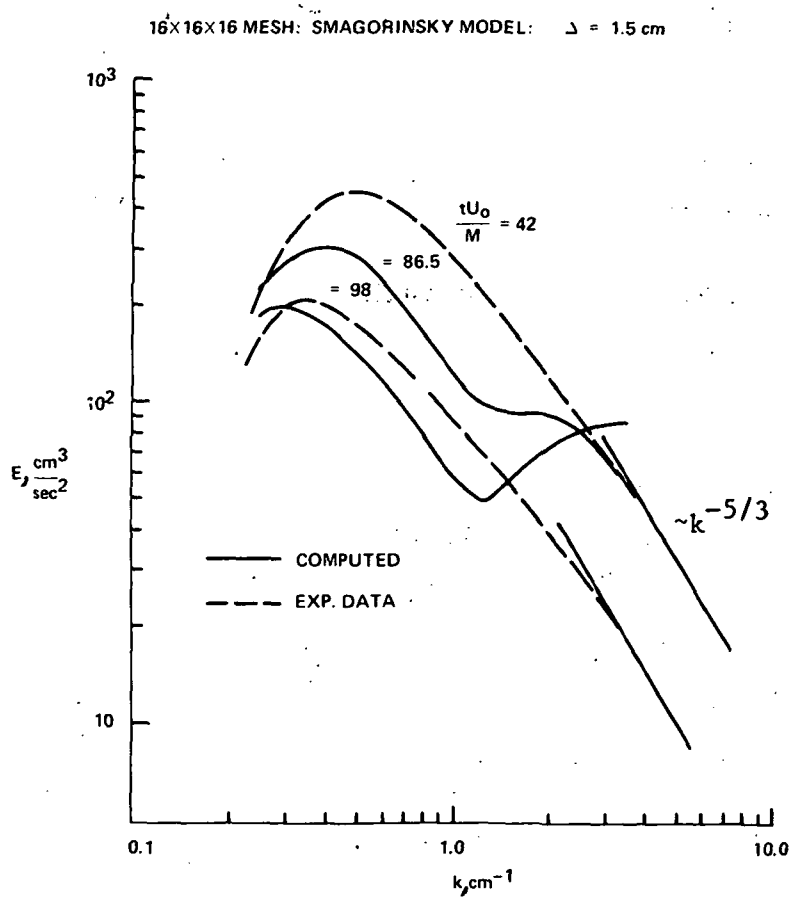

Figure 4. Evolution of energy spectra, $\Delta_{avg} = 0$.

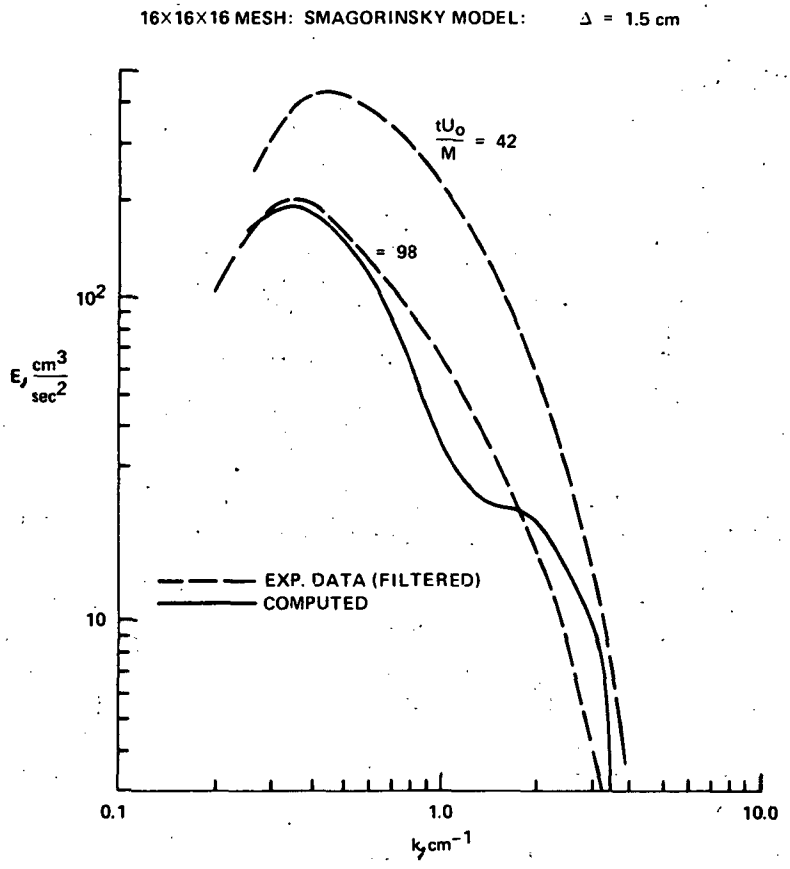

Figure 5. Evolution of energy spectra, $\Delta_{avg} = \Delta$.

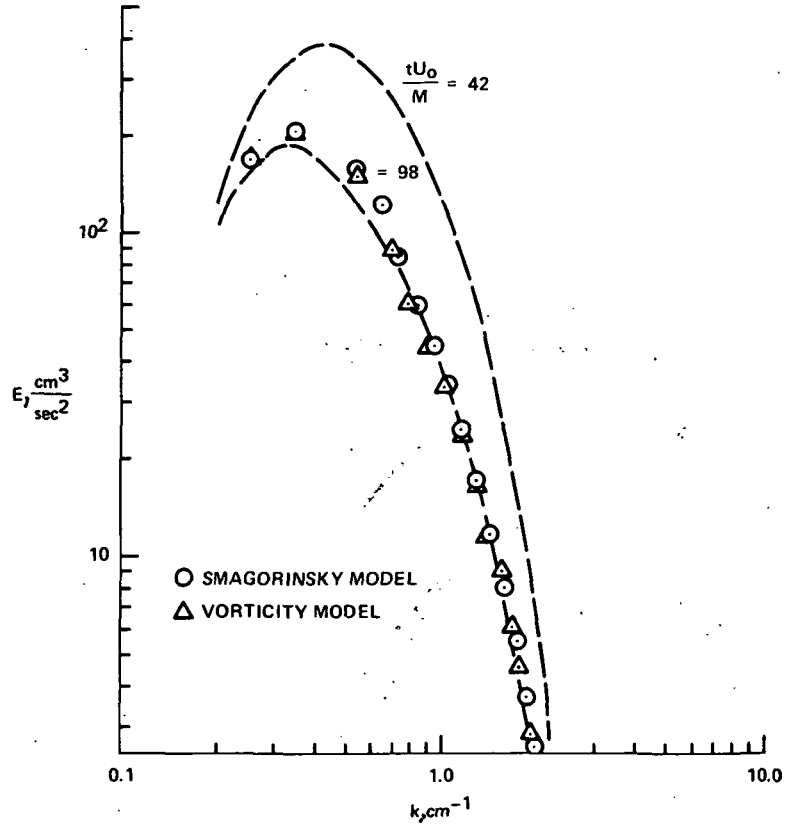

Figure 6. Evolution of energy spectra, $\Delta_{avg} = 2\Delta$.

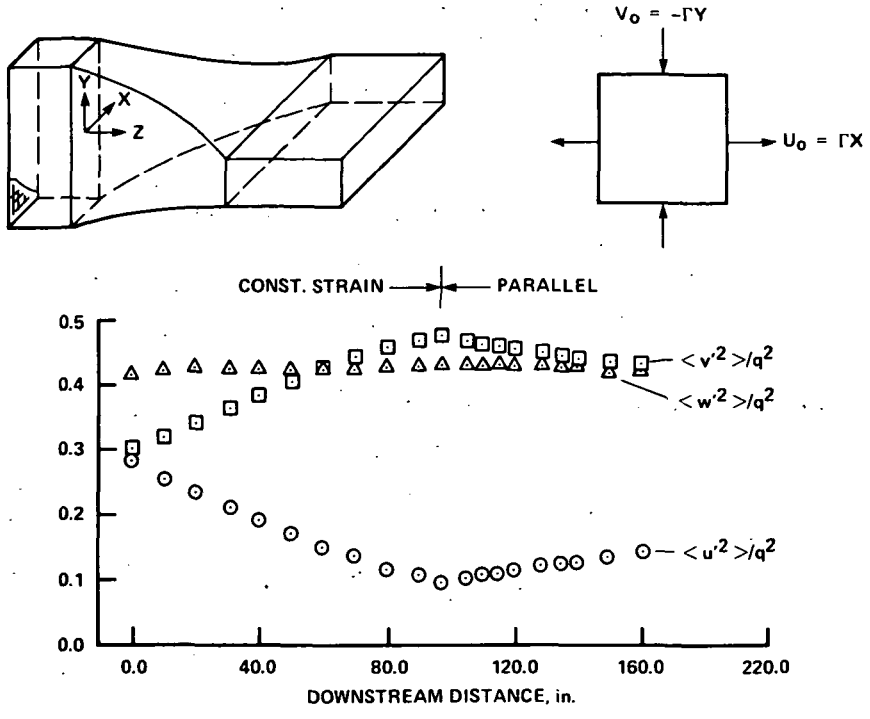

Figure 7. Distortion of homogeneous turbulence by irrotational plane strain.

Page Intentionally Left Blank

INFLUENCE OF EXTERNAL DISTURBANCES AND COMPRESSIBILITY ON FREE TURBULENT MIXING

By Youn H. Oh* and Dennis M. Bushnell
NASA Langley Research Center

SUMMARY

It has been shown that disturbances in external flow can significantly affect, by as much as an order of magnitude, the turbulent mixing rate in free shear layers. A particularly important finding is the fact that the length scale of the external flow disturbances is as important as the amplitude. Also a single parameter correlates the change in entrainment rate remarkably well. The difference between the effect of wide-band and narrow-band disturbances is stressed. The inclusion of the model for pressure fluctuation term in the kinetic energy equation in a two-equation model predicts the reduced spreading rate in high Mach number, high Reynolds number, adiabatic, free turbulent shear layers.

INTRODUCTION

The free turbulent shear layer is a relatively simple flow which is useful for verification of turbulence modeling and has many practical applications such as design of jet engine combustors, slot injection, and gas-dynamic lasers. The requirements of these devices generally vary. The combustor and gas laser require fast mixing and slot flows need slow mixing to be effective as thermal shields or to provide drag reduction.

Of importance in engineering design of such devices is the determination of the relative importance of various parameters upon mixing rate, and whether one can "control" the entrainment. The rate of free turbulent mixing primarily depends on the level and scale of turbulence in the shear layer. There are many things that can affect the structure of free turbulence; for example, large rates of strain and impinging shocks, etc. The purpose of the present investigation is to determine the effect of free-stream disturbances when both free-stream turbulence intensity and scale are varied, and also to determine the influence of Mach number on the entrainment rate of free shear layers. The influence of free-stream disturbances may be particularly important in ground simulation of combustor flows, especially scramjets, where the free-stream flow is heated

*NASA-ODU Research Associate.

by a variety of devices such as arc or vitiated burners which probably produce fairly large disturbance levels and scales. (See fig. 1.)

Experimentalists often fail to measure the intensity of such free-stream disturbances and very rarely measure the dominant or characteristic scale. High Mach number is also found to be a very important factor that affects turbulent free mixing structure. The 1972 Langley Conference on Free Turbulent Shear Flows (ref. 1) indicated that the data on spreading rate for turbulent free shear layers contain disagreement between data and "theory" of up to a factor of 3 or more for supersonic Mach numbers, the larger disagreement occurring at the higher Mach numbers ($M \approx 3$ to 5).

External or free-stream disturbances can be roughly divided into two important classes. The first class is generally referred to as acoustic disturbances. These are isentropic pressure waves having the following characteristics: The magnitudes of pressure, density, and velocity fluctuations are related to each other isentropically (up to moderate amplitude). These disturbances are highly directional, propagate with the speed of sound, and can be transmitted and reflected by the shear layer. This type of disturbance is known to affect laminar shear layer and combustion stability.

Extensive reviews of existing literature on acoustic disturbances can be found in Rockwell (ref. 2) and Borisov and Rozenfel'd (ref. 3). Important experimental data (ref. 4) showing the effect of narrow-band acoustic mode disturbances on fully turbulent shear layers are shown in figure 2 and are discussed in detail in the main body of the paper, particularly in reference to turbulence control.

The second important class of external disturbances is usually referred to as free-stream vorticity or "turbulence." Both of these classes of disturbances can be either wide band or narrow band. Wide-band disturbances generally have typical turbulence spectra. Vinogradov et al. (ref. 5) found the core length of two-dimensional coflowing jets to be strongly affected (factor of 4 difference in spreading rate) by the type of screen applied upstream of the external flow. Rodi (ref. 6) also reports similar findings (Vagt (1970) and Patel (1970)). The present paper describes a study of the effect of wide-band disturbances, employing an equation for the scale of turbulence since disturbances in the "free-stream" (on either or both sides of the mixing layer) would generally have distinct scales which are not related to the local scale of the shear layer. A parametric study of the effect of scale and intensity of free-stream disturbances is presented so that, for example, one can assess the influence of tunnel disturbances on free-flight simulation of scramjet engines. (See fig. 1.)

The present numerical solution of the free turbulent shear layer employs a "two-equation" turbulence model, a turbulent kinetic energy equation for the intensity, and a dissipation equation for the length scale of turbulence. A model for the pressure-velocity correlation term, representing a "compressibility" effect, which was developed by Oh

(ref. 7), based on an eddy-shock-wave concept is included in the turbulent kinetic energy model equation for predictions of the influence of high Mach number upon entrainment in free shear layers.

SYMBOLS

a	mass fraction of species
c_p	specific heat
e	turbulent kinetic energy, $\frac{1}{2}(u''^2 + v''^2 + w''^2)$
f	frequency
H	total enthalpy, $\sum_{i=1}^{n} c_{p,i} a_i T + \frac{1}{2} u^2$
L	reference length
l	length scale
l_{in}	integral length scale
M	Mach number; also grid size
n	total number of species; also exponent of isotropic turbulence energy initial decay law
$N_{Pr,e}$	ratio of turbulent diffusivity in turbulent kinematic energy equation to that of mean momentum
$N_{Pr,t}$	turbulent Prandtl number
$N_{Pr,\epsilon}$	ratio of turbulent diffusivity in dissipation equation to that of mean momentum
p	static pressure
R	gas constant; also Reynolds number

$N_{Sc,t}$ turbulent Schmidt number

T static temperature

u velocity component in x-direction

u_s local sonic speed

v velocity component in y-direction

w velocity component normal to u and v

X_o virtual origin of velocity similarity profiles

x coordinate parallel to outside flows (fig. 1)

x_c core length of jet

x_o initial x where initial conditions are specified

y coordinate normal to x (fig. 3)

$y_{.5}$ y where $(\tilde{u} - \tilde{u}_2)/(\tilde{u}_1 - \tilde{u}_2) = 0.5$

β $= \left(\overline{M}^2 - 1\right)^{1/2} \Big/ \overline{M}$

γ ratio of specific heat

δ shear layer width parameter, $\left|y_{\tilde{u}=0.1} - y_{\tilde{u}=0.9}\right| \Big/ L$

δ_o $= \delta$ at $x = x_o$

ϵ dissipation rate of turbulent kinetic energy

Λ computed shear layer width referred to that implied by linear spreading law with computed σ and X_o, $\left|y_{\tilde{u}=\sqrt{0.1}} - y_{\tilde{u}=\sqrt{0.9}}\right| \Big/ \left[1.32(x - X_o)/\sigma\right]$

λ $\equiv 0.875\delta_o$

μ_e eddy viscosity

ρ density

σ similarity parameter used as a measure of spreading rate

σ_0 σ for low-speed constant-density flows

σ_* $\equiv \lim_{\sqrt{\tilde{e}_\infty} l_\infty \to 0} \sigma$

ϕ $\equiv \dfrac{\tilde{u}_1 + \tilde{u}_2}{\tilde{u}_1 - \tilde{u}_2}\left[\dfrac{\sqrt{e_\infty}}{\tilde{u}_1 - \tilde{u}_2}\right]_{x=0}\left[\dfrac{l_\infty}{\lambda}\right]_{x=0}$

Subscripts and superscripts:

1 conditions on high-velocity side external flow

2 conditions on low-velocity side external flow

i species i

i,j tensor indices

max maximum value

∞ conditions outside of shear layer

$(\bar{\ })$ conventional temporal mean

$(\ )'$ (instantaneous) - $(\bar{\ })$

$(\tilde{\ })$ mass-averaged temporal mean

$(\ )''$ (instantaneous) - $(\tilde{\ })$

GOVERNING EQUATIONS AND ASSUMPTIONS

The physical problem is depicted schematically in figure 3. The shear layer is formed between two parallel uniform flows of different velocities. The higher velocity is called $\tilde{u}_1$ and the slower stream velocity is denoted by $\tilde{u}_2$. The X-axis is alined with the external uniform flows and the Y-axis is the direction normal to the uniform flow. (The flow properties vary most rapidly in the y-direction.) In the subsequent analysis, mass-averaged dependent variables, proposed by Favre (ref. 8), are used for most flow properties. Mass-averaged values are represented by a superscript tilde (~). The following relationships hold:

$$\tilde{u} = \bar{u} + \frac{\overline{\rho' u'}}{\bar{\rho}}$$

$$u'' = u' - \frac{\overline{\rho' u'}}{\bar{\rho}}$$

so that $\overline{\rho u} = \bar{\rho}\tilde{u}$. Both independent and dependent variables are used in their primitive form. The governing equations employed cover both multispecies and high-speed mixing.

Simplifying Assumptions

The following assumptions are made:

(1) The flow is steady on the average

(2) The Reynolds number is sufficiently high so that the mixing layer is fully turbulent and molecular diffusion can be neglected compared with turbulent diffusion

(3) The axial pressure gradient is zero

(4) No chemical reactions occur

Basic Equations

The typical free shear layer with no extraneous strain has an order of magnitude difference in the derivatives of the flow properties in the x- and y-direction and allows the usual boundary-layer-type (quasi-parallel) approximations. The conservation equations describing the problem for the mean flow quantities may be written in the following form (ref. 8):

Continuity:

$$\frac{\partial(\bar{\rho}\tilde{u})}{\partial x} + y^{-J}\frac{\partial\left(y^{J}\overline{\rho v}\right)}{\partial y} = 0 \qquad (1)$$

"x" mean momentum:

$$\bar{\rho}\tilde{u}\frac{\partial\tilde{u}}{\partial x} + \bar{\rho}\tilde{v}\frac{\partial\tilde{u}}{\partial y} + y^{-J}\frac{\partial\left(y^{J}\overline{\rho u''v''}\right)}{\partial y} = 0 \tag{2}$$

"y" mean momentum:

$$\frac{\partial\bar{p}}{\partial y} + \frac{\partial\left(\overline{\rho v''^{2}}\right)}{\partial y} = 0 \tag{3}$$

Mean energy:

$$\bar{\rho}\tilde{u}\frac{\partial\tilde{H}}{\partial x} + \bar{\rho}\tilde{v}\frac{\partial\tilde{H}}{\partial y} - y^{-J}\frac{\partial\left(y^{J}\overline{\rho H''v''}\right)}{\partial y} = 0 \tag{4}$$

Species:

$$\bar{\rho}\tilde{u}\frac{\partial\tilde{a}_i}{\partial x} + \bar{\rho}\tilde{v}\frac{\partial\tilde{a}_i}{\partial y} + y^{-J}\frac{\partial\left(y^{J}\overline{\rho a_i''v''}\right)}{\partial y} = 0 \qquad (i = 1, 2, \ldots, n) \tag{5}$$

Equation of state:

$$\bar{\rho} = \frac{\gamma_1\bar{p}}{(\gamma_1 - 1)\tilde{T}\left(\sum_{i=1}^{n} R_i\tilde{a}_i\right)} \tag{6}$$

In these equations all the variables are rendered dimensionless by referring all lengths to L, velocities to $\tilde{u}_1$, pressure to $\bar{\rho}_1\bar{u}_1^2$, density to $\bar{\rho}_1$, temperature to $\tilde{u}_1^2/c_{p,1}$, total enthalpy to $\tilde{u}_1^2$, specific heat to $c_{p,1}$ $\left(c_{p,i} = \sum_{i=1}^{n} c_{p,1,i}a_{1,i}\right)$, and gas constant to R_1 $\left(R_1 = \sum_{i=1}^{n} R_{1,i}a_{1,i}\right)$. The exponent $J = 0$ for two-dimensional and $J = 1$ for axisymmetric shear layers.

Closure Assumptions

The preceding set of equations are not closed because the turbulent correlations are unknown. Boussinesq's eddy viscosity model is assumed to describe the turbulent shear stress; that is, $\overline{\rho u''v''} = -\mu_e\partial\tilde{u}/\partial y$ along with Prandtl's energy model for the eddy viscosity, $\mu_e = C_\mu l\bar{\rho}\tilde{e}$, where C_μ is a modeling constant and $\tilde{e}$ is the turbulence kinetic energy $\tilde{e} = \overline{\rho(u''^2 + v''^2 + w''^2)}/\bar{\rho}$. Also $\overline{\rho H''v''}/(\partial\tilde{H}/\partial y)$ and $\overline{\rho a_i''v''}/(\partial\tilde{a}_i/\partial y)$ are assumed to be proportional to the eddy viscosity (by constant factors); that is,

$\overline{\rho a'' v''} = \frac{\mu_e}{N_{Sc,t}} \frac{\partial \tilde{a}}{\partial y}$ and $\overline{\rho H'' v''} = \frac{\mu_e}{N_{Pr,t}} c_p \frac{\partial \tilde{T}}{\partial y} + \frac{\mu_e}{N_{Sc,t}} \tilde{T} \left(\sum_{i=1}^{n} c_{p,i} \frac{\partial \tilde{a}_i}{\partial y} \right) + \overline{\rho u} \mu_e \frac{\partial \tilde{u}}{\partial y}$ where

$N_{Sc,t}$ and $N_{Pr,t}$ are the turbulent Schmidt and Prandtl number, respectively.

Turbulence Model

Prandtl's energy model for the eddy viscosity requires the turbulence kinetic energy and length scale. Often the length scale is algebraically related to the width of shear layer itself and yields a reasonable result for the free shear layer. But, in order to study the effect of external disturbances which have their own scale (which is not related to the shear layer), use of an equation governing evolution of the scale of turbulence is essential. Thus a "two-equation" model approach is the minimum necessary to describe the turbulence field in the present problem. The equation for the turbulence dissipation rate is used to compute the turbulence scale. There are other equations which would serve the same purpose, such as a vorticity equation (ref. 9) or an equation for the quantity, energy-times-length scale (ref. 10). Actually, these equations are all very similar (ref. 11).

Equations derived from the Navier-Stokes equations to describe turbulence energy and dissipation include a number of unknown correlations. Modeling of these unknowns requires a delicate balance between mathematical rigor and physical intuition since elaborate mathematical manipulation can be meaningless if not supported by experimental measurement. In general, the higher order correlations in the turbulent kinetic equation are better known than those in the equations for the length scale (ref. 12). Most notoriously difficult to measure, and hence least known of the turbulent fluctuating properties, are the pressure fluctuation terms. A model for the pressure-velocity correlation hypothesized by Oh (ref. 7) is included in the kinetic energy equation. No attempt was made to model pressure fluctuation terms in the dissipation equation. The model used by Spalding's group with their constants (ref. 1) was used herein for the dissipation equation. The final model equations are as follows:

Turbulent kinetic energy:

$$\overline{\rho u} \frac{\partial \tilde{e}}{\partial x} + \overline{\rho v} \frac{\partial \tilde{e}}{\partial y} - y^{-J} \frac{\partial}{\partial y} \left(y^J \frac{\mu_e}{N_{Pr,e}} \frac{\partial \tilde{e}}{\partial y} \right) - \mu_e \left(\frac{\partial \tilde{u}}{\partial y} \right)^2 + C_{e,1} \overline{\rho} D \tilde{e} + \overline{\rho} \epsilon$$

$$- C_{e,2} H(\overline{M} - 1) \beta \tilde{e} \left[\overline{\rho} D + \operatorname{sign}\left(\frac{\partial \overline{M}}{\partial y} \right) u_s \beta \frac{\partial \overline{\rho}}{\partial y} - \beta u_s^{-1} \frac{\partial \overline{\rho}}{\partial y} \right] = 0 \qquad (7)$$

Turbulent dissipation equation:

$$\overline{\rho u} \frac{\partial \epsilon}{\partial x} + \overline{\rho v} \frac{\partial \epsilon}{\partial y} - y^{-J} \frac{\partial}{\partial y} \left(y^J \frac{\mu_e}{N_{Pr,\epsilon}} \frac{\partial \epsilon}{\partial y} \right) - C_{\epsilon,1} \frac{\epsilon}{\tilde{e}} \mu_e \left(\frac{\partial u}{\partial y} \right)^2 + \frac{C_{\epsilon,2} \overline{\rho} \epsilon^2}{\tilde{e}} = 0 \qquad (8)$$

where $J = 0$ for two-dimensional and $J = 1$ for axisymmetric shear layers, H is the Heaviside unit function $H(\zeta) = 0$ when $\zeta < 0$ and $H(\zeta) = 1$ when $\zeta \geq 0$. Also, the following definitions are used: $D \equiv \partial\tilde{u}/\partial x + \partial\tilde{v}/\partial y$; u_s = Local sonic speed; $\beta \equiv \left(\overline{M}^2 - 1\right)^{1/2}/\overline{M}$; $\epsilon \equiv \tilde{e}^{3/2}/l$ so that $\mu_e = C_\mu \overline{\rho}\tilde{e}^2/\epsilon$. The constants used are $C_\mu = 0.09$, $N_{Sc,t} = 0.7$, $N_{Pr,t} = 0.9$, $N_{Pr,e} = 1.0$, $N_{Pr,\epsilon} = 1.3$, $C_{e,1} = 0$, $C_{e,2} = 0.14$, $C_{\epsilon,1} = 1.43$, and $C_{\epsilon,2} = 1.92$.

Initial and Boundary Conditions

Initial conditions.- Initial profiles of all dependable variables are required to start the solution procedure. All the results reported in this paper are computed with a set of initial profiles which were "guessed at" based upon the physics of the flow. The scarcity of experimental data, especially measured profiles for the turbulence energy and length scale, is the reason for using "arbitrary" (but physically reasonable) initial profiles. The quasi-similarity (all the computed results show linear shear layer growth, see fig. 5) of the results is a posteriori justification, that is, the calculations proceeded far enough downstream for the influence of the starting profiles to be "washed out." The initial profiles are generated as follows: First axial velocity $\tilde{u}$ profiles are generated for a given width parameter $\delta_o = \dfrac{\left|y_{\tilde{u}=0.1} - y_{\tilde{u}=0.9}\right|_{x=0}}{L}$

$$\tilde{u}(0,y) = \frac{1}{2}\left[(\tilde{u}_1 + \tilde{u}_2) + (\tilde{u}_1 - \tilde{u}_2)\mathrm{erf}(\zeta)\right] \tag{9}$$

where $\zeta = 2 \times 0.90621514 y/\delta_o$. Then

$$\tilde{e}(0,y) = \underbrace{\frac{1}{2}\left[(\tilde{e}_1 + \tilde{e}_2) + \left|\tilde{e}_1 - \tilde{e}_2\right|\mathrm{erf}(\zeta)\right]}_{\tilde{e}_{fr}} + \underbrace{\frac{1}{2}\left\{\left[\tilde{e}_{max,sh} - \frac{1}{2}(\tilde{e}_1 + \tilde{e}_2)\right]\exp\left(-2\zeta^2\right)\right\}}_{\tilde{e}_{sh}} \tag{10}$$

where the first term $\tilde{e}_{fr}$ is the contribution of free-stream disturbances and the second term $\tilde{e}_{sh}$ is chosen as the contribution of mean shear (from the assumed relation $\tilde{e} \propto \left(\frac{d\tilde{u}}{dy}\right)^2$ when $\tilde{e}_1 = \tilde{e}_2 = 0$). The term $\tilde{e}_{max,sh}$ is another input which is chosen as 0.12 for most incompressible cases and as 0.08 for supersonic cases. The term $\tilde{e}_{sh}$ was neglected when $\tilde{e}_1 + \tilde{e}_2 > 2\tilde{e}_{max,sh}$. Note that these equations are in nondimensional form. In order to estimate dissipation, the distribution of length scale is computed as

$$l(0,y) = \underbrace{\frac{\frac{1}{2}\left[(l_1 + l_2) + |l_1 - l_2|\,\mathrm{erf}(\zeta)\right]\tilde{e}_{fr}}{\tilde{e}}}_{l_{fr}} + \underbrace{\frac{\lambda\tilde{e}_{max,sh} - \frac{1}{4}(l_1 + l_2)(\tilde{e}_1 + \tilde{e}_2)}{\tilde{e}_{max,sh} - \frac{1}{2}(\tilde{e}_1 + \tilde{e}_2)}\,\frac{\tilde{e}_{sh}}{\tilde{e}}}_{l_{sh}} \tag{11}$$

where $\lambda \equiv 0.875\delta_o$ and $l_{sh} = 0$ when $\tilde{e}_{max,sh} < \frac{1}{2}(\tilde{e}_1 + \tilde{e}_2)$. Then ϵ is computed as $\epsilon = \tilde{e}^{3/2}/l$. Total enthalpy is assumed to be initially uniform

$$\tilde{H}(0,y) = 1$$

The static temperature is obtained from the expression

$$\tilde{T}(0,y) = \left[\left(1 + \frac{\gamma - 1}{2}\overline{M}_1^2\right)\tilde{H} - \frac{\gamma - 1}{2}\overline{M}_1^2\tilde{u}^2\right]\frac{\gamma}{c_p(\gamma - 1)R} \tag{12}$$

For static pressure, normal velocity and density, the initial assumptions include:

$$\left.\begin{aligned} \overline{p}(0,y) &= p_\infty \\ \tilde{v}(0,y) &= 0 \\ \overline{\rho}(0,y) &= \overline{M}_1^2\,\frac{p}{\tilde{T}R} \end{aligned}\right\} \tag{13}$$

Boundary conditions.- The external free stream usually contains some type of disturbance. The major disturbances can be divided into two broad groups, acoustic and vortical. The effect of narrow-band acoustic disturbances is fundamentally different than that of free-stream vorticity (turbulence). The present research effort is concerned with the effect of wide-band-type free-stream turbulence only.

The free-stream turbulence could be the result of upstream agitation, diffusion from an adjoining shear layer (wall boundary layer in enclosed flow or free shear layer in case of coaxial jet, etc.), or distributed sources such as chemical reaction or distributed fine obstacles, etc. (that is, dust flows). The most well documented data are for decaying isotropic turbulence. (A good example is grid-generated turbulence.) Therefore, the boundary conditions for the kinetic energy and dissipation equation are limited to isotropic decaying turbulence in the present study.

Batchelor and Townsend (ref. 13) found grid-generated isotropic turbulence decays in the early stage as

$$\frac{\tilde{e}}{u_\infty^2} = B\left(\frac{x}{M} - \frac{x_g}{M}\right)^{-1}$$

$$\frac{l_{in}}{M} = C\left(\frac{x}{M} - \frac{x_g}{M}\right)^{1/2}$$

where A, B, and C are constants, and l_{in}, x_g, and M are the integral length scale, grid location, and grid size, respectively.

In order to study the variation of boundary conditions for the turbulence model equations with x, the turbulence energy is assumed to vary as

$$\tilde{e}_\infty = \tilde{u}_\infty{}^2 A\left(\frac{x}{M} - \frac{x_g}{M}\right)^n$$

In the absence of mean shear, the model equation for the turbulent kinetic energy equation becomes

$$\tilde{u}_\infty \frac{d\tilde{e}_\infty}{dx} = -\epsilon \tag{14}$$

Substituting the expression for $\tilde{e}_\infty$ results in

$$\epsilon = -\tilde{u}_\infty{}^3 \frac{n}{M} A\left(\frac{x}{M} - \frac{x_g}{M}\right)^{n-1} \tag{15}$$

From the relation $l = \frac{\tilde{e}^{3/2}}{\epsilon}$

$$l = -\frac{MA^{1/2}}{n}\left(\frac{x}{M} - \frac{x_g}{M}\right)^{\frac{n}{2}+1} \tag{16}$$

Initial boundary conditions are therefore

$$(\tilde{e}_\infty)_{x=0} = \tilde{u}_\infty{}^2 A\left(\frac{x_0}{M} - \frac{x_g}{M}\right)^n \tag{17}$$

$$(l_\infty)_{x=0} = -\frac{MA^{1/2}}{n}\left(\frac{x_0}{M} - \frac{x_g}{M}\right)^{\frac{n}{2}+1} \tag{18}$$

From equations (14), (15), (17), and (18),

$$\tilde{e}_\infty = (\tilde{e}_\infty)_{x=0}\left\{1 - \left[\frac{x - x_0}{(l_\infty)_{x=0}{}^n}\right]^n \left[\frac{(\tilde{e}_\infty)_{x=0}}{\tilde{u}_\infty{}^2}\right]^{n/2}\right\} \tag{19}$$

$$\epsilon_\infty = \frac{\left(\tilde{e}_\infty^{3/2}\right)_{x=0}}{(l_\infty)_{x=0}} \left\{ 1 - \left[\frac{x - x_o}{(l_\infty)_{x=0}^{n}} \right]^{n-1} \left[\frac{(\tilde{e}_\infty)_{x=0}}{\tilde{u}_\infty^{2}} \right]^{n-\frac{1}{2}} \right\} \tag{20}$$

The recent measurements made by Comte-Bellot and Corrisin (ref. 14) show that $n \approx -1.25$.

Symmetric boundary conditions are imposed on the X-axis in the axisymmetric and two-dimensional jet cases. (Center velocity is allowed to decrease.)

Numerical solution procedure.- The numerical method used to solve the governing equation is the implicit finite-difference method of Crank-Nicholson with the dependent variables in conservation form. Linearization is accomplished by initially lagging the nonlinear coefficient a step and then integrating until convergence.

Variable grid spacing is used in the y-direction. The spacing was increased by a geometrical progression on each side of the shear layer center line. In order to prevent the shear region from outgrowing the computing net, the computing net was continuously expanded in the y-direction by doubling the grid spacing whenever the converged solution for $\tilde{u}$ changes by a predetermined margin at both edges for the pure shear layer case and at the outer edge for the jet case. A typical run, 250 cross-node points and 170 marching steps in x ($\approx$100 times the initial thickness δ_o distance), for the incompressible binary mixing case takes approximately 200 seconds of CPU time on the CDC 6600 computer system. Sixty percent of this time is actually spent in solving the finite-difference equations and the rest of the machine time is spent in data management and plotting routines. A solution for the supersonic shear layer takes approximately three times longer than for an incompressible case. Convergence was tested on $\tilde{u}$, $\tilde{v}$, and $\tilde{e}$ with a convergence criterion 0.1 percent relative (or combined with an equivalent absolute criterion for $\tilde{v}$).

RESULTS AND DISCUSSION

Comparison With Data

Experimental data which can be used to check the validity of the present prediction are extremely scarce. Most often, data are incomplete, that is, the intensity of free-stream disturbances is measured but not the characteristic scale. Also, the core length of the jet may be measured but not the initial boundary-layer thickness (ref. 5), etc.

Thus the comparison with incomplete data becomes no more than finding the missing data which would yield agreement in the results. Nevertheless Rodi (ref. 6) demonstrated, by using a prediction method similar to the present one, that the measured effect of free-stream disturbances (Patel (1970) and Vagt (1970)) on free turbulent mixing could be qual-

itatively simulated. In this vein, a comparison will be made with the Vinogradov et al. (ref. 5) experiment. The experimental setup (see fig. 4) consisted of an enclosed two-dimensional channel with two separating plates which initially divided the channel into three equal size ducts. The ratio of center duct velocity to the velocity of two outer ducts was varied along with the "agitating grids" in the outlet sections of the ducts. The experiment determined the variation of core length of the center jet with velocity ratio and initial intensity of turbulence for incompressible isothermal flow. From the present authors' viewpoint, the data have the following defects: (1) The wall shear layers on either side of the splitter plate were not measured. (The core length depends not only on the spreading rate but also on the virtual origin, that is, initial shear layer thickness.) (2) The core length was measured from schlieren photographs, with smoke in the center jet. However, the end of the core was not defined clearly, that is, whether the concentration was $a_1 = 0.99$ or 0.9, etc. The analytical determination of x_c depends greatly on such a criterion. (3) The location where the grids are placed is not certain. If the grids were placed at the exit of the jet as the article (ref. 5) implies, then the results would have been considerably affected by the immediate wake of the grid. (4) The outer uniform flow carries not only decaying grid-generated turbulence but also turbulence diffused from the outer wall boundary layer. (The nature of such turbulence is much less well known than grid turbulence.) (5) The initial free-stream turbulence energy was measured but the scales were not. However, because of the lack of more complete data, comparisons will be shown for this case by using plausible assumptions.

A number of predictions were made with arbitrary but reasonable initial shear layer widths for the no grid case. (See circle symbol in fig. 4.) The prediction and experimental data are compared in figure 4. The flow quantities assumed in predictions of all cases are $\tilde{u}_1 = 30$ m/sec, $\delta_0 = 0.5875 \times 2$ cm, definition for the core length $\tilde{a}_1 = 0.98$, length scale for the no grid case $l_\infty/\lambda = 1.0$, and Δl_∞ is assumed to be proportional to the grid spacing (or rod diameter). The implication of this comparison is the slope of the no grid case data with velocity ratio is used to define the end of core as $\tilde{a}_1 = 0.98$, the x_c at $\tilde{u}_2/\tilde{u}_1 = 0.3$ for the no grid case is used to calibrate the initial shear layer width $\delta_0 = 0.5875 \times 2$, and the grids with 2-mm rod and 4-mm rod are used to fix $\Delta(l_\infty/\lambda)/(2\text{-mm rod diam}) = 0.15$. Therefore, the results for the 8-mm grid can be looked upon as the real comparison, which is certainly very reasonable and tends to vindicate the present approach.

Parametric Study of Effect of Free-Stream Disturbances

Because of the lack of complete data, the comparison of the present results with experiment is quantitatively inconclusive (but qualitatively satisfactory) as the attempt in the previous section demonstrates.

In this section a parametric study is made of the effect of the intensity and length scale of wide-band-type free-stream disturbances on 2-D incompressible, free, turbulent air-air mixing. A number of computer runs were made with identical flow conditions except for variations in velocity ratio $\tilde{u}_2/\tilde{u}_1$, turbulent intensity $\sqrt{\tilde{e}_\infty}/\tilde{u}_\infty$, and length scale l_∞/λ. All computed cases are summarized in table I with the results σ and X_0.

To show the effects of $\tilde{e}_\infty$ and l_∞ on profiles of shear layer properties, samples of the similarity profiles $\tilde{u}$, $\tilde{e}$, and l/λ as functions of $\sigma y/(x - X_0)$ and $\tilde{u}_{max}$, $\tilde{e}_{max}$, and $\overline{uv}_{max}$, and Λ as a function of x (which represent large disturbances, very small disturbances, and effects of disturbance on both sides of the shear layer and on just one side alone) are shown in figure 5. The spreading parameter σ which is used as the measure for the spreading (see fig. 3) is defined herein by the relation (ref. 15) $\sigma = 1.32/\Delta\eta$ where $\Delta\eta$ is the angular distance between two rays when $(\tilde{u} - \tilde{u}_2)/(\tilde{u}_1 - \tilde{u}_2) = (0.1)^{1/2}$ and $(\tilde{u} - \tilde{u}_2)/(\tilde{u}_1 - \tilde{u}_2) = (0.9)^{1/2}$. The accompanying virtual origin is X_0. The quantities σ and X_0 are evaluated from the last $\tilde{u}$ profile computed and a profile at about $x = 0.8$ of the total distance computed. A single parameter which can be used to compare the rate of spreading of all properties in all flow conditions is not yet known. The parameter σ and other parameters (ref. 16) have their limitations. The quantity σ can be used to compare the growth rate of velocity width (also momentum thickness and entrainment rate for constant-density shear layers) only when the velocity profiles are similar. But the presence of a high level of turbulence in the external flow distorts the profiles; however, they are "self-similar." The self-similar velocity profile for the quiet boundary condition case (fig. 5(a)) is similar to that of Liepmann and Laufer (ref. 17). (A comparison can be found in ref. 7.) The presence of high $\tilde{e}_1$ makes the self-similar velocity profile smoother near the high-velocity side because of the increased shear stress. (See fig. 5(e).) The presence of high free-stream disturbances on both sides stretches the profile at both ends so that the self-similar profile becomes nearly similar again. (Compare figs. 5(a) and 5(i).) The σ values used in table I, figure 6, and figure 7 can be regarded as comparing approximately 80 percent of the momentum thickness because of the way it is defined.

In the course of this study, the following qualitative observations were made: (1) The effects on turbulence intensity is approximately proportional to $\sqrt{\tilde{e}_\infty}/(\tilde{u}_1 - \tilde{u}_2)$; that is, for a given $\sqrt{\tilde{e}_\infty}/\tilde{u}_\infty$, the effects of disturbances in the high-velocity side became more prominent and the effects of external turbulence on the low-velocity side diminishes as $\tilde{u}_2/\tilde{u}_1$ decreases. The higher $\tilde{u}_2/\tilde{u}_1$, the more sensitive the flow is to external disturbances. (2) As $l_\infty \to 0$ and $\sqrt{\tilde{e}_\infty} \to 0$, σ and X_0 approach an asymptotic value. (3) The overall profiles are quasi-similar (i.e., though turbulence properties are still changing the mean velocity profiles are similar) in most of the cases computed even though the boundary conditions imposed are strongly nonsimilar. Note the constancy of $\Lambda = \left|y_{\tilde{u}=\sqrt{0.1}} - y_{\tilde{u}=\sqrt{0.9}}\right| \Big/ \left[1.32(x - X_0)/\sigma\right]$ as a function of X (linear spreading) in fig-

ures 5(d), 5(h), 5(l), and 5(p). (4) Very small $\sqrt{\tilde{e}_\infty}$ causes numerical instability near the edge due to the definition $l = \frac{\tilde{e}^{3/2}}{\epsilon}$. (5) The ratios of diffusivities in $\tilde{e}$ and $\tilde{\epsilon}$ equations have to have a certain value, that is, 1.3 (as Spalding's group used). Otherwise the length scale profile would exhibit an anomalous dip or peak near the edge of the shear layer. (6) Disturbances on the low-velocity side of the external flow can further increase mixing rate up to 10 percent over the correlated results shown in figure 6.

Surprisingly, a single parameter

$$\phi = \frac{\tilde{u}_1 + \tilde{u}_2}{\tilde{u}_1 - \tilde{u}_2}\left(\frac{\sqrt{\tilde{e}_{\infty,1}}}{\tilde{u}_1 - \tilde{u}_2}\right)_{x=0}\left(\frac{l_\infty}{\lambda}\right)_{x=0}$$

correlates the variation of σ/σ_* with "one side" external disturbances as shown in figure 6.

Here σ_* is the limiting value of σ for small ϕ. (Actual σ_* values used are marked in the table.) It should be noted that the present calculations, as correlated in figure 6, indicate potentially large effects of free-stream disturbance on spreading rate for simple shear layers (factor of up to 10 change in spreading rate possible).

In figure 7, predictions made with $\left(\frac{\sqrt{\tilde{e}_1}}{\tilde{u}_1 - \tilde{u}_2}\frac{l_1}{\lambda}\right)_{x=0} = 1.7$ and 0 are plotted with experimental data collected by Birch and Eggers (ref. 1) in the format suggested by Kline for σ as a function of $\tilde{u}_2/\tilde{u}_1$. This comparison suggests that the disturbances in the facility free stream were responsible for at least some of the data scatter which is more than 100 percent at the high velocity ratios $\left(\tilde{u}_2/\tilde{u}_1 \to 1\right)$.[1]

The effect of narrow-band acoustic disturbances could be markedly different from the effects of the wide-band vorticity type so far considered. The difference is very well demonstrated in the experiment conducted by Vlasov and Ginevsky (ref. 4). The experimental setup and the results were shown in figure 2. Narrow-band acoustic disturbances generated by a loud speaker were injected into a fully turbulent free subsonic jet. The center-line velocity decay with x is plotted for the no-sound case and two different disturbance frequencies. The data show that the external disturbances not only accelerate mixing (low-frequency disturbance), but could also attenuate mixing (high-frequency input). This is a very significant result and indicates that the mixing rate can be controlled by artificially inputting narrow-band disturbances. It is currently planned to study this phenomenon with a spectral plane analysis.

[1]Note that the slow rate of development to a "pure shear layer" is also conjectured (ref. 16) for the large scatter of data as $\tilde{u}_2/\tilde{u}_1 \to 1$.

Influence of Mach Number

Oh (ref. 7) modeled the pressure-velocity correlation term $\overline{p' \frac{\partial u^j}{\partial x^j}}$ in the kinetic energy equation based on an eddy shock-wave concept. The prediction (ref. 7) made by a one-equation model was reasonably good. The same cases were computed again with the dissipation equation included. (Note that the p' terms are not yet included in the dissipation equation.)

A prediction with $C_{e,2} = 0.14$ (equivalent to $C_5C_6 = 0.07$ of ref. 7) are shown in figure 8. The plots of σ against $\overline{M}_1$ are qualitatively similar to the results of the one-equation method (ref. 7). Detailed profile comparisons indicate the need for slightly higher diffusivity in the dissipation equation which is a possible indication of the need for a model of the p' term in that equation.

To be noted is that all the data shown in figure 9 are from relatively "clean" configurations. The data that have some sort of wall proximity, which may allow reflection of large noise levels back into the shear layer or allow self generation of low-frequency narrow-band noise such as cavity flows, are excluded. These "noisy flows" generally spread faster. (See fig. 9.)

CONCLUDING REMARKS

It has been shown that disturbances in external flow can significantly affect, by as much as an order of magnitude, the free turbulent mixing rate in shear layers. A particularly important finding is the fact that the length scale of the external flow disturbances is as important as the amplitude.

Also, a single parameter correlates the change in entrainment rate remarkably well. The difference between the effect of wide-band and narrow-band disturbances is stressed. The inclusion of the model for the velocity-pressure correlation term in the kinetic energy equation in a two-equation model predicts the reduced spreading rate in high Mach number, high Reynolds number, adiabatic, free turbulent shear layers.

REFERENCES

1. Anon.: Free Turbulent Shear Flows. Vol. I – Conference Proceedings. NASA SP-321, 1973.

2. Rockwell, Donald O.: The Macroscopic Nature of Jet Flows Subjected to Small Amplitude Periodic Disturbances. Sonochem. Eng., vol. 67, no. 109, 1971, pp. 99-107.

3. Borisov, Yu. Ya.; and Rozenfel'd, É. I.: Action of Acoustic Oscillations on Flow Stability and Structure. Soviet-Phys.-Acoustics, vol. 17, no. 2, Oct.-Dec. 1971, pp. 154-168.

4. Vlasov, Ye. V.; and Ginevskiy, A. S.: Generation and Suppression of Turbulence in an Axisymmetric Turbulent Jet in the Presence of an Acoustic Influence. NASA TT F-15,721, 1974.

5. Vinogradov, Yu. V.; Gruzdev, V. N.; and Talanlov, A. V.: Effect of the Intensity of Turbulence Upon the Process of Mixing Slipstreams at a Different Ratio of Velocities. FTD-HT-23-866-74, U.S. Air Force, Apr. 15, 1974. (Available from DDC as AD 778 798.)

6. Rodi, Wolfgang: The Prediction of Free Turbulent Boundary Layers by Use of a Two-Equation Model of Turbulence. Ph. D. Thesis, Imperial College (London), Dec. 1972.

7. Oh, Y. H.: Analysis of Two-Dimensional Free Turbulent Mixing. AIAA Paper No. 74-594, June 1974.

8. Favre, A.: Statistical Equations of Turbulent Gases. Problems of Hydrodynamics and Continuum Mechanics. Soc. Indust. & Appl. Math., 1969, pp. 231-266.

9. Saffman, P. G.: A Model for Inhomogeneous Turbulent Flow. Proc. Roy. Soc. (London), ser. A, vol. 317, no. 1530, June 1970, pp. 417-433.

10. Rotta, J. C.: Recent Attempts To Develop a Generally Applicable Calculation Method for Turbulent Shear Flow Layers. Turbulent Shear Flows, AGARD-CP-93, Jan. 1972, pp. A-1 – A-11.

11. Wolfshtein, M.; Naot, D.; and Lin, A.: Models of Turbulence. Rep. ME-746(N), Ben-Gurion Univ. Negev (Israel), June 1974.

12. Bradshaw, P. (appendix by V. C. Patel): The Strategy of Calculation Methods for Complex Turbulent Flows. I. C. Aero Rep. 73-05, Aeronaut. Dep., Imp. Coll. Sci. & Technol., Aug. 1973.

13. Batchelor, G. K.; and Townsend, A. A.: Decay of Isotropic Turbulence in the Initial Period. Proc. Roy. Soc., ser. A, vol. 193, no. 1032, Apr. 22, 1948, pp. 539-558.

14. Comte-Bellot, Geneviève; and Corrsin, Stanley: The Use of a Contraction To Improve the Isotropy of Grid-Generated Turbulence. J. Fluid Mech., vol. 25, pt. 4, Aug. 1966, pp. 657-682.

15. Brown, Garry; and Roshko, Anatol: The Effect of Density Difference on the Turbulent Mixing Layer. Turbulent Shear Flows, AGARD-CP-93, Jan. 1972, pp. 23-1 – 23-12.

16. Brown, Garry L.; and Roshko, Anatol: On Density Effects and Large Structure in Turbulent Mixing Layers. J. Fluid Mech., vol. 64, pt. 4, July 1974, pp. 775-816.

17. Liepmann, Hans Wolfgang; and Laufer, John: Investigations of Free Turbulent Mixing. NACA TN 1257, 1947.

18. Maydew, R. C.; and Reed, J. F.: Turbulent Mixing of Axisymmetric Compressible Jets (in the Half-Jet Region) With Quiescent Air. SC-4764(RR), Sandia Corp. (Albuquerque, N. Mex.), Mar. 1963.

19. Sirieix, M.; and Solignac, J. L.: Contribution à l'Etude Expérimentale de la Couche de Mélange Turbulent Isobare d'un Ecoulement Supersonique. Separated Flows, pt. I, AGARD CP No. 4, May 1966, pp. 241-270.

20. Ikawa, Hideo: Turbulent Mixing Layer Experiment in Supersonic Flow. Ph. D. Thesis, California Inst. Technol., 1973.

21. Morrisette, E. Leon; and Birch, Stanley F.: Mean Flow and Turbulent Measurements in a Mach 5 Shear Layer. Pt. I – The Development and Spreading of the Mean Flow. Fluid Mechanics of Mixing, Earl M. Uram and Victor W. Goldschmidt, eds., Amer. Soc. Mech. Eng., c.1973, pp. 79-86.

22. Hill, W. G., Jr.; and Page, R. H.: Initial Development of Turbulent, Compressible, Free Shear Layers. Trans. ASME, Ser. D: J. Basic Eng., vol. 91, no. 1, Mar. 1969, pp. 67-73.

23. Rhudy, J. P.; and Magnan, J. D., Jr.: Turbulent Cavity Flow Investigation at Mach Numbers 4 and 8. AEDC-TR-66-73, U.S. Air Force, June 1966. (Available from DDC as AD 483 748.)

24. Fernandez, F. L.; and Zukoski, E. E.: Experiments in Supersonic Turbulent Flow With Large Distributed Surface Injection. AIAA J., vol. 7, no. 9, Sept. 1969, pp. 1759-1767.

25. Rudy, David H.; and Birch, Stanley F.: Mean Flow Development and Surface Heating for an Attaching Compressible Free Shear Layer. J. Spacecraft & Rockets, vol. 11, no. 5, May 1974, pp. 348-351.

26. Cary, Aubrey M., Jr.; and Hefner, Jerry N.: Film-Cooling Effectiveness and Skin Friction in Hypersonic Turbulent Flow. AIAA J., vol. 10, no. 9, Sept. 1972, pp. 1188-1193.

27. Kenworthy, Michael; and Schetz, Joseph A.: An Experimental Study of Slot Injection Into a Supersonic Stream. NASA CR-2128, 1973.

28. Drewry, J. E.; Neer, M. E.; and Scaggs, N. E.: Supersonic Mixing and Combustion Studies of Ducted Hydrogen-Air Flows at an Inlet Air Mach Number of 2.6. AIAA Paper No. 73-1320, Nov. 1973.

TABLE I.- COMPUTED RESULTS OF SPREADING RATE AS A FUNCTION OF FREE-STREAM DISTURBANCES

Flow conditions for data given in table.

$\tilde{u}_1 = 30$ cm/sec

$T_{total} = 318$ K

$p_{total} = 1$ atm

$M_1 = 0.084$

R/cm = 17296.5802

$\delta_o = 0.3$ cm $\equiv \left| y_{\tilde{u}=1} - y_{\tilde{u}=0.9} \right|_{x=0}$

All cases computed from $x_o = 0$ to $x = 30$ cm $(100\delta_o)$

Varied conditions, at $x = x_o$

$\frac{\tilde{u}_2}{\tilde{u}_1} = 0.5, 0.3, 0.6, 0.9$

$\frac{\sqrt{\tilde{e}_\infty}}{u_\infty} = 0.005$ to $\sqrt{0.03}$

$\frac{l_\infty}{\lambda} = 0.1$ to 10 $\quad (\lambda = 0.875\delta_o)$

(a) $\frac{\tilde{u}_2}{\tilde{u}_1} = 0.05$; $\frac{\sqrt{\tilde{e}_{\infty,2}}}{\tilde{u}_2} = 0.02$; $\frac{l_{\infty,2}}{\lambda} = 0.1$

$\frac{l_{\infty,1}}{\lambda}$	Value of σ and $\frac{x_o}{\lambda}$ for $\frac{\sqrt{\tilde{e}_{\infty,1}}}{\tilde{u}_1}$ of –			
	0.06	0.086	0.1	$\sqrt{0.03}$
1		[a]14.14 -13.41		
4	13.83 -12.99		13.72 -15.01	12.83 -23.47
6	13.69 -12.84		13.10 -16.00	12.24 -24.23
10	13.54 -12.69		12.73 -15.73	

[a]Used as σ_* in figure 6.

TABLE I. - COMPUTED RESULTS OF SPREADING RATE AS A FUNCTION OF FREE-STREAM DISTURBANCES – Continued

(b) $\frac{\tilde{u}_2}{\tilde{u}_1} = 0.3$; $\frac{\sqrt{\tilde{e}_{\infty,2}}}{\tilde{u}_2} = 0.005$; $\frac{l_{\infty,2}}{\lambda} = 0.01$

$\frac{l_{\infty,1}}{\lambda}$	Value of σ and $\frac{X_0}{\lambda}$ for $\frac{\sqrt{\tilde{e}_{\infty,1}}}{\tilde{u}_1}$ of –			
	0.0377	0.06	0.1	$\sqrt{0.03}$
1	23.13 -20.76		23.26 -26.59	
4		21.92 -21.90	20.86 -27.50	19.39 -38.55
6		21.92 -21.37	20.05 -27.31	18.06 -39.73
10		21.07 -21.03	19.01 -26.10	16.26 -38.36

(c) $\frac{\tilde{u}_2}{\tilde{u}_1} = 0.3$; $\frac{\sqrt{\tilde{e}_{\infty,1}}}{\tilde{u}_1} = \frac{\sqrt{\tilde{e}_{\infty,2}}}{\tilde{u}_2}$; $\frac{l_{\infty,1}}{\lambda} = \frac{l_{\infty,2}}{\lambda}$

$\frac{l_{\infty,1}}{\lambda}$	Value of σ and $\frac{X_0}{\lambda}$ for $\frac{\sqrt{\tilde{e}_{\infty,1}}}{\tilde{u}_1}$ of –			
	0.06	0.1	$\sqrt{0.02}$	$\sqrt{0.03}$
0.1				[a]23.36 -9.79
1				22.22 -26.78
2		21.89 -26.10		21.05 -33.75
4	21.86 -21.98	20.74 -27.73	19.78 -34.40	19.21 -39.70
6	21.44 -21.52	19.92 -27.62		17.85 -41.03
10	21.01 -21.26	18.88 -26.63	17.10 -34.13	15.99 -39.62

[a]Used as σ_* in figure 6.

TABLE I.- COMPUTED RESULTS OF SPREADING RATE AS A FUNCTION OF FREE-STREAM DISTURBANCES – Continued

(d) $\frac{\tilde{u}_2}{\tilde{u}_1} = 0.6$; $\frac{\sqrt{\tilde{e}_{\infty,2}}}{\tilde{u}_2} = 0.005$; $\frac{l_{\infty,2}}{\lambda} = 0.1$

$\frac{l_{\infty,1}}{\lambda}$	Value of σ and $\frac{X_0}{\lambda}$ for $\frac{\sqrt{\tilde{e}_{\infty,1}}}{\tilde{u}_1}$ of –			
	0.05	0.06	0.1	$\sqrt{0.03}$
0.1			[a]49.58 -25.83	
1	46.88 -46.06		46.05 -53.56	
4		40.57 -46.48	36.05 -55.85	30.86 -77.98
6		38.73 -45.33	32.90 -53.56	26.58 -79.12
10				[b]21.36 -95.12

[a]Used as σ_* in figure 6.

[b]Similarity profiles are included in figure 5.

(e) $\frac{\tilde{u}_2}{\tilde{u}_1} = 0.6$; $\frac{\sqrt{\tilde{e}_{\infty,1}}}{\tilde{u}_1} = \frac{\sqrt{\tilde{e}_{\infty,2}}}{\tilde{u}_2}$; $\frac{l_{\infty,1}}{\lambda} = \frac{l_{\infty,2}}{\lambda}$

$\frac{l_{\infty,1}}{\lambda}$	Value of σ and $\frac{X_0}{\lambda}$ for $\frac{\sqrt{\tilde{e}_{\infty,1}}}{\tilde{u}_1}$ of –					
	0.005	0.6	0.1	$\sqrt{0.015}$	$\sqrt{0.02}$	$\sqrt{0.03}$
0.1	[a]49.35 -43.81					
1				43.86 -54.36		
4		39.44 -45.60	34.00 -54.59			28.52 -87.43
10	42.20 -43.92				[a]22.79 -63.58	[a]19.71 -98.48

[a]Similarity profiles are included in figure 5.

TABLE I.- COMPUTED RESULTS OF SPREADING RATE AS A FUNCTION OF FREE-STREAM DISTURBANCES – Continued

(f) $\frac{\tilde{u}_2}{\tilde{u}_1} = 0.6$; $\frac{2\sqrt{\tilde{e}_{\infty,2}}}{\tilde{u}_2} = \frac{\sqrt{\tilde{e}_{\infty,1}}}{\tilde{u}_1}$; $\frac{l_{\infty,2}}{\lambda} = \frac{l_{\infty,1}}{\lambda}$

$\frac{l_{\infty,1}}{\lambda}$	Value of σ and $\frac{X_o}{\lambda}$ for $\frac{\sqrt{\tilde{e}_{\infty,1}}}{\tilde{u}_1}$ of –		
	0.06	0.1	$\sqrt{0.03}$
4	40.27 -46.74	35.56 -55.96	29.99 -76.08
6	38.22 -45.03	32.22 -54.74	26.18 -75.24
10	36.03 -42.97	28.56 -50.59	20.42 -101.98

(g) $\frac{\tilde{u}_2}{\tilde{u}_1} = 0.9$; $\frac{\sqrt{\tilde{e}_{\infty,2}}}{\tilde{u}_2} = 0.005$; $\frac{l_{\infty,2}}{\lambda} = 0.1$

$\frac{l_{\infty,1}}{\lambda}$	Value of σ and $\frac{X_o}{\lambda}$ for $\frac{\sqrt{\tilde{e}_{\infty,1}}}{\tilde{u}_1}$ of –				
	0.00526	0.05	0.06	0.1	$\sqrt{0.03}$
0.1	[a]209.47 -179.09				
1		145.61 -153.14			
4			65.71 -122.25	50.31 -117.14	38.91 -116.34
6			53.07 -117.45	40.17 -112.38	31.17 -113.33
10			40.41 -111.35	30.55 -108.84	23.67 -110.55

[a]Used as σ_* in figure 6.

TABLE I.- COMPUTED RESULTS OF SPREADING RATE AS A FUNCTION OF FREE-STREAM DISTURBANCES – Concluded

(h) $\frac{\tilde{u}_2}{\tilde{u}_1} = 0.9$; $\frac{\sqrt{\tilde{e}_{\infty,1}}}{\tilde{u}_1} = \frac{\sqrt{\tilde{e}_{\infty,2}}}{\tilde{u}_2}$; $\frac{l_{\infty,1}}{\lambda} = \frac{l_{\infty,2}}{\lambda}$

$\frac{l_{\infty,1}}{\lambda}$	Value of σ and $\frac{X_0}{\lambda}$ for $\frac{\sqrt{\tilde{e}_{\infty,1}}}{\tilde{u}_1}$ of –	
	0.005	$\sqrt{0.03}$
0.1	209.37 -179.20	
1	199.09 -168.19	
10		23.87 -112.38

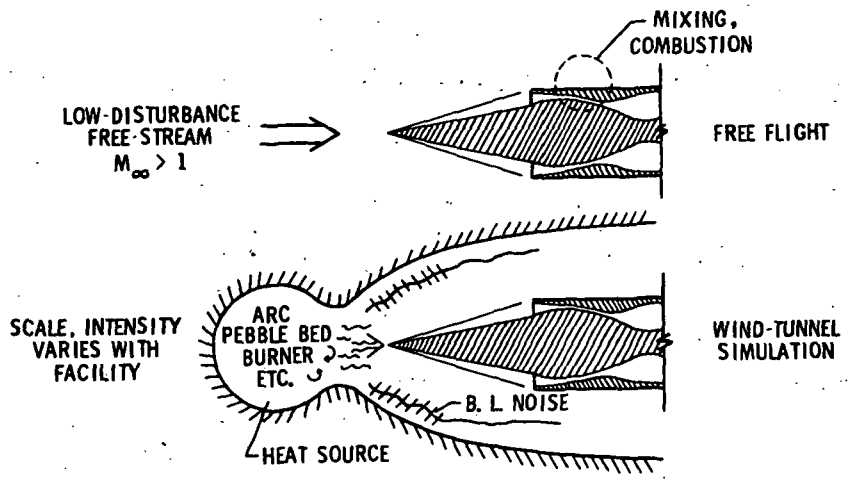

Figure 1.- Schematic of Ramjet/Scramjet engine ground simulation.

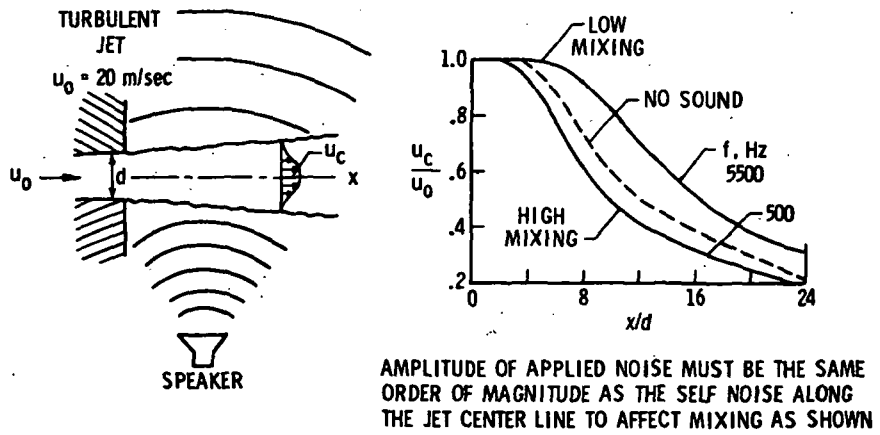

Figure 2.- Effect of narrow-band disturbances.

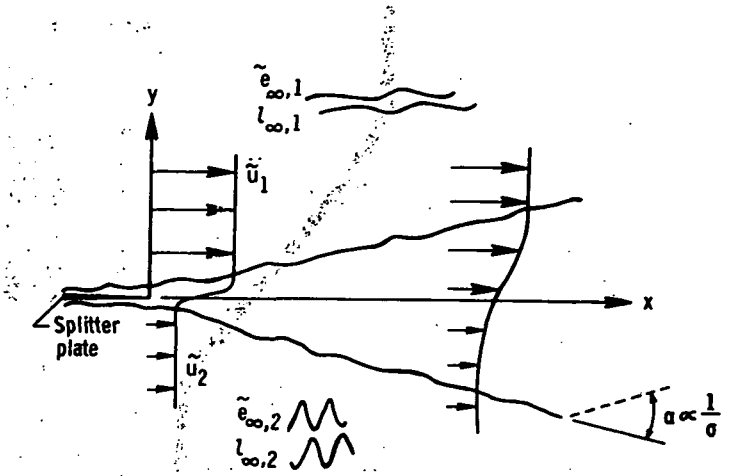

Figure 3.- Sketch of problem.

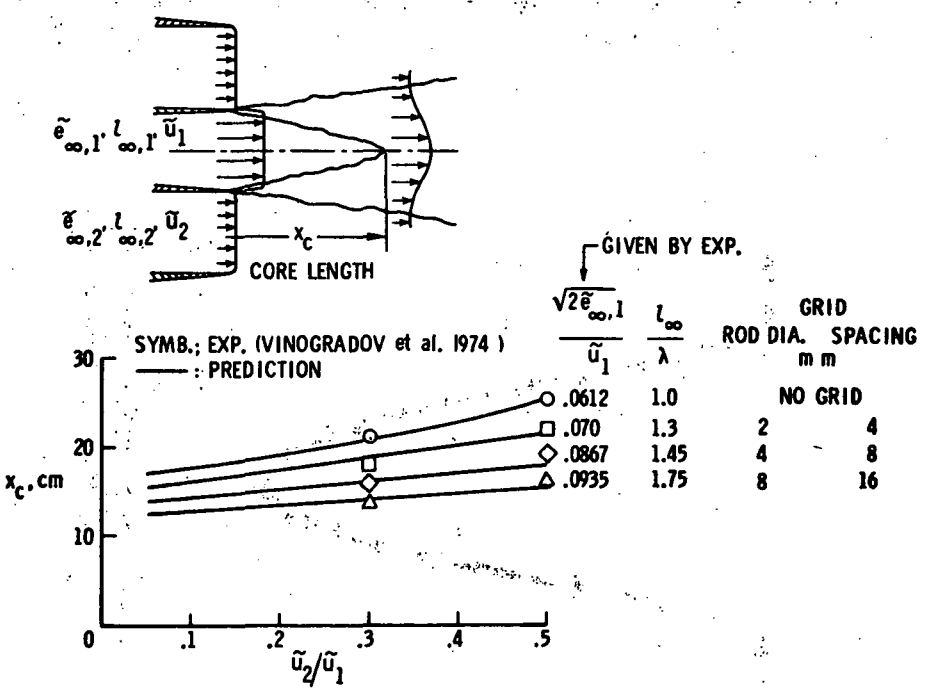

Figure 4.- Effect of wide-band free-stream disturbances on turbulent free mixing (low speed) comparison with data.

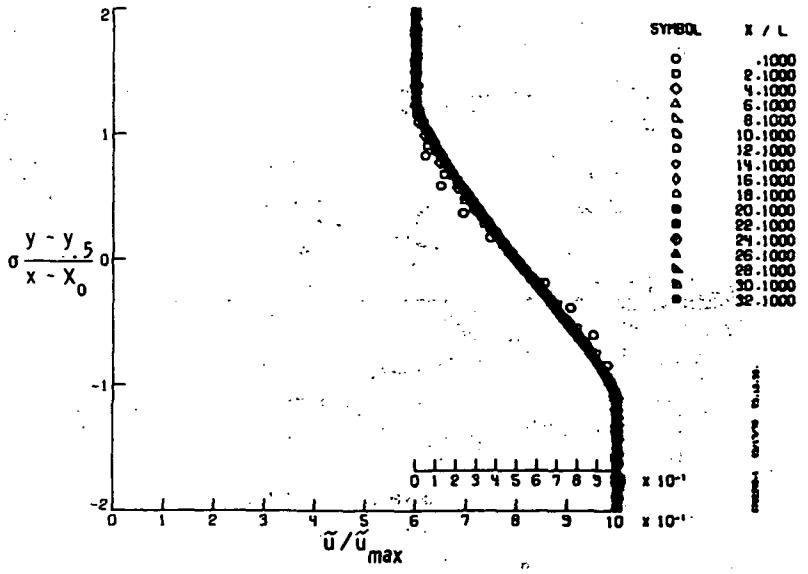

(a) Variation of $\tilde{u}/\tilde{u}_{max}$ with $\sigma(y - y_{.5})/(x - X_0)$ for $\tilde{u}_2/\tilde{u}_1 = 0.6$ with turbulence boundary conditions at $x = 0$; $\sqrt{\tilde{e}_\infty}/\tilde{u}_\infty = 0.005$; $l_\infty/\lambda = 0.1$; $L = \frac{10}{3}\delta_0$; $X_0/L = -11.5034$; $\sigma = 49.3547$.

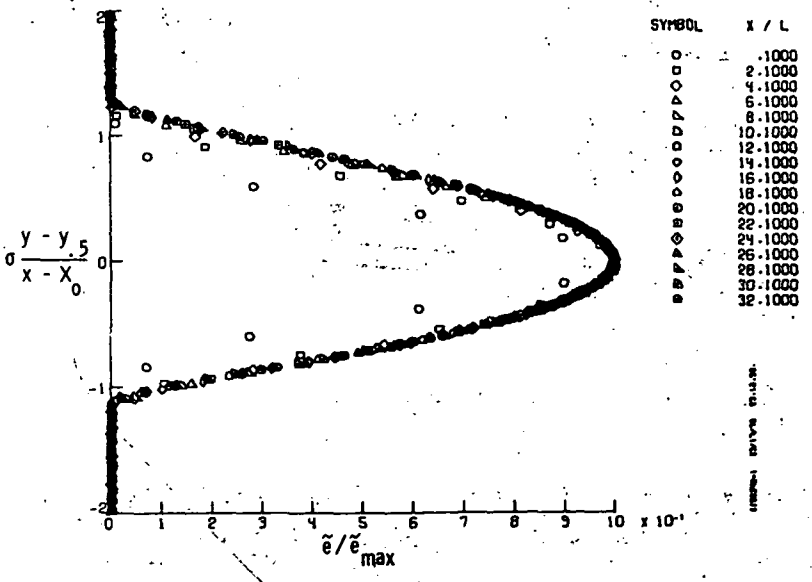

(b) Variation of $\tilde{e}/\tilde{e}_{max}$ with $\sigma(y - y_{.5})/(x - X_0)$. $X_0/L = 11.5034$; $\sigma = 49.3547$.

Figure 5.- Computed profiles.

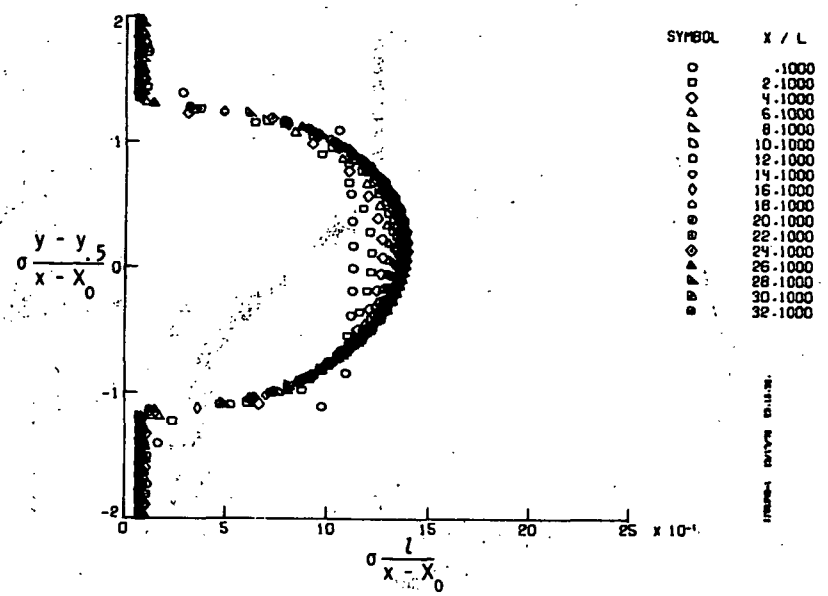

(c) Variation of $\sigma l/(x - X_0)$ with $\sigma(y - y_{.5})/(x - X_0)$. $X_0/L = -11.5034$; $\sigma = 49.3547$.

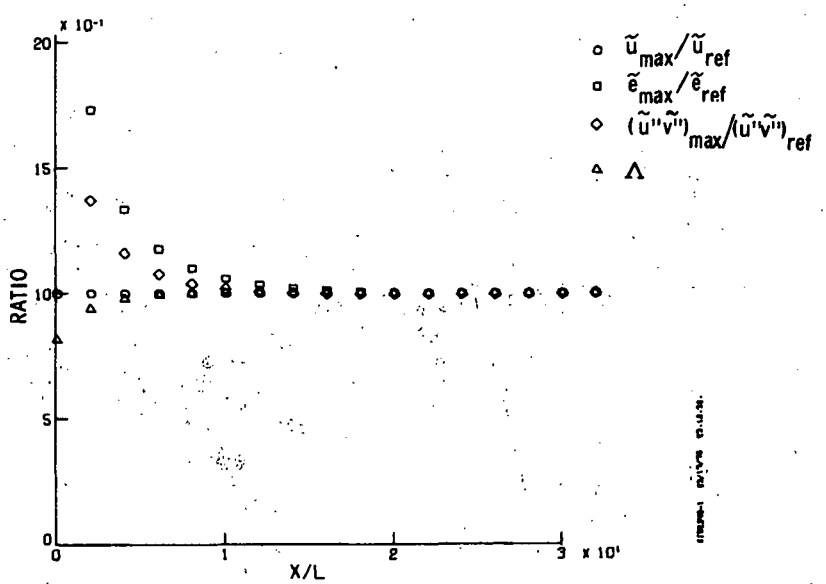

(d) Variation of $\tilde{u}_{max}/\tilde{u}_{ref}$, $\tilde{e}_{max}/\tilde{e}_{ref}$, $(\tilde{u}''\tilde{v}'')_{max}/(\tilde{u}''\tilde{v}'')_{ref}$, and Λ with x/L. $\sqrt{\tilde{e}_{ref}}/(\tilde{u}_1 - \tilde{u}_2) = \sqrt{0.0311}$; $(\tilde{u}''\tilde{v}'')_{ref}/(\tilde{u}_1 - \tilde{u}_2)^2 = 0.0108$; $L = \frac{10}{3}\delta_0$; $X_0/L = -11.5034$; $\sigma = 49.3547$.

Figure 5.- Continued.

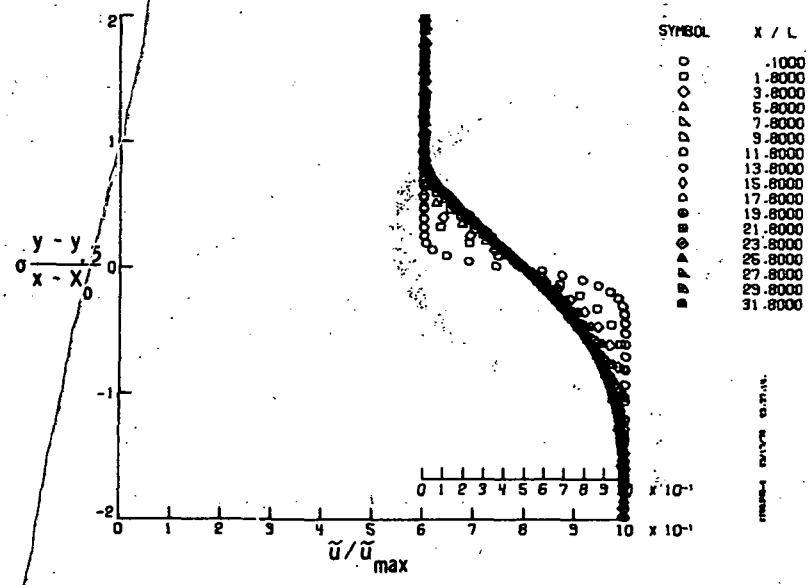

(e) Variation of $\tilde{u}/\tilde{u}_{max}$ with $\sigma(y - y_{.5})/(x - X_0)$ for $\tilde{u}_2/\tilde{u}_1 = 0.6$ with turbulence boundary conditions at $x = 0$; $\sqrt{\tilde{e}_{\infty,1}}/\tilde{u}_1 = \sqrt{0.03}$; $l_{\infty,1}/\lambda = 10$; $\sqrt{\tilde{e}_{\infty,2}}/\tilde{u}_2 = 0.005$; $l_{\infty,2}/\lambda = 0.1$; $L = \frac{10}{3}\delta_0$; $X_0/L = -24.9709$; $\sigma = 21.3565$.

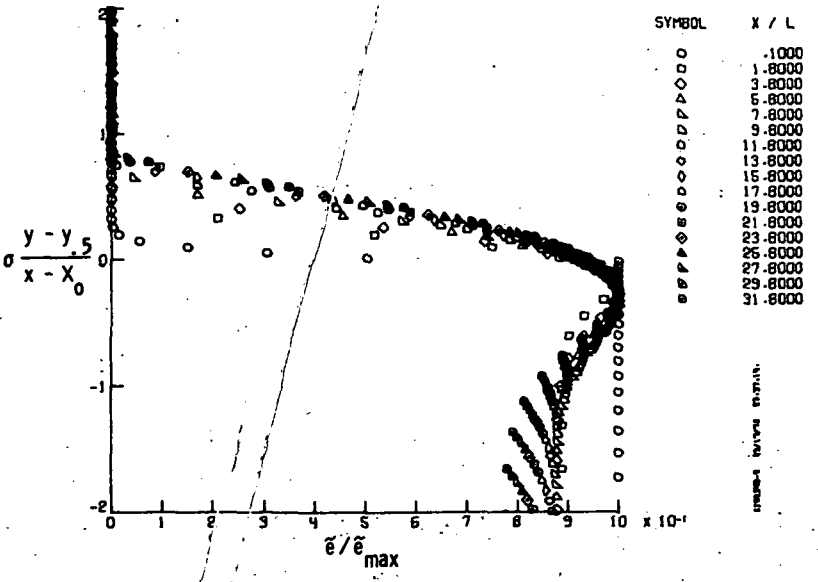

(f) Variation of $\tilde{e}/\tilde{e}_{max}$ with $\sigma(y - y_{.5})/(x - X_0)$. $X_0/L = -24.9707$; $\sigma = 21.3565$.

Figure 5.- Continued.

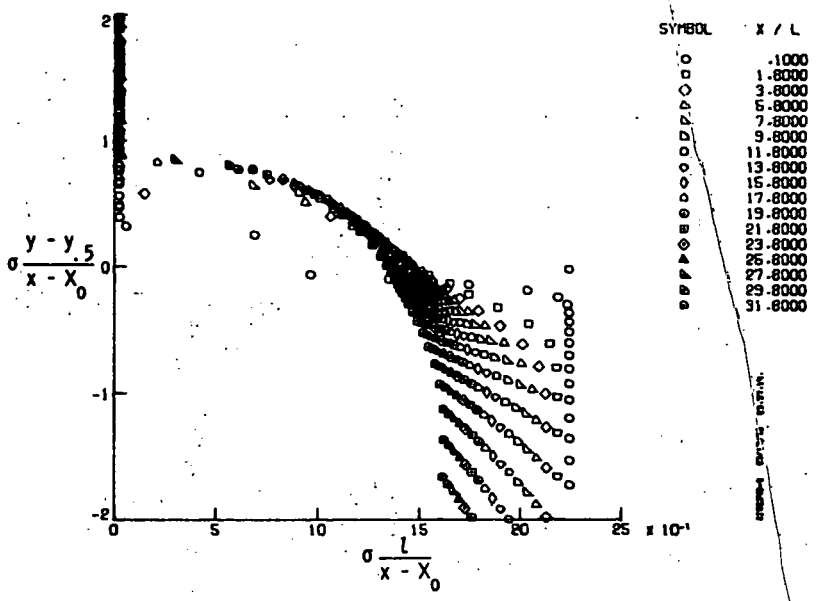

(g) Variation of $\sigma l/(x - X_0)$ with $\sigma(y - y_{.5})/(x - X_0)$. $X_0/L = -24.9707$; $\sigma = 21.3565$.

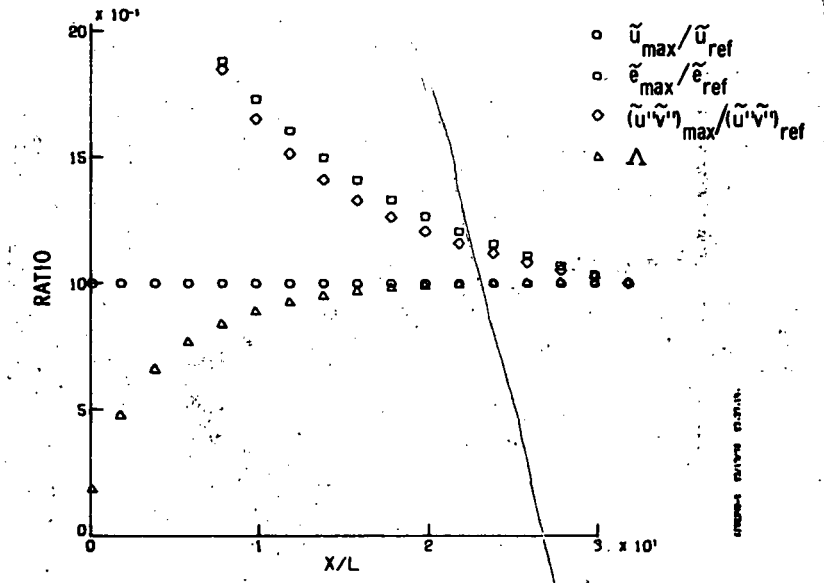

(h) Variation of $\tilde{u}_{max}/\tilde{u}_{ref}$, $\tilde{e}_{max}/\tilde{e}_{ref}$, $(\tilde{u}''\tilde{v}'')_{max}/(\tilde{u}''\tilde{v}'')_{ref}$, and Λ with x/L. $\sqrt{\tilde{e}_{ref}}/(u_1 - u_2) = \sqrt{0.0754}$; $(\tilde{u}''\tilde{v}'')_{ref}/(u_1 - u_2)^2 = 0.0212$; $L = \frac{10}{3}\delta_0$; $X_0/L = -24.9707$; $\sigma = 21.3565$.

Figure 5.- Continued.

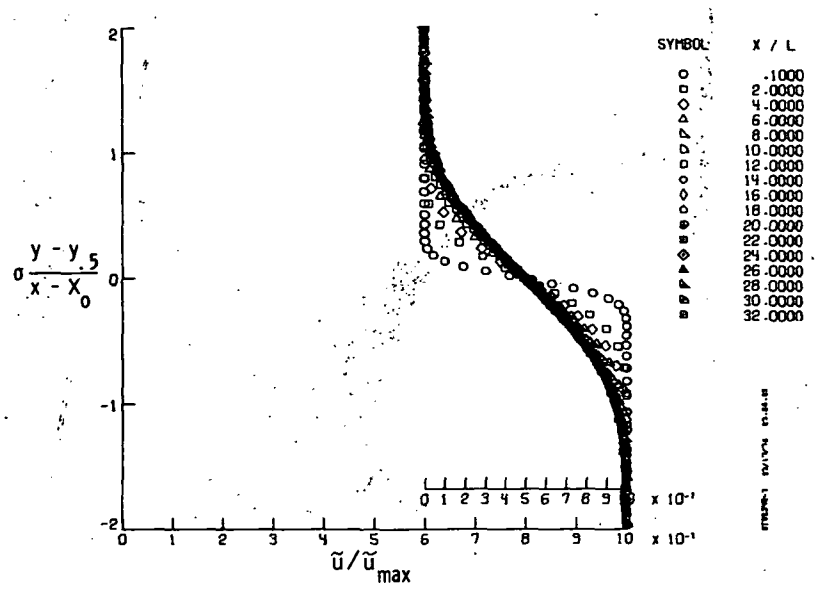

(i) Variation of $\tilde{u}/\tilde{u}_{max}$ with $\sigma(y - y_{.5})/(x - X_0)$ for $\tilde{u}_2/\tilde{u}_1 = 0.6$ with turbulence boundary conditions at $x = 0$; $\sqrt{\tilde{e}_\infty}/u_\infty = \sqrt{0.03}$; $\ell_\infty/\lambda = 10$; uniform initial length scale profile; $X_0/L = -25.8005$; $\sigma = 19.7200$.

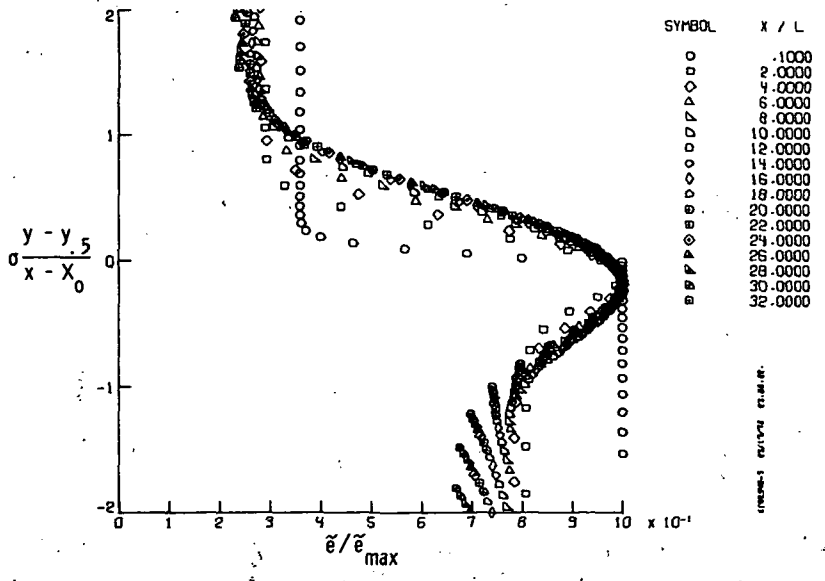

(j) Variation of $\tilde{e}/\tilde{e}_{max}$ with $\sigma(y - y_{.5})/(x - X_0)$. $X_0/L = -25.8005$; $\sigma = 19.7200$.

Figure 5.- Continued.

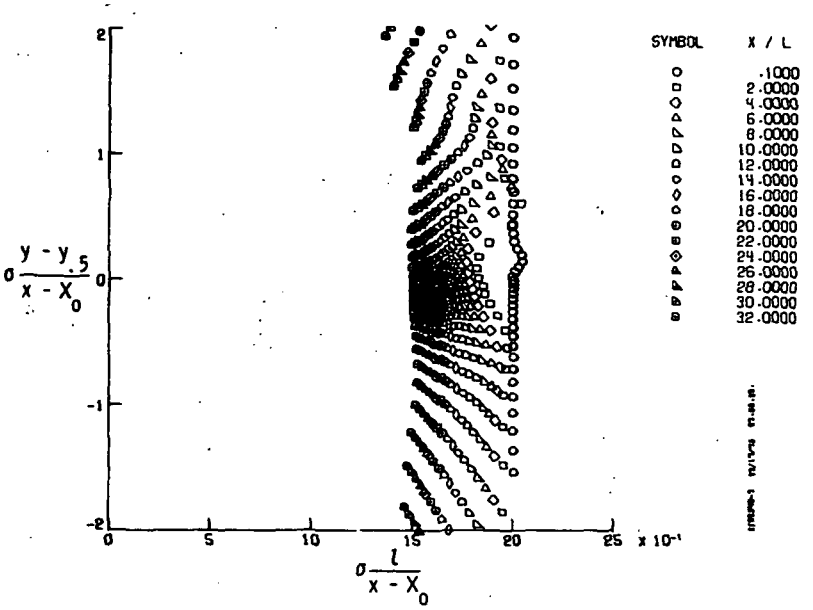

(k) Variation of $\sigma l/(x - X_0)$ with $\sigma(y - y_{.5})/(x - X_0)$. $X_0/L = -25.8005$; $\sigma = 19.7200$.

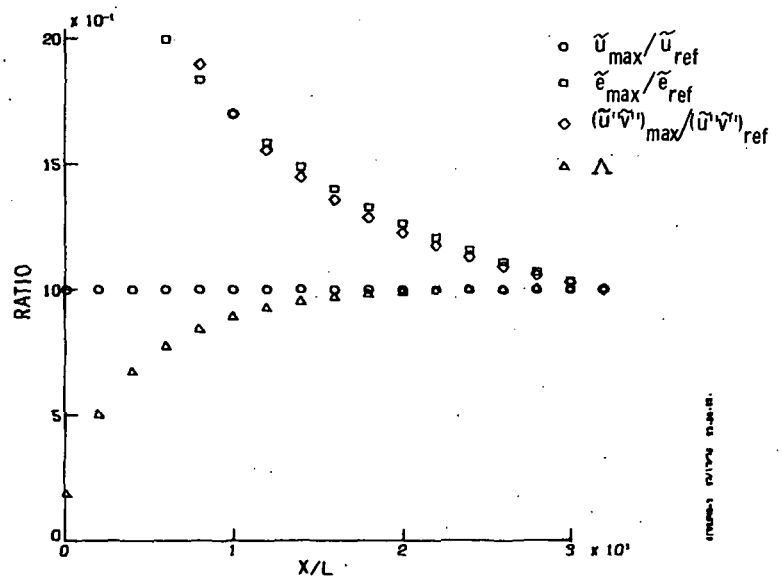

(l) Variation of $\tilde{u}_{max}/\tilde{u}_{ref}$, $\tilde{e}_{max}/\tilde{e}_{ref}$, $(\tilde{u}''\tilde{v}'')_{max}/(\tilde{u}''\tilde{v}'')_{ref}$, and Λ with x/L. $\sqrt{\tilde{e}_{ref}}/(\tilde{u}_1 - \tilde{u}_2) = \sqrt{0.0872}$; $(\tilde{u}''\tilde{v}'')_{ref}/(\tilde{u}_1 - \tilde{u}_2)^2 = 0.0242$; $L = \frac{10}{3}\delta_0$; $X_0/L = -25.8005$; $\sigma = 19.7200$.

Figure 5.- Continued.

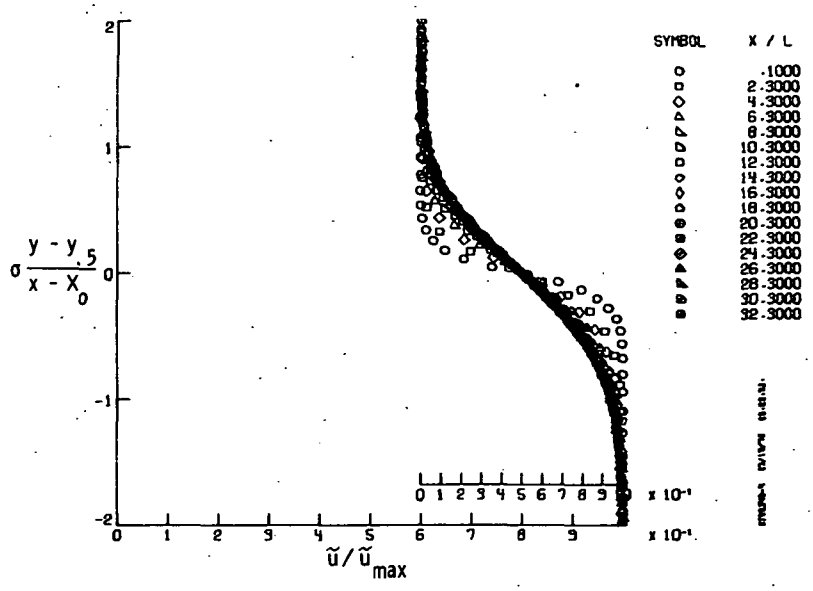

(m) Variation of $\tilde{u}/\tilde{u}_{max}$ with $\sigma(y - y_{.5})/(x - X_0)$ for $\tilde{u}_2/\tilde{u}_1 = 0.6$ with turbulence boundary conditions at $x = 0$; $\sqrt{\tilde{e}_\infty}/\tilde{u}_\infty = 0.02$; $l_\infty/\lambda = 10$; $L = \frac{10}{3}\delta_0$; $X_0/L = -16.6895$; $\sigma = 22.7909$.

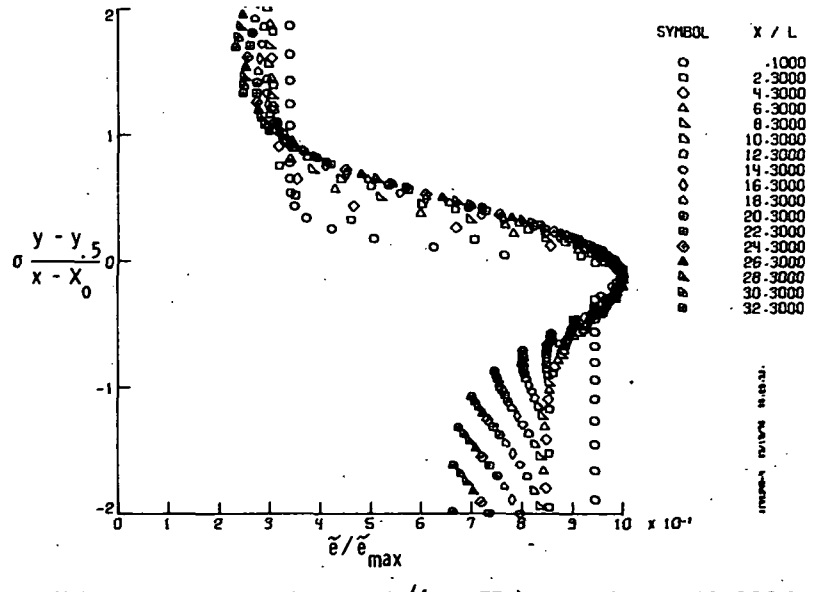

(n) Variation of $\tilde{e}/\tilde{e}_{max}$ with $\sigma(y - y_{.5})/(x - X_0)$. $X_0/L = -16.6895$; $\sigma = 22.7909$.

Figure 5.- Continued.

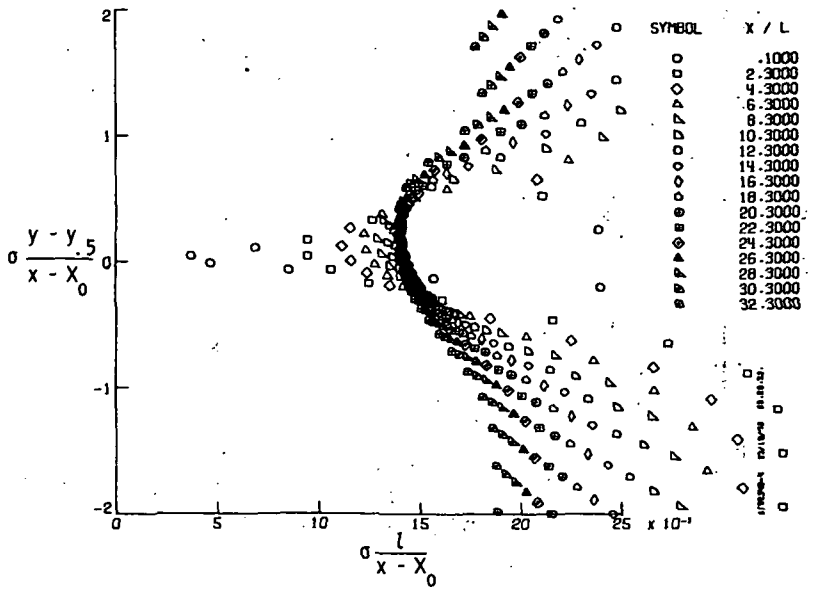

(o) Variation of $\sigma l/(x - X_o)$ with $\sigma(y - y_{.5})/(x - X_o)$. $X_o/L = -16.6895$; $\sigma = 22.7909$.

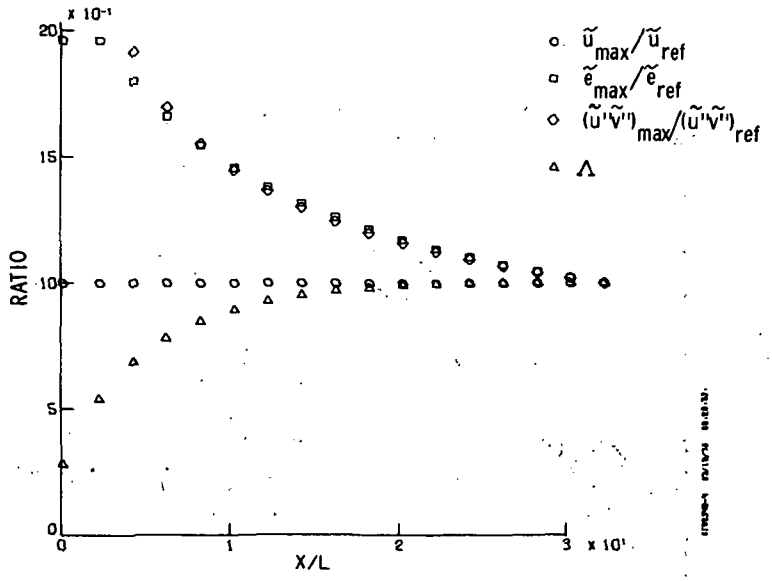

(p) Variation of $\tilde{u}_{max}/\tilde{u}_{ref}$, $\tilde{e}_{max}/\tilde{e}_{ref}$, $(\tilde{u}''\tilde{v}'')_{max}/(\tilde{u}''\tilde{v}'')_{ref}$, and Λ with x/L. $\sqrt{\tilde{e}_{ref}}/(\tilde{u}_1 - \tilde{u}_2) = \sqrt{0.0671}$; $(\tilde{u}''\tilde{v}'')_{ref}/(\tilde{u}_1 - \tilde{u}_2)^2 = 0.0213$; $L = \frac{10}{3}\delta_o$; $X_o/L = -16.6895$; $\sigma = 22.7909$.

Figure 5.- Concluded.

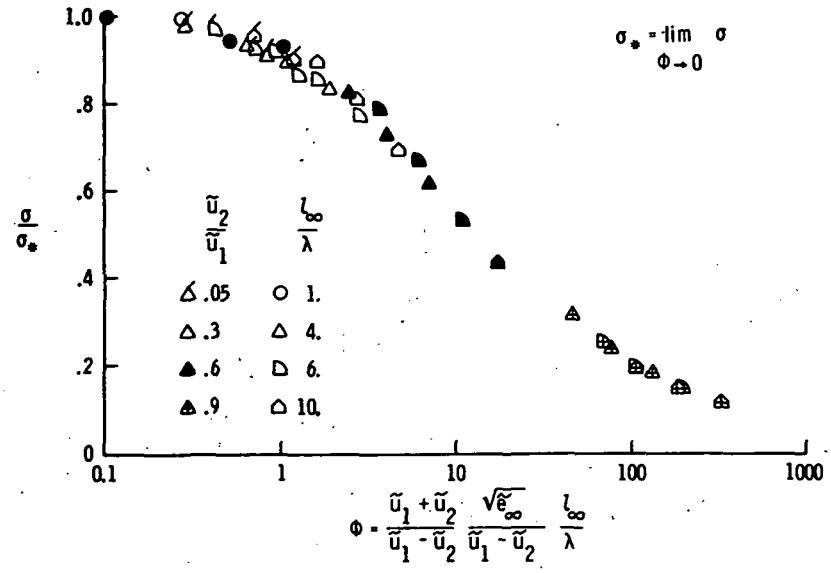

Figure 6.- Parametric correlation of predicted effect of wide-band free-stream disturbances (only one side) on turbulent free mixing (low speed). σ is based on width for 10 percent and 90 percent momentum.

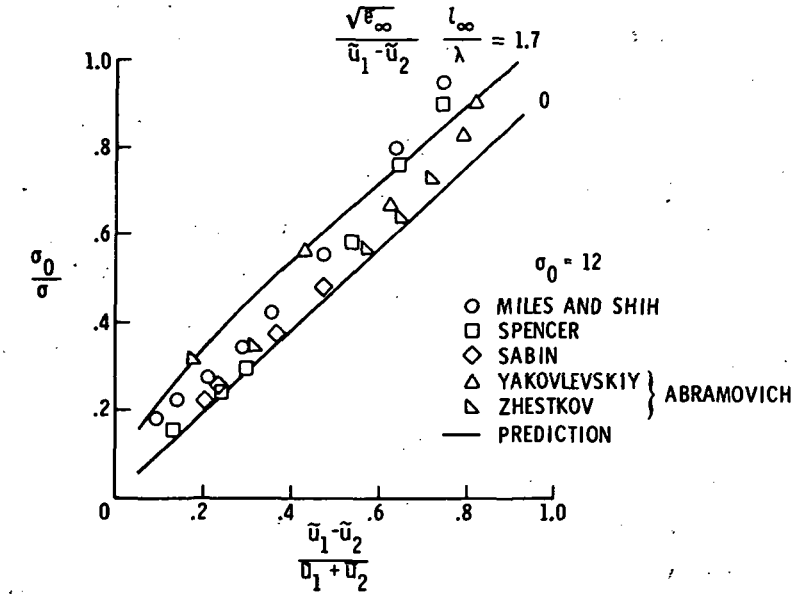

Figure 7.- Effect of wide-band free-stream disturbances. Variation of σ with $(\tilde{u}_1 - \tilde{u}_2)/(\tilde{u}_1 + \tilde{u}_2)$.

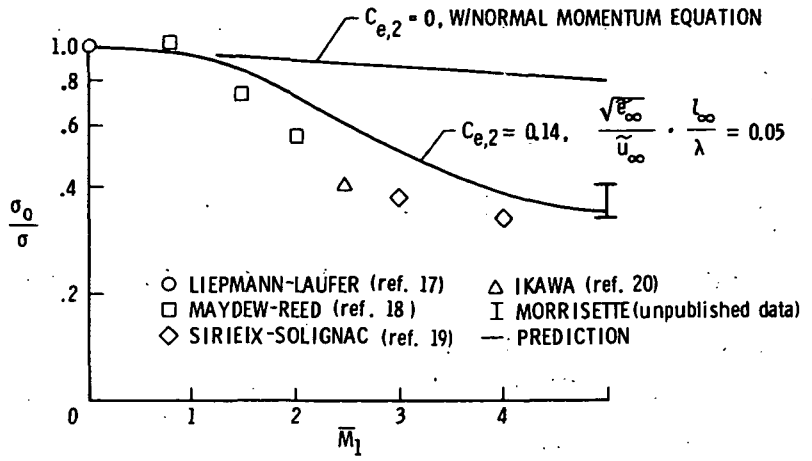

Figure 8.- Effect of Mach number on spreading rate prediction for clean flow.

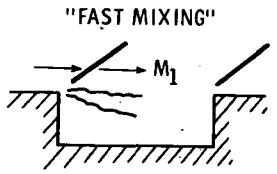

(a) Cavity Flows (refs. 22 and 23).

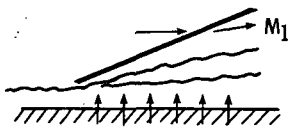

(b) Massive wall injection (ref. 24).

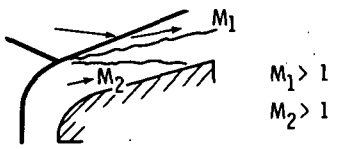

(c) Triple shock intersection (ref. 5).

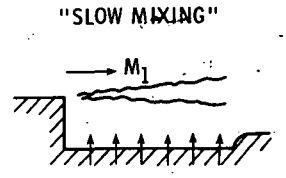

(d) Backward facing step with matched pressure (ref. 20).

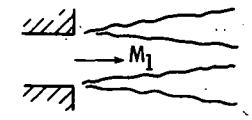

(e) Near field of isolated jets (ref. 21).

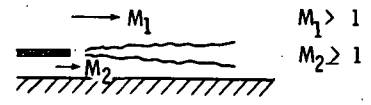

(f) Sonic slot injection into supersonic hypersonic flow (refs. 26 and 27) co-axial jet (ref. 28).

Figure 9.- Experimental configurations used for supersonic shear layer experiment.

AN EXPERIMENTAL AND NUMERICAL INVESTIGATION OF SHOCK-WAVE INDUCED TURBULENT BOUNDARY-LAYER SEPARATION AT HYPERSONIC SPEEDS[†]

By J. G. Marvin, C. C. Horstman, M. W. Rubesin,
T. J. Coakley, and M. I. Kussoy

NASA Ames Research Center

SUMMARY

This paper describes a thoroughly documented experiment that was specifically designed to test and guide computations of the interaction of an impinging shock wave with a turbulent boundary layer. Detailed mean flow-field and surface data are presented for two shock strengths which resulted in attached and separated flows, respectively. Numerical computations, employing the complete time-averaged Navier-Stokes equations along with algebraic eddy-viscosity and turbulent Prandtl number models to describe shear stress and heat flux, are used to illustrate the dependence of the computations on the particulars of the turbulence models. Models appropriate for zero-pressure-gradient flows predicted the overall features of the flow fields, but were deficient in predicting many of the details of the interaction regions. Improvements to the turbulence model parameters were sought through a combination of detailed data analysis and computer simulations which tested the sensitivity of the solutions to model parameter changes. Computer simulations using these improvements are presented and discussed.

INTRODUCTION

The availability of larger, faster computers, the need to reduce wind-tunnel testing, which is time consuming and costly, and the need to provide alternate simulation capability for test conditions beyond the reach of practical wind-tunnel design have resulted in increased emphasis on computational fluid mechanics. Computations that were not feasible several years ago are

[†]Paper to be presented at the Symposium On Flow Separation sponsored by the AGARD Fluid Dynamics Panel at Göttingen, Germany, 27-30 May, 1975.

now being performed routinely. For example: inviscid three-dimensional computations for speeds ranging from transonic to hypersonic are possible (refs. 1 and 2); even flows where dominant viscous interactions occur, such as the interaction of a shock with a boundary layer, are being computed (refs. 3 and 4). These interacting flows present the greatest challenge, however, because most of the practical applications occur at high Reynolds numbers where the flow is turbulent and little is known about turbulence modeling.

Until recently, most of the techniques for predicting the flow behavior in the vicinity of shock boundary-layer interactions were based on experimental correlations or approximate solutions to the boundary-layer equations. But advances in numerical methods and increased computer speed and capacity have resulted in successful attempts to obtain steady-state solutions of the complete time-dependent Navier-Stokes equations. Computations of laminar interactions have been used to illustrate the utility and accuracy of these techniques (refs. 3 and 4). Very recent examples for turbulent flows (refs. 5-7) illustrate that such computations using the time-dependent, time-averaged Navier-Stokes equations‡ are also feasible and that they describe the qualitative features of the flow interactions. In these examples, closure of the conservation equations was accomplished by describing the turbulent shear stress and heat flux by eddy-viscosity models and turbulent Prandtl numbers. However, a lack of sufficient detailed experimental data precluded verification of these models and efforts to modify them so that the quantitative flow features could be more aptly described.

The present study was undertaken to provide a formidable first step toward understanding the mechanisms that must be modeled before successful numerical calculations of these complicated flows can be made. It combines experimental and numerical methods to guide and verify turbulence modeling for two shock boundary-layer interaction flows, one with and one without separation. An axisymmetric experimental arrangement was chosen to assure purely two-dimensional flow (ref. 8). Shocks of two different strengths were impinged on an established turbulent boundary layer to set up both unseparated and separated flows in the interaction zone. Detailed measurements, consisting of surface-pressure, skin-friction, heat-transfer, and boundary-layer profiles of velocity, static pressure, and temperature were obtained at finely spaced intervals along the surface. Analysis of these data was undertaken to define the detailed behavior of the turbulence parameters used to describe the shear stresses throughout the interaction regions. Computations were made using the time-dependent, time-averaged Navier-Stokes equations employing the exact experimental boundary conditions and algebraic eddy-viscosity descriptions for the turbulent shear stress. The authors reported preliminary progress on the separated case in reference 9.

---

‡Time averaging in these equations is over periods long compared to turbulence time scales, but short compared to the time variations of the flow field as a whole.

NOTATION

A, A_w^+	Van Driest damping parameter, Eqs. (5) and (6)
c_p	specific heat at constant pressure
c_v	specific heat at constant volume
C_F	local skin friction coefficient, $\tau_w/(1/2)\rho_\infty u_\infty^2$
C_H	local Stanton number, $q_w/\rho_\infty u_\infty c_p(T_t - T_w)$
e	total specific energy per unit volume, $\rho[c_v T + (v^2 + u^2)/2]$
F, G, H	mass-averaged fluxes, Eqs. (1) and (2)
I	intermittency factor, Eq. (9)
k	thermal conductivity
ℓ	mixing length, Eqs. (4) and (20)
p	time-averaged pressure
Pr	molecular Prandtl number, $\mu c_p/k$
Pr_t	turbulent Prandtl number
q_x	axial heat flux, $-c_p(\mu/Pr + \rho\varepsilon/Pr_t)\partial T/\partial x$
q_r, q	radial heat flux, $-c_p(\mu/Pr + \rho\varepsilon/Pr_t)\partial T/\partial r$
r	radial coordinate, distance from model centerline
t	time
T	temperature
u	mass-averaged velocity component in axial direction
U	mass-averaged conservation variables, Eqs. (1) and (2)
v	mass-averaged velocity component in radial direction
x	axial coordinate, distance from leading edge of shock-wave generator
y	distance normal to model surface
α	shock-wave generator leading-edge angle

δ boundary-layer thickness

δ_o boundary-layer thickness at the upstream location of the first measured profile station

δ_i^* kinematic displacement thickness, Eq. (8)

δ_c^* compressible displacement thickness, Eq. (11)

ε eddy viscosity, Eqs. (4) and (20)

κ Von Kármán constant, Eq. (5)

μ viscosity

ρ time-averaged density

σ_r radial normal stress, $p - 2\mu_T \frac{\partial v}{\partial r} + \frac{2}{3}\mu_T \left(\frac{v}{r} + \frac{\partial v}{\partial r} + \frac{\partial u}{\partial x}\right)$

σ_x axial normal stress, $p - 2\mu_T \frac{\partial u}{\partial x} + \frac{2}{3}\mu_T \left(\frac{v}{r} + \frac{\partial v}{\partial r} + \frac{\partial u}{\partial x}\right)$

σ_θ azimuthal normal stress, $p - 2\mu_T \frac{v}{r} + \frac{2}{3}\mu_T \left(\frac{v}{r} + \frac{\partial v}{\partial r} + \frac{\partial u}{\partial x}\right)$

τ, τ_{xr} total shear stress, Eq. (3)

Subscripts

f final axial grid location

i initial axial grid location

max maximum

o location of incident shock impingement on cylinder surface in the absence of a boundary layer

r radial direction

t stagnation conditions

T total

x axial direction

w wall

∞ local free stream ahead of interaction

APPARATUS AND PROCEDURES

Facility

The experiment was conducted in the NASA Ames Research Center 3.5-Foot Hypersonic Wind Tunnel. This facility operates in a blowdown mode and utilizes contoured axisymmetric nozzles to achieve a uniform Mach number, and an open-jet type test core approximately 0.7 m in diameter and 4 m in length. The present tests were all performed at a nominal free-stream Mach number of 7.2 and with nominal values of total temperature and pressure of 695 K and 34 atmospheres, respectively. The corresponding nominal value of free-stream unit Reynolds number was 10.9×10^6 m^{-1} and the useful test time was about 3 min.

Model

A cone-ogive cylinder, 330 cm in length and 20.3 cm in diameter was used as the test surface (see fig. 1). An annular shockwave generator, 51 cm in diameter, mounted concentric with the cylinder axis was used to generate shock waves of two different strengths by beveling the sharp leading edge at either 7.5° or 15°. The generator could be translated in a direction parallel to the cylinder axis so that the entire interaction region could be passed over selected survey stations.

Interchangeable instrumentation ports, 12 cm in diameter and specifically contoured to match the cylindrical surface, were located at 25 cm intervals along the cylinder in a single line, and every 50 cm in another line 180° around the body. One port was instrumented with a floating element skin-friction balance. Another was used to accommodate either pitot and static pressure probes or total temperature probes. The probes were positioned by a mechanism contained inside the cylinder and automatically actuated from outside the tunnel test section. The remaining ports were instrumented with thermocouples spot-welded to the inner surface every 1.25 cm and with static pressure taps. Static pressure taps were also located every 5 cm along the entire cylinder between ports.

Test Procedure

Data were collected from a series of tests with the tunnel operating at the nominal conditions described above. In separate tests without the generator it was determined that a fully developed turbulent boundary layer with negligible axial pressure gradient was established over the cylinder surface between 100 and 300 cm from the model tip (ref. 10). With the generator in place, the nominal measured boundary-layer parameters ahead of the interaction for the 7.5° and 15° generator angles, respectively, were: edge Mach number, 6.7 and 6.9; boundary-layer thickness, 3.2 cm and 2.7 cm; and Reynolds number based on boundary-layer thickness, 0.23×10^6 and 0.2×10^6. The model wall temperature was essentially constant at a value of 300 K.

Surface pressure, skin friction, and heat transfer were obtained at small intervals by moving the shock-wave generator in an axial direction during the tests. The boundary-layer thickness increased about 10% over the distance of 25 cm which corresponded to the difference between the farthest upstream and downstream positions of the generator. The difference in boundary-layer thickness had little influence on the results, provided they were compared at equivalent distances from the leading edge of the generator.

Skin friction was measured with a contoured floating-element balance whose sensible element was 0.95 cm in diameter. Calibrations of the gage before and after each test run were repeatable to within 5%. The skin-friction data were corrected for buoyancy effects resulting from the axial pressure gradient. Corrections were less than 10% of the measured values, except in the regions of minimum skin friction for the 7.5° generator tests and near separation and reattachment for the 15° generator tests, where they were as high as 50% of the measured upstream zero pressure gradient values. The heat-transfer rate was measured using the thin-wall transient technique. Longitudinal conduction errors were computed and found to be less than 5% of the measured rates and so no corrections were applied to these data.

Velocity, density, and pressure profiles were obtained from pitot and static pressure and total temperature surveys. Each survey was taken during a single test run, and its axial location was established prior to the run by prepositioning the shock generator. In the interaction region, surveys were obtained every 2 cm for the 7.5° generator tests and every 2.5 cm for the 15° generator tests. Downstream of the interaction the corresponding distances between survey stations were increased to 4 cm and 5 cm, respectively, for the two generator angles. In the reversed flow region established with the 15° generator, pitot measurements were obtained in upstream and downstream directions to help establish the extent of separation. When traversing the boundary layer, the probes were stopped at each location for a few seconds to avoid time lags in the measurements, and static pressures at the model surface were monitored continuously to verify interference-free data.

To verify that the model was aligned with the free-stream flow direction, surface-pressure measurements at selected axial positions were obtained at 90° intervals around the model, and skin-friction measurements at selected axial positions 180° apart. Comparisons of these data around the model showed variations that were within the experimental accuracy of the measurements. For the 15° generator tests, separation and reattachment lines around the model were also measured using a surface oil film technique. The results verified an axisymmetric separation zone.

A more complete description of the test procedure and data accuracy along with tabulations of all the test data are given in reference 11.

GOVERNING EQUATIONS AND NUMERICAL PROCEDURES

The equations and numerical procedures were first presented by the authors in reference 9. For completeness, some of that information is presented again in this section.

Equations and Boundary Conditions

The mass-averaged Navier-Stokes equations for compressible flow, expressed in cylindrical coordinates with axial symmetry assumed, were used to predict the flow throughout the interaction region. The equations and the concept of mass averaging are discussed in reference 12. The turbulent Reynolds stress and heat-flux terms in these equations are related to the mean flow gradients of velocity and temperature by eddy-transport coefficients that are added to the molecular-transport coefficients. Additional restrictions on the equation system include the perfect gas assumption, constant specific heats, the Sutherland viscosity law, and zero bulk viscosity. The resulting equations are

$$\frac{\partial U}{\partial t} + \frac{\partial F}{\partial x} + \frac{\partial G}{\partial r} = H \tag{1}$$

$$U = r\begin{pmatrix} \rho \\ \rho u \\ \rho v \\ e \end{pmatrix} \qquad F = r\begin{pmatrix} \rho u \\ \rho u^2 + \sigma_x \\ \rho uv + \tau_{xr} \\ (e+\sigma_x)u + \tau_{xr}v^3 + q_x \end{pmatrix} \tag{2}$$

$$H = \begin{pmatrix} 0 \\ 0 \\ \sigma_\theta \\ 0 \end{pmatrix} \qquad G = r\begin{pmatrix} \rho v \\ \rho uv + \tau_{xr} \\ \rho v^2 + \sigma_r \\ (e+\sigma_r)v + \tau_{xr}u + q_r \end{pmatrix}$$

Figure 2 shows the computational domain. The conditions on the upstream boundary were prescribed by a combination of an inviscid, method of characteristics program (ref. 13), and a boundary-layer program (ref. 14) modified for turbulent flows by Marvin and Sheaffer. At the upstream boundary position, the experimental and computed incident shock waves were aligned and the boundary-layer program was run for an x distance that ensured a match of experimentally and numerically determined displacement thicknesses. Along the cylinder surface, $r = r_w$ or $y = 0$, the boundary conditions used were the viscous, no-slip conditions, $u = v = \partial p/\partial r = 0$, $T = T_w$, while along the outer boundary they were the inviscid, free-slip conditions, $v = \partial p/\partial r = \partial u/\partial r = \partial T/\partial r = 0$. At the downstream boundary the derivatives of all variables were set to zero, e.g., $\partial u/\partial x = 0$. The initial conditions within the computational domain used to start the solutions were obtained by setting the values of all variables equal to their inflow boundary values at the same vertical station, that is, $f(x, r, 0) = f(x_i, r, 0)$, $x_i \le x \le x_f$. To restart solutions or make modifications to turbulence parameters, initial values of the variables were set equal to their computed values obtained during the last time step of the previous solution.

Numerical Procedures

The finite difference scheme used to solve equation (1) is the same as that developed originally by MacCormack (ref. 3) and applied more recently to two-dimensional turbulent shock boundary-layer interactions by Baldwin and MacCormack (ref. 15). The numerical techniques employed in the present study, along with all the pertinent difference equations, and some special procedures are reported in reference 9. The computational domain was subdivided into four subgrids with each subgrid divided into a number of uniform grid cells with spacing Δy. Finer spacing was employed near the wall. A total of 78 cells in the y direction was used; uniformly spaced grid with 48 cells in the x direction was used with spacing $\Delta x = 0.80$ or 0.635 cm for the 7.5° and 15° cases, respectively. Some of the solutions presented later cover axial distances greater than those obtained with the 48 cells in the x direction. Those solutions were achieved by redefining the upstream boundary to coincide with a position about 3 cm ahead of the downstream boundary from converged solutions and then continuing the solutions on downstream for another 48 cell points in the x direction.

The solutions were advanced in time following the procedure described in reference 9. Steady-state convergence was assumed when solutions from at least 20 successive time steps showed little or no change. Computation times to achieve these fully converged solutions on a CDC 7600 were 3-4 hrs for the 15° generator cases and about 1 hr for the 7.5° cases.

RESULTS AND DISCUSSION

Experimentally Determined Flow-Field Features

Figure 2 depicts the major features of the shock-wave, boundary-layer interaction zone. The sketch is based on boundary-layer survey measurements and shadowgraphs taken during the experiments using both the 7.5° and 15° shock-wave generators. The incident shock wave, weakened and curved somewhat by the expansion fan emanating from the corner formed by the leading edge and the body of the shock-wave generator, impinges on the incoming boundary layer. The subsequent increases in surface pressure cause the boundary layer to thicken, or even separate in the case of the strongest incident shock wave, and induce a shock wave. Thereafter rapid flow turning and boundary-layer thinning occur and a recompression shock is formed.

Figure 3 shows the surface measurements obtained for the two shock-wave generator angles. Surface-pressure, skin-friction, and heat-transfer coefficients are shown as functions of a normalized interaction distance centered about x_o, the location of the intersection of the inviscid incident shock wave with the body surface in the absence of a boundary layer. With the 7.5° generator, the pressure rises continually through the interaction; the skin friction decreases initially in the presence of the adverse pressure gradient and rises thereafter in the recompression region where the boundary layer thins. The heat transfer follows a behavior similar to that of the pressure. No separation was observed in this case, either from the skin-friction mea-

surements or from oil-flow patterns that were established and photographed during some special tests. In contrast, with the 15° generator the initial increase in pressure levels off in a plateau, and negative values of skin friction were measured, both characteristics typically associated with separation. Rapid increases in pressure and skin friction occur downstream of reattachment. The heat transfer rises continually through the interaction until the surface pressure decreases. For both generator angles, the decay in pressure, skin friction, and heat transfer downstream of the interaction is a direct result of the expansion fan emanating from the corner of the generator.

Figures 4 and 5 present constant static pressure and velocity contours and illustrate further the details of the two interaction cases under investigation. The contours were constructed from the profiles of velocity and static pressure across the boundary layer obtained from pitot and static pressure and total temperature measurements taken at small Δx and Δy intervals. Complete tabulations of these profile data can be found in reference 11. Locations of the incident, induced, and recompression shocks are easily recognized in the pressure contours. Note that for the 15° generator the pressures are higher than the wall-peak pressure in the compression region downstream of the intersection of the incident and induced shocks. The velocity contours illustrate more dramatically the differences between the two flow cases. For the larger generator angle the flow velocity near the wall in the vicinity of the interaction is highly retarded and achieves negative values associated with the reversed flow in the separated zone.

A precise determination of separation and reattachment points for the separated case was made difficult because of the unsteady nature of the separated flow and the relatively large diameter of the skin friction element. A detailed discussion of this unsteady phenomenon is given in reference 9. A best estimate of the extent of the time-averaged separation region was obtained from data obtained with forward and backward facing pitot tubes. These data, obtained at fixed values of y with x varied by moving the shock generator, indicated a separated region extending from $(x - x_o)/\delta_o = -3.15$ to -1.68. This region is somewhat larger than the skin-friction measurements indicated. Locations of the separation and reattachement points from the pitot measurements are shown on the abscissa of the skin-friction plot.

Numerically Simulated Flow-Field Features

As previously mentioned, the turbulent Reynolds stress and heat-flux terms in equation (2) were assumed to be related to the mean flow gradients of velocity and temperature by algebraic eddy-transport coefficients that were simply added to the molecular-transport coefficients. Mainly, this choice was dictated by considerations of economy in the computer program. Although such a model may be restrictive in its application to other new flow situations, it suits our current objectives of (1) defining the eddy viscosity field that results when a shock impinges on a turbulent boundary layer, and (2) determining whether improvements in the eddy viscosity description used in the numerical simulations can be made by a close examination of the experimental data.

Results using a baseline turbulence model.—The first numerical simulations were obtained with a modified, two-layer, Cebeci-Smith (ref. 16) eddy viscosity model. Modifications suggested by Cebeci to account for pressure gradient effects were not used. The shear was expressed as

$$\tau = -\tau_{xr} = (\mu + \rho\varepsilon)\left(\frac{\partial u}{\partial r} + \frac{\partial v}{\partial x}\right) \tag{3}$$

In the inner layer the following mixing length description for the eddy viscosity was used:

$$\varepsilon = \varepsilon_{inner} = \ell^2\left(\left|\frac{\partial u}{\partial r} + \frac{\partial v}{\partial x}\right|\right) \tag{4}$$

where

$$\ell = \kappa y\left[1 - \exp\left(\frac{-y}{A}\right)\right] \tag{5}$$

$$A = A_w^+ \frac{\mu_w}{\sqrt{|\tau_w|\rho_w}} \tag{6}$$

with the Von Karman constant $\kappa = 0.4$ and the Van Driest constant $A_w^+ = 26$. In the outer layer, the eddy viscosity was given, following Clauser, by

$$\varepsilon = \varepsilon_{outer} = 0.0168 \frac{u_{max}\delta_i^*}{I} \tag{7}$$

where

$$\delta_i^* = \int_0^{y_{max}} \left(1 - \frac{u}{u_{max}}\right) \frac{r_w + y}{r_w}\, dy \tag{8}$$

$$I = 1 + 5.5\left(\frac{y}{\delta}\right)^6 \tag{9}$$

$$\delta = 1.735\,\delta_c^* \tag{10}$$

$$\delta_c^* = \int_0^{y_{max}} \left(1 - \frac{\rho u}{(\rho u)_{max}}\right) \frac{r_w + y}{r_w}\, dy \tag{11}$$

The above definitions of the displacement thicknesses differ somewhat from the conventional ones. The present choice was dictated by the fact that, in the first stages of developing the Navier-Stokes code for the shock interaction

problem, overshoots in the velocity profiles during early time steps made it difficult to select the edge of the viscous layer. Therefore, the value of y_{max} was simply taken as the boundary-layer thickness ahead of the interaction, and u_{max} and $(\rho u)_{max}$ were taken as the local maximum values between the wall and y_{max}. The boundary between the two layers was determined by the value of y where $\varepsilon_{inner} = \varepsilon_{outer}$.

The heat flux was expressed in terms of the eddy viscosity by

$$q = q_r = -\left(\frac{\mu}{Pr} + \frac{\rho\varepsilon}{Pr_t}\right) c_p \frac{\partial T}{\partial r} \tag{12}$$

where $Pr_t = 0.9$.

Results of the computations using this baseline turbulence model are compared with the experimental data in figures 6, 7, and 8. Overall, the computations predict the qualitative features of the two flows remarkably well considering the simplicity of the turbulence model, but a closer examination of the comparisons points out the major limitations of the computations.

The overall surface pressure rise for the flow with the 7.5° shock-wave generator (fig. 6a) is predicted reasonably well, except for the location of the initial rise in pressure. The corresponding predicted rises in both skin friction and heat transfer lag the data in the interaction region, reflecting the inability of the simple turbulence model to predict any upstream influence, but the final predicted levels downstream agree reasonably well with the data. The skin friction prediction shows separation at the surface but the measurements do not. The pressure contour comparisons (fig. 7a) show that the computation predicts only the incident and reflected shocks whereas the experimental data show the presence of an induced shock. The comparison of the streamline contours (fig. 8a) shows the prediction of a zero velocity line just off the surface accompanied by a small region of reversed flow which is not present in the experimental data.

Similar conclusions can be made from comparisons of the numerical computations and the data for the flow with the 15° shock-wave generator (figs. 6b, 7b, and 8b). With the baseline turbulence model, no upstream influence is predicted and in this separated flow case no plateau pressure is predicted. The induced shock wave caused by the large separation in the experiment is not predicted because the computation predicts such a small separation height. For this separated flow case, the baseline turbulence model results in good prediction of the overall pressure and skin friction rises and their subsequent decay; but the heat transfer is substantially underpredicted (see fig. 6b).

Baseline model modifications.—Attempts were made to guide changes in the turbulence model by combining data analysis and trial and error solutions in the actual Navier-Stokes code. Ideally, these changes could have been guided entirely from data if absolutely reliable shear-stress measurements had been available. But, since attempts to directly measure the shear stress through these interactions have so far produced unsatisfactory results, the boundary-

layer profile data were used. A significant degree of uncertainty is introduced in this procedure, however, because the inertial forces dominate the momentum balance, especially in the outer portions of the flow. Conversely, relying solely on trial and error solutions to the code itself to guide modeling changes would be time consuming and perhaps unsuccessful if attention was not confined to physically meaningful changes.

The shear-stress and heat-flux distributions through the boundary layer were evaluated by the use of experimental profile data to solve the following equations based on the boundary-layer approximation:

$$\tau = \frac{1}{(r_w + y)} \left[r_w \tau_w + \frac{\partial}{\partial x} \int_0^y (r_w + y)(p + \rho u^2)\, dy \right.$$

$$\left. - u \frac{\partial}{\partial x} \int_0^y (r_w + y) \rho u\, dy \right] \tag{13}$$

and

$$q - u\tau = \frac{1}{(r_w + y)} \left[r_w q_w + c_p T_t \frac{\partial}{\partial x} \int_0^y (r_w + y) \rho u\, dy \right.$$

$$\left. - \frac{\partial}{\partial x} \int_0^y (r_w + y) \rho u c_p T_t\, dy \right] \tag{14}$$

By performing integration with respect to y before differentiation with respect to x and by employing the conservative form of the variables, for example $(p + \rho u^2)$, it was expected that errors in the momentum and energy balances could be minimized. Despite these precautions, not all the shear profiles approached zero at large distances from the wall where they should have. In some of these cases it was possible to adjust the inertial balance across the boundary layer so that zero shear was achieved at the edge of the thermal boundary layer. These adjustments were usually small for the 7.5° shock wave generator profiles, but somewhat larger for the 15° generator profiles.

Figure 9 shows the shear profiles resulting from these momentum and energy balances for axial locations ahead, within, and downstream of the two interaction regions. For the flow with the 7.5° generator the maximum shear stress within the boundary layer builds up rapidly within the interaction region as the adverse pressure gradient increases; after peak pressure is reached this maximum shear relaxes toward its initial level but at a very slow rate. At the farthest downstream location where the pressure gradient is favorable the shear near the wall decreases and subsequently increases, indicating that the shear in the outer extremes of the boundary layer is adjusting to the local flow gradients more slowly than the shear near the wall. Similar

conclusions can be reached for the separated case using the 15° generator. In this case, data were available for a larger downstream interaction distance, and the shear appears to have adjusted to the local flow gradients. Also, for this separated case, the maximum shear in the boundary layer continues to increase downstream of reattachment and slightly beyond the location of peak pressure.

A maximum mixing length was determined at each of the profile survey stations by dividing the experimentally deduced shear distributions by the measured velocity gradients, plotting the results, and choosing the maximum value of mixing length. For those cases where the mixing length continuously increased with distance from the wall, the value of maximum mixing length was chosen at the point where the first significant departure from a linear mixing length distribution occurred. These maximum values are shown in figure 10 as a function of the interaction length parameter. The extremes on the bars represent the uncertainty introduced by using shear profiles evaluated either directly from the momentum balances or from momentum balances modified by adjusting the inertial terms to insure zero shear at the edge of the thermal boundary layer. The uncertainty was largest in the region downstream of reattachment for the 15° generator case. In both cases the maximum mixing lengths tend to decrease in regions of adverse pressure gradient, where the boundary layer thickens, and to increase in regions of favorable pressure gradient.

Near the surface where the importance of the inertia and convection terms in the momentum and energy balances diminished, attempts were made to evaluate κ and A_w^+. The shear profiles at each survey station were analyzed by integrating the following system of equations to obtain values of velocity and temperature as a function of y out to distances where the estimated errors in the inertial balance became significant compared to the magnitude of the local shear (usually this consisted of about 9 measured points away from the wall):

$$\tau = \left(\mu + \rho \ell^2 \left|\frac{\partial u}{\partial y}\right|\right) \frac{\partial u}{\partial y} \tag{15}$$

$$\ell = \kappa y \left[1 - \exp\left(\frac{-y}{A}\right)\right] \tag{16}$$

$$A = \frac{\mu_w}{\sqrt{|\tau_w|\rho_w}} A_w^+ \tag{17}$$

$$q = -\left(\frac{\mu}{P_r} + \frac{\rho \ell^2}{P_{r_t}} \left|\frac{\partial u}{\partial y}\right|\right) \frac{\partial T}{\partial y} \tag{18}$$

Best fits to the velocity and temperature profile data near the wall were achieved by repeated integration of these equations until the sum of the root mean square of the differences between the predicted and measured velocities and temperatures was minimized. The procedure was automated for solution on a CDC 7600 and initiated by inputting shear and temperature profiles from the

momentum and energy balances along with the measured values of wall shear. An optimization routine (described in ref. 16) was initiated and values of κ and A_w^+ and q_w were sought to satisfy the minimization criteria. (This optimization routine was developed by Garret N. Vanderplaats, of NASA Ames, who helped to implement it for the present application.) The root mean square of the residuals never exceeded 5% and in most cases was less. Exceptions to this residual band occurred for the 15° generator case in the separated region. However, it was still possible to achieve this band at these profile stations, provided the input wall shear was also considered part of the optimization routine along with the other parameters. This was not surprising, however, since accurate skin-friction measurements were difficult to make in this separated region. Examples of the best fits to the velocity and temperature data near the upstream edge of the separated region are shown as the solid lines in figure 11. Two important aspects of this example are noteworthy. First, at this station, the wall shear needed to achieve a best fit was -5.28 N/m^2 whereas the direct measurement was 12.1 N/m^2. Considering that the station is near the separation point where experimental accuracy is poor and that the separation point is unsteady, this disparity is not unreasonable. Second, at this station, values of κ and A_w^+ are significantly lower than their corresponding undisturbed values, 0.4 and 26.

Figure 12 presents the values of κ and A_w^+ required to achieve these best fit velocity and temperature profiles for both of the interaction cases being studied. The error bands on the symbols again represent the uncertainty introduced by using shear profiles evaluated either directly from the momentum balances or from momentum balances modified by adjusting the inertial terms to insure zero shear at the edge of the thermal boundary layer. The results for the 7.5° generator show that A_w^+ decreases in the vicinity of the interaction while κ increases. These results are interpreted as indicating a higher eddy viscosity throughout the region than that predicted by the baseline turbulence model. This could explain why the numerical simulations using the baseline turbulence model predicted separation. For the 15° generator case where separation was present, similar trends in κ and A_w^+ are apparent. However, the uncertainties within the separated region precluded any precise determination of the parameters. Apparently, both κ and A_w^+ decrease ahead of and in the upstream portions of the separated region. At the downstream edge of the separated region near reattachment κ has increased considerably and A_w^+ is also increasing. The physical interpretation of these results suggests that ahead of separation the sublayer or inner region has a somewhat higher eddy viscosity than the baseline model would predict, but in the logarithmic region the viscosity is somewhat lower than the baseline model would predict. In the separated region, an interpretation is more difficult to arrive at, but apparently, at least near the reattachment point, the eddy viscosity is higher across the sublayer and logarithmic regions than would be predicted by the baseline model.

The turbulence model mixing length formulation suggested by the foregoing data analysis was introduced into the Navier-Stokes computer code in the following way:

$$\tau = -\tau_{xr} = (\mu + \rho\varepsilon)\left(\frac{\partial u}{\partial r} + \frac{\partial v}{\partial x}\right) \tag{19}$$

$$\varepsilon = \ell^2\left[\left(\frac{\partial u}{\partial r}\right)^2 + \left(\frac{\partial v}{\partial x}\right)^2\right]^{\frac{1}{2}} \tag{20}$$

In the inner region

$$\ell = \kappa(x)\left[1 - \exp\left(\frac{-y}{A}\right)\right] \tag{21}$$

$$A = A_w^+(x)\frac{\mu_w}{\sqrt{|\tau_w|\rho_w}} \tag{22}$$

In the outer region

$$\ell = \ell_{max}(x) \tag{23}$$

Employing ℓ_{max} in this model formulation eliminated the need for arbitrarily defining compressible and incompressible displacement thickness as was the case with the baseline model. The boundary between the two regions is determined by the value of y where $\ell = \ell_{max}$. The heat flux equation remained the same as for the baseline model (see eq. 12).

Computer simulations were next obtained using the experimental data analysis as a guide for evaluating the parameters $\ell_{max}(x)$, $\kappa(x)$, and $A_w^+(x)$. First, values directly from the data analysis were used. Examination of the resulting computer simulations made it apparent that adjustments to the parameters would be needed before the simulations would predict the experimentally determined features of the flow fields in the interaction region. Therefore, a trial and error procedure was initiated to arrive at more appropriate distributions of the turbulence parameters. The procedure is still underway at this time. Before discussing the results of this procedure to date, some interesting observations can be pointed out. The simulations were all more sensitive to modifications of the inner region model parameters than the outer maximum mixing length parameter. In the inner region itself, $A_w^+(x)$ modifications tended to affect the solutions more than those for $\kappa(x)$, especially in the separated case. However, best results have been achieved with modification to both $A_w^+(x)$ and $\kappa(x)$.

Results using a modified turbulence model.—The turbulence parameter variations used in the latest computer simulations employing the complete Navier-Stokes equations are shown as the solid and dashed lines in figures 10 and 12. The maximum mixing length variation (fig. 10), employed in all simulations, corresponded to the mean variation exhibited by the data analysis. In the inner layer region (fig. 12), values of A_w^+ and κ had to be altered to obtain better predictions of the experimental surface and flow-field data. For the 7.5° generator case these variations in A_w^+ and κ follow the trends exhibited by the data analysis. The largest disparity between the values used in the

simulations and those deduced from data analysis is in A_{w}^{+} at the beginning of the interaction region. As noted before, decreasing A_{w}^{+} and increasing κ both result in a larger eddy viscosity in the inner layer region. For the 15° generator case the variations in the inner layer turbulence parameters follow the same trends as the data analysis except near reattachment. Part of the reason for this disparity is that the data analysis in this region was completed only recently and there was insufficient time to obtain converged simulations before preparing this manuscript.

The results of the computer simulations using the turbulence parameter variations described above are presented in figures 6, 7, and 8. For the 7.5° generator case there is obvious improvement over the baseline predictions of skin friction and heat transfer in the interaction region (see fig. 6a). Separation is not predicted and the upstream influence of the interaction coincides with that observed from the data. Downstream of the peak pressure location the heat-transfer prediction is not as good as the baseline model predictions, but this could be explained by an incorrect choice of a constant turbulent Prandtl number. At this stage of model development this disparity in heating prediction is not considered crucial because the solutions of the momentum and energy equations are loosely coupled. The turbulence model changes had little effect on the surface pressure prediction. The pressure and velocity contours (figs. 7 and 8) are not changed significantly from those for the baseline model, except that no reversed flow region is predicted with the modified model. The reflected shock observed in the data is still not predicted. The main reason for this is that the numerical simulations fail to show a significant thickening of the boundary layer at the start of the interaction region.

Results using the turbulence model modifications for the 15° generator case are also shown in figures 6, 7, and 8. The predicted separation bubble size increased considerably with a corresponding prediction of upstream influence and a plateau in the surface pressure. The pressure contours show the presence of an induced shock wave similar to that observed in the experiment. Obviously, substantial deficiencies still exist in the prediction using the modified model. The separated bubble size is still smaller in height than the experiment indicates; the plateau pressure is only about half the measured value; and all three surface quantities show substantial differences with the measurements in the interaction region. It is felt, however, that a significant improvement in the surface predictions can be made by including the latest data analysis values of A_{w}^{+} and κ near reattachment. This should shorten the extent of predicted separation and shift the rise in skin-friction and heat-transfer upstream.

CONCLUDING REMARKS

A detailed experimental investigation of the mean flow throughout two shock-wave boundary-layer interaction regions, one with separation and one without, has been presented. Although the interactions were very complex, the mean data were of sufficient detail and quality to assess the validity of numerical simulations and to guide turbulence model changes.

Numerical solutions, employing the full time-averaged Navier-Stokes equations along with algebraic eddy-viscosity models appropriate for zero-pressure-gradient flows, predicted the overall features of the flow fields, but they were seriously deficient in predicting the details of the interaction regions. Through a combination of data analysis and trial and error computer simulations, which tested the sensitivity of the solutions to turbulence model parameter changes, the agreement between numerical predictions and experiment was improved.

Although the improvements fell short of identifying an optimum model, several important trends regarding the two-layer, algebraic eddy-viscosity model can be noted. The inner layer model parameters had substantially more influence on the numerical simulations than the outer layer parameter. Where the boundary layer was unseparated, the eddy viscosity in the inner layer region had to be increased substantially over that predicted by a zero-pressure-gradient, two-layer model; otherwise separation was predicted. Therefore the simple zero-pressure-gradient model cannot be used to predict locations of separation. Where separation did occur, the results were less clear, but the eddy viscosity in the sublayer region had to be increased while in the logarithmic region it had to be reduced somewhat; otherwise the separation bubble size was substantially underpredicted.

REFERENCES

1. Ballhaus, W. F., and Bailey, F. R.: Numerical Calculation of Transonic Flow About Swept Wings. AIAA Paper 72-677, June 1972.

2. Rakich, J. V., and Kutler, P.: Comparison of Characteristics and Shock Capturing Methods with Application to the Space Shuttle Vehicle. AIAA Paper 72-191, Jan. 1972.

3. MacCormack, R. W.: Numerical Solution of the Interaction of a Shock Wave with a Laminar Boundary Layer. Lecture Notes in Physics, Vol. 8, Springer Verlag, New York, 1971, p. 151.

4. Hung, M., and MacCormack, R. W.: Supersonic and Hypersonic Laminar Flows Over a Two-Dimensional Compression Corner, AIAA Paper 75-2, Jan. 1975.

5. Baldwin, B. S., and MacCormack, R. W.: Numerical Solution of a Strong Shock Wave with a Hypersonic Turbulent Boundary Layer. AIAA Paper 74-558, June 1974.

6. Wilcox, D. C.: Numerical Study of Separated Turbulent Flows. AIAA Paper 74-584, June 1974.

7. Deiwert, G. S.: Numerical Simulation of High Reynolds Number Transonic Flows. AIAA Paper 74-603, June 1974.

8. Redda, D. C., and Murphy, J. D.: Shock Wave Turbulent Boundary Layer Interactions in Rectangular Channels, Part II: The Influence of Sidewall Boundary Layers on Incipient Separation and Scale of the Interaction. AIAA Journal, vol. 11, no. 10, Oct. 1973, pp. 1367-1368.

9. Horstman, C. C., Kussoy, M. I., Coakley, T. J., Rubesin, M. W., and Marvin, J. G.: Shock Wave Induced Turbulent Boundary-Layer Separation at Hypersonic Speeds. AIAA Paper 75-4, Jan. 1975.

10. Horstman, C. C., and Owen, F. K.: Turbulent Properties of a Compressible Boundary Layer. AIAA Journal, vol. 10, no. 11, Nov. 1972, pp. 1418-1424.

11. Kussoy, M. I., and Horstman, C. C.: An Experimental Documentation of a Hypersonic Shock-Wave Turbulent Boundary-Layer Interaction Flow—With and Without Separation. NASA TM X-62,412, 1975.

12. Rubesin, M. W., and Rose, W. C.: The Turbulent Mean-Flow Reynolds-Stress, and Heat Flux Equations in Mass-Averaged Dependent Variables. NASA TM X-62,248, March 1973.

13. Sorensen, V. L.: Computer Program for Calculating Flow Fields in Supersonic Inlets. NASA TN D-2897, July 1965.

14. Marvin, J. G., and Sheaffer, Y. S.: A Method for Solving the Nonsimilar Boundary-Layer Equations Including Foreign Gas Injection. NASA TN D-5516, Nov. 1969.

15. Baldwin, B. S., and MacCormack, R. W.: Interaction of Strong Shock Wave with Turbulent Boundary Layer. Proceedings of the 4th International Conference on Numerical Methods in Fluid Dynamics, Boulder, Colorado, June 1974.

16. Vanderplaats, Garret N.: CONMIN - A FORTRAN Program for Constrained Function Minimization User's Manual. NASA TM X-62,282, August 1973.

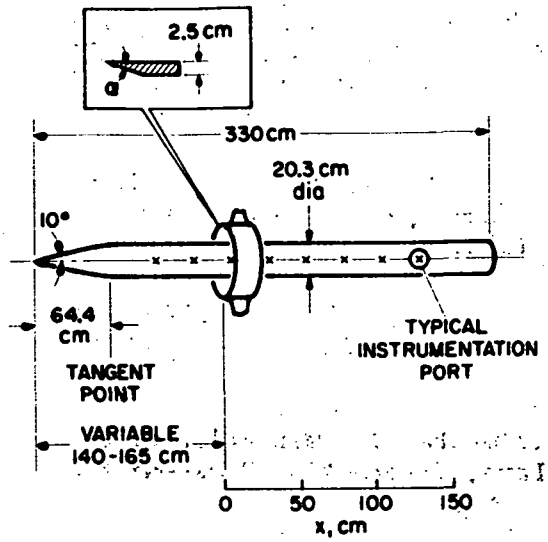

Figure 1.- Test model.

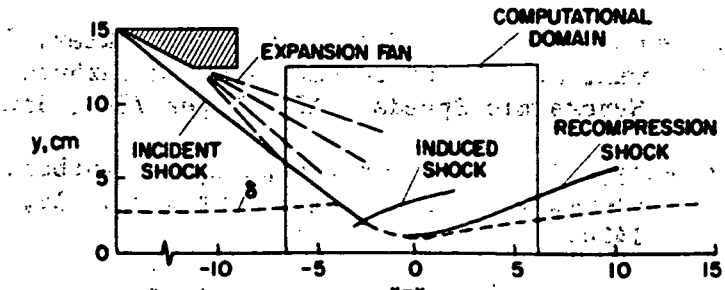

Figure 2.- Flow-field sketch and computational domain.

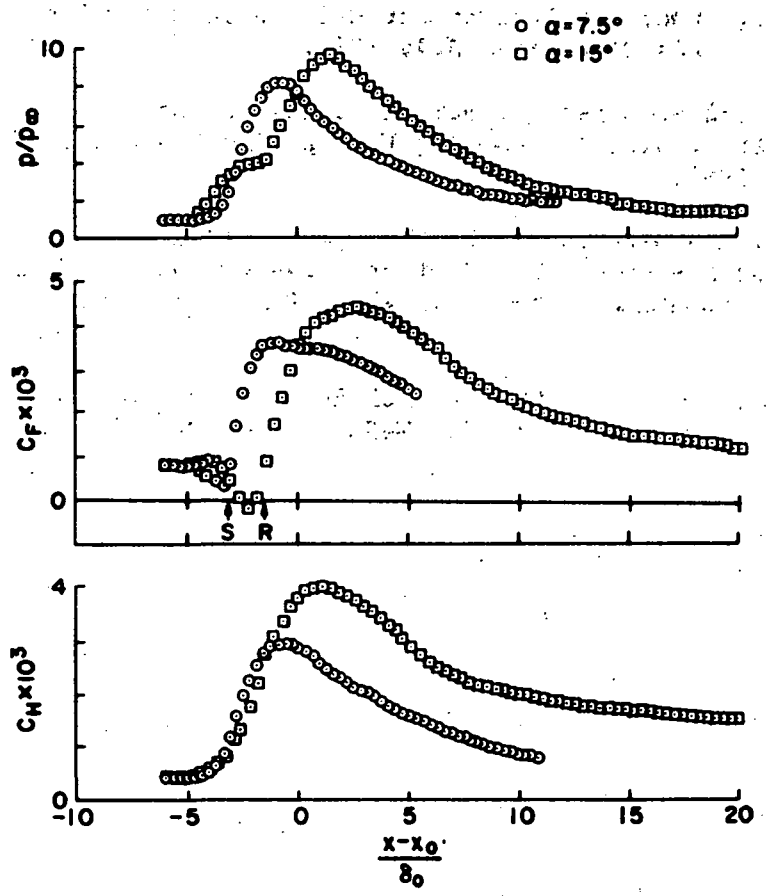

Figure 3.- Measurements along the model surface.

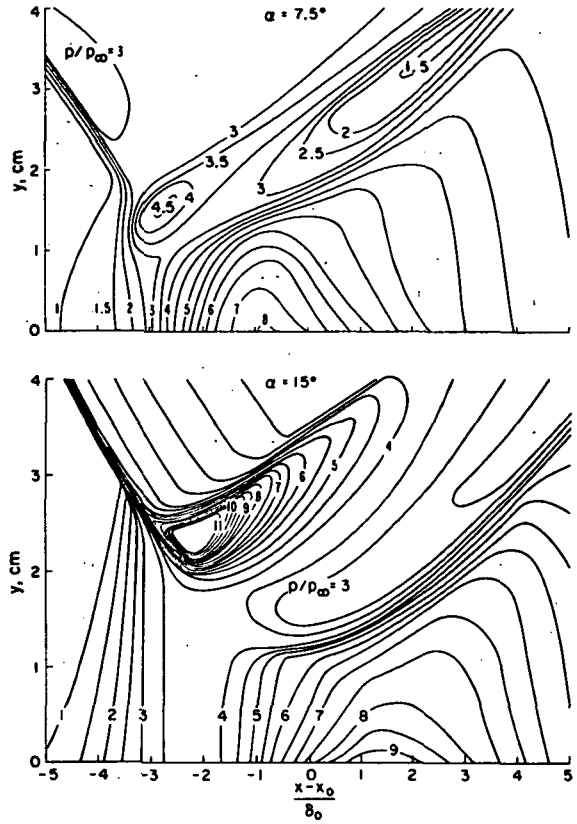

Figure 4.- Static pressure contours obtained from flow-field measurements.

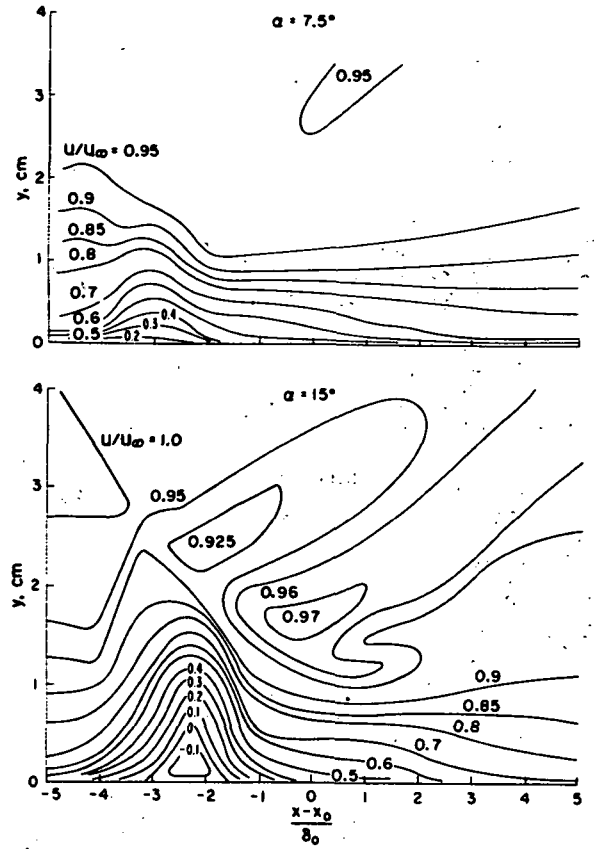

Figure 5.- Velocity contours obtained from flow-field measurements.

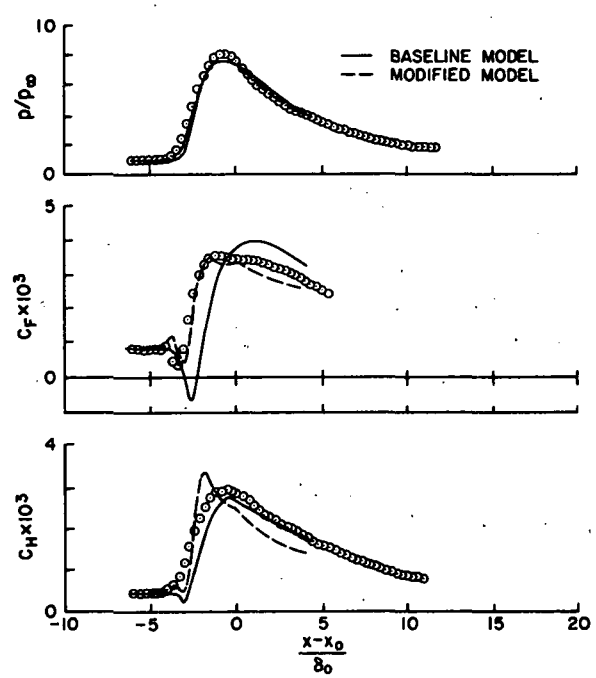

(a) α = 7.5°.

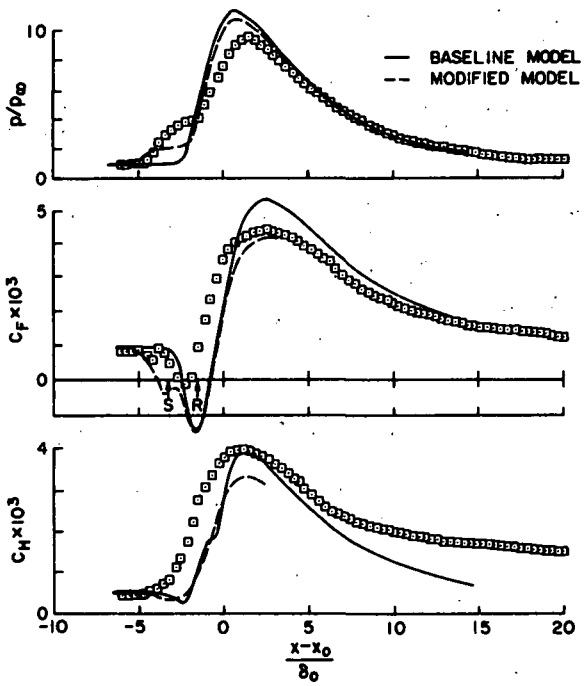

(b) α = 15°.

Figure 6.- Comparisons of computations and measurements along the model surface.

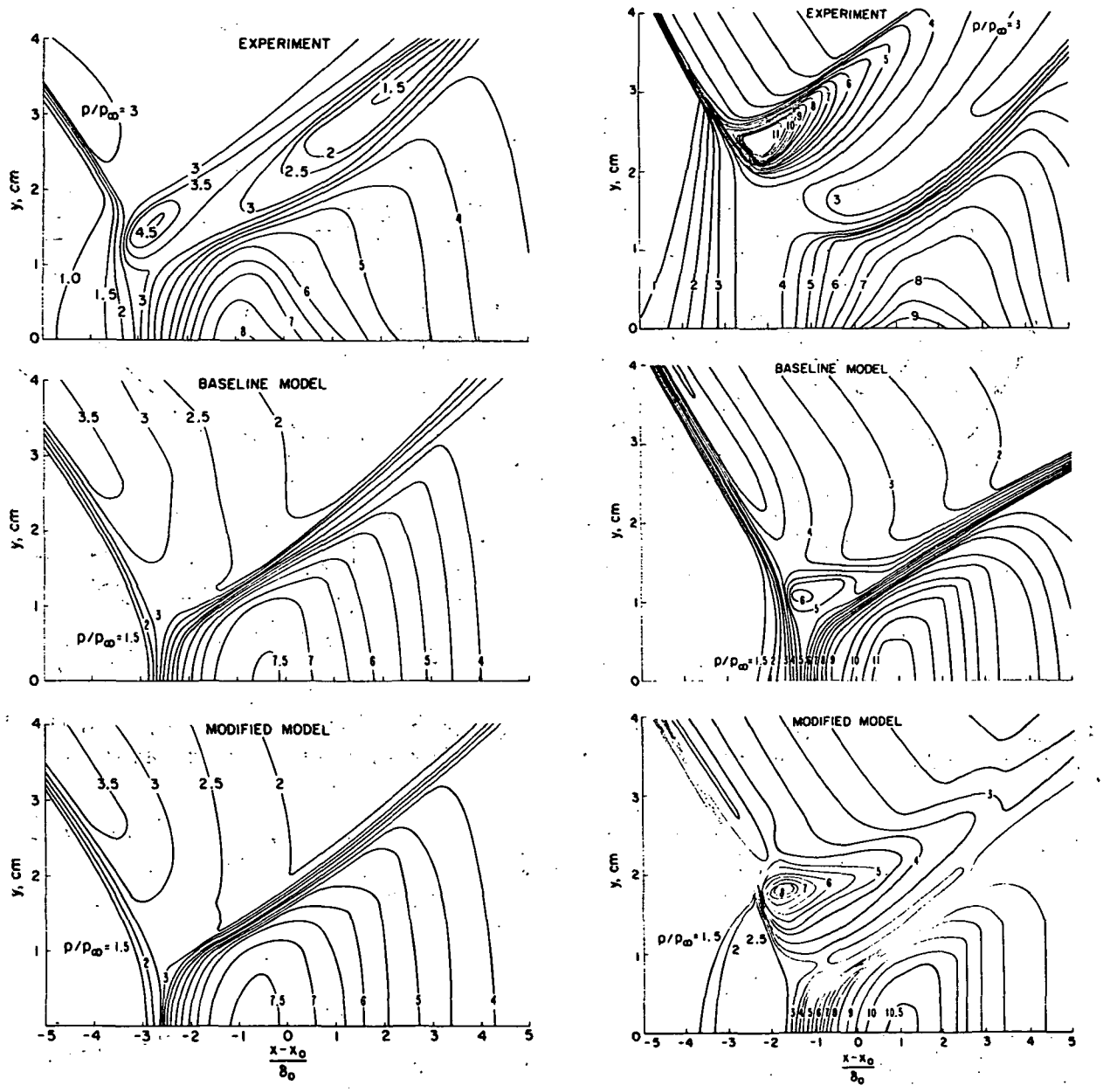

(a) $\alpha = 7.5°$.

(b) $\alpha = 15°$.

Figure 7.- Comparisons of static pressure contours from computations and experiment.

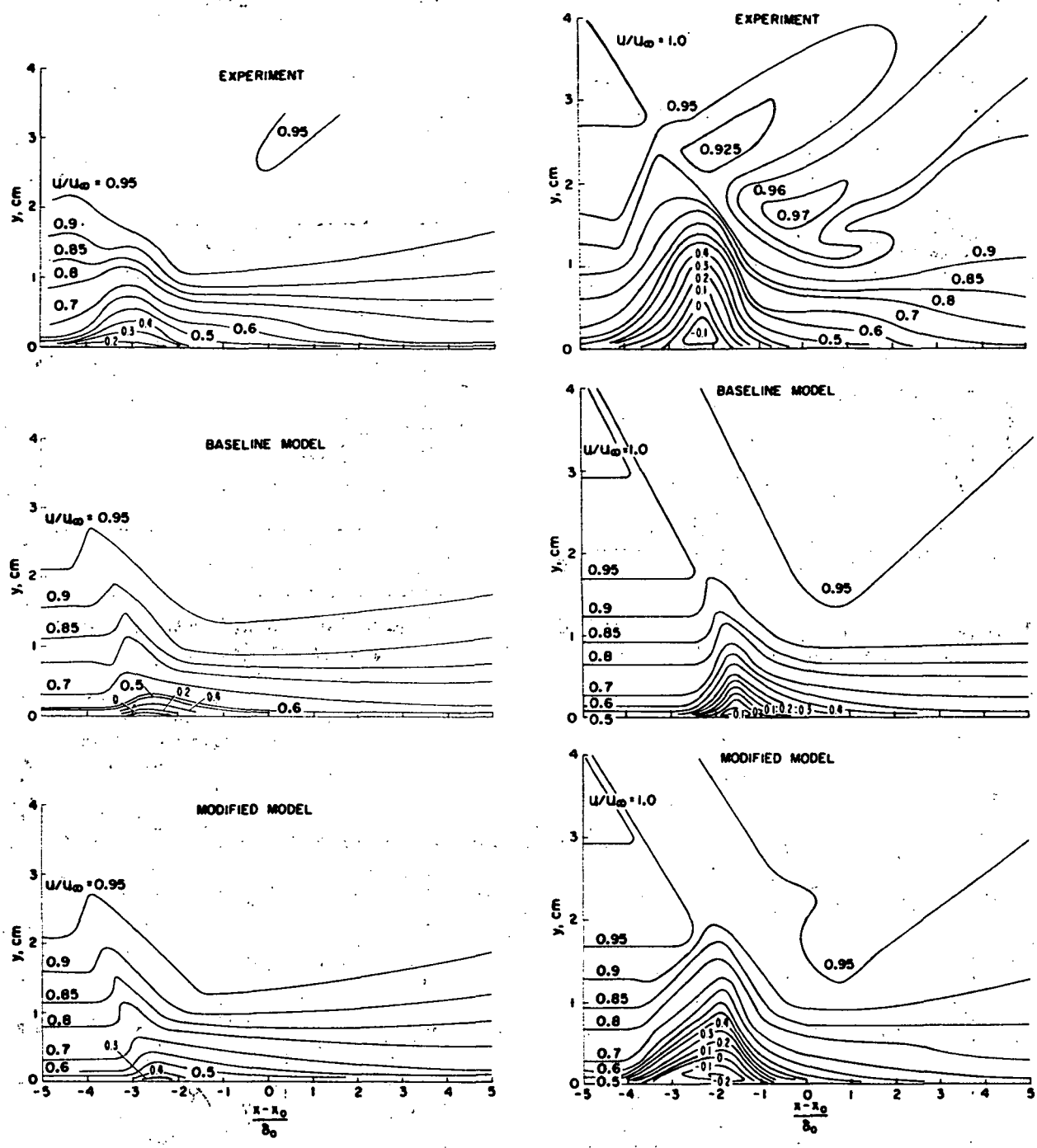

Figure 8.- Comparisons of velocity contours from computations and experiment.

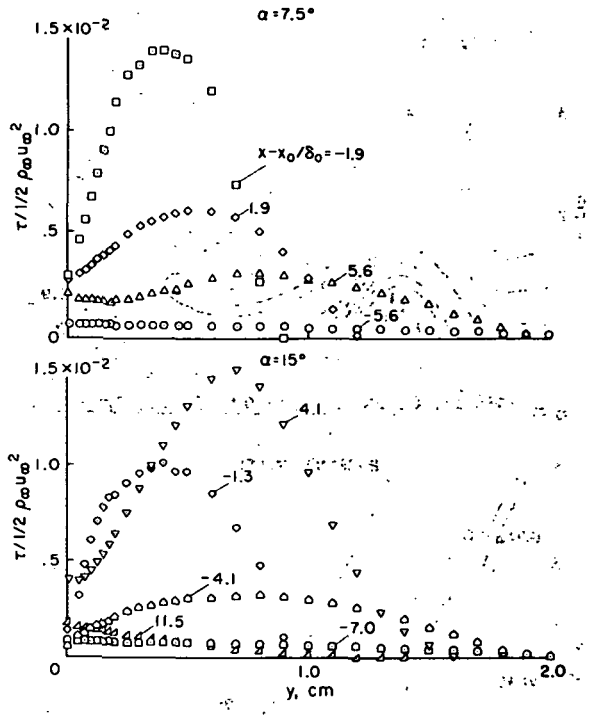

Figure 9.- Shear profiles for various axial locations along the model.

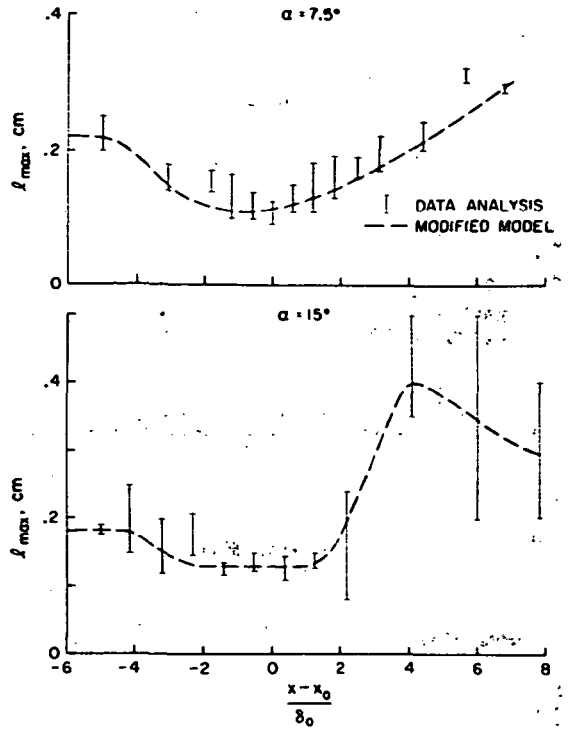

Figure 10.- Axial variation of maximum mixing lengths.

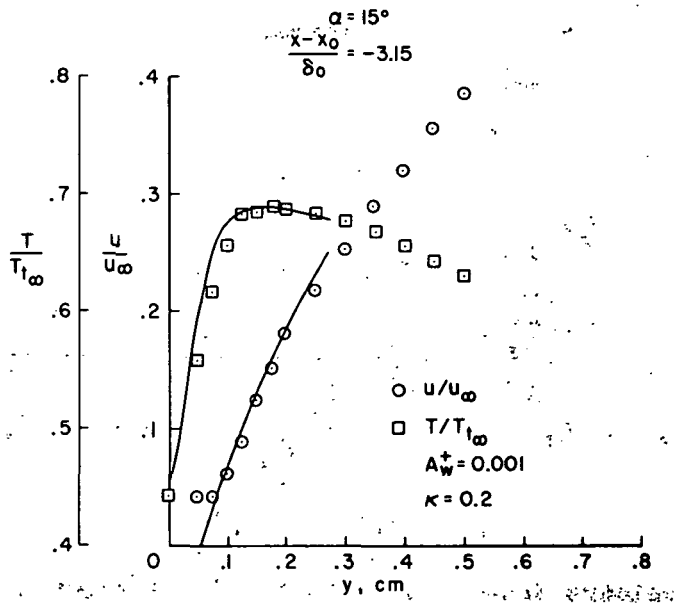

Figure 11.- Comparison of experimental and best fit velocity and temperature profiles employing a modified inner eddy-viscosity model.

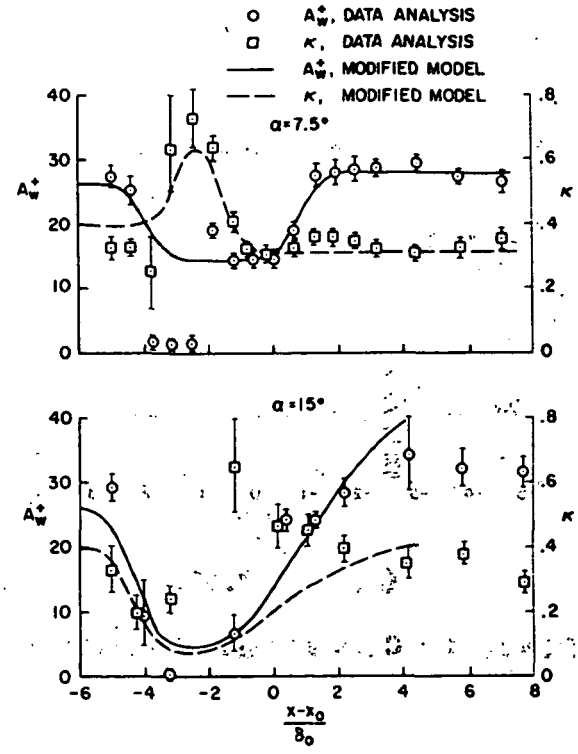

Figure 12.- Axial variation of A_w^+ and κ.

Page Intentionally Left Blank

CALCULATION OF SHOCK-SEPARATED TURBULENT BOUNDARY LAYERS

By B. S. Baldwin and W. C. Rose
NASA Ames Research Center

SUMMARY

Numerical solutions of the complete, time-averaged conservation equations using several eddy-viscosity models for the Reynolds shear stress to close the equations are compared with experimental measurements in a compressible, turbulent separated flow. An efficient time-splitting, explicit difference scheme was used to solve the two-dimensional conservation equations. The experiment used for comparison was a turbulent boundary layer that was separated by an incident shock wave in a Mach 2.93 flow with a unit Reynolds number of 5.7×10^7/m. Comparisons of predicted and experimental values of surface pressure, shear stress along the wall, and velocity profiles are shown. One of the tested eddy-viscosity models which allows the shear stress to be out of equilibrium with the mean flow produces substantially better agreement with the experimental measurements than the simpler models. A tool is thereby provided for inferring additional information about the flow, such as static pressures in the stream, which might not be directly obtainable from experiments.

INTRODUCTION

Development of turbulence models capable of adequately predicting separated compressible flows requires extensive comparisons of calculations with a variety of experiments. At present, the proper role of the calculations is perhaps to aid in the design, interpretation, and documentation of the experiments. For those purposes, it is expedient to seek simple empirical relationships that can be used in the calculations to correlate the experiments. Only after a reliable body of experimental data has been accumulated will definitive verification of the advanced turbulence models be possible.

The adequacy of the numerical method for solving the conservation equations has been established by comparison of calculations with experimental measurements in laminar separated flows (refs. 1 to 3). Methods and procedures for incorporating turbulence models efficiently in the numerical methods are still in a stage of development. Thus, while experience is being gained with these methods and procedures, it is expedient to utilize simple empirical relationships in most of the calculations rather than add the complication of advanced turbulence models.

Several solutions to the conservation equations for compressible turbulent separated flows have been obtained to date (refs. 4 to 8). The present investigation was motivated and guided by interaction with experiments conducted by the authors of references 9 to 11. The class of experiments considered in this study (i.e., non-hypersonic, near-adiabatic wall condition) was chosen for examination to minimize uncertainty with the body of data to be used for comparison with the calculations. In addition, the effects of pressure fluctuations which might influence the turbulence modeling are minimized in such flows. An attempt has been made in the present study to find modifications of a simple algebraic turbulence model that will adequately represent the turbulent shear stress throughout a shock-separated turbulent boundary layer.

SYMBOLS

C_f	skin-friction coefficient $\left(\frac{\tau_w}{0.5\,\rho_\infty u_\infty^2}\right)$
C_p	pressure coefficient
ℓ	mixing length
M	Mach number
p	pressure
Pr	Prandtl number (0.72)
Pr_T	turbulent Prandtl number (0.9)
Re	Reynolds number
T	temperature
u	streamwise velocity
u_{max}	maximum velocity in boundary layer
u_τ	friction velocity
v	velocity in y-direction

x	streamwise coordinate
x_i	inviscid impingement location
y	cross-stream coordinate
δ	boundary-layer thickness
ϵ	eddy viscosity
ϵ_{inner}	eddy viscosity near wall
ϵ_{outer}	eddy viscosity in outer part of boundary layer
μ	absolute viscosity
ρ	density
τ_{xy}	shear stress fluxes in Navier-Stokes equations
τ	total shear stress, $-\tau_{xy}$

Subscripts:

e	edge of boundary layer
o	upstream conditions
t	total conditions
w	wall conditions
∞	free-stream conditions

Superscript:

+	indicates dimensionless boundary-layer quantity

PRELIMINARY CONSIDERATIONS

Description of the Flow

The flow field considered in this study is shown schematically in figure 1. (See ref. 10 for complete detail.) The free-stream Mach number is 2.93 and the unit Reynolds number is 5.7×10^7/m. A shock wave, generated by a plate set at 13^o to the free stream, impinges on the turbulent boundary layer at the upper nozzle wall. This incident and reflected shock system produces a large pressure rise $\left(p_{final}/p_{initial} \approx 5\right)$ and causes the boundary layer to separate. The pressure rise feeds upstream in the subsonic part of the boundary layer and forms a separation bubble containing reversed flow; hence, separation occurs well upstream of the inviscid shock impingement point. An induced shock wave results from the upstream separation and a reflected shock wave also forms. Although care was taken in the experiment to minimize three-dimensional effects, the flow may still contain these effects as noted in reference 10. This is important to consider since the present numerical method applies strictly to two-dimensional flows.

The Numerical Method

The time-averaged Navier-Stokes equations to be solved are listed in reference 5. The numerical method and special numerical procedures used in the calculations presented herein are described in detail in references 2 and 5. The grid used in the present study had 40 nodes in the streamwise direction with $\Delta x = 5.1 \times 10^{-3}$ m and 32 nodes in the cross-stream direction with four different Δy ranging from 2.5×10^{-5} m near the wall to 4.8×10^{-3} m beyond the boundary-layer edge.

A simplified turbulence model used previously (refs. 5 to 7) to gain experience in the numerical solutions while conserving computer time expresses the shear stress as

$$\tau_{xy} = -(\mu + \rho\epsilon)\left(\frac{\partial u}{\partial y} + \frac{\partial v}{\partial x}\right) \tag{1}$$

The eddy viscosity ϵ is modeled in two regions within the boundary layer, the inner region comprising essentially the logarithmic region near the wall and the outer region that consists of the wake or approximately the remaining 75 to 80 percent of the boundary layer. In the inner region, a mixing length formulation for the eddy viscosity is used

$$\epsilon_{inner} = \ell^2\left|\frac{\partial u}{\partial y} + \frac{\partial v}{\partial x}\right| \tag{2}$$

where

$$\ell = ky\left[1 - \exp\left(\frac{-y}{A}\right)\right] \tag{3}$$

with

$$A = A_w^+ \frac{\mu_w}{\sqrt{|\tau_w|\rho_w}} \tag{4}$$

$k = 0.4$, and $A_w^+ = 26$. In the outer region the eddy viscosity is represented by

$$\epsilon_{outer} = 0.0168 \frac{u_{max}\delta_i^*}{I} \tag{5}$$

where

$$\delta_i^* = \int_0^{\delta_o} \left(1 - \frac{u}{u_{max}}\right) dy \tag{6}$$

and

$$I = 1 + \left(\frac{y}{\delta_o}\right)^6 \tag{7}$$

In the calculations, ϵ_{inner} is used in the boundary layer until y is large enough that $\epsilon_{inner} > \epsilon_{outer}$, at which point and beyond ϵ_{outer} is used. The heat flux vector is approximated by

$$\vec{q} = -\left(\frac{\mu}{Pr} + \frac{\rho\epsilon}{Pr_T}\right) C_p \vec{\nabla} T \tag{8}$$

with $Pr = 0.72$ and $Pr_T = 0.9$. The model described in equations (2) to (8) is denoted in the remainder of this paper as the "baseline model."

In addition to the baseline model, various other models or variations of the baseline model were investigated. Calculations using these various models will be described in the "Results and Discussion" section.

The calculations were started at a streamwise station $(x - x_i)/\delta_o = -5.47$ using the experimental turbulent boundary-layer velocity profiles and other information, such as shock-wave location, that is consistent with the experiment. To indicate the resolution of the near-wall region of the boundary layer achieved in the numerical solution, a law of the wall velocity profile is shown in figure 2. The symbols are at the computational mesh points and, as can be seen, at least one point is in the laminar sublayer where $u^+ = y^+$. The flow-field quantities at the mesh points were found by interpolating experimental data. Below the region where experimental data were available (y^+ less than about 500), the quantities were found by setting $\tau = \tau_w$, neglecting streamwise derivatives in the numerical solution using the baseline turbulence model, and constraining the velocity profile to pass through the experimental data beyond $y^+ = 500$. The skin-

friction coefficient $C_f = 1.30 \times 10^{-3}$ calculated in this manner is in close agreement with the experimentally determined value obtained using a Preston tube (ref. 10) and with that obtained from examination of the velocity profile (ref. 12).

RESULTS AND DISCUSSION

Comparison of Baseline Model With Experimental Results

The experimental results of reference 10 are compared with calculations using the baseline model in figures 3 to 6. Figure 3 contains a comparison of experimental and calculated wall pressures as a function of the streamwise coordinate employed in reference 10, namely $(x - x_i)/\delta_o$. Agreement between experiment and theory using the baseline model is poor. In figure 4 the computed skin-friction coefficient is compared with that obtained from velocity profiles from reference 10 analyzed by the method of reference 12. The separation and reattachment points deduced from surface oil-flow observations (ref. 10) are also indicated. Not only is the forward extent of the separation underestimated by the baseline-model calculation but the rearward extent is overestimated. As a result of the apparent inability of the baseline model to describe the observed variation of pressure and skin-friction coefficient, various modifications to that model were made.

Pressure Gradient Modification

To allow for effects of pressure gradients, Cebeci (ref. 13) recommends (in effect) replacement of $A_w^+ = 26$ in equation (4) with

$$A_w^+ = 26\left(1 + 11.8\,\frac{\rho_w}{\rho_e}^{1.5}\,\frac{\mu_e}{\rho_e}\,\frac{dp/dx}{\tau^{1.5}}\right)^{-1/2} \tag{9}$$

where in the present study $\tau = \tau_w + y(\partial p/\partial x)$ (ref. 13) while the eddy viscosity in the outer flow remains unchanged. According to Cebeci, the above correction factor is applicable in the presence of favorable as well as unfavorable pressure gradients. In the present application the modification increases the eddy viscosity in regions ahead of the separation as well as aft of reattachment.

The effect of the Cebeci modification on skin friction is shown in figure 5. The separation bubble is moved slightly forward in the direction of the experiment, but the bubble is also extended farther rearward worsening the agreement with the measurements. Clearly some modification other than that of Cebeci (or in addition to) is needed for the class of separated flows considered here.

Escudier Formulation

An alternative to equation (5) of the baseline model that has been used for attached flows (ref. 14) is

$$\epsilon_{outer} = \ell_{max}^2 \left| \frac{\partial u}{\partial y} + \frac{\partial v}{\partial x} \right|$$

with $\ell_{max} = 0.09\delta$. Results of using the Escudier model are shown also in figure 5. The model, however, is difficult to apply in the present calculation since the local width of the boundary layer δ cannot be defined accurately enough in the numerical calculation because of velocity gradients introduced by curvature of the incident, induced, and reflected shock waves. Slight changes in the definition of δ can change its value by more than a factor of 2. However, as observed in the experiment, the values of δ do not change significantly from the upstream value ahead of the separation. Accordingly, ℓ_{max} based on the upstream boundary-layer thickness $\left(\ell_{max} = 0.09\delta_o\right)$ has been used in several calculations to be described. Figure 6 shows calculated profiles of $\rho\epsilon$ in the separated region according to the baseline model and the Escudier formula. Although, as is well known, the two formulations produce similar variations for attached flows with small pressure gradients, they appear to produce greatly different variations for the present separated flow.

Applying the Escudier formulation in the present calculations greatly reduced the extent of the separation along the wall. As evident in figure 5, the prediction of upstream influence was substantially worse than that of the baseline model, although the rearward extent of the bubble agreed better with indications from oil flow in the experiment. Despite the poor overall agreement shown, the Escudier model can be used as a guide in modifying the turbulence model. The better agreement with reattachment location indicates one type of modification to the turbulence model needed to obtain better agreement with the experimental data. Namely, relative to the baseline model, larger values of eddy viscosity are needed near reattachment to confine the rearward extent of the bubble. However, smaller values are probably needed near separation to promote the proper upstream influence. A model is now discussed that, in fact, does possess these characteristics.

Modification to Account for Nonequilibrium Effects

For separated supersonic flow over a compression corner Shang and Hankey (ref. 8) have obtained remarkably good agreement with experiment by use of a simple modification of an algebraic turbulence model of the form (in the present notation)

$$\rho\epsilon = (\rho\epsilon)_o + \left[(\rho\epsilon)_{equilibrium} - (\rho\epsilon)_o\right] \left\{1 - \exp\left[\frac{-\alpha(x - x_o)}{\delta_o}\right]\right\} \qquad (10)$$

with $\alpha = 1/10$. This type of modification (with $\alpha = 1/10$) has been proposed by many authors and has been shown by Rose and Johnson (ref. 11) to agree generally with the values of ℓ_{max} deduced from direct measurements of the Reynolds shear stress. A value of α between 1/5 and 1/15 is consistent with experimental observations, as noted in reference 11.

Application of equation (10) in the present problem with $\alpha = 1/10$ led to results (not shown) similar to those obtained from the Cebeci viscous sublayer modification. Namely (relative to the baseline model), the upstream influence was improved, but the bubble was also extended far downstream in gross disagreement with the experiment.

The observed effects of various turbulence models on the calculations described so far led to the following attempt to model the turbulent shear stress. A formula like equation (10) should apply only to the flow outside the separation bubble since there probably should be no upstream history passing through the front of the bubble (i.e., the turbulence within the bubble is in local equilibrium). In the present study, equilibrium within the bubble was insured by applying equation (10) only if $(\rho\epsilon)_{equilibrium}$ exceeded $(\rho\epsilon)_o$ which does, in fact, allow a local equilibrium condition to prevail in the separation bubble. Since the Escudier formula produces the large values of eddy viscosity needed to limit the rearward extent of the bubble, $(\rho\epsilon)_{equilibrium}$ is determined from that formulation. For the same reason in the present case, a value of $\alpha = 1/5$ was found to be better than $\alpha = 1/10$. In other words the baseline model is modified by the use of equation (10) with

$$\alpha = \begin{cases} \infty & \text{if } (\rho\epsilon)_{equilibrium} < (\rho\epsilon)_o \\ 1/5 & \text{otherwise} \end{cases} \tag{11}$$

where $(\rho\epsilon)_{equilibrium}$ is determined from

$$(\rho\epsilon_{outer})_{equilibrium} = \ell_{max}^2 \left| \frac{\partial u}{\partial y} + \frac{\partial v}{\partial x} \right|$$

$$\ell_{max} = 0.09\delta_o$$

and $(\rho\epsilon_{inner})_{equilibrium}$ from equations (2) to (4) of the baseline model if $\ell < \ell_{max}$. Profiles of $\rho\epsilon$ produced by these modifications are compared with those from the baseline model in figure 7. The desired variation in the values of $\rho\epsilon$ is obtained; that is, upstream near separation $\rho\epsilon$ is lower than the baseline model and downstream near reattachment $\rho\epsilon$ is higher.

In figure 8, calculated wall pressure distributions are compared to the experimental measurements. The upstream influence predicted by the relaxation model is in better agreement with the measurements than the prediction from the baseline or Escudier

models. However, the wall shear stresses shown in figure 9 indicate that prediction of the reattachment point is still poor. Velocity profiles near the front of the bubble predicted by the baseline, relaxation, and Escudier models are compared with measurements in figure 10. Again, the results using the relaxation model are in much better agreement with the data than the simpler models.

Finally, locations of the experimental shock waves and expansion from a tracing of a schlieren photograph of the flow field are compared in figure 11 with the locations of the shocks and expansion predicted using the relaxation model. The good agreement shown for the relaxation model would not be obtained by any other turbulence models investigated in the present study since none of the other models predict the proper upstream influence. One can thus conclude that the flow-field properties, such as regions of shock waves and expansions, can be adequately predicted when a valid turbulence model is used.

CONCLUDING REMARKS

The complete, time-averaged conservation equations have been numerically solved using several algebraic turbulence models. Information has been gained on the effects of the various turbulence models applied to a separating and reattaching compressible turbulent boundary layer. The information has led to the formulation of a relaxation model for the Reynolds shear stress that produces reasonable agreement with a set of experimental data.

REFERENCES

1. MacCormack, R. W.: Numerical Solution of the Interaction of a Shock Wave With a Laminar Boundary Layer. Lecture Notes in Physics, vol. 8, Springer-Verlag, New York, 1971, p. 151.

2. MacCormack, R. W.; and Baldwin, B. S.: A Numerical Method for Solving the Navier-Stokes Equations With Application to Shock-Boundary Layer Interactions. AIAA Paper 75-1, 1975.

3. Hung, C. M.; and MacCormack, R. W.: Numerical Solutions of Supersonic and Hypersonic Laminar Flows Over a Two-Dimensional Compression Corner. AIAA Paper 75-2, 1975.

4. Wilcox, D. C.: Calculation of Turbulent Boundary Layer Shock Wave Interaction. AIAA J., vol. 11, no. 4, 1973, pp. 1592-1594.

5. Baldwin, B. S.; and MacCormack, R. W.: Numerical Solution of the Interaction of a Strong Shock Wave With a Hypersonic Turbulent Boundary Layer. AIAA Paper 74-558, 1974.

6. Deiwert, G. S.: Numerical Simulation of High Reynolds Transonic Flows. AIAA Paper 74-603, 1974.

7. Horstman, C. C.; Kussoy, M. I.; Coakley, T. J.; Rubesin, M. M.; and Marvin, J. G.: Shock-Wave-Induced Turbulent Boundary-Layer Separation at Hypersonic Speeds. AIAA Paper 75-3, 1975.

8. Shang, J. S.; and Hankey, W. L., Jr.: Numerical Solution of the Navier-Stokes Equations for Supersonic Turbulent Flow Over a Compression Corner. AIAA Paper 75-4, 1975.

9. Rose, W. C.: The Behavior of a Compressible Turbulent Boundary Layer in a Shock-Wave Induced Adverse Pressure Gradient. Ph. D. Thesis, Univ. of Washington, 1972. (Available as NASA TN D-7092, 1973.)

10. Reda, D. C.; and Murphy, J. D.: Shock Wave – Turbulent Boundary Layer Interactions in Rectangular Channels, Part II: The Influence of Sidewall Boundary Layers on Incipient Separation and Scale of the Interaction. AIAA Paper 73-234, 1973.

11. Rose, W. C.; and Johnson, D. A.: A Study of Shock-Wave Turbulent Boundary Layer Interaction Using Laser Velocimeter and Hot-Wire Anemometer Techniques. AIAA Paper 74-95, 1974.

12. Rubesin, M. W.; Murphy, J. D.; and Rose, W. C.: Wall Shear in Strongly Retarded and Separated Compressible Turbulent Boundary Layers. AIAA J., vol. 12, no. 10, Oct. 1974, pp. 1442-1444.

13. Cebeci, T.: Calculation of Compressible Turbulent Boundary Layers With Heat and Mass Transfer. AIAA J., vol. 9, no. 6, 1971, pp. 1091-1097.

14. Launder, B. E.; and Spalding, D. B.: Lectures in Mathematical Models of Turbulence. Academic Press, New York, 1972.

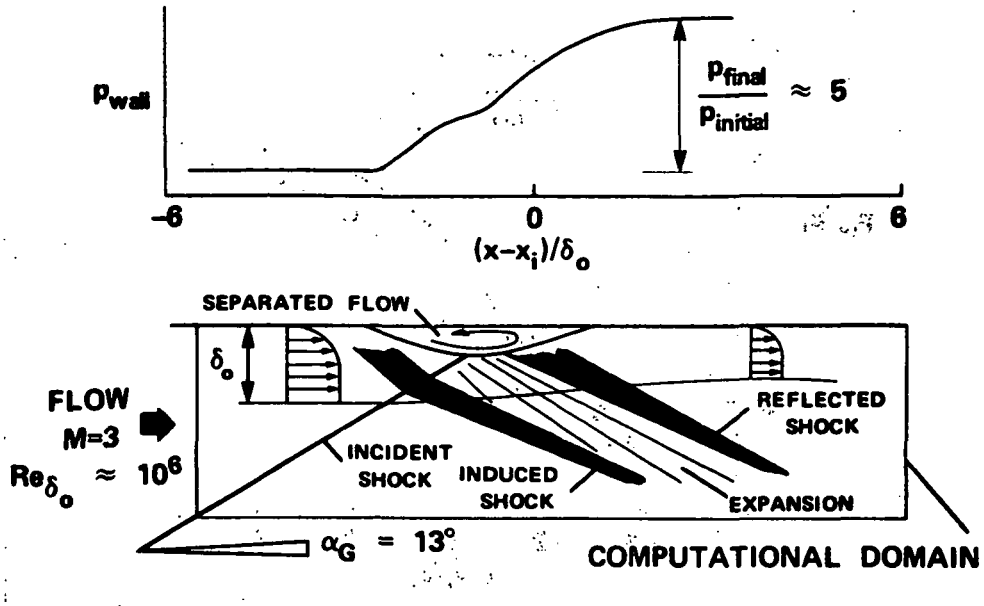

Figure 1.- Schematic drawing of flow field to be calculated.

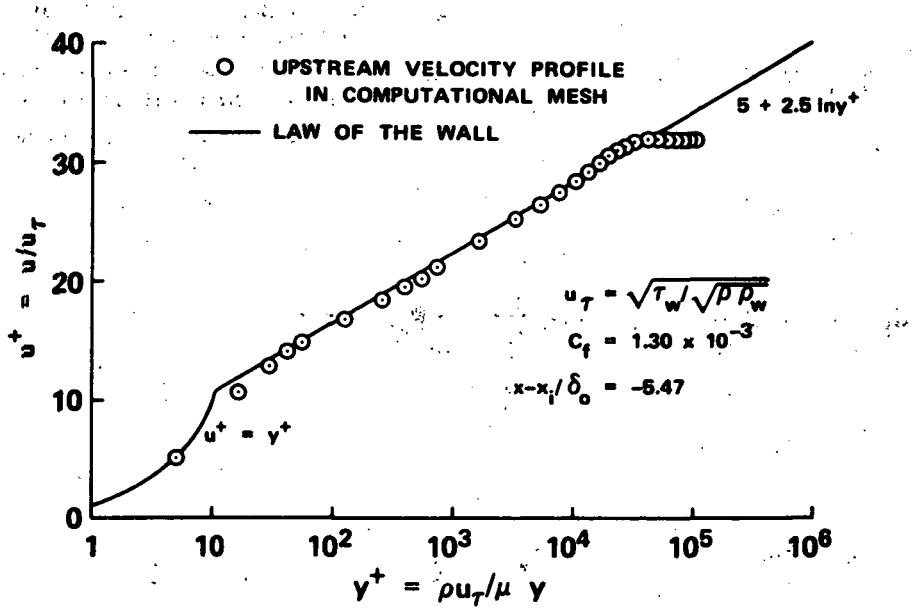

Figure 2.- Upstream velocity profile in law of the wall coordinates.

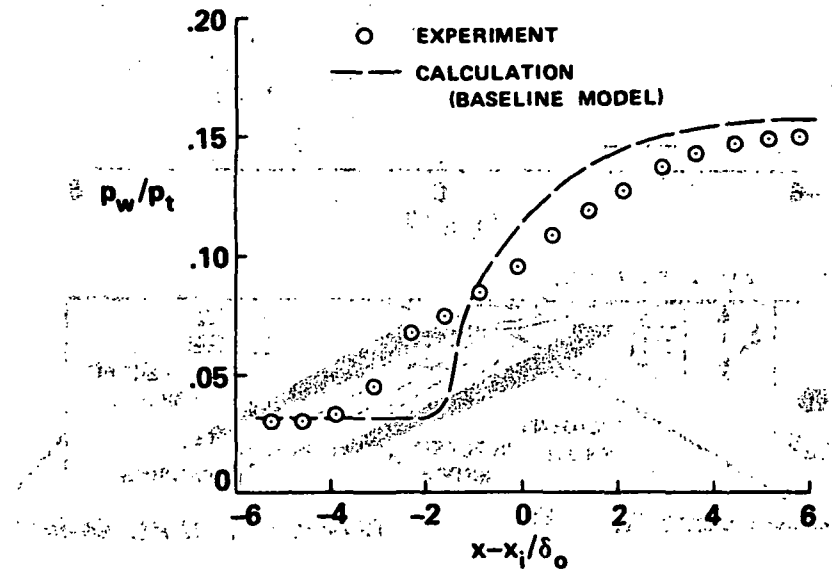

Figure 3.- Comparison of measured pressure with calculation.

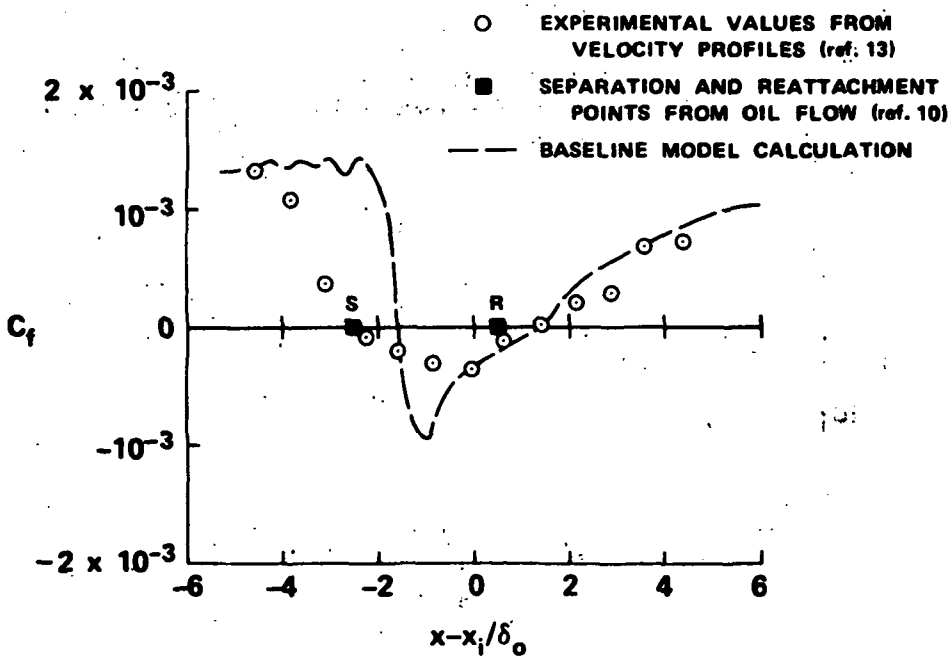

Figure 4.- Comparison of predicted and experimental skin-friction coefficients using baseline model.

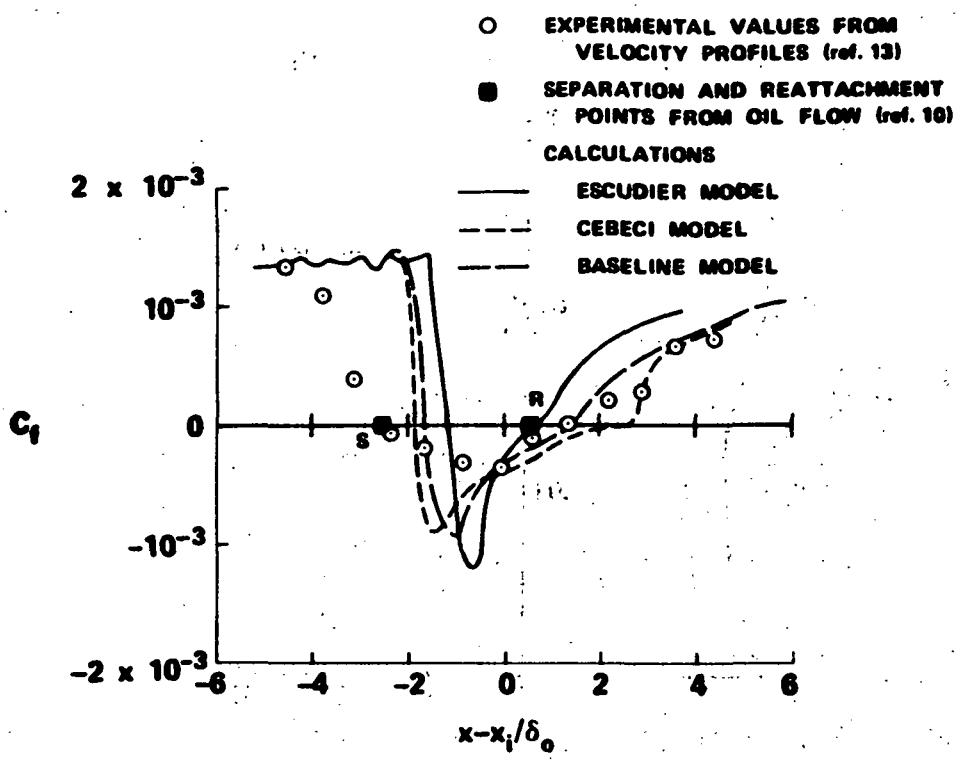

Figure 5.- Comparison of predicted and experimental skin-friction coefficients using various models.

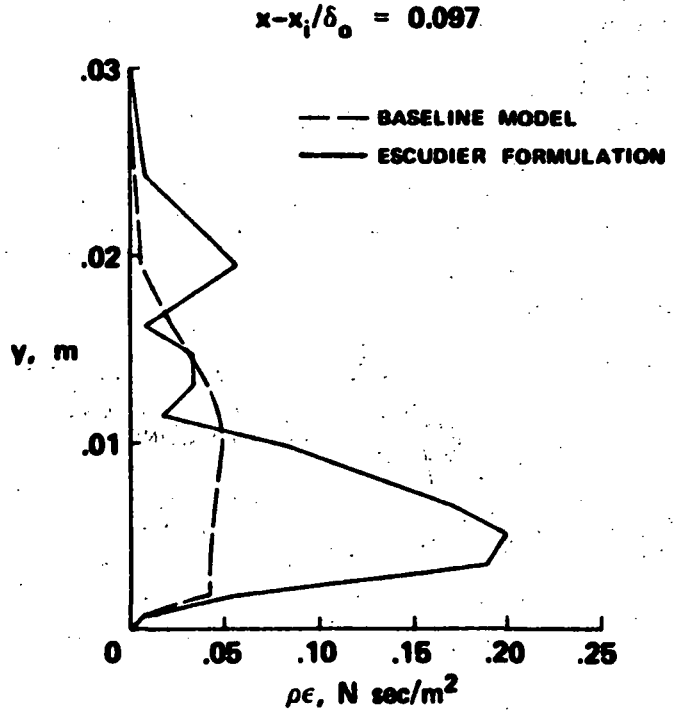

Figure 6.- Comparison of Escudier and baseline eddy-viscosity profiles in separation region.

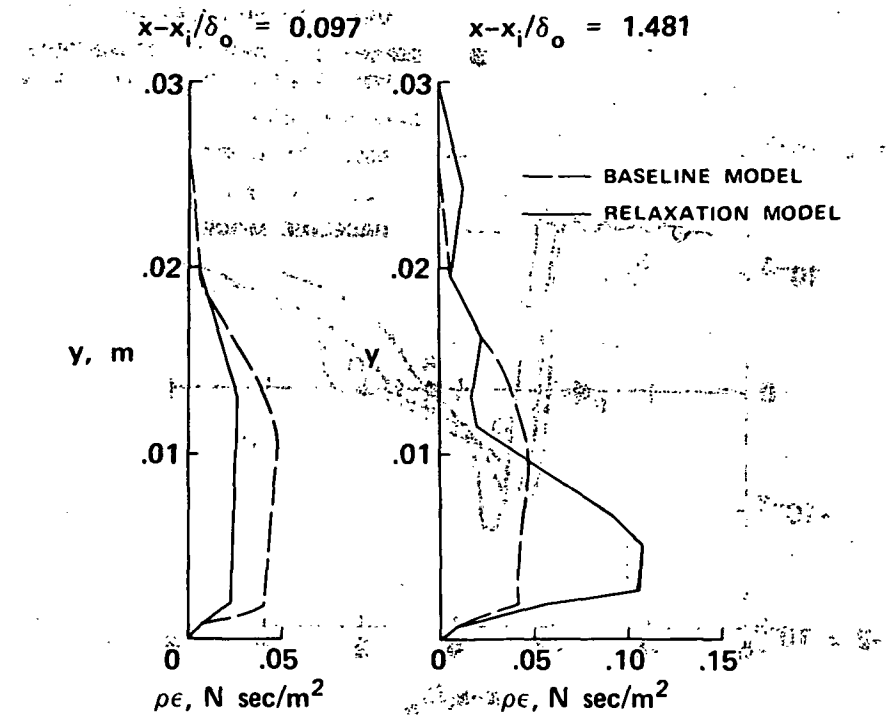

Figure 7.- Comparison of relaxation and baseline eddy-viscosity profiles.

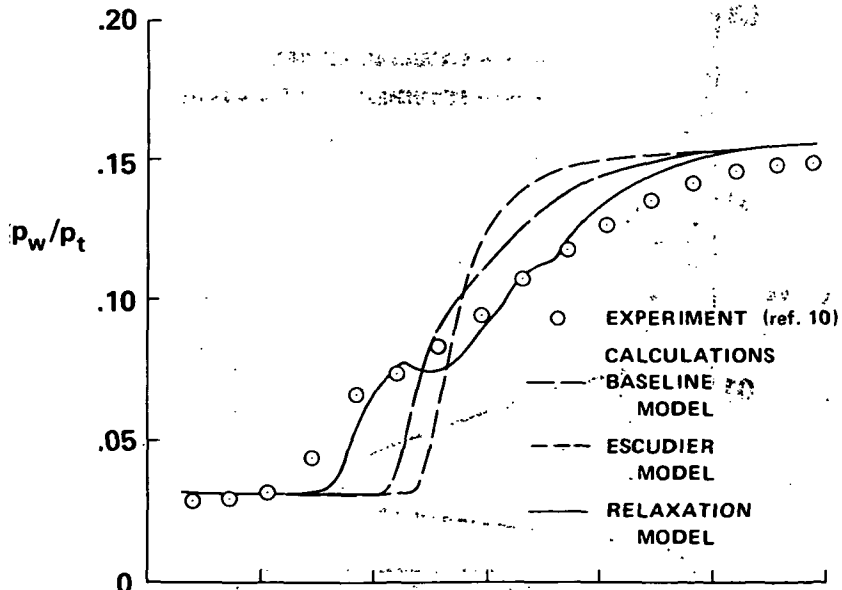

Figure 8.- Comparison of surface static-pressure distributions using various models.

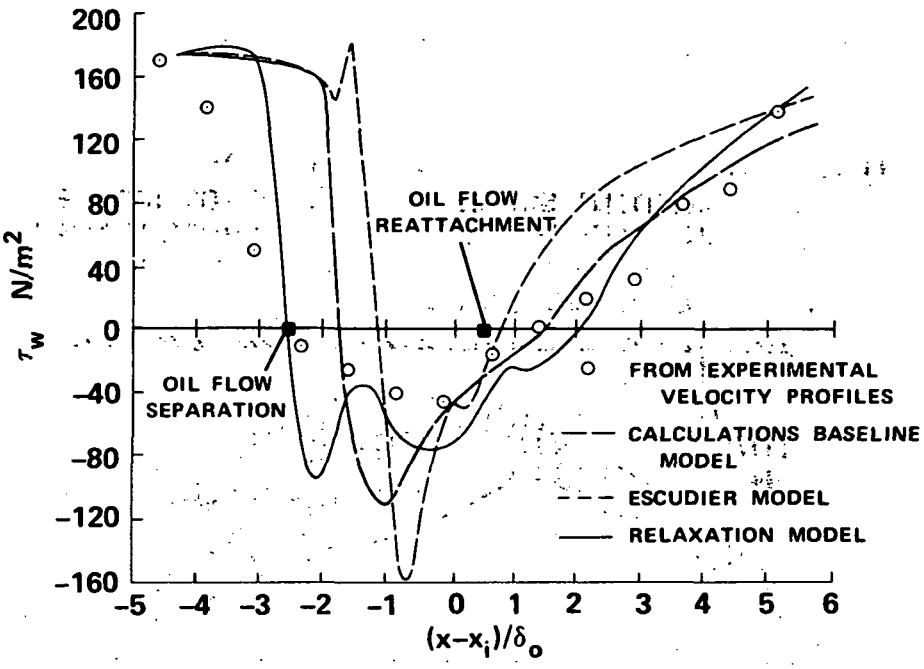

Figure 9.- Comparison of predicted and experimental wall shear stress using various models.

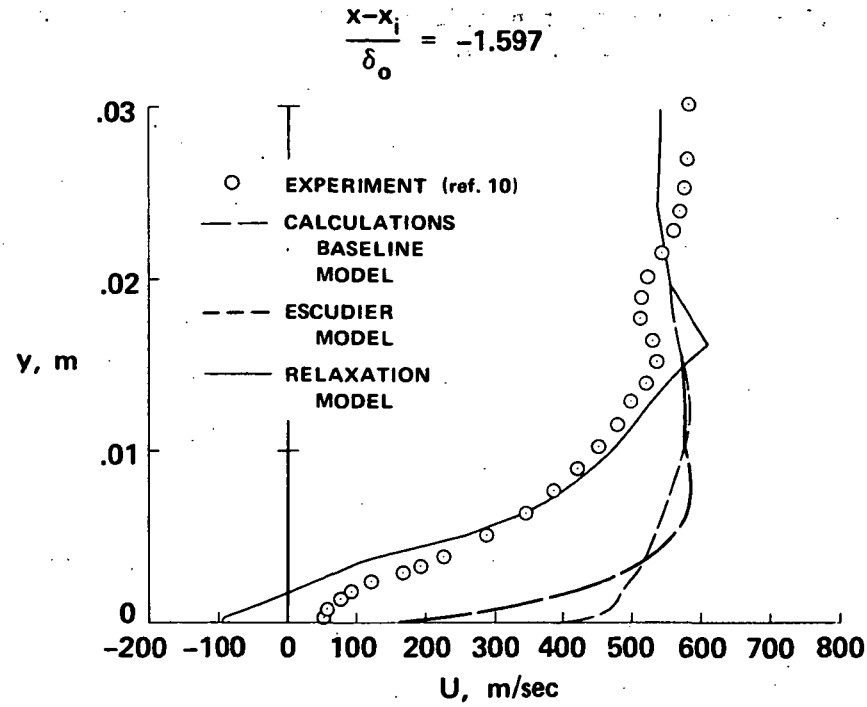

Figure 10.- Comparison of predicted and experimental velocity profiles in separation region.

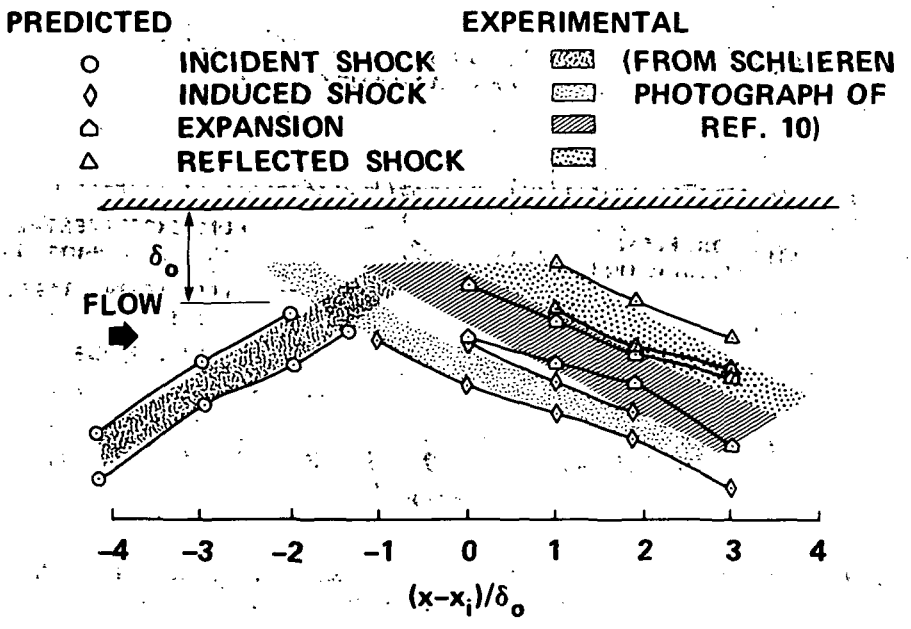

Figure 11.- Comparison of predicted and experimental flow fields using relaxation model.

Page Intentionally Left Blank

SIMULATION OF TURBULENT TRANSONIC SEPARATED FLOW OVER AN AIRFOIL

By George S. Deiwert, John B. McDevitt, and Lionel L. Levy, Jr.

NASA Ames Research Center

SUMMARY

A code has been developed for simulating high Reynolds number transonic flow fields of arbitrary configuration. This code, in conjunction with laboratory experiments, is being used to devise and test turbulence transport models which may be suitable in the prediction of such flow fields, with particular emphasis on regions of flow separation. The solutions describe the flow field, including both the shock-induced and trailing-edge separation regions, in sufficient detail to provide the profile and friction drag.

INTRODUCTION

Transonic flow fields over airfoil configurations are characterized by regions of subsonic flow and regions of supersonic flow. These regions are often separated by standing shock waves. If these shocks are strong enough, flow separation will occur where the shock impinges on the airfoil surface. In addition, separation is likely to occur near the airfoil trailing edge. If the Reynolds number is large, the flow will be turbulent near the airfoil surface and, in all cases, will be turbulent in the far wake.

To simulate such flow fields numerically, it is necessary to use a set of equations capable of supporting a description of all the above phenomena. In the present study the two-dimensional time-averaged Navier-Stokes equations for compressible flow are used. The Reynolds stresses are described by an algebraic eddy-viscosity model and the resulting system is solved by the second-order-accurate explicit difference method developed by MacCormack (refs. 1 and 2).

This paper describes the progress made to date in the development of such a code, the procedure used to validate the code, and the adaptation of the code to advanced computers. Solutions are shown and compared with experiments for the flow field over an 18-percent-thick, biconvex, circular-arc airfoil at zero angle of attack for several values of free-stream Mach number and chord Reynolds number.

SYMBOLS

c	chord length
C_f	skin-friction coefficient
C_p	pressure coefficient
e	internal energy per unit volume
k	thermal conductivity coefficient
ℓ	mixing length
M_∞	free-stream Mach number
p	pressure
Pr	Prandtl number
Pr_t	turbulent Prandtl number
Re_c	chord Reynolds number
s	scalar area
S	integrated surface area
t	time
T	temperature
u,v	velocity vector components in x- and y-direction, respectively
vol	integrated volume element
μ	coefficient of molecular viscosity
ρ	mass density
σ	normal stress
τ	shear stress

Subscript:

w	wall surface

Superscript:

$+$	denotes nondimensionalized boundary-layer quantity

SIMULATION METHOD

Governing Equations

The flow field is described by the two-dimensional compressible equations of motion for turbulent flow. Written in time-dependent integral form, they are:

$$\frac{\partial}{\partial t}\int_{vol} U \, d\,vol + \int_{S} \vec{\vec{H}} \cdot \vec{n} \, ds = 0 \tag{1}$$

where

$$U \equiv \begin{bmatrix} \rho \\ \rho u \\ \rho v \\ e \end{bmatrix} \qquad \vec{\vec{H}} \equiv \begin{bmatrix} \rho\vec{q} \\ \rho u\vec{q} + \vec{\vec{\tau}} \cdot \vec{e}_x \\ \rho v\vec{q} + \vec{\vec{\tau}} \cdot \vec{e}_y \\ e\vec{q} + \vec{\vec{\tau}} \cdot \vec{q} - k\Delta T \end{bmatrix}$$

$$\vec{q} \equiv u\vec{e}_x + v\vec{e}_y$$

$$\vec{\vec{\tau}} \equiv \sigma_x \vec{e}_x\vec{e}_x + \tau_{xy}\vec{e}_x\vec{e}_y + \tau_{yx}\vec{e}_y\vec{e}_x + \sigma_y\vec{e}_y\vec{e}_y$$

and $\vec{e}_x$, $\vec{e}_y$ are unit vectors, and $\vec{n}$ is a unit normal vector. These equations can be solved in the orthogonal x,y coordinate system for an arbitrary quadrilateral volume element (sketch (a)) by application of the split Ly and Lx operators in the manner described by MacCormack (ref. 2).

Ly operator:

$$\text{predictor} \quad \overline{U^{n+1/2}_{i,j}} = U^{n}_{i,j} - \frac{\Delta t}{vol_{i,j}}\left(\vec{\vec{H}}^{n}_{i,j} \cdot \vec{S}_3 + \vec{\vec{H}}^{n}_{i,j-1} \cdot \vec{S}_1\right)$$

$$\text{corrector} \quad U^{n+1/2}_{i,j} = \frac{1}{2}\left[u^{n}_{i,j} + \overline{U^{n+1/2}_{i,j}} - \frac{\Delta t}{vol_{i,j}}\left(\vec{\vec{H}}^{\overline{n+1/2}}_{i,j+1} \cdot \vec{S}_3 + \vec{\vec{H}}^{\overline{n+1/2}}_{i,j} \cdot \vec{S}_1\right)\right]$$

Lx operator:

$$\text{predictor} \quad \overline{U^{n+1}_{i,j}} = U^{n+1/2}_{i,j} - \frac{\Delta t}{vol_{i,j}}\left(\vec{\vec{H}}^{n+1/2}_{i,j} \cdot \vec{S}_4 + \vec{\vec{H}}^{n+1/2}_{i-1,j} \cdot \vec{S}_2\right)$$

$$\text{corrector} \quad U^{n+1}_{i,j} = \frac{1}{2}\left[U^{n+1/2}_{i,j} + \overline{U^{n+1}_{i,j}} - \frac{\Delta t}{vol_{i,j}}\left(\vec{\vec{H}}^{\overline{n+1}}_{i+1,j} \cdot \vec{S}_4 + \vec{\vec{H}}^{\overline{n+1}}_{i,j} \cdot \vec{S}_2\right)\right]$$

$$\vec{S} = \hat{n}S$$

$$\int_S ds = \int_{S_1} ds + \int_{S_2} ds + \int_{S_3} ds + \int_{S_4} ds$$

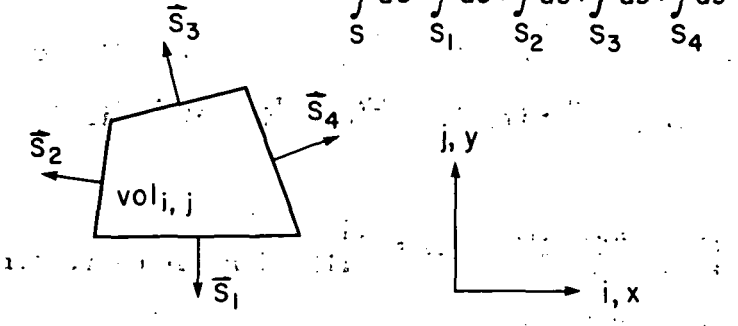

Sketch (a) — Quadrilateral volume element.

The Ly and Lx operators are applied so that equation (1) is satisfied at each time step for each cell of the nonorthogonal nonuniform computational mesh. To evaluate the viscous derivatives for the nonorthogonal mesh, the following transformation is appropriate (ref. 3):

$$\frac{\partial \phi}{\partial x} = \frac{\partial \phi}{\partial \xi}\frac{\partial \xi}{\partial x} + \frac{\partial \phi}{\partial \eta}\frac{\partial \eta}{\partial x} \qquad \frac{\partial \phi}{\partial y} = \frac{\partial \phi}{\partial \xi}\frac{\partial \xi}{\partial y} + \frac{\partial \phi}{\partial \eta}\frac{\partial \eta}{\partial y}$$

where ϕ is a dummy dependent variable, and (ξ,η) are the local coordinates of the nonorthogonal mesh. In terms of the notation in sketch (b),

$$\frac{\partial \phi}{\partial x} = \frac{\Delta\phi_\xi \Delta y_\eta - \Delta\phi_\eta \Delta y_\xi}{\Delta x_\xi \Delta y_\eta - \Delta x_\eta \Delta y_\xi} \qquad \frac{\partial \phi}{\partial y} = \frac{\Delta\phi_\xi \Delta x_\eta - \Delta\phi_\eta \Delta x_\xi}{\Delta y_\xi \Delta x_\eta - \Delta y_\eta \Delta x_\xi}$$

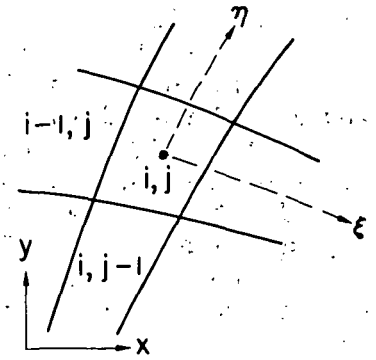

Sketch (b) — Nonorthogonal mesh notation.

For evaluation on surfaces S_3 and S_4, the differences are defined as

$$\Delta\phi_\xi = \phi_{i+1,jj} - \phi_{im,jj} \qquad \Delta\phi_\eta = \phi_{ii,j+1} - \phi_{ii,jm}$$

$$\Delta x_\xi = x_{i+1,jj} - x_{im,jj} \qquad \Delta x_\eta = x_{ii,j+1} - x_{ii,jm}$$

$$\Delta y_\xi = y_{i+1,jj} - y_{im,jj} \qquad \Delta y_\eta = y_{ii,j+1} - y_{ii,jm}$$

and

$$im = \begin{cases} i & \text{for Lx} \\ i-1 & \text{for Ly} \end{cases} \qquad ii = \begin{cases} i & \\ i+1 & \text{for Lx corrector} \end{cases}$$

$$jm = \begin{cases} j-1 & \text{for Lx} \\ j & \text{for Ly} \end{cases} \qquad jj = \begin{cases} j & \\ j+1 & \text{for Ly corrector} \end{cases}$$

This treatment of the viscous derivatives always results in centered differences, maintains second-order accuracy, and provides consistent treatment of discontinuous boundary conditions (such as at the leading and trailing edges of the airfoil).

Control Volume, Mesh, and Boundary Conditions

The airfoil, initially at rest, is impulsively started at time zero at the desired free-stream Mach number and pressure. Figure 1 shows a typical control volume for which the flow-field development is followed in time. At a sufficient distance upstream of the leading edge (in this case six chord lengths), the flow is assumed uniform at the free-stream conditions ($U = U_\infty$) as it is along the far transverse boundary (again, six chord lengths away). The downstream boundary is positioned far enough downstream of the trailing edge (nine chord lengths) so that all gradients in the flow direction may be assumed negligible ($\partial u/\partial x = 0$). The surface of the airfoil is impermeable, and "no slip" boundary conditions are assumed ($u = v = 0$). The airfoil is assumed adiabatic ($\nabla T \cdot \vec{n} = 0$), and the normal surface pressure gradient is zero ($\partial p/\partial n = 0$). Ahead of and behind the airfoil, the flow is symmetric. If the airfoil is thick, and the flow field is transonic, significant boundary-layer separation is likely. To simulate this phenomenon reliably for turbulent flow it is necessary to resolve the boundary layer to the sublayer scale. This sublayer scale is nearly proportional to $1/\sqrt{Re_c}$ so that, for the high Reynolds number flows of interest, the mesh resolution near the surface must be extremely fine. As a rule of thumb, a first mesh spacing of $\Delta y_{min} = 2/3(c/\sqrt{Re_c})$ is adequate.

The mesh used in the studies to date is a 50×38 mesh. In the x-direction, the mesh is uniformly distributed over the surface of the airfoil (20 points) and is exponentially stretched ahead of (10 points) and behind the airfoil (20 points). In the y-direction, a coarse mesh of 26 points is exponentially stretched away from the airfoil. The innermost region is further subdivided

into a medium mesh of 10 exponentially stretched points and a fine mesh of 4 uniformly spaced points.

Turbulence Model

The turbulence modeling is incorporated in the shear stress term τ_{xy} and τ_{yx} in the form of an eddy-viscosity coefficient ε as

$$\tau = \tau_{xy} = \tau_{yx} = (\mu + \varepsilon)\left(\frac{\partial u}{\partial y} + \frac{\partial v}{\partial x}\right)$$

Two different algebraic models have been considered, each expected to perform adequately ahead of the shock-wave—boundary-layer interaction regions but to exhibit different behavior when the flow separates.

The first model considered (model 1) is a van Driest formulation (ref. 4) for the wall region and a plane mixing formulation for the outer region. No special consideration is given to separated regions and the airfoil wake is described by a Clauser (ref. 5) wake formulation.

Wall Region:

$$\varepsilon = \rho \ell^2 \left|\frac{\partial u}{\partial y} + \frac{\partial v}{\partial x}\right|$$

$$\ell = 0.4y\left[1 - \exp(-y/A)\right]$$

$$A \equiv 26 \frac{\mu_w}{\rho_w}\sqrt{\frac{\rho_w}{|\tau_w|}}$$

Outer Region:

$$\varepsilon = \rho \ell^2 \left|\frac{\partial u}{\partial y} + \frac{\partial v}{\partial x}\right|$$

$$\ell = 0.07(\delta - y_o)$$

where δ is the boundary-layer thickness and y_o is the furthest point across the boundary layer where the velocity is zero. (For attached boundary layers $y_o = 0$.)

Airfoil Wake:

$$\varepsilon = 0.001176\rho(\delta - y_o)|u_\delta - u_{\mathfrak{L}}|$$

where u_δ is the velocity at the edge of the wake and $u_{\mathfrak{L}}$ is the velocity at the center line.

Prandtl Number:

$$Pr = Pr_t = 0.90$$

The second model (model 2) uses a van Driest formulation for the wall region and a Clauser formulation with an intermittency factor in the outer region. A limiting minimum value is imposed on velocity gradient used in the separation-bubble description and the airfoil wake is described by the boundary-layer-wake formulation.

Wall Region:

$$\varepsilon = \rho \ell^2 \left[\left(\frac{\partial u}{\partial y} \right)^2 + \left(\frac{\partial v}{\partial x} \right)^2 \right]^{1/2}$$

$$\ell = 0.41y \left[1 - \exp(-y/A) \right]$$

$$A \equiv 26 \frac{\mu_w}{\rho_w} \sqrt{\frac{\rho_w}{|\tau_w|}}$$

Outer Region:

$$\varepsilon = \frac{0.0168 U_\delta \delta_i^*}{1 + \left[(y - y_o)/\delta \right]^6}$$

$$\delta_i^* = \int_{y_o}^{\delta} \left(1 - \frac{u}{u_\delta} \right) dy$$

Separation Bubble: Same as wall region except that

$$\left[\left(\frac{\partial u}{\partial y} \right)^2 + \left(\frac{\partial v}{\partial x} \right)^2 \right]^{1/2} \geq \frac{u_\delta}{\delta}$$

Airfoil Wake: Same as outer region

Prandtl Number:

$$Pr = 0.72 , \quad Pr_t = 0.90$$

The validity of each of these models in the interaction and separated flow regions is highly suspect and requires verification by experiment. While it may be necessary to resort to more rigorous turbulent models in these regions, the simple models used here should permit some insight into the influence of viscosity on such flow fields and are adequate for the early development stages of the computer codes.

Computational Time Step

Six different computational time steps are used in the calculation; one for the Lx operator and one for the Ly operator in each of the three mesh regions. Each time step is determined by the CFL (Courant-Friedrichs-Lewy) and viscous stability requirements from the following relation:

$$\Delta t = \frac{h}{|V| + a + (\alpha/h)(\mu + \varepsilon)/\rho}$$

where h is the appropriate mesh spacing, V is the appropriate velocity component, a is the local speed of sound, and α is a function of the mesh aspect ratio. In the fine mesh in the wake behind the airfoil, the eddy viscosity ε is quite large, and the viscous stability criterion may govern the time step for the Ly operator. To avoid this undesirable restriction and unneeded resolution of the wake, the entire fine mesh region downstream of the airfoil is averaged and treated as part of the medium mesh.

VALIDATION

Because computations of this complexity have not previously been performed, the validity of the present code has been determined by comparison with established computations for certain specific regions of the flow field and with experimental results obtained in the Ames High Reynolds Number Channel.

Inviscid Flow Field

The viscous terms were neglected and the inviscid flow was computed over a 6-percent circular-arc airfoil at a free-stream Mach number of 0.90. The surface pressure distribution is compared in figure 2 with a computation using the small-disturbance-theory program of E. M. Murman of Flow Research, Inc. (refs. 6 to 8 and unpublished information) and an Euler equation computation by R. W. MacCormack of Ames Research Center. Both of these computations employed special considerations at the shock which have not been incorporated in the present code. The agreement between the three computations (all of which solve the conservative form of the equations) is excellent.

Attached Boundary Layer

The flow over an 18-percent-thick circular-arc airfoil at a free-stream Mach number of 0.775 and a chord Reynolds number of 2×10^6 was computed using eddy-viscosity model 1. The computed surface pressure distribution was input to the turbulent boundary-layer code of Marvin and Sheaffer of Ames Research Center (ref. 9 and additional information supplied by Marvin) which uses an implicit Crank-Nicholson method and a Cebeci-Smith eddy-viscosity model (ref. 10). Computed values of local skin friction from this boundary-layer code are compared with the present calculation in figure 3. Ahead of the

separated-flow region the agreement is excellent except for a small region near the leading edge where the Marvin-Sheaffer code assumes a laminar to turbulent transition region.

In addition to skin friction, boundary-layer velocity profiles computed by the present code are compared in figure 4 with the compressible form of the universal "law of the wall." Here the symbols represent the numerical solution and are plotted at y^+ values corresponding to the mesh centers. All profiles are seen to have one point in the sublayer and adequately describe the log-law and wake-flow regions of the boundary layer.

Experimental Comparisons

Surface-pressure measurements, oil-flow studies, and shadowgraph studies were made using an 18-percent-thick circular-arc airfoil in the Ames High Reynolds Number Channel. Chord Reynolds numbers were varied between 1 and 13 million for free-stream Mach numbers between 0.711 and 0.788. In these experiments, flow-field streamlines, determined from the present computer code, were used to design contoured tunnel walls in an attempt to minimize tunnel interference effects.

Figure 5 shows a comparison between experimental and computed surface pressure distributions over the 18-percent-thick circular-arc airfoil at $M_\infty = 0.775$ and $Re_c = 2\times10^6$. Three computed distributions are shown in this figure as determined by the present code. One of these is an inviscid calculation, and the other two were determined using eddy-viscosity models 1 and 2. All comparisons are in excellent agreement ahead of the interaction region. Both viscous computations show a marked improvement over the inviscid results in the interaction region. The solution with model 2 shows the best agreement with experiment with respect to shock location and shock strength. Both viscous solutions indicate a shock-induced separation with the separation bubble extending into the wake. This is denoted in figure 5 by the pressure plateau downstream of the 80-percent-chord point. The experimental pressure distribution does not indicate this extensive separation region, and herein constitutes the greatest disagreement between computation and experiment. As will be shown later, at this particular choice of free-stream Mach number the experimental flow field can be highly unsteady, and direct comparisons in the separated flow region may be invalid.

The first study performed using the code was to assess the influence of Reynolds number on the transonic flow field. Using the 18-percent circular arc at $M_\infty = 0.775$, the chord Reynolds number was parametrically varied from 1×10^6 to 6.67×10^6 and the flow field computed using eddy-viscosity model 1. The results of this study are shown in figure 6 for the surface pressure distribution. Included for reference is the inviscid solution. Three features are apparent in this figure. First the influence of Reynolds number on this flow field is small while the effect of viscosity is large. Second, as the Reynolds number is decreased, the shock strength decreases and the shock moves forward on the airfoil. And third, as the Reynolds number is decreased, the displacement effects in the separation region increase resulting in less pressure recovery near the trailing edge. The displacement effect ahead of the

interaction region is nearly the same for the entire Reynolds number range considered.

A similar study was performed experimentally. Figure 7 shows the measured surface pressure distributions over an 18-percent circular-arc airfoil at $M_\infty = 0.750$. Except for boundary-layer-transition effects at the lower Reynolds number, the experimental study bears out the same conclusions determined from the numerical results. In addition to Reynolds number effect, the influence of free-stream Mach number was also experimentally studied. Figure 8 shows measured surface pressure distribution over an 18-percent circular-arc airfoil at $Re_c = 10 \times 10^6$. Results for four free-stream Mach numbers are included: $M_\infty = 0.74$, 0.76, 0.77, and 0.79. At $M_\infty = 0.74$ the flow is nearly subcritical and the shock is very weak. For $M_\infty = 0.76$ the shock is much stronger but there is still a large pressure recovery at the trailing edge, indicating small separation effects. For $M_\infty = 0.77$ there is a dramatic shift in pressure distribution over the aft portion of the airfoil. This sudden jump is associated with the shock-induced separation merging with existent trailing-edge separation, resulting in a large reverse flow region and large boundary-layer displacement effects. This phenomenon persists at the higher free-stream Mach numbers. This Mach number dependence of onset of massive separation is also a function of Reynolds number, which is discussed in reference 11.

To understand this discontinuous dependence on Mach number, shadowgraph movies were made of the flow over the aft portion of the airfoil as the Mach number was varied through the critical range. Photographs of selected frames of one such film are shown in figure 9 for an 18-percent circular-arc airfoil at $Re_c = 7 \times 10^6$. The Mach number variation is from 0.76 to 0.79 and results are shown for values of 0.76, 0.77, and 0.79. At $M_\infty = 0.76$ the flow is steady and there is some separation at the trailing edge. As the Mach number is increased, the flow becomes unsteady, switching alternately from massive separation to fully attached or small trailing-edge separation. This unsteadiness is most probably an asymmetric phenomenon; hence it is not reasonable to expect to simulate this phenomenon with a symmetric, free boundary code. When the Mach number reaches 0.79, the flow is again steady with massive shock-induced separation. Note that at the lower Mach number the shock is fairly weak and nearly normal to the airfoil surface. At the higher Mach number the shock is stronger and is definitely oblique — probably a lambda shock.

To avoid comparisons in the unsteady flow regimes, subsequent computations were performed only for the lower and higher Mach numbers where the experimental flow is known to be steady. In addition, because of the superior performance indicated in figure 5 of eddy-viscosity model 2 versus eddy-viscosity model 1 in the interaction regime, model 1 has been dropped from further consideration.

Oil-flow photographs of both the low and high Mach number experimental steady-flow regimes are shown in figure 10. At $M_\infty = 0.76$ the line at the

onset of trailing-edge separation is clearly indicated by the oil flow. The symmetry of the separation bubble is indicated in the right-hand photograph of the junction of the airfoil trailing edge and the tunnel side wall. At $M_\infty = 0.79$ the onset of shock-induced separation is indicated. The right-hand photograph of the junction of the airfoil trailing edge and the tunnel side wall clearly indicates the magnitude of the separation bubble. The photographs in figure 10 also serve to indicate the two-dimensional and symmetric character of the flow.

For a chord Reynolds number of 4×10^6 the flow field over the 18-percent circular-arc airfoil was simulated using eddy-viscosity model 2 for $M_\infty = 0.742$ and $M_\infty = 0.788$, corresponding to the two extremes of the experimental steady flows. Figure 11 shows a comparison with experimental data of the surface pressure distributions for the two cases. In figure 11(a) the viscous solution is an improvement over the inviscid result but does not agree with the experiment in the shock—boundary-layer interaction region. The experiment indicates a stronger influence of viscosity than does the calculation, resulting in a weaker, more smeared out shock. Near the trailing edge, however, the agreement is better, both distributions supporting the fact that there is only trailing-edge separation and both indicating the same level of pressure recovery. The reason for the substantial disparity in the interaction region is not yet clear. It may be related to the fact that the shock is near the midchord and, for a chord Reynolds number of only 4×10^6, the boundary layer may actually be transitional in that region. This could lead to the stronger viscous-inviscid interaction effect indicated by the experiment.

In figure 11(b) the viscous solution again is an improvement over the inviscid result. Here the agreement between experiment and viscous calculation is good in the interaction region but is poor over the separation bubble. Unfortunately, there was no experimental data for $Re_c = 4\times10^6$ at $M_\infty = 0.788$ so data are shown for $Re_c = 2\times10^6$ and 7×10^6. It is expected that data for 4×10^6 will fall within the envelope defined by these two limits. Note that both the experimental and calculated pressures tend to plateau over the separation bubble and indicate a similar extent over the aft portion of the airfoil. The computed pressures indicate larger recovery in this region and, as will be seen in the next figure, this is associated with the fact that the shock wave in the experiment is oblique while that simulated is nearly normal. The fundamental reason for this disparity is not yet clear but it is likely attributable to the inability of the simple eddy-viscosity model to support this complicated flow.

Figure 12 shows the flow field detail over the aft portion of the airfoil for the two Mach numbers considered above. The top photographs are shadowgraphs of the experiment. For $M_\infty = 0.742$ the shock is weak and normal to the surface. Separation occurs only at the trailing edge and is small in extent. For $M_\infty = 0.788$ the shock is strong and oblique. Separation is shock induced and extends into the wake. Immediately beneath the photographs are computed Mach number contours. For $M_\infty = 0.742$ the flow features are quite similar to the shadowgraph above. For $M_\infty = 0.788$ the shock is seen

to be nearly normal to the surface as opposed to being oblique in the shadowgraph, but the magnitude of the separated flow region is similar to that shown in the shadowgraph. The bottom part of this figure contains computed velocity vector plots showing the details of the separation bubbles and the effect of the shock in retarding the flow. Subsequent experiments using a laser velocimeter are planned to provide similar experimental data in this region.

COMPUTER REQUIREMENTS

The present code was originally written in FORTRAN and debugged on an IBM 360/67 using the interactive features of the time sharing system. Subsequently, it was run on the CDC 7600, requiring 2 to 10 hours per converged solution, depending on chord Reynolds number. Because of the long run times, the code was completely restructured and written in the vector-oriented Ames-developed CFD language.[1] This code was translated to assembly language for the ILLIAC IV and to FORTRAN for the CDC 7600. The resulting FORTRAN code was further optimized, using COMPASS coded subroutines for *all* vector arithmetic operations. Resultant run times are now 0.8 to 4.2 hours per converged solution on the CDC 7600, and 0.6 to 3.0 hours on the ILLIAC IV. There is substantial room for speed increase on the ILLIAC IV in that (1) the quoted run times were for the ILLIAC operating at 11.5 MHz instead of the design speed of 15-16 MHz, (2) the ILLIAC was operated in non-overlap mode, and (3) each iteration was performed twice and the solutions compared before continuing with the computation. Each of these areas represents potential speed reductions of 0.72, 0.40, and 0.48, respectively, leading to an overall potential speed reduction of 0.14. In this case, the present code would require from 0.08 to 0.42 hour per converged solution — an order of magnitude faster than the vector-coded CDC 7600.

CONCLUDING REMARKS

In conclusion, a code has been written to simulate transonic turbulent flow fields over two-dimensional bodies of arbitrary configuration. At present, only algebraic eddy-viscosity models have been considered to achieve turbulence closure. With these models the code yields valid solutions in the inviscid flow field and in the attached boundary layer ahead of interaction regions. The validity of the numerical simulations in the shock—boundary-layer interaction region and in reverse flow regions is directly related to the turbulence model. For the models considered thus far, comparisons with experiment have been less than good. This is to be expected since the models are developed from flat-plate incompressible boundary-layer data. Nevertheless, the viscous solutions represent a considerable improvement over inviscid solutions and do predict the proper features of the flow.

---

[1] Computational Fluid Dynamics (A FORTRAN-Based Language for the ILLIAC IV developed at Ames Research Center in 1973).

The code has been optimized for the CDC 7600 computer and requires from 0.8 to 4.2 hours to simulate the transonic flow field over an 18-percent circular-arc airfoil. The code has also been written for the ILLIAC IV and presently requires from 0.6 to 3.0 hours to simulate these transonic flows. These ILLIAC run times have a potential reduction to 0.08 to 0.42 hour, if total advantage is taken of certain design features of the ILLIAC.

REFERENCES

1. MacCormack, R. W.: Numerical Solution of the Interaction of a Shock Wave with a Laminar Boundary Layer. Lecture Notes in Physics, vol. 8, Springer-Verlag, pp. 151-163.

2. MacCormack, R. W., and Paullay, A. J.: Computational Efficiency Achieved by Time Splitting of Finite Difference Operators. AIAA Paper 72-154, 1972.

3. Deiwert, G. S.: Numerical Simulation of High Reynolds Number Transonic Flows. AIAA Paper 74-603, June 17-19, 1974.

4. Van Driest, E. R.: On Turbulent Flow Near a Wall. Jour. Aero. Sci., vol. 23, 1956, p. 1007.

5. Clauser, F. H.: The Turbulent Boundary Layer. Adv. in App. Mech. IV, pt. 1, New York, Academic Press, 1956.

6. Murman, E. M., and Cole, J. D.: Calculation of Plane Steady Transonic Flows. AIAA Jour., vol. 9, no. 1, 1971, pp. 114-121.

7. Murman, E. M.: Analysis of Embedded Shock Waves Calculated by Relaxation Methods. Proc. AIAA Computational Fluid Dynamics Conference, 1973, pp. 27-40.

8. Murman, E. M.: Computation of Wall Effects in Ventilated Transonic Wind Tunnels. AIAA Paper 72-1007, 1972, pp. 216-217.

9. Marvin, J. G., and Sheaffer, Y. S.: A Method for Solving the Nonsimilar Laminar Boundary-Layer Equations Including Foreign Gas Injection. NASA TN D-5516, 1969.

10. Inouye, M., Marvin, J. G., and Shaeffer, Y. S.: Turbulent-Wake Calculations with an Eddy-Viscosity Model. AIAA Journal, vol. 10, no. 2, 1972.

11. McDevitt, J. B., Levy, L. L., and Deiwert, G. S.: Transonic Flow About Thick Circular-Arc Airfoils. AIAA Paper 75-875, 1975.

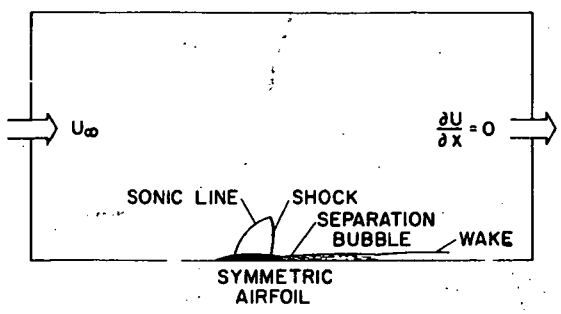

Figure 1.— Computational control volume.

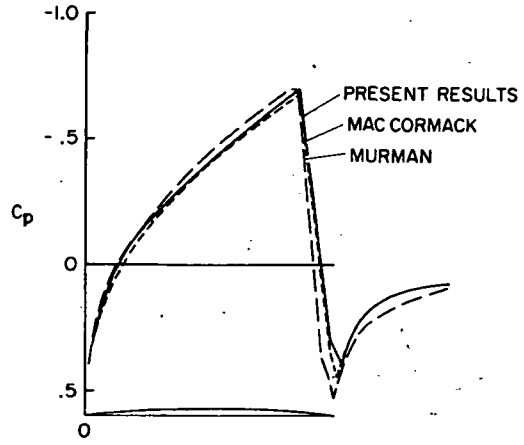

Figure 2.— Inviscid pressure distribution over a 6-percent circular-arc airfoil; $M_\infty = 0.90$.

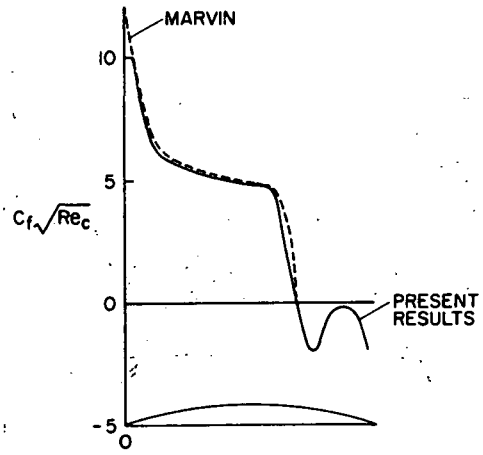

Figure 3.— Skin-friction distribution over an 18-percent circular-arc airfoil; $M_\infty = 0.775$, $Re_c = 2\times10^6$.

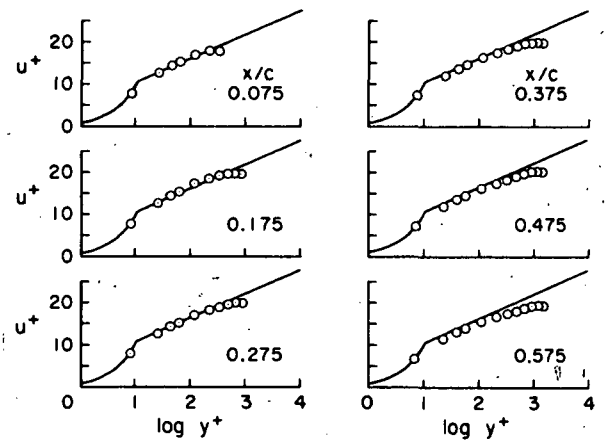

Figure 4.— Velocity profiles ahead of shock; $M_\infty = 0.775$, $Re_c = 2\times10^6$.

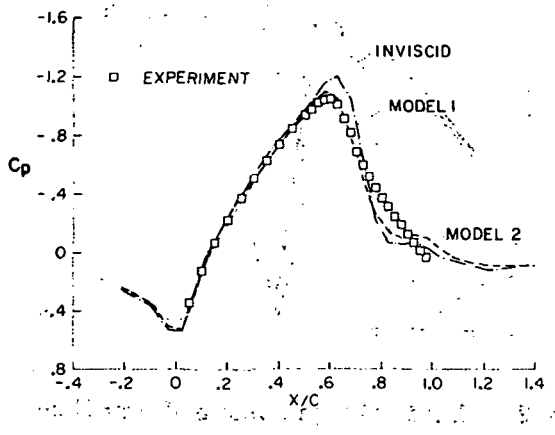

Figure 5.— Pressure distribution over an 18-percent circular-arc airfoil; $M_\infty = 0.775$, $Re_c = 2\times10^6$.

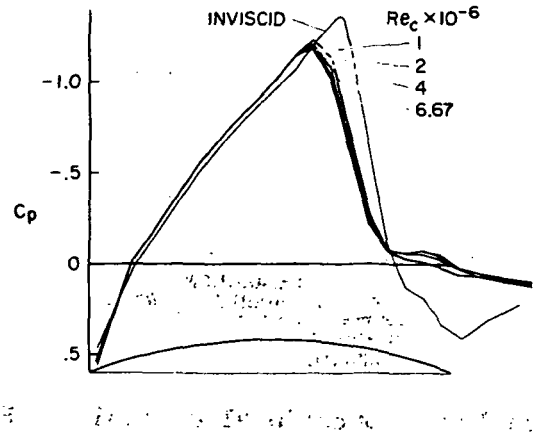

Figure 6.— Pressure distribution over an 18-percent circular-arc airfoil; $M_\infty = 0.775$.

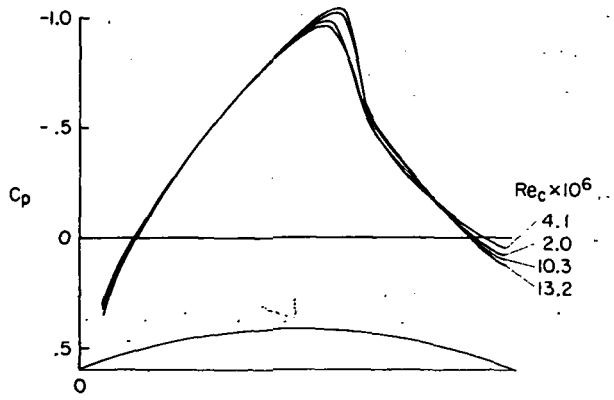

Figure 7.— Experimental pressure distribution over an 18-percent circular-arc airfoil; Reynolds number effect, $M_\infty = 0.750$.

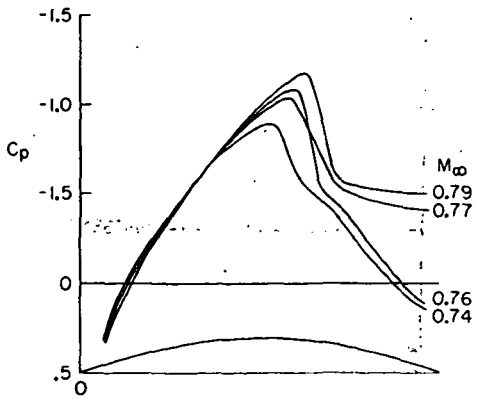

Figure 8.— Experimental pressure distribution over an 18-percent circular-arc airfoil; Mach number effect, $Re_c = 10\times10^6$.

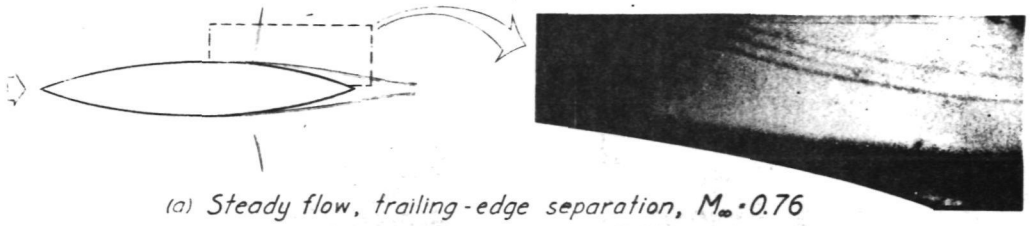

(a) Steady flow, trailing-edge separation, $M_\infty = 0.76$

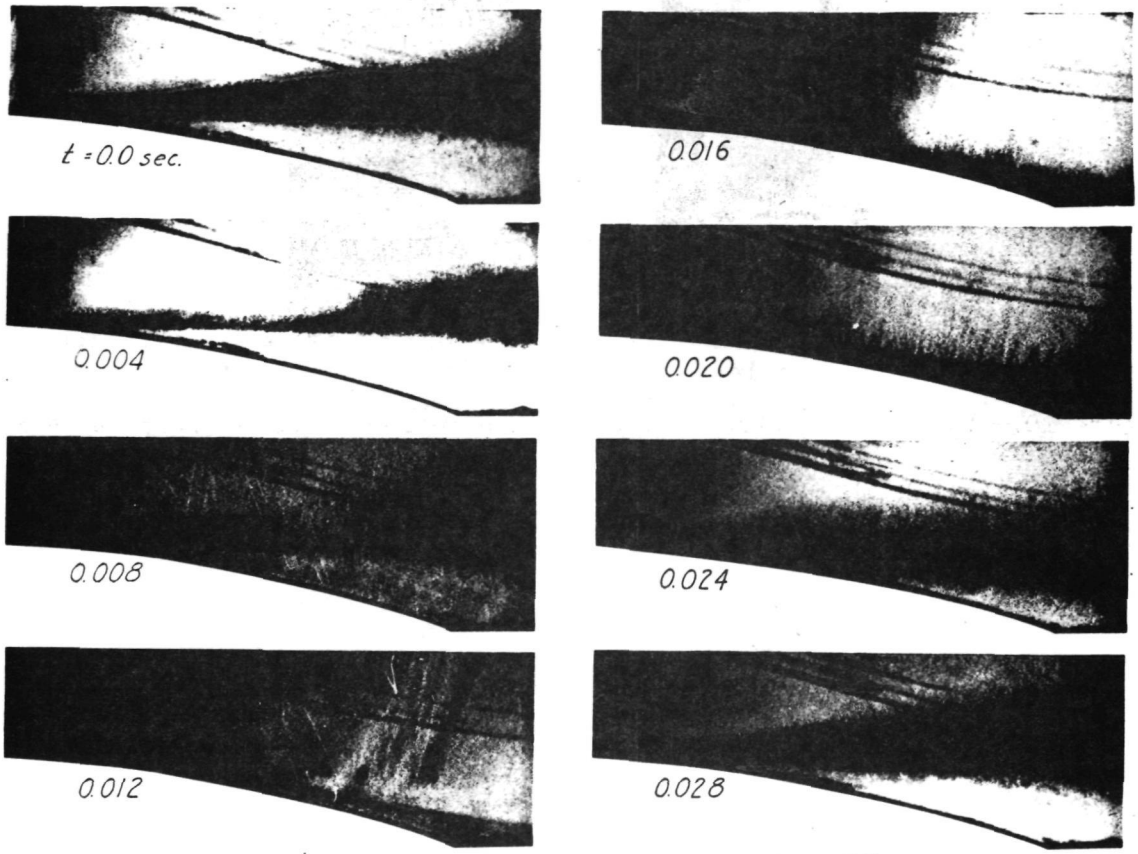

(b) Unsteady flow, oscillatory separation, $M_\infty = 0.77$

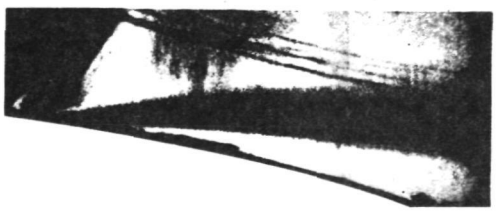

(c) Steady flow, shock-induced separation, $M_\infty = 0.79$

Figure 9.— Photographs of boundary-layer separation from a shadowgraph movie; $t/c = 0.18$, $Re_c = 7 \times 10^6$.

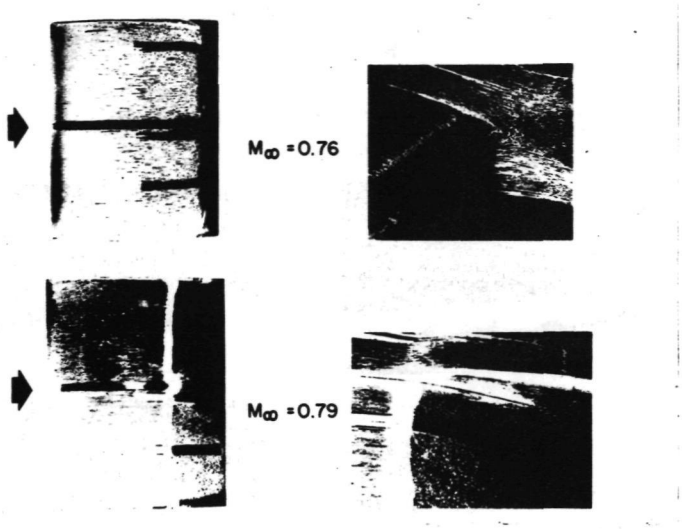

Figure 10.— Oil-flow patterns of separation regions; t/c = 0.18, $Re_c = 10\times10^6$.

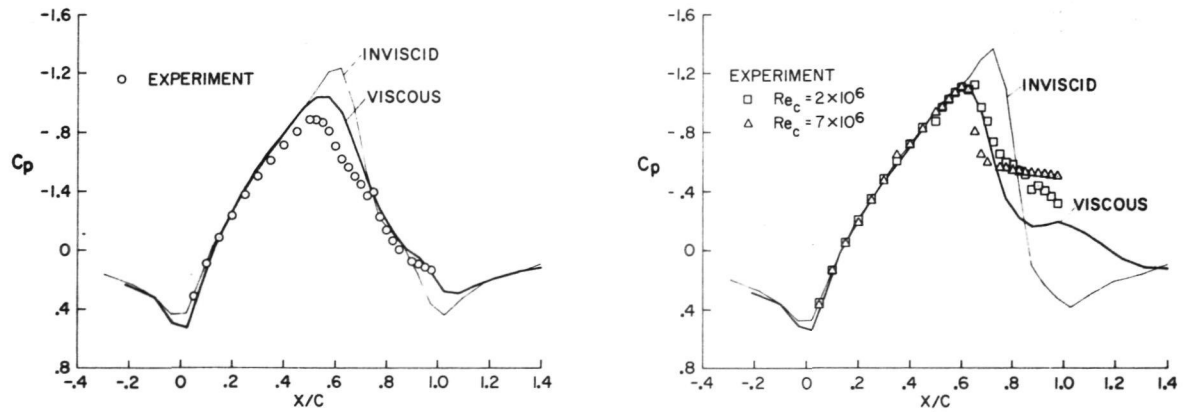

(a) $M_\infty = 0.742$.

(b) $M_\infty = 0.788$.

Figure 11.— Pressure distributions over an 18-percent circular-arc airfoil; $Re_c = 4\times10^6$.

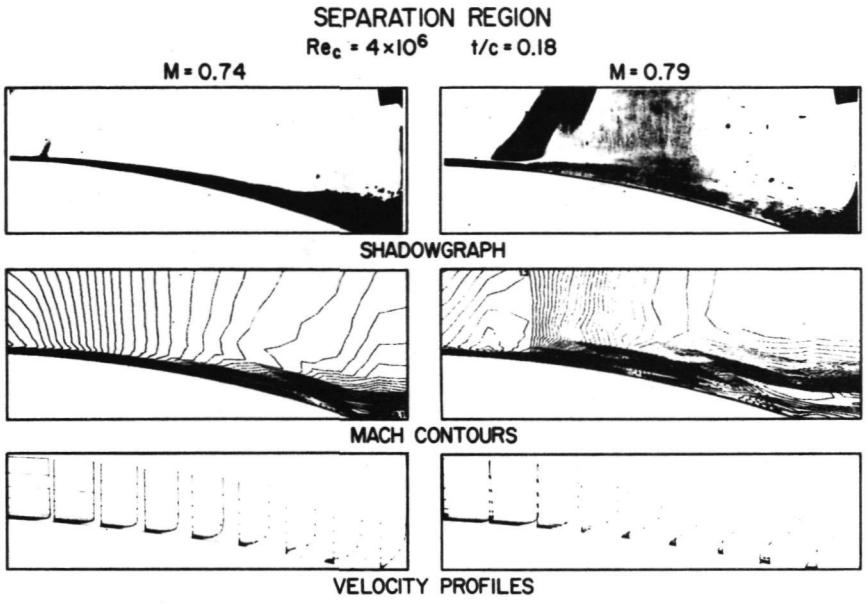

Figure 12.- Flow-field details over the aft portion of an 18-percent circular-arc airfoil.

AN INVESTIGATION OF SEVERAL NUMERICAL PROCEDURES FOR TIME-ASYMPTOTIC COMPRESSIBLE NAVIER-STOKES SOLUTIONS

By David H. Rudy, Dana J. Morris, Doris K. Blanchard,
NASA Langley Research Center

Charlie H. Cooke,
Old Dominion University

and Stanley G. Rubin
Polytechnic Institute of New York

14

SUMMARY

The status of an investigation of four numerical techniques for the time-dependent compressible Navier-Stokes equations is presented. Results for free shear layer calculations in the Reynolds number range from 10^3 to 8.1×10^4 indicate that a sequential alterating-direction implicit (ADI) finite-difference procedure requires longer computing times to reach steady state than a low-storage hopscotch finite-difference procedure. A finite-element method with cubic approximating functions was found to require excessive computer storage and computation times. A fourth method, an alternating-direction cubic spline technique which is still being tested, is also described.

INTRODUCTION

The quasi-parallel assumption successfully used in boundary-layer-type calculations is not applicable for many free mixing flows. The complete Navier-Stokes equations must usually be solved for flows which have no single dominant flow direction. This paper presents the current status of a detailed investigation of several numerical procedures for obtaining steady-state solutions for two-dimensional, high Reynolds number, compressible free shear flows using the time-asymptotic approach. In particular, the research has been directed toward the solution of mixed subsonic-supersonic flow problems.

Most published numerical solutions of the compressible viscous time-dependent Navier-Stokes equations have been for flows with Reynolds numbers much less than 10^3. Peyret and Viviand (ref. 1) have summarized these solutions through mid-1973. Taylor (ref. 2) also analyzed the literature at that time. Most methods up to the time of these surveys used explicit difference schemes. Later, Briley and McDonald (ref. 3) and Baum

and Ndefo (ref. 4) published alternating-direction implicit (ADI) calculations. The high Reynolds number solutions (Victoria and Steiger (ref. 5), Carter (ref. 6), and MacCormack (ref. 7)) were all computed with explicit difference schemes. Recently, additional high Reynolds number solutions have appeared, e.g., Holst and Tannehill (ref. 8) and Baldwin and MacCormack (ref. 9). These solutions were also computed with explicit methods.

Although conceptually simpler and more easily coded than implicit methods, explicit methods are restricted to small time steps relative to the spatial grid size for numerical stability. Consequently, such methods require long computation times to reach a steady state, especially for flows in which a fine mesh has been used such as in regions of high shear. For example, the calculation of a shear layer impinging on a blunt body for a Reynolds number of 10^4 by Holst, Tannehill, and Rakich (ref. 10) using the MacCormack method requires up to 80 min on a CDC 7600 computer.

The methods under investigation are the following: (1) hopscotch (explicit) finite difference, (2) alternating-direction implicit (ADI) finite difference, (3) finite element, and (4) implicit cubic spline integration. In addition, some calculations have been made with the Du Fort-Frankel procedure. The goal of this study is the development of an efficient numerical tool to be used in testing fully two-dimensional turbulence models for a wide range of free shear flow applications such as interference heating (shock/shear layer impingement), separated flows, jet exhaust noise reduction, combustor design, and tangential slot injection. This paper summarizes results of calculations for sample mixing problems with Reynolds numbers ranging from 10^3 to 8.1×10^4. The procedures are compared with respect to their accuracy, computer storage requirements, ease of implementation, and total time to steady state for computation of sample problems.

SYMBOLS

c	speed of sound
D_j	diameter of jet
f,g	general functions
H	enthalpy
L	differential operator
M	Mach number
M_i	second derivative of $S(x_i)$

m_i	first derivative of $S(x_i)$
N	integer
N_{Co}	Courant number, $\dfrac{\Delta t}{\Delta x/(u + v + 2c)}$
N_{Re}	Reynolds number, $\dfrac{\bar{\rho}_s \bar{u}_{ref} D_j}{\bar{\mu}_s}$
p	pressure
R	gas constant
$S(x)$	cubic spline function
T	temperature
t	time
u	streamwise velocity
u_{ref}	reference velocity, $\sqrt{2\bar{H}_s}$
V	vector of unknowns
v	normal velocity
x,y	streamwise and normal directions, respectively
α	artificial diffusion coefficient
γ	ratio of specific heats
Δ	incremental change
μ	molecular viscosity
ν	kinematic viscosity
ρ	density

ϕ_J B-spline function in equation (14)

Subscripts:

i,j index denoting grid point spatial location

J nodal index in finite-element mesh

s stagnation condition

t,x,y derivative with respect to time, x-direction, and y-direction

Superscripts:

n,* index denoting time level

A bar over a symbol denotes a dimensional quantity. An arrow over a symbol denotes a vector quantity.

PROBLEM DEFINITION

To provide a basis for comparison of the numerical procedures, a set of standard test problems was selected.

Sample Problems

Figure 1(a) shows the mixing problem (case 1) originally chosen for use as the standard sample problem. This flow is the mixing of a two-dimensional laminar supersonic (Mach 3) jet and a laminar subsonic flow normal to the jet axis. The peripheral velocity v_p is higher in magnitude than the normal velocity component arising from natural entrainment of the resultant free shear layer for the same jet issuing into quiescent surroundings. As shown in figure 1(a), the solution domain does not extend to infinity in either the positive streamwise or normal directions. The peripheral flow is applied one or more jet diameters above the corner of the wall, and the calculation is truncated one jet diameter downstream from the jet exit plane. This problem thus embodies some complicating factors which are often unavoidable in computations of flow fields for real vehicles, e.g., a sharp corner and the artificial downstream boundary with a significant portion of subsonic outflow. Since the individual effects of these factors are difficult to isolate in the computation of such a flow field, calculations were also made for the related problem, mixing of two parallel streams, shown in figure 1(b). The computational region

begins downstream of the base of the infinitely thin splitter plates. Such a calculation obviously does not require the full Navier-Stokes equations, since solutions can be obtained with the usual quasi-parallel approach (boundary-layer equations with free shear flow boundary conditions). However, since steady-state calculations could be made with another method, solutions were obtained for comparison with computed Navier-Stokes results. The mixing of a subsonic stream and a supersonic stream (case 2) shown in figure 1(b) was chosen for the study of subsonic boundary conditions. Calculations were also made for the mixing of two supersonic (Mach 3 and Mach 1.68) streams (case 3), a flow free from subsonic boundary problems.

Governing Equations

The governing equations can be written in nonconservative forms as follows:

Continuity

$$\rho_t + \rho v_y + \rho u_x + v\rho_y + u\rho_x = 0 \tag{1}$$

x-momentum

$$\rho u_t + \rho v u_y + \rho u u_x = -p_x + \frac{4}{3N_{Re}}\left(\mu u_x\right)_x - \frac{2}{3N_{Re}}\left(\mu v_y\right)_x + \frac{1}{N_{Re}}\left[\mu\left(u_y + v_x\right)\right]_y \tag{2}$$

y-momentum

$$\rho v_t + \rho v v_y + \rho u v_x = -p_y + \frac{4}{3N_{Re}}\left(\mu v_y\right)_y - \frac{2}{3N_{Re}}\left(\mu u_x\right)_y + \frac{1}{N_{Re}}\left[\mu\left(u_y + v_x\right)\right]_y \tag{3}$$

These equations are nondimensionalized with respect to the jet diameter and stagnation flow conditions, i.e.,

$$\rho = \frac{\bar{\rho}}{\bar{\rho}_s} \qquad p = \frac{\bar{p}}{2\bar{\rho}_s \bar{H}_s}$$

$$T = \frac{\bar{T}}{\bar{T}_s} \qquad x = \frac{\bar{x}}{D_j}$$

$$\bar{u}_{ref} = \sqrt{2\bar{H}_s} \qquad y = \frac{\bar{y}}{D_j}$$

$$u = \frac{\bar{u}}{\sqrt{2\bar{H}_s}} = \frac{\bar{u}}{\bar{u}_{ref}} \qquad N_{Re} = \frac{\bar{\rho}_s \bar{u}_{ref} D_j}{\bar{\mu}_s}$$

$$v = \frac{\bar{v}}{\sqrt{2\bar{H}_s}} = \frac{\bar{u}}{\bar{u}_{ref}} \qquad \mu = \frac{\bar{\mu}}{\bar{\mu}_s}$$

The pressure was evaluated by means of the perfect gas equation of state

$$p = \rho RT \tag{4}$$

where $R = \frac{\gamma - 1}{2\gamma}$. Air was the test gas. Only laminar (molecular) viscous effects were considered, the Sutherland law being used to express the viscosity as a function of temperature

$$\mu = T^{3/2} \frac{1 + 198.6/\overline{T}_s}{T + 198.6/\overline{T}_s} \tag{5}$$

To simplify the system of governing equations and to reduce required machine storage, a constant total temperature of 530° R (294 K) was assumed. Calculations for a Mach 3 jet into still air with the quasi-parallel code of Oh (ref. 11), which included the energy equation, showed that the total enthalpy varied less than 5 percent throughout the mixing region from the constant value assumed in other calculations. This small variation had a negligible effect on the other flow parameters. As a result of this assumption, the temperature could be evaluated by the algebraic relationship

$$T = 1 - u^2 - v^2 \tag{6}$$

which eliminated the need for solving the complete energy equation. Constant static pressure was assumed in all calculations to generate initial values of density using equations (4) and (6) along with the given initial velocities. The linearized version of equations (1) to (6) with the viscous terms neglected has been shown by Gottlieb and Gustafsson (ref. 12) to be well-posed for the initial value problem.

DESCRIPTION OF NUMERICAL PROCEDURES

Hopscotch

The hopscotch method is a two-step explicit procedure which was shown to be unconditionally stable for the diffusion equation by Gourlay (ref. 13). It was used by Scala and Gordon (ref. 14) for compressible viscous calculations of low Reynolds number flow around a circular cylinder, and it has been applied to hyperbolic systems with shocks by Gourlay and Morris (ref. 15).

Figure 2 shows the pattern of the two sweeps. Consider, for example, the equation

$$u_t = u_{xx} + u_{yy} \tag{7}$$

With forward time and centered space differencing, $u_{i,j}^{n+1}$ is computed at each time step at the nodes for which $i + j + n$ is even (marked with circles in fig. 2) during the first sweep through the mesh with the equation

$$u_{i,j}^{n+1} = u_{i,j}^{n} + \Delta t\left[\frac{u_{i+1,j}^{n} - 2u_{i,j}^{n} + u_{i-1,j}^{n}}{(\Delta x)^2}\right] + \Delta t\left[\frac{u_{i,j+1}^{n} - 2u_{i,j}^{n} + u_{i,j-1}^{n}}{(\Delta y)^2}\right] \tag{8}$$

This sweep is fully explicit. In the second sweep at this time step,

$$u_{i,j}^{n+1} = u_{i,j}^{n} + \Delta t\left[\frac{u_{i+1,j}^{n+1} - 2u_{i,j}^{n+1} + u_{i-1,j}^{n+1}}{(\Delta x)^2}\right] + \Delta t\left[\frac{u_{i,j+1}^{n+1} - 2u_{i,j}^{n+1} + u_{i,j-1}^{n+1}}{(\Delta y)^2}\right] \tag{9}$$

at the nodes (marked with squares in fig. 2) for which $i + j + n$ is odd. This sweep is implicit in the sense that the values in the computation of the spatial derivatives are at the new time level $n + 1$. However, this implicitness does not require the reduction of a matrix, since these values were computed during the first sweep. Differencing which does not fit into this pattern, such as a five-point difference for u_{xx} using values of $u_{i+2,j}^{n+1}$ and $u_{i-2,j}^{n+1}$, requires special consideration. The conventional nine-point difference analog for cross-derivative terms must receive treatment which usually requires the reduction of a matrix. The computational efficiency of the hopscotch procedure is thus reduced. For the full Navier-Stokes equations, hopscotch has no cell Reynolds number limitation, but the maximum time step is limited by the condition, $\Delta t \leqq \frac{\Delta x}{u + v + 2c}$. For the present application, a sufficient condition for stability is $\Delta t \leqq \frac{\Delta x}{u + v + \sqrt{2}c}$.

The hopscotch version derived for the present investigation is a low-storage procedure (one array per dependent variable). The equations were linearized by lagging the nonlinear coefficients. On the second sweep, values at time $n + 1$ are used only where available. This lagging eliminates the need for matrix reductions and thereby simplifies the coding, maintains the low storage, and minimizes CPU time per nodal point. Gottlieb and Gustafsson (ref. 12), considering the convective terms only, have analyzed the stability of this version of hopscotch with the lagging of some values and have found its stability to be identical to that of the original hopscotch method. The method is different, however, when the diffusion terms are included. The stability limit which was derived from the advection terms is not changed for the range of Reynolds number considered in the present investigation. The lagging of values used to compute the viscous terms introduces slightly more second-order dissipation than in the original hopscotch method. The new procedure is formally not consistent with the time-dependent problem; however, the extra error term

introduced is very small for large Reynolds numbers (such as 10^3). In the present application the interest is not in the transient but in the steady-state solution; therefore, this error term, which goes to zero at steady state, has no detrimental effect.

During each sweep the x-momentum, y-momentum, and continuity equations are solved sequentially at each nodal point with the boundary values then being updated at the end of each time step. To illustrate the present version of hopscotch, the differencing of the x-momentum equation is as follows:

First sweep

$$u_{i,j}^{n+1} = u_{i,j}^{n} + \Delta t \left\{ -u_{i,j}^{n}\left(\frac{\partial u}{\partial x}\right)_{i,j}^{n} - v_{i,j}^{n}\left(\frac{\partial u}{\partial y}\right)_{i,j}^{n} - \frac{1}{\rho_{i,j}^{n}}\left(\frac{\partial p}{\partial x}\right)_{i,j}^{n} \right.$$

$$+ \frac{4}{3N_{Re}\rho_{i,j}^{n}}\left[2A\left(\frac{\mu_{i+1,j}^{n} + \mu_{i,j}^{n}}{2}\right)\left(\frac{u_{i+1,j}^{n} - u_{i,j}^{n}}{\Delta x_i}\right) + 2B\mu_{i,j}^{n}\left(\frac{\partial u}{\partial x}\right)_{i,j}^{n} \right.$$

$$\left. + 2C\left(\frac{\mu_{i,j}^{n} + \mu_{i-1,j}^{n}}{2}\right)\left(\frac{u_{i,j}^{n} - u_{i-1,j}^{n}}{\Delta x_{i-1}}\right)\right] - \frac{2}{3N_{Re}\rho_{i,j}^{n}}\left[A\mu_{i+1,j}^{n}\left(\frac{\partial v}{\partial y}\right)_{i+1,j}^{n} + B\mu_{i,j}^{n}\left(\frac{\partial v}{\partial y}\right)_{i,j}^{n} \right.$$

$$\left. + C\mu_{i-1,j}^{n}\left(\frac{\partial v}{\partial y}\right)_{i-1,j}^{n}\right] + \frac{1}{N_{Re}\rho_{i,j}^{n}}\left[2D\left(\frac{\mu_{i,j+1}^{n} + \mu_{i,j}^{n}}{2}\right)\left(\frac{u_{i,j+1}^{n} - u_{i,j}^{n}}{\Delta y_j}\right) + 2E\mu_{i,j}^{n}\left(\frac{\partial u}{\partial y}\right)_{i,j}^{n} \right.$$

$$\left. + 2F\left(\frac{\mu_{i,j}^{n} + \mu_{i,j-1}^{n}}{2}\right)\left(\frac{u_{i,j}^{n} - u_{i,j-1}^{n}}{\Delta y_{j-1}}\right)\right] + \frac{1}{N_{Re}\rho_{i,j}^{n}}\left[D\mu_{i,j+1}^{n}\left(\frac{\partial v}{\partial x}\right)_{i,j+1}^{n} \right.$$

$$\left.\left. + E\mu_{i,j}^{n}\left(\frac{\partial v}{\partial x}\right)_{i,j}^{n} + F\mu_{i,j-1}^{n}\left(\frac{\partial v}{\partial x}\right)_{i,j-1}^{n}\right]\right\} \qquad (10)$$

where A, B, C, D, E, and F are coefficients arising from the differencing.

Second sweep

$$u_{i,j}^{n+1} = u_{i,j}^{n} + \Delta t \left\{ -u_{i,j}^{n}\left(\frac{\partial u}{\partial x}\right)_{i,j}^{n+1} - v_{i,j}^{n}\left(\frac{\partial v}{\partial y}\right)_{i,j}^{n+1} - \frac{1}{\rho_{i,j}^{n}}\left(\frac{\partial p}{\partial x}\right)_{i,j}^{n+1} \right.$$

(Equation continued on next page)

$$+\frac{4}{3N_{Re}\rho_{i,j}^{n}}\left[2A\left(\frac{\mu_{i+1,j}^{n+1}+\mu_{i,j}^{n}}{2}\right)\left(\frac{u_{i+1,j}^{n+1}-u_{i,j}^{n}}{\Delta x_i}\right)+2B\mu_{i,j}^{n}\left(\frac{\partial u}{\partial x}\right)_{i,j}^{n+1}\right.$$

$$\left.+2C\left(\frac{\mu_{i,j}^{n}+\mu_{i-1,j}^{n+1}}{2}\right)\left(\frac{u_{i,j}^{n}-u_{i-1,j}^{n+1}}{\Delta x_{i-1}}\right)\right]-\frac{2}{3N_{Re}\rho_{i,j}^{n}}\left[A\mu_{i+1,j}^{n+1}\left(\frac{\partial v}{\partial y}\right)_{i+1,j}^{n+1}+B\mu_{i,j}^{n}\left(\frac{\partial v}{\partial y}\right)_{i,j}^{n+1}\right.$$

$$\left.+C\mu_{i-1,j}^{n+1}\left(\frac{\partial v}{\partial y}\right)_{i-1,j}^{n+1}\right]+\frac{1}{N_{Re}\rho_{i,j}^{n}}\left[2D\left(\frac{\mu_{i,j+1}^{n+1}+\mu_{i,j}^{n}}{2}\right)\left(\frac{u_{i,j+1}^{n+1}-u_{i,j}^{n}}{\Delta y_j}\right)+2E\mu_{i,j}^{n}\left(\frac{\partial u}{\partial y}\right)_{i,j}^{n+1}\right.$$

$$\left.+2F\left(\frac{\mu_{i,j}^{n}+\mu_{i,j-1}^{n+1}}{2}\right)\left(\frac{u_{i,j}^{n}-u_{i,j-1}^{n+1}}{\Delta y_{j-1}}\right)\right]+\frac{1}{N_{Re}\rho_{i,j}^{n}}\left[D\mu_{i,j+1}^{n+1}\left(\frac{\partial v}{\partial x}\right)_{i,j+1}^{n+1}\right.$$

$$\left.\left.+E\mu_{i,j}^{n}\left(\frac{\partial v}{\partial x}\right)_{i,j}^{n+1}+F\mu_{i,j-1}^{n+1}\left(\frac{\partial v}{\partial x}\right)_{i,j-1}^{n+1}\right]\right\} \tag{11}$$

Alternating-Direction Implicit Method

The alternating-direction implicit (ADI) technique developed by Peaceman and Rachford (ref. 16) is a two-step procedure requiring reduction of tridiagonal matrices for which an efficient solution algorithm, the Thomas algorithm (ref. 17), exists. The method was originally applied to the two-dimensional heat conduction equation in reference 16 and later to a system of hyperbolic equations by Gourlay and Mitchell (ref. 18). For both of these model problems, it was shown to possess unconditional stability. The method, however, has not been extensively applied to the compressible Navier-Stokes equations. In 1966, Polezhaev (ref. 19) obtained solutions for a natural convection problem. His ADI method removed the diffusion time-step limitation; however, he found experimentally that the time step was still limited to the usual maximum explicit value. In 1973, Baum and Ndefo (ref. 4) published a two-dimensional implicit method based on the Peaceman-Rachford procedure. The Baum-Ndefo method iteratively solves nonlinear difference equations as a sequence of linear equations using a quasi-linearization technique. In a one-dimensional calculation of shock structure, the method was found to be stable for Courant numbers as large as 10. However, reference 4 does not consider the full Navier-Stokes equations. Later in 1973, Briley and McDonald (ref. 3) presented a method based on a fully implicit backward time difference scheme in which nonlinearities at the implicit time level are linearized by a Taylor's series expansion about the known time level. The

resulting system of multidimensional coupled linear difference equations is solved with a noniterative Douglas-Gunn ADI approach. The method was shown to be stable for very large Courant numbers in calculation of three-dimensional subsonic flow in a straight duct with rectangular cross section. For a flow with Mach number of 0.044 and a Reynolds number of 60, stable solutions were obtained for Courant numbers up to 1250. For a Mach number of 0.5 and a Reynolds number of 600, the time step was gradually increased as the solution progressed, resulting in an average Courant number of 73. Thus, the actual Courant number decreases with increasing Reynolds number, perhaps because of diagonal dominance problems as discussed in reference 3. The computational effort per time step was reported to be twice that of most explicit methods.

In the ADI procedure used in the present investigation, a sequential solution of the difference equations is obtained for each row during the first one-half time step (horizontal sweep) and for each column during the second one-half time step (vertical sweep). All spatial derivatives were approximated by centered finite differences; time derivatives, by backward differences. The nonlinear coefficients in the convective terms were lagged one-half time step. In addition, the pressure terms and cross-derivative terms were treated explicitly in each sweep. The temperature and viscosity were updated for the entire field after each sweep. The order of solution for each row and column is (1) x-momentum equation, (2) y-momentum equation, and (3) continuity equation. The solution is then marched to steady state without iteration. This ADI formulation requires two storage arrays for u, v, ρ, and μ and one for T.

To illustrate the ADI method, the finite-difference form of the x-momentum equation is shown. For the horizontal sweep, from time level n to an intermediate time denoted by $*$,

$$\rho_{i,j}^{n}\left(\frac{u_{i,j}^{*}-u_{i,j}^{n}}{\Delta t/2}\right)+\rho_{i,j}^{n}v_{i,j}^{n}\left(\frac{u_{i,j+1}^{n}-u_{i,j-1}^{n}}{2\,\Delta y}\right)+\rho_{i,j}^{n}u_{i,j}^{n}\left(\frac{u_{i+1,j}^{*}-u_{i-1,j}^{*}}{2\,\Delta x}\right)$$

$$=-\left(\frac{p_{i+1,j}^{n}-p_{i-1,j}^{n}}{2\,\Delta x}\right)+\frac{1}{N_{Re}\,\Delta y}\left[\left(\frac{\mu_{i,j+1}^{n}+\mu_{i,j}^{n}}{2}\right)\left(\frac{u_{i,j+1}^{n}-u_{i,j}^{n}}{\Delta y}\right)\right.$$

$$\left.-\left(\frac{\mu_{i,j}^{n}+\mu_{i,j-1}^{n}}{2}\right)\left(\frac{u_{i,j}^{n}-u_{i,j-1}^{n}}{\Delta y}\right)\right]+\frac{1}{N_{Re}\,\Delta y}\left[\mu_{i,j+1}^{n}\left(\frac{v_{i+1,j+1}^{n}-v_{i-1,j+1}^{n}}{2\,\Delta x}\right)\right.$$

$$\left.-\mu_{i,j-1}^{n}\left(\frac{v_{i+1,j-1}^{n}-v_{i-1,j-1}^{n}}{2\,\Delta x}\right)\right]+\frac{4}{3N_{Re}\,\Delta x}\left[\left(\frac{\mu_{i+1,j}^{n}+\mu_{i,j}^{n}}{2}\right)\left(\frac{u_{i+1,j}^{*}-u_{i,j}^{*}}{\Delta x}\right)\right.$$

(Equation continued on next page)

$$-\left(\frac{\mu^{n}_{i,j}+\mu^{n}_{i-1,j}}{2}\right)\left(\frac{u^{*}_{i,j}-u^{*}_{i-1,j}}{\Delta x}\right)\Bigg]-\frac{2}{3N_{Re}\,\Delta x}\Bigg[\mu^{n}_{i+1,j}\left(\frac{v^{n}_{i+1,j+1}-v^{n}_{i+1,j-1}}{2\,\Delta y}\right)$$

$$-\mu^{n}_{i-1,j}\left(\frac{v^{n}_{i-1,j+1}-v^{n}_{i-1,j-1}}{2\,\Delta y}\right)\Bigg] \tag{12}$$

The unknowns are $u^{*}_{i-1,j}$, $u^{*}_{i,j}$, and $u^{*}_{i+1,j}$. Similarly, for the vertical sweep, from * to n+1,

$$\rho^{*}_{i,j}\left(\frac{u^{n+1}_{i,j}-u^{*}_{i,j}}{\Delta t/2}\right)+\rho^{*}_{i,j}v^{*}_{i,j}\left(\frac{u^{n+1}_{i,j+1}-u^{n+1}_{i,j-1}}{2\,\Delta y}\right)+\rho^{*}_{i,j}u^{*}_{i,j}\left(\frac{u^{*}_{i+1,j}-u^{*}_{i-1,j}}{2\,\Delta x}\right)$$

$$=-\left(\frac{p^{*}_{i+1,j}-p^{*}_{i-1,j}}{2\,\Delta x}\right)+\frac{1}{N_{Re}\,\Delta y}\Bigg[\left(\frac{\mu^{*}_{i,j+1}+\mu^{*}_{i,j}}{2}\right)\left(\frac{u^{n+1}_{i,j+1}-u^{n+1}_{i,j}}{\Delta y}\right)$$

$$-\left(\frac{\mu^{*}_{i,j}+\mu^{*}_{i,j-1}}{2}\right)\left(\frac{u^{n+1}_{i,j}-u^{n+1}_{i,j-1}}{\Delta y}\right)\Bigg]+\frac{1}{N_{Re}\,\Delta y}\Bigg[\mu^{*}_{i,j+1}\left(\frac{v^{*}_{i+1,j+1}-v^{*}_{i-1,j+1}}{2\,\Delta x}\right)$$

$$-\mu^{*}_{i,j-1}\left(\frac{v^{*}_{i+1,j-1}-v^{*}_{i-1,j-1}}{2\,\Delta x}\right)\Bigg]+\frac{4}{3N_{Re}\,\Delta x}\Bigg[\left(\frac{\mu^{*}_{i+1,j}+\mu^{*}_{i,j}}{2}\right)\left(\frac{u^{*}_{i+1,j}-u^{*}_{i,j}}{\Delta x}\right)$$

$$-\left(\frac{\mu^{*}_{i,j}+\mu^{*}_{i-1,j}}{2}\right)\left(\frac{u^{*}_{i,j}-u^{*}_{i-1,j}}{\Delta x}\right)\Bigg]-\frac{2}{3N_{Re}\,\Delta x}\Bigg[\mu^{*}_{i+1,j}\left(\frac{v^{*}_{i+1,j+1}-v^{*}_{i+1,j-1}}{2\,\Delta y}\right)$$

$$-\mu^{*}_{i-1,j}\left(\frac{v^{*}_{i-1,j+1}-v^{*}_{i-1,j-1}}{2\,\Delta y}\right)\Bigg] \tag{13}$$

Finite-Element Method

The finite-element method has been used extensively for the numerical solution of structural mechanics problems for a number of years; however, the procedure has only recently been applied to fluid mechanics problems. (See pp. 240-257 of ref. 20.) Using a

stream-function—vorticity approach with linear elements, Baker (ref. 21) has developed an algorithm for steady viscous compressible flows. Solutions have been obtained for Reynolds numbers up to 7750. The present method appears to be the first finite-element procedure for the compressible Navier-Stokes equations in primitive variables.

The solution algorithm uses a Galerkin method with leapfrog time integration. The solution domain is discretized with triangular elements with bicubic trial functions. Figure 3 shows a finite-element mesh for case 1. As an example of a trial function, the density is of the form

$$\rho(x,y,t) = \sum_{J=1}^{10} \rho_J(t)\,\phi_J(x,y) \tag{14}$$

where J is the nodal index and the ϕ_J are the so-called B-spline basis functions which are piecewise cubic over the problem domain.

The unknown parameters in each trial function are the flow variable function values (ρ, u, and v) and their first partial derivatives (ρ_x, ρ_y, u_x, u_y, v_x, and v_y) at the triangle vertices and the function values alone at the triangle centroid. In the Galerkin approach, the weighted residuals formed by using the weights ϕ_J are set equal to zero. This yields a set of algebraic equations for the nodal values. Thus, if the governing equations are of the form

$$L(\omega) = 0$$

where ω is a general function, the Galerkin approach yields a set of equations

$$\iint_{\substack{\text{Solution}\\ \text{domain}}} \phi_J(\omega) = 0 \tag{15}$$

The time discretization scheme is similar to the Crank-Nicolson Galerkin method described by Douglas and Dupont (ref. 22). Centered time differences over two time steps, $n - 1$ to $n + 1$, and the averaging of space derivatives over times $n - 1$ and $n + 1$ yield second-order time truncation error. This spatial averaging also eliminates nonlinearities in the resulting implicit system of difference equations. The system of determining equations has the following form:

Continuity

$$D^n \vec{\rho}^{n+1} = \overline{FD}^{n,n-1} \tag{16}$$

Momentum equations

$$\begin{bmatrix} ZZ & ZR \\ RZ & RR \end{bmatrix}^{n} \begin{Bmatrix} \vec{u} \\ \vec{v} \end{Bmatrix}^{n+1} = \begin{Bmatrix} \overrightarrow{FU} \\ \overrightarrow{FV} \end{Bmatrix}^{n,n-1} \tag{17}$$

where $\vec{\rho}$ is the unknown density vector, $\vec{u}$ and $\vec{v}$ are vectors of unknowns from the x- and y-momentum equations, ZZ, ZR, RZ, RR, and D are nonsymmetric matrices with varying bandwidth, and $\overrightarrow{FD}$, $\overrightarrow{FU}$, and $\overrightarrow{FV}$ are vectors of known quantity.

The matrices in these equations are assembled at each time step. The continuity equation is solved with a standard triangular decomposition method which takes advantage of matrix sparseness. The momentum equations are solved with a unique block iterative LU solver developed during the present investigation. Despite large matrices and the accompanying problem of efficient data management, the use of cubic elements yields fourth-order spatial discretization error. Cubic elements also allow exact incorporation of first-derivative boundary conditions, unlike finite-difference methods which require a discretization. In addition, the triangular mesh allows the method to be easily adapted to nonrectangular solution domains.

Cubic Spline Integration Method

The potential of a cubic spline collocation procedure for the numerical solution of partial differential equations has been demonstrated by Rubin and Graves (ref. 23) for several model problems. This use of a cubic spline approximation for the evaluation of spatial gradients provides a highly efficient and accurate procedure for computation with a nonuniform mesh (which is necessary for high Reynolds number calculations in the physical plane) and/or curvilinear boundaries. The basic spline approximation leads to a second-order accurate expression for second derivatives, e.g., the diffusion terms in the momentum equations, for both a uniform mesh and an arbitrarily nonuniform mesh. First derivatives, i.e., the convective terms, are third-order accurate with a nonuniform mesh and fourth-order accurate with a uniform mesh. With a three-point finite-difference approximation, the order of the truncation error is significantly decreased with even a moderate variation in the mesh spacing (ref. 24). Thus, the spline procedure is more accurate than the usual finite-difference procedures for nonuniform grids. The spline method also allows accurate interpolation if grid realinement becomes necessary.

In addition, first- and second-derivative boundary conditions can be applied more accurately and more easily than with conventional finite-difference methods, since discretization is unnecessary. Unlike the finite-element or other Galerkin procedures, the evaluation of quadratures, which are generally not tridiagonal, is unnecessary.

In reference 23, Rubin and Graves present a detailed discussion of the general spline formulation and methodology for solving second-order quasi-linear partial differential equations. Therefore, only a brief description of the general cubic spline procedure is presented in this paper.

A cubic spline $S(x)$ is a continuous function which has continuous first and second derivatives on an interval $a < x < b$ (a and b are two arbitrary points) and corresponds to a cubic polynomial in each subinterval $x_{i-1} \leq x \leq x_i$. The mesh spacing h_i is defined by $h_i = x_i - x_{i-1}$.

The following tridiagonal formulas are obtained by enforcing the continuity requirements at the collocation points x_i:

$$\frac{h_i}{6} M_{i-1} + \frac{h_i + h_{i+1}}{3} M_i + \frac{h_{i+1}}{6} M_{i+1} = \frac{u_{i+1} - u_i}{h_{i+1}} - \frac{u_i - u_{i-1}}{h_i} \tag{18}$$

$$\frac{1}{h_i} m_{i-1} + 2\left(\frac{1}{h_i} + \frac{1}{h_{i+1}}\right) m_i + \frac{1}{h_{i+1}} m_{i+1} = \frac{3\left(u_{i+1} - u_i\right)}{h_{i+1}^2} + \frac{3\left(u_i - u_{i-1}\right)}{h_i^2} \tag{19}$$

where at $x = x_i$, $S\left(x_i\right) = u_i$, $S'\left(x_i\right) = m_i$, and $S''\left(x_i\right) = M_i$. The following useful relationships also exist between the first and second derivatives:

$$m_{i+1} - m_i = \frac{h_{i+1}}{2}\left(M_i + M_{i+1}\right) \tag{20}$$

$$m_i = \frac{h_i}{3} M_i + \frac{h_i}{6} M_{i-1} + \frac{u_i - u_{i-1}}{h_i} \tag{21}$$

$$m_i = -\frac{h_{i+1}}{3} M_i - \frac{h_{i+1}}{6} M_{i+1} + \frac{u_{i+1} - u_i}{h_{i+1}} \tag{22}$$

For a governing partial differential equation of the form

$$u_t = f\left(u, u_x, u_{xx}\right) \tag{23}$$

the approximate solution is found by considering the solution of

$$\left(u_t\right)_i = f\left(u_i, m_i, M_i\right) \tag{24}$$

where the time derivative is discretized in the usual finite-difference manner, i.e.,

$$\left(u_t\right)_i = \frac{u_i^{n+1} - u_i^n}{\Delta t} \tag{25}$$

As an example, consider an implicit solution of the linearized Burgers' equation, which has the general form of the momentum equations

$$u_t + uu_x = \nu u_{xx} \tag{26}$$

where

$$u = u(x,t) \qquad \nu = \nu(x,t)$$

The approximation for this equation becomes

$$u_i^{n+1} = u_i^n - \Delta t\left(u_i^{n+1} m_i^{n+1}\right) + \Delta t\left(\nu_i^{n+1} M_i^{n+1}\right) \tag{27}$$

With the spline relations (18) and (19), a system of $3N$ equations is generated for $3(N + 2)$ unknowns. This system can be written as

$$A_i \vec{V}_{i-1}^{n+1} + B_i \vec{V}_i^{n+1} + C_i \vec{V}_{i+1}^{n+1} = D_i \vec{V}_i^n \tag{28}$$

where $\vec{V}_i = \left[u_i, m_i, M_i\right]^T$ and A, B, C, and D are 3×3 coefficient matrices. Initial conditions are prescribed so that $u(x,0) = g(x)$. Equations (20) to (22) can be used, if necessary, to relate information at the boundaries and provide a closed system which can then be solved by the standard tridiagonal algorithm.

An alternate procedure can be derived by substituting u_i and m_i as functions of M_i. The resulting tridiagonal system for M_i has the form

$$a_i M_{i-1}^{n+1} + b_i M_i^{n+1} + c_i M_{i+1}^{n+1} = d_i \qquad (i = 1, \ldots, N) \tag{29}$$

This procedure is being used in the present application for the two momentum equations. If the partial differential equation to be solved has no second-derivative terms (e.g., the continuity equation), a tridiagonal system of equations in terms of m_i can also be found.

For the two-dimensional Navier-Stokes equations, a spline ADI procedure has been used. This two-step method applies the spline procedure to each of the one-half step ADI equations. The cross derivatives are found by using equation (19) with the cross derivatives being m_i and the appropriate first derivatives replacing u_i. The three governing equations are solved sequentially at each row and column during the horizontal and vertical sweeps, respectively.

The boundary conditions for u_{xx}, u_{yy}, v_{xx}, v_{yy}, ρ_x, and ρ_y are found by evaluating the appropriate governing equation at the boundary with the time derivative set equal to zero, to give in effect steady-state boundary conditions. The initial values of the second derivatives of u and v and first derivatives of ρ are obtained by fitting cubic splines to the given initial function values.

COMPUTATIONAL RESULTS

Subsonic Boundary Conditions

One of the major difficulties associated with the computation of case 1 is proper specification of boundary conditions for the region of subsonic flow, i.e., for the subsonic portion of the inflow jet profile, the peripheral inflow, and the subsonic portion of the downstream boundary. This boundary-condition problem was therefore studied for case 2 with $N_{Re} = 8.1 \times 10^4$ using hopscotch as well as a second-order Du Fort-Frankel procedure described by Gottlieb and Gustafsson in reference 25.

The mathematical analysis of boundary-condition specification by Gottlieb and Gustafsson (ref. 12) formed the basis for this study. At the left subsonic inflow boundary (see fig. 4), the analysis indicated that two of the three dependent variables (u, v, and ρ) must be specified. Since v was itself a characteristic variable in the x-direction, it had to be one of the two specified functions; u was the logical choice for the second. The density boundary condition was chosen to be $\rho_x = 0$. No difficulties were encountered in any of the calculations with this set of inflow boundary conditions. At the upper inflow boundary, u is a characteristic variable in the y-direction; therefore, again u and v were specified and $\rho_y = 0$ was selected as the third boundary condition. This combination created no numerical difficulties in any calculations. However, the combination of ρ and u specified with $v_y = 0$ usually led to erroneous values for v, especially in the region near the upper boundary where positive values of v, indicating outflow, occurred.

At the subsonic outflow boundary the one-dimensional analysis indicated that one function value, either ρ or u, must be specified. Of course such a boundary condition is not convenient for most applications since downstream function values are generally not known a priori. Figure 5 shows the results of calculations using hopscotch with three

different subsonic downstream boundary conditions. The boundary conditions used in the subsonic region are indicated in figure 4.

The initial flow field was obtained by setting the downstream (outflow) boundary values for u and v equal to one-half of their steady-state values (obtained from the parabolic code described in ref. 11) and linearly interpolating to obtain values at interior nodes. Computed steady-state profiles of the streamwise and normal velocity components u and v, respectively, at the downstream boundary are compared with results obtained with the parabolic technique. The streamwise component is accurately predicted for all three boundary conditions; however, only the specification of ρ gives a smooth and accurate v profile. Specifying u produces large oscillations in the v profile in the viscous region. These oscillations may be critical in turbulent flows when the turbulence model is locally a function of $\partial v/\partial y$. The least accurate results are obtained for linear extrapolation of all three function values.

The results of calculations with the Du Fort-Frankel procedure (see ref. 12) were identical to the hopscotch results with the exception that the linear extrapolation had to be altered to obtain converged solutions. Extrapolation of values at time level $n + 1$ to obtain boundary values does not work for any degree of extrapolation (linear, quadratic, etc.). Linear extrapolation of the form

$$f^{n+1}_{i_{max},j} = 2f^{n}_{i_{max}-1,j} - f^{n-1}_{i_{max}-2,j} \tag{30}$$

for ρ, u, and v, where i_{max} is the outflow boundary, gave results which converged to the correct steady state. The boundary condition

$$f^{n+1}_{i_{max},j} = f^{n}_{i_{max}-1,j} \tag{31}$$

which has been shown to be stable for scalar hyperbolic equations for the pure leapfrog scheme in reference 26, also gave good results. Using both values at $n + 1$ in equation (31) results in an unstable condition.

Parallel Mixing Calculations

Calculations of case 3 were made with the hopscotch and ADI methods for $N_{Re} = 10^3$ and 5×10^3. The supersonic inflow, supersonic outflow, and upper inflow boundary conditions shown in figure 4 were used. The computed steady state u and v velocity profiles and pressure profiles at $x = 0.15$ for $N_{Re} = 10^3$ are compared in figure 6 with the

corresponding calculation using a parabolic method. The ADI and hopscotch results are virtually identical with both procedures accurately predicting u and v. For this grid spacing ($\Delta x = \Delta y = 0.025$), the pressure shows high-frequency oscillations in the viscous mixing region, although the maximum oscillation is only about 2 percent of the correct value. For the initial flow field the $y = 0$ inflow profiles were also specified at all other x-stations downstream. The time step in the hopscotch calculation was 0.9 of the maximum allowed for stability, i.e., the Courant number N_{Co} was 0.9. Identical solutions were also obtained with ADI for $N_{Co} = 6$ but with no decrease in the total number of steps to steady state. The solution diverged for $N_{Co} = 12$.

At both $N_{Co} = 6$ and 12, the large time step was used for the entire solution. The probable cause of divergence at $N_{Co} = 12$ is roundoff error from the tridiagonal matrix inversion occurring when the coefficient matrix did not possess diagonal dominance, a sufficient but not necessary condition for convergence of the matrix reduction. In this instance the continuity equation was not diagonally dominant for any row in the horizontal sweep, and in addition, the two momentum equations lacked diagonal dominance for many rows.

Figure 7 contains the steady-state results at $x = 0.15$ for $N_{Re} = 5.0 \times 10^3$. Figure 7(a) shows that again the hopscotch and ADI results are virtually identical for u and v. With the same grid spacing as in the previous calculation, u is accurately predicted, whereas the v profile exhibits an oscillation in the viscous region. Halving the grid so that $\Delta x = \Delta y = 0.0125$ eliminated this oscillation. The pressure profile shown in figure 7(b) has very small oscillations for both grids with the hopscotch pressure varying less from the constant value given by the parabolic code than the ADI pressure. For $N_{Co} = 0.8$, with either grid, the ADI method required approximately 5 times as many steps for convergence to steady state as hopscotch. The solution was considered to be converged when

$$\frac{f_{i,j}^{n+1} - f_{i,j}^{n}}{\Delta t} \leq 0.01\, g_{i,j}^{n} \tag{32}$$

for $f = \rho$, u, and v at every point in the field and $g = \rho$, u, and u, respectively. Converged ADI solutions were obtained for $N_{Co} = 6$, but the solution again diverged for $N_{Co} = 12$. Hopscotch solutions were not attempted with Courant numbers significantly greater than one.

Figure 8 shows results of hopscotch calculations for case 3 with $N_{Re} = 8.1 \times 10^4$. Profiles of v and p are shown at the downstream boundary $x = 0.45$. The boundary conditions shown in figure 4 were used with function values obtained from the parabolic procedure providing the necessary specifications of v at the upper boundary and ρ at the downstream boundary. The initial field was obtained by using steady-state values of

all functions (obtained from parabolic code) at the downstream boundary and calculating the interior values by linear interpolation. This gives an initial flow field which is a good approximation of the steady-state field. For a grid spacing of $\Delta x = \Delta y = 0.025$, the hopscotch solution converged in 1637 time steps. The u velocity component was accurately predicted, and figure 8 ($\alpha = 0$ curve) shows that v also agreed with the parabolic results; however, small oscillations occurred in the pressure. It was found that the pressure could be smoothed by explicitly adding artificial diffusion to the continuity equation, that is,

$$\rho_t + (\rho u)_x + (\rho v)_y = \alpha(\Delta x)^2 \rho_{xx} + \alpha(\Delta y)^2 \rho_{yy} \tag{33}$$

Victoria and Widhopf (ref. 27) also found it necessary to add artificial diffusion to the continuity equation. For this case, $\alpha = 0.1$ smoothed the pressure without altering u or v; moreover, the solution converged in 1150 time steps. (The coefficient of ρ_{xx} is then approximately 5 to 10 times as large as the average coefficients of the viscous terms in the two momentum equations.) Although the solution converged in 1837 time steps for $\alpha = 1.0$, both p and v show oscillations. For $\alpha = 0$, a significantly different initial flow field was generated by halving u and v at the downstream edge and then linearly interpolating for interior values. Steady state was reached in 3050 steps with u, v, and p found to be identical to the previous results. For this grid, no converged ADI results were obtained with or without artificial diffusion. Oscillations in v in the mixing region grew with time, and the solution diverged.

The Du Fort-Frankel procedure with the downstream boundary condition given by equation (31) for u and v was compared with hopscotch which used linear extrapolation when the initial flow field was obtained by setting the outflow values of u and v to one-half of their steady-state values and linearly interpolating for interior values. Both solutions converged to steady state at approximately the same nondimensional time, although slightly different time steps were used in each method. The maximum difference in the u profiles was approximately 3 percent and occurred in the viscous region. This slight difference is attributed to the difference in explicit artificial diffusion in the two methods. Second-order diffusion with $\alpha = 0.1$ was used in hopscotch, and fourth-order diffusion was added to the Du Fort-Frankel procedure.

Results for Case 1

Computations were attempted for the original test problem, case 1, with a Reynolds number of 8.1×10^4 with the two finite-difference methods and with the finite-element method. A nonuniform grid was used for the finite-difference methods. From the sharp corner, Δy was increased by a factor of 1.05 for each successive spacing in the positive and negative y-directions from the smallest value, $\Delta y = 0.005$. Thus, grid points were

concentrated in the viscous mixing region. The grid also increased in the x-direction by a factor of 1.05 $\left(\Delta x_i / \Delta x_{i-1} = 1.05\right)$ for each successive spacing.

Computations with hopscotch were made with the boundary conditions of figure 4 along with a no-slip wall condition and constant density assumption near the wall. The upper boundary was approximately six jet diameters above the center line. Figure 9 shows steady-state hopscotch results for an interior x-location using linear extrapolation for density in the subsonic portion of the outflow boundary (extrapolation used since ρ is unknown). The magnitude of the peripheral velocity at the upper boundary was 0.07, which is several times greater than the natural entrainment for the same jet issuing into still air. Since the upper boundary effectively models a porous wall with nonuniform mass injestion into the boundary layer, it was necessary to modify the upper boundary conditions by setting $u_y = 0$. The results shown in figure 9 were obtained with $\alpha = 10$ after 3 hr of computing time on a CDC 6600 computer. As expected from the parallel mixing results, the u component is smooth and appears to be qualitatively correct. (There are no known experimental data for such a flow with which to compare the computed results.) The v profile shows the oscillation characteristic of using linear extrapolation for the subsonic outflow density. For some engineering applications, however, these results may be sufficient. The local increase in the pressure profile indicates the presence of a weak shock.

Fully converged ADI results were not obtained for case 1. With linear density extrapolation and the same nonuniform grid, the solutions appeared to be nearly converged after approximately 3 hr of CPU time on the CDC 6600, but the computations were not continued further since the results did not appear to be better than hopscotch. As with hopscotch, the u profiles were smooth and apparently qualitatively correct, although v again exhibited spatial oscillations.

At the present time, converged results have not been obtained with the finite-element method for this problem. The major difficulties appear to be the lack of sufficient spatial resolution in the viscous region and incorporation of the second-derivative downstream continuation boundary conditions. The 103-triangle mesh currently in use (shown in fig. 3) requires excessive machine storage and prohibits a significant increase in resolution.

The cubic spline algorithm has been coded, but presently no steady-state results have been obtained.

CODE COMPARISON

For case 1 the hopscotch code requires machine storage of approximately 50000_8 for 3045 node points, whereas the ADI method requires approximately 150000_8 for the same grid. The 103-triangle finite-element mesh which has 301 nodes requires 330000_8. The cubic spline algorithm will presumably require fewer grid points for accuracy comparable to the finite-difference results.

For each Δt step the CPU time on the CDC 6600 for hopscotch is 1.08×10^{-3} sec/node and for the ADI method, 3.74×10^{-3} sec/node. The finite-element code requires 1.93×10^{-1} sec/node to assemble the matrices and even with the fast block iterative solver, requires 4.25×10^{-2} sec/node for equation solution at each time step. No data are available for the spline code. (The Du Fort-Frankel code requires 1.28×10^{-3} sec/node for each time step.)

CONCLUDING REMARKS

A study of mixed supersonic-subsonic free shear flows has shown that correct calculation of the normal velocity component required specification of the density in the subsonic portion of the outflow boundary. The streamwise velocity was, however, correctly computed even when linear density extrapolation was used for this boundary.

For high Reynolds number flows (flows with small viscous terms in the momentum equations), it was necessary to add artificial diffusion in the continuity equation to eliminate oscillations in the static pressure. The addition of too much artificial viscosity had adverse effects on both the pressure and the normal component of velocity.

For the problems considered, the maximum allowable time step for the sequential alternating-direction implicit (ADI) procedure was less than 10 times the maximum explicit time step. This increase in time step, however, did not significantly improve the convergence rate. The hopscotch procedure, with a time step no greater than the maximum explicit time step, still converged faster than any of the ADI solutions. A fully coupled ADI procedure may allow larger time steps; however, the effect of large steps on convergence rate must be investigated.

The finite-element method with cubic elements appears to have excessive storage requirements and computing times. Therefore, as currently formulated, it does not appear to be a competitive procedure for high Reynolds number calculations in aerospace vehicle analysis.

REFERENCES

1. Peyret, Roger; and Viviand, Henri: Numerical Solution of the Navier-Stokes Equations for Compressible Fluids. ONERA T.P. No. 1319, 1973.

2. Taylor, T. D.: Numerical Methods for Predicting Subsonic, Transonic, and Supersonic Flow. AGARDograph No. 187, Jan. 1974.

3. Briley, W. R.; and McDonald, H.: An Implicit Numerical Method for the Multidimensional Compressible Navier-Stokes Equations. Rep. M911363-6 (Contract No. N00014-72-C-0183), United Aircraft Res. Lab., United Aircraft Corp., Nov. 1973. (Available from DDC as AD 770 224.)

4. Baum, Eric; and Ndefo, Ejike: A Temporal ADI Computational Technique. AIAA Computational Fluid Dynamics Conference, July 1973, pp. 133-140.

5. Victoria, Keith J.; and Steiger, Martin H.: Exact Solution of the 2-D Laminar Near Wake of a Slender Body in Supersonic Flow at High Reynolds Number. IAF Paper 55, Oct. 1970.

6. Carter, James E.: Numerical Solutions of the Navier-Stokes Equations for the Supersonic Laminar Flow Over a Two-Dimensional Compression Corner. NASA TR R-385, 1972.

7. MacCormack, Robert W.: The Effect of Viscosity in Hypervelocity Impact Cratering. AIAA Paper No. 69-354, Apr.-May 1969.

8. Holst, T. L.; and Tannehill, J. C.: Numerical Computation of Two-Dimensional Viscous Blunt Body Flows With an Impinging Shock. NASA CR-138594, 1974.

9. Baldwin, B. S.; and MacCormack, R. W.: Numerical Solution of the Interaction of a Strong Shock Wave With a Hypersonic Turbulent Boundary Layer. AIAA Paper No. 74-558, June 1974.

10. Holst, Terry L.; Tannehill, John C.; and Rakich, John V.: Numerical Computation of Viscous Blunt Body Flows With a Planar Impinging Shock. Aerodynamic Analyses Requiring Advanced Computers, Part II, NASA SP-347, 1975, pp. 1457-1471.

11. Oh, Y. H.: Analysis of Two-Dimensional Free Turbulent Mixing. AIAA Paper No. 74-594, June 1974.

12. Gottlieb, David; and Gustafsson, Bertil: On the Navier-Stokes Equations With Constant Total Temperature. NASA CR-132664, 1975.

13. Gourlay, A. R.: Hopscotch: A Fast Second-Order Partial Differential Equation Solver. J. Inst. Math. & Its Appl., vol. 6, no. 4, Dec. 1970, pp. 375-390.

14. Scala, Sinclaire M.; and Gordon, Paul: Solution of the Time-Dependent Navier-Stokes Equations for the Flow Around a Circular Cylinder. AIAA J., vol. 6, no. 5, May 1968, pp. 815-822.

15. Gourlay, A. R.; and Morris, J. Ll.: Hopscotch Difference Methods for Nonlinear Hyperbolic Systems. IBM J. Res. & Develop., vol. 16, no. 4, July 1972, pp. 349-353.

16. Peaceman, D. W.; and Rachford, H. H., Jr.: The Numerical Solution of Parabolic and Elliptic Differential Equations. J. Soc. Ind. & Appl. Math., vol. 3, no. 1, Mar. 1955, pp. 28-41.

17. Von Rosenburg, Dale U.: Methods for the Numerical Solution of Partial Differential Equations. American Elsevier Pub. Co., Inc., 1969.

18. Gourlay, A. R.; and Mitchell, A. R.: Alternating Direction Methods for Hyperbolic Systems. Numer. Math., Bd. 8, Heft 2, Apr. 4, 1966, pp. 137-149.

19. Polezhaev, V. I.: Numerical Solution of the System of Two-Dimensional Unsteady Navier-Stokes Equations for a Compressible Gas in a Closed Region. Fluid Dyn., vol. 2, no. 2, Mar.-Apr. 1967, pp. 70-74.

20. Norrie, Douglas H.; and De Vries, Gerard: The Finite Element Method. Academic Press, Inc., 1973.

21. Baker, A. J.: A Finite Element Solution Algorithm for the Navier-Stokes Equations. NASA CR-2391, 1974.

22. Douglas, Jim, Jr.; and Dupont, Todd: Galerkin Methods for Parabolic Equations. SIAM J. Numerical Anal., vol. 7, no. 4, Dec. 1970, pp. 575-626.

23. Rubin, Stanley G.; and Graves, Randolph A., Jr.: A Cubic Spline Approximation for Problems in Fluid Mechanics. NASA TR R-436, 1975.

24. Crowder, H. J.; and Dalton, C.: Errors in the Use of Nonuniform Mesh Systems. J. Comput. Phys., vol. 7, no. 1, Feb. 1971, pp. 32-45.

25. Gottlieb, David; and Gustafsson, Bertil: Generalized Du Fort-Frankel Methods for Parabolic Initial-Boundary-Value Problems. NASA CR-132653, 1975.

26. Gustafsson, Bertil; Kreiss, Heinz-Otto; and Sundström, Arne: Stability Theory of Difference Approximations for Mixed Initial Boundary Value Problems. II. Math. Comput., vol. 26, no. 119, July 1972, pp. 649-686.

27. Victoria, Keith J.; and Widhopf, George F.: Numerical Solution of the Unsteady Navier-Stokes Equations in Curvilinear Coordinates: The Hypersonic Blunt Body Merged Layer Problem. Proceedings of the Third International Conference on Numerical Methods in Fluid Mechanics, Volume II. Volume 19 of Lecture Notes in Physics, Henri Cabannes and Roger Teman, eds., Springer-Verlag, 1973, pp. 254-267.

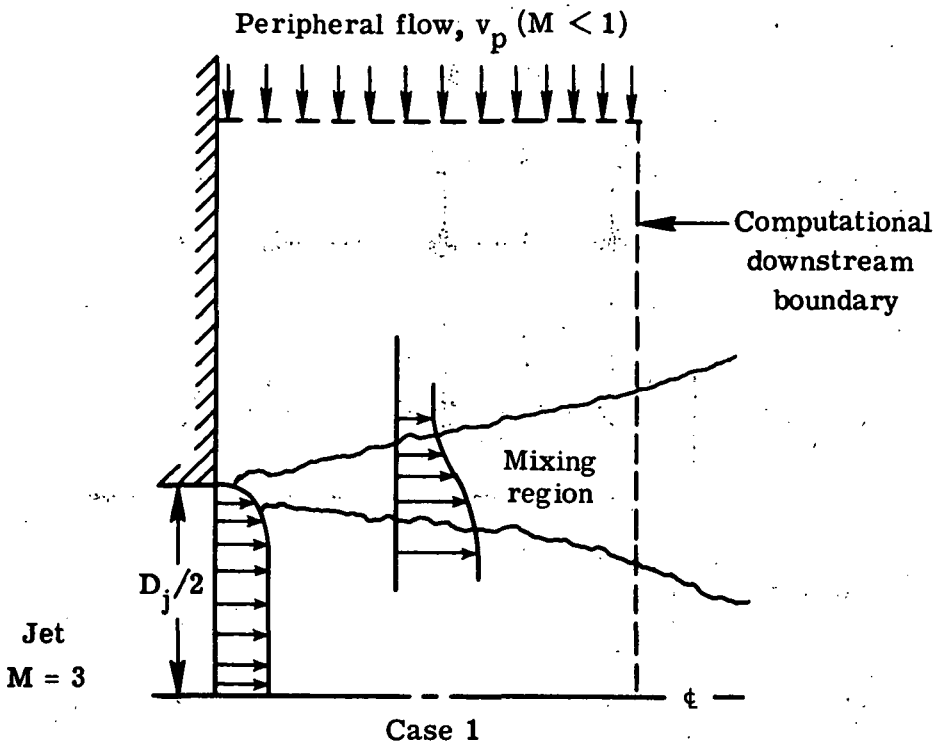

(a) Mixing of laminar supersonic jet with imposed peripheral flow normal to jet center line axis.

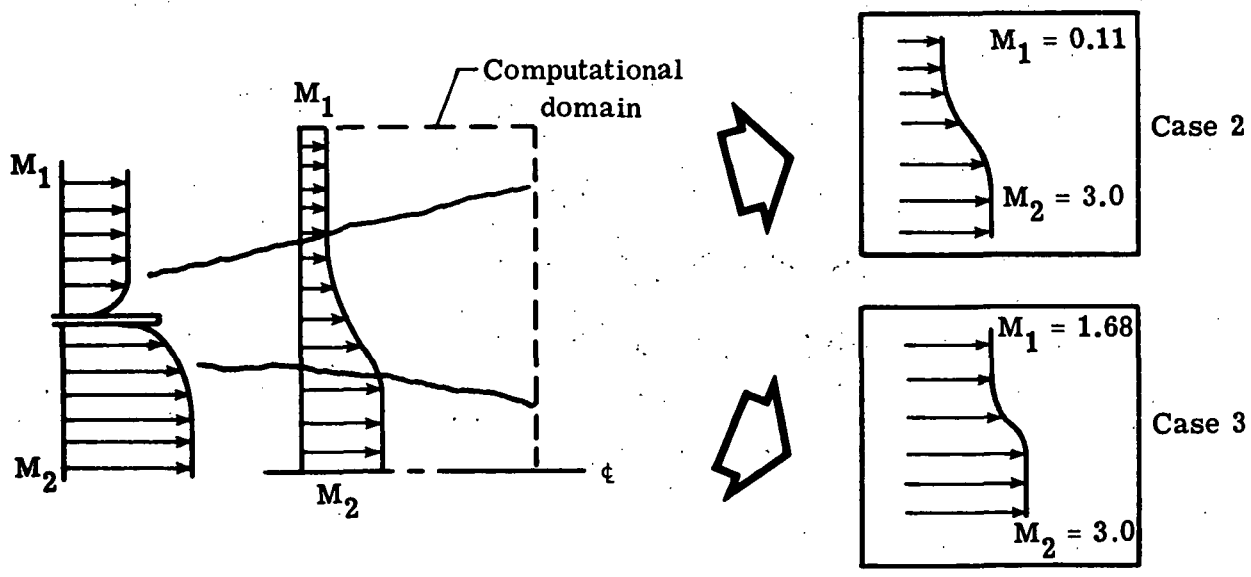

(b) Mixing of two parallel flows.

Figure 1.- Standard sample problems.

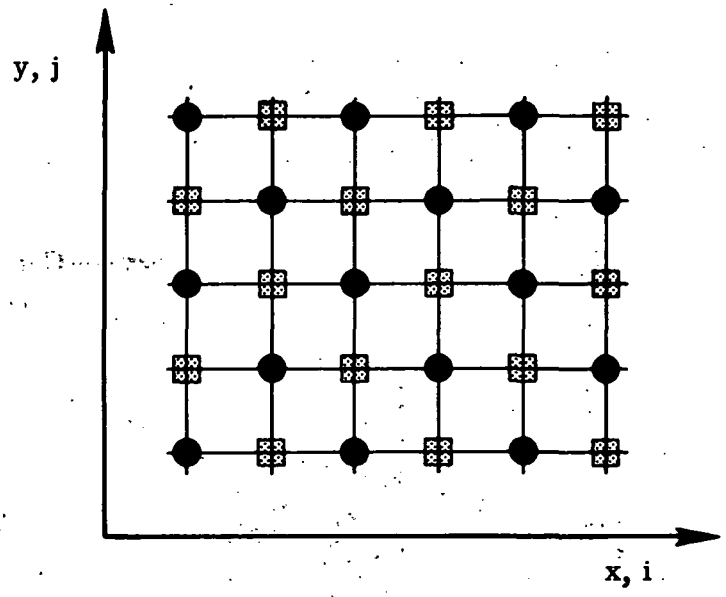

Figure 2.- Hopscotch grid.

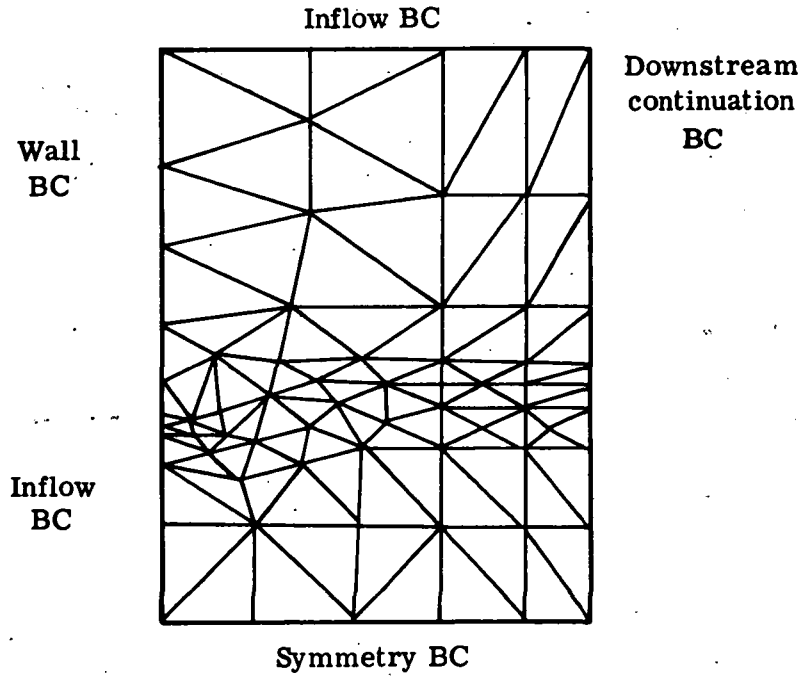

Figure 3.- Solution domain showing finite-element mesh for case 1 with 103 triangles with boundary conditions (BC) indicated.

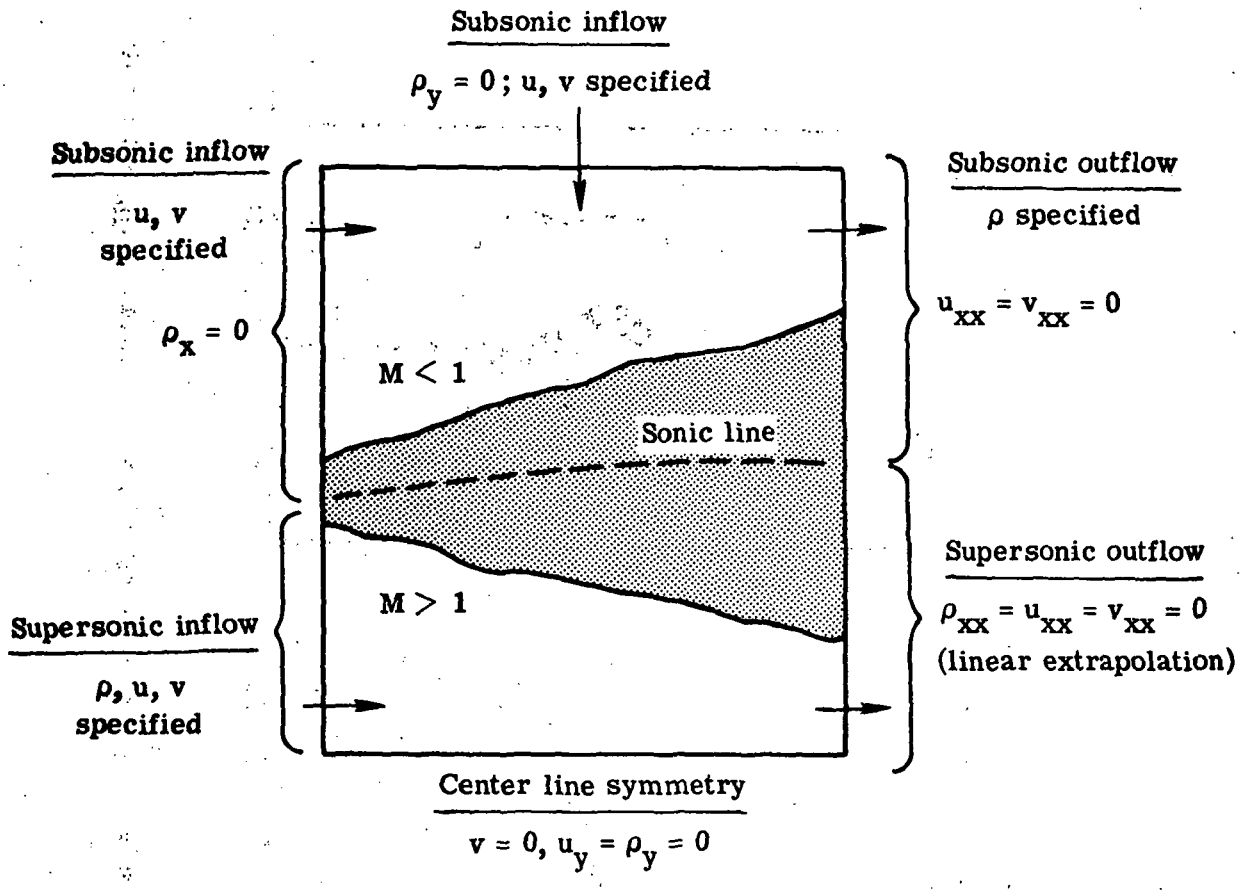

Figure 4. - Schematic of computational domain with best boundary conditions for case 2.

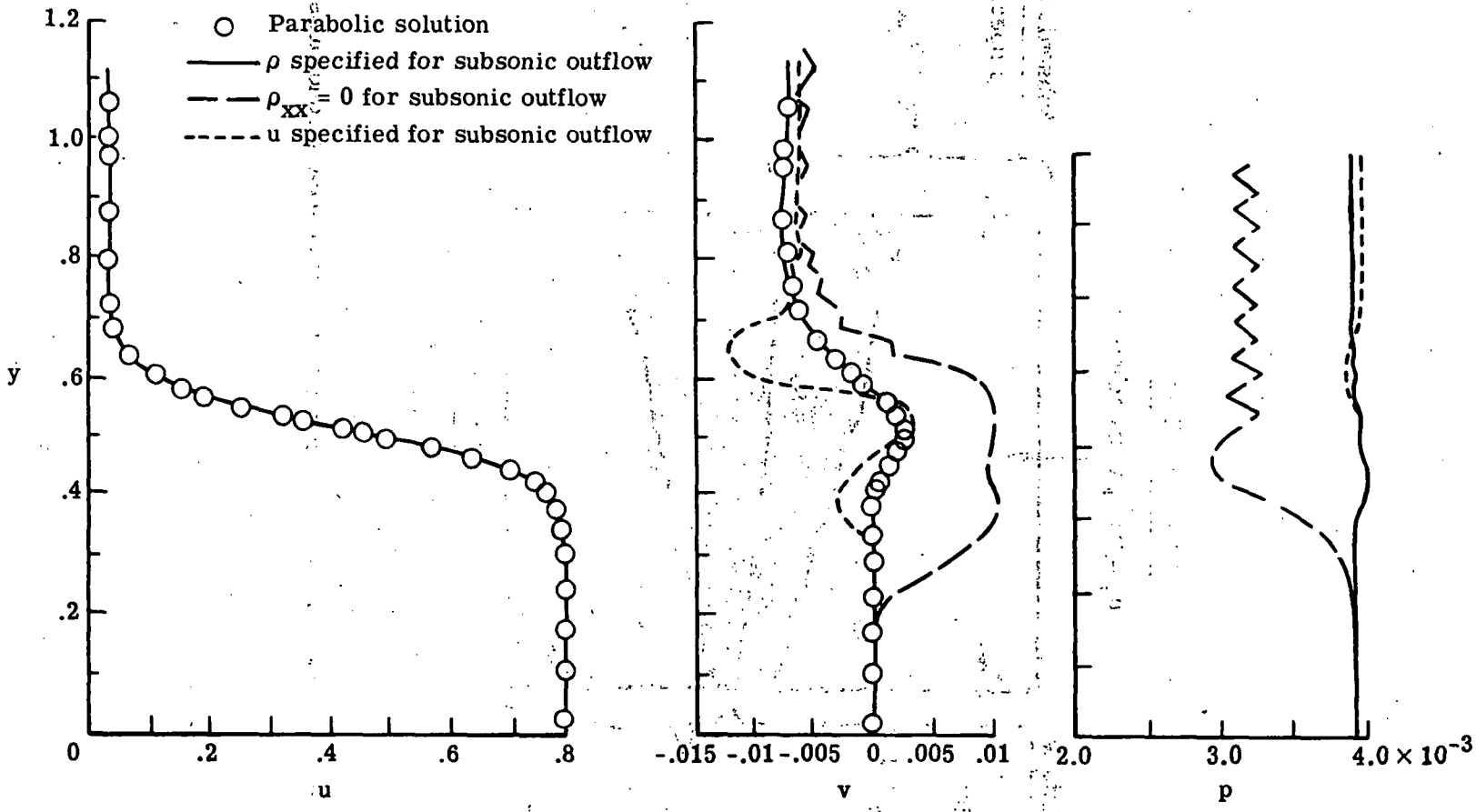

Figure 5.- Boundary-condition study for subsonic boundary. $N_{Re} = 8.1 \times 10^4$; $x = 0.45$.

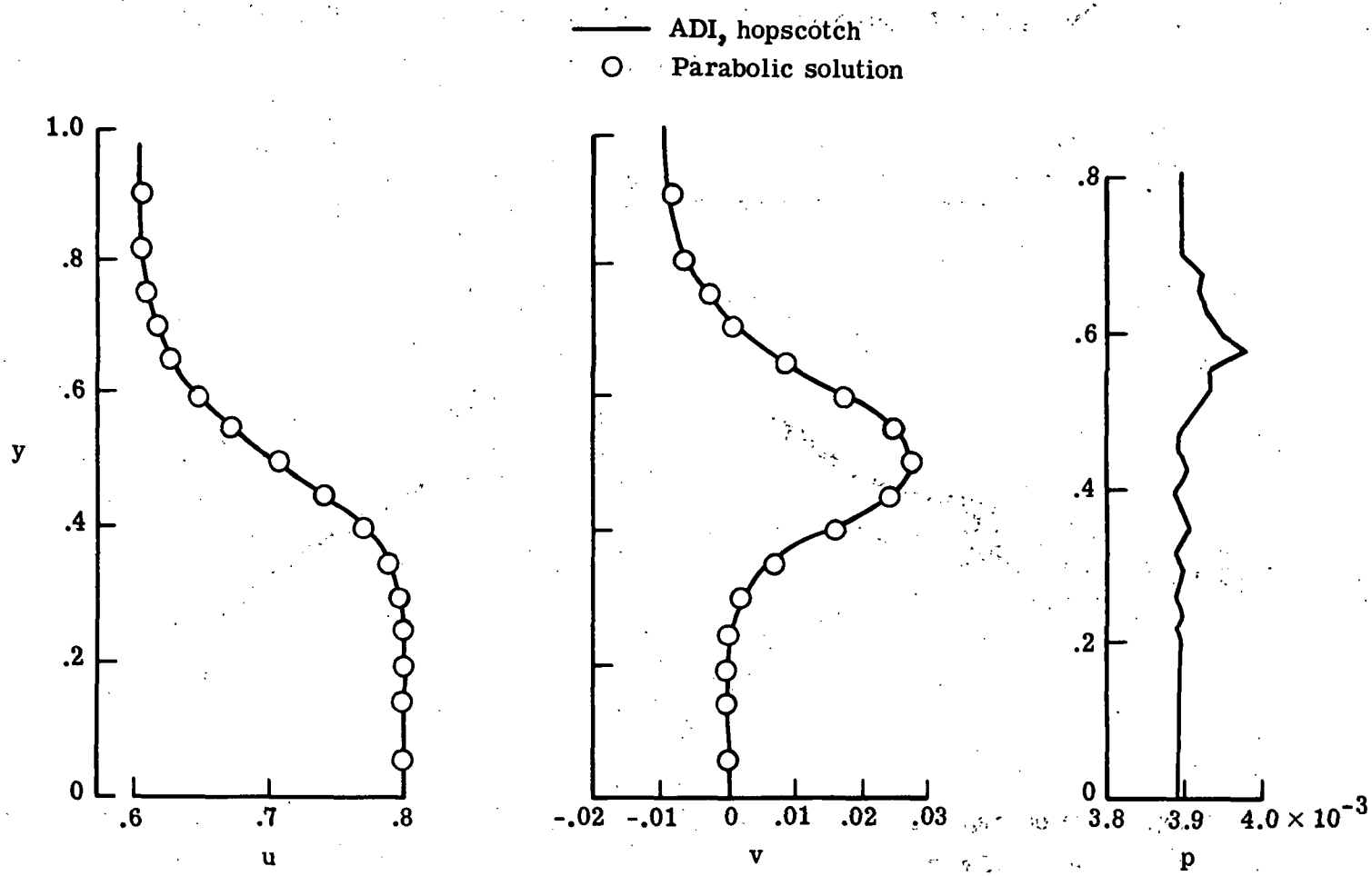

Figure 6.- Supersonic-supersonic mixing for $N_{Re} = 10^3$; $\Delta x = \Delta y = 0.025$; $N_{Co} = 0.9$.

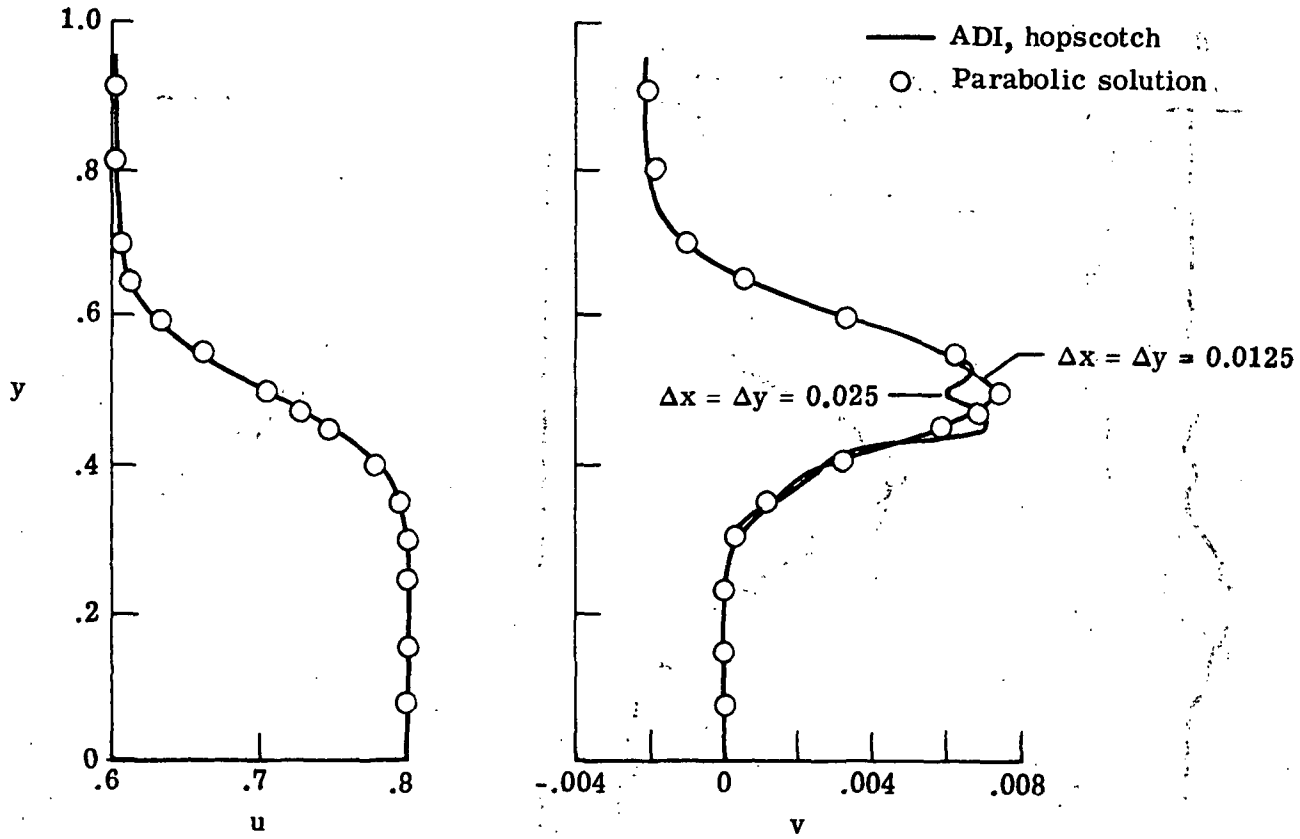

(a) Velocity profiles.

Figure 7.- Subsonic-supersonic mixing for $N_{Re} = 5 \times 10^3$. $x = 0.15$; $N_{Co} = 0.9$.

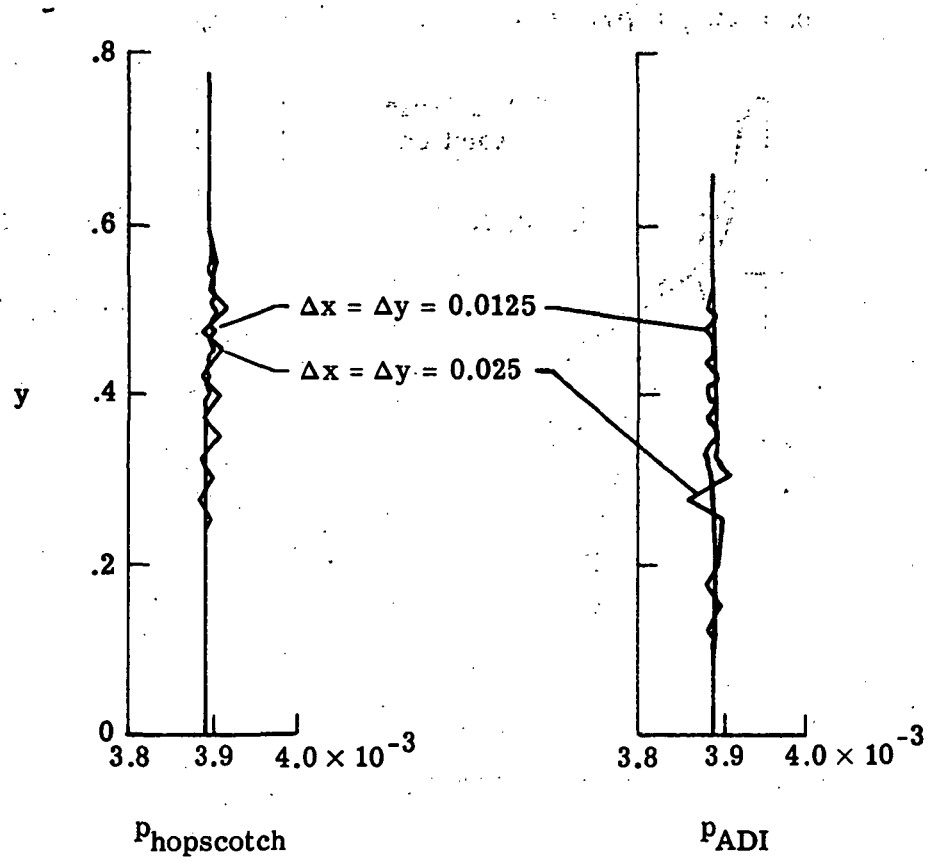

(b) Pressure profiles.

Figure 7.- Concluded.

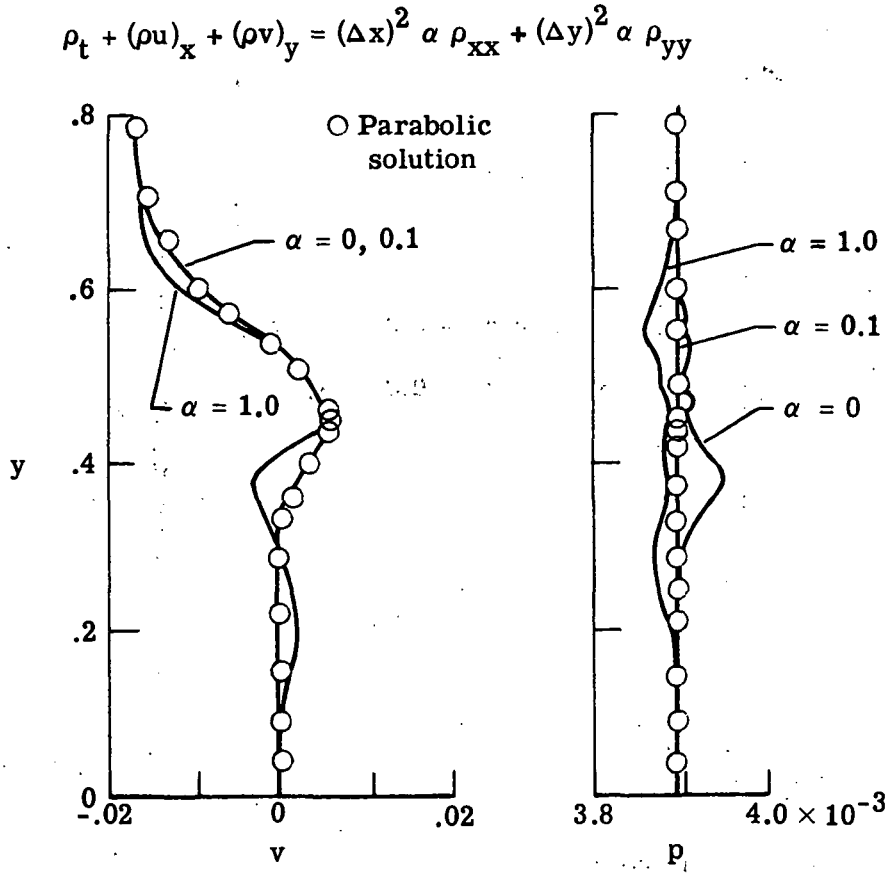

Figure 8.- Effect of artificial diffusion in continuity equation. $N_{Re} = 8.1 \times 10^4$; x = 0.45.

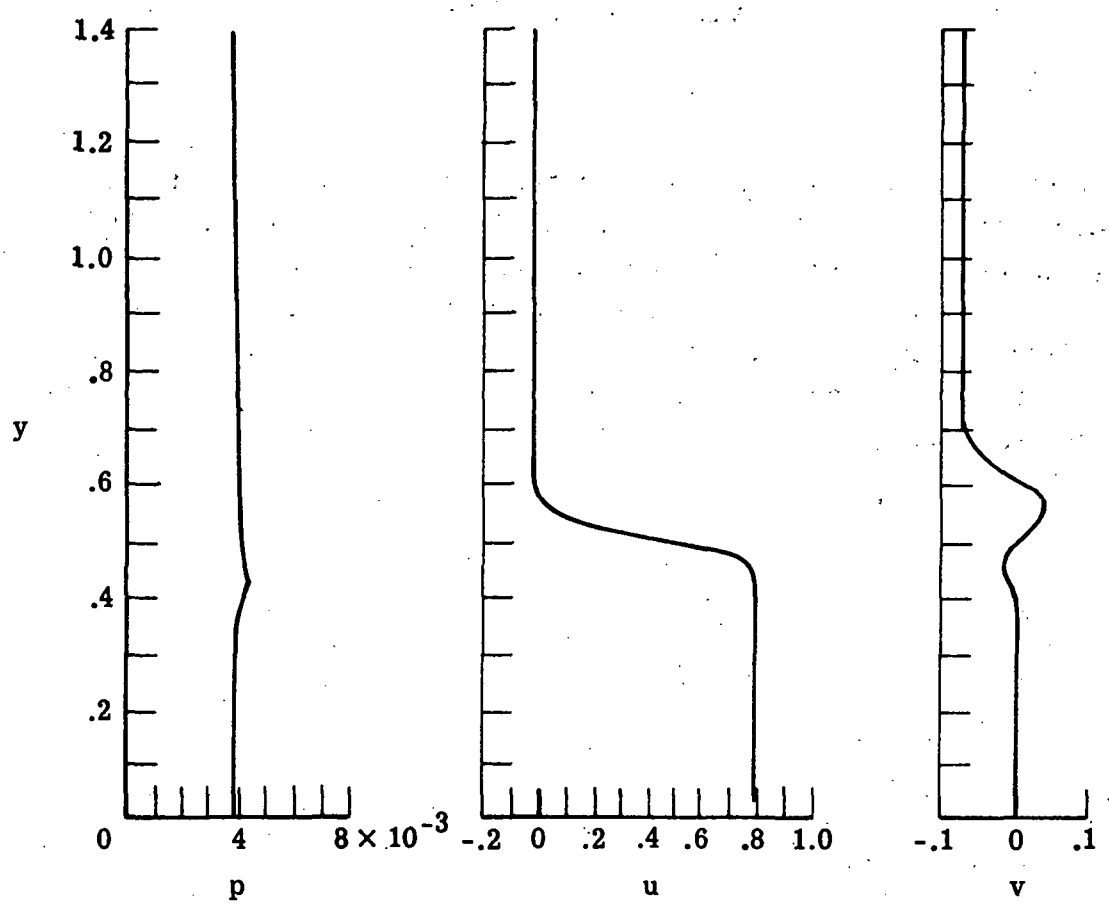

Figure 9.- Steady-state hopscotch results for case 1 with peripheral velocity of -0.07. $N_{Re} = 8.1 \times 10^4$; $x = 0.367$; $\alpha = 10$.

NUMERICAL SOLUTION OF THE NAVIER-STOKES EQUATIONS FOR ARBITRARY TWO-DIMENSIONAL AIRFOILS*

By Frank C. Thames, Joe F. Thompson, and C. Wayne Mastin
Mississippi State University

SUMMARY

A method of numerical solution of the Navier-Stokes equations for the flow about arbitrary airfoils or other bodies is presented. This method untilizes a numerically generated curvilinear coordinate system having a coordinate line coincident with the body contour. Streamlines, velocity profiles, and pressure and force coefficients for several airfoils and an arbitrary rock are given. Potential flow solutions are also presented. The procedure is also capable of treating multiple-element airfoils, and potential flow results are presented therefor.

INTRODUCTION

It is imperative in numerical solution of the Navier-Stokes equations that the boundary conditions be represented accurately in the finite-difference formulation, for the region in the immediate vicinity of solid surfaces is generally dominant in determining the character of the flow. The pressure and forces on solid bodies are directly dependent on the large gradients that prevail in this region near the surface, and accurate pressure and force coefficients require that these large gradients be represented accurately. This problem is accentuated at higher Reynolds numbers as the gradients become more severe.

Therefore, almost all numerical solutions of the Navier-Stokes equations generated to date have treated bodies for which a natural coordinate system is available – circles, ellipses, spheres, Joukowski airfoils, and so forth. (Natural coordinate systems as defined here are those for which the body contour under consideration coincides with a constant coordinate line.) The paper by Mehta and Lavan (ref. 1) has given a solution about a modified Joukowski airfoil accomplished by generating a natural coordinate system with a conformal Joukowski transformation and solving the Navier-Stokes equations on this system. The basic Joukowski transformation was modified somewhat by rounding the trailing edge and contracting the coordinates near the body. Only one case

*Research sponsored by NASA Langley Research Center under Grant NGR 25-001-055.

was run – a stalled flow at a 15° angle of attack and a Reynolds number of 1000. The method is limited to those bodies which can be generated by the Joukowski transformation (symmetric and cambered Joukowski airfoils, flat plates, and circular and elliptic cylinders) and does not have general applicability. Arbitrary two-dimensional bodies have not been successfully attacked as yet, primarily because of the difficulty of accurate representation of the boundary conditions and the large gradients near solid surfaces when no coordinate line is coincident with the body contour. Some solutions have been attempted with interpolation between grid points for boundaries not coincident with coordinate lines, but this necessarily introduces irregularity into an otherwise smooth boundary and places the most inaccurate difference representation in precisely the region of greatest sensitivity. Dawson (ref. 2) attempted to create a method for general bodies by the use of two uniform rectangular grids: a fine inner grid surrounding the body and extending for perhaps one characteristic body dimension, and a coarse outer grid surrounding the inner grid and extending outward for perhaps 10 to 12 body diameters. The two grids overlap to allow for accurate transition between the two mesh systems. Only a circular cylinder solution was attempted, and this solution was restricted to small Reynolds numbers ($R \leq 1000$) because of boundary instabilities.

A method of automatic numerical generation of a general curvilinear coordinate system with coordinate lines coincident with all boundaries of a general multiconnected region containing any number of arbitrarily shaped bodies has, however, been developed which should alleviate this problem with arbitrary bodies (ref. 3). The curvilinear coordinates are generated as the solution of two elliptic partial differential equations with Dirichlet boundary conditions, one coordinate being specified to be constant on each of the boundaries, and a distribution of the other being specified along the boundaries. These equations are solved in finite-difference approximation by successive overrelaxation (SOR) iteration. No restrictions are placed on the shape of the boundaries, which may even be time dependent, and the method is not restricted to two dimensions or single bodies. Coordinate lines may be concentrated as desired along the boundaries. Spacing of the coordinate lines encircling the body may be controlled by adjusting parameters in the partial differential equations for the coordinates.

Regardless of the shape and number of the bodies and regardless of the spacing of the curvilinear coordinate lines, all numerical computations, both to generate the coordinate system and subsequently to solve the Navier-Stokes equations on the coordinate system, are done on a rectangular grid with a square mesh, that is, in the transformed plane. It is also possible to cause the natural coordinate system to change in time as desired and still have all computation done on the fixed rectangular grid with square mesh. This allows the curvilinear coordinate system in the physical plane to deform with a deforming body, blast front, shock, free surface, or any other boundary, keeping a coordinate line always coincident with the boundary at all times. The physical coordinate

system has been, in effect, eliminated from the problem, at the expense of adding two elliptic equations to the original system.

Since the curvilinear coordinate system has coordinate lines coincident with the surface contours of all bodies present, all boundary conditions may be expressed at grid points. Also, normal derivatives on the bodies may be represented by using only finite differences between grid points on coordinate lines, without need of any interpolation, even though the coordinate system is not orthogonal at the boundary. Numerical solutions for the lifting and nonlifting potential flow about Kármán-Trefftz airfoils obtained with this coordinate-system generation show excellent comparison with the analytic solutions.

This method of automatic body-fitted curvilinear coordinate generation has been used to construct a finite-difference solution of the full, incompressible, time-dependent, Navier-Stokes equations for the laminar viscous flow about arbitrary two-dimensional airfoils or any other two-dimensional body (ref. 4). The Navier-Stokes equations are written in the vorticity—stream-function formulation, with the vorticity on the body being determined by a type of false-position iteration so that the no-slip boundary condition is satisfied. The solution is implicit in time, the vorticity and the stream-function equations being solved simultaneously at each time step by SOR iteration. A method of controlling the spacing of the coordinate lines encircling the body has been developed in order to treat high Reynolds number flow, since the coordinate lines must concentrate near the surface to a greater degree as the Reynolds number increases. The solution is designed to provide the velocity field, the surface-pressure distribution, and the lift, drag, and moment coefficients. Results are given for separated flow over two airfoils and an arbitrary rock. Initial application to multiple airfoils has also been made.

SYMBOLS

a,b,c,d	coefficients in equations (5)
C_A	axial-force coefficient
C_D	drag coefficient
C_{D_F}	friction-drag coefficient
C_{D_P}	pressure-drag coefficient
C_L	lift coefficient

C_N	normal-force coefficient
C_p	pressure coefficient
C_p^*	pressure coefficient referenced to trailing-edge pressure
D	differential operator; two-dimensional region (fig. 1)
D*	rectangular region (fig. 1)
ds	increment of arc length along body surface
E	maximum norm
$\underset{\sim}{F}$	force on body
f	function
i,j	computational grid points; i = 1 . . . I; j = 1 . . . J
$\underset{\sim}{i},\underset{\sim}{j}$	unit vectors
J	Jacobian
k	iteration counter
M,N	summation limits (eqs. (5))
m,n	indices
$\underset{\sim}{n}$	unit vector normal to body surface
P,Q	amplitude factors (eqs. (5))
p	pressure
R	Reynolds number
S	body surface

$\underset{\sim}{T}_n$	stress vector on body surface
t	time
t_n	current time
$\underset{\sim}{V}$	velocity
$V_{\underset{\sim}{t}}$	tangential velocity component
x,y	physical coordinates (nondimensionalized by airfoil chord)
α,β,γ	coefficients of natural coordinate transformation (eqs. (3))
$\Gamma_1, \Gamma_2, \ldots, \Gamma_8$	curves in physical plane
$\Gamma_1^*, \Gamma_2^*, \ldots, \Gamma_8^*$	curves in transformed plane
ϵ	convergence factor
δ	relaxation factor
θ	free-stream angle of attack
λ	coefficient in stream-function equation
ξ,η	transformed coordinates
σ,τ	coefficients in equation (9a)
ψ	stream function
ψ_b	value of ψ at body
ω	vorticity
ω_b	value of ω at body

Superscripts:

L	lower surface
U	upper surface
*	transformation

Subscripts:

L	lower surface
o	trailing edge (fig. 4)
T.E.	trailing edge
U	upper surface
x,y	differentiation with respect to x or y
ξ,η	differentiation with respect to ξ or η
∞	free stream

BODY-FITTED CURVILINEAR COORDINATE SYSTEM

Mathematical Development

Let it be desired to transform the two-dimensional, doubly connected region D bounded by two closed contours of arbitrary shape into a rectangular region D*, as shown in figure 1. The general transformation from the physical plane $[x,y]$ to the transformed plane $[\xi,\eta]$ is given by $\xi = \xi(x,y)$, $\eta = \eta(x,y)$. Similarly, the inverse transformation is given by $x = x(\xi,\eta)$, $y = y(\xi,\eta)$. Derivatives are transformed as follows:

$$f_x = \frac{\partial(f,y)/\partial(\xi,\eta)}{\partial(x,y)/\partial(\xi,\eta)} = \frac{y_\eta f_\xi - y_\xi f_\eta}{J} \tag{1a}$$

$$f_y = \frac{\partial(x,f)/\partial(\xi,\eta)}{\partial(x,y)/\partial(\xi,\eta)} = \frac{-x_\eta f_\xi + x_\xi f_\eta}{J} \tag{1b}$$

where J is the Jacobian of the transformation $J = x_\xi y_\eta - x_\eta y_\xi$.

Since the basic idea of the transformation is to generate transformation functions such that all boundaries are coincident with coordinate lines, the natural coordinates $[\xi,\eta]$ are taken as solutions of some suitable elliptic boundary value problem with one of these coordinates constant on the boundaries. Using Laplace's equation as the generating elliptic system gives

$$\xi_{xx} + \xi_{yy} = 0 \tag{2a}$$

$$\eta_{xx} + \eta_{yy} = 0 \tag{2b}$$

with Dirichlet boundary conditions: η = Constant = η_1 on Γ_1, η = Constant = η_2 on Γ_2, and $\xi(x,y)$ a multiple-valued solution with a branch of $\xi(x,y)$ specified (but not constant) on Γ_1 and Γ_2. The curve Γ_1 on the physical plane transforms to the lower boundary Γ_1^* of the transformed plane. Similarly, Γ_2 transforms to Γ_2^*, and so forth. The right and left boundaries of the rectangular transformed plane Γ_3^* and Γ_4^* are coincident in the physical plane. The curve which transforms to these boundaries connects Γ_1 and Γ_2 and determines a branch cut for the multiple-valued function $\xi(x,y)$. Thus the functions and all derivatives are continuous across this cut.

Now since it is desirable to do all numerical computation in the rectangular transformed plane, it is necessary to interchange the dependent and independent variables in equations (2). Thus

$$\alpha x_{\xi\xi} - 2\beta x_{\xi\eta} + \gamma x_{\eta\eta} = 0 \tag{3a}$$

$$\alpha y_{\xi\xi} - 2\beta y_{\xi\eta} + \gamma y_{\eta\eta} = 0 \tag{3b}$$

where

$$\alpha = x_\eta^2 + y_\eta^2 \tag{3c}$$

$$\beta = x_\xi x_\eta + y_\xi y_\eta \tag{3d}$$

$$\gamma = x_\xi^2 + y_\xi^2 \tag{3e}$$

with the transformed boundary conditions: $x = f_1(\xi,\eta_1)$ on Γ_1^*, $y = g_1(\xi,\eta_1)$ on Γ_1^*, $x = f_2(\xi,\eta_2)$ on Γ_2^*, and $y = g_2(\xi,\eta_2)$ on Γ_2^*. (In the present application, x and y are nondimensionalized with respect to the airfoil chord.)

The natural coordinate system so generated has a constant η-line coincident with each boundary in the physical plane. The ξ-lines may be spaced in any manner desired around the boundaries by specification of $[x,y]$ at the equispaced ξ-points on the η_1- and

η_2-lines of the transformed plane. Control of the spacing of the η-lines may be exercised by varying the elliptic system of which ξ and η are solutions.

Extension to Multiple Bodies

The same procedure for natural coordinate generation may be extended to regions that are more than doubly connected, that is, have more than two closed boundaries or, equivalently, more than one body or hole within a single outer boundary. The transformation to the rectangular field is illustrated in figure 2.

The method requires that the η-coordinate be equal to the same constant on all the interior boundaries, that is, on all bodies in the field. Let all the bodies be connected by arbitrary cuts and, similarly, one body be connected to the outer boundary by an arbitrary cut. Since the η-coordinate is equal to the same constant on all the bodies, it is, of course, equal to that constant on the cuts between the bodies also. By contrast, the ξ-coordinate is taken constant on the cut between the body and the outer boundary. Since the locations of these cuts in the physical plane are not specified, the specification of η or ξ as constant on a cut does not overspecify the elliptic problem.

Note that all bodies except one are split into two segments. Each cut appears twice on the transformed field boundary, the two segments, of course, corresponding to the two "sides" of the cut in the physical plane and thus being reentrant boundaries with the functions and all derivatives continuous thereon. Thus x and y have been specified on the portions of the lower boundary of the transformed field that correspond to the bodies – Γ_7^* and Γ_8^* for the right body and Γ_1^* for the left body – and also on the entire upper boundary, corresponding to the outer boundary in the physical field. The remaining portions of the lower boundary and the entire side boundaries are reentrant boundaries and, thus, neither require nor allow specification of $[x,y]$ thereon.

Again an elliptic Dirichlet problem is solved to generate the natural coordinates $[x,y]$, as in the previously considered case with only a single body. All computations, both to generate the coordinates and subsequently to solve the partial differential system of interest, are again done on the rectangular field with square mesh in the transformed plane.

Numerical Solution

The relation between the transformed and physical fields for a single airfoil is shown in figure 3(a). The physical coordinates of I points describing the body surface $[x,y]$ provide the boundary conditions along the $j = 1$ line; those of I points on the physical remote boundary, usually a circle with radius 10 or more chords, supply the boundary conditions along the $j = J$ line of the transformed field. Since the side boundaries of the transformed field are reentrant, corresponding to the cut in the physical

plane, then $f_{I,j} = f_{1,j}$ and $f_{I+1,j} = f_{2,j}$ for all j. Note that the values of x and y are not specified on these side boundaries. All derivatives in equations (3) are approximated by second-order, central-difference expressions ($\Delta\xi$ and $\Delta\eta$ are both unity by construction, the actual values of ξ and η being immaterial):

$$(f_\xi)_{ij} \approx \frac{1}{2}(f_{i+1,j} - f_{i-1,j}) \tag{4a}$$

$$(f_\eta)_{ij} \approx \frac{1}{2}(f_{i,j+1} - f_{i,j-1}) \tag{4b}$$

$$(f_{\xi\xi})_{ij} \approx f_{i+1,j} - 2f_{ij} + f_{i-1,j} \tag{4c}$$

$$(f_{\eta\eta})_{ij} \approx f_{i,j+1} - 2f_{ij} + f_{i,j-1} \tag{4d}$$

$$(f_{\xi\eta})_{ij} \approx \frac{1}{4}(f_{i+1,j+1} - f_{i+1,j-1} - f_{i-1,j+1} + f_{i-1,j-1}) \tag{4e}$$

The resulting set of $2I(J - 1)$ nonlinear difference equations, two for each point $[i,j]$ for $i = 1, 2, \ldots, I - 1$ and $j = 2, 3, \ldots, J - 1$, were solved by accelerated Gauss-Seidel (SOR) iteration. The iteration was considered to have converged when the maximum absolute change on the field between iterations was less than 10^{-5}. A range of acceleration parameters was examined, and a value of 1.85 was nearly optimum for the bodies considered.

The relation between the transformed and physical fields for two airfoils is shown in figure 3(b). The physical coordinates of body 2 at points $i = 1 \ldots I1$, those of body 1 at points $i = I2 \ldots I3$, and finally the remaining points $i = I4 \ldots I$ on body 2 are input as boundary conditions on the $j = 1$ line in the transformed plane. The remaining points $i = (I1 + 1) \ldots (I2 - 1)$ and $i = (I3 + 1) \ldots (I4 - 1)$ on the $j = 1$ line are reentrant points corresponding to the cut between the bodies in the physical plane. Therefore values at these points are not specified, but rather the relations $f_{I1+k,1} = f_{I4-k,1}$ and $f_{I1+k,0} = f_{I4-k,2}$ for $k = 1 \ldots (I2 - I1 - 1)$ hold. The rest of the procedure is unchanged from the case of a single airfoil, except that two difference equations at each of the points $[i,1]$ for $i = (I1 + 1) \ldots (I2 - 1)$ are added to the system, so that the total number of equations is now $2I(J - 1) + 2(I2 - I1 - 1)$.

Control of Coordinate System

Several procedures for controlling the spacing of the coordinate lines in the field are available and the general philosophy of such control is discussed in reference 3. One particularly effective procedure is to add exponential inhomogeneous terms to the

Laplace equations for the curvilinear coordinates, so that the coordinates are generated as the solutions of

$$\xi_{xx} + \xi_{yy} = \sum_{m=1}^{M} a_m \frac{\xi - \xi_m}{|\xi - \xi_m|} \exp\left(-c_m|\xi - \xi_m|\right)$$

$$+ \sum_{n=1}^{N} b_n \frac{\xi - \xi_n}{|\xi - \xi_n|} \exp\left[-d_n\sqrt{(\xi - \xi_n)^2 + (\eta - \eta_n)^2}\right] \equiv P \tag{5a}$$

$$\eta_{xx} + \eta_{yy} = \sum_{m=1}^{M} a_m \frac{\eta - \eta_m}{|\eta - \eta_m|} \exp\left(-c_m|\eta - \eta_m|\right)$$

$$+ \sum_{n=1}^{N} b_n \frac{\eta - \eta_n}{|\eta - \eta_n|} \exp\left[-d_n\sqrt{(\xi - \xi_n)^2 + (\eta - \eta_n)^2}\right] \equiv Q \tag{5b}$$

where the amplitudes and decay factors are not necessarily the same in the two equations. Here the first terms have the effect of attracting ξ-lines to the ξ_m-lines in the ξ-equation, and attracting η-lines to the η_m-lines in the η-equation. The second terms cause ξ-lines to be attracted to the points $[\xi_n,\eta_n]$ in the ξ-equation, with a similar effect on η-lines in the η-equation.

In the transformed plane these equations become

$$\alpha x_{\xi\xi} - 2\beta x_{\xi\eta} + \gamma x_{\eta\eta} = -J^2\left(Px_\xi + Qx_\eta\right) \tag{6a}$$

$$\alpha y_{\xi\xi} - 2\beta y_{\xi\eta} + \gamma y_{\eta\eta} = -J^2\left(Py_\xi + Qy_\eta\right) \tag{6b}$$

POTENTIAL-FLOW SOLUTION

Laplace Equation and Boundary Conditions

The two-dimensional irrotational flow about any number of bodies may be described by the Laplace equation for the stream function ψ:

$$\psi_{xx} + \psi_{yy} = 0 \tag{7}$$

with boundary conditions:

On the body surface,

$$\psi(x,y) = \psi_o \tag{8a}$$

At infinity,

$$\psi(x,y) = y \cos\theta - x \sin\theta \tag{8b}$$

where θ is the angle of attack of the free stream relative to the positive x-axis. Here the stream function is nondimensionalized relative to the airfoil chord and the free-stream velocity. When transformed to the curvilinear coordinate system, this equation becomes

$$\alpha\psi_{\xi\xi} - 2\beta\psi_{\xi\eta} + \gamma\psi_{\eta\eta} + \sigma\psi_{\eta} + \tau\psi_{\xi} = 0 \tag{9a}$$

where α, β, and γ are defined by equations (3c) to (3e) and σ and τ are given by

$$\sigma \equiv \frac{y_{\xi}(Dx) - x_{\xi}(Dy)}{J} \tag{9b}$$

$$\tau \equiv \frac{x_{\eta}(Dy) - y_{\eta}(Dx)}{J} \tag{9c}$$

with

$$Dx \equiv \alpha x_{\xi\xi} - 2\beta x_{\xi\eta} + \gamma x_{\eta\eta} \tag{9d}$$

$$Dy \equiv \alpha y_{\xi\xi} - 2\beta y_{\xi\eta} + \gamma y_{\eta\eta} \tag{9e}$$

Note that Dx and Dy, and hence σ and τ, vanish when no coordinate contraction is used, that is, when the generating system is simply equations (3). The transformed boundary conditions are

On $\eta = \eta_1$ (i.e., on Γ_1^*),

$$\psi(\xi,\eta_1) = \psi_b \tag{10a}$$

On $\eta = \eta_2$ (i.e., on Γ_2^*),

$$\psi(\xi,\eta_2) = y(\xi,\eta_2) \cos\theta - x(\xi,\eta_2) \sin\theta \tag{10b}$$

The uniqueness is implied by insisting that the solution be periodic in $-\infty < \xi < \infty$, $\eta_1 \leq \eta \leq \eta_2$. The coefficients α, β, γ, σ, and τ are calculated during the generation of the natural coordinate system. For the approximation of equations (9), second-order, central differences are used for all derivatives, and the resulting difference equation is solved by accelerated Gauss-Seidel (SOR) iteration on the rectangular transformed field.

The solution of equations (9) on the transformed field is constructed in the same manner that has been previously described for the solution of equations (3). The single equation (9a) replaces the two equations (3a) and (3b), and the boundary conditions are

given by equations (10). The total number of difference equations thus is $I(J - 1)$ for a single airfoil and $I(J - 1) + (I2 - I1 - 1)$ for two airfoils.

Kutta Condition

The boundary value of ψ on the body ψ_b is determined by imposing the Kutta condition. The Kutta condition arises from physical considerations and basically asserts that the flow must leave the sharp trailing edge of an airfoil section in a smooth fashion. In a mathematical sense this smoothness condition is guaranteed by insisting that the velocity on the surface of the airfoil be continuous. The continuity implies that the limit of the velocity at any point on the surface exists and is the same regardless of the path along which this point is approached. In particular, the velocity at the trailing edge of the airfoil must be the same when approached from the upstream direction along the upper and lower surfaces. It is easily shown that the above ideas imply that the trailing edge is a stagnation point for airfoils having an included trailing-edge angle greater than zero, but only a common (possibly nonzero) upper and lower surface velocity limit is required for cusped trailing edges. The common-limit condition has also been applied by Giesing (ref. 5) in a solution utilizing superposition of singularities.

Since the normal velocity component vanishes identically on the airfoil surface, only the tangential velocity component need be considered. If $V_t^{(\eta)}$ is the component of $\underset{\sim}{V}$ tangent to a constant η-line, then

$$V_t^{(\eta_1)} = \frac{\sqrt{\gamma}\psi_\eta}{J} \tag{11}$$

On the surface the ξ-derivatives are approximated by the second-order, central-difference expressions of equation (4a), as in the interior of the field, at all points except those on the cut $i = 1$ and $i = I$, where second-order, one-sided expressions are used. Thus

$$(f_\xi)_{1,1} = \frac{1}{2}(-f_{3,1} + 4f_{2,1} - 3f_{1,1}) \tag{12a}$$

$$(f_\xi)_{I,1} = \frac{1}{2}(f_{I-2,1} - 4f_{I-1,1} + 3f_{I,1}) \tag{12b}$$

The η-derivatives on the surface are approximated at all points by similar one-sided expressions:

$$(f_\eta)_{i,1} = \frac{1}{2}(-f_{i,3} + 4f_{i,2} - 3f_{i,1}) \tag{12c}$$

To implement the condition of a common velocity limit numerically, the tangential velocity component at the airfoil trailing edge is approximated by a three-point, quadratic

extrapolation in which the three points on the airfoil surface immediately adjacent to the trailing-edge point on both upper and lower surfaces are utilized. This procedure is illustrated in figure 4. The extrapolated values are

$$\left(\underset{\sim}{V}_t\right)_o^{(U)} = 3\left(\underset{\sim}{V}_t\right)_{1U,1} - 3\left(\underset{\sim}{V}_t\right)_{2U,1} + \left(\underset{\sim}{V}_t\right)_{3U,1} \tag{13a}$$

$$\left(\underset{\sim}{V}_t\right)_o^{(L)} = 3\left(\underset{\sim}{V}_t\right)_{1L,1} - 3\left(\underset{\sim}{V}_t\right)_{2L,1} + \left(\underset{\sim}{V}_t\right)_{3L,1} \tag{13b}$$

where the subscripts o, 1U, 2U, 3U, 1L, 2L, and 3L refer to the ξ-field position as indicated in figure 4. All η-field position indices are of course unity. The common-limit condition is then

$$\left(\underset{\sim}{V}_t\right)_o^{(U)} = \left(\underset{\sim}{V}_t\right)_o^{(L)} \tag{14}$$

Superposition of Solutions

Since the system to be solved is linear in ψ, the solution for a single airfoil at any angle of attack may be obtained by superposing three component solutions: (1) a solution at 0^o angle of attack with no circulation, (2) a solution at 90^o angle of attack with no circulation, and (3) a solution with circulation but zero free-stream velocity. These three component solutions, written $\psi^{(k)}(\xi,\eta)$, where k = 1, 2, 3, each satisfy equations (9), with the respective boundary conditions

$$\psi_{i,1}^{(1)} = 0 \qquad (i = 1 \ldots I) \tag{15a}$$

$$\psi_{i,J}^{(1)} = y_{i,J} \qquad (i = 1 \ldots I) \tag{15b}$$

$$\psi_{i,1}^{(2)} = 0 \qquad (i = 1 \ldots I) \tag{16a}$$

$$\psi_{i,J}^{(2)} = -x_{i,J} \qquad (i = 1 \ldots I) \tag{16b}$$

$$\psi_{i,1}^{(3)} = 1 \qquad (i = 1 \ldots I) \tag{17a}$$

$$\psi_{i,J}^{(3)} = 0 \qquad (i = 1 \ldots I) \tag{17b}$$

The complete solution with arbitrary circulation then is

$$\psi(\xi,\eta;\lambda) = \psi^{(1)}(\xi,\eta)\cos\theta + \psi^{(2)}(\xi,\eta)\sin\theta + \lambda\psi^{(3)}(\xi,\eta) \tag{18}$$

The Kutta condition is then satisfied by choosing the coefficient λ such that equation (14) is satisfied. Thus it is only necessary to solve the system of difference equations three times for a given airfoil. The solution at any angle of attack may then be obtained without re-solving the difference system.

Surface Pressure and Force Coefficients

The pressure coefficient at any point in the field may be obtained from the velocities via the Bernoulli equation, which in the present nondimensional variables is

$$C_p = 1 - |\underset{\sim}{V}|^2 \tag{19}$$

On the body surface this becomes, through use of equation (11),

$$C_p = 1 - \frac{\gamma}{J^2}\psi_\eta^{\,2} \tag{20}$$

with the derivative evaluated by a second-order, one-sided difference expression. The nondimensional force on the body is given by

$$\underset{\sim}{F} = -\oint C_p \underset{\sim}{n}\, ds \tag{21}$$

where $\underset{\sim}{n}$ is the unit outward normal to the surface, and ds is an increment of arc length along the surface. The lift and drag coefficients are

$$C_L = \oint C_p\left(-x_\xi \cos\theta - y_\xi \sin\theta\right) d\xi \tag{22a}$$

$$C_D = \oint C_p\left(y_\xi \cos\theta + x_\xi \sin\theta\right) d\xi \tag{22b}$$

These integrals were evaluated with numerical quadrature by means of the trapezoidal rule.

Multiple Airfoils

With two airfoils, the boundary condition of equation (8a) is replaced by the two boundary conditions:

On the surface of body 1,

$$\psi(x,y) = \psi_1 \tag{23a}$$

On the surface of body 2,

$$\psi(x,y) = \psi_2 \tag{23b}$$

With reference to figure 3 and the discussion in the previous section of the coordinate system solution, these boundary conditions become, in the transformed field,

$$\psi_{i,1} = \psi_1 \qquad (i = I2 \ldots I3) \tag{24a}$$

$$\psi_{i,1} = \psi_2 \qquad (i = 1 \ldots I1 \text{ and } i = I4 \ldots I) \tag{24b}$$

As in the case of the coordinate system solution, the remaining portions of the $j = 1$ line are reentrant boundaries, so that points thereon are treated as field points rather than boundary points. The ξ-derivatives at the surface points I1, I2, I3, and I4 on the cuts between the bodies are also evaluated by using the one-sided expressions of equations (12) in the calculation of the velocity on the surface.

The Kutta condition must be applied on each body. Therefore, a fourth component solution is added, and the four component solutions each satisfy equation (9a), with the boundary conditions

$$\psi^{(1)}_{i,1} = 0 \qquad (i = 1 \ldots I1, \quad I2 \ldots I3, \quad I4 \ldots I) \tag{25a}$$

$$\psi^{(1)}_{i,J} = y_{i,J} \qquad (i = 1 \ldots I) \tag{25b}$$

$$\psi^{(2)}_{i,1} = 0 \qquad (i = 1 \ldots I1, \quad I2 \ldots I3, \quad I4 \ldots I) \tag{26a}$$

$$\psi^{(2)}_{i,J} = -x_{i,J} \qquad (i = 1 \ldots I) \tag{26b}$$

$$\psi^{(3)}_{i,1} = 0 \qquad (i = 1 \ldots I1, \quad I4 \ldots I) \tag{27a}$$

$$\psi^{(3)}_{i,1} = 1 \qquad (i = I2 \ldots I3) \tag{27b}$$

$$\psi^{(3)}_{i,J} = 0 \qquad (i = 1 \ldots I) \tag{27c}$$

$$\psi^{(4)}_{i,1} = 1 \qquad (i = 1 \ldots I1, \quad I4 \ldots I) \tag{28a}$$

$$\psi^{(4)}_{i,1} = 0 \qquad (i = I2 \ldots I3) \tag{28b}$$

$$\psi^{(4)}_{i,J} = 0 \qquad (i = 1 \ldots I) \tag{28c}$$

The complete solution with arbitrary circulation about each body is

$$\psi(\xi,\eta;\lambda_1,\lambda_2) = \psi^{(1)}(\xi,\eta)\cos\theta + \psi^{(2)}(\xi,\eta)\sin\theta + \lambda_1\psi^{(3)}(\xi,\eta) + \lambda_2\psi^{(4)}(\xi,\eta) \tag{29}$$

The Kutta condition is then satisfied by choosing the coefficients λ_1 and λ_2 such that equation (14) is satisfied on each body. This requires only the simultaneous solution of two linear algebraic equations. Generalizing to N bodies, it is necessary to solve the difference equation system N+2 times for a given multiple airfoil system. The solution at any orientation of the free stream may then be obtained without re-solving the difference system.

Results and Comparisons

The coordinate system for a Kármán-Trefftz airfoil having an integral flap is shown in figure 5, and the streamlines and pressure distribution for this airfoil are compared with the analytic solution (ref. 6) in figure 6. Similar excellent comparisons have been obtained with other Kármán-Trefftz airfoils. Figure 7 shows the coordinate system for a Liebeck laminar airfoil, the solution for which is compared with experimental results (ref. 7) for the pressure distribution and lift curve in figure 8. Finally, the coordinate system for a multiple-element airfoil is shown in figure 9, with the streamlines and pressure distributions shown in figure 10. Here coordinate system control was employed as discussed above to attract the coordinate lines into the concave region formed by the intersections of the cut between the airfoils.

APPLICATION TO THE NAVIER-STOKES EQUATIONS

Basic Equations

The stream-function—vorticity formulation of the two-dimensional, incompressible, viscous-flow equations is given by

$$\omega_t + \psi_y\omega_x - \psi_x\omega_y = \frac{\omega_{xx} + \omega_{yy}}{R} \tag{30}$$

$$\psi_{xx} + \psi_{yy} = -\omega \tag{31}$$

where ψ is the nondimensional stream function, ω the nondimensional vorticity, and R the Reynolds number based on the characteristic velocity and length used to nondimensionalize the basic equations. The transformed equations are

$$\omega_t + \frac{\psi_\eta \omega_\xi - \psi_\xi \omega_\eta}{J} = \frac{\alpha\omega_{\xi\xi} - 2\beta\omega_{\xi\eta} + \gamma\omega_{\eta\eta} + \sigma\omega_\eta + \tau\omega_\xi}{J^2 R} \tag{32}$$

$$\alpha\psi_{\xi\xi} - 2\beta\psi_{\xi\eta} + \gamma\psi_{\eta\eta} + \sigma\psi_\eta + \tau\psi_\xi = -J^2\omega \tag{33}$$

where the coordinate system parameters α, β, γ, J, σ, and τ have already been given. Recall that these coordinate system parameters are fixed and need be calculated only once.

Boundary Conditions

The boundary conditions are given by

On the body surface,

$$\psi(x,y,t) = \psi_b = \text{Constant} \tag{34a}$$

$$\frac{\partial\psi}{\partial n}(x,y,t) = 0 \tag{34b}$$

At infinity,

$$\psi(x,y,t) = y\cos\theta - x\sin\theta \tag{35a}$$

$$\omega(x,y,t) = 0 \tag{35b}$$

where $\underset{\sim}{n}$ is the unit vector normal to the body surface. The function describing the variation of the vorticity on the body $\omega_b(x,y,t)$ is unknown and must be calculated as part of the solution. Initial conditions at $t = 0$ are those resulting from an impulsive start. Equations (34) and (35) may be transformed to yield boundary conditions for equations (32) and (33) in the transformed plane. This procedure yields the following relations:

On $\eta = \eta_1$ $\left(\text{i.e., on } \Gamma_1^*\right)$,

$$\psi(\xi,\eta_1,t) = \psi_b = \text{Constant} \tag{36a}$$

$$\frac{\sqrt{\gamma}}{J}\psi_\eta(\xi,\eta_1,t) = 0 \tag{36b}$$

On $\eta = \eta_2$ $\left(\text{i.e., on } \Gamma_2^*\right)$,

$$\psi(\xi,\eta_2,t) = y(\xi,\eta_2)\cos\theta - x(\xi,\eta_2)\sin\theta \tag{37a}$$

$$\omega(\xi,\eta_2,t) = 0 \tag{37b}$$

where η_1 and η_2 are the values of the η-coordinate for contours Γ_1^* and Γ_2^*, respectively, in the transformed plane (fig. 1). The condition specified by equation (36b) guarantees that the velocity component tangent to the transformed body surface vanishes on the body surface. Since the component normal to the body surface vanishes identically, the satisfaction of equation (36b) implies that the viscous no-slip condition is satisfied on the body surface (i.e., along Γ_1^*, or equivalently Γ_1).

Most solutions in the computational fluids field have relied on a modified evaluation of equation (33) on the boundary to determine the vorticity on the body surface $\omega_b(\xi,\eta_1,t)$. The modification is introduced in an attempt to insure that equation (36b) holds – that is, to satisfy the no-slip condition. A variety of numerical procedures along these lines are documented in reference 8. The principal problem encountered with such an approach is that the vanishing of the tangential velocity component is implied only indirectly rather than directly. Israeli (ref. 9) has shown that these procedures are not only unreliable in producing a zero tangential component, but may, in fact, even be numerically divergent. Israeli suggests that $\omega_b(\xi,\eta_1,t)$ be calculated with an iterative algorithm of the form

$$\omega_b^{(k+1)}(\xi_i,\eta_1,t_n) = \omega_b^{(k)}(\xi_i,\eta_1,t_n) - \delta\left[\frac{\partial\psi}{\partial n}(\xi_i,\eta_1,t_n)\right] \tag{38}$$

for all $1 \leq i \leq I - 1$, where ξ_i refers to the ξ-position along the body, η_1 denotes the η-value for contour Γ_1^*, t_n is the current time, k denotes the iteration counter at step t_n, and δ is a relaxation factor (possibly variable). Obviously, such a procedure can only be employed with implicit methods which require iteration of the parabolic vorticity equation at each time increment. Note that convergence of the vector sequence $\omega_b^{(k)}(\xi_i,\eta_1,t_n)$ implies convergence of $\left[\frac{\partial\psi}{\partial n}(\xi_i,\eta_1,t_n)\right]^{(k)}$ to that function which inherently satisfies the no-slip boundary condition.

Pressure Coefficients

If the primitive variable formulation of the Navier-Stokes equations (velocity-pressure) is evaluated on the body surface, the time derivative and inertia terms vanish to yield

$$\nabla p = \frac{1}{R}\nabla^2 \underset{\sim}{V} \tag{39}$$

where p is the nondimensional pressure, $\underset{\sim}{V}$ the nondimensional velocity, and R the Reynolds number based on the characteristic flow parameters. Utilizing a vector identity to eliminate $\nabla^2 \underset{\sim}{V}$ gives

$$\nabla p = \frac{1}{R}\left(\underset{\sim}{j}\,\omega_x - \underset{\sim}{i}\,\omega_y\right) \tag{40}$$

The pressure differential in the transformed plane then is

$$dp = \frac{1}{RJ}\left(\beta\omega_\xi - \gamma\omega_\eta\right)d\xi \tag{41}$$

Integration of equation (41) along Γ_1 starting at the trailing-edge position yields

$$C_p^*(\xi) \equiv p(\xi) - p_{T.E.} = \frac{1}{R}\int_{\xi_{T.E.}}^{\xi} \frac{1}{J}\left(\beta\omega_\xi - \gamma\omega_\eta\right)d\xi' \tag{42}$$

where $\xi_{T.E.}$ is the ξ-value corresponding to the body trailing edge. The symbol C_p^* is used instead of the more conventional C_p to indicate that the reference pressure is the trailing-edge value $p_{T.E.}$ rather than the free-stream value p_∞. Note that all quantities in equation (42) must be evaluated on the body surface (i.e., along $\eta = \eta_1$). Central-difference approximations were used for all ξ-derivatives appearing in equation (42), while second-order one-sided expressions were used for the η-derivatives. The numerical quadrature was performed by the trapezoidal rule.

Force Coefficients

The force coefficients associated with the stress vector are obtained by integrating the stress vector over the body surface. Let $\underset{\sim}{F} = \underset{\sim}{i}\,C_A + \underset{\sim}{j}\,C_N$ be the total force acting on the body and let $T_{\underset{\sim}{n}} = \underset{\sim}{i}\left(T_{\underset{\sim}{n}}\right)_1 + \underset{\sim}{j}\left(T_{\underset{\sim}{n}}\right)_2$ be the stress vector on the body surface having outward unit normal $\underset{\sim}{n}$. Then,

$$\underset{\sim}{F} = \int_S T_{\underset{\sim}{n}}\,dS \tag{43}$$

where S is the body surface. The stress vector components $\left(T_{\underset{\sim}{n}}\right)_1$ and $\left(T_{\underset{\sim}{n}}\right)_2$ may be expressed in terms of the primitive variables as

$$\left(T_{\underset{\sim}{n}}\right)_1 = -2pn_1 + 4\left(V_1\right)_x\frac{n_1}{R} + 2\left[\left(V_1\right)_y + \left(V_2\right)_x\right]\frac{n_2}{R} \tag{44a}$$

$$\left(T_{\underset{\sim}{n}}\right)_2 = -2pn_2 + 2\left[\left(V_2\right)_x + \left(V_1\right)_y\right]\frac{n_1}{R} + 4\left(V_2\right)_y\frac{n_2}{R} \tag{44b}$$

where n_1 and n_2 are the x- and y-components of the normal to the body surface $\underset{\sim}{n}$. The lift and drag coefficients may then be calculated by means of the conventional wind-axis transformation as follows:

$$C_D = 2\int_{\xi_{min}}^{\xi_{max}} \left(y_\xi \cos\theta - x_\xi \sin\theta\right) C_p^* \, d\xi + 2\int_{\xi_{min}}^{\xi_{max}} \frac{y_\xi \sin\theta - x_\xi \cos\theta}{R} \omega \, d\xi \tag{45a}$$

$$C_L = -2\int_{\xi_{min}}^{\xi_{max}} \left[\cos\theta\left(x_\xi C_p^* - \frac{y_\xi \omega}{R}\right) + \sin\theta\left(y_\xi C_p^* - \frac{x_\xi \omega}{R}\right)\right] d\xi \tag{45b}$$

The two integrals in equations (45) are referred to as the pressure and friction drag coefficients and are denoted C_{D_P} and C_{D_F}, respectively. These integrals were evaluated numerically by use of the trapezoidal rule. The ξ-derivatives were approximated with second-order central-difference expressions.

Difference Equations

A first-order backward difference is used to approximate the time derivative, while second-order central differences are used for the space derivatives in equations (32) and (33). The resulting coupled difference equations, two for each point in the field, were solved simultaneously by point SOR iteration at each time step.

Implementation of the Boundary Conditions

As indicated earlier, the basic idea used to calculate the vorticity on the body surface $\omega_b(\xi,\eta_1,t)$ is to select this function so that the no-slip condition is satisfied. An approach suggested by Israeli (ref. 9) has already been cited in equation (38). This is basically the parallel-chord method (see ref. 10) and has only a linear convergence rate. Another method similar to false-position iteration was used to accelerate the convergence. The iterative sequence is generated by the algorithm

$$\omega_{i,1}^{(k+1)} = \omega_{i,1}^{(k)} - \delta \frac{\omega_{i,1}^{(k)} - \omega_{i,1}^{(k-1)}}{\left(\frac{\sqrt{\gamma}}{J}\psi_\eta\right)_{i,1}^{(k)} - \left(\frac{\sqrt{\gamma}}{J}\psi_\eta\right)_{i,1}^{(k-1)}} \left(\frac{\sqrt{\gamma}}{J}\psi_\eta\right)_{i,1}^{(k)} \tag{46}$$

where δ is again an acceleration parameter. The derivatives in this equation were approximated with second-order one-sided differences for the η-derivatives and central differences for the ξ-derivatives. Another method was used when numerical overflow problems were encountered with the quotient in equation (46). This consisted of modifying the second term on the right side of equation (38) with the algebraic sign of the difference quotient. Several other approaches documented in Roache (ref. 8) were also tried. None of these were as successful as the methods discussed above.

Calculation Procedure

The vorticity and stream-function fields are converged by means of the point SOR technique. New boundary values of the vorticity are calculated as discussed in a previous section. Three conditions must be met before the time step is considered to be converged:

(1) $E(\psi,k) \leqq \epsilon(\psi)$

(2) $E(\omega,k) \leqq \epsilon(\omega)$

(3) $E\left(\frac{\partial\psi}{\partial n},k\right) \leqq \epsilon\left(\frac{\partial\psi}{\partial n}\right)$

where the terms $E(\psi,k)$, $E(\omega,k)$, and $E\left(\frac{\partial\psi}{\partial n},k\right)$ are the maximum norms of the change $E(\psi,k) \equiv \left\|\psi^{(k)} - \psi^{(k-1)}\right\|_\infty$. The terms involving ϵ are simply the required convergence criteria. (Nominal values for $\epsilon(\psi)$, $\epsilon(\omega)$, and $\epsilon\left(\frac{\partial\psi}{\partial n}\right)$ are 10^{-5}, 10^{-5}, and 10^{-2}, respectively.) This procedure is repeated until convergence. Once a time step has converged, time is incremented and the process begins again.

NAVIER-STOKES RESULTS

Solutions About Various Bodies

To illustrate the versatility of the natural coordinate system approach, viscous flows about three different bodies are presented. The bodies and associated flow conditions are

(1) Flapped Kármán-Trefftz airfoil: $\theta = 15^\circ$; $R = 200$

(2) Göttingen 625 airfoil: $\theta = 5^\circ$; $R = 2000$

(3) Cambered rock: $\theta = 5^\circ$; $R = 500$

The coordinates of these bodies are given in reference 4.

Several problems arose with the body vorticity calculations. At times the iterative method used to calculate the body vorticity produced mildly oscillating values along the body boundary. The principal cause of this result was that the method was applied point by point along the boundary. Thus, the only "communication" between the body points was through the field iterations. This tendency was overcome in two ways: First, only small surface vorticity changes were allowed at each body station at each iteration. Second, after the new vorticity values had been calculated, a three-point weighted average was used to smooth the new surface vorticity distribution.

A second problem developed with those bodies having a sharp trailing edge. To preserve continuity of the vorticity, the vorticity at the trailing edge was held at zero. Since the vorticity gradients are extremely large in the neighborhood of the trailing edge, the numerical solution had a tendency to oscillate near this point. This phenomenon is generally known as "wiggles" and, as shown in Roache (ref. 8), is actually the solution of the difference equations. In reality the wiggles are caused by the inability of the net function to resolve large gradients near boundaries.

Flapped Kármán-Trefftz Airfoil

The coordinate system for the flapped Kármán-Trefftz airfoil profile, which possesses a camber of 22 percent at the 0.55-chord point, is shown in figure 5. The free-stream Reynolds number was taken as 200, and the flow angle of attack was 15°. Other data concerning the solution are given in table 1.

Stream-function contours are given for two time steps in figure 11. The contours at the earlier time indicate clearly the large flow velocities over the upper surface of the airfoil and the consequent large difference in overall boundary-layer thickness between the upper and lower surfaces. The manner in which the zero streamline leaves the trailing edge indicates that flow separation on the upper surface is imminent. The contours for $t = 1.06$ illustrate a fully developed laminar separation. The boundary-layer thickness over the aft half of the upper surface has increased approximately 300 percent.

In order to gain some insight into the development of laminar separation, a series of four velocity profiles are shown in figure 12. The profiles for $t = 0.08$ illustrate the upper-surface flow shortly after the impulsive start. The boundary layer is very thin at this time. Separation has already begun at $t = 0.22$, as evidenced by the profiles on the flap portion of the airfoil. Figures 12(c) and 12(d) indicate that the upper-surface separation point has moved rapidly upstream to approximately the 70-percent-chord point. Reverse flow has been well established at $t = 0.54$. Note that the upper-surface boundary-layer thickness has increased substantially over the time span shown.

Göttingen 625 Airfoil

The flow Reynolds number was 2000 at an angle of attack of 5°. Additional summary data of the solution for the Göttingen 625 airfoil appear in table 1. The coordinate system shown in figure 13 was used in this solution. The high density of constant η-lines near the airfoil surface is the result of contraction to the first 15 η-lines. In particular, the amplitude factor appearing in equation (5b) ranged from 20 000 at $\eta = 1$ to 13 000 at $\eta = 15$ (increments of 500/line), while the decay factors were held constant at 1.0 for

η = 1 to 14 and were 0.4 for the 15th η-line. The function P(x,y) defined by equation (5a) was set to zero as were the point-attraction parameters of equation (5b).

This solution developed wiggles near the sharp trailing edge. The effect of the wiggles is dramatically illustrated in figure 14, which shows ψ and ω contours at several times after the impulsive start. Note the distortion of the vorticity contours near the trailing edge. The oscillatory effects are carried upstream along the lower surface of the airfoil and are proceeding downward, away from the trailing edge. The disturbance proceeds away from the airfoil without much damping but has little effect on the flow in the vicinity of the airfoil after the start, as can be seen in figures 15(a) and (b), which show ψ contours at later times. A feature of interest in figures 14(a) and (b) is the starting vortex which is formed and shed at the trailing edge. This vortex appears just above the disturbance due to the wiggles.

Figure 14(c) indicates that flow separation has been initiated on the trailing-edge portion of the airfoil upper surface. The separation point moves rapidly upstream to approximately the half-chord point at t = 1.012. At this time the upstream movement of the separation point slows down considerably. The thickness of the separated region, however, begins to increase, as illustrated in figures 15 and 16. The remainder of the stream-function contours in figures 15(a) and (b) illustrate the growing thickness of the separated region, the increasing back flow, and the separation of flow eddies. At t = 2.23 a bubble begins to form on the trailing edge. This bubble continues to grow and is followed by the formation of another bubble at t = 2.53. The extent of both bubbles continues to increase until a single bubble is formed at t = 3.13. The final ψ contours given indicate that the single bubble has become much larger. The thickness of the separation region is roughly 1.25 times the airfoil thickness at this time, with the forward separation point at approximately 31 percent of the chord.

The separation process may also be examined by viewing the series of upper-surface velocity profiles given in figure 16. The profiles given in figure 16(a) illustrate attached upper-surface flows shortly after the impulsive start. There is a noticeable increase in the boundary-layer thickness at t = 0.336. The remaining parts of figure 16 track the growing thickness of the separated region and the upstream movement of the separation point.

Pressure and force coefficients at an early time are illustrated in figure 17(a). The friction drag constitutes more than 65 percent of the total drag at this time. As the boundary layer becomes thicker, the friction drag decreases rapidly and causes a corresponding decrease in the total drag. The effects of the laminar flow separation are shown in figure 17(b). The peculiar variation in the C_p^* distribution at the trailing edge is again due to inaccuracies in the body vorticity distribution.

Cambered Rock

To show that the natural coordinate method could be used with arbitrary shaped bodies, the viscous flow about the cambered rock at a Reynolds number of 500 was developed. The contracted natural coordinate system used in the solution is given in figure 18. The same amplitude and decay factors given for the Göttingen 625 airfoil were used to create this system. Other summary data are presented in table 1.

With a body such as the cambered rock, reliance must be placed on one's physical intuition in evaluating the resulting flow. For this reason an extended discussion of the flow past the cambered rock will not be given. Instead a significant number of ψ and ω contours will be given. These are shown in figure 19. However, it is felt that some remarks are appropriate. A glance at figure 18 indicates that the rock possesses several concave areas. Intuition would imply that flow stagnation areas should develop quite rapidly in these regions. This, in fact, does occur, as figure 19 indicates. In addition one would expect laminar flow separation and the consequent shedding of vorticity from the body. These events are also borne out by the contours. The ever-increasing size of the region of significant vorticity is quite apparent from the figures. Finally, velocity profiles and surface pressure distributions are shown in figures 20 and 21.

Computer Time Requirements

Numerical solutions to parabolic partial differential equations require extensive amounts of digital computer time. The total CPU times (UNIVAC 1106) used to generate the three solutions discussed in this study are documented in table 1. The average time required to converge each time step is also shown. (No attempt was made to quantify the effects of time-step size on the average times given.)

CONCLUSIONS

The objective of this study was to develop methods to obtain numerical solutions of the two-dimensional, incompressible, time-dependent Navier-Stokes equations about arbitrary bodies. The solutions followed the development of a general numerical curvilinear coordinate transformation which produces a natural coordinate system having a constant coordinate line coincident with each boundary contour in the physical plane. Once the natural coordinates are developed for a given physical domain, the set of partial differential equations of interest may be transformed to the natural system and solved numerically in the transformed plane without regard to the geometry of the physical region. In effect the natural coordinate method eliminates all geometrical considerations from a given solution, as all physical regions have the same appearance in the transformed plane. The computer software utilized to generate the natural coordinates

is independent of the set of partial differential equations whose solution is to be carried out on the transformed plane. The partial differential equations governing potential and viscous flow differ drastically. However, for a given body geometry, the same natural system was used herein for both solutions. The second major advantage of using natural coordinates is that the computer software generated to approximate the solution of a given set of partial differential equations is completely independent of the physical geometry of the problem. The same computer program was utilized to develop all the solutions for the wide variety of bodies discussed herein. Only the input varies with the body. Such a procedure obviously has significant ramifications in numerical mathematics and all areas of physical science.

Significant viscous-flow results were obtained for three different bodies. These included two general airfoil sections and one completely arbitrary body. The airfoil solutions developed computational wiggles near the sharp trailing edge at the start of the impulsive flow. The wiggles were generated as a result of large vorticity gradients which appeared in this region at the start. This disturbance was convected away from the body essentially undamped, but produced no significant disturbance near the body at later times. The solutions show the formation and development of the boundary layer, laminar separation bubbles, and completely separated flow. Present results extend to a Reynolds number of 2000. Although the magnitude of the calculated force coefficients cannot be compared with experimental data, as none exist at this low Reynolds number, the time variation of these parameters agreed quite well with the flow pattern development. The cambered-rock solution proved that the natural coordinate methods could be applied to very general bodies. The manner of this flow development also agreed with intuitive physical reasoning.

There appears to be no basic barrier to higher Reynolds number solutions, since the means are at hand to contract the coordinate system about the body as much as desired. Preliminary runs at a Reynolds number of 10 000 have already been made. Work is also in progress on the solution for multiple airfoils with viscous flow.

REFERENCES

1. Mehta, U. B.; and Lavan, Z.: Starting Vortex, Separation Bubbles and Stall – A Numerical Study of Laminar Unsteady Flow Around an Airfoil. AFOSR-TR-73-0640, Dec. 1972. (Available from DDC as AD 758 831.)

2. Dawson, C.; and Marcus, M.: DMC – A Computer Code To Simulate Viscous Flow About Arbitrary Shaped Bodies. Proceedings of the 1970 Heat Transfer and Fluid Mechanics Institute, 1970, pp. 323-338.

3. Thompson, Joe F.; Thames, Frank C.; and Mastin, C. Wayne: Automatic Numerical Generation of Body-Fitted Curvilinear Coordinate System for Field Containing Any Number of Arbitrary Two-Dimensional Bodies. J. Computational Phys., vol. 15, no. 3, July 1974, pp. 299-319.

4. Thames, Frank C.: Numerical Solution of the Incompressible Navier-Stokes Equations About Arbitrary Two-Dimensional Bodies. Ph. D. Diss., Mississippi State University, 1975.

5. Giesing, Joseph P.: Potential Flow About Two-Dimensional Airfoils. Part I: A Summary of Two-Dimensional Airfoil Methods; Part II: Solution of the Flow Field About One or More Airfoils of Arbitrary Shape in Uniform or Nonuniform Flows by the Douglas Neumann Method. Rep. No. LB31946, Douglas Aircraft Co., Inc., Dec. 1, 1965.

6. Karamcheti, Krishnamurty: Principles of Ideal-Fluid Aerodynamics. John Wiley & Sons, Inc., 1966.

7. Liebeck, Robert H.: A Class of Airfoils Designed for High Lift in Incompressible Flow. AIAA Paper No. 73-86, Jan. 1973.

8. Roache, Patrick J.: Computational Fluid Dynamics. Hermosa Publ., c.1972.

9. Israeli, M.: A Fast Implicit Numerical Method for Time-Dependent Viscous Flows. Studies in Appl. Math, vol. 49, 1970, p. 327.

10. Ortega, J. M.; and Rheinboldt, W. C.: Iterative Sclution of Nonlinear Equations in Several Variables. Academic Press, Inc., 1970.

TABLE 1.- SUMMARY OF DATA FOR VISCOUS-FLOW SOLUTIONS

Body (*)	θ, deg	R	Field size	Convergence criteria			Time steps		Average number of iterations		Total solution time	Total CPU time, hr
				ψ	ω	$\frac{\partial \psi}{\partial n}$	Initial	Final	Initial	Final		
1	15	200	3828 (66 × 58)	10^{-5}	10^{-5}	10^{-2}	0.01	0.03	280	280	1.15	7.104
2	5	2000	4350 (75 × 58)	10^{-5}	10^{-5}	10^{-1}	.001	.01	130	220	3.35	32.40
3	5	500	3132 (54 × 58)	10^{-5}	10^{-5}	0.5	.005	.005	55	95	1.30	6.40

*Body code:

1 Flapped Kármán-Trefftz airfoil
2 Göttingen 625 airfoil
3 Cambered rock

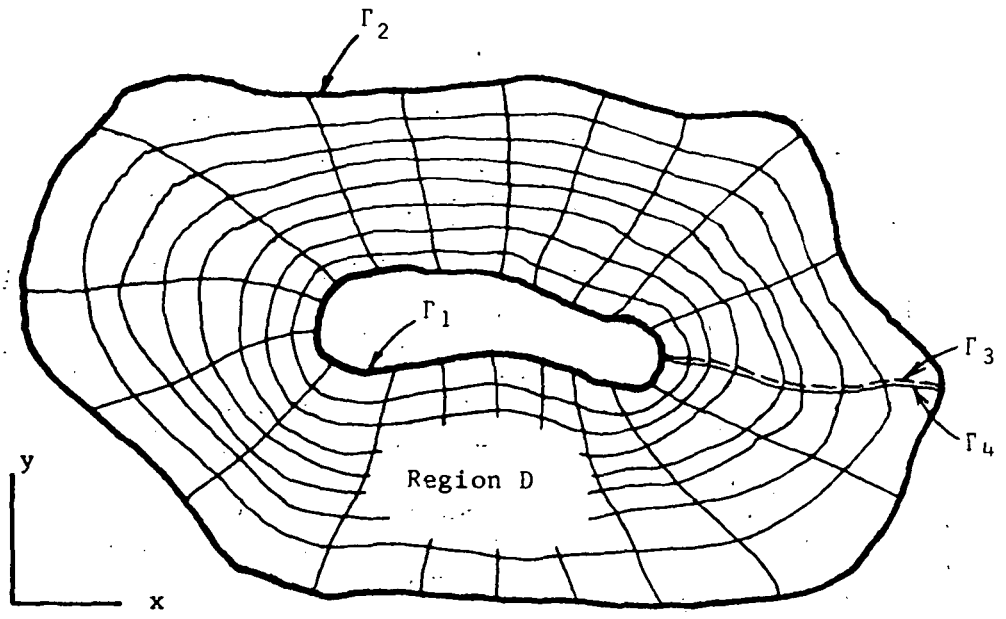

Physical Plane

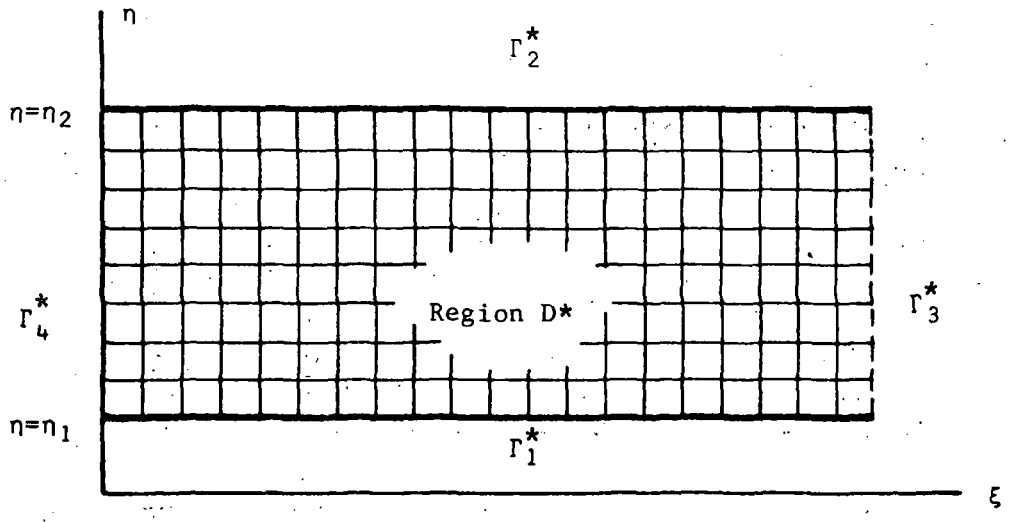

Transformed Plane
(Natural Coordinates)

Figure 1.- Field transformation - single body.

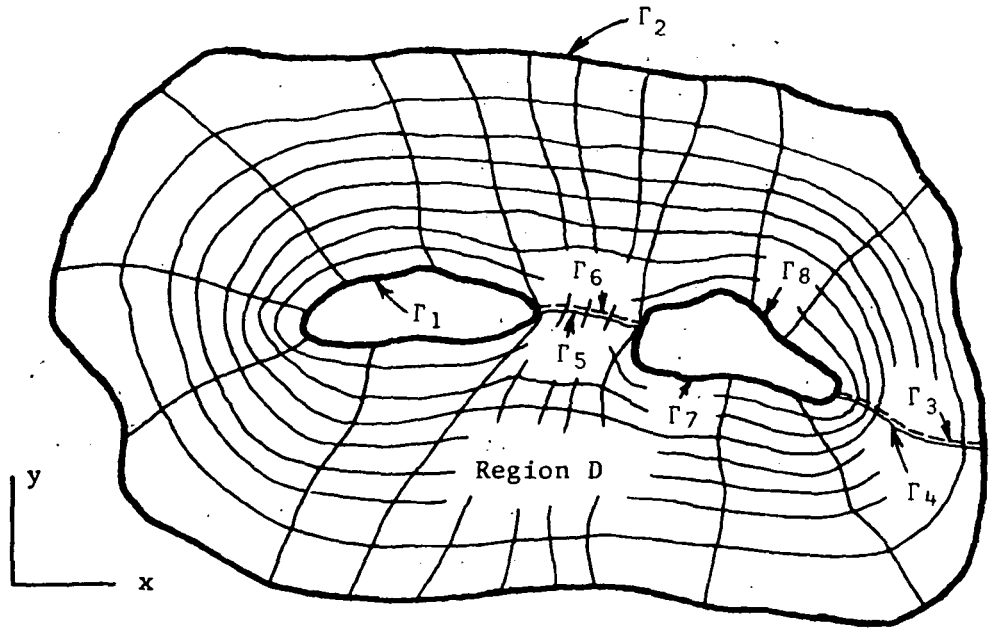

Physical Plane

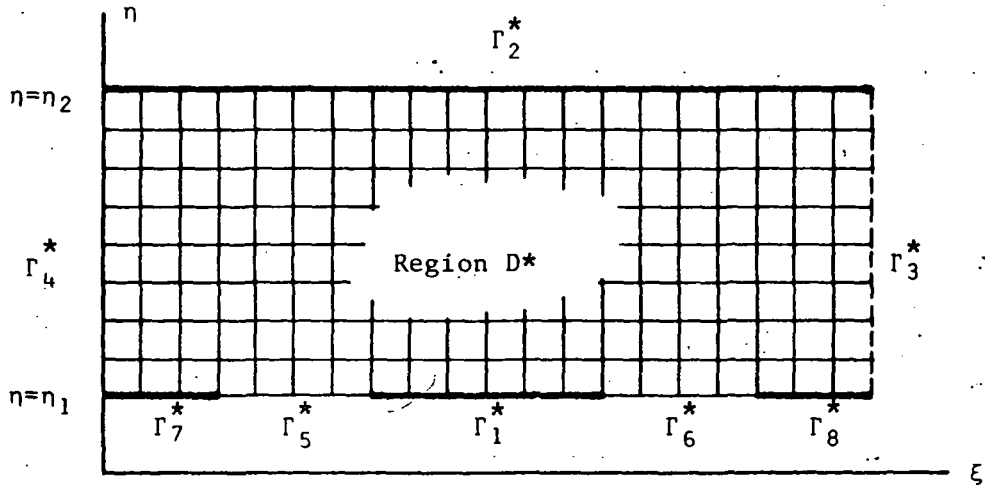

Transformed Plane

Figure 2.- Field transformation - multiple bodies.

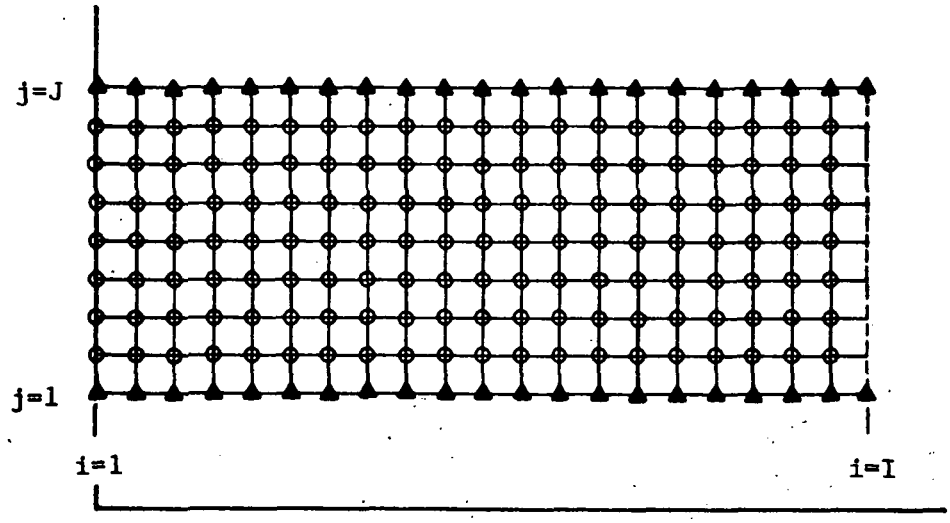

(a) Single-body region.

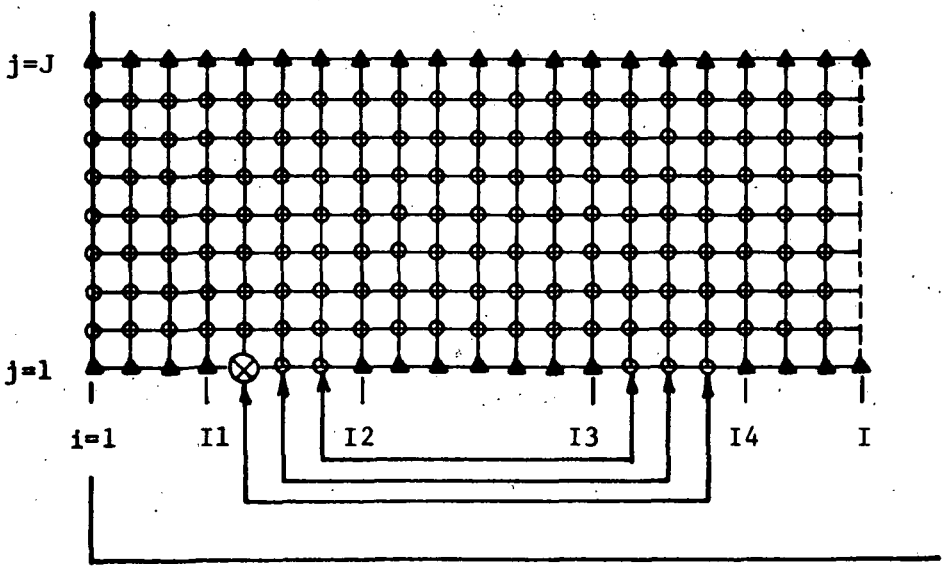

(b) Two-body region.

Figure 3.- Computational grids - single and two-body regions.

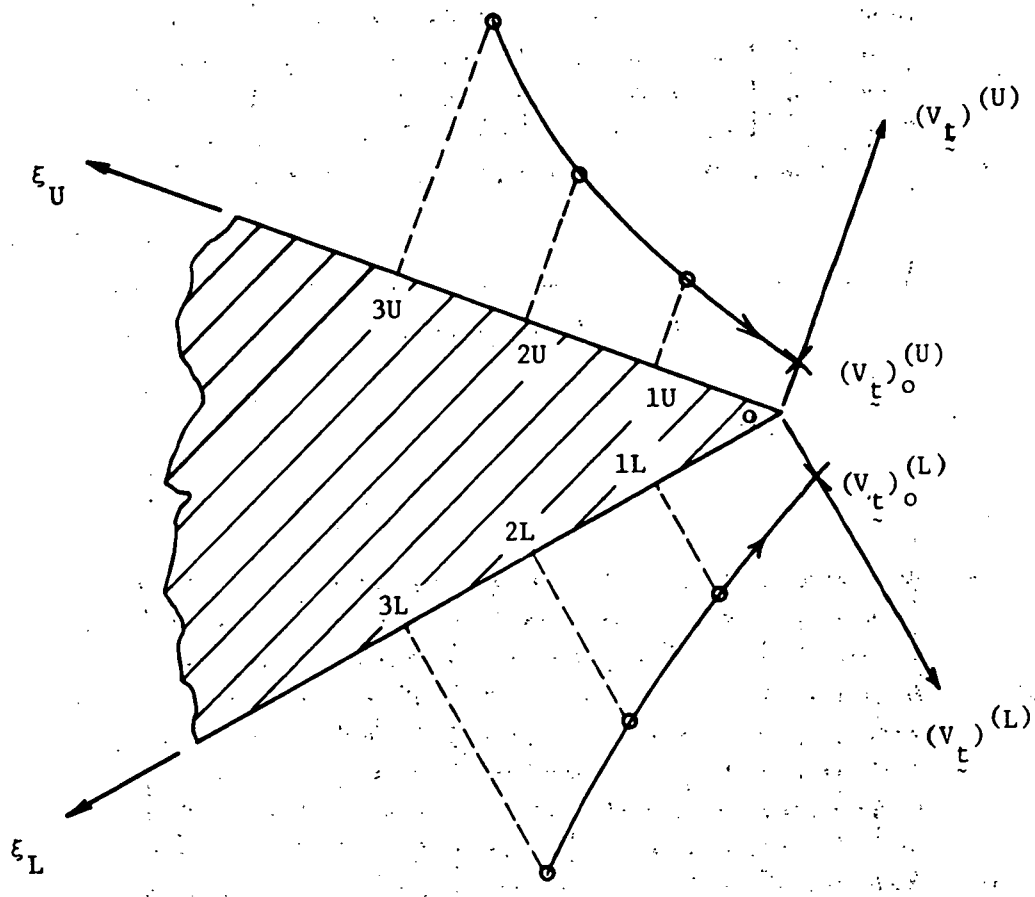

Figure 4.- Velocity extrapolation at airfoil trailing edge.

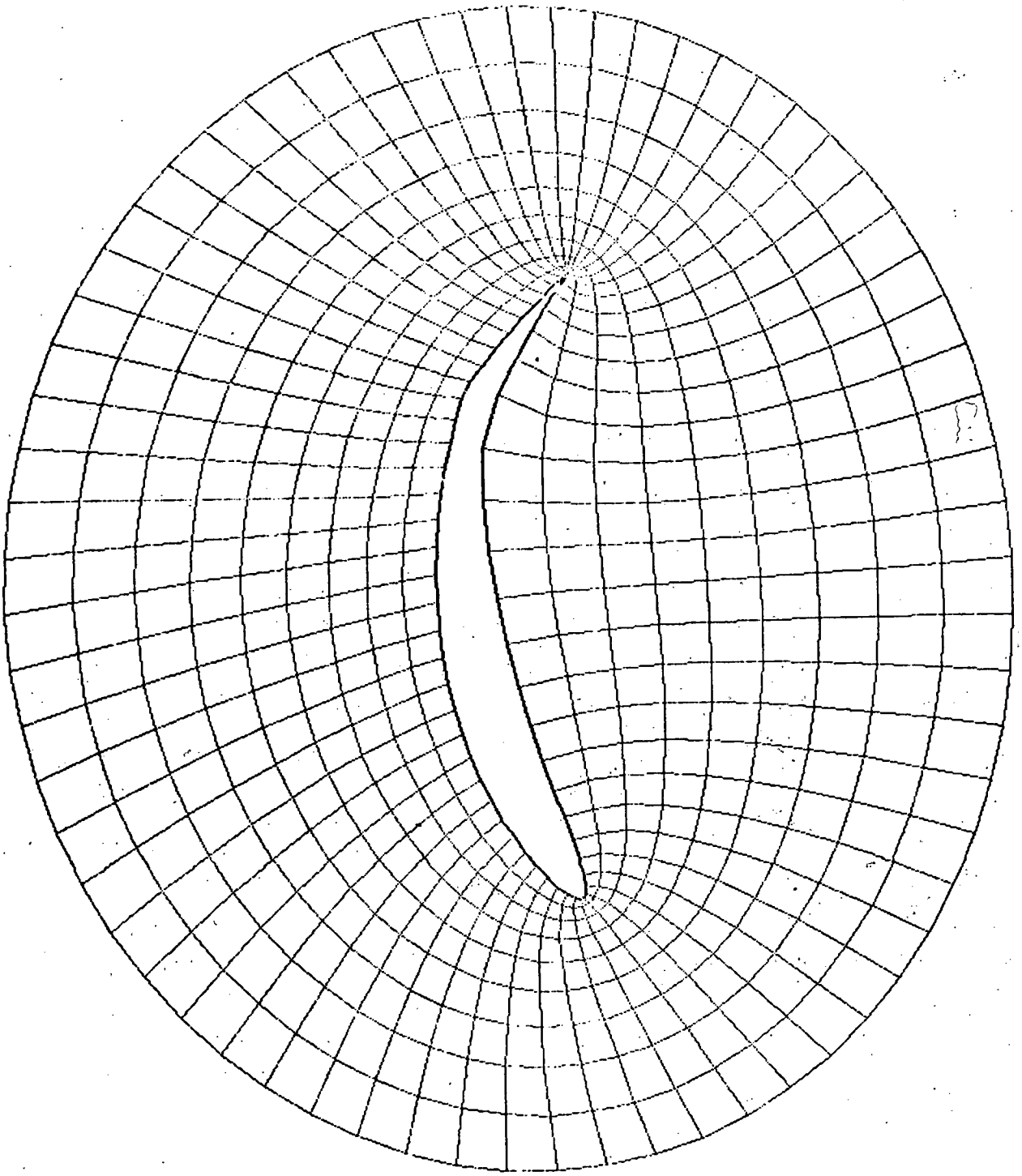

Figure 5.- Coordinate system for flapped Kármán-Trefftz airfoil.

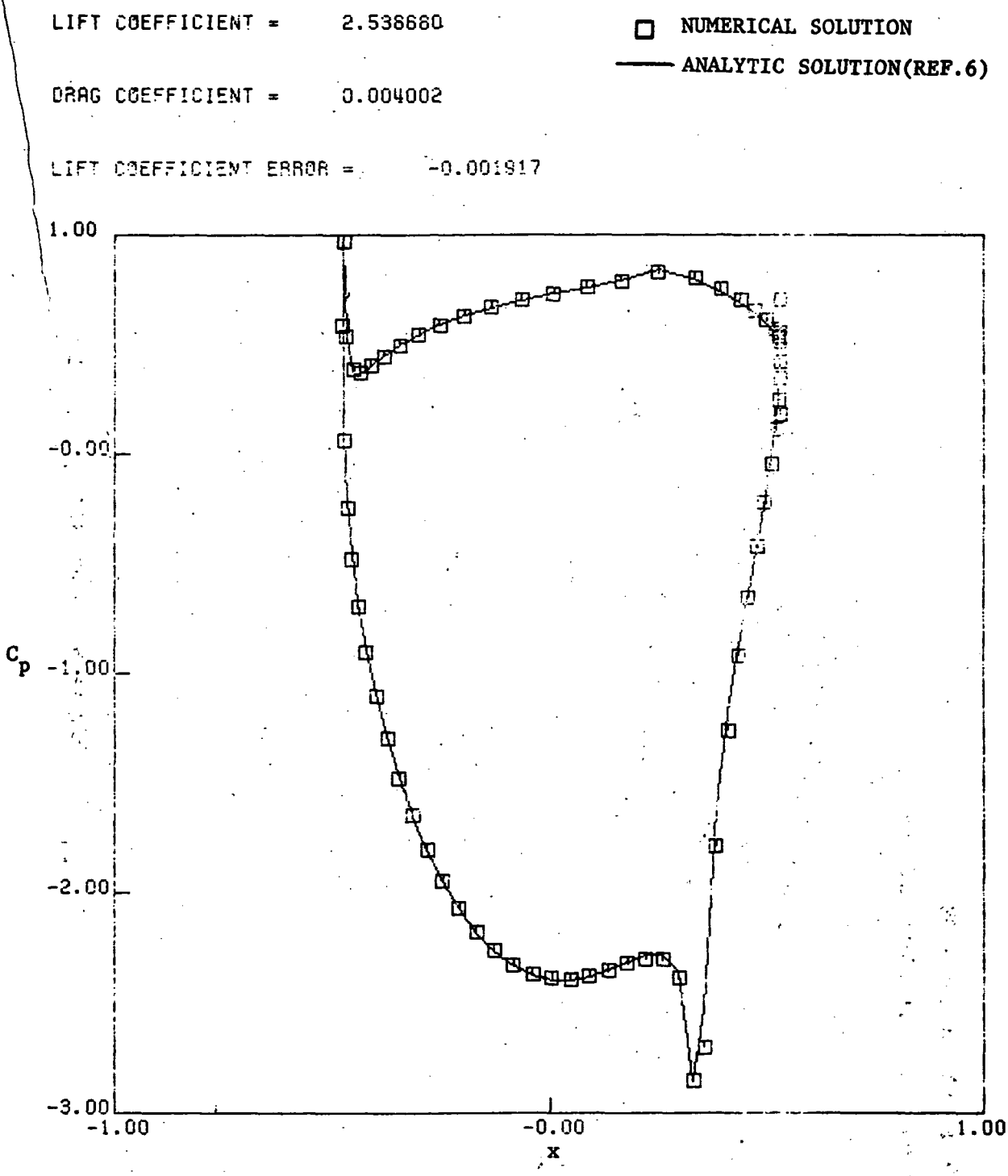

(a) Pressure distribution.

Figure 6.- Analytic and numerical potential-flow results for flapped Kármán-Trefftz airfoil.

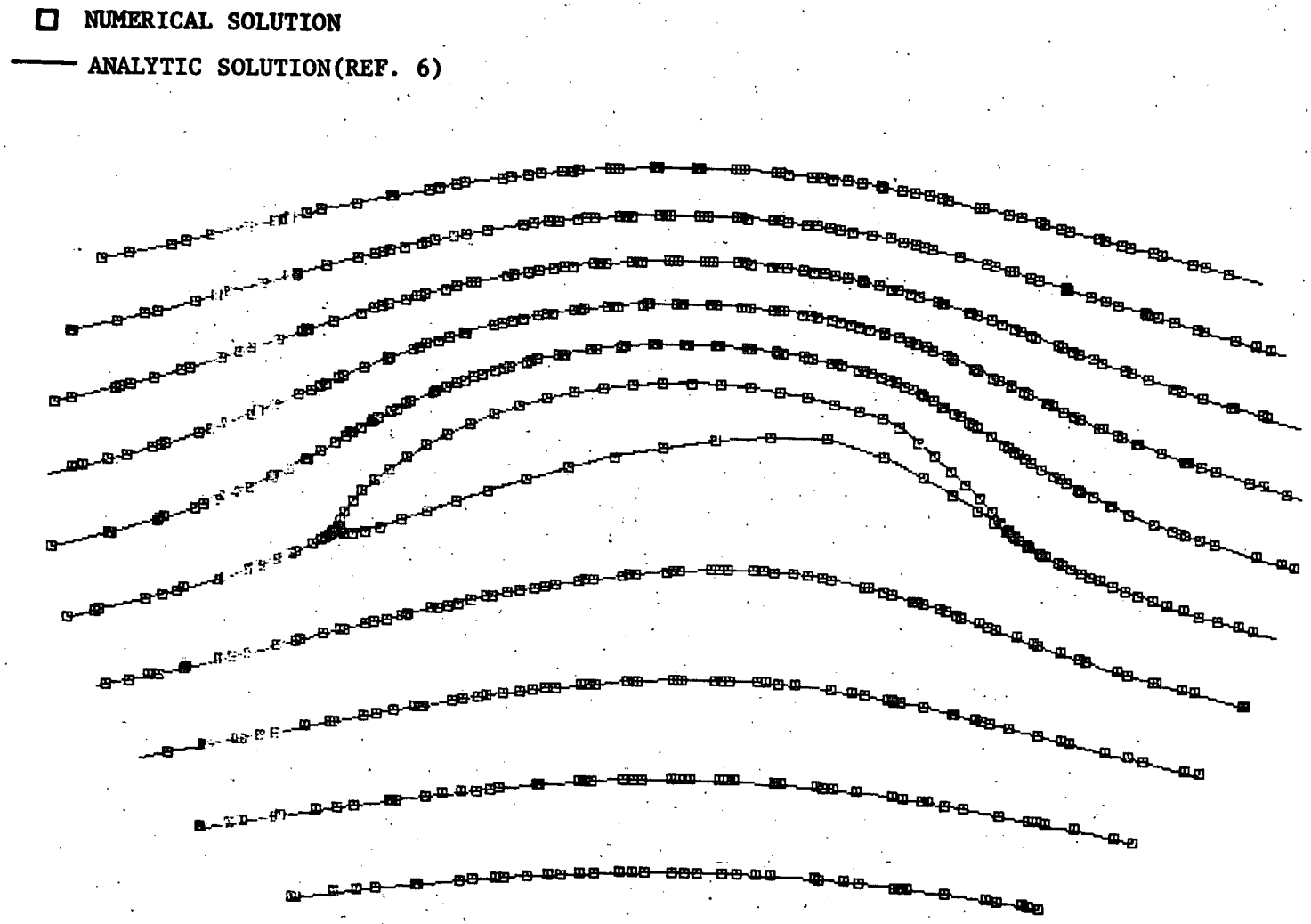

(b) Streamlines.

Figure 6.- Concluded.

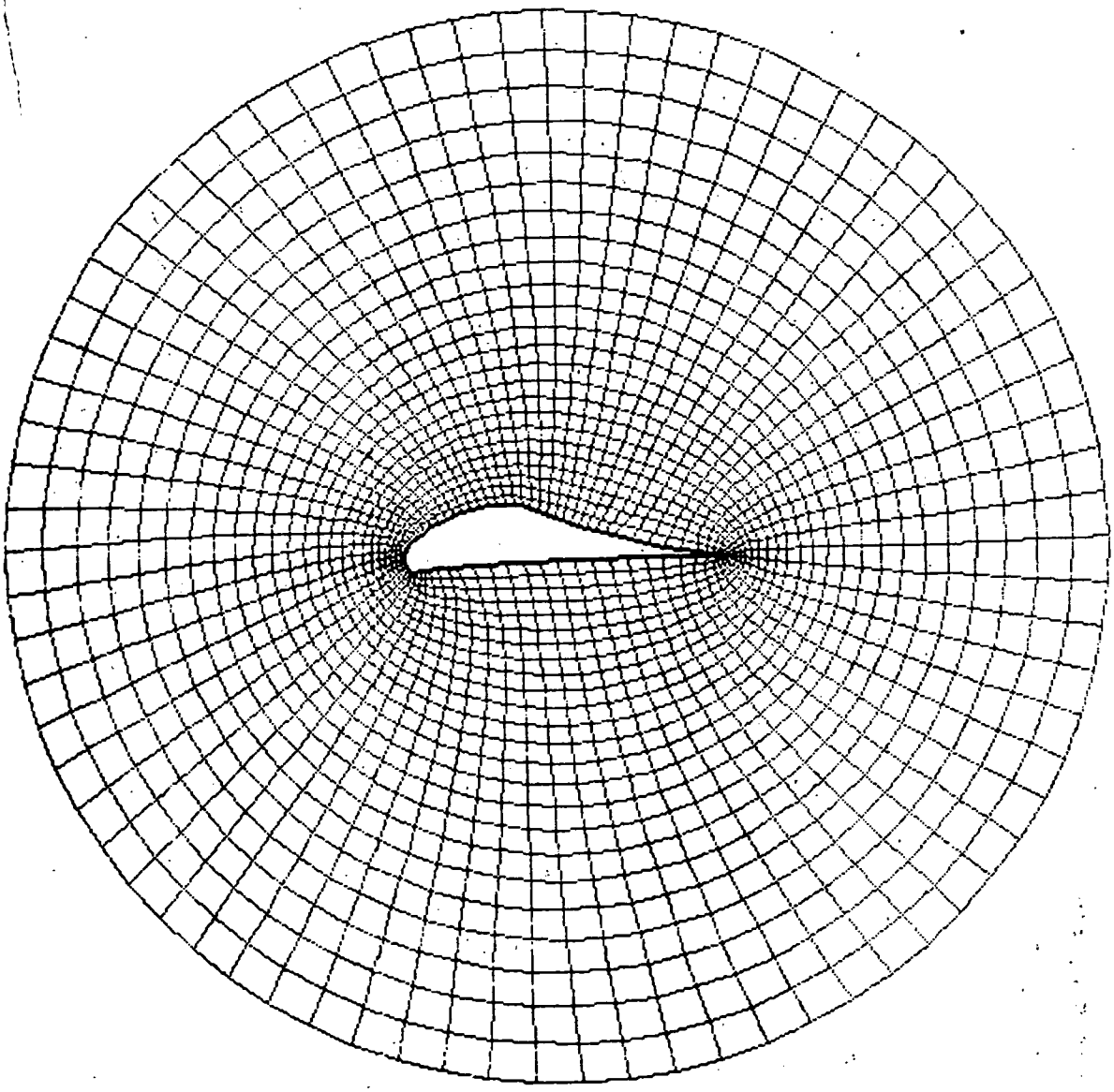

Figure 7.- Coordinate system for Liebeck laminar airfoil.

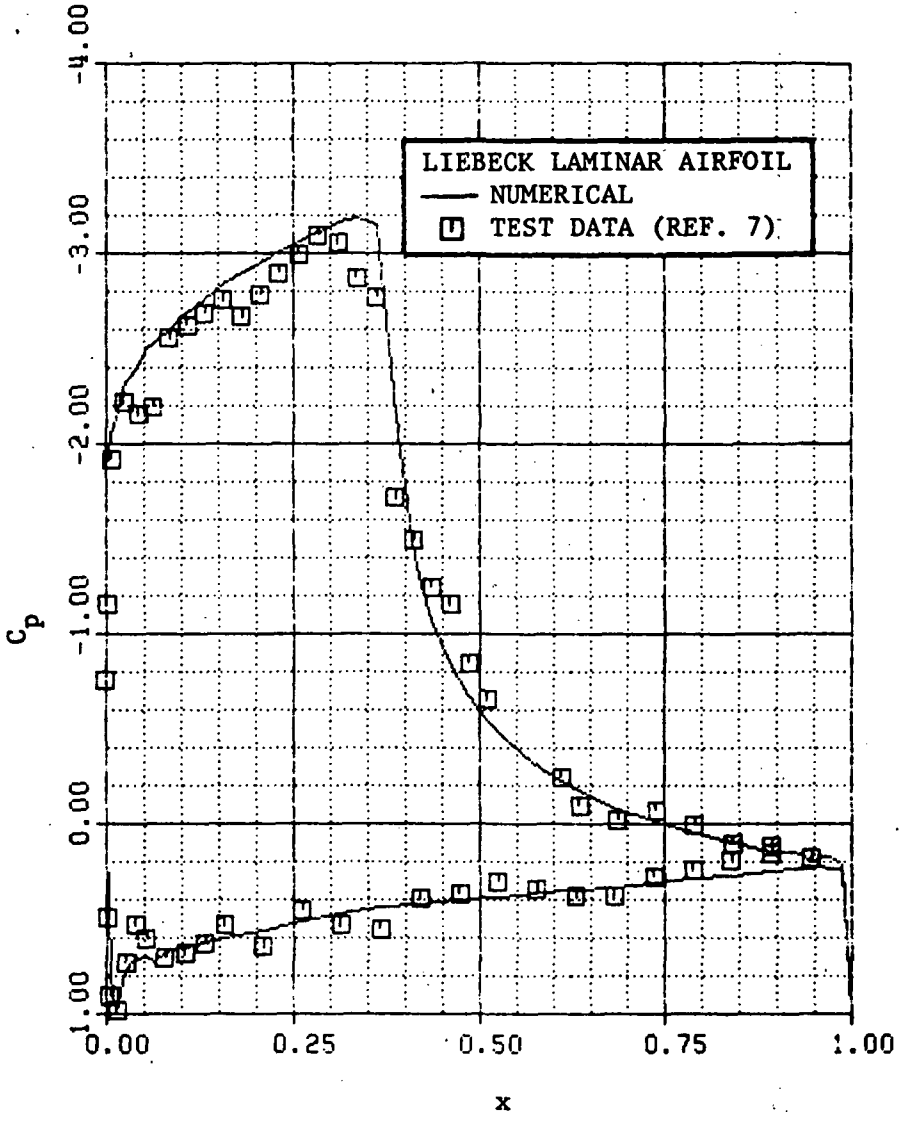

(a) Pressure distribution.

Figure 8.- Experimental and numerical potential-flow results for Liebeck laminar airfoil.

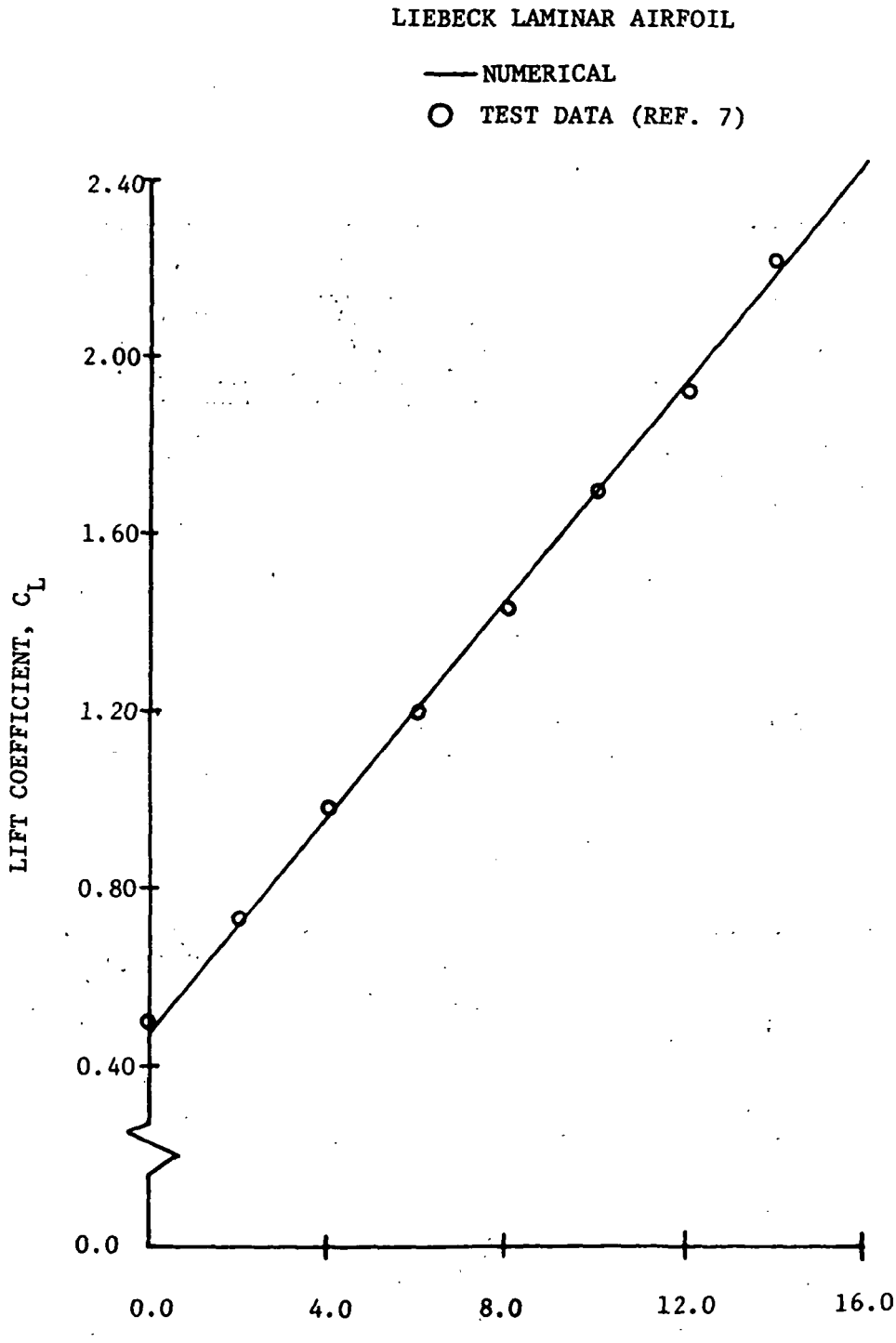

(b) Lift curve.

Figure 8.- Concluded.

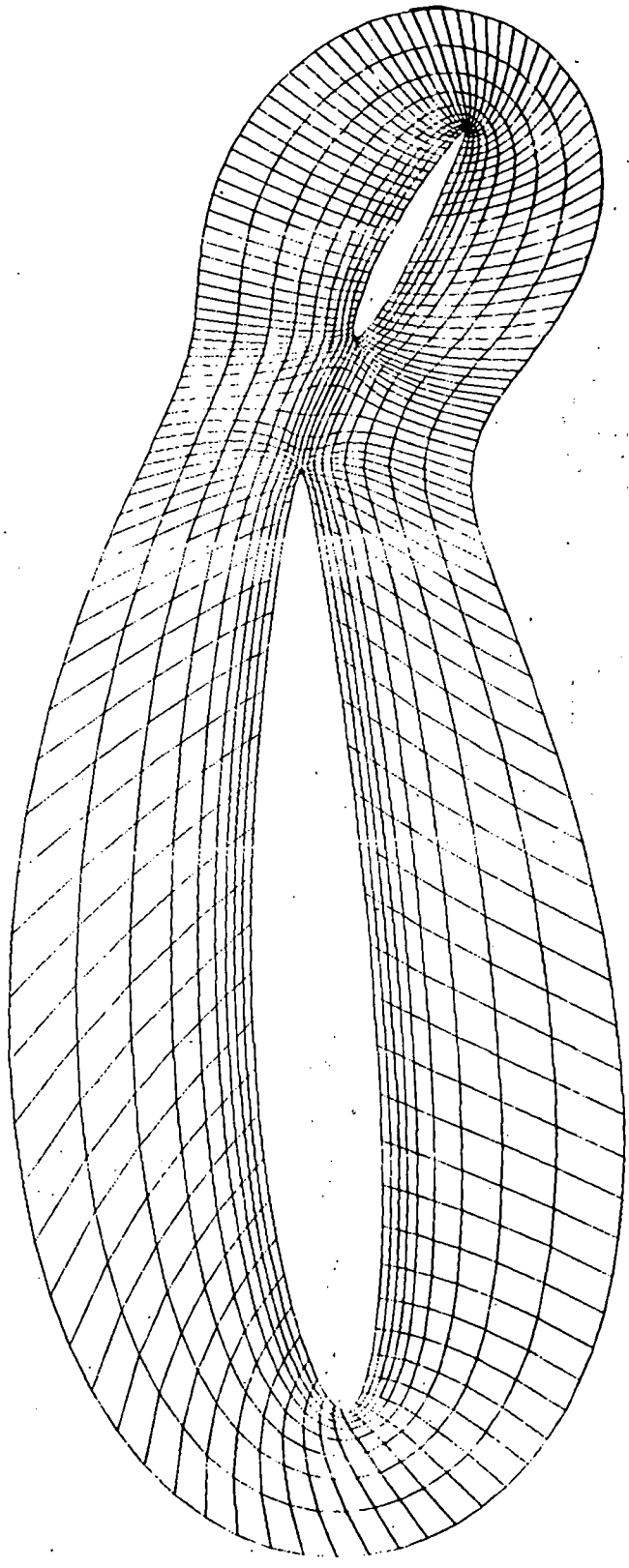

Figure 9.- Coordinate system for multiple airfoil.

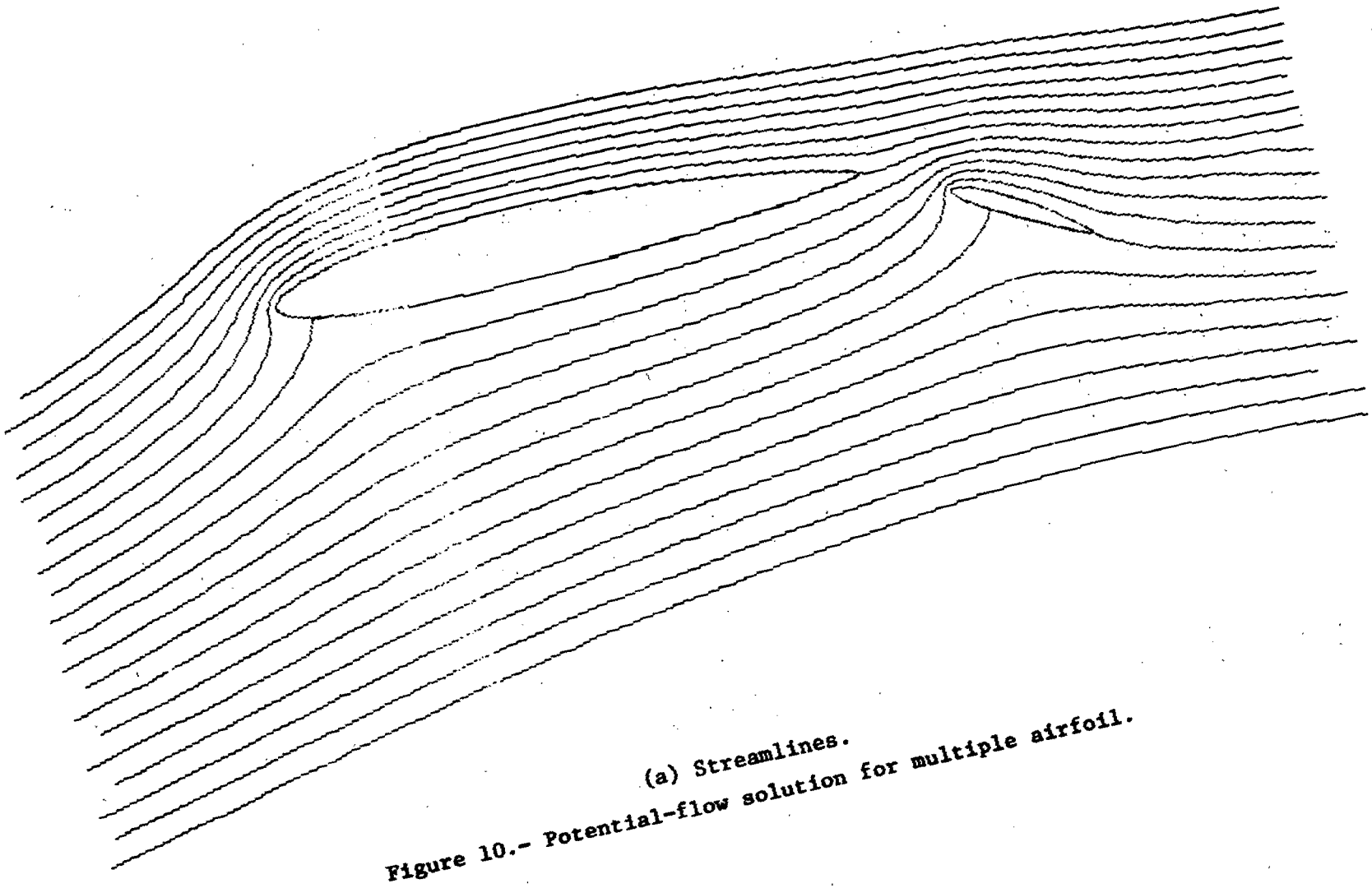

(a) Streamlines.

Figure 10.- Potential-flow solution for multiple airfoil.

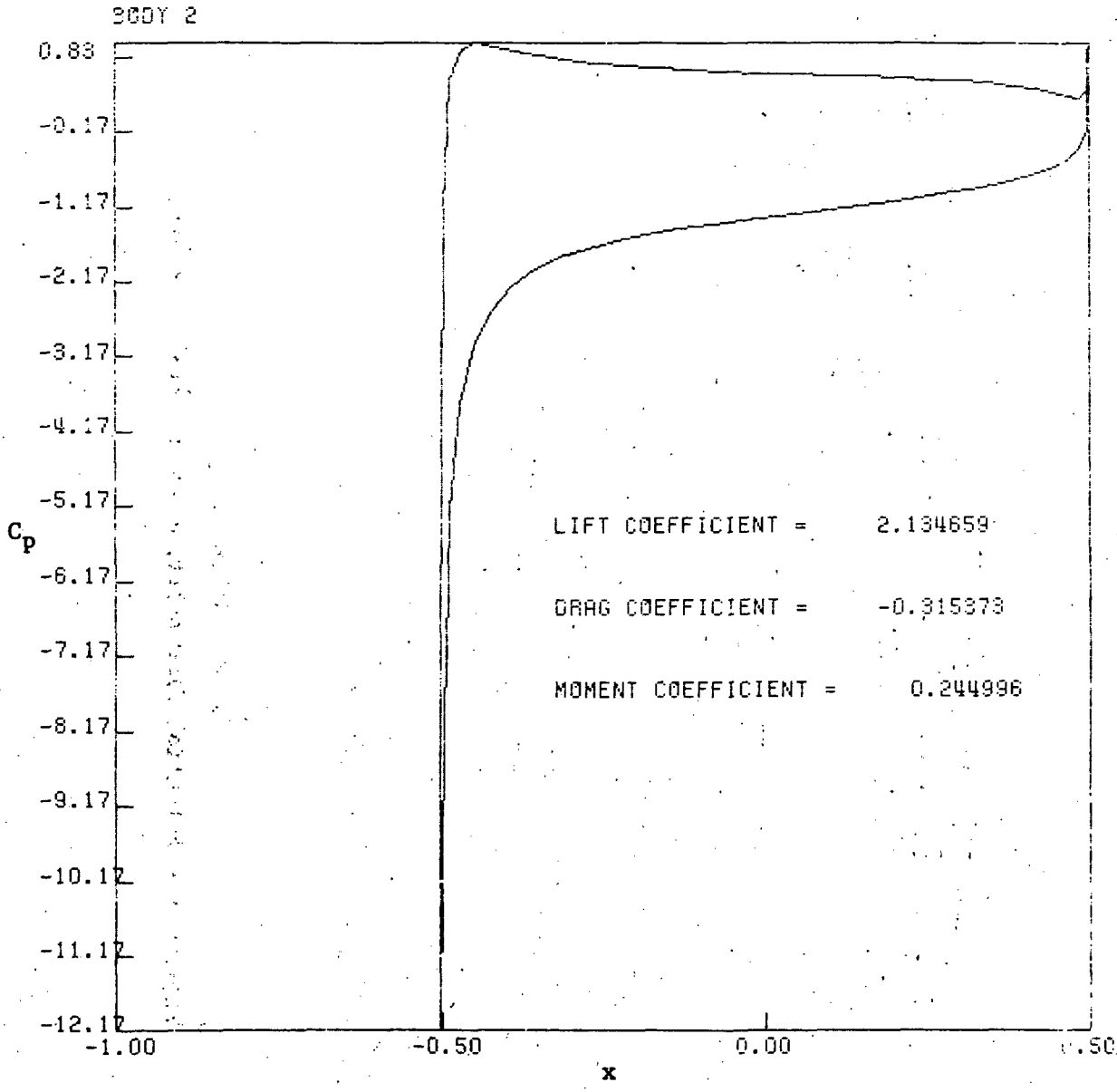

(b) Pressure distribution - fore body.

Figure 10.- Continued.

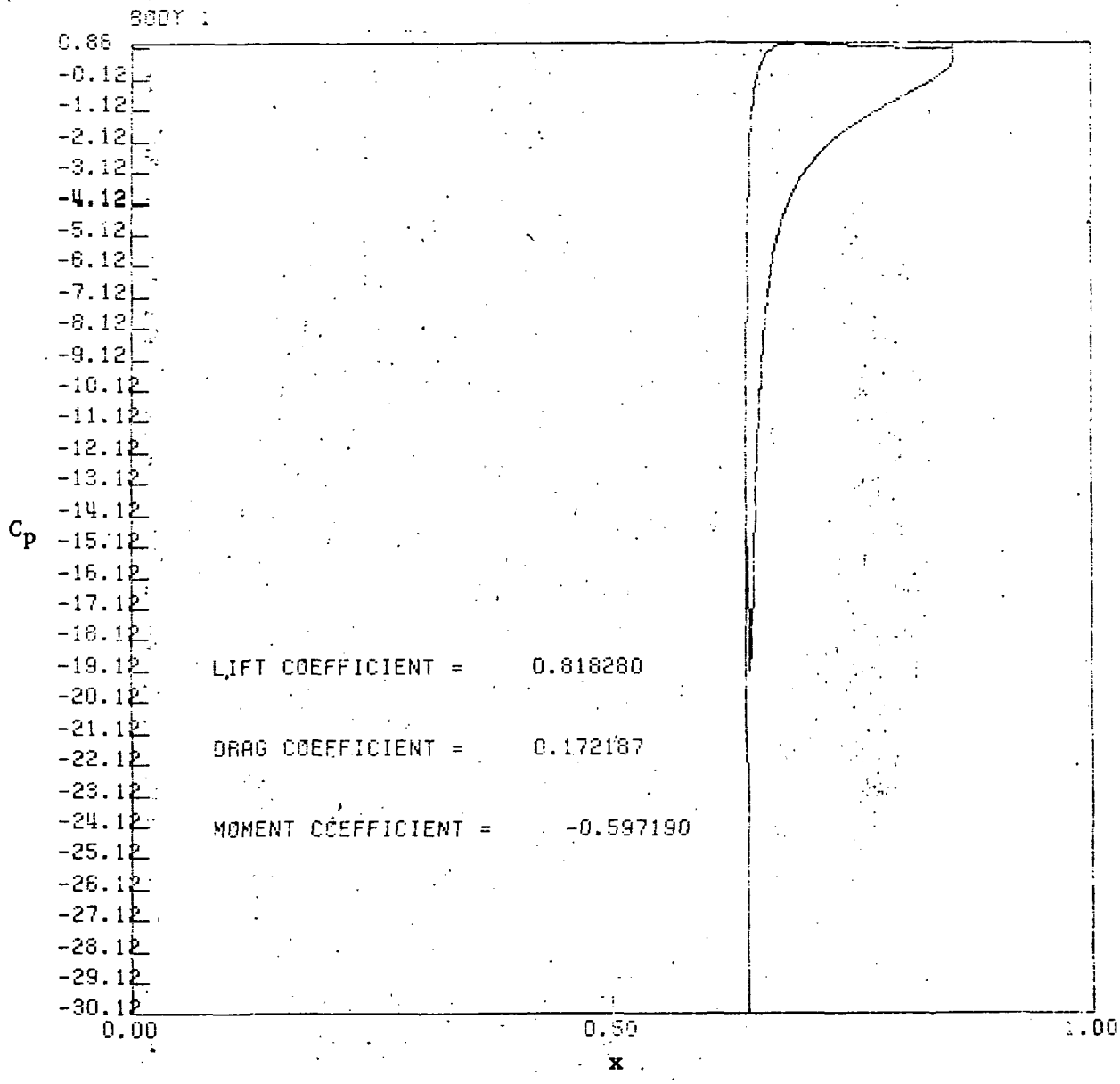

(c) Pressure distribution - aft body.

Figure 10.- Concluded.

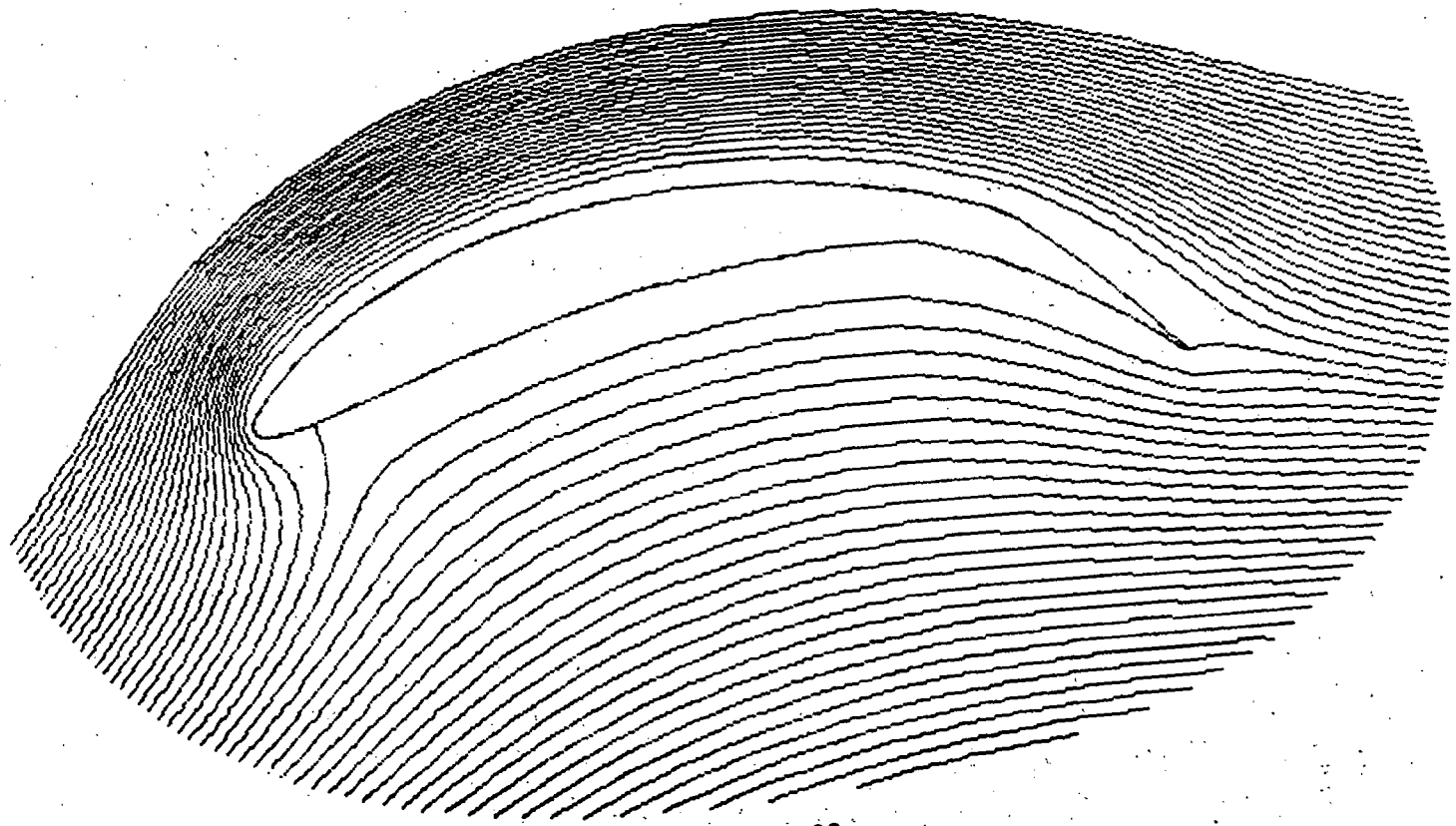

(a) $t = 0.22$.

Figure 11.- Stream-function contours for flapped Kármán-Trefftz airfoil.

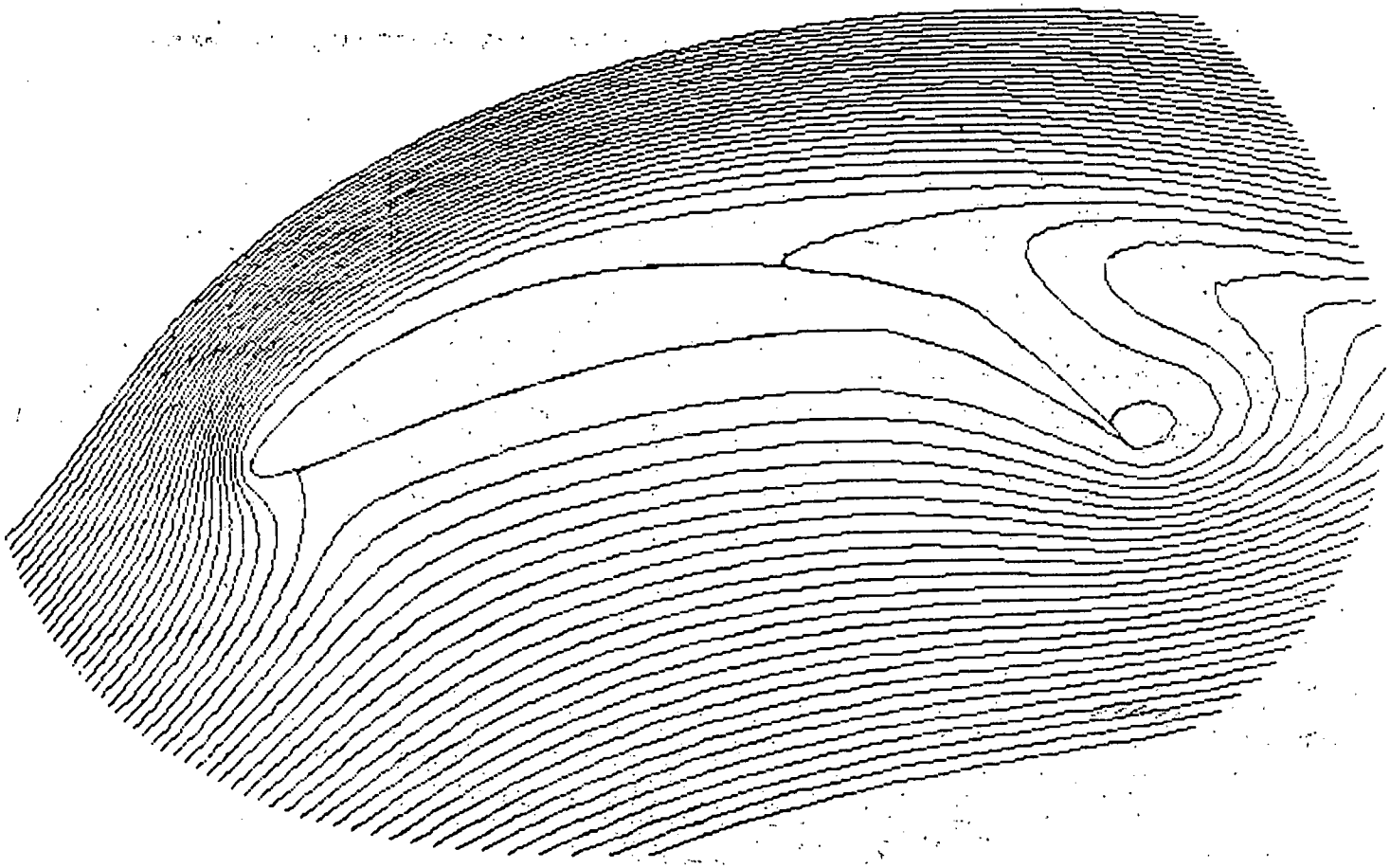

(b) t = 1.06.

Figure 11.- Concluded.

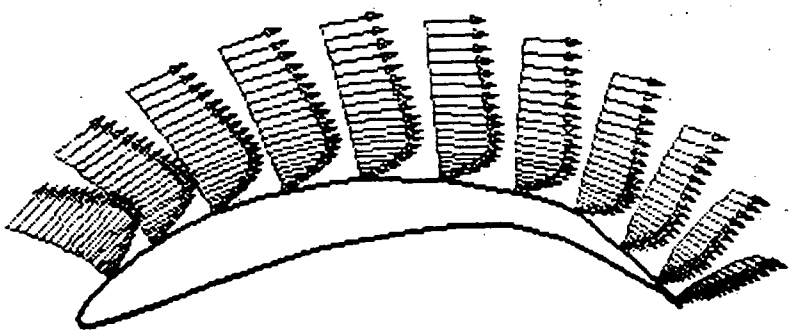

(a) t = 0.08.

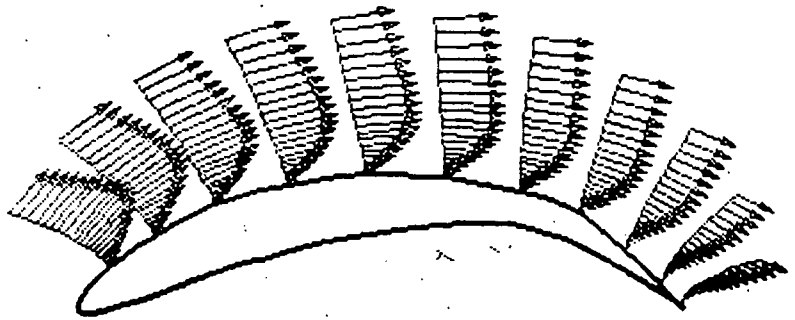

(b) t = 0.22.

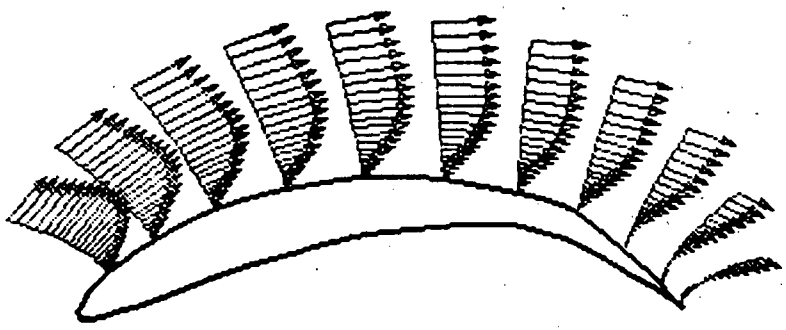

(c) t = 0.38.

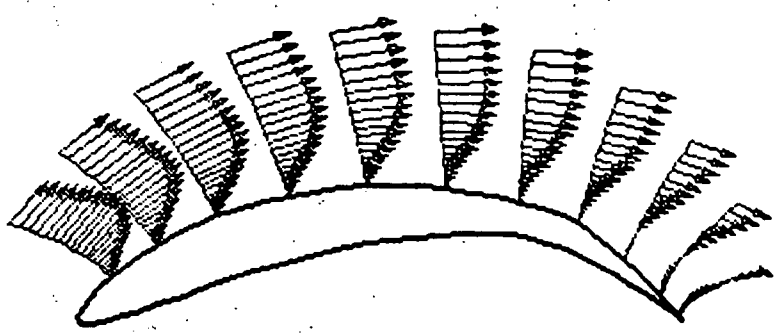

(d) t = 0.54.

Figure 12.- Velocity profiles for flapped Kármán-Trefftz airfoil.

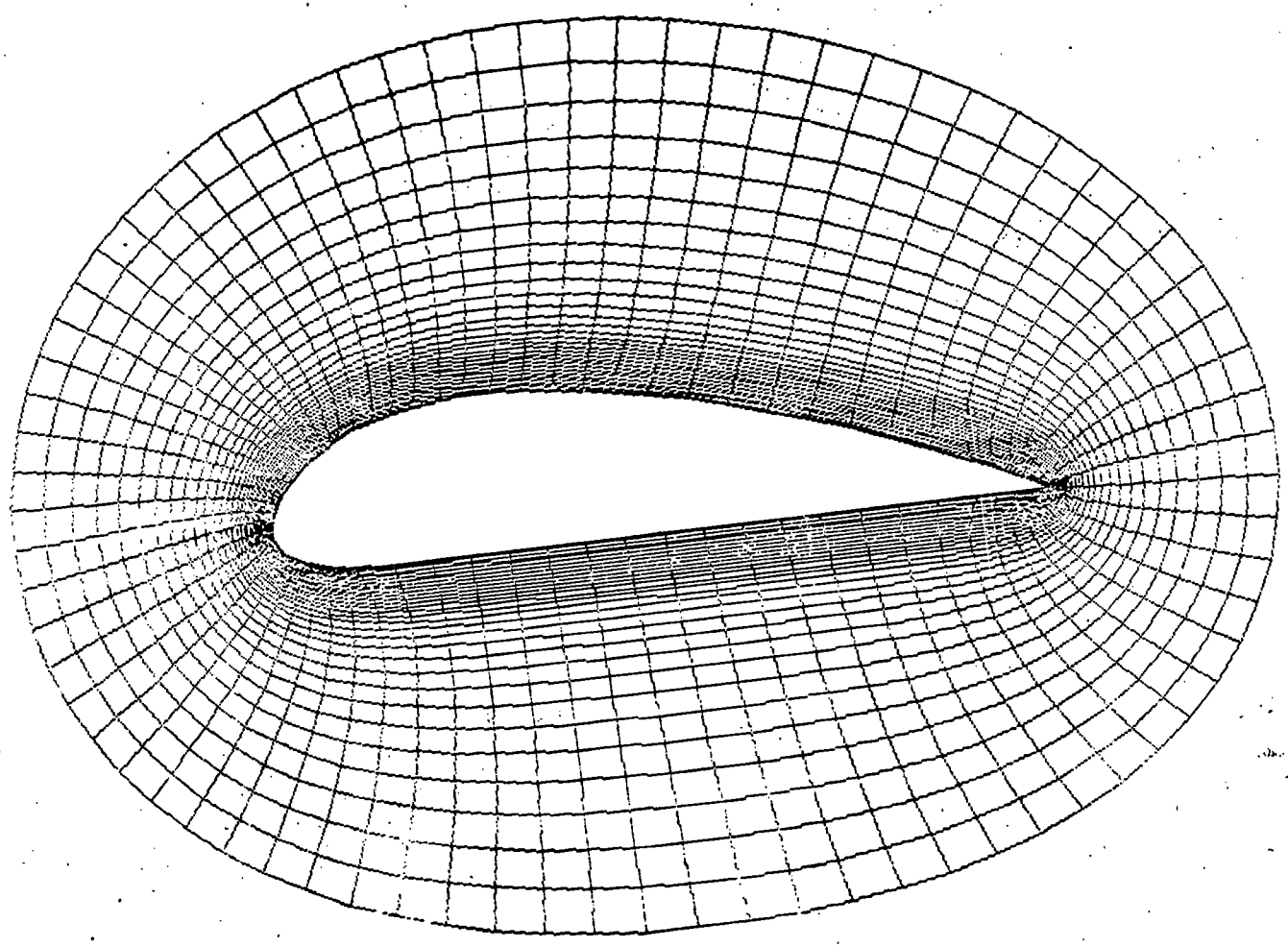

Figure 13.- Contracted coordinate system for the Göttingen 625 airfoil.

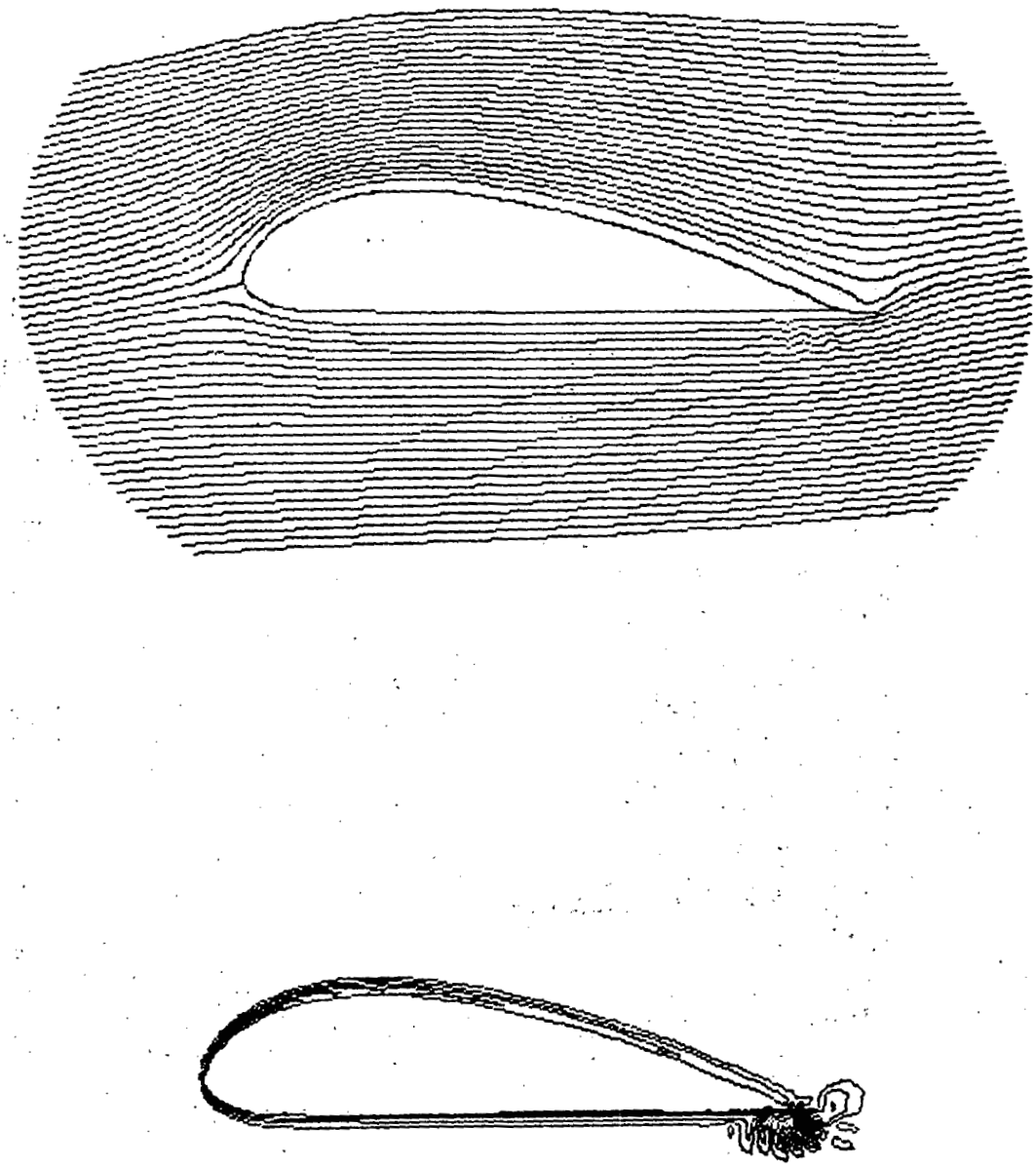

(a) t = 0.118.

Figure 14.- Stream-function and vorticity contours for Göttingen 625 airfoil.

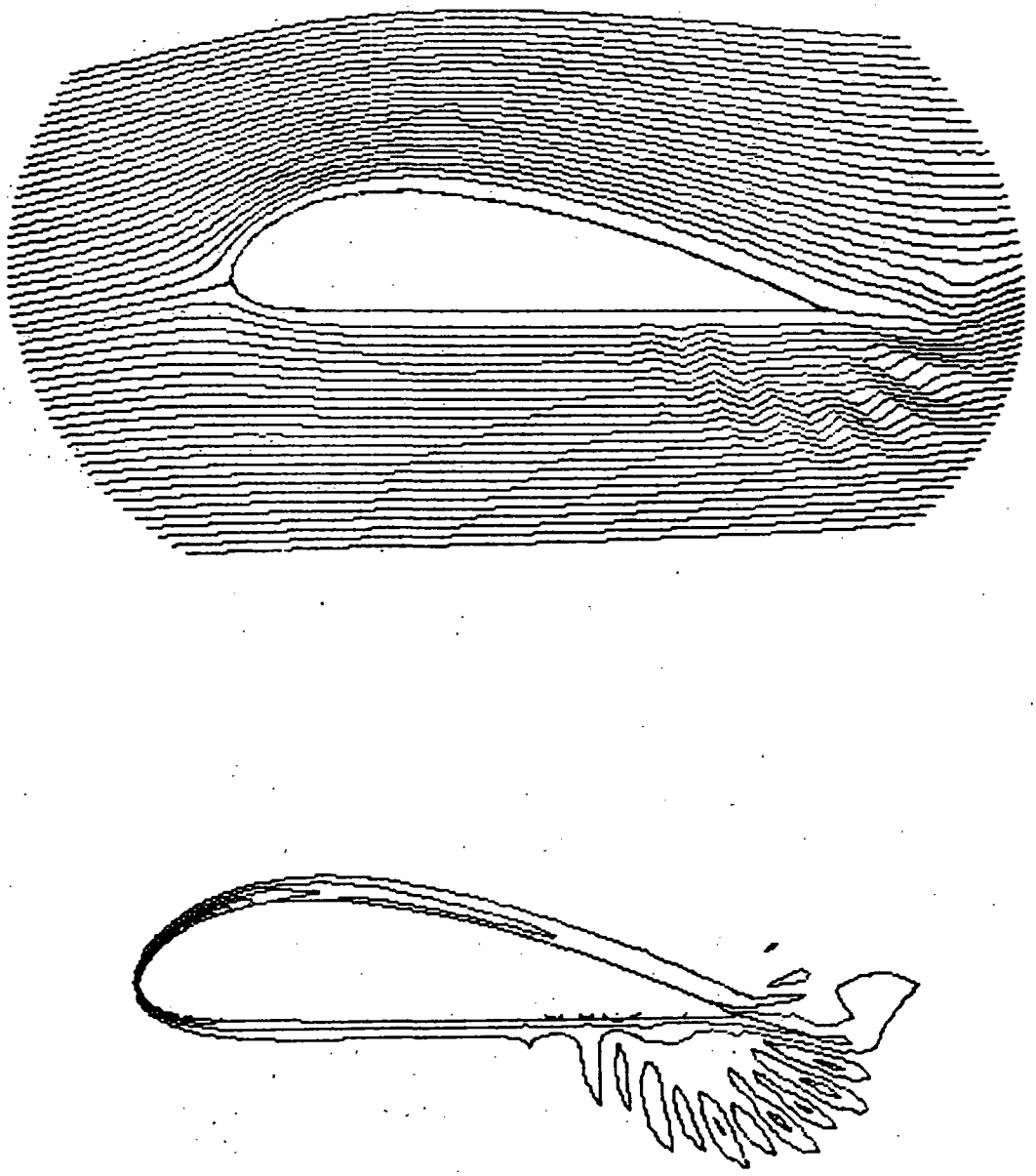

(b) t = 0.336.

Figure 14.- Continued.

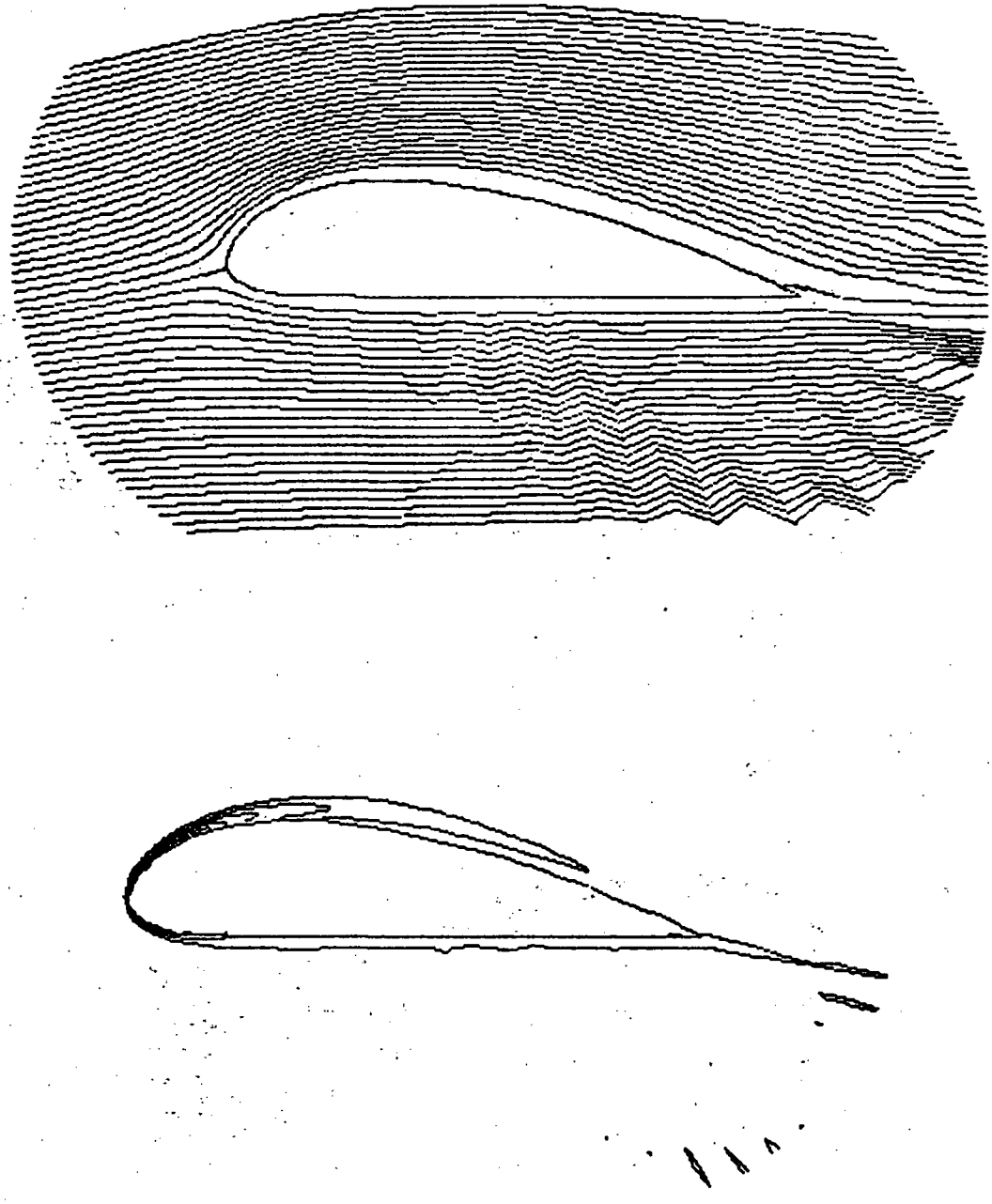

(c) t = 0.658.

Figure 14.- Concluded.

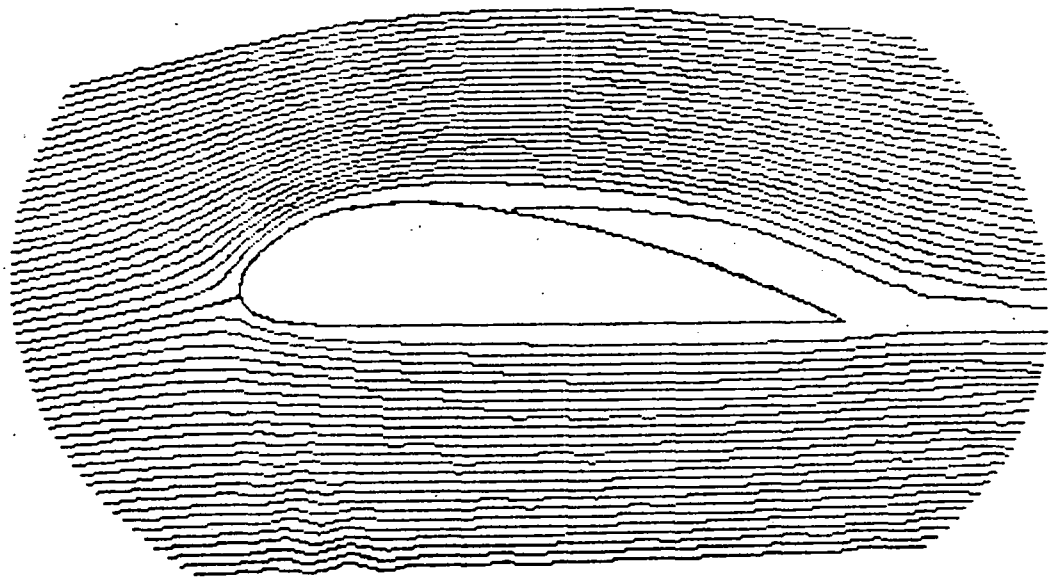

t=1.53

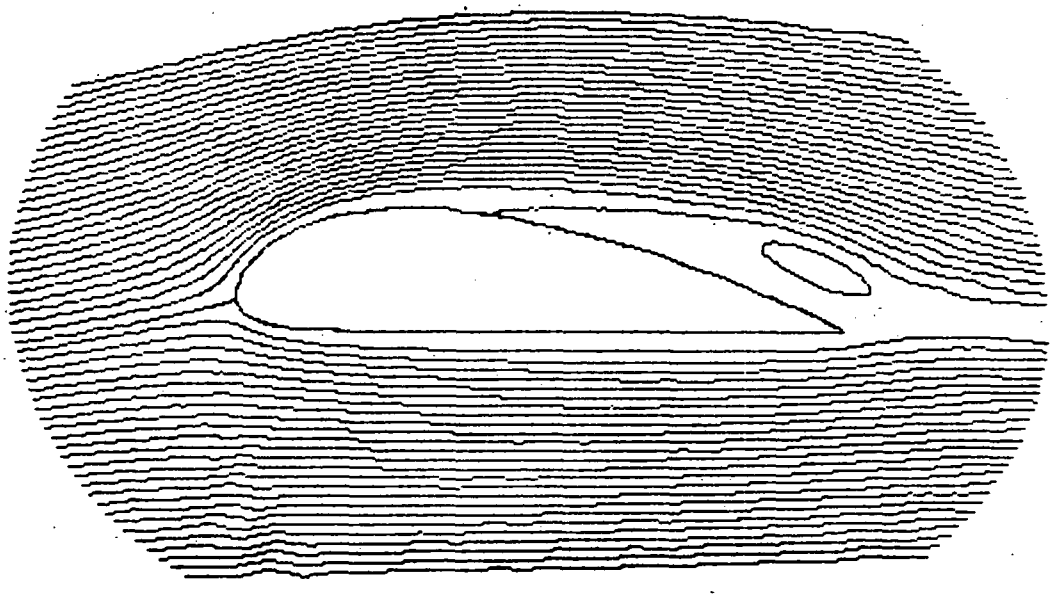

t=1.83

(a) t = 1.53 and 1.83.

Figure 15.- Stream-function contours for Göttingen 625 airfoil.

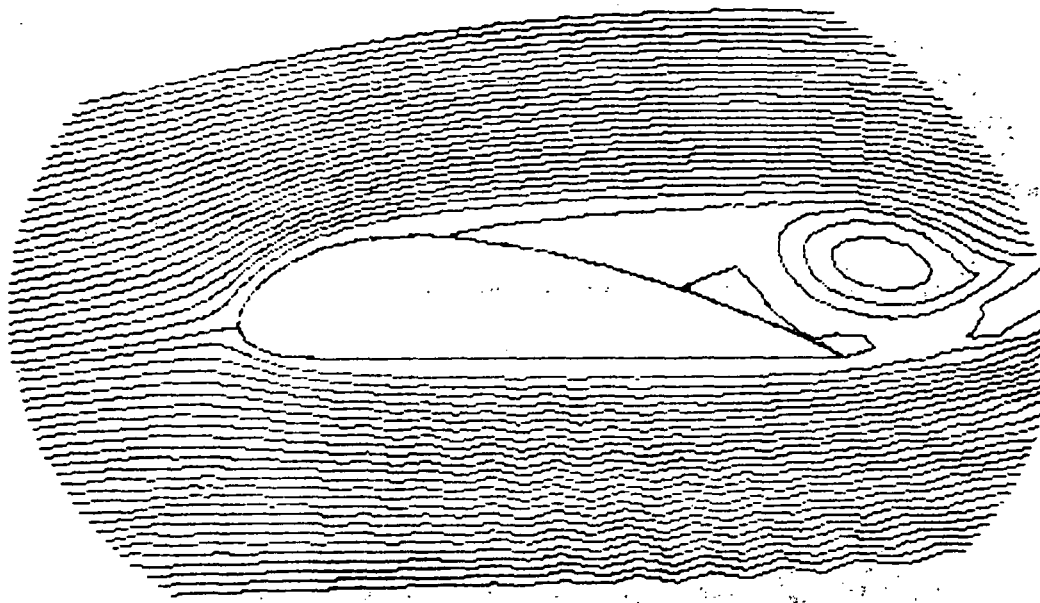

t=3.13

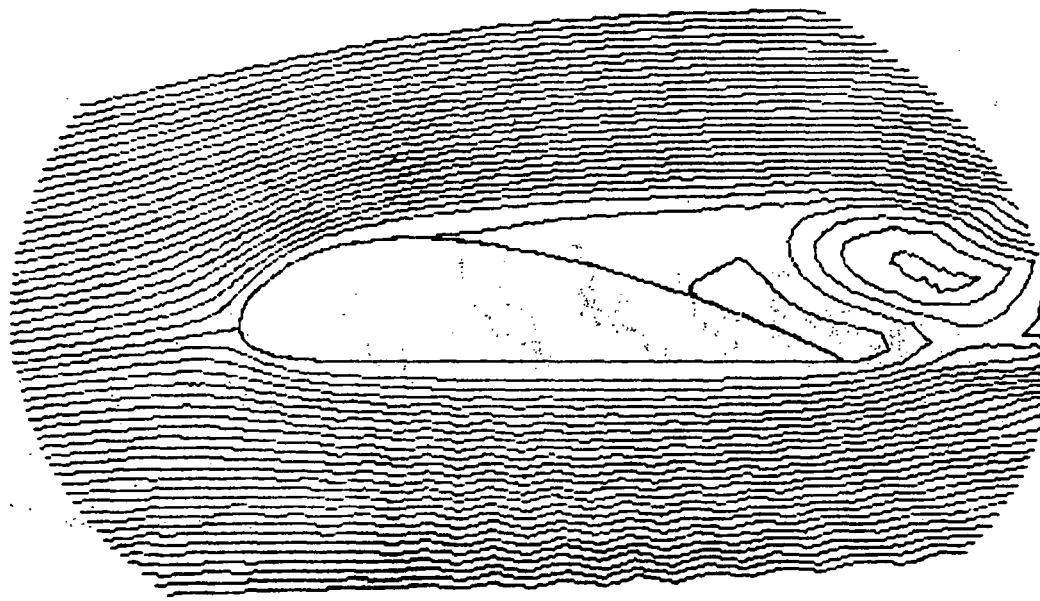

t=3.33

(b) t = 3.13 and 3.33.

Figure 15.- Concluded.

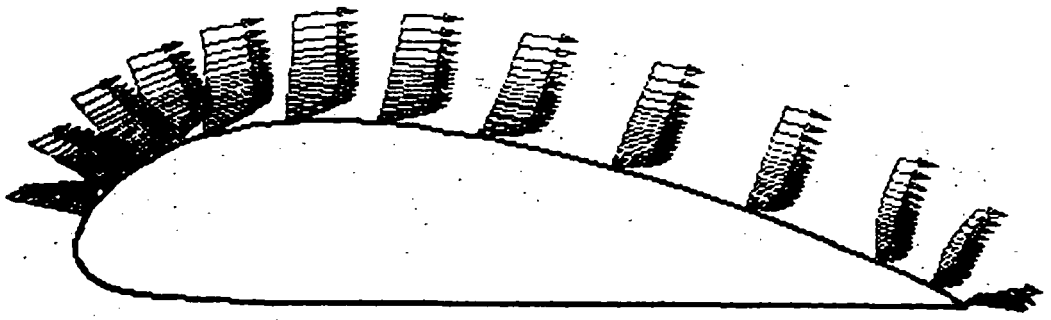

t=0.118

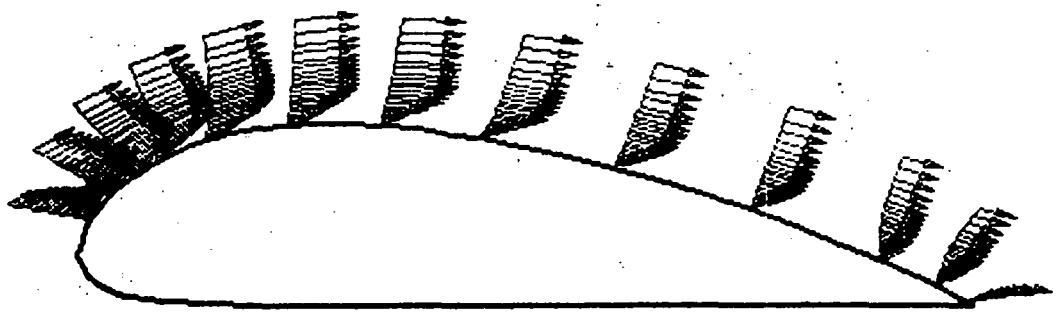

t=0.336

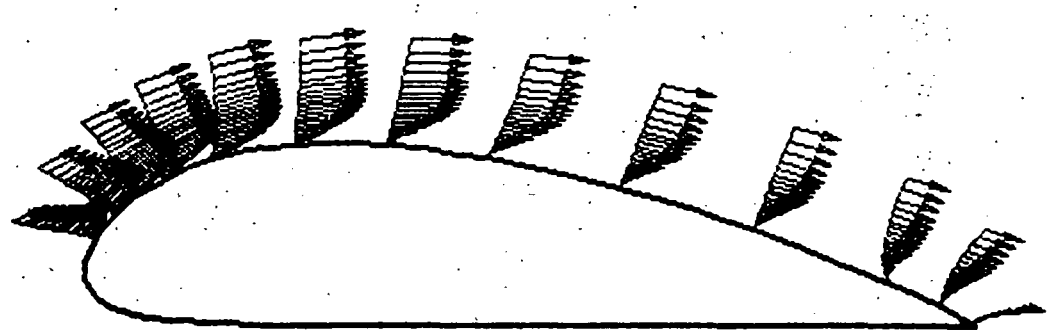

t=0.658

(a) t = 0.118, 0.336, and 0.658.

Figure 16.- Upper-surface velocity profiles for Göttingen 625 airfoil.

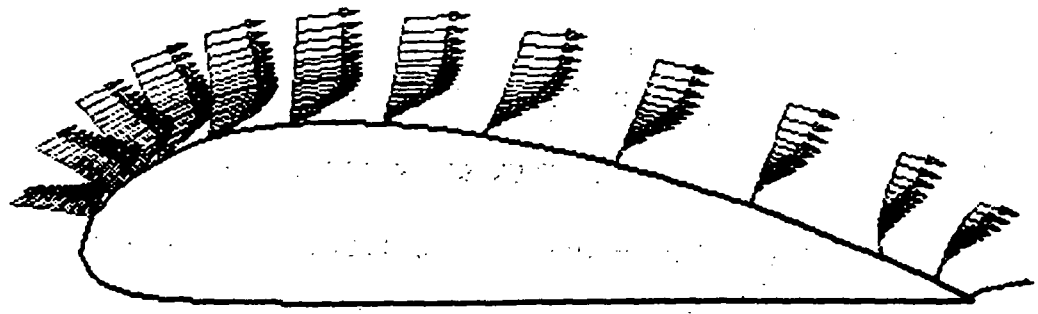

t=1.012

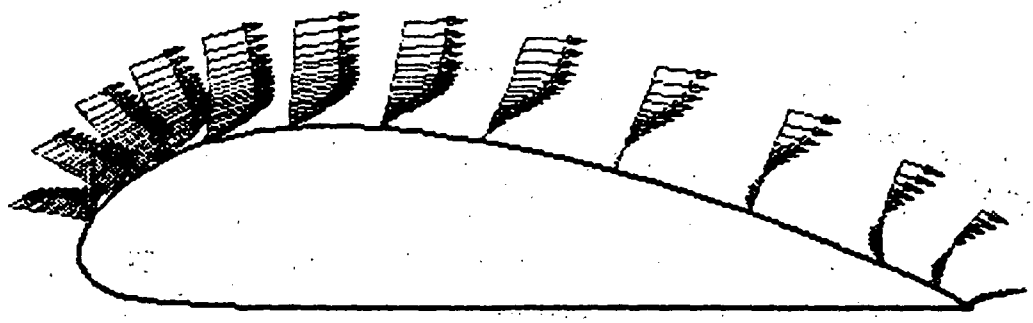

t=1.53

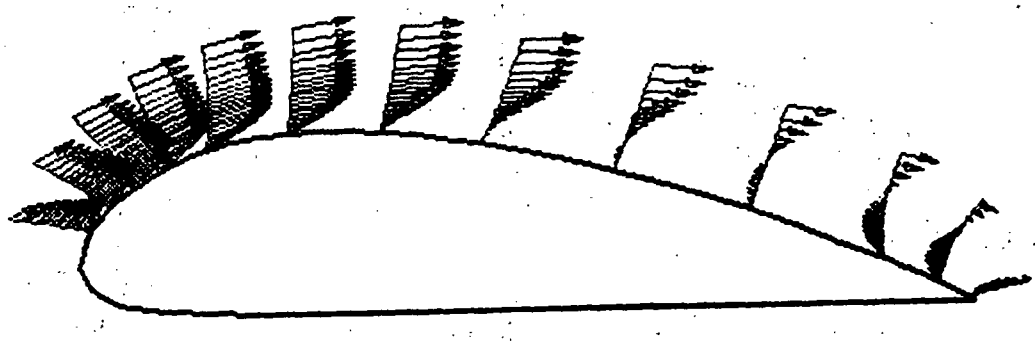

t=1.83

(b) t = 1.012, 1.53, and 1.83.

Figure 16.- Concluded.

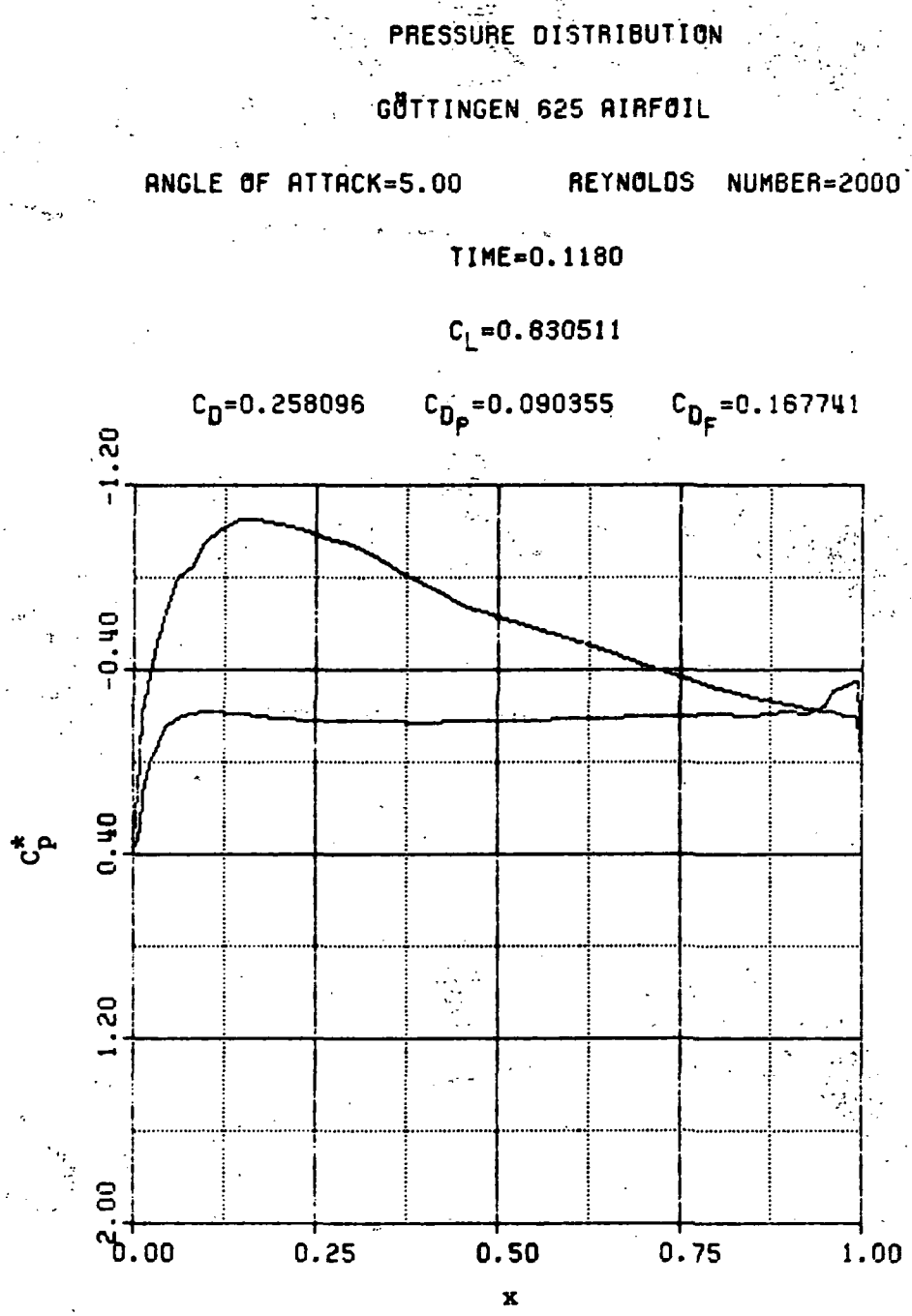

(a) t = 0.118.

Figure 17.- Pressure distribution for Göttingen 625 airfoil.

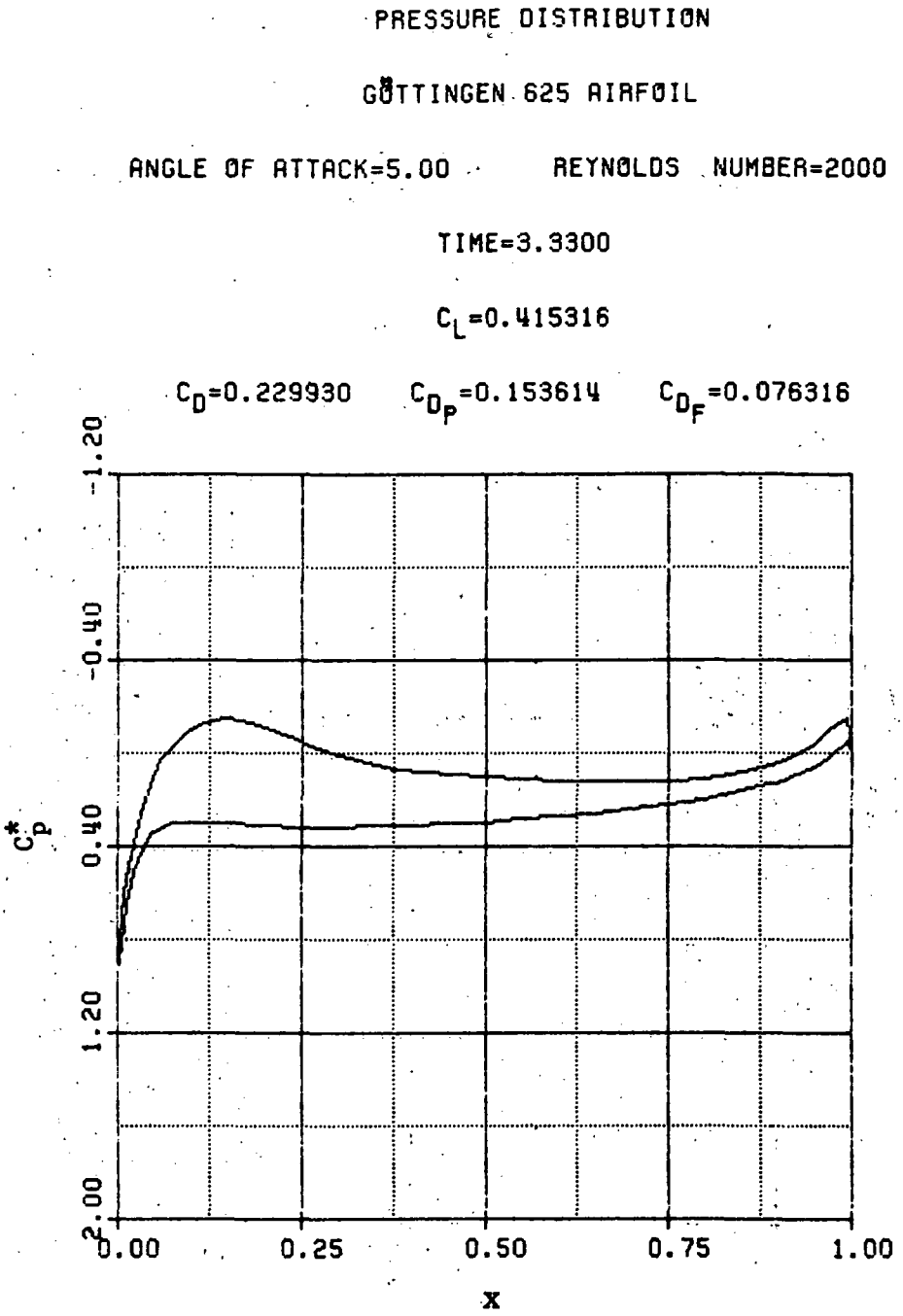

(b) t = 3.33.

Figure 17.- Concluded.

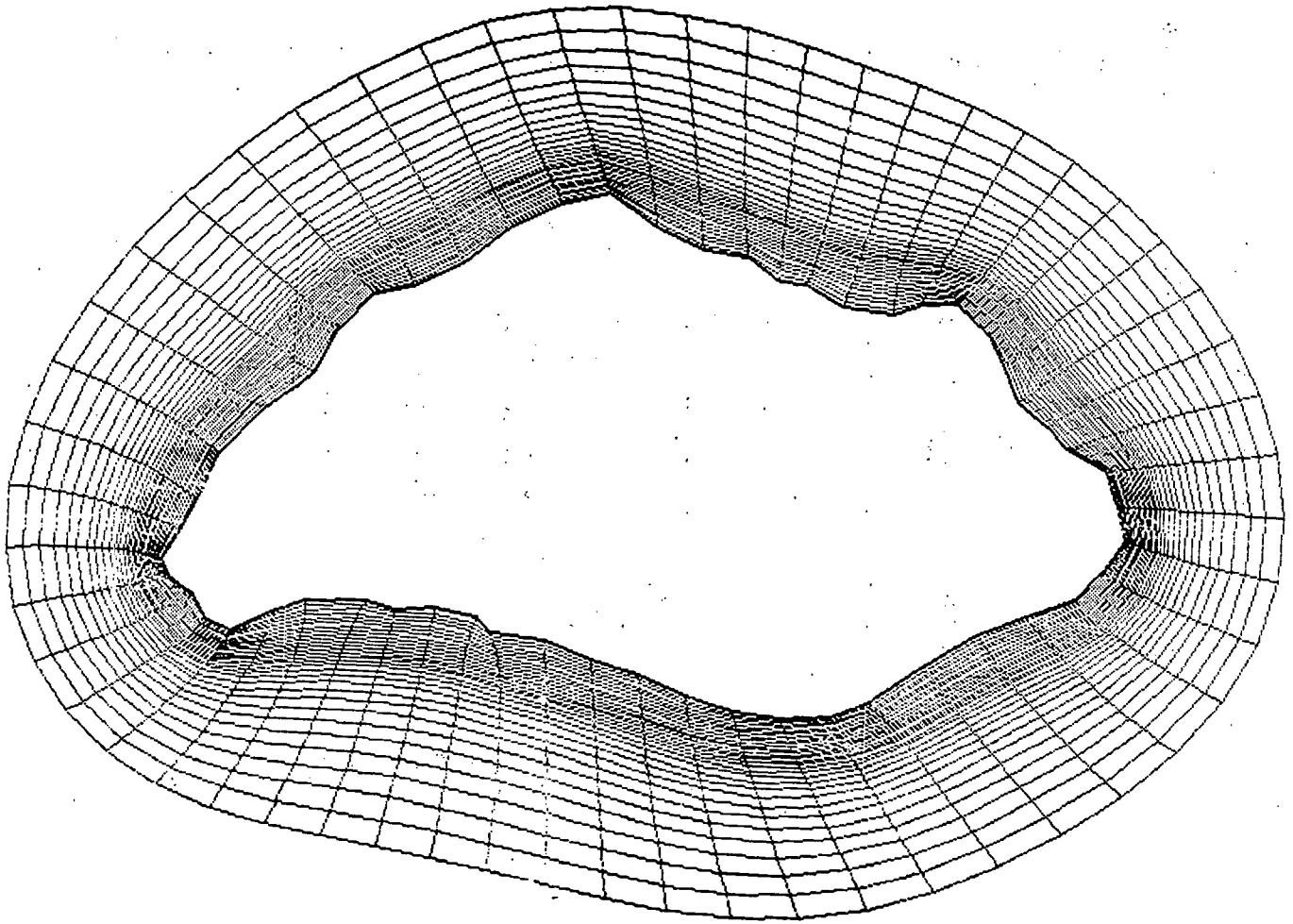

Figure 18.- Contracted coordinate system for cambered rock.

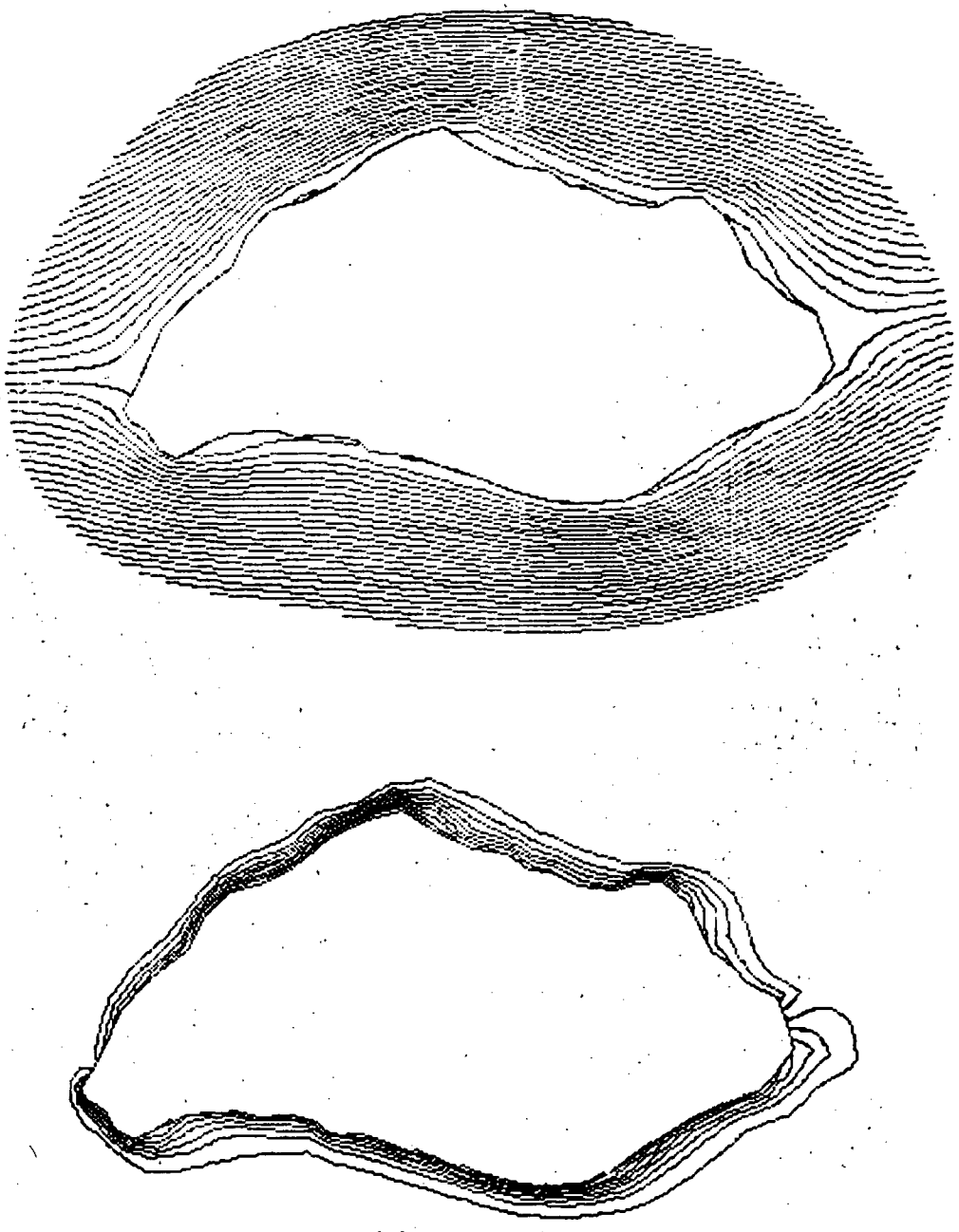

(a) t = 0.15.

Figure 19.- Stream-function and vorticity contours for cambered rock.

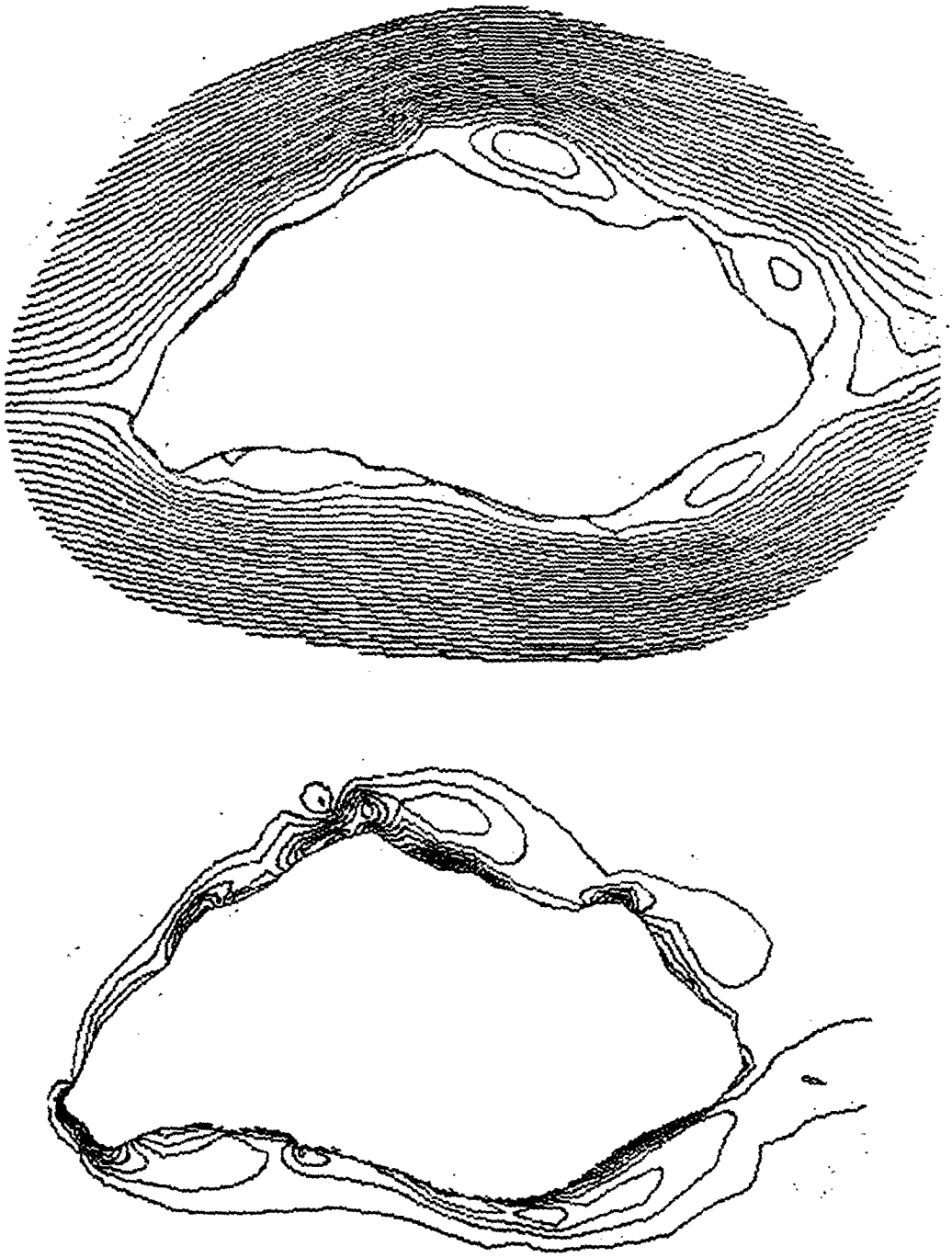

(b) t = 0.5.

Figure 19.- Continued.

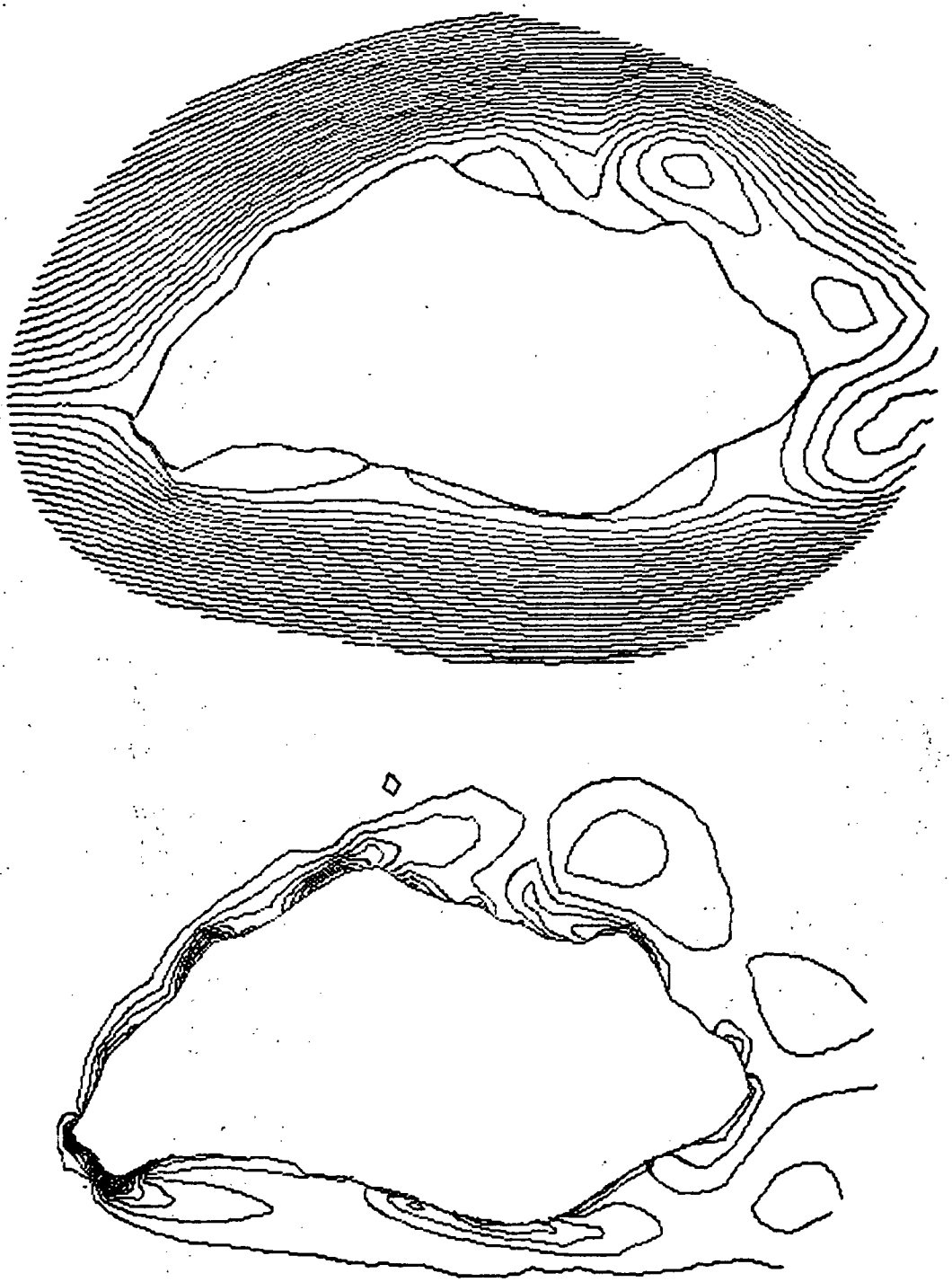

(c) t = 1.0.

Figure 19.- Concluded.

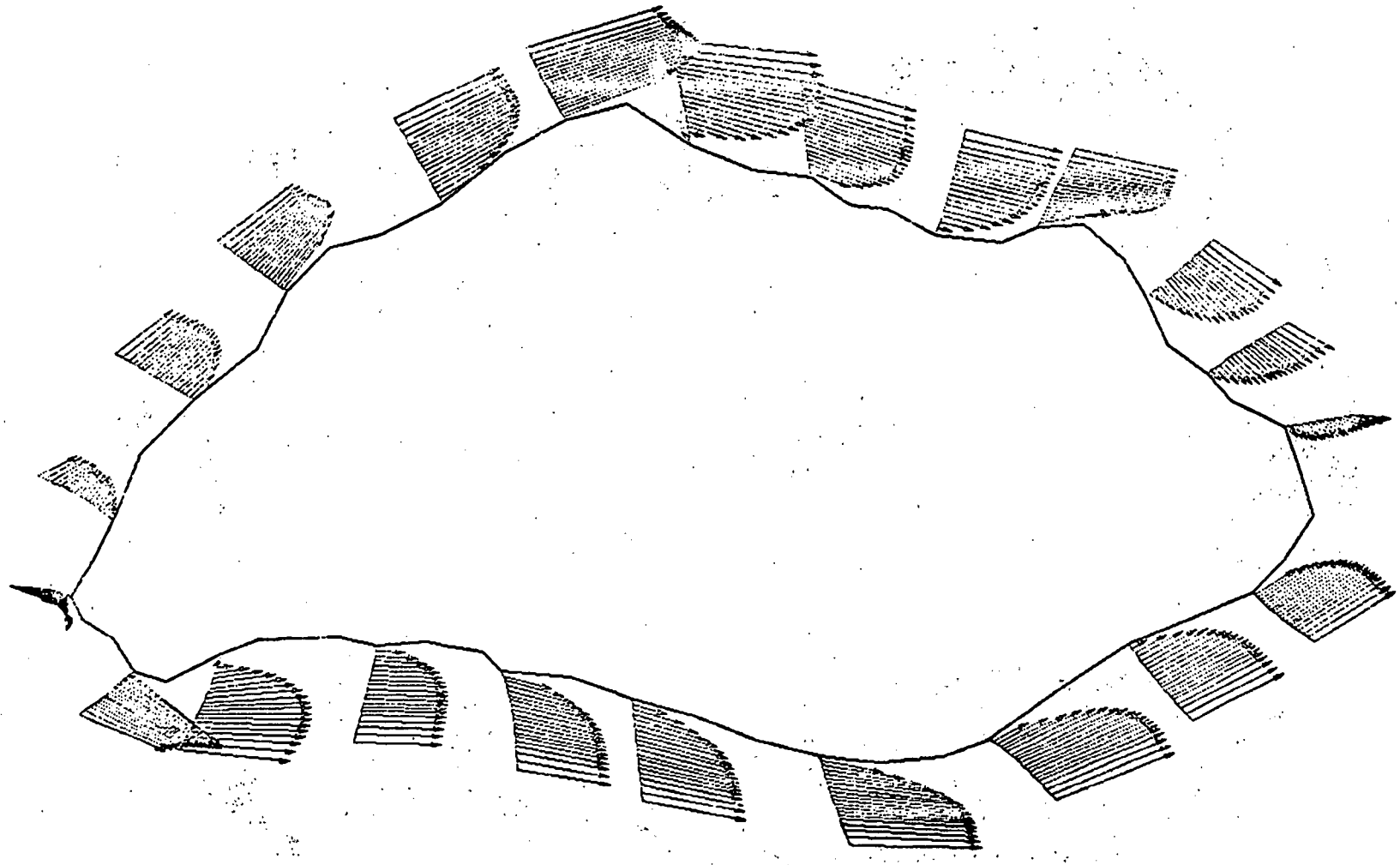

(a) t = 0.1.

Figure 20.- Velocity profiles for cambered rock.

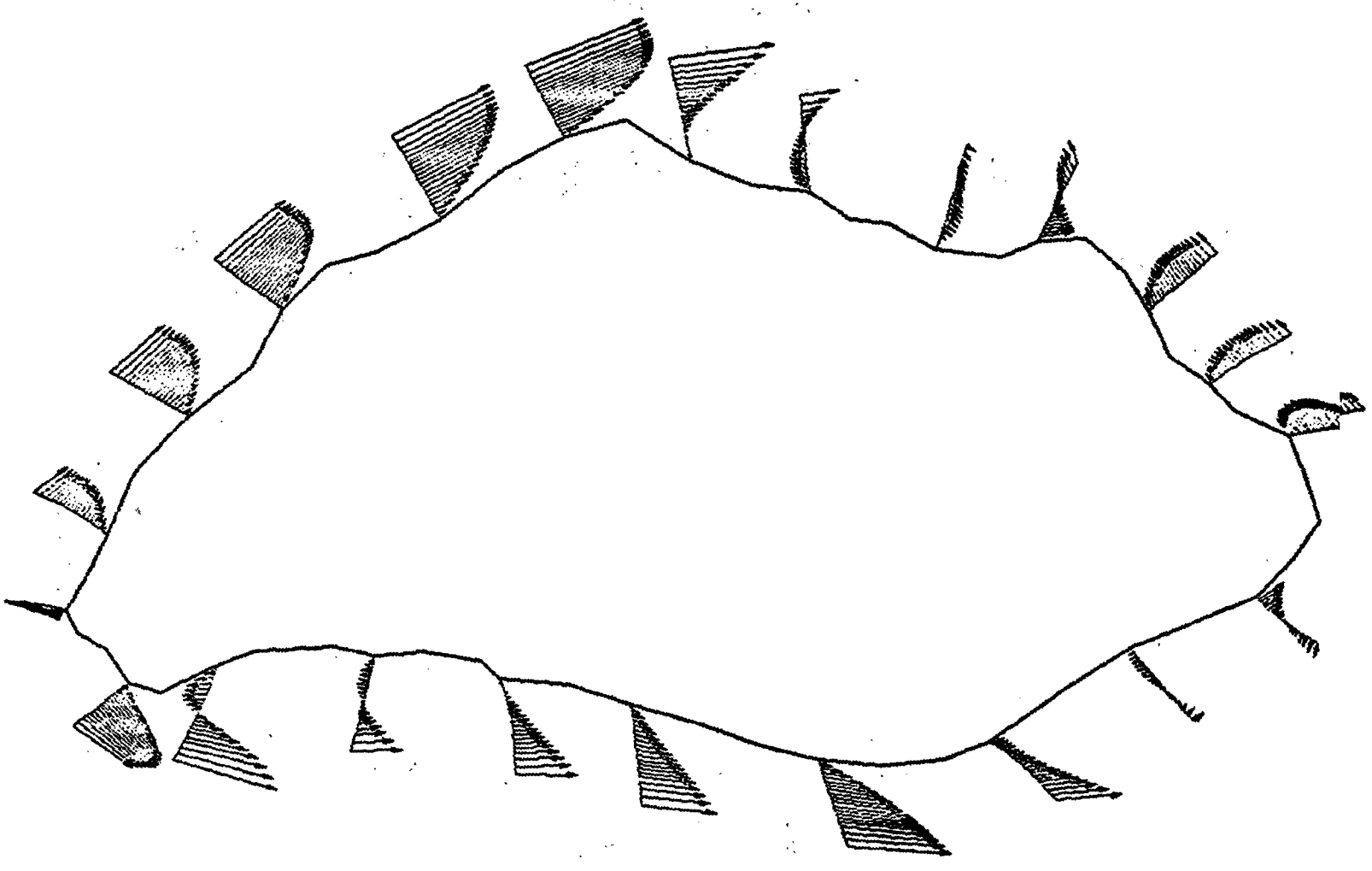

(b) $t = 1.2$.

Figure 20.- Concluded.

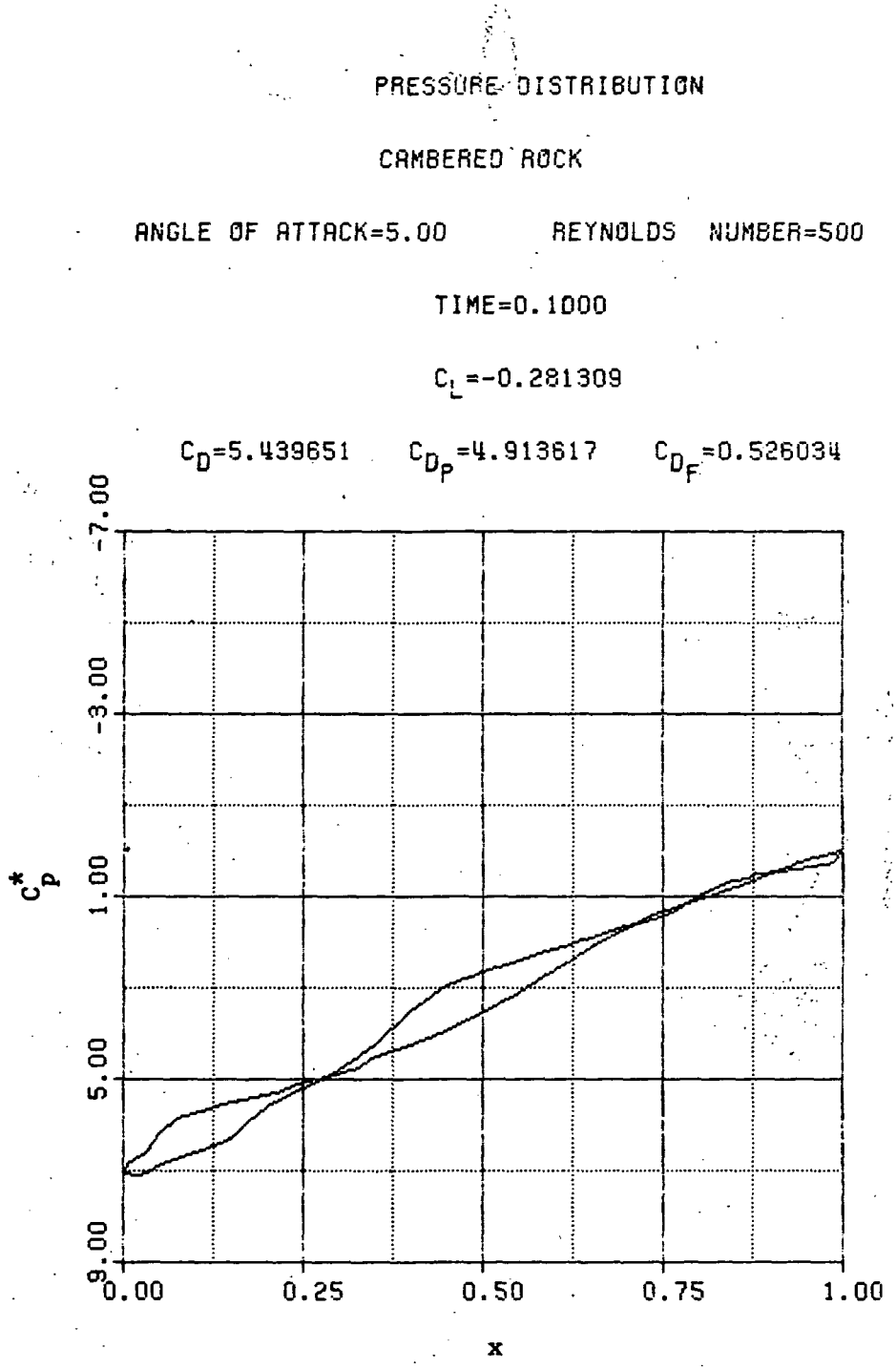

(a) t = 0.1.

Figure 21.- Pressure distribution for cambered rock.

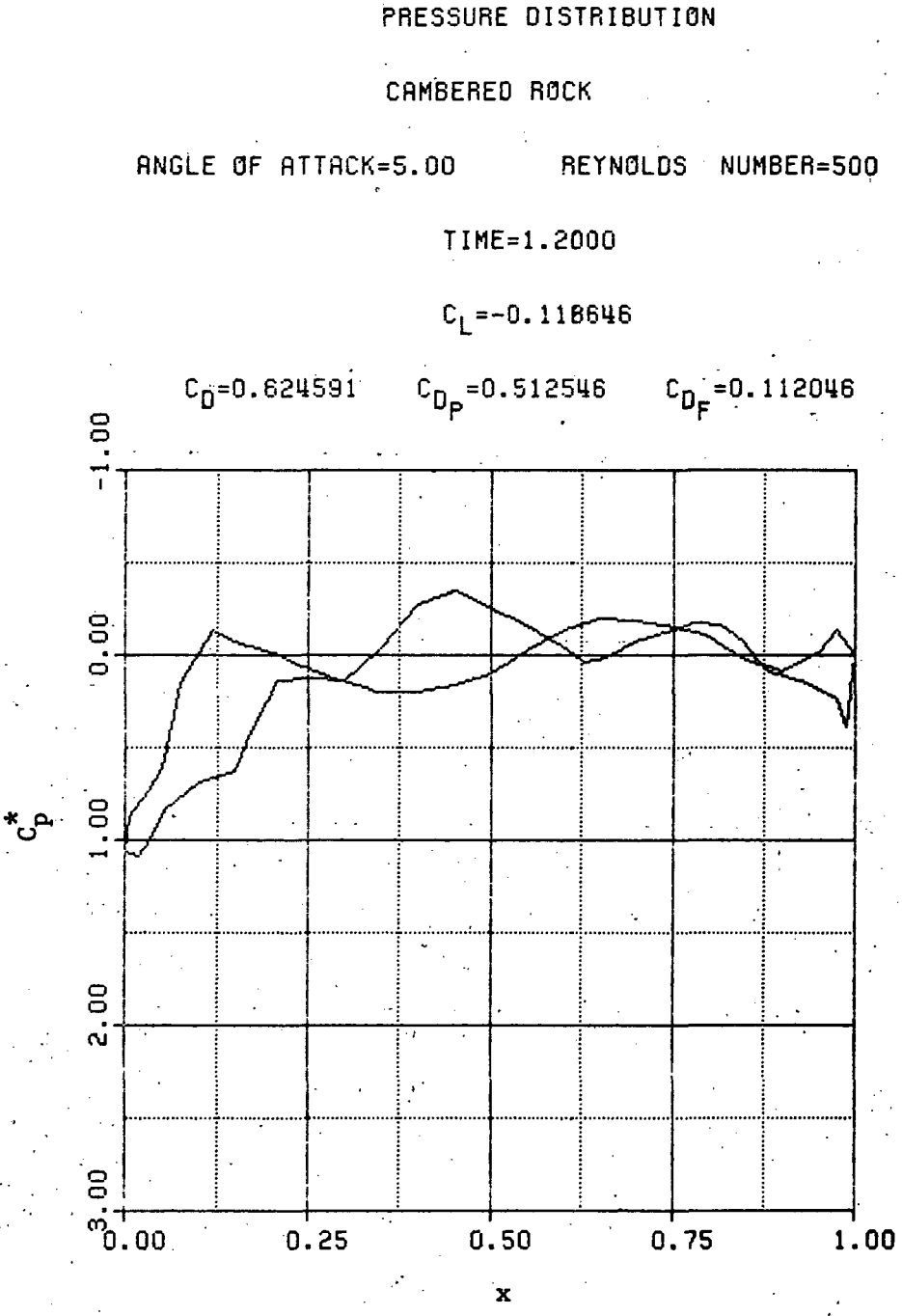

(b) t = 1.2.

Figure 21.- Concluded.

NUMERICAL COMPUTATION OF VISCOUS FLOWS ON THE LEE SIDE OF BLUNT SHAPES FLYING AT SUPERSONIC SPEEDS

By John V. Rakich

NASA Ames Research Center

and

Stephen C. Lubard

RDA Inc.

SUMMARY

A numerical method for solving the parabolic approximation to the steady-state compressible Navier-Stokes equations is critically examined. The approximation neglects only the streamwise gradients of shear stress. An implicit finite difference method is used which advances the solution downstream from an initial data surface and determines the complete viscous-inviscid flow between the body and bow shock wave. It is necessary that the inviscid portion of the flow field be supersonic. Crossflow separation is also determined as part of the solution.

The method is applied to a 15° sphere-cone at 15° angle of attack, and the results are compared with available experiment and with an inviscid method-of-characteristics calculation. Excellent agreement between viscous and inviscid theories is obtained in the inviscid regions of the flow. The viscous calculations agree well with experimental surface and pitot pressures and with surface heating rates.

INTRODUCTION

The flow field on the leeward side of bodies has received considerable attention for many years. The flow is inherently viscous and develops into a vortex at moderate angles of attack. At high speeds, lee-side flows are important because the local heating is difficult to correlate and because the shed vortices can interact with aircraft components such as a canopy, a vertical tail, etc. Recently, for example, lee-side flows have become a factor in the design of the space shuttle orbiter thermal protection system.

Lee-side flows are difficult to calculate because thin-boundary-layer theory is not applicable and the concept of matching inviscid and viscous flow becomes highly questionable. Early attempts to predict lee-side flows were based on vortex tracing methods. However, for such methods the separation point must be specified, a priori, and that point is unknown. Therefore vortex tracing methods are inherently empirical. Recently, two new approaches have been proposed to study the lee-side flow for a pointed cone. One approach utilizes boundary-layer type equations (Lin and Rubin, ref. 1) and requires that the pressure distribution be specified. The second approach (Lubard and Helliwell, ref. 2) makes use of the parabolic approximation to the compressible Navier-Stokes equations and solves for the complete inviscid and viscous regions of flow, including the pressure.

It is the application of the method of Lubard and Helliwell to blunt-nosed bodies that is the topic of the present paper. To use this method it is necessary to first determine an initial data solution in a region where the inviscid portion of the flow is supersonic. The starting solution for the present paper was obtained with the inviscid blunt body and method-of-characteristics codes of references 3 and 4, together with a boundary-layer program, reference 5. The results obtained for a 15° sphere-cone at 15° angle of attack are compared with experiment and with inviscid theory.

ANALYSIS

The so-called "parabolic Navier-Stokes" equations, and the numerical methods employed to solve them, have been described previously in references 2 and 6. Only the main features will be discussed here in order to illustrate the capabilities and limitations of the method.

The parabolic approximation results from the assumption that the stress derivatives in the streamwise direction are small in comparison with derivatives in the normal and circumferential directions. This assumption permits the calculation of the flow to proceed downstream from an initial data surface, provided the inviscid region of flow is supersonic. The equations have a parabolic character with respect to the downstream direction, and are elliptic with respect to the surface normal and circumferential directions. Separation and reverse flow is permitted in the crossflow plane, provided the component of velocity in the marching direction is positive. This crossflow separation causes a spiral flow pattern and is the initial stage of formation of the vortices which trail a lifting body.

To start the solution, it is necessary to determine an initial data surface in the supersonic part of the inviscid flow. For the present application to a sphere cone, the flow at the sphere-cone juncture is not separated and boundary-layer theory is applicable there. Also, the flow on the sphere is axisymmetric with respect to wind axes, which simplifies the boundary-layer solution. Therefore, an axisymmetric boundary-layer code (ref. 5) was applied along streamlines from the stagnation point to the sphere-cone juncture. The edge conditions and the inviscid part of the shock

layer were calculated with a blunt-body technique (ref. 3) coupled with a three-dimensional characteristics program (ref. 4). An approximate starting solution was then obtained by simply patching the inviscid flow to the outer edge of the boundary layer (see fig. 1). This displaces the inviscid flow a little too much but it proved to be an adequate approximation for the present example.

The numerical method is the same one used by Lubard and Helliwell (ref. 2) for pointed cones, and is similar to the technique developed by Rubin and Lin (ref. 7). It is an implicit finite difference scheme which employs an iterative matrix inversion scheme. The circumferential derivatives are evaluated in terms of known quantities from the previous iteration, and the matrix is inverted sequentially, one ray at a time. The radial and circumferential derivatives are iterated such that the converged value is obtained at the solution point. For example, the second derivative of velocity, u, is approximated by

$$\left(\frac{\partial^2 u}{\partial \Phi^2}\right)^n_{j,k,\ell} = \left[\frac{u^{n-1}_{j,k,\ell+1} - 2u^{n}_{j,k,\ell} + u^{n-1}_{j,k,\ell-1}}{(\Delta\Phi)^2}\right] \tag{1}$$

where j,k,ℓ are mesh indices for the x,η,Φ directions (fig. 2), respectively, and n is the iteration index. A backward difference is used for the streamwise derivatives. For example, the streamwise derivative of momentum, ρu, is approximated by

$$\left(\frac{\partial \rho u}{\partial x}\right)^n_{j,k,\ell} = \left[\frac{(\rho u)^{n}_{j,k,\ell} - (\rho u)^{n}_{j-1,k,\ell}}{\Delta x}\right] \tag{2}$$

The finite difference grid had 19 equally spaced planes circumferentially, and 50 unequally spaced points radially. About half the radial points were positioned in the boundary layer. Figure 2 shows the grid and computing time for the sample case, and compares with those for an inviscid solution. Only 87 marching steps were taken in the implicit viscous calculation as compared with 508 steps in the inviscid characteristics calculation, which is constrained by the Courant-Friedrichs-Lewey (CFL) condition. The viscous calculation required 23 minutes of computing time for 950 points per marching plane, and the inviscid calculation required 6 minutes for 399 points per plane. Note, however, that neither code was run at the absolute maximum step size. Also, the characteristics code is not the most efficient method from the computational point of view. Therefore the comparison in figure 2 should only be considered qualitative. On this basis, and considering the finer resolution, the computer time required by the viscous code is not excessive.

Because of a peculiarity of the parabolic Navier-Stokes approximation, the finite difference method has a lower bound on the marching-step size. If too small a step size is attempted, nonphysical branching solutions can be generated (see ref. 2). The reason for this behavior is discussed by Rubin and Lin in reference 7 where it is pointed out that the equations have a singularity at the sonic line in the boundary layer, and at that point some

upstream influence is allowed. The singularity did not cause any difficulty in the present example.

RESULTS

In order to adequately establish the validity of the described numerical technique, it is essential to compare both with experiment and with other numerical methods. Since other viscous flow methods are not available, comparison is made with an inviscid solution obtained with the method of characteristics (ref. 4). The viscous and inviscid results should agree outside the boundary layer in regions where the boundary layer is thin.

The configuration selected for comparison was a 15° half-angle cone with a sphere nose and at 15° angle of attack. This blunt cone model was tested by Cleary in the Ames 3.5-foot hypersonic wind tunnel at $M = 10.6$ (refs. 8-10). Surface pressures and heating rates, as well as shock-layer pitot-pressure distributions were measured in the experiments. The angle of attack selected was the largest value for which complete test data were available, and was large enough to cause crossflow separation. Complete test conditions are shown in figure 3.

Figure 4 shows the surface-pressure coefficient for three meridional planes. There is reasonably good agreement between both numerical methods (viscous and inviscid) on the windward side $\Phi = 0$, as is expected. Note, however, that on the leeward side the inviscid theory breaks away from the viscous theory at about $x/R_N = 5$. This is approximately the region where a crossflow separation first appears in the viscous flow calculation.

Figures 5 and 6 show the pitot-pressure distributions between the shock and body. Here, η is the distance along the outward normal from the body surface, x is the axial distance from the nose, and R_N is the nose radius. At $x/R_N = 3.4$ the inviscid result seems to agree best with experiment. This is attributed to the way in which the inviscid solution was patched to the boundary layer to obtain an approximate starting solution. The displacement effect is too large, especially on the leeward side. At both stations, $x/R_N = 3.4$ and 14.7, the agreement between inviscid and viscous computations is very good on the windward side. Significant deviations between the two theories occur only near the body where the well-known blunt-body entropy layer and the boundary layer tend to merge.

It should be noted that the model used for the pitot-pressure experiment had a relatively hot wall. It is estimated that the ratio of wall to total temperature could have reached 0.6 for the pressure test as compared to a value of 0.26 for the heating test and for the viscous computations. The higher wall temperature would cause a thicker boundary layer and might explain the difference between the viscous theory and experiment for $\Phi = 0$ and 30° in figure 6(a). For $\Phi = 60°$ and 90°, the experimental pitot pressures are lower than both numerical solutions in the region where viscous effects should be small. This difference is attributed to misalinement of

the pitot probe and flow direction in the experiment.

On the leeward side at $x/R_N = 14.7$, there is excellent agreement between the viscous calculations and experiment, while inviscid calculations overpredict the pressure for the entire shock layer.

The heating rates are compared in figure 7 and the agreement is excellent.

Finally, in figure 8 the crossflow velocity field is shown in the vicinity of the leeward side at $x/R_N = 14.7$. Crossflow separation is indicated at about 22° off the leeward plane of symmetry. Experimental data were not available on the separation-point location for the present test case.

CONCLUDING REMARKS

A marching method for calculating the complete viscous/inviscid flow over blunt bodies at angle of attack has been described and tested for a sphere-cone at moderate angle of attack. It is found to give fairly good agreement with available experiments and is in agreement with inviscid theory where viscous effects are small. The lee-side flow field, including crossflow separation, is predicted without the need for any assumptions about the pressure distribution or the separation point. The present method should be capable of following the vortex initiated by crossflow separation as it sheds and moves away from the body surface. Additional tests of the method are needed to establish this capability. In this regard, it may be necessary to allow lateral asymmetry for the calculation to correctly model vortex shedding.

The computation time for the test case was 23 minutes on a CDC 7600 computer. This is only about four times longer than an inviscid calculation with half as many points. The time per step is an order of magnitude longer than for the inviscid calculation but the implicit finite difference scheme allowed larger marching steps.

The methods described can also be applied to bodies with more general cross-sectional shape, and work is currently progressing along these lines. However, the approximate technique used for the starting solution may not work as well for a general nose shape. For general nose shapes a time-dependent method of solution, such as that described in reference 11, would give a better starting solution.

REFERENCES

1. Lin, T. C., and Rubin, S. G.: Viscous Flow Over a Cone at Incidence, Part 2: Boundary Layer. J. Fluid Mech., vol. 1, July 1975, pp. 593-620.

2. Lubard, S. C., and Helliwell, W. S.: Calculation of the Flow on a Cone at High Angle of Attack. AIAA J., vol. 12, no. 7, July 1974.

3. Moretti, G., and Bleich, G.: Three-Dimensional Flow Around Blunt Bodies. AIAA J., vol. 5, no. 9, 1967.

4. Rakich, John V.: A Method of Characteristics for Steady Three-Dimensional Supersonic Flow with Application to Inclined Bodies of Revolution. NASA TN D-5341, 1969.

5. Bartlett, E. P., and Kendall, R. M.: Nonsimilar Solution of the Multicomponent Laminar Boundary Layer by an Integral Matrix Method. Aerotherm Final Report No. 66-7, Part III, March 13, 1967; also AIAA J., 6, pp. 1089-1097, 1968.

6. Lubard, Stephen C., and Rakich, John V.: Calculation of the Flow on a Blunted Cone at a High Angle of Attack. AIAA paper 75-149, 13th Aerospace Sciences Meeting, Pasadena, Calif., Jan. 20-22, 1975.

7. Rubin, S. G., and Lin, T. C.: Numerical Methods for Two- and Three-Dimensional Viscous Flow Problems: Application to Hypersonic Leading Edge Equations. Polytechnic Institute of Brooklyn, PIBAL Rep. no. 71-8, April 1971.

8. Cleary, Joseph W.: An Experimental Theoretical Investigation of the Pressure Distribution and Flow Fields of Blunted Cones at Hypersonic Mach Numbers. NASA TN D-2969, 1965.

9. Cleary, Joseph W.: Effects of Angle of Attack and Bluntness on the Shock-Layer Properties of a 15° Cone at a Mach Number of 10.6. NASA TN D-4909, 1968.

10. Cleary, Joseph W.: Effects of Angle of Attack and Bluntness on Laminar Heating-Rate Distributions of a 15° Cone at a Mach Number of 10.6. NASA TN D-5450, 1969.

11. Tannehill, J. C., and Holst, T. L.: Numerical Computation of Two-Dimensional Viscous Blunt Body Flows with an Impinging Shock. AIAA Paper 75-154, presented at AIAA 13th Aerospace Sciences Meeting, Pasadena, Calif., Jan. 20-22, 1975.

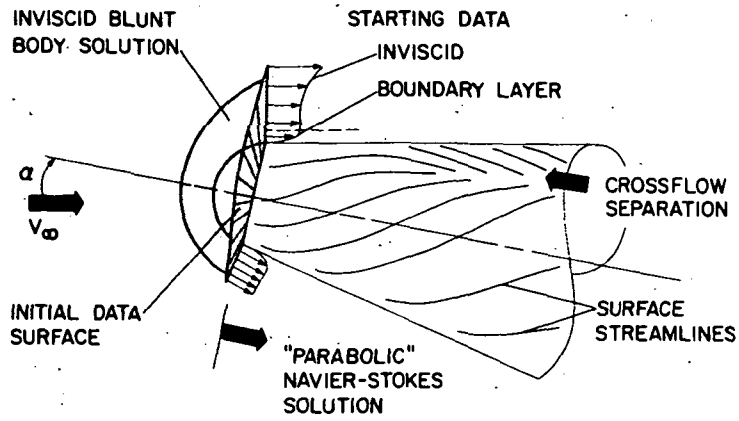

Figure 1.- Laminar viscous vortex flow over a blunt cone.

CALCULATION METHOD:
I VISCOUS IMPLICIT CODE
II INVISCID CHARACTERISTICS CODE

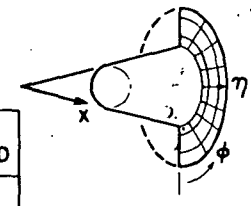

		I VISCOUS	II INVISCID
NUMBER OF MESH POINTS	η	50	21
	ϕ	19	19
	TOTAL	950	399
CDC-7600 COMPUTE TIME (min) $x/R_N = 14.7$	PER STEP	0.26	0.012
	TOTAL	22.9	6.0

Figure 2.- Computational mesh and computer run time.

BLUNT CONE MODEL	
NOSE RADIUS	0.0254 m (1 in.)
CONE HALF-ANGLE	15°
ANGLE OF ATTACK	15°
TEST CONDITIONS (CLEARY)	
MACH NUMBER	10.6
REYNOLDS NUMBER (BASED ON NOSE RADIUS)	1.0×10^5
T_{WALL}/T_{TOTAL}	.26 HEATING TEST .6 PRESSURE TEST

Figure 3.- Conditions for the test case.

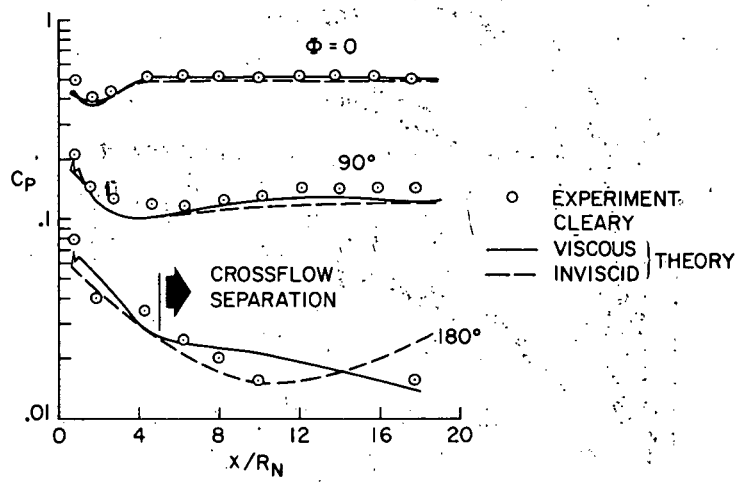

Figure 4.- Surface-pressure coefficient, C_p, for 15° sphere-cone. Angle of attack, 15°; Mach number, 10.6.

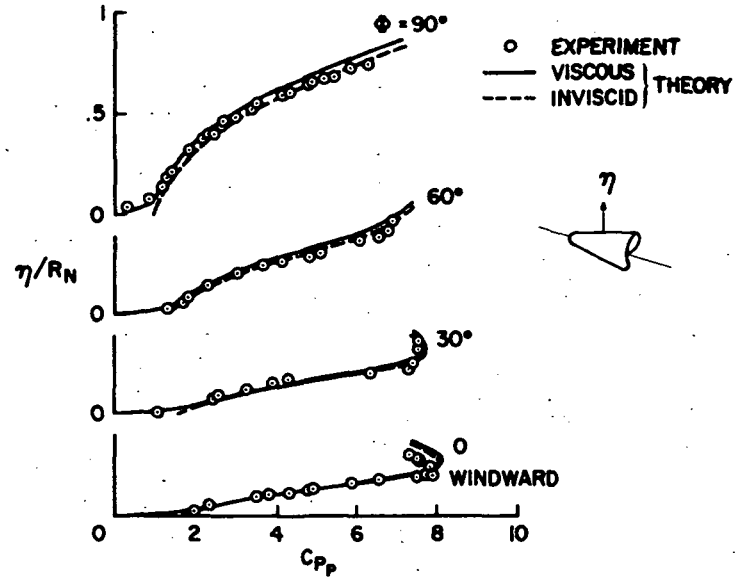

(a) $\Phi = 0° - 90°$.

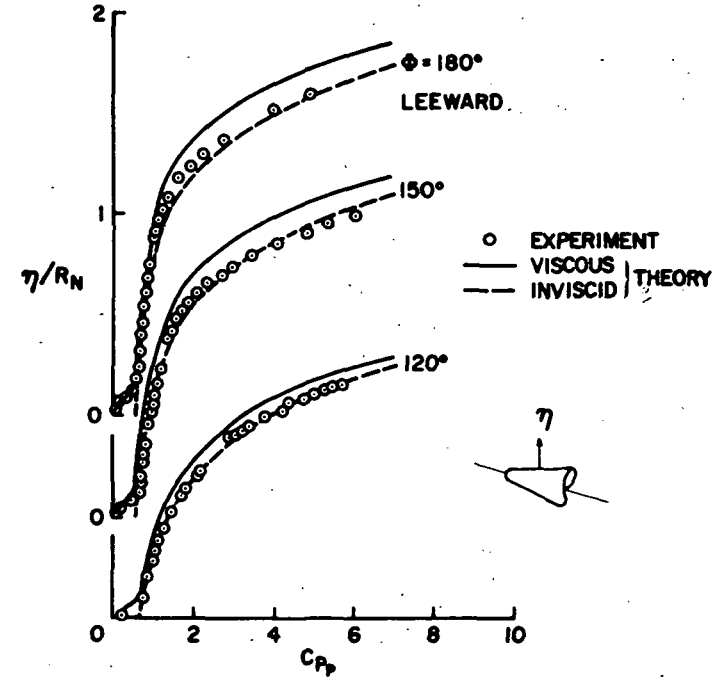

(b) $\Phi = 120° - 180°$.

Figure 5.– Pitot-pressure coefficient, C_{P_p}, across shock layer for 15° sphere-cone. Angle of attack, 15°; Mach number, 10.6; $x/R_N = 3.4$.

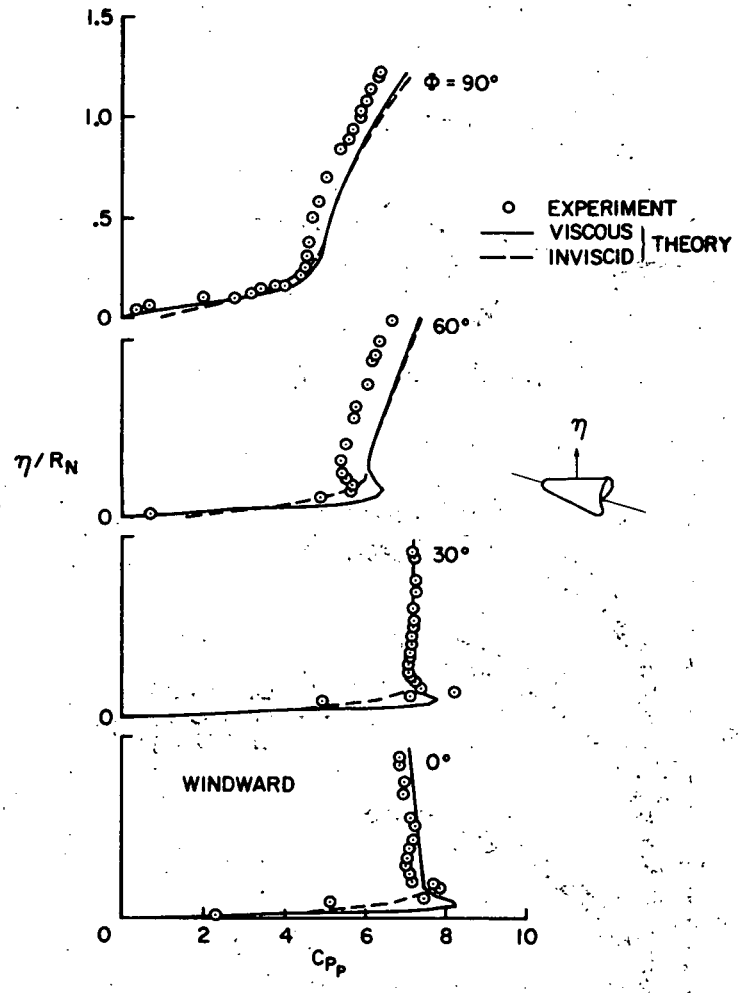

(a) $\Phi = 0° - 90°$.

Figure 6.- Pitot-pressure coefficient, C_{P_p}, across shock layer for 15° sphere-cone. Angle of attack, 15°; Mach number, 10.6; $x/R_N = 14.7$.

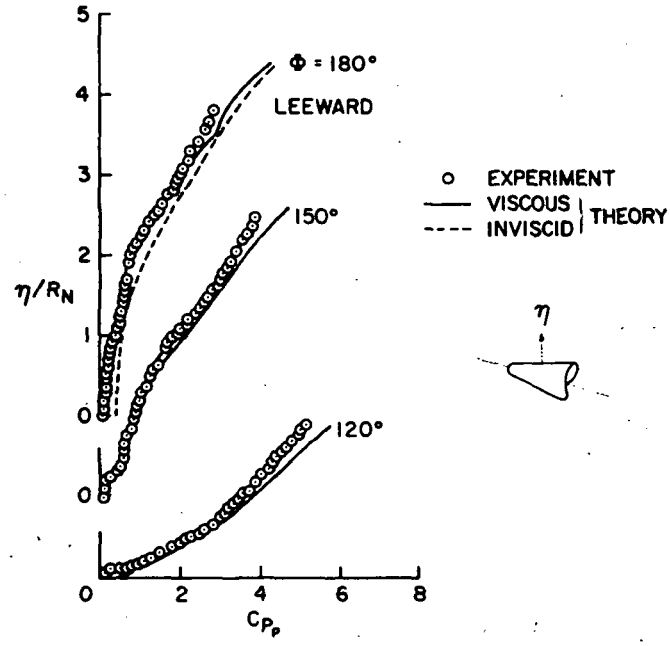

(b) $\Phi = 120° - 180°$.

Figure 6.- Concluded.

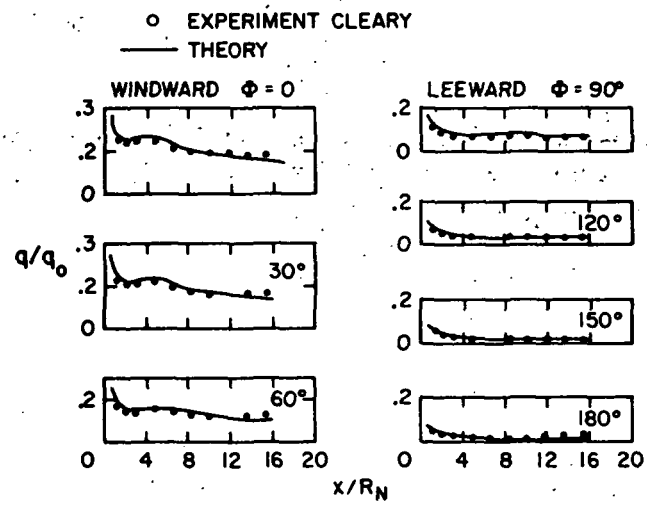

Figure 7.- Surface heating rate ratio, q/q_o, for 15° sphere-cone. Angle of attack, 15°; Mach number, 10.6; $T_{WALL}/T_{TOTAL} = 0.26$; Reynolds number, 1.0×10^5.

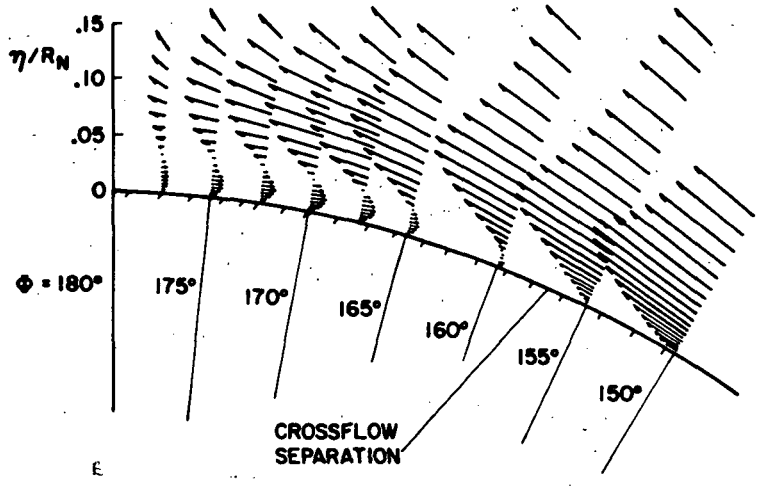

Figure 8.- Crossflow velocity vector field for 15° sphere-cone. Angle of attack, 15°; Mach number, 10.6; $x/R_N = 14.7$; $T_{WALL}/T_{TOTAL} = 0.26$; Reynolds number, 1.0×10^5.

CALCULATION OF SUPERSONIC THREE-DIMENSIONAL FREE-MIXING FLOWS USING THE PARABOLIC-ELLIPTIC NAVIER-STOKES EQUATIONS

By Richard S. Hirsh
NASA Langley Research Center

SUMMARY

A numerical method is presented which is valid for integration of the parabolic-elliptic Navier-Stokes equations. The solution procedure is applied to the three-dimensional supersonic flow of a jet issuing into a supersonic free stream. Difficulties associated with the imposition of free-stream boundary conditions are noted, and a coordinate transformation, which maps the "point at infinity" onto a finite value, is introduced to alleviate these difficulties.

Results are presented for calculations of a square jet and varying-aspect-ratio rectangular jets. The solution behavior varies from axisymmetry for the square jet to nearly two-dimensional for the high-aspect-ratio rectangle, although the computation always calculates the flow as though it were truly three-dimensional.

INTRODUCTION

The calculation of free-mixing flows has, in the past, been accomplished through use of the boundary-layer assumptions in the two-dimensional or axisymmetric Navier-Stokes equations. The accuracy and validity of these procedures have been well documented in the literature (refs. 1 and 2). However, there are numerous situations where the flow cannot be considered either two-dimensional or axisymmetric. Jets issuing from rectangular orifices (see fig. 1), wakes behind any but the simplest bodies, and the flow downstream of a wingtip are examples of three-dimensional free-mixing flows where boundary-layer assumptions are invalid. The characteristic feature of these flows is the importance of diffusion in two spatial coordinates.

These flows have certain characteristics which are common to boundary-layer flows; e.g., the velocities in the planes normal to the main-stream direction are usually much smaller than the main-flow velocity. Consequently, one expects gradients that exist in the cross directions to be larger than the gradients in the main-flow direction. Also, these are usually constant-pressure flows. Therefore, it might be reasonable to

use a boundary-layer scaling on the Navier-Stokes equations to effect some simplification; however, this yields an inconsistent set of equations. To lowest order, the cross-stream momentum equations reduce to statements that the pressure is constant, and the resulting number of equations is not sufficient to determine the remaining unknown quantities.

This paper presents the results of a method which overcomes this difficulty and allows numerical solutions of the parabolized Navier-Stokes equations. The method is applied to a three-dimensional, supersonic, rectangular jet problem in which the aspect ratio is varied from one (square jet) to large values representative of slits. The range of applicability of the procedure is demonstrated from the near axisymmetry of the square, through a true three-dimensional region of moderate aspect ratios, to a quasi-two-dimensional flow in the high-aspect-ratio limit which approximates a two-dimensional jet.

SYMBOLS

A,B	transformation constants
$[A],[B],[C]$	matrices defined by equation (15)
$\vec{D}$	vector defined by equation (15)
$\frac{D}{Dt}$	convective derivative
h	half-width of unit jet (reference length)
M	Mach number
N_{Pr}	Prandtl number
p	pressure
R	Reynolds number
S	$= S^*/T_r$
S^*	Sutherland's constant

T	temperature
U	velocity
u,v,w	component velocities in x-, y-, and z-directions, respectively
x,y,z	coordinate directions
$\Delta x,\Delta y,\Delta z$	grid spacings in x-, y-, and z-directions, respectively
$\vec{W}$	vector of dependent variables (see eq. (16))
γ	ratio of specific heats
Δ	dilatation
δ	central difference operator
η,ζ	transformed y- and z-coordinates
μ	viscosity
ρ	density
Φ	dissipation

Subscripts:

j,k	discretized y- and z-positions, respectively
r	reference quantity
∞	free stream
$+,-$	upper and lower grid spacings used with nonuniform grid

Superscripts:

i	discretized x-position

intermediate step of alternating-direction implicit method

GOVERNING EQUATIONS

Derivation of Equations

The full three-dimensional Navier-Stokes equations are elliptic in character. The core storage available on present computers is insufficient to practicably handle any but the coarsest computational grids. Thus, methods to reduce the equations to a form more tractable for computation must be employed. A true boundary-layer scaling cannot be used since it yields an inconsistent set of equations; however, some of the concepts from boundary-layer theory indicate the means to simplify the equations.

The only assumption which can be made is the predominance of the convection in one main-flow direction. This leads to the (Reynolds number dependent) conclusion that diffusion can be neglected in this direction when compared with convection. Assuming the x-direction to be the convective direction, the Navier-Stokes equations become

for x-momentum:

$$\rho \frac{Du}{Dt} = -\frac{\partial p}{\partial x} + \left\{\frac{\partial}{\partial x}\left[\mu\left(2\frac{\partial u}{\partial x} - \frac{2}{3}\Delta\right)\right]\right\} + \frac{\partial}{\partial y}\left[\mu\left(\frac{\partial u}{\partial y}\right)\right] + \frac{\partial}{\partial z}\left[\mu\left(\frac{\partial u}{\partial z}\right)\right] \tag{1}$$

for y-momentum:

$$\rho \frac{Dv}{Dt} = -\frac{\partial p}{\partial y} + \left\{\frac{\partial}{\partial x}\left[\mu\left(\frac{\partial v}{\partial x}\right)\right]\right\} + \frac{\partial}{\partial y}\left[\mu\left(2\frac{\partial v}{\partial y} - \frac{2}{3}\Delta\right)\right] + \frac{\partial}{\partial z}\left[\mu\left(\frac{\partial v}{\partial z}\right)\right] \tag{2}$$

for z-momentum:

$$\rho \frac{Dw}{Dt} = -\frac{\partial p}{\partial z} + \left\{\frac{\partial}{\partial x}\left[\mu\left(\frac{\partial w}{\partial x}\right)\right]\right\} + \frac{\partial}{\partial y}\left[\mu\left(\frac{\partial w}{\partial y}\right)\right] + \frac{\partial}{\partial z}\left[\mu\left(2\frac{\partial w}{\partial z} - \Delta\right)\right] \tag{3}$$

where the terms in braces are the streamwise x-direction diffusion terms to be neglected. In addition, since the expression

$$\Delta = \frac{\partial u}{\partial x} + \frac{\partial v}{\partial y} + \frac{\partial w}{\partial z}$$

also introduces x-diffusion terms in the y- and z-crossflow momentum equations, these derivatives are also neglected here. The x-momentum equation is the same as would have been produced by a true boundary-layer scaling, but since no quantitative assumptions have been made concerning the relative sizes of the x-, y-, or z-gradients, the y- and z-momentum equations are retained, although in somewhat simpler form.

The energy equation becomes

$$\rho \frac{DT}{Dt} = \frac{Dp}{Dt} + \frac{1}{N_{Pr}} \left(\left\{ \frac{\partial}{\partial x} \left[\mu \left(\frac{\partial T}{\partial x} \right) \right] \right\} + \frac{\partial}{\partial y} \left[\mu \left(\frac{\partial T}{\partial y} \right) \right] + \frac{\partial}{\partial z} \left[\mu \left(\frac{\partial T}{\partial z} \right) \right] \right) + \mu \Phi \tag{4}$$

where the term in braces is to be neglected,

$$\Phi = \left(\frac{\partial u}{\partial y} \right)^2 + \left(\frac{\partial u}{\partial z} \right)^2 + \frac{4}{3} \left[\left(\frac{\partial v}{\partial y} \right)^2 - \left(\frac{\partial v}{\partial y} \right) \left(\frac{\partial w}{\partial z} \right) + \left(\frac{\partial w}{\partial z} \right)^2 \right] + \left(\frac{\partial w}{\partial y} \right)^2 - 2 \left(\frac{\partial w}{\partial y} \right) \left(\frac{\partial v}{\partial z} \right) + \left(\frac{\partial v}{\partial z} \right)^2$$

and the convective derivative $\frac{D}{Dt}$ is given by

$$\frac{D}{Dt} = u \frac{\partial}{\partial x} + v \frac{\partial}{\partial y} + w \frac{\partial}{\partial z}$$

All x-gradients in the dissipation have also been neglected. Finally, the continuity equation remains unchanged:

$$\frac{\partial}{\partial x}(\rho u) + \frac{\partial}{\partial y}(\rho v) + \frac{\partial}{\partial z}(\rho w) = 0 \tag{5}$$

When these equations are supplemented by an equation of state and a viscosity relation,

$$p = \rho R T \tag{6a}$$

$$\frac{\mu}{\mu_r} = \left(\frac{T_r + S^*}{T + S^*} \right) \left(\frac{T}{T_r} \right)^{3/2} \tag{6b}$$

where R is the universal gas constant, a system of five equations for five unknowns is obtained after elimination of the density by the perfect gas equation of state.

The elliptic nature of the Navier-Stokes equations in the x-direction has thus been eliminated; consequently, the equations are parabolic in x and marching integration may be used in the streamwise direction. This is significant computationally since it eliminates the need to store all the field quantities at each x-location which results in a substantial reduction in computer storage. Thus, the name parabolic-elliptic Navier-Stokes equations, since the assumptions allow a march in x away from an initial data plane, yet retain the elliptic character of the crossflow planes (Y-Z planes) due to the inclusion of all second derivatives in y and z. Flows with swirl or possible cross-flow recirculation (vortices) in the Y-Z planes can be computed, and only reverse flow in the main-stream direction is eliminated due to the omission of x-diffusion.

It should be noted that the continuity equation is hyperbolic; however, a march in the streamwise direction is still possible since the x-derivative can be expanded as follows:

$$(\rho u)_x = \left(\frac{pu}{T}\right)_x = \frac{u}{T} p_x + \frac{p}{T} u_x - \frac{pu}{T^2} T_x$$

and the p_x term can be used to advance to the next station. There is no explicit diffusion term present and discontinuities which may be present can be expected to persist for large x-distances; hence, smooth initial profiles are desirable.

Equations similar to these have recently been used for supersonic flow past a sharp cone at incidence (ref. 3) and for hypersonic leading-edge flows, where a more formal analysis and scaling can be invoked (ref. 4). To date, no detailed work has been published on three-dimensional free-mixing flows.

Validity for Supersonic Jet Flows

Free jet and wake flows are common aerodynamic phenomena. These flows are generally turbulent, and the calculation of two-dimensional or axisymmetric turbulent free jets or wakes is difficult (ref. 2) because of problems associated with turbulence modeling; higher order modeling (two-equation models) is necessary in many cases. For three-dimensional flows with two essential cross-plane velocities, very few calculations have been made. To assess the modeling procedures for a three-dimensional flow, a calculation procedure valid for laminar flows, preferably in primitive variables to allow ease of incorporation of the turbulence models, is required. The parabolic-elliptic equations (eqs. (1) to (6)) need to be verified for laminar jet calculations prior to their application to turbulent flows.

If the equations are cast in nondimensional form by using free-stream values of U_∞, p_∞, and T_∞ and some suitable reference length which characterizes the problem, the equations become

for x-momentum:

$$\rho \frac{Du}{Dt} = -\frac{1}{\gamma M_\infty{}^2} \frac{\partial p}{\partial x} + \frac{1}{R}\left\{\frac{\partial}{\partial y}\left[\mu\left(\frac{\partial u}{\partial y}\right)\right] + \frac{\partial}{\partial z}\left[\mu\left(\frac{\partial u}{\partial z}\right)\right]\right\} \tag{7}$$

for y-momentum:

$$\rho \frac{Dv}{Dt} = -\frac{1}{\gamma M_\infty{}^2} \frac{\partial p}{\partial y} + \frac{1}{R}\left\{\frac{\partial}{\partial y}\left[\mu\left(2\frac{\partial v}{\partial y} - \frac{2}{3}\Delta\right)\right] + \frac{\partial}{\partial z}\left[\mu\left(\frac{\partial v}{\partial z}\right)\right]\right\} \tag{8}$$

for z-momentum:

$$\rho \frac{Dw}{Dt} = -\frac{1}{\gamma M_\infty{}^2} \frac{\partial p}{\partial z} + \frac{1}{R}\left\{\frac{\partial}{\partial y}\left[\mu\left(\frac{\partial w}{\partial y}\right)\right] + \frac{\partial}{\partial z}\left[\mu\left(2\frac{\partial w}{\partial z} - \frac{2}{3}\Delta\right)\right]\right\} \tag{9}$$

for energy:

$$\rho\frac{DT}{Dt} = \left(\frac{\gamma - 1}{\gamma}\right)\frac{Dp}{Dt} + \frac{1}{N_{Pr}R}\left\{\frac{\partial}{\partial y}\left[\mu\left(\frac{\partial T}{\partial y}\right)\right] + \frac{\partial}{\partial z}\left[\mu\left(\frac{\partial T}{\partial z}\right)\right]\right\} + \frac{\gamma - 1}{R}M_\infty{}^2\mu\left\{\left(\frac{\partial u}{\partial y}\right)^2 + \left(\frac{\partial u}{\partial z}\right)^2\right.$$

$$\left. + \frac{4}{3}\left[\left(\frac{\partial v}{\partial y}\right)^2 - \left(\frac{\partial v}{\partial y}\right)\left(\frac{\partial w}{\partial z}\right) + \left(\frac{\partial w}{\partial z}\right)^2\right] + \left(\frac{\partial w}{\partial y}\right)^2 - 2\left(\frac{\partial w}{\partial y}\right)\left(\frac{\partial v}{\partial z}\right) + \left(\frac{\partial v}{\partial z}\right)^2\right\} \tag{10}$$

for continuity:

$$\frac{\partial}{\partial x}(\rho u) + \frac{\partial}{\partial y}(\rho v) + \frac{\partial}{\partial z}(\rho w) = 0 \tag{11}$$

and for Sutherland's law:

$$\mu = \left(\frac{1 + S}{T + S}\right)T^{3/2} \tag{12}$$

Rubin and Lin (ref. 5) have shown that equations of this type are singular at $M = 1$ if the p_x term is treated exactly and singular at $M = 0$ if the p_x term is calculated in an explicit manner during the numerical calculation. If the p_x term is neglected entirely or specified from a boundary-layer approximation, then the parabolic march in x can proceed without difficulty. Thus, it was felt that since the p_x term should be included if necessary, the problem chosen to test the overall method should avoid any of these obvious integration difficulties. The $M = 0$ behavior takes place near boundaries (where $u = 0$), and therefore, the free jet problem avoids this singular behavior. However, the jet cannot exhaust into an ambient atmosphere since here too $u = 0$. Thus a jet issuing into a moving free stream is suitable. To avoid any difficulties at $M = 1$ both streams were chosen to be supersonic. Thus, equations (7) to (12) will be solved for a supersonic jet issuing into a supersonic free stream.

NUMERICAL PROCEDURE

Integration Technique

An implicit numerical procedure was chosen to solve the governing equations for a number of reasons. The success of implicit methods on the two- and three-dimensional boundary-layer equations implies that they should be efficient for the boundary-layer-like parabolic-elliptic Navier-Stokes equations (eqs. (7) to (12)). It is expected that solutions will be required at large distances downstream from the initial data plane; consequently, large x-steps are desirable. The need to eliminate the step size restrictions of explicit methods leads to a consideration of unconditionally stable methods which are consistent in their marching variation. The particular implicit method used in this study is the alternating-direction implicit (ADI) method of Peaceman and Rachford (ref. 6). The

ADI method is ideally suited for the solution of equations (7) to (12). There is no stability restriction on the step size, and hence, large x-steps are permitted. The method has second-order truncation error in its marching variation, which is also a requirement for the type of flow envisioned, since the x-history of the flow must be traced accurately at each step. Finally, the method does not require the inversion of a sparse-banded matrix, as a fully implicit or Crank-Nicolson method would. Simple tridiagonal coefficient matrices are generated at each step which require much less storage and time for their inversion in relation to sparse-banded matrices. The method has previously been shown to be effective for a set of equations similar to those used in the present approach (ref. 7).

The ADI procedure is used to difference in x, with the y- and z-derivatives expressed as central differences, with the option of a nonuniform grid included; that is,

$$\delta_z u^i_{j,k} = \frac{\partial u}{\partial z} = \frac{(\Delta z_-)^2 u^i_{j,k+1} - \left[(\Delta z_+)^2 - (\Delta z_-)^2\right] u^i_{j,k} - (\Delta z_+)^2 u^i_{j,k-1}}{(\Delta z_+)(\Delta z_-)\left[(\Delta z_+) + (\Delta z_-)\right]}$$

$$\delta_z{}^2 u^i_{j,k} = \frac{\partial^2 u}{\partial z^2} = 2\left\{\frac{(\Delta z_-) u^i_{j,k+1} - \left[(\Delta z_+) + (\Delta z_-)\right] u^i_{j,k} + (\Delta z_+) u^i_{j,k-1}}{(\Delta z_+)(\Delta z_-)\left[(\Delta z_+) + (\Delta z_-)\right]}\right\}$$

An example of the complete differencing scheme is shown for the x-momentum equation as follows:

$$(\rho u)^{i+\frac{1}{2}}_{j,k}\left(\frac{u^*_{j,k} - u^i_{j,k}}{\Delta x/2}\right) + (\rho v)^{i+\frac{1}{2}}_{j,k}\delta_y u^{i+\frac{1}{2}}_{j,k} + (\rho w)^{i+\frac{1}{2}}_{j,k}\delta_z u^{*}_{j,k} = -\frac{1}{\gamma M_\infty{}^2}\left(\frac{p^*_{j,k} - p^i_{j,k}}{\Delta x/2}\right)$$

$$+ \frac{1}{R}\left\{\frac{1}{2}\left(\frac{\partial \mu}{\partial T}\right)^{i+\frac{1}{2}}_{j,k}\left[\left(\frac{\partial T}{\partial y}\right)^{i+\frac{1}{2}}_{j,k}\delta_y u^i_{j,k} + \left(\frac{\partial u}{\partial y}\right)^{i+\frac{1}{2}}_{j,k}\delta_y T^i_{j,k}\right] + \mu^{i+\frac{1}{2}}_{j,k}\delta_y{}^2 u^i_{j,k} + \frac{1}{2}\left(\frac{\partial \mu}{\partial T}\right)^{i+\frac{1}{2}}_{j,k}\left[\left(\frac{\partial T}{\partial z}\right)^{i+\frac{1}{2}}_{j,k}\delta_z u^*_{j,k}\right.\right.$$

$$\left.\left. + \left(\frac{\partial u}{\partial z}\right)^{i+\frac{1}{2}}_{j,k}\delta_z T^*_{j,k}\right] + \mu^{i+\frac{1}{2}}_{j,k}\delta_z{}^2 u^*_{j,k}\right\} \qquad (13a)$$

$$(\rho u)_{j,k}^{i+\frac{1}{2}}\left(\frac{u_{j,k}^{i+1}-u_{j,k}^{*}}{\Delta x/2}\right)+(\rho v)_{j,k}^{i+\frac{1}{2}}\delta_y u_{j,k}^{i+1}+(\rho w)_{j,k}^{i+\frac{1}{2}}\delta_z u_{j,k}^{*}=-\frac{1}{\gamma M_\infty{}^2}\left(\frac{p_{j,k}^{i+1}-p_{j,k}^{*}}{\Delta x/2}\right)$$

$$+\frac{1}{R}\left\{\frac{1}{2}\left(\frac{\partial\mu}{\partial T}\right)_{j,k}^{i+\frac{1}{2}}\left[\left(\frac{\partial T}{\partial y}\right)_{j,k}^{i+\frac{1}{2}}\delta_y u_{j,k}^{i+1}+\left(\frac{\partial u}{\partial y}\right)_{j,k}^{i+\frac{1}{2}}\delta_y T_{j,k}^{i+1}\right]+\mu_{j,k}^{i+\frac{1}{2}}\delta_y{}^2 u_{j,k}^{i+1}+\frac{1}{2}\left(\frac{\partial\mu}{\partial T}\right)_{j,k}^{i+\frac{1}{2}}\left[\left(\frac{\partial T}{\partial z}\right)_{j,k}^{i+\frac{1}{2}}\delta_z u_{j,k}^{*}\right.\right.$$

$$\left.\left.+\left(\frac{\partial u}{\partial z}\right)_{j,k}^{i+\frac{1}{2}}\delta_z T_{j,k}^{*}\right]+\mu_{j,k}^{i+\frac{1}{2}}\delta_z{}^2 u_{j,k}^{*}\right\} \tag{13b}$$

The only difficulty arises from the cross derivatives of velocity present in the y- and z-momentum equations. These cannot be differenced implicitly since the tridiagonal structure of the resulting matrices would be destroyed. These are treated in the same manner as all the nonlinear coefficients present in the differenced equations.

Linearization Scheme

The ADI procedure, which is second-order accurate, centers the x-derivatives about the point $\left(i+\frac{1}{2}\right)$. (See fig. 2.) This point is not equivalent to the intermediate step of the ADI procedure. Hence, a method must be developed to compute all the nonlinear coefficients (and the cross derivatives) at the $\left(i+\frac{1}{2}\right)$ point. This can be accomplished by a quadratic extrapolation from the two previous x-stations (i) and (i - 1) (ref. 7) or by use of the predictor-corrector procedure of Douglas and Jones (ref. 8). Both of these require additional storage. The procedure used in the present work handles the nonlinear terms by an iterative technique similar to that used for boundary-layer calculations in which a Crank-Nicolson integration is used (ref. 9). Any coefficient Q is calculated at the midpoint $\left(i+\frac{1}{2}\right)$ by the simple formula

$$Q_{j,k}^{i+\frac{1}{2}}=\frac{1}{2}\left(Q_{j,k}^{i+1}+Q_{j,k}^{i}\right) \tag{14}$$

The value at (i + 1) is not known on the first iteration and so the Q^i value is used. After the integration to (i + 1) has been completed, new values of Q^{i+1} are computed, and the integration step to (i + 1) is repeated to either a specified convergence or a specified number of iterations. At convergence this yields second-order-accurate coefficients which match the accuracy of the integration. The cross derivatives are also treated this way.

Solution of Matrix Equation

The resulting linear difference equations are a set of five equations in five unknowns. Rather than make the quite arbitrary choice of the order of solution if a sequential technique of solving each equation in turn were elected, the five equations are solved simultaneously. The resulting matrix equation has a block tridiagonal structure which can be represented as

$$[A_j]\vec{W}_{j+1} + [B_j]\vec{W}_j + [C_j]\vec{W}_{j-1} = \vec{D}_j \tag{15}$$

where the unknown vector $\vec{W}_j$ contains all the five unknowns

$$\vec{W}_j = (u_j, v_j, w_j, T_j, p_j)^T \tag{16}$$

the coefficients $[A]$, $[B]$, and $[C]$ are simply the matrix coefficients of each particular unknown; that is,

$$[A_j] = \begin{pmatrix} a_{11j} & a_{12j} & \cdots & a_{15j} \\ a_{21j} & & & \vdots \\ \vdots & & & \vdots \\ \vdots & & & \vdots \\ a_{51j} & \cdots & \cdots & a_{55j} \end{pmatrix} \tag{17}$$

and the vector $\vec{D}$ is a source term in each equation. The components a_{mnj} represent the coefficient of the nth unknown from the mth equation at point j.

The inversion of this block matrix is particularly simple. It consists of rewriting the usual tridiagonal algorithm with all multiplications replaced by matrix multiples, and all divisions replaced by matrix inversions. This simultaneous solution procedure was used previously by Krause, Hirschel, and Bothmann (ref. 9) where the pressure, of course, was not one of the unknown variables due to the boundary-layer assumptions. The procedure is quite advantageous because, in addition to eliminating the previously mentioned choice of solution order, it models the physics more precisely by allowing changes in any variable to be instantaneously sensed by all the others. It is also believed that this procedure aids in the convergence of the iteration since it eliminates the use of lagged information previously calculated in a sequential solution. Thus it is fully implicit in the sense that a sequential solution is much like a Gauss-Seidel iteration which is explicit.

The number of grid points used for the calculation was governed by conflicting requirements. For acceptable resolution, many points were desirable in the shear layer

between the jet and free stream and in the jet itself. Also, reasonable distances away from the high shear region were necessary to allow boundary conditions in the free stream to be applied without distorting the results interior to the computational domain. However, excessive mesh points result in unacceptable machine storage requirements, increase computational time extravagantly, and impair job turnaround time. An initial compromise was to use a 41×41 grid to compute the quarter-plane of the jet flow, using the symmetry axes of the jet as boundaries. An equally spaced grid of $\Delta y = \Delta z = 0.1$ was first utilized, thereby placing a jet half-width at five grid spacings away from the axis and the outer edge of the domain seven times beyond this (40 grid spacings away from the axis). The required computer storage was $130\ 000_8$ on the CDC 6600 system.

Initial Conditions

The initial conditions at the data plane representing the orifice location $x = 0$ were chosen in a very rudimentary manner. Since too many points would be necessary to describe the merging of the free stream and duct flows just past a jet exit, and storage limitations were severe enough before this consideration, the initial velocity profiles were chosen as shown in figure 3. The jet and free stream are represented by two distinct inviscid flows separated by a sharp boundary. Computationally this yields a one-grid-point discontinuity between u_{jet} and U_∞. This initial condition is probably the most severe that can be imposed while still generating an eventually realistic flow description. The initial conditions on the crossflow velocities were also modeled simply and were set equal to zero.

The pressure distribution was chosen to be uniform at the free-stream level since an unmatched static pressure would undoubtedly produce shocks. These were not consciously sought as part of the problem, and the initial conditions were set to try to avoid their generation. The streamwise velocity and temperature levels were computed by assuming constant total temperature in the jet and free stream and specifying the jet and free-stream Mach numbers.

The free jet problem was expected to encounter few boundary condition troubles due to the avoidance of all $u = 0$ boundary conditions. The conditions placed on the variables were symmetry with no crossflow on the axes of the jet and consistent free-stream conditions. Difficulties encountered with the application of these conditions are discussed in the next section.

RESULTS AND DISCUSSION

A standard test case was chosen to check the numerical procedure: the free-stream Mach number was set equal to 5.0; the jet Mach number at the initial station was 7.5. The reference length was set equal to the minimum initial orifice width of a

1×1 square jet. The Reynolds number based on this reference length was set equal to 10^3, and the Prandtl number was set equal to 1.

Effect of Initial Conditions

The initial behavior (small x) for all cases computed regardless of the grid configuration or boundary conditions applied was essentially the same. The discontinuous velocity and temperature profiles were smoothed out by the diffusive terms, but the continuity equation reacted to these discontinuities differently. The initial and subsequent u, T, and p profiles are shown qualitatively in figure 4. Referring to the figure, in the region below the initial discontinuity, $u_x < 0$ and $T_x > 0$, and above, $u_x > 0$ and $T_x < 0$. The x-gradients in the continuity equation appear as follows:

$$\frac{p}{T}\frac{\partial u}{\partial x} - \frac{pu}{T^2}\frac{\partial T}{\partial x} + (y \text{ and } z \text{ gradients}) = -\frac{u}{T}\frac{\partial p}{\partial x} \tag{18}$$

Above the original discontinuity then, $p_x < 0$, and below, $p_x > 0$, neglecting the y- and z-gradients which are smaller here than the x-gradients. Hence, the pressure develops a blip around the initial discontinuity (see fig. 4) which persists for some distance before the profiles lose the influence of the initial conditions. This high-pressure-gradient profile causes divergence of the normal velocities about the initial breakpoint until the entrainment-induced boundary-layer-like velocities away from the jet axis are established. Eventually the pressure profiles smooth out to the expected constant case, but since the continuity equation is hyperbolic and contains no damping, ripples in the pressure profile of 0.2 percent of the free stream are commonplace. However, this initial behavior is of no concern, except in its influence on the downstream results, since the parabolic approximation is not valid in this region of very high x-gradients.

Since the pressure is expected to be approximately constant in the developed jet, an attempt to artificially drive the pressure to its constant value more quickly was made. An artificial diffusion term was introduced into the continuity equation in the hope of quickly smoothing the pressure profile. However, it was found that any introduction of these terms generated more diffusion in the other variables as well. Only values of an artificial viscosity larger than the actual flow viscosity had any significant effect and no improvement was effected by the incorporation of these fictitious terms. Thus, the flow was permitted to naturally adjust to the initial discontinuity. If this was smoothed initially over a few grid points, the pressure disturbance was smaller and shorter lived. Consequently it appears that no difficulties will be encountered if correct initial data are prescribed from experiments or boundary-layer calculations.

Problems Associated With Application of Boundary Conditions

The expectation that the elimination of solid walls and stagnant regions would ease boundary condition difficulties was not realized. The boundaries of the computational domain were the axes of symmetry of the jet and the point in the free stream considered to approximate infinity. The conditions to be applied at these axes were symmetry of all quantities except the cross-plane velocity normal to the axis which was equal to zero. Thus at $y = 0$, for example, the conditions to be applied were $u_y = w_y = T_y = p_y = 0$ and $v = 0$. Writing the governing equations differenced on the boundary (see fig. 5) and using the above relations to eliminate the unknown points outside the domain created by the central differences resulted in the values of the functions on the boundary becoming an additional row of unknowns to the vector $\vec{W}_j$ in the block tridiagonal system. The inversion technique thus allowed the simultaneous solution of the boundary values as well as the interior points, and the resulting solution was smooth for all variables except the pressure. At the symmetry plane the pressure profile contained a spike (see fig. 6) and the other unknowns had gradients which differed from zero. This entire difficulty was eliminated by imposing a quadratic fit for the zero gradient condition onto each of the variables. The relation

$$u_1 = \frac{4u_2 - u_3}{3} \tag{19}$$

insures a zero gradient with second-order accuracy, which matches the truncation of the difference scheme, and retains the tridiagonal aspect of the solution matrices.

The "infinity" boundary conditions must be imposed at boundaries in the free stream. These boundary conditions could be imposed at a suitable distance from the symmetry plane if asymptotic conditions could be derived far from the jet. However, asymptotic conditions are not known for the three-dimensional jet, and even if they were, the question arises as to a suitable distance at which they could be applied. Treatment of these boundary conditions can be classified into two groups: alterations in the actual conditions imposed at the last grid point and, concurrent with these, changes in the grid size.

At first, all variables were specified at their free-stream values; that is, $u = T = p = 1$ and $v = w = 0$ at the last grid point in the domain with a uniform grid. The calculation proceeded smoothly, but after the usual jet crossflow velocity established itself, a sharp, one-grid-width gradient developed at the outer edge of the computational domain due to the difference between the negative entrainment velocity and the imposed zero value. (See fig. 7.) To alleviate this condition, an expanding nonuniform grid was used in place of the uniform one. Where the uniform 41×41 grid had $y = z = 4$ as the last grid point, the nonuniform grid using the same number of points allowed the edge to be displaced to $y = z = 17.5$, after remaining uniform to $y = z = 1$. This resulted in a

delay in the appearance of this boundary gradient until the solution marched further downstream; however, it did not eliminate the problem.

The expanding jet both deflects the crossflow away from the jet axes and entrains fluid from the free stream. An interaction between the jet and variables such as v, w, and possibly p is quite likely to be present, and consequently, the specification of values for these quantities at some finite near point would be of doubtful validity. Instead, the equations should determine the necessary boundary effects. To do this, a quadratic extrapolation consistent with the second-order differencing was imposed on v, w, and p by using both the uniform and nonuniform grids. The pressure solution quickly deteriorated and the cause was traced to the lack of actual specification of a pressure level. With zero gradient conditions on the axes and extrapolation at the outer edge, no fixed pressure value is specified. Hence, the extrapolation was limited to the crossflow velocities, which proved more successful, and the x-marching proceeded to a distance of approximately 20 jet widths. However, difficulties again occurred at the outer edge of the domain as shown in figure 8. The expected crossflow velocities appeared and the extrapolation did not affect the profiles. But, as the jet proceeds downstream, it grows and the zero velocity point of the crossflow moves out from the axes. Eventually, as shown in figure 8, this point moved completely out of the computational domain, leaving only outflow from the centerline which is not characteristic of a jet.

Until this point was reached, the development of the profiles showed the correct trend for the streamwise velocity (see fig. 9) but, as later calculations indicated, the greatest x-distance achieved was well ahead of the end of the jet core region, even if the nonuniform grid was used. For the square jet initial profile, all the variables were computed symmetrically about the jet axis, and the pressure became uniform to within 0.2 percent of the free-stream value.

All these difficulties with edge conditions arise due to the growth of the jet with x when it is computed by using the unscaled spatial coordinates. To overcome this problem area a transformation was introduced in the Y-Z plane to contain the jet totally within the computational domain.

Transformation of Coordinates

The objective in transforming the coordinates is to aid in the imposition of "infinity" boundary conditions. The uncertainty in these conditions can be overcome only if the exact free-stream conditions can be imposed. To enable this to be accomplished, the point at infinity must be mapped to a finite point in the transformed space. One of the simpler transformations by which this can be accomplished is

$$\eta = \frac{Ay}{1 + Ay} \tag{20a}$$

$$\zeta = \frac{Bz}{1 + Bz} \tag{20b}$$

which maps zero onto zero and infinity in the physical plane onto unity in the η-ζ plane. With equations (20) the governing equations are as follows (with $\xi = x$):

$$\rho u u_\xi + \left[\rho v + 2A\mu(1 - \eta)\right]A(1 - \eta)^2 u_\eta + \left[\rho w + 2B\mu(1 - \zeta)\right]B(1 - \zeta)^2 u_\zeta = -\frac{1}{\gamma M_\infty{}^2}\, p_\xi$$

$$+ \frac{1}{R}\left[A^2(1 - \eta)^4\left(\mu_T T_\eta u_\eta + u_{\eta\eta}\right) + B^2(1 - \zeta)^2\left(\mu_T T_\zeta u_\zeta + u_{\zeta\zeta}\right)\right] \tag{21}$$

$$\rho u v_\xi + \left[\rho v + \frac{8}{3} A\mu(1 - \eta)\right]A(1 - \eta)^2 v_\eta + \left[\rho w + 2B\mu(1 - \zeta)\right]B(1 - \zeta)^2 v_\zeta = -\frac{1}{\gamma M_\infty{}^2} A(1 - \eta)^2 p_\eta$$

$$+ \frac{1}{R}\left\{\frac{4}{3} A^2(1 - \eta)^4\left(\mu_T T_\eta v_\eta + \mu v_{\eta\eta}\right) + B^2(1 - \zeta)^4\left(\mu_T T_\zeta v_\zeta + \mu v_{\zeta\zeta}\right)\right.$$

$$\left. + AB(1 - \eta)^2(1 - \zeta)^2\left[\frac{1}{3}\mu w_{\eta\zeta} + \mu_T\left(T_\zeta w_\eta - \frac{2}{3} T_\eta w_\zeta\right)\right]\right\} \tag{22}$$

$$\rho u w_\xi + \left[\rho v + 2A\mu(1 - \eta)\right]A(1 - \eta)^2 w_\eta + \left[\rho w + \frac{8}{3} B\mu(1 - \zeta)\right]B(1 - \zeta)^2 w_\zeta = -\frac{1}{\gamma M_\infty{}^2} B(1 - \zeta)^2 p_\zeta$$

$$+ \frac{1}{R}\left\{A^2(1 - \eta)^4\left(\mu_T T_\eta w_\eta + \mu w_{\eta\eta}\right) + \frac{4}{3} B^2(1 - \zeta)^4\left(\mu_T T_\zeta w_\zeta + \mu w_{\zeta\zeta}\right)\right.$$

$$\left. + AB(1 - \eta)^2(1 - \zeta)^2\left[\frac{1}{3}\mu v_{\eta\zeta} + \mu_T\left(T_\eta v_\zeta - \frac{2}{3} T_\zeta v_\eta\right)\right]\right\} \tag{23}$$

$$\rho u T_\xi + \left[\rho v + \frac{2\mu}{N_{Pr}} A(1 - \eta)\right]A(1 - \eta)^2 T_\eta + \left[\rho w + \frac{2\mu}{N_{Pr}} B(1 - \zeta)^2\right]B(1 - \zeta)^2 T_\zeta = \frac{\gamma - 1}{\gamma}\left[u p_\xi\right.$$

$$\left. + vA(1 - \eta)^2 p_\eta + wB(1 - \zeta)^2 p_\zeta\right] + \frac{1}{N_{Pr} R}\left[A^2(1 - \eta)^4\left(\mu_T T_\eta{}^2 + \mu T_{\eta\eta}\right) + B^2(1 - \zeta)^4\left(\mu_T T_\zeta{}^2\right.\right.$$

$$\left.\left. + \mu T_{\zeta\zeta}\right)\right] + \frac{(\gamma - 1)M_\infty{}^2}{R}\mu\left[A^2(1 - \eta)^4\left(u_\eta{}^2 + w_\eta{}^2 + \frac{4}{3} v_\eta{}^2\right) + B^2(1 - \zeta)^4\left(u_\zeta{}^2 + v_\zeta{}^2 + \frac{4}{3} w_\zeta{}^2\right)\right.$$

$$\left. + AB(1 - \eta)^2(1 - \zeta)^2\left(w_\eta v_\zeta - \frac{4}{3} v_\eta w_\zeta\right)\right] \tag{24}$$

$$up_\xi - \rho uT_\xi + pu_\xi + A(1 - \eta)^2(vp_\eta - \rho vT_\eta + pv_\eta) + B(1 - \zeta)^2(wp_\zeta - \rho wT_\zeta + pw_\zeta) = 0 \qquad (25)$$

These equations were cast in finite difference form and solved numerically by using the same ADI method, linearization scheme, and block tridiagonal solution algorithm as previously discussed. The boundary conditions $u = T = p = 1$ and $v = w = 0$ are imposed at $\eta = 1$ or $\zeta = 1$, corresponding to infinity in the untransformed plane. A coarse 21×21 equally spaced mesh was used on the unit square in the η-ζ plane to reduce the core storage to more acceptable levels (63000_8) for computation.

Results Computed in Transformed Plane

Cases comparable to the ones calculated on the untransformed variables were computed successfully for a variety of initial geometries with no difficulty. The loss of entrainment velocities never occurred, confirming the usefulness of the transformation.

The first test case was a square jet with unit sides. The streamwise centerline velocity decay of this jet is presented in figure 10. After a lengthy core region the centerline velocity quickly decays according to the laminar relation for axisymmetric jets x^{-1} (ref. 1). Thus, although the equations compute the flow as if it were truly three-dimensional, the axisymmetry is reproduced. Another square jet was computed to test the transformation. A large jet with sides of length equal to four was formed by taking unequal scalings of y and z. That is, five points in ζ sufficed to give $z = 2$ (half the jet width), while 11 points in η were necessary to give the equivalent $y = 2$. The centerline decay for this case is also shown in figure 10. After a much longer core than the 1×1 jet (since the initial shear layer is four times farther from the axis), this configuration also very rapidly begins to decay along the axisymmetric curve. In fact, if the 1×1 curve is displaced to the right by the difference of core lengths, the decay curves coincide.

The three-dimensional capabilities of the method were tested on rectangular jets of varying aspect ratios. A rectangular 2×1 jet gave results for velocity decay shown in figure 10. The initial core region was of the same length as the 1×1 square jet. However, the decay was slower than the 1×1 jet, and in fact there was a region where the two-dimensional laminar jet decay $x^{-1/3}$ described the flow. Eventually though, the decay increased and approached the axisymmetric behavior seen before with slope x^{-1}. Only this far-field behavior could be described by an axisymmetric boundary-layer analysis, whereas the length to its asymptotic decay could not.

A rectangular 4×1 jet is more two-dimensional than either of the previous cases, as indicated by its decay. (See fig. 10.) After the initial core length, characteristic of the distance needed for disturbances one width away from the centerline to reach the axis, the decay curve obviously follows the two-dimensional slope for a greater distance down-

stream to about $x = 500$ (see fig. 10) where it also gradually starts to approach the axisymmetric curve. The length $x = 500$ is not too surprising, for this is the core distance of the 4×4 square jet, the distance needed for disturbances four widths away to reach the axis. The even higher aspect ratio 8×1 jet continued the established trend and is also shown in figure 10.

Finally, note the advantage gained through the use of the transformation. Prior to its use, by using a greatly expanding mesh in the untransformed plane with extrapolation at the last mesh point, complete loss of entrainment took place at approximately $x = 20$. Even at this point the accuracy of the solution is questionable, and this is not even halfway to the end of the core region as computed by using the transformation and depicted in figure 10.

CONCLUDING REMARKS

The parabolic-elliptic Navier-Stokes equations have been shown to be a viable method for computation of three-dimensional supersonic jet flows. The difficulties associated with the unbounded domain of the jet can be eliminated by incorporating a transformation into the equations so that the points of infinity in the cross plane are mapped to a finite value at the transformed plane.

Although the character of the computed flow can be predominantly axisymmetric in the case of the square jet or approach a two-dimensional limit, as is the case for the 8×1 rectangular jet, no prior assumptions to this effect are required. The solution computes the particular flow under investigation as though it were three-dimensional, allowing the initial geometry of the prescribed jet to determine the ultimate nature of the solution.

The present calculations have been for laminar jets; however, jet flows are generally turbulent. Thus, even if some simpler method could be used instead of the present integration scheme to recover the gross characteristic of the laminar flow, the inclusion of turbulence modeling in the fully elliptic crossplane requires numerical treatment.

A subsonic analog of the parabolic-elliptic Navier-Stokes equations, where the streamwise pressure gradient is correctly accounted for, is currently being investigated so that the more advanced state of the higher order incompressible turbulence models can be drawn upon for inclusion into the governing equations. If this proves successful, then the supersonic equations will be used as a means to test various modeling procedures for compressible turbulent flows.

REFERENCES

1. Schlichting, Hermann (J. Kestin, transl.): Boundary Layer Theory. Fourth ed., McGraw-Hill Book Co., Inc., c.1960.

2. Free Turbulent Shear Flows. Volume I – Conference Proceedings. NASA SP-321, 1973.

3. Lubard, Stephen C.; and Helliwell, William S.: Calculation of the Flow on a Cone at High Angle of Attack. AIAA Paper No. 73-636, July 1973.

4. Rudman, S.; and Rubin, S. G.: Hypersonic Viscous Flow Over Slender Bodies With Sharp Leading Edges. AIAA J., vol. 6, no. 10, Oct. 1968, pp. 1883-1890.

5. Rubin, S. G.; and Lin, T. C.: Numerical Methods for Two- and Three-Dimensional Viscous Flow Problems: Application to Hypersonic Leading Edge Equations. AFOSR-TR-71-0778, U.S. Air Force, Apr. 1971. (Available from DDC as AD 726 547.)

6. Peaceman, D. W.; and Rachford, H. H., Jr.: The Numerical Solution of Parabolic and Elliptic Differential Equations. J. Soc. Ind. & Appl. Math., vol. 3, no. 1, Mar. 1955, pp. 28-41.

7. Nardo, C. T.; and Cresci, R. J.: An Alternating Directional Implicit Scheme for Three-Dimensional Hypersonic Flows. J. Comput. Phys., vol. 8, no. 2, Oct. 1971, pp. 268-284.

8. Douglas, Jim, Jr.; and Jones, B. F., Jr.: On Predictor-Corrector Methods for Nonlinear Parabolic Differential Equations. J. Soc. Ind. & Appl. Math., vol. 11, no. 1, Mar. 1963, pp. 195-204.

9. Krause, E.; Hirschel, E. H.; and Bothmann, Th.: Differenzenformeln zur Berechnung Dreidimensionaler Grenzschichten (Finite Difference Equations for Calculating Three-Dimensional Boundary Layers). DLR FB 69-66, Sept. 1969.

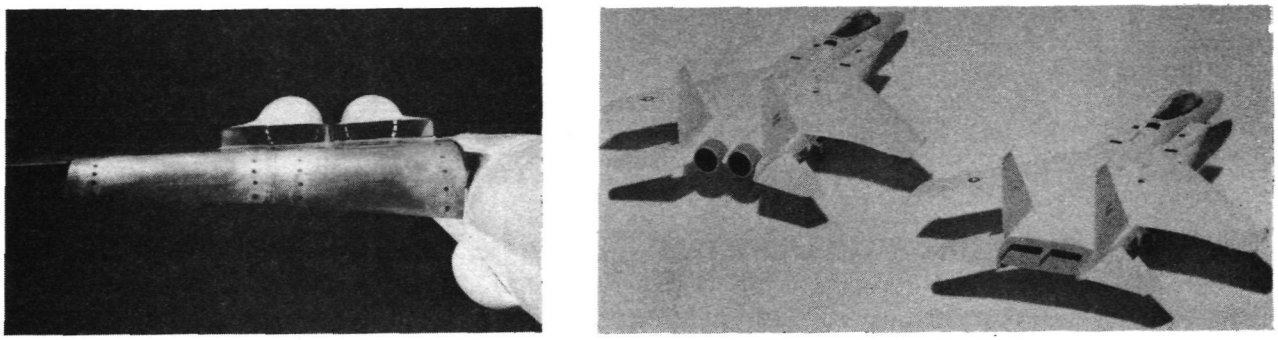

(a) Upper surface blowing. (b) F-15 with proposed rectangular nozzle.

Figure 1.- Examples of three-dimensional jets in aerodynamic flows.

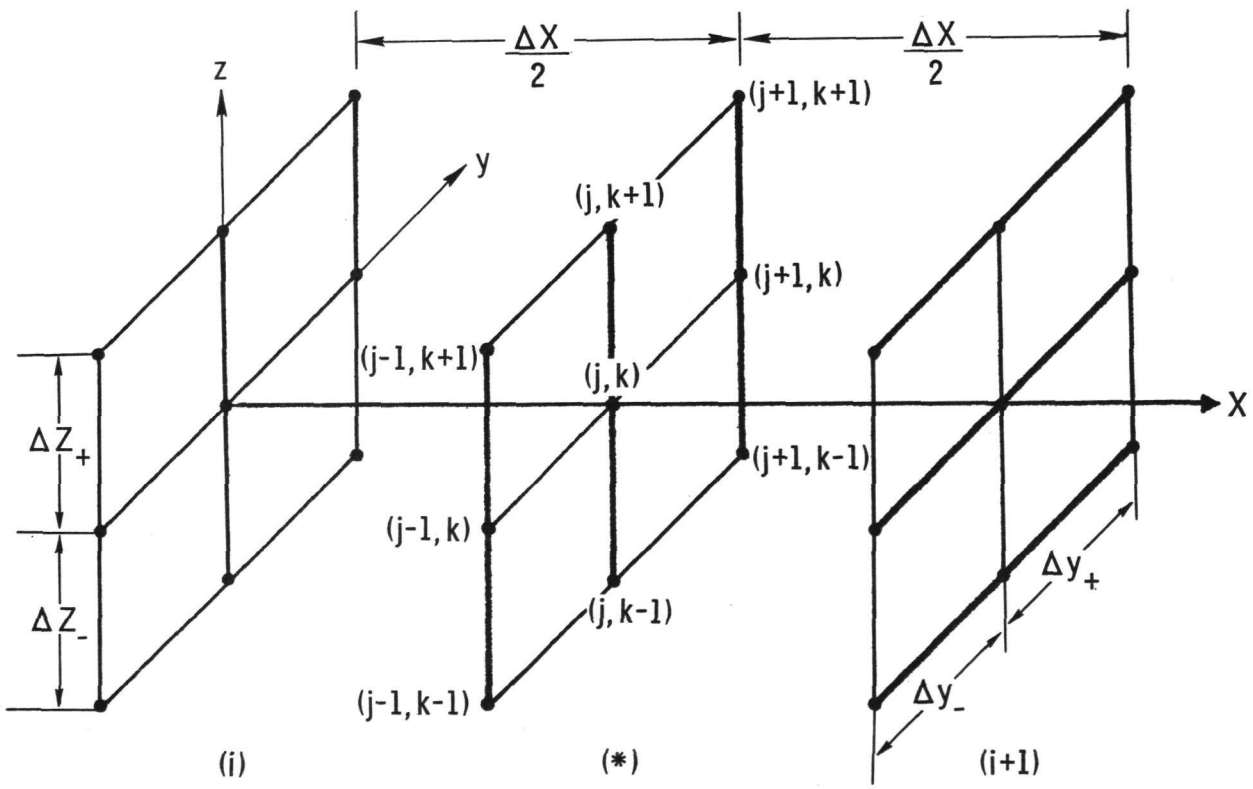

Figure 2.- The ADI procedure: first step implicit in z, explicit in y; second step implicit in y, explicit in z.

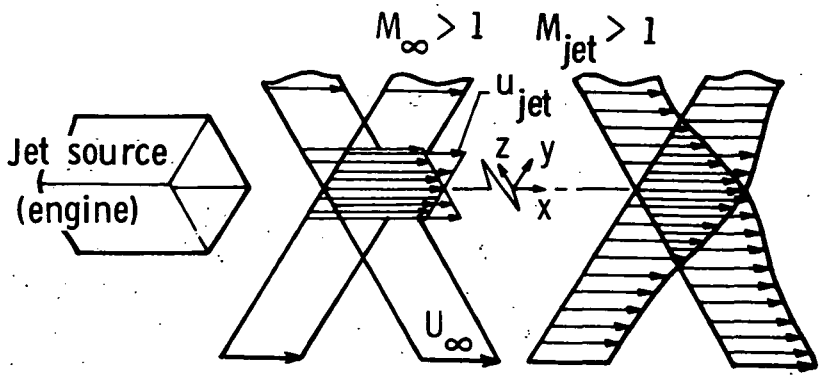

Figure 3.- Conceptual model of three-dimensional supersonic jet flow.

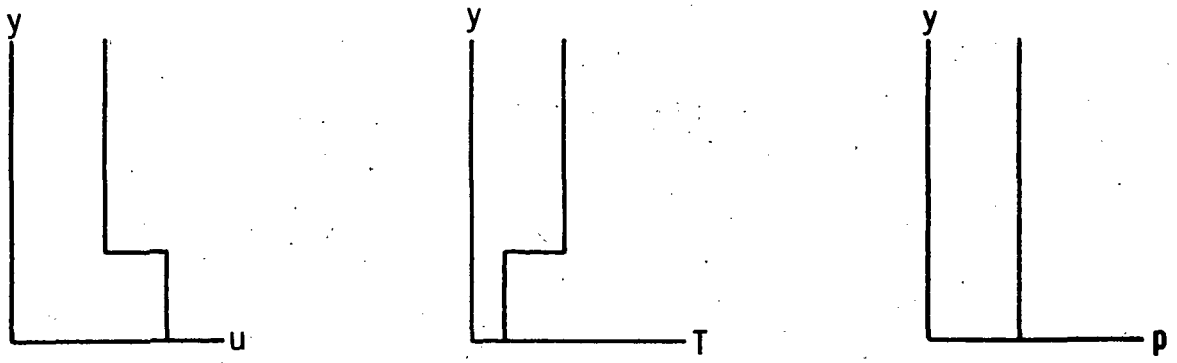

(a) Profiles at x = 0.

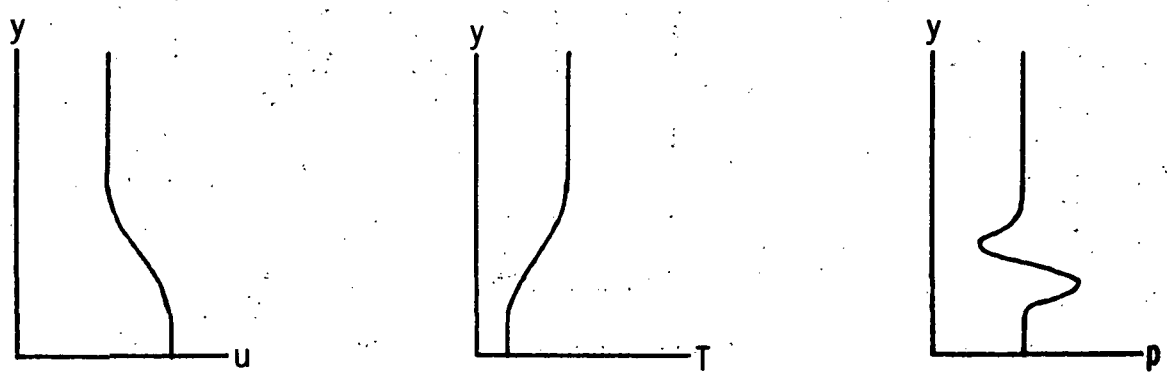

(b) Profiles downstream of initial plane.

Figure 4.- Initial x-behavior of solution profiles.

$$\delta u = 0 \therefore u_2 - u_0 = 0$$

$$\delta^2 u = \frac{u_2 - 2u_1 + u_0}{\Delta^2} = 2\frac{(u_2 - u_1)}{\Delta^2}$$

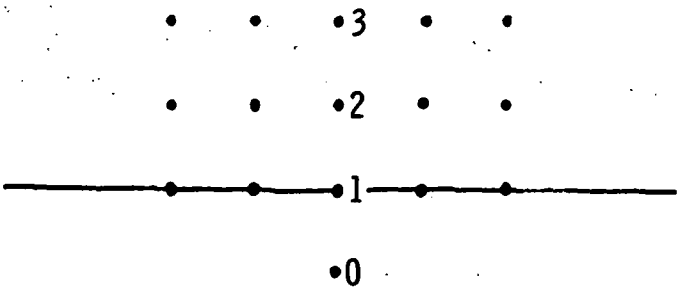

Figure 5.- Differencing used on a boundary.

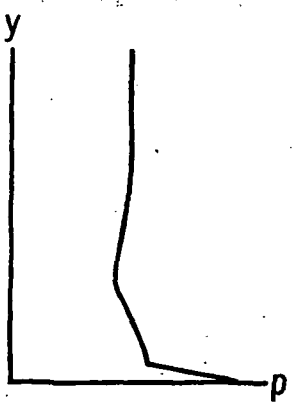

Figure 6.- Qualitative pressure behavior attributed to boundary differencing.

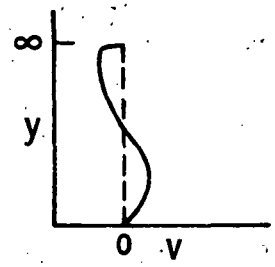

Figure 7.- Crossflow profiles when free-stream conditions imposed.

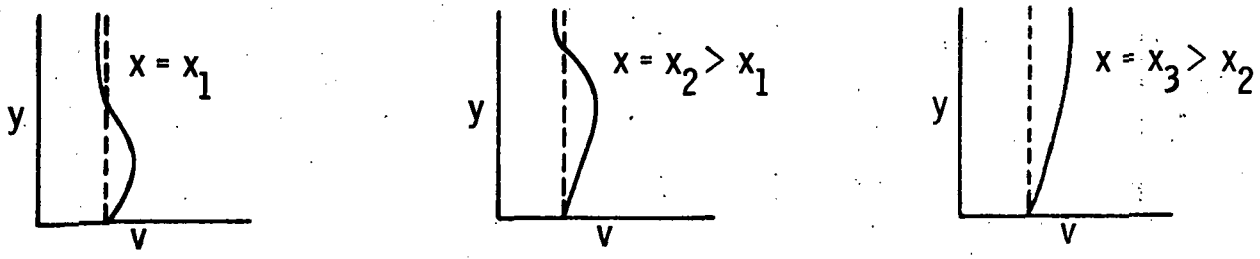

Figure 8.- Crossflow profiles when free-stream conditions extrapolated.

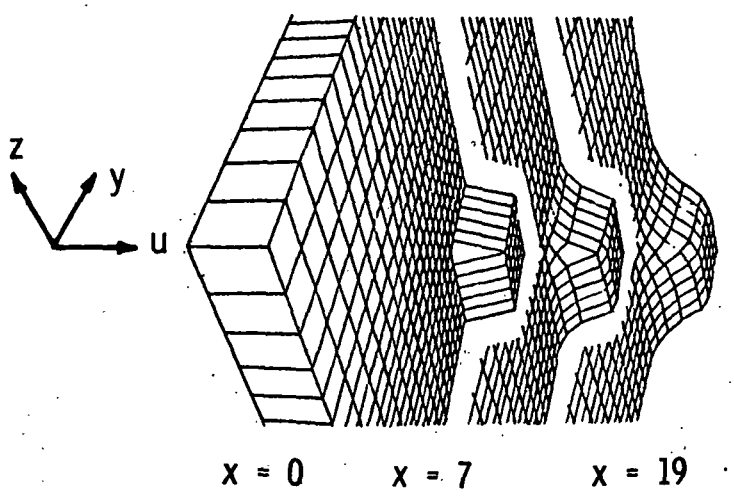

Figure 9.- Computed velocity profiles at various stations.

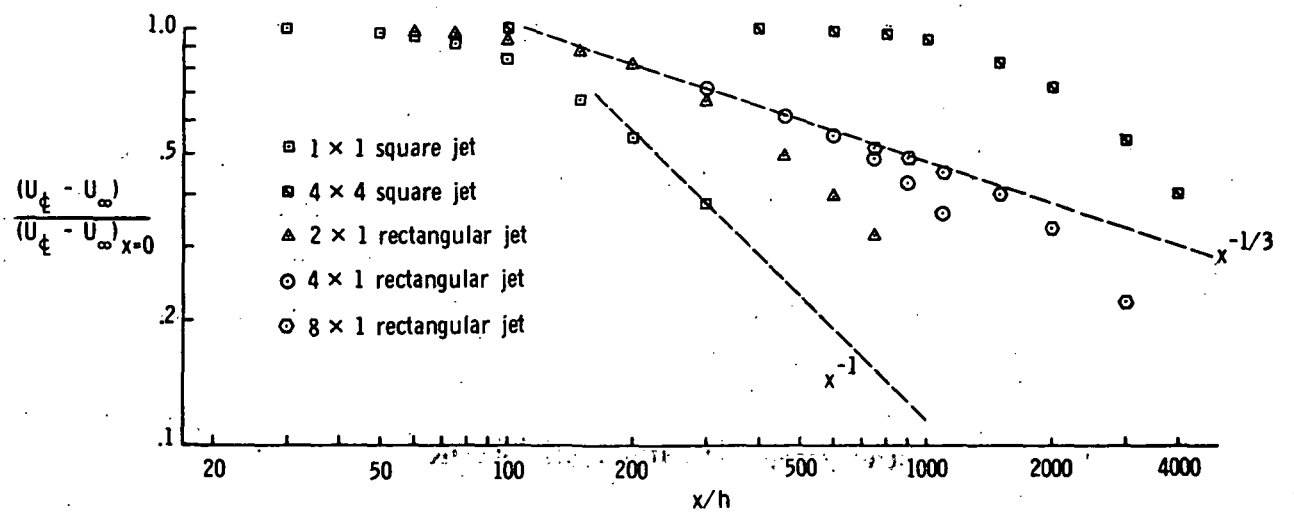

Figure 10.- Centerline velocity decay for three-dimensional jets.

Page intentionally left blank

COMPUTATIONAL ASPECTS OF THE PREDICTION OF MULTIDIMENSIONAL TRANSONIC FLOWS IN TURBOMACHINERY

By David A. Oliver and Panagiotis Sparis
Massachusetts Institute of Technology

INTRODUCTION

The analytical prediction and description of transonic flow in turbomachinery is complicated by three fundamental effects: (1) The fluid equations describing the transonic regime are inherently nonlinear, (2) shock waves may be present in the flow, and (3) turbomachine blading is geometrically complex, possessing large amounts of curvature, stagger, and twist. Simple analytically separable solutions are therefore not readily obtainable. (The complex geometry of a typical transonic compressor rotor is shown in fig. 1.) Because of these analytical difficulties, a computational approach to the prediction and design of transonic turbomachine flows is strongly warranted.

In the present work, a three-dimensional computation procedure for the study of transonic turbomachine fluid mechanics is described. The fluid differential equations and corresponding difference operators are presented, the boundary conditions for complex blade shapes are described, and the computational implementation and mapping procedures are developed. Illustrative results of a typical unthrottled transonic rotor are also presented.

FLUID EQUATIONS AND DIFFERENCE OPERATORS

The densities of mass ρ, momenta m_i, and energy e defined by the fluid state vector $\underline{U}(x_i,t)$ are governed by the fluid conservation laws in cylindrical coordinates $(x_1 = r,\ x_2 = \theta$, and $x_3 = z)$ and time t:

$$\frac{\partial \underline{U}}{\partial t} = \frac{1}{r}\left[\frac{\partial \underline{F}_i}{\partial x_i} + \underline{K}(\underline{U})\right] \tag{1}$$

In a coordinate system fixed to a turbomachine blade rotating at angular velocity Ω, the state vector $\underline{U}$, and the flux vectors $\underline{F}_i(\underline{U})$ and $\underline{K}(\underline{U})$ are

$$\underline{U} = \left[\rho, \rho u_r, \rho u_\theta, \rho u_z, e\right] \tag{2}$$

$$\underline{F}_1 = r\begin{vmatrix} \rho u_r \\ \rho u_r^2 + p \\ \rho u_r u_\theta \\ \rho u_r u_z \\ (e + p)u_r \end{vmatrix} \qquad \underline{F}_2 = \begin{vmatrix} \rho(u_\theta - r\Omega) \\ \rho u_r(u_\theta - r\Omega) \\ \rho u_\theta(u_\theta - r\Omega) + p \\ \rho u_z(u_\theta - r\Omega) \\ (e + p)(u_\theta - r\Omega) \end{vmatrix} \tag{3a}$$

$$\underline{F}_3 = r\begin{vmatrix} \rho u_z \\ \rho u_r u_z \\ \rho u_r u_\theta \\ \rho u_z^2 + p \\ (e + p)u_z \end{vmatrix} \qquad \underline{K} = \begin{vmatrix} 0 \\ \rho u_\theta^2 + p \\ \rho u_r u_\theta \\ 0 \\ 0 \end{vmatrix} \tag{3b}$$

In equations (3), the pressure p appears which is expressed in terms of the state vector $\underline{U}$ through the equation of state.

A time-explicit difference operator S approximating the fluid equations (eq. (1)) with second-order accuracy coupled with a local stabilizing operator D is used to advance the fluid state from time level n to level $n + 1$ over the interval δt as follows:

$$\underline{U}^{n+1} = (S + D)\underline{U}^n \tag{4}$$

Here, following MacCormack (ref. 1), S is formed in two steps as

$$\underline{U}^* = -\frac{1}{r}\left[\frac{\delta t}{\delta x_i}\Delta_i^+ \underline{F}_i(\underline{U}) + \delta t \underline{K}(\underline{U})\right]$$

$$S\underline{U} = \frac{1}{2}\left\{\underline{U}^* + \underline{U} - \frac{1}{r}\left[\frac{\delta t}{\delta x_i}\Delta_i^- \underline{F}_i(\underline{U}^*) + \delta t \underline{K}(\underline{U}^*)\right]\right\} \tag{5}$$

The operators Δ_i^+ and Δ_i^- are the forward and backward difference operators in the coordinate directions x_i:

$$\Delta^+ f(x) = f(x + \delta x) - f(x)$$

$$\Delta^- f(x) = f(x) - f(x - \delta x) \tag{6}$$

If the difference operator (eq. (5)) is applied successively in split steps (ref. 2) for each coordinate direction, the numerical stability conditions are

$$\delta t \leq \min_i \left\{ \frac{\delta x_i}{|u_i| + c} \right\} \tag{7}$$

At stagnation points or sonic points, the linearized version of the difference operator (eq. (5)) is neutrally stable independently of the choice of $\delta t/\delta x_i$. For a genuinely linear difference operator this occurrence is of no consequence and stable solutions of the difference equations can be achieved. In the nonlinear case, however, the true stability of the operator at the neutral point will be determined by the higher order nonlinear terms, and these terms will destabilize the difference operator. This numerical instability is an inherently numerical instability induced by higher order terms in the truncation error. Hence the nonlinear difference operator may be stabilized by the introduction of an artificial dissipation term of the order of the truncation error of the difference operator. In the case of the difference operator (eq. (5)), this term must be of third order in $\delta t, \delta x_i$.

The global damping or stabilizing operator D_o may be summarized in the archetypal form

$$D_o \underline{U} = \kappa \frac{\delta t}{\delta x_i} \frac{\Delta_i^+ Q \Delta_i^- + \Delta_i^- Q \Delta_i^+}{2} \underline{U} \tag{8}$$

where $Q(\underline{U})$ is a matrix diffusion coefficient of order $\delta t, \delta x_i$ and κ is an order unity nondimensional constant. A Taylor's series expansion of this operator shows that it is the difference expression for the continuous diffusion operator

$$\kappa \delta x_i^2 \frac{\delta t}{\delta x_i} \frac{\partial}{\partial x_i} Q \frac{\partial \underline{U}}{\partial x_i} \tag{9}$$

The neutral stability condition of the linearized operator occurs at sonic points and stagnation points. While a sonic point exists in the interior of a shock wave, the nonlinear instability could be just as important in smooth isentropic regions of transonic flow passing continuously through the sonic point as in regions where shocks are present. Calculations performed with the operator (eq. (5)) have confirmed this conjecture. For subsonic flows up into the high subsonic regime, the undamped operators have been demonstrated to be stable. However, where the Mach number was increased into the transonic regime, numerical instabilities occurred which could be eliminated with the use of the damping operator.

On the basis of the observations, the nonlinear instability should be confined to those regions of the flow where the eigenvalues of the amplification matrix are unity, i.e., at sonic and stagnation points. The damping operator D should then be structured such

that it becomes significant only near the sonic and stagnation points and not operative in other portions of the flow. A damping operator with such characteristics is

$$D = f(M)D_0 \tag{10}$$

where $f(M)$ is a distribution function which depends upon the local Mach number such that $f(M) = 1$ for $M = 0$ or $M = 1$, but $f(M) \ll 1$ for $M \neq 0$ and 1. A useful function with such properties is the Lorentz Line shape function

$$f(M) = \frac{1}{1 + \left(\frac{M - 1}{\Delta M}\right)^2} + \frac{1}{1 + \left(\frac{M}{\Delta M}\right)^2} \tag{11}$$

where the parameter ΔM represents the effective width in Mach number of the distribution function which peaks at $M = 0$ and 1. The use of the local damping operator D in place of the global operator D_0 can offer significant improvement in the resolution of the flow while maintaining stability of the difference operator.

The utility of the local damping operator is shown in figure 2 where the supercritical transonic flow of a $\gamma = 1.4$ gas over a right circular cylinder has been computed. This calculation was performed with a minimal number of mesh points (20) distributed over the surface of the half-cylinder to test the utility of the local damping operator. Significant improvement of the flow-field resolution, including the shock wave, results.

BOUNDARY CONDITIONS ON BLADE SURFACES

The appropriate boundary condition on an impenetrable blade surface for an inviscid flow is the single condition

$$u_n = 0 \tag{12}$$

where u_n is the velocity normal to the blade surface in blade coordinates. This boundary condition is not readily implemented in the finite-difference procedures described in the previous section because the full fluid state $\underline{U}$ is required at each point including the boundary points. If, as in figure 3, the boundary points are treated as interior points to which the difference equation (eq. (5)) is to be applied, then the application of the boundary condition, which consists of the determination of the state vector $\underline{U}$ at the auxiliary point, must be such that only the single condition (eq. (12)) is imposed at the blade surface.

If Σ is the surface of a sufficiently smooth three-dimensional body, then at each point M on the surface Σ a triply orthogonal curvilinear coordinate system may be defined consisting of the local normal ζ to the surface Σ at the point M and two curves of the surface $\Sigma(\eta$ and $\xi)$ that are normal to each other at the point M. If dn, $d\tau$, and ds are the differential arc lengths along the axes ξ, η, and ζ, respectively, then

$$\left.\begin{aligned} ds &= h_s\, d\xi \\ d\tau &= h_\tau\, d\eta \\ dn &= h_n\, d\zeta \end{aligned}\right\} \tag{13}$$

The equations of motion may be expressed in the curvilinear coordinate system ξ, η, and ζ. By introducing the boundary condition $u_n = 0$ and the radii of curvature R_s and R_τ of the surface Σ in the direction of the axes ξ and η, the equations of motion may be written in the following form, correct only for points on the surface Σ (ref. 3):

$$\frac{\partial \rho}{\partial t} + \frac{1}{h_s h_\tau}\left[\frac{\partial}{\partial \xi}\left(h_\tau u_s \rho\right) + \frac{\partial}{\partial \eta}\left(h_s u_\tau \rho\right)\right] + \frac{\partial\left(u_n \rho\right)}{\partial \zeta} = 0 \tag{14}$$

$$\frac{\partial u_s}{\partial t} + \frac{u_s}{h_s}\frac{\partial u_s}{\partial \xi} + \frac{u_\tau}{h_\tau}\frac{\partial u_s}{\partial \eta} + \frac{u_\tau u_s}{h_s h_\tau}\frac{\partial h_s}{\partial \eta} - \frac{u_\tau^2}{h_s h_\tau}\frac{\partial h_\tau}{\partial \xi} = -\frac{1}{\rho h_s}\frac{\partial p}{\partial \xi} \tag{15}$$

$$\frac{\partial u_\tau}{\partial t} + \frac{u_s}{h_s}\frac{\partial u_\tau}{\partial \xi} + \frac{u_\tau}{h_\tau}\frac{\partial u_\tau}{\partial \eta} + \frac{u_\tau u_s}{h_s h_\tau}\frac{\partial h_s}{\partial \xi} - \frac{u_s^2}{h_s h_\tau}\frac{\partial h_s}{\partial \eta} = -\frac{1}{\rho h_\tau}\frac{\partial p}{\partial \eta} \tag{16}$$

$$\frac{\rho}{a^2}\left(\frac{u_s^2}{R_s} + \frac{u_\tau^2}{R_\tau}\right) = \frac{1}{a^2}\frac{\partial p}{\partial n} = \frac{\partial \rho}{\partial n} \tag{17}$$

Equations (14) to (17) have been obtained with the isentropic assumption in which a^2 is the square of the speed of sound. By eliminating the space and time derivatives of the density between equations (14) and (17) and replacing the general curvilinear coordinates ξ, η, and ζ with the local s, τ, and n, the following condition on the normal derivatives of the normal velocity is obtained (ref. 3):

$$\rho \frac{\partial u_n^2}{\partial n^2} + 2 \frac{\partial \rho}{\partial n} \frac{\partial u_n}{\partial n} = -\left[\frac{\partial^2 (u_s \rho)}{\partial s \, \partial n} - \frac{1}{R_s} \frac{\partial (u_s \rho)}{\partial s} + \frac{\partial^2 (u_\tau \rho)}{\partial \tau \, \partial n} - \frac{1}{R_\tau} \frac{\partial (u_\tau \rho)}{\partial \tau} + \frac{\partial}{\partial n} \left(\frac{u_s \rho}{R_s} + \frac{u_\tau \rho}{R_\tau} \right) \right.$$

$$\left. + \left(\frac{u_s^2}{R_s} + \frac{u_\tau^2}{R_\tau} \right) \left(\frac{2 - \gamma}{a^2} \right) \frac{\partial \rho}{\partial t} + 2 \left(\frac{u_s}{R_s} \frac{\partial u_s}{\partial t} + \frac{u_\tau}{R_\tau} \frac{\partial u_\tau}{\partial t} \right) \frac{\rho}{a^2} \right] \tag{18}$$

By center differencing the normal first and second derivatives of the normal velocity, an approximation is obtained to u_n^- on the auxiliary point correct to order $(\delta n)^3$ if the right-hand side of equation (18) can be approximated with an error no greater than $O(\delta n)$. Thus, on the surface of the body, equations (14), (15), and (16) have to be solved while a boundary condition is applied for u_n using equation (18). Note also that the radii of curvature of the surface R_s and R_τ are required for this accurate determination of u_n^-. The second normal derivative of the normal velocity is rigorously required for a second-order-accurate boundary condition, the expression for u_n^- being

$$u_n^- = -u_n^+ + O\left[(\delta n)^2 \frac{1}{R} \right] \tag{19}$$

However, for mildly curving shapes with $1/R$ of order δn, a simple reflection of u_n will yield second-order accuracy without the complication of introducing the second normal derivative given by equation (18). This simplification is used in the results to be illustrated in the subsequent sections.

UPSTREAM, DOWNSTREAM BOUNDARY CONDITIONS

For a steady-state one-dimensional duct flow, one is not free to specify the downstream boundary conditions if the upstream conditions are fully specified. This is not so in a transonic multidimensional duct flow. In this case the upstream conditions may be set. However, one can still vary a single downstream variable such as the pressure and achieve different steady-state solutions. This degree of freedom on downstream pressure arises because the oblique shock waves present on the blades in the transonic regime are free to move and alter their strength in response to the different downstream pressure conditions. This range of freedom on downstream pressure is limited. It ceases, for example, if the downstream pressure is set high enough so that the shocks are blown forward out of the cascade.

In the actual calculation, boundary conditions were set so that the mean flow at the inlet plane to the duct was held fixed. Waves generated by the rotor which moved upstream into the inlet plane were then allowed to escape. This escape condition was

formulated as an axially one-dimensional characteristics construction at the inlet plane of the computational domain. At the downstream exit plane the pressure was held fixed and the remaining flow variables forced to take a zero axial gradient condition. This condition allows the mean flow velocity at the exit to adjust itself to the correct mass flow; however, it distorts the structure imposed by the rotor locally in the vicinity of the exit plane. This distortion is a consequence of the condition of uniformity of flow in the axial direction rather than in the streamline direction (which is helical rather than axial).

COMPUTATIONAL IMPLEMENTATION

The geometry of the flow field for an illustrative transonic rotor calculation is shown in figures 4 and 5. On the conical spinner are attached $N = 23$ blades with an average hub to tip ratio of 0.6. Thus the flow field of a blade element is bounded by the machine outer and inner casings in the radial direction and by two surfaces $\theta_1(r,z)$ and $\theta_2(r,z)$ in the angular direction such that

$$\theta_2(r,z) - \theta_1(r,z) = \Delta\theta$$

$$\Delta\theta \equiv \frac{2\pi}{N} \tag{20}$$

Let $r_H(z)$ and $r_T(z)$ be the equations of the inner casing (hub) and the outer casing (tip) surfaces. If $\theta = \theta_s(r,z)$ and $\theta = \theta_p(r,z)$ are the equations of the blade suction and pressure surfaces, respectively, then the computational domain boundary surfaces θ_1 and θ_2 may be constructed by making $\theta_1 = \theta_s$ and $\theta_2 = \theta_p$ in the blade region and then extending these surfaces upstream and downstream as ruled surfaces parallel to the machine axis as shown in figure 4.

The complex geometry formed by the extended blade and casing surfaces may be handled computationally by carrying out the computational work in a computational domain $x_i' = (r',\theta',z')$ obtained as a mapping of the physical domain $x_i = (r,\theta,z)$. The complex turbomachine surfaces should map into planar surfaces in the computational domain. Mapping functions selected for this purpose are

$$r' = \frac{r - r_H(z)}{r_T - r_H(z)} r_T \tag{21}$$

$$\theta' = \frac{\theta - \theta_1(r,z)}{\theta_2(r,z) - \theta_1(r,z)} \Delta\theta \tag{22}$$

$$z' = z \tag{23}$$

The Jacobian derivatives of this transformation $g_{ij} = \frac{\partial x_j'}{\partial x_i}$ appear in the conservation laws (eq. (1)) so that $\frac{\partial \underline{F}_i}{\partial x_i}$ is replaced by $g_{ij} \frac{\partial \underline{F}_i}{\partial x_j'}$. Similarly, the difference operator (eq. (5)) in the computation domain becomes

$$\underline{U}^* = -\frac{1}{r(r',z')}\left[g_{ij} \frac{\delta t}{\delta x_j'} \Delta_j^+ \underline{F}_i(\underline{U}) + \delta t \underline{K}(\underline{U})\right]$$

$$S\underline{U} = \frac{1}{2}\left\{\underline{U}^* + \underline{U} - \frac{1}{r(r',z')}\left[g_{ij} \frac{\delta t}{\delta x_j'} \Delta_j^- \underline{F}_i(\underline{U}^*) + \delta t \underline{K}(\underline{U}^*)\right]\right\} \tag{24}$$

In addition, the blade boundary conditions which require the normal derivatives in the physical domain must be expressed in terms of computational domain coordinates. If ν_i denotes the three direction cosines of the blade surface normal, then the first normal derivative expressed in computational domain coordinates x_j' is

$$\frac{\partial}{\partial n} = \nu_i g_{ij} \frac{\partial}{\partial x_j} \tag{25}$$

and the second normal derivative is

$$\frac{\partial^2}{\partial n^2} = \nu_i \nu_k g_{ij} \frac{\partial}{\partial x_j'} g_{kl} \frac{\partial}{\partial x_l'} \tag{26}$$

The derivative forms (eqs. (25) and (26)) and similar forms for the s and τ derivatives replace those of equations (14) to (18) allowing finite differences to be taken in terms of computational domain coordinates x_j'.

INITIAL RESULTS FOR A TRANSONIC ROTOR

Some initial results obtained with the foregoing method for the single-stage transonic rotor shown in figure 1 are now presented. This rotor operates with a tip Mach number M_T of 1.2 and an average axial Mach number M_a of 0.5. The calculation

illustrated here is for an open throttle situation in which the static pressure behind the rotor remains at a low value relative to the full load design values of the rotor.

The calculation was performed on an IBM 370/168 system. Although this machine has a large primary memory capacity, economic considerations necessitated the use of the secondary memory units for the storage of the U^n and U^{n+1} arrays. Continuous input-output operations between the core and the secondary memory units were required for the calculation.

The computational domain shown in figures 4 and 5 was discretized with 67 points in the axial direction, 30 of which are in the region of the blade. The radial direction was discretized with 12 points, the angular direction with 10 points. This discretization was selected as being the minimum number of points which would provide a representative although not detailed resolution of the flow field. Considerations of economy dictated the use of such a coarse mesh in a developmental calculation such as the one described here. Future calculations may be carried out with expanded mesh densities.

Before going into the details of the obtained results, it might be useful for the reader to familiarize himself with the nature of the coordinate transformation and especially with the shape of the $r' = \text{Constant}$ and $\theta' = \text{Constant}$ surfaces in the physical space. The $r' = \text{Constant}$ surfaces are cylindrical surfaces as indicated in figure 5, ranging between the hub and the tip. Actually the tip and the hub surfaces belong to the $r' = \text{Constant}$ family of surfaces. The $\theta' = \text{Constant}$ surfaces are more complicated and, as it can be seen in figure 4, they have no degree of symmetry. However, it is quite apparent that these surfaces are more geometrically related to the blade shape than the $\theta = \text{Constant}$ planes. Thus, some of the plots of the field properties have been made in the r', θ', and z' coordinate system rather than the r, θ, and z system to improve their clarity.

In figure 6, the Mach number distribution is plotted in r and z coordinates along the span on the $\theta' = \text{Constant}$ surface that passes at the suction surface of the blade ($\theta' = \Delta\theta$).

There is a strong shock wave originating from the trailing edge of the blade; on the other hand, there is hardly any trace of the leading-edge oblique shock. The flow upstream of the blade varies almost linearly from subsonic close to the hub to supersonic at the tip, as expected, due to the solid body rotation of the flow in the rotary frame.

Because of the wide open throttle condition, the flow accelerates near the hub to a higher Mach number (approximately 1.9 compared to 1.6 at the tip). This causes the shock wave at the trailing edge to be strongest near the hub. The flow at the supersonic tip is relatively smooth, the trailing-edge shock decelerating the flow from a Mach number of 1.6 to 1.3.

In figure 7, a similar plot of the Mach number distribution on the pressure side of the blade is illustrated. The effect of the hub geometry becomes more apparent now since the flow on the pressure side is accelerating. The maximum Mach number on the pressure side is 1.55 and occurs at the tip section. A shock is present also on the pressure side; however, its strength is diminishing towards the hub, where the flow becomes nearly sonic. The pressure side shock appears upstream of the trailing edge and, as will become apparent in the next figures, it extends to the trailing edge of the suction side of the adjacent blade.

In figures 8 and 9, the intersections of the sonic surface with the pressure and the suction side have been traced in r and z coordinates. In figure 8, corresponding to the pressure side ($\theta = 0$), the presence of the trailing-edge shock is rather apparent. This shock is normal to the hub surface at the pressure side, changing to an oblique towards the suction side (fig. 9). In figures 10, 11, and 12, the Mach number contours have been plotted in θ and z coordinates on the three r' = Constant cylinders corresponding to the tip, mid, and hub sections of the blade. The location and the strength of the trailing-edge shock can now be easily established.

Figures 13 and 14 show the pressure coefficient

$$C_p = \frac{p - p_\infty}{\rho_\infty a_\infty^2}$$

(where $(\,)_\infty$ indicates the properties far upstream) on the suction and pressure sides at typical blade sections near the tip and the hub, respectively. The location of the trailing-edge shock can be easily established on both blade surfaces.

In figure 13, the leading-edge shock can be clearly identified. This shock appears to be stronger on the suction side of the blade. At the pressure side near the trailing edge, there is evidence of an expansion fan that matches the local static pressure at the two sides of the blade. With respect to the blade's lift distribution along the span, the tip section produces little work at the open throttle condition; on the other hand, the hub sections are working very hard, but in vain, in view of the strong shock at the trailing edge that dissipates much of the stagnation pressure rise produced at the hub.

In figure 15 is plotted the distribution of the crossflow velocity u_r on the θ = Constant surface that passes at the blade's suction surface ($\theta = \Delta\theta$). The behavior of u_r is generally determined by the shape of the hub and tip; however, in the region around the trailing edge of the blade, the appearing shock has a significant effect. Due to the acceleration of the flow, the pressure upstream of the shock is lower at the hub than at the tip; thus, a crossflow is developed from the tip to the hub. On the contrary, downstream of the shock, the crossflow reverses direction because now the hub pressure is higher since the shock is stronger at the hub.

Figures 13 and 14 also clearly show the acceleration of the flow, even in the supersonic region near the blade tips, due to the influence of the subsonic zone near the hub. This is a crucial effect in such a genuinely mixed flow; for even though axially propagating signals cannot influence the supersonic zone, it is possible for disturbances to feed back upstream through the subsonic zone and then radially impact the upstream supersonic flow at the tip.

REFERENCES

1. MacCormack, Robert W.: Numerical Solution of the Interaction of a Shock Wave With a Laminar Boundary Layer. Proceedings of the Second International Conference on Numerical Methods in Fluid Dynamics. Vol. 8 of Lecture Notes in Physics, Maurice Holt, ed., Springer-Verlag, 1971, pp. 151-163.

2. MacCormack, R. W.; and Paullay, A. J.: Computational Efficiency Achieved by Time Splitting of Finite Difference Operators. AIAA Paper No. 72-154, Jan. 1972.

3. Sparis, P.: A Computational Study of the Three Dimensional Flow in a Single Stage Transonic Compressor. Ph. D. Thesis, Massachusetts Inst. Technol., 1974.

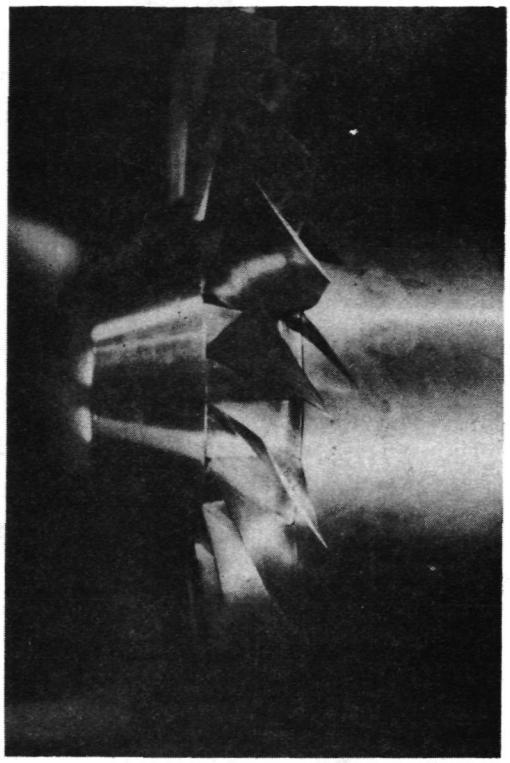

Figure 1.- Single stage transonic compressor rotor designed with average hub-tip radius ratio of 0.6; axial Mach number, 0.5; tip Mach number, 1.2.

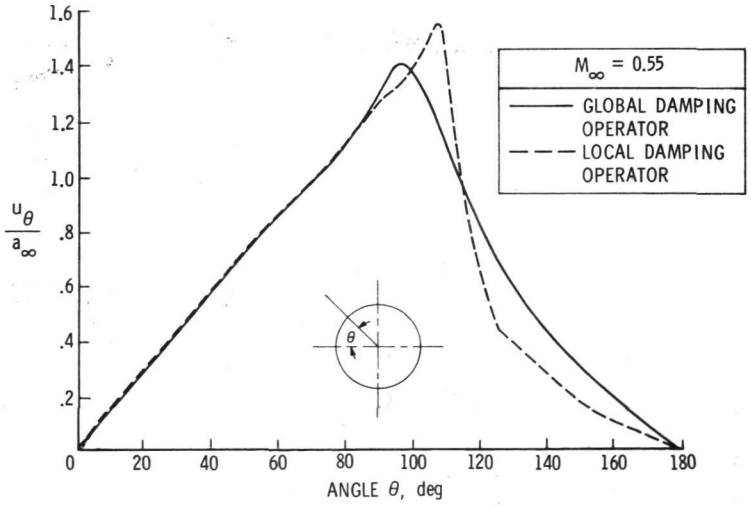

Figure 2.- Test of local damping operator D(M) for transonic flow of $\gamma = 1.4$ gas over right circular cylinder. Twenty points distributed over θ.

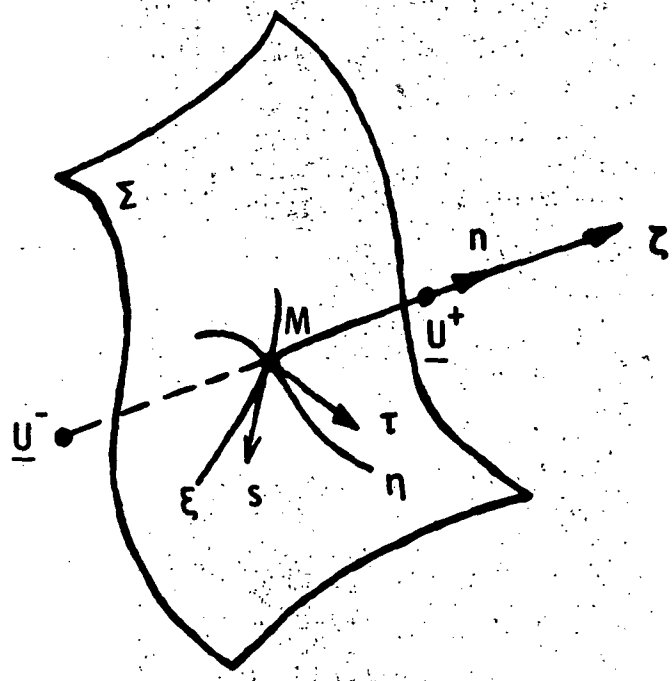

Figure 3.- Surface geometry.

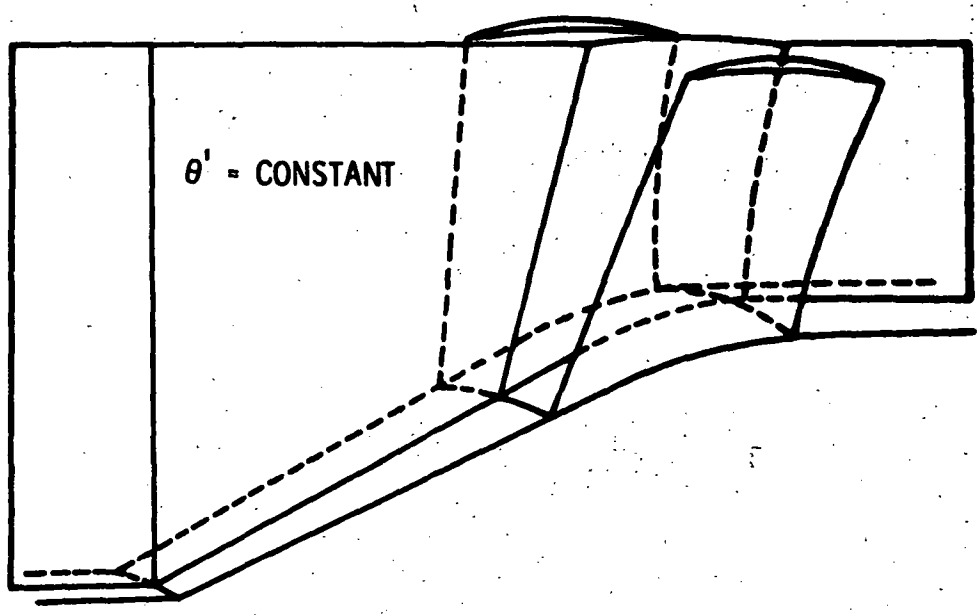

Figure 4.- Computational domain (passage view) illustrating blades and θ' = Constant surface.

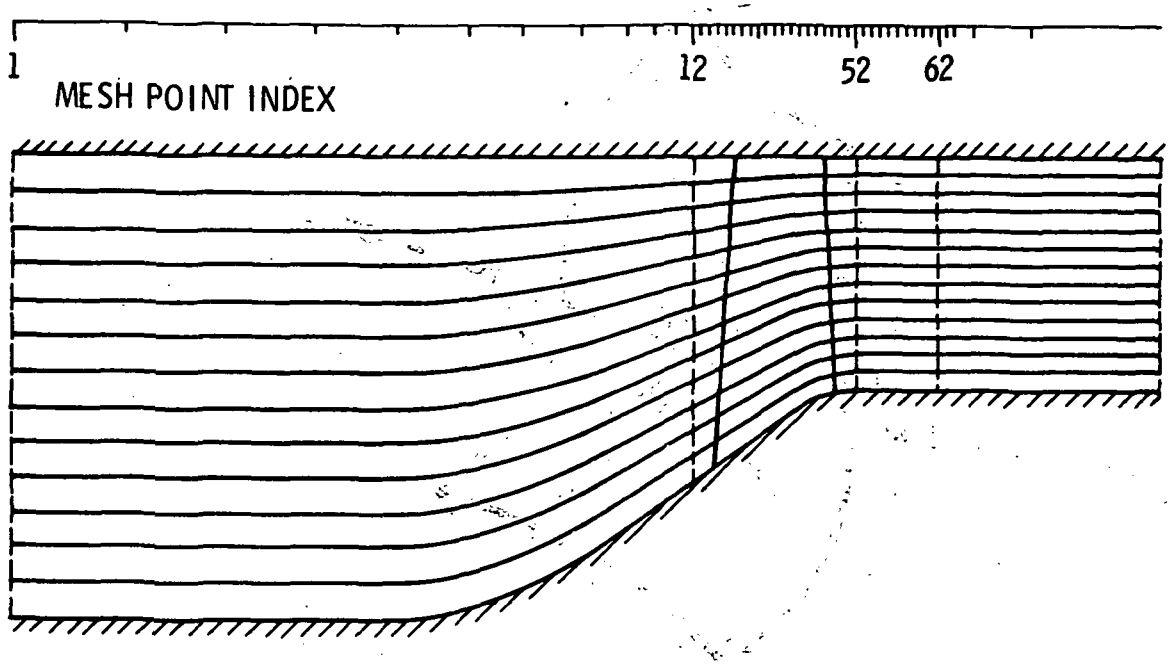

Figure 5.- Computational domain (section view) along axis of machine illustrating r' = Constant surfaces.

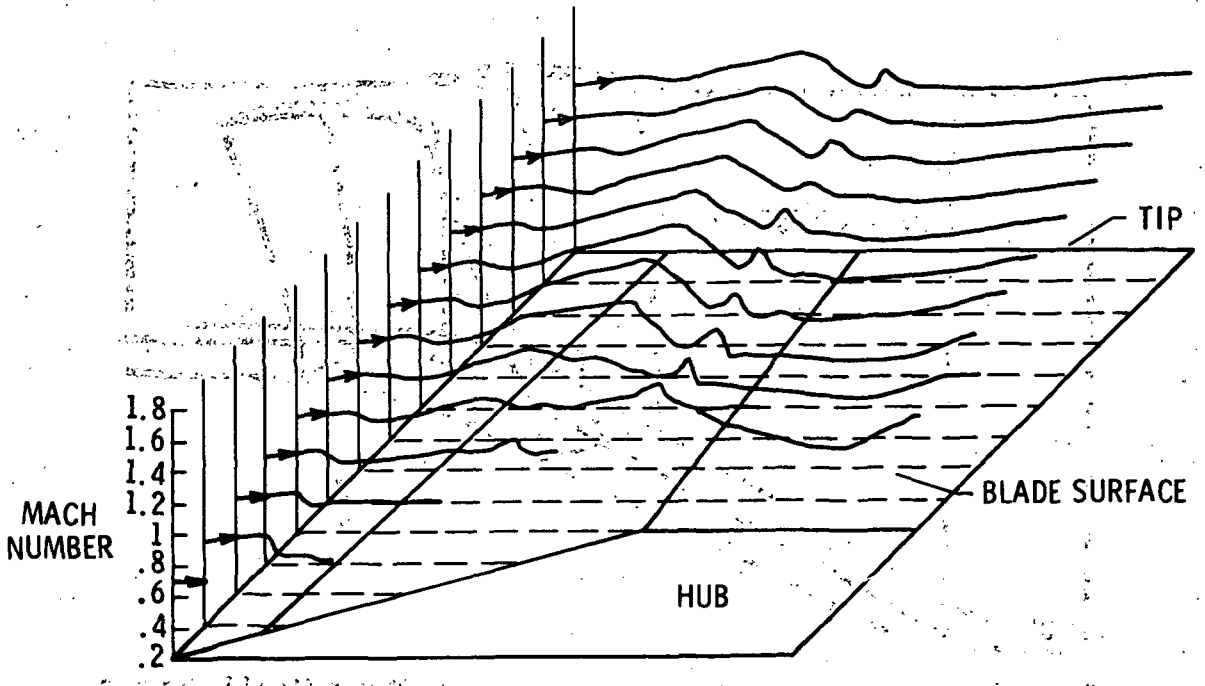

Figure 6.- Mach number distribution over blade surface (suction side).

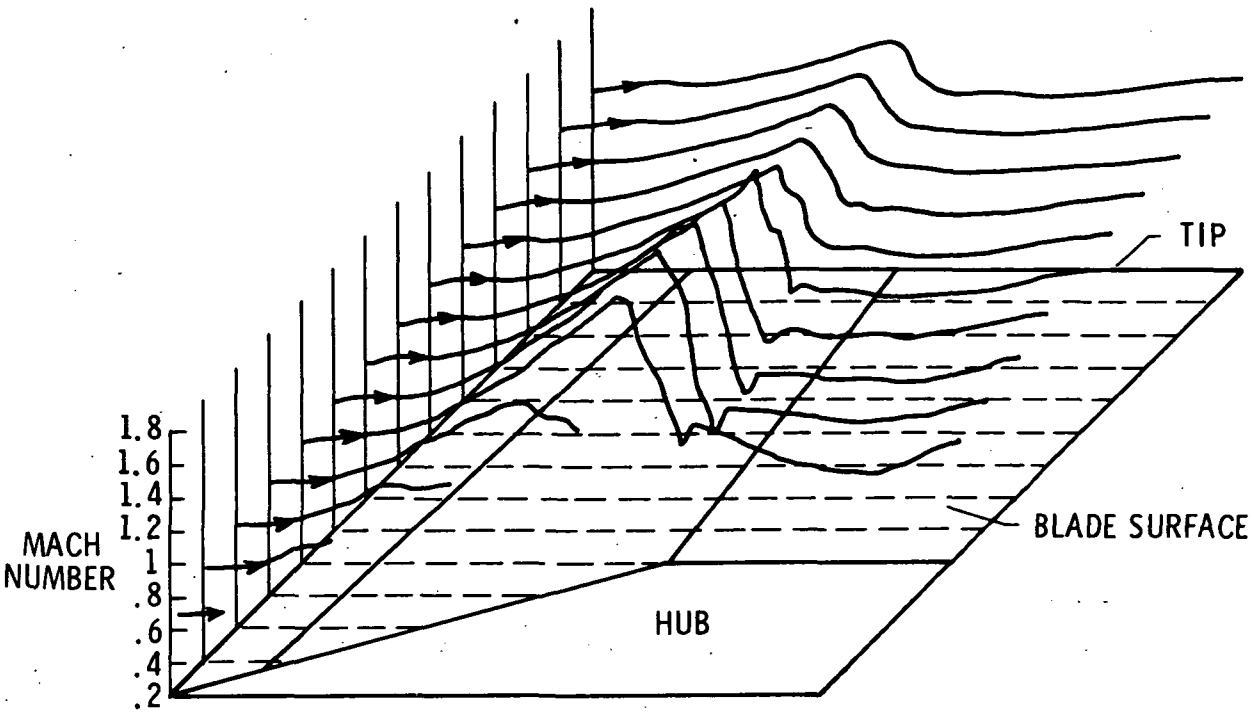

Figure 7.- Mach number distribution over blade surface (pressure side).

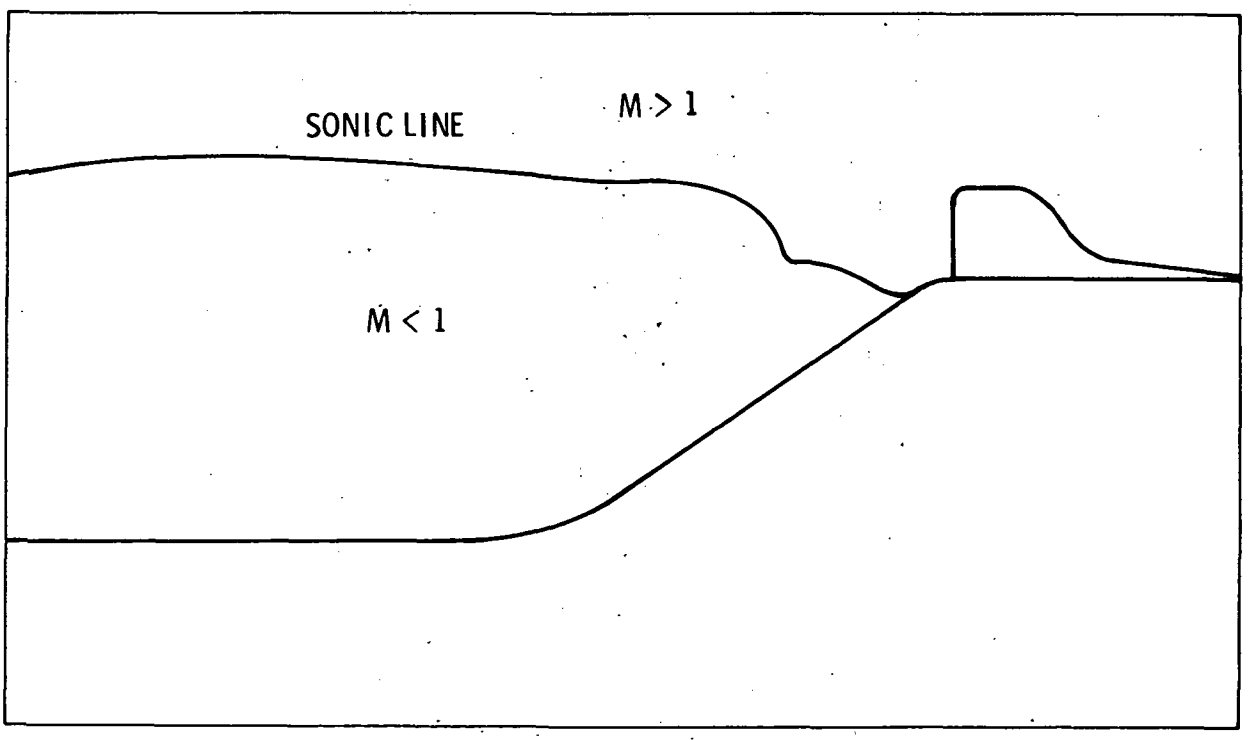

Figure 8.- Sonic surface intersections with $\theta = \theta_1$ surface (pressure side).

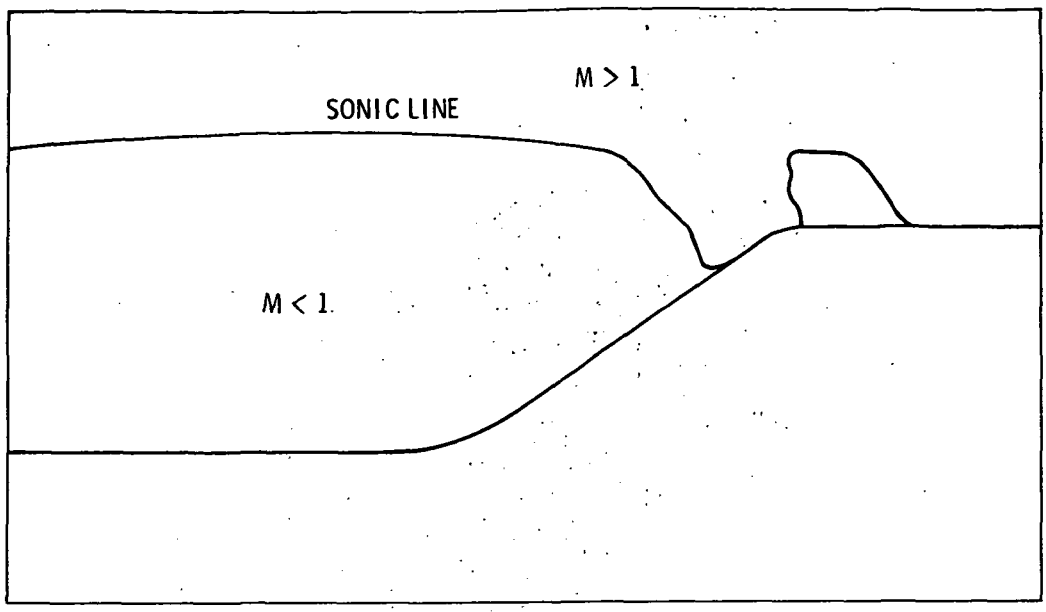

Figure 9.- Sonic surface intersections with $\theta = \theta_2$ surface (suction side).

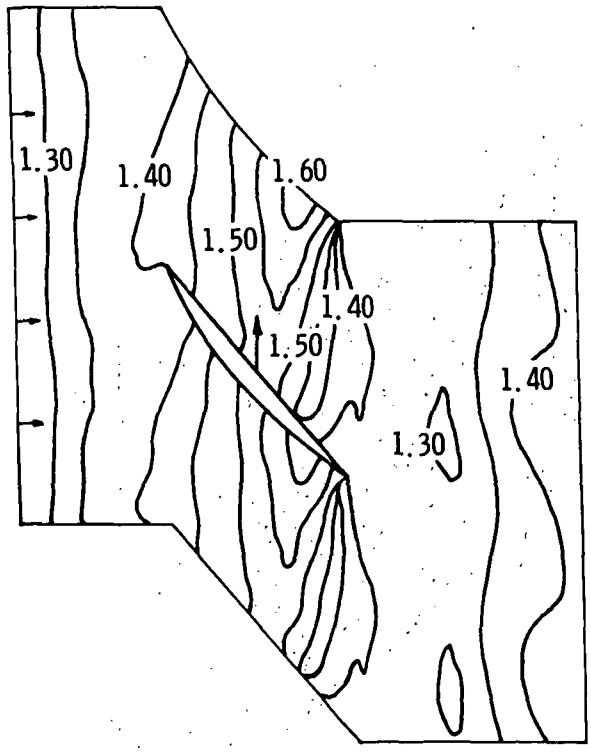

Figure 10.- Mach number contours in interblade region along r' = Constant surface (tip section).

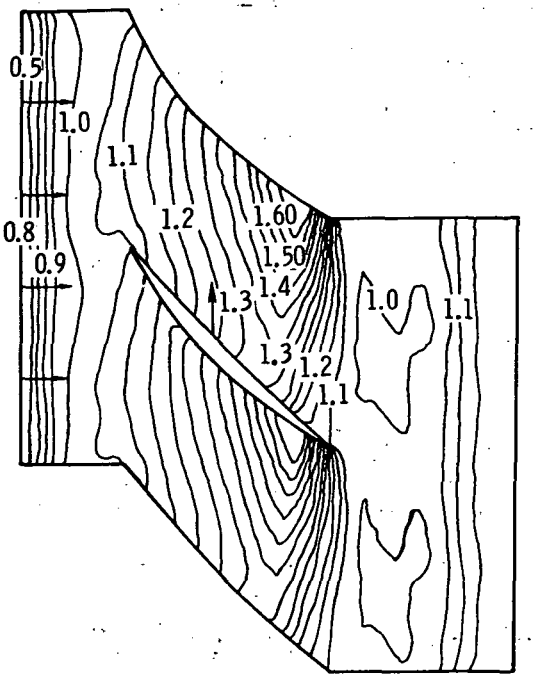

Figure 11.- Mach number contours in interblade region along r' = Constant surface (midspan section).

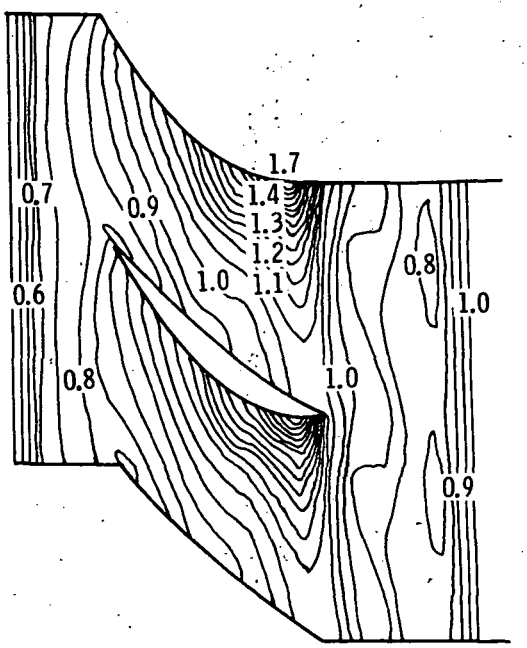

Figure 12.- Mach number contours in interblade region along r' = Constant surface (hub section).

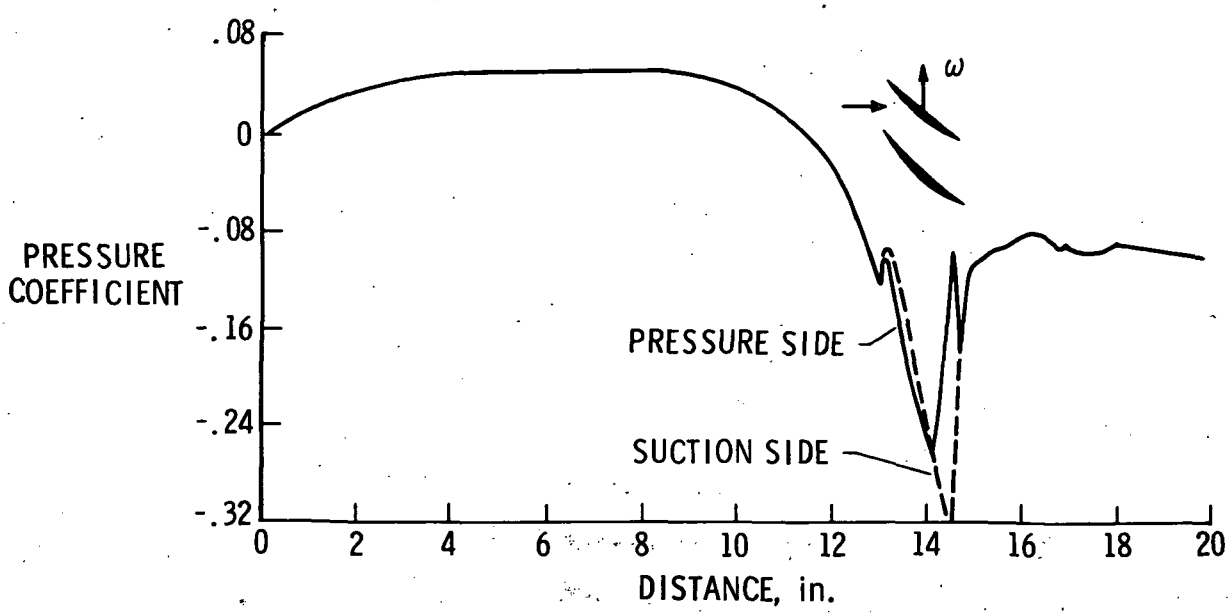

Figure 13.- Pressure coefficient through passage and over blades at tip.
(1 in. = 2.54 cm.)

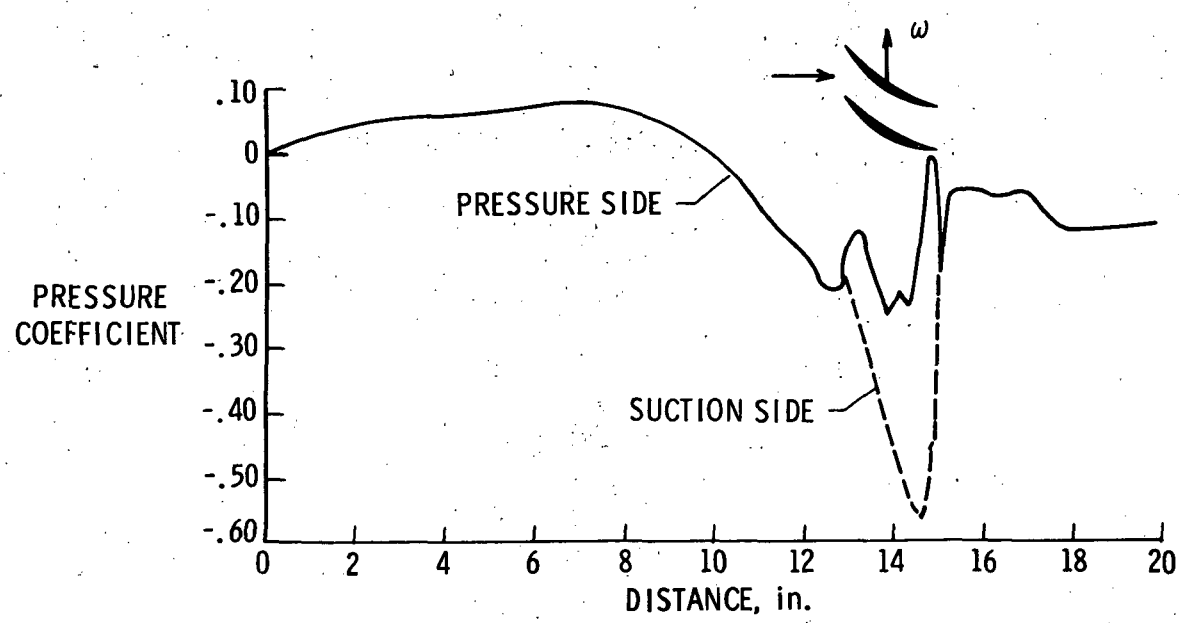

Figure 14.- Pressure coefficient through passage and over blades at hub.
(1 in. = 2.54 cm.)

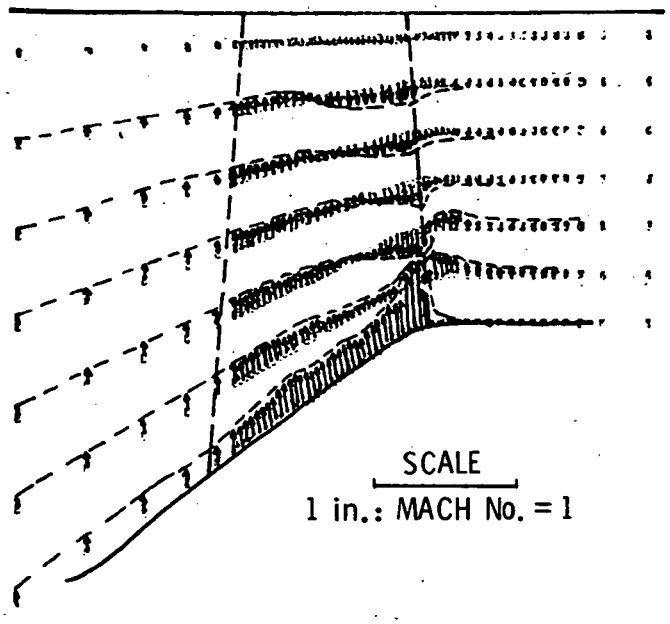

Figure 15.- Crossflow velocity u_r distributions.

Page Intentionally Left Blank

TIME-DEPENDENT TRANSONIC FLOW SOLUTIONS FOR AXIAL TURBOMACHINERY

By John Erdos, Edgar Alzner, Paul Kalben,
Advanced Technology Laboratories, Inc.

William McNally,
NASA Lewis Research Center

and Simon Slutsky
Polytechnic Institute of New York

SUMMARY

Three-dimensional unsteady transonic flow through an axial turbomachine stage is described in terms of a pair of two-dimensional formulations pertaining to orthogonal surfaces, namely, a blade-to-blade surface and a hub-to-casing surface. The resulting systems of nonlinear, inviscid, compressible equations of motion are solved by an explicit finite-difference technique. Separate computer programs have been constructed for each formulation. The blade-to-blade program includes the periodic interaction between rotor and stator blade rows. Treatment of the boundary conditions and of the blade slipstream motion by a characteristic type procedure is discussed in detail. Harmonic analysis of the acoustic far field produced by the blade row interaction, including an arbitrary initial transient, is outlined in an appendix. Results from the blade-to-blade program are compared with experimental measurements of the rotating pressure field at the tip of a high-speed fan. The hub-to-casing program determines circumferentially averaged flow properties on a meridional plane. Blade row interactions are neglected in this formulation, but the force distributions over the entire blade surface for both the rotor and stator are obtained. Results from the hub-to-casing program are compared with a relaxation method solution for a subsonic rotor. Results are also presented for a quiet fan stage designed by the National Aeronautics and Space Administration, which includes transonic flow in both the rotor and stator and a normal shock in the stator.

INTRODUCTION

Flow through a high-speed fan or compressor is highly three-dimensional and can include complex shock wave systems. In addition, flow through a complete stage consisting of a rotor and stator or a fan preceded by inlet guide vanes is unsteady even in the rotating frame of reference. Effects of viscosity and turbulence are known to be signifi-

cant; in fact, the turbulent wakes may be the predominant source of aerodynamic interaction between the rotating and stationary blade rows and responsible for the associated noise. Vortex filaments are known to stream from the rotor tips and undoubtedly interact with the wall boundary layer. Sufficiently far downstream, turbulence generated by the first blade row may encompass the entire flow. Calculation of transonic flow field solutions in high-speed turbomachinery stages is clearly one of the most formidable challenges to present-day capabilities in computational aerodynamics.

A traditional approach to solution of this complex problem has been taken. Description of the inviscid flow field is addressed first, boundary layer and turbulence effects being superimposed as small perturbations. The basic system of equations which is solved numerically consists of the complete nonlinear equations of motion for an inviscid compressible gas:

$$\frac{\partial \rho}{\partial t} + \nabla \cdot \rho V = 0 \tag{1}$$

$$\frac{DV}{Dt} = -\frac{1}{\rho} \nabla p \tag{2}$$

$$\frac{De}{Dt} + p \frac{D}{Dt}\left(\rho^{-1}\right) = 0 \tag{3}$$

where

$$p = \rho R T \tag{4}$$

$$e = \frac{p}{(\gamma - 1)\rho} \tag{5}$$

$$\frac{D}{Dt} = \frac{\partial}{\partial t} + V \cdot \nabla \tag{6}$$

and

e	internal energy
p	pressure
R	gas constant
T	temperature
t	time
V	velocity vector

ρ density

The only essential simplifications introduced pertain to reduction of the spatial dimensions of the problem from 3 to 2. Solution of the full three-dimensional problem is reduced to a pair of two-dimensional solutions on orthogonal surfaces. A separate program tailored to the particular aspects of each formulation has been developed. Both computer programs which will be discussed herein are intended for analysis of a complete stage, that is, rotor and stator, although an isolated blade row can also be treated.

A harmonic type analysis of the acoustic far field due to blade row interactions has also been developed. This analysis provides a direct coupling between the numerical near-field solution and the acoustic far field, with a particular view toward characterizing the acoustic far field. This aspect of the flow model will be only briefly outlined herein, but a complete description is given in reference 1. The boundary-layer and wake representations utilize standard integral methods and it is assumed that the boundary layer and wake are quasi-steady. The reader is again referred to reference 1 for a complete description.

SYMBOLS

A_n, B_n, C_n, . . . Fourier coefficients

a speed of sound

b stream sheet thickness or blade thickness

$\mathfrak{c}$ centerline

c chord

E total internal energy

e internal energy

H total enthalpy

h enthalpy

M Mach number

m	meridional distance along a blade-to-blade stream surface
N_i	number of blades in ith row
n	blade-to-blade distance
P,Q,R	boundary conditions at interface of numerical near-field and acoustic far-field solutions
p	pressure
R	gas constant
r	radial distance from axis of rotation
S	entropy
s	distance along the stream path
T	temperature
t	time
U	a reference velocity
u	meridional component of velocity
$\bar{u}$	velocity component parallel to slipstream or blade surface
V	velocity vector
v	circumferential component of velocity
$\bar{v}$	velocity component normal to slipstream or blade surface
v_r	radial component of velocity; also circumferential velocity component in rotating coordinate system
v_z	axial velocity component

v_θ	circumferential velocity component
x	meridional distance along a blade-to-blade stream surface
$\bar{x}$	distance along slipstream or blade surface
y	circumferential distance
$\bar{y}$	distance normal to slipstream or blade surface
z	axial coordinate
α_n, β_n	acoustic propagation coefficient
γ	ratio of specific heats
θ	circumferential angle
θ_1, θ_2	blade surface coordinates
ρ	density
ϕ	angle between slipstream or blade surface and meridional plane
ψ	ratio of mass flow to total mass flow
Ω	angular speed of rotor
ω	vorticity; also frequency

Subscripts:

o	initial or reference condition
*	reference condition
∞	free stream

A circumflex (^) over a symbol denotes an average value. A bar over a symbol denotes vector quantities except in appendix where it denotes time to frequency transform.

BLADE-TO-BLADE ANALYSIS

In the blade-to-blade formulation the previously stated equations of motion are expressed in a curvilinear coordinate system alined on an axisymmetric stream surface as shown in figure 1. This stream surface is considered to have small but finite thickness $b(z)$ and variable mean radius from the axis of rotation $r(z)$. The velocity component normal to the stream surface is neglected; as a result, a two-dimensional approximation to the flow field is produced. (See refs. 2 and 3.) When the m,θ coordinates are transformed to a rotating system by

$$x = m \tag{7}$$

$$y = r(\theta - \Omega t) \qquad (x = \text{Constant}) \tag{8}$$

and the circumferential velocity component is transformed by

$$v_r = v - \Omega r \tag{9}$$

then the following system of governing equations result:

$$\frac{\partial \rho}{\partial t} + \frac{\partial}{\partial x}(\rho u) + \frac{\partial}{\partial y}(\rho v_r) = -\frac{\rho u}{rb}\frac{drb}{dx} \tag{10}$$

$$\frac{\partial \rho u}{\partial t} + \frac{\partial}{\partial x}\left(\rho u^2 + p\right) + \frac{\partial}{\partial y}(\rho u v_r) = -\frac{\rho u^2}{rb}\frac{drb}{dx} \tag{11}$$

$$\frac{\partial \rho v_r}{\partial t} + \frac{\partial}{\partial x}(\rho u v_r) + \frac{\partial}{\partial y}\left(\rho v_r^2 + p\right) = -\frac{\rho u v_r}{rb}\frac{drb}{dx} - \rho u \Omega \frac{dr}{dx} \tag{12}$$

$$\frac{\partial \rho E_r}{\partial t} + \frac{\partial}{\partial x}\left(\rho u H_r\right) + \frac{\partial}{\partial y}\left(\rho v_r H_r\right) = -\frac{\rho u H_r}{rb}\frac{drb}{dx} - \rho u \Omega \frac{dr}{dx}(\Omega r + v_r) \tag{13}$$

where the relative total energy and total enthalpy are defined by

$$H_r = H - \Omega r v \tag{14}$$

$$E_r = H_r - \frac{p}{\rho} \tag{15}$$

The terms on the right-hand side of the equations result from the variations in cross-sectional area and radius of the stream surface, which are intended to account for the effects of variations in hub and casing radii. The terms on the left-hand side of the equations correspond to the familiar set of two-dimensional unsteady equations of motion

of an inviscid compressible gas. Note that the relative total enthalpy is not the same as the total enthalpy defined on the basis of velocity components in the rotating frame. Numerical solution of this system of equations at interior grid points is accomplished by the MacCormack algorithm (ref. 4). Systematic rotation of the order in which the noncentered differences are evaluated is employed to minimize any bias in the solution due to the alternating directions of the noncentered differences. No artificial damping or stabilization is used.

As shown in figure 1, the computational domain is divided into a maximum of seven segments, not all of which need be included in every case. The grid network extends axially from an inlet station to a discharge station and circumferentially across one blade-to-blade passage. The inlet station is located either 1 axial chord length upstream of the first blade row, in which case domain 1 is deleted, or an arbitrary distance upstream exceeding 1 chord length. Placement of the discharge station can be selected in the same manner as that employed for the inlet station. Domains 2 to 6 are each linearly mapped into a unit square which is spanned by a rectangular grid network. In domains 1 and 7 a linear stretching of the axial coordinate is used to map these domains into unit squares. The axial grid spacing in domains 1, 4, and 7 is determined by the locations of the axial boundaries of these domains. The lateral boundaries of domains 1 and 2 lie on extensions of the mean camber line. The lateral boundaries of domains 3 and 5 lie on the blade surfaces. The instantaneous locations of the blade slipstreams form the boundaries of domains 4, 6, and 7. Domains 1 to 4 are attached to the first blade row and domains 5 to 7 are attached to the second blade row either of which may be selected as the rotating row. It is assumed that the number of blades in the second row equals or exceeds the number in the first row.

It is emphasized that a periodic solution due to the aerodynamic interaction of the rotating and stationary blades is anticipated. The formulation is thus a numerical counterpart of the problem for which Kemp and Sears (ref. 5) obtained an analytic solution pertaining to thin, slightly cambered blades of low solidity in an incompressible flow. Linearized solutions have more recently been obtained for compressible flows, but the authors are not aware of any other attempt to develop nonlinear solutions for the periodic blade-row interaction problem at transonic or supersonic conditions.

In connection with the periodicity of the subject problem, two main points of departure from other numerical solutions for transonic airfoils or cascades should be recognized. First, the slipstreams are moving surfaces of discontinuity across which jumps in tangential component velocity and in total pressure can occur. Only static pressure and the component of velocity normal to the surface must be continuous. It should be noted that the jumps in tangential velocity across the slipstreams are related to the unsteady variations in lift of the blades and therefore cannot be obtained from the conservation form of the equations of motion through a limiting process as in the case of

shock waves. Treatment of the slipstreams as surfaces of discontinuity in the present model is therefore warranted for two reasons: It allows attainment of an accurate periodic solution without requiring a very large grid point density to approximate the slipstream discontinuities, and tracking of the slipstreams is necessary to determine the trajectories of the viscous wakes which diffuse outward from the inviscid slipstreams. The second point is that in the case of an unequal number of blades in the two rows, the angular period of the circumferential variations in the flow field is not the width of a blade-to-blade passage but it is the circumference divided by the difference between the number of blades in the rotor and stator. Furthermore, the flow pattern rotates with an angular velocity which, in general, is a multiple of the wheel speed. Numerical representation of this periodicity condition pertaining to the lateral boundary points of the grid network, as well as to those points along the interface between domains 4 and 5, is accomplished by a cyclic procedure which is discussed later.

BOUNDARY CONDITIONS

The calculation of boundary points and indeed the exposition of proper boundary conditions is facilitated by recasting the equations in the form of characteristic compatibility relations pertaining to a quasi one-dimensional unsteady wave system (as suggested by Moretti and Abbett (ref. 6) and Serra (ref. 7)). Although actual numerical implementation of the characteristic formulation is far more complex than the finite-difference procedure used in the interior points and can possess certain drawbacks, such as inconsistency with the interior point solution, it is nevertheless adopted here for the particular advantages it offers with respect to the slipstream, inlet, and discharge point calculations.

Consider first the inlet station sketched in figure 2. As is well known, the momentum and energy equations can be rewritten in the form:

$$\frac{DS}{Dt} = 0 \quad \text{or} \quad S = \text{Constant} \quad \text{on} \quad \frac{\Delta x}{u} = \frac{\Delta y}{v_r} = \Delta t \tag{16}$$

$$\frac{D(\omega/\rho)}{Dt} = 0 \quad \text{or} \quad \frac{\omega}{\rho} = \text{Constant} \quad \text{on} \quad \frac{\Delta x}{u} = \frac{\Delta y}{v_r} = \Delta t \tag{17}$$

By assuming that no flow reversal occurs at the inlet station, the values of the entropy and ratio of vorticity to density at the inlet station are, therefore, solely properties of the incoming flow and may be specified a priori; both the entropy and vorticity of the incoming flow are assumed to be zero. Three options have been considered with regard to physical interpretation of the inlet boundary conditions. First, if the inlet station represents an open end of a finite length duct, the static pressure can be specified as

$$p = p_{-\infty} \tag{18a}$$

Second, if it is an arbitrary station in a duct of infinite length, the Riemann invariant on the downstream traveling wave can be specified as

$$\frac{2a}{\gamma - 1} + u = \frac{2a_{-\infty}}{\gamma - 1} + u_{\infty} \tag{18b}$$

Use of this relationship implies that the outward traveling waves are one-dimensional (i.e., either planes or helices). As a third option the numerical solution can be matched to the acoustic far-field analysis at the inlet station, in which case all acoustic modes are properly accounted for. This procedure is outlined in an appendix. In any of these cases the solution of the inlet boundary points is completed by first using a compatibility relation on the upstream running wave which originates within the computational domain at point C in figure 2; that is,

$$\frac{a}{\gamma}\Delta \log p - \Delta u = \left[(v_r - v_o)\left(\frac{\partial u}{\partial y} - \frac{a}{\gamma}\frac{\partial \log p}{\partial y}\right) - a\frac{\partial v_r}{\partial y} - ua\frac{d \log rb}{dx}\right]\Delta t$$

$$\left(\text{on } \frac{\Delta x}{\Delta t} = u - a \text{ and } \frac{\Delta y}{\Delta t} = v_o\right) \tag{19}$$

and second by solving the following angular momentum equation, which only involves spatial derivatives of the dependent variables in the circumferential direction, by the MacCormack finite-difference algorithm:

$$\frac{\partial v_r}{\partial t} = -\left(u\frac{\partial u}{\partial y} + v_r\frac{\partial v_r}{\partial y} + \frac{1}{\rho}\frac{\partial p}{\partial y} + u\Omega\frac{dr}{dx}\right) \tag{20}$$

This characteristic compatibility relation may be interpreted as pertaining to the projection of the true characteristic conoid on a reference plane which is alined normal to the inlet station and translates in the circumferential direction with an arbitrary velocity v_o, for example, v_r from the previous time step. The acoustic far-field analysis can be used to replace equation (18a) or (18b).

A similar procedure is employed at the discharge boundary points but here the entropy and vorticity are determined by tracing a particle path from within the computational domain (point B in fig. 2) to the boundary point. The system of equations pertaining to a discharge boundary point are stated below for the case of either a finite length duct or an infinite duct

$$p = p_{\infty} \tag{21a}$$

$$\frac{2a}{\gamma - 1} - u = \frac{2a_{\infty}}{\gamma - 1} - u_{\infty} \tag{21b}$$

Use of the acoustic model would replace equation (21a) or (21b)

$$\left.\begin{aligned} S &= S_* \\ \frac{\omega}{\rho} &= \frac{\omega_*}{\rho_*} \end{aligned}\right\} \qquad \left(\text{on } \frac{\Delta x}{u} = \frac{\Delta y}{v} = \Delta t\right) \tag{22}$$

$$\frac{a}{\gamma}\Delta \log p + \Delta u = \left[-(v_r - v_o)\left(\frac{\partial u}{\partial y} + \frac{a}{\gamma}\frac{\partial \log p}{\partial y}\right) - a\frac{\partial v_r}{\partial y} - ua\frac{d \log rb}{dx}\right]\Delta t$$

$$\left(\text{on } \frac{\Delta x}{\Delta t} = u + a \text{ and } \frac{\Delta y}{\Delta t} = v_o\right) \tag{23}$$

$$\frac{\partial v}{\partial t} = -\left(u\frac{\partial u}{\partial y} + v_r\frac{\partial v_r}{\partial y} + \frac{1}{\rho}\frac{\partial p}{\partial y} + 2\rho u\frac{\omega_*}{\rho_*} + u\Omega\frac{dr}{dx}\right) \tag{24}$$

The boundary condition at the blade surface points is simply vanishing of the component of velocity normal to the surface. At the trailing edge the Kutta condition is satisfied by requiring the pressure to be continuous and the velocity component normal to the mean of the camber line and slipstream to be zero. On the slipstream the pressure and normal component of the velocity must be continuous. Implementation of these conditions is facilitated by recasting the equations into a characteristic form similar to that described; however, in this case the reference planes are normal to the surface and translate in the streamwise direction, as shown in figure 3. Combination of the continuity equation and normal momentum equation results in the following pair of compatibility relations:

$$a\Delta \log p \pm \gamma \Delta \bar{v}_r = (aQ_1 \pm \gamma Q_2)\Delta t \qquad \left(\text{on } \frac{\Delta \bar{y}}{\Delta t} = \bar{v}_r \pm a \text{ and } \frac{\Delta \bar{x}}{\Delta t} = \bar{u}_o\right) \tag{25}$$

where

$$Q_1 = -\left[(\bar{u} - \bar{u}_o)\frac{\partial \log p}{\partial \bar{x}} + \frac{\partial \bar{u}}{\partial \bar{x}} + \gamma u\frac{d \log rb}{dx}\right] \tag{26}$$

$$Q_2 = -\left[(\bar{u} - \bar{u}_o)\frac{\partial \bar{v}_r}{\partial \bar{x}} - u\Omega \cos\phi\frac{dr}{dx}\right] \tag{27}$$

The energy equation is stated as

$$\left.\begin{aligned} \frac{DS}{Dt} &= 0 \\ S &= \text{Constant} \end{aligned}\right\} \qquad (\text{on } \Delta\bar{x} = \bar{u}\,\Delta t \text{ and } \Delta\bar{y} = \bar{v}\,\Delta t) \tag{28}$$

and the streamwise momentum equation is solved in the LaGrangian form

$$-\frac{D\bar{q}}{Dt} = -\frac{a^2}{\gamma}\frac{\partial \log p}{\partial s} - \frac{uv_r}{q}\Omega\frac{dr}{dx} \tag{29}$$

where $\bar{q}^2 = \bar{u}^2 + \bar{v}^2$ and $ds/\bar{q} = d\bar{x}/\bar{u} = d\bar{y}/\bar{v} = dt$.

It is pointed out that the form of the compatibility relations given by equation (25) provides an algebraic solution for the quantities which are continuous across the blade slipstream, namely, the pressure and normal velocity. Thus, the boundary conditions on the blade slipstream can be satisfied without iteration, other than that necessary to locate the characteristic geometrically (points A and D in fig. 3) by successive approximations, of which two are usually sufficient. However, at the trailing edge an iteration is required to determine the slipstream angle which satisfies the Kutta condition.

The overall scheme for imposing the boundary conditions along the blade surface and slipstream points is shown schematically in figure 4. The time axis projects vertically out of the page in this figure. The dashed lines represent the intersections of the translating reference planes with the axisymmetric stream surface and the intersections of the particle paths with the stream surface during a time step Δt.

PERIODICITY CONDITION

Illustration of the nature of the cyclic procedure devised to enforce the periodicity of the solution can best be accomplished with respect to the following simplified configuration. Consider first a stage having three rotor blades and three stator blades. This configuration is shown in figure 5 in both axial and cascade projections. At time t_o all rotor and stator blades are alined, whereas at time $t_o + \Delta t$ the rotor has moved through a fraction of a revolution, and none of the blades are now alined. It is clear in this case that the geometric conditions which determine the flow through the stage are identical in each blade-to-blade passage at any time.[1] In this case the solution along an exterior grid row δ can be equated to that along the interior grid line β and similarly that along exterior line α can be equated to that along interior line γ at any instant. Consider now the case with three blades in the stator and four blades in the rotor as shown in figure 6. At time t_o rotor blade 2 is alined with stator blade b, whereas at time $t_o + \Delta t$ rotor blade 3 is alined with blade c. In this case the geometric conditions pertaining to the passage between blades a and b are obviously different from those for the passage between blades b and c at any time. However, it may be noted that those pertaining to passage bc at $t_o + \Delta t$ are precisely the same as those which pertain to passage ab

[1]It is assumed, of course, that the boundary conditions imposed at the inlet and discharge stations are spatially uniform so that the blade geometry provides the only scale for circumferential variations.

at the previous time t_o. Therefore, the flow conditions along exterior grid line δ at time $t_o + \Delta t$ can be equated to those along interior grid line β at the earlier time t_o. However, in this case those along exterior grid line α at time $t_o + \Delta t$ cannot be equated to those occurring in passage ab at time t_o, but must be equated to those occurring along line γ at an earlier time. Thus a phase shift is introduced in application of the lateral boundary conditions. The necessary boundary information is acquired during the passage of time, and therefore the desired periodicity is attained asymptotically in time.

NUMERICAL EXAMPLE: BLADE-TO-BLADE PROGRAM

Results from the blade-to-blade program have been compared with data for a high-speed (1500-fps) fan tip section for which experimental data are reported in reference 8. The casing wall was instrumented with an array of fast response pressure gages, from which a contour plot of the rotating pressure field around the tip section was reconstructed. This fan was preceded by a set of guide vanes and followed by a row of stators. However, the unsteady interaction was neglected in this case and only the rotor was considered. The grid network was very coarse and consisted of 9 grid rows in the circumferential direction and 11 in the axial direction in each of 3 domains, that is, a total of 297 grid points.

The experimental pressure contour plot is reproduced on the left-hand side of figure 7. The data indicate the presence of an oblique shock off the leading edge of the upper blade which reflects off the lower blade and reimpinges on the upper blade near the trailing edge. A lambda (λ) type shock is apparently formed on the aft portion of the upper blade because of the boundary-layer separation. The isobars constructed from the numerical solutions are shown on the right-hand side of this figure. The numerical results exhibit qualitatively similar behavior, although boundary-layer effects have not been included and the grid is admittedly very coarse. Although a qualitative correlation is apparent with respect to the main features of the flow field, a quantitative comparison is somewhat difficult. Therefore, the experimental isobars have been used to construct pressure distributions along the suction and compression surfaces of the blade and along a mid-channel line. The accuracy of the data obtained in this manner may be somewhat suspect, but the agreement between the data and the numerical solution shown in figure 8 is considered to be very encouraging.

Numerical solutions for interacting blade rows have thus far been limited to idealized test case configurations for which no comparisons with other solutions or experimental data are available. However, results for the full stage consisting of fan and stator tip sections from reference 8 are included in reference 1.

HUB-TO-CASING ANALYSIS

Attention is now shifted to the second program, which considers a hub-to-casing stream surface. The coordinate system and grid network is illustrated in figure 9. The finite-difference grid lies on a meridional plane extending from hub to casing and from an inlet station to a discharge station. Circumferential variations are removed in this case by integration of the governing equations with respect to θ from one blade to the next and defining average properties over this angular interval. The angular velocity component and angular momentum equation are retained because of the presence of a pressure force exerted by the blades. The effects of blockage of the flow area due to the blade thickness and boundary-layer displacement thickness are included. Multiple blade rows can be considered but the effects of periodic interactions between the blade rows are necessarily neglected because of integration of the equations with respect to the angular variable.

In this analysis the basic system of equations given by equations (1) to (6) are stated in cylindrical coordinates, multiplied by $d\theta$ and integrated from $\theta_1(r,z)$ to $\theta_2(r,z)$, which are the surface coordinates of two adjacent blades, as indicated in figure 9. Outside a blade row, the integration interval is taken as $2\pi/N_i$. The blade-to-blade passage width is defined by

$$n = \begin{cases} N_i \int_{\theta_1}^{\theta_2} r \, d\theta & \text{(Within a blade row)} \\ 2\pi r & \text{(Outside a blade row)} \end{cases} \tag{30}$$

Circumferentially averaged values of the dependent variables are defined by

$$\hat{\rho} = n^{-1} N_i \int_{\theta_1}^{\theta_2} \rho r \, d\theta \tag{31}$$

$$\hat{\rho}\hat{v}_z = n^{-1} N_i \int_{\theta_1}^{\theta_2} \rho r v_z \, d\theta \tag{32}$$

It is assumed that the blades are thin and sharp and hence the local blade surface angles can be replaced by the mean camber line angles:

$$\frac{\partial \theta_1}{\partial z} \approx \frac{\partial \theta_2}{\partial z} = \left.\frac{\partial \theta}{\partial z}\right|_{\text{Camber line}} \tag{33}$$

$$\frac{\partial\theta_1}{\partial r} \approx \frac{\partial\theta_2}{\partial r} = \left.\frac{\partial\theta}{\partial r}\right|_{\text{Camber line}} \tag{34}$$

Furthermore, differences between root-mean-square (rms) values and mean squared values are neglected:

$$\left|\hat{v}_z^2 - \hat{v}_z^2\right| \ll a^2 \tag{35}$$

$$\left|\hat{v}_r\hat{v}_z - \hat{v}_r\hat{v}_z\right| \ll a^2 \tag{36}$$

The following system of equations is thereby obtained[2]:

$$\frac{\partial(\rho n)}{\partial t} + \frac{\partial}{\partial z}(\rho n v_z) + \frac{\partial}{\partial r}(\rho n v_r) = 0 \tag{37}$$

$$\frac{\partial}{\partial t}(\rho n v_z) + \frac{\partial}{\partial z}\left(\rho n v_z^2\right) + \frac{\partial}{\partial r}(\rho n v_r) = -n\frac{\partial p}{\partial z} + \Delta p\left(r\frac{\partial\theta}{\partial z}\right) \tag{38}$$

$$\frac{\partial}{\partial t}(\rho n v_r) + \frac{\partial}{\partial z}(\rho n v_r v_z) + \frac{\partial}{\partial r}\left(\rho n v_r^2\right) = -n\frac{\partial p}{\partial r} + \frac{\rho n v_\theta^2}{r} + \Delta p\left(r\frac{\partial\theta}{\partial r}\right) \tag{39}$$

$$\frac{\partial}{\partial t}(\rho n r v_\theta) + \frac{\partial}{\partial z}(\rho n r v_\theta v_z) + \frac{\partial}{\partial r}(\rho n r v_\theta v_r) = -r\,\Delta p \tag{40}$$

$$\frac{\partial}{\partial t}(\rho n E) + \frac{\partial}{\partial z}(\rho u v_z H) + \frac{\partial}{\partial r}(\rho u v_r H) = -r\Omega\,\Delta p \tag{41}$$

where

$$\Delta p(r,z) = p(r,z,\theta_2) - p(r,z,\theta_1) \tag{42}$$

Thus the variable n represents the circumferential distance around the annulus, reduced by the cumulative blockage due to all blades, at fixed r and z. The term Δp represents the cumulative pressure differential across the blades, that is, the pressure differential across each blade times the number of blades. The terms involving Δp in the momentum equations represent the three components of the pressure force exerted by the blades. The term on the right-hand side of the energy equation is the work performed by the rotating blade row.

---

[2]The superscript notation to denote average quantities is dropped in the following discussion.

Within a blade row the velocity vector is assumed to remain tangent to the mean camber surface at all times:

$$v_\theta = \Omega r + v_z\left(r\,\frac{\partial\theta}{\partial z}\right) + v_r\left(r\,\frac{\partial\theta}{\partial r}\right) \tag{43}$$

The tangency condition is used within the blade rows to determine the angular velocity component, and the blade pressure differential Δp is obtained from the angular momentum equation. Outside the blade rows $\Delta p = 0$ and the angular momentum equation is used to determine the angular component of velocity.

Representation of the inlet and discharge boundary conditions and numerical solution of these boundary points follows the general approach described in connection with the blade-to-blade program. However, since a steady, rather than periodic, solution is sought in this case, somewhat less care need be taken in modeling a physically correct boundary condition. In particular, the "infinite duct" condition discussed previously has been replaced in this case by prescription of the total pressure at the inlet station. Similarly, prescription of the components vorticity of the incoming flow can be replaced by direct statement of the flow angles or of the radial and circumferential velocity components. At the discharge boundary the static pressure is specified. Solution at the boundary points along the hub and casing surfaces is accomplished by restating equations (37) to (41) in a body-oriented coordinate system similar to that used to derive equations (25) to (29). In this case, the boundary condition $\bar{v} = 0$ replaces the normal momentum equation. The same finite-difference procedure as used at the interior points is used to accomplish the solution of the remaining members of the system of equations. Noncentered differences are used for the derivatives normal to the walls, which only involve gradients of the normal velocity component. The accuracy of this procedure has been found to compare very well with that of the interior point solution, with considerable less complexity than the characteristic procedure used in the blade-to-blade program.

NUMERICAL EXAMPLES: HUB-TO-CASING PROGRAM

The present hub-to-casing program is analogous in many respects to the relaxation method program developed by Katsanis and McNally at NASA Lewis Research Center. Their program MERIDL (ref. 9) solves the stream function equation on a meridional plane through a blade row for steady subsonic conditions by use of a finite-difference method. The comparison between the present program and their program has been carried out for a case in which their solution should be very accurate. The rotor configuration selected corresponds to the test case used by Katsanis and McNally in reference 9.

The relative swirl angle is shown in figure 10. This angle is defined as that between the velocity vector and the projection of the velocity vector on a meridional plane, measured in a rotating frame of reference. The three curves pertain to the hub surface,

the tip or casing surface, and a mid-channel surface. Within the blade row the relative swirl angle along the hub and casing is completely determined by geometric constraints. However, everywhere else it is obtained from the solution for the three velocity components. The agreement between the two programs is considered to be quite satisfactory.

The magnitude of the velocity vector in the rotating frame is shown in figure 11. The mid-channel values were deleted from this figure for clarity. The only significant difference between the two solutions occurs near the leading edge. Both programs allow grid columns to cross the leading and trailing edges in an arbitrary fashion. However, Katsanis and McNally's program accounts for the effects of bluntness of the leading edge in some detail whereas the present program assumes that these edges are sharp.

Next, a transonic fan stage designed by NASA Lewis Research Center for the Quiet Fan Program has been considered. Designated the QF-1 stage it combines an 1100-fps tip speed rotor with a stator having highly "leaned" blades (up to 45° at the tip). A range of stator positions relative to the rotor location are possible with this stage; position VI was selected in this case. The rotor and stator are relatively close in this position, less than 1 chord length apart.

The pressure distributions along the hub and casing surface are shown in figure 12, and the absolute Mach numbers are displayed in figure 13. The supersonic region which develops in the stator along the hub, due to the combination of the hub curvature and blade thickness, is terminated by a normal shock. This shock is spread over about 4 or 5 grid points, or about 25 percent to 30 percent of the 16 grid points which cover the stator axially in this case. Only 10 grid points cover the rotor tip section; consequently, a shock in the rotor would be difficult to detect with the present grid point density. A rapid compression is evident on the aft portion of the rotor tip section, which corresponds to a reduction in relative Mach numbers from 1.12 near the leading edge to 0.64 at the trailing edge. Therefore, the rotor-tip compression substantially exceeds the normal-shock compression by itself.

COMPUTER EXECUTION TIME AND STORAGE REQUIREMENTS

The blade-to-blade program will fit in small-core memory of a CDC 7600 computer, that is, about 160K octal words, with a maximum of 1000 grid points (not including the exterior points required for the boundary point calculations), exclusive of the storage required for the periodic boundary data needed for unequal numbers of blades. In its present form, disk storage is used for the periodic boundary data, although use of the large-core memory would undoubtedly be more efficient. The blade-to-blade program requires approximately 2×10^{-4} second per grid point per time step for execution on a

CDC 7600 computer by using the FTN (opt = 2) compiler to generate the binary code. The results presented in figures 7 and 8 required less than 1 minute of execution time.

The hub-to-casing program also fits in small-core memory with a maximum of 1600 grid points. It requires approximately 4×10^{-4} second per grid point per time step for execution. The additional time relative to the blade-to-blade program is believed to be associated with calculation of the blade pressure differential Δp, solution of an additional momentum equation, and continuous reevaluation of the maximum permissible time step. (A variable time step is not allowed in the blade-to-blade program because of the procedure for storing and retrieving boundary data.) The subsonic rotor case discussed in connection with figures 10 and 11 required less than 1 minute of execution time with a 27 by 17 grid network. The transonic stage results shown in figures 12 and 13 required approximately 7 minutes of execution time.

CONCLUDING REMARKS

A blade-to-blade formulation and a hub-to-casing formulation have been developed for analysis of transonic unsteady flow through an axial turbomachine stage and implemented in two computer programs. Both employed an explicit finite-difference technique for solution at the interior grid points, and a characteristic type procedure at the inlet and discharge boundaries. The blade-to-blade program can treat periodic interactions between rotating and stationary blade rows, and particular attention has been given to correct representation of the blade slipstreams and their motion due to unsteady blade loading. A comparison with experimental measurements of the rotating pressure field of a high-speed fan tip section is considered to be very encouraging. The computer execution time for this case was very modest, less than 1 minute on a CDC 7600, and use of a higher grid point density to improve the numerical accuracy is therefore practical.

The hub-to-casing program compares favorably with a relaxation time solution for a flow condition when the latter should be very accurate. Results have also been obtained for a quiet fan stage which includes transonic flow in both the rotor and stator and a normal shock in the stator. The program resolves the shock reasonably well, although a higher grid point density would probably be beneficial in this case.

These programs offer a substantial improvement in the predictive capabilities available to aerodynamicists involved in design and evaluation of high-speed turbomachinery stages. However, it is clear that a complete description of the three-dimensional, unsteady, turbulent flow prevailing in such stages will require continued development of the computational models.

APPENDIX

ACOUSTIC FAR-FIELD ANALYSIS

Under the conditions typically prevalent in highly loaded transonic fan or compressor stages, the linearized, small-perturbation approximations to the equations of motion cannot be expected to be descriptive of the flow in the vicinity of the blades. Thus, recourse is made to the numerical solution of the complete nonlinear system of equations as discussed in connection with the blade-to-blade program. However, sufficiently far from the blade rows, the amplitude of the flow disturbances will decay to acoustic levels and the linearized, small-perturbation approximations will be descriptive of the far field. Therefore, an intermediate region in which both analyses are valid should exist at some distance from the blades. The inlet and discharge stations of the blade-to-blade computational domain can serve as the interfaces between the near-field (numerical) and far-field (acoustic) analyses. The present far-field analysis is formulated with respect to an infinite duct model, namely, outgoing waves should propagate without reflection. It differs, however, from conventional inlet duct analyses in that the signal may begin with an arbitrary transient, associated with the deviation of the assumed initial data in the near field from the periodic solution which is sought as the asymptotic limit in time. Therefore, the acoustic analysis must recognize that a transient signal will occur during startup and that a simple harmonic time dependence, which is the usual basis of inlet duct acoustics, cannot be assumed. The analysis should allow the transient to radiate outward without reflection, and should be capable of identifying the attainment of a periodic solution by the growth of discrete harmonic components in the solution.

The inlet and discharge stations indicated in figure 1 as the axial boundaries of domains 1 and 7 (or possibly of domains 2 and 6 if 1 and 7 are deleted) form the axial boundaries of the acoustic far field. However, the lateral boundary should extend over that fraction of the circumference which corresponds to the fundamental period of the stage configuration (that is, an integer number of blade-to-blade passages). This will require storage and retrieval of numerical data along this interface in the same manner as is performed along the interface between domains 4 and 5 of the near field.

As discussed in connection with the characteristic procedure used at the inlet and discharge boundaries, the compatibility relation on the outward running waves (eqs. (19) and (23)) provide a connection between the combination of pressure and axial velocity on the boundary points at time $t + \Delta t$ and the known interior point solution at time t. This information provides the mechanism for matching the acoustic far-field solution with the numerical near-field solution on a point-by-point, step-by-step basis. Since the blades are capable of producing a vorticity field which will convect downstream, additional information is necessary to define the downstream far field. (Recall that the inlet flow is

assumed to be irrotational.) If the standard small-disturbance approximations are employed, the numerical data to be provided at the inlet consist of

$$P(y,t) = \frac{p - p_{-\infty}}{\rho_{-\infty} a_{-\infty}} - (u - u_{-\infty}) \tag{A1}$$

and at the discharge station

$$Q(y,t) = \frac{p - p_{\infty}}{\rho_{\infty} a_{\infty}} + (u - u_{\infty}) \tag{A2}$$

$$R(y,t) = v \tag{A3}$$

where the subscripts denote the reference states at $x \to \pm\infty$, which are not necessarily the same. Equations (A1), (A2), and (A3) form, in effect, the boundary conditions for the far-field analysis, from which the instantaneous values of the pressure perturbation and velocity perturbation at the inlet and discharge stations are obtained.

With these preliminaries in hand, attention is now focused on the acoustic far-field analysis. In the following discussion the subscript $(\,)_0$ will be used to denote the reference conditions for either boundary, that is, $x \to \pm\infty$, and all variables without subscript will refer to perturbations with respect to the reference state, namely, $p = p - p_0$ and $u = u - u_0$.

Since the present effort is addressed toward a cascade formulation, the governing equations are written in a two-dimensional Cartesian coordinate system. It is noted that the two-dimensional problem could be described by a solution of the wave equation alone, were it not for the fact that the time dependent force distribution on the blades is capable of producing a convected vorticity field (as well as a corresponding entropy field, which, however, is not relevant to the present problem). It will be seen that the convected vorticity field (characterized by a solenoidal velocity component) does not contribute to the acoustic pressure field by itself, as distinguished from the irrotational component of the velocity field which is directly coupled with the acoustic pressure. Therefore, the velocity perturbation field downstream of the discharge boundary station and upstream of the inlet boundary station is characterized by the sum of an irrotational velocity vector $\bar{u}_1$ and a solenoidal velocity vector $\bar{u}_2$, which satisfy the linearized conservation equations[3]:

$$\frac{dp}{dt} + \rho_0 a_0^2 \nabla \cdot \bar{u} = 0 \tag{A4}$$

$$\rho_0 \frac{d\bar{u}}{dt} + \nabla p = 0 \tag{A5}$$

[3]Note that $u_2 = 0$ upstream of the inlet; however, the analysis is developed with respect to the more general case pertaining to the flow downstream of the discharge station.

$$\frac{dp}{dt} - a_o^2 \frac{d\rho}{dt} = \frac{p}{C_v} \frac{dS}{dt} = 0 \tag{A6}$$

where

$$\nabla \times \bar{u}_2 = \omega \neq 0 \qquad \frac{d}{dt} = \frac{\partial}{\partial t} + U \frac{\partial}{\partial x}$$

$$\nabla \cdot \bar{u}_2 = 0 \qquad \bar{u}_1 = \bar{i} u_1 + \bar{j} v_1$$

$$\nabla \times \bar{u}_1 = 0 \qquad \bar{u}_2 = \bar{i} u_2 + \bar{j} v_2$$

$$\bar{u} = \bar{u}_1 + \bar{u}_2 \qquad U = M_o a_o$$

It can be implied from these equations that solutions for p and $\bar{u}_1$ are purely radiative (propagating acoustically in a coordinate system convecting at the mean flow velocity U) whereas solutions for $\bar{u}_2$ are purely convective. These results can be expressed in terms of a Fourier integral representation:

$$\begin{Bmatrix} p(x,y,t) \\ u_1(x,y,t) \\ v_1(x,y,t) \end{Bmatrix} = \sum_n e^{-i\alpha_n y} \int_{-\infty}^{\infty} \begin{Bmatrix} \rho_o a_o A_n(\omega) \\ B_n(\omega) \\ C_n(\omega) \end{Bmatrix} e^{i(\omega t - \beta_n x)} \frac{d\omega}{2\pi} \tag{A7}$$

$$\begin{Bmatrix} u_2(x,y,t) \\ v_2(x,y,t) \end{Bmatrix} = \sum_n e^{-i\alpha_n y} \int_{-\infty}^{\infty} \begin{Bmatrix} D_n(\omega) \\ E_n(\omega) \end{Bmatrix} e^{i\omega(t-x/U)} \frac{d\omega}{2\pi} \tag{A8}$$

The boundary data can be expressed as

$$\begin{Bmatrix} P(y,t) \\ Q(y,t) \\ R(y,t) \end{Bmatrix} = \sum_n e^{-i\alpha_n y} \int_{-\infty}^{\infty} \begin{Bmatrix} \bar{P}_n{}^o(\omega) \\ \bar{Q}_n{}^o(\omega) \\ \bar{R}_n{}^o(\omega) \end{Bmatrix} e^{i\omega t} \frac{d\omega}{2\pi} \tag{A9}$$

where a bar over a symbol denotes the time to frequency transform, and the superscript o indicates transformation from spatial location y to spatial harmonic n which will be discussed later.

Substitution of these integral forms into the governing equations gives

$$C_n = \frac{\alpha_n}{\beta_n} B_n \tag{A10}$$

$$E_n = \frac{\omega}{U\alpha_n} D_n \tag{A11}$$

$$B_n = \frac{\hat{a}_o \beta_n}{\omega - U\beta_n} A_n \tag{A12}$$

$$A_n + B_n + D_n = \overline{Q}_n{}^o \tag{A13}$$

$$C_n + E_n = \overline{R}_n{}^o \tag{A14}$$

The value of A_n, and thus B_n, C_n, D_n, and E_n, can thereby be expressed in terms of the transform of the boundary data as

$$A_n = \frac{\omega - U\beta_n}{\omega^2 + (a_o - U)\beta_n\omega + Ua_o\alpha_o{}^2}\left(\omega\overline{Q}_n + U\alpha_n\overline{R}_n{}^o\right) \tag{A15}$$

The propagation coefficient β_n is determined by substituting the integral relation for pressure into the convected wave equation as

$$\beta_n = \frac{-\omega M_o \pm \left[\omega^2 - \alpha_n{}^2 a_o{}^2\left(1 - M_o{}^2\right)\right]^{1/2}}{a_o\left(1 - M_o{}^2\right)} \tag{A16}$$

where the + sign refers to downstream propagation (the discharge boundary) and the - sign to upstream propagation (the inlet boundary).

The selected representation of the solutions and boundary conditions as Fourier series in the y-direction is appropriate for enforcement of the periodicity boundary condition pertaining to spatial variations in this direction. The coefficient α_n is defined accordingly as

$$\alpha_n = \frac{2\pi n}{Y} \tag{A17}$$

where Y is the fundamental period of the stage cascade configuration. In addition, the fact that the boundary data are specified at a discrete number of grid points, say N, on the boundaries implies that the Fourier series can only include N terms, that is, $n = 0, 1, 2, \ldots, N - 1$. Since the distance y to each point can be written as mY/N, where $m = 0, 1, 2, \ldots, N - 1$ also, the Fourier series can be expressed in the standard Discrete Fourier Transform (DFT) notation:

$$\begin{Bmatrix} P(y,t) \\ Q(y,t) \\ R(y,t) \end{Bmatrix} = \begin{Bmatrix} P_m(t) \\ Q_m(t) \\ R_m(t) \end{Bmatrix} = \sum_{n=0}^{N-1} \begin{Bmatrix} P_n{}^o(t) \\ Q_n{}^o(t) \\ R_n{}^o(t) \end{Bmatrix} e^{-2\pi inm/N} \tag{A18}$$

The inverse DFT is then

$$\begin{Bmatrix} P_n^{o}(t) \\ Q_n^{o}(t) \\ R_n^{o}(t) \end{Bmatrix} = \frac{1}{N} \sum_{m=0}^{N-1} \begin{Bmatrix} P_m(t) \\ Q_m(t) \\ R_m(t) \end{Bmatrix} e^{2\pi inm/N} \tag{A19}$$

The desired solution for the pressure perturbation on the boundaries is accomplished after some manipulation as

$$p_m(t) = \rho_o a_o \sum_{n=0}^{N-1} e^{-2\pi inm/N} \begin{Bmatrix} H_n^{o}(t) * Q_n^{o}(t) + J_n^{o}(t) * R_n^{o}(t) \\ K_n^{o}(t) * P_n^{o}(t) \end{Bmatrix} \tag{A20}$$

where $p_m(t)$ refers to the value at one of the N boundary grid points on the inlet or discharge boundary. Use of DFT techniques for $P_m(t)$, $Q_m(t)$, and $R_m(t)$ and similar DFT expansions for H_m, J_m, and K_m then leads to the convolution:

$$p_m(t) = \frac{\rho_o a_o}{N} \sum_{n=0}^{N-1} \begin{Bmatrix} H_n(t) * Q_{m-n}(t) + J_n(t) * R_{m-n}(t) \\ K_n(t) * P_{m-n}(t) \end{Bmatrix} \tag{A21}$$

on the discharge and inlet boundaries, respectively. Thus a double convolution over both time and distance (in the y-direction) is required. The functions $P_m(t)$, $Q_m(t)$, and $R_m(t)$, therefore, represent the point sources of time-varying strength which are alined along the considered boundaries, spatial resolution being consistent with the number of grid points specified. The functions $H_m(t)$, $J_m(t)$, and $K_m(t)$ are the duct response functions defined by

$$\begin{Bmatrix} H_m(t) \\ J_m(t) \\ K_m(t) \end{Bmatrix} = \sum_{n=0}^{N-1} \begin{Bmatrix} H_n^{o}(t) \\ J_n^{o}(t) \\ K_n^{o}(t) \end{Bmatrix} e^{-2\pi inm/N} = \begin{Bmatrix} \frac{1}{2}\delta(t) \\ 0 \\ \frac{1}{2}\delta(t) \end{Bmatrix} + \sum_{n=1}^{N-1} \begin{Bmatrix} H_n^{o}(t) \\ J_n^{o}(t) \\ K_n^{o}(t) \end{Bmatrix} e^{-2\pi inm/N} \tag{A22}$$

$$H_n^{o}(\tau) = \frac{1}{n^2\left(1 - M_o^2\right)} \int_{-\infty}^{\infty} (\Omega - T_n)\Omega e^{i\Omega\tau} \frac{d\Omega}{2\pi} \tag{A23}$$

$$J_n^{o}(\tau) = \frac{1}{n\left(1 - M_o^2\right)} \int_{-\infty}^{\infty} (\Omega - T_n) e^{i\Omega\tau} \frac{d\Omega}{2\pi} \tag{A24}$$

$$K_n^{o}(\tau) = \frac{1}{n(1 - M_o^2)(1 + M_o)} \int_{-\infty}^{\infty} (\Omega - T_n)(\Omega + M_o T_n) e^{i\Omega\tau} \frac{d\Omega}{2\pi} \qquad \text{(A25)}$$

where δ is the Dirac delta function and

$$T_n = \left[\Omega^2 - (1 - M_o^2)n^2\right]^{1/2}$$

$$\Omega = \frac{\omega}{\alpha} a_o$$

$$\tau = \frac{\alpha}{a_o t}$$

$$\alpha = \frac{2\pi}{Y}$$

A group of subroutines including an efficient Fast Fourier Transform routine has been developed for use in conjunction with the blade-to-blade computer program to carry out the indicated convolutions numerically. Results have been thus far limited to test cases with a simple harmonic input signal. For example, in one of the calculations the discharge station was assumed to be divided into 8 intervals covering a total circumferential distance of 0.1 foot. The selected reference (average) Mach number of the discharge flow was 0.8. The flow was assumed to be irrotational so that only one input function $Q(y,t)$ was required, and the second input function $R(y,t)$ could be considered as a response function (that is, it was calculated from $Q(y,t)$). The input function $Q(y,t) = \cos\left(\Omega\tau - \frac{2\pi n}{N}\right)$, with $Q(y,t) = 0$ for $\tau < 0$, was selected for this case, where $\tau = 2\pi N a_o t/Y$, $n = 1, 2, \ldots, N$, $N = 8$, $Y = 0.1$ foot, $a_o = 10^3$ fps, and $\Omega = 1$. The input function Q and response function R at $n = 1$ are plotted in figure (A1). It should be noted that the response function is initially out of phase with the input function because of the assumption that $Q = 0$ for $\tau < 0$. However, the effect of the transient at $\tau = 0$ dies quickly, and after about 1/3 millisecond the response function closely approximates the input function and indicates the desired harmonic solution is being approached asymptotically. The nondimensional perturbation pressure is plotted in figure (A2). The complete history is shown for the point $n = 1$, whereas the history of the points $n = 2$ and 3 is only shown at early times, where a difference in amplitude as well as phase exists. At later times (that is, after about 1/3 millisecond) the pressure solutions at the various grid points only differ noticeably by the phase angle corresponding to the input fuction, as the differences in amplitude asymptotically decay.

REFERENCES

1. Alzner, Edgar; and Erdos, John: Computation of Unsteady Transonic Flows Through Rotating and Stationary Cascades. Volume 1 – Method of Analysis. ATL TR 205 (Contract No. NAS 3-16807), Advanced Technology Labs., Inc., May 1975.

2. Vavra, Michael H.: Aero-Thermodynamics and Flow in Turbomachines. John Wiley & Sons, Inc., 1960.

3. Katsanis, Theodore: FORTRAN Program for Calculating Transonic Velocities on a Blade-To-Blade Stream Surface of a Turbomachine. NASA TN D-5427, 1969.

4. MacCormack, Robert W.: Numerical Solution of the Interaction of a Shock Wave With a Laminar Boundary Layer. Proceedings of the Second International Conference on Numerical Methods in Fluid Dynamics, Vol. 8 of Lecture Notes in Physics, Maurice Holt, ed., Springer-Verlag, 1971, pp. 151-163.

5. Kemp, Nelson H.; and Sears, W. R.: Aerodynamic Interference Between Moving Blade Rows. J. Aeronaut. Sci., vol. 20, no. 9, Sept. 1953, pp. 585-612.

6. Moretti, Gino; and Abbett, Michael: A Time-Dependent Computational Method for Blunt Body Flows. AIAA J., vol. 4, no. 12, Dec. 1966, pp. 2136-2141.

7. Serra, Raymond A.: Determination of Internal Gas Flows by a Transient Numerical Technique. AIAA J., vol. 10, no. 5, May 1972, pp. 603-611.

8. Bilwakesh, K. R.; Koch, C. C.; and Prince, D. C.: Evaluation of Range and Distortion Tolerance for High Mach Number Transonic Fan Stages. Final Report on Task II: Performance of a 1500 Feet per Second Tip Speed Transonic Fan Stage With Variable Geometry Inlet Guide Vanes and Stator. NASA CR-72880, 1972.

9. Katsanis, Theodore; and McNally, William D.: FORTRAN Program for Calculating Velocities and Streamlines on the Hub-Shroud Mid-Channel Flow Surface of an Axial- or Mixed-Flow Turbomachine. I – User's Manual. NASA TN D-7343, 1973.

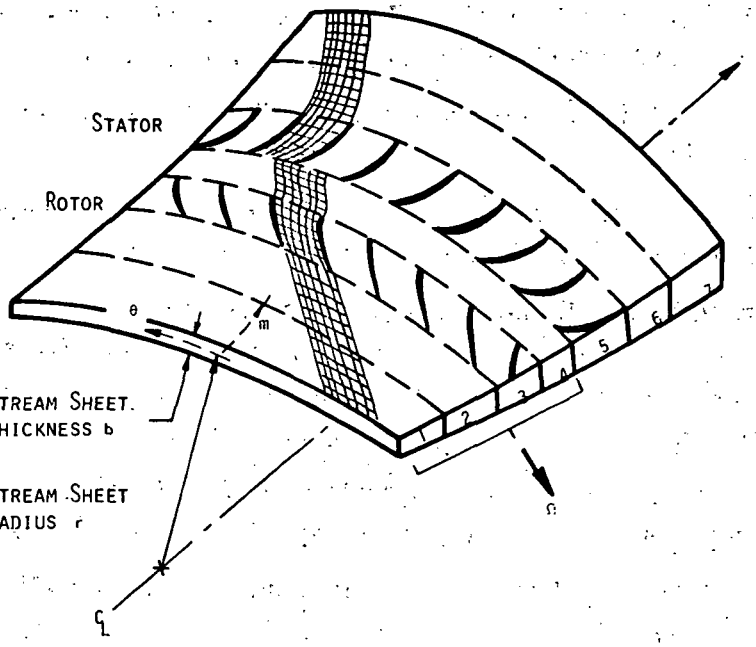

Figure 1.- Blade-to-blade coordinate system and grid network.

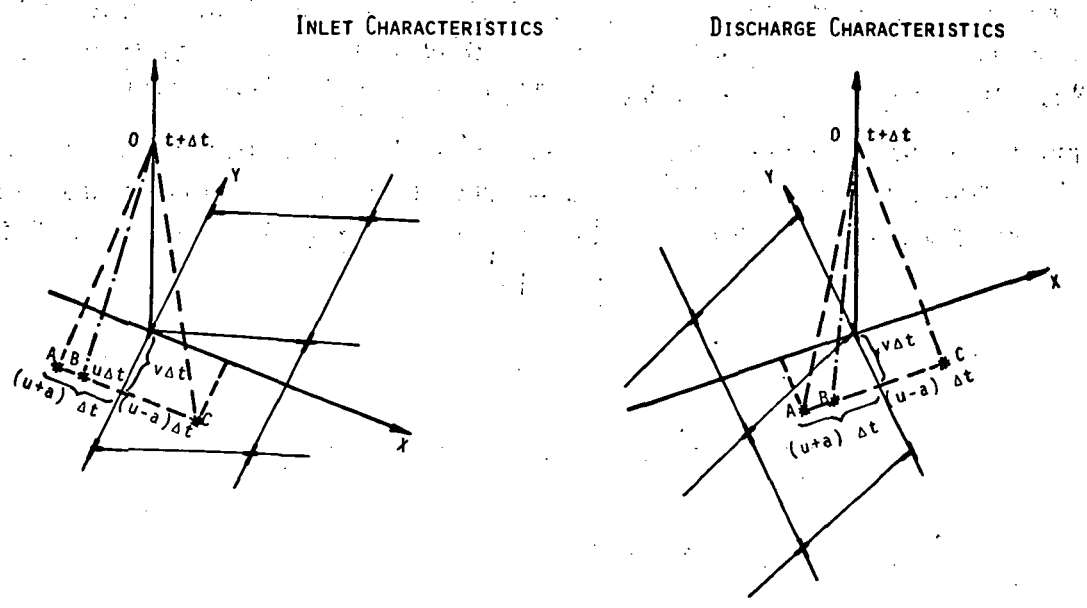

Figure 2.- Characteristic surfaces and grid points at inlet and discharge stations.

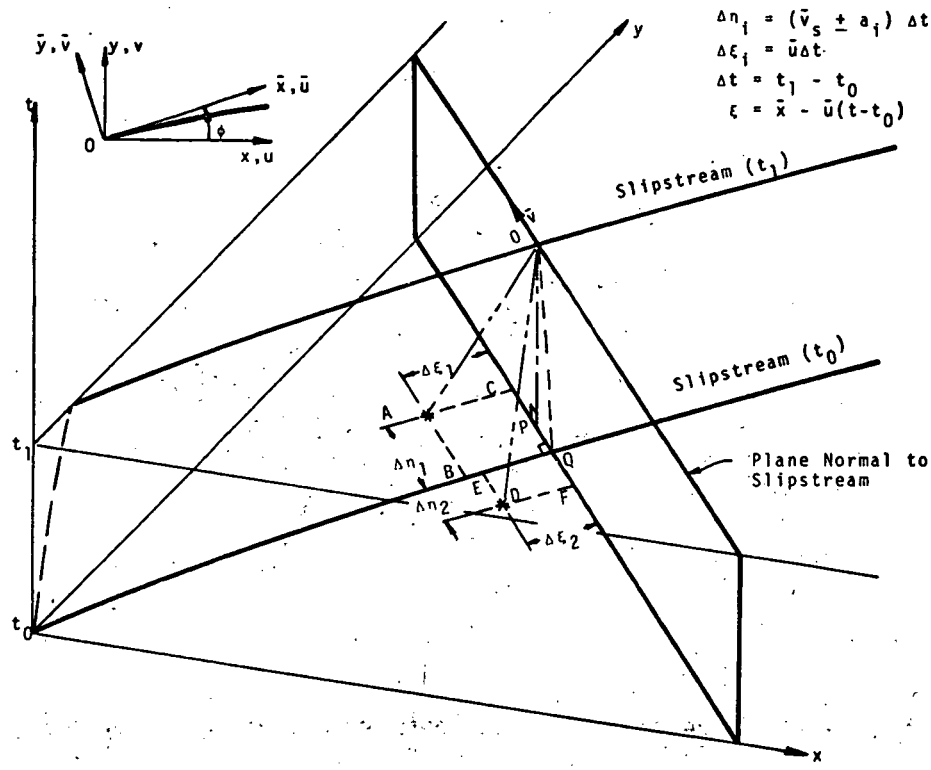

Figure 3.- Slipstream and blade surface characteristic geometry.

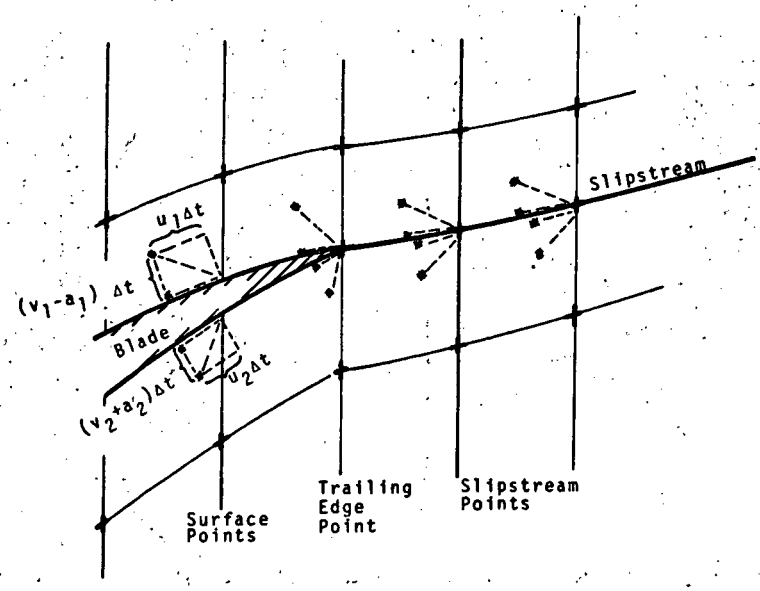

Figure 4.- Blade and slipstream characteristic system.

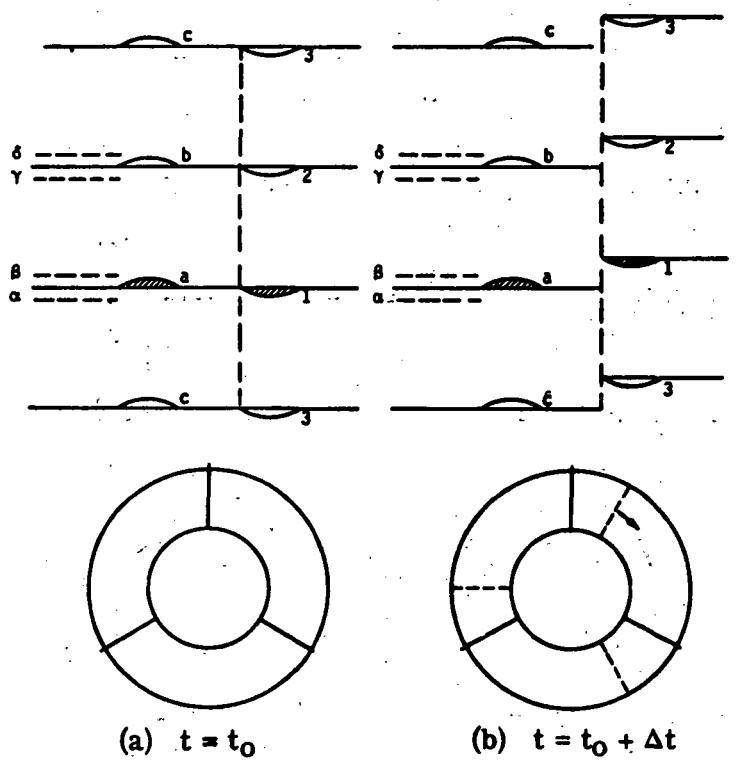

Figure 5.- Illustration of cyclic algorithm for stage with equal number of blades in stator and rotor. $N_1 = 3$, $N_2 = 3$.

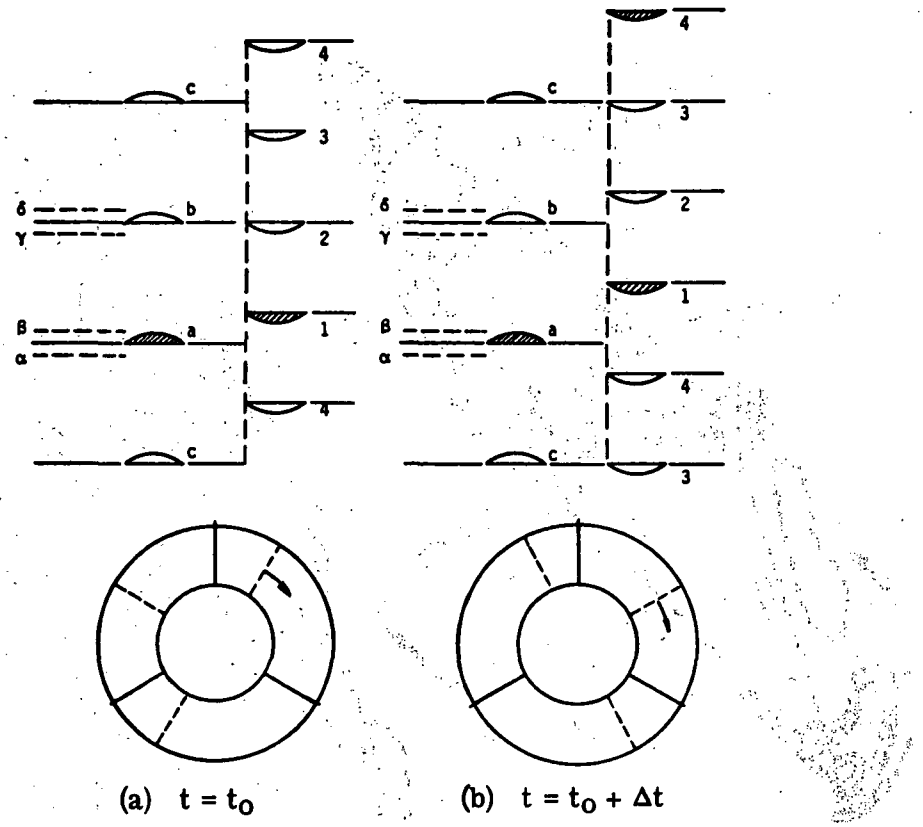

Figure 6.- Illustration of cyclic algorithm for stage with unequal number of blades in stator and rotor. $N_1 = 3$, $N_2 = 4$.

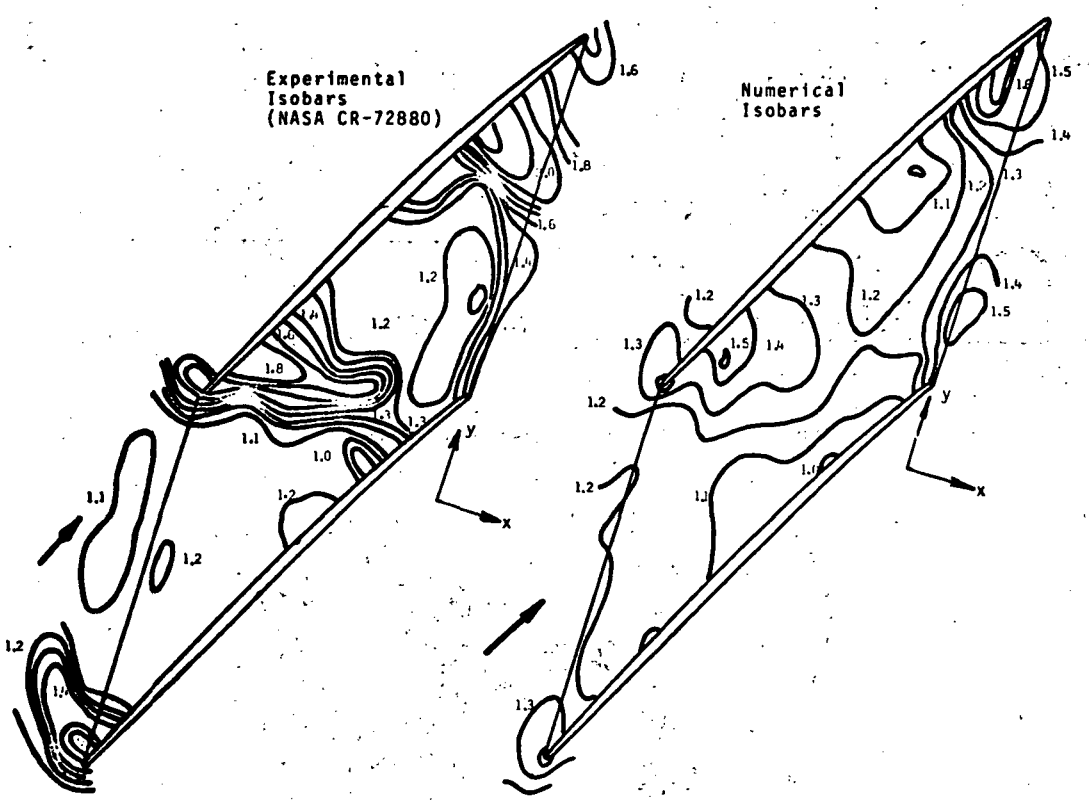

Figure 7.- Comparison of experimental and numerical pressure distributions for 1500 fps rotor.

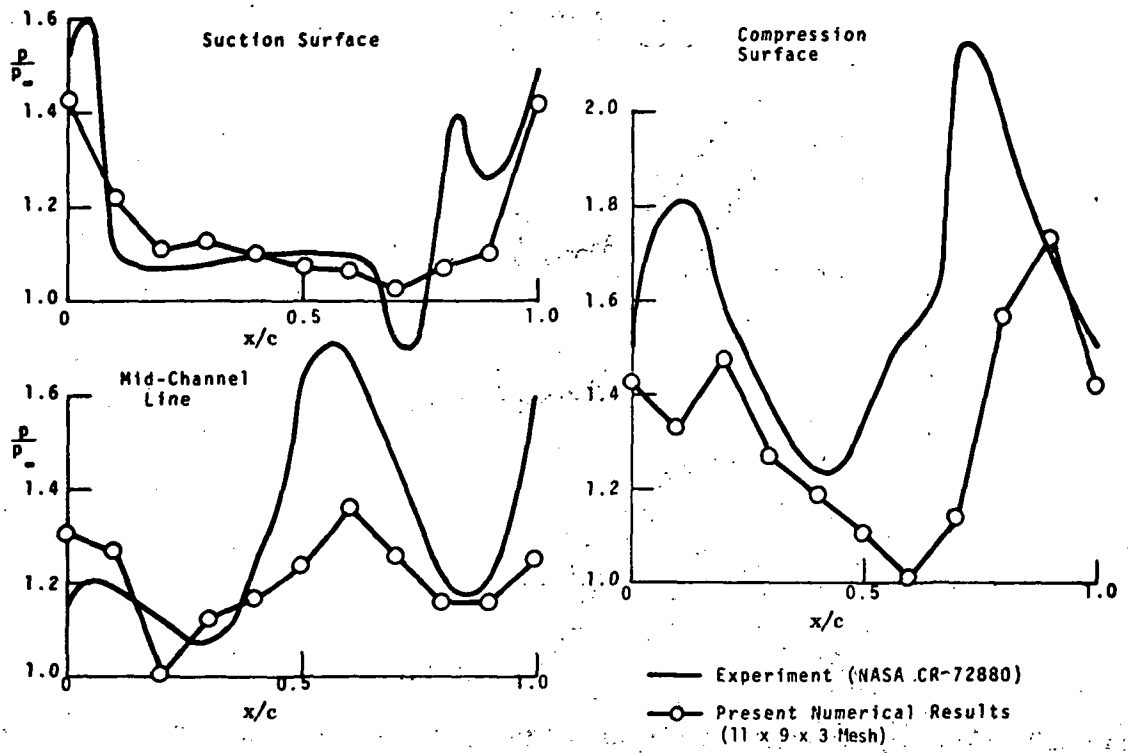

Figure 8.- Rotor pressure distributions.

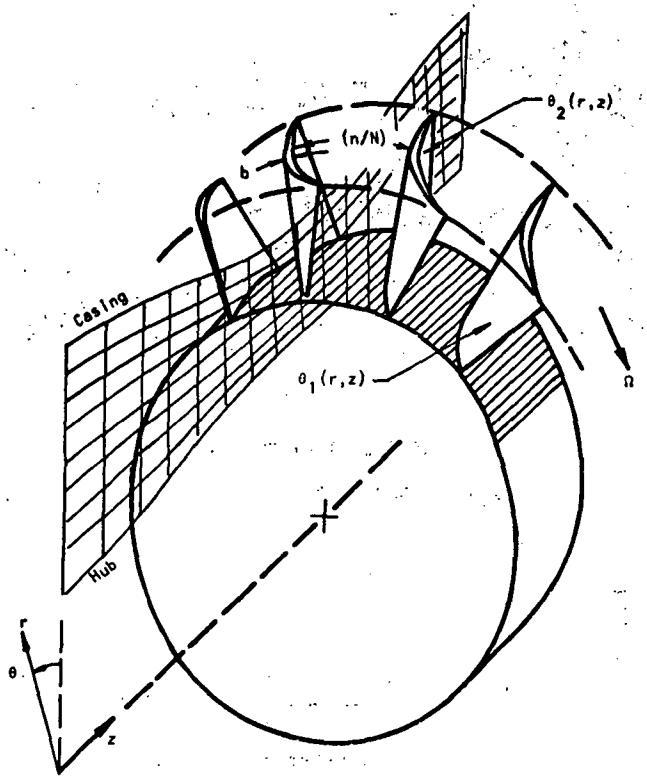

Figure 9.- Hub-to-casing coordinate system and grid network.

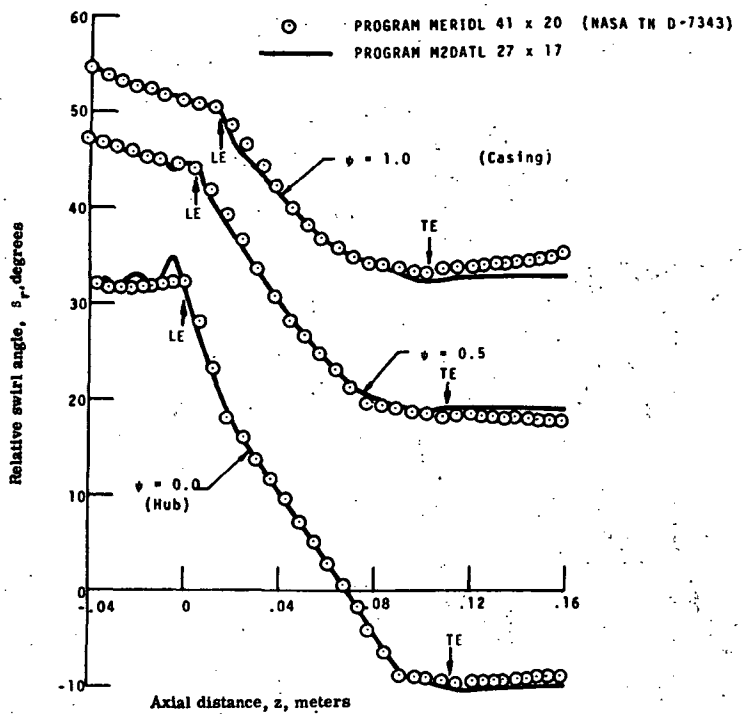

Figure 10.- Comparison of relative swirl angle variations through a subsonic rotor.

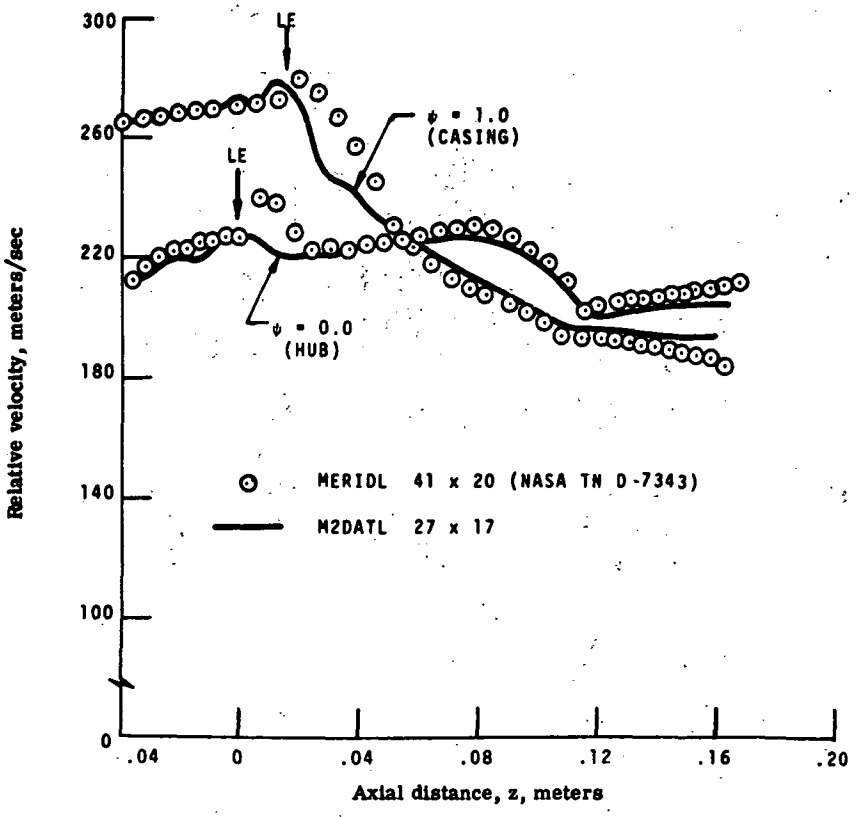

Figure 11.- Comparison of relative velocity distributions through a subsonic rotor.

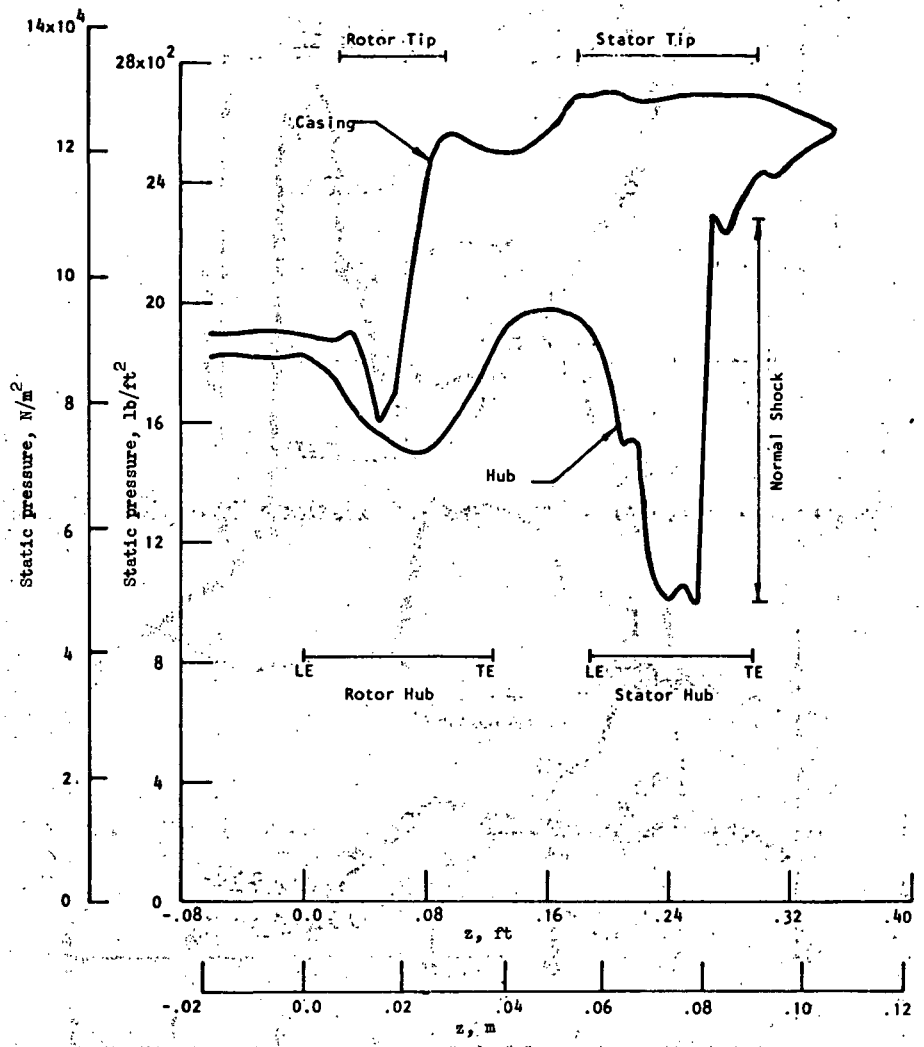

Figure 12.- Variation of static pressure along hub and casing through NASA QF-1 stage. Rotor 15; stator S9D – 45°; position VI.

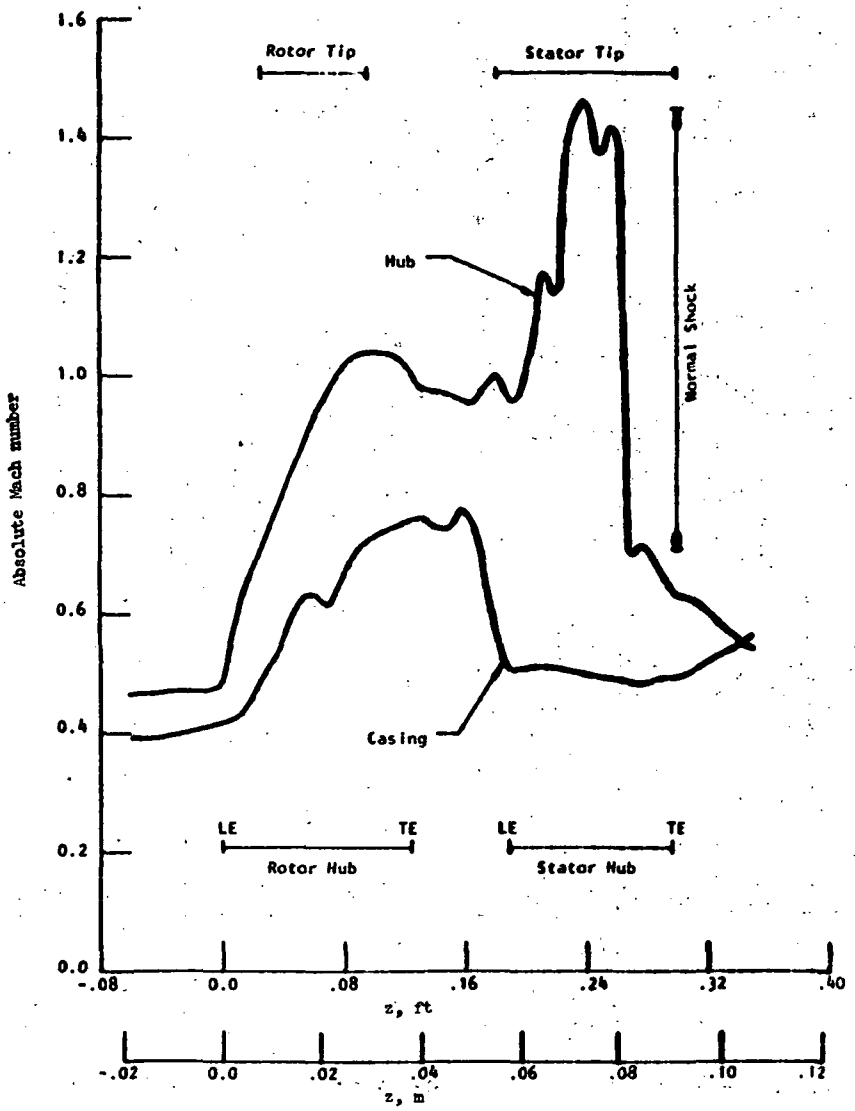

Figure 13.- Variation of Mach number along hub and casing through NASA QF-1 stage.

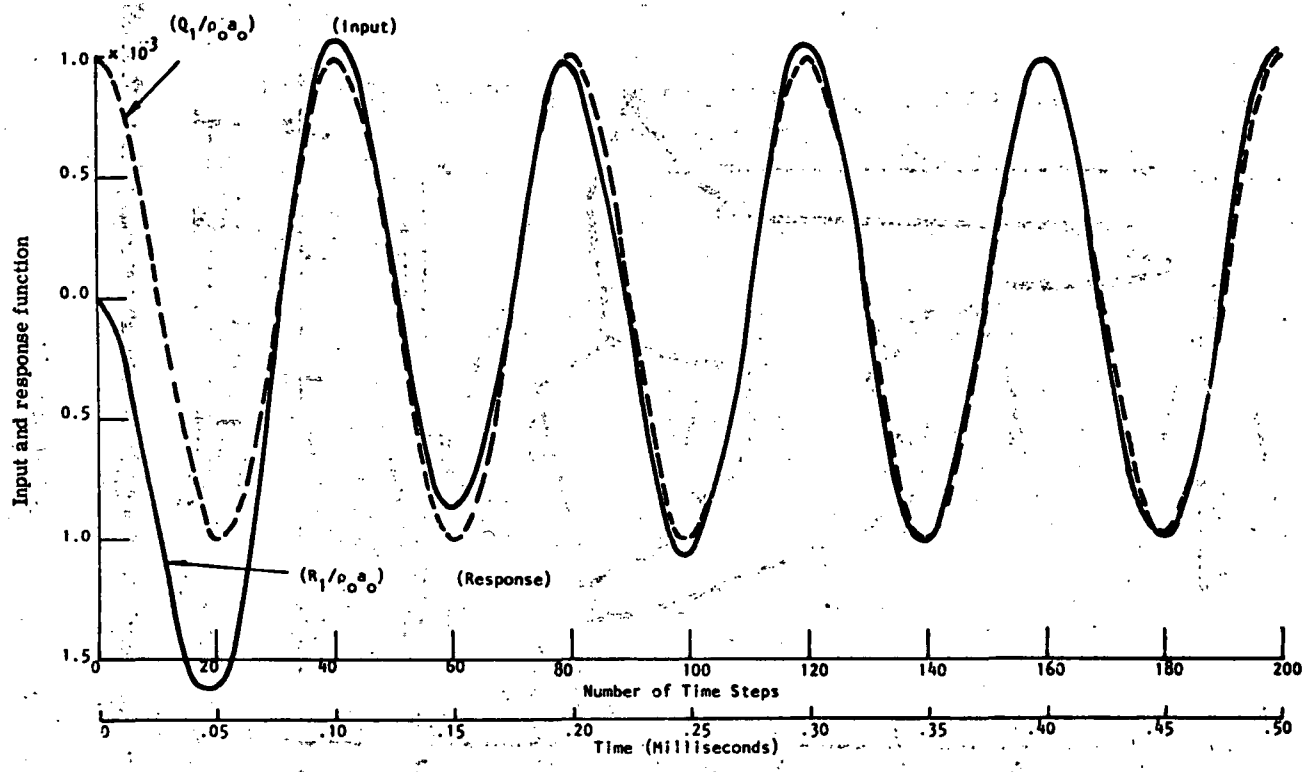

Figure 14.- Input and response functions for test cases.

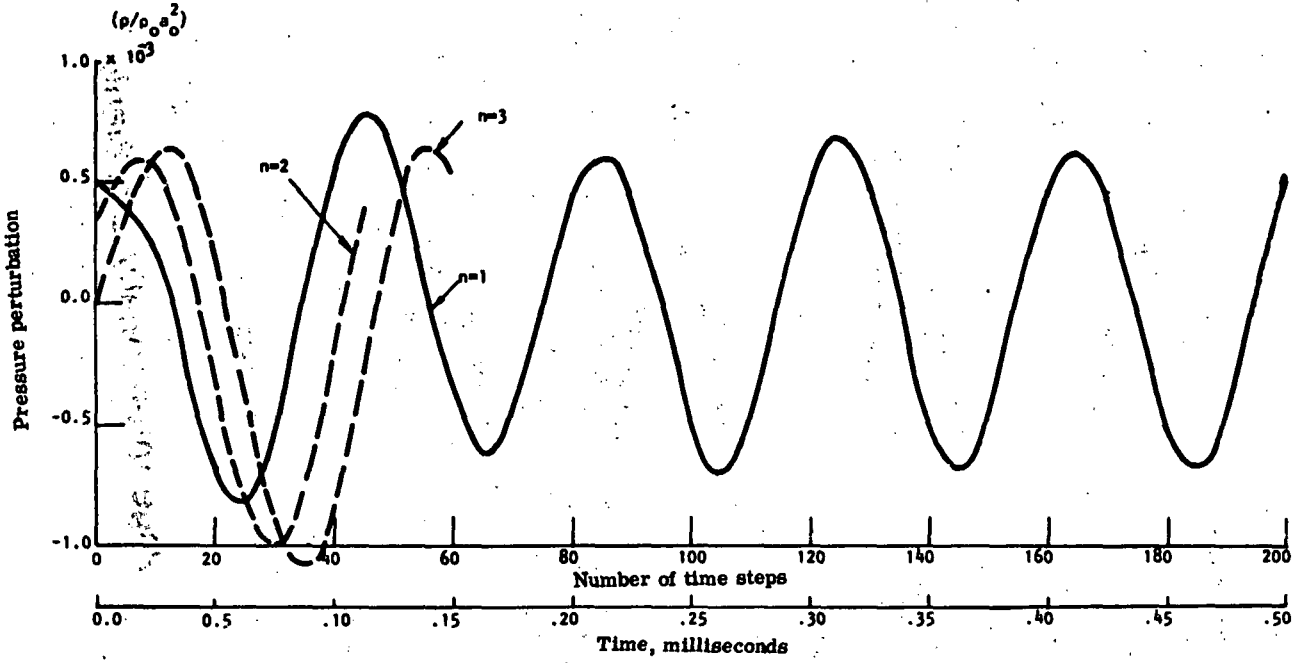

Figure 15.- Pressure perturbations at several grid points.

Page Intentionally Left Blank

A COMPARISON OF A SHOCK-CAPTURING TECHNIQUE WITH EXPERIMENTAL DATA FOR THREE-DIMENSIONAL INTERNAL FLOWS

By Leroy L. Presley
NASA Ames Research Center

SUMMARY

Shock-capturing solutions for an axisymmetric supersonic inlet at small angles of attack have been obtained. Good overall agreement between the shock-capturing solutions and experimental data have been shown except in regions of strong viscous effects or boundary-layer removal. Although the results indicate a strong potential for the use of shock-capturing or finite-difference solutions for internal flows, improvement in the ability to handle the reflection of strong shockwaves having downstream Mach numbers near 1 is needed.

INTRODUCTION

Traditional approaches to the design of axisymmetric supersonic inlets have employed the method of characteristics (refs. 1 to 3). References 2 and 3 include engineering modeling of the viscous effects, with reference 3 incorporating the effects of the boundary layer on the inviscid core flow. For two-dimensional flows — including axisymmetric flows — the method of characteristics provides a standard for any other computational technique. However, extension of the method of characteristics to three-dimensional flows, particularly complex internal flows, presents a very formidable task.

Recent developments in the use of finite-difference techniques show promise for application to three-dimensional internal flows. References 4 and 5 have been concerned with solutions to the flow about shuttle-type vehicles, both with diffuse (captured) and discrete bow shockwaves. References 6 and 7 describe techniques to fit discrete shockwaves into the computational mesh. A comparison of a discrete-shock, finite-difference technique with the method of characteristics for planar internal flows was given in reference 7; agreement between the two techniques was excellent. An advantage in using the finite-difference codes referenced above, as opposed to the method of characteristics, is that embedded shockwaves are captured in the finite-difference mesh without requiring any special logic.

The present paper describes an adaptation of the shock-capturing technique of reference 4 to the particular problem of inviscid flow in axisymmetric supersonic inlets at small angles of attack. (Many helpful suggestions concerning the present paper were made by Paul Kutler.) Comparison of the theoretical solutions with experimental data for the $M_\infty = 3.5$ inlet described in reference 2 is presented. The present shock-capturing solutions represent the

first step in a long range program that will ultimately incorporate discrete shockwaves, boundary-layer effects, mass exchange, and an arbitrary body cross section. The computer code for this analysis was developed by Dennis J. Maine, Computer Science Corporation.

SYMBOLS

a local speed of sound

k $\frac{\gamma - 1}{2\gamma}$

M Mach number

p pressure normalized by the free-stream stagnation pressure

q total velocity normalized by the maximum adiabatic velocity

r radius from axis of symmetry

u z-component of velocity

v r-component of velocity

w ϕ-component of velocity

Z axial coordinate from centerbody tip

α angle of attack

γ ratio of specific heats

δ boundary surface angle

ρ density

ϕ meridional coordinate

Subscripts:

a annulus

b centerbody

c end of cone

i index in ξ direction

j index in ϕ direction

o outer boundary

t stagnation conditions

∞ free-stream conditions

Superscripts:

n array of known flow properties

n+1 advanced array of flow properties

METHOD OF ANALYSIS

General Equations

The technique used in the present analysis is a direct adaptation of the shock-capturing technique presented in references 4 and 5. The major details of the analysis will be presented here, primarily for reasons of completeness. The equations of motion can be written in conservative form, using vector notation and cylindrical coordinates as

$$\tilde{E}_Z + \tilde{F}_r + \tilde{G}_\phi + \tilde{H} = 0 \tag{1}$$

where the $\tilde{E}$, $\tilde{F}$, $\tilde{G}$ and $\tilde{H}$ vector components are defined as:

$$\tilde{E} = \begin{bmatrix} \rho u \\ kp + \rho u^2 \\ \rho uv \\ \rho uw \end{bmatrix} ; \quad \tilde{F} = \begin{bmatrix} \rho v \\ \rho uv \\ kp + \rho v^2 \\ \rho vw \end{bmatrix} ; \quad \tilde{G} = \frac{1}{r} \begin{bmatrix} \rho w \\ \rho uw \\ \rho vw \\ kp + \rho w^2 \end{bmatrix} ; \quad \tilde{H} = \frac{1}{r} \begin{bmatrix} \rho v \\ \rho uv \\ \rho(v^2 - w^2) \\ 2\rho vw \end{bmatrix}$$

Equation (1), which represents the continuity and the three momentum equations, comprises a complete set when coupled with the energy equation in the following form:

$$p = \rho(1 - q^2) \tag{2}$$

where

$$q = \sqrt{u^2 + v^2 + w^2} \tag{3}$$

In applying shock-capturing techniques to the computation of internal flows, it is most convenient to transform the physical coordinate system to one wherein the distance between the inner and outer computational boundaries is normalized. This is done by the following coordinate transformation:

$$Z = Z ; \quad \xi = \frac{r - r_b}{r_o - r_b} = \frac{r - r_b}{\omega} ; \quad \phi = \phi \tag{4}$$

where, for the case considered here and as shown in figure 1(a), the inner and outer boundaries are given respectively by

$$r_b = r_b(Z) \; ; \; r_o = r_o(Z) \tag{5}$$

It should be noted that, for an axially symmetric configuration, the inner and outer boundaries are independent of the meridional angle.

The conservative form of the equations of motion, equation (1), can be retained in the transformed coordinate system as:

$$E_Z + G_\xi + G_\phi + H = 0 \tag{6}$$

where new variables are defined as follows:

$$\left.\begin{aligned} E &= \tilde{E} \\ F &= \tilde{F}\frac{\partial \xi}{\partial r} + \tilde{E}\frac{\partial \xi}{\partial Z} \\ G &= \tilde{G} \\ H &= \tilde{H} - \tilde{E}\frac{\partial^2 \xi}{\partial Z\, \partial \xi} \end{aligned}\right\} \tag{7}$$

The transformation derivatives are

$$\frac{\partial \xi}{\partial Z} = \frac{-\frac{\partial r_b}{\partial Z} - \xi\left(\frac{\partial r_o}{\partial \xi} - \frac{\partial r_b}{\partial \xi}\right)}{\omega} \; ; \; \frac{\partial \xi}{\partial r} = \frac{1}{\omega} \; ; \; \frac{\partial^2 \xi}{\partial Z\, \partial \xi} = \frac{-\left(\frac{\partial r_o}{\partial \xi} - \frac{\partial r_b}{\partial \xi}\right)}{\omega} \tag{8}$$

A plane of known flow quantities at some constant Z^n is required to initiate the solution. Within this plane, an array of discrete points is identified (fig. 1(b)) such that along each meridional ray, there are N_ξ points indexed by $1 \leq i \leq N_\xi$, and there are N_ϕ meridional rays indexed by $1 \leq j \leq N_\phi$. A step size consistent with the stability requirements of the differential equations is first determined for advancing the solution to Z^{n+1}. Since only supersonic flows are considered in the present analysis, the Z-axis is the hyperbolic coordinate. For each point in the flow field a minimum of four step sizes, corresponding to the four characteristic directions, must be found as follows:

$$\Delta Z = \frac{\Delta \xi}{\sigma_p}$$

and

$$\Delta Z = \frac{\Delta \phi}{\sigma_q} \tag{9}$$

The maximum eigenvalues are given by

$$\left.\begin{aligned} \sigma_p &= [\sigma(p)]_{\text{local max}} = \max\left(|\sigma_1^M|, |\sigma_2^M|\right) \\ \sigma_q &= [\sigma(\alpha)]_{\text{local max}} = \max\left(|\sigma_1^N|, |\sigma_2^N|\right) \end{aligned}\right\} \tag{10}$$

where

$$\left.\begin{aligned} \sigma_{1,2}^M &= \frac{\partial \xi}{\partial Z} + \frac{uv \pm a\sqrt{u^2 + v^2 - a^2}}{\omega(u^2 - a^2)} \\ \text{and} \\ \sigma_{1,2}^N &= \frac{1}{r}\left(\frac{uw \pm a\sqrt{u^2 + w^2 - a^2}}{(u^2 - a^2)}\right) \end{aligned}\right\} \tag{11}$$

Advancing the solution to Z^{n+1} is controlled by the smallest step size determined for the entire array at Z^n.

New conservative variables, $E_{1,2,3,4}$, are found at step Z^{n+1} using MacCormick's second-order predictor-corrector technique. Some modification to the indexing for these equations is required, depending upon the region of the flow being analyzed, as shown in figure 1(a). These predictor difference equations are given by

(a) For conical, external, and internal flows, where $1 \leq i \leq N_\xi - 1$ and $1 \leq j \leq N_\phi$,

$$\overline{E_{ij}^{n+1}} = E_{ij}^n - \frac{\Delta z}{\Delta \xi}\left(F_{i+1,j}^n - F_{ij}^n\right) - \frac{\Delta Z}{\Delta \phi}\left(G_{i,j+1}^n - G_{ij}^n\right) - \Delta Z H_{ij}^n \tag{12}$$

(b) For conical and external flows, where $i = N_\xi$ and $1 \leq j \leq N_\phi$, the predicted values are set equal to the free-stream values, which will be defined later.

(c) For internal flows, where $i = N_\xi$ and $1 \leq j \leq N_\phi$,

$$\overline{E_{N_\xi,j}^{n+1}} = E_{N_\xi,j}^n - \frac{\Delta Z}{\Delta \xi}\left(F_{N_\xi,j}^n - F_{N_\xi-1,j}^n\right) - \frac{\Delta Z}{\Delta \phi}\left(G_{N_\xi,j+1}^n - G_{N_\xi,j}^n\right) - \Delta Z H_{N_\xi,j}^n \tag{13}$$

where the superbar denotes predicted values at Z^{n+1}. The computations are carried out on only one side of the plane of symmetry, $0 \leq \phi \leq \pi$. For the predictor step, information at $\phi = \pi + \Delta\phi$ is needed, while (as will be seen shortly) information at $\phi = -\Delta\phi$ is needed for the corrector step. This information is obtained by simply mirroring w (i.e., changing the sign of w) across the plane of symmetry at the appropriate points and using the values of p, ρ, u, and v from the mirror image point.

The corrector difference equations are given by

(a) For conical and external flows, where $2 \le i \le N_\xi$ and $1 \le j \le N_\phi$, and for internal flows, where $2 \le i \le N_\xi - 1$ and $1 \le j \le N_\phi$,

$$E_{i,j}^{n+1} = \frac{1}{2}\left[E_{i,j}^{n} + \overline{E_{i,j}^{n+1}} - \frac{\Delta Z}{\Delta \xi}\left(\overline{F_{i,j}^{n+1}} - \overline{F_{i-1,j}^{n+1}}\right) - \frac{\Delta Z}{\Delta \phi}\left(\overline{G_{i,j}^{n+1}} - \overline{G_{i,j-1}^{n+1}}\right) - \Delta Z H_{i,j}^{n+1}\right] \tag{14}$$

(b) For conical, external, and internal flows, where $i = 1$ and $1 \le j \le N_\phi$,

$$E_{1,j}^{n+1} = \frac{1}{2}\left[E_{1,j}^{n} + \overline{E_{1,j}^{n+1}} - \frac{\Delta Z}{\Delta \xi}\left(\overline{F_{2,j}^{n+1}} - \overline{F_{1,j}^{n+1}}\right) - \frac{\Delta Z}{\Delta \phi}\left(\overline{G_{1,j}^{n+1}} - \overline{G_{1,j-1}^{n+1}}\right) - \Delta Z \overline{H_{1,j}^{n+1}} + \frac{\Delta Z}{\Delta \xi}\left(F_{3,j}^{n} - 2F_{2,j}^{n} + F_{1,j}^{n}\right)\right] \tag{15}$$

(c) For internal flows, where $i = N_\xi$ and $1 \le j \le N_\phi$,

$$E_{N_\xi,j}^{n+1} = \frac{1}{2}\left[E_{N_\xi,j}^{n} + \overline{E_{N_\xi,j}^{n+1}} - \frac{\Delta Z}{\Delta \xi}\left(\overline{F_{N_\xi,j}^{n+1}} - \overline{F_{N_\xi-1,j}^{n+1}}\right) - \frac{\Delta Z}{\Delta \phi}\left(\overline{G_{N_\xi,j}^{n+1}} - \overline{G_{N_\xi,j-1}^{n+1}}\right) - \Delta Z \overline{H_{N_\xi,j}^{n+1}} + \frac{\Delta Z}{\Delta \xi}\left(F_{N_\xi,j}^{n} - 2F_{N_\xi-1,j}^{n} + F_{N_\xi-2,j}^{n}\right)\right] \tag{16}$$

After both the predictor and the corrector steps, the conservative variables $E_{1,2,3,4}$ must be decoded to yield the physical variables $p, \rho, u, v,$ and w such that new predicted or corrected conservative variables $F, G,$ and H can be found. Decoding is accomplished by the following equations:

$$\left.\begin{aligned} v &= \frac{E_3}{E_1} \\ w &= \frac{E_4}{E_1} \\ u &= \frac{E_2 + \sqrt{E_2^2 - 4kE_1^2(1-k)(1-v^2-w^2)}}{2E_1(1-k)} \\ \rho &= \frac{E_1}{u} \\ p &= \rho(1 - u^2 - v^2 - w^2) \end{aligned}\right\} \tag{17}$$

After the advanced array is decoded, the flow along the centerbody and annulus boundaries will not necessarily satisfy the tangency requirement. As described in reference 8, the velocity vector at the wall must be rotated through a small angle, $\Delta\nu$, and the wall pressure corrected using the Prandtl-Meyer relationship. The turning angle $\Delta\nu$ for all j is found as follows:

(a) For the centerbody,

$$\Delta\nu = \sin^{-1} \frac{-\hat{u}_1^{n+1} \tan \delta_b^{n+1} + \hat{v}_1^{n+1}}{\hat{q}_1^{n+1} \left(\tan^2 \delta_b^{n+1} + 1\right)^{1/2}} \tag{18}$$

where the carets over the symbols denote the decoded values from the corrector equations (i.e., those values that do not satisfy tangency).

(b) For the annulus,

$$\Delta\nu = \sin^{-1} \frac{\hat{u}_{N_\xi}^{n+1} \tan \delta_o^{n+1} - \hat{v}_{N_\xi}^{n+1}}{\hat{q}_{N_\xi}^{n+1} \left(\tan^2 \delta_o^{n+1} + 1\right)^{1/2}} \tag{19}$$

The pressure ratio associated with this turning angle is found from

$$\frac{p^{n+1}}{\hat{p}^{n+1}} = 1 - \gamma \mathcal{M}^{n+1} \Delta\nu + \gamma \left(\frac{\mathcal{M}^{n+1}}{M^{n+1}}\right) \left[\frac{\gamma + 1}{4} \left(\mathcal{M}^{n+1}\right)^2 - 1\right] \Delta\nu^2 \tag{20}$$

where:

$$\mathcal{M} = \frac{M}{\sqrt{M^2 - 1}}$$

and

$$M = \frac{\hat{q}^2}{1 - \frac{1}{5} \hat{q}^2}$$

Note that if $\Delta\nu > 0$, an expansion will result, while, if $\Delta\nu < 0$, a compression will result. The new corrected wall pressure, consistent with the tangency condition, is

$$p^{n+1} = \hat{p}^{n+1} \frac{p^{n+1}}{\hat{p}^{n+1}} \tag{21}$$

and the corresponding density is

$$\rho^{n+1}\left(p^{n+1}\right)^{1/\gamma} \tag{22}$$

This relationship for density assumes that the entropy on the centerbody and annulus is everywhere equal to the free-stream values. Once the pressure and density are known, the total velocity is found from

$$q^{n+1} = \sqrt{1 - \left(\frac{p}{\rho}\right)^{n+1}} \tag{23}$$

and the individual velocity components are

$$\left.\begin{aligned} u^{n+1} &= \frac{q^{n+1}\left[\hat{u}^{n+1} + (M/N^2)\tan\delta\right]}{L} \\ v^{n+1} &= \frac{q^{n+1}\left(\hat{v}^{n+1} - M/N^2\right)}{L} \\ w^{n+1} &= \frac{q^{n+1}\hat{w}^{n+1}}{L} \end{aligned}\right\} \tag{24}$$

The quantities L, M, and N are

$$\left.\begin{aligned} L &= \left[\left(\hat{u}^{n+1} + \frac{M}{N^2}\tan\delta\right)^2 + \left(\hat{v}^{n+1} - \frac{M}{N^2}\right)^2 + \left(\hat{w}^{n+1}\right)^2\right]^{1/2} \\ M &= \hat{u}^{n+1}\tan\delta + \hat{v}^{n+1} \\ N &= \sqrt{\tan^2\delta + 1} \end{aligned}\right\} \tag{25}$$

The angle δ in equations (24) and (25) can be either the surface angle of the centerbody or the annulus at Z^{n+1}.

Method of Solution

Input to the program consists of the free-stream Mach number, the number of points N_ξ and N_ϕ (both of which are held constant throughout the solution), body coordinates (which herein are only a function of Z), and the initial angle of the conical tip. The remaining free-stream input quantities are calculated as follows:

$$p_\infty = \left(1 + \frac{1}{5}M_\infty^2\right)^{-7/2} \tag{26a}$$

$$\rho_\infty = \left(1 + \frac{1}{5}M_\infty^2\right)^{-5/2} \tag{26b}$$

$$q_\infty = \left[\frac{M_\infty^2}{5}\left(1 + \frac{1}{5}M_\infty^2\right)^{1/2}\right] \qquad (26c)$$

$$n_\infty = q_\infty \cos\alpha \qquad (26d)$$

$$v_\infty = q_\infty \sin\alpha \cos\phi \qquad (26e)$$

$$w_\infty = q_\infty \sin\alpha \sin\phi \qquad (26f)$$

The body coordinates are entered at discrete Z locations. For any three points on either the centerbody or annulus, a quadratic of the form $r = aZ^2 + bZ + c$ was determined. Choice of which coordinates to use for defining the coefficients was determined such that for any Z^{n+1}, determined from $Z^{n+1} = Z^n + \Delta Z$, two of the three points should have $Z > Z^{n+1}$. No explicit attempt at smoothing the angles at the input points was made; however, the present technique has been found to provide a satisfactory representation of the actual contours. The slope of any Z location was found by differentiating the above.

Solution of the conical flow is obtained by an iterative method. First, an outer computational boundary for both the conical and external flowfield must be found that will allow the shockwave from the cone tip to be captured between the centerbody surface and the outer boundary. As shown in figure 1, this boundary is taken to be inclined at an angle, relative to the axis of symmetry of the inlet, that is, equal to the angle of attack plus the planar shockwave angle for a flow deflection equal to the cone half-angle. Similar to the technique of reference 9, the free-stream quantities are assigned between the outer boundary and the cone surface at some initial Z start. The solution is advanced N_ξ steps in Z. Since the flow is conical, these values can be inserted at Z start and the solution again advanced N_ξ steps in Z. This cycling continues until the pressures on the cone at the end of the N^{th} cycle agree to within an ε of 0.0001 of those on the $N\text{-}1^{th}$ cycle. The solution was then taken to have converged, and these final flow quantities were assigned to the end of the conical flow zone Z_c. (The location of Z_c is somewhat arbitrary, here taken as $Z_c = 1$ (see fig. 1(a)), but it should always be less than or equal to the portion of the centerbody that can be represented as a cone.) Usually, convergence was obtained within eight cycles for the cases considered here.

After the conical flow was defined, the solution was advanced to the plane of the annulus lip. Here, the mesh is renoded to provide N_ξ points between the centerbody and the annulus lip. For the remainder of the solution, the outer boundary r_o is the radius of the annulus. If the external flow outer boundary fell outside the annulus lip, the flow properties at the renoded radial points were found using linear interpolation in the external flow solution. If the external flow outer boundary fell inside the annulus lip, linear interpolation was still used, but free-stream flow quantities were assigned between the external flow outer boundary and the annulus lip.

Computation of the internal flow continues until the end of the input coordinates. No attempt to define the external flow beyond the plane of the annulus lip was made in this study.

RESULTS AND DISCUSSION

Coordinates of the $M_\infty = 3.5$ axisymmetric supersonic inlet, for which shock-capturing solutions have been obtained herein, are given in table 1, and shown schematically in figure 2. This inlet, which resulted from the design study of reference 2, has the feature that the minimum area remains in nearly the same location, relative to the annulus, as the centerbody is translated forward for off-design ($M_\infty < 3.5$) operation. To obtain maximum performance with this inlet, it is necessary to remove the boundary layer in regions of strong adverse pressure gradients, such as produced by shockwave boundary-layer interactions. Regions of boundary-layer removal remain fixed on the annulus but, through a complicated porting system, move rearward on the centerbody as it is translated forward. (See ref. 2 for details.) Since, in this analysis, boundary-layer effects and mass exchange through the boundaries were not considered, discussion of this boundary-layer removal system is important only insofar as indicating regions wherein good agreement between theoretical calculations and experimental data should not be expected.

Any new computational technique should be compared with a standard solution before being applied to more generalized problems. As shown in reference 7, excellent agreement between a discrete-shock, finite-difference technique and the method of characteristics was obtained for planar internal flows, with good qualitative agreement also being obtained with a straight finite-difference method (shock-capturing technique). It remains to be shown that similar agreement between a shock-capturing solution and the method of characteristics can be obtained for axisymmetric flows, particularly when using a shock-capturing technique developed for three-dimensional flows. A shockwave pattern obtained from the method of characteristics for the inlet at $M_\infty = 3.5$, $\alpha = 0°$, with the centerbody in the design position (herein defined as the position wherein the shockwave from the centerbody tip hits the annulus lip at $M_\infty = 3.5$) is shown in figure 3. Corresponding static pressure distributions on the centerbody and annulus, obtained using the method of characteristics, are shown in figure 4, along with the pressure distributions obtained by using the shock-capturing technique. For all shock-capturing solutions obtained herein, 20 intervals in the ξ direction and 10 intervals in the ϕ direction were used. The shock-capturing solution agrees very well with the method of characteristics up to the second shockwave reflection on the centerbody. This is a fairly strong shockwave reflection, with the method of characteristics indicating a downstream Mach number less than 1.2. Failure of the shock-capturing solution at this point is due to the Mach number becoming subsonic in the interaction region. Overshoots in static pressure, and hence undershoots in Mach number, are typical of the solution of reflecting oblique shockwaves using MacCormack's second-order-accurate differencing in a shock-capturing technique (ref. 10). Several possibilities exist that can possibly resolve this situation: (1) incorporation of higher-order differencing terms, as described in reference 10; (2) incorporation of a damping term near the

shockwaves, as was used in reference 11; (3) incorporation of a technique for allowing the wall entropy to change across reflection regions; or (4) incorporation of discrete shockwaves into the solution. At present, all four of these possibilities are being examined. However, it can be said at this point that until the failure occurs, the solution obtained by the shock-capturing technique agrees well with that obtained by the method of characteristics.

A comparison of the shock-capturing solution discussed above with experimental data is shown in figure 5. Good overall agreement with the experimental data is obtained at $\alpha = 0°$, except in the regions of boundary-layer removal. The experimental data indicate shockwave intersections with the annulus and centerbody slightly ahead of the predictions of the shock-capturing technique. This is reasonable, since the presence of boundary-layer effects in the experimental data would tend to displace the shockwave interactions forward.

An angle of attack solution ($\alpha = 5°$ for the same centerbody location and M_∞ as the above calculations) is shown in figure 6. Again, the solution fails (at station $Z/r_a = 4.5$) due to the Mach number becoming subsonic in the strong interaction region; nevertheless, some qualitative conclusions concerning angle-of-attack effects can be drawn. Static pressures along the windward, $\phi = 0$, and leeward, $\phi = \pi$ meridians for both the annulus and centerbody are shown. Comparison with the solution shown in figure 5 shows that the magnitude of the pressure rise across the shockwave reflections is markedly increased, particularly on the centerbody. Further, evidence that the solution is producing a plausible reproduction of the physical flow is indicated by the behavior of the pressure distribution near the annulus lip on the windward meridian. Here, the shockwave from the centerbody tip should pass inside of the annulus lip and, since the initial angle of the annulus lip is about one degree, a local expansion should be generated at the annulus lip. The decrease of pressure indicated by the solution on the windward meridian near the annulus lip $2.86 \leq Z/r_a \leq 3.1$ is in agreement with the postulated physical flow.

All of the angle-of-attack experimental data that will be discussed herein is for angles of attack of 3°. In the following paragraphs, two different Mach numbers, and hence, two sets of different centerbody location data, will be discussed. The pattern will be first to show an $\alpha = 0°$ solution for the inlet and then an angle of attack solution and corresponding comparison with experimental data. Angle-of-attack effects on the internal flow pattern will thereby be identified.

The first Mach number data that will be discussed is for $M_\infty = 3.3$, where a forward centerbody translation $\Delta Z/r_a = 0.356$ was required. Note that even a small change in angle of attack requires a change in centerbody position for optimum inlet operation. At this M_∞ and $\alpha = 0°$, complete solutions were obtained to $Z/r_a = 5.0$, which is beyond the minimum area of the inlet (fig. 7). The corresponding solution for $\alpha = 3°$ is shown in figure 8. Although the angle-of-attack effects here are not as large as shown in figure 6, there is an indication that the strength of the shock reflections on the leeward side are increased. Here again, a complete solution was not obtained because the Mach number became subsonic in the strong reflection region near $Z/r_a = 4.8$ on the centerbody. Most of the experimental data are for the leeward side, with good qualitative agreement being obtained (except for the viscous effects

noted earlier). Some data on the windward side of the annulus were obtained and these show the same qualitative behavior with respect to the leeward data as indicated by the shock-capturing solutions.

The last Mach number data that will be discussed is for $M_\infty = 2.5$, where a forward translation $\Delta Z/r_a = 0.855$ was required. The $\alpha = 0^\circ$ solution is shown in figure 9, where a complete solution beyond the minimum area was obtained. At this Mach number, a complete solution was also obtained at angle of attack, and again the strength of the shockwave reflections was increased (fig. 10). For this case, the centerbody was extended sufficiently far forward that some expansion to pressures lower than the conical values was expected, and this is shown by both the data and the shock-capturing solution. Again invoking the qualifications on the agreement due to viscous effects, good qualitative agreement between the shock-capturing solution and experimental data was obtained.

CONCLUDING REMARKS

For all of the internal flows examined herein, several observations can be made:

(1) A solution given by the shock-capturing technique agrees well with one given by the method of characteristics for $\alpha = 0^\circ$.

(2) Second-order-accurate differencing can fail in regions near the reflection of strong shockwaves where the downstream Mach number is near 1. Several possibilities such as higher-order differencing, damping terms near the shockwaves, wall entropy correction, and discrete shockwaves are being investigated to determine if this failure can be overcome.

(3) Shock-capturing solutions agree well with experimental data, except in regions of strong viscous effects and boundary-layer removal.

REFERENCES

1. Sorenson, V. L.: Computer Program for Calculating Flow Fields in Supersonic Inlets. NASA TN D-2897, 1965.

2. Syberg, J., and Hickcox, T. E.: Design of a Bleed System for a Mach 3.5 Inlet. NASA CR-2187, 1974.

3. Maslowe, S. A., and Benson, J. L.: Computer Program for the Design and Analysis of Hypersonic Inlets. NASA CR-77749, 1964.

4. Kutler, P., Lomax, H., and Warming, R. F.: Computation of Space Shuttle Flow Fields Using Noncentered Finite-Difference Schemes. AIAA Paper 72-193, 1972.

5. Kutler, P., Reinhardt, W. A., and Warming, R. F.: Numerical Calculations of Multishocked Three-Dimensional Supersonic Flow Fields with Real Gas Effects. AIAA Journal, vol. 11, May 1973, pp. 651-664.

6. Moretti, G.: Complicated One-Dimensional Flows. Polytechnic Institute of Brooklyn, PIBAL Report No. 71-25, September 1971.

7. Presley, L. L., and Kutler, P.: Comparison of a Discrete-Shock Finite-Difference Technique and the Method of Characteristics for Calculating Internal Supersonic Flows. NASA paper presented at AIAA Computational Fluid Dynamics Conference (Palm Springs, Calif.), July 19-24, 1973.

8. Abbett, M. J.: Boundary Condition Calculation Procedures for Inviscid Supersonic Flow Fields. Proceedings, AIAA Computational Fluid Dynamics Conference (Palm Springs, Calif.), July 19-24, 1973, pp. 153-172.

9. Kutler, P., and Lomax, H.: Shock-Capturing, Finite-Difference Approach to Supersonic Flows. J. Spacecraft and Rockets, vol. 8, no. 12, pp. 1175-1182.

10. Anderson, D. A.: A Comparison of Numerical Solutions to the Inviscid Equations of Fluid Motion. Journal of Computational Physics, vol. 15, no. 1, pp. 1-20.

11. Kutler, P., Sakel, L., and Aiello, G.: On the Shock-on-Shock Interaction Problem. AIAA Paper 74-524, 1974.

TABLE 1.- $M_\infty = 3.5$ INLET CONTOUR DEFINITION

Z/r_a	r/r_a	Z/r_a	r/r_a
Centerbody		Annulus	
0.0	0.0	2.86	1.0
4.0	0.70532	3.1	1.004188
4.1	0.7228	3.2	1.0054
4.2	0.7387	3.4	1.0051
4.3	0.7512	3.6	0.99996
4.4	0.759	3.8	0.9882
4.5	0.7625	4.0	0.9681
4.55	0.763	4.1	0.954
4.6	0.7625	4.2	0.9364
4.65	0.7611	4.25	0.9261
4.7	0.7585	4.3	0.9154
4.8	0.7504	4.4	0.8949
4.9	0.7391	4.5	0.8768
5.1	0.7120	4.55	0.8695
5.3	0.6829	4.6	0.864
5.5	0.6525	4.65	0.86
5.6	0.6362	4.7	0.8572
5.7	0.618	4.8	0.8533
5.8	0.5973	4.9	0.8511
5.9	0.5744	5.0	0.8502
6.0	0.5467	5.1	0.85
		5.6	0.85
		5.8	0.8574
		5.9	0.8646
		6.0	0.8735

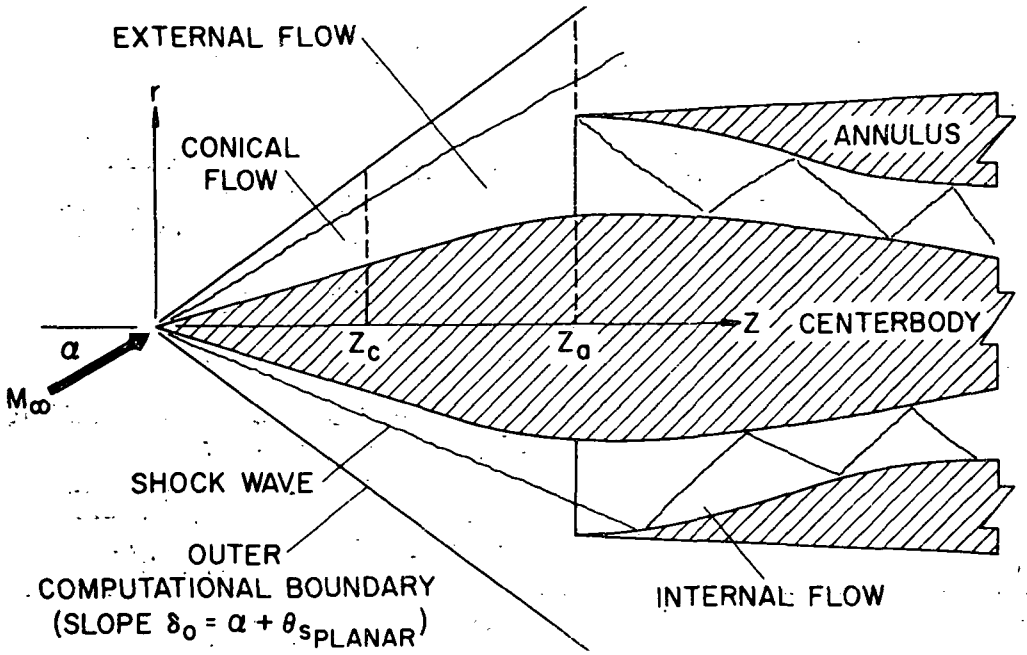

(a).— Schematic diagram of computational domains.

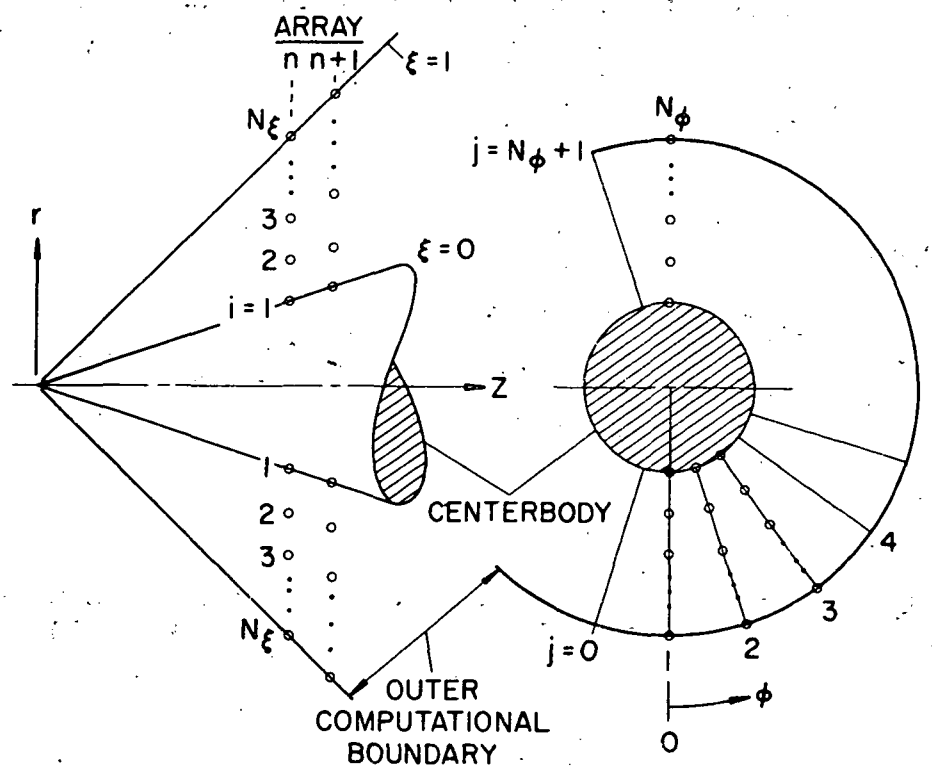

(b).— Diagram of indexing scheme for shock-capturing technique.

Figure 1.— Details of flow-field model.

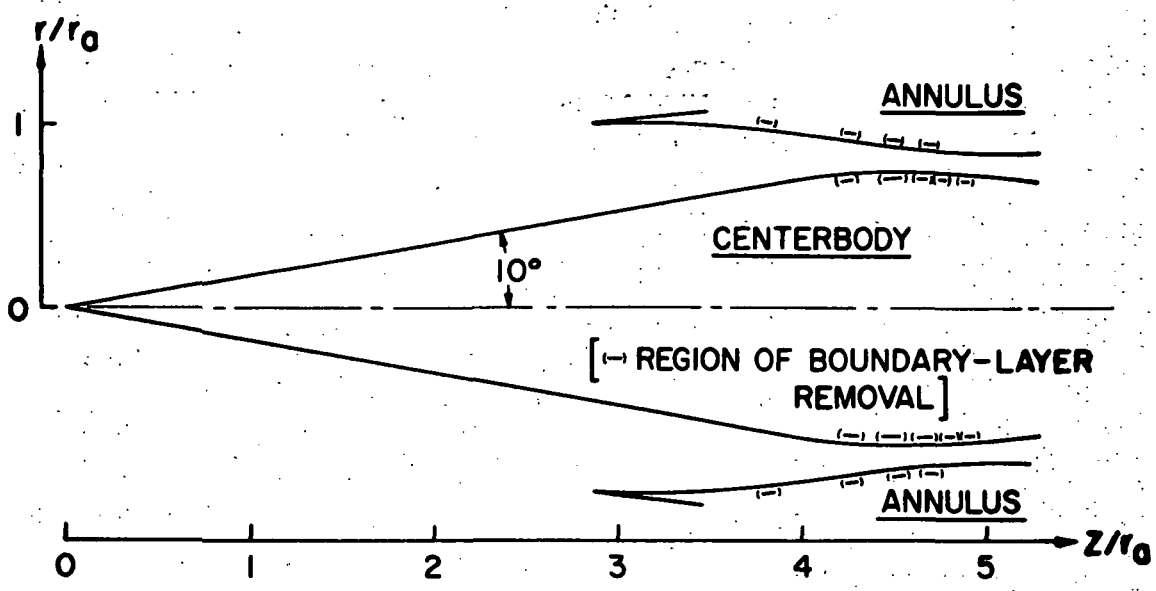

Figure 2.— Contours of $M_\infty = 3.5$ inlet.

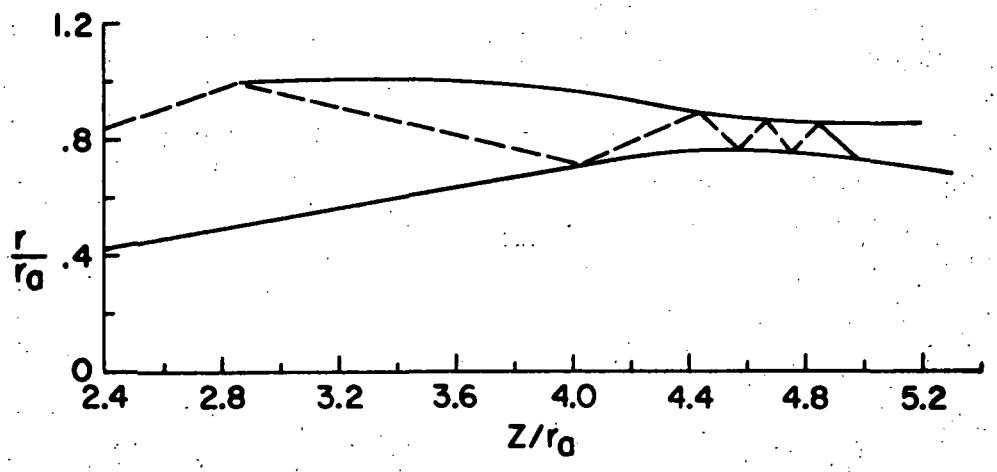

Figure 3.— Shock wave pattern given by the method of characteristics for $M_\infty = 3.5$, $\alpha = 0°$, and design centerbody location, $\Delta Z/r_a = 0$.

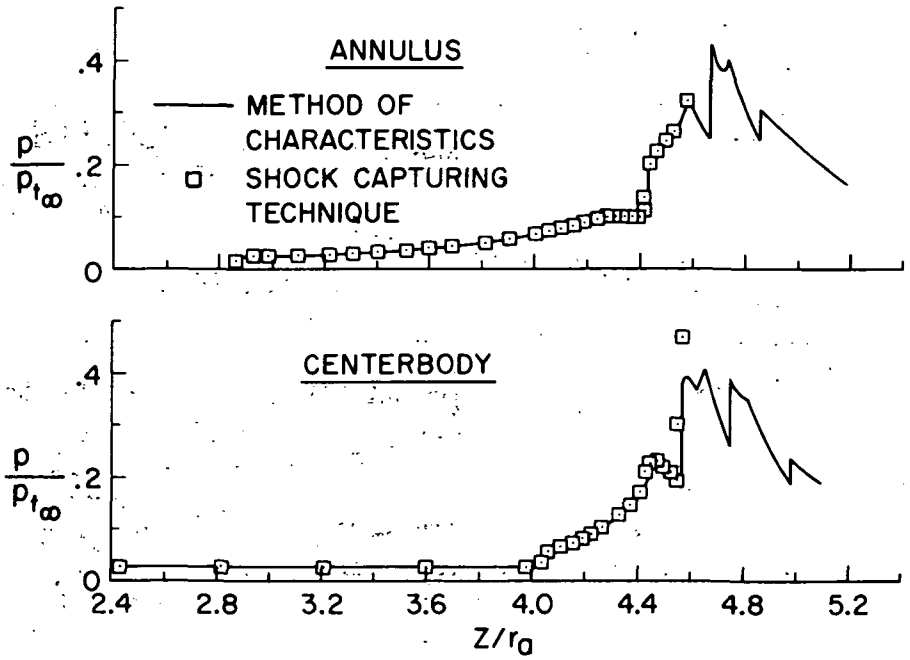

Figure 4.— Comparison of pressure distributions given by the shock-capturing technique and the method of characteristics for $M_\infty = 3.5$, $\alpha = 0°$, and design centerbody location, $\Delta Z/r_a = 0$.

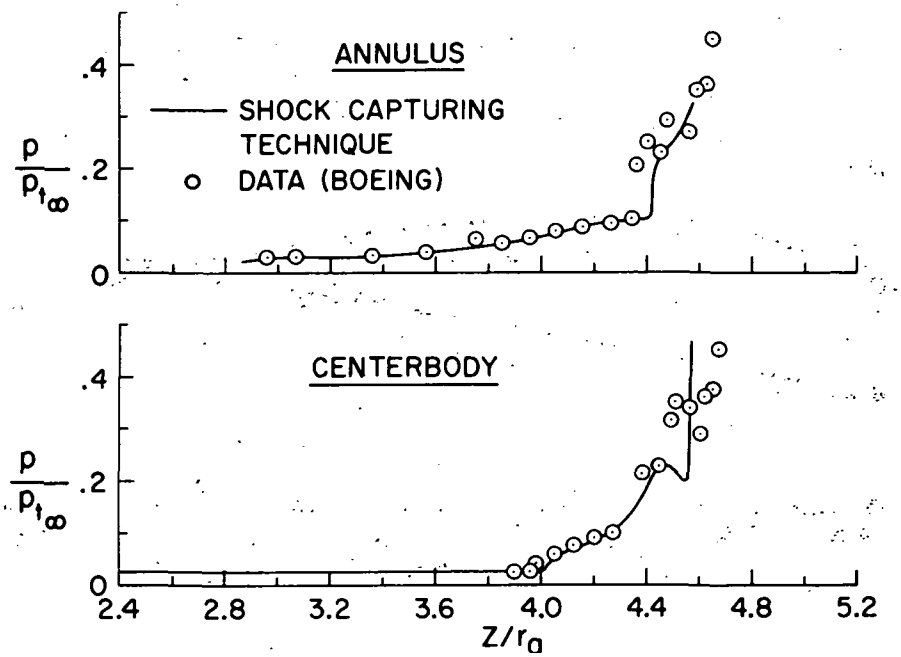

Figure 5.— Comparison of pressure distribution given by the shock-capturing technique with experimental for $M_\infty = 3.5$, $\alpha = 0^6$, and design centerbody location, $\Delta Z/r_a = 0$.

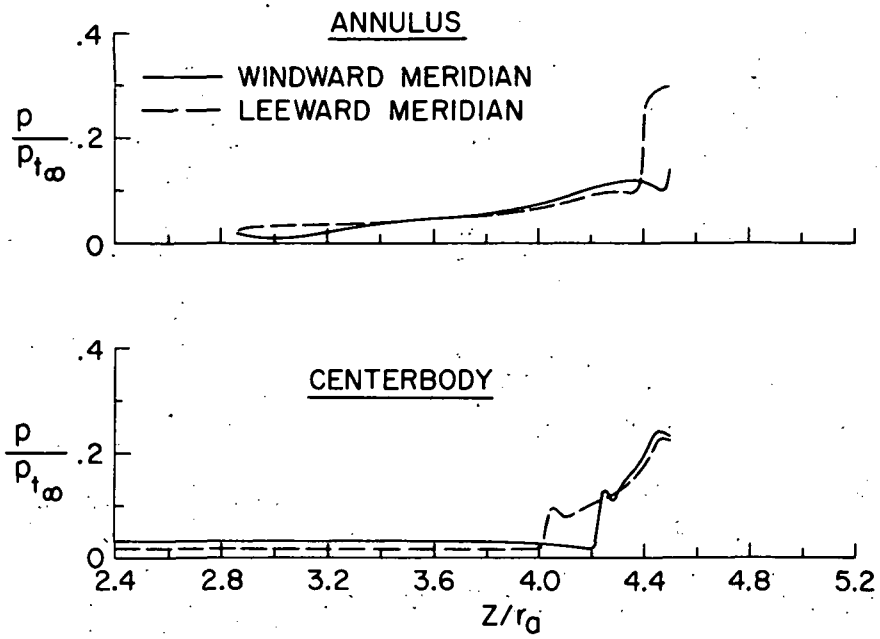

Figure 6.— Shock-capturing solution for $M_\infty = 3.5$, $\alpha = 5^\circ$, and design centerbody position, $\Delta Z/r_a = 0$.

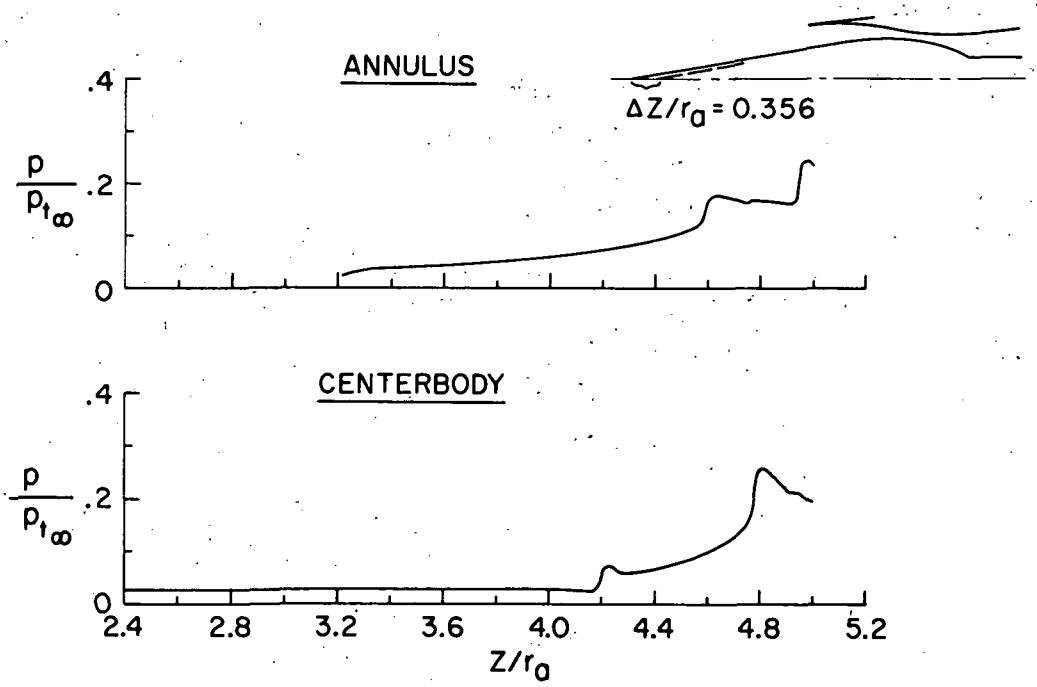

Figure 7.— Shock-capturing solution for $M_\infty = 3.3$, $\alpha = 0^\circ$, and $\Delta Z/r_a = 0.356$.

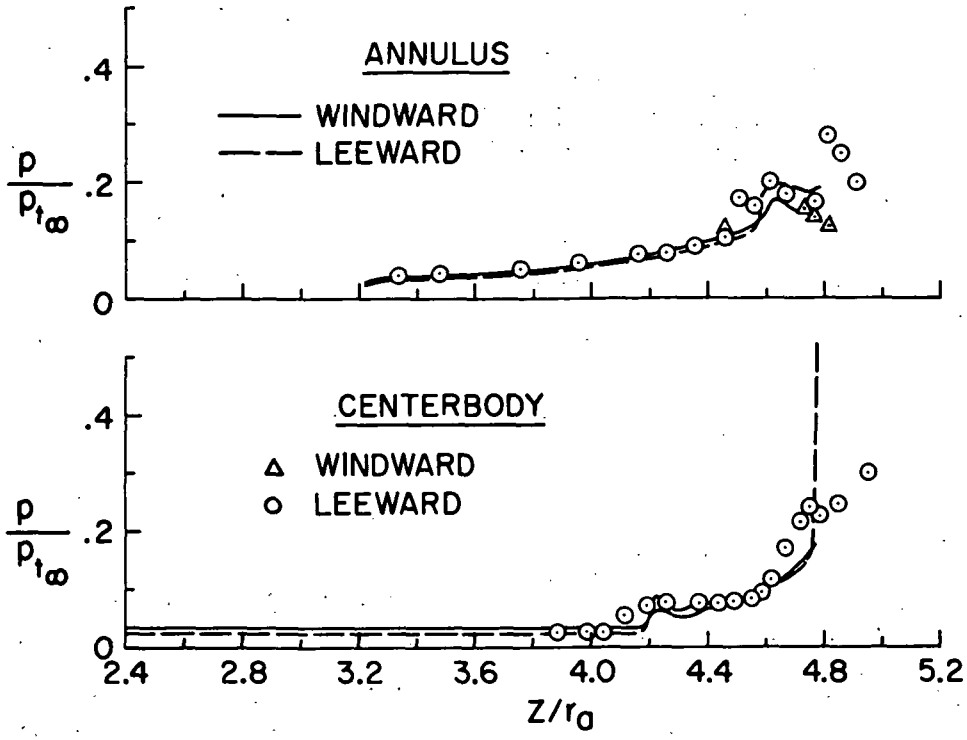

Figure 8.— Comparison of pressure distributions given by shock-capturing technique with experimental data for $M_\infty = 3.3$, $\alpha = 3°$, and $\Delta Z/r_a = 0.356$.

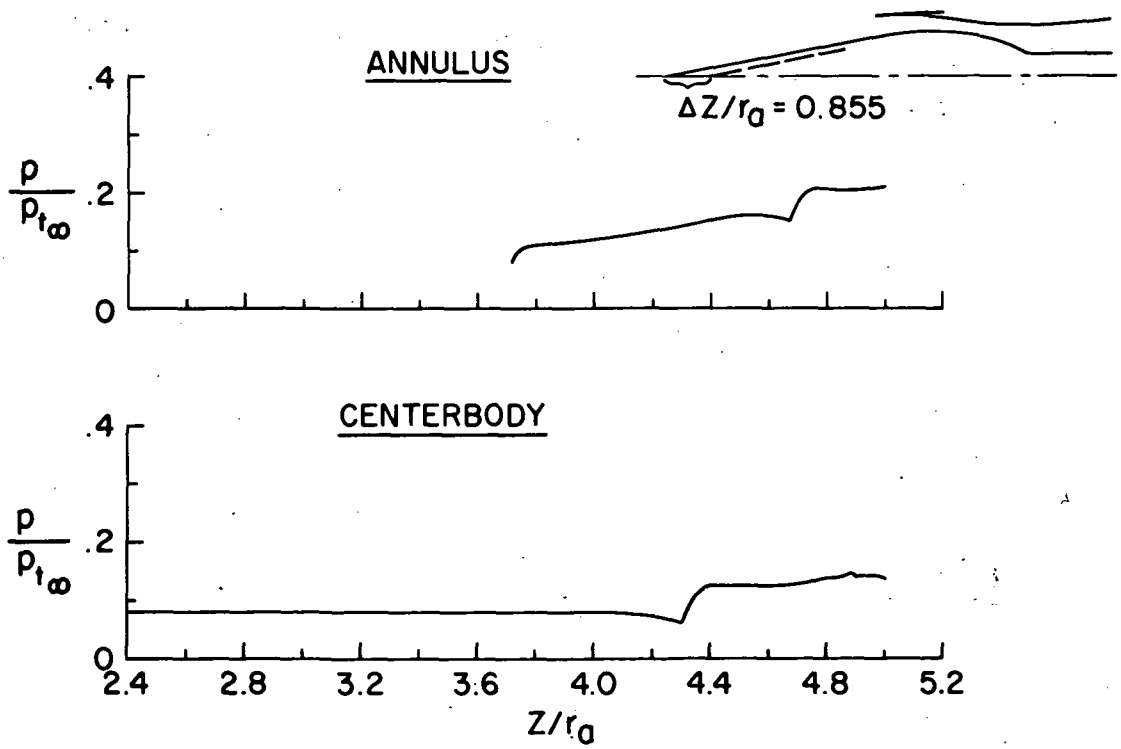

Figure 9.— Shock-capturing solution for $M_\infty = 2.5$, $\alpha = 0°$, and $\Delta Z/r_a = 0.855$.

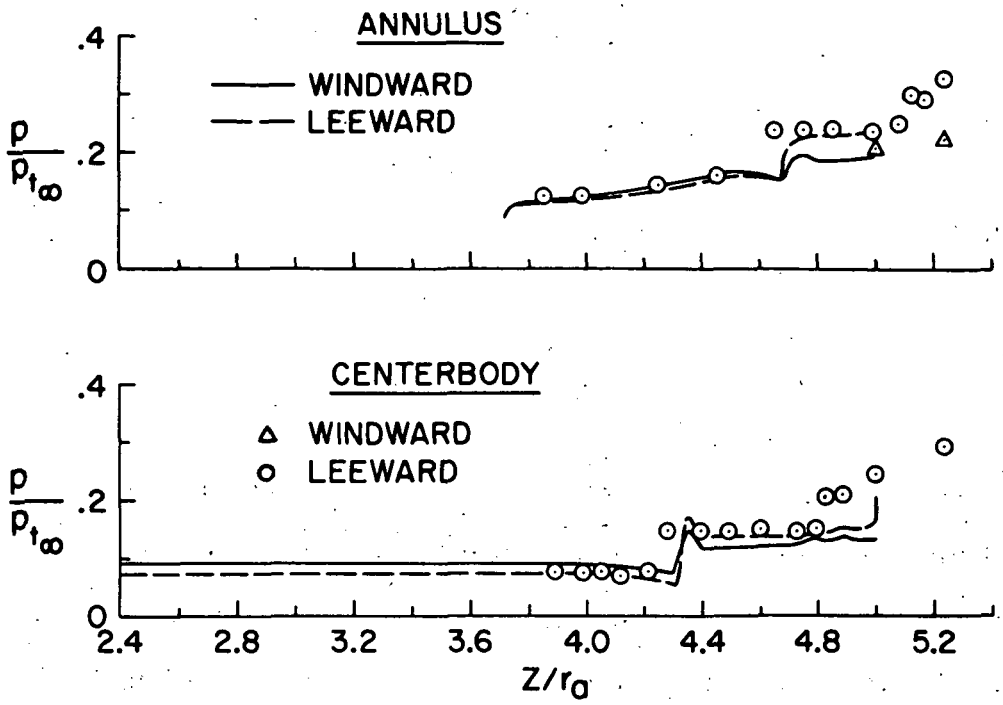

Figure 10.— Comparison of pressure distributions given by shock-capturing technique with experimental data for $M_\infty = 2.5$, $\alpha = 3°$, and $\Delta Z/r_a = 0.855$.

INTERNAL AND EXTERNAL AXIAL CORNER FLOWS

By Paul Kutler,
NASA Ames Research Center

Vijaya Shankar, Dale A. Anderson,
Iowa State University

and Reese L. Sorenson
NASA Ames Research Center

SUMMARY

The inviscid, internal and external axial corner flows generated by two intersecting wedges traveling supersonically are obtained by use of a second-order shock-capturing, finite-difference approach. The governing equations are solved iteratively in conical coordinates to yield the complicated wave structure of the internal corner and the simple peripheral shock of the external corner. The numerical results for the internal flows compare favorably with existing experimental data.

INTRODUCTION

Existing supersonic aircraft such as the B-1, F-14, F-15, Concorde, and recently proposed designs of advanced hypersonic research aircraft such as that shown in figure 1, possess engine inlets which are composed of planar compression or expansion surfaces with swept and unswept leading edges. These surfaces form various combinations of internal and external axial corners. Such a corner configuration can generate a rather complicated interference flowfield whose prediction is of considerable interest to the vehicle designer, because of the severe pressure gradients and high local heating that can occur at the surface.

The typical internal corner configuration studied in this paper and the coordinate system used are shown in figure 2. The flow direction is aligned with the x-axis. The vertical wedge is unswept and is always considered a compression surface; i.e., $\delta_2 > 0$. The horizontal or base wedge can have a sweep of Λ and be either a compression or an expansion surface; i.e., $\delta_1 \lesssim 0$.

The conical wave structure for a typical swept, compression-compression configuration is also shown in figure 2. The shock structure consists of a planar shock emanating from the leading edge of each wedge, a corner shock that joins the two wedge shocks, and two embedded shocks that stretch from the body to the triple points. A slip surface exists between each of the triple points and the axial corner at which there exists a vortical singularity.

If the base wedge is an expansion surface; i.e., $\delta_1 > 0$, then a Prandtl-Meyer expansion fan emanates from the leading edge and intersects the vertical wedge shock perpendicularly. As a result of the interaction, the wedge shock is bent and shifted slightly towards the axial corner, becoming weakened in the process. The expansion fan, after interaction with the wedge shock, becomes concave with respect to the corner.

A typical external corner configuration is shown in figure 3 and consists of two intersecting compression surfaces with angles δ_1 and δ_2 and sweeps Λ_1 and Λ_2. The flow structure about the external corner is considerably simpler than that of the internal corner. It consists of a single continuous shock wave whose strength in rounding the corner transitions from that of the δ_1-wedge shock to that of the δ_2-wedge shock. Like the internal flow problem, there also exists a vortical singularity at the axial corner due to the convergence of the cross-flow streamlines (each with different values of entropy).

Both the internal and external axial corner flows are conical since there is no characteristic length associated with the body. Viscous effects are assumed to be minimal, and therefore the flow is governed by the three-dimensional steady-flow Euler equations. These equations, under a nonorthogonal coordinate transformation which introduces conical self-similarity and aligns certain independent variables with the body, are hyperbolic and can be integrated in an iterative fashion using MacCormack's finite-difference algorithm (ref. 1). The internal corner problem with its complicated wave structure is solved using the shock-capturing philosophy (ref. 2) while the external corner problem with its single peripheral shock is solved using both the shock-capturing and shock-fitting approaches.

THEORY

The governing partial differential equations (continuity, x, y, and z momentum) in Cartesian coordinates (see figs. 2 and 3) are first written in the dimensionless strong conservation-law form:

$$E_x^{**} + F_y^{**} + G_z^{**} = 0 \qquad (1)$$

where

$$E^{**} = \begin{bmatrix} \rho u \\ kp + \rho u^2 \\ \rho uv \\ \rho uw \end{bmatrix} \quad F^{**} = \begin{bmatrix} \rho v \\ \rho uv \\ kp + \rho v^2 \\ \rho vw \end{bmatrix} \quad G^{**} = \begin{bmatrix} \rho w \\ \rho uw \\ \rho vw \\ kp + \rho w^2 \end{bmatrix}$$

and where $k = (\gamma-1)/2\gamma$, γ being the ratio of specific heats.

In equation (1), pressure p and density ρ are made dimensionless with respect to free-stream stagnation conditions, and velocity components u, v, and w are made dimensionless with respect to the maximum adiabatic velocity. The above system of equations is made complete by the addition of the steady-flow energy equation which can be written in the following dimensionless form:

$$p = \rho\left(1 - u^2 - v^2 - w^2\right) \tag{2}$$

It is desirable when solving fluid flow problems to transform the independent variables so that the new coordinates are aligned with the surface of the body. This alleviates the numerical difficulties associated with satisfying the tangency conditions for an unequally spaced grid. A transformation which satisfies the above criterion and also includes conical self-similarity is

$$\left.\begin{aligned} \zeta &= x \\ \eta &= y/(x - z \tan \Lambda_1) \\ \xi &= z/(x + y \tan \Lambda_2) \end{aligned}\right\} \tag{3}$$

where Λ_1 and Λ_2 are depicted in figure 3 for the external corner. For the internal corner, $\Lambda_1 = \Lambda$ and $\Lambda_2 = 0$.

Under the above transformation equation (1) becomes

$$E^*_\zeta + F^*_\eta + G^*_\xi + H^* = 0 \tag{4}$$

where

$$E^* = E^{**}cd$$

$$F^* = -E^{**}\eta c + F^{**}c + G^{**}\eta c + \tan \Lambda_1$$

$$G^* = -E^{**}\xi d - F^{**}\xi d \tan \Lambda_2 + G^{**}d$$

$$H^* = E^*[-c(-b + (\xi/e))\tan \Lambda_1 - d(a - (\eta/e))\tan \Lambda_2]$$
$$+ F^*[-d(-1 + (1/e))\tan \Lambda_2 - \xi(c/e)\tan \Lambda_1 \tan \Lambda_2]$$
$$+ G^*[-c(1 - (1/e))\tan \Lambda_1 - \eta(d/e)\tan \Lambda_1 \tan \Lambda_2]$$

$$a = \eta(1 - \xi \tan \Lambda_1)/e$$

$$b = \xi(1 + \eta \tan \Lambda_2)/e$$

$$c = \zeta(1 + a \tan \Lambda_2)$$

$$d = \zeta(1 - b \tan \Lambda_1)$$

$$e = 1 + \eta\xi \tan \Lambda_1 \tan \Lambda_2$$

Thus equation (4) governs the flow over both the internal and external corners and can be solved without any further relations using the shock-capturing approach.

In order to treat the peripheral shock of the external problem as a sharp discontinuity, equation (4) is first normalized between the surface of each wedge and the shock. This requires a separate coordinate transformation for each of the two regions outlined by points 1-2-3-4-1 and 5-6-7-8-5 in figure 4. The necessary equations will be developed for the horizontal region only, since the derivation of the analogous equations for the vertical region is the same.

The required transformation is

$$\left.\begin{aligned} \zeta &= \zeta \\ \lambda &= (\eta - \eta_b)/[\eta_s(\zeta,\xi) - \eta_b] \\ \xi &= \xi \end{aligned}\right\} \tag{5}$$

and when applied to equation (4) yields

$$E_\zeta + F_\lambda + G_\xi + H = 0 \tag{6}$$

where

$$E = E^*$$

$$F = E^*\lambda_\zeta + F^*\lambda_\eta + G^*\lambda_\xi$$

$$G = G^*$$

$$H = H^* - E^*\lambda_{\zeta_\lambda} - G^*\lambda_{\xi_\lambda}$$

$$\lambda_\zeta = -\lambda(\eta_s)_\zeta/(\eta_s - \eta_b)$$

$$\lambda_\eta = 1/(\eta_s - \eta_b)$$

$$\lambda_\xi = -\lambda(\eta_s)_\xi/(\eta_s - \eta_b)$$

$$\lambda_{\zeta_\lambda} = -(\eta_s)_\zeta/(\eta_s - \eta_b)$$

$$\lambda_{\xi_\lambda} = -(\eta_s)_\xi/(\eta_s - \eta_b)$$

The equation of the shock is $y_s = y_s(x,z)$, and the quantity $(\eta_s)_\zeta$ of equation (6) can be expressed as a function of the derivatives $(y_s)_x$ and $(y_s)_z$ as follows:

$$(\eta_s)_\zeta = \frac{y_\zeta - (y_s)_x - (y_s)_z z_\zeta}{z_\eta (y_s)_z - y_\eta} \tag{7}$$

where

$$(y_s)_z = \frac{y_\xi + y_\eta (\eta_s)_\xi}{z_\xi + z_\eta (\eta_s)_\xi}$$

$$y_\zeta = \frac{y}{\zeta}$$

$$y_\eta = \frac{y}{\eta e}$$

$$y_\xi = -\frac{\eta \tan \Lambda_1}{\xi e}$$

$$z_\zeta = \frac{z}{\zeta}$$

$$z_\eta = \frac{\xi \tan \Lambda_2}{\eta e}$$

$$z_\xi = \frac{z}{\xi e}$$

$$y = \frac{\eta\zeta(1 - \xi \tan \Lambda_1)}{e}$$

$$z = \frac{\xi\zeta(1 + \eta \tan \Lambda_2)}{e}$$

The quantity $(\eta_s)_\xi$ is evaluated numerically and $(y_s)_x$ is computed from the Rankine-Hugoniot equations:

$$
\left.
\begin{aligned}
\left(y_s\right)_x &= \left[u_\infty\left(v_\infty - w_\infty\left(y_s\right)_z\right) \right. \\
&\quad \left. + \tilde{u}_1\sqrt{\left(v_\infty - w_\infty\left(y_s\right)_z\right)^2 + \left(u_\infty^2 - \tilde{u}_1^2\right)\left(1 + \left(y_s\right)_z^2\right)}\right] \Big/ \left(u^2 - \tilde{u}_1^2\right) \\
\tilde{u}_1^2 &= \frac{\gamma^2 - 1}{4\gamma}\,\frac{p_1}{\rho_1}\left[\frac{p_2}{p_1} + \frac{\gamma - 1}{\gamma + 1}\right] \\
\rho_2 &= \rho_1 \frac{\dfrac{p_2}{p_1} + \dfrac{\gamma - 1}{\gamma + 1}}{1 + \dfrac{\gamma - 1}{\gamma + 1}\dfrac{p_2}{p_1}} \\
\vec{q}_2 &= \left(u_\infty - \left(y_s\right)_x a\right)\hat{i} + \left(v_\infty + a\right)\hat{j} + \left(w_\infty - \left(y_s\right)_z a\right)\hat{k}
\end{aligned}
\right\} \qquad (8)
$$

where

$$
a = \frac{\left|\tilde{u}_1\right|\left(1 - \rho_1/\rho_2\right)}{\sqrt{\left(y_s\right)_x^2 + 1 + \left(y_s\right)_z^2}}
$$

and the subscript ∞ indicates the free-stream condition.

Following the approach developed by Thomas et al. (ref. 3), it is only necessary to know the pressure behind the shock in order to propagate it. The remaining flow quantities can be found from equation (8). Shock pressure is determined by a finite-difference approximation of the governing partial differential equations at the shock (refs. 4 and 5).

Equation (4), which governs both corner flows (via shock-capturing), and equation (6), which governs only the external corner flow (via shock-fitting), are hyperbolic with respect to the conical coordinate ζ. These equations can therefore be solved iteratively until E_ζ^* of equation (4) and E_ζ of equation (6) are zero, indicating the establishment of conical flow.

The boundary condition at the surface of each wedge requires that the flow be tangent to it. Since an iterative procedure is employed to solve the governing equations, a simple Euler predictor/modified Euler corrector with one-sided normal derivatives is used at each surface. The following condition on the velocity components is imposed after the corrector step to satisfy tangency:

$$v = u \tan \delta_1 - w \tan \delta_1 \tan \Lambda_1; \text{ horizontal wedge}$$
$$w = u \tan \delta_2 + v \tan \delta_2 \tan \Lambda_2; \text{ vertical wedge}$$

The axial corner is treated as a multiple-valued point to account for the vortical singularity that exists there. Although pressure is continuous, density and velocity are discontinuous.

The computational boundaries for both the internal and external corner flows are shown in figure 4. Region I corresponds to the uniform free stream, region II to the horizontal wedge flow, region III to the vertical wedge flow, and region IV represents the unknown conical flow. Regions I, II, and III are known flow regions and are hyperbolic zones in the cross-flow planes. Region IV is unknown and elliptic in the cross-flow plane. It is the determination of this region that is the crux of the present problem.

RESULTS

Numerical results for the internal corner flow problem are shown in figures 5-10. These results were computed by Kutler (ref. 6) and Shankar and Anderson (ref. 7).

Some of the most recently published experimental data obtained for the corner-flow problem are by West and Korkegi (ref. 8). They tested an equal wedge angle ($\delta_1 = \delta_2 = 9.49°$) configuration in Mach 2.98 flow over a Reynolds number range from 0.4×10^6 to 60×10^6, which included laminar, transitional, and turbulent boundary layers. A numerical solution for this same case was obtained, and the shock wave and slip surface structure are compared with the high Reynolds number experiment in figure 5.

The inviscid embedded shock is slightly concave when viewed from the origin falling inside the location of the corresponding experimental shock. The corner shock, which is slightly convexed when viewed from the origin, also falls inside the experimental shock. The positions of the experimental and numerical wedge shocks agree exactly. It appears, therefore, that the displacement effects of the boundary layer in the region bounded by the corner and embedded shocks result in an effective thickening of the body, and this forces the shock structure outward.

The location of the slip surfaces for this case can be found from plots of density and is shown as the thin double line in figure 5 stretching from the triple point to the origin. The slip surface is slightly curved and asymptotically approaches the bisector near the origin. The experimental shear layer is also curved but appears to merge before the origin is reached. Since the positions of the numerical and experimental triple points are different, the comparison between the inviscid slip surface and viscous shear layer, which originate at the triple points, is unfair. But, qualitatively, their basic shapes are the same.

A comparison of the numerical and experimental (turbulent boundary layer) surface pressures is shown in figure 6. The first pressure rise in

the experimental data (decreasing) indicates the onset of separation. This is followed by a reduced gradient region that indicates separation and again a rapid pressure rise that indicates reattachment. The pressure between the reattachment point and the origin is greater than that of the inviscid result. This higher pressure indicates an apparent thickening of the body in this region due to boundary-layer displacement effects.

Nangia (ref. 9) performed an experimental study on the wave interactions in supersonic intakes and obtained some rather interesting data. Figures 7-9 are numerical solutions which compare with Nangia's results. Figure 7 is a pressure contour plot for an unswept configuration with $\delta_1 = -5°$ and $\delta_2 = 7.5°$ for a Mach number of 3. It is interesting to note that the wave structure does not exhibit any corner shock or slip surfaces. This appears to be correct because changes through the expansion fan occur isentropically. However, an auxiliary compression wave is formed in the corner region. The wedge expansion fan, after the interaction with the wedge shock, turns away from the axial corner and is concave when viewed from the origin, whereas the wedge shock turns toward the axial corner and appears to be slightly convex.

The inviscid numerical wave structure compares very well with the experimental results of Nangia. The auxiliary compression fan in the corner region, as predicted by the numerical solution, is not observed in the experimental results, however.

A pressure contour plot for a $\Lambda = 30°$, $\delta_1 = 5°$, and $\delta_2 = 7.5°$ configuration at a Mach number of 3 is shown in figure 8. The numerical solution is again compared with the experimental data of Nangia. The computed surface-pressure distribution for both the horizontal and vertical wedges is compared with Nangia's experimental measurements in figure 9.

The final case considered on the internal corner problem consists of a $\Lambda = 30°$, $\delta_1 = -5°$, and $\delta_2 = 7.5°$ configuration at a Mach number of 3. The pressure contour plot of the numerical solution is shown in figure 10. The wedge expansion fan, after interacting with the wedge shock, turns away from the axial corner and appears to be concave when viewed from the origin. The intersecting wedge shock is deflected towards the axial corner under the influence of the wedge expansion fan. An auxiliary weak shock is formed in the corner region which merges with the weak embedded shock and forms a strong shock near the horizontal wedge surface. The shock impingement on this surface is nearer the axial corner than the wedge shock. The strength of the impinging shock appears to increase with increasing sweep angle. Furthermore, the interference region decreases as the sweep angle increases.

Numerical solutions for two external corner configurations were generated and are shown in figures 11-14. Results are presented for both the shock-capturing and shock-fitting techniques. Figure 11 shows the shock shape and cross-flow sonic line for an unswept equal-angled ($\delta_1 = \delta_2 = 10°$) configuration at a Mach number of 3. The surface-pressure distribution for this case compared to linear theory is shown in figure 12.

The shock and cross-flow sonic-line locations for a swept ($\Lambda_1 = \Lambda_2 = 30°$), equal wedge angle ($\delta_1 = \delta_2 = 10°$) configuration at Mach number 3 is

shown in figure 13. The shock-capturing results are almost identical to the shock-fitting solution. The surface pressure distribution for this configuration is shown figure 14, and again both the shock-capturing and shock-fitting results agree.

All of the numerical results presented here were obtained on serial machines but employed a numerical procedure which is particularly well suited for the parallel processing philosophy. Should the computing power of an ILLIAC IV be required for a more complicated problem, such as a multiple-corner configuration, some of the coding techniques used for the solutions presented here could easily be applied.

REFERENCES

1. MacCormack, R. W.: The Effect of Viscosity in Hypervelocity Impact Cratering. AIAA Paper 69-354, 1969.

2. Kutler, P., and Lomax, H.: Shock-Capturing, Finite Difference Approach to Supersonic Flows. J. of Spacecraft and Rockets, vol. 8, 1971, pp. 1175-1182.

3. Thomas, P. D., Vinokur, M., Bastianon, R., and Conti, R. J.: Numerical Solution for the Three-Dimensional Inviscid Supersonic Flow of a Blunt Delta Body. AIAA Jour., vol. 10, no. 7, July 1972, pp. 887-894.

4. Kutler, P., Reinhardt, W. A., and Warming, R. F.: Multishocked, Three-Dimensional Supersonic Flowfields with Real Gas Effects. AIAA Jour., vol. 11, no. 5, May 1973, pp. 657-664.

5. Kutler, P.: Computation of Three-Dimensional, Inviscid Supersonic Flows. Computational Methods in Fluid Dynamics, Lecture Notes in Physics, AGARD, 1975. (To be published.)

6. Kutler, P.: Supersonic Flow in the Corner Formed by Two Intersecting Wedges. AIAA Jour., vol. 12, 1974, pp. 577-578.

7. Shankar, V., and Anderson, D. A.: Numerical Solutions for Inviscid Supersonic Corner Flows. Final Report ISU-ERI-AMES-74090, May 1974.

8. West, J. E., and Korkegi, R. H.: Supersonic Interactions in the Corner of Intersecting Wedges at High Reynolds Numbers. AIAA Journal, vol. 10, May 1972, pp. 652-656.

9. Nangia, R. K.: Three-Dimensional Wave Interactions in Supersonic Intakes. Second International Symposium on Air Breathing Engines (Sheffield, United Kingdom), March 1974.

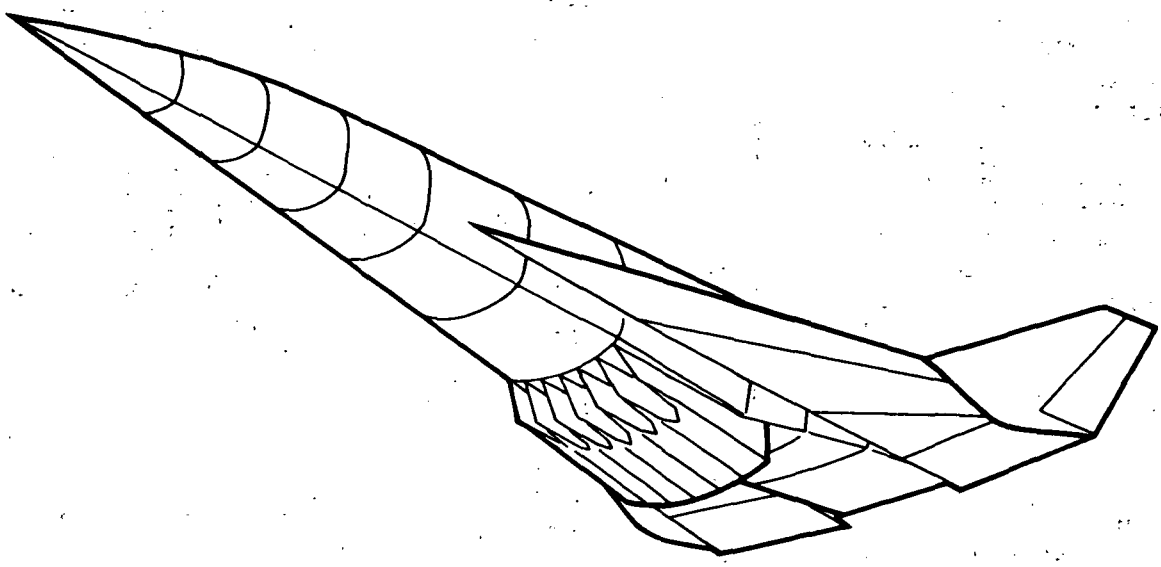

Fig. 1 Hypersonic airbreathing aircraft

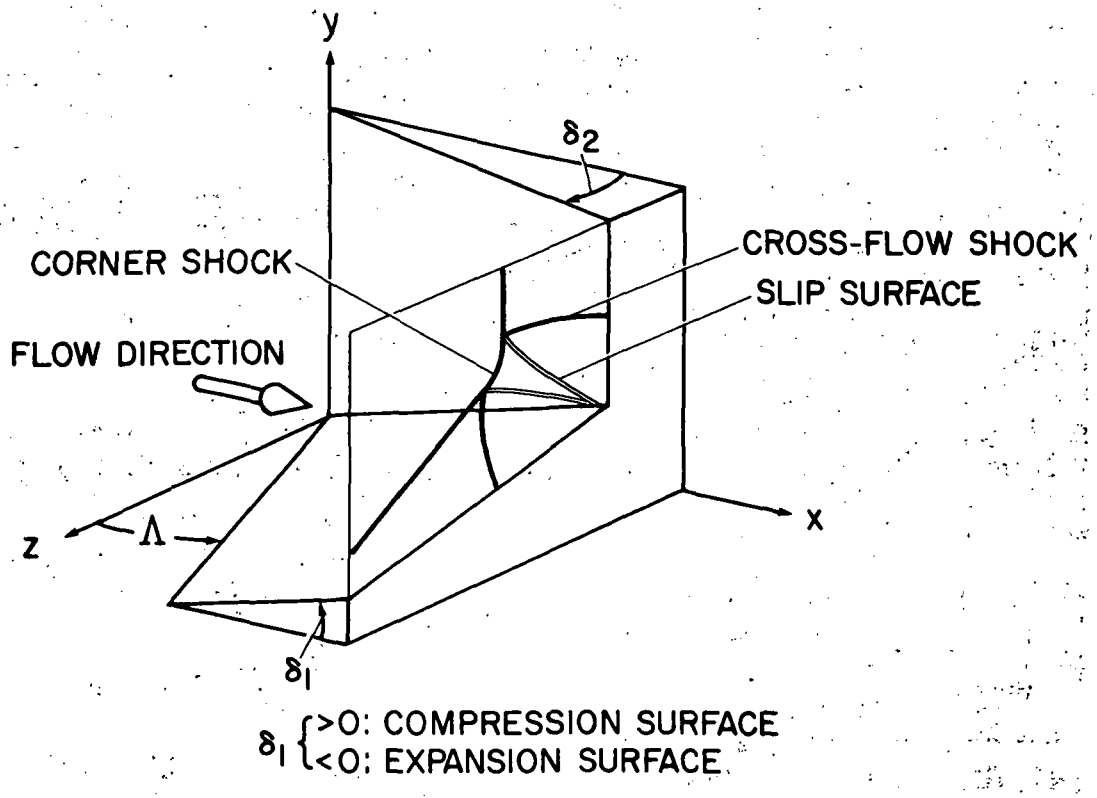

Fig. 2 Coordinate system and wave structure for internal axial corner.

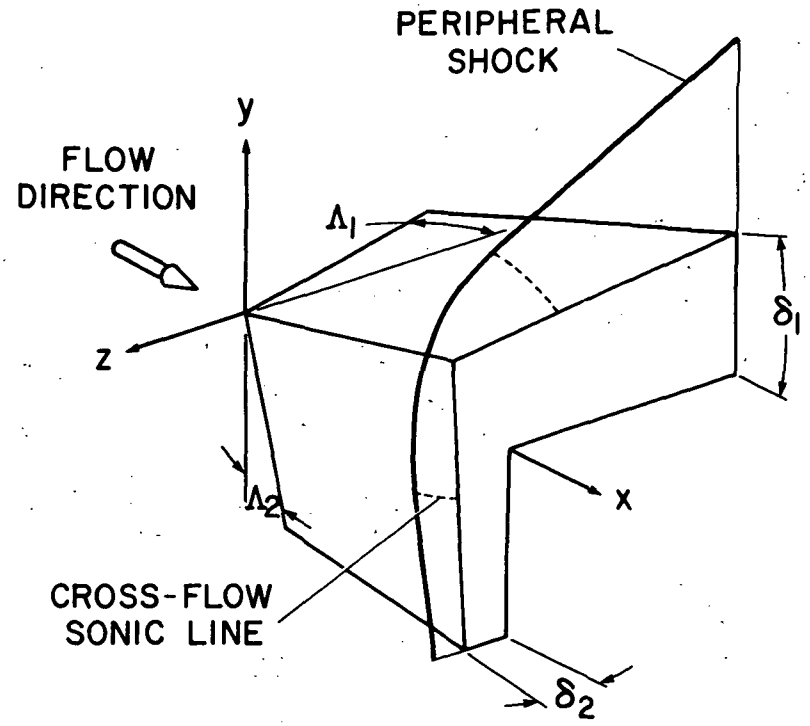

Fig. 3 Coordinate system and shock structure for external axial corner.

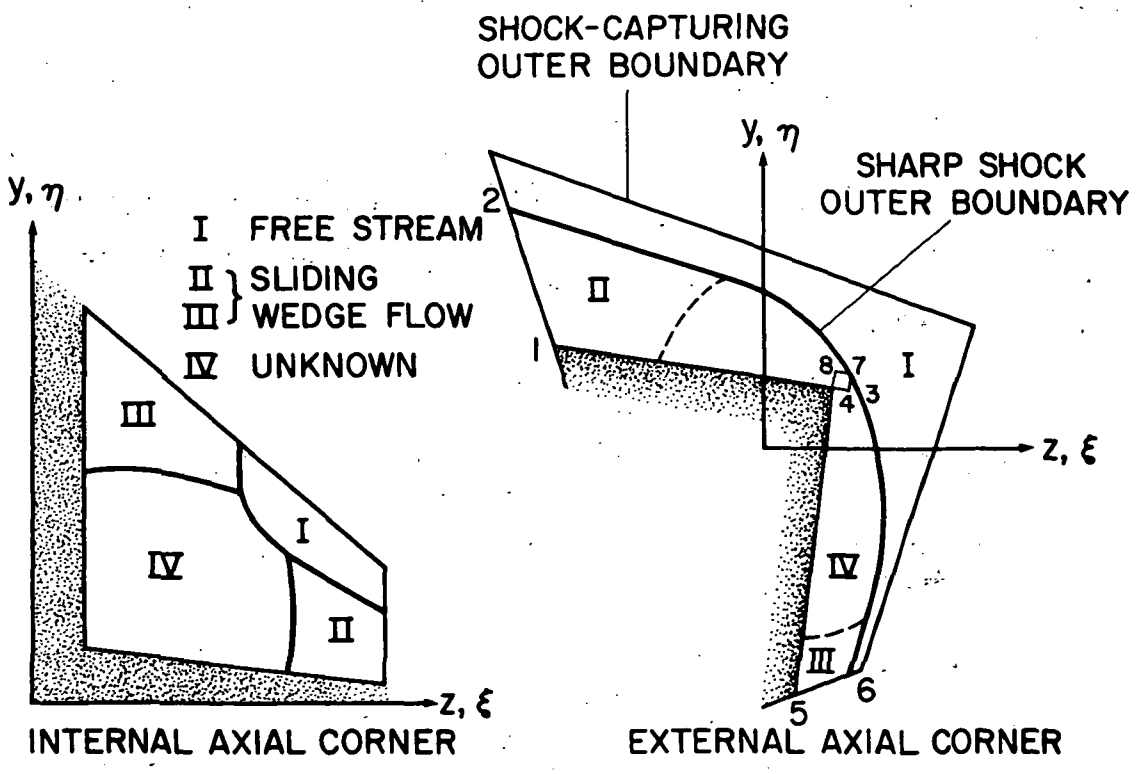

Fig. 4 Computational boundaries for internal and external axial corners.

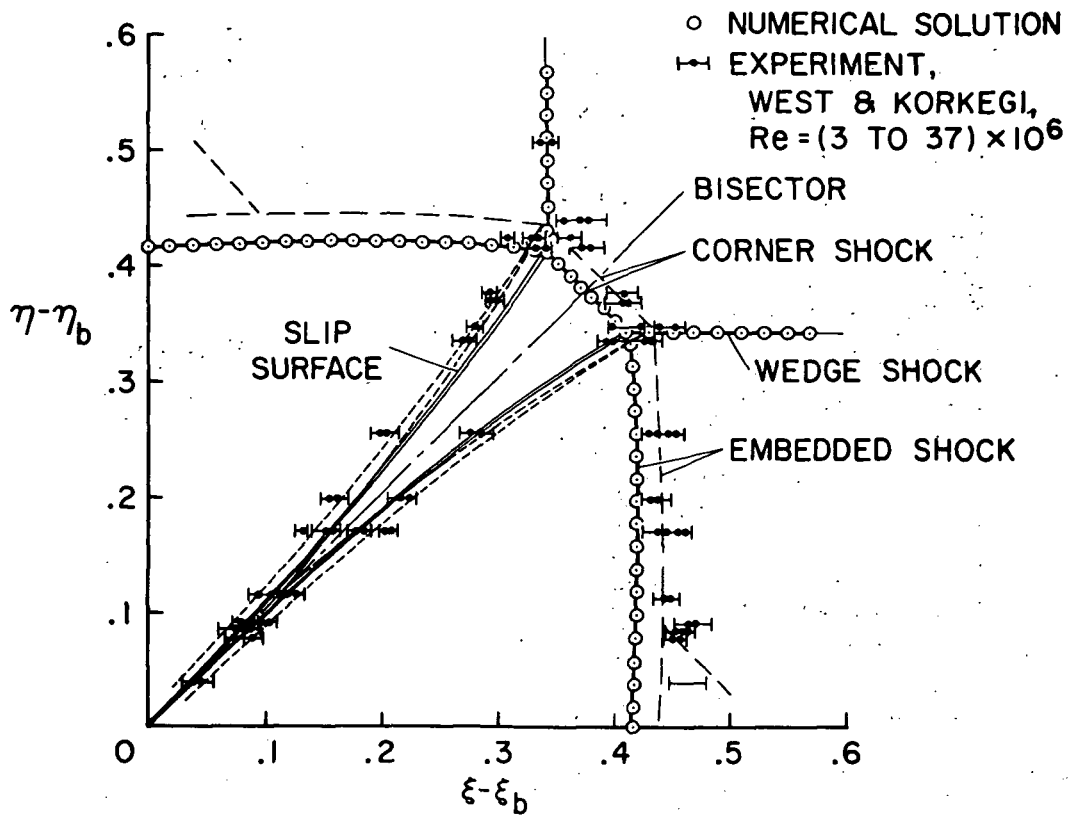

Fig. 5 Comparison of numerical and experimental shock patterns; M = 2.98, $\delta_1 = \delta_2 = 9.49°$.

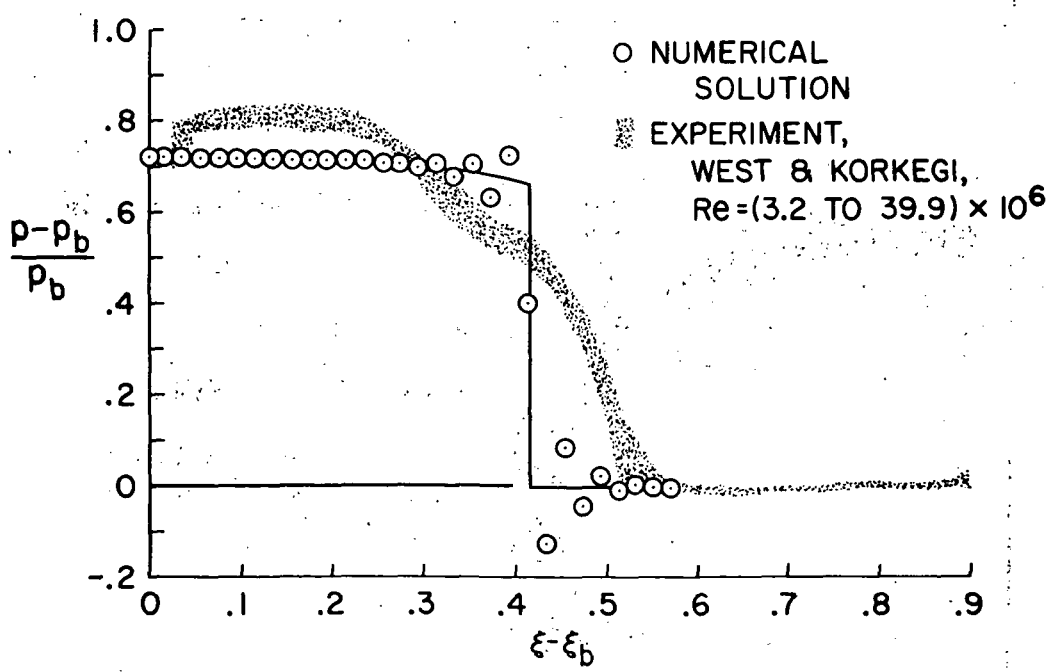

Fig. 6 Comparison of numerical and experimental surface-pressure distribution; M = 2.98, $\delta_1 = \delta_2 = 9.49$, $\Lambda = 0°$.

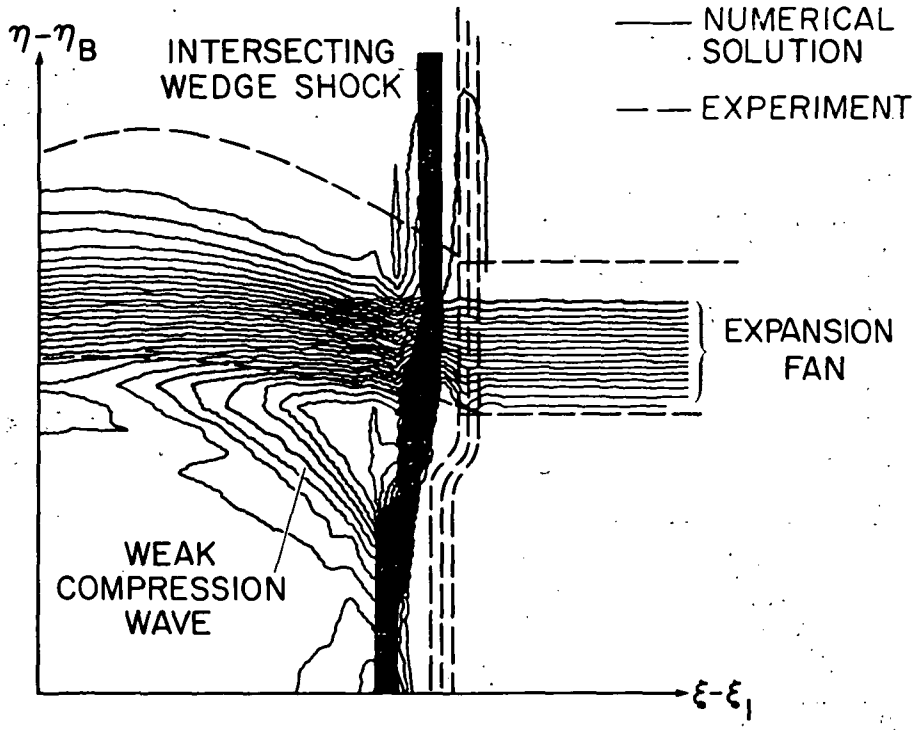

Fig. 7 Comparison of numerical and experimental wave structure; M = 3, $\delta_1 = -5°$, $\delta_2 = 7.5°$, $\Lambda = 0°$.

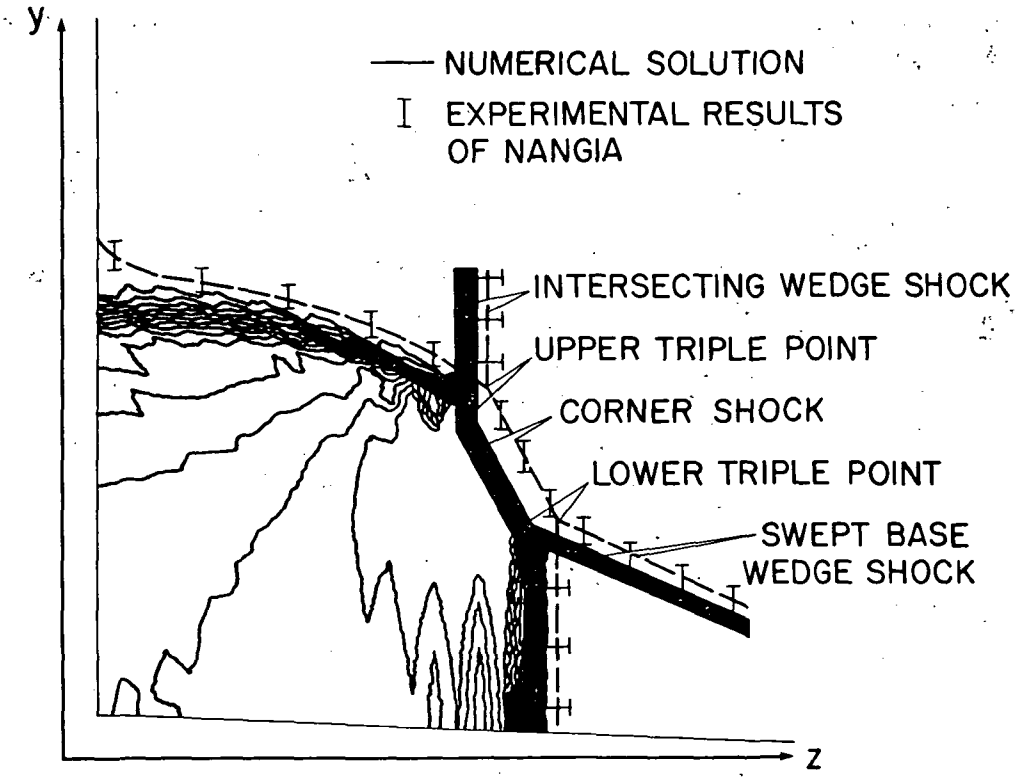

Fig. 8 Comparison of numerical and experimental shock structure; M = 3, $\delta_1 = 5°$, $\delta_2 = 7.5°$, $\Lambda = 30°$.

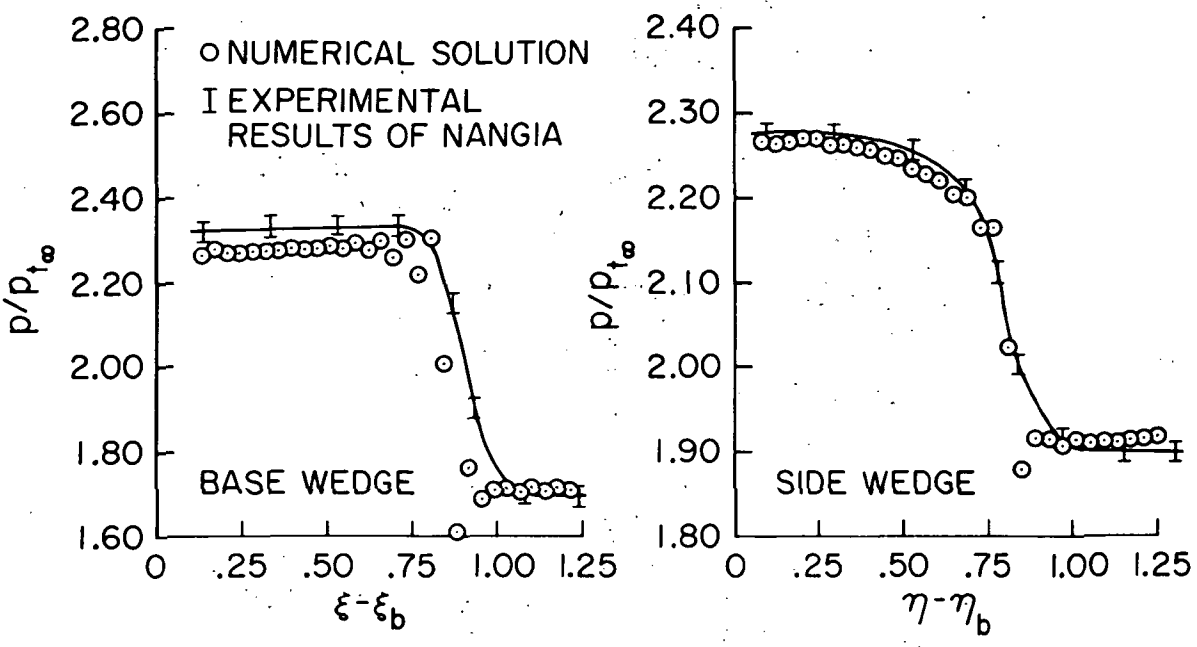

Fig. 9 Comparison of numerical and experimental surface-pressure distribution; M = 3, $\delta_1 = 5°$, $\delta_2 = 7.5°$, $\Lambda = 30°$.

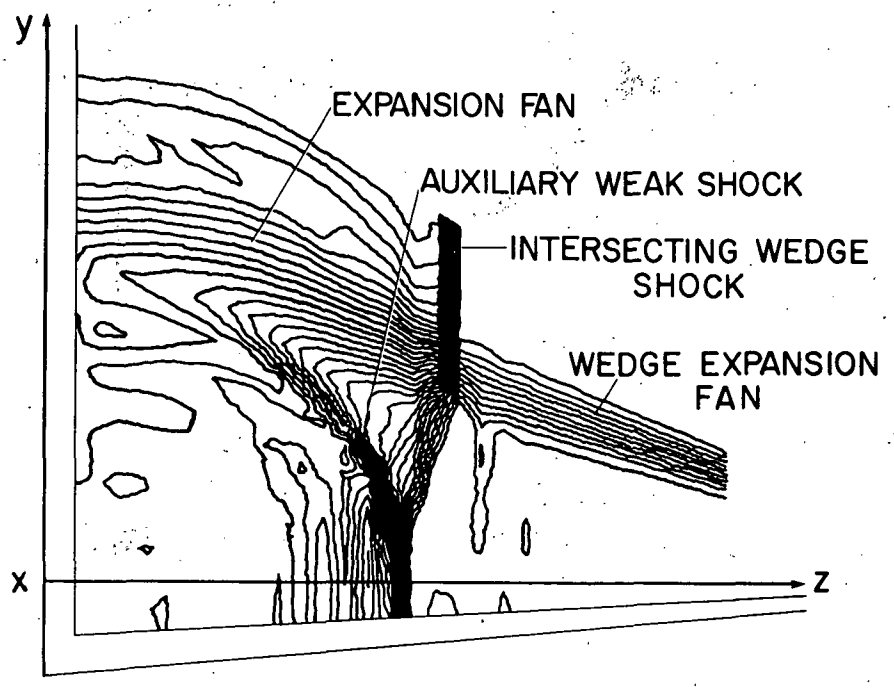

Fig. 10 Pressure contour plot of computational plane; M = 3, $\delta_1 = -5°$, $\delta_2 = 7.5°$, $\Lambda = 30°$.

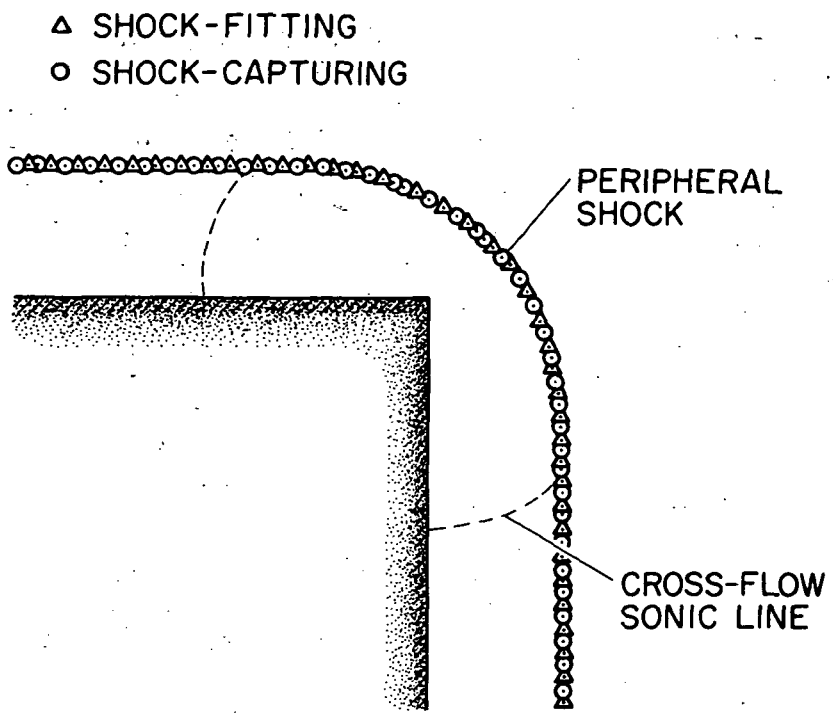

Fig. 11 Shock structure for symmetric external corner; M = 3, $\delta_1 = \delta_2 = 10°$, $\Lambda_1 = \Lambda_2 = 0°$.

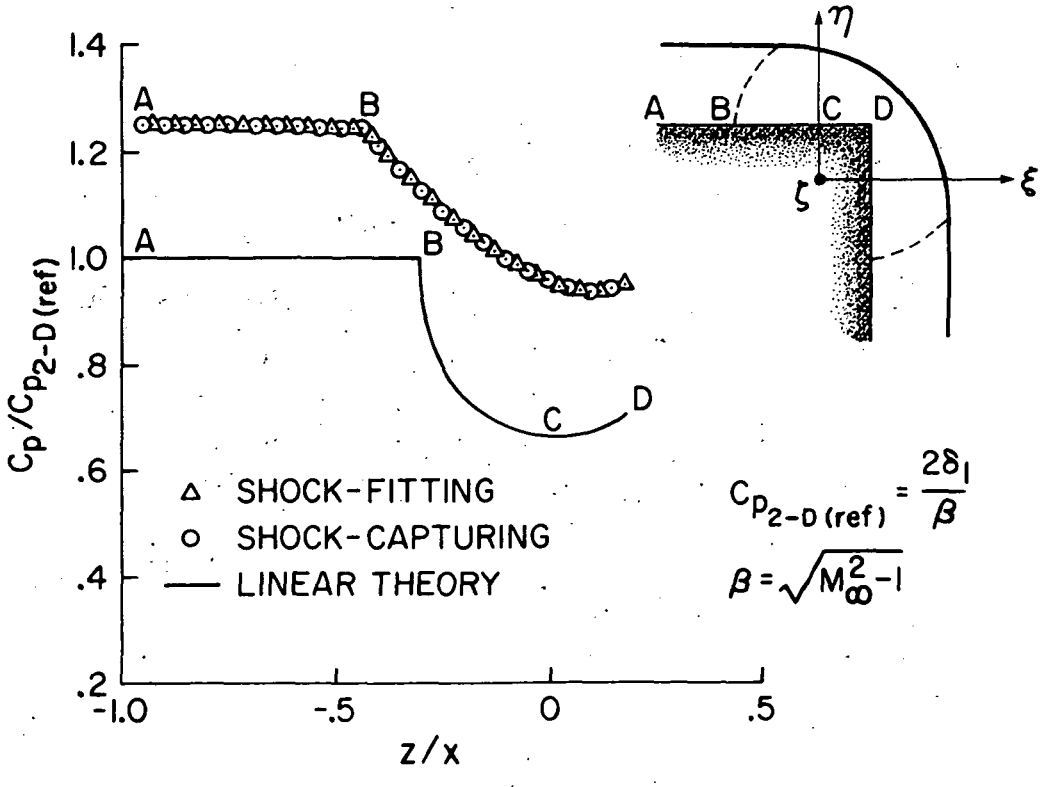

Fig. 12 Surface-pressure distribution for symmetric external corner; M = 3, $\delta_1 = \delta_2 = 10°$, $\Lambda_1 = \Lambda_2 = 0°$.

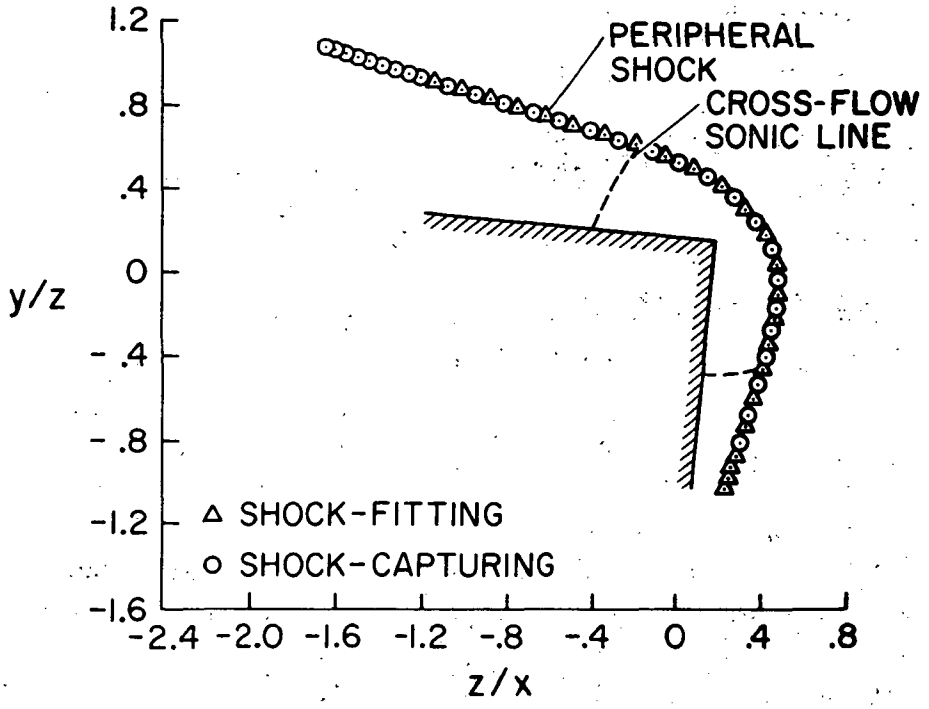

Fig. 13 Shock structure for swept external corner; M = 3, $\delta_1 = \delta_2 = 10°$, $\Lambda_1 = \Lambda_2 = 30°$.

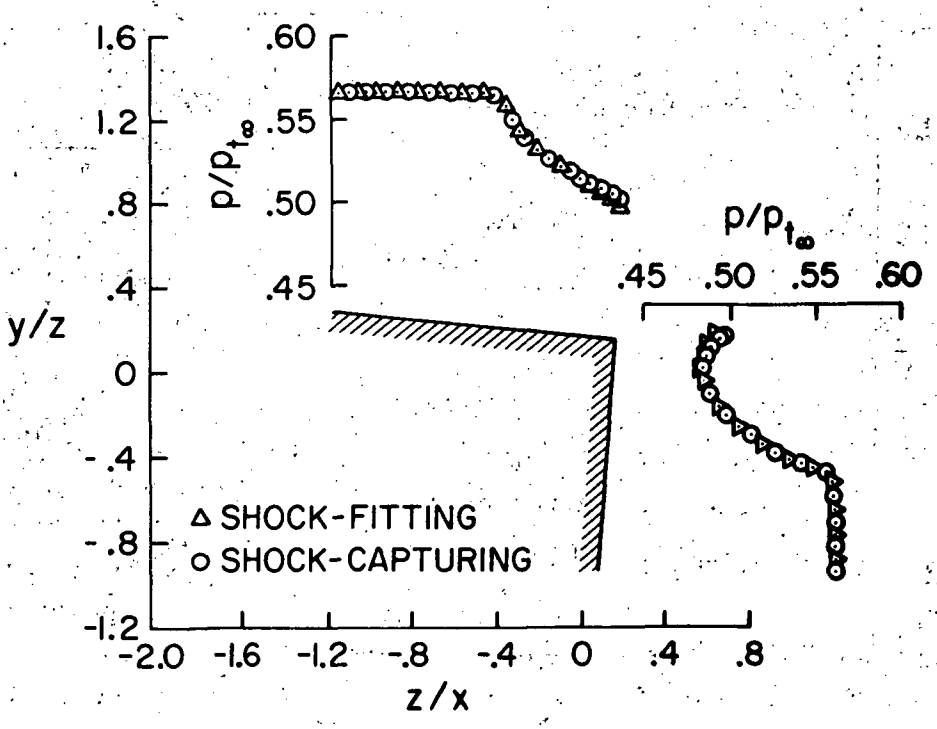

Fig. 14 Surface-pressure distribution for swept external corner; M = 3, $\delta_1 = \delta_2 = 10°$, $\Lambda_1 = \Lambda_2 = 30°$.

NUMERICAL METHODS FOR THE CALCULATION OF THREE-DIMENSIONAL NOZZLE EXHAUST FLOW FIELDS*

By Sanford M. Dash and Paul D. Del Guidice
Advanced Technology Laboratories, Inc.

SUMMARY

Two numerical codes have been developed for the calculation of three-dimensional nozzle exhaust flow fields associated with hypersonic airbreathing aircraft. Both codes employ reference plane grid networks with respect to three coordinate systems. Program CHAR3D is a characteristic code utilizing a new wave preserving network within the reference planes, while program BIGMAC is a finite difference code utilizing conservation variables and a one-sided difference algorithm. Secondary waves are numerically captured by both codes, while the underexpansion shock and plume boundary are treated discretely. The exhaust gas properties consist of hydrogen-air combustion product mixtures in local chemical equilibrium. Nozzle contours are treated by a newly developed geometry package based on dual cubic splines. Results are presented for simple configurations demonstrating two- and three-dimensional multiple wave interactions.

INTRODUCTION

Hypersonic aircraft with airbreathing propulsion will require a high degree of engine/airframe integration in order to achieve optimized performance. The engine exhaust flow, because of physical area limitations, will generally be underexpanded at the nozzle exit, and in order to obtain maximum propulsive efficiency, the vehicle afterbody undersurface is used to provide additional expansion. This results in a three-dimensional nozzle flow whose boundaries are defined both by the solid boundary of the nozzle wall and by the boundary separating the nozzle flow from the vehicle external flow. A typical exhaust nozzle (fig. 1) may be characterized as having nozzle modules with cross sections which are rectangular in shape. These nozzles may be arranged in multiples and discharge into a common nozzle. The flow fields to be analyzed start at the combustor exit and each module may be analyzed individually until its merger with adjacent modules and the external flow field.

*This research was performed under Contract No. NAS 1-12726.

In developing a numerical model for this flow field, the following dominant features must be accounted for:

(1) The flow properties at the combustor exit are highly nonuniform. Burning and mixing in the combustor yield regions of highly varying composition, temperature, and stagnation properties. In addition, shock waves are produced in the vicinity of the injectors. Although the strength of these waves decays rapidly as they propagate through the burner, they are generally present at the burner exit and must be accounted for.

(2) The exhaust gas mixture consists of hydrogen-air combustion products and significant burning may still occur in the initial regions of nozzle expansion.

(3) The flow field geometry is quite complex. The engine modules consist of multiple surfaces with sharp interior corners, and flow fences to contain the external exhaust flow may be present.

(4) The interior nozzle flow field is dominated by complex wave interactions with waves generated and reflected off multiple surfaces. In addition, sharp interior corner regions must be accounted for.

(5) The nozzle exhaust flow interacts with the nonuniform vehicle external flow field. This complex interaction for underexpanded exhaust flows results in an expansion system propagating toward the vehicle undersurface from the cowl trailing edge and a spanwise expansion generated by the sidewall interaction. An underexpansion shock propagates outward into the nonuniform vehicle external flow, and the exhaust and external flow are separated by a plume boundary. In addition, pressure and flow deflection mismatch between adjacent modules may occur, resulting in a spanwise multiple shock system.

To best accommodate highly rotational variable composition flow fields, a grid network which follows streamlines is preferred. For nonstreamline networks, large errors may be associated with streamline interpolation procedures for nonequilibrium flow calculations, as discussed by Sedney (ref. 1). For two-dimensional flow fields, a grid network following the flow streamlines is readily obtained. Such a system is employed in references 2 and 3 for the calculation of chemical reacting nozzle flow fields and supersonic combustor flow fields, employing a "viscous" characteristics technique. In this approach, a uniform marching step Δx is taken, new streamline grid points are obtained, and characteristic data are obtained by interpolation on the initial data line. Such a scheme can readily be extended to three dimensions via the reference plane approach. This approach involves the definition of a reference plane system in which the three-dimensional volume under consideration is spanned by an appropriately selected series of planes which intersect the boundaries of the considered volume. The equations of motion within the reference planes are expressed in a quasi-streamline coordinate system,

where quasi-streamlines are the projections of the actual stream surfaces onto these reference planes. Then, although the actual streamlines are not traced, streamline interpolation procedures are minimized.

In addition to minimizing streamline interpolation procedures, use of the reference plane approach has other distinct advantages. By developing the equations of motion with respect to different reference plane systems (Cartesian, cylindrical, and line source), complex geometric configurations may be analyzed. In figure 2(a), a reference plane network is depicted for a typical nozzle module, wherein the line source system shown alleviates the need for adding reference planes as the sidewall opens. The addition or deletion of reference planes is provided for automatically, based on their proximity to walls. A more complex situation is depicted in figure 2(b) for the flow field downstream of the modules. For this calculation, a combination of several systems is employed and provisions are included for automatic switching from one system to another as the character of the boundary surfaces changes. The reference plane system also caters to the usage of reference plane characteristics at all boundary points. This approach is generally recognized as the most accurate boundary calculational procedure (ref. 4). However, it proves cumbersome when employed in conjunction with nonreference plane networks due to the complex interpolation procedures then required.

The reference plane characteristic technique has been widely used for the calculation of three-dimensional supersonic flow fields, and the authors had previously developed a program employing this technique for the calculation of nozzle exhaust flow fields (refs. 5 and 6), which is in current usage at NASA Langley Research Center (refs. 7 and 8). That program, as well as most reference plane characteristic (refchar) codes in common usage (refs. 9 and 10), employs an inverse scheme wherein interpolations are performed to obtain data at the intersection of the quasi-characteristics with the initial data surface. Comparisons of such refchar codes with shock capturing finite difference codes (ref. 11) have led to the general conclusion that such difference codes are better able to analyze complex flow fields with multiple secondary shocks. From experience gained with the authors' original refchar code, it was felt that the inability to successfully analyze such flow fields was primarily due to the inverse interpolation procedures employed. Such procedures tend to ignore the presence of weak waves by allowing the quasi-characteristic lines to arbitrarily cross each other. The numerical diffusion associated with these interpolations can become significant, particularly when the local Courant number (ratio of overall marching step to local maximum allowable marching step) is much less than one. The smearing of these weak waves is enhanced by resorting to higher order interpolations on the initial data line.

To treat complex multiwave flow fields and still retain the advantages that reference plane methods afford, two new numerical codes have been developed. Program CHAR3D

is a refchar code which employs the wave preserving network depicted in figure 3(a) as compared to the standard inverse network of figure 3(b). This new network tends to preserve wave systems and secondary shock waves have been successfully captured with it with a minimum of smearing. In addition, CHAR3D employs a nonisentropic pressure-density relation along streamlines to calculate shock entropy losses and utilizes conservation variables in constructing derivatives normal to the reference plane. Program BIGMAC is a reference plane finite difference code utilizing a quasi-streamline grid in the reference planes as depicted in figure 3(c). BIGMAC captures shock waves via the use of conservation variables in conjunction with a one-sided difference algorithm.

SYMBOLS

a_e	equilibrium sound speed, ft/sec (m/sec)
C_v	specific heat at constant volume
E(k)	conservation variables (k = 1 to 6) defined in text (see eq. (1))
F(k)	conservation variables (k = 1 to 6) defined in text (see eq. (1))
G(k)	conservation variables (k = 1 to 6) defined in text (see eq. (1))
H(k)	conservation variables (k = 1 to 6) defined in text (see eq. (1))
H	stagnation enthalpy, ft^2/sec^2 (m^2/sec^2)
h	static enthalpy, ft^2/sec^2 (m^2/sec^2)
h_1,h_2,h_3	defined in text (see eq. (1))
I	index of data point in reference plane
J	index of reference plane
J_1,J_2	defined in text (see eq. (1))
K	index of marching step
M	Mach number in reference plane, q/a_e

$\hat{n}$	unit normal to surface
p	pressure, lb/ft^2 (N/m^2)
q	magnitude of velocity in reference plane, ft/sec (m/sec)
S	entropy, $ft^2/sec^2\text{-}^oR$ $(m^2/sec^2\text{-}K)$
T	temperature, ^oR (K)
$\vec{V}$	flow velocity vector
u	velocity component in marching direction in reference plane, ft/sec (m/sec)
v	velocity component normal to reference plane, ft/sec (m/sec)
w	velocity component in reference plane normal to marching direction, ft/sec (m/sec)
x,y,z	Cartesian coordinates
r,θ,z	line source coordinates
x,θ,r	cylindrical coordinates
Γ	equilibrium isentropic exponent
ρ	density, $slugs/ft^3$ (kg/m^3)
Φ	fuel-air equivalence ratio
ϕ	velocity direction in reference plane, rad
ψ	velocity direction with respect to reference planes, rad

Arrows over symbols denote vector quantities. Coordinate subscripts denote differentiation with respect to the coordinate.

GOVERNING EQUATIONS

Program BIGMAC

The equations of motion for the steady inviscid flow of a gas mixture in chemical equilibrium, written in conservation form with respect to the streamline reference plane system described, are:

$$\vec{E}_x + \vec{F}_y + \vec{G}_z + \vec{H} - \frac{h_1}{h_3}\frac{w}{u}\vec{E}_z - \frac{h_2}{h_3}\vec{F}_z \tan\alpha = 0 \tag{1}$$

where $\tan\alpha$ is $\partial z/\partial y$ at constant x and for $k = 1$ to 6

$$\vec{E}(k) = h_2h_3\begin{vmatrix} \rho u \\ P + \rho u^2 \\ \rho uv \\ \rho uw \\ \rho uH \\ \rho u\Phi \end{vmatrix} \qquad \vec{F}(k) = h_1h_3\begin{vmatrix} \rho v \\ \rho uv \\ P + \rho v^2 \\ \rho vw \\ \rho vH \\ \rho v\Phi \end{vmatrix}$$

$$\vec{G}(k) = h_1h_2\begin{vmatrix} \rho w \\ \rho uw \\ \rho vw \\ P + \rho w^2 \\ \rho wH \\ \rho w\Phi \end{vmatrix} \qquad \vec{H}(k) = \begin{vmatrix} 0 \\ -J_1h_3(P + \rho v^2) \\ (J_1h_3u + J_2h_1w)\rho v \\ -J_2h_1(P + \rho v^2) \\ 0 \\ 0 \end{vmatrix}$$

System	J_1	J_2	h_1	h_2	h_3
Cartesian	0	0	1	1	1
Line source	1	0	1	x	1
Cylindrical	0	1	1	z	1

Program CHAR3D

In nonconservation form, these equations (in continuous regions of the flow field) may be written

$$\left.\begin{aligned} &\nabla \cdot (\rho \vec{V}) = 0 \\ &\rho(\vec{V} \cdot \nabla)\vec{V} + \nabla P = 0 \\ &\vec{V} \cdot \nabla H = 0 \\ &\vec{V} \cdot \nabla \Phi = 0 \end{aligned}\right\} \tag{2}$$

The equations may be cast in characteristic form with respect to the reference plane systems described by writing the above equations in scalar form and transposing those terms not involving variations in the x- or z-direction onto the right side. Then, the left side is identical to the corresponding two-dimensional system in the X,Z plane. The equations in reference plane characteristic form (ref. 6) may be written:

Along

$$\lambda^{\pm} = \frac{dz}{dx} = \frac{M^2 \cos\phi \sin\phi \pm \beta}{M^2 \cos^2(\phi) - 1} \tag{3}$$

where $M^2 = \left(u^2 + w^2\right)/a_e^2$ and $\beta^2 = M^2 - 1$

$$d\phi \pm \frac{\beta}{\Gamma M^2} d(\ln P) = F^{\pm} d\tilde{x} \tag{4}$$

where

$$F^{\pm} = (\sin\phi - \lambda^{\pm} \cos\phi)\left[(\tan\psi)_y + \frac{\tan\psi}{\Gamma}(\ln P)_y\right]$$

$$- \phi_y \tan\psi (\cos\phi + \lambda^{\pm} \sin\phi) + \left(J_2 - \lambda^{\pm} J_1\right) \tan^2\psi$$

and

$$d\tilde{x} = \frac{dx}{z^{J_2}} + J_1 \, d(\ln x)$$

Along

$$\lambda_{SL} = \frac{dz}{dx} = \tan\phi \tag{5}$$

$$d(\tan\psi) = \frac{\tan\psi}{\Gamma M^2} d(\ln P) + G \, d\tilde{x} \tag{6}$$

where

$$G = \frac{-1}{\cos \phi}\left[\frac{(\ln P)_y}{\Gamma M^2} + \tan \psi \, (\tan \psi)_y + \tan \psi \left(1 + \tan^2 \psi\right)\left(J_1 \cos \phi + J_2 \sin \phi\right)\right]$$

The flow deflection angles ϕ and ψ, velocity components u, v, and w, and streamline and characteristic orientations $\lambda^{\pm}$ are shown in figure 4. A detailed description of orientations with respect to the various reference plane systems may be found in references 5 and 6.

CALCULATIONAL PROCEDURES

Interior Point Calculation

Properties are desired at the grid point $(\bar{I},J,K)$ shown in figure 4. The allowable step size Δx is determined by satisfying the CFL condition. For BIGMAC, this requires that the intersection of the Mach cone from $(\bar{I},J,K)$ with the initial data surface falls within the numerical domain as depicted (i.e., the quadrilateral (I,J+1), (I-1,J), (I,J-1), (I+1,J)). Note that the effective numerical domain for the characteristic calculation includes the points $I + 1$ and $I - 1$ on planes $J - 1$ and $J + 1$; hence, a larger step may be taken with CHAR3D $\left(\Delta x_{CHAR3D} \approx \sqrt{2}\, \Delta x_{BIGMAC}\right)$.

BIGMAC.- The MacCormack (ref. 12) scheme, used to difference equation (1), yields

$$\tilde{E}_{\bar{I},J} = E_{I,J} - 2\,\Delta x\left(F_y + G_z - \frac{h_1}{h_3}\frac{w}{u} E_z - \frac{h_2}{h_3} F_z \tan \alpha + \frac{H}{2}\right)_{I,J} \tag{7a}$$

where

$$\tan \alpha = \pm 2\left(\frac{z_{I,J\pm1} - z_{I,J}}{\Delta y_1 + \Delta y_2}\right)\left(\frac{\Delta y_1}{\Delta y_2}\right)^{\pm 1}\left(\frac{h_3}{h_2}\right)$$

$$\left.\frac{\partial f}{\partial y}\right|_{I,J} = \pm\left(\frac{f_{I,J\pm1} - f_{I,J}}{\Delta y_1 + \Delta y_2}\right)\left(\frac{\Delta y_1}{\Delta y_2}\right)^{\pm 1}$$

$$\left.\frac{\partial f}{\partial z}\right|_{I,J} = \pm\left(\frac{f_{I\pm1,J} - f_{I,J}}{\Delta z_1 + \Delta z_2}\right)\left(\frac{\Delta z_1}{\Delta z_2}\right)^{\pm 1}$$

$$\Delta y_1 = y_{I,J} - y_{I,J-1} \qquad \Delta y_2 = y_{I,J+1} - y_{I,J}$$

$$\Delta z_1 = z_{I,J} - z_{I-1,J} \qquad \Delta z_2 = z_{I+1,J} - z_{I,J}$$

for any variable f and

$$E_{\bar{I},J} = \frac{1}{2}\left\{\left(\tilde{E}_{\bar{I},J} + E_{I,J}\right) - 2\,\Delta x\left[\tilde{F}_y + \tilde{G}_z - \frac{h_1}{h_3}\left(\frac{\tilde{w}}{u}\right)\tilde{E}_z - \frac{h_2}{h_3}\tilde{F}_z \tan\tilde{\alpha} + \frac{\tilde{H}}{2}\right]_{\bar{I},J}\right\} \tag{7b}$$

where

$$\tan\tilde{\alpha} = \mp 2\left(\frac{\tilde{z}_{I,J\mp1} - \tilde{z}_{I,J}}{\Delta y_1 + \Delta y_2}\right)\left(\frac{\Delta y_2}{\Delta y_1}\right)^{\pm 1}\left(\frac{h_3}{h_2}\right)$$

$$\left.\frac{\partial\tilde{f}}{\partial y}\right|_{\bar{I},J} = \mp\left(\frac{\tilde{f}_{I,J\mp1} - \tilde{f}_{I,J}}{\Delta y_1 + \Delta y_2}\right)\left(\frac{\Delta y_2}{\Delta y_1}\right)^{\pm 1}$$

$$\left.\frac{\partial\tilde{f}}{\partial z}\right|_{\bar{I},J} = \mp\left(\frac{\tilde{f}_{I\mp1,J} - \tilde{f}_{I,J}}{\Delta\tilde{z}_1 + \Delta\tilde{z}_2}\right)\left(\frac{\Delta\tilde{z}_2}{\Delta z_1}\right)^{\pm 1}$$

$$\tilde{z}_{\bar{I},J} = z_{I,J} + \left(\frac{h_1}{h_3}\frac{w}{u}\right)_{I,J}\Delta x$$

$$z_{\bar{I},J} = z_{I,J} + \frac{1}{2}\left[\left(\frac{h_1}{h_3}\frac{w}{u}\right)_{I,J} + \left(\frac{\tilde{h_1}}{h_3}\frac{\tilde{w}}{u}\right)_{\bar{I},J}\right]\Delta x$$

The physical variables are obtained by the following iterative procedure. A value of u is assumed. Then,

$$\rho = E(1)/u \tag{8a}$$

$$P = E(2) - E(1)\,u \tag{8b}$$

$$v = E(3)/E(1) \tag{8c}$$

$$w = E(4)/E(1) \tag{8d}$$

$$H = E(5)/E(1) \tag{8e}$$

$$\Phi = E(6)/E(1) \tag{8f}$$

$$h = H - \frac{1}{2}\left(u^2 + v^2 + w^2\right) \tag{8g}$$

The following three parameter curve fits (based on data from ref. 13) are incorporated into this code and are described in detail in the appendix of reference 6.

$$h = h(P,\Phi,T) \tag{9a}$$

$$\rho = \rho(P,\Phi,T) \tag{9b}$$

$$\Gamma = \Gamma(P,\Phi,T) \tag{9c}$$

The value of h obtained in equation (8g) yields T via an inversion of equation (9a). Equation (9b) yields an alternate value of the density compared to that obtained in equation 8(a). The value of u is perturbed and the procedure repeated until the two values of density agree to within a specified tolerance.

CHAR3D.- Point $\bar{I}$ in figure 5 is located along the quasi-streamline by the relation

$$z_{\bar{I},J} = z_{I,J} + \left(a \tan \phi_{I,J} + b \tan \phi_{\bar{I},J}\right) \Delta x$$

where $a = 1$, $b = 0$ in the predictor step and $a = \frac{1}{2}$, $b = \frac{1}{2}$ in the corrector step. In this new wave preserving network, the calculation proceeds upward from the lower boundary where points $(\bar{I}-1,J)$ are calculated for all reference planes J to second order prior to calculating points $(\bar{I},J)$. In addition to the standard initial data array (the points (I,J)), an extra array $(\hat{I},J)$ is required. To calculate properties at $(\bar{I},J)$, the standard initial data grid in the reference plane $(I-1,J)$, (I,J), and $(I+1,J)$ is employed to calculate the forcing function terms involving derivatives normal to the reference planes. Properties are known at points H_1, G_1, and $\bar{I} - 1$ from the calculation of point $(\bar{I}-1,J)$ to second order.

Point A is located between H_1 and G_1 on the quasi-characteristic $\lambda^+(A\bar{I})$ where $\lambda^{\pm}$ is defined in equation (3). All properties (including forcing functions) are

obtained via linear interpolation[1] between H_1 and G_1. Then, H_2 is located between $\hat{I}$ and $I+1$ such that the downrunning quasi-characteristic from G_2 (or B) passes through $(\bar{I},J)$. To first order, properties at $(\bar{I},J)$ are calculated using points B and A, where P_B and ϕ_B are determined using compatibility relations (eq. (4)) along IB and H_2B.

Then $P_{\bar{I}}$ and $\phi_{\bar{I}}$ are calculated employing the compatibility relations

$$\left.\begin{aligned}
&(\phi_{\bar{I}} - \phi_A) + \left[a\left(\frac{\beta}{\Gamma M^2}\right)_A + b\left(\frac{\beta}{\Gamma M^2}\right)_{\bar{I}}\right] \ln\left(\frac{P_{\bar{I}}}{P_A}\right) = \left(aF_A^+ + bF_{\bar{I}}^+\right)\Delta\tilde{x}_{\bar{I}A} \\
&\text{and} \\
&(\phi_{\bar{I}} - \phi_B) - \left[a\left(\frac{\beta}{\Gamma M^2}\right)_B + b\left(\frac{\beta}{\Gamma M^2}\right)_{\bar{I}}\right] \ln\left(\frac{P_{\bar{I}}}{P_B}\right) = \left(aF_B^- + bF_{\bar{I}}^-\right)\Delta\tilde{x}_{\bar{I}B}
\end{aligned}\right\} \quad (10)$$

Remaining properties are determined at $\bar{I}$ via the following streamline relations:

$$(\tan\psi)_{\bar{I}} = (\tan\psi)_{\bar{I}} + \left[a\left(\frac{\tan\psi}{\Gamma M^2}\right)_I + b\left(\frac{\tan\psi}{\Gamma M^2}\right)_{\bar{I}}\right] \ln\left(\frac{P_{\bar{I}}}{P_I}\right) + \left(aG_I + bG_{\bar{I}}\right)\Delta\tilde{x}_{I\bar{I}} \quad (11)$$

$$H_{\bar{I}} = H_I - \left[a\left(\frac{\tan\psi}{\cos\phi}H_y\right)_I + b\left(\frac{\tan\psi}{\cos\phi}H_y\right)_{\bar{I}}\right]\Delta\tilde{x}_{I\bar{I}} \quad (12)$$

$$\phi_{\bar{I}} = \phi_I - \left[a\left(\frac{\tan\psi}{\cos\phi}\Phi_y\right)_I + b\left(\frac{\tan\psi}{\cos\phi}\Phi_y\right)_{\bar{I}}\right]\Delta\tilde{x}_{I\bar{I}} \quad (13)$$

and in continuous regions of the flow

$$\left(P/\rho^\Gamma\right)_{\bar{I}} = \left(P/\rho^\Gamma\right)_I - \left\{a\left[\frac{\tan\psi}{\cos\phi}\left(P/\rho^\Gamma\right)_y\right]_I + b\left[\frac{\tan\psi}{\cos\phi}\left(P/\rho^\Gamma\right)_y\right]_{\bar{I}}\right\}\Delta x_{I\bar{I}} \quad (14)$$

---

[1]Linear interpolation along a characteristic line calculated to second order is consistent to second order. (See appendix.)

The flow velocity is obtained via the relation

$$V_{\bar{I}} = \sqrt{2}\left[H_{\bar{I}} - h\left(P_{\bar{I}}, \Phi_{\bar{I}}, T_{\bar{I}}\right)\right]^{1/2} \tag{15}$$

where $T_{\bar{I}}$ is obtained via an inversion of equation (9b) (with $\rho_{\bar{I}}$, $P_{\bar{I}}$, and $\Phi_{\bar{I}}$ known) and $h_{\bar{I}}$ is obtained employing equation (9a). Then, $\Gamma_{\bar{I}}$ is obtained from equation (9c) and $a_e^2 = \Gamma_{\bar{I}} P_{\bar{I}}/\rho_{\bar{I}}$.

This calculation is performed for points $\bar{I}$ in <u>all</u> reference planes to first order. Then, cross derivatives $\partial/\partial y$ are evaluated at $\bar{I}$ employing the relation

$$\left(\frac{\partial f}{\partial y}\right)_{x,z} = \left(\frac{\partial f}{\partial y}\right)_{x,\eta} - \tan\alpha \left(\frac{\partial f}{\partial z}\right)_{x,y} \tag{16}$$

where

$$\left(\frac{\partial f}{\partial y}\right)_{x,\eta} = \frac{f_{\bar{I},J+1}\left(\frac{\Delta y_1}{\Delta y_2}\right) + f_{\bar{I},J}\left(\frac{\Delta y_2}{\Delta y_1} - \frac{\Delta y_1}{\Delta y_2}\right) - f_{\bar{I},J-1}\left(\frac{\Delta y_2}{\Delta y_1}\right)}{\left(\Delta y_1 + \Delta y_2\right)}$$

$$\Delta y_1 = y_{\bar{I},J} - y_{\bar{I},J-1} \qquad \Delta y_2 = y_{\bar{I},J+1} - y_{\bar{I},J}$$

$$\tan\alpha = \left(\frac{\partial z}{\partial y}\right)_{x,\eta}$$

$$\left(\frac{\partial f}{\partial z}\right)_{x,y} = \frac{f_{\bar{I},J} - f_{\bar{I}-1,J}}{z_{\bar{I},J} - z_{\bar{I}-1,J}}$$

Derivatives are made the same way at the initial station I, except here $\partial f/\partial z$ is evaluated by

$$\left(\frac{\partial f}{\partial z}\right)_{x,y} = \frac{f_{I+1,J} - f_{I,J}}{z_{I+1,J} - z_{I,J}}$$

CHAR3D, in addition to the centered difference algorithm described above, has the option of evaluating cross derivatives via an alternating one-sided difference algorithm. For this option, derivatives are evaluated as described in the section for BIGMAC. Cross

derivatives are required for the variables P, ϕ, ψ, H, Φ, and P/ρ^{Γ}. In evaluating cross derivatives for P, ϕ, and ψ, conservation variables are employed as follows:

$$\left.\begin{aligned} P_y &= F(3)_y - F(1)\, v_y - v\, F(1)_y \\ \phi_y &= \frac{w_y \cos\phi - u_y \sin\phi}{q} \\ (\tan\psi)_y &= \frac{q v_y - (u u_y + w w_y)\tan\psi}{q^2} \end{aligned}\right\} \tag{17}$$

where

$$u = q\cos\phi \qquad w = q\sin\phi \qquad v = q\tan\psi$$

$$q^2 = u^2 + w^2$$

and

$$\left.\begin{aligned} v_y &= \frac{E(3)_y - v\, E(1)_y}{E(1)} \\ u_y &= \frac{E(2)_y - h_2 h_3 P_y - u\, E(1)_y}{E(1)} \\ w_y &= \frac{E(4)_y - w\, E(1)_y}{E(1)} \end{aligned}\right\} \tag{18}$$

The conservation variables $E(k)$ and $F(k)$ are given by equation (1). The use of conservation variables in construction of these cross derivatives tends to suppress oscillations that occur when employing physical variables to difference across shock waves. However, the use of a one-sided difference algorithm in conjunction with CHAR3D tends to produce spurious results in regions of large cross flow.

In the characteristic reference plane algorithm, cross flow variations are expressed via the forcing function terms $F^{\pm}$ appearing in the right side of the compatibility relations (eq. (4)). These terms are assumed to vary mildly within an integration step. When a one-sided algorithm is employed to evaluate cross derivatives in the vicinity of shocks, the values of the forcing function terms may vary greatly between the predictor and corrector steps. In addition, the numerical domain of dependence is somewhat vague for the characteristic reference plane approach in conjunction with one-sided differences, so that

part of the problem may be due to stability. The recommended approach for evaluating cross derivatives in CHAR3D is to employ conservation variables in conjunction with a centered difference algorithm, although this matter requires further study.

In CHAR3D, secondary shocks are captured as rapid changes spread over approximately three grid points. These discontinuities are preserved by use of the wave network described which performs all interpolations off quasi-characteristic surfaces. The entropy change associated with these shocks is evaluated employing a nonisentropic pressure-density relation (illustrated here for a perfect gas)

$$\vec{V} \cdot \nabla \ln \left(P/\rho^{\Gamma}\right) = \vec{V} \cdot \frac{\nabla S}{C_v} \tag{19}$$

For a shock of strength ξ (pressure ratio across shock), this change is determined employing the relation (for perfect gas)

$$\frac{\Delta S}{C_v} = \ln \xi - \Gamma \ln \left[\frac{(\Gamma + 1)\xi + (\Gamma - 1)}{(\Gamma - 1)\xi + (\Gamma + 1)}\right] \tag{20}$$

where ΔS is the entropy change along a streamline produced by the captured shock. This relation involves only the pressure distribution in the vicinity of the shock and is readily applied in regions of noninteracting shocks as follows. Let

$$F(\xi,\Gamma) = \frac{(\Gamma + 1)\xi + (\Gamma - 1)}{(\Gamma - 1)\xi + (\Gamma + 1)}$$

Assume a shock is spread over the marching interval $K = 1$ to 6 (fig. 6) for a typical quasi-streamline. Then 1 represents free stream conditions for this shock. The entropy change in the interval $K - 1$ to K is then expressed by

$$\left(\frac{\Delta S}{C_v}\right)_{K-1,K} = \left(\frac{\Delta S}{C_v}\right)_{1,K} - \left(\frac{\Delta S}{C_v}\right)_{1,K-1} = \ln \left[\frac{\xi_{1,K}}{\xi_{1,K-1}} \left(\frac{F_{1,K-1}}{F_{1,K}}\right)^{\Gamma}\right]$$

where

$$\xi_{1,K} = P_K/P_1$$

Then

$$\left(P/\rho^{\Gamma}\right)_K = \left[\left(P/\rho^{\Gamma}\right)_{K-1} - \frac{\tan \psi}{\cos \phi} \left(P/\rho^{\Gamma}\right)_y \Delta\tilde{x}_{K-1,K}\right] \exp \left(\frac{\Delta S}{C_v}\right)_{K-1,K}$$

Since the shock geometry does not appear in the entropy jump relation, the entropy rise associated with extremely complex three-dimensional shocks can be accurately obtained. Special provisions have been incorporated into the program for the computation of singular points at the juncture of intersecting shock waves and/or shock reflection points. At such points the streamline undergoes a discontinuous pressure rise corresponding to that through both shock waves. If the shock intensities are different, an entropy discontinuity occurs separating the different zones, and a vortex of infinite intensity results. Numerically, the entropy procedure described would predict an entropy rise associated with this pressure jump. Theoretically, this occurs in the limit of vanishing mass flow, while numerically the finite mass within this region would lead to unduly large entropy levels. Special coding has been incorporated at such singular points to suppress these "numerical" peaks.

Wall Point Calculation

Solid surfaces are prescribed via discrete contour data and fitted via a newly developed method based on the use of partial cubic splines (ref. 14). The surface fitting is done by a separate geometry package and the array of coefficients generated is stored on tape. BIGMAC and CHAR3D employ this coefficient data in conjunction with a surface interpolation procedure yielding highly accurate values of the dependent variable and surface unit normal.

In both BIGMAC and CHAR3D, wall point calculations are performed employing a reference plane characteristic calculation. In figure 7, CD is the intersection of the reference plane $y = y_C$ with the surface $z = f(x,y)$. Reference planes are oriented so that the surface normal lies nearly within the reference plane. For sidewall calculations, this is accomplished via local coordinate rotations.

In CHAR3D, P_C, ϕ_C, and ψ_C are evaluated utilizing the characteristic compatibility relation (eq. (4)) along BC, the normal momentum equation (eq. (6)) along the streamline projection CD^*, and the relation $\vec{V} \cdot \hat{n} = 0$ applied at C, which yield the relation

$$\sin \phi_C = (f_x)_C \cos \phi_C + (f_y)_C \tan \psi_C \tag{21}$$

The compatibility equation yields a relation between P_C and ϕ_C, and the normal momentum equation yields a relation between P_C and ψ_C. This system is solved in the context of the wave preserving network previously described by a simple iterative procedure.

In BIGMAC, this iterative procedure is eliminated by combining the normal momentum equation with the quasi-streamline momentum equation, yielding the following system of equations for P_C, $(w/u)_C$, and $(v/u)_C$:

$$\begin{vmatrix} (\rho u^2/\beta P)_{BC} & \pm 1 & 0 \\ 1 & 0 & -(f_y)_C \\ (\tan\psi \sin\phi)_{CD^*} & \left(\frac{P \tan\psi \cos\phi}{\rho u^2}\right)_{CD^*} & -1 \end{vmatrix} \begin{vmatrix} (w/u)_C \\ \ln P_C \\ (v/u)_C \end{vmatrix} = \begin{vmatrix} R_1 \\ R_2 \\ R_3 \end{vmatrix} \qquad (22)$$

where

$$R_1 = -\frac{1}{\beta P h_1 h_2 h_3}\left[(\lambda^{\pm} u - w)A - \lambda^{\pm} B + C\right]_{BC} \Delta x \pm \ln P_B + \left(\frac{\rho u^2}{\beta P}\right)_{BC}\left(\frac{w}{u}\right)_B$$

$$R_2 = (f_x)_C$$

$$R_3 = \frac{1}{\rho u^2 h_1 h_2 h_3}\left[E_{SL} - \tan\psi\,(B\cos\phi + C\sin\phi)\right]_{CD^*} \Delta x$$

and

$$A = h_1 h_3\left(\frac{v P_y}{a_e^2} + \rho v_y\right) + J_1 \frac{E(1)}{h_2} + J_2 \frac{G(1)}{h_2}$$

$$B = F(2)_y - u\,F(1)_y - J_1 \frac{v\,F(1)}{h_1}$$

$$C = F(4)_y - w\,F(1)_y - J_2 \frac{v\,F(1)}{h_3}$$

$$E_{SL} = F(3)_y - v\,F(1)_y + J_1 \frac{F(2)}{h_1} + J_2 \frac{F(4)}{h_3}$$

Then, relations applied along the streamline projection CD^* yield remaining flow variables at C, in conjunction with the equilibrium curve fits (eq. (9)), for both programs. The process is then repeated with coefficients averaged for second order accuracy.

Interior Corner

Interior corners occur in the internal modules and are discretely treated as the intersection of specified surfaces, as depicted in figure 8. A detailed description of these corner calculations with respect to the various reference plane coordinate systems may be found in reference 6. The procedure is outlined here for a Cartesian system where the intersecting surfaces are prescribed by $z = f(x,y)$ and $y = g(x,z)$.

The relation $\vec{V} \cdot \hat{n} = 0$ applied to both intersecting surfaces at C (the point to be calculated) yields the flow deflection angles ϕ_C and ψ_C explicitly

$$\left.\begin{aligned} \phi_C &= \tan^{-1}\left(\frac{f_x + g_x f_y}{1 - g_z f_y}\right) \\ \psi_C &= \tan^{-1}\left(\cos\phi_C \frac{g_x + f_x g_z}{1 - f_y g_z}\right) \end{aligned}\right\} \tag{23}$$

Then, a redundant procedure is employed wherein reference plane calculations for the pressure at C are performed in the reference planes $z = z_C$ and $y = y_C$. This yields two values of pressure P_{C_1} and P_{C_2} which differ due to evaluating the cross derivative forcing function terms in the compatibility relations via backward differences. A weighting of these pressures is performed by accounting for the relative wave strengths in each of these reference planes. This gives the stronger weighting to the calculation performed in the reference plane containing the dominant waves via the relation

$$P_C = \frac{\Delta\psi_{A_1C}}{\Delta\psi_{A_1C} + \Delta\phi_{A_2C}} P_{C_1} + \frac{\Delta\phi_{A_2C}}{\Delta\psi_{A_1C} + \Delta\phi_{A_2C}} P_{C_2} \tag{24}$$

Streamline relations are performed along the corner CD, and the process is repeated for second order accuracy.

Shock Point Calculation

A discrete three-dimensional shock point calculation is performed for the nozzle underexpansion shock, which propagates into the nonuniform external stream surrounding the vehicle. In figure 9, subscript 2 refers to the shock free stream. Shock geometry is defined in terms of the direction cosines of α and β, where β is the angle made by the shock cut with the reference plane and α is the crosscut angle. For given values of α and β, the shock normal is

$$\hat{n}_S = \hat{i}_X \cos\alpha \sin\beta - \hat{i}_Y \sin\alpha + \hat{i}_Z \cos\alpha \cos\beta \tag{25}$$

where $\hat{i}_X, \hat{i}_Y, \hat{i}_Z$ are the unit vectors in the x-, y-, and z-directions. The characteristic relations on the free stream side yield flow properties at C_2. The Hugoniot relations in a shock normal system yield properties at C_1. The compatibility relation along A_1C_1 yields an alternate value of pressure $P^*_{C_1}$. The angle β is perturbed locally until P_{C_1} from the jump relations equals $P^*_{C_1}$ from the compatibility relations to within a specified tolerance. This procedure is performed in all reference planes, and the process is then repeated using updated values of the crosscut angle α. The complete details of this procedure including rotation into the shock oriented system, jump relations, and iterative procedures may be found in references 5 and 6.

Contact Surface Calculation

A three-dimensional contact surface is significantly more complex than its two-dimensional counterpart, since the streamlines on each side of the discontinuity not only differ in velocity magnitude but also may be highly skewed with respect to each other. In figure 10, α and β are as previously defined for the shock calculation, and the streamlines passing through C emanate from D_1 on the lower side and D_2 on the upper side. Hence, discontinuities exist in the flow angles ϕ and ψ at point C. The boundary relation $\vec{V} \cdot \hat{n} = 0$ applied at C_1 and C_2 yields the relations

$$\left.\begin{aligned} \sin\left(\beta - \phi_{C_1}\right) + \tan\alpha \tan\psi_{C_1} = 0 \\ \sin\left(\beta - \phi_{C_2}\right) + \tan\alpha \tan\psi_{C_2} = 0 \end{aligned}\right\} \tag{26}$$

Then, characteristic compatibility relations may be applied along A_1C_1 and B_2C_2 yielding $P_{C_1} - \phi_{C_1}$ and $P_{C_2} - \phi_{C_2}$ relations. The normal momentum relations applied along the streamline projections $C_1D_1^*$ and $C_2D_2^*$ yield relations between $P_{C_1} - \psi_{C_1}$ and $P_{C_2} - \psi_{C_2}$. For a given value of the crosscut angle α, a value of β is obtained via an iterative process satisfying the above relations and the boundary condition $P_{C_1} = P_{C_2}$. This procedure is performed in all reference planes and repeated with updated values of the crosscut angle α. Again, complete details may be found in references 5 and 6.

RESULTS

Internal corners represent just one segment of the overall boundary calculational procedure and hence must be calculated as part of the overall marching procedure.

Recently, inviscid corner flow fields have been studied in detail (refs. 15 and 16) utilizing conical coordinates in a timelike marching procedure until conical invariance was achieved. While these schemes do yield the flow field details in the corner region, they are not applicable to general three-dimensional flow problems which are nonconical.

Corner results are presented using the general interior corner point calculation outlined above and previously described in references 5 and 6. Results for a 5^{o} double expansion corner are depicted in figures 11 and 12. These results were obtained with CHAR3D starting from uniform initial flow conditions $(P_{\infty} = 845, \quad M_{\infty} = 2.94, \quad \phi = \psi = 0)$ with an 11×11 Cartesian grid. Results are shown after nine axial marching steps and the axial pressure variation at the corner is also indicated. Similar results have been obtained with BIGMAC.

An expansion-compression has been calculated using BIGMAC which yielded the results depicted in figure 13. These results were obtained with an 11×11 Cartesian grid for initially uniform flow $(M_{\infty} = 2)$ and are depicted after 10 axial marching steps. Results are compared with the detailed solution of Shankar (ref. 16) and the experimental results of Nangia (ref. 17).

Results for the double compression corner, as obtained by BIGMAC, are shown in figure 14 after 35 axial marching steps. A 12×12 line source network was employed with initially uniform flow at $M_{\infty} = 3.17$. A comparison is made with Shankar's numerical results (ref. 16) and the experimental results of Charwat and Redekeopp (ref. 18).

The above results verify the accuracy and validity of the interior corner procedure employed and, hence, yield credibility to the application of this procedure for general corner calculations within "truly" three-dimensional flow fields.

To demonstrate results obtainable with the new wave preserving network of CHAR3D, a simple two-dimensional inlet flow field is calculated. Calculation was performed with a uniform equally spaced initial profile ($P = 845$, $M = 2.94$) employing 11 and 21 grid points. Wall pressures are depicted in figures 15 and 16 for three shock reflections. After the fourth reflection, the flow on the upper boundary is subsonic, and thus the program could not calculate past this region. Note that both the pressures obtained as well as the propagation rates are in excellent agreement with the exact solution and no additional smearing results from wall reflections.

A complex internal module flow field calculation (square nozzle) as depicted in figure 17 has been performed using BIGMAC. This flow field is characterized by the initial interactions of expansion waves emanating from mutually perpendicular surfaces and the subsequent interaction of enveloping shock systems generated by recompression on the upper wall and sidewall. This calculation employed a 21×11 Cartesian network, with

additional reference planes being inserted as the sidewall opened. At the straight section the final network was 21×18. Uniform flow properties $(P_\infty = 845, \ M_\infty = 2.94)$ were stipulated at the nozzle entrance. Pressure contours on the symmetry plane are depicted in figure 18. Of particular interest is the intersection of four three-dimensional shock surfaces at $x \approx 17$ and $z = y = 0$. This results from the reflection of the envelope shock produced by the sidewall and the reflection of the envelope shock produced by the upper wall, resulting in an approximate 15/1 pressure ratio at this location. The axial pressure variation along the corner is depicted in figure 19 and pressure variations along several streamlines in the symmetry plane are depicted in figure 20.

All results presented employed a perfect gas option with $\Gamma = 1.4$ for the sake of simplicity. The equilibrium option has been extensively used and tested (refs. 5, 6, 7, and 8) and provides no further insight into these problems. The results were all obtained with relatively crude grid networks, yet provided accurate and detailed flow field results. Further grid refinement would yield somewhat better flow resolution, if desired or necessary. It should be noted that due to the use of disc storage techniques, as employed in both programs, flow field resolution is not limited by machine core storage.

CONCLUDING REMARKS

Two new computer codes have been developed for analyzing complex three-dimensional supersonic flow fields. Their use of a quasi-streamline network in conjunction with a reference plane grid allows for the calculation of complex geometric configurations and caters to highly rotational, variable composition flow fields. Both BIGMAC and CHAR3D are currently running internal flow codes with perfect gas or equilibrium hydrogen-air chemistry options.

CHAR3D employs a totally new grid network which caters to both the following of streamlines and the preservation of wave systems. This is done in conjunction with an axial marching procedure. Hence, in addition to its application to three-dimensional reference plane systems, it is equally applicable to "viscous" characteristic techniques, since forcing functions are also employed.

BIGMAC employs the commonly used MacCormack algorithm in conjunction with conservation variables and hence falls in the general classification of finite difference shock capturing codes. However, it does this in conjunction with a reference plane streamline grid which provides significant advantages for the flow fields treated.

Both programs treat complex three-dimensional flow fields accurately, locating secondary shock waves and evaluating flow field properties in their vicinity including wall and interior flow entropy. From our limited experience with these codes, CHAR3D appears best suited to flow fields wherein the predominant wave propagation occurs within

the reference planes. For such flow fields, CHAR3D with half the grid points yields results comparable to those of BIGMAC. In addition, no overshoots occur in the vicinity of shock waves and a larger marching step may be taken. However, when the assumption of a mildly varying forcing function is violated (i.e., in the vicinity of strong crosswise compressions) BIGMAC would be the preferred code. This program has no preferential direction and has been shown capable of calculating arbitrary multishocked three-dimensional flow fields.

Our current effort is devoted to extending both these codes for the calculation of the flow field downstream of the engine modules. This calculation is performed in the authors' previous code and similar procedures will be incorporated. Future efforts will involve the incorporation of finite-rate hydrogen-air chemistry, frozen chemistry, and associated sudden freezing criterion. In addition, the extension of these codes to mixing calculations along the plume interface is anticipated.

It should be noted that while the calculation of nozzle exhaust flow fields has been specifically discussed, both codes are capable of analyzing quite general three-dimensional flow fields. Results to date indicate that these techniques yield minimum smearing of captured shocks, even after multiple reflections and/or intersections. Thus, these codes appear capable of calculating inlet type flow fields and can readily be modified to calculate the simpler problem of external supersonic flows.

APPENDIX

LINEAR INTERPOLATION ON CHARACTERISTIC

A SECOND ORDER PROCEDURE

In previous reference plane characteristic codes (employing inverse interpolation procedures), data are interpolated on a noncharacteristic surface. To achieve full second order accuracy, most codes resort to higher order interpolation procedures. Such procedures are helpful in smooth regions of the flow field but are detrimental in regions of weak discontinuities. In such regions, linear interpolation is more accurate as explicitly discussed by Sedney (ref. 1). The authors had performed an independent study (unpublished) on such higher order interpolation procedures and concluded that for general multiwave flow fields, linear interpolations provide the most accurate results.

Now, with this new "wave preserving" network, all interpolations are performed on characteristic lines. Employing a linear interpolation procedure on a characteristic line calculated to second order is consistent with a second order algorithm. This point can be inferred from Ferri's article (ref. 19) but apparently, is not universally accepted. (See ref. 1.) Hence, a simple proof of this statement is presented.

Along any line AC, a series expansion for the pressure and flow deflection are written

$$P_C = P_A + (P_x)_A \Delta x + (P_{xx})_A (\Delta x)^2/2 + 0 (\Delta x)^3 \tag{A1}$$

$$\phi_C = \phi_A + (\phi_x)_A \Delta x + (\phi_{xx})_A (\Delta x)^2/2 + 0 (\Delta x)^3 \tag{A2}$$

but

$$(P_x)_C = (P_x)_A + (P_{xx})_A \Delta x + 0 (\Delta x)^2 \tag{A3}$$

$$(\phi_x)_C = (\phi_x)_A + (\phi_{xx})_A \Delta x + 0 (\Delta x)^2 \tag{A4}$$

where x denotes distance along AC.

Substituting equation (A3) into equation (A1) and equation (A4) into equation (A2) results in

$$P_C = P_A + \left[(P_x)_A + (P_x)_C\right] (\Delta x/2) + 0 (\Delta x)^3 \tag{A5}$$

$$\phi_C = \phi_A + \left[(\phi_x)_A + (\phi_x)_C\right] (\Delta x/2) + 0 (\Delta x)^3 \tag{A6}$$

The previous expressions are valid along any line AC. Assuming that AC is a down-running characteristic, the compatibility relations at points A and C are

$$(\phi_x)_A - A_A(P_x)_A = 0 \tag{A7}$$

$$(\phi_x)_C - A_C(P_x)_C = 0 \tag{A8}$$

where

$$A = \frac{\beta}{\Gamma M^2 P}$$

Solving the system of equations (A5) to (A8) for $(P_x)_A + (P_x)_C$ results in

$$(P_x)_A = \frac{-2}{\Delta x(A_C - A_A)}\left[(\phi_C - \phi_A) - A_C(P_C - P_A)\right] \tag{A9}$$

and

$$(P_x)_C = \frac{2}{\Delta x(A_C - A_A)}\left[(\phi_C - \phi_A) - A_A(P_C - P_A)\right] \tag{A10}$$

Now consider a point x^* between A and C. The pressure at this point to second order is given by

$$P^* = P_A + (P_x)_A(x^* - x_A) + \frac{(P_x)_C - (P_x)_A}{\Delta x_{AC}}(x^* - x_A)^2 + 0\,(\Delta x)^3 \tag{A11}$$

where $(P_x)_A$ and $(P_x)_C$ are given by equations (A9) and (A10). Up to this point, all relations are quite general and have not required that a second order compatibility relation exist between A and C. We now make use of this relation by stating that by second order, we imply that the relation

$$(\phi_C - \phi_A) - \left(\frac{A_A + A_C}{2}\right)(P_C - P_A) = 0 \tag{A12}$$

is satisfied between points A and C in a convergent fashion as detailed in reference 19. Then, substituting equation (A12) into equations (A9) and (A10) results in

$$(P_x)_C - (P_x)_A = 0 \tag{A13}$$

and

$$(P_x)_A = \frac{P_C - P_A}{x_C - x_A} \tag{A14}$$

Hence, substituting these relations into equation (A11) yields

$$P^* = P_A + (P_C - P_A)\left(\frac{x^* - x_A}{x_C - x_A}\right) + 0\,(\Delta x)^3$$

which clearly demonstrates that a linear interpolation for pressure (or flow deflection) on a characteristic calculated to second order is consistent with a fully second order approach.

REFERENCES

1. Sedney, R.: The Method of Characteristics. Nonequilibrium Flows, Part II, Marcel Dekker Inc., New York (1970).

2. Dash, S.: An Analysis of Internal Supersonic Flows With Diffusion, Dissipation and Hydrogen-Air Combustion. NASA CR-111783, 1970.

3. Dash, S.; and Del Guidice, P.: Analysis of Supersonic Combustion Flow Fields With Embedded Subsonic Regions. NASA CR-112223, 1972.

4. Abett, M. J.: Boundary Condition Calculational Procedures for Inviscid Supersonic Flow Fields. AIAA Computational Fluid Dynamics Conference Proceedings, July 1973.

5. Dash, S.; and Del Guidice, P.: Three Dimensional Nozzle Exhaust Flow Field Analysis by a Reference Plane Technique. AIAA Paper No. 72-704, June 1972.

6. Dash, S.; and Del Guidice, P.: Analysis and Design of Three-Dimensional Supersonic Nozzles, Vol. I. NASA CR-132350, 1972.

7. Edwards, C. L. W.; Small, W. J.; and Weidner, J. P.: Studies of Scramjet/Airframe Integration Techniques for Hypersonic Aircraft. AIAA Paper No. 75-58, Jan. 1975.

8. Small, W. J.; Weidner, J. P.; and Johnston, P. J.: Scramjet Nozzle Design and Analysis as Applied to a Highly Integrated Research Airplane. NASA TM X-71972, 1974.

9. Rakich, J. V.: Three-Dimensional Flow Calculation by the Method of Characteristics. AIAA J., vol. 5, no. 10, 1967.

10. Katskova, O. N.; and Chuskin, P. I.: Three-Dimensional Supersonic Equilibrium Flow of Gas Around Bodies at Angles of Attack. NASA TT F-9790, 1965.

11. Rakich, J. V.; and Kutler, P.: Comparison of Characteristics and Shock Capturing Methods With Application to the Space Shuttle Vehicle. AIAA Paper No. 72-191, Jan. 1972.

12. MacCormack, R. W.: The Effect of Viscosity in Hypervelocity Impact Cratering. AIAA Paper No. 69-354, 1969.

13. Barnes, B.; McIntyre, R. W.; and Sims, J. A.: Properties of Air and Combustion Products With Kerosine and Hydrogen Fuels. Published by Bristol Siddley Engines Ltd. on behalf of Group for Aerospace R&D, 1967.

14. Dash, S.; and Kalben, P.: Three-Dimensional Surface Representation and Interpolation Procedures Employing Cubic Spline Functions. ATL TR-193, Jan. 1974.

15. Kutler, P.: Supersonic Flow in the Corner Formed by Two Intersecting Wedges. AIAA J., vol. 12, no. 5, May 1974.

16. Shankar, V. S. V.: Numerical Solutions for Inviscid Supersonic Corner Flows. AIAA Paper No. 75-221, Jan. 1975.

17. Nangia, P. K.: Three-Dimensional Wave Interactions in Supersonic Intakes. 2nd Int. Symposium on Air Breathing Engines, Sheffield, England, Mar. 1974.

18. Charwat, A. F.; and Redekeopp, L. G.: Supersonic Interference Flow Along the Corner of Intersecting Wedges. AIAA J., vol. 5, no. 3, Mar. 1967.

19. Ferri, A.: The Method of Characteristics. Section G of The General Theory of High Speed Aerodynamics, Vol. VI of Princeton Series, Princeton University Press, 1954.

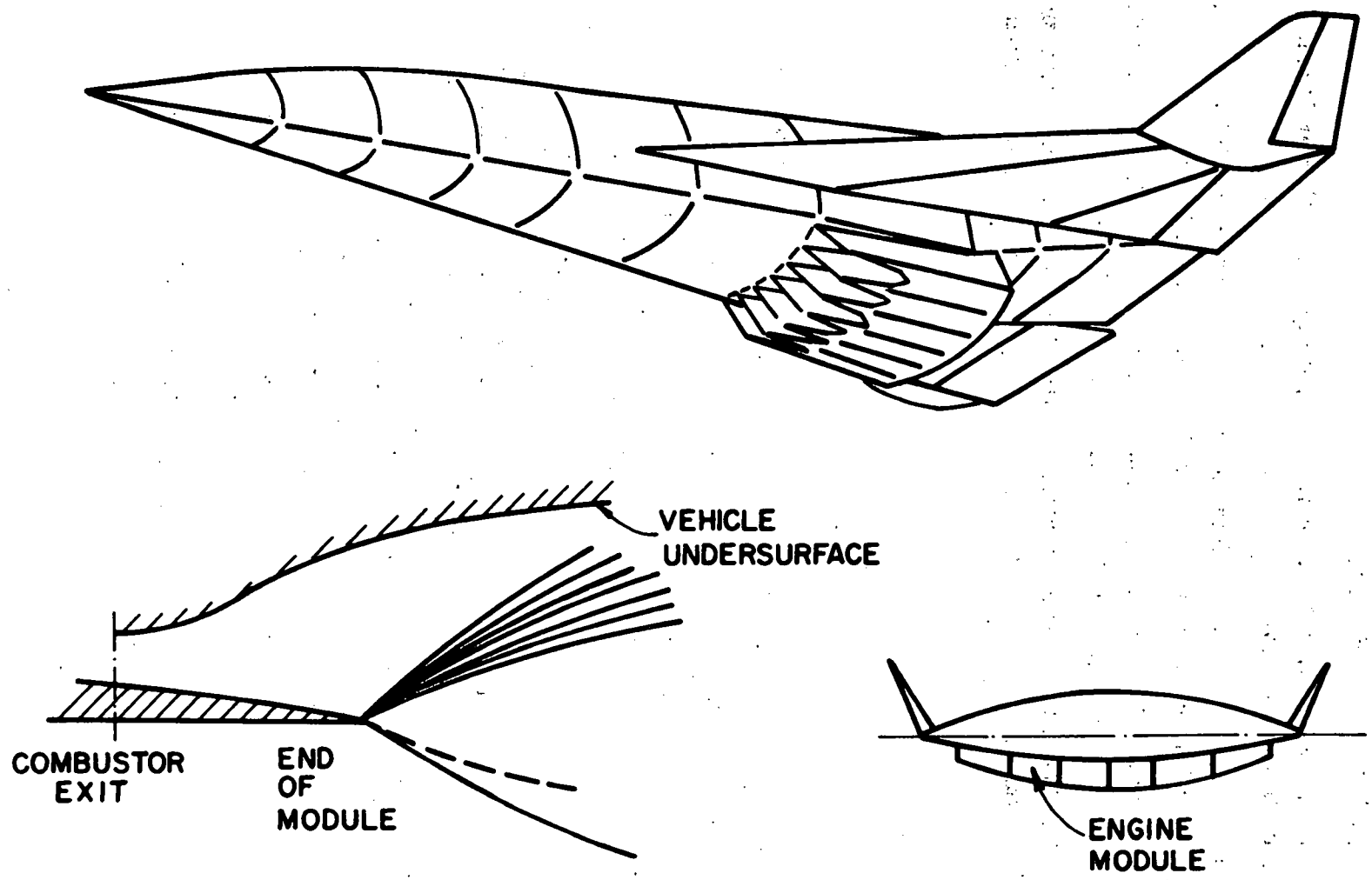

Figure 1.- Hypersonic research airplane.

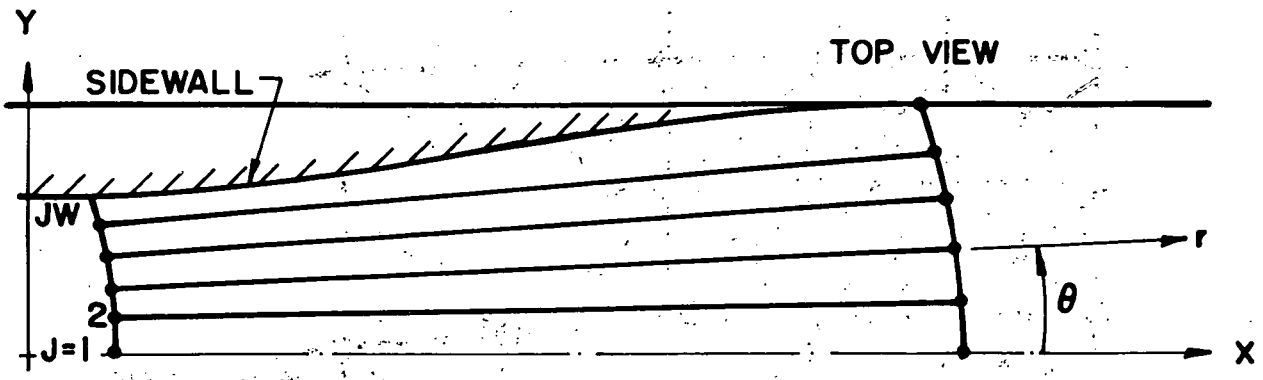

(a) In line source system for internal nozzle module. JW designates sidewall.

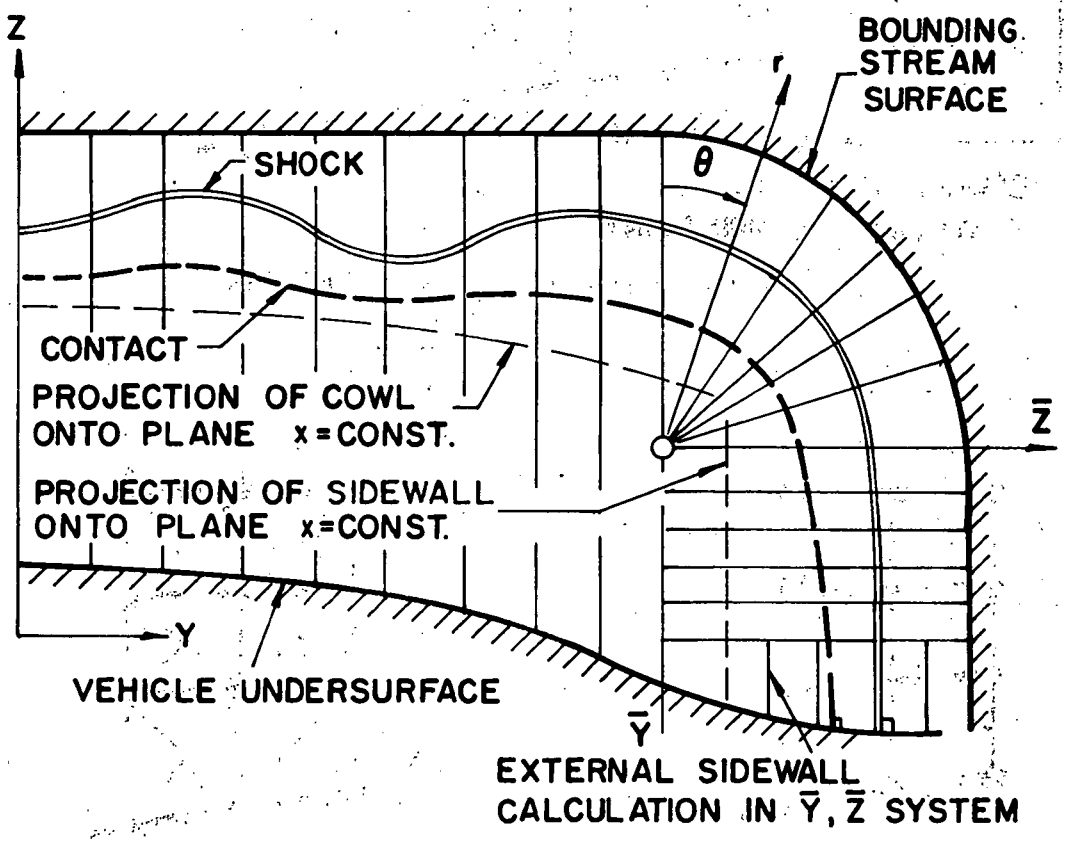

(b) Downstream of modules.

Figure 2.- Reference plane configuration.

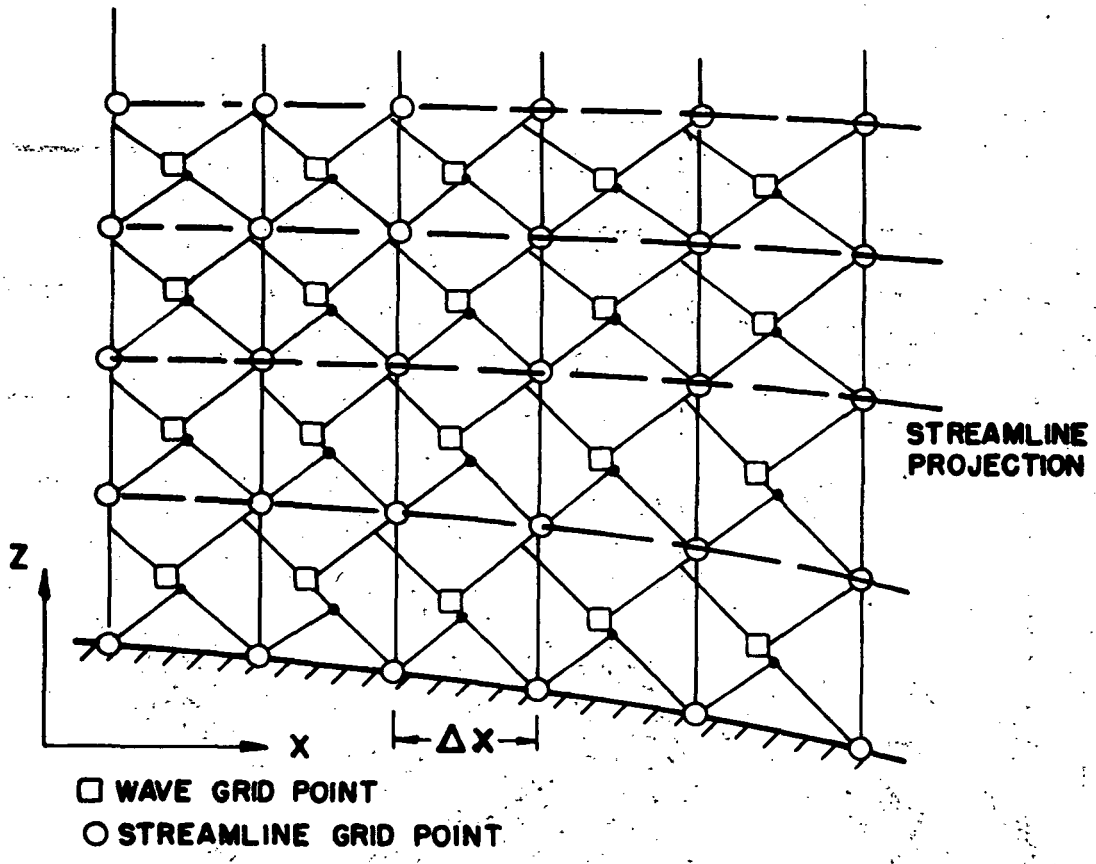

(a) Reference plane grid network for CHAR3D.

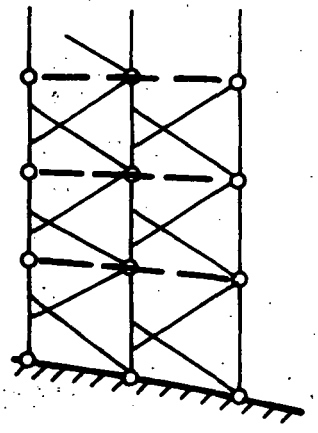

(b) Standard reference plane characteristic network.

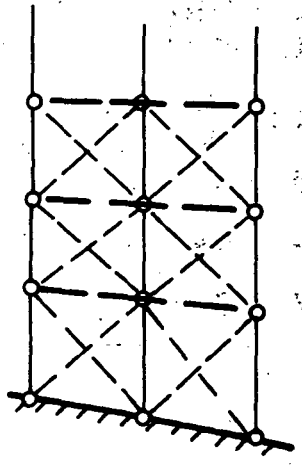

(c) Finite difference network.

Figure 3.- Reference plane networks.

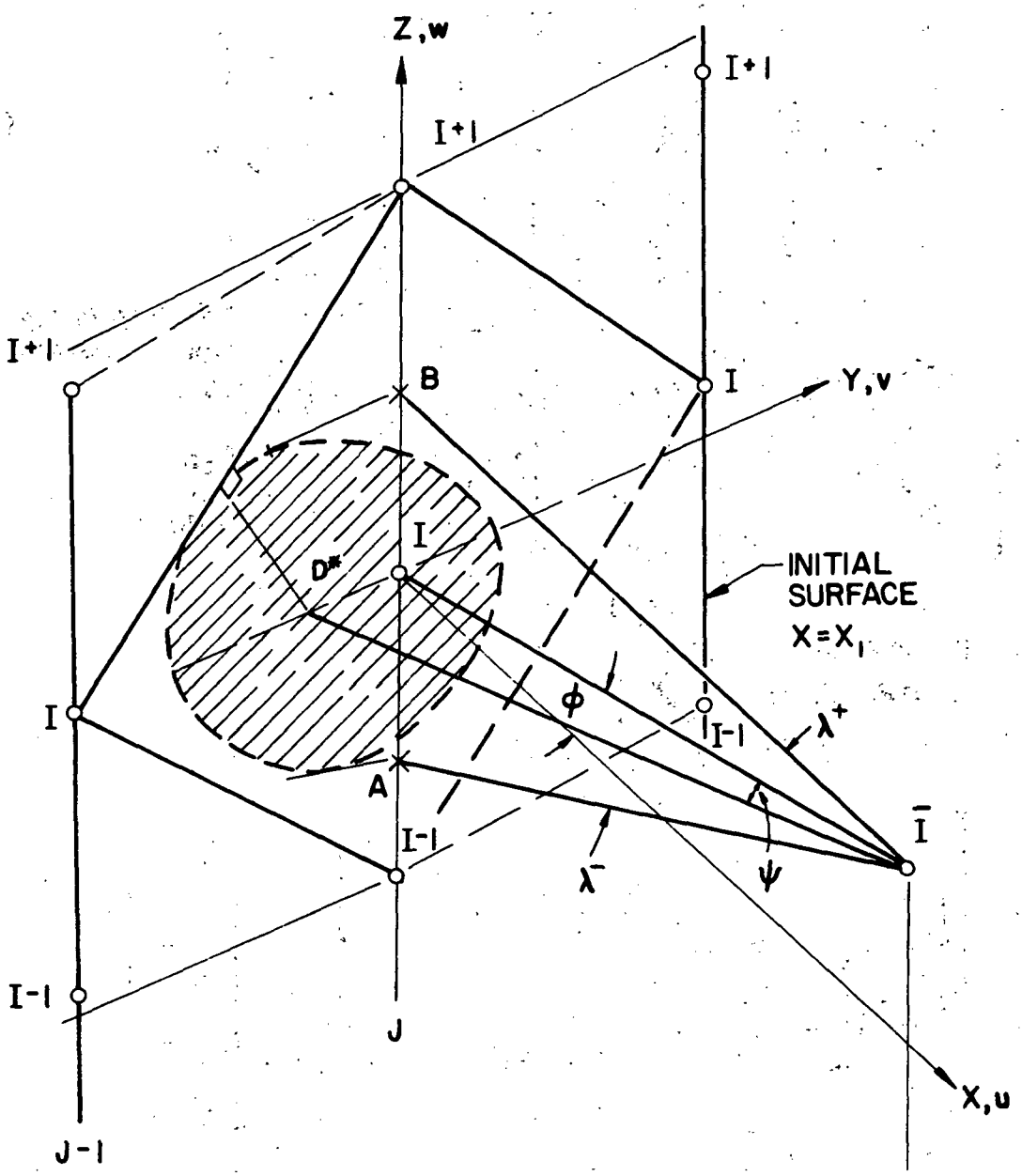

Figure 4.- Interior grid point.

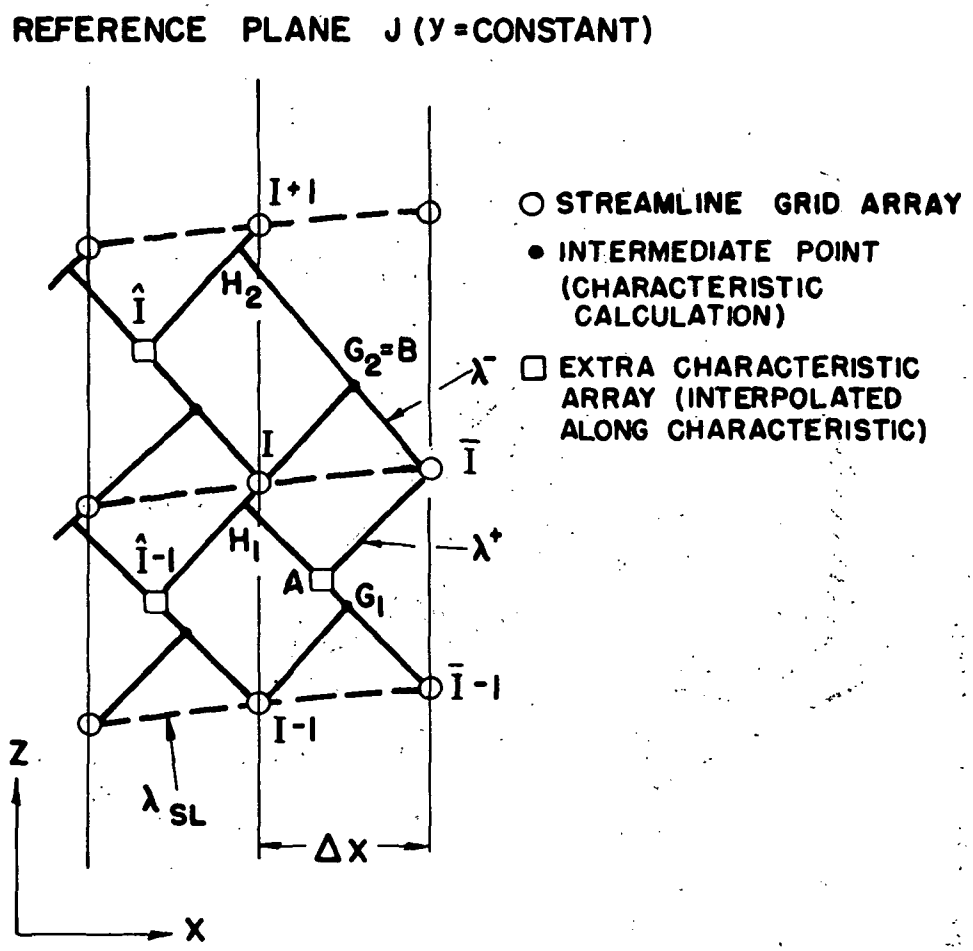

Figure 5.- CHAR3D interior point grid.

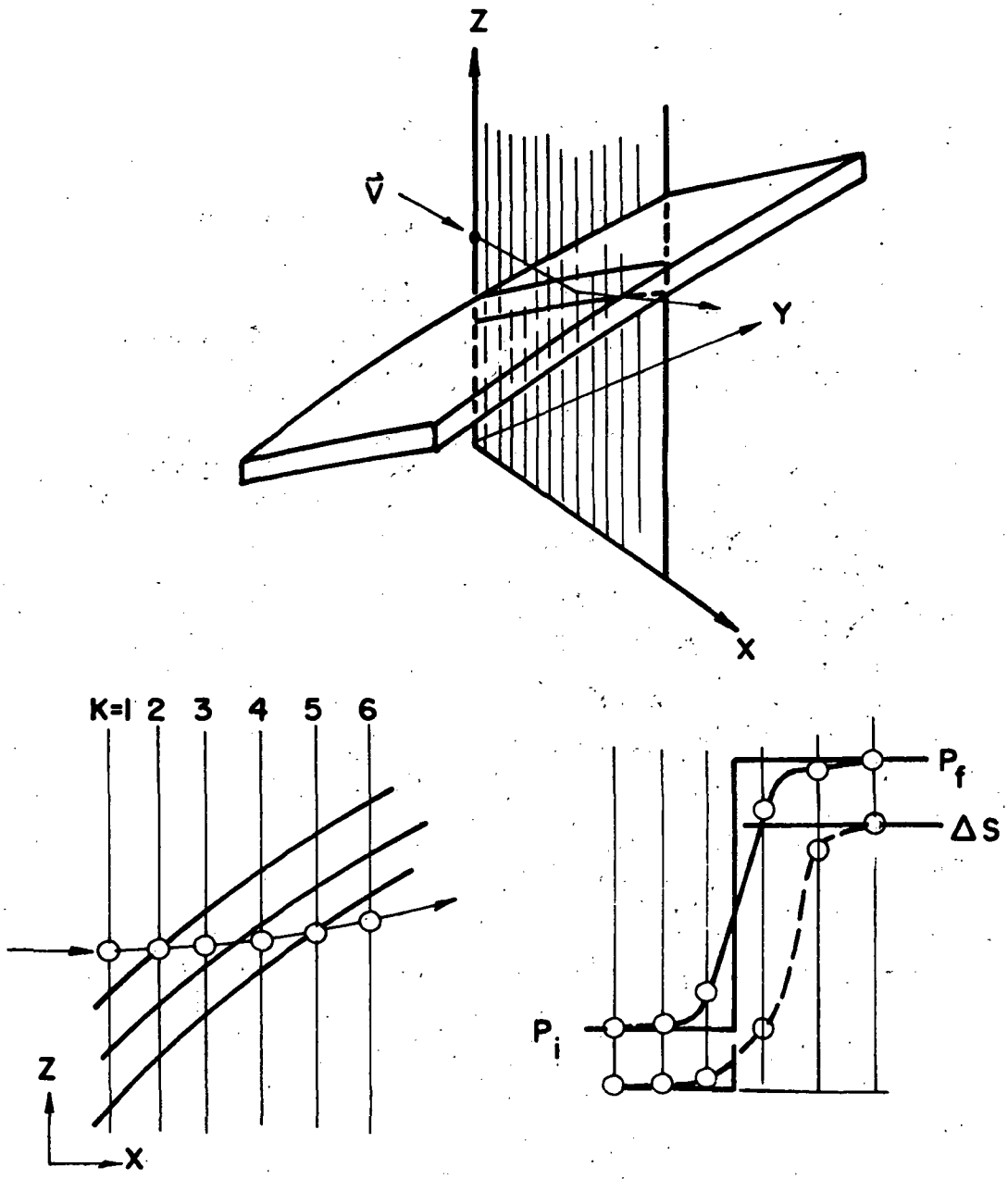

Figure 6.- Entropy calculational procedure. P_i is initial pressure; P_f is final pressure.

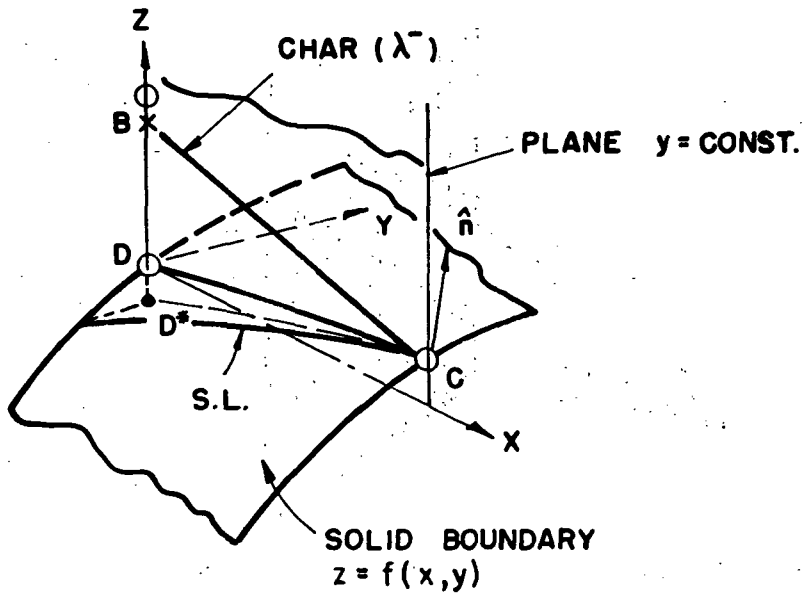

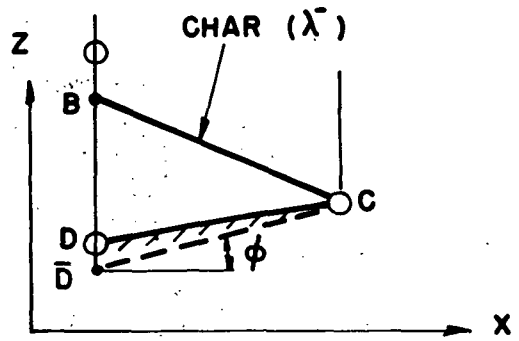

Figure 7.- Solid boundary calculation.

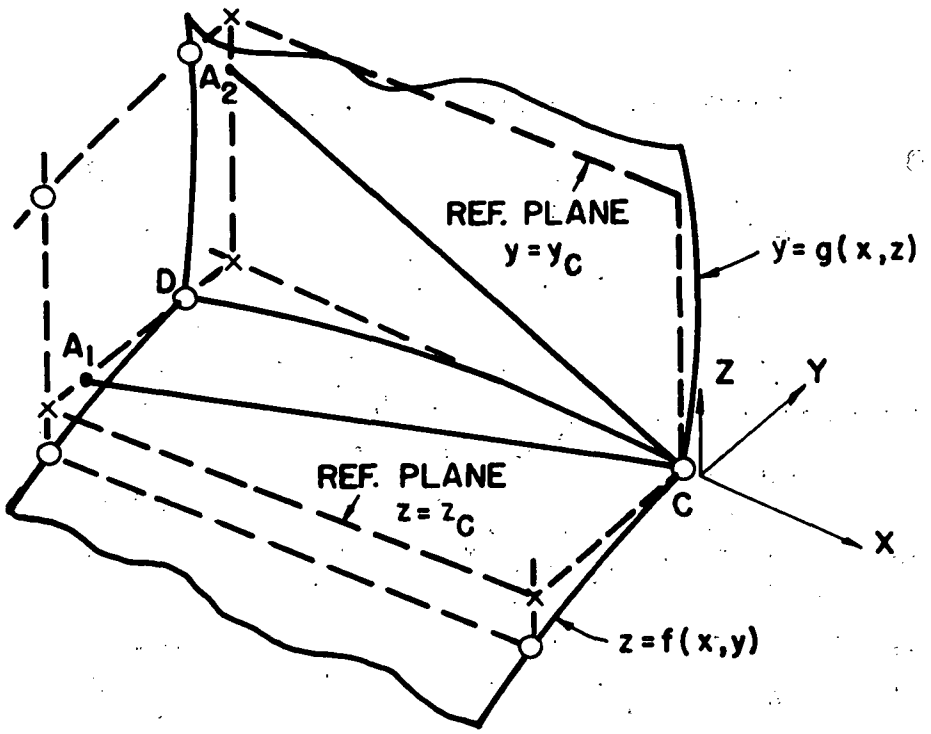

Figure 8.- Internal corner calculation.

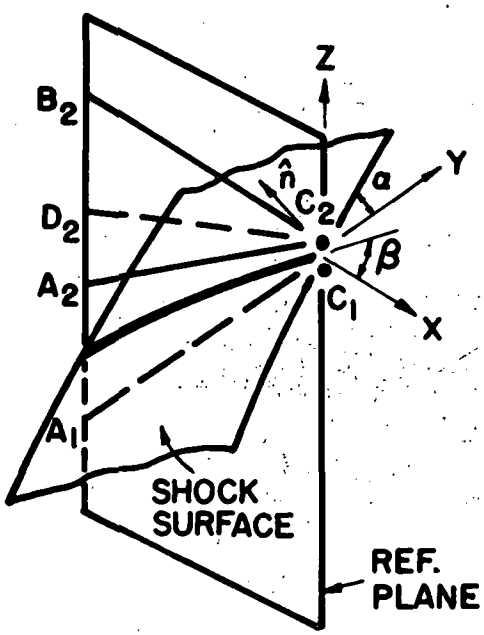

Figure 9.- Shock surface calculation.

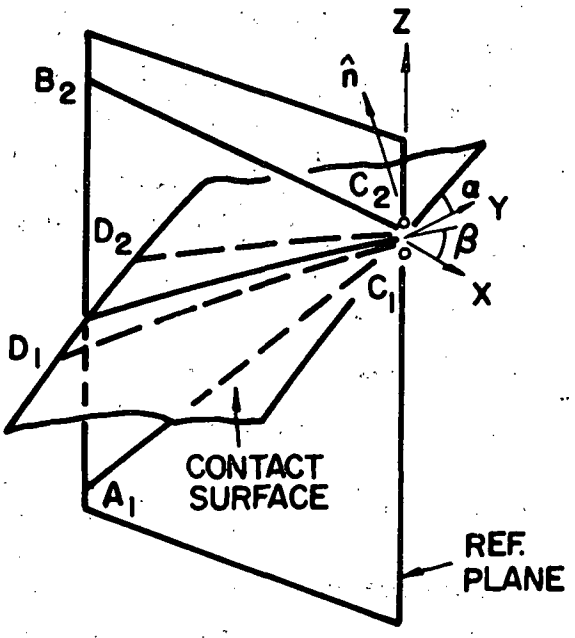

Figure 10.- Contact surface calculation.

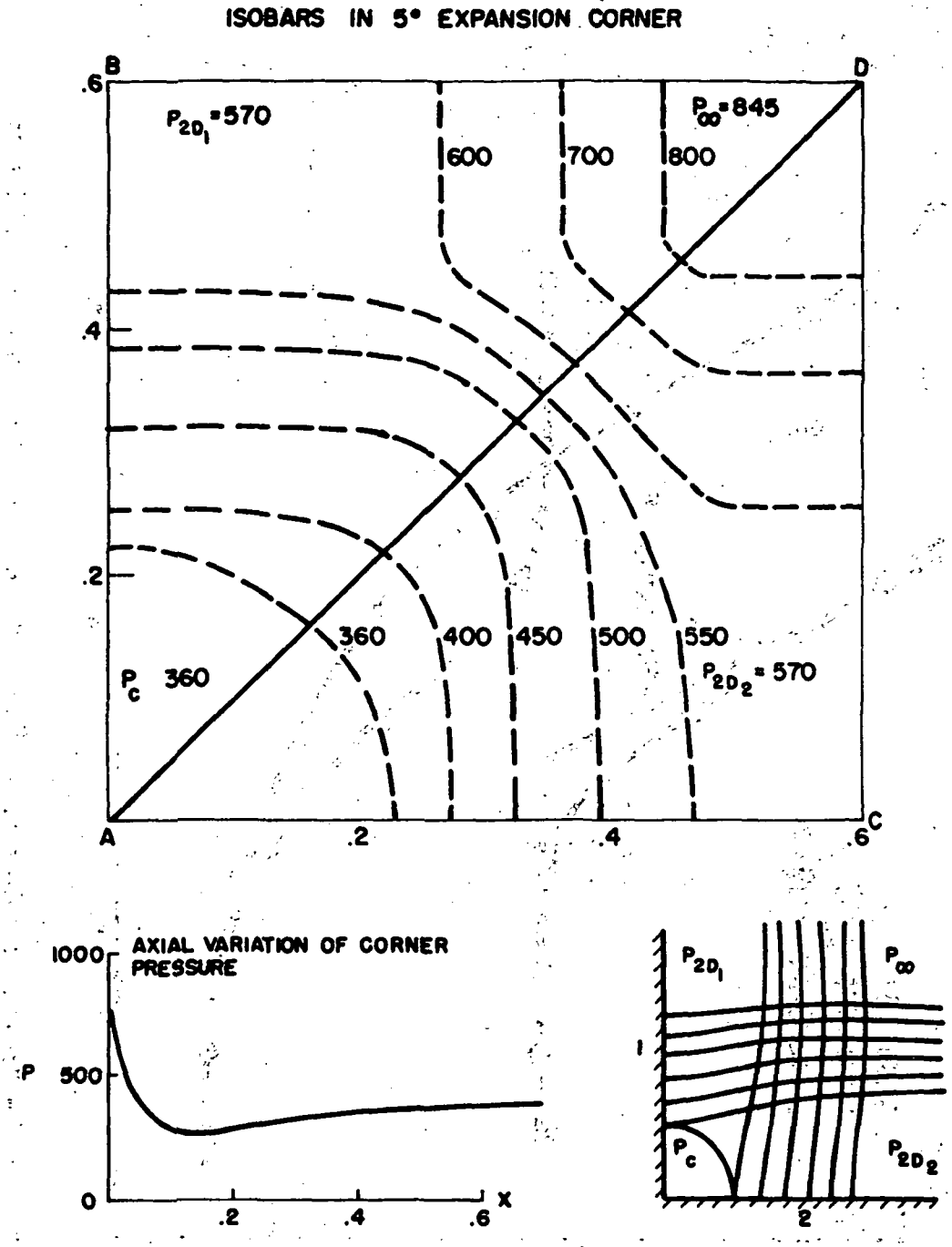

Figure 11.- Results for 5° expansion corner. P_C is corner pressure; P_{2D} is two-dimensional wall pressure.

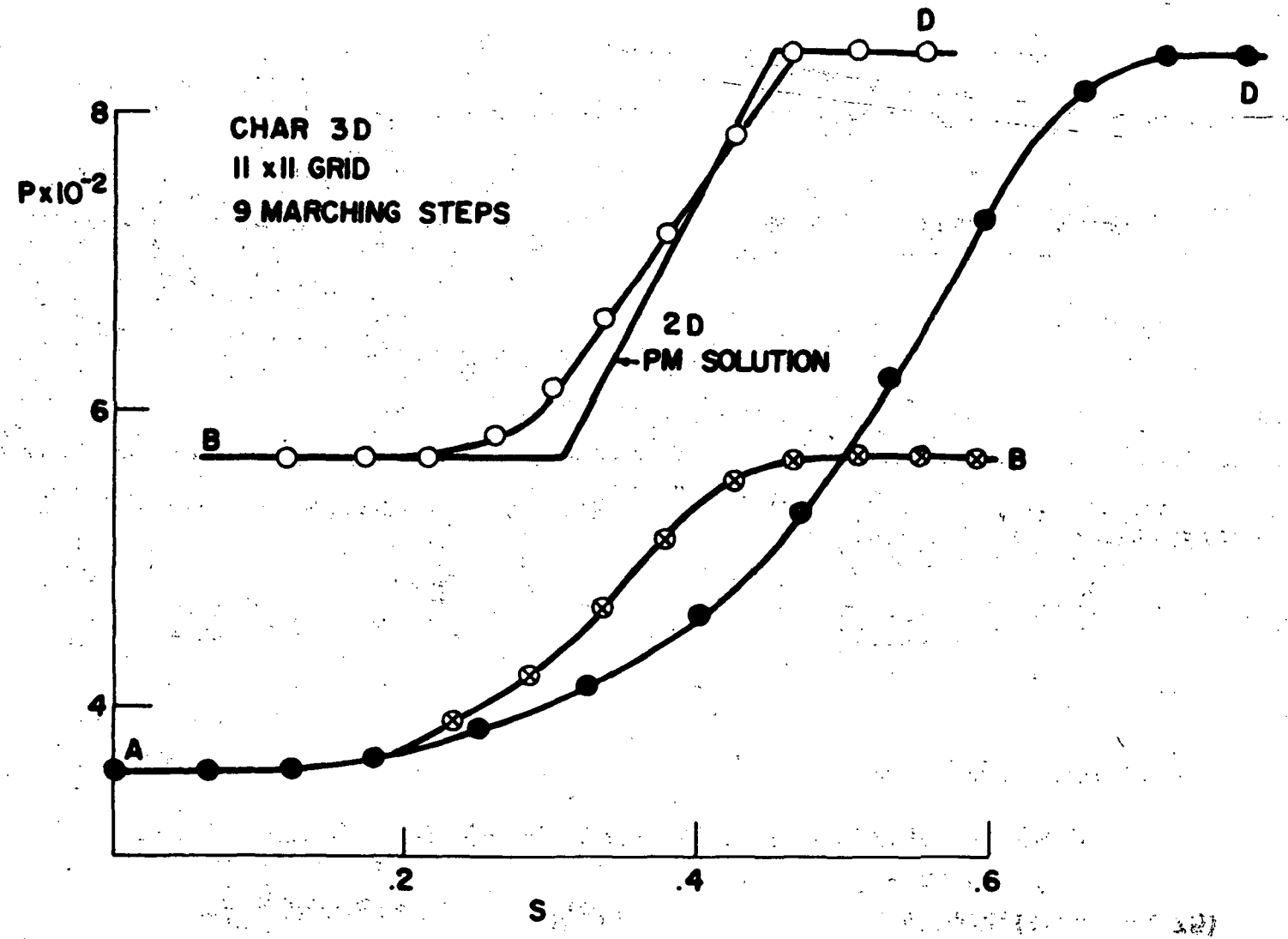

Figure 12.- Pressure distribution for 5^{o} expansion corner. PM means Prandtl-Meyer.

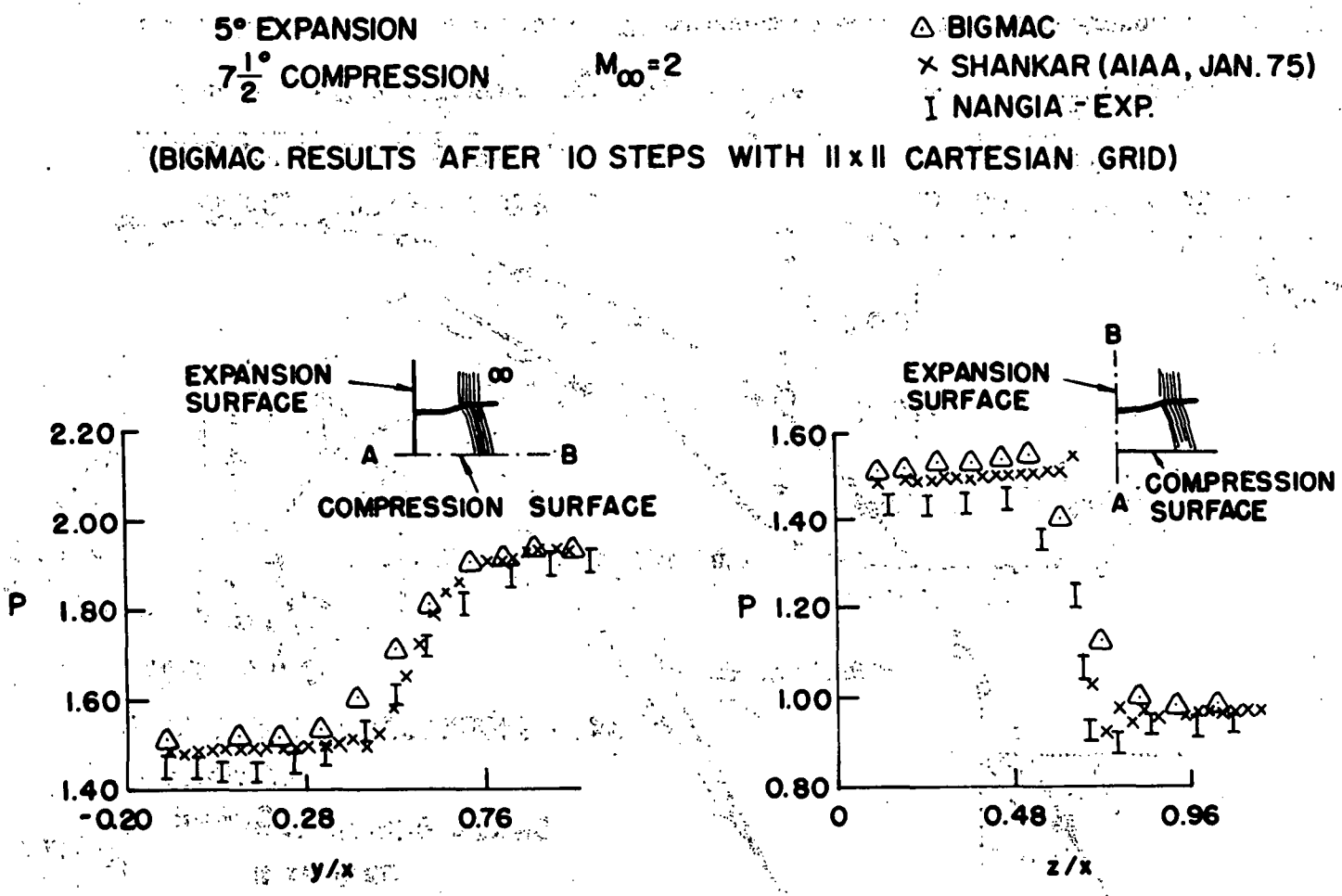

Figure 13.- Results for an expansion-compression corner.

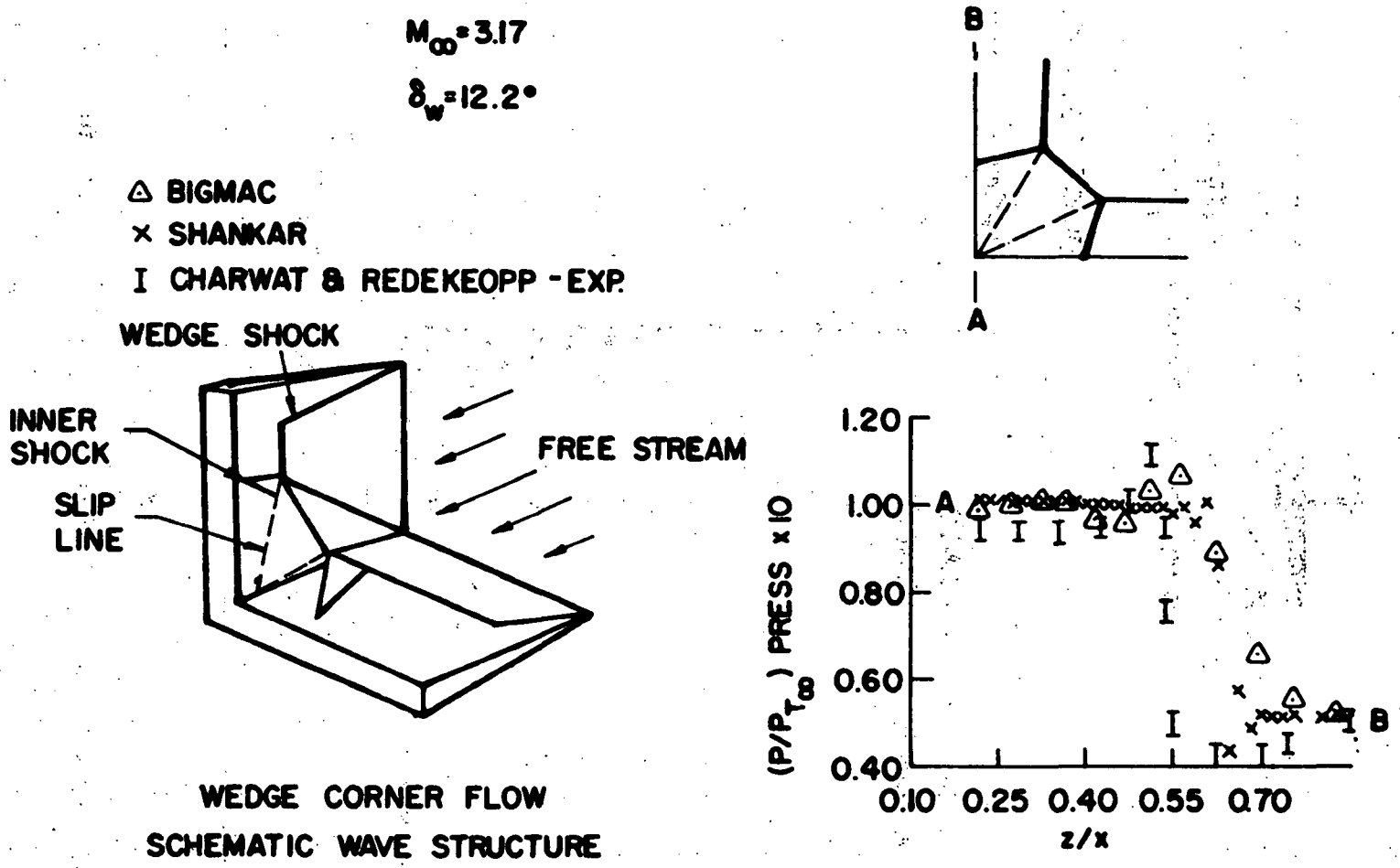

Figure 14.- Compression corner. δ_w is wedge angle; P_{T_∞} is total pressure.

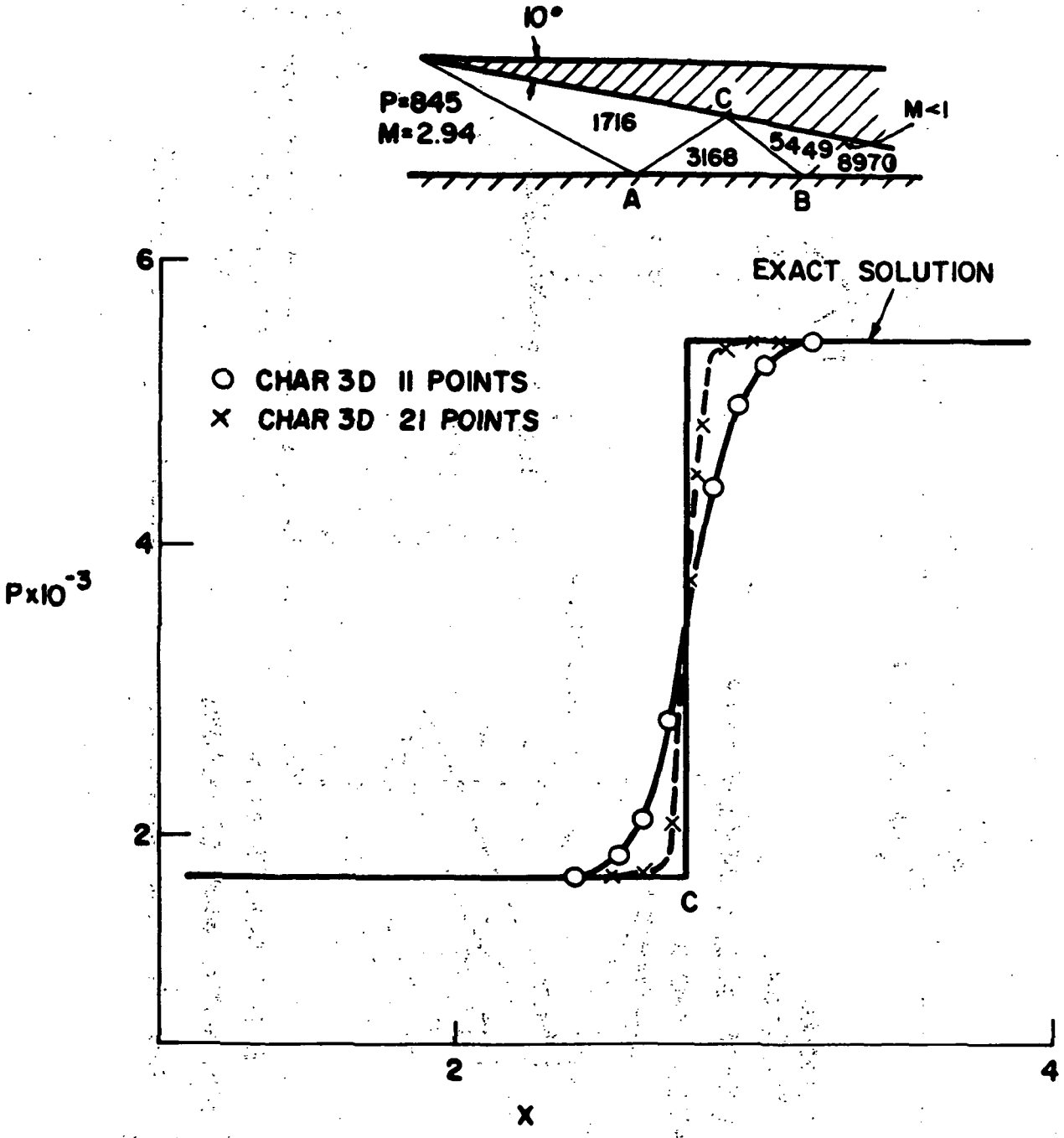

Figure 15.- Upper wall pressure distribution for 10° wedge inlet flow field.

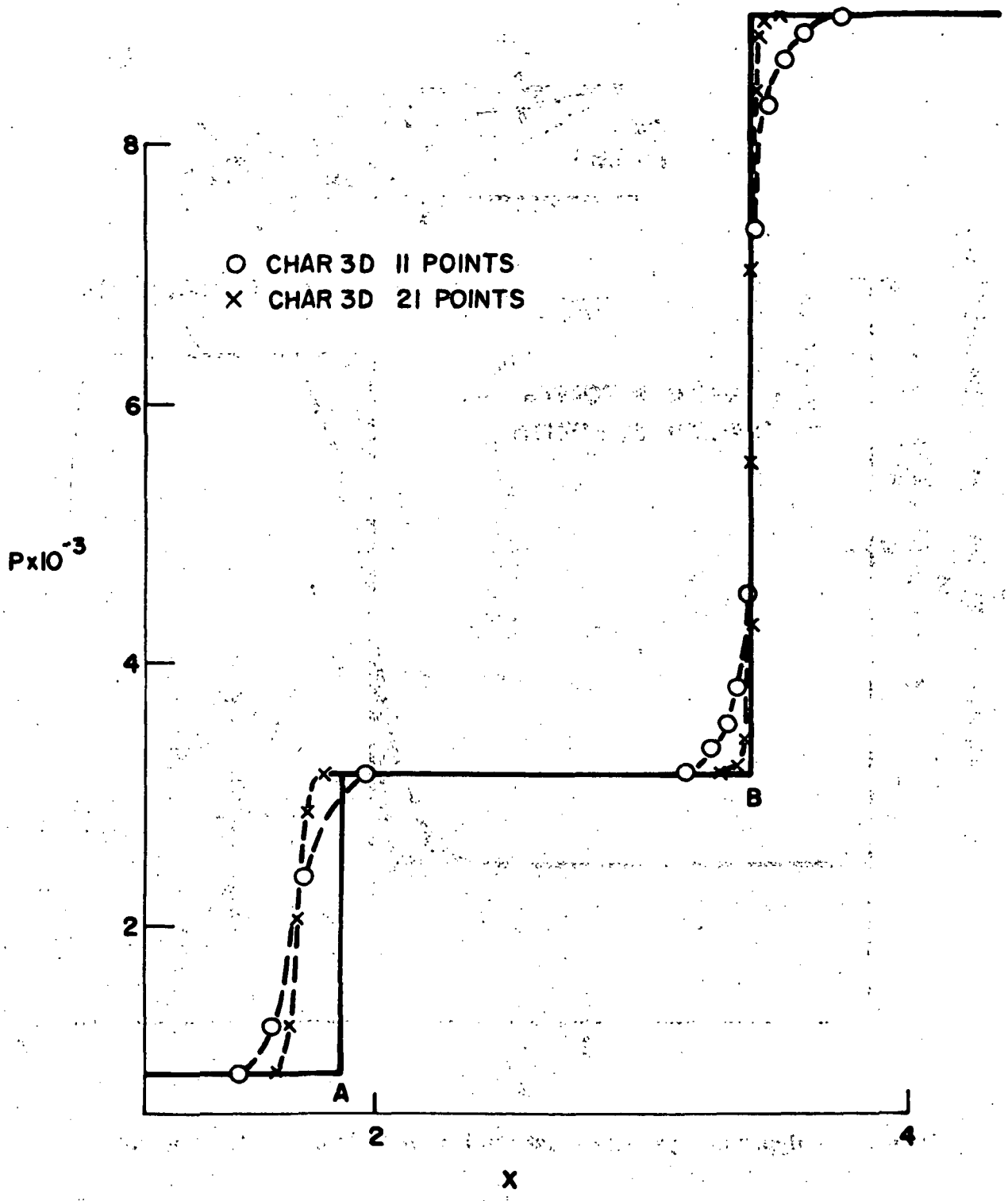

Figure 16.- Lower wall pressure distribution for 10^{o} wedge inlet flow field.

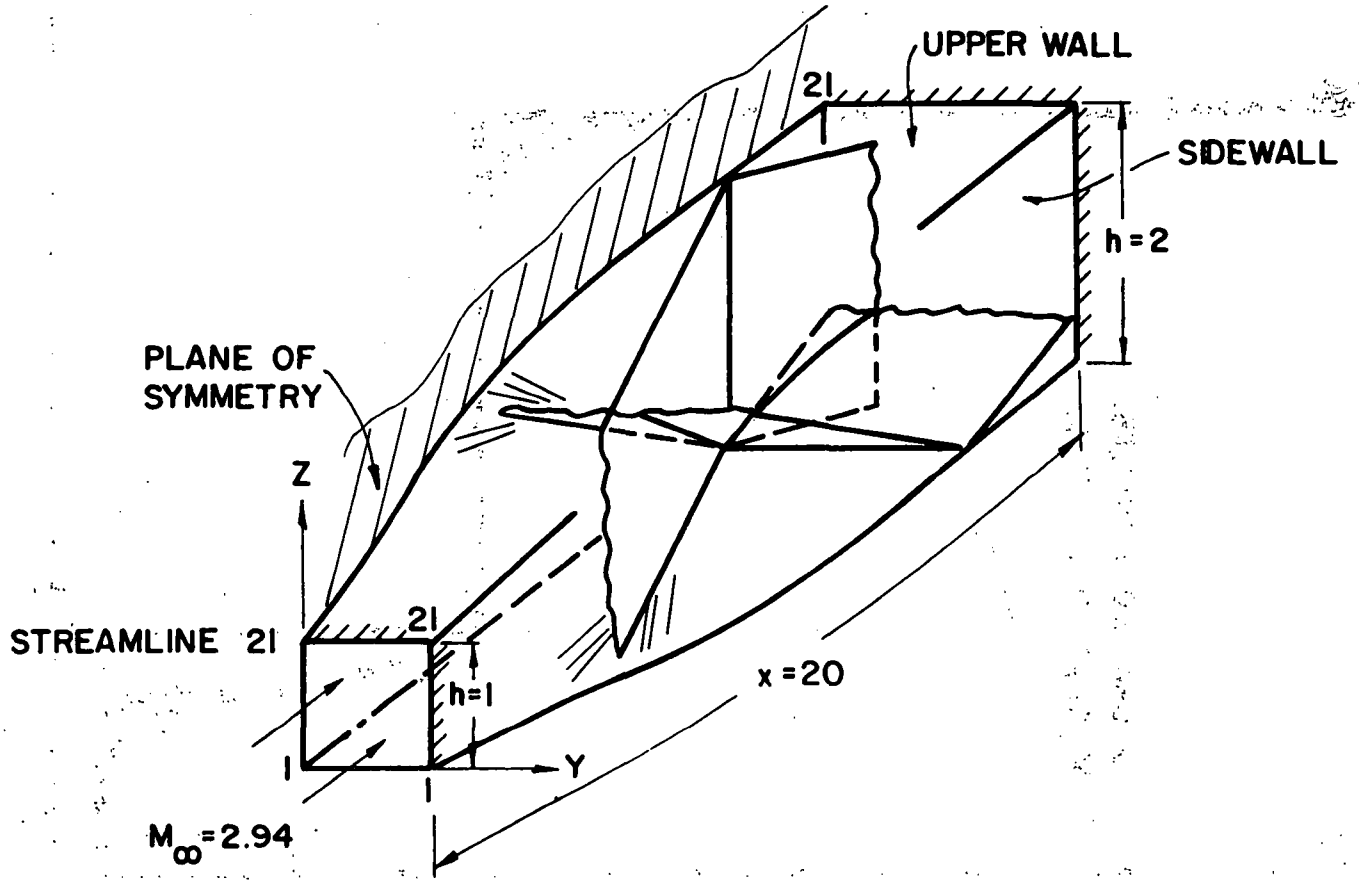

Figure 17.- Square nozzle; h is height.

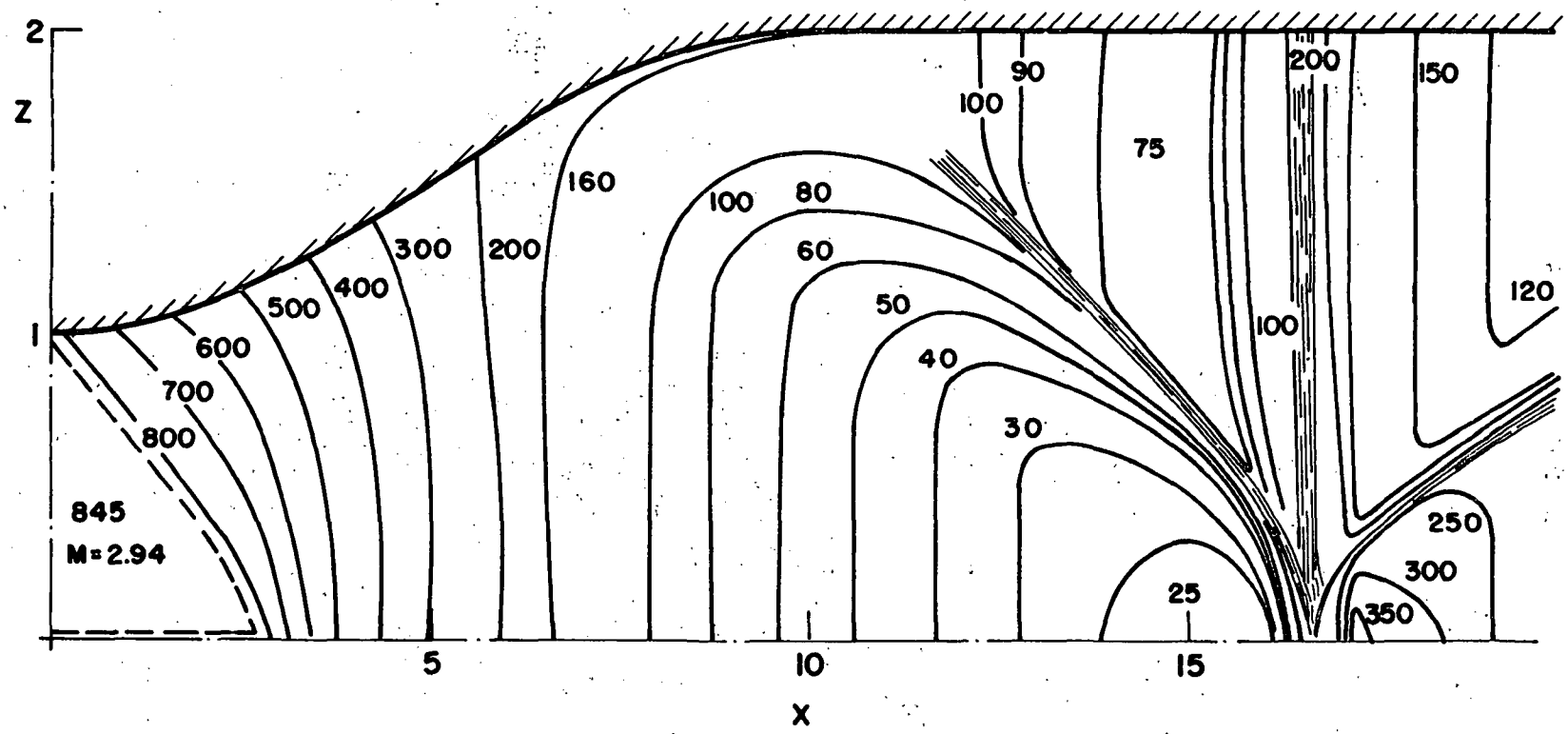

Figure 18.- Pressure contours on symmetry plane of square nozzle.

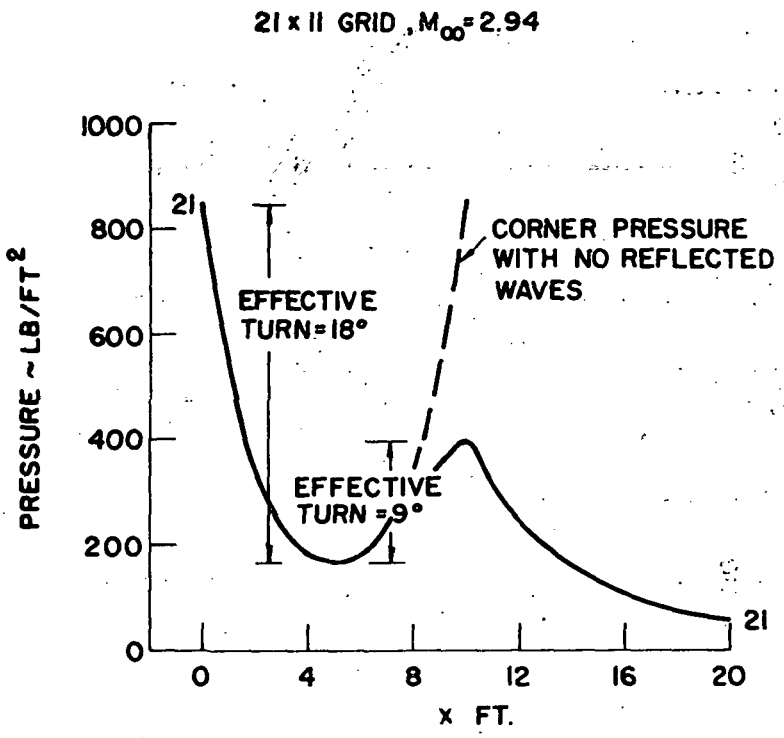

Figure 19.- Streamline pressure distribution at sidewall corner of square nozzle.

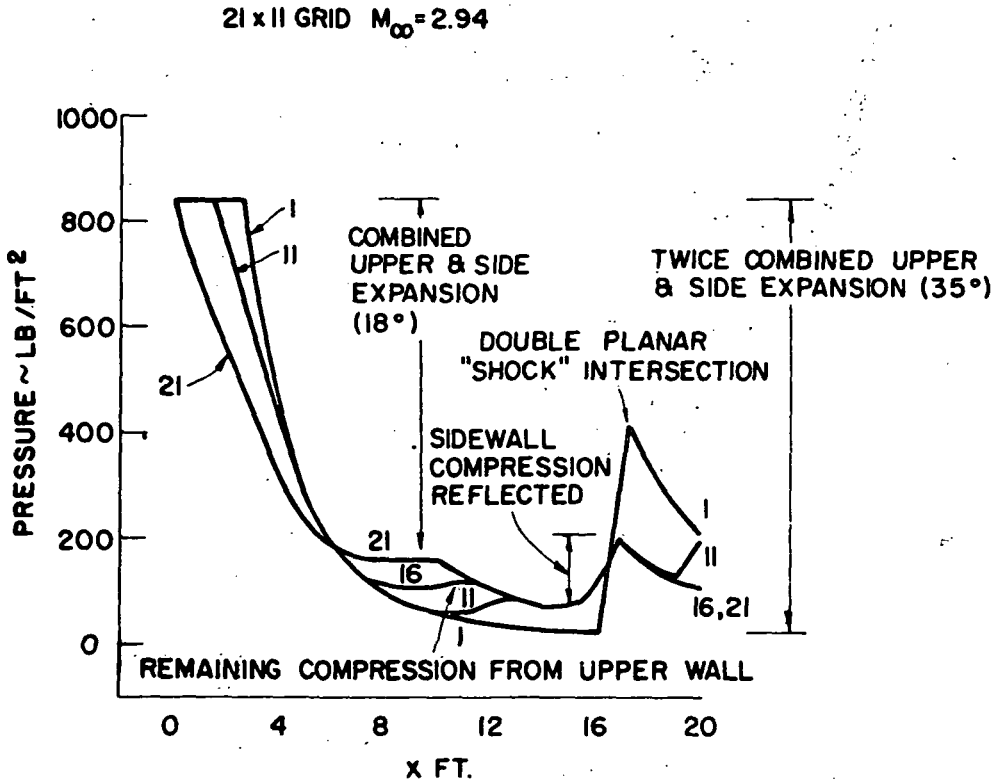

Figure 20.- Streamline pressure distribution in plane of symmetry of square nozzle.

*U.S. GOVERNMENT PRINTING OFFICE: 1975 - 635-275/17

"The aeronautical and space activities of the United States shall be conducted so as to contribute . . . to the expansion of human knowledge of phenomena in the atmosphere and space. The Administration shall provide for the widest practicable and appropriate dissemination of information concerning its activities and the results thereof."

—NATIONAL AERONAUTICS AND SPACE ACT OF 1958

NASA SCIENTIFIC AND TECHNICAL PUBLICATIONS

TECHNICAL REPORTS: Scientific and technical information considered important, complete, and a lasting contribution to existing knowledge.

TECHNICAL NOTES: Information less broad in scope but nevertheless of importance as a contribution to existing knowledge.

TECHNICAL MEMORANDUMS: Information receiving limited distribution because of preliminary data, security classification, or other reasons. Also includes conference proceedings with either limited or unlimited distribution.

CONTRACTOR REPORTS: Scientific and technical information generated under a NASA contract or grant and considered an important contribution to existing knowledge.

TECHNICAL TRANSLATIONS: Information published in a foreign language considered to merit NASA distribution in English.

SPECIAL PUBLICATIONS: Information derived from or of value to NASA activities. Publications include final reports of major projects, monographs, data compilations, handbooks, sourcebooks, and special bibliographies.

TECHNOLOGY UTILIZATION PUBLICATIONS: Information on technology used by NASA that may be of particular interest in commercial and other non-aerospace applications. Publications include Tech Briefs, Technology Utilization Reports and Technology Surveys.

Details on the availability of these publications may be obtained from:

SCIENTIFIC AND TECHNICAL INFORMATION OFFICE

NATIONAL AERONAUTICS AND SPACE ADMINISTRATION

Washington, D.C. 20546